Springer Series in Optical Sciences 212

Hiroyuki Fujiwara · Robert W. Collins
Editors

Spectroscopic Ellipsometry for Photovoltaics

Volume 1: Fundamental Principles and Solar Cell Characterization

Springer Series in Optical Sciences

Volume 212

Founded by

H. K. V. Lotsch

Editor-in-chief

William T. Rhodes, Florida Atlantic University, Boca Raton, FL, USA

Series editors

Ali Adibi, School of Electrical and Computer Engineering, Georgia Institute of Technology, Atlanta, GA, USA
Toshimitsu Asakura, Hokkai-Gakuen University, Sapporo, Hokkaido, Japan
Theodor W. Hänsch, Max-Planck-Institut für Quantenoptik, Garching, Bayern, Germany
Ferenc Krausz, Garching, Bayern, Germany
Barry R. Masters, Cambridge, MA, USA
Katsumi Midorikawa, Laser Technology Laboratory, RIKEN Advanced Science Institute, Saitama, Japan
Bo A. J. Monemar, Department of Physics and Measurement Technology, Linköping University, Linköping, Sweden
Herbert Venghaus, Ostseebad Binz, Germany
Horst Weber, Berlin, Germany
Harald Weinfurter, München, Germany

Springer Series in Optical Sciences is led by Editor-in-Chief William T. Rhodes, Georgia Institute of Technology, USA, and provides an expanding selection of research monographs in all major areas of optics:

- lasers and quantum optics
- ultrafast phenomena
- optical spectroscopy techniques
- optoelectronics
- information optics
- applied laser technology
- industrial applications and
- other topics of contemporary interest.

With this broad coverage of topics the series is useful to research scientists and engineers who need up-to-date reference books.

More information about this series at http://www.springer.com/series/624

Hiroyuki Fujiwara · Robert W. Collins
Editors

Spectroscopic Ellipsometry for Photovoltaics

Volume 1: Fundamental Principles and Solar Cell Characterization

Editors
Hiroyuki Fujiwara
Department of Electrical, Electronic
and Computer Engineering
Gifu University
Gifu, Japan

Robert W. Collins
Department of Physics and Astronomy
The University of Toledo
Toledo, OH, USA

ISSN 0342-4111 ISSN 1556-1534 (electronic)
Springer Series in Optical Sciences
ISBN 978-3-319-75375-1 ISBN 978-3-319-75377-5 (eBook)
https://doi.org/10.1007/978-3-319-75377-5

Library of Congress Control Number: 2018931482

© Springer International Publishing AG, part of Springer Nature 2018
This work is subject to copyright. All rights are reserved by the Publisher, whether the whole or part of the material is concerned, specifically the rights of translation, reprinting, reuse of illustrations, recitation, broadcasting, reproduction on microfilms or in any other physical way, and transmission or information storage and retrieval, electronic adaptation, computer software, or by similar or dissimilar methodology now known or hereafter developed.
The use of general descriptive names, registered names, trademarks, service marks, etc. in this publication does not imply, even in the absence of a specific statement, that such names are exempt from the relevant protective laws and regulations and therefore free for general use.
The publisher, the authors and the editors are safe to assume that the advice and information in this book are believed to be true and accurate at the date of publication. Neither the publisher nor the authors or the editors give a warranty, express or implied, with respect to the material contained herein or for any errors or omissions that may have been made. The publisher remains neutral with regard to jurisdictional claims in published maps and institutional affiliations.

This Springer imprint is published by the registered company Springer Nature Switzerland AG
The registered company address is: Gewerbestrasse 11, 6330 Cham, Switzerland

Preface

In recent years, spectroscopic ellipsometry has been applied extensively to characterize the optical properties of various materials incorporated into photovoltaic devices. Among many physical parameters, the band gap and absorption coefficient of light absorbers are the most important physical quantities from which the potential efficiency and cost of solar cells can be speculated. The ellipsometry technique remains the only method by which the band gap and the optical functions (i.e., the refractive index, extinction coefficient, and absorption coefficient spectra) can be determined accurately. The ellipsometry characterization further allows us to evaluate multilayered solar cell structures from small area cells to large area modules. Based on the optical data deduced from spectroscopic ellipsometry, detailed device analyses can further be performed.

Unfortunately, however, the principles of the ellipsometry technique are often considered challenging, as ellipsometry measures the change in the polarized state of light upon light reflection, and the measured quantities are not straightforwardly interpretable in terms of material properties. The extreme surface sensitivity of the technique and the resulting influence of surface non-idealities generate additional challenges. In thin film photovoltaic technologies, however, spectroscopic ellipsometry is becoming a quite important technique for verifying the optical and structural properties of solar cells. Thus, an increasing number of photovoltaic specialists are overcoming the barriers to first-time use, and the application of ellipsometry to solar cell characterization has been increasing steadily over the last decade. The development of various optical simulation techniques further strengthens the need of accurate optical data for solar cell component layers.

The purpose of this first volume of the book is to provide a basic understanding of spectroscopic ellipsometry for photovoltaic specialists who are not familiar with the method. In particular, this book is organized so that first-time users will be able to conduct spectroscopic ellipsometry measurements and data analyses properly, with a focus on the characterization of solar cell materials/devices. To serve readers at different levels of expertise, this book consists of the following two major parts: fundamental principles of spectroscopic ellipsometry (Part I) and characterization of various solar cell materials/structures (Part II).

More specifically, after an introductory chapter which gives (i) a general introduction into the field of ellipsometry and (ii) an overview over the contents of the subsequent chapters in the book (Chap. 1), in Part I, the fundamental ellipsometry measurement technique is reviewed (Chap. 2). Since excellent ellipsometry instruments are commercially available, data analysis procedures in spectroscopic ellipsometry are explained extensively in Part I (Chaps. 3–6). In particular, in addition to the overall explanation of the data analysis (Chap. 3), the optical properties of materials (Chap. 4) and their modeling (Chap. 5) are addressed. The treatment of surface roughness in the data analysis (Chap. 6) is very important for accurate ellipsometry analyses.

In Part II, since researchers in the photovoltaic community specialize in a wide variety of materials technologies, this book covers the broad range from traditional solar cell materials [thin film Si:H (Chap. 7), crystalline Si (Chaps. 8 and 9), $Cu(In,Ga)Se_2$ (Chaps. 10 and 11), CdTe (Chap. 13), and group III–V compounds (Chap. 14)] to more advanced emerging materials [$Cu_2ZnSnSe_4$ (Chap. 12), organics (Chap. 15), and hybrid perovskites (Chap. 16)]. The reviews for photonic structures of solar cells (Chap. 17) and transparent conductive oxides (Chaps. 18 and 19) are also provided.

The second volume of this book further explains spectroscopic ellipsometry applications, including current loss analysis of the devices, real-time monitoring/control of semiconducting layers and large area analysis as well as the complete optical data of solar cell component layers (a total of 148 materials), which are crucial for ellipsometry analyses and optical simulations of devices. From these two volumes of the book, quite general spectroscopic ellipsometry techniques, which have been applied widely for material/device characterization, can be learned and understood.

Gifu, Japan — Hiroyuki Fujiwara
Toledo, USA — Robert W. Collins

Acknowledgements

The editors would like to thank all authors for their great contributions and helpful suggestions. HF thanks Drs. Shigeru Niki and Koji Matsubara for their kind support. HF gratefully acknowledges Dr. Claus E. Ascheron who has supported the publication of this book. HF wishes to express sincere gratitude to Shohei Fujimoto, Akihiro Nakane, Takemasa Fujiseki, Masato Kato, Mitsutoshi Nishiwaki, and Masayuki Kozawa for their enthusiastic efforts for the preparation of this book.

RWC acknowledges data and graphics assistance from chapter contributors, Drs. Puruswottam Aryal, Lila Dahal, Zhiquan Huang, Abdel-Rahman Ibdah, Prakash Koirala, Jian Li, and Puja Pradhan. RWC also acknowledges motivating collaborations with faculty colleagues, Profs. Hiroyuki Fujiwara, Nikolas Podraza, Sylvain Marsillac, Angus Rockett, and Xunming Deng, as well as with colleagues from the photovoltaics and glass industries, Kenneth Kormanyos, Wenhui Du, Simon Cao, and David Strickler. Finally, RWC would like to thank Linda Collins for her continuous support.

Gifu, Japan — Hiroyuki Fujiwara
Toledo, USA — Robert W. Collins

Contents

1 Introduction 1
Hiroyuki Fujiwara
1.1 Ellipsometry Technique 1
1.1.1 Principles of Ellipsometry 2
1.1.2 Data Analysis Procedure 5
1.1.3 Effect of Rough Surface 6
1.1.4 Structural Characterization 8
1.2 Optical Properties of Solar Cell Materials 8
1.2.1 Optical Constants 9
1.2.2 Dielectric Function 11
1.2.3 Absorption Spectra 13
1.3 Overview of This Book 13
References 15

Part I Fundamental Principles of Ellipsometry

2 Measurement Technique of Ellipsometry 19
Robert W. Collins
2.1 Introduction and Preliminaries 20
2.1.1 Step 1: Polarization Generation 21
2.1.2 Step 2: Interaction with the Sample 22
2.1.3 Step 3: Polarization Detection 23
2.1.4 Step 4: Determination of Ellipsometry Data 24
2.1.5 Step 5: Deduction of Sample Information 26
2.1.6 Overview 28
2.2 Polarization of Light 29
2.3 Oblique Reflection of Polarized Light 34
2.4 Optical Properties of Materials 38

2.5 Fresnel (or Complex Amplitude Reflection) Coefficients for Single and Multiple Interfaces 42
2.5.1 Single Interface 42
2.5.2 Multiple Interfaces 43
2.5.3 Through-the-Glass Ellipsometry 45
2.6 Instrumentation: Rotating Compensator Ellipsometer 47
2.6.1 Formalism 47
2.6.2 Data Reduction 51
2.6.3 Instrument Calibration 53
2.7 Summary 54
2.8 Selected Readings 56
2.8.1 Optics 56
2.8.2 Ellipsometry 56
2.8.3 Optical Properties of Solids 56
2.8.4 Photovoltaics 57
References 57

3 Data Analysis 59
James N. Hilfiker, Jianing Sun and Nina Hong
3.1 Analysis Flow 59
3.2 SE Measurement 60
3.3 Data Interpretation 61
3.4 Model 65
3.4.1 Model Structure and Optical Constants 65
3.4.2 Representing Optical Constants 67
3.4.3 Model Calculations 70
3.5 Data Fitting 73
3.5.1 Direct Conversion 73
3.5.2 Model-Based Data Fitting 74
3.6 Evaluating Results 77
3.7 Analysis Strategies for Common Sample Structures 80
3.7.1 Transparent Thin Films 80
3.7.2 Films that Absorb at Some Wavelengths 82
3.7.3 Absorbing Films 85
3.7.4 Complications to the Sample Structure 86
References 88

4 Optical Properties of Semiconductors 89
Maria Isabel Alonso and Miquel Garriga
4.1 Introduction 89
4.2 Electronic Band Structures 90
4.2.1 Energy Considerations 90
4.2.2 Symmetry Considerations 92
4.2.3 Band Structure Diagrams 94

4.3 Dielectric Function . . . 98
4.3.1 Critical Points . . . 99
4.4 Inorganic Semiconductors . . . 104
4.4.1 Crystalline . . . 106
4.4.2 Amorphous . . . 108
4.5 Organic Semiconductors . . . 109
4.5.1 Molecules . . . 109
4.5.2 Solids . . . 111
4.6 Summary . . . 112
References . . . 113

5 Dielectric Function Modeling . . . 115
James N. Hilfiker and Tom Tiwald
5.1 Optical Absorption and Dispersion Features . . . 115
5.1.1 Refractive Index and Dielectric Function . . . 116
5.1.2 Resonance . . . 118
5.1.3 Kramers-Kronig Relations . . . 120
5.1.4 Absorption Phenomena . . . 121
5.2 Representing the Dielectric Function . . . 124
5.2.1 Representing Absorption Features . . . 124
5.2.2 Absorptions Outside Measured Spectral Range . . . 126
5.3 Common Dispersion Relations . . . 127
5.3.1 Sellmeier . . . 128
5.3.2 Cauchy . . . 130
5.3.3 Lorentz . . . 132
5.3.4 Drude . . . 134
5.3.5 Harmonic Oscillator Approximation . . . 135
5.3.6 Gaussian . . . 137
5.3.7 Tauc-Lorentz . . . 139
5.3.8 Cody-Lorentz . . . 141
5.3.9 Critical Point Models . . . 143
5.3.10 Polynomials, Splines and B-Spline . . . 147
References . . . 152

6 Effect of Roughness on Ellipsometry Analysis . . . 155
Hiroyuki Fujiwara
6.1 Introduction . . . 155
6.2 Effect of Surface Roughness on Dielectric Function . . . 159
6.2.1 $CuInSe_2$ . . . 159
6.2.2 $CH_3NH_3PbI_3$ . . . 166
6.3 Effect of Surface Roughness on EQE Analysis . . . 168
References . . . 170

Part II Characterization of Materials and Structures

7 Ex Situ Analysis of Multijunction Solar Cells Based on Hydrogenated Amorphous Silicon 175
Zhiquan Huang, Lila R. Dahal, Prakash Koirala, Wenhui Du, Simon Cao, Xunming Deng, Nikolas J. Podraza and Robert W. Collins
7.1 Introduction and Overview 176
7.2 General Strategy and Approaches 178
7.3 Substrate and Individual Solar Cell Materials 182
7.4 Single-Junction *a*-Si:H and *a*-$Si_{1-x}Ge_x$:H Solar Cells 192
7.5 Tandem *a*-$Si_{1-y}Ge_y$:H/*a*-$Si_{1-x}Ge_x$:H Solar Cells 195
7.6 Summary 197
References 199

8 Crystalline Silicon Solar Cells 201
Gerald E. Jellison Jr. and Pooran C. Joshi
8.1 Introduction 201
8.2 Optical Properties of Silicon: UV to Near IR (200–1200 nm) 203
8.2.1 Measurement Techniques 203
8.2.2 Optical Functions of Silicon 205
8.2.3 Origins of the Optical Functions of Silicon 208
8.2.4 Modifications to the Optical Properties of Silicon 212
8.3 Spectroscopic Ellipsometry of Thin Films on Silicon 218
8.4 Addendum: Optical Data Tables 223
References 224

9 Amorphous/Crystalline Si Heterojunction Solar Cells 227
Hiroyuki Fujiwara
9.1 Introduction 227
9.2 Ellipsometry Analysis of a-Si:H/c-Si Structures 229
9.2.1 Analysis of a-Si:H Layers on c-Si Substrates 230
9.2.2 Real-Time Characterization of a-Si:H Growth 234
9.3 Epitaxial Growth at a-Si:H/c-Si Heterointerface 237
9.3.1 SE Analysis of a-Si:H/c-Si Interface with Epitaxial Growth 237
9.3.2 Effect of Epitaxial Growth on Solar Cells 238
9.4 Dielectric Functions of a-Si:H, a-SiO:H and a-SiC:H 239
9.4.1 Dielectric Function of a-Si:H 240
9.4.2 Dielectric Functions of a-SiO:H and a-SiC:H 244
References 250

10 Optical Properties of $Cu(In,Ga)Se_2$ 253
Hiroyuki Fujiwara
10.1 Introduction 253
10.2 GEM Analysis 256
10.2.1 Mathematical Inversion 256
10.2.2 Analysis Procedure of GEM 257
10.2.3 GEM Analysis of CIGSe 259
10.3 Dielectric Function of CIGSe 261
10.3.1 Variations with the Ga and Cu Composition 261
10.3.2 E_g and CP Analyses 264
10.3.3 Optical Transition 268
10.3.4 Effect of Compositions 269
10.4 CIGSe Optical Database 271
10.4.1 Energy Shift Model 272
10.4.2 Calculation of CIGSe Optical Constants 273
References 276

11 Real Time and In-Situ Spectroscopic Ellipsometry of $Cu_yIn_{1-x}Ga_xSe_2$ for Complex Dielectric Function Determination and Parameterization 281
Abdel-Rahman A. Ibdah, Puruswottam Aryal, Puja Pradhan, Sylvain Marsillac, Nikolas J. Podraza and Robert W. Collins
11.1 Introduction 282
11.2 Experimental Details 283
11.3 Data Analysis and Results: Effect of Cu Content 284
11.3.1 RTSE of CIGS Growth Versus Cu Content at 570 °C 284
11.3.2 CIGS at Room Temperature 296
11.4 Results: Effect of Ga Content 312
11.5 Comparison and Discussion of Results 320
11.6 Applications 322
11.7 Summary 327
References 329

12 $Cu_2ZnSn(S,Se)_4$ and Related Materials 333
Sukgeun Choi
12.1 Introduction 333
12.1.1 Emergence of $Cu_2ZnSn(S,Se)_4$-Based Solar Cells 333
12.1.2 Fundamental Physical Properties of $Cu_2ZnSn(S,Se)_4$ 334
12.1.3 Spectroscopic Ellipsometric Studies of $Cu_2ZnSn(S,Se)_4$ and Related Compounds 337
12.2 Strategies in Sample Preparation 337
12.2.1 Pseudobulk Approach 338

12.2.2 Chemomechanical Polishing 339
12.3 Studies of $Cu_2ZnSnSe_4$ and Cu_2ZnSnS_4 341
12.3.1 $Cu_2ZnSnSe_4$ 341
12.3.2 Cu_2ZnSnS_4 346
12.4 Studies of Other Related Compounds 348
12.4.1 $Cu_2ZnGeSe_4$ 348
12.4.2 $Cu_2ZnSiSe_4$ 349
12.4.3 Cu_2SnSe_3 350
12.5 Summary and Outlook 352
References 353

13 Real Time and Mapping Spectroscopic Ellipsometry for CdTe Photovoltaics 357
Prakash Koirala, Jian Li, Nikolas J. Podraza and Robert W. Collins
13.1 Introduction 358
13.2 Real Time Spectroscopic Ellipsometry 359
13.2.1 Experimental Methods 359
13.2.2 Optical Model with Dielectric Functions 360
13.2.3 Structural Evolution of CdS/CdTe 371
13.2.4 Application: Role of Ar Pressure in CdS Sputter Deposition 380
13.3 Mapping Spectroscopic Ellipsometry of CdTe Solar Cells 385
13.3.1 Experimental Methods 386
13.3.2 Dielectric Function Model for CdS and CdTe 388
13.3.3 Maps of SnO_2:F and CdTe Properties 393
13.3.4 Maps of CdS/CdTe/Cu Structures 396
13.3.5 Application: Structure-Performance Correlations for Devices 400
13.4 Mapping Spectroscopic Ellipsometry for Full Scale Solar Modules 408
13.5 Summary 410
References 412

14 High Efficiency III–V Solar Cells 415
Nikolas J. Podraza
14.1 Background of III–V Photovoltaic Devices 416
14.2 Challenges for Spectroscopic Ellipsometry Measurements and Analysis 419
14.3 Optical Properties 422
14.3.1 Composition Dependence 423
14.3.2 Compressive and Tensile Stress 425
14.3.3 Defects 426
14.3.4 Temperature Dependence 427

14.4 Infrared and THz Spectroscopic Ellipsometry 428
14.4.1 Infrared Active Phonon Modes 428
14.4.2 Free Carrier Absorption and Electrical Transport 429
14.5 In Situ and Real Time Spectroscopic Ellipsometry 431
14.5.1 Surface Oxidation. 431
14.5.2 Deposition Monitoring and Control 433
14.6 Future Outlook 435
References 436

15 Organic Solar Cells 439
Maria Isabel Alonso and Mariano Campoy-Quiles
15.1 Introduction 439
15.2 Ellipsometric Characterization of Organic Semiconductors 441
15.2.1 Single Crystals 441
15.2.2 Vacuum Evaporated Films 443
15.2.3 Solution Processed Films 445
15.3 Device Architectures 447
15.3.1 Vertical Structures 448
15.3.2 Bulk Heterojunctions 449
15.3.3 Full Devices. 451
15.4 Monitoring Organic Solar Cells 452
15.4.1 Monitoring Thermal Stability 452
15.4.2 Monitoring Morphology Evolution 453
15.4.3 Monitoring Fabrication 456
15.4.4 Monitoring Degradation 456
15.5 Hybrid Approaches 457
15.6 Summary 458
References 458

16 Organic-Inorganic Hybrid Perovskite Solar Cells 463
Hiroyuki Fujiwara, Nikolas J. Podraza, Maria Isabel Alonso,
Masato Kato, Kiran Ghimire, Tetsuhiko Miyadera
and Masayuki Chikamatsu
16.1 Introduction 464
16.2 Optical Properties 466
16.2.1 Optical Constants of Hybrid Perovskites 466
16.2.2 Optical Transitions in Hybrid Perovskites 473
16.2.3 Universal Rules for Light Absorption in $APbX_3$
Perovskites. 479
16.3 Operating Principles of Hybrid Perovskite Solar Cells. 485
16.3.1 Optical Simulation of a $CH_3NH_3PbI_3$ Solar Cell 486
16.3.2 Carrier Loss Mechanisms 488
16.4 Real Time Spectroscopic Ellipsometry of Thin Film
Perovskites 493

16.4.1 RTSE During Vapor Deposition 495
16.4.2 RTSE Post-deposition 497
16.5 Characterization of Degradation in Hybrid Perovskite Materials 499
References 503

17 Solar Cells with Photonic and Plasmonic Structures 509
Peter Petrik
17.1 Introduction 509
17.2 Nanostructure-Based Solar Cells 510
17.2.1 Nanostructured Surfaces and Photonic Crystals 510
17.2.2 Plasmonic Nanostructures 512
17.2.3 Nanoparticles and Quantum Dots 512
17.2.4 Metamaterials 512
17.2.5 Nano- and Microwires 512
17.2.6 Device Performance 513
17.3 Characterization of Nanomaterials 513
17.3.1 Effective Medium Methods in Specular Configuration 513
17.3.2 Direct Methods 514
17.3.3 Surface Correction 514
17.3.4 Ellipsometry and Mueller Polarimetry in Specular Configuration 515
17.3.5 Ellipsometric Scatterometry 515
17.4 Summary and Outlook 517
References 518

18 Transparent Conductive Oxide Materials 523
Hiroyuki Fujiwara and Shohei Fujimoto
18.1 Introduction 523
18.2 Optical Properties of TCO Materials 529
18.2.1 Optical Transitions in TCO Materials 529
18.2.2 Drude Model 532
18.2.3 Modeling of TCO Dielectric Functions 536
18.3 Analyses of TCO Layers 538
18.3.1 SE Measurement 538
18.3.2 SE Analysis of an ITO Layer 539
18.3.3 Analysis of Effective Mass 541
18.3.4 Nonparabolicity of TCO Conduction Bands 543
18.3.5 Analysis of Interband Transition 546
18.4 Carrier Transport Properties 548
18.4.1 Carrier Scattering in TCO 548
18.4.2 Thickness Variation of Grain Boundary Scattering 551

18.5 SE Analysis of Textured TCO Layers 555
18.5.1 Analysis of an Asahi-U Substrate 557
18.5.2 Analysis of TEC Substrates 559
References 560

19 High-Mobility Transparent Conductive Oxide Layers 565
Takashi Koida
19.1 Introduction 566
19.1.1 Optical and Electrical Properties of Transparent Conductive Oxide Layers 566
19.1.2 High-Mobility TCO Layers 568
19.2 Spectroscopic Ellipsometry Analysis of High-Mobility TCO Layers 573
19.2.1 SE Analysis for TCO Layers 573
19.2.2 Dielectric Functions of In_2O_3:H Layers 574
19.2.3 Analysis of Dielectric Functions of In_2O_3:H Layers . . . 578
19.3 Application of High-Mobility TCO Layers to Solar Cells 580
References 583

Index 587

Contributors

Maria Isabel Alonso Institut de Ciència de Materials de Barcelona (ICMAB-CSIC), Campus de la Universitat Autònoma de Barcelona, Bellaterra, Spain

Puruswottam Aryal Department of Physics & Astronomy and Center for Photovoltaics Innovation & Commercialization, University of Toledo, Toledo, OH, USA

Mariano Campoy-Quiles Institut de Ciència de Materials de Barcelona (ICMAB-CSIC), Bellaterra, Spain

Simon Cao Department of Physics & Astronomy and Center for Photovoltaics Innovation & Commercialization, University of Toledo, Toledo, OH, USA

Masayuki Chikamatsu Research Center for Photovoltaics, National Institute of Advanced Industrial Science and Technology, Tsukuba, Japan

Sukgeun Choi Department of Electrical and Computer Engineering, University of California, Santa Barbara, CA, USA

Robert W. Collins Department of Physics & Astronomy and Center for Photovoltaics Innovation & Commercialization, University of Toledo, Toledo, OH, USA

Lila R. Dahal Department of Physics & Astronomy and Center for Photovoltaics Innovation & Commercialization, University of Toledo, Toledo, OH, USA

Xunming Deng Department of Physics & Astronomy and Center for Photovoltaics Innovation & Commercialization, University of Toledo, Toledo, OH, USA

Wenhui Du Department of Physics & Astronomy and Center for Photovoltaics Innovation & Commercialization, University of Toledo, Toledo, OH, USA

Shohei Fujimoto Gifu University, Gifu, Japan

Hiroyuki Fujiwara Gifu University, Gifu, Japan

Miquel Garriga Institut de Ciència de Materials de Barcelona (ICMAB-CSIC), Campus de la Universitat Autònoma de Barcelona, Bellaterra, Spain

Kiran Ghimire University of Toledo, Toledo, OH, USA

James N. Hilfiker J.A. Woollam Co., Inc., Lincoln, NE, USA

Nina Hong J.A. Woollam Co., Inc., Lincoln, NE, USA

Zhiquan Huang Department of Physics & Astronomy and Center for Photovoltaics Innovation & Commercialization, University of Toledo, Toledo, OH, USA

Abdel-Rahman A. Ibdah Department of Physics & Astronomy and Center for Photovoltaics Innovation & Commercialization, University of Toledo, Toledo, OH, USA

Gerald E. Jellison Jr. Oak Ridge National Laboratory, Oak Ridge, TN, USA

Pooran C. Joshi Oak Ridge National Laboratory, Oak Ridge, TN, USA

Masato Kato Gifu University, Gifu, Japan

Takashi Koida Research Center for Photovoltaics, National Institute of Advanced Industrial Science and Technology, Tsukuba, Japan

Prakash Koirala Department of Physics & Astronomy and Center for Photovoltaics Innovation & Commercialization, University of Toledo, Toledo, OH, USA

Jian Li Department of Physics & Astronomy and Center for Photovoltaics Innovation & Commercialization, University of Toledo, Toledo, OH, USA

Sylvain Marsillac Virginia Institute of Photovoltaics, Old Dominion University, Norfolk, VA, USA

Tetsuhiko Miyadera Research Center for Photovoltaics, National Institute of Advanced Industrial Science and Technology, Tsukuba, Japan

Peter Petrik Institute for Technical Physics and Materials Science, Centre for Energy Research, Hungarian Academy of Sciences, Budapest, Hungary

Nikolas J. Podraza Department of Physics & Astronomy and Center for Photovoltaics Innovation & Commercialization, University of Toledo, Toledo, OH, USA

Puja Pradhan Department of Physics & Astronomy and Center for Photovoltaics Innovation & Commercialization, University of Toledo, Toledo, OH, USA

Jianing Sun J.A. Woollam Co., Inc., Lincoln, NE, USA

Tom Tiwald J.A. Woollam Co., Inc., Lincoln, NE, USA

Chapter 1
Introduction

Hiroyuki Fujiwara

Abstract Ellipsometry is an optical technique from which the optical constants (refractive index n and extinction coefficient k), dielectric function and absorption coefficient (α) of materials are characterized. The performance of solar cells is essentially governed by the light absorption characteristics of semiconducting light absorbers incorporated into solar cells and the understanding of the absorber optical properties is crucial for the interpretation and improvement of the device performance. In particular, the optical processes in solar cells, including unfavorable light absorption and back-side reflection by a metal layer, are determined primarily by the optical constants of solar-cell component layers. Accordingly, accurate knowledge of the layer optical properties is essential to maximize solar-cell conversion efficiencies. From ellipsometry measurements, layer structures of solar cells can also be characterized non-destructively. In this chapter I review the fundamental principles and basic idea of the ellipsometry technique. This chapter will also provide an overview for the contents of subsequent chapters in this book.

1.1 Ellipsometry Technique

Ellipsometry was developed more than 100 years ago by Drude [1]. Today, his name is known more widely by a physical model that bears his name (i.e., the Drude model, Chap. 5). The unique feature of the ellipsometry technique is that it determines the optical constants (i.e., refractive index n and extinction coefficient k) of samples based on the change in the light polarization upon the light reflection. In this section, the basic principles of ellipsometry and data analysis procedure are

H. Fujiwara (✉)
Gifu University, 1-1 Yanagido, Gifu 501-1193, Japan
e-mail: fujiwara@gifu-u.ac.jp

© Springer International Publishing AG, part of Springer Nature 2018

H. Fujiwara and R. W. Collins (eds.), *Spectroscopic Ellipsometry for Photovoltaics*,
Springer Series in Optical Sciences 212,
https://doi.org/10.1007/978-3-319-75377-5_1

overviewed. For the data analysis, the importance of proper modeling for surface roughness is emphasized.

1.1.1 Principles of Ellipsometry

Figure 1.1 explains the basic principle of ellipsometry. As known well [2, 3], light is an electromagnetic wave and has the electric and magnetic field components. In Fig. 1.1, however, only the electric field ($\mathbf{E}_\mathrm{f}$) component of the light waves is illustrated. When light waves are polarized, their electric fields are oriented in specific directions and, for the light reflection on samples, the light polarization is classified into *p*- and *s*-polarizations depending on the oscillatory direction of the electric field. As shown in Fig. 1.1, the oscillatory direction of the *p*-polarization is parallel to the incident plane, while that of the *s*-polarization is perpendicular.

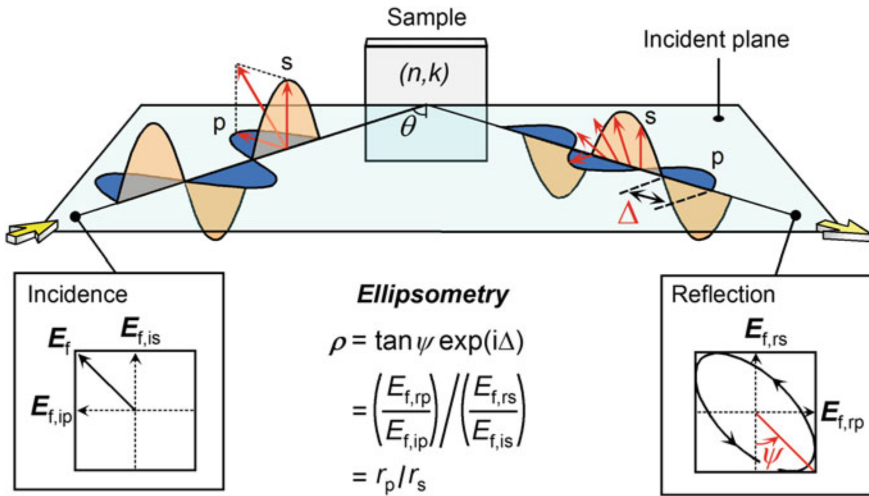

Fig. 1.1 Basic principle of ellipsometry. The waves indicated as "*s*" and "*p*" represent *s*- and *p*-polarized light waves. The oscillatory direction of the *p*-polarization is parallel to the incident plane of samples. Ellipsometry measures the amplitude ratio ψ and the phase difference Δ between the *p*- and *s*-polarizations. The *n* and *k* show the refractive index and extinction coefficient of the sample, whereas θ indicates the incident angle. The $\mathbf{E}_\mathrm{f}$ shows the electric field vector and the subscripts "*i*", "*r*", "*s*", and "*p*" for $\mathbf{E}_\mathrm{f}$ denote the incidence, reflection, *s*-polarization and *p*-polarization, respectively. The synthesized vectors for the *p*- and *s*-polarizations are indicated by red arrows. The ellipsometry parameters (ψ, Δ) are defined by the amplitude reflection coefficients for *p*-polarization (r_p) and *s*-polarization (r_s)

In ellipsometry, *p*- and *s*-polarized light waves are irradiated to a sample. When light waves propagate in the same direction, the state of polarization is expressed by superimposing the waves propagating along two orthogonal axes (Sect. 2.2). To express the superposition of polarized states, the electric field vectors ($\mathbf{E}_{\mathrm{f}}$) are generally used. In ellipsometry, the polarization states of incident and reflected light waves are described by the coordinates of *p*- and *s*-polarizations. In Fig. 1.1, $\mathbf{E}_{\mathrm{f},ip}$ and $\mathbf{E}_{\mathrm{f},is}$ represent the electric field vectors of incident *p*- and *s*-polarizations, respectively. When these vectors are superimposed ($\mathbf{E}_{\mathrm{f}} = \mathbf{E}_{\mathrm{f},ip} + \mathbf{E}_{\mathrm{f},is}$), $\mathbf{E}_{\mathrm{f}}$ oscillates in a plane, which is inclined by 45° from the incident plane.

Quite interestingly, due to the difference in the oscillatory direction between $\mathbf{E}_{\mathrm{f},ip}$ and $\mathbf{E}_{\mathrm{f},is}$, each polarization shows quite different light reflection [2]. In particular, the amplitude of the *p*- and *s*-polarized waves and the phase between these polarizations change depending on the optical constants (n, k) and film thickness [4–7]. In Fig. 1.1, the peak and valley positions of the reflected *p*- and *s*-polarizations are no longer consistent and the synthesized vector of the reflected *p*- and *s*-polarizations (i.e., $\mathbf{E}_{\mathrm{f}} = \mathbf{E}_{\mathrm{f},rp} + \mathbf{E}_{\mathrm{f},rs}$) rotates as the reflected light propagates. The name of the technique "ellipsometry" originates from the fact that polarized light often becomes "elliptical" upon light reflection, as depicted in Fig. 1.1. Notice that the directions of the basis vectors on the incident and reflection sides in Fig. 1.1 are chosen so that these vectors overlap completely when the incident angle is $\theta = 90°$.

Ellipsometry measures the two values (ψ, Δ), which represent the amplitude ratio ψ and phase difference Δ between the *p*- and *s*-polarizations [4–11]. When sample structures are simple (i.e., only substrates), the amplitude ratio ψ is characterized by n, while Δ represents light absorption described by k or the absorption coefficient α [4–7]. Thus, the two values (n, k) can be determined directly from the two ellipsometry parameters (ψ, Δ) obtained from a measurement. In other words, in ellipsometry, the optical constants are determined by characterizing the polarization change upon light reflection.

In conventional transmittance/reflectance (T/R) measurements, absolute light intensities are characterized. In this case, the measured light intensities are influenced directly by the imperfections of the instrument, calibration and samples (i.e., light scattering, see Fig. 6.8). Thus, the T/R techniques are generally more prone to measurement errors. In contrast, the relative amplitude and phase of reflected polarized light are characterized in ellipsometry, and this principle allows high-precision evaluation of material optical properties. Moreover, in T/R analysis, k (or α) is often deduced assuming a constant n in a light absorbing region [12], which is not a valid assumption for most of materials. Accordingly, ellipsometry can be considered as the most reliable technique for the determination of (n, k). When the optical properties in weak absorbing regions ($\alpha < 500$ cm^{-1}) are characterized, however, a transmission measurement still needs to be used as a complementary technique (see Fig. 8.3), as reflection-type ellipsometry has limited sensitivity for light absorption [6].

The (ψ, Δ) measured from ellipsometry are defined by

$$\rho \equiv \tan\psi \exp(i\Delta) \equiv \left(\frac{E_{\mathrm{f},rp}}{E_{\mathrm{f},ip}}\right) \Big/ \left(\frac{E_{\mathrm{f},rs}}{E_{\mathrm{f},is}}\right), \tag{1.1}$$

Although the above equation is slightly complicated, $E_{\mathrm{f},ip} = E_{\mathrm{f},is}$ holds in Fig. 1.1 since the amplitudes of the p- and s-polarizations are the same and the phase difference between the polarizations is zero. For the case of Fig. 1.1, therefore, we obtain a quite simple relation of $\tan\psi\exp(i\Delta) = E_{\mathrm{f},rp}/E_{\mathrm{f},rs}$. As known well [4, 6], the amplitude reflection coefficients for the p- and s-polarizations are expressed as

$$r_p \equiv \frac{E_{\mathrm{f},rp}}{E_{\mathrm{f},ip}} = |r_p| \exp(i\delta_p), \tag{1.2}$$

$$r_s \equiv \frac{E_{\mathrm{f},rs}}{E_{\mathrm{f},is}} = |r_s| \exp(i\delta_s), \tag{1.3}$$

where $|r|$ and δ show the amplitude ratio and phase difference between the incident and reflected waves, respectively (Sect. 2.3). By applying these relations, we obtain the following equation using (1.1):

$$\rho \equiv \tan\psi \exp(i\Delta) \equiv \frac{r_p}{r_s}. \tag{1.4}$$

From (1.2)–(1.4), it follows that

$$\tan\psi = |r_p|/|r_s|, \quad \Delta = \delta_p - \delta_s. \tag{1.5}$$

Since the reflectances for the p- and s-polarizations are given by $R_p = |r_p|^2$ and $R_s = |r_s|^2$ [2–8], respectively, $\tan\psi$ can be interpreted as the reflectance ratio [i.e., $\tan\psi = (R_p/R_s)^{1/2}$]. On the other hand, when there is no light absorption ($k = \alpha = 0$), we obtain $\Delta = 0°$ or $180°$. Thus, the phase difference between the reflected p-polarization (δ_p) and s-polarization (δ_s) represents the light absorption characteristics [4–7]. Quite importantly, r_p and r_s can be calculated from the optical constants and layer thicknesses using optical models (Chaps. 3 and 5) and the ellipsometry analyses of samples can be performed systematically from (1.4). It should be emphasized that (1.1) and (1.4) correspond to the ones when the complex refractive index is defined by $N \equiv n - ik$ (Sect. 1.2.1). If the definition of $N \equiv n + ik$ is applied, we need to rewrite the above equation as $\rho \equiv \tan\psi\exp(-i\Delta)$. Note that the definition of $\rho \equiv \tan\psi\exp(i\Delta)$ (i.e., $N \equiv n - ik$) will be used throughout this book.

For actual ellipsometry measurements, various optical elements, including polarizer, analyzer and compensator, are used [4–8]. In conventional ellipsometry instruments, these optical parts are rotated, and the polarization state of the reflected light is determined based on the variation of the reflected light intensity with the

rotation angle of the optical element (Chap. 2). In spectroscopic ellipsometry (SE), white light generated by xenon, halogen and/or deuterium lamps is used as a probe, and (ψ, Δ) values for all the wavelengths are measured simultaneously using multichannel detectors [5–8]. In SE measurements, the rotation frequency of the optical element is high (~50 Hz) and one ellipsometry spectrum can be measured in a few seconds with sufficient accuracy. Accordingly, ellipsometry characterization can be carried out non-destructively in a short time, which is one of the important features of the ellipsometry technique. By taking this advantage, the on-line monitoring of large-area module production (Chap. 5 in Vol. 2) and the real-time control of thin film structures (Chap. 6 in Vol. 2) have also been performed.

1.1.2 Data Analysis Procedure

Figure 1.2 summarizes the procedure of SE data analysis. In the first step of the analysis, for measured (ψ, Δ) spectra, an optical model is constructed (Chap. 3). The optical model is an assumed flat layered structure defined by the thicknesses of component layers (d_1 and d_2 in Fig. 1.2) and the optical constants of all the layers and the substrate. The simplest optical model is when there is only the substrate. In the second step, we select the optical constants (or dielectric functions) for the layers and substrate. The dielectric function of a substrate can be obtained quite easily if there are no overlayers (Sect. 3.5.1). When appropriate optical data are not available, the optical constants are calculated using a dielectric function model. In this case, depending on material optical properties (i.e., semiconductor, insulator, metal, etc.), different types of models are adopted (Chap. 5). By employing the constructed optical model and the optical data, the SE spectra are calculated using (1.4). For this calculation, Fresnel equations are used and the effect of optical interference induced by thin film structures is also taken into account (Chap. 3). When the incident angle of the ellipsometry measurement is not known, the value is estimated from a measurement using a standard sample. In the next step, the calculated SE spectra are fitted to the experimental spectra using some analytical parameters as fitting parameters. Finally, from the parameters that provide the best fitting, the optical constants and thin film structure are determined. By analyzing the extracted optical spectrum, the band gap (E_g) of semiconductor materials can further be determined (see Figs. 9.3 and 10.10, for example).

One drawback of the ellipsometry technique is an indirect nature of this characterization method and the optical model is almost always necessary for the analysis. In particular, the optical model constructed for the analysis represents merely an approximate structure and the analysis result may include artifacts or large errors even when the fitting is sufficiently good. Accordingly, ellipsometry results must be justified using other measurement and analysis results. For thin film structures, the validity of ellipsometry analyses can be confirmed by comparing structural parameters deduced from ellipsometry with those determined from scanning electron microscopy (SEM) and transmission electron microscopy (TEM).

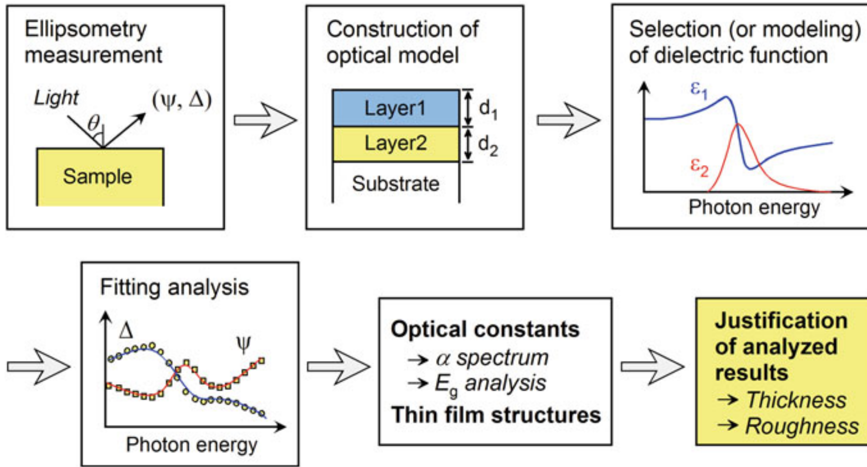

Fig. 1.2 Data analysis procedure for spectroscopic ellipsometry measurements. The d_1 and d_2 of the optical model show the layer thicknesses

It should be emphasized that quite reliable SE results can be obtained from multi-sample analyses, in which the optical constants of layers are determined self-consistently by analyzing more than two samples having different layer thicknesses on substrates (Sect. 10.2).

1.1.3 Effect of Rough Surface

The remarkable feature of ellipsometry is a very high sensitivity for layer thicknesses (~0.1 Å) [6]. However, the high thickness sensitivity could also become disadvantage if samples have complex structures and the precise optical modeling of the sample structures is difficult. In particular, the Δ spectrum is extremely sensitive to surface structures and the roughness of a few angstroms still affects the extracted optical constants (Fig. 6.5). Thus, the proper modeling of the surface roughness is critical for accurate analysis. Quite inconsistent α spectra reported for $CuInSe_2$ and $CH_3NH_3PbI_3$ hybrid perovskite have been confirmed to originate from inappropriate roughness modeling (Chap. 6).

Figure 1.3 shows the influence of surface roughness on ellipsometry analysis [13]. In Fig. 1.3a, reported α spectra of $CH_3NH_3PbI_3$ [13–22] are summarized. The arrow indicates the E_g position of $CH_3NH_3PbI_3$ (1.61 eV) determined from the critical point analysis (Fig. 16.7). It can be seen that the reported α differs significantly in a range from 2.5×10^4 to 8.7×10^4 cm^{-1} at 2.0 eV and this large difference in α leads to a substantial variation in the device simulation (see Fig. 6.11). Furthermore, some of the α spectra show relatively large values in the energy region below E_g, as

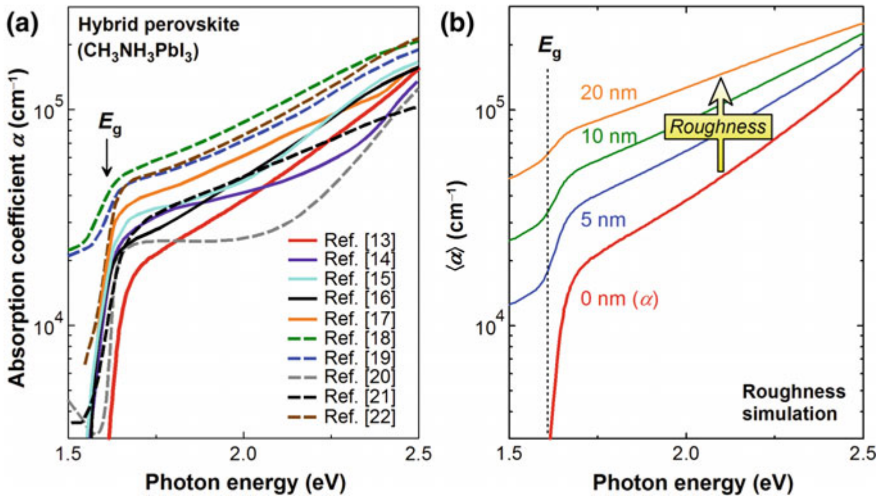

Fig. 1.3 **a** α spectra of $CH_3NH_3PbI_3$ reported in [13–22] and **b** variation of the pseudo-α spectrum ($\langle\alpha\rangle$) with roughness layer thickness. In the simulation of (**b**), a hypothetical roughness was assumed using an optical model of (surface roughness layer)/($CH_3NH_3PbI_3$ bulk layer) and the optical data of [13] in (**a**) were employed for the calculation. The data of (**a**) and (**b**) are adopted from [13]

indicated by the dotted lines. Rather surprisingly, the large variation of α observed in Fig. 1.3a is artifact and can be interpreted primarily by large surface roughness of $CH_3NH_3PbI_3$ samples (Chap. 6).

In general, when surface roughness is present, a surface roughness layer is incorporated into the optical model and the optical properties of this layer are calculated using the effective medium approximation (Sect. 3.4.2). However, $CH_3NH_3PbI_3$ layers fabricated by solution-based processing exhibit large roughness structures with sizes comparable to the wavelength (λ) of the visible/ultraviolet (UV) light [15, 23]. In such cases, the roughness modeling becomes quite difficult (Chap. 6) and, when the SE analysis is performed using an oversimplified optical model (i.e., single roughness layer), the extracted optical data generally show strong artifacts, such as non-zero α values in the energy region even below E_g [24]. On the other hand, the α spectrum of [13] has been extracted from a very smooth $CH_3NH_3PbI_3$ layer using multi-sample analysis (Chap. 16) and this spectrum shows the lowest α value near E_g. When this spectrum is employed for the external quantum efficiency (EQE) analysis, the calculated spectrum shows excellent agreement with the experimental result (Fig. 6.11).

To reveal the effect of the roughness, the pseudo-α spectrum $\langle\alpha\rangle$ (see Sect. 6.2.1) is calculated from the α spectrum of [13] by providing a hypothetical surface roughness layer. In Fig. 1.3b, the variation of $\langle\alpha\rangle$ with roughness layer thickness is shown. It can be seen that $\langle\alpha\rangle$ increases rather significantly with increasing thickness of the hypothetical roughness layer and the simulated $\langle\alpha\rangle$ spectrum reproduces the

high α values reported in [18, 19] quite well. A similar trend has also been observed for $CuInSe_2$ (Fig. 6.3). It should be noted that, when the α values are overestimated, the E_g value is in turn underestimated [13], as confirmed from the results of Fig. 1.3a. Accordingly, the overall optical data are affected seriously if the surface roughness is modeled improperly. Quite fortunately, the artifacts generated by the large roughness can be corrected rather easily using a simple procedure (Fig. 6.10). The result of Fig. 1.3 recalls the important fact that the influence of surface roughness is significant in ellipsometry analysis. For the confirmation of the SE analysis, the roughness characterization by atomic force microscopy (AFM) is quite effective as the root-mean-square roughness obtained from AFM shows a clear linear relationship with the surface roughness layer thickness determined by SE (Fig. 6.1) [25]. Thus, it is important to perform the structural characterization by AFM and SEM (TEM) to justify SE results.

1.1.4 Structural Characterization

In addition to the determination of optical constants, the ellipsometry technique can be applied to characterize detailed layer structures. In the field of solar cells, the SE technique has been employed widely to determine the optical constants and thickness of SiN layers formed on crystalline Si (c-Si) substrates [26]. In this case, only the SiN thickness is deduced as the layer structure. However, if advanced optical modeling technique is employed, even multilayered textured structures can be evaluated by SE (Chap. 4 in Vol. 2). Such analyses are expected to be quite useful when the structural inhomogeneity in large-area solar modules is characterized by SE mapping measurements (Chap. 5 in Vol. 2). If an optical database is constructed for semiconductor alloys, the alloy composition of the layer can also be deduced. Such characterization has already been demonstrated for $Cu(In,Ga)Se_2$ (CIGSe) absorber layers [27, 28].

1.2 Optical Properties of Solar Cell Materials

The conversion efficiency of solar cells is ultimately governed by the absorption characteristics of solar-cell absorber layers. Thus, the understanding of the absorption properties is of utmost importance. In this section, the basic ideas of light absorption and optical constants are addressed. This section will further provide the comparison of optical spectra obtained from various solar cell materials.

1.2.1 Optical Constants

The optical constants (n, k) can be defined by considering the propagation of electromagnetic waves in media. Figure 1.4 schematically illustrates the propagation of light at an air/semiconductor interface when k of the semiconductor is (a) low and (b) high. In Fig. 1.4, λ shows the wavelength of the incident electromagnetic wave. Classically, the refractive index is defined by

$$n \equiv c/v, \tag{1.6}$$

where c and v indicate the speed of light in vacuum and in a medium, respectively [2]. The n value of air is 1.0003 [2] and can be approximated as $n = 1$. Equation (1.6) shows the physical phenomenon that the speed of light becomes slower in a medium with high n. As a result, when the light advances into the semiconductor, λ decreases to $\lambda' = \lambda/n$, as depicted in Fig. 1.4. On the other hand, the light absorption in media is represented by the extinction coefficient k. Specifically, when $k > 0$, the amplitude of the electromagnetic wave decreases gradually as the light propagates deeper into the semiconductor due to light absorption. As a result, n modifies λ in the medium, while k varies the amplitude of the electromagnetic wave.

Using the complex number ($i = \sqrt{-1}$), the light waves in Fig. 1.4 are described by a unified expression [6]:

$$E_{\mathrm{f}} = E_{\mathrm{f0}} \exp[i(\omega t - Kx + \delta)], \tag{1.7}$$

where E_{f0} is the amplitude of the electromagnetic wave at the interface (see Fig. 1.4a) The ω, t, x and δ show the angular frequency, time, distance from the interface (surface) and initial phase, respectively, whereas K indicates the propagation number given by

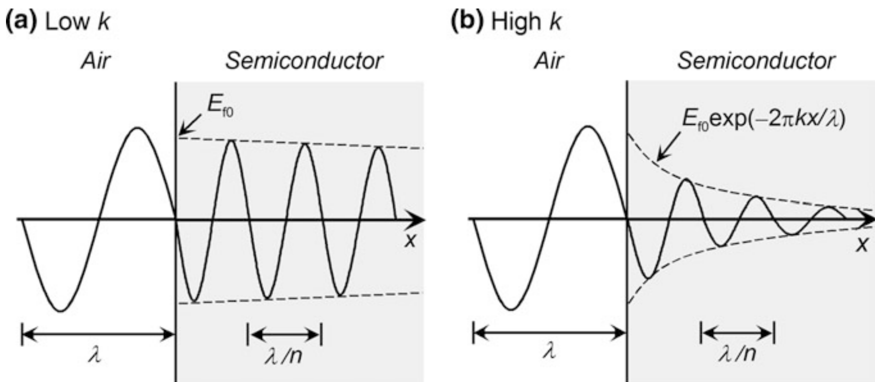

Fig. 1.4 Propagation of electromagnetic waves at air/semiconductor interfaces when the extinction coefficient k of the semiconductor is (**a**) low and (**b**) high. The λ and n show the wavelength of the light in air and refractive index of the semiconductor. The E_{f0} shows the amplitude of the electric field at the interface. The variations of the wave amplitude along the distance x from the interface are indicated by the dotted lines

$$K = \frac{2\pi}{\lambda} N. \tag{1.8}$$

Here, N shows the complex refractive index defined by

$$N \equiv n - ik. \tag{1.9}$$

By inserting (1.8) into (1.7), we further get

$$E_\mathrm{f} = E_\mathrm{f0} \exp\left(-\frac{2\pi k}{\lambda} x \right) \exp\left[i\left(\omega t - \frac{2\pi n}{\lambda} x + \delta \right) \right] \tag{1.10}$$

By treating k as a complex number, the wave amplitude reduction by light absorption is expressed simply as $\exp(-2\pi kx/\lambda)$. In (1.10), the reduction of λ in the medium is also described by $\lambda' = \lambda/n$. If the definition of $N \equiv n - ik$ is used, therefore, the propagation of the electromagnetic wave can be expressed from a single expression. Note that δ in (1.2) and (1.3) can be related to δ in (1.10) and shows the change in δ upon light reflection (Sect. 2.3).

The light intensity of electromagnetic waves is given by $I \propto |E_\mathrm{f}|^2$ [2]. If (1.10) is inserted into this equation, we obtain

$$I = \left| E_\mathrm{f0} \exp\left(-\frac{2\pi k}{\lambda} x \right) \right|^2 = |E_\mathrm{f0}|^2 \exp\left(-\frac{4\pi k}{\lambda} x \right) \tag{1.11}$$

using $|\exp(i\varphi)|^2 = 1$. Experimentally, the light intensity variation by absorption is described using Beer's law:

$$I = I_0 \exp(-\alpha d), \tag{1.12}$$

where α and d show the absorption coefficient and the distance from the surface (i.e., x in Fig. 1.4). By comparing (1.11) and (1.12), we notice that

$$\alpha = \frac{4\pi k}{\lambda}. \tag{1.13}$$

This shows an important relation between k and α. If there is no light absorption, it follows that $\alpha = k = 0$.

1.2.2 Dielectric Function

Although the propagation of electromagnetic waves in media is expressed completely by (n, k), the value of N is determined from a complex dielectric constant defined by

$$\varepsilon \equiv \varepsilon_1 - i\varepsilon_2. \tag{1.14}$$

From Maxwell's equations, we can define the relation between ε and N [6]:

$$N^2 \equiv \varepsilon. \tag{1.15}$$

Using (1.9), (1.14) and (1.15), we get

$$\varepsilon_1 = n^2 - k^2, \tag{1.16}$$

$$\varepsilon_2 = 2nk. \tag{1.17}$$

Note that, when $k = 0$, we obtain $\varepsilon_2 = 0$ ($\varepsilon_1 = n^2$). Thus, ε_2 essentially shows the absorption characteristics. On the other hand, from (ε_1, ε_2), (n, k) can also be calculated:

$$n = \left\{ \left[\varepsilon_1 + \left(\varepsilon_1^2 + \varepsilon_2^2 \right)^{1/2} \right] \Big/ 2 \right\}^{1/2}, \tag{1.18}$$

$$k = \left\{ \left[-\varepsilon_1 + \left(\varepsilon_1^2 + \varepsilon_2^2 \right)^{1/2} \right] \Big/ 2 \right\}^{1/2}. \tag{1.19}$$

From k, α can further be obtained using (1.13).

Figure 1.5 shows ε_1 and ε_2 spectra in the infrared and visible/UV regions. As illustrated in this figure, the real part ε_1 and imaginary part ε_2 show complicated changes, and the dielectric response for photon energy E is generally referred to as the dielectric function. The variation of ε_1 and ε_2 can be understood based on the dielectric polarization (Chap. 5). Specifically, when the light advances into a medium, positive and negative charges in the medium receive electric forces in the opposite direction by $\mathbf{E}_\mathrm{f}$ of the incident light (see the insets of Fig. 1.5). However, electric charges in the medium are bound by springs in the classical view and cannot move freely. As a result, the charges present in the medium are separated into regions that are more electrically positive and negative, creating a dipole moment. The dielectric polarization P is the sum of the dipole moment per unit volume and, using P, ε is expressed by the following equation [6, 29]:

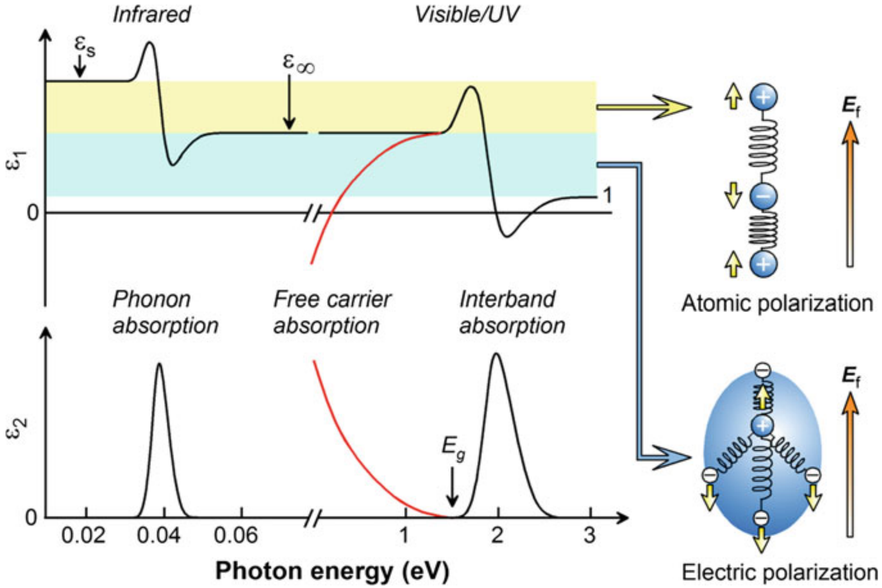

Fig. 1.5 Real part ε_1 and imaginary part ε_2 of a dielectric function in the infrared and visible/UV regions ($\varepsilon = \varepsilon_1 - i\varepsilon_2$). The ε_s and ε_∞ show a static dielectric constant and a high-frequency dielectric constant, respectively. The red lines indicate the contribution of free carrier absorption observed in TCO materials and metals. The dielectric polarizations (atomic and electric polarizations) induced by the electric field of light are also illustrated

$$\varepsilon = 1 + \frac{P}{\varepsilon_0 E_f}, \tag{1.20}$$

where ε_0 shows the free-space permittivity. The above equation shows clearly that ε becomes larger as P increases.

The dielectric polarization can be categorized into (i) atomic polarization and (ii) electric polarization. The atomic polarization occurs mainly in ionic crystals, whereas the electric polarization is induced by electrons and a nucleus in atoms. When the photon energy of the incident light is low, ε_1 shows a constant value referred to as the static dielectric constant ε_s. At low energy, the modulation frequency of the ac electric field of light is low (i.e., $\omega = 1.519 \times 10^{15}E$ [6]) and both atomic and electric polarizations occur. Thus, ε_s includes the contributions of these polarizations. Quite importantly, in the classical view, light is absorbed at a resonant oscillatory frequency of the spring and ε_2 increases in a specified energy region (Chap. 5). The light absorption caused by the atomic polarization is observed in the infrared region, while the resonant oscillation for the electric polarization occurs in the visible/UV region. At high energies, the atomic polarization disappears as the modulation frequency becomes higher and ε_1 decreases to a constant value referred

to as the high-frequency dielectric constant ε_∞. At even higher energies, no polarization occurs ($P = 0$) and ε_1 shows the value of vacuum (i.e., $\varepsilon_1 = 1$, $\varepsilon_2 = 0$).

The charge separation and the resulting generation of the dielectric polarization are quite important concepts even when we analyze dielectric function based on first-principles calculation (see Fig. 16.13, for example). In the quantum mechanical view, the light absorption in the infrared region is caused by the phonon absorption, while that in the visible/UV region is explained by the interband optical transition (i.e., a transition from valence to conduction bands). For the interband transition, the onset of the ε_2 peak is consistent with E_g if there is no absorption tail. When there are many electrons and holes in a medium at a high concentration (typically $> 10^{20}$ cm^{-3}), free carrier absorption (Sect. 18.2) occurs as indicated by the red line in Fig. 1.5. The free carrier absorption is observed in many transparent conductive oxide (TCO) layers (Chap. 11 in Vol. 2) and relatively strong parasitic absorption occurs in these layers. Thus, the suppression of the free carrier absorption in TCO layers is quite important to reduce the current loss in solar cells (Chap. 19).

1.2.3 Absorption Spectra

Figure 1.6 summarizes the α spectra of various solar cell materials versus (a) E and (b) λ. The complete optical data of these materials can be found in Chaps. 8 and 10 in Vol. 2. In the figure, the E_g positions of each material are indicated by the closed circles. For a high efficiency CIGSe solar cell [30], the alloy composition of $CuIn_{0.8}Ga_{0.2}Se_2$ was employed and the corresponding spectrum calculated from the CIGSe optical database (Sect. 10.4) is shown. It can be seen that many direct-transition semiconductors show similar α values of $\sim 10^4$ cm^{-1} and, at the exact E_g positions, the α values are around 5×10^3 cm^{-1}. In contrast, the indirect-transition semiconductors, including Si, Ge, GaP and AlAs, exhibit much lower α values. In Part II of this book, the detailed characterizations of individual absorber materials are described.

1.3 Overview of This Book

This book aims to provide general understanding of various SE techniques used for the characterization of solar cell materials/devices and is consisting of two major parts. In Part I, the basic SE measurement and data analysis methods are introduced, whereas Part II describes how individual materials and device structures can be analyzed. More specifically, after a general introduction into the field of ellipsometry and into the topics covered by the book (Chap. 1), Part I continues with a review of the fundamental measurement technique (Chap. 2). In the SE applications to solar cells, data analysis is practically more important and fundamental

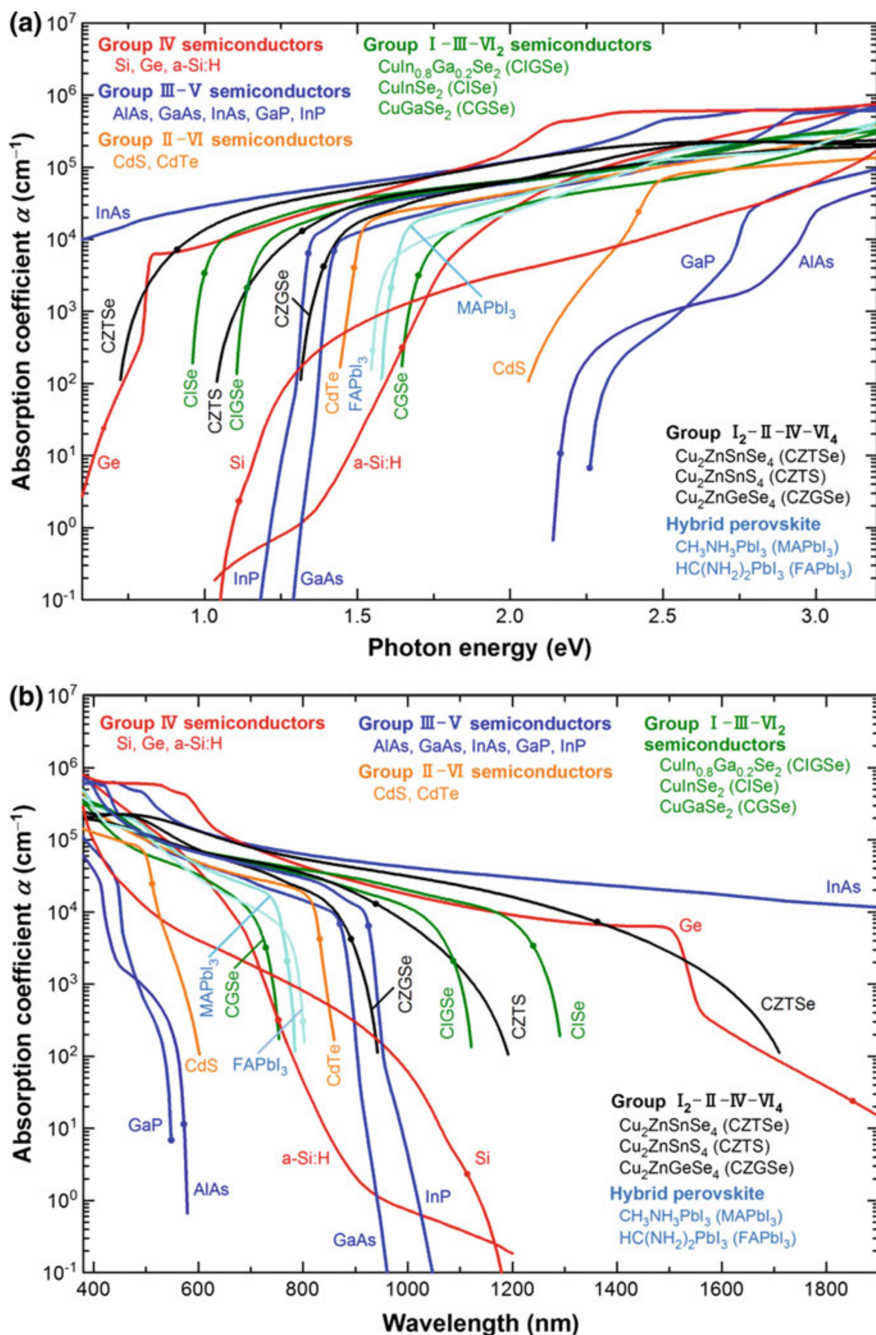

Fig. 1.6 α spectra of various solar cell materials versus **a** photon energy and **b** wavelength. The complete optical data of these materials are shown in Chaps. 8 and 10 in Vol. 2. The closed circles indicate the E_g positions of each absorber material. For high efficiency Cu(In, Ga)Se_2 solar cells, the composition of $CuIn_{0.8}Ga_{0.2}Se_2$ has been used and the corresponding spectrum is shown. It should be noted that the optical constants of a-Si:H are process dependent (Sect. 9.4)

explanation for SE data analysis is provided (Chap. 3). For accurate SE analyses, background knowledge for semiconductor optical properties (Chap. 4) and understanding of dielectric function models (Chap. 5) are critical. As mentioned above (Sect. 1.1.3), the effect of surface roughness is quite significant in the SE analysis and the treatment of the roughness is also explained (Chap. 6).

Part II covers a quite broad area of solar cell materials/devices. For Si-based solar cells, the characterizations of a-Si:H solar cells (Chap. 7), c-Si solar cells (Chap. 8) and a-Si:H/c-Si heterojunction solar cells (Chap. 9) are treated. For CIGSe solar cells, the basic optical properties of quaternary CIGSe alloy semiconductors (Chap. 10) and the real-time SE characterization of CIGSe layers (Chap. 11) are shown. The optical characteristics of emerging CZTSe-related kesterite (Chap. 12), CdTe (Chap. 13) and group III–V (Chap. 14) semiconductors are also summarized. In the following chapters, the SE analyses performed for organic materials (Chap. 15) and hybrid perovskite materials (Chap. 16) are indicated. In particular, for the hybrid perovskites, extensive research results obtained from the material and device characterizations are discussed. The recent progress for photonic and plasmonic solar cells is further reviewed (Chap. 17). As mentioned earlier, the free carrier absorption in TCO layers directly influences the photocurrent of the device. Thus, the fundamental optical properties of various TCO materials (Chap. 18) and high-mobility TCO layers (Chap. 19), which can suppress the free carrier absorption in solar cells, are described in details.

In the second volume of “Spectroscopic Ellipsometry for Photovoltaics”, detailed descriptions for more advanced SE and external quantum efficiency (EQE) analyses, which employ new optical modeling and calculation techniques, are given. More specifically, real-time monitoring/control of solar cell structures and large-area module characterization by SE are described. Moreover, optical and recombination loss analyses based on EQE characterization have been highlighted. The second volume further provides a quite complete optical database for numerous solar cell component materials (a total of 148 materials), which can be used for SE analyses and optical/EQE simulations. In particular, tabulated (n, k) data and completely parameterized dielectric function parameters for inorganic/organic/hybrid-perovskite semiconductors, transparent conductive oxide, metal and substrate materials are summarized in the book. Through the above overall descriptions, in-depth knowledge and understanding for SE characterization of solar cells can be gained.

Acknowledgements The author acknowledges Shohei Fujimoto for the preparation of Fig. 1.6.

References

1. P. Drude, *The Theory of Optics* (Dover Phoenix Editions, NY, 1959)
2. E. Hecht, *Optics*, 4th edn. (Addison Wesley, San Francisco, 2002)

3. M. Born, E. Wolf, *Principles of Optics*, 7th edn. (Cambridge University Press, Cambridge, 1999)
4. R.M.A. Azzam, N.M. Bashara, *Ellipsometry and Polarized Light* (Elsevier Science B. V, Amsterdam, 1977)
5. H.G. Tompkins, W.A. McGahan, *Spectroscopic Ellipsometry and Reflectometry: A User's Guide* (Wiley, New York, 1999)
6. H. Fujiwara, *Spectroscopic Ellipsometry: Principles and Applications* (Wiley, West Sussex, UK, 2007)
7. H.G. Tompkins, J.N. Hilfiker, *Spectroscopic Ellipsometry: Practical Application to Thin Film Characterization* (Momentum Press, New York, 2016)
8. H.G. Tompkins, E.A. Irene (eds.), *Handbook of Ellipsometry* (William Andrew, New York, 2005)
9. M. Schubert, *Infrared Ellipsometry on Semiconductor Layer Structures: Phonons, Plasmons, and Polaritons* (Springer, Heidelberg, 2004)
10. M. Losurdo, K. Hingerl (eds.), *Ellipsometry at the Nanoscale* (Springer, Heidelberg, 2013)
11. K. Hinrichs, K.-J. Eichhorn (eds.), *Ellipsometry of Functional Organic Surfaces and Films* (Springer, Heidelberg, 2014)
12. J.R. Tuttle, D. Albin, R.J. Matson, R. Noufi, J. Appl. Phys. **66**, 4408 (1989)
13. M. Shirayama, H. Kadowaki, T. Miyadera, T. Sugita, M. Tamakoshi, M. Kato, T. Fujiseki, D. Murata, S. Hara, T.N. Murakami, S. Fujimoto, M. Chikamatsu, H. Fujiwara, Phys. Rev. Applied **5**, 014012 (2016)
14. Q. Lin, A. Armin, R.C.R. Nagiri, P.L. Burn, P. Meredith, Nat. Photon **9**, 106 (2015)
15. P. Löper, M. Stuckelberger, B. Niesen, J. Werner, M. Filipič, S.-J. Moon, J.-H. Yum, M. Topič, S. De Wolf, C. Ballif, J. Phys. Chem. Lett. **6**, 66 (2015)
16. Y. Jiang, M.A. Green, R. Sheng, A. Ho-Baillie, Sol. Eng. Mater. Sol. Cells **137**, 253 (2015)
17. S. De Wolf, J. Holovsky, S.-J. Moon, P. Löper, B. Niesen, M. Ledinsky, F.-J. Haug, J.-H. Yum, C. Ballif, J. Phys. Chem. Lett. **5**, 1035 (2014)
18. J.M. Ball, S.D. Stranks, M.T. Hörantner, S. Hüttner, W. Zhang, E.J.W. Crossland, I. Ramirez, M. Riede, M.B. Johnston, R.H. Friend, H.J. Snaith, Energy Environ. Sci. **8**, 602 (2015)
19. G. Xing, N. Mathews, S.S. Lim, N. Yantara, X. Liu, S. Dharani, M. Grätzel, S. Mhaisalkar, T. C. Sum, Nat. Mater. **13**, 476 (2014)
20. A.M.A. Leguy, Y. Hu, M. Campoy-Quiles, M.I. Alonso, O.J. Weber, P. Azarhoosh, M. van Schilfgaarde, M.T. Weller, T. Bein, J. Nelson, P. Docampo, P.R.F. Barnes, Chem. Mater. **27**, 3397 (2015)
21. G. Xing, N. Mathews, S. Sun, S.S. Lim, Y.M. Lam, M. Grätzel, S. Mhaisalkar, T.C. Sum, Science **342**, 344 (2013)
22. S. Sun, T. Salim, N. Mathews, M. Duchamp, C. Boothroyd, G. Xing, T.C. Sum, Y.M. Lam, Energy Environ. Sci. **7**, 399 (2014)
23. H.S. Jung, N.-G. Park, Small **11**, 10 (2015)
24. H. Fujiwara, S. Fujimoto, M. Tamakoshi, M. Kato, H. Kadowaki, T. Miyadera, H. Tampo, M. Chikamatsu, H. Shibata, Appl. Surf. Sci. **421**, 276 (2016)
25. H. Fujiwara, J. Koh, P.I. Rovira, R.W. Collins, Phys. Rev. B **61**, 10832 (2000)
26. G.E. Jellison Jr., F.A. Modine, P. Doshi, A. Rohatgi, Thin Solid Films **313–314**, 193 (1998)
27. V. Ranjan, T. Begou, S. Little, R.W. Collins, S. Marsillac, Prog. Photovolt. **22**, 77 (2014)
28. S. Minoura, T. Maekawa, K. Kodera, A. Nakane, S. Niki, H. Fujiwara, J. Appl. Phys. **117**, 195703 (2015)
29. C. Kittel, *Introduction to Solid State Physics* (Wiley, New York, 1986)
30. P. Jackson, D. Hariskos, R. Wuerz, O. Kiowski, A. Bauer, T.M. Friedlmeier, M. Powalla, Phys. Status Solidi RRL **9**, 28 (2015)

Part I
Fundamental Principles of Ellipsometry

Chapter 2
Measurement Technique of Ellipsometry

Robert W. Collins

Abstract Ellipsometry is an optical measurement technique that involves generating a light beam in a known polarization state and reflecting it from a sample having a planar surface. By measuring the polarization state of the specularly reflected beam, the ellipsometry angles (ψ, Δ) can be determined. These angles are specific to the wavelength λ_0 of the light beam and the angle of incidence θ_i of the beam at the sample surface. Upon detailed analysis, the angles (ψ, Δ), along with the associated known values of λ_0 and θ_i, yield information on the sample. Such information for a bulk sample includes the optical properties, i.e. the index of refraction n and the extinction coefficient k, which depend on the wavelength λ_0. Information deduced for samples consisting one or more thin films having plane-parallel surface/interfaces includes the layer thicknesses d and (n, k) of the components. Considering samples that are isotropic, which describe most structures of interest in photovoltaics applications, (ψ, Δ) are defined by $\tan \psi \exp(i\Delta) = r_p/r_s$, where r_p and r_s are the complex amplitude reflection coefficients for linear p and s-polarization states. For these states, the electric field vibrates parallel (p) and perpendicular (s) to the plane of incidence, defined by the incident and reflected beam propagation directions. Several variations of the ellipsometry experiment have been developed with the goals to obtain a large set of (ψ, Δ) pairs that facilitates data interpretation and to extract as much information as possible on the sample. In spectroscopic ellipsometry, (ψ, Δ) are measured continuously versus the wavelength of the light beam, and in real time ellipsometry, (ψ, Δ) are measured versus time at fixed λ_0. The latter two modes can be integrated to yield real time spectroscopic ellipsometry, utilizing an instrument with a linear detector array for high speed data acquisition in parallel for a continuous distribution of wavelengths. In expanded beam imaging spectroscopic ellipsometry, (ψ, Δ) are measured along a line on the surface of the sample using an instrument with a two-dimensional detector array. One array index is used for the line imaging function and the second array index is used for spectroscopy. Two-dimensional spectroscopic mapping is

R. W. Collins (✉)
Department of Physics & Astronomy and Center for Photovoltaics Innovation & Commercialization, University of Toledo, Toledo, OH 43606, USA
e-mail: robert.collins@utoledo.edu

© Springer International Publishing AG, part of Springer Nature 2018

H. Fujiwara and R. W. Collins (eds.), *Spectroscopic Ellipsometry for Photovoltaics*,
Springer Series in Optical Sciences 212,
https://doi.org/10.1007/978-3-319-75377-5_2

possible by translating the sample. In general, the most widely used ellipsometers for photovoltaics applications are spectroscopic and span the range from the ultraviolet to the near-infrared (200–2000 nm). Over this spectral range, the (n, k) spectra deduced from spectroscopic ellipsometry provide information on the processes of absorption and dispersion originating from the valence electrons in semiconductors and dielectrics and from the conduction electrons in transparent conducting oxides and metals. Spectroscopic ellipsometry is of great interest in photovoltaics research and development due to its ability to extract {d, (n, k)} information for the multiple layers of the solar cell and (n, k) for the bulk materials, e.g. wafers or substrates. Once this information has been established for the solar cell, it becomes possible to simulate the external quantum efficiency of the device as well as the optical losses due to reflection, absorption in inactive layers, and transmission (if any). Comparisons of simulation and measurements give insights into electronic losses in active layers via recombination.

2.1 Introduction and Preliminaries

Ellipsometry is an optical measurement technique that derives its name from the analysis of the ellipse of polarization that is generated when a polarized light beam interacts with a sample [1]. An ellipsometer system describes the instrumentation designed to perform the following sequence of five steps of the ellipsometry measurement [2]:

(1) *Polarized beam generation*: the generation of a light beam in a known state of polarization using optical components such as a light source, monochromator, polarizer, and retarder (often referred to as a compensator);
(2) *Polarized beam interaction*: interaction of the light beam with a sample, most commonly via oblique specular reflection, resulting in an emergent beam in a second polarization state;
(3) *Polarized beam detection*: the measurement of the emerging polarization state using optical elements such as a compensator, polarizer, spectrometer, and solid state detector;
(4) *Data reduction*: determination of sample parameters, i.e. the ellipsometry data, that describe the interaction, applying the information on the two polarization states and instrument calibration information obtained in separate measurements; and
(5) *Data analysis*: deduction of useful information on the sample, such as optical properties and film thicknesses, from the ellipsometry data, the geometry of the interaction, e.g. angle of incidence, and the wavelength of the light beam.

Figure 2.1 shows a schematic of the polarization state generator, sample, and polarization state detector for an ellipsometer designed for high speed spectroscopic

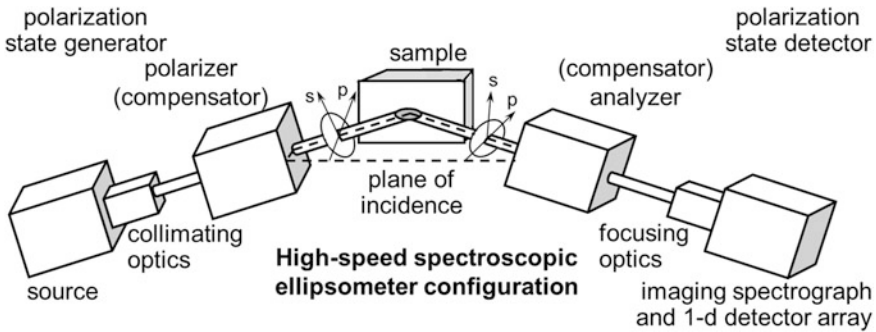

Fig. 2.1 Configuration of an ellipsometer consisting of a polarization state generator, sample, and polarization state detector. Oblique reflection from the sample defines the *p-s* coordinate system that serves as the reference system for measurement of the polarization state and the orientations of the optical elements of polarizer, retarders (or compensators), and analyzer

measurements. Preliminary discussion of all five steps of ellipsometry will be provided in this section before the detailed mathematical development is presented.

2.1.1 Step 1: Polarization Generation

In step (1), the goal of the equipment described as the polarization state generator is to produce a light beam in an identifiable polarization state starting from one or more sources of light irradiance. The output of the light source of the ellipsometer can be either single wavelength from a laser, multiple wavelengths from one or more lasers, quasi-monochromatic from a lamp and spectrometer, or broadband, the latter implying a continuous distribution of wavelengths directly from a lamp. In the case of a broadband source, dispersion of the light beam into its individual spectral components must be performed as a capability of the polarization detection, step (3).

The most general polarization state of the incident light beam for a given wavelength can be described by two ellipse parameters, the tilt angle and the axial ratio. The axial ratio, or the ratio of the length of the semi-minor axis of the ellipse to that of the semi-major axis, is referred to as the ellipticity here for consistency with [2]. In some circumstances, for example, if a reflectance measurement is performed simultaneously with ellipsometry, the size of the polarization ellipse, i.e. the irradiance, is also determined for the incident beam in addition to the shape of its polarization ellipse [3]. A simple and effective approach for polarizing the light beam after the source adopts a single polarizer fabricated from birefringent crystals. In ideal form, this optical element permits one component of the incident beam to pass through, that having linear polarization parallel to the transmission axis. The component with orthogonal linear polarization along the extinction axis of the

device is diverted and blocked. Optionally, a birefringent retarder can be added after the polarizer which enables generation of elliptically polarized light from the linearly polarized light at the exit of the polarizer. This is accomplished by shifting the phase of the linearly polarized component along the fast axis of the retarder relative to that of the component along the orthogonal slow axis.

Because the interaction of the beam from the source with the optical elements (polarizer, retarder) in general depends on the wavelength of the beam, the process of polarization state generation, step (1), must be considered wavelength by wavelength. This is also the case for the interaction with the sample, and for polarization state detection, steps (2) and (3). If the output of the polarization generator is a continuous distribution of wavelengths, the measurement approach is referred to as spectroscopic ellipsometry [4]. The most widely applied versions of the spectroscopic ellipsometer span wavelength ranges from the ultraviolet to near-infrared (200–2000 nm), corresponding to the ranges possible with readily available lamps (xenon, deuterium, and tungsten-halogen), birefringent polarizers and retarders (quartz, MgF_2), and solid state detectors (silicon, gallium-indium arsenide) and photomultiplier tubes. The spectroscopic ellipsometer range of 200–2000 nm is also of direct applicability for photovoltaic (PV) materials and devices as it encompasses the range of the solar spectrum of greatest interest. Additional spectral ranges for ellipsometry are possible with specialized equipment that probes the physics of PV materials including the terahertz, the mid-infrared, and the vacuum ultraviolet ranges.

2.1.2 Step 2: Interaction with the Sample

The most common approach for probing the sample surface with incident polarized light, step (2), relies on a collimated beam characterized by a single angle of incidence at the planar sample surface. Typical collimated beam sizes in spectroscopic ellipsometry range from 0.5 to 5 mm. A collimated beam is desirable because the interaction of the beam with the sample, as well as with the optical elements in general, depends on the angle of incidence. In some circumstances, for example, small samples or fine scale mapping, the incident beam is focused, enabling beam sizes as small as ~10 μm or less [5]. In the case of a converging beam, the beam-sample interaction can be approximated by a single average angle of incidence if the f-number of the optical system is sufficiently large. Otherwise "effective" ellipsometry data are determined in step (4). Then an angular distribution must be introduced in the determination of useful information on the sample in step (5). In a more recent instrument, a diverging or expanding beam is used to illuminate a stripe along the sample surface, which is then imaged via an additional function provided by the polarization detection system [6]. This allows the deduction of useful uniformity or patterning information along the sample surface in parallel without mapping. In contrast to the imaging approach, mapping would entail moving a collimated or focused beam relative to the fixed sample or moving

the sample relative to the fixed beam. When focusing or expanding beams are used to probe the sample, it must be ensured that the polarization generation and detection elements are operating properly. For example, the semi-field angle of the polarizer must not be exceeded; otherwise leakage of the linear polarization component along the extinction axis will occur. In addition, a mixture of polarization states can be generated at the retarder output when polarized focused or expanded beams are transmitted through the device.

2.1.3 Step 3: Polarization Detection

In step (3), the goal is to determine two parameters that describe the ellipse shape, for example the tilt angle and ellipticity (Q, e), of the polarization state emerging upon reflection from the sample. If a reflectance measurement is performed simultaneously with ellipsometry, the irradiance of the reflected beam is also measured [3]. Once oblique reflection from the sample has occurred, a plane of incidence is defined which contains the incident and reflected beam propagation directions. Then the tilt angle Q of the incident and reflected beam polarization states are measured relative to the intersection line between the plane of incidence and the plane normal to the beam direction. Although there are varied ways to determine the shape of a polarization ellipse, the simplest method is to measure the light irradiance at different rotation angles that define the transmission axis of a polarizer (called the analyzer) mounted after the sample [7]. The axis of rotation of the analyzer is aligned with the beam direction, and the reference coordinate system for the rotation angle of the transmission axis is the same as that used for Q. This simplest rotating analyzer approach has accuracy limitations for the detection of polarized light with small ellipticity e. For this reason, a rotatable retarder (often referred to as a rotating compensator in this role) can be used immediately after the sample in conjunction with a fixed (non-rotating) analyzer mounted after the retarder. Then the irradiance is measured at different angles of the fast axis of the retarder. This approach provides more uniform accuracy in measuring the full range of reflected beam polarization states, including tilt angles Q: $-90° < Q \leq 90°$ and ellipticities e: $-1 \leq e \leq 1$. Here, $e > 0$ and $e < 0$ refer to right and left elliptical polarization states, respectively, using the convention of this chapter.

Based on this discussion, it is clear that different ellipsometer configurations using fixed and rotating optical elements can be used [7]. The simplest as described in the previous paragraph can be denoted PSA_r, where P designates the polarizer, S the sample, and A the analyzer. The subscript 'r' identifies the element that is rotated about its optical axis to measure the polarization state. In this simple configuration, the polarization state generator consists of a single fixed polarizer so that the sample is illuminated with linearly polarized light (with $e = 0$). The configuration described in the previous paragraph in which the retarder is rotated is designated PSC_rA, where C designates the retarder or compensator. Considerable effort has been devoted to optimizing polarization generation and detection for sample

analysis with highest accuracy and precision. In this effort, advantages are obtained by placing the rotating compensator in front of the sample as part of the polarization generator, yielding the configuration PC_rSA. The reason is that variations in sample alignment perturb polarization state detection less strongly when detection is performed with a single fixed analyzer. It should be noted that the PSC_rA and PC_rSA are symmetric configurations, and for purely polarized incident and reflected beams, they provide similar sample measurement capabilities.

Polarization detection system components in addition to the polarization analyzer are needed, of course. When the light reflected from the sample is single wavelength or quasi-monochromatic, a single detector element such as a photomultiplier tube or a silicon photodiode can be used for irradiance detection at the different angles of the rotating optical element (analyzer or compensator). When multiple wavelength or broadband light is reflected from the sample, spectral dispersion is required before irradiance detection can proceed. In one approach, spectroscopy can be performed serially using a spectrometer in conjunction with a single detector element [8]. The spectrometer is stepped via rotation of a grating through a series of wavelengths, and at each wavelength, the irradiance is measured at the different optical element angles. A much higher speed approach for spectroscopic ellipsometry involves using a spectrograph and a linear detector array which measures all wavelengths in parallel at each of the angles of the rotating optical element. This latter approach can reduce the measurement time for spectroscopic ellipsometry from hours/minutes to tens of milliseconds [9]. A more advanced detection system for imaging spectroscopic ellipsometry using an expanded incident beam incorporates a silicon charge-coupled device as a two-dimensional detector array. One index of the array spans the wavelength, and the second index of the array spans the position along a line on the sample surface which is in turn imaged along the length of the spectrograph slit [10].

2.1.4 Step 4: Determination of Ellipsometry Data

Step (4) of the ellipsometry measurement is most easily handled for the commonly encountered situation in PV materials and device analysis—when a pure polarization state is reflected from the sample and the sample is isotropic. Rather than using the shapes of the incident and reflected beam polarization states, the optical electric fields associated with the polarization states are resolved into their p and s orthogonal vector components [2]. The p-direction is parallel to the plane of incidence whereas the s-direction is perpendicular. The p/s ratio of the amplitudes and the p-s difference in the phases represent the most mathematically convenient method for describing the pure polarization states of the incident and reflected beams in oblique reflection. Then a complex phasor description of the incident and

reflected beam polarization states can be used, and the sample parameters in step (4) can be obtained conveniently as a reflected/incident ratio of phasors.

Under some circumstances the sample can depolarize the incident light beam, leading to a distribution of polarization states in the reflected beam. The most common depolarization effect occurs when the sample is non-uniform over the area of the beam. Depolarization also occurs when components of the incident beam are reflected from top and back surfaces of a thick (>10 μm) semi-transparent substrate medium, and both such beams enter the detection system. This depolarization effect occurs in through-the-glass measurements of PV structures in the superstrate configuration. In measurements that involve superposition of front and back surface reflections from a substrate, depolarization occurs because the path length within the substrate is longer than the coherence length of the light wave, meaning a random phase jump has occurred between the superposed beams. Generally when depolarization occurs, effective values of the ellipsometry data are acquired, and expanded data analysis that accounts for the depolarization is performed in Step (5). For example, information on sample non-uniformity or stress in glass substrates can be deduced from in-depth analyses of depolarization behavior [11].

Most sample structures used in bulk silicon wafer and thin film PV technologies are isotropic. This implies that incident linear p and s-polarization states are unchanged upon reflection [2]. As a result, to obtain a polarization change upon reflection and thus useful information on such samples, the incident polarization state must consist of a superposition of p and s linear polarization states. In other words if $e = 0$, implying linear polarized light, then Q must not be 0° or 90°. For the same reason, the light beam must reflect from the sample at oblique incidence in order to generate a polarization state change that provides sample information in ellipsometry. The polarization state change for an isotropic sample can be expressed as the ratio of the phasors describing the reflected and incident polarization states. Because the ratio of two phasors generates a third phasor, then the ellipsometry data for an isotropic sample is given by two parameters, described as the angles (ψ, Δ). A sample that is anisotropic exhibits different properties in response to optical electric fields vibrating along two or three principal axis directions. For such a sample, depending on its orientation, incident p and s linear polarization states can be converted upon reflection to a mixture of linear p and s states. As a result, as many as six parameters are needed to describe the reflection process uniquely. In such cases, a generalized form of ellipsometry is used, implying that the response of the sample to different incident polarization states is determined in the (PCA$_r$, PSC$_r$A) configurations, or different reflected beam polarization states are resolved in the (P$_r$CA, PC$_r$SA) configurations. Such measurements involve performing the ellipsometry experiment with different polarizer or analyzer angles, respectively [12]. Because of the isotropic nature of most PV materials, the treatment of anisotropic samples is beyond the mathematical scope of this chapter.

2.1.5 Step 5: Deduction of Sample Information

In the standard ellipsometry measurement technique to be discussed, two data values (ψ, Δ) are obtained at given (known) wavelength λ_0 and angle of incidence θ_i values. These two data values can provide at most two sample characteristics [2]. If the sample consists of an atomically-smooth, film-free material that can be represented as a single interface, then the complex index of refraction N of the material can be obtained at the wavelength λ_0 of the incident/reflected beams assuming that N is known for the ambient medium. N describes the linear optical properties of an isotropic material and includes as its real part the real index of refraction n and as its imaginary part the extinction coefficient k, i.e. $N = n - ik$. For an ambient medium of vacuum, $n = 1$ and $k = 0$, independent of λ_0, and these values are appropriate for the laboratory ambient medium, as well. Thus, ellipsometry is the preferred method of measuring N for absorbing bulk materials and opaque thin films, e.g. semiconductors and metals that comprise PV devices, at λ_0 values within the spectral range of conventional ellipsometers, from the ultraviolet to near-infrared (200–2000 nm). Because this range covers the solar spectrum, the optical properties deduced here are of direct interest in PV. One limitation of ellipsometry, however, is its inability to measure low k values or low absorption coefficients α, where $\alpha = 4\pi k/\lambda_0$. The ellipsometry measurement is limited by accuracy to $k > 1 \times 10^{-3}$ or $\alpha > 3 \times 10^{2}$ cm^{-1} for $\lambda_0 = 500$ nm. This limitation is not generally encountered in transmittance spectroscopy in which case the ratio of the transmitted irradiance to incident irradiance is determined, and increasing sample thickness may be exploited to measure decreasing α values. The ultimate limitation on accuracy in the determination of both n and k, however, arises from the inability to fabricate an atomically-smooth, film free surface with the intention to achieve the ideal single interface that is assumed in data analysis.

Most PV structures of interest employ single or multiple thin films on a substrate. If the sample consists of a non-absorbing film (i.e. with $k = 0$) on a substrate of known N, then n of the film and its thickness d can be determined from the two data values (ψ, Δ) within certain limitations (i.e. if an approximate thickness is available to identify the appropriate value from multiple solutions) [2]. Because of the high sensitivity in the measurement of Δ, ellipsometry can detect changes in the nominal thickness of a surface layer equivalent to 0.01 monolayers. In fact, the accuracy in the measurement of thickness by ellipsometry, typically 0.1–0.2 nm, arises from the inability of the real films—with their surface and interfacial imperfections—to be simulated by the ideal laminar optical models assumed in data analysis. Because of the high sensitivity and accuracy in the determination of thickness, ellipsometry is the most widely applied method for the analysis of non-absorbing layers on semiconductors and dielectrics, such as anti-reflection coatings on PV device structures. An absorbing, but semi-transparent, thin film on a known substrate surrounded by a known ambient medium can be modeled as a two interface system. Three parameters describe this system at a given wavelength $\{d, (n, k)\}$ where the added parameter over the one interface system is the film thickness d. Given two ellipsometry data values, (ψ, Δ), determination of $\{d, (n, k)\}$

is not possible. As a result, multiple measurement capabilities and associated data analysis must be developed to handle even the simplest situation of a single thin film.

Spectroscopic ellipsometry is the most common multiple measurement strategy for determining useful information on thin film samples [13]. In a spectroscopic ellipsometry measurement, the data consist of $2N_\lambda$ values, $\{(\psi_i, \Delta_i); i = 1, \ldots N_\lambda\}$, where N_λ is the number of spectral points. Because the useful sample information for a single unknown film on a known substrate is $\{d, (n_i, k_i); i = 1, \ldots N_\lambda\}$ (assuming ambient vacuum or air), there will always be one more sample parameter than available experimental data values. The problem is solvable by expressing $N = n - ik$ as an analytical complex function of wavelength, which reduces the number of unknown parameters in the data analysis problem. In fact, the complex dielectric function, given by $\varepsilon = \varepsilon_1 - i\varepsilon_2 = N^2 = (n - ik)^2$, where ε_1 and ε_2 are its real and imaginary parts, can expressed assuming a sum of N_L damped, driven harmonic (or Lorentz) oscillators, each defined in turn by an amplitude A_{Ln}, resonance energy E_{Ln}, and broadening parameter Γ_{Ln}, (and possibly additional parameters for more general oscillator forms) [14]. A constant contribution to the real part of ε, ε_{1o}, can also be added. Thus, the useful information to be determined becomes $\{\varepsilon_{1o}, (A_{Ln}, E_{Ln}, \Gamma_{Ln}); n = 1, \ldots, N_L\}$, which can then be smaller than the number of data values as long as $3N_L + 1 < 2N_\lambda$. Thus, conversion of the spectra in n and k to analytical forms based on physical principles enables data analysis in terms of wavelength-independent parameters. Such analysis can be handled by non-linear least-squares regression. Using such an analysis approach, even more complicated problems than a single film on a substrate can be solved through spectroscopic ellipsometry. For multilayer stacks, however, further reduction in the number of free parameters is desirable. For example, the dielectric functions of some layers can be fixed at those obtained in measurements of single layers, and/or the dielectric function parameters $\{\varepsilon_{1o}, (A_{Ln}, E_{Ln}, \Gamma_{Ln}); n = 1, \ldots, N_L\}$ can be expressed as functions of a smaller set of physical properties such as void fraction, composition, stress, grain size, etc.

Other multiple measurement approaches can be applied or combined with the spectroscopic measurement to extract useful sample information. The angle of incidence can be varied which, when combined with the wavelength variation, is referred to as variable angle of incidence spectroscopic ellipsometry. Performing multiple ellipsometry measurements of the same spot on the sample in-situ during its deposition is referred to as real time ellipsometry. For a film growing uniformly versus thickness (i.e. with a thickness independent complex index N), this approach enables analysis of the (n, k) values at a single wavelength and the thickness versus time. For samples that are spatially non-uniform in thickness over the area of the sample, but uniform in N, mapping ellipsometry can serve the same multiple measurement role as real time ellipsometry. Real time and mapping *spectroscopic* ellipsometry can be performed for even greater useful information on PV materials. In summary, the wavelength variation in spectroscopic ellipsometry is of greater interest in PV applications than any other single measurement parameter variation because the outcome of the experiment includes not only layer thicknesses, but also

the wavelength dependence of (n, k). The combined information is of utmost importance in the analysis of PV devices because it can be applied to predict the optical performance of the multilayer stack, including the overall reflectance, individual layer absorbances, and overall transmittance. Furthermore with wavelength as the single variable, spectroscopic ellipsometry data can be collected over a wide spectral range in a time as short as 16 ms using a detection system consisting of a spectrograph and a linear detector array [9].

The influence of non-ideality of surfaces and thin films on spectroscopic ellipsometry data and the need for incorporating such non-ideality in data analysis was identified early in the development of the data analysis techniques [15]. Standard data analysis procedures in ellipsometry are based on the assumption of mathematically abrupt planar surfaces and interfaces, relying on Fresnel equations derived from boundary conditions on the electromagnetic fields. In practice, surfaces and interfaces exhibit roughness or mixed inter-diffusion regions having in-plane and out-of-plane scales that can vary considerably. If homogeneous roughness exists at surfaces or interfaces with an in-plane correlation length and out-of-plane length (thickness) scales of less than $\sim 0.1\lambda_0$, i.e. so-called “microscopic roughness”, then analysis of ellipsometry data can proceed by the standard methods. To do this, intermediate layers can be incorporated into the optical model at film surfaces or interfaces that simulate the roughness region. The dielectric functions of such intermediate layers can be approximated using an effective medium theory with the volume fractions of the underlying and overlying media as fixed or variable parameters [16]. Inter-diffusion regions can also be modeled similarly with the difference being in the assignment of the dielectric function as a chemically distinct phase rather than a mixture of phases [17]. In comparison to reflectance spectroscopy, which relies on irradiance measurements, spectroscopic ellipsometry provides very good immunity to inhomogeneous surface features such as localized defects that scatter light irradiance out of the specular beam. If the sample is very rough or inhomogeneous with a correlation length of the structure greater than $\sim 0.1\lambda_0$, however, conventional ellipsometry may fail due to light scattering that can depolarize the beam and lead to unmanageable complexities in data analysis. If the correlation length of the surface inhomogeneity is greater than $\sim 10\lambda_0$, however, then high resolution focusing and mapping methods or imaging spectroscopic ellipsometry can be applied to characterize the sample as described in earlier subsections.

2.1.6 Overview

The component of this chapter on the formalisms of the measurement technique of ellipsometry starts in Sect. 2.2 with a mathematical description of the polarization of light waves relevant for steps (1–3). Section 2.2 includes the vector description that incorporates phasors to describe the orthogonal electric field components, taken

as projections along the x and y-directions of a general right-handed Cartesian coordinate system such that z defines the propagation direction.

In Sect. 2.3, the treatment will focus on the polarization change that occurs upon reflection of polarized light from an ideal sample, and two ways of describing the ellipsometry angles (ψ, Δ) mathematically in terms of beam polarization and isotropic sample properties, specifically describing step (4). In this case, the general x-y coordinate system of the polarization state of Sect. 2.3 becomes the p-s coordinate system in the plane perpendicular to the beam propagation direction. Here p and s are the axes parallel and perpendicular to the plane of incidence for the incident and reflected beams, and z continues to serve as the propagation directions of the two beams.

A discussion of the foundations of data analysis, step (5) must start with a description of the complex index of refraction and complex dielectric functions of materials; this description is provided in Sect. 2.4. The simplest step (5) analysis problem will be addressed first in Sect. 2.5, namely, a single specularly reflecting surface of an isotropic medium, and how the complex dielectric function or complex index of refraction can be deduced from (ψ, Δ) for this ideal sample situation. Also treated in Sect. 2.5 is the general mathematical problem of multilayer samples analyzed applying matrix methods that enable computation of (ψ, Δ) for the arbitrary m-layer system. This method serves as the basis for non-linear least-squares regression analysis which starts with a model for the sample incorporating wavelength-independent structural parameters (e.g., thicknesses as well as composite and roughness layer volume fractions) and optical parameters (amplitudes, resonance energies, and broadening parameters). The analysis determines the parameters in a simulation of the (ψ, Δ) spectra that best fits the experimental results. As a third and final topic, the approach applied for data reduction and analysis in through-the-glass ellipsometry is described.

The last component of this chapter, Sect. 2.6, is more advanced and focuses on the mathematical methods used to analyze general ellipsometer configurations useful for steps (1)–(3). As an example, one of the most powerful spectroscopic ellipsometer configurations is presented, namely that based on the PC_rSA sequence of optical elements, and the importance of instrument calibration is discussed as it is required for data reduction in step (4).

2.2 Polarization of Light

Initially, plane wave propagation of light in free space is considered [2]. A light wave is a transverse wave, meaning that the wave vibrations occur perpendicularly to the direction of wave propagation which is the ray direction, defined here as the z axis. The vibrations of a light wave are associated with the wave's electric field **E** and magnetic induction **B** vectors. It should be noted that because **E** and **B** are vector quantities with magnitude and direction, then they define a polarization property of the wave. Because the electric forces are far stronger than the magnetic

forces when a light wave interacts with a solid surface, then one is concerned with the **E**-field in a description of the polarization of the light wave. As a result of the transverse nature of the wave propagating along z, the **E**-field is confined to planes parallel to the x-y plane, considering its vibration at a given location versus time or its oscillation with distance along z at a given time. In these planes, the **E**-field vector is resolved along reference x and y axes and the two vector components, although having the same frequency and wavelength, can differ in their amplitude and phases; these differences result in the different polarization states. Thus, the **E**-field of a plane wave can be expressed as:

$$\mathbf{E}(z,t) = E_{0x}\cos[\omega t - (2\pi/\lambda_0)z + \delta_x]\hat{\mathbf{x}} + E_{0y}\cos[\omega t - (2\pi/\lambda_0)z + \delta_y]\hat{\mathbf{y}}. \tag{2.1}$$

In this equation, $\hat{\mathbf{x}}$ and $\hat{\mathbf{y}}$ are unit vectors along the x and y-directions, E_{0x} (>0) and E_{0y} (>0) are the vector component amplitudes, which do not depend on location for a plane wave, and the cosine function arguments are expressed in radians. In addition, ω is the frequency of the light wave with $\tau = 2\pi/\omega$ as the temporal period and λ_0 as the spatial period, or wavelength in free space (in laboratory ambient medium, as well). This means that the arguments of the cosine functions advance by 2π (implying they repeat) when time advances by $\Delta t = \tau$ and when distance increases along z by $\Delta z = \lambda_0$.

The shape of the polarization state is determined by the amplitude ratio $|\gamma| = E_{0x}/E_{0y}$ of the two field components and the phase difference $\delta = \delta_x - \delta_y$ between the arguments of the two cosine functions. The ratio and phase difference conventions y/x and $y - x$ are also used [2]; however, once the coordinate system is changed to the p-s coordinate system for polarized light reflection with $x \to p$ and $y \to s$, then the ratio p/s and phase difference $p - s$ become the universally accepted conventions. The relationships between the shape parameters of tilt and ellipticity (Q, e) and the field parameters of amplitude ratio and phase difference ($|\gamma|$, δ) are given in Fig. 2.2. When the phase difference is $2n\pi$ radians (n an integer), then the light beam is linearly polarized at an angle $Q = \tan^{-1}(1/|\gamma|)$; $0 \le Q \le \frac{1}{2}\pi$, as measured with respect to the x-axis. When the phase difference is $(2n + 1)\pi$ radians, then the light beam is linearly polarized at an angle $Q = -\tan^{-1}(1/|\gamma|)$; $-\frac{1}{2}\pi < Q < 0$, as measured with respect to the x-axis. If $E_{0x} = E_{0y}$ (or $|\gamma| = 1$), then left circular polarization results when $\delta_x - \delta_y = (2n + \frac{1}{2})\pi$ radians, and right circular polarization results when $\delta_x - \delta_y = (2n - \frac{1}{2})\pi$ radians. These are special cases as indicated in Fig. 2.3; for any other phase shift values, the polarization is more general—elliptical polarization, left for positive phase shifts over the range $0 < \delta < \pi$ and right for negative phase shifts over the range $-\pi < \delta < 0$. If one fixes the location $z = 0$ along its direction of travel, the polarization of the wave describes the motion of the endpoint of the **E**-field within the x-y plane versus time. For right circular and elliptical polarizations, the **E**-field rotates clockwise when the beam is propagating toward the observer; for left polarizations the **E**-field rotates counter-clockwise. If one views the fields as a snapshot at a fixed time, the progression with

Conversion Equations between Polarization Shape [(Q, e)] and (Field Amplitude Ratio, Phase Difference) [$|\gamma| \equiv E_{0x}/E_{0y}$, $\delta \equiv \delta_x - \delta_y$]

E-field endpoint shape depends only on the x/y amplitude ratio and the x–y phase difference

$$\delta \equiv \delta_x - \delta_y = \tan^{-1}\left\{\frac{-e\,(1+\tan^2 Q)}{(1-e^2)\tan Q}\right\}$$

$$Q = \tfrac{1}{2}\tan^{-1}\left\{\frac{2|\gamma|\cos\delta}{|\gamma|^2 - 1}\right\}$$

$$|\gamma| \equiv \frac{E_{0x}}{E_{0y}} = \left\{\frac{1 + e^2\tan^2 Q}{e^2 + \tan^2 Q}\right\}^{1/2}$$

$$e = \pm\left\{\frac{|\gamma|^2\tan^2 Q - 2|\gamma|\tan Q\cos\delta + 1}{|\gamma|^2 + 2|\gamma|\tan Q\cos\delta + \tan^2 Q}\right\}^{1/2}$$

δ: 90°; 180° 2 | 1 0°; −180° 3 | 4; −90°

NOTES:
Quadrant corrections for δ:
If e < 0 and Q < 0 add 180° to δ (4th → 2nd)
If e > 0 and Q < 0 subtract 180° from δ (1st → 3rd)

NOTES:
If tanQ cosδ < 0 the following changes are made to the final results of the above equations:
$e \to e^{-1}$ and $Q \to Q \pm 90°$; the sign of Q ± 90° is chosen to ensure that $-90° < Q \le 90°$
For left elliptical polarization e < 0
For right elliptical polarization e > 0.

Fig. 2.2 Relationships between the two different representations of polarized light described in this chapter

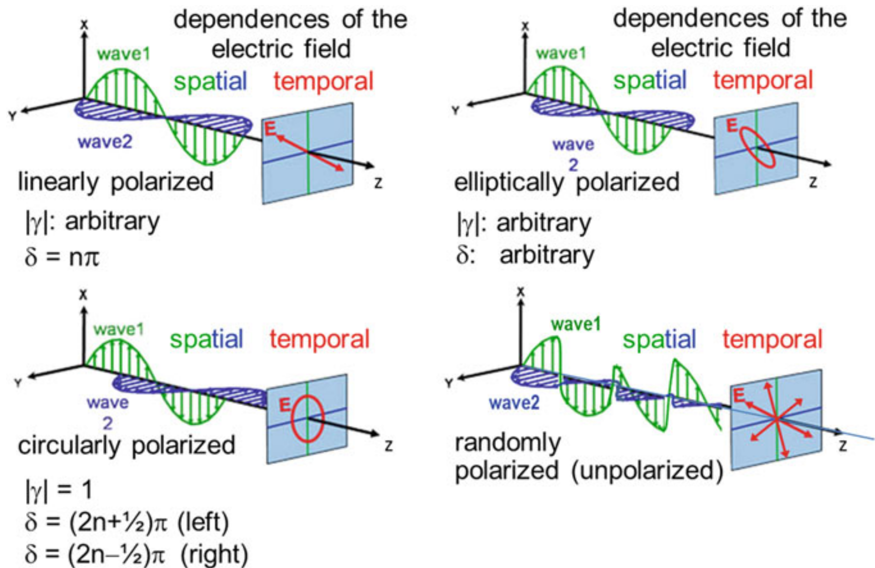

Fig. 2.3 Examples depicting the electric field vector as a function of position along z. Here $|\gamma| = E_{0x}/E_{0y}$ is the x/y ratio of the two field components and $\delta = \delta_x - \delta_y$ is the $x - y$ phase difference of the field components. For circular and elliptical polarization, the trajectory of the vector endpoint is shown versus position and time. At the front of each plot the evolution of the field vector is shown versus time at a fixed position. The direction of travel is along $+z$, out of the page. Unpolarized light consists of a random progression of different polarization states versus position and time [Adapted figure with acknowledgment to J. A. Woollam Co.]

distance along the positive z axis is opposite: right $\Rightarrow$ counterclockwise rotation; left $\Rightarrow$ clockwise rotation.

The mathematics of polarization can be described in different ways. In addition to the description of (2.1), polarization can be described as a column vector:

$$\mathbf{E}(z,t) = \begin{pmatrix} E_{0x}\cos[\omega t - (2\pi/\lambda_0)z + \delta_x] \\ E_{0y}\cos[\omega t - (2\pi/\lambda_0)z + \delta_y] \end{pmatrix}, \tag{2.2}$$

with the x and y components as the (1, 1) and (2, 1) positions of the column, respectively. To facilitate the mathematics of oscillations, it is convenient to convert (2.1) to phasor notation. Considering $z = 0$, the $\mathbf{E}$-field vector is:

$$\mathbf{E}(t) = E_x\hat{\mathbf{x}} + E_y\hat{\mathbf{y}} = E_{0x}\cos(\omega t + \delta_x)\hat{\mathbf{x}} + E_{0y}\cos(\omega t + \delta_y)\hat{\mathbf{y}}. \tag{2.3}$$

In phasor notation, given by $e^{i(\omega t + \delta_j)} = \cos(\omega t + \delta_j) + i\sin(\omega t + \delta_j)$ with $j = (x, y)$ and with i the imaginary unit, the field becomes:

$$\mathbf{E}(t) = E_{0x}\,e^{i(\omega t + \delta_x)}\hat{\mathbf{x}} + E_{0y}\,e^{i(\omega t + \delta_y)}\hat{\mathbf{y}}. \tag{2.4}$$

In this notation, for mathematical convenience, the oscillatory motion of real E_x along the x-axis has been converted to circular motion of complex E_x in the complex [Real(E_x), Imaginary(E_x)] plane as illustrated in Fig. 2.4. The same conversion has been applied to the y component E_y. To regain an experimental observable, one must project the complex phasor of each vector component onto the real axis by taking the real part of $\mathbf{E}$, Re{$\mathbf{E}$}:

$$\mathrm{Re}\,\{\mathbf{E}(t)\} = \mathrm{Re}\,\{E_{0x}\,e^{i(\omega t + \delta_x)}\}\,\hat{\mathbf{x}} + \mathrm{Re}\,\{E_{0y}\,e^{i(\omega t + \delta_y)}\}\hat{\mathbf{y}} \tag{2.5a}$$

$$= E_{0x}\,\cos(\omega t + \delta_x)\,\hat{\mathbf{x}} + E_{0y}\,\cos(\omega t + \delta_y)\hat{\mathbf{y}}. \tag{2.5b}$$

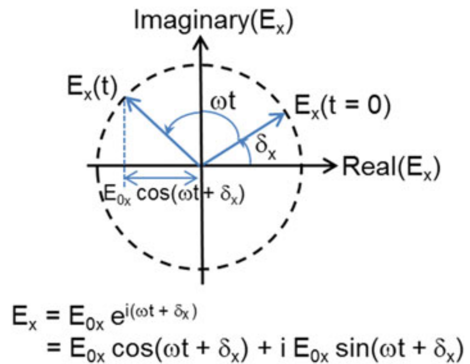

Fig. 2.4 Phasor notation for the x component of the optical electric field associated with a polarization state

Using the phasor notation, the column vector of (2.2) can be written as:

$$\mathbf{E}(z,t) = \mathrm{e}^{-2\pi i(z/\lambda_0)} \begin{pmatrix} E_{0x}\,\mathrm{e}^{i(\omega t+\delta_x)} \\ E_{0y}\,\mathrm{e}^{i\left(\omega t+\delta_y\right)} \end{pmatrix}. \tag{2.6}$$

For the purposes of describing the polarization state of a wave at a given point in space, one is primarily interested in the ratios of the amplitudes of the field components along x and y and the phase difference between x and y. So if one divides each component of the vector by the y component of the vector, $E_{0y}\,\mathrm{e}^{-2\pi i(z/\lambda_0)}\;\mathrm{e}^{i\left(\omega t+\delta_y\right)}$, then one arrives at a simpler vector $\mathbf{P}$ to describe the polarization state:

$$\mathbf{P} = \begin{pmatrix} \dfrac{E_{0x}}{E_{0y}}\,\mathrm{e}^{i\left(\delta_x-\delta_y\right)} \\ 1 \end{pmatrix} = \begin{pmatrix} |\gamma|\,\mathrm{e}^{i\delta} \\ 1 \end{pmatrix}. \tag{2.7}$$

This vector approach is convenient for use in determining how an optical element, for example, a polarizer or a reflecting surface modifies the polarization state. The approach will be utilized in Sect. 2.3. Other texts normalize to the x-component [2]; however, the reason for deviating from this convention becomes clear when the reflection process is treated.

Using the vector of (2.7), a convenient second method for describing polarization is available. This second method involves plotting the polarization state as a number γ, the (1, 1) component of $\mathbf{P}$, in the complex plane:

$$\gamma = \frac{E_{0x}\,\mathrm{e}^{i(\omega t+\delta_x)}}{E_{0y}\,\mathrm{e}^{i\left(\omega t+\delta_y\right)}} = \frac{E_{0x}}{E_{0y}}\,\mathrm{e}^{i\left(\delta_x-\delta_y\right)} = |\gamma|\,e^{i\delta}. \tag{2.8}$$

Figure 2.5 shows examples of the polarization state shapes associated with the locations of γ in the complex plane [2].

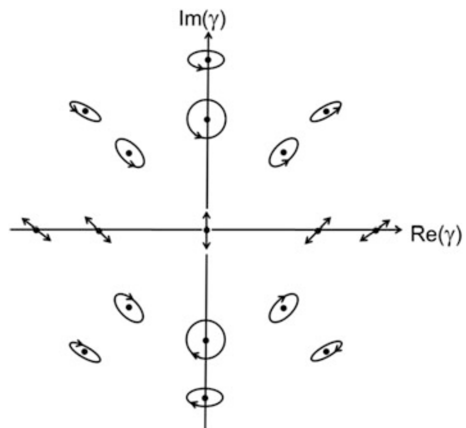

Fig. 2.5 The shapes of the polarization states for γ in the complex plane. This plot uses the complex number $\gamma = \left(E_{0x}/E_{0y}\right)\mathrm{e}^{i\left(\delta_x-\delta_y\right)}$ to describe the polarization state. Thus, γ includes as its amplitude (>0) the x/y ratio of the two amplitudes and as its phase the $x-y$ difference between the phases of the two vector components of the **E**-field

2.3 Oblique Reflection of Polarized Light

In the process of oblique reflection of a plane light wave from a planar, specularly reflecting surface, the incident and reflected propagation directions or rays form a plane, the plane of incidence. The perpendicular or normal to the surface also lies within the plane of incidence and the angles of incidence and reflection are measured from this perpendicular (see Fig. 2.6) [2]. The plane of incidence allows one to define a unique Cartesian coordinate system for the **E**-fields of each of the incident and reflected waves, the *p*-*s* system. The *p*-direction (analogous to *x*) is defined to lie parallel to the plane of incidence and the *s*-direction (analogous to *y*) is defined to lie perpendicular to the plane of incidence. Thus, if the ray direction is defined as *z*, then the *p*-*s*-*z* axes define a right-handed Cartesian coordinate system for each wave. It should be noted that in the reflection process, the *s*-direction remains unchanged, whereas the *p* and *z* axes change their orientation so as to ensure that the angle of incidence equals the angle of reflection.

Using the phasor notation, and assuming that the reflection process at the interface occurs at $z = 0$, then one can write the electric fields of the incident and reflected waves in their individual *p*-*s*-*z* coordinate systems, respectively, as:

$$\mathbf{E}_i(0,t) = E_{pi}\,\mathrm{e}^{i\left(\omega t + \delta_{pi}\right)}\hat{\mathbf{p}} + E_{si}\,\mathrm{e}^{i(\omega t + \delta_{si})}\hat{\mathbf{s}}, \tag{2.9a}$$

$$\mathbf{E}_r(0,t) = E_{pr}\,\mathrm{e}^{i\left(\omega t + \delta_{pr}\right)}\hat{\mathbf{p}} + E_{sr}\,\mathrm{e}^{i(\omega t + \delta_{sr})}\hat{\mathbf{s}}. \tag{2.9b}$$

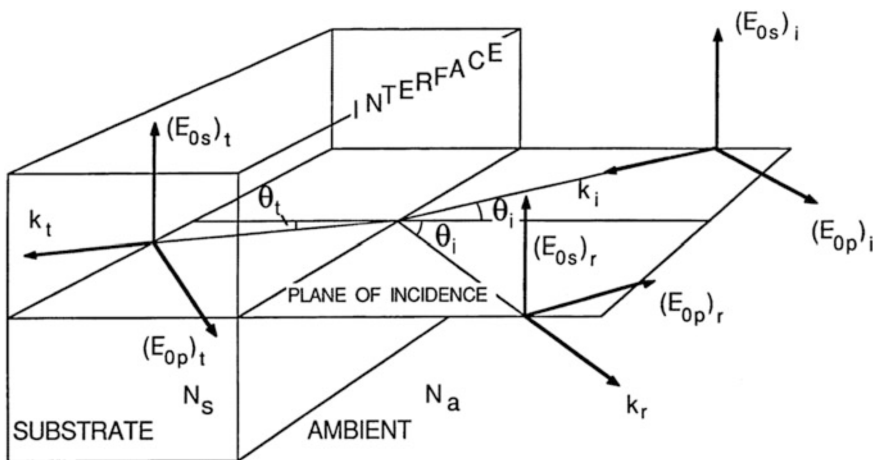

Fig. 2.6 Geometry of the reflection process at the interface between two media showing the incident (*i*), reflected (*r*), and transmitted (*t*) electric field components in the *p* and *s*-directions. The ray or propagation directions are designated by the vectors **k**, and the angles of incidence and transmission are θ_i and θ_t. The two media are assumed to have complex indices of refraction N_a for the ambient and N_s for the substrate although, in a single interface reflection, N_a is most often a non-absorbing medium such that $N_a = n_a$, a real quantity

In these equations, $\hat{\mathbf{p}}$ and $\hat{\mathbf{s}}$ indicate the unit vectors for the individual coordinate systems, and the subscripts 'i' and 'r' distinguish the incident and reflected waves. Also the subscripts '0' on the field amplitudes are now suppressed for simplicity. It is noted that ω is unchanged upon reflection, which is a characteristic of linear optical processes at low light irradiance levels. To determine the irradiances associated with the incident and reflected waves, two operations must be taken as shown:

$$I_i = (1/2)\varepsilon_0 c \mathbf{E}_i^* \cdot \mathbf{E}_i = (1/2)\varepsilon_0 c \left(E_{pi}^2 + E_{si}^2\right), \tag{2.10a}$$

$$I_r = (1/2)\varepsilon_0 c \mathbf{E}_r^* \cdot \mathbf{E}_r = (1/2)\varepsilon_0 c \left(E_{pr}^2 + E_{sr}^2\right). \tag{2.10b}$$

First the complex conjugate of $\mathbf{E}$, indicated $\mathbf{E}^*$ and obtained from $\mathbf{E}$ through the change $i \to -i$, is taken, and then the scalar product indicated by '•' is applied. These operations yield an observable quantity. In (2.10a), (2.10b), ε_0 is the permittivity of free space and c is the speed of light; thus, the equations are based on the assumption that the incident medium is vacuum or air.

The polarization states associated with the incident and reflected waves can also be defined as numbers in the complex plane:

$$\gamma_i = \frac{E_{pi} e^{i(\omega t + \delta_{pi})}}{E_{si} e^{i(\omega t + \delta_{si})}} = \frac{E_{pi}}{E_{si}} e^{i(\delta_{pi} - \delta_{si})}, \tag{2.11a}$$

$$\gamma_r = \frac{E_{pr} e^{i(\omega t + \delta_{pr})}}{E_{sr} e^{i(\omega t + \delta_{sr})}} = \frac{E_{pr}}{E_{sr}} e^{i(\delta_{pr} - \delta_{sr})}. \tag{2.11b}$$

Equations (2.10a), (2.10b) and (2.11a), (2.11b) describe the irradiance and polarization states associated with the incident and reflected waves and can be considered as establishing the basis of reflectance and ellipsometry, respectively; this will be demonstrated shortly. Note that in forming the irradiance, information on the phase difference of the wave components is lost whereas it is retained in considering the polarization. For this reason ellipsometry is a more powerful experiment than reflectance, but more challenging to perform as will be discussed in Sect. 2.6.

One can consider the surface as acting on the incident wave and changing its irradiance and polarization. To describe this process, the complex amplitude reflection coefficients (or Fresnel reflection coefficients) of the surface are defined individually for the p and s $\mathbf{E}$-field components as follows:

$$r_p = \frac{E_{pr} e^{i(\omega t + \delta_{pr})}}{E_{pi} e^{i(\omega t + \delta_{pi})}} = \frac{E_{pr}}{E_{pi}} e^{i(\delta_{pr} - \delta_{pi})}, \tag{2.12a}$$

$$r_s = \frac{E_{sr} e^{i(\omega t + \delta_{sr})}}{E_{si} e^{i(\omega t + \delta_{si})}} = \frac{E_{sr}}{E_{si}} e^{i(\delta_{sr} - \delta_{si})}. \tag{2.12b}$$

Thus, each Fresnel reflection coefficient describes the ability of the reflecting surface to reduce the amplitude of the reflected field component relative to the incident field component and shift the phase upon reflection. The ratio of these reflection coefficients is considered a characteristic of the reflecting sample and is assigned the complex quantity ρ, which is a function of the wavelength of the source (or the energy of the emitted photons) as well as the angle of incidence. The phasor description of ρ is given as $\rho \equiv \tan \psi \exp(i\Delta)$, with its amplitude being $\tan \psi$ and its phase being Δ. The quantities (ψ, Δ) are described as the ellipsometry angles. Thus:

$$\rho = \tan \psi e^{i\Delta} = \tan \psi \cos \Delta + i \tan \psi \sin \Delta \equiv \frac{r_p}{r_s} = \frac{\left(\frac{E_{pr}}{E_{pi}}\right) e^{i\left(\delta_{pr} - \delta_{pi}\right)}}{\left(\frac{E_{sr}}{E_{si}}\right) e^{i(\delta_{sr} - \delta_{si})}}. \tag{2.12c}$$

In order to obtain such reflection characteristics of a sample, one can perform reflectance spectroscopy, which involves measuring the reflectance R as a function of wavelength λ_0. R is the ratio of the reflected to incident irradiances according to:

$$R = \frac{I_r}{I_i} = \frac{E_{pr}^2 + E_{sr}^2}{E_{pi}^2 + E_{si}^2}. \tag{2.13}$$

Alternatively, R can be plotted as a function of the energy of the photons $E = hc/\lambda_0$. Here c is the speed of light in free space and h is Planck's constant. The reflectance experiment is relatively easy to perform, and in general unpolarized light is used, yielding the result $R = ½(|r_p|^2 + |r_s|^2)$ expressed in terms of the sample properties. Much of the challenge of reflectance spectroscopy involves calibration of the incident irradiance which can be done with a standard sample or by measuring the beam with a separate calibrated detector. In either case, inaccuracies are introduced when moving the sample between the two measurements or in detector calibration. Most commercial instruments use dual-beam spectrophotometers to overcome these accuracy issues.

An alternative approach for studying the properties of the reflecting surface is spectroscopic ellipsometry, which can be defined as a measurement of the polarization state change versus λ_0 or E, in turn expressed as a ratio of the reflected to incident polarization states. Thus, one can write:

$$\frac{\gamma_r}{\gamma_i} = \frac{\left(\frac{E_{pr}}{E_{sr}}\right) e^{i\left(\delta_{pr} - \delta_{sr}\right)}}{\left(\frac{E_{pi}}{E_{si}}\right) e^{i\left(\delta_{pi} - \delta_{si}\right)}}. \tag{2.14}$$

It is easy to see that by rearranging terms, this polarization state ratio, analogous to the irradiance ratio that defines reflectance, provides $\rho = \tan\psi\, e^{i\Delta}$ directly. Thus, the ellipsometry experiment on an isotropic sample can be described as measuring equivalently a ratio of Fresnel reflection coefficients or a ratio of polarization states. The two approaches yield the same two informative expressions for (ψ, Δ) expressed with different arrangements of the amplitudes and phases. The results in terms of the ratio of the p and s reflection coefficients are:

$$\tan\psi = \frac{\left(\frac{E_{pr}}{E_{pi}}\right)}{\left(\frac{E_{sr}}{E_{si}}\right)}; \qquad \Delta = \left(\delta_{pr} - \delta_{pi}\right) - \left(\delta_{sr} - \delta_{si}\right). \tag{2.15a}$$

The equivalent results in terms of the ratio of the reflected and incident polarizations are:

$$\tan\psi = \frac{\left(\frac{E_{pr}}{E_{sr}}\right)}{\left(\frac{E_{pi}}{E_{si}}\right)}; \qquad \Delta = \left(\delta_{pr} - \delta_{sr}\right) - \left(\delta_{pi} - \delta_{si}\right). \tag{2.15b}$$

Now to describe ellipsometry in words, the following terminology can be proposed to explain the measurement:

Amplitude ratio ⇔ p/s
Phase difference ⇔ $p - s$
Relative amplitude ⇔ r/i
Phase shift ⇔ $r - i$.

The underlying concept of these assignments is that the interest lies in the amplitude of the reflected beam relative to the incident beam in the reflection process and also the phase shift that occurs upon reflection. Furthermore these behaviors upon reflection differ for the p and s linear polarizations. Thus, one can describe Δ and tan ψ in words as the:

- phase difference ($p - s$) shift ($r - i$) upon reflection and the
- ratio (p/s) of relative (r/i) reflected electric field amplitudes, or equivalently as the:
- phase shift ($r - i$) difference ($p - s$) between components and the
- relative (r/i) electric field amplitude ratio (p/s) for the components.

The terminology results from considering ellipsometry equivalently as measuring either a ratio of polarization states or, more directly for sample analysis, a ratio of the Fresnel reflection coefficients.

Another approach to understanding an ellipsometry experiment is to consider the reflecting surface of an isotropic sample as an optical element described by a 2 × 2 complex matrix $\mathbf{J}_S$ acting on a 2 × 1 complex vector $\mathbf{P}_i$, which is the incident beam polarization state, to yield $\mathbf{P}_r$ the reflected beam polarization state. The 2 × 2

matrix is called the Jones matrix of the sample and the 2 × 1 vector is called the Jones vector of the polarization state. The matrix equation can be written as:

$$\mathbf{P}_r = \mathbf{J}_S \mathbf{P}_i. \tag{2.16}$$

It is easy to see from the definitions of the Fresnel coefficients that the appropriate equation is:

$$\begin{pmatrix} E_{pr}\,\mathrm{e}^{i\delta_{pr}} \\ E_{sr}\,\mathrm{e}^{i\delta_{sr}} \end{pmatrix} = \begin{pmatrix} r_p & 0 \\ 0 & r_s \end{pmatrix} \begin{pmatrix} E_{pi}\,\mathrm{e}^{i\delta_{pi}} \\ E_{si}\,\mathrm{e}^{i\delta_{si}} \end{pmatrix}. \tag{2.17}$$

This equation demonstrates that the p and s linear polarization states are the eigenmodes of the reflecting surface. By "eigenmodes", it is meant that when linearly polarized light along the p-direction, which has $E_{si} = 0$, is incident on the surface, then the reflected wave is also p-polarized with $E_{sr} = 0$ (i.e. the reflected and incident beam polarization states are the same). Thus, when linearly polarized light along the s-direction, which has $E_{pi} = 0$, is incident on the surface, then the reflected wave is also s-polarized with $E_{pr} = 0$ (i.e. the reflected and incident polarization states are the same). For any other polarization states, the different complex values of r_p and r_s act on the two field components differently, thus modifying the polarization state, meaning the tilt angle and the ellipticity of the ellipse changes in general. One can factor out the (2, 1) vector component on the left side of (2.17) and one can also factor out the (2, 2) matrix element and the (2, 1) vector component on right side of (2.17) and cancel from both sides. This leads to the simpler equation:

$$\begin{pmatrix} \gamma_r \\ 1 \end{pmatrix} = \begin{pmatrix} \rho & 0 \\ 0 & 1 \end{pmatrix} \begin{pmatrix} \gamma_i \\ 1 \end{pmatrix}. \tag{2.18}$$

This expression yields two equations, one stating that $\gamma_r = \rho\gamma_i$ and the other being trivial (1 = 1). The non-trivial equation states that the ratio of the reflected-to-incident polarization states is simply the p-to-s ratio of the Fresnel reflection coefficients. The factored form of the Jones matrix of the sample in (2.18) will be used to describe the operation of the ellipsometer in Sect. 2.6.

2.4 Optical Properties of Materials

The propagation of electromagnetic radiation in free space can be described by Maxwell's Equations which, in the International System (SI) of units, can be written as [14]:

$$\nabla \cdot \mathbf{E} = \frac{\rho}{\varepsilon_0}, \tag{2.19a}$$

$$\nabla \times \mathbf{E} = -\frac{\partial \mathbf{B}}{\partial t}, \tag{2.19b}$$

$$\nabla \cdot \mathbf{B} = 0, \tag{2.19c}$$

$$\nabla \times \mathbf{B} = \mu_0 \left(\varepsilon_0 \frac{\partial \mathbf{E}}{\partial t} + \mathbf{J} \right), \tag{2.19d}$$

where **E**, **B**, **J**, and ρ represent the spatial averages of microscopic quantities of electric field vector, magnetic induction vector, current density vector, and charge density, respectively. Here ε_0 and μ_0 are the electric permittivity and magnetic permeability of free space, respectively. In order to describe the propagation of electromagnetic radiation in matter, two additional vectors are introduced, the displacement vector **D** and the magnetic field intensity vector **H** given as:

$$\mathbf{D} = \varepsilon_0 \varepsilon \mathbf{E}, \tag{2.20a}$$

$$\mathbf{B} = \mu_0 \mu \mathbf{H}, \tag{2.20b}$$

where ε, the relative electric permittivity or more commonly called the dielectric function, and μ, the relative magnetic permeability, are properties of the material. These quantities can be described using complex scalars for isotropic materials, but second-rank complex tensors are needed for anisotropic materials. They describe the response of the material to propagating electromagnetic radiation and can be described as functions of the frequency $\omega = 2\pi c/\lambda_0$, wavelength λ_0, or photon energy $E = \hbar\omega = hc/\lambda_0$ of the radiation. Here c is the speed of light in free space, $\hbar = h/2\pi$, where h is Planck's constant. Thus, $\varepsilon(E)$ and $\mu(E)$ are called "optical functions" of the material. Here, the medium is assumed to be isotropic, so only scalar functions $\varepsilon(E)$ and $\mu(E)$ are considered.

In the case of a homogeneous medium, there is no spatial dependence of ε and μ, and in a non-magnetic medium the value of μ is unity, the latter relevant for PV materials over the photon energy range of interest. Finally, if it is assumed that the material is electrically neutral, interpreting (2.19a), (2.19b), (2.19c), (2.19d) as spatially averaged behavior, then $\rho = 0$ and this results in further simplification of (2.19a), (2.19b), (2.19c), (2.19d) in materials. The solutions of Maxwell's Equations under these conditions yield polarized transverse electromagnetic plane waves. If the propagation direction of the electromagnetic wave is considered as the z-axis of a Cartesian coordinate system, then the electric field of the electromagnetic plane wave solution can be represented by:

$$\mathbf{E}(z,t) = \{E_{0x}\exp(i\delta_x)\hat{\mathbf{x}} + E_{0y}\exp(i\delta_y)\hat{\mathbf{y}}\}\exp\{i[\omega t - (2\pi N/\lambda_0)z]\}, \quad (2.21)$$

where the function "exp(iz)" is used to denote e^{iz}, the exponential of iz, and $N = \varepsilon^{1/2}$ is the complex index of refraction which depends on wavelength or photon energy. The complex index of refraction can be written as $N = n - ik$, where n is the real part or simply "the index of refraction" and k is the imaginary part or "extinction coefficient". The first term on the right describes the polarization of the wave and the second exponential term describes the oscillation and decay of the wave. Expanding N in terms of its real and imaginary parts yields:

$$\mathbf{E}(z,t) = \{E_{0x}\exp(i\delta_x)\hat{\mathbf{x}} + E_{0y}\exp(i\delta_y)\hat{\mathbf{y}}\}\ \exp[-(2\pi k/\lambda_0)z]\exp\{i[\omega t - (2\pi n/\lambda_0)z]\}. \quad (2.22)$$

Such easy separation of the wave into individual exponential factors representing oscillating and decaying components is not possible when trigonometric functions are used, and this demonstrates the convenience of the complex exponential function. If the x component of the oscillating term is projected to the real axis, one obtains $\cos[\omega t - (2\pi n/\lambda_0)z + \delta_x]$. This is similar to the oscillating term of (2.1) but with the replacement of λ_0, the wavelength in vacuum or air in that equation, by λ_0/n, which is the wavelength within the medium. The extinction coefficient k, as its name implies, generates an exponentially decaying plane wave in the medium, leading to the irradiance in the x-y plane at z given by:

$$I = (1/2)n\varepsilon_0 c\,\mathbf{E}^* \cdot \mathbf{E} = (1/2)n\varepsilon_0 c\left(E_{0x}^2 + E_{0y}^2\right)\exp[-(4\pi k/\lambda_0)z] = I_0\exp(-\alpha z), \quad (2.23)$$

where I_0 is the irradiance in the x-y plane at $z = 0$ and α is the absorption coefficient. Thus, the absorption coefficient is related to the extinction coefficient by $\alpha = 4\pi k/\lambda_0$.

One description of the linear optical response of a material to an electromagnetic wave is through the photon energy dependent complex index of refraction $N(E) = n(E) - ik(E)$ as used in (2.21). A second approach is through the complex dielectric function $\varepsilon(E) = \varepsilon_1(E) - i\varepsilon_2(E)$, introduced in Sect. 2.1.5. The relationship between the two descriptions is $N(E) = [\varepsilon(E)]^{1/2}$ so that:

$$\varepsilon_1 - i\varepsilon_2 = (n - ik)^2. \quad (2.24a)$$

Expanding N^2 and equating the real parts on both sides, and then the imaginary parts on both sides, give:

$$\varepsilon_1 = n^2 - k^2; \quad \varepsilon_2 = 2nk. \quad (2.24b)$$

Inverting these equations yields:

$$n = \{(1/2)[|\varepsilon| + \varepsilon_1]\}^{1/2}; \quad k = \{(1/2)[|\varepsilon| - \varepsilon_1]\}^{1/2}; \quad |\varepsilon| = (\varepsilon_1^2 + \varepsilon_2^2)^{1/2}. \qquad (2.24c)$$

Many different forms for the photon energy dependence of ε have been developed based on physical principles of the interaction of the electromagnetic wave with the electrons in energy states of the solid [14]. The simplest physical approach is based on a treatment the electron in the presence of the **E**-field as a damped, driven harmonic oscillator. For electrons that are bound in states with their transition energies occurring within the photon energy range of measurement, the damped, driven harmonic oscillator description yields a Lorentz oscillator term in the expression for ε. In contrast, if the transitions occur outside the spectral range of measurement, then a Sellmeier term in the expression for ε_1 can be used (no ε_2 contribution). For electrons that are free, a Drude term in the expression for ε can be used. If a single material combines all types of transitions, then the complex dielectric function can be expressed by:

$$\varepsilon(E) = \varepsilon_{1o} - \sum_{n=1}^{N_D} \frac{A_{Dn}^2}{E^2 - i\Gamma_{Dn}E} + \sum_{n=1}^{N_S} \frac{A_{Sn}^2}{E_{Sn}^2 - E^2} + \sum_{n=1}^{N_L} \frac{A_{Ln}^2}{(E_{Ln}^2 - E^2) + i\Gamma_{Ln}E}, \qquad (2.25)$$

where the first term on the right describes a constant contribution to the real part of $\varepsilon(E)$. The second, third, and fourth summations incorporate the Drude, Sellmeier, and Lorentz oscillator terms, respectively. Thus (2.25) allows for multiple electronic transitions, N_D, N_S, and N_L in number, for each type with amplitudes of A_{Dn}, A_{Sn}, and A_{Ln}, respectively. The Sellmeier and Lorentz oscillator resonance energies are E_{Sn} and E_{Ln}, respectively, and the Drude and Lorentz broadening parameters are Γ_{Dn} and Γ_{Ln}, respectively. It can be noted that each Sellmeier term is obtained from the Lorentz oscillator by setting $\Gamma_{Ln} = 0$. This yields singularities at $E = E_{Sn}$; as a result, the resonance energies of the Sellmeier term must lie outside the photon energy range. It can be noted as well that each Drude term can be obtained from the Lorentz oscillator by setting $E_{Ln} = 0$, meaning that, in contrast to the bound electrons of the Lorentz oscillator, the free electrons lack a restoring force in the damped, driven harmonic oscillator description. Although a sum of Drude terms is shown in (2.25) for generality, only a single term is needed in most situations. Finally, it should be noted that the individual Lorentz oscillator terms of the last summation on the right can be replaced by alternative oscillator forms such as the critical point oscillator developed for crystalline solids, or the Tauc-Lorentz oscillator or Cody-Lorentz oscillator developed for amorphous solids. In contrast, the Drude and Sellmeier terms generally retain the same forms as given in (2.25) irrespective of the nature of the solid.

The first part of the discussion of this section has treated plane wave propagation in infinite media, either free space or a medium with complex index of refraction $N = \varepsilon^{1/2}$. Next, the discussion will focus on plane wave interaction with one or more interfaces as is relevant in the analysis of ellipsometry data.

2.5 Fresnel (or Complex Amplitude Reflection) Coefficients for Single and Multiple Interfaces

2.5.1 *Single Interface*

Reflection from a single ideal interface between a semi-infinite ambient and a semi-infinite isotropic, homogeneous, and uniform medium can be considered the simplest analysis problem in ellipsometry. The goal is to determine N_s, the complex index of refraction of the reflecting medium which can be considered optically as the substrate (hence the subscript '*s*') [2]. In this particular case, the Fresnel reflection coefficients for *p* and *s* polarized light are given by:

$$r_p = \frac{N_s \cos\theta_i - n_a \cos\theta_t}{N_s \cos\theta_i + n_a \cos\theta_t}, \tag{2.26a}$$

$$r_s = \frac{n_a \cos\theta_i - N_s \cos\theta_t}{n_a \cos\theta_i + N_s \cos\theta_t}, \tag{2.26b}$$

where n_a is the assumed real index of refraction of the ambient medium; N_s is given by $N_s = n_s - ik_s$, where n_s is the real index of refraction of the substrate medium and k_s is its extinction coefficient; θ_i is the angle of incidence; and θ_t is the complex angle of transmission. The geometry of the reflection is shown in Fig. 2.6.

Equations (2.26a), (2.26b) appear to incorporate three unknown values, n_s, k_s, and θ_t. Snell's Law can be applied, however, given by:

$$n_a \sin\theta_i = N_s \sin\theta_t, \tag{2.26c}$$

to eliminate $\cos\theta_t$ via:

$$\cos\theta_t = (1 - \sin^2\theta_t)^{1/2} = [1 - (n_a/N_s)^2 \sin^2\theta_i]^{1/2}. \tag{2.26d}$$

Then, the two ellipsometric angles ψ and Δ can be expressed in terms of N_s, n_a, and θ_i through the defining equation:

$$\tan\psi \exp(i\Delta) = \frac{r_p}{r_s} = \rho. \tag{2.27}$$

Using (2.26a), (2.26b), (2.26c), (2.26d) and (2.27), n_s and k_s (or complex N_s) can be determined from the ellipsometry data values ψ and Δ (or complex ρ) using the assumed known quantities n_a and θ_i. The equation for doing this becomes somewhat simpler in form when the optical functions $n_a = N_a$ and N_s are expressed as the corresponding complex dielectric functions:

$$\varepsilon_a = N_a^2; \quad \varepsilon_s = N_s^2, \tag{2.28a}$$

where ε_s is the complex dielectric function of the reflecting substrate medium, and ε_a is the complex dielectric function of the ambient. The final result, which relates the measured ellipsometry parameters to the complex dielectric function of the reflecting substrate medium, is given as:

$$\varepsilon_s = \varepsilon_a \sin^2 \theta_i \left[1 + \tan^2 \theta_i \left(\frac{1-\rho}{1+\rho} \right)^2 \right]. \tag{2.28b}$$

It is more common to express the ellipsometry angles in degrees rather than radians. For a single interface, the requirements on ε_s, i.e. that the imaginary part be positive, implies that $0° \leq \psi \leq 45°$ and $0° \leq \Delta \leq 180°$.

2.5.2 *Multiple Interfaces*

A single interface between an ambient and a substrate is rare in real samples. A more widely encountered problem is the general sample structure consisting of m layers on a substrate and $m + 1$ interfaces [2]. In addressing this problem, depicted in Fig. 2.7, the 2×2 scattering matrix given by $\mathbf{S}_\nu$ is determined, where ν designates either p or s-polarization. This matrix, given by:

$$\mathbf{S}_{\nu,(m+1)} = \mathbf{I}_{\nu,01}\,\mathbf{L}_1\,\mathbf{I}_{\nu,12}\,\mathbf{L}_2 \ldots \mathbf{I}_{\nu,j-1,j}\,\mathbf{L}_j \ldots \mathbf{L}_m\,\mathbf{I}_{\nu,m,(m+1)} \tag{2.29}$$

is a product of $m + 1$ interface matrices (**I**) and m layer matrices (**L**), where index 0 represents the semi-infinite ambient, and index $m + 1$ represents the semi-infinite substrate. The interface and layer matrices are given by:

$$\mathbf{I}_{\nu,(j-1),j} = \frac{1}{t_{\nu,(j-1),j}} \begin{pmatrix} 1 & r_{\nu,(j-1),j} \\ r_{\nu,(j-1),j} & 1 \end{pmatrix}, \tag{2.30a}$$

$$L_j = \begin{bmatrix} Z_j & 0 \\ 0 & Z_j^{-1} \end{bmatrix}, \tag{2.30b}$$

for both p and s-polarizations. In the interface matrix, $r_{\nu,\,j-1,\,j}$ and $t_{\nu,\,j-1,\,j}$, can be determined from the following formulae:

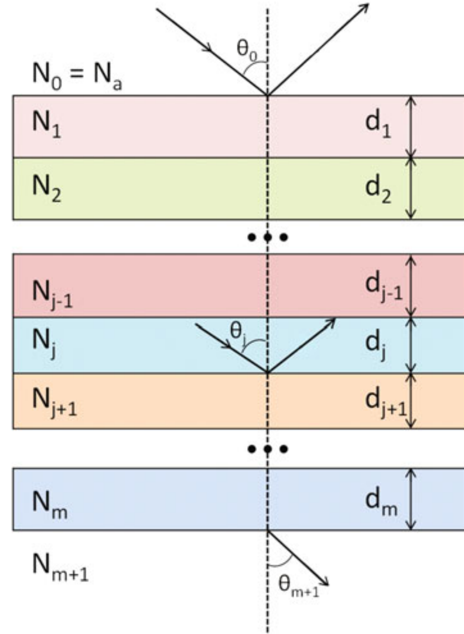

Fig. 2.7 Schematic of a multilayer thin film stack. N_a is the complex index of refraction of the ambient, N_j is the complex index of refraction of the jth layer, and N_{m+1} is the complex index of refraction of the substrate. θ_0 is the angle of incidence that the light beam makes with the first layer, θ_j is the angle of incidence at the interface between the jth and the (j+1)st layer, and θ_{m+1} is the angle of transmission into the substrate

$$\left(r_{j-1,j}\right)_p = \frac{N_j \cos\theta_{j-1} - N_{j-1}\cos\theta_j}{N_j \cos\theta_{j-1} + N_{j-1}\cos\theta_j}, \tag{2.31a}$$

$$\left(r_{j-1,j}\right)_s = \frac{N_{j-1} \cos\theta_{j-1} - N_j\cos\theta_j}{N_{j-1} \cos\theta_{j-1} + N_j\cos\theta_j}, \tag{2.31b}$$

$$\left(t_{j-1,j}\right)_p = \frac{2N_{j-1}\cos\theta_{j-1}}{N_j \cos\theta_{j-1} + N_{j-1}\cos\theta_j}, \tag{2.31c}$$

$$\left(t_{j-1,j}\right)_s = \frac{2N_{j-1}\cos\theta_{j-1}}{N_{j-1} \cos\theta_{j-1} + N_j\cos\theta_j}. \tag{2.31d}$$

These four equations are the complex amplitude reflection (r) and transmission (t) coefficients for the interface between layers $j - 1$ and j. In addition, Z_j in the layer matrix of (2.30b) is given by:

$$Z_j = \exp\left(\frac{2\pi i d_j}{\lambda_0} N_j \cos\theta_j\right), \tag{2.32}$$

where d_j is the thickness of layer j. The angle of incidence θ_{j-1} for the interface between layer $j - 1$ and layer j is obtained from successive applications of Snell's Law:

$$N_0 \sin\theta_0 = N_1 \sin\theta_1 = \cdots = N_{j-1} \sin\theta_{j-1} = N_j \sin\theta_j = \cdots = N_m \sin\theta_m = N_{m+1} \sin\theta_{m+1}. \tag{2.33}$$

After determining the scattering matrix from (2.29), the Fresnel reflection coefficients for the entire stack can be determined by:

$$r_{p,m+1} = \frac{\left[\mathbf{S}_{p,m+1}\right]_{21}}{\left[\mathbf{S}_{p,m+1}\right]_{11}}, \tag{2.34a}$$

$$r_{s,m+1} = \frac{[\mathbf{S}_{s,m+1}]_{21}}{[\mathbf{S}_{s,m+1}]_{11}}, \tag{2.34b}$$

where the subscripts '11' and '21' identify the elements of the 2 × 2 scattering matrix.

Once these reflection coefficients are determined, the (ψ, Δ) values corresponding to this layer stack can also be found, using the following equation:

$$\rho_{m+1} = \frac{r_{p,m+1}}{r_{s,m+1}} = \tan\psi \exp(i\Delta). \tag{2.35}$$

Here, the subscript $m + 1$ on ρ and the Fresnel coefficients indicates that the results have been derived for an m-layer system. For an m-layer structure such as this, the ellipsometry angles can span the full ranges of $0° \le \psi \le 90°$ and $-180° < \Delta \le 180°$. Thus, the approach of (2.29)–(2.35) can be applied for any number of layers. These equations relate the measured quantities (ψ, Δ) to λ_0, θ_0, N_0, …, N_{m+1}, and d_1, …, d_m and must be solved for the useful information on the film stack using computer software. Solutions can be obtained either numerically from a single pair of (ψ, Δ) spectra, for example, with the user inputting λ_0, θ_0, and d_j values along with known N_j spectra to extract a single unknown N wavelength by wavelength in spectroscopic ellipsometry analysis, or by fitting spectra in the (ψ, Δ) values, for example, with the user inputting initial values for wavelength-independent free parameters that describe N_j and initial values for the thicknesses d_j. Non-linear least-squares regression is then used to adjust the initial values iteratively until the best fit set of wavelength-independent values are found.

2.5.3 Through-the-Glass Ellipsometry

Through-the-glass ellipsometry imposes additional challenges in data reduction and analysis [18]. In this experiment, the goal is to block the reflected light beam from the top surface of the glass and only collect the beam making a single reflection from the back surface where the multilayer films are located. In this case the glass is "optically thick" meaning one need only worry about one beam—the primary beam

passing through the front ambient/glass interface, reflecting from the glass/multilayer interface at the back, and returning through the front glass/ambient interface again. The top-surface-reflected beam and multiply-reflected secondary beams, i.e. those making more than one pair of passes through the glass, can be ignored in the analysis since they are displaced spatially and effectively blocked by an aperture placed after the sample. The reflection at the glass/multilayer interface is modified relative to a sample in air by the index of refraction of the glass n_g which serves as the ambient; the extinction coefficient of the glass can be neglected in any interface reflection/transmission processes. In addition, the angle of incidence at the back glass/multilayer interface $\theta_{i,b}$ is the angle of transmission θ_t at the glass/ambient interface. According to Snell's Law:

$$\theta_{i,b} = \theta_t = \sin^{-1}(\sin\theta_{i,f}/n_g), \tag{2.36}$$

where $\theta_{i,f}$ is the angle of incidence at the front air/glass interface and n_g is the index of refraction of the glass.

Under ideal circumstances, three polarization changes occur in this measurement, and the Jones matrix product describing these changes can be written as:

$$\mathbf{P}_r = \mathbf{T}_r \mathbf{J}_S \mathbf{T}_i \mathbf{P}_i, \tag{2.37}$$

where

$$\mathbf{T}_i \mathbf{P}_i = \begin{pmatrix} E_{pt}\,\mathrm{e}^{i\delta_{pt}} \\ E_{st}\,\mathrm{e}^{i\delta_{st}} \end{pmatrix} = \begin{pmatrix} t_p & 0 \\ 0 & t_s \end{pmatrix} \begin{pmatrix} E_{pi}\,\mathrm{e}^{i\delta_{pi}} \\ E_{si}\,\mathrm{e}^{i\delta_{si}} \end{pmatrix} \tag{2.38}$$

describes the first transmission through the ambient/glass interface. Here the **E**-field is resolved into the p and s components of the incident (i) and transmitted (t) waves at the ambient/glass interface, and t_p and t_s are the complex amplitude (or Fresnel) transmission coefficients, given previously in (2.31c) and (2.31d) for an interface between two media in a multilayer stack. In applying these general equations to (2.38), $j-1$ represents the ambient air and j represents the glass. $\mathbf{J}_S$ in (2.37) is the matrix for reflection from the glass/film-stack interface given by the first matrix on the right side of (2.17), but with r_p and r_s replaced by $r_{p,m+1}$ and $r_{s,m+1}$ of (2.34a), (2.34b) and (2.35) for an m-layer film stack at the back of the glass. A similar equation to that of (2.38) is used to elaborate $\mathbf{T}_r$, but with glass serving as medium $j-1$ and ambient as medium j.

As noted previously, each matrix and vector of the complete matrix equation for $\mathbf{P}_r$ can be factored such that the (2, 2) element and (2, 1) component are unity. Doing so yields the single equation for the polarization state ratio:

$$\gamma_r/\gamma_i = \tan\psi\exp(i\Delta) = \left(t_{pr}/t_{sr}\right)\left[\tan\psi'\exp(i\Delta')\right]\left(t_{pi}/t_{si}\right) = \left(t_{pi}/t_{si}\right)^2\tan\psi'\exp(i\Delta'), \tag{2.39a}$$

where ψ and Δ are the measured ellipsometry angles in through-the-glass ellipsometry. The angles ψ' and Δ' are generated from ψ and Δ, and are simulated in data analysis assuming that a wave is incident from an ambient of glass onto a glass/multilayer at an angle of incidence of $\theta_{i,b}$. Based on (2.39a), one finds that $\Delta' = \Delta$ and $\tan\psi' = (t_{si}/t_{pi})^2 \tan\psi$. For this situation, the factor that modifies $\tan\psi$ is given by:

$$\frac{t_{pi}}{t_{si}} = \frac{\cos\theta_{i,f} + n_g \cos\theta_{i,b}}{n_g \cos\theta_{i,f} + \cos\theta_{i,b}}. \tag{2.39b}$$

The above (2.39a), (2.39b) describe the basic principle of through-the-glass ellipsometry under ideal conditions. Non-idealities occur that may complicate the situation [18]. First, stress in the glass modifies the polarization state upon each of the two transmissions through the glass. Second, the detector may collect some fractions of the beams associated with ambient/glass and higher order reflections in addition to that of the single primary beam of interest. Third, float glass exhibits a region typically at the air/glass interface in PV superstrate structures that is modified by the Sn bath. This region has a different index of refraction than bulk glass and can lead to a more complicated top surface structure than a single air/glass interface. All three effects can be incorporated into the data analysis with added free or fixed parameters. These include the collected fraction of the top surface and secondary reflections, the stress parameters that describe the stress birefringence and its optical dispersion, and the thickness and index of refraction parameters of the Sn-modified region. Incorporation of stress requires adding two more matrices to the matrix product in (2.37) to account for the polarization modifications that occur.

2.6 Instrumentation: Rotating Compensator Ellipsometer

2.6.1 Formalism

One of the most widely used commercial research and development instruments for high speed spectroscopic ellipsometry of PV materials is the rotating compensator multichannel ellipsometer in the PC$_r$SA configuration (M2000, J. A. Woollam Co.) [19]. Here P represents a polarizer, C$_r$ represents a rotating compensator, S represents the sample, and A represents an analyzer. The analyzer is a polarizer on the polarization detection side of the instrument. In order to understand how such an instrument can measure ψ and Δ spectra for an unknown sample, one must understand the action of each of the optical elements on the polarization state, including the action of the sample on the state exiting the polarizer-compensator combination. In the analysis of such an instrument configuration, one multiplies the Jones vector that describes the polarization state at the output of the polarizer $\mathbf{P}_{o,P}$ by a product of Jones matrices that represent the compensator $\mathbf{J}_C$, sample $\mathbf{J}_S$, and

analyzer $\mathbf{J}_A$ in the sequence, $\mathbf{P}_{o,A} = \mathbf{J}_A\mathbf{J}_S\mathbf{J}_C\mathbf{P}_{o,P}$. The result of this product is the electric field associated with the polarization state $\mathbf{P}_{o,A}$ exiting the analyzer. From the electric field, the irradiance can be determined. Each optical element including the sample can be described by a diagonal Jones matrix in the frame of reference of the optical element. Although the coordinate system of each element lies in the plane normal to the ray direction z, the orientations of these individual coordinate systems are different, in general, and so a reference coordinate system for the entire instrument is needed. The instrument reference coordinate system is selected to be that of the sample, the *p*-*s* coordinate system.

The linear polarization state at the entrance to the compensator $\mathbf{P}_{i,C}$ can be described in the *p*-*s* coordinate system by the following product:

$$\mathbf{P}_{i,C} = \mathbf{R}(-P)\begin{pmatrix}1\\0\end{pmatrix}. \tag{2.40}$$

The vector on the right represents the linear polarization state of the wave in the polarizer's transmission-extinction (*t*-*e*) reference frame after the wave has passed through the polarizer. This vector indicates that there is an electric field along the transmission axis and no electric field along the extinction axis. In a conventional ellipsometry experiment, one is concerned only with changes in the shape of the polarization ellipse and not in the amplitude of the field along the transmission axis. As a result, for simplicity a normalized Jones vector can be used.

The matrix $\mathbf{R}(-P)$ represents a rotation matrix by the angle $-P$ that transforms the polarization vector from the polarizer *t*-*e* coordinate system to the reference *p*-*s* coordinate system. The angle P is the rotational orientation of the transmission axis of the polarizer relative to the *p*-direction as measured in a counter-clockwise positive sense when the beam is viewed so as to enter the observer's eye. Thus, to transform the polarization vector from the *t*-*e* to the *p*-*s* frame, the *t*-*e* coordinate system is rotated by $-P$ (which is clockwise for $P > 0$). The rotation matrix for an arbitrary angle Θ is given by:

$$\mathbf{R}(\Theta) = \begin{pmatrix}\cos\Theta & \sin\Theta\\ -\sin\Theta & \cos\Theta\end{pmatrix}. \tag{2.41}$$

Now the polarization vector at the output of the analyzer in the *t*-*e* frame of reference of the analyzer can be written as:

$$\begin{pmatrix}E_{t,A}\\0\end{pmatrix} = \mathbf{J}_A\,\mathbf{R}(A)\,\mathbf{J}_S\,\mathbf{R}(-C)\,\mathbf{J}_C\,\mathbf{R}(C)\begin{pmatrix}\cos P\\ \sin P\end{pmatrix}. \tag{2.42}$$

This vector equation can be understood as follows. The polarization state vector at the right is that entering the compensator in the *p*-*s* frame of reference, as obtained from (2.40) and (2.41). The rotation matrices $\mathbf{R}(C)$ and $\mathbf{R}(-C)$ transform the polarization state from the *p*-*s* reference frame of the sample to the fast-slow axes (*F*-*S*) reference frame of the compensator and then back again, respectively. The

rotation matrix $\mathbf{R}(A)$ transforms the polarization state from the *p*-*s* frame of reference of the sample to the *t*-*e* frame of the analyzer. Because the irradiance, rather than the polarization state itself, is measured after the analyzer a final rotation back to the *p*-*s* frame is not needed. The reason is that coordinate rotations have no effect on the irradiance.

It now remains to define $\mathbf{J}_C$, $\mathbf{J}_S$, and $\mathbf{J}_A$, the Jones matrices of the compensator, sample, and analyzer, respectively. The Jones matrix for the sample was given previously by:

$$\mathbf{J}_S = \begin{pmatrix} (|r_p|/|r_s|)\exp\left[i(\delta_p - \delta_s)\right] & 0 \\ 0 & 1 \end{pmatrix} = \begin{pmatrix} \tan\psi \exp(i\Delta) & 0 \\ 0 & 1 \end{pmatrix}. \tag{2.43}$$

There are different methods for expressing $\mathbf{J}_C$, which is a transmission device. One method in which the (1, 1) element is normalized to unity used most commonly is given by:

$$\mathbf{J}_C = \begin{pmatrix} 1 & 0 \\ 0 & (|t_S|/|t_F|)\exp[i(\delta_S - \delta_F)] \end{pmatrix} = \begin{pmatrix} 1 & 0 \\ 0 & \cot\psi_C \exp(-i\delta_C) \end{pmatrix}, \tag{2.44}$$

where $t_F = |t_F|\exp(i\delta_F)$ and $t_S = |t_S|\exp(i\delta_S)$ are the fast and slow axis transmission coefficients described as phasors and the following definitions are conventional: $\delta_C = \delta_F - \delta_S$ and $\tan\psi_C = |t_F|/|t_S|$.

The operational principle of the compensator is light transmission through a birefringent medium such that the wave linearly polarized with the field along the *F*-axis experiences an index of refraction of n_F and the wave linearly polarized with the field along the *S*-axis experiences an index of refraction of n_S. Because the speed of the wave in a medium is given by $v = c/n$, then the wave polarized linearly along the fast axis has $n_F < n_S$, meaning that the wave moves faster than that polarized linearly along the slow axis. Setting $z = 0$ as the entrance of the device and d as the distance of travel through the birefringent medium, then the phase shift between the fast and slow waves upon transmission is:

$$\delta_C = \delta_F - \delta_S = [-(2\pi n_F/\lambda_0)d] - [-(2\pi n_S/\lambda_0)d] = (2\pi\Delta n/\lambda_0)d, \tag{2.45a}$$

where $\Delta n = n_S - n_F > 0$ is the birefringence. Most compensators are non-dichroic, meaning $|t_F| = |t_S|$ so that $\tan\psi_C = 1$.

The above description is appropriate for a single plate of birefringent material. It is desirable, however, to employ a biplate compensator, or a combination of biplates. The reason for the use of a biplate is that one seeks to operate in the lowest possible order, meaning that $0 < \delta_C < \pi$ over the spectral range of interest in order to minimize $d\delta_C/d\lambda_0$. For typical birefringence magnitudes, the plate thickness d is impractically small under these conditions. To overcome this problem, a biplate compensator can be used such that the fast axes of the two plates are orthogonal. If the thicknesses of the two plates were the same, the phase shifts from the two plates would completely cancel. By arranging a small difference between the

practically-designed thicknesses of the plates, lowest order operation of the compensator is ensured according to:

$$\delta_C = (2\pi\Delta n/\lambda_0)d_1 - (2\pi\Delta n/\lambda_0)d_2 = (2\pi\Delta n/\lambda_0)\Delta d, \tag{2.45b}$$

where d_1 and d_2 (with $d_1 > d_2$) are the thicknesses of the two plates and Δd is the thickness difference. Considering this equation for the phase shift, when δ_C = ½π rad = 90°, then one has a quarter-wave plate at the given λ_0 operating in lowest order. In that case, if linear polarization with its **E**-field tilted at Q = 45° with respect to the F-axis enters the compensator, then left circular light exits the compensator. If the tilt is Q = −45° then right circular polarization results. In this section, the convention is used in which the argument of the phasor is $\{\omega t - (2\pi n/\lambda_0)z\}$ [2].

Returning to the analyzer, which is a much easier optical element to describe, the Jones matrix in the frame of its transmission-extinction axes is given by:

$$\mathbf{J}_A = \begin{pmatrix} 1 & 0 \\ 0 & 0 \end{pmatrix}, \tag{2.46}$$

where we have ignored any prefactors that reduce the field amplitude, for example, due to extinction or to reflection losses. This simple matrix makes sense since it takes any electric field vector input and eliminates the component along the extinction axis.

With the above elaborations, the electric field vector along the transmission axis of the analyzer $E_{t,A}$ can be expressed as a complex quantity with the following functional dependence:

$$E_{t,A} = \mathrm{Re}\,[E_{t,A}(P, C, \delta_C, \psi_C, \psi, \Delta, A)] + i\,\mathrm{Im}[E_{t,A}(P, C, \delta_C, \psi_C, \psi, \Delta, A)], \tag{2.47}$$

where 'Re' and 'Im' indicate real and imaginary parts of $E_{t,A}$. Although $\psi_C = 45°$ is a valid assumption for the MgF_2 biplate compensator instrument, ψ_C is allowed to vary for a more general compensator design. Because a value proportional to the irradiance I (rather than the field) is measured at the detector, then I after the analyzer is given by:

$$I \propto E_{t,A}{}^{*}E_{t,A} = \{\mathrm{Re}\,[E_{t,A}(P, C, \delta_C, \psi_C, \psi, \Delta, A)]\}^2 + \{\mathrm{Im}[E_{t,A}(P, C, \delta_C, \psi_C, \psi, \Delta, A)]\}^2, \tag{2.48}$$

where $E_{t,A}{}^{*}$ is the complex conjugate of $E_{t,A}(P, C, \delta_C, \psi_C, \psi, \Delta, A)$. In various types of ellipsometers, one or more of the instrument parameters P, C, δ_C, and A are modulated and Fourier analysis is performed to deduce the ellipsometry angles ψ and Δ. For example, in the case of the PC_rSA instrument under discussion, the compensator is rotated and measurements are performed at the different values of C,

which is the angle of the fast axis measured with respect to the *p* axis of the coordinate system that defines reflection from the sample.

In fact, there are two possible configurations for the single rotating-compensator ellipsometer as described in Fig. 2.1, depending on whether the compensator is located before or after the sample. These are denoted PC_rSA or PSC_rA, where P, C_r, S, and A represent the polarizer, rotating compensator, reflecting sample, and analyzer, respectively. By placing the rotating compensator before the sample, the path of the beam through the compensator is fixed irrespective of the optical alignment of the sample, and greater reproducibility is possible. In this case, the compensator is aligned independently of the sample as a component of the polarization generation arm of the instrument. By placing the rotating compensator after the sample, however, the operation is conceptually simpler since the C_rA optical element configuration acts as polarization state detector.

2.6.2 Data Reduction

For both single rotating-compensator configurations of the multichannel ellipsometer, the irradiance waveform at the detector is given by [20]:

$$I(t) = I_0 a_0 \{1 + \alpha(2C)\cos 2C + \beta(2C)\sin 2C + \alpha(4C)\cos 4C + \beta(4C)\sin 4C\}. \tag{2.49}$$

$\{\alpha(2nC), \beta(2nC); n = 1, 2\}$ are the dc-normalized cosine and sine Fourier coefficients, respectively, where C is the angle of the fast axis of the compensator. In the PC_rSA configuration, the Fourier coefficients are given by:

$$\alpha(2C) = \frac{-(\mu_{A1}\cos 2P + \mu_{A2})\cos 2\psi_C - \mu_{A4}\,\sigma_C \sin 2P}{a_0}, \tag{2.50a}$$

$$\beta(2C) = \frac{-(\mu_{A1}\sin 2P + \mu_{A3})\cos 2\psi_C + \mu_{A4}\,\sigma_C \cos 2P}{a_0}, \tag{2.50b}$$

$$\alpha(4C) = \frac{s_C\mu_{A2}\cos 2P - s_C\mu_{A3}\sin 2P}{a_0}, \tag{2.50c}$$

$$\beta(4C) = \frac{s_C\mu_{A2}\sin 2P + s_C\mu_{A3}\cos 2P}{a_0}, \tag{2.50d}$$

where $a_0 = \mu_{A1} + c_C\,\mu_{A2}\cos 2P + c_C\,\mu_{A3}\sin 2P$ and $\mu_{Aj}\ (j = 1, \ldots, 4)$ are defined according to:

$$\mu_{A1} = 1 - \cos 2\psi \cos 2A, \tag{2.51a}$$

$$\mu_{A2} = -\cos 2\psi + \cos 2A, \tag{2.51b}$$

$$\mu_{A3} = \sin 2\psi \cos \Delta \sin 2A, \tag{2.51c}$$

$$\mu_{A4} = \sin 2\psi \sin \Delta \sin 2A. \tag{2.51d}$$

In (2.50a), (2.50b), (2.50c), (2.50d), the compensator parameters are:

$$\sigma_C = \sin 2\psi_C \sin \delta_C, \tag{2.52a}$$

$$c_C = (1/2)(1 + \sin 2\psi_C \cos \delta_C), \tag{2.52b}$$

$$s_C = (1/2)(1 - \sin 2\psi_C \cos \delta_C). \tag{2.52c}$$

These equations are developed in such a way that the first set, (2.50a), (2.50b), (2.50c), (2.50d), depends explicitly on the polarizer angle and the compensator properties, the second set, (2.51a), (2.51b), (2.51c), (2.51d), introduces the analyzer angle and the ellipsometry parameters, and the third set, (2.52a), (2.52b), (2.52c) defines more convenient compensator parameters. Being general, the polarizer and analyzer angles can be optimized for the specific sample. One approach for data reduction is to determine ψ and Δ from the ac Fourier coefficients as ratios in order to eliminate a_0 and provide immunity to ambient light. In fact, the ellipsometry parameters are over-determined by the ac Fourier coefficients, and the method of calculation can be also optimized for the specific sample. The five Fourier coefficients (one dc and four ac) are obtained with a minimum of five detector acquisitions at different compensator angles. Taking $\psi_C = 45°$ and one possible case of $P = 0°$, $A = 45°$, then a simple relationship exists between the Fourier coefficients and ψ and Δ:

$$\tan \Delta = \frac{[R_C \beta(2C)]}{[\beta(4C)]}, \tag{2.53a}$$

$$\tan 2\psi = -\frac{\left\{[R_C \beta(2C)]^2 + [\beta(4C)]^2\right\}^{1/2}}{\alpha(4C)}, \tag{2.53b}$$

where

$$R_C = (1/2)\tan(\delta_C/2). \tag{2.53c}$$

Taking $\psi_C = 45°$ and a second possible case of $P = -45°$, $A = 45°$, then an alternative relationship exists between the Fourier coefficients and ψ and Δ:

$$\tan \Delta = \frac{[R_C \alpha(2C)]}{[\alpha(4C)]}, \tag{2.54a}$$

$$\tan 2\psi = \frac{\left\{[R_C \alpha(2C)]^2 + [\alpha(4C)]^2\right\}^{1/2}}{\beta(4C)}. \tag{2.54b}$$

The advantage of the rotating compensator configuration is the ability to measure (ψ, Δ) with high precision and accuracy and without ambiguity over their full ranges of $0 \leq \psi \leq 90°$ and $-180° < \Delta \leq 180°$. The lack of ambiguity in ψ is clear because $\tan 2\psi$ is measured, whereas the lack of ambiguity in Δ arises from the fact that both $\cos \Delta$ and $\sin \Delta$ can be determined from (2.50a), (2.50b), (2.50c), (2.50d)–(2.52a), (2.52b), (2.52c). The optimum compensator value δ_C typically selected for the center of the photon energy range depends on the type of sample to be measured [21]. One approach is to notice that when $R_C = 1$ in (2.53c), the $2C$ and $4C$ coefficients are weighted equally. This gives the result that $\delta_C = 126.9°$ as a possible value for selection at the center of the photon energy range.

2.6.3 Instrument Calibration

In order to obtain high accuracy data, calibration of the ellipsometer is very important. In (2.50a), (2.50b), (2.50c, (2.50d)–(2.52a), (2.52b), (2.52c), it is assumed that P, C, δ_C, ψ_C, and A are known and that ψ and Δ of the sample are the only unknowns. For calibration of the three angles P, C, and A, the sample must be in place and the desired angle of incidence set. Approximate values of these angles are known and define the settings P^*, C^*, A^*, such that $P = P^* + \Delta P$, $C = C^* + \Delta C$, and $A = A^* + \Delta A$. The goal of calibration is to find the small offset angles ΔP, ΔC, and ΔA by which the optical elements must be rotated so that the settings match the correct values for use in the data reduction equations. Typical approaches for determining the offset angles involve measurements at different angles of the polarizer and analyzer [20]. Although such measurements can be done on the sample to be studied, calibration of the instrument is often performed with a specific sample chosen for high accuracy calibration results. Finally, a test of the instrument and calibration quality for spectroscopic ellipsometry relies on the fact that the angular offsets ΔP and ΔA of the polarizer and analyzer are independent of wavelength. Depending on the detection scheme, ΔC for the rotating compensator may be also constant or vary linearly with wavelength.

The calibration to determine the spectra in δ_C and ψ_C can be performed with the instrument in the straight-through configuration, in which case the sample is removed and the polarization generation arm and the polarization detection arm are aligned. In this case, the common reference axis of the calibrated polarizer and analyzer becomes the reference for the fast axis of the compensator. In this

configuration, the compensator is fixed (i.e. not rotating) and a calibration procedure is used to determine ΔC. Then the compensator angle is set to $C = 0°$, and in this configuration, irradiance measurements at the detector versus polarizer and/or analyzer angle provide δ_C and ψ_C. For a MgF_2 biplate, $\psi_C = 45°$, independent of photon energy, and this is a suitable test for a quality biplate and a quality calibration. Because $\delta_C = (2\pi \Delta n/\lambda_0)\Delta d$, and the birefringence can be given as a polynomial function of energy, then the compensator phase shift, also called the retardance, can be fit with:

$$\delta_C(E) = E\left(c_0 + c_2E^2 + c_4E^4\right), \tag{2.55}$$

where E is the photon energy and $\{c_j; j = 0, 2, 4\}$ are constants determined in the fit. This equation results from $E = hc/\lambda_0$, and the assumption that $n_F(E)$ and $n_S(E)$ follow Cauchy expressions, in which the indices of refraction are given as polynomials in E with even terms. Because the Cauchy expression is an approximation, odd terms in E can also be included in the summation in parenthesis in (2.55) [22].

2.7 Summary

The optical analysis technique of ellipsometry provides powerful capabilities that can be applied in the development and optimization of thin film photovoltaic (PV) materials and devices. Because the technique is indirect and requires in-depth analysis of the acquired data to extract useful information on materials and devices, a key toward success is the acquisition of multiple data sets through variation of the measurement or sample conditions. Collecting multiple data sets is time consuming, and as a result, high speed measurements are desirable for rapid feedback to the user on materials and device properties. High speed spectroscopic ellipsometry is made possible through the use of linear detector arrays that can collect continuous spectra in parallel with acquisition times as short as 16 ms. High speed line imaging spectroscopic ellipsometry is also possible by using two-dimensional detector arrays with one array index for spectroscopy and a second array index for imaging across a line on the sample. For the latter instrument, high speed mapping is possible by linear translation of the sample. A popular ellipsometry configuration for high speed spectroscopic ellipsometry is based on rotating compensator polarization modulation, which provides high accuracy and precision for a wide variety of sample types from dielectric substrates to semiconductors and opaque metal contacts.

Considering ex-situ ellipsometry measurements restricted to a single sample location, data acquired as a function of both wavelength (or photon energy) and angle of incidence, i.e. variable angle of incidence spectroscopic ellipsometry, are useful for extracting layer thicknesses in multilayer stacks and the parameters that describe the optical properties (n, k) of individual layers. In order to make the

analysis problem tractable for multilayers, it is important to develop a database of (n, k) spectra for PV materials that can be used in the analysis, either as initial estimates or as fixed spectra. The challenge, however, is that for many of the materials used in PV, (n, k) cannot be fixed, given their sensitivity to the details of the fabrication process and to the nature of the substrate. As a result, it is helpful to develop analytical expressions for (n, k) versus wavelength (or photon energy) that incorporate several wavelength-independent parameters associated with a collection of electronic oscillators in the complex dielectric function $\varepsilon = (n - ik)^2$. Even more useful still as components of the database are expressions of the complex dielectric function or its oscillator parameters in terms of physical properties of the material including void content, alloy composition, stress, grain size, carrier concentration, and carrier mobility, as examples. The reduction of the analysis problem to the determination of wavelength-independent parameters enables non-linear least-squares regression for determination of the physical parameters that specify (n, k) along with the layer thicknesses of multilayer stacks from the ex-situ measurements. The significant challenge of state-of-the-art analysis involves the roughness on the surfaces of device-relevant substrate structures such as thin film metal back contacts and transparent conducting oxide top contacts that then propagate throughout the multiple layers of the device.

In addition to ex-situ measurements performed as a function of wavelength and angle of incidence, the high speed of spectroscopic ellipsometry enables in-situ measurements versus time as well in order to track film growth or surface modification. In fact, this capability of real time spectroscopic ellipsometry enables one to study the physical mechanisms of growth for thin film PV materials, ranging from the initial nucleation and coalescence stages to the final film structural characteristics, including the bulk and surface roughness layer thicknesses. The ability to obtain accurate structural information in-situ from multiple measurements versus time in turn yields high accuracy (n, k) spectra in the absence of surface oxidation, also accurately corrected for the surface non-idealities associated with roughness. These high accuracy (n, k) spectra (or complex dielectric functions ε) for films deposited under different conditions can be applied in physics-based analyses that relate parameters in oscillator models of ε to physical parameters. The relationships can be used in ex-situ spectroscopic ellipsometry analysis of complete solar cell device structures using non-linear least-squares regression analysis as described in the previous paragraph.

Complete information $\{d, (n, k)\}$ for full device structures enables the simulation of the external quantum efficiency based on the assignment of the active layer or layers, the prediction of the current density for the device under air mass 1.5 illumination, and the identification of the optical losses due to reflection, absorption in inactive layers, and transmission (if any). Thus, spectroscopic ellipsometry, given optimized analysis strategies, can provide comprehensive information on the optical performance of solar cells and can identify directions for improvements. In fact, the significant increases in thin film PV laboratory efficiencies to >22% have been achieved predominantly through improvements in optical design of the structures and increases in current density. Excellent prospects also exist for expansion of the

spectroscopic ellipsometry methodologies from the laboratory scale to the pilot scale and full scale production environments, given a high speed spectroscopic line imaging capability. This approach also motivates high resolution mapping spectroscopic ellipsometry, in which case maps of thickness and parameters that define the optical properties can provide predictions of the current output for the sub-cells of full scale modules from measurements performed on production lines.

2.8 Selected Readings

2.8.1 Optics

- R. D. Guenther, *Modern Optics*, (John Wiley & Sons, New York, 1990)
- M. Born and E. Wolf, *Principles of Optics*, *7th Edition* (Pergamon, Oxford, UK, 1999)
- E. Hecht, *Optics, 5th Edition* (Pearson, New York, 2017)

2.8.2 Ellipsometry

- R. M. A. Azzam and N. M. Bashara, *Ellipsometry and Polarized Light*, (North-Holland, Amsterdam, The Netherlands, 1977)
- H. G. Tompkins and E. A. Irene, editors, *Handbook of Ellipsometry*, (William Andrew, Norwich, NY, 2005)
- H. Fujiwara, *Spectroscopic Ellipsometry: Principles and Applications*, (John Wiley & Sons, Chichester, UK, 2007)
- H. G. Tompkins and J. N. Hilfiker, *Spectroscopic Ellipsometry: Practical Application to Thin Film Characterization*, (Momentum, New York, 2016)

2.8.3 Optical Properties of Solids

- F. Wooten, *Optical Properties of Solids*, (Academic, New York, 1972)
- R. W. Collins and A. S. Ferlauto, "Optical physics of materials," in: *Handbook of Ellipsometry*, edited by H. G. Tompkins and E. A. Irene, (William Andrew, Norwich, NY, 2005), Chapter 2, pp. 93–235
- M. Fox, *Optical Properties of Solids, 2nd Edition* (Oxford, Oxford, UK, 2010)

2.8.4 Photovoltaics

- A. Luque and S. Hegedus, editors, *Handbook of Photovoltaic Science and Engineering, 2nd Edition*, (John Wiley & Sons, New York, 2011)
- J. Nelson, *The Physics of Solar Cells*, (Imperial College, London, UK, 2003)
- S. J. Fonash, *Solar Cell Device Physics, 2nd Edition*, (Academic Press, Oxford, UK, 2010)
- D. Abou-Ras, T. Kirchartz, and U. Rau, editors, *Advanced Characterization Techniques for Thin Film Solar Cells, 2nd Edition*, (Wiley-VCH, Weinheim, Germany, 2016)

References

1. A. Rothen, Rev. Sci. Instrum. **16**, 26 (1945)
2. R.M.A. Azzam, N.M. Bashara, *Ellipsometry and Polarized Light* (North-Holland, Amsterdam, The Netherlands, 1977)
3. W.-K. Paik, J.O'M. Bockris, Surf. Sci. **28**, 61 (1971)
4. H. Fujiwara, *Spectroscopic Ellipsometry: Principles and Applications* (Wiley, Chichester, UK, 2007)
5. M. Erman, J.B. Theeten, J. Appl. Phys. **60**, 859 (1986)
6. G. Juhász, Z. Horváth, C. Major, P. Petrik, O. Polgár, M. Fried, Phys. Stat. Sol. (c) **5**, 1081 (2008)
7. P.S. Hauge, Surf. Sci. **96**, 108 (1980)
8. D.E. Aspnes, A.A. Studna, Appl. Opt. **14**, 220 (1975)
9. I. An, Y.M. Li, H.V. Nguyen, R.W. Collins, Rev. Sci. Instrum. **63**, 3842 (1992)
10. A. Shan, M. Fried, G. Juhász, C. Major, O. Polgár, A. Németh, P. Petrik, L.R. Dahal, J. Chen, Z. Huang, N.J. Podraza, R.W. Collins, IEEE J. Photovolt. **4**, 355 (2013)
11. J. Lee, P.I. Rovira, I. An, R.W. Collins, Appl. Phys. Lett. **72**, 900 (1998)
12. M. Schubert, Theory and application of generalized ellipsometry, in *Handbook of Ellipsometry*, ed. by H.G. Tompkins, E.A. Irene (William Andrew, Norwich, NY, 2005), pp. 637–717
13. G.E. Jellison Jr., Data analysis for spectroscopic ellipsometry, in *Handbook of Ellipsometry*, ed. by H.G. Tompkins, E.A. Irene (William Andrew, Norwich, NY, 2005), pp. 237–296
14. R.W. Collins, A.S. Ferlauto, Optical physics of materials, in *Handbook of Ellipsometry*, ed. by H.G. Tompkins, E.A. Irene (William Andrew, Norwich, NY, 2005), pp. 93–235
15. D.E. Aspnes, Thin Solid Films **89**, 249 (1982)
16. H. Fujiwara, J. Koh, P.I. Rovira, R.W. Collins, Phys. Rev. B **61**, 10832 (2000)
17. Y. Cong, I. An, K. Vedam, R.W. Collins, Appl. Opt. **21**, 2692 (1991)
18. J. Chen, P. Aryal, J. Li, M.N. Sestak, L.R. Dahal, Z. Huang, R.W. Collins, *Conference Record of the 37th IEEE Photovoltaics Specialists Conference, June 19–24, 2011, Seattle WA* (New York, NY, IEEE, 2011), pp. 3486–3491

19. B. Johs, J. Hale, N.J. Ianno, C.M. Herzinger, T. Tiwald, J.A. Woollam, Recent developments spectroscopic ellipsometry for in-situ applications, in *Optical Metrology Roadmap for the Semiconductor, Optical, and Data Storage Industries II, SPIE Proceedings 4449*, ed. by A. Duparre, B. Singh (SPIE, Bellingham, WA, 2001), pp. 41–57
20. J. Lee, P.I. Rovira, I. An, and R. W. Collins. Rev. Sci. Instrum. **69**, 1800 (1998)
21. M.H. Smith, Appl. Opt. **41**, 2488 (2002)
22. J. Lee, P.I. Rovira, I. An, R.W. Collins, J. Opt. Soc. Am. A **18**, 1980 (2001)

Chapter 3
Data Analysis

James N. Hilfiker, Jianing Sun and Nina Hong

Abstract Data analysis is an important aspect of spectroscopic ellipsometry (SE). The measurement is directly related to the polarization change of probing light upon reflection from a sample surface. Data analysis enables determination of physical material properties of interest, such as film thickness, material dielectric functions, composition, crystallinity, conductivity, and more. This is achieved through model-based regression analysis. In this chapter, we detail the typical SE data analysis procedures. The fundamentals of optical modeling are outlined. Different ways to describe material dielectric functions are reviewed. Principles of fitting and evaluation of results are discussed. The chapter concludes with a review of strategies for common sample structures, categorized as transparent thin films, absorbing thin films, or films which are both transparent and absorbing, depending on the wavelength considered.

3.1 Analysis Flow

Spectroscopic ellipsometers use polarized light to characterize material properties. The polarization is altered as light interacts with the thin films and substrate materials. Thus, SE is sensitive to film thickness and optical constants of each material. Data analysis is the process of extracting sample properties from the measured SE data. The procedure is shown in Fig. 3.1. First, the SE data are measured (Sect. 3.2). This involves reflecting polarized light from the sample surface and determining the change in polarization. The experimental data are represented by psi (ψ) and delta (Δ) at each measured wavelength and angle of incidence. Features in the spectral data curves indicate the sample properties. In Sect. 3.3 we demonstrate how to interpret the SE spectra. Next, a model is built to describe the sample structure (Sect. 3.4). The model contains estimates for thickness and optical constants of each material that interacts with the probing light.

J. N. Hilfiker (✉) · J. Sun · N. Hong
J.A. Woollam Co., Inc., 645 M Street, Suite 102, Lincoln, NE 68508, USA
e-mail: jhilfiker@jawoollam.com

© Springer International Publishing AG, part of Springer Nature 2018

H. Fujiwara and R. W. Collins (eds.), *Spectroscopic Ellipsometry for Photovoltaics*,
Springer Series in Optical Sciences 212,
https://doi.org/10.1007/978-3-319-75377-5_3

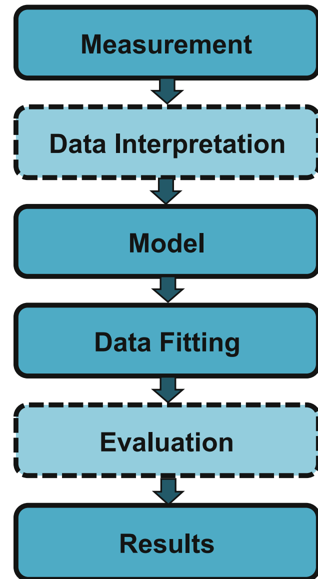

Fig. 3.1 Spectroscopic ellipsometry data analysis flow chart is illustrated with essential (solid border) and optional (dashed border) steps

Theoretical calculations are made from the model description to compare with the experimental SE data. The comparison proceeds by adjusting unknown sample properties until agreement is reached between the experimental data and the model-calculations. This is referred to as regression analysis and is described in Sect. 3.5. While often overlooked, the results are then evaluated (Sect. 3.6). This ensures the analysis produces unique sample properties which are physically plausible. When successfully followed, these steps provide the resultant thin film thickness and material properties from the measured SE data.

3.2 SE Measurement

Spectroscopic ellipsometers shine light with known polarization onto a bulk material or a thin film coated substrate, i.e. a sample. Reflection from the sample changes the light polarization. The measurement is described by two parameters, ψ and Δ, which are related to changes in amplitude and phase, respectively. Together, ψ and Δ represent a link between the incoming light with known polarization and the altered polarization of the detected light (Fig. 3.2). The change in polarization results from interactions between light and sample, which forms the foundation of ellipsometry characterization.

SE data are typically collected at angles between 45° and 85° to optimize changes in polarization. Both ψ and Δ vary at each wavelength (λ), producing spectral curves for each measured angle of incidence (θ). While ψ and Δ are

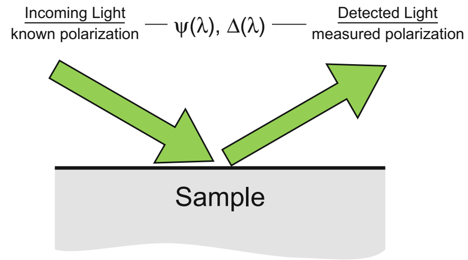

Fig. 3.2 Reflection of light produces a change in polarization reported as two measured spectra: $\psi(\lambda)$ and $\Delta(\lambda)$

common SE data descriptions, the experimental curves can also be shown using related parameters, such as:

- $\tan(\psi)$ and $\cos(\Delta)$
- $N = \cos(2\psi)$, $C = \sin(2\psi)\cos(\Delta)$, and $S = \sin(2\psi)\sin(\Delta)$.

For simplicity, ψ and Δ are used throughout this chapter, but all data analysis concepts are relevant regardless of measurement notation.

3.3 Data Interpretation

Features in the raw SE spectra carry information about sample structure and film properties. Understanding these features can help the user construct an appropriate model and estimate film properties. In this section we describe typical features from single-layer films. The interaction of a measurement beam with a transparent film is shown in Fig. 3.3. Because the film is transparent the detected light consists of reflections both from the surface and light that travels through the film.

The most prominent features in SE data are oscillations when the film is transparent. The measured spectra exhibit peaks and valleys, referred to as *interference features*, due to constructive and destructive interference as the light recombines. The number and position of interference features depend on film thickness (d) and refractive index (n). An increase in either thickness or film index produces more interference features. Figure 3.4 shows three spectra from

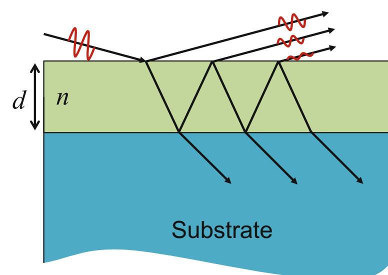

Fig. 3.3 Interaction of light with a transparent film involves both reflection from the surface and light traveling through the film

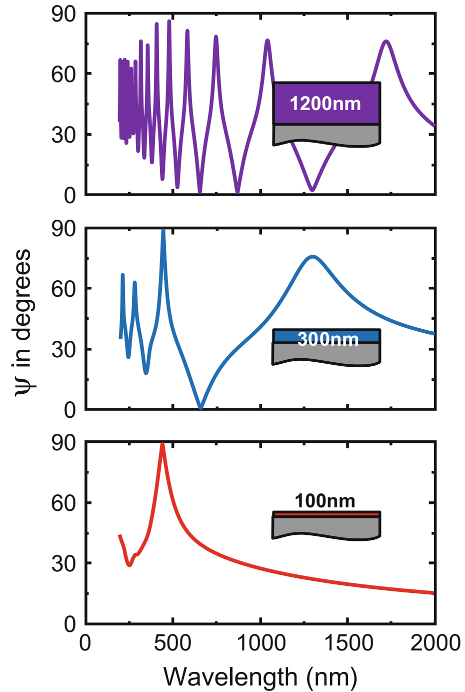

Fig. 3.4 SE ψ spectra from transparent SiO_2 films on Si show the increasing number of interference features (peaks and valleys) as the film thickness increases

transparent SiO_2 films on silicon substrate. Clearly, there are more interference features across the spectra as the film thickness increases.

The ψ oscillation amplitude is affected by optical contrast between film and substrate. The ψ peak-to-valley variation generally increases with larger index contrast (Δn). Thus, we expect smaller oscillations from Al_2O_3 on glass ($\Delta n \sim 0.1$–0.2) than for hydrogenated amorphous silicon (a-Si:H) on glass ($\Delta n \sim 2$–3). For a known substrate the ψ oscillation amplitude can be used to estimate the index of a transparent film.

If a thin film absorbs light, only the front reflection is detected and no interference occurs. Consider the SE spectra from an a-Si:H film on glass in Fig. 3.5. Both ψ and Δ oscillate at longer wavelengths where the a-Si:H film is transparent. At shorter wavelengths the oscillations are dampened and eventually disappear.

The absorption transition, identified near 600 nm in Fig. 3.5, occurs when the photon energy of light exceeds the a-Si:H film bandgap (E_g). Because a-Si:H shows weak absorption near E_g, the absorption onset is gradual. Once the film optical constants are accurately determined through data analysis, the bandgap can be better estimated ($E_g \sim 1.78$ eV for this film) based on traditional methods [1].

Direct bandgap materials have a sharper transition between transparent and absorbing regions which allows easier visual estimation directly from the raw data. Figure 3.6 shows SE spectra from a CdMgTe thin film on glass. The interference oscillations diminish abruptly at the material bandgap near 1.6 eV. Here, data are

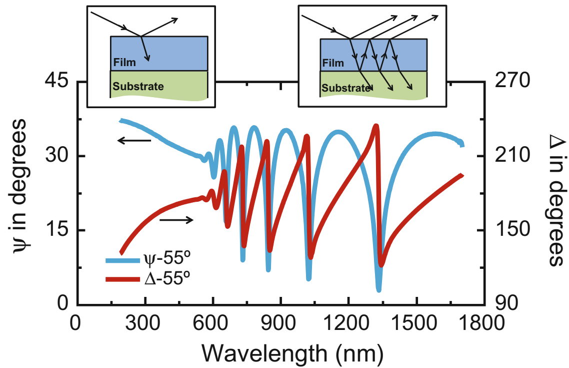

Fig. 3.5 SE data from an a-Si:H film on glass show the absorbing region (λ < 600 nm) where only the surface of the a-Si:H is measured and the transparent wavelength region where interference features result from light traveling through the film

plotted in a unique manner. First, the data are graphed versus photon energy (in eV), which is inversely related to the wavelength (in nm):

$$E = \frac{1239.8}{\lambda} \tag{3.1}$$

Second, the ψ and Δ spectra have been converted to “pseudo” dielectric functions. Pseudo dielectric functions (Sect. 3.5.1) are often confused with actual material properties. Rather, they are directly calculated from ψ and Δ assuming a single surface reflection from an isotropic, uncoated, bulk material. If the sample contains a thin film, the pseudo dielectric functions calculated from the SE data are not physical properties and should not be interpreted as the dielectric functions of individual materials. To avoid confusion, we add triangle brackets to the pseudo curves ($<\varepsilon_1>$, $<\varepsilon_2>$) to differentiate from the actual material dielectric functions (ε_1, ε_2).

Still, the pseudo dielectric functions are a helpful data visualization tool for estimating film properties. Where the film is transparent, the pseudo dielectric functions will oscillate just like ψ and Δ. When the film is absorbing the pseudo dielectric functions are similar for different angles of incidence, making it easier to estimate bandgap and other electronic transition energies. Each absorption peak in $<\varepsilon_2>$ can be associated with an interband transition in the material band structure [2]. For the CdMgTe film in Fig. 3.6, there are three critical points associated with $<\varepsilon_2>$ peaks at 3.5, 3.9 and 5 eV [3]. However, roughness or surface layers, such as a native oxide, contribute to shifts between the pseudo curves and actual material dielectric functions [2, 3]. Thus, pseudo-dielectric functions only provide estimates of real material properties.

For single-layer films the oscillations in the transparent wavelength region should center on zero in $<\varepsilon_2>$. This is no longer true if the film is rough. Consider the $<\varepsilon_2>$ oscillations in Fig. 3.6 which are centered above zero due to an 11 nm surface layer. When pseudo dielectric function curves from different angles do not overlap, each angle may contain complementary information. Curves from two angles plotted in Fig. 3.6 overlap in the absorbing region, but are shifted with

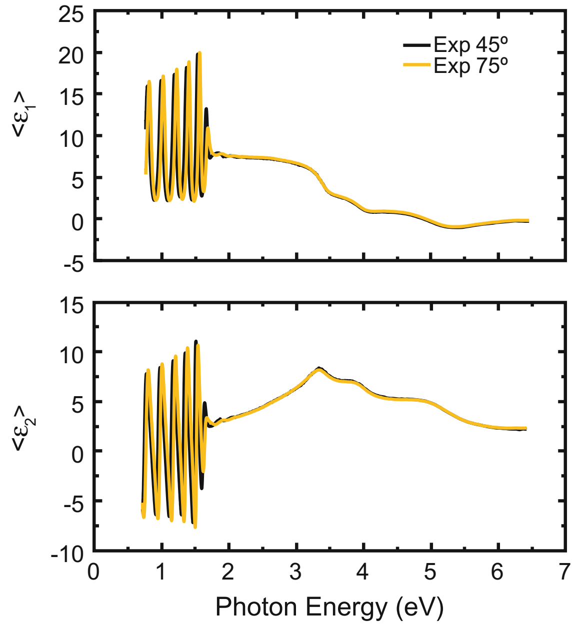

Fig. 3.6 Pseudo dielectric function data curves from a CdMgTe thin film deposited on glass

wavelength in the transparent region below 1.6 eV. Changing angle provides a different path length within the film which affects the interference feature positions. The additional information from multiple angles of incidence proves necessary when analyzing certain complicated samples.

In Fig. 3.7, we consider SE spectra from a transparent conductive oxide (TCO) on glass. TCOs are widely used in photovoltaics. They offer transparency at visible wavelengths yet absorb light in both ultraviolet and infrared due to electronic transitions and free-carriers, respectively [4]. Without modeling the sample structure, we can distinguish the transparent region ($\lambda < 1500$ nm) from the absorbing region at longer wavelengths based on corresponding data features. TCO thickness is determined from data in the transparent wavelength region, where interference features exist. The strong absorption at near infrared (NIR) wavelengths produces a transition in the measured SE spectra where the film changes from dielectric to metallic behavior. This is identified by a step in ψ at a wavelength near 2000 nm. The step position and shape are related to the film conductivity. As a film becomes more conductive, the step position shifts toward shorter wavelengths. Thus, for TCO films there is a trade-off between high conductivity and visible transparency.

In summary, spectral features help identify both transparent and absorbing regions. We can then predict the thin film properties and build an appropriate optical model.

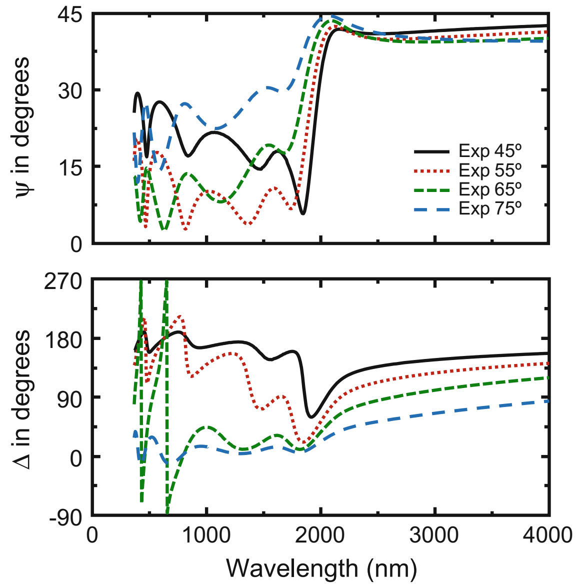

Fig. 3.7 SE data from a transparent conductive oxide layer on glass

3.4 Model

The measured ψ and Δ are not typically of direct interest. Rather, we wish to determine layer thicknesses and material optical constants. The relationships between these sample properties and ψ and Δ are generally transcendental. Thus, we are not able to directly solve for the sample quantities of interest. To obtain the desired sample information we must apply the Inverse Approach—we predict the result, calculate if we are correct, and then refine our prediction. This method is referred to as model-based regression analysis, as our prediction takes the form of a model which describes the measured sample.

The model describes each material by its optical constants and film thickness. We examine the basic model structures used in ellipsometry and define the optical constants in Sect. 3.4.1. The optical constants vary versus wavelength, which is referred to as dispersion. In Sect. 3.4.2, we describe common methods to represent the optical constant dispersion. In Sect. 3.4.3, we review the underlying equations related to the model which allow us to calculate ψ and Δ.

3.4.1 Model Structure and Optical Constants

A model is simply a description of the measured sample structure. For SE data analysis, the model predicts how the light polarization is altered. Models for a bare

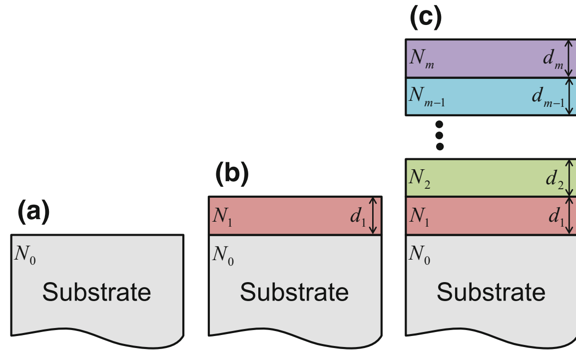

Fig. 3.8 Illustrations of **a** bare substrate, **b** single-layer film, and **c** multi-layered film

substrate, single-layer film, and multi-layered film are illustrated in Fig. 3.8. Each material is described by its thickness and optical constants.

Note that substrate thickness is not shown. For the purpose of simple calculations the substrate is ideal and treated as semi-infinite. For actual ellipsometry samples, any material can be used as a substrate. Examples include crystalline semiconductors such as silicon wafers, glass panels, or polished metal surfaces. In fact, a thin metal can exist anywhere in an actual sample structure, but be treated as an effective substrate if it completely absorbs the light.

There are two common descriptions for the optical constants of a material: the complex dielectric function and the complex refractive index. The complex dielectric function is given as:

$$\varepsilon \equiv \varepsilon_1 - i\varepsilon_2 \tag{3.2}$$

where the real and imaginary components, ε_1 and ε_2, describe the material response to electric fields associated with the probing light beam.

The complex refractive index is given as:

$$N \equiv n - ik \tag{3.3}$$

where n is the index of refraction and k is the extinction coefficient. The index of refraction describes the phase velocity of light within a material (v) compared to the velocity in vacuum (c):

$$n = \frac{c}{v} \tag{3.4}$$

The extinction coefficient informs the absorption of light as it travels through a material. When the extinction coefficient is non-zero, the light intensity decreases exponentially with traveled distance (z) from the initial intensity (I_0):

$$I(z) = I_0 e^{-\alpha z} \tag{3.5}$$

Here, α is the absorption coefficient and is related to the extinction coefficient by:

$$\alpha = \frac{4\pi k}{\lambda} \tag{3.6}$$

The complex dielectric function and complex refractive index are related by:

$$\varepsilon = N^2 \tag{3.7}$$

Either representation of optical constants can be used to describe the materials in our model. However, optical constants are not inherently constant values and actually vary with wavelength and temperature. Next, we describe different methods to represent the wavelength-dependent nature of material optical functions.

3.4.2 Representing Optical Constants

The optical constants must be entered for each layer in the model. However, optical constants vary with wavelength so the model needs to incorporate values for each measured wavelength. In addition, we need to consider how optical constants can be adjusted in case our estimation is incorrect.

The most direct way to introduce optical constants into a model is to list their values at each measured wavelength. Representative optical constants can be obtained from literature references and books such as the compilations of Palik and Adachi [5–7]. In fact, updated optical constants for photovoltaic materials are provided in Part II of Volume II. Tabulated lists work well for stable and reproducible materials. However, the optical constants of many materials depend on microstructure, composition, process conditions, and so forth. For these materials, tabulated lists are not practical except to provide initial estimations.

It is more efficient and useful to describe optical constants using mathematical functions, referred to as dispersion equations. These equations offer many advantages: 1. They significantly reduce the number of parameters used to both *describe* and *adjust* the optical constant shape. 2. They generally maintain smooth and continuous curves. 3. They impose controls between the optical constants at different wavelengths. 4. Many enforce a physically plausible shape. Chapter 5 contains a review of many common dispersion equations. In Fig. 3.9, the optical functions of indium tin oxide (ITO) are graphed. Dispersion equations are used to describe the ITO complex dielectric function over the measured energy range.

Both tabulated lists and dispersion equations describe the optical constants of single, homogenous materials. Composites of more than one material are often described by "effective" dielectric functions or *effective medium approximations*

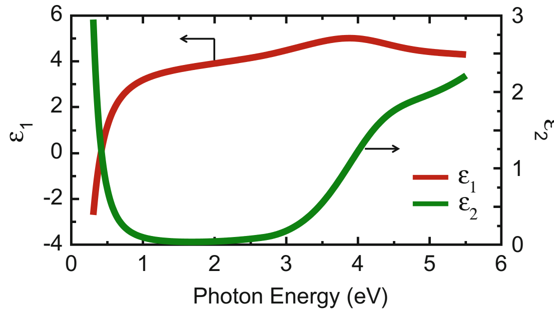

Fig. 3.9 Dielectric function for indium tin oxide described by a sum of Kramers-Kronig consistent dispersion equation shapes

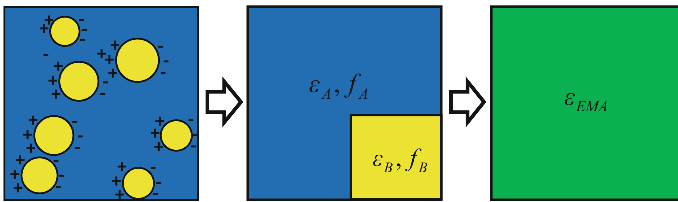

Fig. 3.10 Effective medium approximation (EMA) considers mixing of materials based on the dielectric functions (ε_a and ε_b) and volume fractions (f_a and f_b) of each constituent, along with possible effects from charge screening to be approximated by a single dielectric function (ε_{EMA})

(EMA). Figure 3.10 illustrates a composite with two constituents. The effective dielectric function (ε_{EMA}) is calculated by considering the volume fraction (f_a and f_b) and dielectric functions (ε_a and ε_b) of each constituent along with possible charge screening. As evident from the figure, when two materials are mixed, the volume fractions must sum to the total such that $f_b = 1 - f_a$.

If charge screening is ignored, as is the case when the external electric field is parallel to the boundaries between materials, ε_{EMA} is simply the volume average of the constituents:

$$\varepsilon_{EMA} = f_a \varepsilon_a + (1 - f_a)\varepsilon_b \tag{3.8}$$

which is easily extended for more than two constituents. For general material shapes, screening charges appear along the boundaries due to the discontinuity of the electric field. Here, the theoretical approximations must consider the shape of each material when calculating the effect of screening [8]. A further simplification assumes the charge screening from spherical materials in a host material to derive corresponding EMA equations. While the mathematical details of the EMA are beyond the scope of this chapter, we will consider the Bruggeman EMA, which

finds common use when describing rough surfaces and interfacial mixing between layers. Here, the two constituents are mixed without distinction of host and inclusion and the EMA equation becomes:

$$f_a \frac{\varepsilon_a - \varepsilon_{EMA}}{\varepsilon_a + 2\varepsilon_{EMA}} + (1 - f_a) \frac{\varepsilon_b - \varepsilon_{EMA}}{\varepsilon_b + 2\varepsilon_{EMA}} = 0 \tag{3.9}$$

In general, EMA theories are used when the dielectric function of each material is already known and can be fixed in the model. The volume fraction and layer thickness are often the only fit parameter.

EMA calculations are useful within certain limitations. If the length-scale of individual materials is large compared to the measurement wavelength, there can be light scattering which is not considered by the EMA. The length-scale must be much smaller than the wavelength of light; however, it also must not be too small. Each material must maintain its own identity for the EMA to remain valid. If mixing occurs at an atomic level, the underlying band structure is affected and an EMA will not correctly describe the optical functions. Here, a composition-shifting algorithm is often applied. Figure 3.11 shows the complex dielectric function for a series of $Al_xGa_{1-x}As$ alloys. The critical points of the crystalline semiconductor shift as composition (x) varies [9].

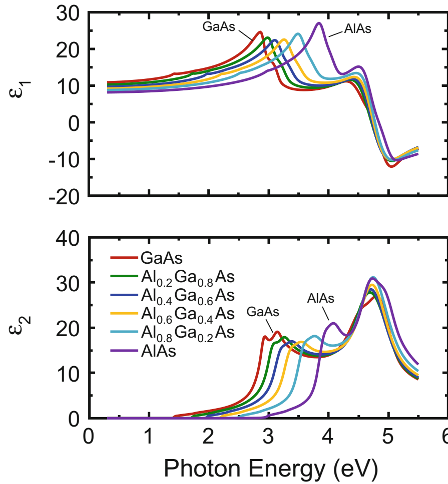

Fig. 3.11 Composition-shifting algorithm adjusts the optical functions of $Al_xGa_{1-x}As$ in relation to the specified composition, x

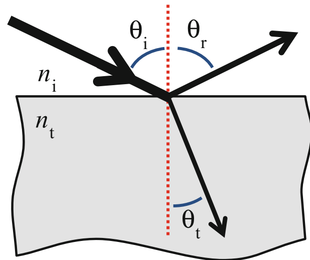

Fig. 3.12 Reflection and refraction of light from an interface between a transparent ambient and a bulk material

3.4.3 Model Calculations

After a model is constructed, we can calculate the expected ψ and Δ values associated with such a sample. In this section, we review the basic equations for this calculation. Recall that ψ and Δ are related to the change of light polarization state. Thus, we start with a brief description of light at an interface.

When a light beam reaches the interface between two media, reflection and refraction occur. Figure 3.12 illustrates the light at the interface between an ambient and a bulk material. Reflection describes the partial light that returns to the original medium. For a smooth interface, the reflection is specular and the reflection angle is the same as the incident angle of the incoming light:

$$\theta_r = \theta_i \tag{3.10}$$

Refraction describes the partial light that transmits into the second medium. The transmitted light changes direction depending on both the incident angle and the change in refractive index across the interface. For a transparent material, the light refracts at a new angle as described by Snell's law [10]:

$$n_i \sin\theta_i = n_t \sin\theta_t \tag{3.11}$$

where n_i and n_t are the refractive index of the incident and transmitted materials, respectively.

The polarization of a light wave can be described by two perpendicular electric fields; each with an amplitude (E_{x0}, E_{y0}) and phase (δ_x, δ_y). A Jones vector represents a light wave traveling in the z-direction as [11]:

$$\begin{bmatrix} E_x \\ E_y \end{bmatrix} = \begin{bmatrix} E_{x0}e^{i\delta_x} \\ E_{y0}e^{i\delta_y} \end{bmatrix} \tag{3.12}$$

For ellipsometry measurements, we choose a Cartesian coordinate system for the orthogonal electric field directions [12], as shown in Fig. 3.13. The plane containing the incident beam and the sample normal is called the plane of incidence. The specular reflection from a smooth surface also lies in the plane of incidence.

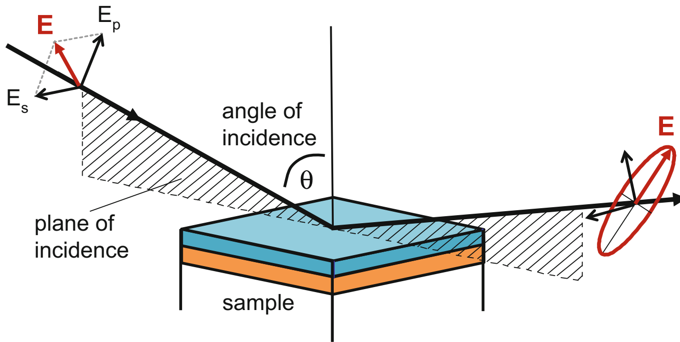

Fig. 3.13 SE measurement coordinate system

The electric field parallel to this plane is called the *p*-wave or the *p*-component of the electric field (E_p). The electric field perpendicular to the plane of incidence is called the *s*-wave or the *s*-component of the electric field (E_s).

By the nature of light interaction with an isotropic surface, incident *p*-waves will remain *p*-waves upon reflection and transmission. Similarly, the incident *s*-waves will remain *s*-waves. Each will experience amplitude and phase changes but they will not convert orientations. Thus, *p*-waves and *s*-waves remain orthogonal and can be treated independently. We relate the reflected electric field in the *p*- and *s*-directions to the incident electric fields using amplitude reflection coefficients (r_p, r_s) as:

$$E_{rp} = r_p E_{ip} \tag{3.13a}$$

$$E_{rs} = r_s E_{is} \tag{3.13b}$$

where the subscripts refer to the incident (i) and reflected (r) electric fields.

Ellipsometry is not a measurement of the polarization of the detected light. Rather, ellipsometry describes the *change* in polarization. With this in mind, an ellipsometry measurement is given as the ratio of the interaction of *p*-waves to *s*-waves:

$$\tan(\psi)e^{i\Delta} = \frac{E_{rp}/E_{ip}}{E_{rs}/E_{is}} = \frac{r_p}{r_s} \tag{3.14}$$

This definition shows how ψ and Δ are related to the change in polarization. We calculate the reflected electric field components predicted by our model by studying the interaction of light with our sample. First, we consider a single interface. The reflected and transmitted electric field components are related to the incident electric field by Fresnel's equations [10]:

$$r_p \equiv \frac{E_{rp}}{E_{ip}} = \frac{N_t \cos\theta_i - N_i \cos\theta_t}{N_t \cos\theta_i + N_i \cos\theta_t} \tag{3.15a}$$

$$r_s \equiv \frac{E_{rs}}{E_{is}} = \frac{N_i \cos\theta_i - N_t \cos\theta_t}{N_i \cos\theta_i + N_t \cos\theta_t} \tag{3.15b}$$

$$t_p \equiv \frac{E_{tp}}{E_{ip}} = \frac{2N_i \cos\theta_i}{N_i \cos\theta_t + N_t \cos\theta_i} \tag{3.15c}$$

$$t_s \equiv \frac{E_{ts}}{E_{is}} = \frac{2N_i \cos\theta_i}{N_i \cos\theta_i + N_t \cos\theta_t} \tag{3.15d}$$

Notice there are different reflection and transmission coefficients for the *p*-waves and *s*-waves. Additionally, the reflected and transmitted light depends only on the angle of incidence and the optical constants of each material.

Now consider a single-layer film on a substrate as show in Fig. 3.14. If the film is completely transparent, we can draw an infinite number of reflected and transmitted beams. The first reflected beam can be calculated using (3.15a–3.15d) for both *p*- and *s*-polarization directions. Additional detected light beams will contain thickness information since they travel through the film. This is represented by tracking the phase difference between the first reflection and the light beams that have traveled through the film. The phase variation, β, is calculated as [13]:

$$\beta = \frac{2\pi d}{\lambda} N_1 \cos\theta_1 \tag{3.16}$$

Because the refracted light travels twice through the film before transmitting to air, the phase difference between first and second detected reflections is 2β. The total reflection can be obtained by the superposition of every reflected wave collected at the detector:

$$r_{\text{tot}} = r_{01} + t_{01}t_{10}r_{12}e^{-i2\beta} + t_{01}t_{10}r_{10}r_{12}^2e^{-i4\beta} + t_{01}t_{10}r_{10}^2r_{12}^3e^{-i6\beta} + \ldots \tag{3.17}$$

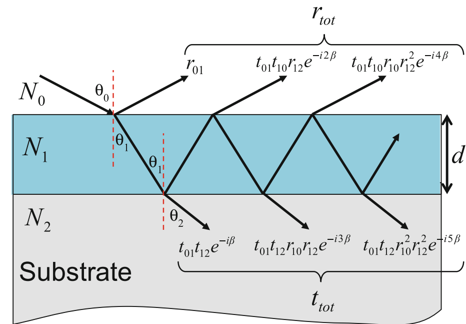

Fig. 3.14 Interaction of measurement beam with a thin film

where r_{jk} and t_{jk} represent the reflection or transmission coefficient with j and k referring to the incident and transmitted media, respectively. Equation (3.17) leads to an infinite series and exact expressions for p- and s-waves can be easily found elsewhere [13]. The ellipsometric measurement quantities described in (3.14) are now given by $r_{\mathrm{tot},p}/r_{\mathrm{tot},s}$ which contains the film thickness in addition to the complex refractive indices.

We conclude that the ellipsometric model contains all of the information to calculate ψ and Δ. The *angle of incidence* is defined by the measurement. The substrate is represented by its *optical constants*. If we describe the optical constants and thickness of each layer in our model, we can calculate ψ and Δ for any measurement angle. Next, we compare the model calculations to the experimental results in an attempt to obtain useful sample properties.

3.5 Data Fitting

Data analysis is the process of determining sample properties that produce the best match to the measured data. The SE measurements consist of two values (ψ, Δ) which allow calculation of two sample properties for each measured wavelength. In the case of a bare substrate, the measured data can be directly transformed to determine bulk optical constants, as described in Sect. 3.5.1. However, it is more common that sample properties are determined through model-based data fitting (Sect. 3.5.2).

3.5.1 Direct Conversion

Not all ellipsometry measurements require a model. Interaction of light with an ideal substrate produces a single, specular reflection from the surface of a bulk, uncoated material. The optical functions of such a material, commonly referred to as *pseudo-dielectric functions*, are directly calculated from the raw ellipsometric data as [13]:

$$\langle \varepsilon \rangle = \langle N \rangle^2 = \sin^2\theta \left[1 + \tan^2\theta \left(\frac{1-\rho}{1+\rho} \right)^2 \right] \tag{3.18}$$

where $\rho = \tan(\psi)e^{i\Delta}$.

If more than a single reflection is detected, the optical functions calculated from (3.18) will not match the actual material optical functions and have little meaning. Few samples satisfy the requirements of an ideal substrate. Most surfaces are microscopically rough or coated with thin layers such as a native oxide. Measurements from transparent substrates, such as glass or plastic, may not qualify as an

ideal bulk material due to additional reflections from the back surface of the substrate. Triangular brackets are added around the direct-calculated optical functions to distinguish these values from the intrinsic material properties. Because <*ε*> and <*N*> are directly related to the measured data, they are called "pseudo" optical functions.

The pseudo optical functions are just another way of representing the measurement quantities. While metal substrates may not be ideal due to oxidization or roughness, pseudo-optical functions are often used to approximate their bulk properties. Figure 3.15 shows measured ψ and Δ from an opaque molybdenum film. These measurement curves are also transformed to show corresponding pseudo optical constants. In this case, measurements from different angles transform to the same <*n*> and <*k*> curves because any surface layers are very thin. The <*n*> and <*k*> are used as an approximation for the bulk optical functions (*n, k*) even though the actual values may be offset by 10% or more.

There are inevitable limitations to the pseudo optical transformation. For this reason, optical modeling is commonly applied to samples even when direct transformation can be performed.

3.5.2 Model-Based Data Fitting

Data fitting, or regression analysis, is an iterative process of determining unknown sample properties from the measured data. The equations which relate the measured data to the sample structure are very complex and often transcendental. This means the equations can't be simplified to express the sample properties in terms of

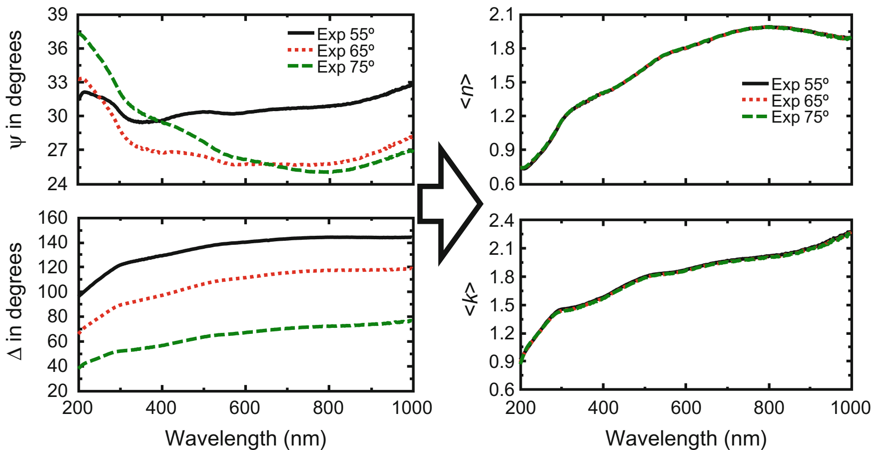

Fig. 3.15 Measured SE spectra from an opaque Mo film along with corresponding pseudo optical function curves

measurement parameters (ψ, Δ). As a result, we take an inverse approach: guessing the sample properties and comparing the "expected" ψ and Δ to the experiments.

As discussed in Sect. 3.4, our guess takes the form of a model, which describes the entire sample structure. All *known* properties, such as substrate optical constants, are fixed. An initial guess is entered for any *unknown* model parameters. Because they are unknown, they are allowed to vary and are referred to as *fitting parameters*. With all model values entered, the initial ψ and Δ values are calculated. Data fitting begins by examining the match between model-calculations and experimental measurements. Inevitably, there are differences between these values. The fitting parameters adjust to minimize these differences. The fitting process iterates until no further improvement is achieved, resulting in the *best-fit*. The fitting parameters are now at values that produce the best model-calculated match to the experimental data. The user must assess whether these are the correct results, as discussed in Sect. 3.6.

To find the best-fit, the fitting parameters adjust to minimize a merit function, which quantifies the match between model calculations and data. Example merit functions include the mean squared error (MSE) and Chi-Square [14]. In simplest form, the MSE is proportional to the total difference between measured data (Exp) and model calculations (Mod):

$$\mathrm{MSE} \propto \sum (\mathrm{Mod} - \mathrm{Exp})^2 \tag{3.19}$$

In this equation, measurement data can be represented in any form. For example, the MSE can be calculated using ψ and Δ, as [15]:

$$\mathrm{MSE} = \sqrt{\frac{1}{2N - M} \sum_{i=1}^{N} \left[\left(\frac{\psi_i^{\mathrm{Mod}} - \psi_i^{\mathrm{Exp}}}{\sigma_{\psi,i}^{\mathrm{Exp}}} \right)^2 + \left(\frac{\Delta_i^{\mathrm{Mod}} - \Delta_i^{\mathrm{Exp}}}{\sigma_{\Delta,i}^{\mathrm{Exp}}} \right)^2 \right]} \tag{3.20}$$

where N is the number of ψ and Δ pairs, M is the number of variables in the model and σ is the standard deviation for each experimental data point. Regardless of definition, a lower merit function value signifies a better match between model and experimental data and "suggests" a better result. We use MSE as a generic term for further discussion.

Consider the data fitting process for a thick silicon film on glass, as shown in Fig. 3.16. The optical constants for each material are known. Nominal thickness for the bulk film (d_b) and SiO_2 surface layer (d_s) are estimated in the initial model. For the initial model, calculated ψ and Δ curves are compared to the experimental curves as shown in the upper-right graph. Both curves have similar shape, but their interference features are not aligned. The initial MSE of 204 quantifies the large differences between curves. The fitting process proceeds by adjusting the two thicknesses to minimize the differences. After a single iteration, the silicon film thickness decreases to 885 nm while the surface oxide increases. There are noticeable

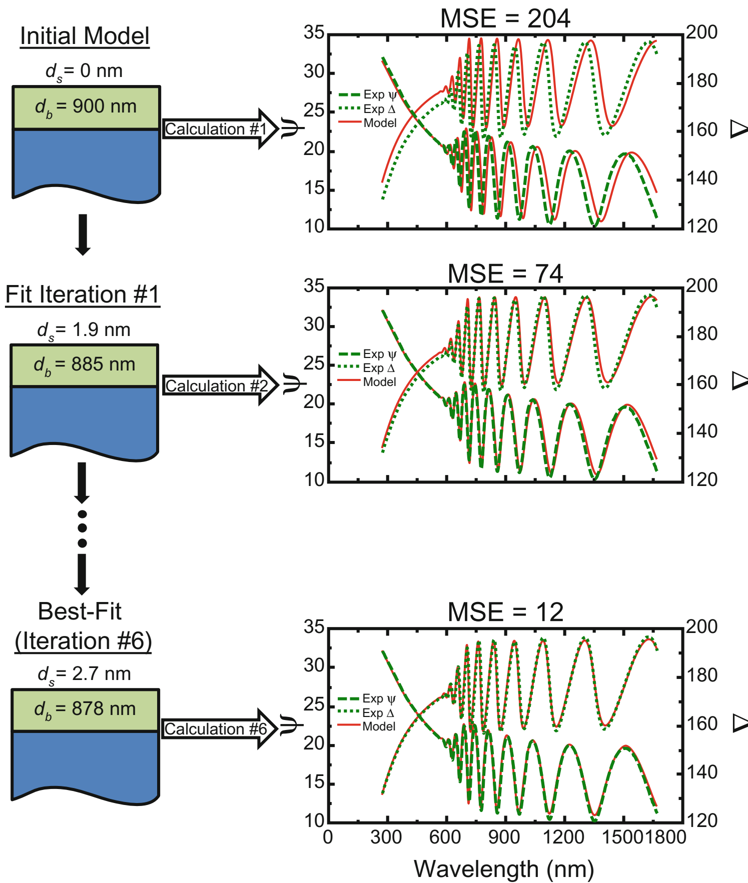

Fig. 3.16 Iterative fitting process is demonstrated where two parameters (silicon film thickness, d_b, and surface oxide thickness, d_s) are adjusted to find the best agreement between experimental data and model calculations

improvements in the match between model and experimental curves. The fitting process continues to iterate—adjusting the thicknesses to further improve the agreement between curves until the MSE reaches a minimum. The final result, which occurs after 6 iterations, produces an MSE of 12, d_b = 878 nm and d_s = 2.7 nm. The model-calculated curves now lie on top of the experimental curves. Thus, the fitting process successfully adjusted the fitting parameters from their initial guesses to their best-fit results to match the experimental data, as quantified by a low MSE.

Computer algorithms facilitate minimization of the merit function [16]. In simplest sense, the algorithm adjusts the fitting parameters to find the best MSE minimum (also called the global minimum). However, success depends greatly on the initial estimates of each fitting parameter. A different MSE minimum (local

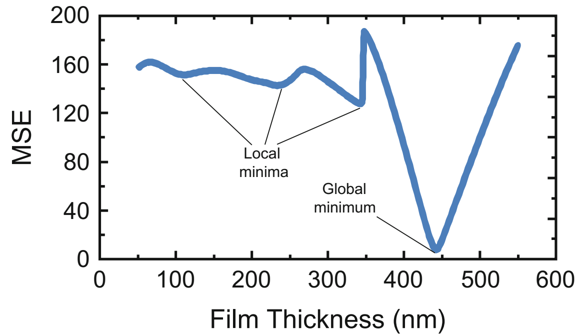

Fig. 3.17 MSE profile versus film thickness

minimum) may be found if the initial estimates are not close to the correct results. An MSE profile is shown in Fig. 3.17. There are several local minima (not the lowest value) and only one global MSE minimum for different thicknesses. In this example, a starting thickness less than 350 nm will converge into a local minimum rather than the best-fit result of 445 nm. If the algorithm finds a local minimum, the reported results will be useless. While easy to visualize for this simple case, an actual model may have many fitting parameters which increases the dimensionality of the problem.

Reasonable estimates for each fitting parameter help guide the algorithm to the global minimum. When difficult to estimate, advanced algorithms can search for the global MSE minimum from multiple starting values. Such global search algorithms are commonly included in commercial software.

Typically, all measured data are fit simultaneously. However, fitting can also be applied on a wavelength-by-wavelength basis, referred to as point-by-point fitting. Here, data at each wavelength are considered separately. Thus, the model should be constrained to a limited number of fitting parameters that vary with wavelength. The thickness of a film is not wavelength dependent and thus should not be determined using this approach. Point-by-point fitting is demonstrated in Sect. 3.7.2.

3.6 Evaluating Results

After data analysis is complete, the user must judge whether the results are valid. Often, only the visual match between model-calculated and experimental data curves is examined. While important, this evaluation is not adequate. Below is a check-list of considerations to increase confidence in the final results.

1. Do model calculations agree with the experimental data? Can the MSE be further reduced?

When the model calculations do not match the experimental data curves, the results are meaningless. In this case, the model needs to be refined until a match is found. If the fit converges to a local minimum, the fitting parameters should be moved to better estimates and data analysis repeated to find the global MSE minimum. It may also be necessary to modify the underlying model. Typically, the simplest model in agreement with experiment is the best answer. Thus, a more complex model should significantly improve the MSE to warrant consideration. What constitutes significant MSE improvement? This is subjective, but an MSE decrease of 20% or more often justifies additional model complexity.

2. Is the result unique?

Next, we confirm that the current result provides the only realistic match to the experimental data. The results are tested by moving the fitting parameters to different starting values in search of additional MSE minima. This test is visualized by calculating an MSE profile versus each fitting parameter, such as shown in Fig. 3.18. One fitting parameter (i.e. the test parameter) is fixed at different values surrounding the suspected final answer. The remaining fitting parameters are allowed to adjust until the best MSE is found at each point. A unique result corresponds to a single MSE minimum that is significantly lower than any additional (local) minima. This is demonstrated with the black solid-line in Fig. 3.18. Results are difficult to assess when additional MSE minima exist, such as with the blue long-dashed curve. Here the fit can easily converge into a local minimum with MSE similar to the global minimum. An obvious case where the result is not unique is shown for the red short-dashed curve. The same minimum MSE is found for a wide range of test parameter values, indicating that no unique answer is available. When a result is not unique, additional data content is needed or the number of fitting parameters needs to be reduced.

3. Is there correlation between fitting parameters?

One reason the result may not be unique is due to parameter correlation. *Correlation* is a measure of the independence of each fitting parameter. When correlation exists, similar modification to the model-calculated curves is achieved by adjustment of multiple correlated parameters. Strong parameter correlation signifies the model has too many fitting parameters. To reduce correlation, one of the correlated

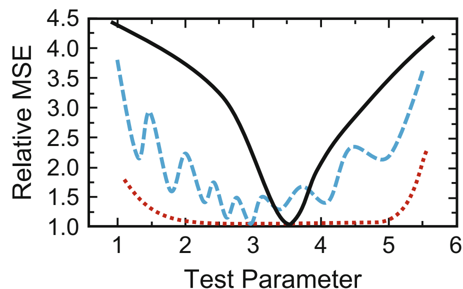

Fig. 3.18 Profiles of relative MSE (=MSE/Global MSE minimum) are shown for three different scenarios: a single unique answer (solid-line), multiple MSE minima (long-dash), and a non-unique, broad MSE minimum (short-dash)

fitting parameters should be removed and the data analysis repeated. If parameter correlation was truly the problem, the MSE should return to a similar minimum value.

4. What is the sensitivity to each fitting parameter?

The algorithm used for data analysis may also generate confidence limits for each result. The confidence limits can be used to check whether each fitting parameter is required. Fitting parameters with large confidence limits in relation to their value can be removed due to lack of sensitivity. Minimizing the number of fitting parameters improves confidence for the remaining adjustable parameters.

5. Are the final results physically plausible?

Regression analysis is a mathematical process to determine the best fitting parameters. However, this does not guarantee the solutions are indeed physically plausible. Negative values for parameters such as thickness, void fraction, or oscillator amplitude are simple examples of non-physical results. Each hints that the model needs to be modified to allow a physically plausible result.

It is also important that resulting optical constants are physically plausible. The simplest test is to ensure each parameter is within its correct range: k and ε_2 are not negative, n is greater than zero, and ε_1 can be positive or negative. A more advanced test is to consider the relationship between real and imaginary optical functions. In Chap. 5, Kramers-Kronig (KK) consistency will be introduced, which describes a physical "tie" between the real and imaginary optical functions. These relationships help explain normal and anomalous dispersion. For transparent films (k equal to or close to zero) the index of refraction exhibits normal dispersion, where n increases towards short wavelengths. This is shown in Fig. 3.19 for the refractive index above 600 nm. At wavelengths where the material is absorbing, the optical functions will show anomalous dispersion. Near the absorption peak, the index will change directions and decrease toward short wavelengths, as shown near 400 nm in Fig. 3.19.

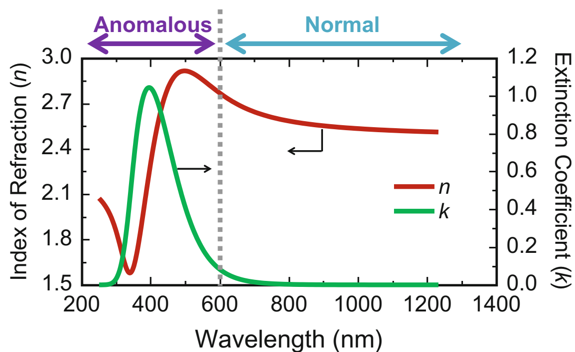

Fig. 3.19 Normal and anomalous dispersion of a Kramers-Kronig consistent refractive index

3.7 Analysis Strategies for Common Sample Structures

SE is typically used to determine film thickness and optical constants. While we may measure hundreds of different thin films with ellipsometry, they are generally: (i) transparent at all wavelengths, (ii) transparent at some wavelengths and absorbing at others, or (iii) absorbing at all wavelengths. The preferred analysis strategy depends on this classification.

In Sect. 3.7.1 we consider measurements of both thickness and index of refraction for transparent films. This approach is also used for films that absorb at some wavelength by restricting characterization to wavelengths where the film is transparent. Further steps can extend data analysis to both transparent and absorbing wavelength regions, as described in Sect. 3.7.2. To determine thickness from a film that absorbs light at all wavelengths, the layer must be thin enough for light to penetrate. For metals, this requirement generally limits the maximum thickness between 50–100 nm. Special strategies for absorbing films are covered in Sect. 3.7.3. Finally, in Sect. 3.7.4 we discuss non-ideal model structures to describe real-world samples.

3.7.1 Transparent Thin Films

The most common application of SE is the characterization of thickness and index of refraction for a thin transparent film. Transparent films have an extinction coefficient equal to zero or low enough to be below the detection limit for typical ellipsometry ($k < 0.001$). Materials in this category include dielectrics, organics, and even semiconductors if we restrict the wavelength range.

As discussed in Sect. 3.3, data from transparent films oscillate due to interference between the surface reflection and light rejoining after traveling through the film. The light traveling through the film is delayed by both thickness and index of refraction. In addition, the reflection characteristics at each interface depend on the index of refraction of the film and underlying material. Thus, the data features contain information about both film thickness and refractive index.

The index of refraction for transparent materials maintains normal dispersion, in other words the index rises toward shorter wavelengths. Transparent films are most commonly modeled with the Cauchy or Sellmeier equations (see Chap. 5) to describe their index versus wavelength. In this manner, the index dispersion can be described with 2–3 adjustable parameters.

Consider the SE data in Fig. 3.20 for a thin SiO_2 film on glass substrate. The oxide layer is transparent over the entire measured spectral range. A Cauchy dispersion equation is used to describe the SiO_2 film index of refraction, while the glass substrate optical constants are fixed at reference values. Regression analysis leads to a SiO_2 film thickness of 171.85 nm with 2.7 nm of roughness. The model calculations are graphed in red solid curves for Fig. 3.20 and show excellent

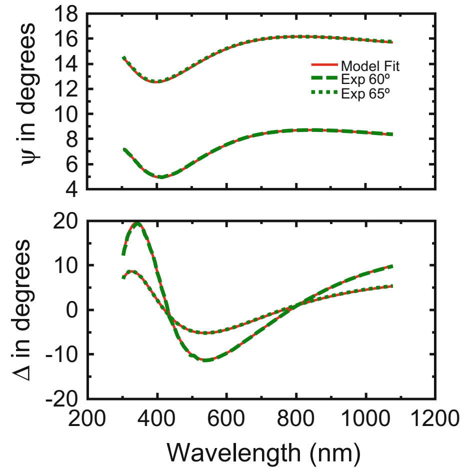

Fig. 3.20 Data Fit for SiO_2 film on glass, where the film index of refraction is described using a Cauchy dispersion relation

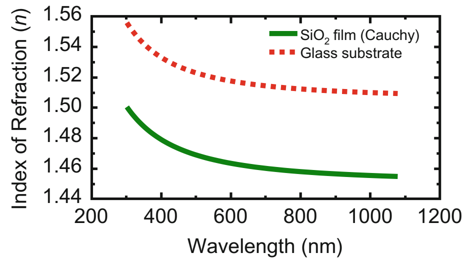

Fig. 3.21 Cauchy dispersion for SiO_2 film compared to glass substrate

agreement to the data curves for both measured angles. The index of refraction for the SiO_2 film described with the Cauchy equation is compared to that of the glass substrate in Fig. 3.21.

This example demonstrates the typical scenario of a transparent layer on a known substrate, whether that substrate is glass, plastic, silicon, or even metal. The substrate optical constants are determined in advance and fixed during the film characterization. The measured ψ and Δ data easily over-determine the unknown thickness and refractive index for the transparent film. To demonstrate SE sensitivity to both thickness and index, consider the simulated curves in Figs. 3.22 and 3.23. In Fig. 3.22 the final fit at 65° is compared with theoretical curves where the modeled SiO_2 thickness is adjusted by ±10 nm. The model-calculated curves shift to shorter wavelengths when the film thickness is underestimated. As thickness increases, the interference features in both ψ and Δ shift toward longer wavelengths.

In Fig. 3.23 the same data fit is compared to adjustments of the index of refraction. Increasing the index of refraction by 0.02 decreases the optical contrast between film and substrate which suppresses the amplitude of the interference features in both ψ and Δ. When the film index decreases by 0.02, the feature amplitude increases because the optical contrast also increases.

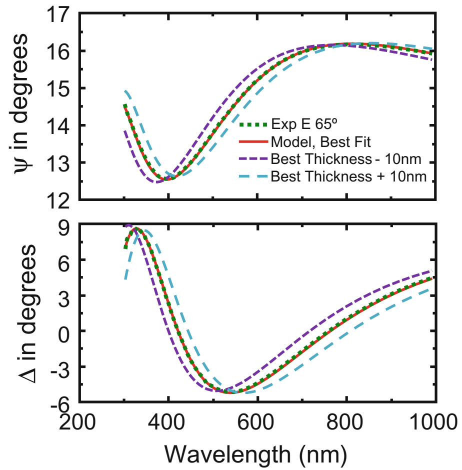

Fig. 3.22 Simulations of ±10 nm thickness variation for the SiO_2 film show the wavelength-shift of interference features for both ψ and Δ

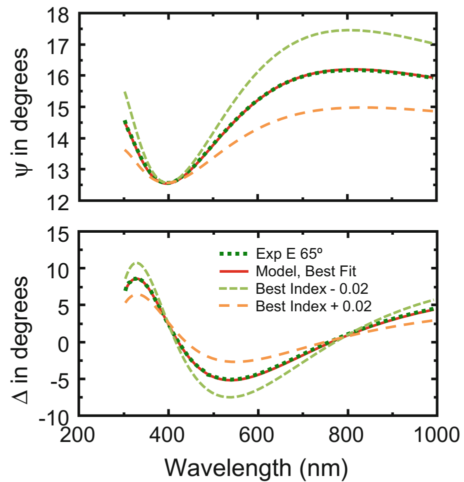

Fig. 3.23 Simulations of ±0.02 variation for the SiO_2 index show the variation in amplitude of interference features for both ψ and Δ

3.7.2 Films that Absorb at Some Wavelengths

Most films will absorb at some wavelengths if the measurement and analysis are extended to the full range of modern SE instruments. The absorbing region adds extra analysis complexity, but comes with a new wealth of information about the materials. The absorbing region can inform about electronic transitions, conductivity, composition, and even crystallinity. To gain more information about the material, the analysis strategy needs to determine thickness and both n and k. Common approaches divide the analysis into stages. First, the wavelength range where the film remains transparent is analyzed with the approach in the previous

section to determine film thickness and refractive index. The thickness is a physical property and does not depend on measurement wavelength. Thus, the thickness can be fixed for subsequent analysis steps. Second, the optical constants are determined at each wavelength using a point-by-point fit. With fixed thickness, this is similar to a direct calculation except the data are still analyzed to find the best match considering a single wavelength at a time. Figure 3.24 shows the resulting index of an organic film. The Cauchy fitting result was used to determine the index above 650 nm, and more importantly, the film thickness. With the thickness fixed, both n and k were determined using point-by-point fitting. These results are compared to the Cauchy in Fig. 3.24. Extension of the Cauchy to shorter wavelengths does not match the actual material properties due to absorption in the film. Point-by-point fitting determines the optical constants in both transparent and absorbing regions. These optical constants may be an adequate final result, but it is often preferred to ensure the final result is physically plausible. Thus, it is common to match any "point-by-point" fit results with Kramers-Kronig dispersion equations (see Chap. 5).

Consider a nanocrystalline germanium film deposited on SiN_x coated glass substrate. The glass and SiN_x film are already characterized such that their values are fixed when determining the top-layer optical constants. As seen in Fig. 3.25, the ψ and Δ curves oscillate at smaller photon energies where the germanium film is transparent. In this region, the thickness of both germanium and SiN_x films are determined and fixed. Next, a point-by-point fit determines both n and k of the nano-crystalline germanium film at all wavelengths. This result may include noise and possibly give incorrect values if the model is not accurate, as determined from fitting the transparent-wavelength range. For example, it is important to include an oxidized surface; otherwise the calculations will not match the experimental data for all wavelengths and will produce incorrect germanium optical constants. To

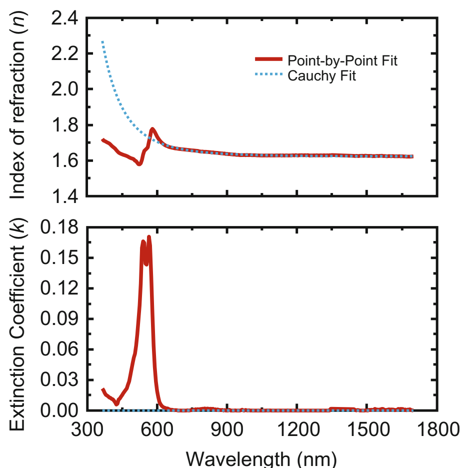

Fig. 3.24 Point-by-point fit results for an organic layer compared to the initial Cauchy fit for transparent region used to determine film thickness. *Note* The Cauchy equation is not applicable to regions where k is non-zero, such as below 600 nm

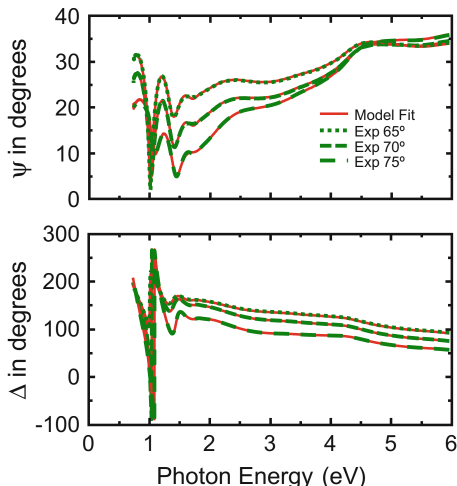

Fig. 3.25 Experimental data and fits for a nanocrystalline germanium film deposited on SiN_x coated glass substrate. The germanium film optical constants were modeled using a summation of Kramers-Kronig consistent oscillators

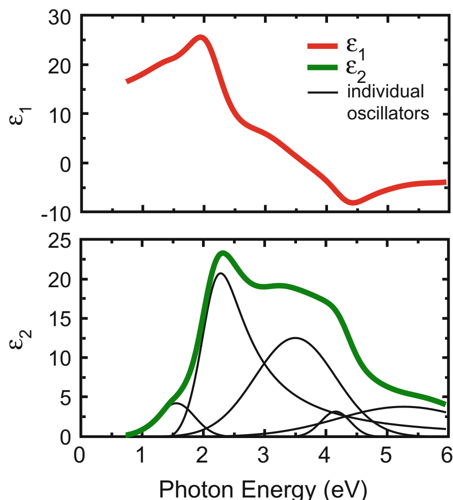

Fig. 3.26 Complex dielectric function for the nanocrystalline germanium film as described by a summation of Kramers-Kronig consistent oscillator functions

ensure better results, the point-by-point optical constants are converted to a summation of oscillator functions, as shown in Fig. 3.26.

This approach works well for semiconducting films, organic films, and even dielectrics where we are extending to high photon energies (above their bandgap). To get accurate thickness from photovoltaic materials, it is often necessary for SE measurements to cover the near infrared spectral region where the materials are transparent.

3.7.3 Absorbing Films

Absorbing films are often modeled in a simple manner. For opaque films, the optical constants are directly solved from the measured SE data (see Sect. 3.5.1). However, there is no sensitivity to the film thickness for opaque layers. Non-opaque absorbing films are more challenging to analyze. Films thin enough to transmit light (generally < 50 nm) have unknown thickness, n and k—all need to be solved simultaneously. The question is whether enough measured information content is acquired to solve all unknown values. Special approaches are required to ensure the data analysis of absorbing films is not under-determined. General methods for absorbing films have been reviewed [17, 18] and each operates by either reducing the unknown sample properties or increasing the measured data information content, as illustrated in Fig. 3.27.

While a full review of methods is beyond the scope of this chapter, we illustrate two common and often successful approaches—both increase measurement content. The first requires a transparent substrate, as SE data are supplemented by transmission intensity data. Transmitted intensity (T) adds adequate extra measurement information for a unique solution. This approach is illustrated in Fig. 3.28a, where the unknown parameters (n, k and d) are determined from measured data (ψ, Δ and T).

The second approach works with absorbing substrates, but requires the addition of a thick transparent film underneath the thin absorbing film. This is referred to as *Interference Enhancement* and exploits significantly different light interaction with the absorbing film for different angles of incidence. The absorbing film can now be characterized using the data from different angles of incidence, as illustrated in Fig. 3.28b. Each method further benefits from a dispersion model to reduce the number of fitting parameters describing the optical functions of the absorbing layer.

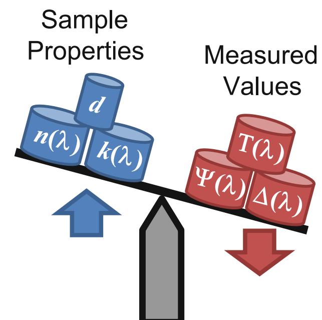

Fig. 3.27 Approaches used for absorbing films require gathering extra information (more measured values) or reducing the total number of unknowns (fewer sample properties)

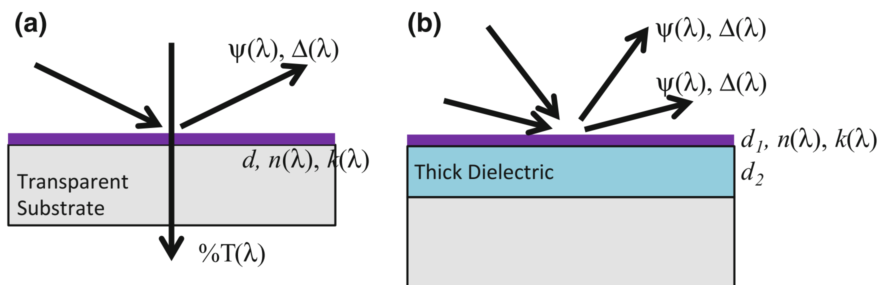

Fig. 3.28 Additonal information can be obtained by **a** SE + T or **b** multi-angle data when interference enhancement provides new information

3.7.4 Complications to the Sample Structure

To this point, the model has consisted of uniform, isotropic, smooth layers. Real samples are often more complex and SE measurements are sensitive to many non-ideal structural properties. Figure 3.29a illustrates an ideal sample structure for a single-layer film. In comparison, the other figures present non-ideal situations. A film with surface roughness is in Fig. 3.29b. When the roughness dimensions are much smaller than the wavelength, they will not scatter light but will affect the measured ψ and Δ. Thus, it may be necessary to model the effects of roughness. This is often done by including an EMA with 50%/50% mixture between the film optical constants and those of air (void). In fact, SE is sensitive to the surface roughness of a few angstroms. If the roughness scale increases beyond 10 nm, additional modeling complexity may be required. The EMA approach may still be applicable but may require more than one EMA layer and there may be sensitivity to the volume fraction in each layer [19].

Figure 3.29c, d show features similar to roughness; however they do not produce the same effect. The surface of Fig. 3.29c is varying, but on a length-scale much larger than the measurement wavelength. In fact, the film thickness is gradually varying within our entire measurement area. This is referred to as thickness non-uniformity and has the effect of averaging the data curves as if multiple uniform films were measured, but each with a different thickness. This tends to broaden any sharp data features and is approximated by using a superposition of models with different film thickness.

When the roughness scale becomes comparable to the wavelength the surface feature will be large enough to cause light scattering. Figure 3.29d illustrates the textured surface used in photovoltaic applications to help capture the incoming sunlight. The accurate characterization can still be performed for textured solar cell structures by using EMA multilayer models (Chap. 4 in Vol. 2). For some special cases the texturing has very repeatable features and dimensions which may scatter the measurement beam to a specific non-specular angle of incidence [20].

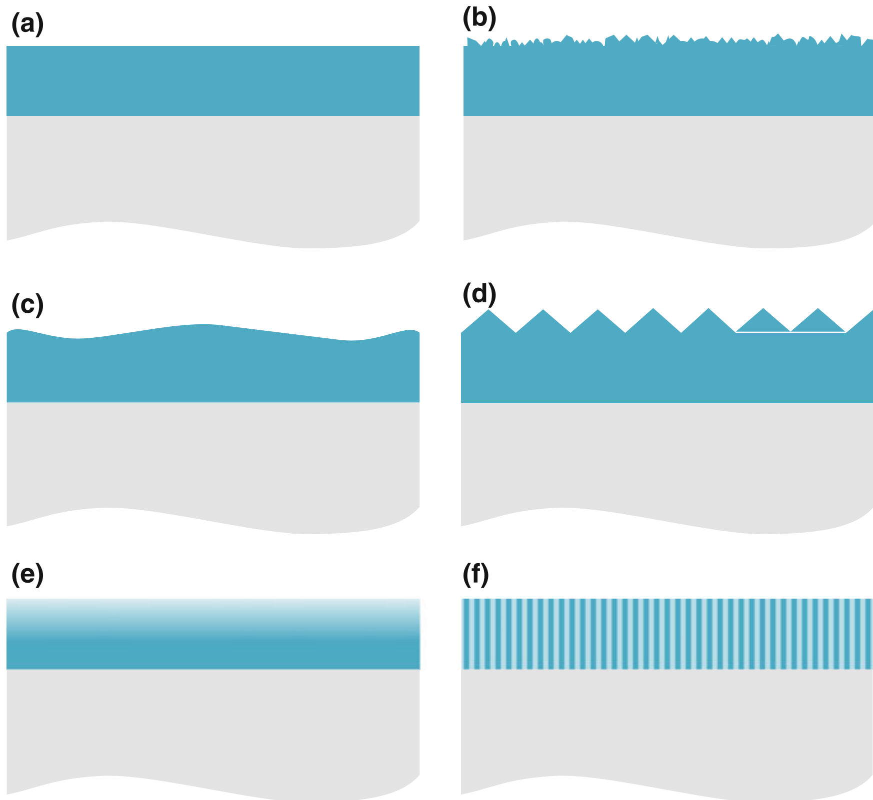

Fig. 3.29 **a** Ideal model consists of planar, homogenous layer with perfect interfaces. Non-ideal models may incorporate **b** rough surface, **c** non-uniform film thickness, **d** textured surface, **e** graded film index, or **f** anisotropic films

Figure 3.29e shows a film with depth-dependent optical constants. To model such a film, the single-layer is represented by a series of thin layers. The optical constants of each layer are allowed to vary to approximate the changes within the graded layers.

Finally, materials can be anisotropic, having different optical response to light from different directions. Figure 3.29f considers a nanostructured film. Here, the film properties appear different for electric fields parallel to the film surface compared to electric fields perpendicular to the surface. This may produce anisotropic effects. Such films are modeled by describing different optical constants for in-plane and out-of-plane orientations [21].

References

1. P.Y. Yu, M. Cardona, *Fundamentals of Semiconductors: Physics and Materials Properties* (Springer, Berlin, 2001)
2. D.E. Aspnes, A.A. Studna, Phys. Rev. B **27**, 985 (1983)
3. Y.S. Ihn, T.J. Kim, D.E. Aspnes, J. Kossut, Y.D. Kim, Appl. Phys. Lett. **84**, 693 (2004)
4. R.A. Synowicki, Thin Solid Films **313–314**, 394 (1998)
5. E.D. Palik (ed.), *Handbook of Optical Constants of Solids I, II, III* (Academic Press, San Diego, 1998)
6. S. Adachi, *Optical Constants of Crystalline and Amorphous Semiconductors: Numerical Data and Graphical Information* (Kluwer Academic Publishers, Boston, 1999)
7. S. Adachi, *Optical Constants of Crystalline and Amorphous Semiconductors: Materials and Fundamental Principles* (Kluwer Academic Publishers, Boston, 1999)
8. M. Losurdo, K. Hingerl (eds.), *Ellipsometry at the Nanoscale* (Springer, Berlin, 2013)
9. P.G. Snyder, J.A. Woollam, S.A. Alterovitz, B. Johs, J. Appl. Phys. **68**, 5925 (1990)
10. E. Hecht, *Optics*, 4th edn. (Addison-Wesley, San Francisco, 2002)
11. R.C. Jones, J. Opt. Soc. Am. **31,** 488 (1941)
12. R.M.A. Azzam, N.M. Bashara, *Ellipsometry and Polarized Light* (North Holland, Amsterdam, 1977)
13. H. Fujiwara, *Spectroscopic Ellipsometry: Principles and Applications* (Wiley, West Sussex, UK, 2007)
14. G.E. Jellison, Jr., *Handbook of Ellipsometry*, ed. by H.G. Tompkins, E.A. Irene (William Andrew, New York, 2005), pp. 241–245. Chap. "Data Analysis for Spectroscopic Ellipsometry"
15. J. Woollam, B. Johs, C. Herzinger, J. Hilfiker, R. Synowicki, C. Bungay, SPIE Proc. **CR72**, 10 (1999)
16. W.H. Press, B.P. Flannery, S.A. Teukolsky, W.T. Vetterling, *Numerical Recipes in C* (Cambridge University Press, Cambridge, 1988)
17. J.N. Hilfiker, N. Singh, T. Tiwald, D. Convey, S.M. Smith, J.H. Baker, H.G. Tompkins, Thin Solid Films **516**, 7979–7989 (2008)
18. J.N. Hilfiker, R.A. Synowicki, H.G. Tompkins, SVC Proc. 511–516 (2008)
19. D.E. Aspnes, F. Hottier, J.B. Theeten, Phys. Rev. B **20**, 3292 (1979)
20. M.F. Saenger, J. Sun, M. Schadel, J.N. Hilfiker, M. Schubert, J.A. Woollam, Thin Solid Films **518**, 1830 (2010)
21. S.-H. Hsu, E.-S. Liu, Y.-C. Chang, J.N. Hilfiker, Y.D. Kim, T.J. Kim, C-J. Lin, G.-R. Lin, Phys. Status Solid A **205**, 876 (2008)

Chapter 4
Optical Properties of Semiconductors

Maria Isabel Alonso and Miquel Garriga

Abstract In this chapter we present basic concepts which are relevant to link the results obtained from ellipsometry data analysis with fundamental properties of semiconductors for photovoltaic applications. The linear optical properties of semiconductors are best discussed in terms of the relationship between the dielectric function ε and the band structure.

4.1 Introduction

The subject of this chapter is so broad that we shall not attempt to give here a comprehensive and theoretically rigorous description. Alternatively, we will focus on some aspects which are helpful to bridge the gap between basic concepts and more complete textbooks beyond the scope of this contribution [1–4]. We shall pay particular attention to topics relevant for the understanding and interpretation of ellipsometry spectra of semiconductors in the essential spectral range for photovoltaic (PV) applications, i.e., the optical energy range.

In terms of the linear optical properties of a material and from an experimental perspective, we can distinguish a semiconductor by quite structured optical functions in the optical energy range. The spectra of both insulators and metals are comparatively featureless. However, insulators are transparent and exhibit low reflectivity whereas metals display high absorption and high reflectivity. We find the origin of these properties in the different electronic structures of the diverse materials and it is possible to understand them based on electronic band theory. The dielectric function ε for some crystalline Silicon-Germanium alloys with different compositions is displayed in Fig. 4.1. The overall shape of the various ε is alike, but even for so similar

M. I. Alonso (✉) · M. Garriga
Institut de Ciència de Materials de Barcelona (ICMAB-CSIC), Campus de la Universitat Autònoma de Barcelona, 08193 Bellaterra, Spain
e-mail: isabel@icmab.es

M. Garriga
e-mail: miquel@icmab.es

© Springer International Publishing AG, part of Springer Nature 2018

H. Fujiwara and R. W. Collins (eds.), *Spectroscopic Ellipsometry for Photovoltaics*, Springer Series in Optical Sciences 212,
https://doi.org/10.1007/978-3-319-75377-5_4

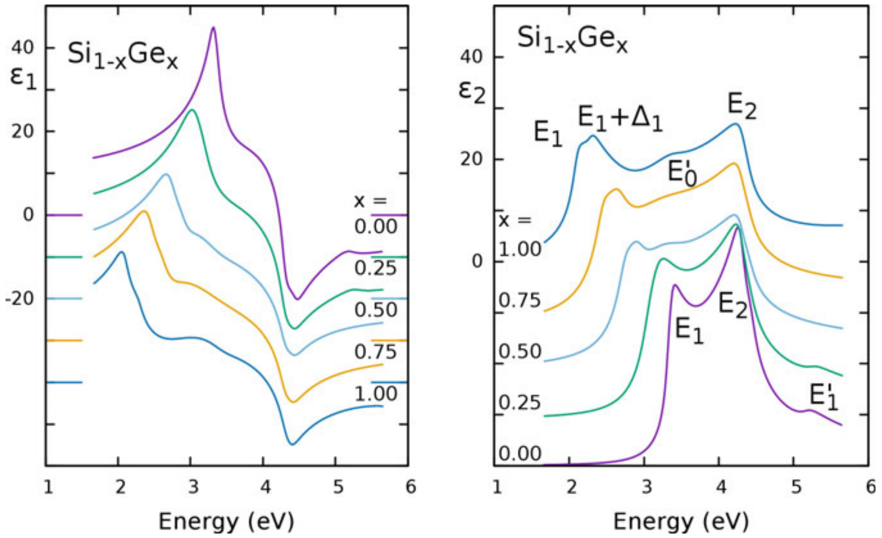

Fig. 4.1 Real and imaginary parts of the dielectric function of SiGe alloys measured by ellipsometry [5]. The critical points observed in this spectral range are labelled with the standard notation according to their assignments. The curves are shifted vertically for clarity, as indicated

semiconductors, the details are quite different. The specific features reveal critical points (CPs) due to Van Hove singularities and the labels of the CPs (i.e., E_0', E_1, $E_1 + \Delta_1$, E_1', and E_2) are related to the band structures. The connection between all these elements will be elaborated in this chapter.

4.2 Electronic Band Structures

The electronic structure of a crystalline solid originates from the interactions between atoms. It is important to notice that there are two kinds of contributions to these interactions. First, the nature of the atoms determines their strength and, second, the spatial order introduces a modulation that promotes or restricts that strength depending on the symmetry of the arrangement. Both contributions determine which is the most stable structure and are reflected in the electronic band structure, that is, the possible electronic energy states as a function of the wavevector.

4.2.1 Energy Considerations

Energy bands evolve from atomic energy levels when individual atoms interact to build the solid. The bonds between atoms are mainly formed by the outer valence

electrons because the inner electrons are more strongly attached to the nucleus. We may then consider the solid as composed of cores and valence electrons. To describe most PV semiconductors we consider as example the C atom. Its valence electronic structure is $(2s)^2(2p)^2$. Having 4 outermost electrons, C atoms can crystallize in a diamond structure with covalent bonding in tetrahedral arrangement by means of the sp^3 hybridization of the valence orbitals in the bonding process which is the basis of most inorganic semiconductors, among them Si, Ge, and also compound semiconductors of the zinc blende, wurtzite, and chalcopyrite structures. Diamond is an insulator and is metastable; the most stable binding among C atoms occurs in graphite by the sp^2 hybridization that results in a planar disposition of bonds. The non-hybridized p orbitals from neighboring C atoms overlap forming π bonds and allow for delocalization of electrons, that is, conjugation. This kind of bonds is fundamental for organic semiconductors. In graphite there is no band gap and therefore, the material is conductor. The conducting versus insulating behavior is due to the presence versus absence of π-electrons. The C–C bond length is quite short in both cases, around 1.42 Å for the sp^2 and 1.55 Å for the sp^3 bond. Therefore, the energy difference between filled binding and empty anti-binding hybrid orbitals is quite large. At larger bond lengths this energy is smaller, accordingly Si (2.35 Å) and Ge (2.45 Å) are semiconductors whereas α-Sn (2.81 Å) is a semi-metal. For compound semiconductors like GaAs, AlAs, ZnSe (examples of zinc blende) or CdS, CdSe, CdTe (wurtzite) not only the length but also the ionicity of the bonds makes a contribution. For compounds with the same bond length, like in Ge and GaAs, the latter has a larger gap due to the bond ionicity contribution in GaAs. In ternary compounds like $Cu(In,Ga)Se_2$ (examples of chalcopyrite) the energy schema is also mainly given by sp^3 bonds, although d-valence electrons from Cu modify the energy balance.

Concerning the π bonds, the dominant factor that determines the bandgap is the bandwidth given by the number of interacting C atoms. In graphite a very large number of atoms participate in the conjugated system; on the other extreme, in small molecules the energy difference between the highest occupied π molecular orbital (HOMO) and the lowest unoccupied $\pi^\star$ molecular orbital (LUMO) is larger. As a rule, the band gap is reduced when the size of the conjugated system increases. For example, in the series of polyacene molecules, the band gap decreases when the number of C rings increases, from $\sim$4.8 eV in benzene down to visible energies such as $\sim$2.1 eV in pentacene. In crystals made from these molecules, the interaction among them is usually of the van-der-Waals type which is much weaker than the intra-molecular covalent bonds. Hence, each molecular identity is well-preserved and with it the semiconducting properties. Interaction among molecules gives also rise to bands, which are narrower than those of sp^3 connected inorganic crystals. Even if there are extended bands for electrons in molecular crystals, in most practical situations the conjugated π-electron systems are still mostly restricted to molecular sites. This is due to the strong interaction between the electrons and the vibrations that scatter electrons at each molecular site even in ideal molecular crystals [6, 7].

Detailed description of methods to calculate the energy bands are beyond the scope of this chapter, however, in Sect. 4.2.3 we will briefly mention some of the

methods that describe the energies of electrons in the extended band regime. These methods are remarkably successful to describe inorganic semiconductors but are insufficient for organics in which inclusion of the interaction with molecular vibrations (and disorder) is necessary to accurately describe the electronic levels. Further insight into particularities of inorganic and organic semiconductors will be given in Sects. 4.4 and 4.5, respectively.

4.2.2 Symmetry Considerations

Symmetry plays an essential role in many aspects that determine the resulting energy bands. To begin with, the atomic energy states possess characteristic symmetries and obviously, the combinations of these states in a solid will reflect them in a certain way. A collection of symmetry operations form a group, a mathematical structure providing us with tools to take advantage of symmetry [8]. One of the most important consequences is that every electron state will always transform as one of the group's irreducible representations (irreps). Thus, electron states can be *labelled* according to the irrep they obey. To examine the atomic energy states, let's consider the hydrogen atom as example. Due to its spherical symmetry, its eigenstates can be constructed making use of the spherical harmonic functions Y_{lm}, i e., these functions are basis of the irreducible representations of the group of rotations in space, and the quantum numbers l and m are good labels for the atomic eigenstates. The orbital angular momentum $l = 0$ describes s states, whereas $l = 1$ describes p states. The irreducible representations not only encode the symmetry operations but also simplify the insight into the system's behavior. For example, when a perturbation is applied to the atom, p energy levels can split into three components, but not s levels. The group of spherical symmetry also describes other important systems in solids like impurities and excitons.

Molecular orbitals that result from the process of bonding display different symmetries but, in general, bonding orbitals are symmetric with respect to the interchange of the two atoms and antibonding orbitals are antisymmetric. Inversion is just one of the possible symmetry elements where a point is kept fixed, in this case the inversion center. We refer to these operations as point group symmetries and besides inversion (I) there may be mirror planes (σ), rotations (C_n), and rotation-inversions (S_n), where $n = 1, 2, 3, 4, 6$ indicates rotation by an angle of $2\pi/n$ radians. Crystals formed by different arrangements of tetrahedral sp^3 bonds result in crystal structures with different point symmetries, as displayed in Fig. 4.2: In diamond and zinc blende the tetrahedra are oriented in a staggered configuration along $\langle 111 \rangle$ generating cubic structures. In wurtzite, an eclipsed configuration of tetrahedra produces an hexagonal crystal structure.

Within group theory, every point symmetry operation can be specified by a linear transformation called representation, described by a matrix that performs the symmetry operation. For practical purposes in spectroscopy, the information needed from groups is gathered in the table of characters, which are the traces of the matrices

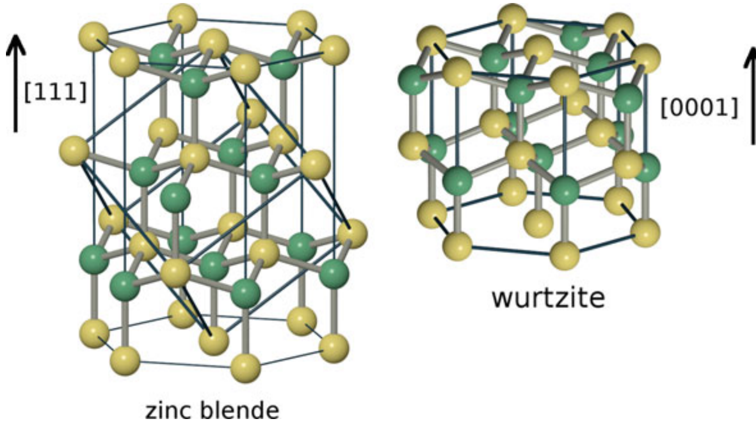

Fig. 4.2 Comparison of the conventional unit cells of zinc blende (cubic) and wurtzite (hexagonal), showing that the different relative orientation of sp^3 tetrahedral units (staggered versus eclipsed) gives rise to crystals of different crystal systems

that describe the irreducible representations. Any set of complete functions can be used as a basis to describe the electronic states but, in general, the group representations generated by those functions are reducible and can be decomposed into a direct sum of irreducible representations. The number and dimensions of the irreducible representations are characteristic of each symmetry group [9]. Therefore, like for the hydrogen atom, the irreducible representations are suitable as labels of physical properties including the electronic energy levels.

An additional unique symmetry that defines a crystal is its invariance under specific translations (translational symmetry). The point operations plus the lattice translations form the space group of the crystal. The three primitive lattice vectors $\mathbf{a_1}$, $\mathbf{a_2}$, $\mathbf{a_3}$ span the direct lattice forming a commutative group. In such a group all irreducible representations are one dimensional with a matrix given by $e^{i\mathbf{kr}}$, where the wavevector $\mathbf{k}$ provides a good quantum number to label the electronic energy states of the crystal in the band structure. The possible values of $\mathbf{k}$ are restricted to those within the first Brillouin Zone (BZ) of the reciprocal lattice generated by the vectors $\mathbf{b_i} = 2\pi(\mathbf{a_j} \times \mathbf{a_k})/[\mathbf{a_1} \cdot (\mathbf{a_2} \times \mathbf{a_3})]$. For each $\mathbf{k}$ we have different states with additional labels coming from the point group symmetries, cf. Sect. 4.3.1. Points and lines of high symmetry within the BZ are designated by greek or roman letters when they are inside or at the border of the BZ, respectively. Significant points are indicated in Fig. 4.3 for the BZs of the two related crystal structures zinc blende and chalcopyrite. Because chalcopyrite can be viewed as a superstructure of zinc blende, the larger BZ of the latter can be folded into the smaller BZ of the former. The zone-folding concept provides approximated dispersions of electronic states starting from known parent materials.

For completeness, we mention that sometimes space-group operations may involve a fractional translation (smaller than a primitive one). These operations are

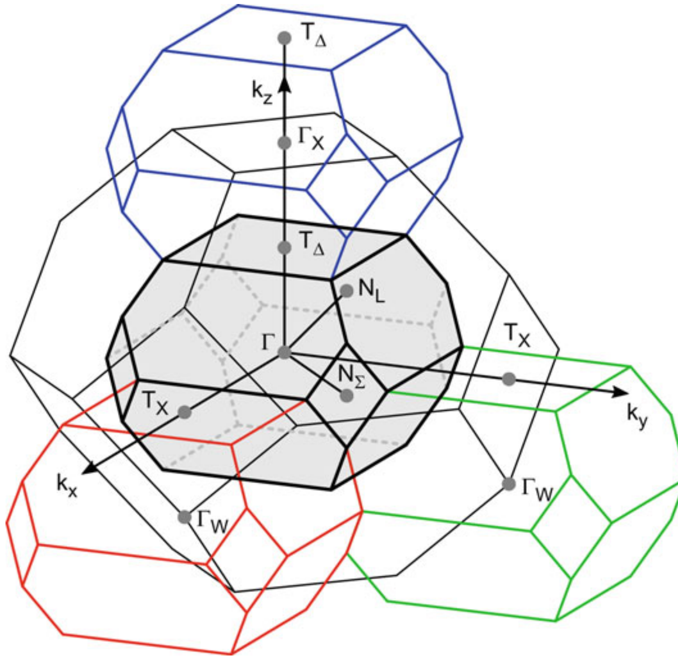

Fig. 4.3 Brillouin zones of the zinc blende and chalcopyrite crystal structures and their relationship. All BZs are truncated octahedra, the main labels refer to high-symmetry points of the smaller chalcopyrite BZ, and the subindices denote the related points of the larger zinc blende BZ. Adapted from [10]

screw rotations or *glide reflections* and give rise to non-symmorphic space groups in which the crystal, such as diamond, is not globally invariant under the point group. Crystals with symmorphic space symmetry, such as zinc blende, are globally invariant under the point group.

4.2.3 Band Structure Diagrams

Electronic band structure diagrams combine the elements that we have described in the preceding pages, in Sects. 4.2.1 and 4.2.2, giving a representation of allowed electron energies in the semiconductor together with their transform properties, obeying both translational symmetry, described by the wavevector **k**, and point group symmetry, given by the specific irreducible representations to which the electron states belong. Most methods to calculate band diagrams consider the semiconductor as a periodic arrangement of static atom cores surrounded by the valence electrons and reduce the problem to solving a one-electron Schrödinger equation:

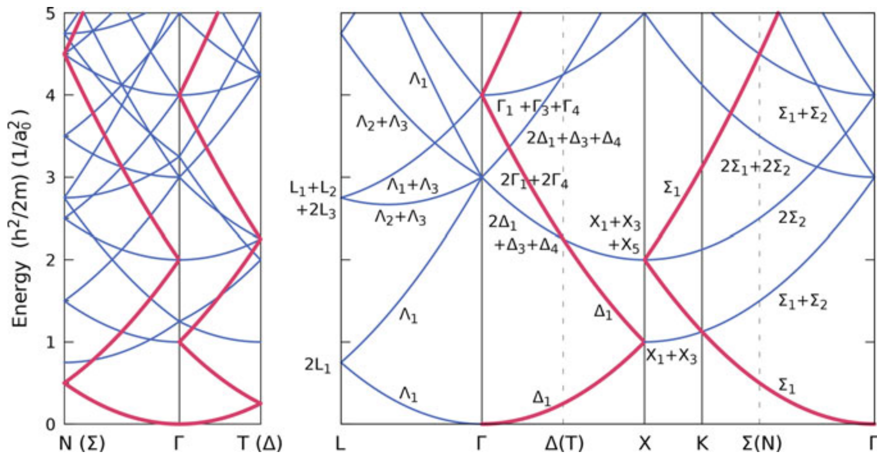

Fig. 4.4 Empty lattice electronic bands along high-symmetry lines of the Brillouin Zone of chalcopyrite (left) and zinc blende (right). The points N and T of chalcopyrite are indicated on the zinc blende scheme to illustrate the zone-folding relationship between both structures. A corresponding band for each direction is highlighted with thicker lines

$$H_{1e}\Psi_n(\mathbf{r}) = \left[\frac{p^2}{2m} + V(\mathbf{r})\right]\Psi_n(\mathbf{r}) = E_n\Psi_n(\mathbf{r}), \tag{4.1}$$

where $V(\mathbf{r})$ is a periodic potential and $\Psi_n(\mathbf{r}) = e^{i\mathbf{kr}}\Phi(\mathbf{r})$ is a Bloch wave function with $\Phi(\mathbf{r})$ also periodic. In this simplification, the strongly interacting valence electrons are replaced by weakly interacting quasi-electrons with effective mass m. The differences between theoretical approaches arise from the definition of $V(\mathbf{r})$ and the basis functions proposed to solve the Schrödinger equation by variational methods. It is illustrative to consider the simplest solution of (4.1) when $V(\mathbf{r}) = 0$, referred to as empty lattice model. In this case, the electronic bands are paraboloids $E_{\mathbf{k}} = \hbar^2\mathbf{k}^2/2m$ folded into the first BZ, as displayed in Fig. 4.4 for zinc blende and chalcopyrite crystals. The zone-folding relationship between electronic bands is evident in the empty lattice simplification.

Obviously, a realistic description of the band structures and band gaps requires to consider $V(\mathbf{r}) \neq 0$. In the following, we give short descriptions of band energy calculations methods that are usually applied to describe the optical properties of semiconductors.

Tight-binding calculations are similar to the method of Linear Combination of Atomic Orbitals (LCAO). The electronic wavefunctions of the solid are built as a linear combination of wavefunctions at each atomic site. Appropriate relative phases between the atomic states are considered to ensure the required translational symmetry. It is assumed that interactions between atomic states are limited to a few nearest neighbors. Thus, a small number of physically sound overlap parameters, with

explicit dependence on bond length, provides a quite good description of the valence band structure for a variety of similar compounds.

The $\mathbf{k} \cdot \mathbf{p}$ method uses perturbation theory to obtain details of the band structure near a $\mathbf{k}$ point in the BZ (usually the center, Γ) starting from the energy gaps and the matrix elements of $\mathbf{p}$ at that specific $\mathbf{k}$ point. The method is quite useful to describe optical properties as it provides gaps, oscillator strengths and effective masses. It can also be easily extended to include spin-orbit interaction and the effects of external perturbations such as stress or electric and magnetic fields [11].

In the Pseudo-potential approach, the complicated interaction of nucleus and core electrons with the valence electrons is replaced by a smoother effective pseudo-potential that allows to use a much smaller basis function set to solve for valence electron eigenstates. Translational symmetry allows to describe the pseudo-potential as a Fourier series with a coefficient for each reciprocal space vector $\mathbf{g}$. Usually, about three Fourier coefficients per atom are sufficient since their value decays with increasing $\mathbf{g}$ length. These coefficients can be obtained either empirically, by adjusting calculated properties to experimental data, or calculated within an ab initio density functional method [1].

Density functional theory (DFT) has progressed in parallel with the increasing availability of computing power. Several ab-initio methods have been developed to obtain very detailed and precise electronic band structures. Those methods replace the correlation and exchange interactions between many electrons by a one-electron problem described by a functional of the local electron density (local density approximation, LDA). Available codes differ in the problems they are designed to solve, going from simple basis functions and potentials that allow to calculate systems with very large numbers of atoms to very accurate models of the exchange and correlation potentials that include functionals of electron density gradient (generalized gradient approximations, GGA). In the framework of these sophisticated models, the interaction of electrons with lattice vibrations, neglected in (4.1), can also be considered, either as a perturbation or dealing with electrons and vibrations on a same footing, the latter usually needed for molecular semiconductors.

Whichever calculation method is chosen, zone-folding remains helpful to ascribe electronic transitions based on parent compounds. In establishing this relationship, electronic levels may be not merely folded but also shifted and splitted by the lower superstructure symmetry, usually referred to as crystal field. A different source of splittings is due to the fact that quasi-electrons are fermions with half-integral spin angular momentum. In many semiconductors there is a significant interaction of the particle spin with its motion (spin-orbit coupling). Considering the spin requires a new point group symmetry operation $\bar{E}$, a 2π rotation that changes the sign of the spin functions. As a consequence, the number of group elements is doubled and the identity operation E of the double group becomes a 4π rotation. The electron states must be labelled with the additional irreducible representations of the double group which carry the spin symmetry. However, in many cases the spin interaction is a perturbation and the symmetry traits of the single group approximately prevail. Figure 4.5 represents the correspondence between single and double group symmetries for the electronic states that are important for the band gap of chalcopyrite semiconductors,

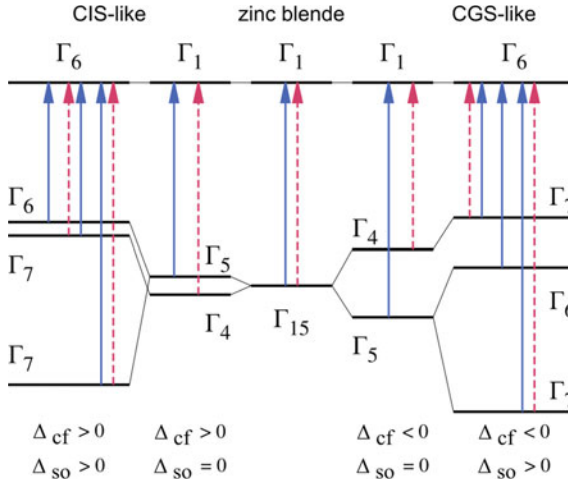

Fig. 4.5 Schematic diagram of the gap energy states at the Γ point of zinc blende and correspondence to chalcopyrite without (single group labels) and with inclusion of spin-orbit interaction $\Delta_{so} \neq 0$ (double group). Solid (dashed) arrows represent transitions allowed by symmetry in $\mathbf{E} \perp c$ ($\mathbf{E} \parallel c$) polarization. The ordering of the topmost valence bands depends on the sign of the crystal field Δ_{cf}, positive for $CuInSe_2$ (CIS) and negative for $CuGaSe_2$ (CGS)

Table 4.1 Character table of the double D_{2d} point group. Notice that in this case both unbarred and barred two-fold rotations and reflection symmetries have the same characters, i.e., belong to the same class. The correspondence between single-group and additional representations may be deduced by considering the characters for the $J = 1/2$ spin operator ($D_{1/2}$) leading to the direct product relations $\Gamma_4 \otimes D_{1/2} = \Gamma_7$ and $\Gamma_5 \otimes D_{1/2} = \Gamma_6 \oplus \Gamma_7$

D_{2d}	E	$2S_4^z$	C_2^z	$2C_2$	$2\sigma_d$	$\bar{E}$	$2\bar{S}_4^z$
			$\bar{C}_2^z$	$2\bar{C}_2$	$2\bar{\sigma}_d$		
Γ_1	1	1	1	1	1	1	1
Γ_2	1	1	1	−1	−1	1	1
Γ_3	1	−1	1	1	−1	1	−1
Γ_4	1	−1	1	−1	1	1	−1
Γ_5	2	0	−2	0	0	2	0
Γ_6	2	$\sqrt{2}$	0	0	0	−2	$-\sqrt{2}$
Γ_7	2	$-\sqrt{2}$	0	0	0	−2	$\sqrt{2}$
$D_{1/2}$	2	$\sqrt{2}$	0	0	0	−2	$-\sqrt{2}$

occurring at the Γ point (cf. Fig. 4.3). This correspondence may be inferred from the table of characters of all point group operators, [9] listed in Table 4.1. The relationship to the zinc blende parent symmetry is also indicated. This example will be further developed in the rest of this chapter.

4.3 Dielectric Function

The relationship between band structure and dielectric function is a two-way street. The experimental knowledge of the dielectric function, extracted from measurements after data analysis as described in Chap. 3, is a source of information of fundamental physical parameters, among them, those of the band structure. Likewise, according to the physical properties of the studied materials, their dielectric function can be parametrized using suitable models as will be shown in Chap. 5. To formulate the basic links we must consider the interaction between light and the electrons in the solid.

The interaction of the electrons with the electromagnetic field of a plane wave can be calculated by writing the electron momentum $\mathbf{p}$ of (4.1) as $\mathbf{p} + e\mathbf{A}$, where $\mathbf{A} = \hat{\mathbf{e}}A_0 \exp(i\mathbf{qr} - \omega t)$ is the vector potential of the electromagnetic field with light wavevector $\mathbf{q}$ and frequency ω, and $\hat{\mathbf{e}}$ its polarisation vector. The resulting Hamiltonian contains the unperturbed term and two time-dependent extra terms that describe the interaction between the radiation and the electrons. To obtain the linear optical response, we keep the dominant term $(e\mathbf{A} \cdot \mathbf{p})/m$ and neglect the smaller quadratic term $e^2\mathbf{A}^2/(2m)$.

Using time-dependent perturbation theory, the transition probability per unit time W for an electronic transition from the valence state $|v\mathbf{k}\rangle$ to the conduction state $|c\mathbf{k}'\rangle$ is [2]:

$$\begin{aligned} W(v, c, \mathbf{k}) &= \frac{e^2 A_0^2}{m^2} \left|M_{cv}(\mathbf{k}, \mathbf{k}')\right|^2 \frac{2\pi}{\hbar} \delta(E_{ck'} - E_{vk} - \hbar\omega), \text{ with} \\ M_{cv}(\mathbf{k}, \mathbf{k}') &= \langle c\mathbf{k}' |\, \hat{\mathbf{e}} \cdot \mathbf{p} \mathrm{e}^{i\mathbf{qr}} \,| v\mathbf{k}\rangle \,. \end{aligned} \quad (4.2)$$

Equation (4.2) is known as Fermi golden rule. Evaluation of the matrix element $M_{cv}(\mathbf{k}, \mathbf{k}')$ is facilitated by applying the space group selection rules. For instance, translational symmetry requires wavevector conservation $\mathbf{k}' = \mathbf{k} + \mathbf{q} + \mathbf{g}$, where $\mathbf{g}$ is a reciprocal lattice vector. Because in the optical range the light wavevector $\mathbf{q}$ is $\approx 10^{-4}$ times smaller than the reciprocal lattice vectors, we have $\mathbf{k}' \simeq \mathbf{k}$ in (4.2). This condition gives rise to *direct* interband transitions. In some semiconductors, (f. i., Si and Ge) the fundamental absorption edge is given by processes in which phonons participate. For those *indirect* interband transitions $\mathbf{k}' = \mathbf{k} + \mathbf{q} \pm \mathbf{Q} + \mathbf{g}$, i.e., $\mathbf{k}' \simeq \mathbf{k} \pm \mathbf{Q}$, where $\mathbf{Q}$ is the wavevector of the absorbed or emitted phonon. On the other hand, the particular symmetries of the electronic levels allow to predict if two states can be connected by the dipolar interaction operator (in this case $\mathbf{p}$) and also assign the relative weight in case of splitting, either by a crystal field or spin-orbit interaction. The matrix element is nonzero, that is, $\langle \Psi_c|\mathbf{p}|\Psi_v\rangle \neq 0$, only if the representation of $\mathbf{p}$ appears in the direct product of the representations of the two interacting states. This enunciate is known as matrix-element or Wigner-Eckart theorem and specifies the selection rules. Note that, since $\mathbf{p}$ is a vector, it changes sign under inversion. Consequently, if the symmetry group of the crystal contains the inversion, all allowed transitions must connect states of opposite parity.

The absorbed energy per unit time and unit volume is obtained by multiplying the transition rate by $\hbar\omega$ and adding over all transitions between filled $|v\rangle$ and empty $|c\rangle$ states for all $\mathbf{k}$ vectors of the BZ. The result of dividing this sum by the incident energy is the absorption coefficient $\alpha(\omega)$ from which the imaginary part of the dielectric function can be calculated:

$$\varepsilon_2(\omega) = \frac{\pi e^2}{3\varepsilon_0 m^2 \omega^2} \sum_{cv} \int_{BZ} \frac{2d\mathbf{k}}{(2\pi)^3} \left|M_{cv}(\mathbf{k})\right|^2 \delta(E_{ck} - E_{vk} - \hbar\omega). \tag{4.3}$$

Equation (4.3) can be evaluated from the electronic structure theory methods and further, the Kramers-Kronig relations give the complete dielectric function. The δ function in (4.3) transforms the volume integral over the BZ into a surface integral over the surface of constant energy difference $\hbar\omega = E_{ck} - E_{vk}$. Considering the contribution to ε_2 of a small interval of the BZ, the matrix element M_{cv} can be taken as constant. Then, $\varepsilon_2(\omega)$ is proportional to the *Joint Density of States* (JDOS):

$$\varepsilon_2(\omega) \propto J_{cv}(\omega) = \frac{2}{(2\pi)^3} \int_{E_{ck}-E_{vk}=\hbar\omega} \frac{dS}{\left|\nabla_k(E_{ck} - E_{vk})\right|} \tag{4.4}$$

that has large values (singularities) at energies where the valence and conduction bands are parallel. Those singularities give rise to structures in the dielectric function.

4.3.1 Critical Points

According to (4.4) a *Critical Point* (CP) appears at every $\mathbf{k}$, for which $\nabla_k(E_{ck} - E_{vk})$ vanishes. Most features of the dielectric function of semiconductors can be identified with CPs, also denominated Van Hove singularities. The structures observed in the optical spectra are labelled according to the position of the corresponding CP at the BZ. The labels E_0, $E_0+\Delta_0$, E'_0 and $E'_0+\Delta'_0$, are used for interband transitions located at or near the BZ center, the Γ-point. The singularities that occur at the L-point or along $\langle 111\rangle$ are labelled E_1, $E_1+\Delta_1$, E'_1. The labels E_2 are used for interband transitions along $\langle 100\rangle$ or occasionally, other parts of the BZ.

The strength of a CP is given in first approximation by the JDOS, that is, by the volume of the BZ that contributes to each structure, provided that the transition is not symmetry forbidden, i.e., the matrix element $\left|M_{cv}(\mathbf{k})\right|^2$ is not zero. The contributing volume is given by the $\mathbf{k}$-dependence of the energy difference between the valence and the conduction band. A series expansion of this difference around the wavevector $\mathbf{k_0}$ of the CP gives:

$$E_{ck} - E_{vk} \approx E_g + \frac{\hbar^2}{2}\left[\frac{(k_x - k_{0x})^2}{\mu_x} + \frac{(k_y - k_{0y})^2}{\mu_y} + \frac{(k_z - k_{0z})^2}{\mu_z}\right], \tag{4.5}$$

where μ_x, μ_y, μ_z are the principal components of the reduced inverse effective mass tensor:

$$\frac{\overleftrightarrow{1}}{\mu_{ij}} = \frac{1}{\hbar^2} \frac{\partial^2}{\partial k_i \partial k_j} \left(E_{ck} - E_{vk} \right) . \tag{4.6}$$

It follows from (4.5) that the values of μ_i determine the JDOS at the CP and with it its strength. From (4.4) it is obvious that a small relative curvature of the bands (i.e., larger reduced effective mass) means an increase of electronic interband transitions with energy E_g and therefore a stronger structure in $\varepsilon_2(\omega)$. Further, when one mass is large compared to the others the corresponding term in (4.5) does not contribute and the energy difference in that direction shows practically no dispersion. As a consequence, the JDOS increases and originates stronger structures in the spectra. The number of contributing terms gives the *dimensionality* of the CP. Besides, the signs of the different μ_i determine the form of the surface of constant energy and therefore the *kind* of CP.

There are four kinds of three dimensional (3D) CPs in which the masses are of similar values: a minimum (M_0), two kinds of saddle points (M_1, M_2), and a maximum (M_3) characterized by 0, 1, 2, and 3 negative masses, respectively. The constant energy surfaces are ellipsoids (M_0 and M_3) or hyperboloids (M_1 and M_2). For two-dimensional (2D) CPs one of the masses is much larger than the other two. We have then a minimum, a saddle point or a maximum when 0, 1, or 2 of those two masses are negative, respectively. The constant energy surfaces are elliptic cylinders when both masses are of the same sign and hyperbolic cylinders for the saddle point. When one of the masses is much smaller than the other two, the CP is one-dimensional (1D), either a minimum or a maximum if that mass is positive or negative, respectively. The constant energy surfaces are parallel planes whose distance increases (minimum) or decreases (maximum) with the energy difference to the CP. Finally, zero-dimensional (0D) CPs are also possible when within a certain finite volume of the BZ the change in the energy difference between conduction and valence bands vanishes or is very small, that is, the bands are quite flat and parallel. Such 0D CPs also describe the lineshape of excitonic transitions. The fact that the energy band diagram is periodic in the reciprocal space imposes strong restrictions on the number and kind of critical points, so that a minimum number of determined singularities must appear in the optical JDOS of a semiconductor [1].

Inserting (4.5) in (4.4) and performing the surface integration in the BZ region close to a CP, a general expression for the most resonant term contribution of an interband transition to the imaginary part of the dielectric function is obtained [12]. As a result, the dielectric function due to a CP can be written as:

$$\varepsilon(\omega) = C - Ae^{i\varphi}(\hbar\omega - E_g + i\Gamma)^{\ell} . \tag{4.7}$$

Here, $\ell = d/2 - 1$ where d is the dimensionality of the CP and the phase angle φ is a multiple of $\pi/2$ that distinguishes between kinds of CPs, A is the amplitude, E_g the transition energy, and Γ a phenomenological lifetime broadening. The parameter C

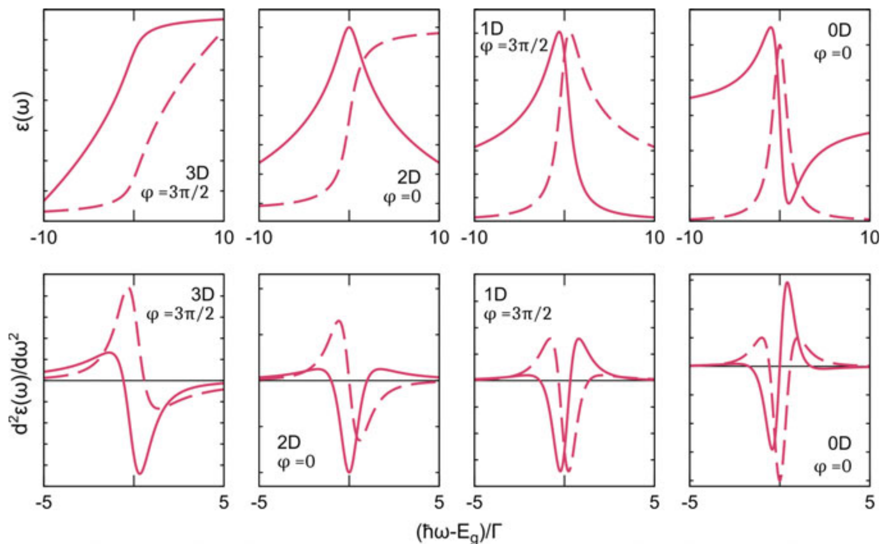

Fig. 4.6 Critical point lineshapes of minima with different dimensionalities. Upper row: dielectric function. Lower row: second derivatives

describes a constant background. Fitting experimental data to (4.7) allows to obtain the parameters that describe the lineshape of the involved electronic interband transition. If several CPs are close, a sum of lineshapes can be fitted, one term for each CP.

Because (4.7) only describes the most resonant term of the CP contribution to the dielectric function, the rest adds a background with a much weaker variation with energy. Thus, to improve the fitting of CP parameters it is advantageous to perform numerical derivatives of the experimentally obtained dielectric function and fit them to an extension of (4.7) to the nth derivative of $\varepsilon(\omega)$ with respect to energy:

$$\frac{d^n\varepsilon(\omega)}{d\omega^n} = -fAe^{i\varphi}(\hbar\omega - E_g + i\Gamma)^{\ell}$$
$$\text{with } \ell = d/2 - 1 - n \text{ and } f = \prod_{\substack{j=1\\ j\neq d/2}}^{n} (d/2 - j). \tag{4.8}$$

For the case $d = 2, n = 0$ the polynomial function is the natural logarithm $\ln(\hbar\omega - E_g + i\Gamma)$. Figure 4.6 shows as example the line shapes associated to minima with different dimensionalities.

Therefore, derivatives eliminate the background and at the same time CP structures become more pronounced. Modulation spectroscopies are based on this fact. In those techniques, applying a periodically modulated external perturbation to the sample and using lock-in detection techniques results in a signal proportional to derivatives (f. i., 1st in piezoreflectance and 3rd in electroreflectance) of the optical response with respect to energy. In spectroscopic ellipsometry there is no external

modulation but current experimental equipments provide measurements with a signal to noise ratio large enough to allow numerical derivatives up to at least second or third order, with the advantage of the absence of possible spurious effects of the external perturbation. The lineshape function of (4.8) has more zero crossings and sharper structures for increasing derivative order n as well as for lower dimensionality, as shown in Fig. 4.6. There are several methods to perform numerical derivatives of SE spectra. The main goal of those methods is to obtain the nth derivative of the spectra without significant distortion of spectral features while at the same time to smooth out as much as possible the experimental noise. The smoothing polynomials method [13, 14] consists in taking a set of $2r + 1$ consecutive experimental data points (r before and r after a specific point) and then, a polynomial of m-degree is fitted to the ε values at those points. The nth derivative at that point is calculated as the value of the nth derivative of the fitted polynomial at the central position. The process is repeated for all points in the spectra. In practice, when the interval between spectral points is constant, the process is equivalent to a convolution of the spectra with a smoothing kernel. The polynomial degree m and the number $2r + 1$ of considered points can be chosen to control the smoothing effect. Usually increasing r and decreasing m accounts for larger noise suppression but care has to be taken to not distort the spectral features with too much smoothing. The optimum r and m depend on the spectral energy step and the sharpness of the specific CP to be analyzed.

Another method of performing numerical derivatives is by using cubic smoothing splines [15, 16]. A series of cubic smoothing splines with increasing level of smoothing is fitted to experimental spectra, and their derivatives evaluated from the spline coefficients. The optimal derivative spectrum is that in the series which shows maximum noise reduction while keeping the amplitude of spectral features unaffected. The appropriate smoothing level can be chosen either subjectively by visual comparison of derivative spectra or estimate it numerically with a generalized cross validation [17] or similar methods. When properly used, the smoothing spline method gives similar results to those of smoothing polynomials and has as advantage that the same smoothing level can be used for the whole spectrum.

Usually, the second derivative is built and a regression analysis of the numerical experimental derivative with the theoretical lineshapes of (4.8) gives insight into the dimensionality of the CPs and the parameters of interest. The fit of nonlinear functions is done with the Levenberg-Marquardt algorithm, obtaining as result the best fit parameters and their error bars. The true error bars may sometimes be larger due to systematic errors, but not all parameters are affected in the same way. The CP energy E_g is nearly insensitive to systematic errors, like f.i., a poorly built derivative, and is therefore the best determined parameter. A difficult case is when the JDOS near the CP is very asymmetric because then the energy can depend on the order of the derivative. A higher derivative is preferred because it represents a smaller region of the BZ. The broadening Γ is strongly correlated with the amplitude A and if the derivative is too smoothed the fit tends to overestimate Γ and underestimate A. To minimize the correlation it is useful to choose fit parameters of similar magnitude, usually multiplying Γ by a factor or choosing Γ^{-1} as fit parameter. The phase angle φ distinguishes between different kinds of CPs of the same dimensionality and in

(4.7) takes only values which are multiples of $\pi/2$. However, the fits improve when φ is taken as freely varying parameter.

The deviation of the phase from standard values is mainly due to two causes: Systematic errors in the evaluation of the spectrum and many-body effects. A common systematic error is due to the influence of overlayers. For example, a thin oxide layer causes a mixture of the real and the imaginary part of the dielectric function which depends on the oxide thickness. Exactly the same effect is obtained by a change in the phase angle. Another factor to keep in mind is that (4.7) is only valid in the close vicinity of the CP and the tails of the structure should be given a smaller weight in the fit but not eliminated because they are important to distinguish between different dimensionality. By minimizing these errors, changes in the phase can be ascribed to many-body (or excitonic) effects in optical interband transitions related to the generated electron-hole pairs. In the one-electron approximation to calculate the dielectric function it is assumed that between the excited electron and the corresponding hole there is no interaction. This approximation cannot explain many experimental details of the spectra for which the Coulomb and the exchange interactions must be included.

The model of Mott-Wannier excitons describes those effects with a weakly attractive potential between the electron and hole. These effects are most evident near the bandgap, where a discrete excitonic spectrum appears just below the interband continuum. However, they are important also for CPs above the gap, where the exciton states are superimposed with the continuum of band states. A description of the interaction between localized exciton and delocalized band states is possible with the aid of simple approximations. The interaction with the continuum leads to a broadening of Mott-Wannier excitons larger than their binding energy. Therefore, details in the shape of the interaction are of secondary importance. It is mainly important that there is an attractive potential between the electron and hole. The simplest model is the Slater-Koster *contact exciton*. It assumes that there is only an attraction if the electron and the hole are on the same lattice site. This kind of interaction can modify amplitudes, for example it leads to an increase for a M_1 CP and a decrease for a M_2 CP. For all kinds of lineshapes the many-body interaction leads to a line shape that is a mixture of two adjacent types of CPs so that the mixture can be modelled as a change in the values of φ taking non integer multiples of $\pi/2$. The values of φ can then be used to investigate the change of the many-body interaction with the temperature or the doping, for instance. In the particular case of a 0D lineshape, the phase angle can be related to the asymmetry parameter q of the Fano-Breit-Wigner profile that describes the interaction between a discrete excitation and a continuum, being $q = -ctg\varphi - sin^{-1}\varphi$.

An alternative approach to obtain relevant information on the electronic interband transitions is the reciprocal-space analysis [18]. In this method, the dielectric function spectra are Fourier transformed and analyzed in reciprocal space (RS) where the baseline contribution, interband transitions information, and experimental noise, are given by the low, intermediate, and high index Fourier coefficients, respectively. Best results are obtained when the starting spectrum is uniformly spaced in energy and suitable procedures to eliminate endpoint discontinuity artifacts are adopted. Recent developments suggest that a combined approach with RS used to suppress

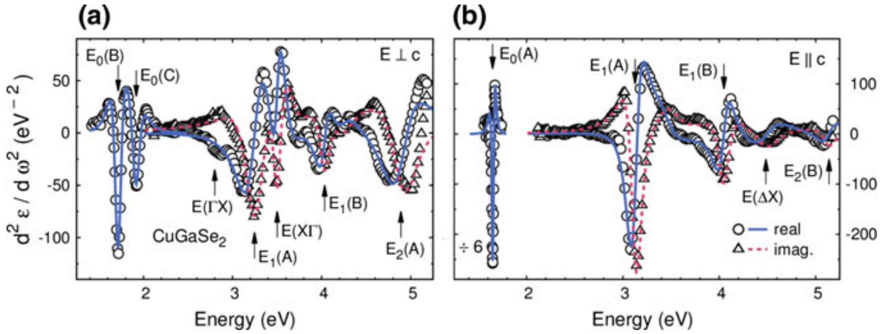

Fig. 4.7 Second derivative spectra of $CuGaSe_2$. Experimental points are plotted by symbols and their best fits are given by lines. **a** Ordinary and **b** extraordinary components. Arrows mark the fitted critical point energies and their assignments. Adapted from [10]

noise and baseline contributions transformed back to direct space derivative spectra can provide further improvement in CP's parameter determinations [19].

As an example, second derivative spectra of $CuGaSe_2$ are plotted in Fig. 4.7. The ordinary ($\mathbf{E} \perp c$) and extraordinary ($\mathbf{E} \parallel c$) spectra were obtained from point-by-point analysis of experimental measurements. Then, numerical derivatives were calculated by smoothing polynomials of degree $m = 5$. The number of correlated points $2r + 1$ were chosen depending on the density of experimental points (energy step) and the intensity and sharpness of the structures. The transitions of the extraordinary polarization, Fig. 4.7b, were more intense than those of the ordinary one, Fig. 4.7a. In both cases $r = 4$ was chosen for the sharp band gap transitions, although the energy steps were different: $\Delta E = 10$ meV for (a) and $\Delta E = 2$ meV for (b). For the higher transitions, energy steps of $\Delta E = 20$ meV were suitable for both cases, with $r = 9$ for (a) and $r = 6$ for (b). Best fits were obtained with 0D transitions for all three E_0 components (A, B, and C), indicating excitonic character. For the other strong structures, E_1 and E_2, 2D line shapes provided the best fits. Then, for weaker structures for which dimensionality was ambiguous, 2D lineshapes were used as well. From this analysis, precise energies and polarizations of transitions were obtained. Some transitions are present in only one polarization whereas others are polarization insensitive. These symmetry properties are very helpful to look for plausible assignments for the observed transitions.

4.4 Inorganic Semiconductors

In inorganic PV semiconductors the strong bonds connecting all atoms and the long-range order allow for delocalization of the electronic states into wide bands and result in low binding energy of the electron-hole pairs and high mobility of the free carriers. The one-electron picture considered in Sect. 4.2.3 describes rather well

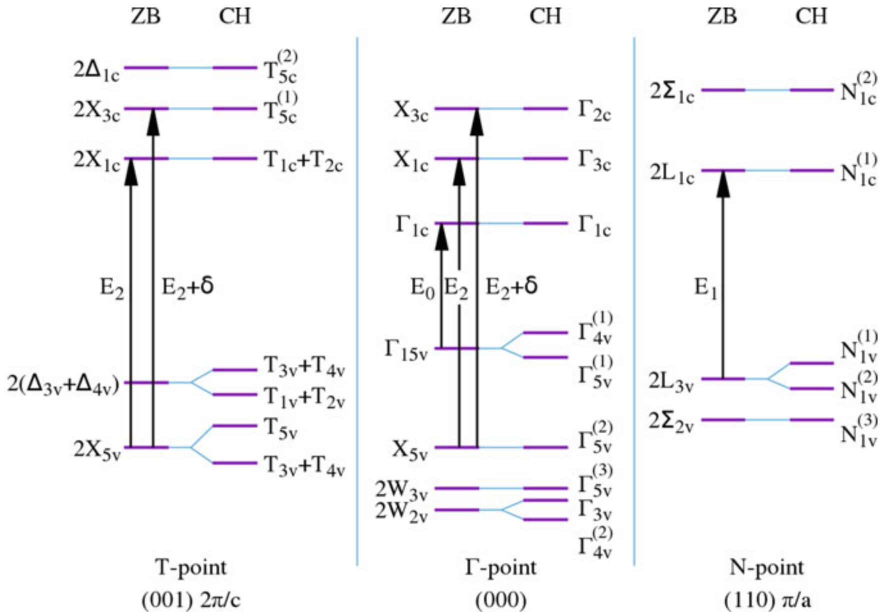

Fig. 4.8 Schematic representation of energy levels and their symmetry in ZB and CH structures. The main transitions of ZB that map onto CH are indicated. The superscripts in parentheses indicate the number of states. Adapted from [10]

Table 4.2 Character tables of the T_d and D_{2d} point group symmetries, valid at the Brillouin zone center. The top valence band states at the zone center are related using the character tables for T_d and D_{2d} symmetries: $\Gamma_{15} \rightarrow \Gamma_4 \oplus \Gamma_5$

T_d	E	$6S_4$	$3C_2$	$8C_3$	$6\sigma_d$	Basis	D_{2d}	E	$2S_4^z$	C_2^z	$2C_2$	$2\sigma_d$	Basis
Γ_1	1	1	1	1	1	xyz	Γ_1	1	1	1	1	1	xyz
Γ_2	1	−1	1	1	−1		Γ_2	1	1	1	−1	−1	
Γ_{12}	2	0	2	−1	0		Γ_3	1	−1	1	1	−1	
Γ_{25}	3	1	−1	0	−1		Γ_4	1	−1	1	−1	1	z
Γ_{15}	3	−1	−1	0	1	x, y, z	Γ_5	2	0	-2	0	0	x, y

their electronic structures. For applications, different morphologies of the materials are required, from single crystalline to micro- or nano-crystalline to amorphous. Although the actual optical behavior of the semiconductor materials used in devices depend on the particular structural arrangements, the basis to understand their optical properties is the extended crystalline structure.

4.4.1 Crystalline

As illustrative example of crystalline symmetry we will further consider the chalcopyrite (CH) structure, in particular the ternary Cu-III-Se_2 compounds. Polycrystalline alloy thin films of Cu(In,Ga)Se_2 are employed for PV application, discussed in detail in Ch 9. Here, we focus on the symmetry properties of the electronic bands of CH, with tetragonal space symmetry D_{2d}^{12} (I$\bar{4}$2*d*) and their relationship to the zinc blende (ZB) binary parent compounds of symmetry T_d^2 (F$\bar{4}$3*m*). The body-centered elementary cell of CH contains eight atoms (Cu_2-III_2-VI_4) and is four times larger than that of ZB. Consequently, both Brillouin zones can be related by zone-folding, as was depicted in Fig. 4.2. Sets of four different wavevectors of ZB fold into a single point of the CH Brillouin zone. The main symmetry points of CH are (in units of π/a): $\Gamma_{CH}(000)$ with ZB states originated from $\Gamma(000)$, $X(002)$, $W(201)$, and $W(021)$; $T_{CH}(001)$ with states from $\Delta(001)$, $\Delta(00\bar{1})$, $X(200)$, and $X(020)$; and $N_{CH}(110)$ with states from $L(111)$, $L(\bar{1}\bar{1}1)$, $\Sigma(1\bar{1}0)$, and $\Sigma(\bar{1}10)$. The relationship between point symmetries of the tetragonal versus the cubic structures are D_{2d} at Γ_{CH} versus $T_d(\Gamma), D_{2d}(X), S_4(W)$; $D_{2d}(T_{CH})$ versus $C_{2v}(\Delta), D_{2d}(X)$; and $C_{2v}(N_{CH})$ versus $C_{3v}(L), C_{1h}(\Sigma)$. Figure 4.8 shows the correspondences. Forced degeneracies or splittings when passing from one symmetry to another can mostly be deduced from the character tables, taking into account the multiple foldings. In this case the CH space group is non-symmorphic as expected from the presence of more than one atom of the same kind per point of the Bravais lattice. Then, the relationship for points at the Brillouin zone boundary is less straightforward than for points within the zone such as the Γ point, shown as example in Table 4.2.

The observed splittings and polarizations are mostly originated in the symmetry lowering from cubic to tetragonal, as depicted in Fig. 4.8. The spectral dependence of the optical functions and the critical point analysis of compounds of the same family, taking into account appropriate selection rules, allows to assign the most important transitions, corroborated by results from band structure calculations [20]. In the case of Cu(In,Ga)Se_2, despite the influence of Cu-3*d* states on the electronic band structure, the main transitions in the optical range originate between hybridized sp^3 bands, bearing a rather close relationship with their ZB parent compounds.

The effect of spin-orbit splitting is practically only important at the fundamental band gap transitions, justifying the general labelling by single-group notations. At the bandgap region, this simplified view leads to considering the two lowest transitions $E_0(A)$ and $E_0(B)$ as a crystal-field-split gap, with the higher-lying $E_0(C)$ a spin-orbit split component. The crystal field Δ_{cf} corresponds to the tetragonal distortion of the unit cell given by the difference between the lattice parameters a and $c/2$. For III = In the distortion is positive and small. For III = Ga, $c/2 < a$ gives $\Delta_{cf} < 0$, which is reflected in the different selection rules of the band gap levels that were indicated in Fig. 4.5. The final assignments for the case of Cu$GaSe_2$ are depicted in Fig. 4.9.

In general, the spectra of polycrystalline films are less resolved than those of single crystals, not only because they contain all possible transitions coming from differently oriented domains with slightly disordered boundaries, but also because

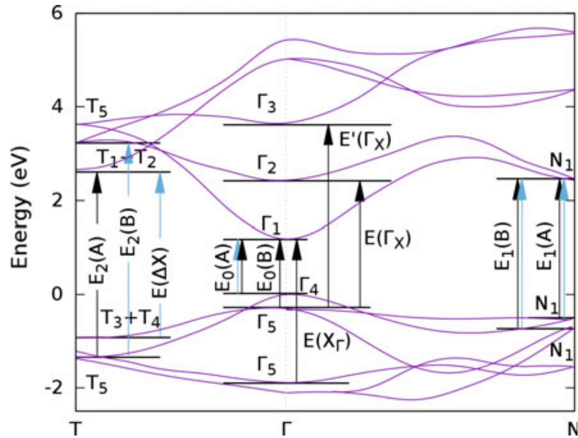

Fig. 4.9 Optical transitions observed in $CuGaSe_2$ in the optical range, depicted on a generic band structure using the single group notation. Dark and light arrows represent optical transitions allowed in $E \perp c$ and $E \parallel c$, respectively. Adapted from [10]

when the crystallite size is reduced the meaning of the wavevector and with it the **k**-conservation is progressively *"relaxed"* as the size of the crystallites decreases. This is also true in well-ordered heterostructures and superlattices in which the translational symmetry in one dimension is lost. In a nanocrystal (NC) the translational symmetry is lost in all three dimensions of real space for the atoms which are at or near the surface. But even a rather small nanocrystal of several nm average size contains thousands of atoms, too large to calculate their electronic structure in a totally realistic structure. A common practice to introduce modifications of periodicity, also due to other causes such as defects or alloying, is to consider an enlarged cell called supercell as elementary cell of the system, maintaining standard periodic boundary conditions. The larger the supercell, the smaller is the first Brillouin Zone and the more bands get folded into it. In the limiting case of very small NCs, the large number of folded segments resemble the density of states, leading to an increasing broadening of the transitions. The use of supercells avoids the problem of dangling bonds at the NC surface. In realistic calculations of small clusters, surface atoms are considered bonded to H atoms to avoid the dangling bonds.

The optical spectra of small nanocrystals are not only broadened compared to the bulk but display also two main effects: Quantum and dielectric confinement. The first entails a blue shift of the spectrum and the second, which is due to the dielectric mismatch between the NCs and the surrounding medium, has as a consequence the change of absolute dielectric function value. In Si NCs embedded in SiO_2 both effects have a huge impact on the optical spectra, as shown in Fig. 4.10. Above NC sizes around 5 nm the dielectric function of the crystallites is reminiscent of the bulk with broad but clear E_1 and E_2 CPs. Below this size, the E_1 transition becomes quite broad and weak and tends to disappear. The remaining broad structure for smaller NCs seems related then to E_2. Curiously, about 5–6 nm is around the size for which the number of atoms in the volume is about the same as at the surface of a spherical crystallite so that surface effects start to dominate the bulk effects.

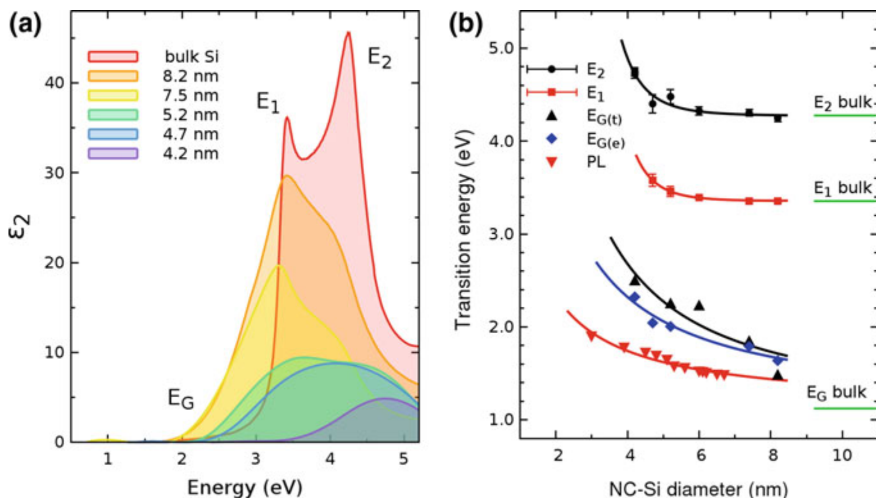

Fig. 4.10 Dependence on the nanocrystal diameter of **a** the imaginary part of the dielectric function and **b** the observed transition energies of nc-Si embedded in SiO_2. Adapted from [21]

4.4.2 *Amorphous*

Amorphous inorganic semiconductors, such as a-Si, still consist of sp^3 bonded units with certain short-range order but lacking long range order. The loss of translational order means that **k** is no longer a good quantum number and, as in the nanocrystals, the changes in electronic spectra in an amorphous structure can also be viewed as folding of bands and still be related to the electronic structure of a parent crystallyne structure. This is because in these amorphous semiconductors the majority of the valence and conduction states still form delocalized states, i.e., the one-electron picture applies. In this case the supercell approach is useful to contain a sufficient representative number of local configurations, [22] in other words represent the distortion of the perfect tetrahedral structure, then the optical spectrum of the amorphous is similar to the JDOS of the crystal with some additional inhomogeneous broadening. The distortion of the structure implies that there are some dangling bonds which act as defects and induce localization. In addition, disorder itself always leads to localization (Anderson localization). Localized states have somewhat larger binding energy, inducing states into the gap. The distribution of these localized states is exponential and the separation between extended and localized states gives rise to a mobility edge.

4.5 Organic Semiconductors

Organic semiconductor materials contain mainly carbon and hydrogen atoms and a few other atoms such as sulfur, oxygen, and nitrogen. Other carbon-based compounds associated with organic semiconductors are fullerenes and carbon nanotubes. The semiconducting behavior of organic semiconductors is quite different from inorganic ones. One of the main causes is that, being composed of light atoms and having smaller packing densities, their dielectric constant ε_1 takes lower values, leading to low dielectric screening of the interactions between electrons. Hence, the Coulomb interaction and the exchange energy between electron pairs with parallel or antiparallel spin is much stronger in organic compared to inorganic semiconductors. In contrast, intermolecular interactions are typically weak. Consequently, the HOMO and LUMO bands are narrow, a few 100 meV, and the optical properties of the solids approximately preserve those of a molecule [4, 6, 7].

4.5.1 Molecules

In a simple picture, absorption of light in a semiconducting molecule takes place by promoting one of the electrons from the HOMO to the LUMO, thus creating an excited state of the molecule. A better description of the excited state including electron-electron interactions is represented by the combination of several possible one-electron transitions in which the predominant term is the mentioned one electron in the HOMO, one in the LUMO. In addition, the relative spins of these electrons also define different excited states which must be considered to account for the exchange interactions. In the simple mentioned case, anti-parallel spins result in $s = 0$ (singlet state) and parallel spins mean $s = 1$ (triplet state), the latter having lower energy due to the exchange term. To reflect these combinations, the energy diagrams drawn for molecules do not usually represent single-electron levels but configurations, that is, many-electron states. The rate of an electronic transition, and thus the intensity of the resulting absorption can be calculated from the Fermi golden rule (cf. 4.2) and the selection rules given by the symmetry of the wavefunctions and the point group of the molecule apply. In most cases there is an even number of π-electrons and the ground state is totally symmetric (1Ag). Allowed transitions from this even state can only reach excited states of odd parity (u) of the centrosymmetric molecule. Since the exchange interaction is strong, the spin wavefunction also imposes a selection rule, the conservation of spin. This means that allowed transitions must connect either singlet S or triplet T states. However, spin-forbidden transitions also known as intersystem crossing may occur. The main mechanism that can flip the spin and cause admixture between singlet and triplet states is spin-orbit coupling, especially important in molecules containing relatively heavy atoms such as Br or I. The transition rate of such a $T - S$ transition will be small but is observable for instance in the

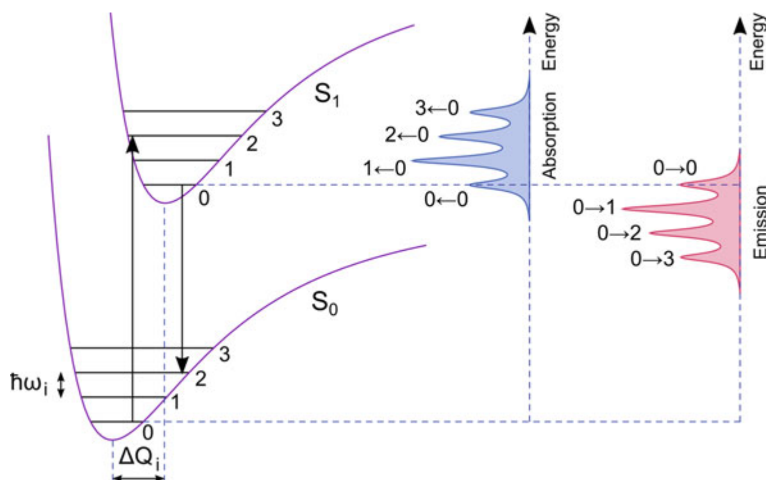

Fig. 4.11 Configuration diagram of the two first singlet states and schematic illustration of the Franck-Condon progression

case of phosphorescence, being the lowest energy radiative transition of the molecule from the lowest triplet to the singlet ground state $T_1 \rightarrow S_0$.

In conjugated molecules the electronic transitions are significantly coupled with vibrations, that is, the electronic transition is accompanied by a distortion of the molecule. Then, the vibrational normal modes are also included in the configuration diagram, as depicted in Fig. 4.11. The energies of the states are then represented as a function of normal mode coordinates Q_i for each normal mode with vibration energy $\hbar\omega_i$ and the superposition of configurations giving the absorption spectra is known as Franck-Condon progression. Several normal modes usually contribute to the coupling but it is not always possible to resolve them in the experimental spectra. Frequently, a mean effective mode energy is observed. In Fig. 4.11 the electronic transitions are drawn as vertical arrows in virtue of the Franck-Condon principle that considers the Q_i coordinates fixed during the electronic transition. The rate of the electronic transitions, and thus the intensity of the resulting absorption or emission signal, depends on the spatial overlap between initial and final state wavefunctions. This is reasonably large for $\pi - \pi^*$ transitions between orbitals which are delocalized over a similar area of the molecule. The overlap is reduced when the π HOMO and the π^* LUMO are located on different regions of the molecule, as is the case for a charge transfer (CT) transition. Also, the intensity distribution of transitions depends on the molecule distortion. The transition probability from the 0th vibrational level of the ground state to the mth vibrational level of the excited state, I_{0-m}, usually corresponds to a Poisson distribution given by $I_{0-m} = (S^m/m!)e^{-S}$, where S is the Huang-Rhys parameter that indicates the number of quanta involved in the vibrational excitation. The dominant transition is the 0–0 (or $S_{0-1} \leftarrow S_{0-0}$) only when the molecule distortion is small. Note that the spectral shape of the emission spectrum

corresponds to the same formula, leading to mirror symmetry from the absorption to lower energies about the zero-phonon line, as depicted in Fig. 4.11.

4.5.2 Solids

Optical spectra of molecular crystals resemble those of their constituent molecules although generally shifted and broadened by the weak intermolecular interaction. Some examples are presented in Chap. 15. In molecular crystals, we define Frenkel excitons as the excited states (quasi-particles) which upon absorption of light are created in an individual molecule and delocalize over the crystalline array forming a narrow exciton band $E(\mathbf{k})$, whereas the ground state is dispersionless because there is no excitation. In an ideal crystal, excitons with a definite value of $\mathbf{k}$ are coherent over the entire crystal. Interaction with phonons and defects change the momentum $\mathbf{k}$ and break this coherence. A measure of the coherence time of excitons is the inverse optical linewidth. During its coherence time τ the exciton remains in its $\mathbf{k}$-state and it travels a distance L, its coherence length. One refers to coherent excitons when L is large compared to the lattice constant a. When $L \leq a$, exciton motion is an incoherent hopping from one lattice site to another. Strictly speaking, when the propagation is incoherent, the quasi-particle is no longer an exciton. However, the denomination exciton is adopted also in this case.

Even if the spectra have strong molecular character, the crystalline order has influence on the symmetry of the electronic transitions. In crystals with multiple (Z) non-translationally equivalent molecules per unit cell, there is a splitting of the exciton levels, which is known as Davydov splitting, due to interaction of the physical Z-mer which constitutes the unit cell. The Davydov components of the spectra differ in their polarisation. For example, in monoclinic aromatic crystals with $Z = 2$ (dimer), like anthracene, one of the transitions connects the A_g ground state with the A_u and the other with the B_u state, resulting in a Davydov component polarized parallel to the monoclinic axis and another perpendicular to it. Other splittings originate in degeneracy breaking of levels because of lower symmetry of the crystals compared to the molecules. The symmetry change from molecule to crystal can also change the selection rules and activate some transition. For example, the pure electronic transition $S_{0-1} \leftarrow S_{0-0}$ is forbidden in the benzene molecule and becomes allowed in benzene crystals.

Molecular solids frequently crystallize in low symmetry systems and they display quite anisotropic optical properties. These anisotropies, concerning both distinct energy positions of electronic transitions and different values of the dielectric tensor components, tend to be reduced in less ordered solids. In this regard, molecular semiconductors other than crystals may show different degrees of disorder and hence, of anisotropic optical behavior. In general, the molecular character of the absorption features prevails but the shifts and broadenings of the spectra depend on the particular arrangements and distributions of molecules. Comparing to molecular spectra, the optical spectra in these solids display an inhomogeneously broadened average

due to different orientations and variable distances between molecules. A particular case most relevant for OPV is that of polymers. We can consider a polymer chain like an ensemble of molecules with a certain length distribution and a certain degree of coherence given by an effective coherence or conjugation length. Over this length L, in average, delocalized coherent excitons may exist. The molecular nature of the absorption features is manifested as a Franck-Condon progression, and the transition energy shift evolves with the average length in rough agreement with a particle-in-a-box model. The polymer is built from such conjugated segments which gradually loose coherency after such average distance. The conjugation length increases with the structural regularity of the chain and its planarity, and decreases when disorder and irregularities such as bends and kinks that disturb the electronic coupling appear. The proximity of neighboring chains or segments may promote interaction between them and develop a certain degree of crystallinity that implies an additional delocalization of the π-electron system. All these factors affect the optical properties and it is quite complex to decouple the different contributions. Even in the case of crystalline polymers, these systems always have a certain degree of disorder. We may distinguish between crystalline polymers in which there are crystalline domains and amorphous polymers in which no such ordered domains exist. As in the case of inorganic semiconductors, disorder leads to localization. However, the excitations in an organic semiconductor are already localized. In this case, further localization means reduction of conjugation which in principle leads to an increase of the band gap in the amorphous polymer compared to the crystalline one. In many cases, a tail to lower energies in the optical spectrum of the amorphous material is evident. The origin of this tail is not related to Anderson localization like in amorphous inorganic semiconductors but to the larger inhomogeneous broadening characteristic of these materials.

4.6 Summary

In this chapter, we have reviewed some fundamental concepts that are important to understand the relationship between the dielectric function of a semiconductor and its electronic band structure. Physical properties that determine the linear optical properties can be deduced from spectroscopic ellipsometry experimental data. Key ingredients to delve into this way are the analysis of experimental dielectric function spectra and band structure diagrams, where symmetry properties are an essential aspect.

As semiconductors applied in solar cells have usually complex structures, simplifications to understand their optical properties are useful. For inorganic materials, the starting point is knowledge of the properties of perfect crystals to which nanostructured or amorphous structures are related. Likewise, the study of superstructures benefits from their relationship to simpler parent crystals. For organic or molecular semiconductors, a good starting point are the optical properties of the constituent molecules. Different strength of the interactions in organic crystals leads to

contrasted semiconducting behavior compared to inorganic ones. One of the most important differences is the resulting dielectric function as reviewed in this chapter.

Acknowledgements The authors thank the Spanish Ministry of Economy and Competitiveness (MINECO) for funding through grants CSD2010-00044, MAT2015-70850-P, and the "Severo Ochoa" Programme for Centres of Excellence in R&D (SEV- 2015-0496).

References

1. M.L. Cohen, J.R. Chelikowski, *Electronic Structure and Optical Properties of Semiconductors* (Springer, 1988)
2. P. Yu, M. Cardona, *Fundamentals of Semiconductors: Physics and Materials Properties* (Springer, Berlin, 2010)
3. H. Ibach, H. Lüth, *Solid-State Physics: An Introduction to Principles of Materials Science* (Springer, Berlin, Heidelberg, 2009)
4. M. Fox, *Optical Properties of Solids* (Oxford University Press, Oxford, 2001)
5. J. Humlíček, M. Garriga, M.I. Alonso, M. Cardona, J. Appl. Phys. **65**, 2827 (1989)
6. M. Schwoerer, H.C. Wolf, *Organic Molecular Solids* (Wiley-VCH, Weinheim, 2005)
7. A. Köhler, H. Bässler, *Electronic Processes in Organic Semiconductors* (Wiley-VCH GmbH & Co. KGaA, Weinheim, 2015)
8. G. Burns, A. Glazer, *Space Groups for Solid State Scientists*, 3th edn. (Academic Press, Oxford, 2013)
9. G.F. Koster, J.O. Dimmock, R.G. Wheeler, H. Statz, *Properties of the thirty-two point groups* (M.I.T. Press, Cambridge, Massachusetts, 1963)
10. M.I. Alonso, K. Wakita, J. Pascual, M. Garriga, N. Yamamoto, Phys. Rev. B **63**, 075203 (2001)
11. L.C.L.Y. Voon, M. Willatzen, *The kp Method* (Springer, Berlin Heidelberg, 2009)
12. D.E. Aspnes, in *Handbook on Semiconductors*, ed. by T.M. Balkanski (North-Holland, Amsterdam, 1980), vol. 2, chap. 4A, p. 110
13. A. Savitzky, M.J.E. Golay, Anal. Chem. **36**, 1627 (1964)
14. J.W. Mueller, Bureau International des Poids et Mesures. Technical Report bIPM-74/1 (1974)
15. C. de Boor, *A Practical Guide to Splines* (Springer, New York, 1978)
16. J. Humlíček, M. Garriga, in *Silicon-Germanium-Carbon Alloys*, ed. by S.T. Pantelides, S. Zollner (Taylor & Francis, New York, 2002), p. 483
17. M.A. Lukas, F.R. de Hoog, R.S. Anderssen, J. Comput. Appl. Math. **235**, 102 (2010)
18. D.E. Aspnes, S.D. Yoo, Phys. Status Solidi B **215**, 715 (1999)
19. S.G. Choi, D.E. Aspnes, N.A. Stoute, Y.D. Kim, H.J. Kim, Y.-C. Chang, C.J. Palmstrom, Phys. Status Solidi A **205**, 884 (2008)
20. J.E. Jaffe, A. Zunger, Phys. Rev. B **28**, 5822 (1983)
21. M.I. Alonso, I.C. Marcus, M. Garriga, A.R. Goñi, J. Jedrzejewski, I. Balberg, Phys. Rev. B **82**, 045302 (2010)
22. F. Wooten, D. Weaire, J. Non-Cryst, Sol. **64**, 325 (1984)

Chapter 5
Dielectric Function Modeling

James N. Hilfiker and Tom Tiwald

Abstract Spectroscopic ellipsometry (SE) is commonly used to measure the optical constants of thin films and bulk materials. The optical constants vary with wavelength, which is referred to as dispersion. Rather than independently determine the optical constants at each wavelength, it is convenient to use an equation to describe their dispersion. A dispersion equation simplifies the description of the optical constants and improves the efficiency of data analysis. We begin this chapter by describing the optical constants, optical resonance, and the Kramers-Kronig relations. Different absorption phenomena are also briefly described. Many dispersion equations relate an optical resonance or absorption in terms of the complex dielectric function. Multiple resonance and absorption features can be summed to describe the overall dielectric function for the material. Finally, we review the common dispersion equations used for photovoltaic materials. The Cauchy and Sellmeier equations are used to describe transparent materials. The Lorentz, Harmonic, and Gaussian equations describe a resonant absorption. The Tauc-Lorentz and Cody-Lorentz were developed for amorphous semiconductors with dispersion features necessary to describe the optical functions near the bandgap energy. Additional dispersion equations are designed to describe the critical points in semiconductor band structure. We conclude this review with a description of polynomials, splines, and basis-splines, which are used to empirically match the optical functions of many materials.

5.1 Optical Absorption and Dispersion Features

In this section, we introduce the definitions for optical constants and consider the general shapes and origins of optical dispersion. We then introduce the Kramers-Kronig relations, which provide a formal connection between the real and

J. N. Hilfiker (✉) · T. Tiwald
J.A. Woollam Co., Inc., 645 M Street, Suite 102, Lincoln, NE 68508, USA
e-mail: jhilfiker@jawoollam.com

© Springer International Publishing AG, part of Springer Nature 2018

H. Fujiwara and R. W. Collins (eds.), *Spectroscopic Ellipsometry for Photovoltaics*,
Springer Series in Optical Sciences 212,
https://doi.org/10.1007/978-3-319-75377-5_5

imaginary optical constants. Finally, we review the phenomena which lead to optical absorption at typical spectroscopic ellipsometry (SE) measurement frequencies.

5.1.1 Refractive Index and Dielectric Function

There are two common expressions for the optical constants of a material: the complex refractive index ($N = n - ik$) and the complex dielectric function ($\varepsilon = \varepsilon_1 - i\varepsilon_2$) [1]. While both were introduced in Chap. 3, we expand the discussion to describe their general shape and behavior. They are related by:

$$\varepsilon = \varepsilon_1 - i\varepsilon_2 = N^2 = (n - ik)^2 \tag{5.1}$$

with

$$\varepsilon_1 = n^2 - k^2 \tag{5.2a}$$

$$\varepsilon_2 = 2nk \tag{5.2b}$$

Because each term varies with wavelength, λ, we refer to $N(\lambda)$ and $\varepsilon(\lambda)$ as the *optical functions* of a material. The optical functions of amorphous germanium are graphed in Fig. 5.1, where N is plotted versus wavelength while ε is shown versus photon energy. Recall from (3.1) that photon energy is inversely related to wavelength. Both representations are acceptable and the graphs contain the same information, just modified by (5.1). In Sect. 5.3, we show that many dispersion equations describe ε versus photon energy because photon energy scales directly with frequency.

The complex refractive index generally describes how light is altered by interaction with a material. For example, the index of refraction, n, is related to the phase velocity (3.4). At an interface between two materials, the difference in the refractive index governs both the direction of the transmitted light (3.11) and the division of light amplitudes between reflection and transmission (3.15a–d). The extinction coefficient, k, is related to the absorption of light as it travels through a material (3.5) and (3.6).

The complex dielectric function also describes the interaction between light and materials. As light travels through a material, the light's oscillating electric fields create oscillating charge dipoles within atoms or between atoms. Each dipole reradiates an electromagnetic field, and will absorb some of the energy at certain oscillation frequencies. Each dipole field combines with the fields from other dipoles as well as the incident field resulting in the total macroscopic field within the material. The dielectric function, ε, describes the constitutive relation between

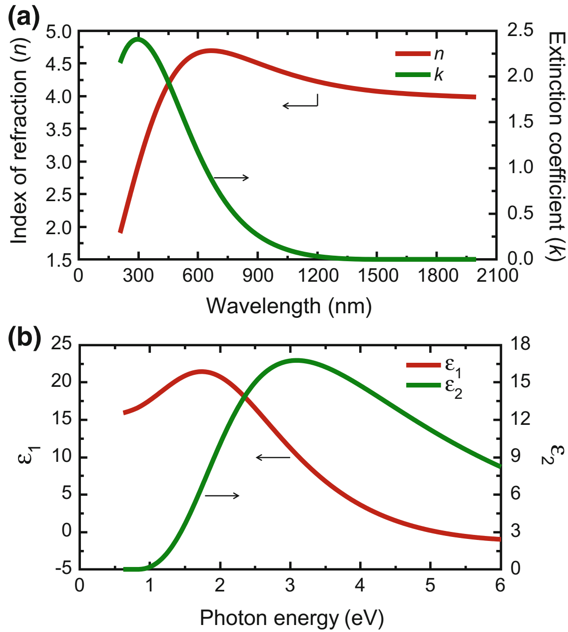

Fig. 5.1 **a** Refractive index versus wavelength and **b** dielectric function versus photon energy for amorphous germanium. While the graphs appear to be quite different, they contain the same information in different forms

the displacement field (**D**) (this is the total macroscopic field), the incident electric field (**E**), and the electric polarization (**P**) [2]:

$$\mathbf{D} = \varepsilon_0 \mathbf{E} + \mathbf{P} = \varepsilon\, \varepsilon_0 \mathbf{E} \tag{5.3}$$

where ε_0 is the permittivity of free space and ε is the relative dielectric constant. Since ε_0 is a constant, in this chapter we will concentrate on ε and simply call it the *dielectric constant*, dropping the term “relative”. Rewriting (5.3) as

$$\varepsilon = \frac{\mathbf{D}}{\varepsilon_0 \mathbf{E}} = \frac{\varepsilon_0 \mathbf{E} + \mathbf{P}}{\varepsilon_0 \mathbf{E}} = 1 + \frac{\mathbf{P}}{\varepsilon_0 \mathbf{E}}. \tag{5.4}$$

we see that ε is a constant of proportionality for **D/E** and describes the contribution from **P**, which is a function of the volume density and strength of the dipoles contained within the material. The dipole response, and therefore **P**, depends on how quickly the **E**-fields oscillate. Thus ε is a function of frequency, $\varepsilon(\omega)$. The dipole response will also generally differ in both amplitude and phase from the oscillating **E**-fields of the incident light, making $\varepsilon(\omega)$ a complex value. Thus, the dielectric function contains a great deal of information about the material properties [2, 3].

5.1.2 Resonance

We now consider how the dipole behavior affects the dielectric function. The dipoles are treated as a collection of classical oscillators, with a resonant frequency, driven by an externally applied harmonically oscillating force. This classical approach provides a reasonable description of the dielectric function shape versus frequency. It is a good starting model for the dipole-field interactions and energy absorption processes of materials. However it does not accurately describe band-gaps, absorption at critical points and other phenomena, which are more accurately described by semi-classical and quantum mechanical models.

Most SE measurements cover the ultraviolet (UV), visible, and near infrared (NIR) wavelengths. At these wavelengths, the light interacts primarily with electrons, as their mass is sufficiently small that they can respond to time-varying electric fields of a very high frequency. The time-varying electric field displaces the negatively-charged electron clouds relative to the heavier, positively-charged nuclei, forming dipoles as shown in Fig. 5.2a. The dipoles oscillate at the same frequency as the E-fields of incoming light; and in turn they reradiate light at that same frequency but with a phase and amplitude that is generally different than the incident field.

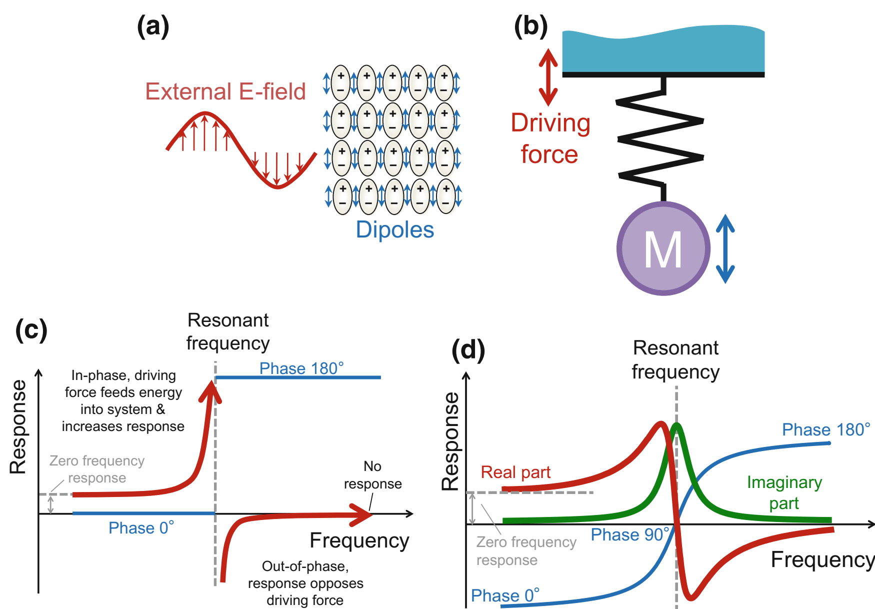

Fig. 5.2 **a** An oscillating electric field induces oscillating dipoles within a material. **b** A mass on a spring responds to an external driving force. **c** The frequency response of a lossless system and **d** the frequency response of a lossy system

This phenomenon has many similarities to a mechanically resonant system driven by an external, harmonic oscillating force, such as the mass on a spring being driven at a specific frequency in Fig. 5.2b. Classical resonant systems are discussed in elementary physics textbooks, but we repeat a few concepts here that help describe the overall shape of a dielectric function. The frequency response of any resonant system can be described as a complex function, as shown in Figs. 5.2c, d for lossless and lossy systems, respectively. The real part represents the portion of the response that is in-phase with the driving force (when positive), or 180° out-of-phase with the driving force (when negative). The imaginary part represents the portion of the response that is 90° out-of-phase with the driving force. The imaginary part is also proportional to the energy loss at a given frequency.

When a zero frequency (static) force is applied, the system responds in the direction of the force, and the response function (in our case, the dipole displacement) is positive and real. The strength of the response depends upon the system particulars, such as mass, strength of the restoring force, and so on. As the applied force begins to oscillate at low frequencies, the real part of the response increases because the response and force are exactly in-phase (lossless system) or mostly in-phase (lossy system); therefore the driving force adds to the response.

In a lossless system (Fig. 5.2c), the response function is always real-valued because the phase is either 0° or 180°. As the frequency increases from zero to the resonant frequency, the response approaches positive infinity (and the phase remains zero). At the resonant frequency, the phase of the response abruptly transitions to 180°, such that it is out-of-phase with the force and the response becomes infinitely negative. As the driving frequency increases beyond the resonant frequency the response becomes smaller and smaller, because the force changes direction faster than the system can respond.

A lossy system will absorb energy, so the response remains finite at all frequencies (Fig. 5.2d). At low frequencies the response function of a lossy system looks very similar to that of a lossless system: the real part is positive and increases with frequency, and the imaginary part is nearly zero. As the frequency increases, the phase of the response lags further and further behind the driving force, which means they are more and more in opposition. At some frequency the driving force opposition is sufficiently large that the real part of the response reaches a maximum and begins to decrease. At about the same frequency, the imaginary part increases sharply. At the resonant frequency the real part of the response is zero, the imaginary part reaches a maximum, and the phase lag is 90°. Beyond the resonant frequency, the real part becomes more negative until at some point the force changes faster than the system can respond. The imaginary part declines from its maximum. At frequencies significantly higher than resonance, both the real and imaginary parts approach zero.

The dielectric function, ε, has a similar form to the frequency response of a classical oscillator. This is because the oscillating dipole displacements give rise to the polarization **P**, which means that **P** has the same form as the response functions shown in Fig. 5.2c, d. Since ε is a function of **P** (5.4), it also takes on a similar

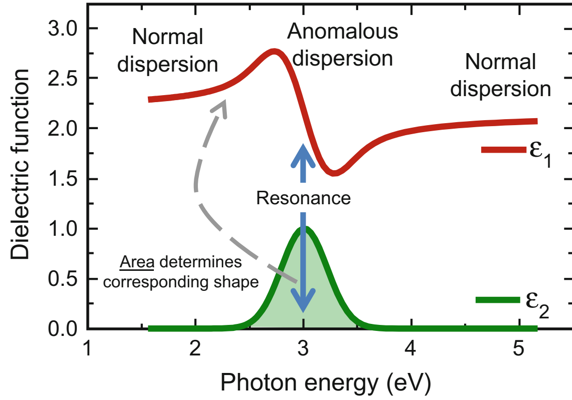

Fig. 5.3 Typical resonance absorption with normal and anomalous dispersion regions. The dispersion goes hand-in-hand with the absorption to maintain causality. Kramers-Kronig relations show that the area integrated under the ε_2 curve corresponds to the shape of the ε_1 curve

form. As an example, the dielectric function for transparent spectral regions is often modeled using a lossless dielectric function that looks very similar to Fig. 5.2c. We shall discuss this type of function when we consider the Sellmeier relation in Sect. 5.3.1.

For absorbing materials, the response function will look very similar to the ε_1 and ε_2 as shown in Fig. 5.3. Note the strong similarities between Figs. 5.2d and 5.3. The ε is usually described as a function of photon energy (in electron volts or eV), which is directly proportional to the electromagnetic field oscillation frequency. The energy loss, or light absorption, goes hand-in-hand with the optical dispersion and leads to regions of normal and anomalous dispersion. *Normal dispersion* describes the increasing ε_1 value as photon energy (or frequency) increases. Normal dispersion occurs at all photon energies where the absorption of light is negligible ($\varepsilon_2 \sim 0$). At energies where the material absorbs light, the slope of ε_1 becomes negative and its value decreases with increasing energy. This is referred to as *anomalous dispersion*. In Fig. 5.3, ε_2 reaches a peak at the resonant condition of 3 eV and we see that ε_1 has a negative slope. The actual shapes of ε_1 and ε_2 are related, as will be discussed in the next section.

5.1.3 Kramers-Kronig Relations

The Kramers-Kronig (KK) relations establish a physical connection between ε_1 and ε_2 as [4]:

$$\varepsilon_1(E) = 1 + \frac{2}{\pi} P \int_0^\infty \frac{E' \varepsilon_2(E')}{E'^2 - E^2} \mathrm{d}E' \qquad (5.5\text{a})$$

$$\varepsilon_2(E) = -\frac{2E}{\pi} P \int_0^\infty \frac{\varepsilon_1(E')}{E'^2 - E^2} \mathrm{d}E' \tag{5.5b}$$

where P is the principal part of the integral and E is the photon energy of the light. Please note that these equations define the dielectric function as $\varepsilon = \varepsilon_1 + i\varepsilon_2$. These equations are the result of causality, where the response cannot precede the cause. In our case the material dipole response and absorption must occur after the electric field is applied. The KK relations help illustrate a few physical properties of the optical functions.

1. The shapes of ε_1 and ε_2 are not independent. The KK relations provide the connection between their values. In theory, if we can describe one function (either ε_1 or ε_2), the second can be calculated. In practice, we can calculate the general shape of the corresponding function but are often prevented from the exact calculation (see #3).
2. The KK relations involve integration, thus the ε_1 shape depends on the area under the ε_2 curve, as shown in Fig. 5.3. Simply stated, absorption causes anomalous dispersion and the larger the area under ε_2, the larger the effect on ε_1.
3. The KK relations integrate over *all* photon energies. Thus, ε_1 at a given energy is affected by ε_2 at all energies. In practice, we can generally describe ε_2 within our measured spectral range. However, absorptions outside the measured spectral range also affect the ε_1 curve. Thus, the KK calculation does not necessarily provide an exact match to our desired ε_1 curve. However, it does provide the correct general shape. We discuss this issue in Sect. 5.2.2.

The KK relations are very important during SE data analysis. They help limit the possible optical functions to only those that are physically plausible. They also greatly reduce the number of free parameters needed to describe complex optical functions. This is generally accomplished by using equations to describe the shape of ε_2 and then calculating ε_1 from (5.5a). For this reason, we consider the mechanisms which produce absorption within a material in the next section.

5.1.4 Absorption Phenomena

We consider three absorption phenomena which may affect the material optical functions at typical SE wavelengths: electronic transitions, free-carrier absorption and vibrational absorption.

5.1.4.1 Electronic Transitions

Most SE measurements use wavelengths from the UV to the NIR. At these wavelengths, the most common absorptions involve electrons. Electronic transitions occur when light of the correct photon energy causes an electron to transition between energy bands, which is why these are also called interband transitions. This absorption mechanism is commonly found in dielectrics, organics, and semiconductors. It also occurs in the UV and visible optical functions of metals, although it is less obvious because the absorptions from electronic transitions can be masked by the effects of conductivity. Electronic transitions also form the basis for the photovoltaic process—light is absorbed by the material and transformed into electrical energy. Thus, absorption from electronic transitions is of significant interest for PV materials. SE can be used to determine which wavelengths (or photon energies) will be absorbed and the amount of absorption.

The bandgap energy is the minimum energy required to initiate electronic transitions between bands. Recall that the photon energy of light is inversely related to wavelength. At longer wavelengths no absorption occurs, because the energy is insufficient to excite electrons to transition across the energy gap between two bands. Above the bandgap energy, the shape of the absorption indicates whether the material has a direct or indirect bandgap. Consider the indirect and direct bandgap absorption curves in Fig. 5.4. The onset of absorption for a direct bandgap appears as a step, while that for an indirect bandgap is much more gradual. The shape of the absorption curve at energies higher than the bandgap is affected by the long-range order within the material. For this reason, the optical functions often indicate whether a material is amorphous, polycrystalline, or monocrystalline. Organic materials also exhibit absorption due to electronic transitions, but their band structure is related to molecular bonding [5].

The electronic transitions are the most commonly measured absorption phenomena, and their exact shape is related to the shape and symmetries of the energy bands. Therefore, they are represented by the largest variety of dispersion models. The Tauc-Lorentz (Sect. 5.3.7) and Cody-Lorentz (Sect. 5.3.8) describe the absorption of amorphous materials near their bandgap. The CPPB, Adachi, and

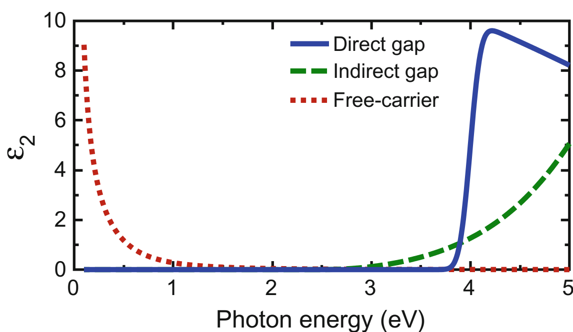

Fig. 5.4 Comparison between the ε_2 curves associated with direct and indirect interband transitions near the bandgap, along with intraband transitions associated with free carrier absorption

PSEMI (Sect. 5.3.9) are useful for crystalline materials and direct bandgap transitions. For organic materials, it is more common to apply a sum of Gaussians (Sect. 5.3.6) or an empirical equation such as the b-spline (Sect. 5.3.10).

5.1.4.2 Conductivity or Free-Carriers

The second type of absorption we consider is that of free-carriers. This absorption occurs from electrons (or holes) which are no longer bound to an atom. Another way to consider this is that the electrons are already in the conduction band (holes in the valence band) and can absorb light to move within the band—in other words intraband transitions [6]. This is the common absorption mechanism for conductive materials such as metals and transparent conductive oxides (TCOs). They are generally modeled with some form of the Drude oscillator, described in Sect. 5.3.4. Figure 5.4 shows an example ε_2 spectra related to free-carrier absorptions. Unlike the electronic transitions, free carriers absorb more strongly as photon energy decreases, which corresponds to slower frequencies. As the frequency decreases, there is higher probability for energy transfer between the electromagnetic wave and the material.

5.1.4.3 Vibrational and Phonon Absorption

The final absorption mechanism we consider is due to interactions with molecular and lattice (phonon) vibrational modes. Because atoms are significantly heavier than electrons, the resonant frequencies of molecular vibrations are generally lower than electronic transition frequencies. Thus, this type of absorption primarily occurs at infrared (IR) wavelengths. The resonant frequency for a particular vibrational mode depends upon the mass and bond strengths of the atoms involved, as well as the molecular and lattice symmetry. Vibrational modes can be symmetric and antisymmetric, and include stretching, twisting and scissor motions, as illustrated in Fig. 5.5. Infrared light can only be absorbed by "infrared active" modes, which are modes with a pre-existing dipole moment because of ionic or polar bonds. As IR ellipsometry is not as common as UV, visible, and NIR ellipsometry, we will give

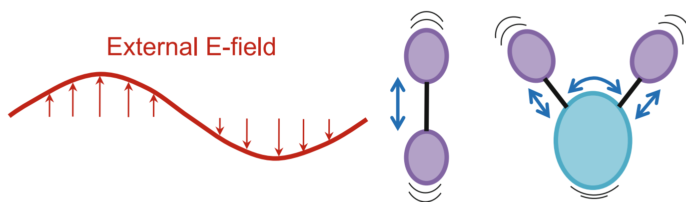

Fig. 5.5 Oscillating molecular vibrations can occur at slower frequencies such as used by Infrared SE

less consideration to the dispersion equations for this region. The reader is directed to two excellent books on IR ellipsometry, one by Roseler [7] and another by Schubert [8]. However, we must point out that these infrared vibrational absorptions can alter the shape of ε_1 at NIR wavelengths through the Kramers-Kronig relationship and this influence can be modeled using a Sellmeier function (Sect. 5.3.1).

5.2 Representing the Dielectric Function

While a few dispersion equations are strictly empirical with no underlying physical basis, the majority incorporate the KK relations to connect the real and imaginary optical functions and maintain a physically plausible shape. In this section, we consider the general approach to describe the optical functions. We start by describing a resonance or absorption. Multiple absorptions are summed together to create the overall optical functions which describe contributions from different phenomena. Finally, we describe how to handle the contributions from absorptions outside the measured spectral range.

5.2.1 Representing Absorption Features

As described in Sect. 5.1, the dielectric function is strongly influenced by dipoles within a material. The form of the complex dielectric function that is described in Sect. 5.1.2 is a result of the strength of the dipole response combined with the level of energy loss near resonance. Most dispersion equations define the shape of ε_2 and then apply the KK integral relations to calculate ε_1. If we consider a single absorption (or resonance) as pictured in Fig. 5.3, the general shape of ε_2 can be described by the absorption amplitude, a broadening term, and the resonant energy (or frequency). Additional terms may be added to modify this basic shape depending on the type of dispersion model. Once the absorption shape is defined, the area under the ε_2 curve is integrated per (5.5a) to determine ε_1. Because of their resemblance to mechanical oscillators, these types of functions are often called "oscillator functions" or simply "oscillators". These functions will be seen time and again as we consider the actual dispersion equations in Sect. 5.3.

Most materials exhibit multiple absorptions, which occur at different energies, and the total optical function versus photon energy is the result of a combination of these phenomena. Figure 5.6 represents a material which has three different absorption phenomena occurring at different energies. Each can be described as a separate resonance and then summed together to describe the material's overall complex optical function. When comparing the three "oscillators" in Fig. 5.6, note that the narrower ε_2 absorptions are associated with a sharper dispersion feature in

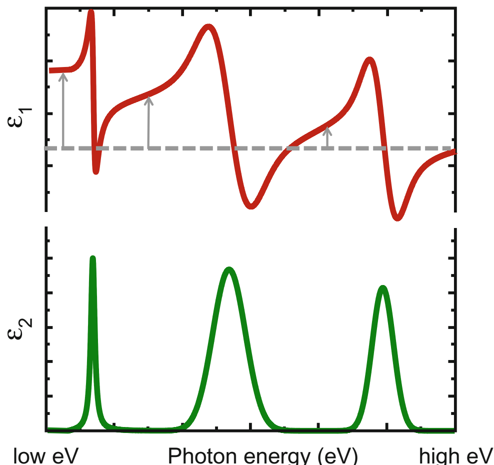

Fig. 5.6 Material dielectric function is influenced by absorption phenomena at different energies

ε_1. The dashed line and arrows illustrate how each resonant absorption increases the overall level of ε_1 as the incident light changes from higher to lower photon energies.

It is easy to visualize the absorption features as isolated resonant phenomena occurring at different energies. However, real materials are generally much more complex. The absorption phenomena, such as electronic transitions, can have multiple contributions and overlap to form the final shape of the material optical functions. Fortunately, many dispersion functions remain valid when summed together. This is shown in Fig. 5.7 for a CdTe material. The final shape consists of five individual dispersion equations, each contributing to the overall shape of ε_2.

When multiple absorptions overlap, it becomes difficult to connect the oscillator parameters—amplitude, broadening, etc.—to the physical origins of the absorption. Furthermore, in most cases more than one combination of oscillators can successfully describe the same dielectric function. If one of the primary goals of the measurement is to determine a material's complex optical function, it can be argued that any combination of oscillators that faithfully reproduces ε is acceptable. In these circumstances, an ad hoc combination of oscillators can be chosen to match

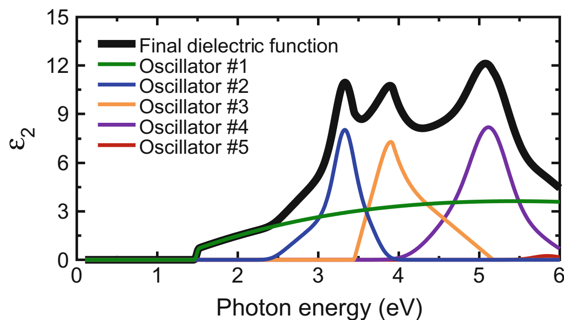

Fig. 5.7 Summation of multiple oscillators that "build-up" to give the overall shape of dielectric function (CdTe for the example)

the overall shape of the function, and no attempt is made to tie oscillator parameters to specific physical properties such as bandgap energy, etc. The goal then is to create an optical function that is physical (i.e., fulfills the Kramer's Kronig relationship), and that best matches the measured SE data. It is also preferred that the optical function use a minimum number of free parameters while still accurately modeling the SE data.

5.2.2 Absorptions Outside Measured Spectral Range

SE measurements can only cover a limited range of energies, and this may be further limited during data analysis—restricting the final *investigated spectral range*. As mentioned earlier, the shape of the optical functions are influenced by their values at all energies. Thus, we need to consider what occurs outside the investigated spectral range. As a simple example, consider a material that is transparent throughout the investigated spectral range. While transparent, ε_1 still increases toward higher energies; that is, it must maintain normal dispersion. As discussed earlier, normal dispersion is the result of the contribution of the oscillating dipoles to the polarization field as the photon energy approaches their resonant energy. Thus, it is the resonance at higher photon energies that causes ε_1 to increase at shorter wavelengths (higher photon energies). The Sellmeier equation approximates normal dispersion by placing a resonance at higher photon energy outside the investigated spectral range.

Even when absorption occurs within the investigated spectral range, the overall ε_1 shape is altered by any absorption at higher or lower photon energies. This is shown in Fig. 5.8 where three ε_2 absorption phenomena occur between 1 and 6 eV. Our measured photon energies only access the middle absorption. If we were to describe only this middle ε_2 absorption, the KK integration would produce the dashed ε_1 curve in Fig. 5.8. However, this ε_1 would not match our experimental SE data, since it does not retain the influence of the absorptions outside the measured energy range. The correct ε_1 shape is shown by the solid curve, because it includes contributions from the out-of-range absorptions. Comparing the solid and dashed curves, the primary difference is an offset and upward tilt to the general ε_1 shape at higher photon energies. We can raise the ε_1 curve by adding an offset, often called $\varepsilon_1(\infty)$. The offset accounts for absorptions that are well beyond the investigated spectral range. If absorptions occur close to our investigated spectral range, they may also "tilt" the ε_1 curve. This effect can be modeled by using "poles" (Sect. 5.3.1). A pole alters ε_1 in the same manner as an absorption that is located outside the investigated spectral range, without describing the actual shape of that absorption. A pole placed at higher photon energies both raises and tilts the ε_1 curve upward toward high energies (shorter wavelengths). A pole placed at lower energies will lower and tip the ε_1 curve downward as it extends toward lower photon

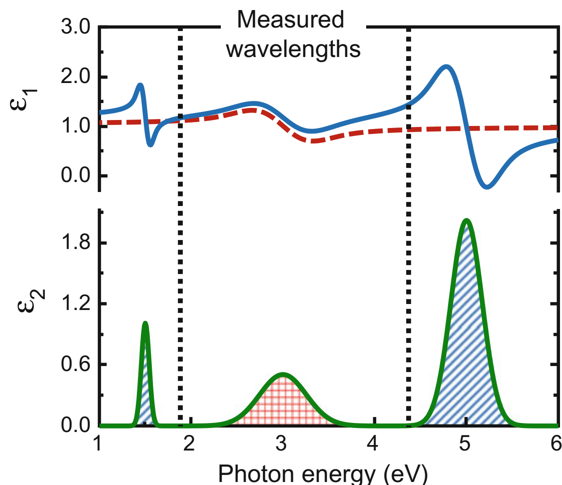

Fig. 5.8 Three absorptions are shown, but only the center peak is within the measured wavelength range. A KK integral from this center absorption (hatched area) would produce the dashed ε_1 curve shown above. However, the absorptions outside the measured spectral range still affect the shape of ε_1 as shown in the solid ε_1 curve which is calculated by the KK integral under all three ε_2 features

energies (longer wavelengths). Thus, the effect on ε_1 from absorptions that are external to the investigated spectral range can be approximated using high and low energy poles, along with an offset—$\varepsilon_1(\infty)$.

5.3 Common Dispersion Relations

We will now review some dispersion relations that are commonly used to describe photovoltaic materials. For each relation, we provide the underlying equations, describe their general shape, and list the free parameters used to modify the shape during data analysis. We also discuss the merits and limitations of each equation and mention common applications. For each equation, a table is provided so that the reader can conveniently locate pertinent information.

While the equations are discussed individually, most can be added together to describe more complex dispersion shapes. For example, the complex dielectric function may be represented by a linear summation of terms, such as:

$$\varepsilon = \varepsilon_1 - i\varepsilon_2 = \varepsilon_1(\infty) + \text{Sellmeier}(A_1, E_1) + \text{Lorentz}(A_2, E_{02}, \Gamma_2) + \text{Gaussian}(A_3, E_{03}, \Gamma_3) \tag{5.6}$$

Each absorption or resonance feature in ε_2 is represented by a corresponding "oscillator" equation and the corresponding variables. In many cases, the real part, ε_1, of an oscillator is derived using Kramers-Kronig integral relationship. The real part, ε_1, is often supplemented by one or two Sellmeier terms and the constant offset, denoted $\varepsilon_1(\infty)$. Note that these only affect ε_1, and they account for any high-frequency resonances which are not already considered by the listed equations.

While many of the individual equations have an offset equal to +1, this can be replaced by the variable offset of $\varepsilon_1(\infty)$ to add more flexibility to the final dielectric function shape.

5.3.1 Sellmeier

The Sellmeier dispersion [9] function models a material as a collection of oscillating dipoles, which resonate at a specific energy (frequency or wavelength) as discussed in Sect. 5.1.2. Sellmeier theory assumes that the oscillating dipoles have no absorption, so the oscillators have zero broadening and the resulting equations can be written as:

$$\varepsilon_1(\lambda) = 1 + \frac{A\lambda^2}{\lambda^2 - \lambda_0^2} \tag{5.7}$$

or equivalently,

$$\varepsilon_1(E) = 1 + \frac{A E_0^2}{E_0^2 - E^2} \tag{5.8}$$

where there are two free parameters for each Sellmeier term: amplitude A, and a resonant wavelength λ_0 or resonant energy E_0. Alternative Sellmeier expressions exist with different numerator terms. This will be discussed in Sect. 5.3.3 for the corresponding Lorentz equations. A very simplified Sellmeier expression, referred to as a *Pole* is given as:

$$\varepsilon_1(E) = 1 + \frac{A}{E_0^2 - E^2} \tag{5.9}$$

Because there is no broadening term, the Sellmeier and Pole equations are purely real ($\varepsilon_2 = 0$) and each term approaches $+\infty$ or $-\infty$ at the resonant condition. This is demonstrated in Fig. 5.9 for a single Sellmeier term per (5.7) with $\lambda_0 = 200$ nm. With this single Sellmeier term, ε_1 approaches +1 at short wavelengths (large E) and approaches $1 + A$ at long wavelengths (small E).

The Sellmeier equations are used to describe transparent materials that exhibit normal dispersion within the investigated spectral range. The resonant frequency is generally located at UV wavelengths, beyond the shortest wavelength of the investigated spectral range. Multiple Sellmeier terms can be summed to represent the effect from multiple resonances, as:

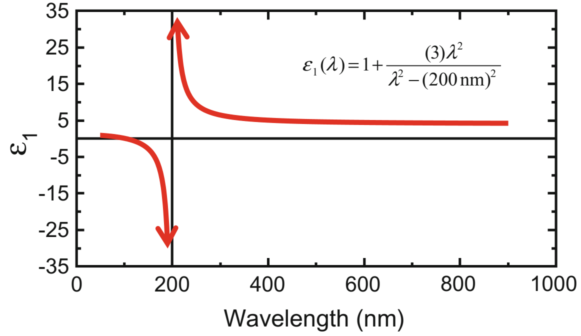

Fig. 5.9 Sellmeier dispersion shown for (5.7) with amplitude equal to 3 and resonant wavelength set to 200 nm

$$\varepsilon_1(\lambda) = \varepsilon_1(\infty) + \sum_j \frac{A_j\lambda^2}{\lambda^2 - \lambda_{0j}^2} \tag{5.10}$$

or

$$\varepsilon_1(E) = \varepsilon_1(\infty) + \sum_j \frac{A_j E_0^2}{E_{0j}^2 - E^2} \tag{5.11}$$

The variable offset, $\varepsilon_1(\infty)$, has been added to accommodate additional resonances well outside the investigated spectral range, because an offset other than +1 may be required to accomplish the desired effect of raising or lowering ε_1. It is common practice to use two Sellmeier terms where a UV term describes the higher energy electronic transitions while an IR term describes molecular vibrations at lower energy. The UV term tips ε_1 upward toward short wavelengths, while the IR term tips ε_1 down toward longer wavelengths and is only needed for materials with strong IR resonance. There is less sensitivity to the IR term unless the investigated spectral range extends well into the infrared. For this reason, it is common to fix the resonant energy of the IR term at a nominal value (e.g. 0.001 eV) and only fit the IR amplitude, which helps reduce correlation by decreasing the total number of variable parameters.

There are several commonly seen forms of the Sellmeier function. One is used in the data sheets supplied with Schott glass, where (5.10) is rewritten in the following form [10]:

$$n^2(\lambda) - 1 = \frac{B_1\lambda^2}{(\lambda^2 - C_1)} + \frac{B_2\lambda^2}{(\lambda^2 - C_2)} + \frac{B_3\lambda^2}{(\lambda^2 - C_3)} \tag{5.12}$$

Note that the C parameters are the *square* of the resonant wavelengths. Another form of the Sellmeier explicitly defines the term $-C\lambda^2$, which curves the optical function downward at longer wavelengths [11]:

Table 5.1 Details of the Sellmeier equation

Sellmeier equation	
# of free parameters	2 or 3 with $\varepsilon_1(\infty)$
for $\varepsilon_{2:}$	0
for $\varepsilon_{1:}$	2–3 [A, E_0] or [A, λ_0] with $\varepsilon_1(\infty)$ optional
Primary applications:	Transparent spectrum of dielectrics and organics

$$n^2(\lambda) = \varepsilon_1(\infty) + \frac{A\lambda^2}{\lambda^2 - B^2} - C\lambda^2 \tag{5.13}$$

This is equivalent to a two-term version of (5.10), where the resonant wavelength of the second term, λ_{02}, is set to a very large, finite value.

The Sellmeier model works well in spectral regions where there is no absorption. It provides a physically plausible normal dispersion shape with the amplitude and curvature needed for ε_1 by varying the two adjustable parameters, amplitude and resonant frequency. However, the relationship between the adjustable parameters and the final shape is not as intuitive as the Cauchy equation (Sect. 5.3.2). In addition, care must be taken to avoid placing the resonant condition within the investigated spectral range to avoid the large singularity which occurs, as shown near $\lambda = 200$ nm in Fig. 5.9. Table 5.1 provides an overview of the Sellmeier equation.

5.3.2 Cauchy

The Cauchy is actually an empirical model that predates the Sellmeier equation. However, it can be derived as a binomial series expansion of a single Sellmeier term. The Cauchy function [12] is written as:

$$n(\lambda) = A + \frac{B}{\lambda^2} + \frac{C}{\lambda^4} + \ \ldots \tag{5.14a}$$

$$k(\lambda) = 0 \tag{5.14b}$$

The simplicity of the Cauchy equation makes it very convenient and it is the most widely-used model for transparent materials. The Cauchy equation is also intuitive to use: A sets the amplitude of the index while B and C add curvature to produce normal dispersion. When wavelength is limited to a small range, two terms (A and B) are often adequate. The C term helps to define the index curvature over a broader wavelength range. With wavelength units in microns, the typical range for B and C is from +0.001 to +0.05 and −0.001 to +0.005, respectively.

The Cauchy is only accurate when $n(\lambda)$ follows normal dispersion. The standard 3-term Cauchy does not have a mechanism to produce downward tip of the index at

NIR wavelengths caused by an IR resonance. However, the Cauchy equation can be modified to the following form:

$$n(\lambda) = A + \frac{B}{\lambda^2} + \frac{C}{\lambda^4} - D\lambda^2 \tag{5.15}$$

where D allows a downward tip at long wavelengths. The "$D\lambda^2$" term is equivalent to the last term of the Sellmeier function in (5.13). The downward tip is demonstrated in Fig. 5.10, which compares a 3-term Cauchy (5.14a), a 4-term modified Cauchy (5.15) and a sum of two-term Sellmeier [Pole form, (5.9)]. In this case, the Sellmeier is still generally preferred as it reduces the total number of free-parameters because the IR resonant energy was fixed at a nominal value.

The Cauchy equation can also be extended to handle the onset of absorption by replacing (5.14b) with Urbach absorption [13]:

$$k(E) = \alpha e^{\beta(E - E_b)} \tag{5.16}$$

The Urbach equation represents a small exponentially decaying absorption below the bandgap of many amorphous materials. The extinction coefficient is described by an amplitude α, an exponent factor β, and the band-edge energy E_b. The Urbach absorption is only accurate when the exponential absorption is sufficiently small ($k < 0.01$) such that the index does not exhibit anomalous dispersion.

The main drawback of the Cauchy equation is that it can create physically implausible shapes that defy normal dispersion if either B or C is a strong negative value. It is advisable to always view a plot of the final index dispersion after data fitting is completed. If the index decreases toward short wavelengths, it defies normal dispersion and calls into question the resulting model. This often indicates the model is still missing some important detail, such as roughness, index gradient or even absorption.

The Cauchy and Sellmeier relations are used to model a wide variety of dielectrics and organics. The main constraint for both is that they can only be applied to a spectral range where the material is transparent. The Sellmeier is

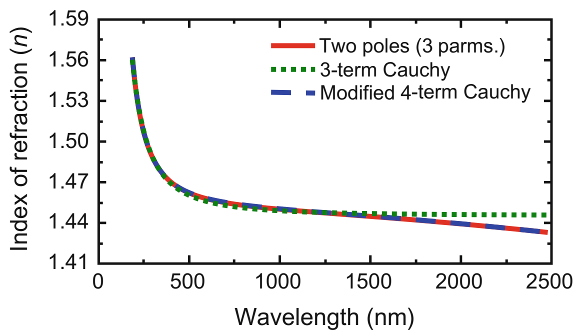

Fig. 5.10 Index of fused silica described using a 3-term Cauchy, a 4-term Cauchy, and a sum of two Sellmeier terms. The standard 3-term Cauchy index remains flat in the NIR while the IR Sellmeier relation and the 4th term of the Cauchy can provide the downward index tip due to IR resonance

Table 5.2 Details of the standard 3-term Cauchy equation

3-term Cauchy equation	
# of free parameters	3
for $\varepsilon_{2:}$	0
for $\varepsilon_{1:}$	3 [A, B, C]
Primary applications:	Transparent spectrum of dielectrics and organics

preferred if the investigated spectral range extends far enough into the NIR such that the index begins to tilt downward due to strong IR phonon resonances (such as with SiO_2) or in response to IR absorption from free-carriers (such as with SnO_2:F). If absorption extends into the investigated spectral range, then neither the Cauchy nor Sellmeier will be adequate. In the following sections, we cover a variety of models which describe absorbing optical functions. Table 5.2 provides an overview of the Cauchy equation.

5.3.3 Lorentz

The Lorentz oscillator model assumes that the response of electrons to the oscillating electric field is similar to the response of a harmonically driven mass on a spring subject to a dissipative force. In this analogy, the mass corresponds to the electron cloud, the spring represents the electrostatic forces on the electron cloud due to all other electrons and nuclei in the solid, and the dissipative force (friction for the mass on a spring) represents the energy loss due to emission of a photon [14]. This model is classical in that the electrons may possess any amount of kinetic energy as opposed to the allowed energy levels and bands of quantum theory. The Lorentz oscillator model is generally formulated as:

$$\varepsilon(E) = \varepsilon_1(E) - i\varepsilon_2(E) = 1 + \frac{A}{E_0^2 - E^2 + i\Gamma E} \tag{5.17}$$

Each oscillator is described by three parameters: the oscillator strength A, center energy E_0, and broadening Γ. The Lorentz (5.17) reduces to the Pole of (5.9) when $\Gamma = 0$. The broadening term, Γ, can be visualized as the full width of ε_2 at half its maximum value (FWHM). When Γ is small, the region of anomalous dispersion extends approximately $\pm\Gamma/2$ around E_0 as shown in Fig. 5.11.

The Lorentz equation can also be constructed with different choice of numerator, as in:

$$\varepsilon(E) = \varepsilon_1(E) - i\varepsilon_2(E) = \varepsilon_1(\infty) + \frac{A\,\Gamma\,E_0}{E_0^2 - E^2 + i\Gamma E} \tag{5.18}$$

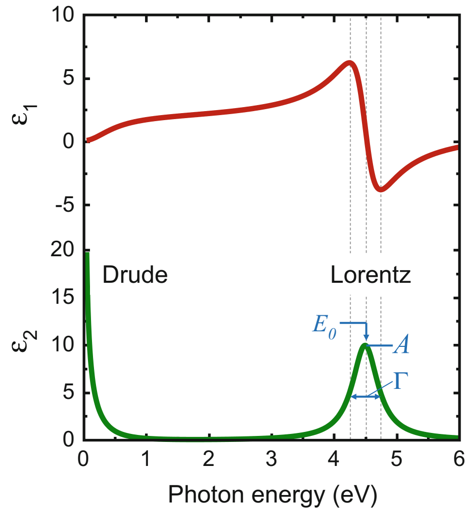

Fig. 5.11 The complex dielectric function associated with a Drude and a Lorentz oscillator function

$$\varepsilon(E) = \varepsilon_1(E) - i\varepsilon_2(E) = \varepsilon_1(\infty) + \frac{A\,E_0}{E_0^2 - E^2 + i\Gamma E} \tag{5.19}$$

or

$$\varepsilon(E) = \varepsilon_1(E) - i\varepsilon_2(E) = \varepsilon_1(\infty) + \frac{A\,E_0^2}{E_0^2 - E^2 + i\Gamma E} \tag{5.20}$$

These three equations provides a similar ε_2 shape, but with different meanings for A. In (5.18), A is the height of ε_2 at the center energy E_0. For (5.19), A is proportional to the area under the ε_2 curve and the ε_2 value at E_0 equals A/Γ. For (5.20), A is equivalent to the difference between ε_1 at energies significantly higher and lower than the oscillator's center energy. Interestingly, for each of these Lorentz equations, the actual peak in ε_2 shifts to energies below E_0 as Γ increases.

A Lorentz oscillator of the form from (5.18) is shown in Fig. 5.11. The oscillator resonance is at 4.5 eV with amplitude $A = 10$ and broadening $\Gamma = 1$ eV. Note the near-symmetric shape of the absorption and the relatively long tails extending on each side of the resonant absorption before ε_2 nears zero. For this reason, the Lorentz oscillator is seldom used to model dielectrics or semiconductors which require a transparent spectral region. Rather, the Lorentz model is useful for metals which remain absorbing across the entire spectrum. The Lorentz (5.17) also reduces to the Drude function (Sect. 5.3.4) as E_0 approaches zero energy, which is very useful for describing the free electron absorption that occurs in transparent conducting oxides and heavily doped semiconductors. Table 5.3 provides an overview of the Lorentz oscillator equation.

Table 5.3 Details of the Lorentz oscillator equation

Lorentz oscillator equation	
# of free parameters	4
for $\varepsilon_{2:}$	3 [A, E_0, Γ]
for $\varepsilon_{1:}$	1 [$\varepsilon_1(\infty)$]
Primary applications:	Metals and other absorbing materials

5.3.4 Drude

The Drude model [15] is a classical kinetic model of conductivity (1/resistivity) that was developed by Drude and Sommerfeld in the late 1800's. It describes the interaction of time-varying electric fields with *free carriers*—electrons or "holes" [15]—which move freely in conductive materials.

The form of the Drude oscillator is that of a Lorentz oscillator (5.17) with zero center energy (no restoring force):

$$\varepsilon(E) = \varepsilon_1(E) - i\varepsilon_2(E) = \varepsilon_1(\infty) - \frac{A}{E^2 - i\Gamma E} \tag{5.21}$$

where the quantity $\varepsilon_1(\infty)$ is the high-frequency dielectric constant and the two free parameters are amplitude, A, and broadening, Γ. Interestingly, the Drude equation can also be written such that the free parameters are the optical resistivity ρ_{opt} (units are Ω-cm), and the mean scattering time τ (units are seconds) [16]:

$$\varepsilon(E) = \varepsilon_1(E) - i\varepsilon_2(E) = \varepsilon_1(\infty) - \frac{\hbar^2}{\varepsilon_0 \rho_{opt}(\tau \cdot E^2 - i\hbar E)} \tag{5.22}$$

where $\hbar$ is the reduced Plank's constant (~6.582 × 10^{-16} eV · s) and ε_0 is the vacuum dielectric constant (~8.854 × 10^{-14} s/Ω-cm). Related parameters of interest include the carrier effective mass m*, the optical carrier concentration N_{opt}, and the optical carrier mobility μ_{opt}, which are related to optical resistivity by:

$$\rho_{opt} = \frac{m^*}{N_{opt} q^2 \tau} = \frac{1}{q \mu_{opt} N_{opt}} \tag{5.23}$$

where q is the single electron charge equal to 1.6 × 10^{-19} C.

Regardless which equation is chose, the Drude has two free parameters to describe a shape with increasing absorption toward lower frequencies (lower E, longer λ) as shown in Fig. 5.11. The primary application of the Drude oscillator is to describe the free-carrier absorption prevalent in metals, heavily-doped semiconductors, and transparent conductive oxides. Table 5.4 provides an overview of the Drude oscillator equation. For a material such as indium tin oxide (ITO), it is common to use the Drude oscillator to describe the free-carrier absorption and then

Table 5.4 Details of the Drude oscillator equation

Drude equation	
# of free parameters	3
for ε_2:	2 [A, Γ] or [ρ_{opt}, τ] or [N_{opt}, μ_{opt}]
for ε_1:	1 [$\varepsilon_1(\infty)$]
Primary applications:	Metals, heavily-doped semiconductors, and transparent conductive oxides (TCOs)

supplement the short-wavelength shape with Tauc-Lorentz or Gaussian equations to describe the effects of electronic transitions. We describe these additional dispersion equations next.

5.3.5 Harmonic Oscillator Approximation

The classic Harmonic oscillator model is very similar to the Lorentz oscillator, but is derived from quantum mechanical perturbation theory:

$$\varepsilon(E) = \varepsilon_1(E) - i\varepsilon_2(E) = 1 + \frac{A}{E + E_0 - i\gamma} - \frac{A}{E - E_0 - i\gamma} \tag{5.24}$$

which can be rearranged as:

$$\varepsilon(E) = \varepsilon_1(E) - i\varepsilon_2(E) = 1 + \frac{2AE_0}{E_0^2 - E^2 + i2\gamma E + \gamma^2} \tag{5.25}$$

If we substitute $\Gamma = 2\gamma$ and then multiply the numerator by Γ, we can rewrite the Harmonic oscillator as:

$$\varepsilon(E) = \varepsilon_1(E) - i\varepsilon_2(E) = \varepsilon_1(\infty) + \frac{A\Gamma E_0}{E_0^2 - E^2 + i\Gamma E + \frac{1}{4}\Gamma^2} \tag{5.26}$$

such that amplitude, A, is approximately the peak of ε_2 at the resonant energy and Γ is approximately the FWHM value found with the Lorentz oscillator. Equation (5.26) is nearly identical to the corresponding Lorentz oscillator of (5.18), except for the $\frac{1}{4}\Gamma^2$ term in the denominator. Interestingly, the energy position for the ε_2 peak of the Harmonic oscillator is less sensitive to the broadening term and shifts slightly to higher photon energies rather than to lower photon energies like with the Lorentz oscillator behavior.

The Lorentz and Harmonic oscillator shapes are compared in Fig. 5.12. The two oscillators appear different if the same parameters are used for A, E_0, and Γ. However, this is a result of the $\frac{1}{4}\Gamma^2$ term in the denominator. A simple adjustment

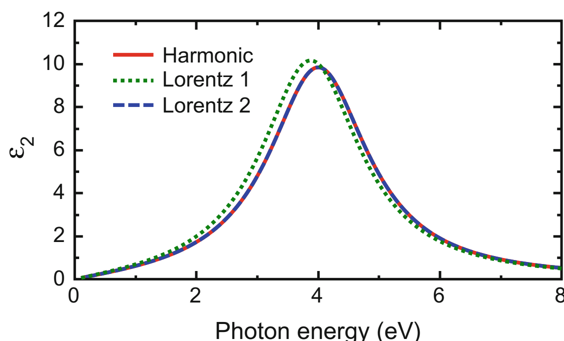

Fig. 5.12 Comparison of a harmonic oscillator [(5.25): A = 10 eV, E_0 = 4 eV, Γ = 2 eV] with two Lorentz oscillators (5.17). The first Lorentz has the same parameter values as the harmonic and it has a noticeable peak shift to lower photon energies with increased amplitude. The second Lorentz has parameters (A = 9.7014 eV, E_0 = 4.1231 eV, Γ = 2 eV) adjusted to match the harmonic shape

of Lorentz oscillator parameters, $E_{0-\mathrm{Lor}} = \sqrt{E_{0-\mathrm{Har}}^2 + \frac{1}{4}\Gamma^2}$ and $A_{\mathrm{Lor}} = A_{\mathrm{Har}} \cdot E_{0-\mathrm{Har}} / \sqrt{E_{0-\mathrm{Har}}^2 + \frac{1}{4}\Gamma^2}$, allows the Lorentz to perfectly match the Harmonic. Thus, when fitting measured SE data, the Harmonic and Lorentz oscillators can produce equivalent shapes and can be used interchangeably; however, the center energies and amplitudes will generally be different.

Based on its origin, the harmonic oscillator is often used to describe semiconductor electronic transitions. While the shape can adequately describe the absorption very close to a critical point energy, it requires many extra oscillators that have no intrinsic physical meaning in order to match the background spectral dispersion effectively. If the data extend below the bandgap of the material, the Harmonic oscillator will extend too much beyond the transparent region to be effective. For this reason, the Harmonic oscillator is reserved for absorbing materials and relegated to the same applications of the Lorentz oscillator. Table 5.5 provides an overview of the Harmonic oscillator equation. In the following sections, we describe dispersion equations which can be used with both an absorbing and a transparent region (Gaussian, Tauc-Lorentz, and Cody-Lorentz).

Table 5.5 Details for the harmonic oscillator equation

Harmonic oscillator equation	
# of free parameters	4
for $\varepsilon_{2:}$	3 [A, E_0, Γ]
for $\varepsilon_{1:}$	1 [$\varepsilon_1(\infty)$]
Primary applications:	Metals and other absorbing materials

5.3.6 Gaussian

The main drawback of the Lorentz and Harmonic oscillators is the long ε_2 tail outside of the central absorption spectrum defined as the following region surrounding the center energy:

$$E-\frac{\Gamma}{2}<E_0<E+\frac{\Gamma}{2} \tag{5.27}$$

This often leads to unwanted absorption extending into spectral regions where the material should be transparent. One alternative is to replace the Lorentz shape with a Gaussian line shape to describe ε_2 as [17, 18]:

$$\varepsilon_2(E)=Ae^{-\left(\frac{E-E_0}{\sigma}\right)^2}-Ae^{-\left(\frac{E+E_0}{\sigma}\right)^2} \tag{5.28}$$

where our free parameters are amplitude A, center energy E_0, and broadening σ. We can modify the equation with

$$\sigma=\frac{\Gamma}{2\sqrt{\ln(2)}} \tag{5.29}$$

to define the broadening, Γ, with respect to the FWHM value and approximate the region of anomalous dispersion per (5.27). The form of (5.28) defines a Gaussian at both positive and negative frequencies to maintain the odd symmetry for ε_2, as required by Kramers-Kronig criteria [specifically (5.30b)]:

$$\varepsilon_1(-E)=\varepsilon_1(E) \tag{5.30a}$$

and

$$\varepsilon_2(-E)=-\varepsilon_2(E) \tag{5.30b}$$

such that the real part, ε_1, can be effectively calculated from the Kramers-Kronig relation (5.5a).

Just like the Lorentz, there are three free parameters to describe the ε_2 absorption shape: amplitude A, broadening Γ, and center energy E_0. Figure 5.13 compares the dielectric functions of a Gaussian to a Lorentz oscillator. The ε_2 for the Gaussian oscillator approaches zero much more rapidly than the Lorentz outside the central absorption region. The absorption shapes for both Lorentz and Gaussian remain roughly symmetric about the resonant condition.

In real materials, the absorption is seldom this symmetric and contributions from more than one absorption phenomena require combination of more than one Lorentz or Gaussian to match the material's optical functions. It is very common to use

Fig. 5.13 Shape of Gaussian with parameters, possible with Lorentz for comparison

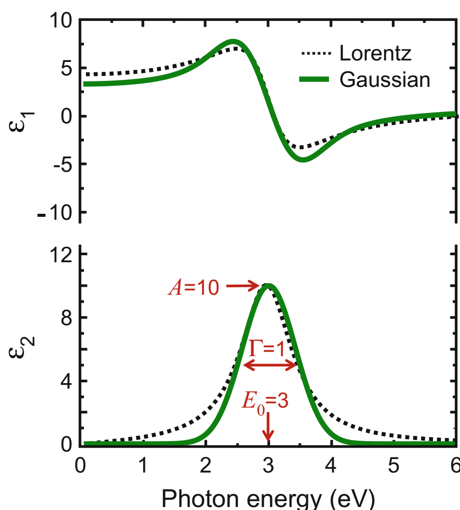

Fig. 5.14 The ε_2 spectra for an organic photoresist composed of seven individual Gaussian oscillators

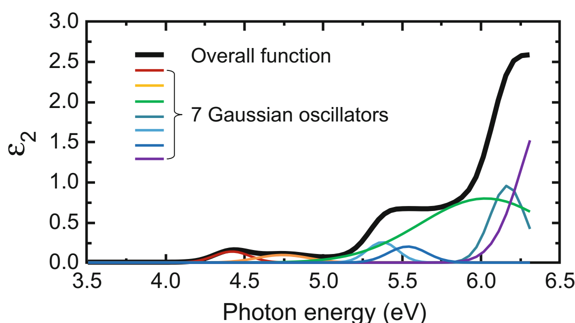

several Gaussian oscillators to describe the dielectric function of organic films. For example, the ε_2 spectrum for an organic photoresist material is shown in Fig. 5.14. The overall ε_2 function results from the summation of seven individual Gaussian oscillators, which are also shown. Another common application of Gaussian oscillators is to supplement other dispersion functions when describing the electronic transitions of dielectrics and semiconductors. Table 5.6 provides an overview of the Gaussian oscillator equation.

Table 5.6 Quick details for the Gaussian oscillator equation

Gaussian oscillator equation	
# of free parameters	4
for ε_{2}:	3 [A, E_0, Γ]
for ε_{1}:	1 [$\varepsilon_1(\infty)$]
Primary applications:	Organics, dielectrics, and semiconductors

5.3.7 Tauc-Lorentz

The Tauc-Lorentz model was developed by Jellison and Modine [19] to provide a dispersion equation which only absorbs light above the material bandgap. It models the dielectric function of many amorphous materials particularly well. Close to the band edge, the absorption of the Tauc-Lorentz equation follows a Tauc law formula:

$$\varepsilon_2(E) \propto \frac{\left(E - E_g\right)^2}{E^2} \tag{5.31}$$

The absorption from the Tauc-Lorentz is separated into two regions:

$$\varepsilon_2(E) = \frac{AE_0C\left(E - E_g\right)^2}{\left(E^2 - E_0^2\right)^2 + C^2E^2} \cdot \frac{1}{E} \quad E > E_g \tag{5.32a}$$

$$\varepsilon_2(E) = 0 \quad E \le E_g \tag{5.32b}$$

Using the KK integral [(5.5a), but repeated here for convenience]:

$$\varepsilon_1(E) = \varepsilon_1(\infty) + \frac{2}{\pi} P \int_{E_g}^{\infty} \frac{E' \varepsilon_2(E')}{E'^2 - E^2} \mathrm{d}E' \tag{5.33}$$

where the integration need consider only energies above the bandgap, as $\varepsilon_2 = 0$ for energies less than E_g. Jellison and Modine provide the closed form solution for ε_1 [19, *specifically the erratum*]:

$$\begin{aligned} \varepsilon_1(E) = \varepsilon_1(\infty) &+ \frac{A\,C}{\pi\,\zeta^4} \cdot \frac{a_{\ln}}{2\alpha\,E_0} \ln\left(\frac{E_0^2 + E_g^2 + \alpha\,E_g}{E_0^2 + E_g^2 - \alpha\,E_g}\right) - \frac{A}{\pi\zeta^4} \cdot \frac{a_{\mathrm{atan}}}{E_0}\left[\pi - \mathrm{atan}\left(\frac{2E_g + \alpha}{C}\right) + \mathrm{atan}\left(\frac{-2E_g + \alpha}{C}\right)\right] \\ &+ 2\frac{A\,E_0}{\pi\,\zeta^4\,\alpha} E_g(E^2 - \gamma^2)\left[\pi + 2\,\mathrm{atan}\left(2\frac{\gamma^2 - E_g^2}{\alpha\,C}\right)\right] - \frac{A\,E_0\,C}{\pi\,\zeta^4} \cdot \frac{E^2 + E_g^2}{E} \ln\left(\frac{\left|E - E_g\right|}{E + E_g}\right) \\ &+ 2\frac{A\,E_0\,C}{\pi\,\zeta^4} E_g \ln\left(\frac{\left|E - E_g\right| \cdot \left(E + E_g\right)}{\sqrt{\left(E_0^2 - E_g^2\right)^2 + E_g^2C^2}}\right) \end{aligned} \tag{5.34}$$

with

$$a_{\ln} = \left(E_g^2 - E_0^2\right)E^2 + E_g^2C^2 - E_0^2\left(E_0^2 + 3E_g^2\right) \tag{5.35a}$$

$$a_{\text{atan}} = \left(E^2 - E_0^2\right)\left(E_0^2 + E_g^2\right) + E_g^2 C^2 \tag{5.35b}$$

$$\zeta^4 = \left(E^2 - \gamma^2\right)^2 + \frac{\alpha^2 C^2}{4} \tag{5.35c}$$

$$\alpha = \sqrt{4E_0^2 - C^2} \tag{5.35d}$$

$$\gamma = \sqrt{E_0^2 - \frac{C^2}{2}} \tag{5.35e}$$

While these equations are quite intimidating, a close inspection shows that only five free parameters describe the dielectric function: amplitude A, resonant energy E_0, broadening C, bandgap energy E_g, and $\varepsilon_1(\infty)$. Unlike the Lorentz, Harmonic, and Gaussian, the Tauc-Lorentz produces a more asymmetric ε_2 shape. A Tauc-Lorentz with optical functions matching those of an amorphous silicon film is shown in Fig. 5.15 with $A = 124$, $E_0 = 3.44$ eV, $C = 2.52$ eV and $E_g = 1.2$ eV. Looking closely at the Tauc-Lorentz shape, the energy where ε_2 reaches a peak will shift to values above E_0 as the broadening increases.

The Tauc-Lorentz provides a more realistic representation of real-world materials and is widely used to describe many amorphous dielectrics and semiconductors. Most importantly, it remains transparent below the bandgap of the material. Table 5.7 provides an overview of the Tauc-Lorentz equation.

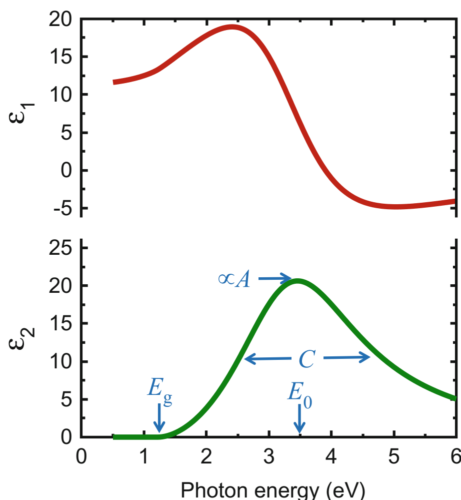

Fig. 5.15 Tauc-Lorentz with parameters matched to the shape of the optical functions for a-Si:H

Table 5.7 Details of the Tauc-Lorentz equation

Tauc-Lorentz equation	
# of free parameters	5
for $\varepsilon_{2:}$	4 $[A, E_0, C, E_g]$
for $\varepsilon_{1:}$	1 $[\varepsilon_1(\infty)]$
Primary applications:	Amorphous semiconductors and dielectrics

5.3.8 Cody-Lorentz

The Cody-Lorentz function, developed by Ferlauto et al. [20] was designed to model amorphous materials, just like the Tauc-Lorentz. It is similar to the Tauc-Lorentz in that it defines the bandgap energy E_g and a Lorentzian absorption peak (parameters A, E_0, and Γ). However, the two models behave differently in the absorption-onset at photon energies slightly greater than E_g. In that region, the Tauc-Lorentz follows a Tauc law formula (5.31) while the Cody-Lorentz assumes:

$$\varepsilon_2(E) \propto (E - E_g)^2 \tag{5.36}$$

The Cody-Lorentz also includes an Urbach absorption term for the small absorptions that may occur below the bandgap. The ε_2 portion of the Cody-Lorentz oscillator model is separated into two energy regions and given as:

$$\varepsilon_2(E) = \frac{E_1}{E}\exp\left(\frac{E - E_t}{E_u}\right) \quad 0 < E \le E_t \tag{5.37a}$$

$$\varepsilon_2(E) = G(E)L(E) = \left[\frac{(E - E_g)^2}{(E - E_g)^2 + E_p^2}\right]\left[\frac{AE_0\Gamma E}{(E^2 - E_0^2)^2 + \Gamma^2 E^2}\right] \quad E > E_t \tag{5.37b}$$

where

$$E_1 = E_t G(E_t) L(E_t) \tag{5.37c}$$

The KK integration must now be split into multiple terms to cover integration of the Urbach and the Lorentz contributions as:

$$\varepsilon_1(E) = \varepsilon_1(\infty) + \frac{2E_1}{\pi} P \int_0^{E_t} \frac{\exp\left[(E' - E_t)/E_u\right]}{E'^2 - E^2} dE' + \frac{2}{\pi} P \int_{E_t}^{\infty} \frac{E' G(E') L(E')}{E'^2 - E^2} dE' \tag{5.38}$$

In the equation above, E_t is the separation between the Urbach tail transitions and the band-to-band transitions. In the above equations, Ferlauto defines E_t as an absolute energy. In commercial software (WVASE®, for example), E_t is defined as an offset from the bandgap energy:

$$E_t = E_t^{\mathrm{Ferlauto}} - E_g \tag{5.39}$$

The G(E) and L(E) functions define the Cody absorption behavior and the Lorentz oscillator function, respectively. The parameter E_p allows the user to define the energy, $E_g + E_p$, where the function transitions from a Cody absorption behavior (5.36) to the Lorentzian absorption.

Unlike the *Cauchy* model, this Urbach absorption tail is fully Kramer-Kronig consistent—that is, the exponential Urbach absorption in $\varepsilon_2(E)$ has a Kramers-Kronig transformed counterpart in $\varepsilon_1(E)$. The internal parameter E_1 guarantees that the ε_2 function transitions smoothly at E_t. The quantity E_1/E guarantees that the Urbach exponential function exactly matches $G(E)L(E)$ at E_t. The quantity E_u defines the exponential rate of decay; specifically where the Urbach absorption equal e^{-1} of its maximum value of E_1/E.

In the absence of the Urbach absorption tail, the Cody-Lorentz shape is very similar to the Tauc-Lorentz, with slight difference in how the absorption increases near the bandgap. The primary Cody-Lorentz parameters of interest become A, E_0, C, E_g, and E_p. This leads to slightly improved fits to amorphous semiconductor data with only a single extra parameter compared to the Tauc-Lorentz.

Standard SE measurements are generally insensitive to the low absorption values described by the Urbach tail (see log-scale plot of Fig. 5.16). Thus, it is most practical to use the Cody-Lorentz without the Urbach absorption. To set $\varepsilon_2 = 0$ below the bandgap, Ferlauto's E_t parameter should equal E_g and $E_1 = 0$ (accomplished with $E_u \rightarrow 0$). In (5.39), this can be accomplished by setting $E_t = 0$. In either case, the seven parameters describing ε_2 are now reduced to the common five parameters we listed in the previous paragraph. Table 5.8 provides an overview of the Cody-Lorentz equation.

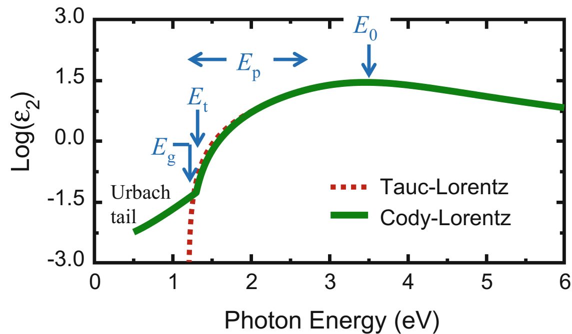

Fig. 5.16 Shape of Cody-Lorentz with parameters

Table 5.8 Details of the Cody-Lorentz equation

Cody-Lorentz equation	
# of free parameters	8 or 6*
for ε_2:	7* [A, E_0, C, E_g, E_p, E_t, E_u] *most often used without Urbach tail: 5 [A, E_0, C, E_g, E_p]
for ε_1:	1 [$\varepsilon_1(\infty)$]
Primary applications:	Amorphous semiconductors and dielectrics

5.3.9 Critical Point Models

For crystalline or polycrystalline semiconductors, the dielectric function can have a very complex shape, especially in the spectral region near critical points [3, 6]. A few models have been developed to describe these specific shapes, including the critical point parabolic band (CPPB), those of Adachi, and the parametric semiconductor (PSEMI) functions.

The CPPB function [21–24] models the shape of the dielectric function near critical points using five parameters: amplitude A, phase projection factor θ, threshold energy E_g, broadening parameter Γ, and exponent n:

$$\varepsilon(E) = \varepsilon_1(E) + i\varepsilon_2(E) = C - Ae^{i\theta}(E - E_g + i\Gamma)^n \quad \text{for } n = \pm\frac{1}{2} \tag{5.40a}$$

$$\varepsilon(E) = \varepsilon_1(E) + i\varepsilon_2(E) = C - Ae^{i\theta}\ln(E - E_g + i\Gamma) \quad \text{for } n = 0 \tag{5.40b}$$

where the exponent n has three discrete values: −½, 0, or +½ for one dimensional (1-D), two dimensional (2-D) and three dimensional (3-D) critical points, respectively. Discrete excitons with a Lorentzian line-shape are represented by $n = -1$. Equation (5.40a) can be rewritten to resemble the form of a Lorentz oscillator, with $\mu = -n$, and some rescaling of Γ and A as:

$$\varepsilon(E) = \varepsilon_1(E) + i\varepsilon_2(E) = \varepsilon_1(\infty) + Ae^{i\theta}\left(\frac{\Gamma}{2E_g - 2E - i\Gamma}\right)^{\mu} \quad \text{for } \mu \neq 0 \tag{5.41a}$$

The CPPB functions are not very useful for fitting SE spectra directly, as the functions produce unphysical shapes with negative ε_2 occurring at some photon energies. They were developed to fit derivative or modulation spectra, in which case they can be successfully applied to locate the critical point features in semiconductors. Table 5.9 provides an overview of the CPPB functions.

Adachi [25, 26] developed four functions that describe the dielectric functions at semiconductor critical points, which he refers to as Model Dielectric Functions (MDFs). The different functions refer to the type of 3-D critical point based on the joint density of states near the corresponding electronic transition [3, 6]:

Table 5.9 Details of the critical point parabolic band functions

CPPB equations	
# of free parameters	6
for $\varepsilon_{2:}$	5 [A, E_g, Γ, θ, n]
for $\varepsilon_{1:}$	1 [$\varepsilon_1(\infty)$]
Primary applications:	Used to fit derivative spectra of crystalline semiconductors

$$\varepsilon_{CPM0} = \varepsilon_1(E) + i\varepsilon_2(E) = \frac{A}{E_0^{1.5}\chi'^2} \cdot \left[2 - \sqrt{1+\chi'} - \sqrt{1-\chi'}\right] \tag{5.42a}$$

$$\varepsilon_{CPM1} = \varepsilon_1(E) + i\varepsilon_2(E) = \frac{-A}{\chi'^2} \cdot \ln\left[1 - \chi'^2\right] \tag{5.42b}$$

$$\varepsilon_{CPM2} = \varepsilon_1(E) + i\varepsilon_2(E) = \frac{-A}{\chi''^2} \cdot \ln\left[1 - \chi''^2\right] \tag{5.42c}$$

$$\varepsilon_{CPM3} = \varepsilon_1(E) + i\varepsilon_2(E) = \frac{A}{E_0^{1.5}\chi''^2} \cdot \left[2 - \sqrt{1+\chi''} - \sqrt{1-\chi''}\right] \tag{5.42d}$$

where

$$\chi' = (E + i\Gamma)/E_0 \tag{5.43a}$$

and

$$\chi'' = (E_0 - E + i\Gamma)/E_0 \tag{5.43b}$$

Again, it is possible to produce unphysical shapes with these oscillators and their primary applications are either modeling dielectric functions near the critical point energies, or fitting derivative spectra. See Schubert et al. [27] for an example of their use. Table 5.10 provides an overview of the Adachi equations.

Herzinger and Johs developed the parametric semiconductor (PSEMI) model, also referred to as the Gaussian-Broadened Polynomial Superposition (GBPS) parametric dispersion model, as a highly-flexible functional shape with KK

Table 5.10 Details of the Adachi equations

Adachi equations	
# of free parameters	4
for $\varepsilon_{2:}$	3 [A, E_0, Γ]
for $\varepsilon_{1:}$	1 [$\varepsilon_1(\infty)$]
Primary applications:	Crystalline semiconductors and fitting derivative spectra

consistent properties to describe semiconductor critical points [3, 28–31]. While extremely flexible, it is also very complicated with up to 12 variable parameters to describe each critical point. The mathematical details are beyond the scope of this chapter, but can be found in the references listed. The primary advantage of this model is that it allows precise control of the ε_2 absorption shape. Figure 5.17 shows one example shape for a single PSEMI oscillator. It is based on the connection of four Gaussian broadened polynomials—two above the center energy E_c and two below—shown as F_I, F_{II}, F_{III}, and F_{IV}. There are five controllable energies; the critical point energy E_c, the minimum (left) and maximum (right) energies, E_L and E_R, and relative mid-point energies on the left and right sides, E_{ML} and E_{MR}. The E_L and E_R positions define where absorption begins and ends on the left and right sides of the oscillator, respectively. The E_{ML} and E_{MR} define the mid-points where two outer polynomials connect to the two inner polynomials. As shown in the figure, E_{ML} and E_{MR} are defined by their relative position between the min/max energies and the center energy. Thus, $E_{MR} = 0.8$ is at an energy position 80% of the distance from E_R toward E_c. The mid-point connections of polynomials is further controlled by relative amplitudes A_{ML} and A_{MR} and coefficients for the 2nd order terms in the polynomials, O_{2L} and O_{2R}. Finally, there is even the possibility of a discontinuity, *Disc*, between the left and right polynomials, positioned at the center energy. The values shown in Fig. 5.17 are for a PSEMI oscillator representing the E_1 critical point of a semiconductor.

The wide variety of PSEMI oscillator shapes is demonstrated in Fig. 5.18 where six different functions are summed to describe the ε_2 shape for CdTe. Each PSEMI oscillator maintains Kramers-Kronig consistency and ε_1 is calculated via (5.5a). The Gaussian broadened line shapes allow each oscillator to go to zero at E_L and E_R, which is a key advantage when describing materials close to their bandgap. In fact, the PSEMI is especially useful for describing the onset of absorption in direct bandgap materials, as demonstrated with "PSEMI1" in Fig. 5.18. Some of the key advantages for the PSEMI are that ε_2 remains positive and can go to zero to maintain a transparent region.

Because it is a highly flexible curve, the PSEMI is generally not a unique model. The final parameter values depend upon how the various oscillators are initially

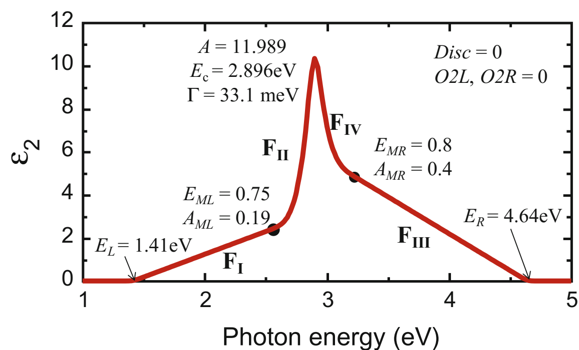

Fig. 5.17 PSEMI oscillator representing the E_1 critical point. F_I, F_{II}, F_{III}, and F_{IV} are the four polynomials connected at the two mid-point energies as well as the center energy

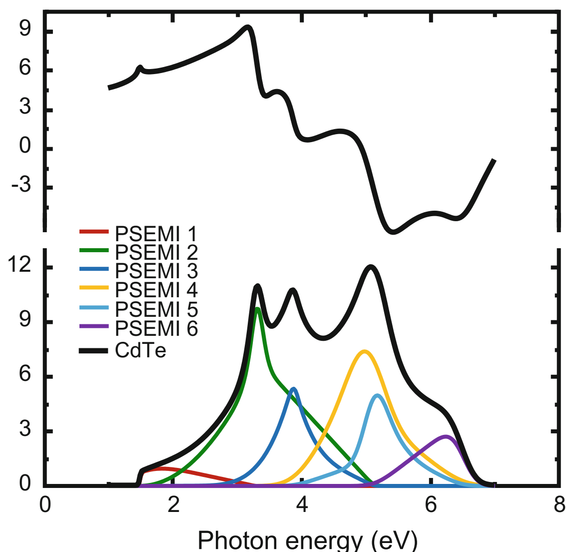

Fig. 5.18 Example Material using PSEMI for direct-bandgap material (CdTe)

configured, which means that more than one PSEMI model can produce essentially the same dielectric function and equally good fits to the data, even though they have different parameters. For this reason, one should be cautious when comparing PSEMI parameters from one model to another.

The PSEMI model's primary contribution to the understanding of the physical properties of a material is in the optical constants it generates, not the internal parameters that define the model. The PSEMI parameter values have no direct physical relationship to critical point parameters, such as energy and broadening, that one might obtain from a derivative or other type of analysis. However, the optical function generated by the PSEMI model can be subjected to a derivative analysis. Figure 5.19 shows the seven PSEMI oscillators representing the critical points of GaAs.

The primary drawback of this model is its complexity; its effective use generally requires some study and practice. Also, its parameters can be strongly correlated to other parameters within the same model. These difficulties can be overcome, and for certain situations this model is worth the time and effort. It is especially helpful for direct bandgap materials, such as CdTe, as shown in Fig. 5.18, where each individual PSEMI function is shown along with the final dielectric functions produced by the sum of six functions. Table 5.11 provides an overview of the PSEMI equations.

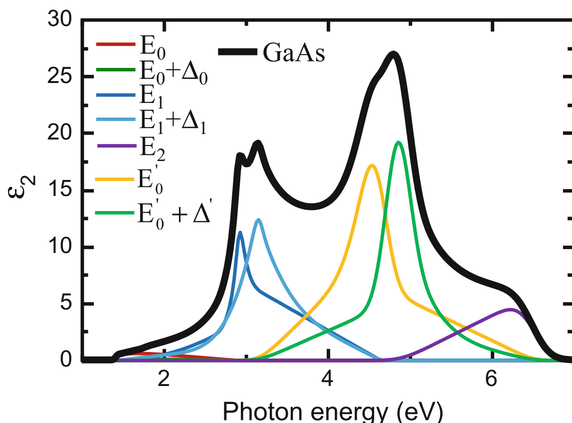

Fig. 5.19 GaAs ε_2 showing contributions of all 7 PSEMI oscillators, representing the 7 critical points

Table 5.11 Details of the parametric semiconductor equations

PSEMI equation	
# of free parameters	13
for $\varepsilon_{2:}$	12 [A, E_c, Γ, E_L, E_R, E_{ML}, E_{MR}, A_{ML}, A_{MR}, O_{2L}, O_{2R}, and Disc]
for $\varepsilon_{1:}$	1 [$\varepsilon_1(\infty)$]
Primary applications:	Crystalline semiconductors

5.3.10 Polynomials, Splines and B-Spline

Often, we wish to match our experimental SE data to accurately determine the optical functions of our material, but we are not sure which type of dispersion equation is suitable. We could adopt a direct fit, where the optical constants are independently varied at each wavelength to best match the measured SE data. However, this is highly inefficient and may produce noisy or even physically implausible results. For this reason, we prefer to choose a dispersion equation. If we are not concerned with the underlying physical phenomena that produced the optical functions, we could choose *any* equation with the ability to describe a smooth spectral curve such that a few "free" parameters adjust the shape to describe the optical functions. One such equation is a polynomial, which is shown to degree m as:

$$p_m(x) = a_m x^m + a_{m-1} x^{m-1} + \cdots + a_1 x + a_0 \tag{5.44}$$

where the a values are the real coefficients of the polynomial. The degree of the polynomial is associated with the highest power of x, with common lower degrees

such as 1, 2, 3 and 4 corresponding with linear, quadratic, cubic, and quartic equations, respectively. We can rewrite (5.44) for use with spectroscopic ellipsometry versus wavelength:

$$p_m(\lambda) = a_m\lambda^m + a_{m-1}\lambda^{m-1} + \cdots + a_1\lambda + a_0 \tag{5.45}$$

or versus photon energy:

$$p_m(E) = a_m E^m + a_{m-1} E^{m-1} + \cdots + a_1 E + a_0 \tag{5.46}$$

In each of these equations, the function p could stand for any of the optical functions that we wish to describe: n, k, ε_1, or ε_2. In fact, for an absorbing material, we may need to use two separate equations, one for the real function and one for the imaginary function. As an example, the Cauchy dispersion relationship of (5.14a) can be written in terms of energy as a quartic polynomial:

$$n(E) = A + B\left(\frac{E}{1.24}\right)^2 + C\left(\frac{E}{1.24}\right)^4 \tag{5.47}$$

While polynomials work well for the transparent region which exhibits normal dispersion, it is more difficult to describe the anomalous dispersion without using polynomials of a much higher degree. A more flexible solution is the use of a spline function. The spline divides the total wavelength range into intervals with a simple function, such as a polynomial, described over each interval. With the spline, the interval size can be increased or decreased depending on the variation required over each spectral range. Splines offer the advantage of combining polynomials over regions of energy or wavelength in a piecewise continuous manner. When combining at each end-point, we wish the curves to remain continuous, which places limits on the end-points of each function. In fact, we typically desire more than just continuity from one function to the next. The type of spline is designated by the degree of the polynomials used within each function. Given a function consisting of a spline of degree k, we can enforce continuity not only on the function but also on its derivatives, up to $k - 1$. Thus, the lower order splines are not very useful for optical functions because we can't make their derivatives continuous at the joining points.

The most commonly encountered spline is cubic (polynomial degree = 3) because this allows continuity of the function, its slope (1st derivative), and its curvature (2nd derivative). The interval of each polynomial is delineated by "knots", which are the positions, t, along the wavelength or energy axis. The knot positions can be equally spaced or can have varied spacing, as shown in Fig. 5.20.

The basis-spline (b-spline) offers an interesting alternative for describing the optical functions of a material [32]. Rather than joining curves that are described for each segment, the b-spline sums individual basis functions to construct the final curve. An example basis function is shown in Fig. 5.21. Each individual basis

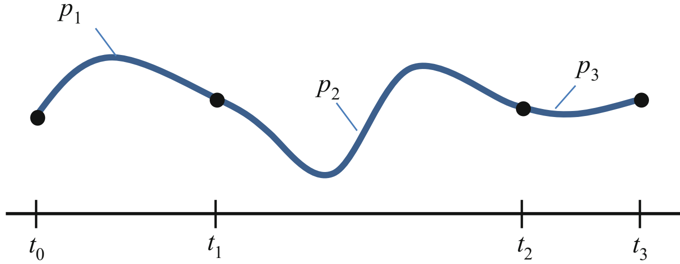

Fig. 5.20 Spline consisting of three polynomials (p) varying between knot positions (t) connected to maintain a smooth, continuous curve

Fig. 5.21 A single 3rd degree basis function shows the four polynomial sections used to create a single shape, with the overall amplitude controlled by the coefficient of the basis function

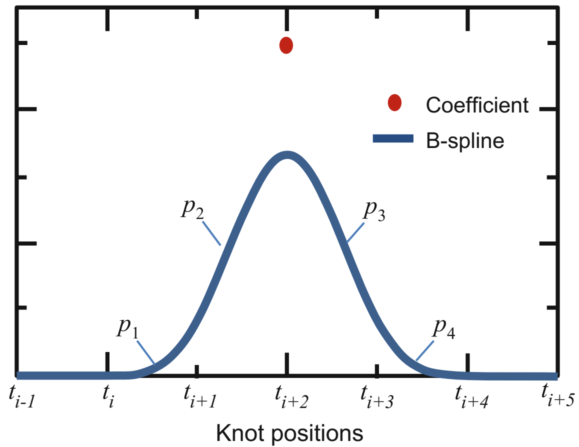

function is constructed from multiple polynomials; in this case four polynomials are required to describe the 3rd degree basis function.

The basis function can be written in recursive form as:

$$B_i^0(x) = \begin{cases} 1 & t_i \le x < t_{i+1} \\ 0 & \text{otherwise} \end{cases} \tag{5.48a}$$

$$B_i^k(x) = \left(\frac{x - t_i}{t_{i+k} - t_i}\right) B_i^{k-1}(x) + \left(\frac{t_{i+k+1} - x}{t_{i+k+1} - t_{i+1}}\right) B_{i+1}^{k-1}(x) \tag{5.48b}$$

where "k" is the degree of the b-spline. These equations describe a single basis function. However, multiple basis functions, or "spline components" are summed to describe the overall shape of our basis-spline function, with coefficients, c, to adjust each spline components amplitude:

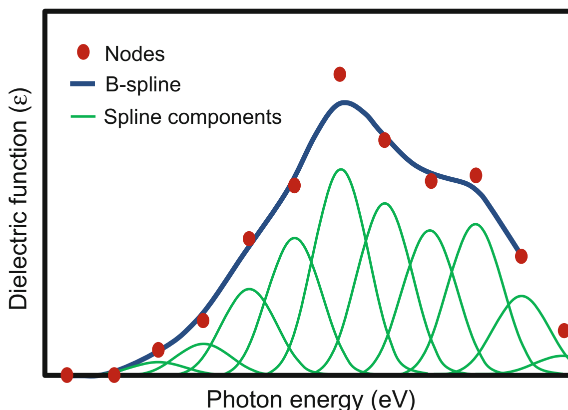

Fig. 5.22 Example of a b-spline curve to describe the dielectric function of a material with a summation of basis functions, each controlled by their node amplitude

$$S(x) = \sum_{i=1}^{n} c_i B_i^k(x) \tag{5.49}$$

Figure 5.22 shows the individual spline components summed together to form the basis-spline curve describing ε_2 of a material. Each basis function maintains its specific shape and is controlled by an associated coefficient, shown here as the nodes. The final function does not have to go through each node, but the node amplitude (amplitude of the spline coefficient) adjusts the general shape of the curve in a local region. The spacing between nodes (which also adjusts the corresponding "knot" spacing) can be reduced to increase control over the shape of the final b-spline curve. This introduces more "free" parameters, which are the individual coefficients or node values for each basis function. In this manner, the b-spline can be optimized by increasing or decreasing the node spacing based on the variability of the optical function it is being used to describe.

Dielectric functions are usually represented by a 3rd order recursive basis polynomial function [32]. The 3rd order b-spline curves have many desirable properties [33] for modeling dielectric functions:

- The function and its 1st and 2nd order derivatives are smooth and continuous.
- Each basis function affects only the "local" shape of the curve. For example, changing a node amplitude in the UV does not affect the curve in the NIR.
- B-spline curves exhibit a "convex hull" property, where the summed function can't exceed the highest or lowest node amplitude. This allows the b-spline to remain non-negative as long as all spline coefficients (nodes) are ≥ 0, thus avoiding non-physical negative ε_2 values. This is demonstrated in Fig. 5.23.
- Since the basis functions depend only on the node positions, the node amplitudes which define the resulting curve are linearly independent, which greatly increases computation efficiency.

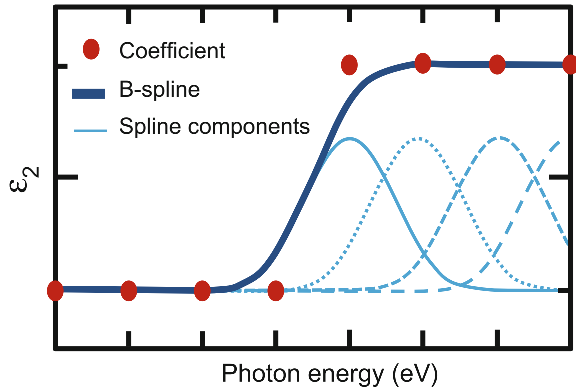

Fig. 5.23 Example b-spline showing the convex hull property where the final b-spline summation does not exceed the lower or upper node coefficient values. This is especially useful when describing the ε_2 curve such that it will not go to negative values

- The KK integral can be applied to the b-spline recursion formula to generate KK consistent basis functions. In other words, the ε_1 curve can be defined by the KK transform of ε_2.

When applying b-splines to the optical functions of materials, there are generally two options:

- The first option is to generate separate b-spline curves for the real and imaginary components, as shown in Fig. 5.24 for an organic material. The total number of free parameters is slightly more than twice the number of node positions. Here, the number of free parameters is tied to the total number of nodes and efficient minimization of "free" parameters is achieved by optimizing the node spacing—even allowing different spacing for different spectral regions.
- The second option is to use a single b-spline to describe the imaginary function, and then calculate the real function using the KK integral. This significantly reduces the number of free parameters, as only one of the curves has free parameters at every node. In this latter case, care must be taken with any b-spline nodes that are located outside the investigated spectral range, as these

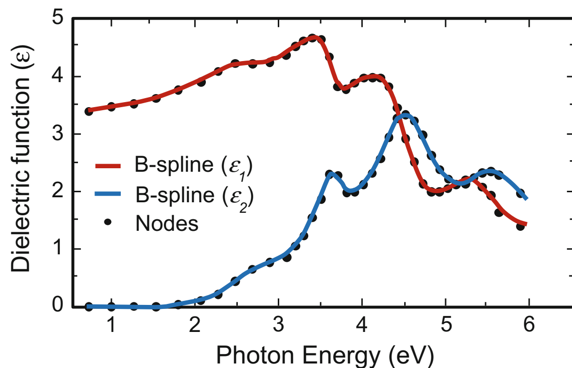

Fig. 5.24 Example of b-spline for organic material, where separate b-spline curves are used to describe ε_1 and ε_2

Table 5.12 Details of the basis-spline functions

B-spline	
# of free parameters	~2 × number of nodes (non KK) ~1 × number of nodes (KK)
for $\varepsilon_{2:}$	~1 × number of nodes
for $\varepsilon_{1:}$	~1 × number of nodes (non KK) 1–3 (KK)
Primary applications:	Organics, dielectrics, semiconductors, and metals

will also affect the KK integration. An offset and "poles" may be added to correct for absorption features outside the investigated spectral range. For materials with a transparent region, it is also very efficient to enforce this transparency by setting the nodes for ε_2 equal to zero over transparent spectral region. Table 5.12 provides an overview of the b-spline functions.

References

1. H. Fujiwara, *Spectroscopic Ellipsometry: Principles and Applications* (Wiley, West Sussex, UK, 2007), pp. 347–348
2. J.D. Jackson, *Classical Electrodynamics*, 3rd edn. (Wiley, New York, 1999)
3. R.W. Collins, A.S. Ferlauto, in *Handbook of Ellipsometry*, ed. by H.G. Tompkins, E.A. Irene (William Andrew, New York, 2005). pp. 93–235, Chap. "Optical Physics of Materials"
4. H. Fujiwara, *Spectroscopic Ellipsometry: Principles and Applications* (Wiley, West Sussex, UK, 2007), pp. 357–360
5. S. Logothetidis, *Ellipsometry of Functional Organic Surfaces and Films,* ed. by K. Hinrichs, K.-J. Eichorn, (Springer, Berlin, 2014). pp. 173–195, Chap. "Polymer Blends and Composites"
6. P.Y. Yu, M. Cardona, *Fundamentals of Semiconductors: Physics and Materials Properties* (Springer, Berlin, 2001)
7. A. Röseler, *Infrared Spectroscopic Ellipsometry* (Akademie-Verlag, Berlin, 1990)
8. M. Schubert, *Infrared Ellipsometry on Semiconductor Layer Structures: Phonons, Plasmons, and Polaritons* (Springer, Berlin, 2004)
9. W. Sellmeier, Annalen der Physik und Chemie **143**, 271 (1871)
10. Schott Glass Catalog, p. 69 (2014)
11. C.M. Herzinger, B. Johs, W.A. McGahan, J.A. Woollam, W. Paulson, J. Appl. Phys. **83**, 3323 (1998)
12. L. Cauchy, Bull. Des. Sc. Math. **14**, 9 (1830)
13. F. Urbach, Phys. Rev. **92**, 1324 (1953)
14. F. Wooten, *Optical Properties of Solids* (Academic Press, New York, 1972)
15. C. Kittel, *Introduction to Solid State Physics*, 5th edn. (Wiley, New York, 1976)
16. T.E. Tiwald, D.W. Thompson, J.A. Woollam, W. Paulson, R. Hance, Thin Solid Films **313–314**, 661 (1998)
17. D. De Sousa Meneses, M. Malki, P. Echegut, J. Non-Cryst. Solids **351**, 769–776 (2006)
18. K.-E. Peiponen, E.M. Vartiainen, Phys. Rev. B **44**, 8301 (1991)
19. G.E. Jellison, Jr., F.A. Modine, Appl. Phys. Lett. **69**, 371 (1996); Erratum, Appl. Phys. Lett. **69**, 2137 (1996)

20. A.S. Ferlauto, G.M. Ferreira, J.M. Pearce, C.R. Wronski, R.W. Collins, Xunming Deng, Gautam Ganguly, J. Appl. Phys. **92**, 2424 (2002)
21. M. Cardona, *Solid State Physics*, ed. by F. Seitz, D. Turnbull, H. Ehrenreich (Academic, New York, 1969). Suppl. 11 “Modulation Spectroscopy”
22. D.E. Aspnes, *Handbook on Semiconductors*, vol. 2, ed. by M. Balkanski (North Holland, 1980), pp. 125–127, Chap. “Modulation Spectroscopy/Electric Field Effects on the Dielectric Function of Semiconductors”
23. P. Lautenschlager, M. Garriga, L. Vina, M. Cardona, Phys. Rev. B **36**, 4821 (1987)
24. P. Lautenschlager, M. Garriga, S. Logothetidis, M. Cardona, Phys. Rev. B **35**, 9174 (1987)
25. S. Adachi, Phys. Rev. B **35**, 7454 (1987)
26. S. Adachi, J. Appl. Phys. **66**, 6030 (1989)
27. Mathias Schubert, Tino Hofmann, Bernd Rheinländer, Ines Pietzonka, Torsten Sass, Volker Gottschalch, John A. Woollam, Phys. Rev. B **60**, 16618 (1999)
28. B. Johs, C.M. Herzinger, J.H. Dinan, A. Cornfeld, J.D. Benson, Thin Solid Films **313–314**, 137 (1998)
29. US Patent #5,796,983, Dielectric function parametric model, and method of use
30. B. Johs, J.A. Woollam, C.M. Herzinger, J. Hilfiker, R. Synowicki, C.L. Bungay, SPIE Proc. **CR72**, 29 (1999)
31. Y.S. Ihn, T.J. Kim, T.H. Ghong, Y.D. Kim, D.E. Aspnes, J. Kossut, Thin Solid Films **455–456**, 222 (2004)
32. B. Johs, J.S. Hale, Phys. Stat. Sol. A **205**, 715 (2008)
33. E. Cheney, D. Kincaid, *Numerical Mathematics and Computing*, 3rd edn. (Brooks/Cole Publishing, 1994)

Chapter 6
Effect of Roughness on Ellipsometry Analysis

Hiroyuki Fujiwara

Abstract In spectroscopic ellipsometry (SE), appropriate modeling of surface roughness structures is critical for the accurate characterization of optical constants. In particular, when a simple SE analysis is performed for rough surfaces with dimensions comparable to the SE measurement wavelengths (>300 nm), the optical response of the rough surfaces cannot be expressed properly, leading to serious overestimation of absorption coefficients of solar cell materials. Accordingly, extra care is necessary when samples with rough surfaces are analyzed. Large discrepancies observed between reported dielectric functions of $CuInSe_2$ and $CH_3NH_3PbI_3$ are found to originate from underestimated roughness contributions, induced primarily by oversimplification of optical models. Quite fortunately, analysis errors generated by the roughness components can be corrected rather easily based on a simple procedure, referred to as extra roughness correction. When this correction scheme is applied, all the dielectric functions and absorption spectra show excellent agreement. It is further demonstrated that the analytical treatment of roughness in SE influences the optical simulation result of solar cells. In this chapter, we will examine the effect of roughness on SE results and discuss the proper SE analysis method for solar cell materials.

6.1 Introduction

Spectroscopic ellipsometry (SE) is a surface-sensitive characterization technique and careful optical modeling is required for high-precision determination of optical constants. Nevertheless, solar cell materials in thin film form often exhibit quite rough surface, which makes the SE analysis quite difficult. When the absorber layers have large roughness, the short-circuit current density (J_{sc}) of solar cells improves due to light scattering. As a result, "device grade materials" are often the most unsuitable materials for SE analysis. For reliable SE characterization, it is of

H. Fujiwara (✉)
Gifu University, 1-1 Yanagido, Gifu 501-1193, Japan
e-mail: fujiwara@gifu-u.ac.jp

© Springer International Publishing AG, part of Springer Nature 2018

H. Fujiwara and R. W. Collins (eds.), *Spectroscopic Ellipsometry for Photovoltaics*,
Springer Series in Optical Sciences 212,
https://doi.org/10.1007/978-3-319-75377-5_6

paramount importance to (i) prepare samples with smoother surfaces [1, 2] and (ii) use a proper optical model particularly for roughness structures [3].

When sample surface is not atomically flat and there is a roughness component, a surface roughness layer is usually incorporated into the optical model in SE analysis (Sect. 3.7.4). In general, the optical properties of this roughness layer are calculated as a mixture of bulk material and void components by using the Bruggeman effective medium approximation (EMA) (Sect. 3.4.2) [4–7]. It has been confirmed that, among several effective medium theories, the surface-roughness optical constants obtained by EMA provide the best fit to (ψ, Δ) spectra, although SE results are essentially independent of effective medium theories used in the analyses [6]. For the SE analyses of solar cell materials, EMA has been used quite commonly.

Figure 6.1a shows the ε_2 spectra of a $CuInSe_2$ (CISe) bulk component [1] and its corresponding surface roughness component calculated by EMA. The complete CISe dielectric function [$\varepsilon_{CISe}(E)$] is shown in Fig. 8.24 (Vol. 2). In Fig. 6.1a, the onset of ε_2 ($\varepsilon_2 > 0$) at 1.0 eV corresponds to the band gap (E_g) of CISe. The dielectric function of the surface roughness is calculated directly from (3.9) assuming a 50:50 vol.% mixture of CISe and voids. In this case, by setting $\varepsilon_a = \varepsilon_{CISe}$, $\varepsilon_b = \varepsilon_{void} = 1$ and $f_a = f_b = 0.5$ in (3.9), the dielectric function of the surface roughness is obtained as ε_{EMA}. It can be seen that the ε_2 amplitude of the roughness component is quite small, compared with the bulk component. This is caused by the screening effect of polarized charges [7]. Specifically, when two components of ε_a and ε_b ($\varepsilon_a > \varepsilon_b$) are considered, the dielectric constant of a two-phase composite does not become a simple average value of $(\varepsilon_a + \varepsilon_b)/2$ but is more influenced by a phase having a lower dielectric constant (i.e., ε_b in the case of $\varepsilon_a > \varepsilon_b$) due to the screening effect. In Fig. 6.1a, therefore, we observe $\varepsilon_2 \sim 0$ for the

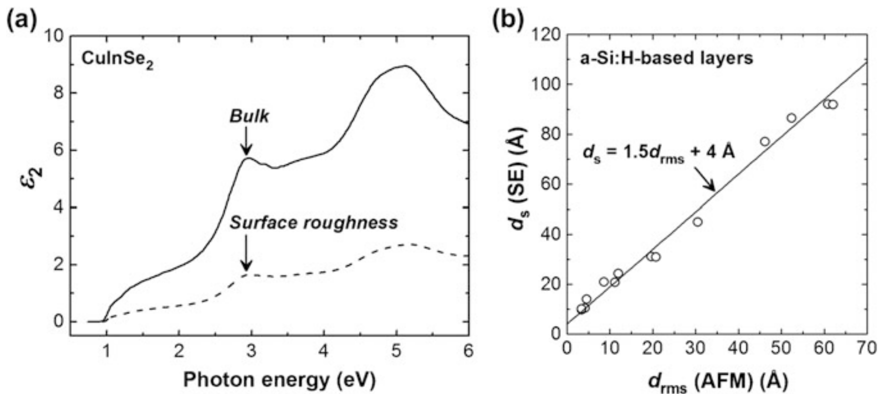

Fig. 6.1 **a** ε_2 spectra of a $CuInSe_2$ (CISe) bulk component [1] and its corresponding surface roughness component calculated by EMA assuming a 50/50 vol.% mixture of CISe and voids and **b** surface roughness layer thickness (d_s) of a-Si:H-based layers estimated by SE as a function of root-mean-square roughness (d_{rms}) characterized by AFM [6]

roughness component because $\varepsilon_2 = 0$ for voids. Consequently, the optical properties of the surface roughness layer resemble closely those of a transparent material ($\varepsilon_2 = 0$).

Figure 6.1b shows surface roughness layer thickness (d_s) estimated by SE as a function of root-mean-square roughness (d_{rms}) characterized from atomic force microscopy (AFM) [6]. In this figure, the SE analysis results obtained from various hydrogenated amorphous silicon (a-Si:H)-based layers are shown. The optical constants of the surface roughness layer were modeled from EMA assuming a fixed void volume fraction of 50 vol.% ($f_{void} = 0.5$). The d_s determined from SE shows a clear linear relationship with d_{rms}, expressed by $d_s = 1.5d_{rms} + 4$ Å [6, 8]. The intercept of 4 Å implies that the SE results include the influence of microscopic roughness on the atomic scale, which cannot be detected by AFM due to a large cantilever-tip radius of curvature (50 ~ 100 Å) [6, 9]. On the other hand, a slope of d_s/d_{rms} increases with the AFM scan size due to a statistical aspect of d_{rms}; namely, if the AFM scan size is small, the higher resolution in the AFM measurement leads to larger d_{rms}, resulting in a smaller d_s/d_{rms} value [10]. In fact, for similar a-Si:H layers, a different slope of $d_s/d_{rms} = 0.88$ has been reported for a scan size of $2 \times 2\ \mu m^2$ [9], while a larger scan size of $5 \times 5\ \mu m^2$ results in $d_s/d_{rms} = 1.5$ (Fig. 6.1b). However, d_s and d_{rms} values are essentially similar and exhibit a quite good relationship. Thus, SE results can be justified by d_{rms} and, conversely, SE analyses could be performed by referring to d_{rms} values. In general, the assumption of $f_{void} = 0.5$ provides a good approximation for surface roughness modeling by EMA [6].

Although EMA is indispensable for SE analysis of many materials, there is a limitation for EMA; the size of a phase (D) in a composite material should be much smaller than the wavelength (λ) of a SE light probe and the condition of $D < 0.1\lambda$ needs to be satisfied [4, 5]. For example, in the surface roughness analysis by EMA, the dimension of roughness structures (D) should be less than 310 Å for a measurement photon energy of $E = 4$ eV ($\lambda \sim 3100$ Å). When D exceeds this limit, a complex EMA-multilayer model is generally necessary for the SE analysis [11–13]. As examples, Fig. 6.2 shows the surface scanning microscope (SEM) images of $CuIn_{1\text{-}x}Ga_xSe_2$ (CIGSe) layers ($x = 0.34$) with layer thicknesses of (a) 500 Å and (b) 3600 Å [1], together with appropriate optical models for each roughness structure. It can be seen that the surface roughness developed by the crystallographic grain growth becomes significantly large as the layer thickness increases and the roughness size becomes comparable to λ of the SE light probe ($D \sim \lambda$). When $D < 0.1\lambda$, a single EMA layer can be employed and the roughness structure is analyzed using two structural parameters (d_s, f_{void}). In conventional analysis, a value of $f_{void} = 0.5$ can be assumed, as mentioned earlier. In the thin CIGSe layer of Fig. 6.2a, the actual size of the roughness is $D \sim 0.1\lambda$ but the single EMA model does not generate artifacts (Sect. 10.2). On the other hand, in the condition of $D > 0.1\lambda$ it may be necessary to use a EMA multilayer model in which more than two surface roughness layers with different void fractions are incorporated (Chap. 4 in Vol. 2). In particular, when D and λ are comparable ($D \sim \lambda$), the EMA multilayer model needs to be used and, if this structure is analyzed by applying a

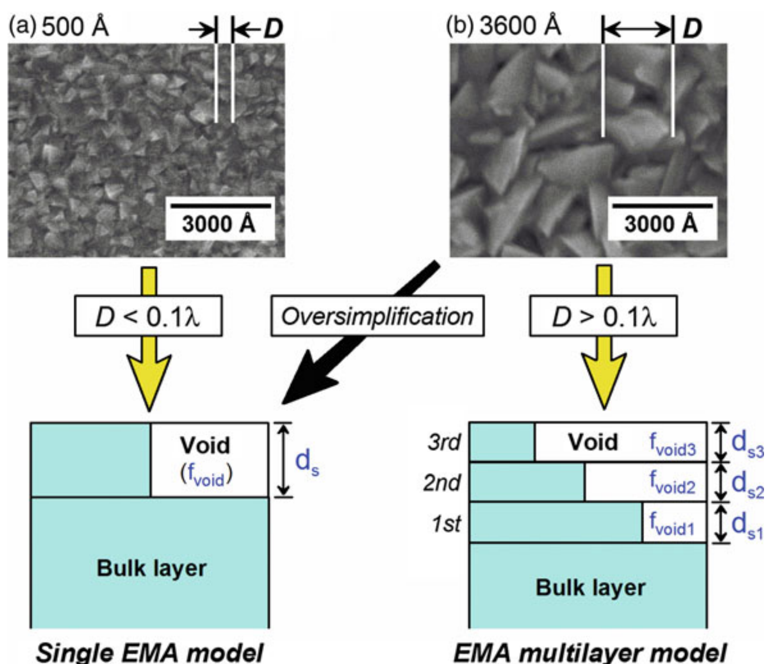

Fig. 6.2 SEM images of $CuIn_{1-x}Ga_xSe_2$ layers ($x = 0.34$) with layer thicknesses of **a** 500 Å and **b** 3600 Å [1]. An appropriate optical model for the roughness structure (single EMA model or EMA multilayer model) can be selected by the condition of $D < 0.1\lambda$ (or $D > 0.1\lambda$), where D and λ represent the roughness size and λ of the SE light probe. In the optical model, f_{void} and d_s denote the void volume fraction and thickness of the surface roughness layer. When the rough surface structure ($D \sim \lambda$) is analyzed using a single EMA model, the oversimplification of the optical model generates SE analysis errors, such as non-zero ε_2 and α values in a region of $E < E_g$

single EMA model, artifacts are likely to be generated by the oversimplification of the optical model.

Since solar cell materials often exhibit rough surface morphology, the SE analyses of these materials have been rather difficult. Specifically, the thick CIGSe layer in Fig. 6.2b and methylammonium lead iodide ($MAPbI_3$, $CH_3NH_3PbI_3$) prepared by solution-based processes [14, 15] show quite rough surfaces with D = 2000–8000 Å. One general and quite effective way to suppress the effect of roughness in SE analysis is to characterize thin layers (<1000 Å) [1, 2]. In this case, the roughness size tends to become smaller, as confirmed from Fig. 6.2, and the SE analysis can be performed relatively easily using a single EMA model. In the analyses of thin layers, other detrimental effects, including thickness non-uniformity and compositional fluctuation, can also be suppressed.

Moreover, to obtain reliable optical data, it is quite helpful to perform multi-sample SE analysis in which some samples having slightly different structures (or layer thicknesses) are analyzed self-consistently. Although there have been

some ways to perform the multi-sample analysis [6, 7, 16, 17], the global error minimization (GEM) scheme has been used for the analysis of solar cell materials [1, 2, 6, 7]. The dielectric function of CISe in Fig. 6.1a has also been extracted from the GEM analysis described in detail in Sect. 10.2.

In this chapter, we will examine how surface roughness modeling affects the resulting optical constants. This chapter further explains a simple procedure, which is quite helpful for the correction of analytical errors generated by rough surfaces [3]. Here, the effect of the roughness analysis on external quantum efficiency (EQE) simulation is also described. The SE analyses for rough surface (textured) structures will be treated in Chap. 4 (Vol. 2).

6.2 Effect of Surface Roughness on Dielectric Function

In this section, the origin of inconsistent optical data reported for CISe [1, 18, 19] and $MAPbI_3$ hybrid perovskite [2, 20, 21] is discussed. Quite importantly, the large discrepancies observed between the reported dielectric functions can be interpreted as a roughness effect and the analysis errors are reduced drastically by applying the extra roughness correction [3]. In this section, as examples, the roughness analyses for CISe and $MAPbI_3$ are described.

6.2.1 CuInSe₂

Figure 6.3 summarizes (a) the ε_2 spectra and (b) absorption coefficient (α) of CISe extracted from polycrystalline layers [1, 19] and a single crystal [18]. The CISe data of [1] have been determined from the multi-sample (GEM) analysis of smooth thin layers. In this analysis, a pair of quite thin CISe layers (around 300 and 500 Å) were used (Sect. 10.2.3), and the surface morphology of these layers is quite similar to that shown in Fig. 6.2a. All the ε_2 spectra in Fig. 6.3 have been extracted using a single EMA model. It is known well that CISe single crystals exhibit optical anisotropy in the direction along the *a* and *c* axes of the chalcopyrite unit cell (see Fig. 10.8) [18, 22, 23] and the ε_2 spectrum of [18] corresponds to that when the polarization direction is perpendicular to the *c* axis.

It can be seen from Fig. 6.3a that the absolute ε_2 values of [1, 18, 19] are quite different, although the ε_2 peak energies are almost identical. In the ε_2 spectra of [18, 19], the ε_2 values show none-zero values even below $E_g = 1.0$ eV, while the ε_2 values at $E < E_g$ are completely zero when the smooth CISe layers are analyzed [1]. This effect can be identified more clearly in the corresponding α spectra shown in Fig. 6.3b. The absolute values of α are also quite different and the maximum difference in α is more than 200% at $E = 1.2$ eV.

The origin of the α-value variation observed in CISe can be understood from a simple optical simulation (Fig. 6.4). Specifically, it was assumed that the change

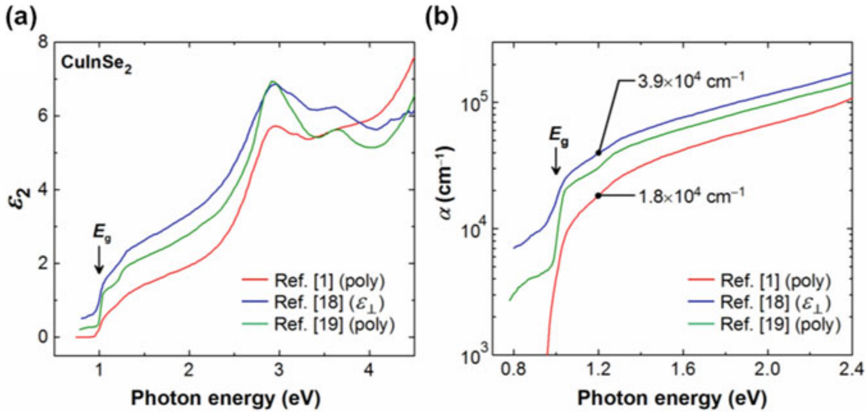

Fig. 6.3 **a** ε_2 spectra and **b** α spectra of CISe extracted from polycrystalline layers [1, 19] and a single crystal [18]. The CISe data of [1] have been determined by the multi-sample analysis of smooth thin layers (<600 Å). The arrows indicate the E_g position of CISe (1.00 eV). In (**b**), the α values of [1, 18] at 1.2 eV are indicated. The data are taken from [3]

between the optical spectra of Fig. 6.3 is caused solely by the effect of the surface roughness and the influence of the rough surface was simulated from the optical model of Fig. 6.4a. In this calculation, the CISe dielectric function of [1] (Fig. 8.24 in Vol. 2) was employed to represent the CISe bulk component and a hypothetical surface roughness layer was further incorporated into the optical model. The optical

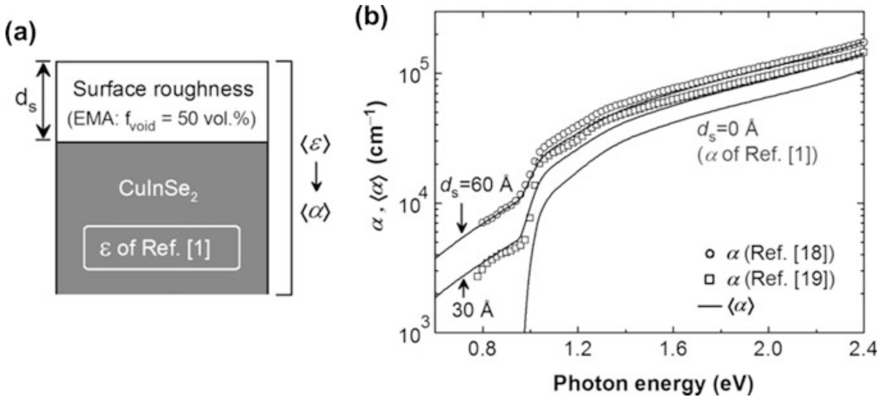

Fig. 6.4 **a** Optical model of surface roughness layer/substrate (CISe bulk component), constructed to simulate the effect of rough surface and **b** experimental α spectra of [18, 19] (open circles) and $\langle\alpha\rangle$ spectra obtained from the simulation. In (**a**), the pseudo-dielectric function $\langle\varepsilon\rangle$ calculated from the optical model is further converted to the pseudo-absorption coefficient $\langle\alpha\rangle$. In (**b**), the simulation results were obtained by varying the thickness of a hypothetical surface roughness layer [d_s in (**a**)] and the $\langle\alpha\rangle$ spectrum corresponds to the α spectrum of [1] when d_s = 0 Å. The data of (**b**) are taken from [3]

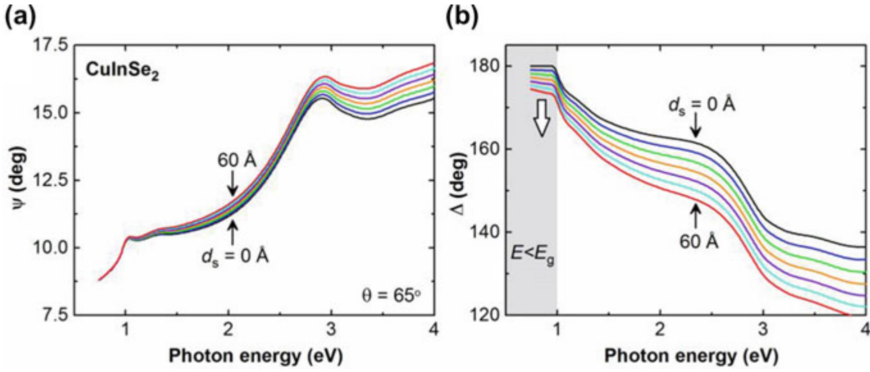

Fig. 6.5 Variation of **a** ψ spectrum and **b** Δ spectrum when d_s is increased from 0 to 60 Å with a step of 10 Å. These (ψ, Δ) spectra were calculated from the optical model of Fig. 6.4a assuming an incident angle of 65°

properties of the roughness layer were calculated from EMA assuming $f_{\text{void}} = 0.5$. Based on the optical model and the optical constants of the surface roughness and substrate (CISe), the ellipsometry spectra were calculated first, which were then converted to the pseudo-dielectric function $(\langle\varepsilon\rangle = \langle\varepsilon_1\rangle - \mathrm{i}\langle\varepsilon_2\rangle)$ using (3.18). The $\langle\varepsilon\rangle$ spectra were changed further to the pseudo-refractive index $\langle n\rangle$ and pseudo-extinction coefficient $\langle k\rangle$ $\left(\langle\varepsilon\rangle = \langle N\rangle^2\right)$, from which the pseudo-absorption coefficient $\langle\alpha\rangle$ was finally calculated using $\langle\alpha\rangle = 4\pi\langle k\rangle/\lambda$.

In Fig. 6.4b, the simulated results (solid lines) are compared with the experimental spectra of [18, 19] (open circles). The simulation results of $\langle\alpha\rangle$ were obtained by varying the thickness of the hypothetical surface roughness layer and, when $d_s = 0$ Å, the $\langle\alpha\rangle$ spectrum corresponds to the α spectrum of [1] in Fig. 6.3b. It can be confirmed from Fig. 6.4b that the $\langle\alpha\rangle$ spectra obtained from the simulation show excellent agreement with the experimental α spectra when d_s values of 30 and 60 Å are assumed. More importantly, the simulated $\langle\alpha\rangle$ spectrum shows a marked upward shift with increasing d_s. Accordingly, the large variation observed in the reported α spectra can be explained primarily by the effect of the surface roughness.

To interpret the simulation result, the (ψ, Δ) spectra were calculated by varying d_s in the optical model of Fig. 6.4a. Figure 6.5 summarizes the variation of (a) the ψ spectrum and (b) the Δ spectrum with increasing d_s from 0 to 60 Å with a step of 10 Å. For this calculation, an incident angle of 65° is assumed. In Fig. 6.5, the ψ spectra show minor variation particularly at low energies ($E < 3$ eV), while Δ exhibits large change as d_s increases. It should be pointed out that, since the optical model is simple, the shape of the Δ spectrum basically determines that of the $\langle\varepsilon\rangle$ spectrum. Thus, although the Δ spectrum is upside down, the variations of the Δ spectrum in Fig. 6.5b and ε_2 spectrum in Fig. 6.3a are quite similar. In particular, we observe $\Delta = 180°$ at $E < E_g$ when $d_s = 0$ Å because $\varepsilon_2 = 0$ in this region, but the whole Δ spectrum shifts downward systematically with increasing d_s.

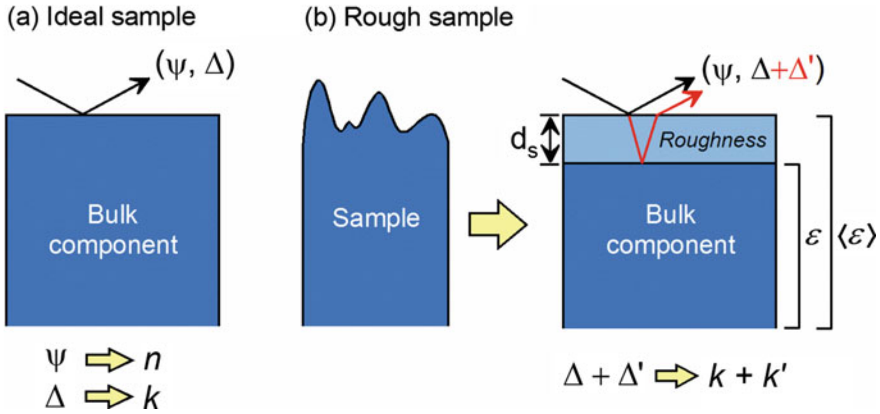

Fig. 6.6 Optical models for **a** an ideal sample and **b** a rough sample. In (**b**), Δ' shows an additional phase shift induced by a remaining roughness layer, which is generated by the oversimplification of an optical model for rough surface

We can understand all the above results from the optical models shown in Fig. 6.6. In an ideal case of Fig. 6.6a, there is only a bulk (substrate) component in the optical model and the ellipsometry parameters of (ψ, Δ) can be related to the optical constants (n, k) of the bulk component (i.e., $\psi \rightarrow n$ and $\Delta \rightarrow k$) [7]. More specifically, we obtain $k = 0$ when Δ is 180° (or 0°). When a single EMA model in Fig. 6.2a is applied for the SE analysis of rough surface, however, the roughness component cannot be removed completely due to the oversimplification of the optical model, and the resulting dielectric function still contains the roughness (or void) contribution, as illustrated in Fig. 6.6b. In this case, ψ does not change significantly, compared with ψ of the ideal case, as confirmed from the simulation result of Fig. 6.5a. In contrast, the Δ value changes largely due to the additional phase shift induced by the roughness layer (Δ' in Fig. 6.6b). This extra phase variation caused by the roughness component can be expressed by

$$\Delta' = 4\pi d_s N_s \cos\theta_s / \lambda, \tag{6.1}$$

where N_s and θ_s denote the complex refractive index and transmission angle for the roughness layer [7]. As we have seen in Fig. 6.1, the surface roughness layer has rather transparent optical properties. Thus, the phase shift of Δ' is determined primarily by the thickness and refractive index of the roughness layer.

As mentioned above, Δ has a direct link with k, and the extra phase shift Δ' increases nominal k (or α) as $\Delta + \Delta' \rightarrow k + k'$. Furthermore, (6.1) implies that nominal α increases when d_s is thicker and λ is shorter (or larger E) because of the increase in Δ'. These are the exact trends that are confirmed in the experimental and simulated spectra of Figs. 6.3, 6.4 and 6.5. In particular, the variation of Δ' with d_s can be confirmed directly from the shift of the Δ spectrum in Fig. 6.5b.

Consequently, by the increase in Δ', the whole α spectrum is lifted upward with the same transition energies and Δ' increases more notably at higher energies. In other words, the underestimation of roughness components leads to serious overestimation of α values [3]. The corresponding ε_2 spectrum also shows a similar increase by $\varepsilon_2 = 2n(k + k')$. It can be noticed that the change of ε_2 at $E < E_g$ in Fig. 6.3a is consistent with the Δ shift observed in Fig. 6.5b. Accordingly, the underestimation of d_s can be judged rather easily from the non-zero ε_2 component and the increase in ε_2 (or α) with E in the region of $E < E_g$.

The above results indicate clearly that the CISe optical functions reported in [18, 19] are actually the pseudo-optical functions (i.e., $\langle\varepsilon\rangle$ and $\langle\alpha\rangle$), and the optical constants of the bulk component can still be obtained by correcting the underestimated roughness contribution. This extra roughness correction can be performed by removing remaining d_s in the optical model of Fig. 6.6b using the mathematical inversion (point-by-point fitting) described in Sect. 10.2.1 [3]. In this analysis, the extra roughness layer is removed so that the ε_2 values become completely zero at $E < E_g$. If the d_s value of the assumed extra roughness is too large, however, the ε_2 values show negative values at $E < E_g$. In commercial software, the unphysical negative ε_2 values are corrected automatically to $\varepsilon_2 = 0$ and the (ψ, Δ) values calculated from the mathematical inversion deviate from the experimental data. In the extra roughness correction, therefore, the d_s value needs to be selected carefully.

Figure 6.7 shows (a) the ε_2 spectra and (b) the α spectra of CISe obtained after the extra roughness correction of the optical data reported in [18, 19], together with the uncorrected CISe optical spectra of [1]. The optical spectra for [18] and [19] shown in this figure were extracted by removing the extra roughness thicknesses (d_s) of 55 Å and 24 Å, respectively. Rather surprisingly, after the extra roughness correction, all the ε_2 and α spectra show similar trends and the difference in α at

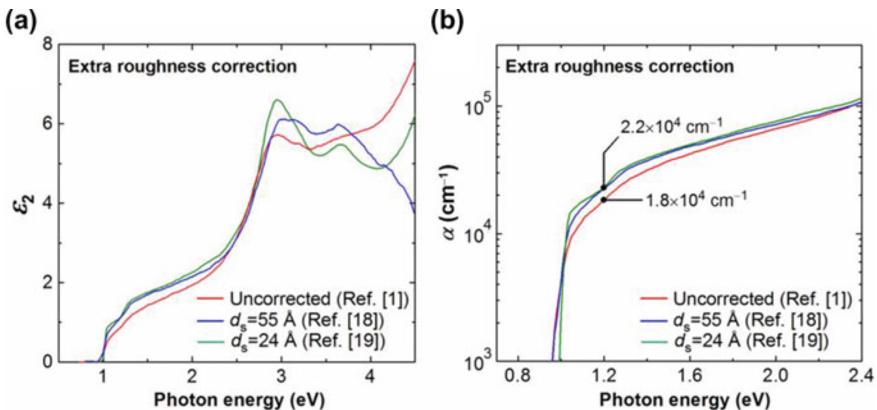

Fig. 6.7 **a** ε_2 spectra and **b** α spectra of CISe obtained after the extra roughness correction of the optical data reported in [18, 19], together with the uncorrected CISe optical spectra of [1]. The d_s values for [18, 19] represent the thicknesses of the extra roughness layers assumed in the extra roughness correction. The data of (**b**) are taken from [3]

$E = 1.2$ eV, for example, reduces drastically from over 200% (Fig. 6.3b) to within 25% (Fig. 6.7b). Thus, the underestimated roughness contribution has a significant impact on absolute ε_2 and α values. In a high energy region ($E \geq 2.8$ eV), however, the ε_2 values show notable differences as λ is shorter and the effect of inappropriate roughness modeling is more significant. Thus, to obtain reliable data at higher energies, the analysis of smooth layers is quite favorable.

It is obvious from the above results that nominal α values increase as the underestimated d_s value increases. In fact, the α values of [18] are higher than those of [19] because the corrected roughness value of [18] ($d_s = 55$ Å) is larger than that of [19] ($d_s = 24$ Å). Since the single EMA model has been employed for these analyses, the underestimated d_s value is expected to increase as the surface roughness increases. In other words, when a simple SE analysis is performed for rough surfaces, nominal α values increase as analyzing samples become rougher. If the extra roughness layer is removed by the mathematical inversion, more realistic optical spectra are obtained and the overall agreement improves drastically. When the increase in ε_2 (or α) with E is observed in the region of $E < E_g$, therefore, it is necessary to perform the extra roughness correction. As an alternative method, surface roughness and bulk layer thicknesses used in thin film analysis can be adjusted so that the artifacts at $E < E_g$ are eliminated. It should be mentioned that variable-angle SE measurements do not solve the problem of rough surface, as the optical spectrum of [19] has been obtained based on the variable-angle SE analysis.

The α spectra of solar cell materials have been characterized widely from optical transmission measurements, but in this case the effect of large surface roughness is even more significant. Figure 6.8a compares the α spectra of CISe determined from SE [1] and transmission [24] measurements. The ellipsometry data are identical to those shown in Fig. 6.7b. It can be seen that the α values are overestimated seriously when the transmission measurement is applied. This reason can be understood by considering the effective optical pass length in a thin film structure. Figure 6.8b illustrates the optical responses in flat and textured structures. For optical transmission, it is known widely that there is a relation of $R + A + T = 1$, where R, A and T represent the reflectance, absorptance and transmittance of an optical system, respectively. For the assumed flat structure, a relation of $R_{flat} + A_{flat} + T_{flat} = 1$ holds. However, when the thin film has a quite rough surface structure ($D \sim \lambda$), intense light scattering occurs on the surface, varying the transmission angle of the incident (probe) light. In this case, the effective optical pass length increases due to the contribution of the inclined transmission angles, which in turn enhances the absorptance of the textured structure (A_{tex}). This is the same phenomenon used to improve the optical confinement of incident light in solar cells. The increased A_{tex} in the optical system further results in smaller transmittance (T_{tex}). Since $T_{flat} > T_{tex}$, if (i) a simple analysis assuming a flat structure is carried out by completely neglecting light scattering effect and (ii) the increased A_{tex} is misinterpreted as the intrinsic properties of the material, nominal α (α_{tex}) increases considerably, compared with α obtained from a flat structure (i.e., $\alpha_{tex} > \alpha_{flat}$). In the actual analysis of [24], the optical interference effect in the film/substrate structure was neglected and the observed T spectrum was converted

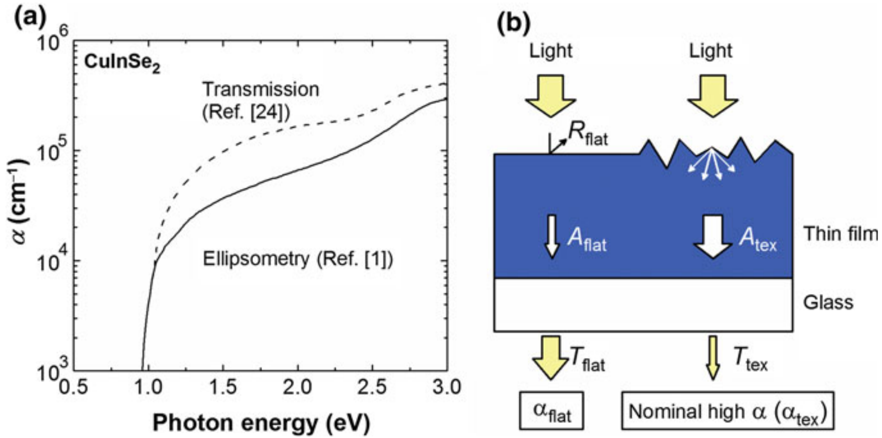

Fig. 6.8 **a** α spectra of CISe determined from SE [1] and transmission [24] measurements and **b** optical responses in flat and textured structures. In (**a**), the α spectrum of [1] corresponds to that shown in Fig. 6.7b. In (**b**), *R, A* and *T* represent the reflectance, absorptance and transmittance of the optical system and the subscripts of "flat" and "tex" show the flat and textured structures. The resulting α values (α_{flat} and α_{tex}) are also indicated

directly to the α spectrum without considering a light scattering effect. Thus, these procedures increase the nominal α values significantly. Moreover, in conventional transmission analysis, the refractive index of a film is often treated as a constant value [25], which is not valid for most of materials. Accordingly, for accurate determination of α, SE characterization is generally required.

So far, for α of CISe at 2.0 eV, a variety of values ranging from 7.5×10^4 to 1.7×10^5 cm^{-1} have been reported [18, 19, 22–33], while the corresponding α value estimated in [1] is 6.6×10^4 cm^{-1} and shows the smallest value. As mentioned above, the variation in the α values can be interpreted as roughness effect. When the dielectric functions of CIGSe extracted from the GEM analysis [1, 34] are applied for the optical simulation of a high-efficiency CIGSe solar cell, the EQE spectrum is reproduced almost perfectly [35] (see Fig. 2.9 in Vol. 2). Furthermore, these CIGSe dielectric functions provide excellent fitting to thicker CIGSe layers when a EMA multilayer model is applied (see Sect. 4.3.4 in Vol. 2).

The α spectrum of [24] in Fig. 6.8a, which shows very high α values exceeding 10^5 cm^{-1}, has been cited quite widely in the last three decades and had generated a belief that CISe (or CIGSe) is the highest α material among all the solar cell materials [36], even though the actual α values of CISe are comparable to those of other semiconductors, such as GaAs and CdTe (Fig. 1.6). Unfortunately, in the solar cell community, there is a tendency to believe in the highest α value reported ever. Thus, it is vital to follow the analysis method and roughness information to judge the validity of optical data.

As shown above, to eliminate the artifact induced by microscopic surface roughness, SE analysis of smooth thin layers is quite effective. We can also detect

the underestimated roughness component by comparing d_s with d_{rms} obtained from AFM (see Fig. 6.1). It should be emphasized that multi-sample analysis is of significant importance to obtain reliable SE results. For example, if similar CISe dielectric functions are extracted from samples with different CISe layer thicknesses, the analysis results are more reliable. To check the validity of dielectric functions, the dielectric function extracted from a thin layer can further be applied to the analysis of a thicker layer. In this case, if a satisfactory fitting is obtained, the accuracy of the analysis can be validated. A more complete SE analysis can be performed in a similar manner using a self-consistent GEM analysis (Sect. 10.2).

6.2.2 $CH_3NH_3PbI_3$

So far, the optical properties of $MAPbI_3$ have been studies quite extensively and apparently conflicting optical data have been reported [15, 20, 21, 37–42] (see Fig. 1.3). As mentioned earlier, $MAPbI_3$ layers fabricated by solution processes have quite rough surfaces ($D \sim \lambda$), and thus the condition of $D < 0.1\lambda$ is not satisfied. For the SE analysis of the solution-processed layers, however, a single EMA layer has been applied widely to simplify the SE analysis [15, 20, 21, 41].

Figure 6.9a summarizes the ε_2 spectra of $MAPbI_3$ determined by SE. The result of [2] has been obtained from the GEM analysis of the smooth thin films (Sect. 16.2). In particular, to prepare very smooth $MAPbI_3$ layers, a laser evaporation technique

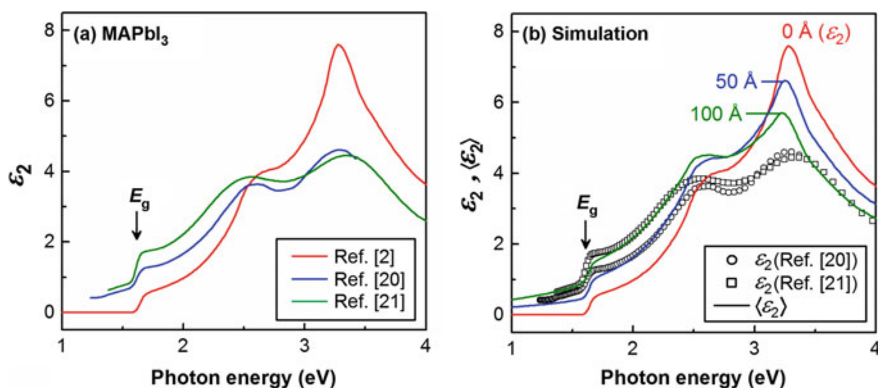

Fig. 6.9 **a** ε_2 spectra of $MAPbI_3$ reported in [2, 20, 21] and **b** $\langle\varepsilon_2\rangle$ spectra calculated by varying a hypothetical surface-roughness layer thickness (d_s) in a surface roughness layer/substrate ($MAPbI_3$ bulk component) structure (solid lines), together with the experimental ε_2 spectra reported in [20, 21] (open circles and squares). The result of [2] has been obtained from the GEM analysis of smooth $MAPbI_3$ layers prepared by laser evaporation (Sect. 16.2), while the results of [20, 21] have been obtained from solution-processed $MAPbI_3$ layers. The arrows indicate the E_g position of $MAPbI_3$ (E_g = 1.61 eV) [2]. The $\langle\varepsilon_2\rangle$ spectrum corresponds to the ε_2 spectrum of [2] when d_s = 0 Å. The data are taken from [3]

(Fig. 16.3) has been employed. To eliminate the degradation effect observed in humid air, the SE measurements were performed in N_2 without exposing the samples to air. The critical point (CP) analysis of the extracted dielectric function shows that E_g of $MAPbI_3$ is 1.61 eV (Fig. 16.7a), as indicated by the arrow in Fig. 6.9a. On the other hand, the ε_2 spectra of [20, 21] have been extracted from solution-processed $MAPbI_3$ layers. For all the SE analyses, a single EMA model has been adopted. In Fig. 6.9a, the overall ε_2 values of [20, 21] are quite larger in the low energy region ($E < 2.5$ eV), compared with those reported in [2]. In the ε_2 spectra of [20, 21], the ε_2 value increases with E in a region of $E < E_g$, suggesting that these optical data are influenced strongly by the roughness.

To find the effect of the remaining roughness, the $\langle\varepsilon_2\rangle$ spectra were calculated by the same procedure used in Fig. 6.4. In this simulation, the $\langle\varepsilon_2\rangle$ spectra were calculated by adding the surface roughness component to the $MAPbI_3$ dielectric function extracted from the smooth layer [2]. Figure 6.9b shows the simulated result obtained by varying d_s in a range of 0–100 Å (solid lines), together with the experimental ε_2 spectra reported in [20, 21] (open circles and squares). It can be seen that the ε_2 spectra of [20, 21] are reproduced quite well by incorporating the additional roughness layer with d_s of 50–100 Å, confirming that the quite large variation observed in the ε_2 spectra is induced mainly by the surface roughness. The remaining disagreement between the experimental and simulated spectra at high energies (~3.2 eV) has been attributed to the formation of a hydrate phase [2, 42, 43], such as $(CH_3NH_3)_4PbI_6 \cdot 2H_2O$, formed by $MAPbI_3$ degradation in humid air (Sect. 16.5).

The extra roughness correction has also been performed for the experimental spectra of [20, 21]. Figure 6.10 shows the SE results obtained (a) before and (b) after the extra roughness correction. Before the correction, the α values of [20,

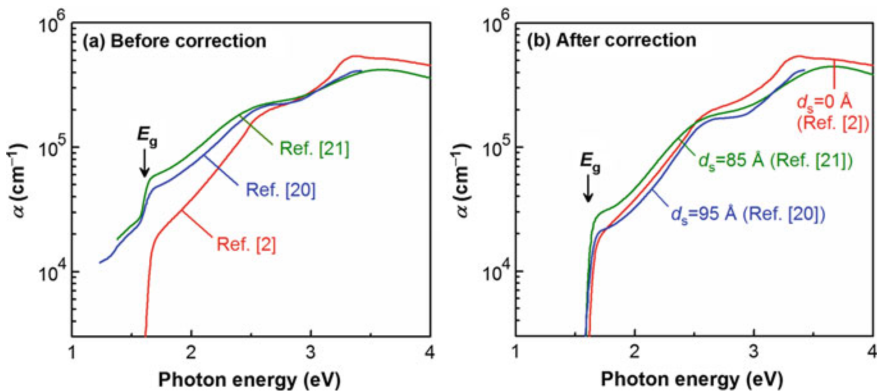

Fig. 6.10 α spectra of $MAPbI_3$ **a** before and **b** after the extra roughness correction of the optical data reported in [20, 21], together with the uncorrected optical spectrum of [2]. The optical spectra of (**a**) correspond to the ε_2 spectra shown in Fig. 6.9a, and the α spectra of [2] in (**a**) and (**b**) are identical. The arrows indicate E_g of $MAPbI_3$ (1.61 eV) [2]. The d_s values represent the thicknesses of the extra roughness layers assumed in the correction. The data are taken from [3]

21] show non-zero values below E_g and the absolute α values near E_g are notably higher than those of [2]. The α spectra determined by transmission measurements also show constant values below E_g [37, 38] most likely due to the contribution of transmission loss caused by surface scattering, as discussed in Fig. 6.8b. Quite remarkably, after the extra roughness correction, all the α spectra show the consistent trend, supporting the effectiveness of this method. In these corrections, the d_s values of 85 Å and 95 Å were removed from the spectra of [21] and [20], respectively. The larger d_s values used for the correction of the $MAPbI_3$ data (d_s = 85–95 Å), compared with the CISe data in Fig. 6.7 (d_s = 24–55 Å), indicate that the roughness of solution-processed $MAPbI_3$ layers is more significant and the larger d_s is required for the correction. For $MAPbI_3$, however, even after the extra roughness correction, the disagreement of α is still relatively large (~40% at 1.7 eV) probably due to the large d_s values used for the correction. It should be noted that the corrected d_s value of [21] is smaller than that of [20] even though the ε_2 values at $E < E_g$ are larger in [21]. This is caused by higher ε_1 values of $MAPbI_3$ in [21] (or higher N_s in (6.1)). In Fig. 1.3, the simulated $\langle\alpha\rangle$ spectra of $MAPbI_3$ have been compared with the experimental values of [15, 20, 21, 37–42].

All the analysis results obtained from CISe and $MAPbI_3$ indicate a simple fact that quite large artifacts (high α values) are generated when rough surface structures are analyzed improperly. Quite fortunately, the extra roughness correction provides a universal solution for this problem, and the disagreement observed in the reported optical spectra can be reduced drastically after the correction. The above results confirm that the analytical treatment of surface roughness is a critical factor for obtaining accurate optical data in a surface-sensitive SE technique.

6.3 Effect of Surface Roughness on EQE Analysis

For $MAPbI_3$, the effect of the α values on the EQE simulation has been investigated [2]. In this optical simulation, the EQE spectrum of an experimental perovskite solar cell fabricated by a standard solution process [44] was analyzed. In conventional hybrid solar cells having metal back contacts (Ag or Au), however, the back-side reflection is strong (Fig. 12.3 in Vol. 2) and the influence of the optical constants on EQE becomes ambiguous. Thus, to determine the effect of the α spectrum more precisely, the EQE spectrum obtained from a "semi-transparent $CH_3NH_3PbI_3$ solar cell", developed originally for a 4-terminal tandem solar cell ($MAPbI_3$/CIGSe) [44], has been characterized. Figure 6.11a shows the optical model constructed for the $MAPbI_3$ top cell consisting of MgF_2/glass/SnO_2:F/ compact TiO_2 (300 Å)/mesoporous TiO_2-$MAPbI_3$ (1500 Å)/$MAPbI_3$ (2400 Å)/ spiro-OMeTAD/MoO_x/ZnO:Al/(Ni-Al grid)/MgF_2 [2]. For this solar cell, a conversion efficiency of 12.1% with a J_{sc} of 16.7 mA/cm^2, open-circuit voltage of 1.03 V and fill factor of 0.703 is reported [44]. In the optical model, the optical response within the mesoporous TiO_2-$MAPbI_3$ mixed-phase layer (1500 Å) was expressed by the two separate flat layers of a TiO_2 layer (600 Å) and a $MAPbI_3$

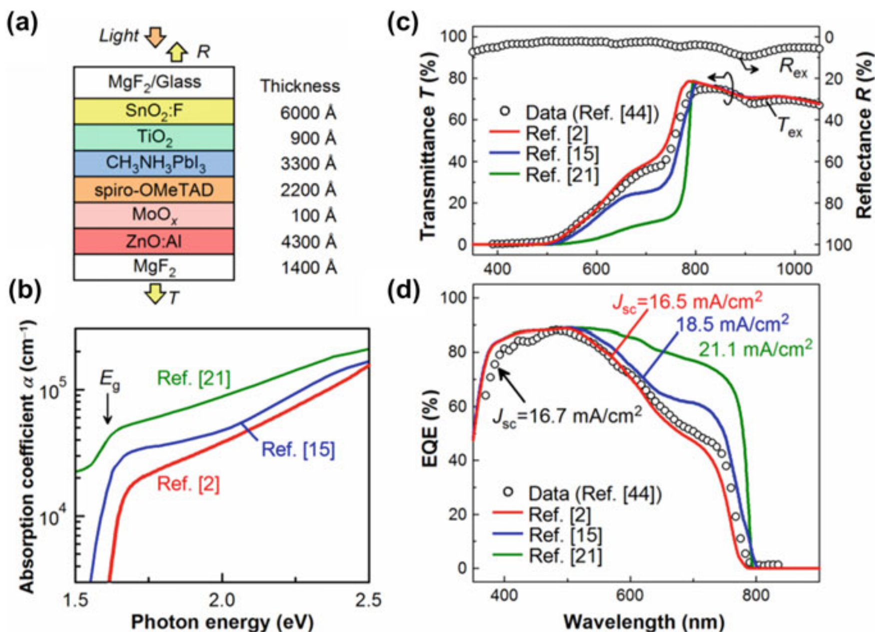

Fig. 6.11 **a** Optical model constructed for a semi-transparent $MAPbI_3$ solar cell consisting of MgF_2/glass/SnO_2:F/compact TiO_2 (300 Å)/mesoporous TiO_2-$MAPbI_3$ (1500 Å)/$MAPbI_3$ (2400 Å)/spiro-OMeTAD/MoO_x/ZnO:Al/(Ni-Al grid)/MgF_2 reported in [44], **b** α spectra of $MAPbI_3$ [2, 15, 21] used in the optical simulation, **c** T and R spectra obtained experimentally from the semi-transparent solar cell (T_{ex}, R_{ex}: open circles) [44], together with the simulated T spectra (solid lines) and **d** EQE spectrum obtained experimentally from the semi-transparent solar cell (open circles) [44], together with the simulated EQE spectra (solid lines). In (**c**) and (**d**), the simulated T and EQE spectra are obtained by assuming different $MAPbI_3$ optical constants represented by the α spectra in (**b**). The J_{sc} values calculated from the EQE spectra are also indicated. The data of (**c**) and (**d**) are taken from [2]

layer (900 Å) assuming a TiO_2 volume fraction of 40% (porosity of 60%) [2], to simplify optical modeling.

Figure 6.11b shows the α spectra of $MAPbI_3$ used for the EQE simulation. Specifically, the dielectric functions that show the highest α ([21] in Fig. 6.10a), the moderate α [15] and the α obtained from the smooth layer ([2] in Fig. 6.10a) were selected. In the optical simulation for [21], however, the nominal light absorption below E_g (1.6 eV) was eliminated by modeling the dielectric function using the Tauc-Lorentz model (Sect. 5.3.7) and this modified optical data was used. For the optical constants of the other layers, the numerical values summarized in Part II (Vol. 2) of this book were used: i.e., MgF_2 (Fig. 13.10 in Vol. 2), glass (Fig. 13.1 in Vol. 2), SnO_2:F (Fig. 11.11 in Vol. 2), TiO_2 (Fig. 11.12 in Vol. 2), $MAPbI_3$ (Fig. 10.2 in Vol. 2), spiro-OMeTAD (Fig. 9.18 in Vol. 2), MoO_x (Fig. 11.8 in Vol. 2), and ZnO:Al (Fig. 11.18 in Vol. 2).

The EQE simulation of the solar cell was performed by using the optical admittance method assuming the flat structure (Sect. 2.2.3 in Vol. 2). In this semi-transparent solar cell, unlike other conventional solar cells, there is a transmission component expressed by $T_{ex} + R_{ex} + A_{ex} = 1$, where the subscript "ex" shows the experimental spectrum. In the simulation, R_{ex} obtained from the actual solar cell was adopted to calculate the A and T spectra more accurately. More details for the EQE calculation can be found in Sects. 16.3 (Vol. 1) and 2.2 (Vol. 2).

Figure 6.11c shows the T_{ex} and R_{ex} spectra of the solar cell reported in [44] (open circles), together with the T spectra calculated from the optical model of Fig. 6.11a (solid lines). In this figure, three T spectra obtained from the different α spectra in Fig. 6.11b are shown. It can be seen that the T spectrum calculated from the optical constants of [2] shows good agreement with T_{ex}, whereas the calculated T values deviate from T_{ex} when the optical constants of [21] (green line) and [15] (blue line) are employed.

Figure 6.11d shows the EQE spectrum reported in [44] (open circles), together with the calculated EQE spectra determined simultaneously in the above simulation (solid lines). The simulated EQE spectra are obtained directly from the calculated A spectra assuming 100% collection of carriers generated within the $MAPbI_3$ layer. As confirmed from Fig. 6.11d, the EQE spectrum calculated from the optical constants of [2] shows excellent agreement with the experimental EQE spectrum, indicating that the T and A (EQE) spectra of a $MAPbI_3$ solar cell fabricated by a standard solution process can be reproduced quite well from the simple optical simulation. The slight disagreement observed between the experimental and simulated EQE spectra at $\lambda > 600$ nm can be attributed to the enhanced carrier generation by light scattering, which is not assumed in the optical simulation. On the other hand, when the $MAPbI_3$ optical constants with higher α values are employed in the calculation, EQE (or light absorption within the $MAPbI_3$) is overestimated seriously particularly in the low α region ($\lambda > 490$ nm) and the resulting T decreases significantly, compared with T_{ex}.

In Fig. 6.10d, the J_{sc} value estimated from the integration of the calculated EQE spectrum at $\lambda > 350$ nm is indicated and J_{sc} obtained using α of [2] (16.5 mA/cm^2) agrees quite well with the experimental J_{sc} of 16.7 mA/cm^2. When the high α values are assumed, J_{sc} is overestimated largely by 1.8 mA/cm^2 [15] and 4.4 mA/cm^2 [21]. Accordingly, the simulated EQE spectrum and the resulting J_{sc} vary considerably with the α spectrum used for $MAPbI_3$. Since the variation of the α spectrum in Fig. 6.11b is caused primarily by the surface roughness, its effect is significant and extra care is necessary for the interpretation of device simulation results.

References

1. S. Minoura, K. Kodera, T. Maekawa, K. Miyazaki, S. Niki, H. Fujiwara, J. Appl. Phys. **113**, 063505 (2013)

2. M. Shirayama, H. Kadowaki, T. Miyadera, T. Sugita, M. Tamakoshi, M. Kato, T. Fujiseki, D. Murata, S. Hara, T.N. Murakami, S. Fujimoto, M. Chikamatsu, H. Fujiwara, Phys. Rev. Appl. **5**, 014012 (2016)
3. H. Fujiwara, S. Fujimoto, M. Tamakoshi, M. Kato, H. Kadowaki, T. Miyadera, H. Tampo, M. Chikamatsu, H. Shibata, Appl. Surf. Sci. **421**, 276 (2017)
4. D.E. Aspnes, Thin Solid Films **89**, 249 (1982)
5. D.E. Aspnes, Phys. Rev. B **25**, 1358 (1982)
6. H. Fujiwara, J. Koh, P.I. Rovira, R.W. Collins, Phys. Rev. B **61**, 10832 (2000)
7. H. Fujiwara, *Spectroscopic Ellipsometry: Principles and Applications* (Wiley, West Sussex, UK, 2007)
8. J. Koh, Y. Lu, C.R. Wronski, Y. Kuang, R.W. Collins, T.T. Tsong, Y.E. Strausser, Appl. Phys. Lett. **69**, 1297 (1996)
9. H. Fujiwara, M. Kondo, A. Matsuda, Phys. Rev. B **63**, 115306 (2001)
10. P. Petrik, L.P. Biró, M. Fried, T. Lohner, R. Berger, C. Schneider, J. Gyulai, H. Ryssel, Thin Solid Films **315**, 186 (1998)
11. D.E. Aspnes, J.B. Theeten, F. Hottier, Phys. Rev. B **20**, 3292 (1979)
12. M. Akagawa, H. Fujiwara, J. Appl. Phys. **110**, 073518 (2011)
13. S. Yamaguchi, Y. Sugimoto, H. Fujiwara, Thin Solid Films **565**, 222 (2014)
14. H.S. Jung, N.-G. Park, Small **11**, 10 (2015)
15. P. Löper, M. Stuckelberger, B. Niesen, J. Werner, M. Filipič, S.-J. Moon, J.-H. Yum, M. Topič, S. De Wolf, C. Ballif, J. Phys. Chem. Lett. **6**, 66 (2015)
16. S. Logothetidis, J. Appl. Phys. **65**, 2416 (1989)
17. C.M. Herzinger, B. Johs, W.A. McGahan, J.A. Woollam, W. Paulson, J. Appl. Phys. **83**, 3323 (1998)
18. A. Kreuter, G. Wagner, K. Otte, G. Lippold, A. Schindler, M. Schubert, Appl. Phys. Lett. **78**, 195 (2001)
19. P.D. Paulson, R.W. Birkmire, W.N. Shafarman, J. Appl. Phys. **94**, 879 (2003)
20. G. Xing, N. Mathews, S.S. Lim, N. Yantara, X. Liu, D. Sabba, M. Grätzel, S. Mhaisalkar, T. C. Sum, Nat. Mater. **13**, 476 (2014)
21. J.M. Ball, S.D. Stranks, M.T. Hörantner, S. Hüttner, W. Zhang, E.J.W. Crossland, I. Ramirez, M. Riede, M.B. Johnston, R.H. Friend, H.J. Snaith, Energy Environ. Sci. **8**, 602 (2015)
22. T. Kawashima, S. Adachi, H. Miyake, K. Sugiyama, J. Appl. Phys. **84**, 5202 (1998)
23. M.I. Alonso, K. Wakita, J. Pascual, M. Garriga, N. Yamamoto, Phys. Rev. B **63**, 075203 (2001)
24. W. Horig, H. Neumann, H. Sobotta, Thin Solid Films **48**, 67 (1978)
25. J.R. Tuttle, D. Albin, R.J. Matson, R. Noufi, J. Appl. Phys. **66**, 4408 (1989)
26. C.A. Durante Rincon, E. Hernandez, M.I. Alonso, M. Garriga, S.M. Wasim, C. Rincon, M. Leon, Mater. Chem. Phys. **70**, 300 (2001)
27. S. Han, F.S. Hasoon, H.A. Al-Thani, A.M. Hermann, D.H. Levi, Appl. Phys. Lett. **86**, 021903 (2005)
28. S. Han, C. Persson, F.S. Hasoon, H.A. Al-Thani, A.M. Hermann, D.H. Levi, Phys. Rev. B **74**, 085212 (2006)
29. S. Han, F.S. Hasoon, A.M. Hermann, D.H. Levi, Appl. Phys. Lett. **91**, 021904 (2007)
30. S. Theodoropoulou, D. Papadimitriou, K. Anestou, C. Cobet, N. Esser, Semicond. Sci. Technol. **24**, 015014 (2009)
31. F.A. Abou-Elfotouh, G.S. Horner, T.J. Coutts, M.W. Wanlass, Solar Cells **30**, 473 (1991)
32. M.L. Hidalgo, M. Lachab, A. Zouaoui, M. Alhamed, C. Llinares, J.P. Peyrade, J. Galibert, Phys. Status Solidi B **200**, 297 (1997)
33. T. Begou, J.D. Walker, D. Attygalle, V. Ranjan, R.W. Collins, S. Marsillac, Phys. Status Solidi RRL **5**, 217 (2011)
34. S. Minoura, T. Maekawa, K. Kodera, A. Nakane, S. Niki, H. Fujiwara, J. Appl. Phys. **117**, 195703 (2015)
35. T. Hara, T. Maekawa, S. Minoura, Y. Sago, S. Niki, H. Fujiwara, Phys. Rev. Appl. **2**, 034012 (2014)

36. J.E. Jaffe, A. Zunger, Phys. Rev. B **29**, 1882 (1984)
37. G. Xing, N. Mathews, S. Sun, S.S. Lim, Y.M. Lam, M. Grätzel, S. Mhaisalkar, T.C. Sum, Science **342**, 344 (2013)
38. S. Sun, T. Salim, N. Mathews, M. Duchamp, C. Boothroyd, G. Xing, T.C. Sum, Y.M. Lam, Energy Environ. Sci. **7**, 399 (2014)
39. S. De Wolf, J. Holovsky, S.-J. Moon, P. Löper, B. Niesen, M. Ledinsky, F.-J. Haug, J.-H. Yum, C. Ballif, J. Phys. Chem. Lett. **5**, 1035 (2014)
40. Q. Lin, A. Armin, R.C.R. Nagiri, P.L. Burn, P. Meredith, Nat. Photon. **9**, 106 (2015)
41. Y. Jiang, M.A. Green, R. Sheng, A. Ho-Baillie, Sol. Eng. Mater. Sol. Cells **137**, 253 (2015)
42. A.M.A. Leguy, Y. Hu, M. Campoy-Quiles, M.I. Alonso, O.J. Weber, P. Azarhoosh, M. van Schilfgaarde, M.T. Weller, T. Bein, J. Nelson, P. Docampo, P.R.F. Barnes, Chem. Mater. **27**, 3397 (2015)
43. M. Shirayama, M. Kato, T. Miyadera, T. Sugita, T. Fujiseki, S. Hara, H. Kadowaki, D. Murata, M. Chikamatsu, H. Fujiwara, J. Appl. Phys. **119**, 115501 (2016)
44. L. Kranz, A. Abate, T. Feurer, F. Fu, E. Avancini, J. Löckinger, P. Reinhard, S.M. Zakeeruddin, M. Grätzel, S. Buecheler, A.N. Tiwari, J. Phys. Chem. Lett. **6**, 2676 (2015)

Part II
Characterization of Materials and Structures

Chapter 7
Ex Situ Analysis of Multijunction Solar Cells Based on Hydrogenated Amorphous Silicon

Zhiquan Huang, Lila R. Dahal, Prakash Koirala, Wenhui Du, Simon Cao, Xunming Deng, Nikolas J. Podraza and Robert W. Collins

Abstract Multiple angle of incidence spectroscopic ellipsometry (SE) has been applied ex situ to support a roll-to-roll photovoltaics (PV) technology applying multijunction thin film hydrogenated amorphous silicon (*a*-Si:H) based device structures deposited on flexible steel foil. This application demonstrates how PV specialists can adopt currently-available SE methodologies to assist in PV production line development, operation, and troubleshooting. Because this thin film production line employs optically opaque steel foil exclusively as the substrate, a reflection optical experiment based on SE is the natural approach for characterization of the output of the line in terms of layer thicknesses and optical properties. Such information is of direct interest in PV as it enables prediction of the photocurrent generated by solar cells and modules. In this chapter, SE approaches are described for extracting the optical properties of a steel foil substrate and the component films deposited on this substrate that comprise hydrogenated amorphous silicon-germanium alloy (a-$Si_{1-x}Ge_x$:H) tandem PV in the *n*-*i*-*p* device configuration. These approaches apply analytical models for the complex dielectric functions that describe the doped and intrinsic amorphous semiconductors and transparent conducting oxide (TCO) layers. Application of these models in analyses of measurements performed on complete tandem device structures enables characterization of the thicknesses of the top TCO, which also serves as an anti-reflection coating, and the top *p*-type window layer, which controls the external quantum efficiency of the device in the blue, as well as the bandgaps of the top cell *p*-layer and *i*-layer, and in some cases the bottom cell *i*-layer. Limitations occur in such analyses when absorption by overlying layers reduces the spectral range of light that reflects from underlying layers, coupled with the similarity in the complex dielectric functions of adjoining underlying layers over the reduced spectral range. For example, it is

Z. Huang · L. R. Dahal · P. Koirala · W. Du · S. Cao · X. Deng · N. J. Podraza (✉)
R. W. Collins
Department of Physics & Astronomy and Center for Photovoltaics Innovation & Commercialization, University of Toledo, Toledo, OH 43606, USA
e-mail: Nikolas.Podraza@utoledo.edu

© Springer International Publishing AG, part of Springer Nature 2018

H. Fujiwara and R. W. Collins (eds.), *Spectroscopic Ellipsometry for Photovoltaics*, Springer Series in Optical Sciences 212,
https://doi.org/10.1007/978-3-319-75377-5_7

difficult to separate the *i*-layer and underlying *n*-layer thicknesses for this reason. It is also difficult to characterize the bottom cell *i*-layer when its bandgap is close to that of the overlying top cell *i*-layer, e.g. in a same-bandgap tandem. In spite of these limitations, analysis of multiple angle SE data establishes critical information on structure and properties that provides guidance to thin film PV specialists on the operation of PV manufacturing equipment and on the expected performance of the manufactured product.

7.1 Introduction and Overview

Hydrogenated silicon (Si:H) thin films serve as the foundation for one of the three major commercialized thin film photovoltaics (PV) technologies [1]. The motivation for developing thin film solar cells incorporating amorphous Si:H (*a*-Si:H) is its strong above-bandgap absorption relative to crystalline Si (*c*-Si) due to the loss of crystal momentum conservation that occurs in an amorphous material. This enables the use of very thin *a*-Si:H absorber layers (~0.3 μm) in device structures. Because the doped forms of *a*-Si:H exhibit high defect concentrations, *a*-Si:H solar cells are fabricated in *p*-*i*-*n* or *n*-*i*-*p* configurations with the *p*-type layer (or *p*-layer) serving as a front window layer of the cell and the *n*-type layer (or *n*-layer) operating with the *p*-layer to generate an electric field across the intrinsic absorber layer (or *i*-layer) [2]. Any light absorbed in the doped layers does not generate photocurrent, and as a result, a very thin wide bandgap Si:H *p*-layer is needed to serve as the window layer of the solar cell.

Although the bandgap of intrinsic *a*-Si:H suitable for the absorber layer of the solar cell can be adjusted through the use of H_2 dilution of SiH_4 in the fabrication process, the accessible range of ~1.6–1.8 eV is above the optimum bandgap of ~1.3–1.4 eV for efficient single-junction solar cells. Thus, in the highest efficiency Si:H based solar cells, tandem or triple-junction *p*-*i*-*n* or *n*-*i*-*p* configurations have been employed. These designs exploit top cell *a*-Si:H with a typical bandgap of 1.7 eV and bottom cell *a*-$Si_{1-x}Ge_x$:H or hydrogenated nanocrystalline Si:H (*nc*-Si:H) with bandgaps of 1.4 and 1.1 eV, respectively. Because the grain size of *nc*-Si:H exceeds the range associated with quantum effects in single crystalline silicon (*c*-Si), the bandgap of this material is similar to that of *c*-Si. Although the effects of grain boundaries result in stronger absorption compared to *c*-Si, the above-gap absorption is still weak in *nc*-Si:H compared to *a*-Si:H, and as a result, much thicker *nc*-Si:H layers are required for the bottom cell of the *a*-Si:H/*nc*-Si:H tandem. In contrast, very thin *a*-$Si_{1-x}Ge_x$:H *i*-layers (~0.2 μm) can be used in both tandem and triple-junction devices.

A traditional advantage of Si:H based solar cell technology lies in the ability to fabricate the devices on flexible substrates such as polymer and steel foils in

roll-to-roll processes. This enables a wider range of applications for photovoltaic energy conversion. When steel foils are used, then the solar cell is fabricated in the substrate configuration so that the associated device structure is deposited in the *n-i-p* semiconductor sequence. In contrast, when rigid glass sheets are used, then the cell is fabricated most often in the superstrate configuration and the associated structure is deposited in the *p-i-n* sequence. In both cases, the solar irradiance enters through the *p*-layer which is deposited last in the substrate configuration and first in the superstrate configuration. The single-junction and tandem *n-i-p* substrate configurations are shown in Fig. 7.1 along with representative thickness and bandgap values. These configurations that employ steel foil substrates are relevant to the examples presented in this chapter.

Multijunction Si:H based solar cells, exhibit greater complexity as shown in Fig. 7.1b than the cells of other thin film PV technologies. Other PV technologies employ single junctions due to absorber layer bandgaps closer to the optimum (CdTe, $E_g \sim 1.5$ eV; $CuIn_{0.7}Ga_{0.3}Se_2$, $E_g \sim 1.2$ eV). As a result, spectroscopic ellipsometry (SE) methods for multijunction structure and optical property determinations are particularly useful [3]. In this chapter, the application of ex situ multiple angle of incidence SE will be described for analysis of the components of three different single-junction a-$Si_{1-x}Ge_x$:H *n-i-p* solar cells (narrow, middle, and wide bandgap) and two different tandem *n-i-p* cells using middle/wide (a-$Si_{1-x}Ge_x$:H/a-Si:H) and narrow/middle (a-$Si_{1-y}Ge_y$:H/a-$Si_{1-x}Ge_x$:H; $y > x$) bandgap materials in the configurations shown in the schematics of Fig. 7.1 [4].

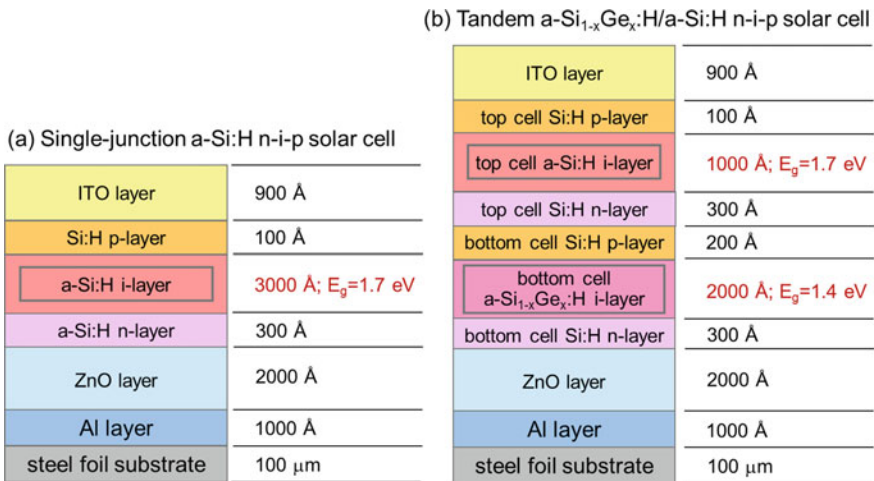

Fig. 7.1 Schematic configurations for **a** single-junction a-Si:H and **b** tandem a-$Si_{1-x}Ge_x$:H/a-Si:H solar cells in the *n-i-p* or substrate configuration shown on flexible steel foil

7.2 General Strategy and Approaches

Ex situ SE analysis of structures as complicated as tandem solar cells can be made possible through determination of the complex dielectric functions of the individual layer components in simplified but relevant sample structures. Ideally, once the dielectric functions are known, the complicated multilayer stacks can be analyzed by least squares regression, yielding photon energy independent structural parameters including interface roughness, bulk, and surface roughness layer thicknesses and the roughness layer compositions [3]. The dielectric functions of the roughness layers used in the analysis are obtained from an effective medium theory assuming a mixture of the underlying and overlying materials using compositions as free parameters. Among such theories, the Bruggeman effective medium approximation (EMA) has been demonstrated to provide the best fits in such analyses [5]. Thus, in an ideal analysis of the complicated multilayer stack, only thicknesses and compositions would be the free parameters.

The assumption underlying the idealized ex situ SE data analysis procedure as described above is that the complex dielectric functions obtained from the simplified sample structures are applicable to the complicated structures of the complete solar cell. In reality, however, the dielectric functions for amorphous and nano/polycrystalline solar cell materials can depend on the nature of the substrate and on the preparation conditions. For complicated structures, however, it is not possible to extract one or more unknown dielectric functions point-by-point as a function of photon energy (>100 values) along with all the required structural parameters. An alternative approach involves fitting the dielectric functions deduced from the simplified sample structures using physics-based analytical models with a handful of photon energy independent parameters (<10 values) [6]. Once the appropriate analytical expression is identified from optimization of dielectric function fitting, then the expression can be introduced to describe the dielectric function in the fitting of the complicated multilayer stacks. In this way, the determination of dielectric functions in these stacks is reduced to determining not >100 values, but rather <10 values. With this more realistic approach, the analysis of the complicated multilayer stack involves determination of thicknesses, roughness layer compositions, and photon energy independent parameters that describe the dielectric functions.

An example of an analytical expression versus photon energy deduced for the complex dielectric function of amorphous semiconductors is the Cody-Lorentz expression given by:

$$\varepsilon_2 = \begin{cases} \frac{E_1}{E}\exp\left(\frac{(E - E_g - E_t)}{E_u}\right) & 0 < E \leq (E_g + E_t) \\ G(E)L(E) = \frac{(E-E_g)^2}{(E-E_g)^2 + E_p^2} \times \frac{AE_0\Gamma E}{(E^2 - E_0^2)^2 + \Gamma^2 E^2}; & E > (E_g + E_t) \end{cases} \quad (7.1)$$

where

$$E_1 = (E_g + E_t)G(E_g + E_t)L(E_g + E_t), \tag{7.2}$$

and ε_1 is given by a Kramers-Kronig integral of ε_2 [7]. In this expression, E_u is the Urbach tail slope, E_g is the bandgap defined by Cody's method [8] through the prescription $G(E) = [(E - E_g)^2/[(E - E_g)^2 + E_p^2]$, $E_g + E_t$ is the tail-to-band-edge transition energy, E_p is the band-edge-to-oscillator transition energy, and E_0 is the resonance energy of the Lorentz oscillator $L(E)$. A and Γ are the amplitude and broadening parameter of the Lorentz oscillator. For SE of a device quality amorphous semiconductor, the Urbach tail can be neglected by fixing $E_t = 0$, which yields $E_1 = 0$. With this expression for ε_2, along with a constant contribution to ε_1, designated here as ε_{1o}, the number of photon energy independent parameters that define $\varepsilon(E)$ is six: $\{\varepsilon_{1o}, E_g, E_p, E_0, A, \Gamma\}$. Further simplification is possible by setting $\varepsilon_{1o} = 1$, based on the assumption that there are no higher energy resonances above E_0 that contribute to ε_1. These equations are referred to as physics based, as they are derived based on the assumptions that the absorption onset is defined by valence and conduction bands with square-root densities of states versus hole and electron energies and that the dipole matrix element is photon energy independent.

The Cody-Lorentz oscillator of (7.1) and (7.2) is similar in nature to the Tauc-Lorentz oscillator [9, 10] in that it defines a bandgap energy, E_g, as well as the parameters associated with an above-gap Lorentzian absorption feature. The models behave differently in the absorption onset region, in particular at photon energies E just above E_g. In this region, the Tauc-Lorentz model follows the Tauc Law, with $G(E) \propto [(E - E_g)^2/E^2]$ in (7.1), based on the assumption of a constant momentum matrix element versus E, whereas the Cody-Lorentz model simulates the function $G(E) \propto (E - E_g)^2$ just above E_g based on the assumption of a constant dipole matrix element first proposed by Cody [8] and subsequently supported by a combination of electron spectroscopies [11]. In order to simulate the latter function for $G(E)$ with E near E_g, while ensuring the limit $G(E) \rightarrow 1$ for $E >> E_g$, then the expression $G(E) = [(E - E_g)^2/[(E - E_g)^2 + E_p^2]$ is used as shown in (7.1). The Cody-Lorentz model differs from the Tauc-Lorentz model in that it includes an additional parameter E_p, which allows one to adjust the transition energy between the band edge region and the Lorentz oscillator region.

As an example of these approaches, Fig. 7.2 shows five parameter fits to the complex dielectric function of an a-$Si_{1-x}Ge_x$:H alloy with $x = 0.34$, measured in situ under vacuum after growth by plasma-enhanced chemical vapor deposition and cooling to room temperature. A c-Si substrate was used and real time SE was performed during growth in order to establish accurate values of the bulk and surface roughness layer thicknesses. These thicknesses were then used to extract the dielectric functions of the bulk layer by exact inversion of the ellipsometry angles (ψ, Δ), yielding its complex dielectric function $(\varepsilon_1, \varepsilon_2)$. Table 7.1 shows the best fit parameters for $(\varepsilon_1, \varepsilon_2)$ as described by the Tauc-Lorentz and Cody-Lorentz expressions obtained for the alloy of Fig. 7.2 along with those for alloys having

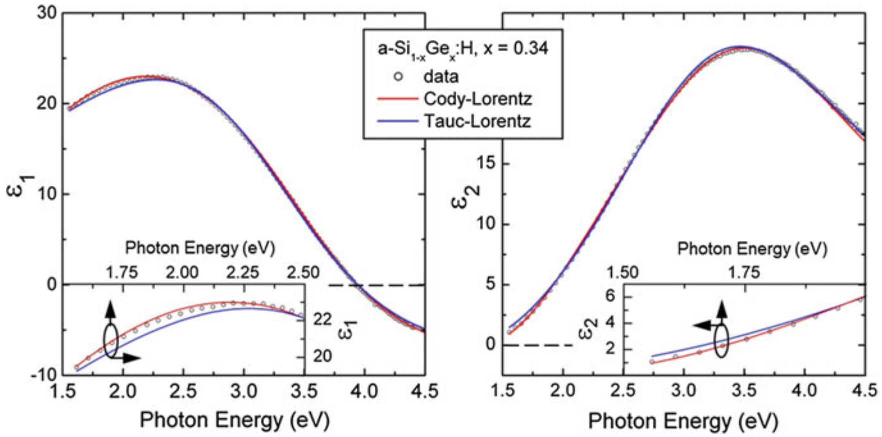

Fig. 7.2 Complex dielectric function measured in situ at room temperature (points) for an a-$Si_{1-x}Ge_x$:H alloy thin film with x = 0.34. Best fits employ five-parameter Tauc-Lorentz and Cody-Lorentz expressions to the dielectric function. For the Cody-Lorentz fitting expression ε_{1o} was fixed at unity. The best fit parameters are given in Table 7.1

compositions $x = 0$ and 0.17. By fixing the constant term in ε_1 for the Cody-Lorentz expression ($\varepsilon_{1o} = 1$), five parameter fits are performed in each case. The value of σ in Table 7.1 is a measure of the quality of the fit, and demonstrates the improvement possible through the Cody-Lorentz expression as described by (7.1) and (7.2).

Even with the simplest general form of the Cody-Lorentz oscillator, five free parameters are introduced, and if the dielectric functions of the remaining materials of the complicated device structure require similar complexity, then fitting continues to be a challenge due to the sheer number of free parameters. In addressing this problem, Ferlauto et al. [7] found that for high quality intrinsic amorphous semiconductor alloys used in solar cells, the four parameters $\{E_p, E_0, A, \Gamma\}$ could be expressed as piecewise linear functions of the most important parameter E_g. As a result, the dielectric function of an intrinsic PV-quality amorphous semiconductor can be completely specified using a single parameter, E_g, which is the most important one because it controls the performance of the material in devices. For poorer quality materials, a second parameter such as a void volume fraction can be introduced. The success in this particular case suggests a methodology that could be applicable for a variety of PV material systems.

Real time and mapping SE are effective approaches for obtaining dielectric functions for parameterization, as described above, since the sample can be probed in a large number of states [12, 13]. In real time SE, as long as the dielectric function of a growing material is independent of thickness, a point-by-point representation of the dielectric function of the material and the structural parameters of the stack can be determined through multi-time analysis. Similarly in mapping SE, as long as the thickness of a film is non-uniform over the area and its dielectric function does not depend on thickness, the dielectric function and the structural

Table 7.1 Best fit parameters obtained in analyses of the complex dielectric functions for three a-$Si_{1-x}Ge_x$:H alloy thin films with $x = 0$, 0.17, and 0.34 as measured in situ at room temperature after deposition with results for $x = 0.34$ shown in Fig. 7.2. Five free parameters were employed in both Tauc-Lorentz and Cody-Lorentz expressions. In the latter expression, the constant contribution to the real part of the dielectric function ε_{1o} was fixed at unity. The fit quality σ describes the root mean square deviation between the measured and best fit dielectric functions. The results demonstrate the consistent improvement in fit made possible by the Cody-Lorentz expression

x	Model	A (eV)	Γ (eV)	E_0 (eV)	E_g (eV)	E_p (eV)	ε_{1o}	σ
0.00	TL	207.1 ± 4.8	2.269 ± 0.017	3.644 ± 0.009	1.65 ± 0.02	–	0.06 ±0.10	0.29
	CL	80.7 ± 1.2	2.406 ± 0.009	3.823 ± 0.009	1.80 ± 0.02	0.97 ± 0.04	1	0.17
0.17	TL	197.4 ± 3.6	2.848 ± 0.019	3.599 ± 0.009	1.47 ± 0.01	–	0.35 ±0.082	0.21
	CL	93.7 ± 1.6	3.037 ± 0.012	3.787 ± 0.010	1.49 ± 0.02	1.20 ± 0.05	1	0.15
0.34	TL	171.1 ± 3.5	3.012 ± 0.021	3.458 ± 0.009	1.18 ± 0.02	–	0.04 ±0.09	0.23
	CL	82.3 ± 1.0	3.051 ± 0.012	3.691 ± 0.009	1.29 ± 0.02	0.82 ± 0.04	1	0.16

parameters of the stack can be determined through a multi-spot analysis. Ex situ SE analysis at a single location is a challenge because the sample is accessible in only one state. In this case, one seeks to gain the additional information content by varying the angle of incidence [14, 15] which serves to vary the penetration depth of the probe beam. In the multiple angle of incidence method, two or three structural parameters can often be determined in addition to a point-by-point dielectric function.

7.3 Substrate and Individual Solar Cell Materials

Figure 7.3 shows the outcome of multiple angle of incidence SE, including the point-by-point dielectric function and structural parameters, performed on an opaque sample of stainless steel foil used as a substrate for roll-to-roll deposition of multijunction a-$Si_{1-x}Ge_x$:H solar cells [4]. SE data were collected at three angles of incidence with a rotating-compensator multichannel ellipsometer (J.A. Woollam Co., M2000-DX) [16, 17]. From this data set, a surface roughness layer thickness and a void volume percent in the roughness layer can be determined in addition to the point-by-point dielectric function. The mean-square error (MSE) presented in Fig. 7.3 employs the deviations between measured and calculated Mueller matrix parameters $N = \cos 2\psi$, $C = \sin 2\psi \cos \Delta$, and $S = \sin 2\psi \sin \Delta$. The stainless steel is

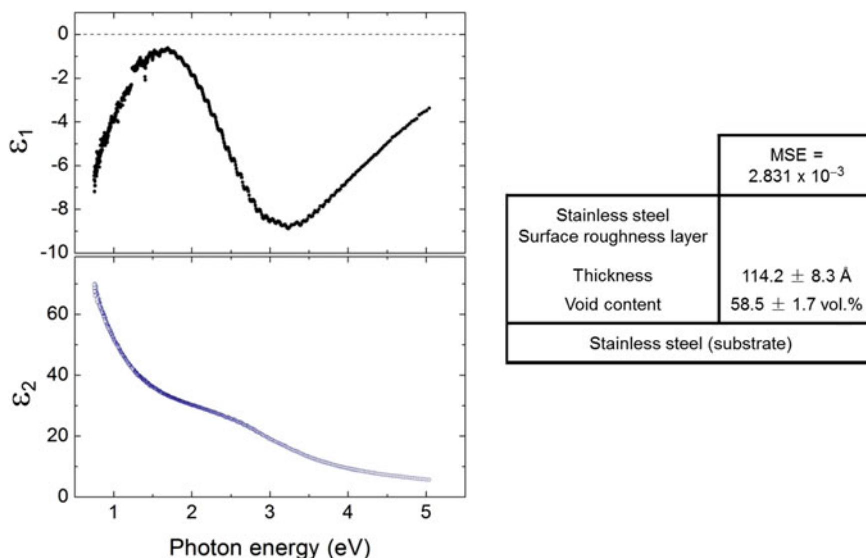

Fig. 7.3 (Left) Real (ε_1) and imaginary (ε_2) parts of the complex dielectric function of stainless steel obtained at room temperature by fitting ex situ SE data (ψ, Δ) at three angles of incidence, 55°, 65°, and 75°. The sample structure deduced in the analysis is shown at right

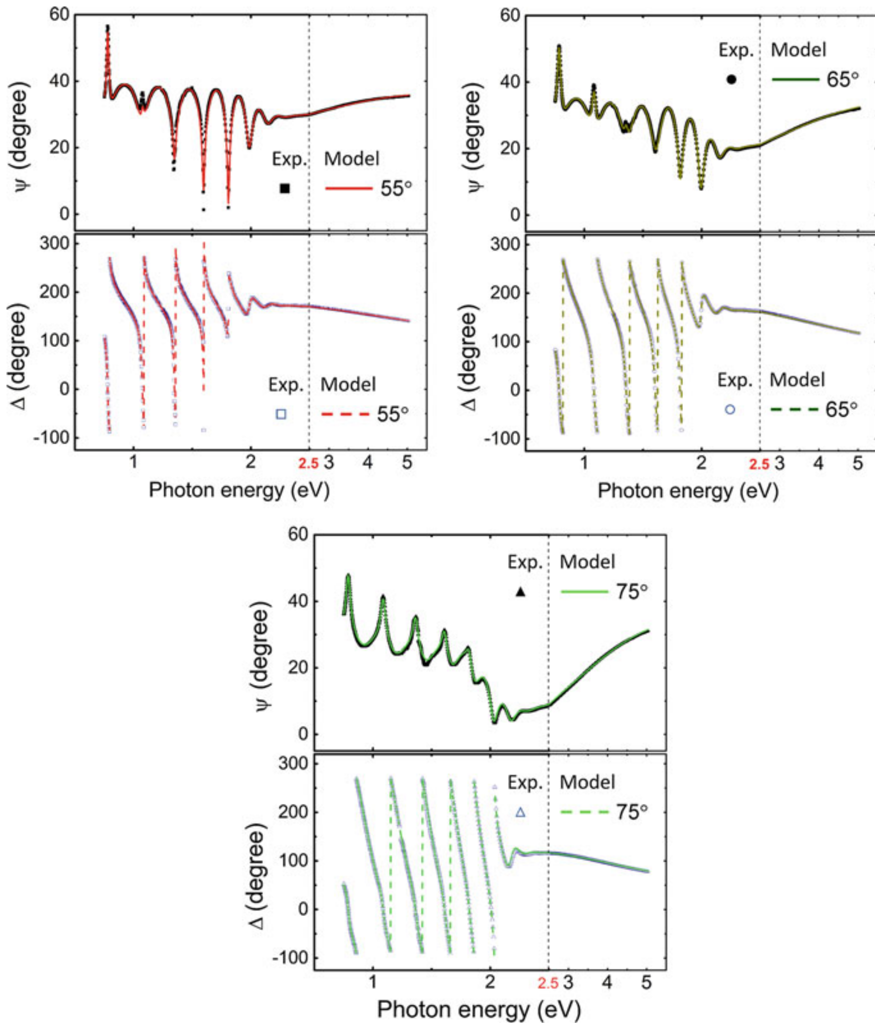

Fig. 7.4 SE data for a sample consisting of an *a*-Si:H *i*-layer on stainless steel at angles of incidence of 55°, 65°, and 75° (points). The lines represent the best ten-parameter fit; the data and their best fit are indistinguishable on these scales

used as a substrate in the plasma-enhanced chemical vapor deposition (PECVD) of intrinsic, *p*, and *n* type *a*-Si:H.

Figure 7.4 shows experimental (ψ, Δ) spectra at three angles of incidence for a steel/(*a*-Si:H *i*-layer) sample deposited by PECVD for the purpose of evaluating its structural and dielectric function parameters. In this analysis, the sample structure consists of steel/(interface-roughness)/*a*-Si:H/(surface-roughness), where the interface roughness derives from the surface roughness on the steel, and the surface roughness on the *a*-Si:H has both substrate-induced and film-growth related

Table 7.2 Parameters added step by step in order to analyze SE data for an *a*-Si:H *i*-layer on a stainless steel substrate and to obtain the best fit *p*-parameter results with $p = 1, 2, \ldots, 11$. Each additional parameter is selected based on its ability to provide the largest reduction in the mean square error (MSE) as given in the third column

# of fitting parameters	Parameter added to improve MSE	MSE (10^{-2})
1	d_b	11.14
2	E_g	7.229
3	d_s	3.529
4	d_i	3.116
5	Γ	3.074
6	E_0	2.481
7	f_{mi}	2.469
8	f_{vs}	2.465
9	f_{vb}	2.467
10	E_p	2.468
11	A	2.465

components. Because of the possibility of five structural parameters, three thicknesses and two roughness layer compositions, along with one unknown dielectric function, multiple angle data analysis is a challenge. In this case, the dielectric function is assumed to follow (7.1) and (7.2) with five free parameters, yielding a total of ten parameters in all. A step-by-step analysis is used to identify the most important of the parameters as shown in Table 7.2 and Fig. 7.5.

In step-by-step analysis, one starts with fixed values for all parameters, and allows each to vary one at a time and identifies the 1, 2, 3, … variable parameter model that provides the lowest mean-square error (MSE). The initial assigned values include a nominal bulk layer thickness d_b, a nominal bandgap E_g, and zero interface and surface roughness layer thicknesses, $d_i = d_s = 0$. Unless independently varied, the Cody-Lorentz parameters are linked to the value of E_g. Once an interface or surface roughness layer is introduced, the volume percent of *a*-Si:H in the interface layer f_{mi} or the volume percent of void in the surface layer f_{vs} becomes an allowable variable to evaluate with the fixed default values being 50 vol.%. In addition, the presence of voids in the bulk layer can be evaluated applying the EMA, and the void content f_{vb} can serve as an 11th possible parameter. Table 7.2 indicates that d_b is the parameter that generates the 1-parameter model with lowest MSE. Variations in d_b, d_s, and E_g combine to generate the best 3-parameter fit. Larger numbers of variable parameters generate weaker improvements in the MSE, indicating that the analysis is less sensitive to the buried interface roughness layer, and that the relationships of Ferlauto et al. [7] give relatively good estimates of $\{\Gamma, E_0, E_p, \text{and } A\}$, given the value of E_g. The results also indicate that the amplitude A can be used as a parameter linked to E_g, and that the bulk layer void percentage f_{vb} is not needed to reduce the oscillator amplitude relative to the linked value A.

Figure 7.6 shows a plot of the best fit analytical expression for the dielectric function of the intrinsic *a*-Si:H film using all five values of $\{E_g, \Gamma, E_0, E_p, \text{and } A\}$ as

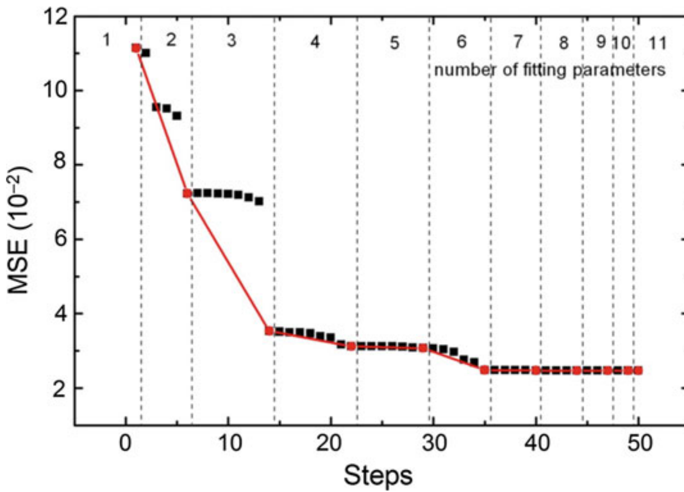

Fig. 7.5 Step by step MSE reduction performed by adding one fitting parameter at a time. Starting with the thickness of the *i*-layer as a single variable, each additional parameter was subsequently incorporated into the model for the sample. It was shown that the addition of E_g as a fitting parameter provided the greatest improvement in the MSE among all 2-parameter attempts. The remaining nine parameters were evaluated similarly. The parameters providing the best *p*-parameter fit for $p = 1, 2, \ldots, 11$ are highlighted as the circles, connected by a line

free in a 10-parameter model. Figure 7.7 shows the location of these parameters on an E_g plot relative to the Ferlauto et al. [7] relationships for high quality intrinsic PV materials. These results indicate that best fit values of E_0, E_p, and A are close to the piece-wise linear relations at left appropriate for *a*-Si:H and its alloys with Ge. The broadening parameter Γ for the intrinsic *a*-Si:H is larger than that obtained for the PV quality sample set as measured by Ferlauto et al., however; this is an indication that the material quality is poor. According to the relation $\Gamma = \hbar/\tau$, where $\hbar$ is Planck's constant h divided by 2π and τ is the scattering time, it is reasonable to expect that excited carriers in the *a*-Si:H are scattered by disorder and defects. A shorter τ and larger Γ implies greater disorder and/or a higher defect concentration. This may be expected due to the direct deposition on the steel which may result in the diffusion of metallic contaminants into the *a*-Si:H. The ten parameters are given along with the confidence limits and final 10-parameter MSE in Table 7.3. Very high sensitivity to the bandgap value is evident in this table. Corresponding results are shown in Figs. 7.6 and 7.7, and Table 7.3 for the *n*-type and *p*-type *a*-Si:H samples, each on a steel foil substrate. Of interest is the wider bandgap of the *p*-layer, as it is normally deposited with higher H_2 dilution to improve its functionality as a window layer. Also of interest is the larger broadening parameters for the two doped *a*-Si:H samples attributed to dopant-induced defects.

A set of samples including steel/Al, steel/Al/ZnO, and steel/Al/ZnO/ITO was prepared by sputtering of Al, ZnO, and In_2O_3:Sn (ITO) targets and studied by multiple angle of incidence SE. The goal is to determine the complex dielectric

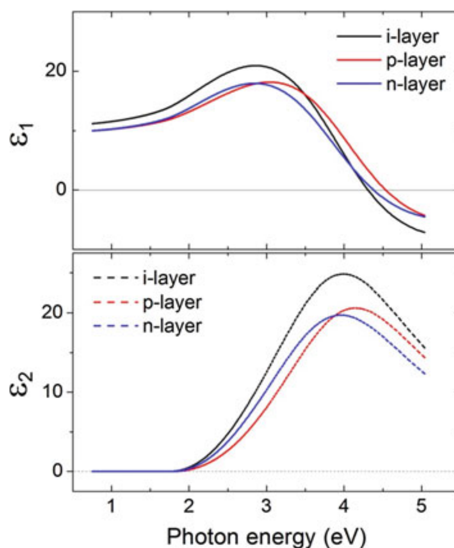

Fig. 7.6 Real (ε_1) and imaginary (ε_2) parts of the *i*-layer, *p*-layer, and *n*-layer complex dielectric functions obtained at room temperature by the step-by-step MSE reduction method. A Cody-Lorentz parameterization was assumed with five free parameters in each case

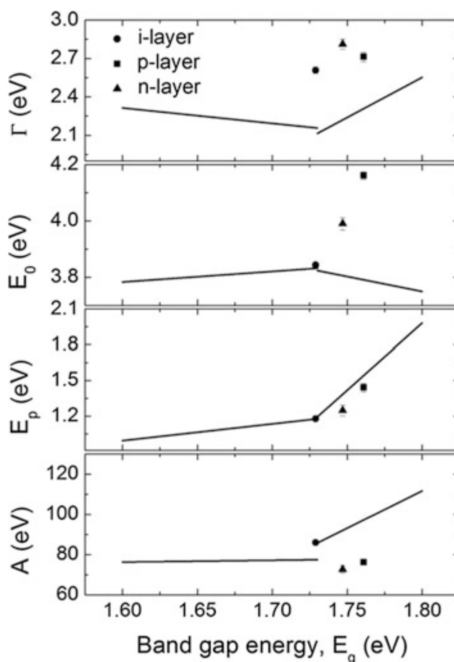

Fig. 7.7 Room temperature Cody-Lorentz parameters Γ, E_0, E_p, and A plotted versus the best fit bandgap energy (E_g) from the final best fitting results for undoped and doped samples of *a*-Si:H deposited on stainless steel substrates. All five Cody-Lorentz parameters were varied. The solid lines are the results for a sample set of photovoltaic quality *a*-$Si_{1-x}Ge_x$:H (left line) and *a*-$Si_{1-x}C_x$:H (right line) materials given in the study by Ferlauto et al. [6, 7]

functions of the Al back-contact and back-reflector, the ZnO back-reflector component, and the ITO top contact, also serving as an anti-reflection coating. These are the multilayer components of the solar cell structure as shown in Fig. 7.1. In fact,

Table 7.3 Best fitting structural and room temperature Cody-Lorentz parameters along with their confidence limits for *i*, *p*, and *n*-layers deposited on stainless steel, as determined by step-by-step MSE reduction. All five Cody-Lorentz parameters were varied in the analysis

	Model with all five Cody-Lorentz parameters varied		
	i	*p*	*n*
MSE	2.465×10^{-2}	1.717×10^{-2}	1.967×10^{-2}
Surface roughness layer thickness (Å)	51.2 ± 2.2	59.5 ± 1.9	39.9 ± 1.5
Roughness void vol. percentage (vol.%)	50.7 ± 2.6	75.2 ± 1.7	48.1 ± 2.4
Bulk layer thickness (Å)	5816 ± 16	779.2 ± 3.5	1338 ± 2
EMA interface (stainless-steel/a-Si:H) roughness layer thickness (Å)	137.3 ± 59.1	41.5 ± 16.2	80.7 ± 8.8
Interface stainless steel volume percentage (vol.%)	67.8 ± 17.6	71.4 ± 12.5	59.6 ± 6.9
A (eV)	85.91 ± 0.27	76.07 ± 1.38	72.61 ± 1.75
Γ (eV)	2.608 ± 0.025	2.712 ± 0.036	2.812 ± 0.039
E_0 (eV)	3.843 ± 0.009	4.160 ± 0.013	3.990 ± 0.022
E_g (eV)	1.729 ± 0.003	1.761 ± 0.007	1.747 ± 0.006
E_p (eV)	1.177 ± 0.012	1.441 ± 0.037	1.247 ± 0.046
Bulk layer void volume percentage vol.% (fixed)	0	0	0

the steel/Al and steel/Al/ZnO samples are in the relevant sequence for solar cell fabrication; however, for the third sample of the set, the ITO is added to the structure for convenience in the deposition and analysis. In the actual solar cell structure, the ITO is added to the top of the final *p*-layer as shown in Fig. 7.1. Thus, the possibility of a dependence of the ITO dielectric function on the nature of the underlying film must be considered. Figure 7.8 shows the results of the analysis of the opaque Al coating on the steel foil substrate. In addition to the point-by-point determination of the complex dielectric function of the Al bulk layer, the surface roughness layer thickness and void content in the surface roughness layer can be obtained. The point-by-point dielectric function of Al can be used in the subsequent analyses of the steel/Al/ZnO and the steel/Al/ZnO/ITO samples.

Because the Al film is opaque, this sample structure is simple enough for a point-by-point complex dielectric function analysis, even though a parameterized form of this dielectric function is available [18]. For the steel/Al/ZnO sample, however, the structure is more complicated and an analytical form for the dielectric function of the polycrystalline ZnO is needed. A general expression for the dielectric function of a polycrystalline transparent conducting oxide can be given as follows

$$\varepsilon(E) = \varepsilon_{1o} + \varepsilon_D(E) + \sum_n \varepsilon_{CP,n}(E), \tag{7.3}$$

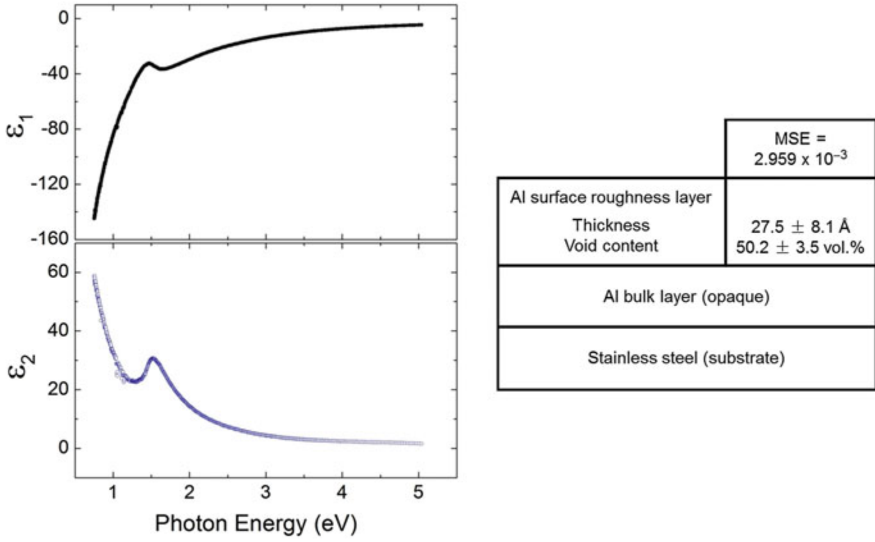

Fig. 7.8 (Left) Real (ε_1) and imaginary (ε_2) parts of the complex dielectric function at room temperature for an aluminum (Al) film obtained by comprehensive analysis of ex situ SE data (ψ, Δ) collected at three angles of incidence. The Al film was deposited to opacity on stainless steel. The structural model used to deduce the dielectric function is given at the right

where ε_{1o} is a real-valued constant contribution and

$$\varepsilon_D(E) = \frac{-\hbar^2}{\varepsilon_0 \rho(\tau \cdot E^2 + i\hbar E)}. \tag{7.4}$$

Equation (7.4) describes a Drude term where ε_0 is the permittivity of free space, τ is the scattering time, and ρ is the resistivity, given by $\rho = m_e{}^*/Ne^2\tau = 1/e\mu N$ [6]. In these expressions for the resistivity, $m_e{}^*$ is the effective mass of the charge carrier, which is the electron in this case, and e, μ, and N are the electron charge, mobility, and concentration, respectively. The term under the summation in (7.3) describes a general critical point (CP) oscillator given as

$$\varepsilon_{CP,n}(E) = A_n\{\exp(i\phi_n)\}\{(\Gamma_n/2)/[E_n - E - i(\Gamma_n/2)]\}^{\mu_n}, \tag{7.5}$$

where A_n, E_n, Γ_n, μ_n, and ϕ_n are the amplitude, resonance energy, broadening parameter, exponent, and phase of the nth CP, respectively [6].

For the ZnO, the layer is only weakly conductive with a sufficiently low carrier concentration that $\varepsilon_D(E)$ in (7.3) can be neglected. Two CPs in the form of (7.5) are required to model the sharp onset and peak in $\varepsilon_2(E)$ at the ZnO bandgap and the broad absorption above the gap. For the bandgap CP, the exponent μ_1 could be fixed at 0.5 for the best fit, whereas the higher energy feature is much less sensitive

to the value of μ_2 and so could also be fixed at 0.5 for simplicity. The fixed parameters led to a model for the ZnO dielectric function with nine parameters, including the four from each of the two CPs along with ε_{1o}. Thus, for the steel/Al/ZnO sample, a total of 13 free parameters are required; four parameters are structural in nature including the Al/ZnO interface roughness, ZnO bulk, and ZnO surface roughness layer thicknesses. The ZnO content in the Al/ZnO interface is taken as 50 vol.%, which is a value consistent with the assumption that the voids in the roughness layer on the Al surface appearing in Fig. 7.8 (right) are completely filled with ZnO. The structural parameters are given on the right side of Fig. 7.9, and the dielectric function and its associated parameters are given in the left side of Fig. 7.9 and in Table 7.4, respectively.

For the third sample, consisting of steel/Al/ZnO/ITO, the multiple angle SE data are shown in Fig. 7.10, as an example of the experimental results obtained in these TCO studies. In the analysis of these data, the Al and ZnO complex dielectric functions from the studies of the steel/Al and steel/Al/ZnO samples are applied. Because of the complexity of the structure, the analysis of the steel/Al/ZnO/ITO sample requires an analytical expression for the unknown ITO dielectric function. In this case, (7.3)–(7.5) are used, but a single broad CP oscillator is sufficient. Because of the much higher carrier concentration of this contact material, the Drude term of (7.4) must be incorporated as well. This leads to a 14-parameter model which includes seven parameters that define the dielectric function, and seven parameters

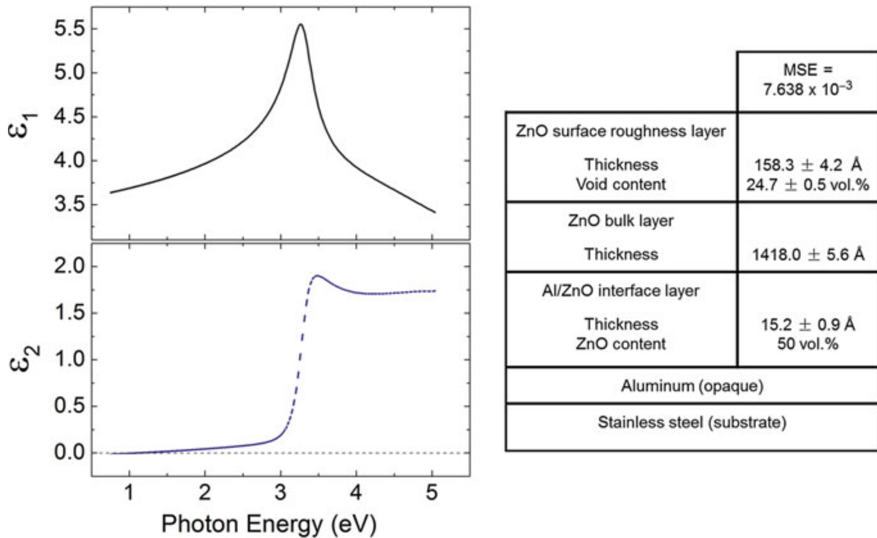

Fig. 7.9 (Left) Real (ε_1) and imaginary (ε_2) parts of the complex dielectric function at room temperature for a ZnO film deposited on stainless steel covered by an opaque Al film, as parameterized using two critical point oscillators. The oscillator parameters along with their confidence limits are given in Table 7.4. The structural parameters obtained in this analysis are given at right

Table 7.4 Best fitting parameters along with their confidence limits for the dielectric function of a ZnO layer on a stainless-steel/Al substrate, as simulated by two generalized critical point oscillators. Results are also provided for an ITO layer on a stainless-steel/Al/ZnO back-reflector structure, as parameterized by one Drude term and one generalized critical point oscillator. Results for both materials define the room temperature complex dielectric functions

ε_{1o}	ρ (Ω cm)	τ (fs)	A_n (unitless)	E_n (eV)	Γ_n (eV)	ϕ_n (°)	μ_n
Intrinsic ZnO							
2.196 ± 0.019	–	–	1.501 ± 0.014	4.566 ± 0.028	3.603 ± 0.111	0.199 ± 0.046	0.5
			2.227 ± 0.008	3.295 ± 0.001	0.297 ± 0.002	−27.079 ± 0.262	
Tin-doped indium oxide (ITO)							
2.253 ± 0.019	$(9.144 \times 10^{-3}) \pm (0.423 \times 10^{-3})$	1.099 ± 0.062	2.783 ± 0.014	4.078 ± 0.006	1.802 ± 0.022	−11.180 ± 0.294	0.5

that define the sample structure. The seven dielectric function parameters consist of ε_{1o}, two Drude term parameters, and four CP parameters, again fixing $\mu = 0.5$. By depositing the ITO roll-to-roll on the previously studied steel/Al/ZnO sheet and measuring the same location for the two structures, one can simplify the analysis by fixing the past history of the sample including the Al/ZnO interface roughness and the ZnO bulk layer thickness, reducing the number of structural parameters from seven to five. The final best fit is shown as the lines in Fig. 7.10; the five best fit

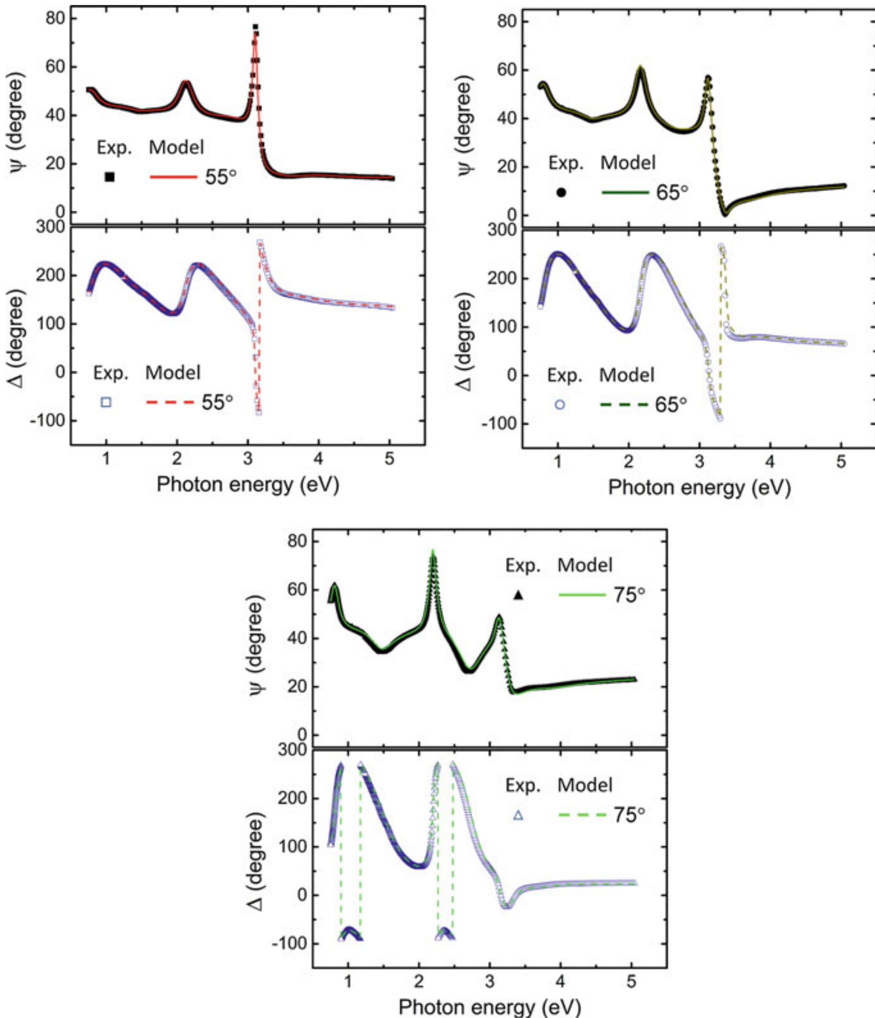

Fig. 7.10 Ellipsometric spectra at the angles of incidence of 55°, 65°, and 75° for a sample consisting of ITO deposited on a stainless-steel/Al/ZnO back-reflector structure. The solid and dashed lines represent the results of the best fit structural model and dielectric function as shown in Fig. 7.11 with dielectric function parameters given in Table 7.4. The data and their best fit are indistinguishable on these scales

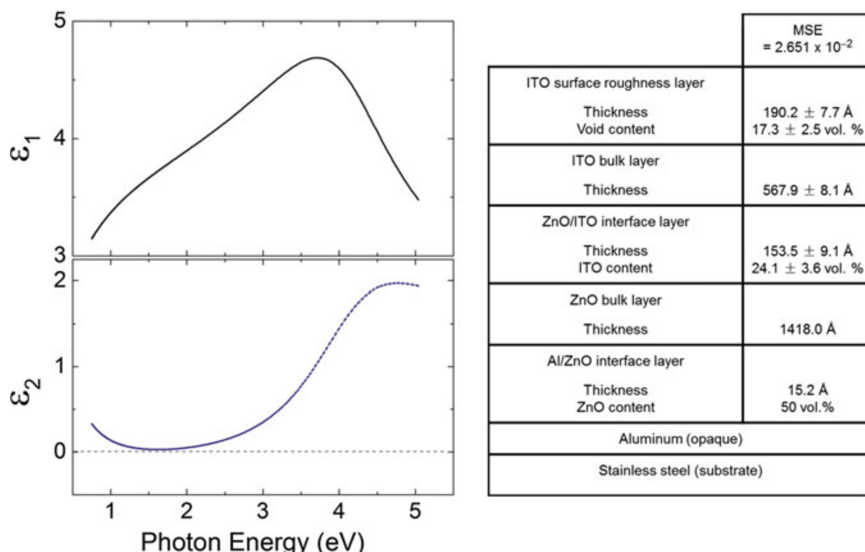

	MSE = 2.651 x 10^{-2}
ITO surface roughness layer Thickness Void content	190.2 ± 7.7 Å 17.3 ± 2.5 vol. %
ITO bulk layer Thickness	567.9 ± 8.1 Å
ZnO/ITO interface layer Thickness ITO content	153.5 ± 9.1 Å 24.1 ± 3.6 vol. %
ZnO bulk layer Thickness	1418.0 Å
Al/ZnO interface layer Thickness ZnO content	15.2 Å 50 vol.%
Aluminum (opaque)	
Stainless steel (substrate)	

Fig. 7.11 (Left) Real (ε_1) and imaginary (ε_2) parts of the complex dielectric function at room temperature for ITO deposited on a stainless-steel/Al/ZnO back-reflector as parameterized by one generalized critical point oscillator and one Drude free electron term. The oscillator parameters along with the confidence limits are given in Table 7.4. The structural parameters obtained in this analysis are given at the right

structural parameters are shown on the right side of Fig. 7.11; and the dielectric function and its best fit parameters are shown on the left side of Fig. 7.11 and in Table 7.4, respectively.

7.4 Single-Junction *a*-Si:H and *a*-$Si_{1-x}Ge_x$:H Solar Cells

The challenging goal of these SE studies is to characterize materials in solar cell configurations as they emerge directly from a continuous roll-to-roll production line, i.e., without the fabrication of special configurations or the use of special substrates. Characterization is more straightforward in the research laboratory when witness substrates can be added in individual depositions. For example, in laboratory PECVD of an amorphous semiconductor, a glass sample can be added to the substrate holder along with the substrate/device-structure. This sample enables individual measurements of transmittance and reflectance or SE to determine thickness and bandgap. In a roll-to-roll production line, one is limited to the steel foil or polymer substrates for the sample measurements, and in continuous roll-to-roll processes, one may also be limited to the available device structures. For single-junction *a*-Si:H based solar cells, the key parameters of interest include the ITO thickness since it serves as an anti-reflection coating, the thickness and

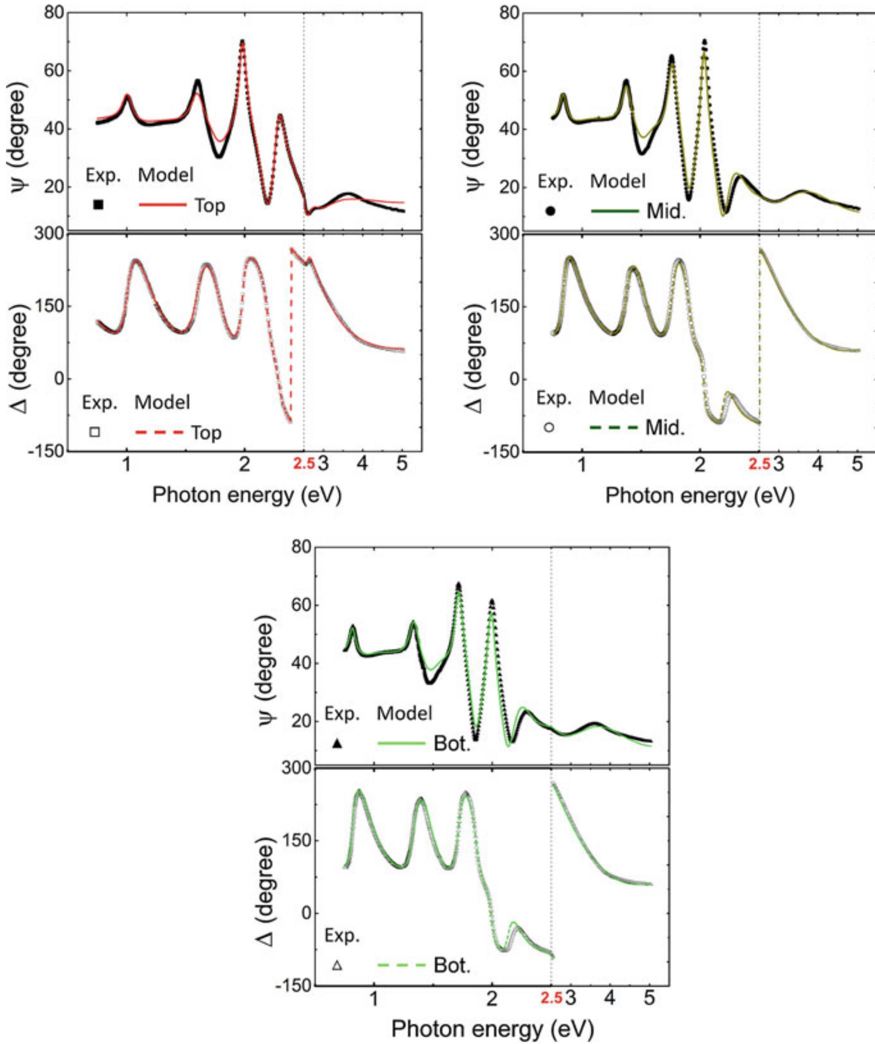

Fig. 7.12 Ex-situ SE data measured at an angle of incidence of 65° for three single-junction solar cells on back-reflector substrate structures consisting of stainless-steel/Al/ZnO. The cells are classified as top, middle, and bottom according to their decreasing *i*-layer bandgaps achieved by increasing the gas flow ratio $[GeH_4]/\{[SiH_4] + [GeH_4]\}$. The symbols represent the experimental spectra in (ψ, Δ) whereas the lines represent the results of the best fit models shown in Table 7.5

bandgap of the *p*-layer since it serves as an inactive window layer, and the thickness and bandgap of the absorber since it serves as the active absorber layer of the device.

Figure 7.12 shows single angle of incidence data collected for three solar cell structures in which the *i*-layers were fabricated with different $[GeH_4]/\{[SiH_4] + [GeH_4]\}$ gas

flow ratios [4]. Steel sheets with previously deposited and measured steel/Al/ZnO back-reflectors were used as the substrate structures for the solar cells. This approach reduces the number of free structural parameters by four, and can also be applied if the ZnO sputter deposition process is highly stable, yielding reproducible bulk and roughness layer thicknesses. Other simplifications include using 50 vol.% void content in the ITO surface roughness layer, and a fixed ZnO/a-$Si_{1-x}Ge_x$:H interface layer thickness with 24.1 vol.% a-$Si_{1-x}Ge_x$:H in accordance with the structure of Fig. 7.11. Even with these simplifications, a limitation in the analysis is encountered. Specifically, the n-layer cannot be clearly distinguished from the i-layer. The reason for the lack of sensitivity to the n-layer is that much of the above bandgap light is absorbed before reaching the n-layer, and in addition its sub-bandgap index of refraction spectrum is not significantly different than that of the i-layer. So rather than incorporating two highly correlated parameters of i and n-layer thicknesses in the model, the two layers are grouped as a single $(i + n)$-layer. A final simplification for the p and $(i + n)$-layers involves linking the four Cody-Lorentz parameters Γ, E_0, E_p, and A to E_g which serves as the single variable to define each of the two complex dielectric functions [7]. Figure 7.12 includes the best fits for the three solar cells and Table 7.5 shows the seven structural and optical parameters. It is clear from the results in the table that accurate measurements of the ITO surface roughness and bulk layer thicknesses, the p-layer thickness and bandgap, and the $(i + n)$-layer thickness and bandgap can be determined. Also given in Table 7.5 are the ITO, p-layer, and $(i + n)$-layer effective thicknesses which are calculated by determining the product of thickness and volume fraction of the material of interest and then summing

Table 7.5 Multilayer structure, effective thicknesses, and bandgaps for single-junction solar cells using the i-layers to be incorporated into the top, middle, and bottom cell components of tandem and triple-junction solar cells. The Cody-Lorentz oscillator model was used to represent the complex dielectric functions of the p-layers and i-layers with parameters linked to the bandgap. The n-layers were not distinguishable from the i-layers

	Top	Middle	Bottom
MSE	5.423×10^{-2}	5.748×10^{-2}	6.809×10^{-2}
ITO surface roughness layer thickness (Å)	133.0 ± 7.7	124.3 ± 7.0	121.7 ± 8.0
ITO bulk layer thickness (Å)	849.6 ± 10.6	799.1 ± 8.5	806.8 ± 10.0
ITO effective thickness (Å)	**977**	**952**	**961**
Interface (p-layer/ITO) roughness layer thickness (Å)	84.4 ± 2.8	152.0 ± 3.5	159.5 ± 3.5
p-layer bulk thickness (Å)	231.2 ± 3.5	229.9 ± 4.3	270.2 ± 3.3
***p*-layer effective thickness (Å)**	**273**	**306**	**350**
$(i + n)$-layer bulk thickness (Å)	1489.8 ± 4.4	1830.2 ± 5.9	1833.9 ± 4.1
$(i + n)$-layer effective thickness (Å)	**1526**	**1867**	**1871**
Interface [ZnO/$(i + n)$-layer)] layer thickness (Å)	153.5	153.5	153.5
E_g (p-layer) (eV)	1.821 ± 0.001	1.768 ± 0.002	1.769 ± 0.001
E_g (i-layer) (eV)	1.722 ± 0.001	1.598 ± 0.002	1.526 ± 0.002

that product for all layers that incorporate the material. Thus, the general expression for effective thickness including interface, bulk, and roughness layers (e.g., relevant for the ITO) is:

$$d_{\text{eff}} = d_i f_{mi} + d_b(1 - f_{vb}) + d_s(1 - f_{vs}), \tag{7.6}$$

where d_i, d_b, and d_s are the interface roughness, bulk, and surface roughness layer thicknesses, and f_{mi}, f_{vb}, and f_{vs} are the material fraction in the interface layer, and the void fractions in the bulk and the surface roughness layers, respectively. The effective thicknesses represent the volume/area of material, and are appropriate for comparison with target thicknesses when the layers of interest are deposited on rough surfaces.

The results of Table 7.5 are promising in a number of aspects. First, in spite of the large differences in the sample structure and the (ψ, Δ) data, the ITO effective thicknesses, intended to be the same for all devices, are determined to lie within the range of ±13 Å for all three structures. The deduced thicknesses of (i + n)-layer are also consistent to the extent that the middle and bottom cells are intended to have the same i and n-layer thickness whereas the top cell is designed with a thinner i-layer. The bandgap values are all consistent with expectations. The highest bandgap for the topmost p-layer arises from its highest H_2 dilution level used in the gas mixture, and the reduction in bandgaps in the order of the top, middle, and bottom cells is consistent with the increase in the $[GeH_4]/\{[SiH_4] + [GeH_4]\}$ gas flow ratios in the same order. In addition, the confidence limits on these bandgaps are quite small indicating that they can be determined to within the level needed to predict the current collection by the solar cell.

7.5 Tandem *a*-$Si_{1-y}Ge_y$:H/*a*-$Si_{1-x}Ge_x$:H Solar Cells

Similar, but even more challenging analyses have been performed on two tandem solar cells combining relatively narrower and wider bandgap *a*-$Si_{1-x}Ge_x$:H absorber layer components (from back to front) [4]. The experimental SE data obtained at a single angle of incidence are shown in Fig. 7.13. Table 7.6 shows the best fit MSE and the deduced structural and dielectric function parameters along with their confidence limits. It is clear that the fits become poorer as the complexity of the structures increase and errors associated with each of the additional components accumulate. Poor agreement occurs particularly at high photon energies also due to the accumulated surface and interface roughness layers which are likely to require more complicated multilayer models. Parameters in Table 7.6 without confidence limits are either the effective thickness values or were fixed in the analysis at values determined from simpler sample structures. In this case as well, the structural parameters determined from measurements of the underlying steel/Al/ZnO structures were used and fixed in the analysis. Interface and surface roughness layer compositions were

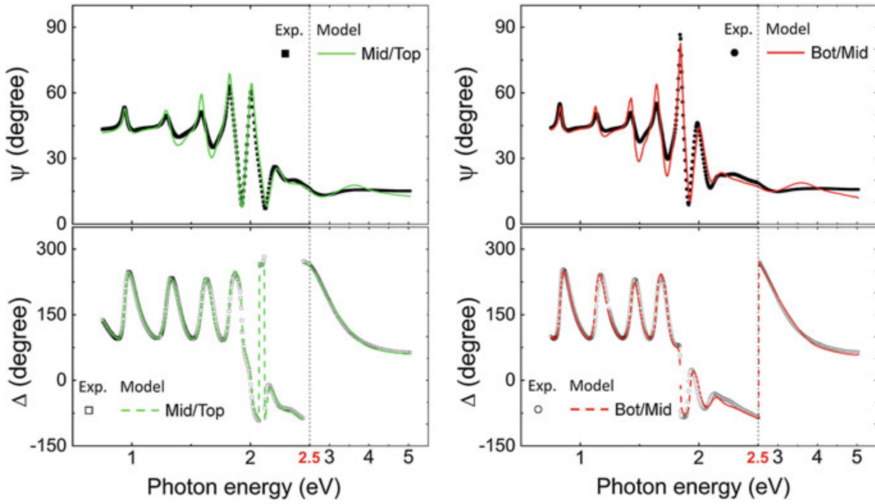

Fig. 7.13 Ellipsometric spectra measured at an angle of incidence of 65° for two tandem solar cells on stainless-steel/Al/ZnO back-reflectors including intermediate/wide bandgap and narrow/intermediate bandgap structures. The symbols represent the experimental spectra in (ψ, Δ) whereas the lines represent the results of the best fit models shown in Table 7.6

Table 7.6 Multilayer structure, component layer effective thicknesses, and room temperature bandgaps of two tandem *a*-$Si_{1-y}Ge_y$:H/*a*-$Si_{1-x}Ge_x$:H ($y > x$) solar cells. Values without confidence limits (excluding the effective thicknesses) were fixed in the analysis. Cody-Lorentz oscillator models with parameters linked to the bandgap were used to represent the complex dielectric functions of the *p*-layers and *i*-layers. The *n*-layers were indistinguishable from the *i*-layers

	Middle/Top	Bottom/Middle
MSE	6.563×10^{-2}	1.009×10^{-1}
ITO surface roughness layer thickness (Å)	121.9 ± 7.6	117.1 ± 6.7
ITO bulk layer thickness (Å)	836.6 ± 10.6	833.8 ± 15.0
ITO effective thickness (Å)	**969**	**963**
Interface (*p*-layer/ITO) roughness layer thickness (Å)	142.9 ± 6.9	141.1 ± 7.4
p-layer (upper) bulk thickness (Å)	261.2 ± 5.6	271.6 ± 5.1
***p*-layer effective thickness (Å)**	**332**	**342**
($i + n$)-layer (upper) bulk thickness (Å)	1145.6 ± 11.9	1651.0 ± 8.2
p-layer (lower) bulk thickness (Å)	306	350
($i + n$)-layer (lower) bulk thickness (Å)	1928.9 ± 4.9	2083.3 ± 4.9
($i + n$)-layer effective thickness (Å)	**1990**	**2160**
Interface [ZnO/($i + n$)-layer] layer thickness (Å)	153.5	153.5
E_g of *p*-layer (upper)	1.813 ± 0.003	1.784 ± 0.002
E_g of *i*-layer (upper)	1.759 ± 0.001	1.580 ± 0.003
E_g of *p*-layer (lower)	1.768	1.769
E_g of *i*-layer (lower)	1.571 ± 0.002	1.526

fixed to the same values used in the analysis of the corresponding interface in single-junction solar cells. The *i* and *n*-layers were grouped for both top and bottom cells, and the *p* and ($i + n$)-layers used dielectric function parameters linked to E_g applying the Ferlauto et al. [7] relationships. Even with these limitations, the bandgap of the bottom cell *a*-$Si_{1-y}Ge_y$:H cannot be determined for the middle/low bandgap tandem and must be fixed at the value obtained for the identically-prepared single-junction solar cell. This limitation occurs only when the top and bottom cells have bandgaps that are relatively close; in the case of the middle/low bandgap tandem, these values are ~1.58 and 1.53 eV from Tables 7.5 and 7.6.

In spite of the limitations, positive outcomes are found. The effective thicknesses of the ITO layers are within a few Ångstroms of the average value obtained for the single-junction devices, as was intended in the fabrication process. The top *p*-layer thicknesses are also consistent within ±16 Å with average values for the single-junction devices. The bandgap of the top and middle cells extracted from the tandem are within ±0.02 and ±0.01 eV of the single-junction counterparts. These results again are sufficiently accurate for developing realistic models of the device for predictions of current matching of individual cells and external quantum efficiency analyses.

7.6 Summary

Standard ex situ SE methods enable routine analysis of a single uniform thin film on an ideal smooth substrate whose properties are known, such as glass or wafer silicon. Analysis is not as simple, however, as the extraction of a single complex dielectric function and a single thickness. Inevitably the surfaces of amorphous, nanocrystalline, and polycrystalline thin films exhibit surface roughness as well as a thin conformal region that incorporates oxidized material and contaminants from the laboratory atmosphere. As a result, for accurate evaluation of the thin film in terms of its complex dielectric function and bulk layer thickness, the measurement must be performed as soon as possible after removal from the processing chamber and analysis must attempt to take into account the surface layer. For thin surface layers attributed predominantly to roughness ($d_s < 0.1\lambda$; λ: minimum probe wavelength in the material), accurate modeling can be performed with the Bruggeman effective medium approximation (EMA) [5]. Application of this approach requires the determination of one or more additional free parameters in the model for the sample, for example, a single thickness of the roughness layer and its void content. For the thinnest surface roughness layers (<50 Å), the void content often can be fixed at 50 vol.%. Under such circumstances, the simplest thin film analysis problem involves determination of a complex dielectric function, including real and imaginary parts which depend on photon energy, and two photon energy independent parameters, the bulk and roughness layer thicknesses. Given that a single SE data set consists of the two photon energy dependent parameters (ψ, Δ), multiple such spectra are generally needed to extract the complex dielectric function

and, at minimum, the two thicknesses. Multiple angle of incidence SE is one possible approach that can be applied routinely with commercial instrumentation to solve this problem and extract a spectral point-by-point representation of the complex dielectric function along with the two thicknesses.

Due to deposition system limitations or due to the substrate dependence of film properties, however, it may be necessary to use the substrate structures specific to the solar cell (rather than the ideal smooth substrates as described in the previous paragraph) for the evaluation of photovoltaic thin films in order to obtain accurate and relevant information. For flexible PV modules, as an example, a substrate such as steel foil may be required in the evaluation of films deposited by roll-to-roll deposition. For rigid PV modules, a substrate such as transparent conducting oxide coated glass may be required to evaluate interactions between the top-most substrate layer and the first deposited device layer. Also, it may be necessary to evaluate films in combinations of two or more layers without the ability to separate the layers and extract the layer properties individually. Ultimately, it is even desirable to develop the capability of analyzing completed devices, enabling determination of layer thicknesses as well as complex dielectric functions of the key components that control the external quantum efficiency of the device.

Clearly in many of these situations it is unreasonable to expect that determination of one or more complex dielectric functions point-by-point versus photon energy is possible. Thus, a critical component of the analyses of more complicated structures is a reduction in the number of variable parameters used to describe the dielectric functions in the sample structure. If the dielectric function of a given material component has been determined previously and is not expected to vary in the process, then this dielectric function can be used in the analysis without free parameters. If one is seeking to extract property information on a film beyond its layer thickness, however, a physics-based model for dielectric function model can be developed, applying measurements of a large number of individual materials [6]. Such a physics-based model employs a collection of photon energy independent parameters that define the dielectric function and depend on the physical properties of interest such as composition, crystalline grain size, and stress. Thus, a very important goal in ex situ SE analysis of PV materials is to develop such dielectric function models and a database of parameters.

In this chapter, the approaches described in the above paragraphs were illustrated. The analysis presentation and discussion focused on the determination of complex dielectric functions of a steel foil substrate and the individual thin films deposited on this substrate that make up tandem *n-i-p* solar cells based on hydrogenated amorphous silicon-germanium alloys (a-$Si_{1-x}Ge_x$:H) fabricated in a roll-to-roll process [4]. Critical components of this capability are the dielectric function models that describe the amorphous semiconductor and transparent conducting oxide (TCO) layers. For the amorphous semiconductor layers, all photon energy independent parameters in the analytical model for the dielectric function can be linked to the single most important parameter, the bandgap [7]. Such a parameter reduction capability has yet to be fully developed for the TCO layers, and as a result, the parameters in their dielectric functions are fixed in tandem cell

analysis. Application of these models enables characterization of complete tandem device structures including the ability to extract the thicknesses of the TCO anti-reflection coating and top window *p*-layer as well as the bandgaps of the top *p*-layer, the top cell *i*-layer, and in some cases the bottom cell *i*-layer. Limitations in this analysis occur because of the absorption by overlying layers and the similarity in the dielectric functions of deeper adjoining layers. For example, it is difficult to separate *i*-layer and *n*-layer thicknesses for this reason. It is also difficult to characterize the bottom cell *i*-layer when its bandgap is close to that of the overlying top cell *i*-layer. Because of this difficulty in distinguishing between layers whose optical properties are similar over the accessible spectral range, for example, intrinsic and doped layers of the same material, real time and on-line SE are important capabilities at both laboratory and production scales for addressing these ambiguities.

References

1. A. Luque, S. Hegedus (eds.), *Handbook of Photovoltaic Science and Engineering* (Wiley, New York, NY, 2003)
2. A. Shah (ed.), *Thin Film Silicon Solar Cells* (CRC, Boca Raton, FL, 2010)
3. H. Fujiwara, *Spectroscopic Ellipsometry: Principles and Applications* (Wiley, Chichester, UK, 2007)
4. Z. Huang, *Spectroscopic Ellipsometry Studies of Thin Film a-Si:H/nc-Si:H Micromorph Solar Cell Fabrication in the p-i-n Superstrate Configuration*. Ph.D. Dissertation, University of Toledo, Toledo, OH, 2016
5. H. Fujiwara, J. Koh, P.I. Rovira, R.W. Collins, Phys. Rev. B **61**, 10832 (2000)
6. R.W. Collins, A.S. Ferlauto, in *Handbook of Ellipsometry*, ed. by H. Tompkins, E.A. Irene, (William Andrew, Norwich, NY, 2005), Chapter 2, p. 93
7. A.S. Ferlauto, G.M. Ferreira, J.M. Pearce, C.R. Wronski, R.W. Collins, X. Deng, G. Ganguly, J. Appl. Phys. **92**, 2424 (2002)
8. G.D. Cody, in *Semiconductors and Semimetals Vol. 21 B, Hydrogenated Amorphous Silicon Optical Properties*, ed. by J.I. Pankove (Academic, New York, NY, 1984), Chapter 2, p. 11
9. G.E. Jellison Jr., F.A. Modine, Appl. Phys. Lett. **69**, 371 (1996)
10. G.E. Jellison Jr., F.A. Modine, Appl. Phys. Lett. **69**, 2137 (1996)
11. W.B. Jackson, S.M. Kelso, C.C. Tsai, J.W. Allen, S.-J. Oh, Phys. Rev. B **31**, 5187 (1985)
12. R.W. Collins, A.S. Ferlauto, G.M. Ferreira, C. Chen, J. Koh, R.J. Koval, Y. Lee, J.M. Pearce, C.R. Wronski, Solar Ener. Mater. Solar Cells **78**, 143 (2003)
13. Z. Huang, J. Chen, M.N. Sestak, D. Attygalle, L.R. Dahal, M.R. Mapes, D.A. Strickler, K.R. Kormanyos, C. Salupo, R.W. Collins, in *Conference Record of the 35th IEEE Photovoltaic Specialists Conference*, Honolulu, HI, 20–25 June 2010 (IEEE, New York, NY 2010), p. 1678
14. J.A. Woollam, B. Johs, C. Herzinger, J. Hilfiker, R. Synwicki, C. Bungay, in *Optical Metrology: A Critical Review*, ed. by G.A. Al-Jumaily, *SPIE Proceedings*, vol. CR 72 (SPIE, Bellingham, WA, 1999), p. 3
15. B. Johs, J.A. Woollam, C. Herzinger, J. Hilfiker, R. Synowicki, C. Bungay, in *Optical Metrology: A Critical Review*, ed. by G.A. Al-Jumaily, *SPIE Proceedings*, vol. CR 72 (SPIE, Bellingham WA, 1999), p. 29
16. B. Johs, J. Hale, N.J. Ianno, C.M. Herzinger, T. Tiwald, J.A. Woollam, in *Optical Metrology Roadmap for the Semiconductor, Optical, and Data Storage Industries II*, ed. by A. Duparre, B. Singh, *SPIE Proceedings*, vol. 4449 (SPIE, Bellingham WA, 2001), p. 41

17. I. An, J.A. Zapien, C. Chen, A.S. Ferlauto, A.S. Lawrence, R.W. Collins, Thin Solid Films **455**, 132 (2004)
18. H.V. Nguyen, I. An, R.W. Collins, Phys. Rev. Lett. **68**, 994 (1992)

Chapter 8
Crystalline Silicon Solar Cells

Gerald E. Jellison Jr. and Pooran C. Joshi

Abstract Most solar cells are fabricated from crystalline or semicrystalline silicon since they are relatively inexpensive starting materials and the resulting solar cells are very efficient. As a result, the optical properties of silicon are extremely important in many aspects of solar cell manufacture, and have been determined by many groups using several techniques. The most reliable values of the optical functions of silicon have been determined using spectroscopic ellipsometry, augmented by optical transmission measurements of the absorption coefficient for wavelengths greater than 700 nm. Obviously, these optical functions depend on the wavelength of light, but they also depend significantly on temperature and morphology. Several thin films are very important to solar cell manufacture, including silicon nitride, silicon dioxide, and aluminum oxide. While the optical properties of these thin films are strong functions of deposition conditions, spectroscopic ellipsometry is ideal for characterizing them. This work will present recent spectroscopic ellipsometry data and optical transmission data from which the optical functions of silicon are obtained. The optical transmission data have been fit from 700 to 1200 nm to a modification of Macfarlane's et al. formula [Phys. Rev. 111, (1958) 759], resulting in a reduced χ^2 of 0.84. This formulation is particularly valuable in that it gives the optical absorption coefficient from 700 to 1200 nm as a function of both wavelength and temperature.

8.1 Introduction

Elemental silicon (atomic number 14) is the 2nd most abundant element in the earth's crust (28% by mass), following only oxygen (46% by mass). It is most often found in nature bonded to oxygen and a variety of other elements to form various

G. E. Jellison Jr. (✉) · P. C. Joshi
Oak Ridge National Laboratory, Oak Ridge, TN 37830, USA
e-mail: jellisongejr@ornl.gov

P. C. Joshi
e-mail: joshipc@ornl.gov

© Springer International Publishing AG, part of Springer Nature 2018
H. Fujiwara and R. W. Collins (eds.), *Spectroscopic Ellipsometry for Photovoltaics*,
Springer Series in Optical Sciences 212,
https://doi.org/10.1007/978-3-319-75377-5_8

silicates. Using a variety of chemical and thermal treatments, silicon can be separated from oxygen and other elements to make a very pure material with impurity concentrations less than one part in a billion (9 N purity). Using a variety of crystal growth techniques, this material can be grown into nearly perfect single crystals (mono-crystalline silicon) or using less expensive techniques, grown into semi-crystalline silicon with grain sizes ~1 mm in diameter. Mono-crystalline silicon can be produced as less-pure, less expensive solar grade silicon or as electronic grade silicon, which is of much higher purity, more expensive, but is useful for the greater electronics industry. Solar cells made from multi-crystalline silicon will have efficiencies up to ~22%, while 25% single junction monocrystalline silicon solar cells have been made from electronic grade silicon.

Above 1414 °C, silicon is liquid. While crystalline silicon is semiconducting, liquid silicon is metallic and very reactive with air. Like water (and unlike most other materials), liquid silicon is denser than the solid. This characteristic means that solid silicon will float on liquid silicon, making crystal growth much easier.

Crystalline silicon has the cubic diamond structure, where each silicon atom is bonded to 4 other silicon atoms forming a perfect tetrahedron. The diamond lattice is highly symmetric with a point group m3m (O_h Schönflies) and space group number 227 (Fd-3m). Therefore, the optical properties of silicon are isotropic. At room temperature, photons greater than ~1.05 eV are absorbed; according to the Shockley-Queisser limit [1] the maximum possible efficiency of a single-junction silicon solar cell is ~31.5%. The fundamental band edge of silicon is indirect; that is, photon absorption requires the absorption or the emission of a phonon to excite an electron from the valence band to the conduction band. This is both good and bad for photovoltaics. It is good because electron-hole recombination is much less likely, dramatically increasing the minority carrier lifetime and diffusion length. In silicon, the minority carrier lifetime is primarily determined by impurities and defects in the material, which act as recombination centers. These centers can trap either a free electron from the conduction band or a free hole in the valence band, which then can be recombined with a free hole or free electron. The bad part is that the indirect gap and resultant requirement that a phonon be either generated or absorbed also results in a much less efficient light absorption process. As a result, many photo-generated electron-hole pairs are created much deeper into the material than for direct gap materials, which must then diffuse to the junction to be collected. Much of the recent work in silicon photovoltaics has focused on minimizing the bad (long penetration depth) and maximizing the good (long minority carrier lifetime), resulting in gradually improving efficiencies over time.

In this chapter, we will discuss the optical properties of silicon and related materials. While ellipsometry has been the technique of choice for much of this work, it has not been the only choice, so we will also discuss these other techniques as appropriate. Since the primary interest in this book is the application of ellipsometry to photovoltaics, we will focus on the optical properties from 200 to 1200 nm. While there is very little sunlight in the spectral region 200–350 nm that reaches the earth, this spectral region contains interesting insights into silicon and

related materials, and is used in many diagnostics for photovoltaics, so this region is discussed as well.

8.2 Optical Properties of Silicon: UV to Near IR (200–1200 nm)

The linear optical functions of an isotropic material can be expressed as either the complex refractive index $N(\lambda)$ or the dielectric function $\varepsilon(\lambda)$. The two are related by

$$\varepsilon(\lambda) = \varepsilon_1 - i\,\varepsilon_2 = N(\lambda)^2 = (n(\lambda) - ik(\lambda))^2 \tag{8.1}$$

where the real and imaginary parts of the dielectric function are given by ε_1 and ε_2, n is the refractive index and k is the extinction coefficient. The wavelength λ is related to the photon energy E (eV) = 1239.8/λ (nm). Since silicon is an isotropic material, the dielectric function is a scalar, requiring only a single complex quantity at each wavelength. The optical functions are directly related to the normal incidence reflectivity R (where there is no surface over layer) and is given by

$$R = \frac{(n-1)^2 + k^2}{(n+1)^2 + k^2}. \tag{8.2}$$

The optical absorption coefficient α is given by

$$\alpha = \frac{4\pi k}{\lambda}, \tag{8.3}$$

where the fraction of light not absorbed at a depth d into the material is given by $f = \exp(-\alpha d)$.

8.2.1 *Measurement Techniques*

The earliest measurements of the optical properties of single-crystal silicon were performed using specular reflectivity, transmission, and minimum deviation [2–11]. Specular reflectivity measurements are relatively simple to perform and can be done in vacuum, making it possible to do these measurements at high photon energies ($E > 6$ eV corresponding to $\lambda < 200$ nm). However, reflectivity measurements suffer from two disadvantages. First of all, the optical functions are not determined directly from the reflectivity measurements, but must be calculated using Kramers-Kronig integration. This integration requires reflectivity data in the energy range from 0 to ∞, which does not exist, so extrapolations beyond the measured data are required. Secondly, reflected light that is not collected by the detector (such

as scattered light) will result in a lower reflectivity, distorting the final result. Specular transmission measurements can be converted directly into the optical absorption coefficient α using the expression for the internal transmission T (correcting for reflection and non-specular losses)

$$T = \exp(-ad), \tag{8.4}$$

where d is the thickness of the sample. Transmission is particularly useful for wavelengths where the light penetration is large; with silicon, this occurs for wavelengths $\lambda > \sim 700$ nm. Transmission gives no information concerning the refractive index. Minimum deviation measurements require that the sample be transparent and that the sample can be constructed as a prism with well-polished faces. For silicon, this technique can only be used in the infrared range with $\lambda > \sim 1200$ nm.

Recently, spectroscopic ellipsometry has become an important technique for the determination of the optical functions of silicon. For ellipsometric measurements, polarized light is reflected from the sample surface, which changes the polarization state of the light. The resulting polarization state is then analyzed to characterize the change in the polarization state generated by the sample. (This is discussed in Chap. 2.) For an isotropic sample, the measured ellipsometric parameters can be expressed in several different ways. The fundamental measured quantity is complex ρ:

$$\rho = (\rho_r + i\rho_i) = \frac{r_p}{r_s} = \frac{C + iS}{1 + N} = \tan(\psi)e^{i\Delta}. \tag{8.5}$$

The complex reflection ratios r_p and r_s are for p- and s-polarized light, (ψ, Δ) are the traditional ellipsometric angles, and $N = \cos(2\psi)$ [not to be confused with the complex refractive index of (8.1)], $S = \sin(2\psi)\,\sin(\Delta)$, and $C = \sin(2\psi)\,\cos(\Delta)$ are elements of the sample Mueller matrix with the requirement that $N^2 + S^2 + C^2 = 1$. Figure 8.1 shows representative spectroscopic ellipsometry data for silicon with only the native oxide overlayer, expressed in terms of ρ and (ψ, Δ).

The quantity ρ can be converted directly into the pseudo-dielectric function

$$\langle\varepsilon\rangle = \langle\varepsilon_1\rangle - i\langle\varepsilon_2\rangle = \sin(\theta)^2\left[1 + \tan(\theta)^2\left(\frac{1-\rho}{1+\rho}\right)^2\right], \tag{8.6}$$

where θ is the angle of incidence. If there is no surface overlayer, then the pseudo-dielectric function becomes the actual dielectric function. Unfortunately, this is seldom the case. For silicon, there always is an overlayer consisting of oxides of silicon, hydrogen termination, surface roughness, etc., depending upon surface treatment. Even an overlayer of a few tenths of a nanometer can significantly distort the pseudodielectric function from the actual dielectric function.

8.2.2 Optical Functions of Silicon

In the spectral range λ = 200–1200 nm, the most reliable optical functions of silicon are determined from spectroscopic ellipsometry measurements in conjunction with optical transmission measurements. Spectroscopic ellipsometry measurements (described in Sect. 8.4) have been performed on a single crystal wafer of silicon, and the results are shown in Fig. 8.1. The dielectric functions and complex refractive indices are determined from the ellipsometry data using a procedure outlined in [12], where the surface overlayer was assumed to be a-SiO_2 using the refractive indices of Malitson [13]. The resulting values of n and k are shown in Fig. 8.2, along with an estimate of the errors.

As can be seen from Fig. 8.1, the value of Δ is close to 180° for wavelengths longer than ~500 nm, so it is important that the ellipsometric technique measure Mueller matrix elements proportional to sin(Δ) very accurately. This was very difficult using the older rotating polarizer or analyzer ellipsometers, since they did not contain a compensating element. This limitation does not exist with most modern ellipsometers based on rotating compensators or photoelastic modulators.

The optical functions of silicon have been the subject of many studies over the last 35 years, where the values that have been honed to such an extent that the disagreements are minimal [14–19]. For photon energies above the direct band gap (~3.4 eV or 365 nm), ellipsometry has been the experimental technique of choice,

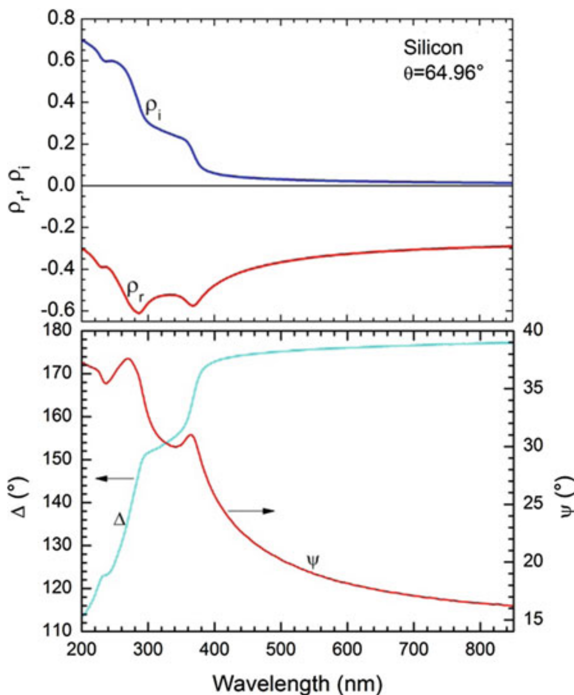

Fig. 8.1 Spectroscopic ellipsometry data for crystalline silicon with a native oxide layer, taken at an angle of incidence of 64.96°. The top panel expresses the data in terms of ρ_r and ρ_i and the bottom panel in terms of ψ and Δ

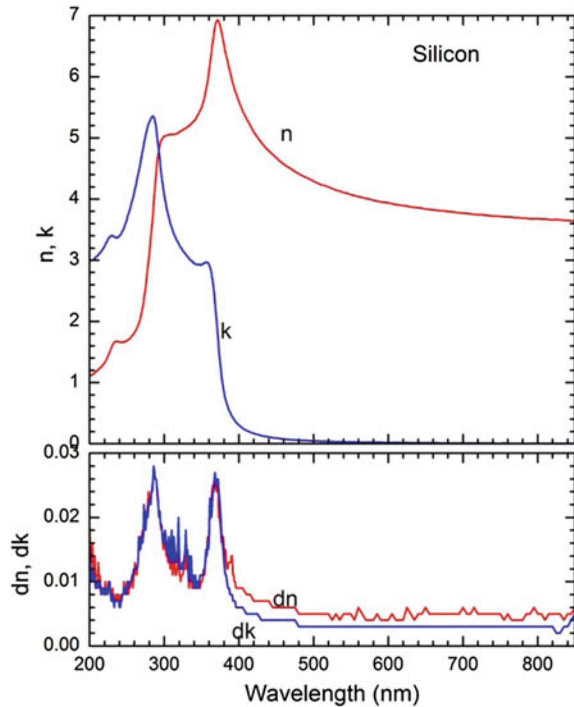

Fig. 8.2 The refractive index n and extinction coefficient k determined from the spectroscopic ellipsometry data shown in Fig. 8.1

although many different varieties of ellipsometers have been used. Interestingly, three of the most important considerations are sample preparation, surface orientation, and data analysis. The surface treatment (such as using an HF etch to clean the surface prior to measurement, or just using a sample with a stabilized native oxide) has a small but quite measurable effect on the data, as does the crystallographic orientation of the surface studied. If the surface layer is not entirely removed, it must be removed mathematically [15–17] to get the actual dielectric functions of silicon from the ellipsometry data, and that requires an appropriate model which will depend on the technique used to clean the silicon surface prior to measurement.

As might be expected, the primary disagreements between the data sets are small (~1–2%) and are focused near the critical points (290 and 370 nm) where the optical penetration depth is small, increasing the importance of the surface overlayer. For photon energies less than the direct band gap, a combination of spectroscopic ellipsometry and transmission measurements produce the most reliable values of the optical functions of silicon. Ellipsometry measurements produce reliable values of the refractive index (or ε_1) throughout the wavelength range, but produce increasingly inaccurate values of the extinction coefficient (or ε_2) as it becomes small. This is discussed in more detail in Sect. 8.4.

Using (8.2) and (8.3), the measured values of n and k can be transformed into reflectivity and absorption coefficient, as shown in Fig. 8.3. As can be seen from the

error bars on the ellipsometric determination of the absorption coefficient, this quantity becomes increasingly less accurate as k and α become smaller. For wavelengths longer than ~700 nm, transmission measurements become much more accurate than ellipsometric measurements in the determination of α or k and should be used instead of ellipsometric measurements. The transmission measurements show two interesting characteristics: First of all, there is a well-defined feature in the absorption coefficient curve at ~1050 nm. This is due to the optical absorption process for indirect gap semiconductors, which involve both the emission and absorption of a phonon; this was first discussed by Macfarlane et al. [5], and will be discussed later. Secondly, the transmission measurements show that the minimum photon energy for absorption in silicon at room temperature is ~1180 nm (=1.051 eV). This energy is somewhat less than the fundamental band gap, since a phonon can be absorbed to make up the energy difference.

In addition to the actual measurements of the dielectric functions of silicon, there have been several papers that have compiled the data [20–23], attempting to reconcile the small differences between the published data sets. Geist et al. [20, 21] fit the available room-temperature data resulting in a multi-parameter fit for both the refractive index and extinction coefficient from 3.1 to 1.1 eV (400–1127 nm). Green's compilation [23] tabulated data from 250 to 1450 nm and included an estimate of temperature coefficients.

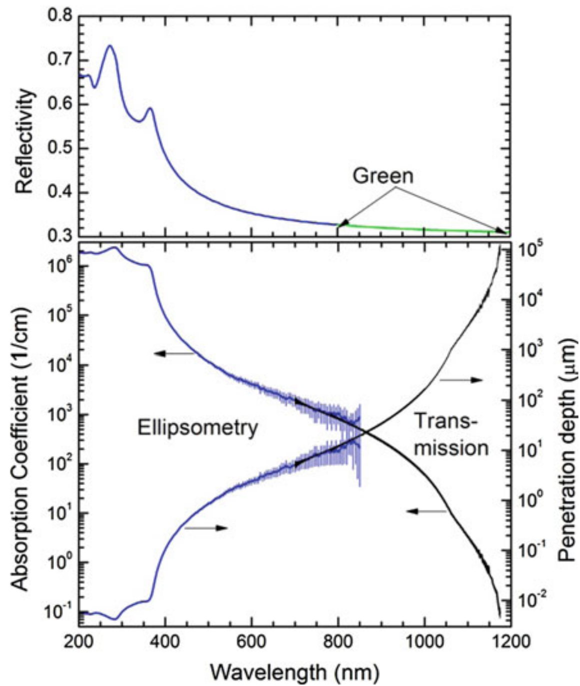

Fig. 8.3 The reflectivity (R, top) and optical absorption coefficient (α, bottom) for silicon. Ellipsometry measurements are shown from 200 to 850 nm for R and α, as well as the error limits for α. The compilation data from Green [22] is shown for R from 800 to 1200. Independent transmission data is shown for the absorption coefficient from 700 to 1200 nm. The equivalent penetration depth (in μm) is also shown in the bottom panel

8.2.3 *Origins of the Optical Functions of Silicon*

8.2.3.1 Band Structure and Critical Points

Many of the features observed in the refractive index and extinction coefficient of silicon (Fig. 8.2) below 400 nm are a result of direct optical transitions in crystalline silicon and can be understood from band structure. The details of band structure calculations are discussed in Chap. 4 (see also [24]). Briefly, the band structure of a material is a theoretical construct that calculates the energy levels that a single electron can have, given its wavevector **k**. The band structure will have the same symmetry that the crystal has, thus simplifying the calculation. As a result, points in the Brillouin zone can be labeled according to the symmetry of the crystal.

Figure 8.4 shows the dielectric function of silicon, plotted as a function of energy; this is the same data as presented in Fig. 8.2, using (8.1) to convert N to ε. The calculated band structure of silicon [25] is shown to the right of Fig. 8.4, which is plotted in two symmetry directions. The Γ point occurs for the wavevector $\mathbf{k} = (0, 0, 0)$ and is the center of Brillouin zone, while the L and X points represent the wavevector $\mathbf{k} = (\pi/a) * (1, 1, 1)$ and $= (\pi/a) * (1, 0, 0)$, respectively, where a is the dimension of the unit cell. The intermediate points are notated as Λ and Δ (not to be confused with the ellipsometric parameter Δ). The valence bands are represented by the electronic states less than 0 while the conduction bands all have energies greater than 0.

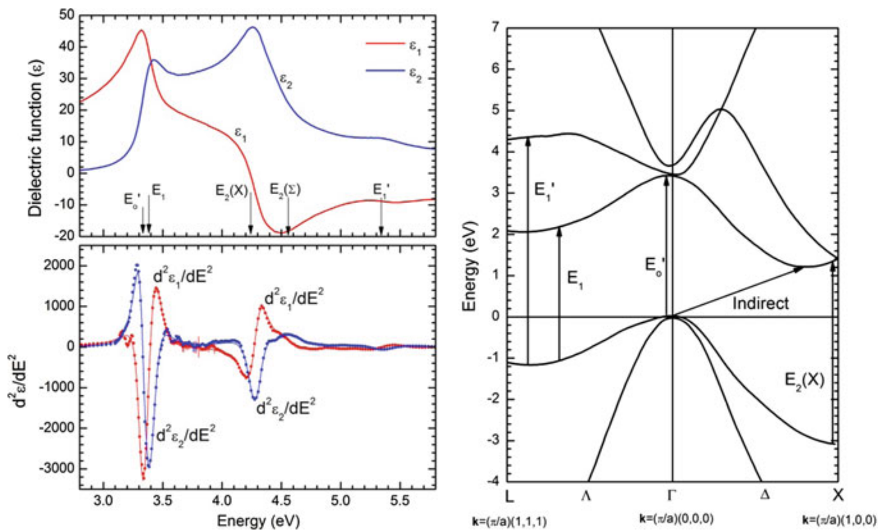

Fig. 8.4 Complex dielectric function of silicon as a function of energy and the 2nd derivative of the dielectric function with respect to energy (left). The energy positions of the 5 critical points are noted. The band structure of silicon [25] with the optical transitions noted (right)

Optical transitions in crystals can occur when a photon of a particular energy interacts with an electron in a filled state which is then excited to an unfilled state. For this discussion, the filled states will be in the valence band and the empty states in the conduction band. A direct transition occurs when there is no change in the wavevector **k** (vertical on the band structure diagram) and an indirect transition occurs when a change in the wavevector **k** is required. To conserve momentum, the indirect transition requires either the absorption or emission of a phonon (quantum of lattice vibration). The probability of transition depends on many things, including the probability that the valence band state is occupied and the conduction band state is unoccupied, the matrix element connecting the two states, and, for indirect transitions, the probability that a phonon of a particular **k**-vector exists or can be created. Since the indirect transition requires a phonon while a direct transition does not, generally direct transitions have a much higher transition probability, resulting in a much higher absorption coefficient. For direct transitions, the imaginary part of the dielectric function is given by [24]

$$\varepsilon_2\left(E_{\text{photon}}\right)\propto \sum_{\vec{k}}\left|P_{cv}\left(\vec{k}\right)\right|^2\delta\left[E_c\left(\vec{k}\right)-E_v\left(\vec{k}\right)-E_{\text{photon}}\right]\propto|P_{cv}|^2J_{cv}\left(E_{\text{photon}}\right) \quad (8.7)$$

where $P_{cv}(\mathbf{k})$ is the probability of transition (related to the symmetry of the critical point) and J_{cv} is the joint density of states.

In some cases, the energy positions of critical points in a crystal can be determined from the dielectric function spectra by taking the 2nd derivative of ε with respect to energy [25] (see Chap. 4),

$$\frac{\mathrm{d}^2\varepsilon(E)}{\mathrm{d}E^2}\approx Ae^{i\Phi}(E-E_\mathrm{o}+i\Gamma)^{n-2}=Fe^{i\Phi}(\varsigma+i)^{n-2}. \quad (8.8)$$

In (8.8), A is the amplitude of the transition, Φ is the phase, E_o is the threshold energy, and Γ is the broadening. The exponent n depends on the dimensionality of the critical point (n = −1/2 (1-D), 0 (2-D), ½ (3-D), −1 (discrete exciton)). The second expression in (8.8) represents a re-parameterization that eliminates some correlations, where $F = A/\Gamma^{n-2}$ and $\zeta = (E - E_\mathrm{o})/\Gamma$.

The bottom left of Fig. 8.4 shows the 2nd derivative of ε with respect to energy for silicon at 295 K, along with a fit to the data using 5 critical points. The energies of these critical points are shown in Table 8.1, along with the energies determined by Lautenschlager et al. [25], and can then be related to critical points in the Brillouin zone of silicon, as plotted on the band structure diagram of silicon to the right of Fig. 8.4. The lowest energy direct transition (E_o') occurs at the Γ point and is often called the direct transition edge. This transition is accompanied by another direct transition (E_1) near the L-point. The largest value of ε_2 occurs near 4.25 eV and is represented by the critical points at $E_2(X)$ and $E_2(\Sigma)$. The E_1' transition occurs near the L point and is quite weak.

Table 8.1 Critical point energies as determined by taking 2nd derivatives of the dielectric function as a function of energy and fitting to (8.8)

	Lautenschager et al. [24]	This work
E_o'	3.320 ± 0.005	3.327 ± 0.002
E_1	3.396 ± 0.005	3.382 ± 0.005
$E_2(X)$	4.270 ± 0.002	4.283 ± 0.003
$E_2(\Sigma)$	4.492 ± 0.010	4.551 ± 0.021
E_1'	5.317 ± 0.025	5.346 ± 0.023

8.2.3.2 Indirect Absorption

Over most of the solar spectrum, optical absorption in silicon is indirect and requires a phonon to conserve the wavevector **k**. The phonon can be either emitted (Stokes) or absorbed (anti-Stokes). For the case of silicon, there are two primary phonons involved: the transverse acoustic and the longitudinal acoustic. Therefore, there are 4 primary contributions to the absorption coefficient near the band edge. These absorption coefficients will be functions of both the photon energy and the temperature of the material and can be expressed as:

$$\alpha(E,T) = \alpha_{LS}(E,T) + \alpha_{LaS}(E,T) + \alpha_{TS}(E,T) + \alpha_{TaS}(E,T), \tag{8.9}$$

where the subscripts indicate either the longitudinal (L) or the transverse (T) acoustic phonon, and phonon emission (Stokes, S) or phonon absorption (anti-Stokes aS).

The phonon absorption process is proportional to the probability that a phonon state is occupied for the absorption process (anti-Stokes), which is given by Bose-Einstein statistics:

$$f_{BE}(T,\theta) = \frac{1}{\left(\exp\left(\frac{\theta}{k_B T}\right) - 1\right)} \tag{8.10a}$$

where T is the temperature in Kelvin, θ is the energy of the phonon in eV, and k_B is Boltzmann's constant = 8.617×10^{-5} eV/K. Conversely, the phonon emission process requires that the phonon state be empty, which is $[1 - f_{BE}(\theta,T)]$. The other factors involved in the determination of optical absorption are the joint density of states and the matrix element which connects an occupied state in the valence band with an unoccupied state in the conduction band.

Figure 8.5 shows the absorption coefficient data for silicon near the band edge, along with a fit to the data using the expressions:

$$\alpha_{LS}(E,T) = (1 - f_{BE}(\theta_L,T))\left(A_L\sqrt{E_{LS}} + B_L(E_{LS})^{\beta}\right) \quad E_{LS} = E - E_g(T) - \theta_L \tag{8.10b}$$

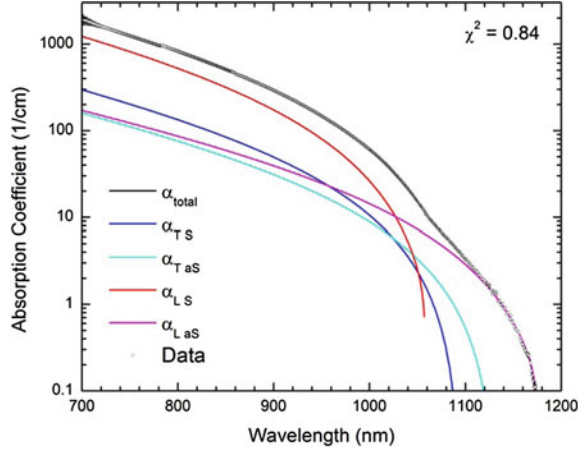

Fig. 8.5 Absorption Coefficient of silicon data (black) compared with calculated absorption coefficients described in the text. The 4 partial absorption coefficients are indicated by the subscripts L and T for the longitudinal and transverse acoustic phonons and S and aS for the Stokes (emission) and anti-Stokes (absorption) processes

$$\alpha_{\mathrm{LaS}}(E,T) = f_{\mathrm{BE}}(\theta_{\mathrm{L}},T)\left(A_{\mathrm{L}}\sqrt{E_{\mathrm{LaS}}} + B_{\mathrm{L}}(E_{\mathrm{LaS}})^{\beta}\right) \quad E_{\mathrm{LaS}} = E - E_{\mathrm{g}}(T) + \theta_{\mathrm{L}} \tag{8.10c}$$

$$\alpha_{\mathrm{TS}}(E,T) = (1 - f_{\mathrm{BE}}(\theta_{\mathrm{T}},T))\left(B_{\mathrm{T}}(E_{\mathrm{TS}})^{\beta}\right) \quad E_{\mathrm{TS}} = E - E_{\mathrm{g}}(T) - \theta_{\mathrm{T}} \tag{8.10d}$$

$$\alpha_{\mathrm{TaS}}(E,T) = f_{\mathrm{BE}}(\theta_{\mathrm{T}},T)\left(B_{\mathrm{T}}(E_{\mathrm{TaS}})^{\beta}\right) \quad E_{\mathrm{TaS}} = E - E_{\mathrm{g}}(T) + \theta_{\mathrm{T}} \tag{8.10e}$$

The fitting parameters are A_{L}, B_{L}, θ_{L}, B_{T}, θ_{T}, E_{g}(T) and the exponent β. The fundamental indirect gap energy of silicon is given by $E_{\mathrm{g}}(T)$, where the temperature dependence is expressed explicitly. The phonon energies θ_{L} and θ_{T} are given in eV. This formulation is very similar to that given in [5], with the exception that their β function is replaced with the exponent β, which is treated as a fitting parameter. For parabolic bands with a constant transition matrix element, $\beta = 2$.

The fitted parameters of (8.9) and (8.10a–8.10e) have been determined by minimizing the reduced χ^2 using the Levenberg-Marquardt algorithm resulting in the values given in Table 8.2. Seven (7) parameters were fit, including fundamental band gap. As can be seen the fit is excellent with a reduced $\chi^2 = 0.84$, indicating that the model fits the data.

Table 8.2 Fitted parameters to the data shown in Fig. 8.5. The sample temperature was 295 K

A_{L}	19.85 ± 0.38	1/cm
B_{L}	2846 ± 22	1/cm
θ_{L}	0.0585 ± 0.0001	eV
B_{T}	355 ± 25	1/cm
θ_{T}	0.0185 ± 0.0010	eV
β	1.874 ± 0.003	
$E_{\mathrm{g}}(T)$	1.1134 ± 0.0002	eV

The values given in Table 8.2 are somewhat different from those used in [5, 11], but this is to be expected since the measured absorption coefficients in this work were considerably larger than those measured in [5] (<~2000 cm^{-1} compared to <~40 cm^{-1}) and the wavelengths examined in this work are quite different from that of [11] (700–1200 nm compared to a single wavelength 1152 nm). Clearly, the dominant phonon in the indirect optical absorption is the longitudinal acoustic phonon, and both the emission (Stokes) and absorption (anti-Stokes) processes are important, depending on the wavelength. The kink in the absorption coefficient curve is real and the result of both the emission and absorption of a phonon playing a role in the total absorption coefficient. The deviation of the exponent β from 2 is an indication that the valence and conduction bands are no longer parabolic when photon energies much larger than the fundamental band gap are considered. Temperature also plays a significant role as discussed in the next section.

8.2.4 Modifications to the Optical Properties of Silicon

While the optical properties are often labeled as optical constants, this is actually a misnomer, since they are anything but constant. Obviously, the optical properties depend significantly on wavelength, as has been discussed in the previous section. However, several other factors can also affect the optical properties, including temperature, morphology, doping, and stress. Of these modifications, temperature and morphology are the most important to photovoltaics. Spectroscopic ellipsometry measurements, along with transmission measurements where appropriate, have been used to quantify the dependence of the optical properties of silicon on these perturbations.

It has been known for some time that the optical functions of silicon depend significantly on temperature [5, 10, 11, 25–30]. Figure 8.6 shows the changes in the optical functions of silicon with increasing temperature [30]. The critical points broaden and increase in wavelength (see Lautenschlager [25] for a complete description). From the thermodynamic arguments of Thurmond, the fundamental indirect gap energy is given by [26]

$$E_g(T) = 1.155 - \frac{4.73 \cdot 10^{-4} T^2}{635 + T}, \tag{8.11}$$

where the temperature T is expressed in Kelvin. At room temperature (295 K), E_g = 1.1107, which compares to the fitted value of 1.1134 eV, given in Table 8.2.

Figure 8.7 shows the temperature dependence of the absorption coefficient, plotted semilogarithmically, with the temperature-dependent fundamental band gap from (8.11) shown in the insert. The short wavelength region (<850 nm) is taken from the data shown in Fig. 6 [30], while the long wavelength region (>700 nm) is determined from (8.9) and (8.10a–8.10e) and is labeled “Transmission.” Clearly, the transmission and ellipsometry values of the absorption coefficient agree within

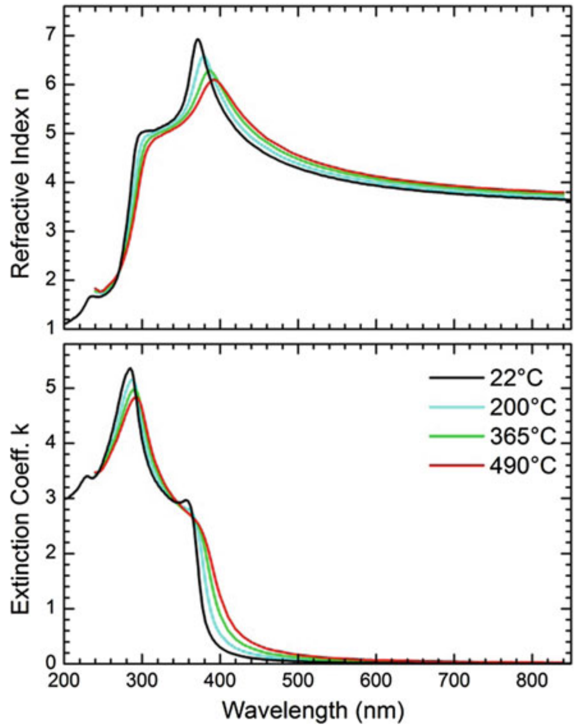

Fig. 8.6 The refractive index and extinction coefficient of silicon as a function of temperature, determined by spectroscopic ellipsometry [30]

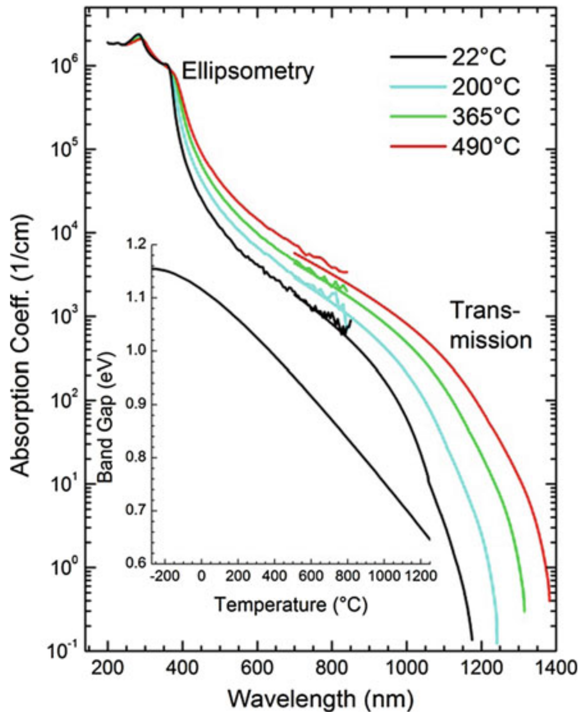

Fig. 8.7 The absorption coefficient of silicon as a function of temperature. The short wavelength region (<850 nm) was determined using spectroscopic ellipsometry data [30], while the long wavelength data (700–1400 nm) was calculated using (8.9) and (8.10a–8.10e). The inset shows the fundamental band gap energy of silicon as a function of temperature, calculated using (8.11)

error for the 22, 200 and 365 °C spectra, while the ellipsometry value of the absorption coefficient is a little larger than the transmission values for the 490 °C sample. This is likely due to an under-estimate of the overlayer thickness used in reducing the ellipsometry data to n and k.

In the region of primary interest to photovoltaics (below the direct band edge or for wavelengths greater than 400 nm), it can be seen that the refractive index, extinction coefficient and absorption coefficient all increase with temperature. The refractive index increase is small, well-ordered, and shows dispersive behavior, being larger for smaller wavelengths. The extinction coefficient and absorption coefficient are far more complicated, and increase dramatically with temperature over the entire wavelength range 400–1200 nm. In the region from 400 to 700 nm, early ellipsometry results [27, 28] showed that the absorption coefficient depended exponentially on temperature, which is validated here. Near the indirect band edge (900–1400 nm), the behavior is even more complicated due to the decrease in the fundamental band gap with temperature and the importance of the temperature dependence on the phonon population. Specifically, the anti-Stokes process, which requires the absorption of a phonon, will become more important at higher temperatures, since there are more phonons available. As Macfarlane et al. [5] showed, reducing the temperature well below room temperature significantly reduces the availability of phonons, thus reducing the anti-Stokes process. This is all accounted for in (8.9) and (8.10a–8.10e).

In the wavelength region of 400–850 nm, the data shown in Fig. 8.6 has been parameterized, using 5 parameters for the refractive index and 6 parameters for the extinction coefficient [30]. The resulting expressions are given by:

$$n(E,T) = n_o + a(E)T \tag{8.12a}$$

$$n_o(E) = \sqrt{4.565 + \frac{97.3}{E_{dg}^2 - E^2}} \tag{8.12b}$$

$$a(E) = 10^{-4}\left(-1.864 + \frac{53.94}{E_{dg}^2 - E^2}\right) \tag{8.12c}$$

$$k(E,T) = k_o(E)\exp\left(\frac{T}{T_o(E)}\right) \tag{8.13a}$$

$$k_o(E) = -0.0805 + \exp\left(-3.1893 + \frac{7.946}{E_{dg}^2 - E^2}\right) \tag{8.13b}$$

$$T_o(E) = 369.9 - \exp(-12.92 + 5.509E) \tag{8.13c}$$

where the parameter $E_{dg} = 3.648$ eV and is common to both n and k. It is important to understand that these expressions are only valid for wavelengths longer than the

direct band edge in silicon, which will increase with increasing temperature. At room temperature, these expressions are valid from 375 to 850 nm, and at 500 °C, the expressions are valid from 410 to 850 nm.

Near room temperature, the change in refractive index and absorption coefficient can be calculated using the expressions given in (8.9)–(8.13a–8.13c), and are shown in Fig. 8.8, where $(1/n)\ \mathrm{d}n/\mathrm{d}T$ and $(1/\alpha)\ \mathrm{d}\alpha/\mathrm{d}T$ are plotted. The temperature coefficient of the refractive index is shown in the top panel of Fig. 8.8, and shows typical dispersive behavior, where the coefficient decreases at longer wavelengths. The bottom panel in Fig. 8.8 shows the temperature coefficient for the absorption coefficient plotted semilogarithmically. Below 700 nm, the derivatives were determined numerically from (8.13a–8.13c), while above 700 nm, the derivatives were determined from (8.9) and (8.10a–8.10e). The nearly constant temperature coefficient of the absorption coefficient observed from 450 to 750 nm is consistent with the observed exponential behavior of the absorption coefficient from early ellipsometry experiments [27]. The expression for the temperature coefficient of α is decidedly non-linear near the band edge, since the fundamental band gap is shifting to lower energies with increasing temperature and the population of phonons is increasing with increasing temperature. Therefore, the data presented in Fig. 8.8 is only valid near room temperature. However, one might use the expressions presented in (8.9) and (8.10a–8.10e) to calculate the temperature coefficient at other temperatures.

The optical functions of silicon are also dependent on the doping concentrations, as seen in Fig. 8.9. These samples were prepared by ion implantation followed by laser annealing [31], which results in higher doping densities than are attainable using traditional dopant activation techniques. The optical effects are similar for other n-type dopants such as phosphorus or antimony, but significantly less for p-type dopants such as boron. With very high doping densities, the critical points are broadened, and significant changes occur below the direct band gap. This effect is usually of no concern for photovoltaic applications, since conventional

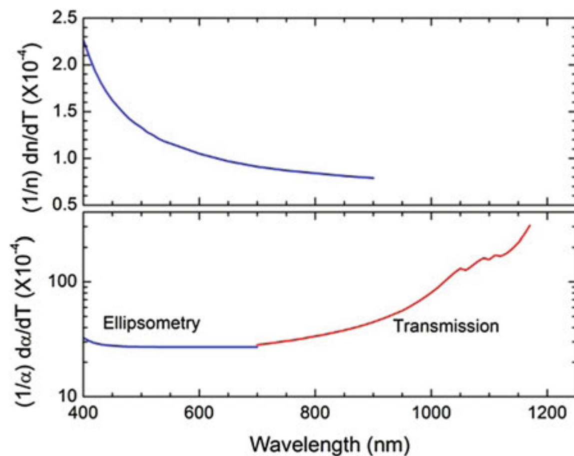

Fig. 8.8 The temperature coefficients of the refractive index and absorption coefficient determined from (8.9), (8.10a–8.10e), (8.12a–8.12c) and (8.13a–8.13c)

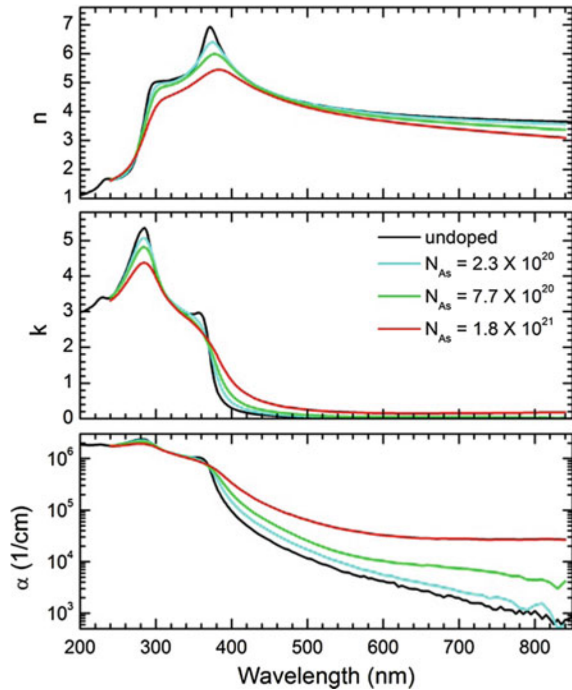

Fig. 8.9 Spectroscopic ellipsometry measurements of the refractive index, extinction coefficient, and absorption coefficient for silicon as a function of doping level (from [31])

photovoltaic doping densities are much lower than is required to see a change in the optical functions.

As might be expected, the optical functions of silicon are also dependent upon the morphology of the material, shown in Fig. 8.10 [32]. The optical functions of semicrystalline silicon (typical grain size of ~0.1–1 mm) show nearly the same optical functions as crystalline silicon, but polycrystalline silicon shows quite different values of the optical functions. Large grain polycrystalline silicon (p-Si LG, grain size ~250 nm) shows optical functions very similar to crystalline silicon, but with broadened critical points and increased absorption below the direct band edge. Small grain polycrystalline silicon (p-Si SG, grain size ~10–20 nm) shows optical functions that are even more broadened, but still resemble the optical functions of crystalline silicon. Amorphous silicon shows significantly different values in the optical functions, and loses any semblance of critical points which are still observable in large-grain and small-grain polycrystalline silicon.

If silicon is strained [33, 34], then the material is no longer strictly cubic, but must be treated as an anisotropic material. The effects on the optical properties near the critical points have been studied by Etchegoin et al. [33], where strains in excess of 0.1 GPa will shift critical points sufficiently to be observed. Similarly, the indirect gap energy will be affected by similar strains [34]. Since the required strains are so large to generate differences in the optical spectra, these effects can normally be ignored in photovoltaics.

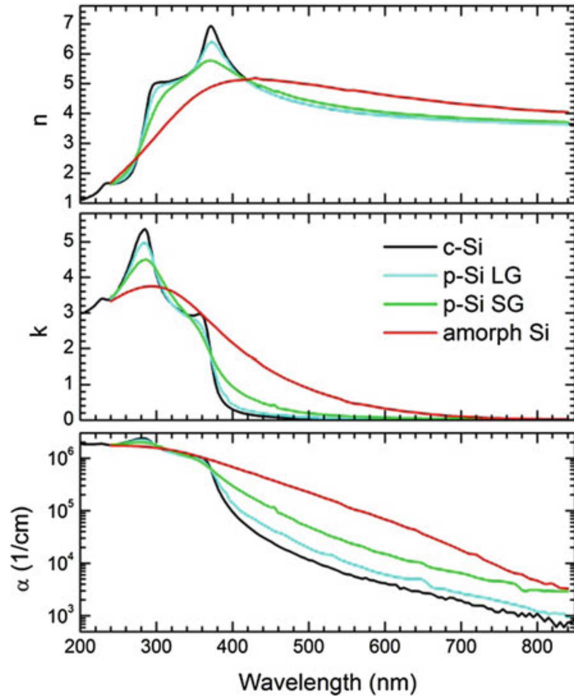

Fig. 8.10 Spectroscopic ellipsometry measurements of the refractive index, extinction coefficient, and absorption coefficient for various morphologies of silicon (from [32])

Silicon melts at 1414 °C, where it becomes metallic. Therefore, its optical properties are considerably different from the solid. Moreover, liquid silicon is very reactive in air, so performing optical measurements on a liquid pool would mean that a significant overlayer would form, which would have to be taken into account in the data analysis. To avoid this complication, measurements of the optical functions of liquid silicon were performed at several cw laser wavelengths using

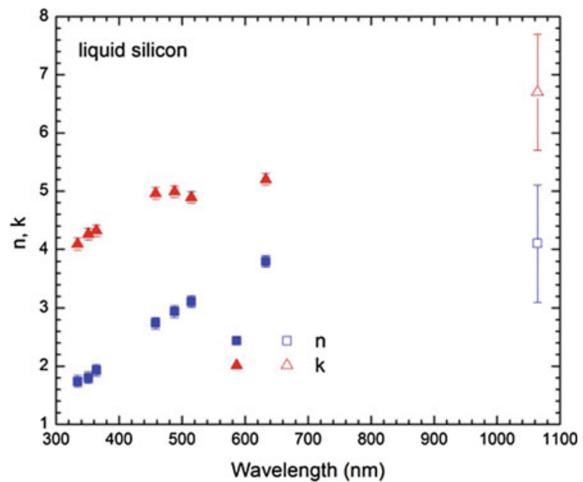

Fig. 8.11 Refractive index n and extinction coefficient of liquid silicon. The solid data points were obtained from [35, 36] where an excimer laser was used to liquefy the silicon surface for ~100 ns. The open points were obtained from [37]

time-resolved ellipsometry [35, 36] during a laser annealing experiment, where the sample surface remains molten for ~100 ns. Similar measurements were done at 1065 nm by Li and Fauchet [37], where the reflectivity was monitored. These results are shown in Fig. 8.11.

8.3 Spectroscopic Ellipsometry of Thin Films on Silicon

There are several dielectric and semiconductor thin films that are commonly used in the silicon photovoltaics industry that are routinely characterized using spectroscopic ellipsometry. As has been shown in Sect. 8.2.4, the optical properties of silicon are dependent on several factors, only one of which is the wavelength of light. This is also true for thin films. Obviously, the optical properties will depend on wavelength and on the constituents of the film. Not so obviously, the optical properties can also depend upon morphology, deposition technique, thickness, impurity type and concentration, etc. Since spectroscopic ellipsometry is non-destructive and is very sensitive to thickness, refractive index, and extinction coefficient, it often is the ideal technique to monitor thin film quality.

Since the optical functions of thin films can vary considerably with deposition conditions, it is important to be able to parameterize these optical functions to analyze spectroscopic ellipsometry measurements. If the material has a band gap that is considerably larger than the highest measured energy, then it is usually a good approximation to model the optical functions of the film using either the Sellmeier equation or the Cauchy expression (discussed in Chap. 5). The Sellmeier approximation is based on the Lorentz oscillator model, where it is assumed that the absorptive part is zero. This expression is given by

$$\varepsilon(\lambda) = n^2(\lambda) = \varepsilon_\infty + \frac{A\lambda^2}{\lambda^2 - \lambda_o^2}, \tag{8.14a}$$

where λ_o is the resonance wavelength of the oscillator (assumed to be less than the smallest measured wavelength), A is the amplitude of the oscillator, and ε_∞ is the dielectric constant at large energy or very small wavelength (this is often 1). If it can be assumed that $\varepsilon_\infty = 1$, then the Sellmeier approximation requires only two fitting parameters A and λ_o. The Sellmeier approximation is often a good model for SiO_2 films on silicon, where $A = 1.099$ and $\lambda_o = 93$ nm.

The Cauchy formula is an empirical relationship that is given by

$$n(\lambda) = A + \frac{B}{\lambda^2} + \frac{C}{\lambda^4} + \cdots, \tag{8.14b}$$

where it is assumed that the absorptive part is zero. Often, the first two parameters are sufficient to fit the spectroscopic variation of the refractive index. For fused silica in the visible range (400–700 nm), $A = 1.458$, $B = 0.00354$ and $C = 0$.

Generally, the Sellmeier expression (8.14a) is more accurate, particularly if the wavelength range of interest extends into the ultraviolet.

If the band gap of the film falls within the wavelength range of the spectroscopic ellipsometry measurement, then the Sellmeier or Cauchy approximations will not be appropriate and a more sophisticated model must be employed. In this case, the extinction coefficient (or the imaginary part of the dielectric function) will be non-zero and needs to be modeled as well as the refractive index. One such model that works quite well for amorphous thin films is the Tauc-Lorentz model [38], which is based on the Tauc band edge [39] convoluted with a Lorentz oscillator to approximate the joint density of states and optical transition probabilities. The imaginary part of the complex dielectric function of the Tauc-Lorentz model is given by

$$\varepsilon_2(E) = 2n(E)k(E) = \frac{A\left(E - E_g\right)^2}{E\left[\left(E^2 - E_o^2\right)^2 + C^2E^2\right]}\Theta\left(E - E_g\right) \tag{8.15a}$$

The real part is determined by performing the Kramers-Kronig integral of $\varepsilon_2(E)$:

$$\varepsilon_1(E) = n^2(E) - k^2(E) = \varepsilon_1(\infty) + \frac{2}{\pi}P\int_{E_g}^{\infty}\frac{\xi\varepsilon_2(E)}{\xi^2 - E^2}\mathrm{d}\xi \tag{8.15b}$$

In (8.15a, 8.15b), E_g is the band gap of the amorphous semiconductor, E_o is the maximum energy of the Lorentz oscillator, C is the broadening parameter, and A is the amplitude. As with the Sellmeier approximation, $\varepsilon_1(\infty)$ is often 1, but can be greater than 1 if there are significant optical transitions at energies greater than sampled by the ellipsometer. The Kramers-Kronig integral can be evaluated exactly, but is too long to be presented here (see [38]). Please note that the amplitude A given here is somewhat different from the expression given in [38], where $A_{new} = A_{old}E_oC$.

Another approach to the modeling of the optical properties of amorphous materials was presented by Ferlauto et al. [40] where Urbach tail absorption is included and the formulation of ε_2 is based on the Cody assumption (parabolic bands and constant dipole matrix element) [41] rather than the Tauc assumption (parabolic bands and constant momentum matrix element). This formulation has a decided advantage of the Tauc-Lorentz formulation when optical transmission studies are included in the data analysis, but the Cody-Lorentz formulation does involve more fitting parameters. In many cases, the difference between the two models is marginal.

As an example of spectroscopic ellipsometry characterization of a thin film system, consider a film of amorphous silicon nitride doped with significant hydrogen (a-Si_xN_y:H) grown on a film of SiO_2 with a silicon substrate. The resulting spectroscopic ellipsometry data (taken from [42]) and the resulting fit are shown in Fig. 8.12. The model used is shown graphically in Fig. 8.12 and consisted of a rough layer, a layer of amorphous non-stoichiometric, hydrogen incorporated

silicon nitride (a-Si_xN_y:H), a layer of silicon dioxide(a-SiO_2), and a substrate of crystalline silicon (c-Si). The rough layer was modeled using the Bruggeman effective medium approximation (see Chap. 3), the silicon nitride layer was modeled by the Tauc-Lorentz formulation [see (8.15a, 8.15b)], and the silicon dioxide layer was modeled by the Sellmeier approximation [see (8.14a)]. The results of the fits are detailed in Table 8.3. Fit 1 utilized 9 fitting parameters, and resulted in significant correlations between the two a-SiO_2 fitting parameters and other parameters in the model. Since the a-SiO_2 parameters are close to those expected for a-SiO_2, a second fit was attempted, where the values of the two a-SiO_2 parameters where held constant at the a-SiO_2 values. As can be seen from Table 8.3, the resulting χ^2 is only marginally higher than that for fit 1, yet the correlated errors for the SiO_2 thickness and some of the Tauc-Lorentz parameters have decreased significantly. The resulting values of the refractive index and extinction coefficient of the a-Si_xN_y:H film are shown in Fig. 8.13, labeled with the energy gap $E_g = 3.82$ eV.

Figure 8.13 shows the refractive index and extinction coefficient for several silicon nitride films determined using spectroscopic ellipsometry measurements analyzed using the Tauc-Lorentz model [43, 44]. The films were grown using plasma-enhanced chemical vapor deposition (PECVD), where the various optical properties are obtained by varying the growth and post-growth conditions. The resulting amorphous film composition is non-stoichiometric silicon nitride with some hydrogen incorporation. As can be seen from Fig. 8.13, the various growth conditions result in quite different optical properties. Generally speaking, the refractive index is controlled by controlling the silane to ammonia flow rate. If the silicon to nitrogen ratio is close to 3–4, then the refractive index tends to be low (~2.02 at 600 nm) with a high-energy band gap. If there is considerably more silicon, then the refractive index tends to be higher, but the band gap tends to be lower. Depending on deposition conditions, there can be significant hydrogen and

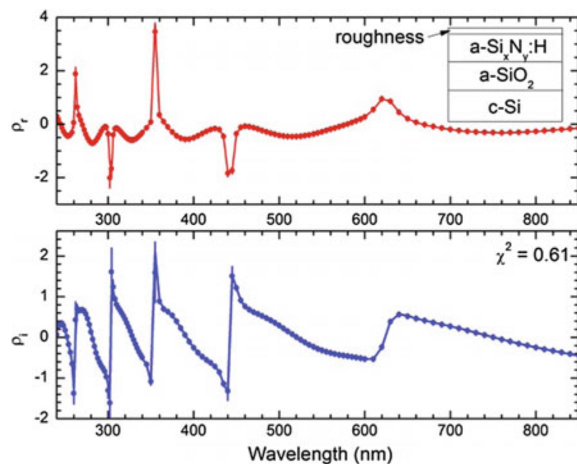

Fig. 8.12 Real and imaginary parts of ρ from a spectroscopic ellipsometry measurement on a-Si_xN_y:H on SiO_2 on c-Si film [42]. The fit line is shown as are the errors. Table 8.3 shows the fitting results

Table 8.3 The fitting results from the spectroscopic ellipsometry data shown in Fig. 8.12. Fit 1 optimized 9 parameters while Fit 2 optimized only 7 parameters, where the Sellmeier coefficients for the SiO_2 layer (indicated with NF) were held constant. The errors shown are the correlated errors

Parameter	Fit 1 ($\chi^2 = 0.61$)	Fit 2 ($\chi^2 = 0.62$)
Rough thick (nm)	2.6 ± 0.3	2.6 ± 0.3
SiN thick (nm)	232.2 ± 0.6	232.4 ± 0.5
SiN TL *A*	4044 ± 455	4243 ± 380
SiN TL E_g (eV)	3.82 ± 0.03	3.82 ± 0.03
SiN TL E_0 (eV)	9.18 ± 0.09	9.24 ± 0.04
SiN TL *C* (eV)	4.14 ± 0.33	4.29 ± 0.27
SiO_2 Thick (nm)	294.7 ± 1.5	295.9 ± 0.2
SiO_2 Sel *A*	1.112 ± 0.014	1.099 (NF)
SiO_2 Sel λ_o (nm)	91.2 ± 2.4	93 (NF)

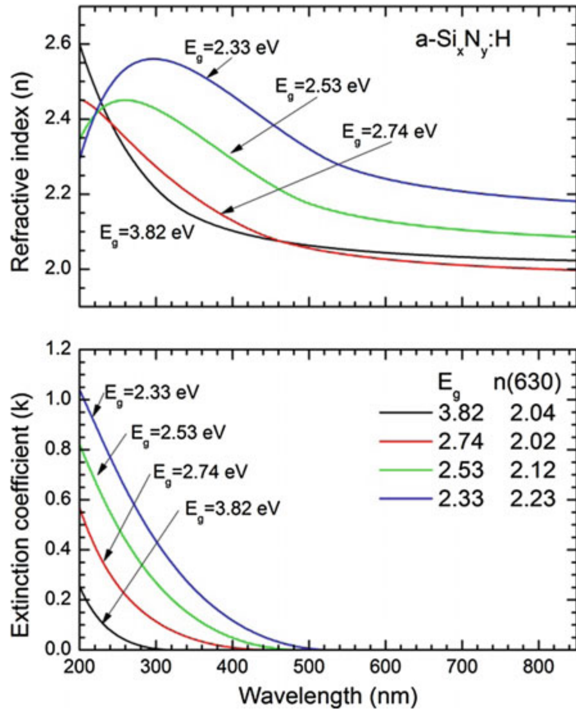

Fig. 8.13 The refractive index *n* and extinction coefficient *k* for several silicon nitride films measured using spectroscopic ellipsometry and analyzed using the Tauc-Lorentz model. The lines are labeled according to the resulting band gap (E_g) and the refractive index at 630 nm

void incorporation, which will also affect the refractive index and extinction coefficient. While a higher refractive index may be better for some applications, the lower band gap means that more of the ultraviolet light will be absorbed in the coating, and this trade-off must be taken into account in coating design.

Since silicon nitride can have such a wide range of optical properties, all controlled by the growth conditions, it makes an ideal material for anti-reflection coatings on silicon solar cells. Reference [44] describes an early study, where a variety of silicon nitride films were grown, measured using spectroscopic

ellipsometry, and then evaluated as potential anti-reflection coatings. Since the refractive index is a function of growth conditions, it is possible to deposit multiple layers of silicon nitride that will be more efficient as an antireflection coating than a single layer. Since the band gap of amorphous silicon nitride falls within the part of the spectrum of interest to photovoltaics, light absorption from the silicon nitride must be taken into account in the anti-reflection coating design.

Generally speaking, spectroscopic ellipsometry measurements are best carried out on smooth surfaces. Small amounts of surface roughness can be addressed using the Bruggeman effective medium approximation, as was done above for the data shown in Fig. 8.12. However, many high-efficiency silicon solar cells have a very rough surface that has been textured using a preferential etch. On single crystal silicon solar cells, this texturing results in the formation of pyramidal structures that are randomly positioned, but of the same orientation. The size of these pyramids is 2–8 μm, which is considerably greater than the wavelength of light used in ellipsometry experiments, resulting in significant light scatter. One solution to this is to tilt the sample in the ellipsometer to 54.7°, such that the ellipsometer light reflects off the sides of the pyramids [45]. This scheme has been used to characterize a-Si_xN_y:H films even on textured mono-crystalline silicon solar cells.

Thin films of amorphous silicon dioxide (a-SiO_2) are commonly found in any silicon technology, including solar cell manufacture. Left in air, silicon will naturally oxidize, stabilizing at a thickness of ~2 nm over several years. The most accurate values of the spectroscopic refractive index of bulk fused silica (a-SiO_2) were determined using the minimum deviation method [13]. The band edge of a-SiO_2 is ~9 eV (~140 nm), so the Sellmeier approximation (8.14a) is sufficient for most ellipsometric measurements. Relatively thick a-SiO_2 films (>100 nm) have spectroscopic refractive indices similar to fused silica, but may vary slightly with differing deposition conditions and water content. Some work has shown that the refractive index of very thin film a-SiO_2 is somewhat higher than bulk a-SiO_2 [46, 47], but others [48] disagree; this probably depends on deposition conditions. Note that the refractive index and thickness of a very thin film become more coupled as the film thickness decreases, making a separate measurement of film thickness and refractive index more difficult. Obviously, if a film growth technique is employed that results in non-stoichiometric a-SiO_x, then the optical functions will be considerably different from thin-film SiO_2 and the Tauc-Lorentz or Cody-Lorentz formulations will be the more appropriate model.

Another film of interest to photovoltaics is Al_2O_3, which can act as a surface passivation layer [49]. Near-stoichiometric Al_2O_3 films will have a refractive index $n \sim 1.60$–1.65 at 620 nm with no observable absorption in the wavelength range 190–1000 nm. This refractive index is considerably less than the refractive index of crystalline Al_2O_3 ($n(o) = 1.7675$, $n(e) = 1.7594$ at 620 nm [50]). As a result, the refractive index of Al_2O_3 films can also be monitored using either the Sellmeier or Cauchy expressions [(8.14a) and (8.14b)]. For solar cell passivation, typical thicknesses are thin (7–30 nm), making spectroscopic ellipsometry the ideal diagnostic for this application. In [49], these films were grown using plasma-assisted atomic layer deposition resulting in surface recombination velocities of 2–6 cm/s.

8.4 Addendum: Optical Data Tables

The spectroscopic ellipsometry room temperature optical data shown in Figs. 8.1, 8.2, 8.3, 8.4, 8.6, 8.7, 8.9, and 8.10 were taken using the two-modulator generalized ellipsometer (2-MGE) [51] on an n-type (100) silicon wafer where the oxide layer was stabilized for several years. The raw data is shown in Fig. 8.1, where the dielectric function and complex refractive index are determined by mathematically removing the surface overlayer using the Newton-Raphson algorithm described in [12], where the a-SiO_2 refractive index values of Malitson [13] were taken for the overlayer. The angle of incidence was $64.96 \pm 0.01°$ and the thickness of the overlayer was 2.19 ± 0.01 nm. Error limits were determined that included the stochastic errors, as well as the systematic errors of the angle of incidence, the overlayer thickness and accidental misalignment of the optics. Additional error, not included, arises from the model chosen to represent the optical functions of the overlayer. The thickness of the a-SiO_2 overlayer was chosen such that the value of k as measured by spectroscopic ellipsometry measurements matched up with the value of k determined from transmission measurements in the 700–800 nm range. If the error limits are taken into account, there is no significant difference between this data and the data presented in [15] although the instruments were quite different.

The absorption coefficients from 700 to 1200 nm shown in Figs. 8.3 and 8.5 were determined using optical transmission measurements of several samples of double-sided polished silicon wafers of various thicknesses from 40 to 240 μm. The transmission measurements were taken using a Perkin-Elmer Lambda 900 spectrophotometer, and the absorption coefficients were determined from the transmission measurements as described in Sect. 8.2. Errors were also determined from estimates of the spectrometer error and the error in the measurement of the thickness of the various wafers. These errors are most pronounced in the 700–800 nm range (see Fig. 8.5) where there is very little light transmission even through the thinnest silicon wafer.

The data shown in Part II Chapter 8.2.1 (Vol. 2) of this book is a compilation of this data. The refractive index data from 300 to 850 nm was taken from the 2-MGE measurements, and the refractive index from 850 to 1200 nm was taken from the work of Herzinger [17] and Green [23]. The 2-MGE data was used for the extinction coefficient from 300 to 700 nm. From 700 to 1200 nm, the calculated absorption coefficient (transformed to extinction coefficient) from (8.9) and (8.10a–8.10e) was used, where the coefficients of Table 8.2 were used. Recall that this expression was a fit to the experimental data and associated error with a reduced $\chi^2 = 0.84$. This data set agrees with the compilation of Geist [21] and the measurements of Schinke [18] within 1–2%, which is within the error of the measurement. However, this data set is ~5% less than the compilation of Green [22], which may be due to small differences in the actual sample temperature during measurement.

Table 8.4 shows a comparison between the various data sets obtained from ellipsometry measurements as well as the compilations of Geist [21] and Green [23]. Three wavelengths were chosen for comparison: 350 nm (just above the direct band

Table 8.4 Comparison of various data sets, including the average and an estimate of the standard deviation. The data used in this work is also shown, along with the error associated with each data point

Author	*n*(350)	*n*(400)	*n*(700)	*k*(350)	*k*(400)	*k*(700)
Aspnes (1983) [14]	5.484	5.587	3.772	2.904	0.298	0.011
Jellison (1992) [15]	5.486	5.585	3.772	2.914	0.296	0.011
Yasuda (1994) [16]	5.507	5.587	3.780	2.960	0.308	0.012
Herzinger (1998) [17]	5.531	5.632	3.773	2.942	0.286	0.009
Schinke(2015) [18]				2.908	0.326	0.011
Geist (1988) [21]		5.583	3.775		0.296	0.010
Green (2008) [23]	5.494	5.613	3.772	2.938	0.296	0.011
This work (2015)	5.498	5.595	3.770	2.924	0.304	0.011
Error	0.010	0.009	0.006	0.011	0.006	0.003
Average	5.500	5.597	3.773	2.927	0.301	0.011
Std. dev.	0.016	0.017	0.003	0.019	0.011	0.001
% error	0.3	0.3	0.1	0.6	3.6	9.1

edge), 400 nm (just below the direct band edge) and 700 nm (well below the direct band edge). Table 8.4 also shows the average values and the standard deviation from the average. Clearly, there is very little difference between the various data sets in the refractive index, where the % error is ~0.3%; we know the refractive index of silicon very well. There is considerably more error in the extinction coefficient, particularly when the extinction coefficient is small. This is an inherent limitation of ellipsometry measurements of small extinction coefficients, where it is more advantageous to use optical transmission measurements.

Acknowledgements GEJ acknowledges Oak Ridge National Laboratory for the use of facilities in the preparation of this manuscript. The work of PCJ was supported by the Department of Energy, Laboratory Directed Research and Development program at Oak Ridge National Laboratory, under contract DE-AC05-00OR22725.

References

1. W. Shockley, H.J. Queisser, J. Appl. Phys. **32**, 510 (1961)
2. W.C. Dash, R. Newman, Phys. Rev. **99**, 1151 (1955)
3. C.D. Salzberg, J.J. Villa, J. Opt. Soc. Am. **47**, 244 (1957)
4. W.G. Spitzer, H.Y. Fan, Phys. Rev. **106**, 882 (1957)
5. G.G. Macfarlane, T.P. McLean, J.E. Quarrington, V. Roberts, Phys. Rev. **111**, 1245 (1958)
6. H.R. Philipp, E.A. Taft, Phys. Rev. **120**, 37 (1960)
7. W. Primak, Appl. Opt. **10**, 759 (1971)
8. H.R. Philipp, J. Appl. Phys. **43**, 2835 (1972)
9. H.W. Icenogle, B.C. Platt, W.L. Wolfe, Appl. Opt. **15**, 2348 (1976)
10. H.A. Weakliem, D. Redfield, J. Appl. Phys. **50**, 1491 (1979)
11. G.E. Jellison Jr., D.H. Lowndes, Appl. Phys. Lett. **41**, 594 (1982)

12. G.E. Jellison Jr. in Ch. 3 of *Handbook of Ellipsometry*, ed. by H.G. Tompkins, E.A. Irene (William Andrew, Norwich, NY, 2005)
13. I.H. Malitson, J. Opt. Soc. Am. **55**, 1205 (1965)
14. D.E. Aspnes, A.A. Studna, Phys. Rev. B **27**, 985 (1983)
15. G.E. Jellison Jr., Opt. Mat. **1**, 41 (1992)
16. T. Yasuda, D.E. Aspnes, Appl. Opt. **33**, 7435 (1994)
17. C.M. Herzinger, B. Johs, W.A. McGahan, J.A. Woollam, W. Paulson, J. Appl. Phys. **83**, 3323 (1998)
18. C. Schinke, K. Bothe, P.C. Peest, J. Schmidt, R. Brendel, Appl. Phys. Lett. **104**, 081915 (2014)
19. C. Schinke, P.C. Peest, J. Schmidt, R. Brendel, K. Bothe, M.R. Vogt, I. Kroger, S. Winter, A. Schirmache, S. Lim, H.T. Nguyen, D. MacDonald, AIP Adv. **5**, 067168 (2015)
20. J. Geist, A. Migdall, H.P. Baltes, Appl. Opt. **27**, 3777 (1988)
21. J. Geist, in *Handbook of Optical Constants*, ed. by E.D. Palik (Academic Press, London, 1998)
22. M.J. Keevers, M.A. Green, Appl. Phys. Lett. **66**, 174 (1995)
23. M.A. Green, Sol. Energy Mater. Sol. Cells **92**, 1305 (2008)
24. P.Y. Yu, M. Cardona, *Fundamentals of Semiconductors: Physics and Materials Properties*, 3rd edn. (Springer, Berlin, 2005)
25. P. Lautenschlager, M. Garriga, L. Viña, M. Cardona, Phys. Rev. B **36**, 4821 (1987)
26. C.D. Thurmond, J. Electrochem. Soc. **122**, 1133 (1975)
27. G.E. Jellison Jr., F.A. Modine, Appl. Phys. Lett. **41**, 180 (1982)
28. G.E. Jellison Jr., F.A. Modine, Phys. Rev. B **27**, 7466 (1983)
29. G.E. Jellison Jr., H.H. Burke, J. Appl. Phys. **60**, 841 (1986)
30. G.E. Jellison Jr., F.A. Modine, J. Appl. Phys. **76**, 3758 (1994)
31. G.E. Jellison Jr., S.P. Withrow, J.W. McCamy, J.D. Budai, D. Lubben, M.J. Godbole, Phys. Rev. B **52**, 14607 (1995)
32. G.E. Jellison Jr., M.F. Chisholm, S.M. Gorbatkin, Appl. Phys. Lett. **62**, 3348 (1993)
33. P. Etchegoin, J. Kircher, M. Cardona, Phys. Rev. B **47**, 10292 (1993)
34. F.H. Pollak, Surf. Sci. **37**, 863 (1973)
35. G.E. Jellison Jr., D.H. Lowndes, Appl. Phys. Lett. **47**, 718 (1985)
36. G.E. Jellison Jr., D.H. Lowndes, Appl. Phys. Lett. **51**, 352 (1987)
37. K.D. Li, P.M. Fauchet, Solid State Commun. **61**, 207 (1987)
38. G.E. Jellison Jr., F.A. Modine, Appl. Phys. Lett. **69**, 371 (1996); ibid. 2137 (1996)
39. J. Tauc, R. Grigorovici, A. Vancu, Phys. Status Solidi **15**, 627 (1966)
40. A.S. Ferlauto, G.M. Ferreira, M. Pearce, C.R. Wronski, R.W. Collins, X. Deng, G. Ganguly, J. Appl. Phys. **92**, 2424 (2002)
41. G.D. Cody, in *Semiconductors and Semimetals*, vol. 21B ed. by J.I. Pankove (Academic, Orlando, FL, 1984), p. 11
42. G.E. Jellison Jr., V.I. Merkulov, A.A. Puretzky, D.B. Geohegan, G. Eres, D.H. Lowndes, J.B. Caughman, Thin Solid Films **377–378**, 68 (2000)
43. G.E. Jellison Jr., F.A. Modine, P. Doshi, A. Rohatgi, Thin Solid Films **313–314**, 193 (1998)
44. P. Doshi, G.E. Jellison Jr., A. Rohatgi, Appl. Opt. **36**, 7826 (1997)
45. M.F. Saenger, J. Sun, M. Schadel, J. Hilfiker, M. Schubert, J.A. Woollam, Thin Solid Films **518**, 1830 (2010)
46. E.A. Taft, L. Cordes, J. Electrochem. Soc. **126**, 131 (1979)
47. G.E. Jellison Jr., J. Appl. Phys. **69**, 7627 (1991)
48. C.M. Herzinger, B. Johs, W.A. McGahan, W. Paulson, Thin Solid Films **313–314**, 281 (1998)
49. B. Hoex, J. Schmidt, P. Pohl, M.C.M. van de Sanden, W.M.M. Kessels, J. Appl. Phys. **104**, 044903 (2008)
50. I.H. Malitson, M.J. Dodge, J. Opt. Soc. Am. **62**, 1405 (1972)
51. G.E. Jellison Jr., F.A. Modine, Appl. Opt. **36,** 8184 (1997); Appl. Opt. **36**, 8190 (1997)

Chapter 9
Amorphous/Crystalline Si Heterojunction Solar Cells

Hiroyuki Fujiwara

Abstract For characterization of hydrogenated amorphous silicon (a-Si:H)/crystalline silicon (c-Si) heterojunction structures, spectroscopic ellipsometry (SE) has been applied extensively. The ellipsometry method is particularly powerful for the determination of quite thin a-Si:H structures (~50 Å) incorporated into the devices. In a-Si:H/c-Si heterojunction solar cells, the formation of ideal a-Si:H/c-Si interface is critical to achieve high conversion efficiencies. For the detection of unfavorable interface formation, such as epitaxial growth of intended a-Si:H layers, SE provides an easy and quick tool. In this chapter, we will overview the ellipsometry analysis of a-Si:H layers formed on c-Si substrates. The analysis examples for detrimental Si epitaxial growth that occurs rather easily at low process temperatures are also presented. This chapter further addresses the interpretation of a-Si:H dielectric functions based on local amorphous networks. The variation of optical constants in a-SiO:H and a-SiC:H alloys, which have been applied to c-Si heterojunction solar cells, is also reviewed in this chapter.

9.1 Introduction

In crystalline silicon (c-Si) solar cells, suppression of carrier recombination at both the front and rear interfaces is crucial to realize high conversion efficiencies. In heterojunction solar cells based on c-Si, to prevent interface recombination, heterostructures with hydrogenated amorphous silicon (a-Si:H) are formed [1–7]. The a-Si:H/c-Si heterojunction architecture allows the fabrication of high efficiency devices with a conversion efficiency of ~26% [7, 8], which is the highest among various designs of c-Si solar cells [8]. Furthermore, in a-Si:H/c-Si solar cells, a lower temperature coefficient has been observed for the efficiency reduction at high operating temperatures [2–5]. Thus, a-Si:H/c-Si solar cells can be considered as one of the most promising solar cells particularly in warmer regions.

H. Fujiwara (✉)
Gifu University, 1-1 Yanagido, Gifu 501-1193, Japan
e-mail: fujiwara@gifu-u.ac.jp

© Springer International Publishing AG, part of Springer Nature 2018

H. Fujiwara and R. W. Collins (eds.), *Spectroscopic Ellipsometry for Photovoltaics*,
Springer Series in Optical Sciences 212,
https://doi.org/10.1007/978-3-319-75377-5_9

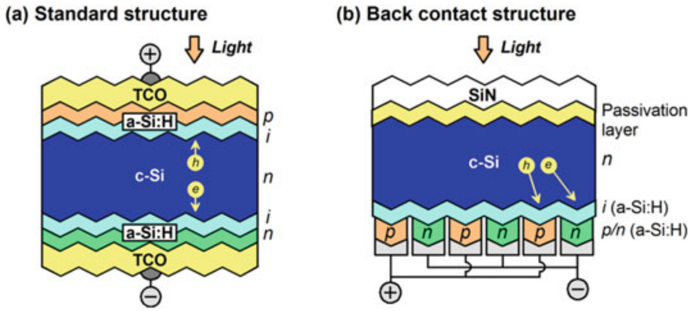

Fig. 9.1 **a** Standard [2–6] and, **b** back contact [7] structures of a-Si:H/c-Si heterojunction solar cells. In the figures, "e" and "h" denote the electron and hole generated within the c-Si by light, respectively

Figure 9.1 shows (a) standard [2–6] and (b) back contact [7] structures of a-Si:H/c-Si heterojunction solar cells. In the standard a-Si:H/c-Si solar cells, a-Si:H *p-i* and *i-n* layers are introduced at the c-Si front and rear interfaces, respectively. This photovoltaic device has a *p-i-n* structure in the front, while the rear a-Si:H *i*/*n* layers serve as the back-surface field (BSF) layers. In particular, the a-Si:H *i* layer introduced at the front side plays a vital role in suppressing carrier recombination [1–4]. Because of low conductivities of a-Si:H layers, however, transparent conductive oxide (TCO) layers are provided as the front and rear electrodes [2–6]. For the TCO, In_2O_3:Sn (ITO) layers are generally employed. In this solar cell, to lower series resistance, metal-grid electrodes are also provided. For the structure of Fig. 9.1a, an efficiency of 24.7% with an open-circuit voltage (V_{oc}) of 750 mV, a short-circuit current density (J_{sc}) of 39.5 mA/cm^2 and a fill factor (FF) of 83.2% is reported [6]. The quite high V_{oc} is consistent with the effective suppression of interface recombination in the solar cell.

In the standard solar cells, however, the optical losses caused by (i) strong free carrier absorption in the ITO layer [5, 9–13] (Chaps. 18 and 19) and (ii) shadow loss due to the front grid electrode [6, 9, 12] (typically ~5% of a cell area) are present. In this structure, the thickness of the front TCO layer is limited to the maximum thickness of ~700 Å to satisfy the anti-reflection condition at the wavelength of $\lambda \sim 560$ nm (Fig. 18.4). To lower series resistance in the 700-Å-thick ITO layers, a high carrier concentration of 10^{20}–10^{21} cm^{-3} is generally necessary [10, 11]. In this case, however, the ITO layers show intense free carrier absorption, which in turn reduces J_{sc} [10–13]. To suppress free carrier absorption, high mobility TCO layers have also been applied for a-Si:H/c-Si solar cells [10, 13] (Chap. 19).

In the back contact configuration of Fig. 9.1b, the optical losses due to the TCO and metal-grid electrode can be eliminated completely. In this structure, a SiN anti-reflection/passivation layer is provided on the front side, while a-Si:H *i-p* and *i-n* structures are placed on the rear side. For a-Si:H/c-Si back-contact solar cells, a

record efficiency of 26.3% has been reported (V_{oc} = 743 mV, J_{sc} = 42.2 mA/cm^2, FF = 83.8%) [8]. One drawback of this solar cell structure is complicated processing steps required for the *p*/*n* region formation on the rear side.

Device performance of a-Si:H/c-Si solar cells is quite sensitive to the quality and structure of a-Si:H layers. For the characterization of a-Si:H layers incorporated into a-Si:H/c-Si, spectroscopic ellipsometry (SE) has been applied extensively [14–25]. In general, for a-Si:H/c-Si solar cells, quite thin a-Si:H *p*-*i* layers with a thickness of ~50 Å are used to suppress the parasitic light absorption [1, 15]. The SE technique is particularly effective for the characterization of such thin layers. The SE measurements can be performed even for a-Si:H layers formed on pyramid-type c-Si textures [23–25] (Chap. 4 in Vol. 2). In this case, the measurements are carried out in a special configuration (tilt-angle configuration) to detect the specular light reflection on the Si {111} facets (see Fig. 4.3 in Vol. 2).

In a-Si:H/c-Si heterojunction solar cells, formation of ideal a-Si:H/c-Si heterointerface is of significant importance to realize high V_{oc} and low temperature coefficient. More specifically, intended a-Si:H *i* layers formed on c-Si substrates often show the epitaxial growth in plasma-enhanced chemical vapor deposition (PECVD) even when substrate temperatures are sufficiently low (>130 °C) [16, 17], and the formation of the epitaxial layer at the a-Si:H/c-Si interface deteriorates the conversion efficiency and passivation quality of a-Si:H/c-Si solar cells significantly [16–20]. The presence of the epitaxial layers can be detected rather easily from SE (Sect. 9.3) and thus SE is a desirable tool for characterizing detailed a-Si:H/c-Si interface structures.

To suppress the epitaxial growth on c-Si substrates, hydrogenated amorphous silicon oxide (a-SiO:H) layers have been applied for Si heterojunction solar cells [26, 27]. In addition, the a-SiO:H/c-Si solar cell exhibits a temperature coefficient even lower than that of the a-Si:H/c-Si [28] and research efforts continue to realize better efficiencies in a-SiO:H/c-Si devices [28–31]. More recently, a high conversion efficiency of 19.4% has been reported by replacing a-Si:H *p* and *n* layers with transparent MoO_x and LiF layers, respectively [32] (see Fig. 18.1f). In this solar cell, due to a high band gap (E_g) of the MoO_x front layer, the parasitic absorption of the a-Si:H *p* layer is reduced, although the a-Si:H *i* layer is still necessary to maintain high V_{oc}. SE can also be applied to characterize such advanced solar cell structures.

9.2 Ellipsometry Analysis of a-Si:H/c-Si Structures

In this section, simple SE analyses for a-Si:H layers formed on flat c-Si substrates are explained. Moreover, we will examine the a-Si:H growth processes in PECVD based on real-time SE measurements.

9.2.1 Analysis of a-Si:H Layers on c-Si Substrates

The SE analysis of a-Si:H/c-Si structures can be performed rather easily, as the c-Si substrate is atomically flat and the surface roughness of a-Si:H layers is generally quite small (~10 Å). Figure 9.2 shows (a) optical model for a-Si:H/c-Si structures and (b) SE analysis performed for a single a-Si:H *i* layer (~200 Å) formed by PECVD at 130 °C. In the optical model, the a-Si:H layer is expressed by two components: i.e., the surface roughness layer and bulk layer with thicknesses of d_s and d_b, respectively. The dielectric function of a-Si:H layers can be modeled by the Tauc-Lorentz model [33] (Sect. 5.3.7) or Cody-Lorentz model [34]. In this chapter, to simplify the analysis, we use the Tauc-Lorentz model described by five free parameters: the amplitude parameter (A), peak transition energy (E_0), broadening parameter (C), Tauc optical gap (E_g) and energy-independent contribution to ε_1 at high energies [$\varepsilon_1(\infty)$] (see Fig. 5.15).

The optical properties of the surface roughness layer can be calculated as a mixture of the bulk layer and void components using the Bruggeman effective medium approximation (EMA) [35, 36] (see Fig. 3.10). For conventional a-Si:H layers fabricated by PECVD, the void volume fraction of 50 vol.% within the surface roughness layers provides a good approximation [36, 37]. In particular, d_s obtained under this assumption shows high correlation with the root-mean-square roughness estimated from atomic force microscopy (AFM) measurements [36, 37] (Fig. 6.1b). Thus, the validity of the SE analysis can be confirmed from AFM. Conversely, d_s values used in SE analyses can be determined by referring to AFM results.

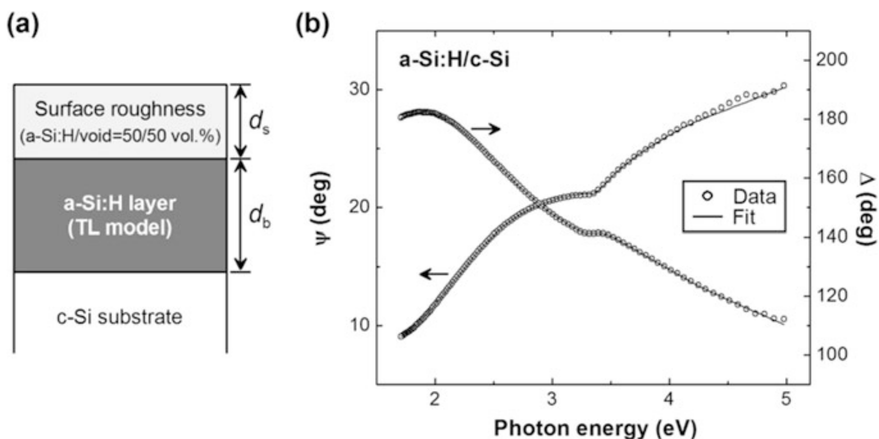

Fig. 9.2 **a** Optical model for an a-Si:H layer formed on c-Si and, **b** SE analysis for a single a-Si:H *i* layer (~200 Å) deposited by PECVD at 130 °C. In **a**, d_s and d_b denote the thicknesses of the surface roughness and bulk layers, respectively. The dielectric function of the a-Si:H layer is calculated by the Tauc-Lorentz (TL) model

For the dielectric function of the c-Si substrate, reported values can be employed. However, there are slight inconsistencies in reported c-Si dielectric functions in the ultraviolet (UV) region (Fig. 8.4 and [38], for example). Thus, depending on c-Si optical constants used in the analysis, the SE result may change slightly. Furthermore, for the fabrication of a-Si:H/c-Si solar cells, c-Si substrates are generally treated by a HF or a NH_4F solution to prepare H-terminated c-Si surface (hereafter described as H/c-Si). Unfortunately, the c-Si surface obtained from this treatment is not perfectly flat and exhibits micro-roughness (<5 Å). In addition, the H-termination modifies the c-Si optical properties in the UV region slightly [39, 40]. One effective way to avoid uncertainties in the SE analysis is to calculate a pseudo-dielectric function ($\langle \varepsilon \rangle$, Sect. 3.5.1) from experimental (ψ, Δ) spectra obtained from a H/c-Si sample and apply this as "ε" of the c-Si substrate. In this case, however, H/c-Si samples need to be sufficiently flat (<5 Å). It should be noted that oxidation of the H-terminated surface still occurs after air exposure and the H/c-Si surface should be characterized immediately after HF/NH_4F etching [39, 40].

In the optical model of Fig. 9.2a, the (ψ, Δ) spectra are calculated by total seven parameters [i.e., $(A, E_0, C, E_g, \varepsilon_1(\infty))_{\text{Tauc-Lorentz}}$, d_b, d_s]. The result of the SE fitting analysis using these parameters is shown in Fig. 9.2b. The experimental SE spectra were obtained at room temperature using an incident angle of $\theta = 70.6°$. It can be seen that the calculated spectra (solid lines) show excellent agreement with the experimental spectra (open circles) in a wide energy region. The slight disagreement observed in the UV region is caused by measurement errors induced by low light intensities of a Xe light source in this region [35]. The numerical parameters determined by the analysis are $A = 216.7 \pm 0.7$ eV, $E_0 = 3.616 \pm 0.003$ eV, $C = 2.287 \pm 0.005$ eV, $E_g = 1.765 \pm 0.002$ eV, $\varepsilon_1(\infty) = 0.78 \pm 0.02$, $d_b = 204.2 \pm 0.3$ Å and $d_s = 10.5 \pm 0.3$ Å. From such analyses, the quantitative evaluation of a-Si:H/c-Si structures can be performed rather easily.

Figure 9.3 shows (a) the a-Si:H dielectric function extracted from the SE spectra of Fig. 9.2b and (b) the E_g analysis of the a-Si:H assuming the Cody gap. In Fig. 9.3a, the open circles show the experimental dielectric function obtained using the mathematical inversion (point-by-point fitting) described in Sect. 10.2.1 [35]. More specifically, in the optical model of Fig. 9.2a, $\rho = \tan\psi \exp(i\Delta)$ is expressed by the following equation:

$$\tan\psi \, \exp(i\Delta) = \rho(\varepsilon_{a\text{-}Si:H}, \varepsilon_{c\text{-}Si}, \theta, d_b, d_s), \tag{9.1}$$

where $\varepsilon_{\text{a-Si:H}}$ and $\varepsilon_{\text{c-Si}}$ denote the dielectric functions of the a-Si:H and c-Si, respectively. The actual calculation of (9.1) is made by considering optical interference effect in thin film structures (see Fig. 3.14). Since (i) $\varepsilon_{\text{c-Si}}$ and θ are known and (ii) d_b and d_s are already determined from the SE analysis using the Tauc-Lorentz model, the two parameters ($\varepsilon_{\text{a-Si:H}} = \varepsilon_1 - i\varepsilon_2$) at each photon energy can directly be extracted from the (ψ, Δ) values based on the fitting analysis using (9.1) (mathematical inversion). On the other hand, the solid lines in Fig. 9.3a represent the a-Si:H dielectric function calculated from the Tauc-Lorentz model

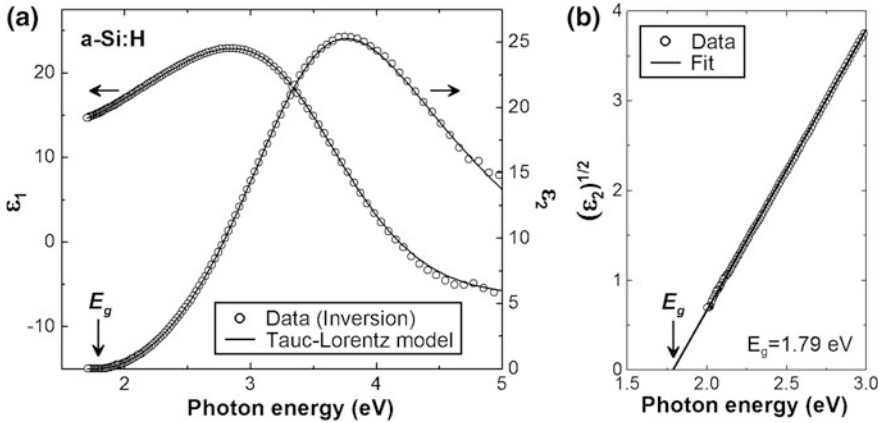

Fig. 9.3 **a** Room-temperature dielectric function of a-Si:H, extracted from the SE spectra of Fig. 9.2b, and, **b** E_g analysis of the a-Si:H assuming the Cody gap. In **a**, the open circles show the experimental dielectric function obtained from the mathematical inversion, while the solid lines show the result calculated from the Tauc-Lorentz parameters. The E_g position in **a** represents the Cody gap position determined by the analysis of **b**. In **b**, the solid line shows the linear fitting result

using the parameter values described above. It can be seen that the dielectric functions obtained from the mathematical inversion and Tauc-Lorentz model are quite consistent.

The dielectric function of the a-Si:H shows a broad single peak with a peak position of $E_0 = 3.62$ eV and the onset of ε_2 ($\varepsilon_2 > 0$) corresponds to E_g. The E_g of amorphous semiconductors can be expressed from the Cody gap, $(\varepsilon_2)^{1/2} = A(E - E_g)$, where A is a proportional constant [41]. Thus, the Cody gap is estimated simply from the energy position of $(\varepsilon_2)^{1/2} = 0$ in $(\varepsilon_2)^{1/2}$–E plots. Superior linearity of the experimental data is observed in the analysis assuming the Cody gap, compared with $(E^2\varepsilon_2)^{1/2} = A(E - E_g)$ that defines the Tauc gap [41]. In Fig. 9.3b, the Cody-gap analysis is performed for the experimental a-Si:H dielectric function extracted by the mathematical inversion. As a result, E_g of 1.79 eV is determined for the a-Si:H layer prepared at a low temperature (130 °C). This Cody gap is slightly larger than the Tauc gap (E_g) defined in the Tauc-Lorentz model ($E_g = 1.765$ eV in the analysis of Fig. 9.2b), as E_g of the Tauc-Lorentz model is deduced from the highest energy position of $\varepsilon_2 = 0$.

Similar SE analyses can be performed for various a-Si:H materials (*p*, *i* and *n* layers) and their a-Si:H alloys (a-SiO:H and a-SiC:H). The dielectric function of a-Si:H *p* layers is resemble to that of the *i* layer, although the ε_2 amplitude and E_g of the *p* layers are smaller. As a result, a-Si:H *p-i* layers on c-Si substrates can be analyzed assuming a single a-Si:H layer on the c-Si substrate [14–17]. Furthermore, if the a-Si:H *p-i* layers are analyzed separately, the thickness parameters of the *p-i* layers may show a high correlation factor in the fitting analysis due to the similar dielectric functions. The validity of SE analyses can basically be judged from the error ranges (confidence limit) of estimated layer thicknesses.

More reliable SE analysis can be carried out based on multi-sample analysis (Sect. 10.2). If similar a-Si:H dielectric functions are obtained, independent of the a-Si:H layer thickness, the analysis results are more reliable. To check the validity of dielectric functions, the a-Si:H dielectric function extracted from a thinner layer can be applied to the analysis of a thicker layer. In this case, if a satisfactory fitting is obtained, the accuracy of the analysis can be validated. AFM measurements can further be employed to justify the d_s value estimated in the SE analysis.

For actual a-Si:H/c-Si heterojunction solar cells, pyramid-type c-Si textures are employed. As mentioned earlier, to determine a-Si:H layer thicknesses on the textured structures, SE measurements in a tilt-angle configuration are necessary [23–25]. However, the a-Si:H thickness on the textures can still be deduced from the a-Si:H layer thickness on the flat substrates since these thicknesses are correlated. Figure 9.4 shows the relation of the a-Si:H thicknesses on the textured c-Si substrates (d_{tex}) and the flat c-Si substrates (d_{flat}) [23]. The a-Si:H thickness in Fig. 9.4 indicates a total thickness calculated from $d_t = d_b + 0.5d_s$, where the coefficient of 0.5 for d_s shows 50 vol.% of voids assumed in the roughness layer. Note that d_{tex} indicates the thickness of an a-Si:H layer measured toward the perpendicular direction to the facet plane, as shown in the inset. It can be seen that both a-Si:H thicknesses show a high linearity expressed by $d_{tex} = 0.69d_{flat} + 14$ Å. Thus, d_{tex} can be deduced from d_{flat}. The offset of 14 Å, however, implies that the initial growth rate of a-Si:H is faster on the textured substrate, compared with the flat substrate.

The thickness reduction in d_{tex} has been interpreted by the change in the surface area [23]. Specifically, on the textured substrate, the total surface area increases rather significantly. Based on the top angle of the pyramid (80°) obtained experimentally, the surface area ratio is estimated to be $S_{tex}/S_{flat} = 1.56$, where S_{tex} and S_{flat} indicate the surface areas of the textured and flat substrates, respectively. If the number of precursors arriving at the surface determines the a-Si:H deposition rate, d_{tex} is expressed as $(S_{flat}/S_{tex})d_{flat} \sim 0.64d_{flat}$, which agrees well with the coefficient of 0.69 in Fig. 9.4. Accordingly, the decrease in d_{tex} can be understood by the

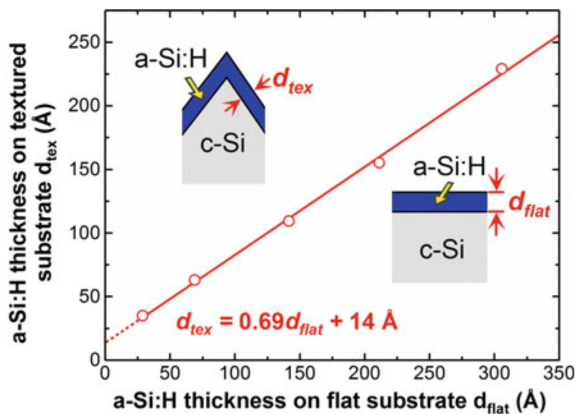

Fig. 9.4 Thickness of an a-Si:H layer formed on the textured c-Si substrate (d_{tex}) versus thickness of an a-Si:H layer formed on the flat c-Si substrate (d_{flat}) [23]. The linear fitting result is shown by the solid line

change in the surface area in the textured structure. The detail of the SE analysis for textured a-Si:H/c-Si structures is described in Chap. 4 (Vol. 2).

9.2.2 Real-Time Characterization of a-Si:H Growth

The growth processes of a-Si:H layers on H-terminated c-Si substrates can be studied in more detail using real-time SE measurements. The SE analysis for real-time spectra is basically similar to that of a standard procedure described in the previous section. However, at process temperatures, the optical properties of materials change and room-temperature data cannot be used for the analysis. For the a-Si:H/c-Si analysis, the dielectric function of H/c-Si at a process temperature can be obtained from the corresponding pseudo-dielectric function, whereas the a-Si:H dielectric function at a process temperature can be determined using the Tauc-Lorentz model. If these dielectric functions are applied, the time evolution of (d_s, d_b) during the a-Si:H growth can be deduced from real-time spectra. More complete SE analysis can be performed using the global error minimization scheme [35, 36]. In this method, the analysis of real-time data is performed self-consistently based on the assumption that the optical properties of the depositing layer do not change within the analyzing thickness range (Sect. 10.2).

Figure 9.5 shows (a) the influence of growth substrate on a-Si:H growth at 130 °C and (b) the models for thin film growth (Volmer-Weber and Stranski-Krastanov). In Fig. 9.5a, the variations of d_s with thickness (d_t) on H/c-Si and SiO_2(native oxide)/c-Si substrates are summarized. On the SiO_2 native oxide, a-Si:H island formation occurs (Volmer-Weber growth) and d_s increases rapidly to ~20 Å at the initial stage of the growth. In this case, after the substrate is covered completely with the islands, a clear smoothening is observed on the growing surface [36]. On the H-terminated surface, however, the island growth is suppressed and d_s shows a smaller value. Thus, the deposition process on the H/c-Si is more close to the Stranski-Krastanov mode, in which the first layer is formed uniformly on a substrate, followed by gradual surface roughening. Real-time infrared spectroscopy performed simultaneously during the real-time SE, however, revealed that a SiH_2-rich layer (~20 Å) is formed at the a-Si:H/c-Si interface [14, 15]. In particular, a quite high SiH_2 concentration of ~30 at.% has been confirmed near the interface region. The formation of the SiH_2-rich porous layer can be interpreted as a consequence of rapid surface roughening observed during the initial growth. Accordingly, the growth process on the substrate directly affects the a-Si:H interface structure.

Figure 9.6 shows (a) the time evolution of d_s and d_b during the a-Si:H *p*-*i* layer growth (130 °C) on a H/c-Si substrate and (b) the transmission electron microscopy (TEM) image of the fabricated a-Si:H/c-Si heterojunction solar cell [14]. In Fig. 9.6, real-time control of a-Si:H layer thickness was performed by SE and the thicknesses of the a-Si:H *p* and *i* layers were adjusted to 50 Å. For the SE analysis of the *p* layer, the dielectric function of the *i* layer was employed and the

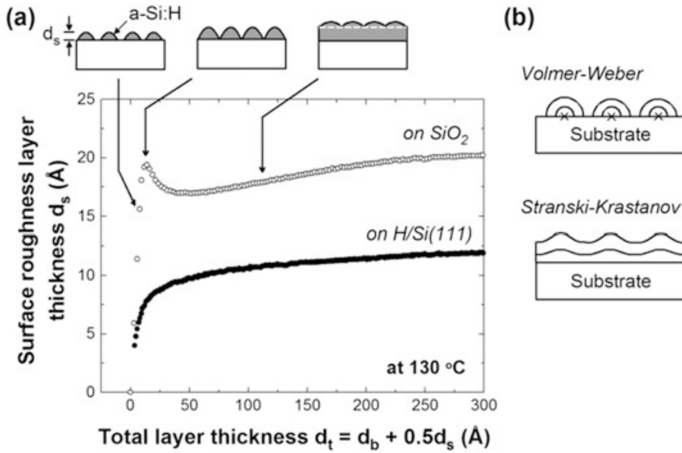

Fig. 9.5 **a** Influence of growth substrate on a-Si:H growth at 130 °C and, **b** models for thin film growth (Volmer-Weber and Stranski-Krastanov)

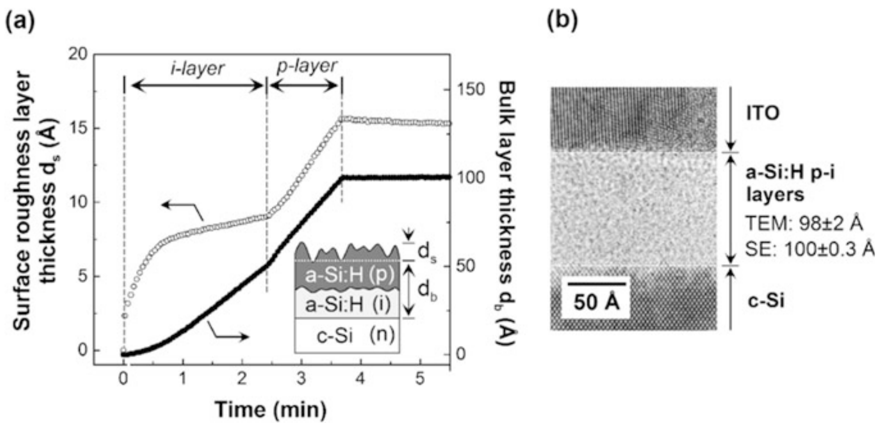

Fig. 9.6 **a** Time evolution of d_s and d_b during a-Si:H *p-i* layer growth at 130 °C on a H/c-Si substrate and, **b** TEM image of the fabricated a-Si:H/c-Si heterojunction solar cell [14]. In this experiment, the thicknesses of the a-Si:H *p* and *i* layers were adjusted to 50 Å by real-time control using SE

intermixing of the *p-i* layers at the interface was neglected. Thus, the a-Si:H *p-i* layer thicknesses were determined using a simple surface roughness layer/bulk layer/substrate structure.

The a-Si:H *i* layer growth in Fig. 9.6a is essentially similar to that shown in Fig. 9.5, but d_s and d_b increase drastically during the *p*-layer growth. These effects can be interpreted by a higher dangling bond density on the *p*-layer surface than that on the *i*-layer surface [42]. The higher *p*-layer dangling bond density is expected to

enhance SiH_3-precursor adsorption on the surface, increasing the roughness by secondary island formation. As confirmed from Fig. 9.6, accurate control of the a-Si:H layer thickness with a precision better than ±1 Å can be achieved by applying SE. In fact, the a-Si:H thickness estimated from the TEM image in Fig. 9.6b shows excellent agreement with the SE result.

Figure 9.7 shows the characteristics of a-Si:H/c-Si:H heterojunction solar cells fabricated by the real-time control of (a) the *i* layer thickness and (b) the *p* layer thickness [15]. The structure of the solar cells is (Ag grid)/ITO(700 Å)/a-Si:H(*p*)/a-Si:H(*i*)/c-Si(*n*)/Al. In Fig. 9.7a, the *i*-layer thickness is varied with a fixed *p*-layer thickness of 50 Å, whereas a fixed *i*-layer thickness of 40 Å was used for the variation of the *p*-layer thickness (Fig. 9.7b). It can be seen that the solar cell characteristics change systematically with the *p*-*i* layer thicknesses and the result indicates the optimum *p*/*i* layer thicknesses of 30/40 Å. For the a-Si:H *i* layer, the best solar cell efficiency is obtained approximately at the thickness where the a-Si:H growth reaches a steady state after the formation of the SiH_2-rich interface layer, as confirmed from Fig. 9.5. Thus, the optimum *i*-layer thickness of 40 Å can be related to the generation of the porous SiH_2-rich structure formed near the a-Si:H/c-Si heterointerface [15].

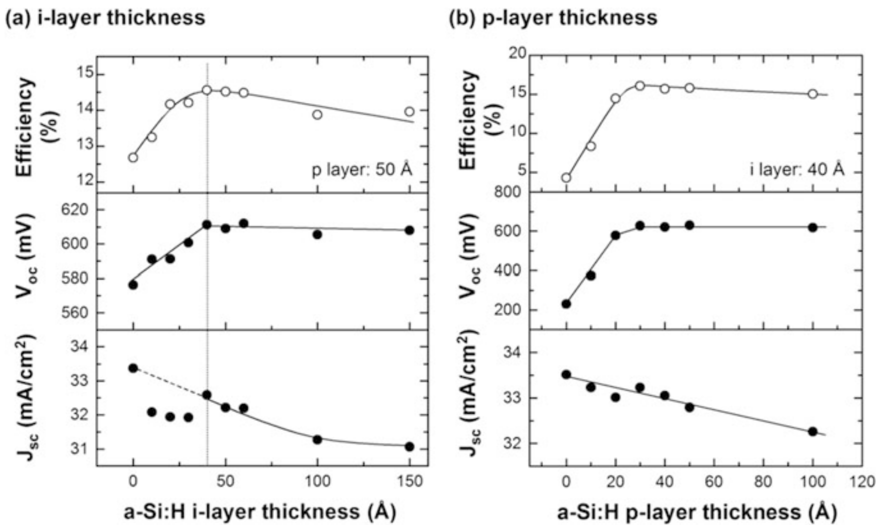

Fig. 9.7 Characteristics of a-Si:H/c-Si heterojunction solar cells fabricated by the real-time control of **a** the *i*-layer thickness and, **b** the *p*-layer thickness [15]. The structure of the solar cells is (Ag grid)/ITO(700 Å)/a-Si:H(*p*)/a-Si:H(*i*)/c-Si(*n*)/Al. In **a**, the *p*-layer thickness is fixed at 50 Å, while the *i* layer thickness is maintained at 40 Å in **b**

9.3 Epitaxial Growth at a-Si:H/c-Si Heterointerface

The structure of a-Si:H/c-Si heterointerface has a significant impact on the solar cell performance. In particular, unintentional Si epitaxial growth occurs on c-Si substrates in PECVD [16–20] and how-wire CVD [43] and the solar cell efficiency decreases significantly by the epitaxial layer formation. The epitaxial growth at the interface can be monitored systematically by applying SE. In this section, the characterization of the a-Si:H/c-Si interface structure by SE is described.

9.3.1 SE Analysis of a-Si:H/c-Si Interface with Epitaxial Growth

Figure 9.8 shows the variation of pseudo-dielectric function ($\langle \varepsilon_2 \rangle$ spectrum) during the plasma deposition of the a-Si:H. In PECVD, the epitaxial growth occurs on H/c-Si even at low temperatures (~140 °C) [16, 17], but the formation of the epitaxial layer is negligible in Fig. 9.8 because of a low process temperature of 130 °C. Before the growth, the dielectric function shows two intense peaks at 3.4 and 4.3 eV due to the E_1 and E_2 transitions in c-Si (Fig. 8.4). During the a-Si:H growth, the amplitude of the E_2 peak reduces significantly even if the thickness of the a-Si:H overlayer is quite thin (d_t = 44 Å at 2.0 min). In contrast, when the epitaxial growth occurs, the ε_2 spectrum shows minor change as the dielectric function of the Si epitaxial layer is essentially the same as that of the c-Si substrate. Thus, when the deposited layer is completely epitaxial, an ex situ SE measurement will confirm no a-Si:H layer formation on the substrate. Furthermore, in the case of the partial epitaxial growth, the a-Si:H thickness decreases from the intended thickness. In

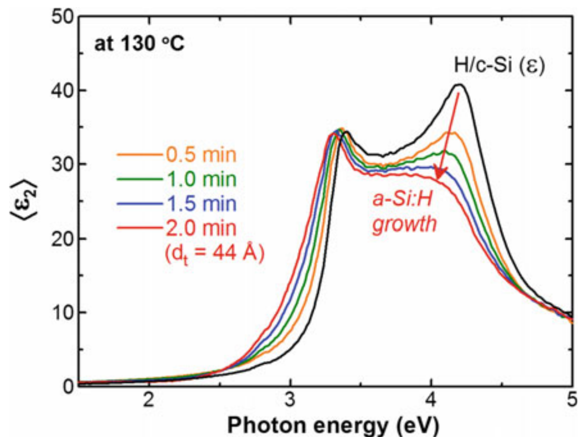

Fig. 9.8 Variation of $\langle \varepsilon_2 \rangle$ spectrum during the PECVD growth of a-Si:H on the H/c-Si at 130 °C. The growth time of each spectrum is indicated

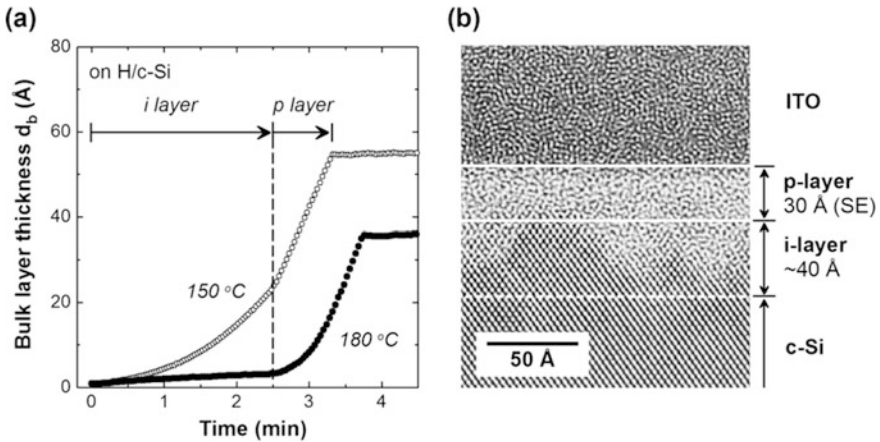

Fig. 9.9 **a** Time evolution of d_b during the Si layer growth on H/c-Si substrates at 150 and 180 °C and, **b** cross-sectional TEM image of the a-Si:H/c-Si solar cell with the partial epitaxial *i* layer formed at 150 °C [16, 17]

other words, the extent of the epitaxial growth can be assessed quite easily from the thickness of the deposited a-Si:H layer.

Figure 9.9 shows (a) the variation of the Si epitaxial growth with processing temperature, characterized by real-time SE, and (b) the cross-sectional TEM image of the a-Si:H/c-Si solar cell with the partial epitaxial *i* layer formed at 150 °C [16, 17]. In Fig. 9.9a, the a-Si:H bulk layer thickness on the H/c-Si is determined using the optical model shown in Fig. 9.6a. In Fig. 9.9a, a fixed process time of 2.5 min was employed for the *i* layer deposition. In this condition, the a-Si:H *i* layer thickness is expected to be ~50 Å, but the nominal *i*-layer thickness at 2.5 min decreases at the high process temperatures due to Si epitaxial growth. The partial epitaxial growth at 150 °C can be confirmed clearly in the corresponding TEM image (Fig. 9.9b). At 180 °C, the complete epitaxial growth occurs and the *i*-layer thickness becomes almost zero. Quite interestingly, the epitaxial growth does not occur in the *p*-layer growth. It has been confirmed from SE that the epitaxial growth occurs on Si (100) substrates, but not on the (111) substrates [19, 20]. In the case of Si pyramid textures with {111} facets, the epitaxial growth is found to occur in the groove region [44].

9.3.2 *Effect of Epitaxial Growth on Solar Cells*

Figure 9.10 summarizes the solar cell efficiencies obtained using various growth temperature and rf power density in PECVD [17]. The solar cells have a structure of (Ag grid)/ITO (700 Å)/a-Si:H *p* layer (30 Å)/a-Si:H *i* layer (40 Å)/c-Si/Al. Because of the lack of the BSF structure (i.e., no a-Si:H *i*-*n* layers on the rear side), the

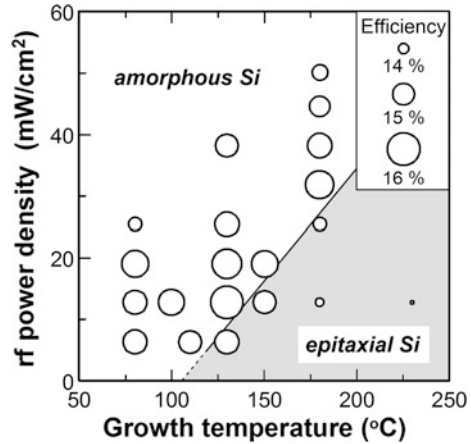

Fig. 9.10 Solar cell efficiencies obtained using various growth temperatures and rf power densities in the PECVD process [17]. The conversion efficiencies of the a-Si:H/c-Si heterojunction solar cells [(Ag grid)/ITO (700 Å)/a-Si:H *p* layer (30 Å)/ a-Si:H *i* layer (40 Å)/c-Si/Al] are represented by the size of the circle, and the amorphous/ epitaxial phase boundary deduced from real-time SE is also indicated

efficiencies of these solar cells are moderate (~16%). In Fig. 9.10, the conversion efficiencies of the a-Si:H/c-Si solar cells are represented by the size of the circle, and the amorphous/epitaxial phase boundary deduced from real-time SE is also indicated. The epitaxial growth takes place at high growth temperatures and low rf powers, and the solar cell efficiency decreases significantly in the epitaxial regime. Even when the growth temperatures are high, the epitaxial growth can be suppressed by increasing ion bombardment (rf power) or growth rate. In a-Si:H/c-Si solar cells, however, the best efficiency is obtained near the amorphous/epitaxial boundary [16, 17]. Accordingly, the control of the Si epitaxial growth is critical in achieving high performance.

The detrimental epitaxial growth of the *i* layer can be suppressed by adopting a-SiO:H *i* layers, instead of a-Si:H *i* layers [26, 27]. In particular, only a small fraction of O is sufficient (O $\geq$ 4 at.%) to prevent the epitaxial growth [26]. As a result, high-efficiency solar cells can be fabricated more easily by applying a-SiO:H *i* layers, although at some deposition conditions the epitaxial growth still occurs [30, 45]. Since a-SiO:H layers have higher E_g, the parasitic light absorption in the thin layers can also be suppressed [28–31]. At this stage, however, the conversion efficiencies of reported a-SiO:H/c-Si solar cells are 17–20% [28–31], and their efficiencies are not comparable to those of the a-Si:H/c-Si, most likely due to the increase of the defect density by O incorporation [46–50].

9.4 Dielectric Functions of a-Si:H, a-SiO:H and a-SiC:H

The fabrication of c-Si heterojunction solar cells has been demonstrated by applying a variety of a-Si:H and its alloy layers. The optical properties of a-Si:H-based materials are influenced strongly by the microvoid formation in the amorphous matrix. In particular, the dielectric function of a-Si:H alloys (a-SiO:H and

a-SiC:H) varies largely with the alloy composition primarily by the drastic increase in a microvoid fraction. In this section, we will examine the effect of local network structure on the dielectric function of a-Si:H and its alloys.

9.4.1 Dielectric Function of a-Si:H

The network structure and optoelectronic properties of a-Si:H have been discussed intensely [51]. Often, the network structure of a-Si:H is represented by continuous random network [52–56], but a-Si:H layer properties change rather significantly with H introduced into the amorphous matrix [57–62] and E_g of a-Si:H increases with the total hydrogen content (C_{total}) [57]. Furthermore, many studies have reported that deformation of the amorphous network occurs by H and microvoids are formed within the a-Si:H matrix [63–73]. Thus, H introduced during a-Si:H growth varies the structure and properties of a-Si:H significantly.

For a-Si:H layers prepared by PECVD, a clear correlation has been observed between the a-Si:H dielectric function in the visible/UV region and SiH_n (n = 1–2) local bonding states in the amorphous network [70]. Figure 9.11 shows (a) ε_2 spectra of a-Si:H layers prepared at different substrate temperatures (T_s) and (b) ε_2 peak value as a function of SiH_2 hydrogen content (C_{SiH2}) in the a-Si:H [70]. The ε_2 spectra of these a-Si:H layers with a thickness of 1000 Å were obtained at room temperature and were extracted by applying the global error minimization scheme (Sect. 10.2). As confirmed from Fig. 9.11a, the ε_2 spectra show a relatively large variation with growth temperature. In particular, the amplitude of the broad ε_2 peak at 3.6 eV decreases as the growth temperature decreases. Moreover, the whole dielectric function shifts toward higher energies with decreasing growth temperature. At $T_s \geq 280$ °C, however, the ε_2 peak amplitude is constant and only a slight ε_2-spectral shift occurs. The result of Fig. 9.11a indicates clearly that the fundamental light absorption in a-Si:H decreases at lower growth temperatures. In addition, the onset of the light absorption ($\varepsilon_2 > 0$) at ~1.7 eV shifts toward higher energy at low temperatures, indicating the optical gap widening in the a-Si:H prepared at low T_s.

The ε_2 peak value in Fig. 9.11b simply represents the ε_2 value at the peak position around 3.6 eV in Fig. 9.11a, and these values obtained at different growth temperatures are plotted as a function of C_{SiH2} determined by infrared spectroscopy. When the a-Si:H growth temperature is reduced in Fig. 9.11, C_{SiH2} increases significantly from 1.1 at.% ($T_s \geq 280$ °C) to 13.1 at.% ($T_s = 80$ °C), while the SiH content (C_{SiH2} shows the moderate changes from 5.4 at.% ($T_s = 310$ °C) to 9.0 at.% ($T_s \leq 180$ °C) [70]. It can be seen that the ε_2 peak value decreases quite linearly with increasing C_{SiH2}, and the amplitude of the ε_2 peak is described quite well by C_{SiH2} in the a-Si:H matrix. The ε_2 amplitude reduction is consistent with the microvoid formation in the a-Si:H network and the light absorption decreases in void-rich a-Si:H layers. The strong correlation between the microvoid and SiH_2

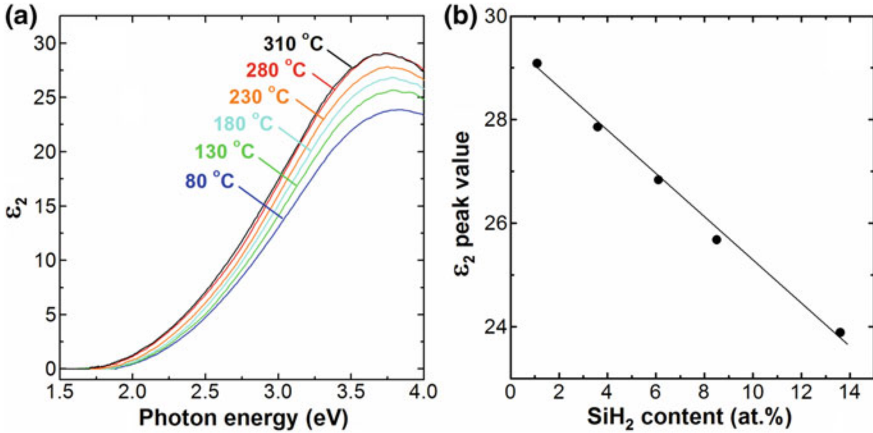

Fig. 9.11 **a** Room-temperature ε_2 spectra of the a-Si:H layers deposited at different substrate temperatures of 80–310 °C and, **b** ε_2 peak value as a function of SiH_2 hydrogen content in the a-Si:H [70]

formation indicates that microvoids present in the a-Si:H network are surrounded by the SiH_2 bondings [70].

On the other hand, when the growth temperature is reduced from 310 to 280 °C, C_{SiH2} shows no change (C_{SiH2} = 1.1 at.%) and only C_{SiH2} increases from 5.4 to 7.1 at.%. In this case, the ε_2 amplitude is constant, but the ε_2 spectrum shifts slightly toward higher energy (Fig. 9.11a). This result confirms that the generation of the SiH local bonding leads to no significant void formation and induces the spectral shift toward higher energy.

The a-Si:H dielectric functions of Fig. 9.11a have been parameterized by applying the Tauc-Lorentz model (Sect. 5.3.7), and good fittings to the experimental data have been confirmed in the whole measured region. In this modeling, a fixed value of C = 2.33 eV is assumed. Figure 9.12 summarizes the variation of the Tauc-Lorentz parameters [A, E_g, E_0, $\varepsilon_1(\infty)$] with $C_{total} = C_{SiH2} + C_{SiH}$ in a-Si:H [70]. The solid lines show the results of liner and polynomial fittings given by

$$A = 217.473 + 0.364C_{total} - 5.076 \times 10^{-2}C_{total}^2 \quad (9.2)$$

$$E_g = 1.562 + 8.260 \times 10^{-3}C_{total} \quad (9.3)$$

$$E_0 = 3.590 + 6.550 \times 10^{-3}C_{total} - 1.267 \times 10^{-4}C_{total}^2 \quad (9.4)$$

$$\varepsilon_1(\infty) = \begin{cases} 0.073 & (C_{total} \leq 8.2\text{ at.\%}) \\ -0.383 + 5.644 \times 10^{-2}C_{total} & (C_{total} > 8.2\text{ at.\%}) \end{cases} \quad (9.5)$$

The units of (A, E_g, E_0) and C_{total} in the above equations are eV and at.%, respectively. With increasing C_{total}, A decreases gradually due to the amplitude

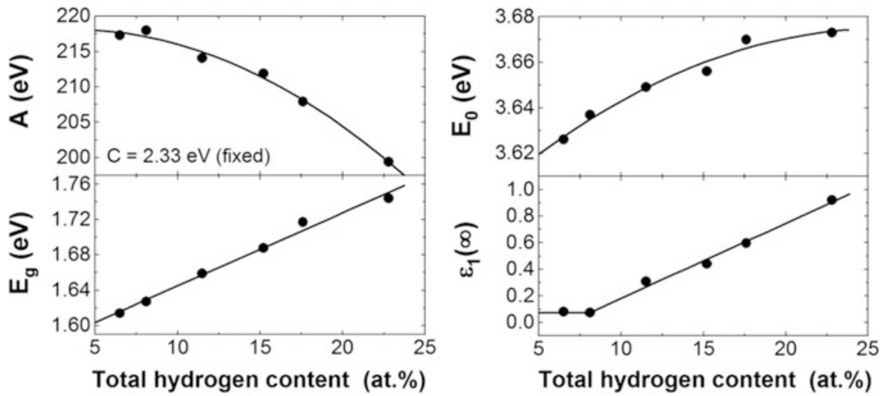

Fig. 9.12 Variation of the Tauc-Lorentz parameters [A, E_g, E_0, $\varepsilon_1(\infty)$] with total hydrogen content in the a-Si:H layers [70]. The sold lines show the fitting results

reduction observed in the ε_2 spectra. The linear variations of E_g and E_0 indicate that the ε_2 spectrum shifts toward higher energies with C_{total}. From (9.2) – (9.5), the dielectric function of a-Si:H can be calculated. However, this model is rather too simple to express various a-Si:H structures, as in this case a-Si:H layer properties are expressed only by C_{total}.

A more complete dielectric function model for a-Si:H has been established by taking the change in a-Si:H network into account. Figure 9.13 represents the plane view of the a-Si:H network assumed in the dielectric function model (a-Si:H network model) [70]. This structural model assumes that (i) microvoids are terminated with SiH_2 bonds and (ii) SiH bonds are embedded into dense network regions. In this model, the ε_2 amplitude reduction is deduced from the amount of C_{SiH2} by considering the volume factor (V_{cav}) and dielectric constant (ε_{cav}) of the SiH_2-microvoid cavity, as described below. Moreover, the ε_2-spectral shift induced by SiH_n is expressed from linear coefficients (k_1 for C_{SiH} and k_2 for C_{SiH2}).

In the above model, the microvoids surrounded by SiH_2 bonds are described based on EMA:

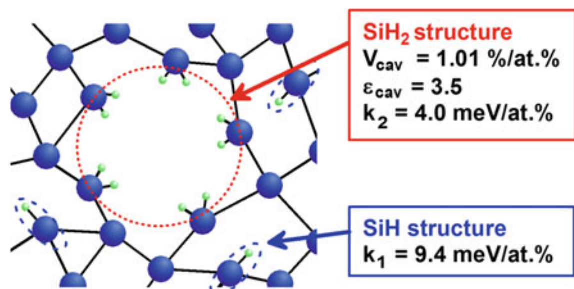

Fig. 9.13 Plane view of the a-Si:H structure assumed in the a-Si:H network model [70]. The red circle shows the microvoid terminated by SiH_2 bonds. The parameter values of the a-Si:H network model are also indicated

$$f_{a\text{-}Si}\frac{\varepsilon_{a\text{-}Si}(E)-\varepsilon_m(E)}{\varepsilon_{a\text{-}Si}(E)+2\varepsilon_m(E)}+f_{cav}\frac{\varepsilon_{cav}-\varepsilon_m(E)}{\varepsilon_{cav}+2\varepsilon_m(E)}=0, \tag{9.6}$$

where $\varepsilon_{\text{a-Si}}(E)$ denotes the dielectric function of a-Si without H. In this model, ε_{cav} is assumed to be an energy-independent constant. In (9.6), the volume fractions of the a-Si and microvoid cavity are described by $f_{\text{a-Si}}$ and f_{cav} ($f_{\text{a-Si}} + f_{\text{cav}} = 1$), respectively. By solving (9.6), we can estimate the dielectric function of the a-Si layer with the SiH_2-microvoid cavity as $\varepsilon_m(E)$. In the actual analysis, $\varepsilon_{\text{a-Si}}$ is represented by $\varepsilon_{\text{a-Si:H}}(E)$ of the highest temperature (310 °C), and f_{cav} is described as $f_{\text{cav}} = V_{\text{cav}}\Delta C_{\text{SiH2}}$, where ΔC_{SiH2} shows the change in C_{SiH2} from the a-Si:H layer deposited at 310 °C (i.e., $\Delta C_{\text{SiH2}} = C_{\text{SiH2}} - 1.1$ at.%). Accordingly, when C_{SiH2} increases at low process temperatures, ΔC_{SiH2} increases and the resulting f_{cav} ($V_{\text{cav}}\Delta C_{\text{SiH2}}$) further reduces the ε_2 amplitude.

On the other hand, the shift of $\varepsilon_{\text{a-Si:H}}(E)$ induced by SiH_n is described simply by

$$\varepsilon_{\text{a-Si: H}}(\text{E}) = \varepsilon_{\text{m}}(E - \Delta E_{\text{SiH}} - \Delta E_{\text{SiH2}}), \tag{9.7}$$

where ΔE_{SiH} and ΔE_{SiH2} show the shift values of the dielectric function for C_{SiH} and C_{SiH2}, respectively. By assuming the linear variation of ΔE with C_{SiH} and C_{SiH2}, ΔE is calculated by $\Delta E_{\text{SiH}} = k_1\Delta C_{\text{SiH}}$ and $\Delta E_{\text{SiH2}} = k_2\Delta C_{\text{SiH2}}$. Here, ΔC_{SiH} shows the change in C_{SiH}, which is given by $\Delta C_{\text{SiH}} = C_{\text{SiH}} - 5.4$ at.%.

The parameter values of (V_{cav}, ε_{cav}, k_1, k_2) have been estimated from the fitting of the a-Si:H dielectric functions of Fig. 9.11a. In particular, the dielectric functions calculated from (9.6) and (9.7) show almost perfect agreement with the experimental data, and the parameter values deduced from this analysis are summarized in Fig. 9.13. The above results indicate that the variation of a-Si:H optical properties in the visible/UV region is caused almost completely by the change in SiH_n local network structures.

If the a-Si:H network model is applied, $\varepsilon_{\text{a-Si:H}}(E)$ is calculated from only two parameters: i.e., C_{SiH} and C_{SiH2}. Figure 9.14 shows the ε_2 spectra of a-Si:H layers calculated from the a-Si:H network model [71]. In Fig. 9.14, variations of ε_2 spectra with (a) C_{SiH2} and (b) C_{SiH} in a-Si:H are shown. When C_{SiH2} increases with a fixed C_{SiH} of 9 at.%, the amplitude of the ε_2 spectrum decreases drastically due to the SiH_2-microvoid formation. On the other hand, when C_{SiH} is varied with $C_{\text{SiH2}} = 9$ at.%, the ε_2 spectrum shifts toward higher energies with no ε_2 amplitude variation. Although a similar spectral shift also occurs with C_{SiH2} ($k_2 = 4.0$ meV/at.%), the shift value is much larger for C_{SiH} ($k_1 = 9.4$ meV/at.%). It should be noted that the energy states of SiH_n are located deeply into the valence band [74–77], and the top of the valence band shifts downward with increasing C_{total} because of the decrease in the density of states by the Si(3*p*)-H(1*s*) interaction [74]. The smaller energy shift

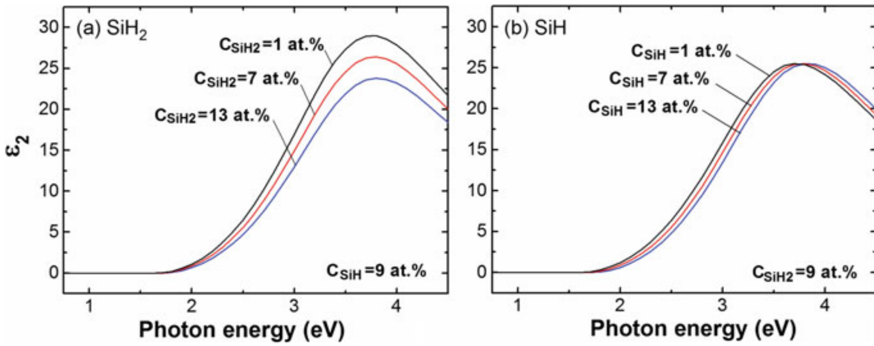

Fig. 9.14 Variations of ε_2 spectrum with **a** C_{SiH2} and **b** C_{SiH}, calculated by the a-Si:H local network model [71]. In **a**, C_{SiH} is fixed at 9 at.%, while C_{SiH2} is fixed at 9 at.% in **b**

for C_{SiH2}, compared with C_{SiH}, suggests that the SiH_2 bonding state is more localized and the interaction with the valence-band top is weaker [74].

The a-Si:H network model is appropriate for a wide variety of a-Si:H layers deposited at different substrate temperatures and plasma conditions [70, 71]. Conversely, C_{SiH} and C_{SiH2} can be extracted from the fitting analysis of experimental $\varepsilon_{a\text{-}Si:H}(E)$. From this model, C_{SiH} and C_{SiH2} in very thin a-Si:H layers (~100 Å) formed on the H/c-Si can be characterized. However, the effect of C_{SiH} on the a-Si:H dielectric function is rather limited, as confirmed from Fig. 9.14b. Since C_{SiH} shows a constant value at $T_s \leq 230$ °C (~9.0 at.%), the SE analysis of a-Si:H layers can be performed by using a fixed value of $C_{SiH} = 9.0$ at.% to reduce the correlations among the analysis parameters. It has been reported that C_{SiH2} obtained directly from infrared ellipsometry analysis agrees well with C_{SiH2} deduced from the a-Si:H network model [71].

9.4.2 Dielectric Functions of a-SiO:H and a-SiC:H

Systematic dielectric function analyses have been made for a-SiO:H [78] and a-SiC:H [79]. Figure 9.15 shows the room-temperature dielectric functions of (a) a-$Si_{1-x}O_x$:H [78] and (b) a-$Si_{1-x}C_x$:H [79] layers fabricated by PECVD at 180 °C. These alloy layers were deposited using different gas flow ratios of $z = [CO_2]/[SiH_4]$ for a-SiO:H or $z = [CH_4]/[SiH_4]$ for a-SiC:H, and the O and C contents in the a-Si:H alloys increase with increasing z. The other growth conditions of a-SiO:H and a-SiC:H are essentially similar to those of a-Si:H in the previous section.

In a-$Si_{1-x}O_x$:H and a-$Si_{1-x}C_x$:H layers, the increase in the alloy content x leads to the significant reduction in the ε_2 amplitude. For example, when $x = 32.2$ at.% in a-$Si_{1-x}O_x$:H, the ε_2 peak value becomes only ~25% of the original ε_2 value of the a-Si:H ($x = 0$ at.%). Since the ε_2 peak value shows a direct relationship with the

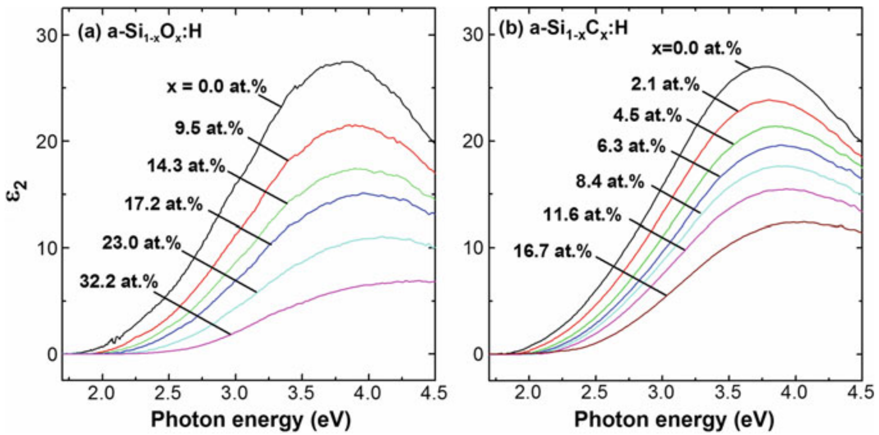

Fig. 9.15 Room-temperature dielectric functions of **a** a-$Si_{1-x}O_x$:H [78] and, **b** a-$Si_{1-x}C_x$:H [79] layers fabricated by PECVD at 180 °C

microvoid formation in a-Si:H, the drastic reduction in the ε_2 peak value indicates the significant microvoid formation in the a-SiO:H and a-SiC:H [26, 28, 78, 79]. On the other hand, the onset of the light absorption shifts toward higher energies with increasing x due to the increase of E_g in the a-SiO:H and a-SiC:H.

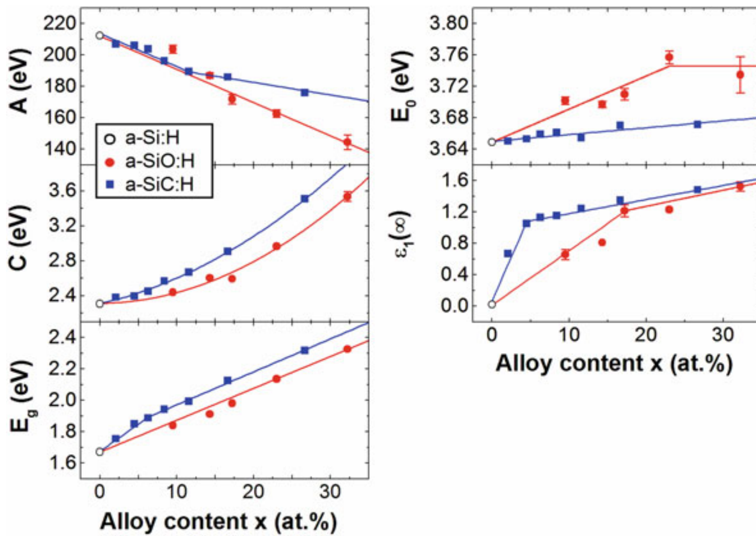

Fig. 9.16 Variation of the Tauc-Lorentz parameters [A, C, E_g, E_0, $\varepsilon_1(\infty)$] with alloy content x in a-$Si_{1-x}O_x$:H and a-$Si_{1-x}C_x$:H layers [78]. The solid lines show the fitting results

All the dielectric functions of the a-Si:H alloys in Fig. 9.15 have been parameterized using the Tauc-Lorentz model and the extracted parameter values are summarized in Fig. 9.16 [78]. The solid lines in this figure show the results obtained from liner and polynomial fittings. For the a-SiO:H, the parameters are expressed by

$$A = 212.128 - 211.781x \tag{9.8}$$

$$C = 2.313 + 6.281 \times 10^{-2}x + 11.600x^2 \tag{9.9}$$

$$E_g = 1.670 + 2.032x \tag{9.10}$$

$$E_0 = \begin{cases} 3.649 + 0.422x & (x \le 0.230) \\ 3.746 & (x > 0.230) \end{cases} \tag{9.11}$$

$$\varepsilon_1(\infty) = \begin{cases} 0.013 + 6.945x & (x \le 0.172) \\ 0.861 + 2.060x & (x > 0.172) \end{cases} \tag{9.12}$$

The unit of (9.8)–(9.11) is eV. For the a-SiC:H, the following relations have been obtained:

$$A = \begin{cases} 213.848 - 211.800x & (x \le 0.116) \\ 198.501 - 79.500x & (x > 0.116) \end{cases} \tag{9.13}$$

$$C = 2.309 + 2.000x + 9.334x^2 \tag{9.14}$$

$$E_g = \begin{cases} 1.674 + 3.500x & (x \le 0.063) \\ 1.762 + 2.100x & (x > 0.063) \end{cases} \tag{9.15}$$

$$E_0 = 3.650 + 8.700 \times 10^{-2}x \tag{9.16}$$

$$\varepsilon_1(\infty) = \begin{cases} 0.059 + 22.700x & (x \le 0.045) \\ 0.999 + 1.800x & (x > 0.045) \end{cases} \tag{9.17}$$

The above result indicates that E_0 of the a-SiO:H is larger, compared with the a-Si:H, while the E_0 shift is smaller in the a-SiC:H. This result implies that the O atom interacts more strongly in the interband transition. By applying above equations, the optical constants of the a-SiO:H and a-SiC:H can be obtained if the deposition temperature is similar (180 °C in Fig. 9.16). When the process temperature is higher, the ε_2 amplitude increases due to the decrease in the SiH_2-microvoid density, as shown in Fig. 9.14.

Figure 9.17 shows (a) ε_2 peak value, (b) E_g (Cody gap) extracted from the a-$Si_{1-x}O_x$:H and a-$Si_{1-x}C_x$:H dielectric functions versus x, together with the ε_2 peak value versus E_g (Cody gap). For the a-$Si_{1-x}O_x$:H layers, the ε_2 peak value decreases linearly with increasing x, whereas E_g increases with x. Similar trends have also

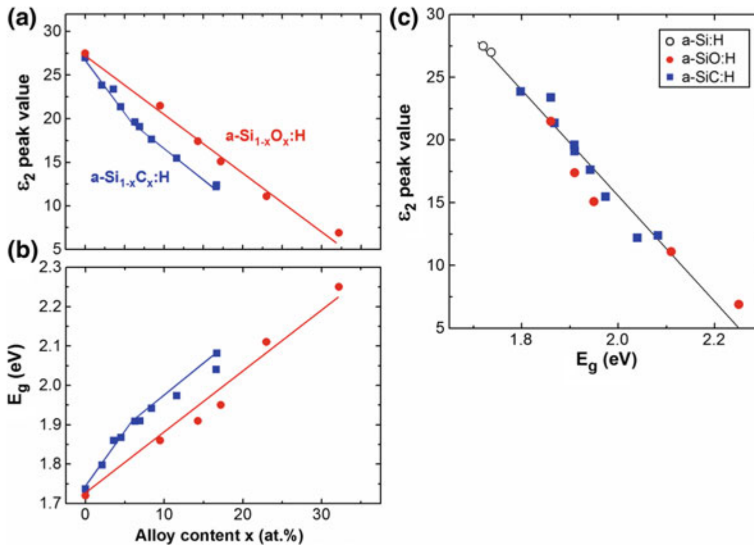

Fig. 9.17 **a** ε_2 peak value and, **b** E_g (Cody gap) extracted from the a-$Si_{1-x}O_x$:H and a-$Si_{1-x}C_x$:H dielectric functions versus x, together with the ε_2 peak value versus E_g (Cody gap) [78]

been confirmed for the a-$Si_{1-x}C_x$:H layers, but the slope of the linear variation changes slightly at $x = 6.3$ at.%. This behavior has been explained by the structural transition at this composition [79]. More specifically, the infrared spectroscopy revealed that the incorporation of CH_m ($m = 2, 3$) and sp^2 C=C bonds is enhanced at $x > 6.3$ at.%. The suppression of the E_g widening observed at $x > 6.3$ at.% can be interpreted by the generation of C=CH_2 bonds in the a-SiC:H matrix [79]. In Fig. 9.17c, the ε_2 peak value of an a-Si:H layer is 27.5 with $E_g = 1.72$ eV ($T_s = 180$ °C). This value decreases strongly as E_g increases. Interestingly, the change of the ε_2 peak value with E_g is almost identical in the a-SiO:H and a-SiC:H.

Figure 9.18 shows the proposed microvoid structures in (a) a-SiO:H [78] and (b) a-SiC:H [79]. The infrared spectra show that the local bondings in the a-SiO:H are dominated by SiH_2 and $SiH_n(O_{4-n})$ ($n \le 2$) with a small amount of C=O and O-H bonds. These local modes are proposed to exist in the void-rich region. However, although the microvoid in the a-SiO:H is terminated with SiH_2, $SiH_n(O_{4-n})$ and C=O, the actual microvoids in the a-SiO:H are modified mainly by $SiH_2(Si_2)$, as C_{SiH2} (15 at.%) is much higher than C_{SiH2O2} (3 at.%) and C_{SiHO3} (1 at.%) in the a-SiO:H ($x = 17$ at.%), for example [78]. On the other hand, the local bonding states of the a-SiC:H alloy can be interpreted as a mixture of SiH_2 and CH_m [79]. In particular, at $x > 6.4$ at.%, the incorporation of CH_2, CH_3 and C=CH_2 are enhanced and the microvoids are most likely terminated with these bonds. In fact, the hydrogen contents of the a-SiC:H layer ($x = 17$ at.%) are $C_{SiH2} = 33$ at.%, $C_{CH3} = 6$ at.% and $C_{CH2} = 2$ at.% with $C_{SiH} = 1$ at.%. Thus, the contributions of $SiH_2(Si)_2$ and CH_3 are particularly large in a-SiC:H. It should be noted that, when $x = 17$ at.%, C_{SiH2} of the a-SiC:H (33 at.%) is far larger than C_{SiH2} of the a-SiO:H (15 at.%). Accordingly, in the

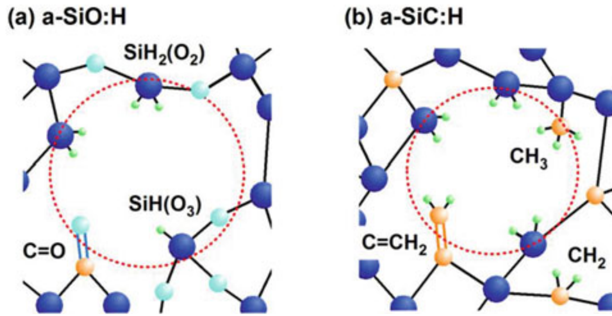

Fig. 9.18 Plane view of **a** a-SiO:H [78] and, **b** a-SiC:H [79] structures with microvoids indicated by red circles

a-SiO:H, the incorporation of H is more suppressed and a denser amorphous network is formed, compared with the a-SiC:H. This effect has also been confirmed from more detailed analyses of average coordination number and Young's modulus of amorphous networks [78].

The microvoid formation in a-SiO:H and a-SiC:H alloys has been investigated further by applying the a-Si:H network model described in the previous section. Figure 9.19 shows (a) the ε_2 peak value of the a-SiO:H as a function of $C_{\mathrm{SiH2}} + C_{\mathrm{SiH2O2}}$ and (b) $\Delta\varepsilon_2$ estimated from (a) as a function of $C_{\mathrm{SiH2O2}} + C_{\mathrm{SiHO3}}$. In Fig. 9.19a, the ε_2 peak values are obtained from the result of Fig. 9.15 and the solid line represents the result calculated by the a-Si:H local network model. In the a-SiO:H, the ε_2 peak value decreases significantly with the $\mathrm{SiH_2}$ bond density in the amorphous network [i.e., $C_{\mathrm{SiH2}} + C_{\mathrm{SiH2O2}}$], but the variation of ε_2 deviates largely from those predicated by the a-Si:H model. The result supports that the void formation is enhanced in the a-SiO:H, compared with the a-Si:H.

In Fig. 9.19a, the difference in the ε_2 peak value between the experimental a-SiO:H and the a-Si:H local network model is further evaluated. This particular value corresponds to the difference between the solid circles and the solid line and is defined as $\Delta\varepsilon_2$. In Fig. 9.19b, $\Delta\varepsilon_2$ is plotted as a function of $C_{\mathrm{SiH2O2}} + C_{\mathrm{SiHO3}}$. It can be seen that the reduction of the ε_2 peak amplitude in the a-SiO:H shows quite good correlation with $C_{\mathrm{SiH2O2}} + C_{\mathrm{SiHO3}}$. Thus, the generation of the void-rich a-SiO:H structure can be attributed to the formation of local $\mathrm{SiH}_n(\mathrm{O}_{4-n})$ bondings in the network.

A similar analysis has also been made for the a-SiC:H (Fig. 9.19c, d). In the case of the a-SiC:H, the ε_2 peak value is expressed quite well by the a-Si:H network model up to $C_{\mathrm{SiH2}} = 22$ at.%, which corresponds to $x = 6.3$ at.% [79]. Thus, the a-SiC:H network is quite similar to the a-Si:H network at $x \leq 6.3$ at.%. At higher x (>6.3 at.%) or C_{SiH2} (>22 at.%), however, the ε_2 value reduces rapidly and $\Delta\varepsilon_2$ becomes larger. As shown in Fig. 9.19d, the change in $\Delta\varepsilon_2$ at $x > 6.3$ at.% is correlated strongly with the CH_m formation in the a-SiC:H matrix. Thus, the enhanced microvoid formation in the a-SiC:H network at high x can be interpreted

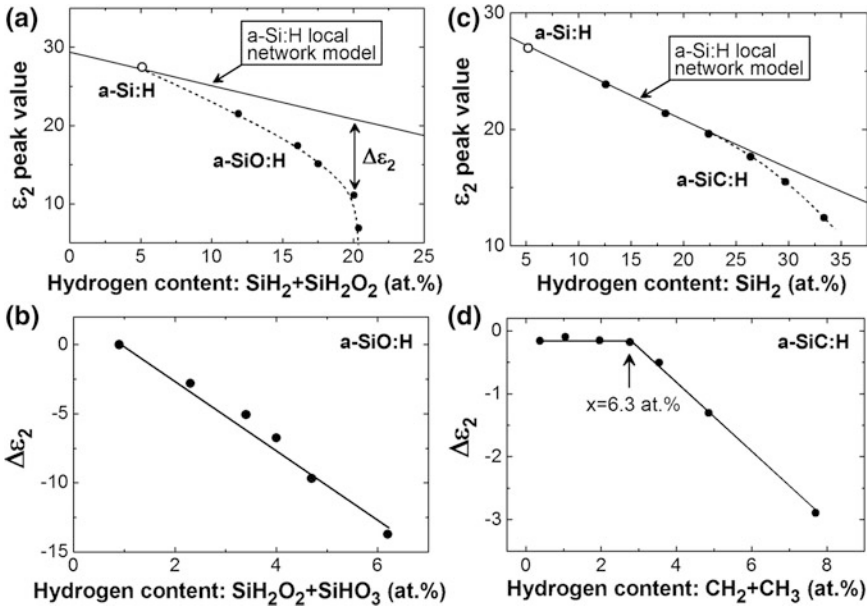

Fig. 9.19 **a** ε_2 peak values of the a-SiO:H as a function of $C_{SiH2} + C_{SiH2O2}$, **b** $\Delta\varepsilon_2$ estimated from **a** as a function of $C_{SiH2O2} + C_{SiHO3}$, **c** ε_2 peak values of the a-SiC:H as a function of C_{SiH2} and, **d** $\Delta\varepsilon_2$ estimated from **c** as a function of $C_{CH2} + C_{CH3}$. For **a** and **b**, the data reported in [78] are shown, while the data of **c** and **d** are adopted from [79]

by the CH_m generation, which prevents the cross-linking reaction of the amorphous network.

The microvoid formation triggered by $SiH_n(O_{4-n})$ in a-SiO:H and CH_m in a-SiC:H can be understood from surface reactions in PECVD. Figure 9.20 illustrates the growing surface of an a-SiO:H layer [78]. It is known well that, in PECVD, the H abstraction reaction occurs by SiH_3 (i.e., $SiH_3 + H \rightarrow SiH_4$) [80]. After the dangling bond is created by this reaction, the SiH_3 adsorption occurs on this site, leading to a-Si:H growth. When O atoms are incorporated into a-Si:H, however, due to a higher electronegativity of a O atom than of a Si atom, the electron charge is pulled toward the O atom, generating positive and negative polarized charges denoted as δ^+ and δ^- in Fig. 9.20, respectively. This induction effect most likely reduces the electron charge density on the H atom, which in turn makes the abstraction of H from SiH_2 bonds more difficult. In fact, in a-Si:H growth by PECVD, $SiH_2(O_2)$ formed on SiO_2 is confirmed to be quite unreactive and remains at the a-Si:H/SiO_2 interface [81]. Thus, the surface reactivity is expected to be hindered by the creation of the $SiH_n(O_{4-n})$, preventing dense a-Si:H network formation. This phenomenon explains the creation of the void-rich a-$Si_{1-x}O_x$:H structure at high x, since the $SiH_n(O_{4-n})$ density simply increases by the

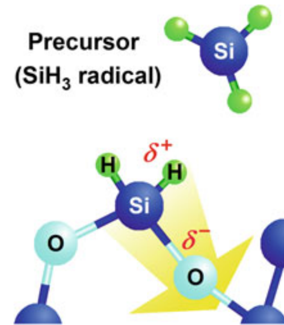

Fig. 9.20 Microvoid formation process during a-SiO:H growth [78]

O incorporation. The formation of the porous a-SiC:H networks can also be explained by a similar process, as a C atom has a high electronegativity.

The results obtained for a-SiO:H and a-SiC:H indicate that the optical properties of a-Si:H-based alloys are modified strongly by the microvoid formation, and microscopic structures of a-Si:H alloys are quite different from amorphous structures obtained assuming continuous random network.

References

1. M. Tanaka, M. Taguchi, T. Matsuyama, T. Sawada, S. Tsuda, S. Nakano, H. Hanafusa, Y. Kuwano, Jpn. J. Appl. Phys. **31**, 3518 (1992)
2. M. Taguchi, K. Kawamoto, S. Tsuge, T. Baba, H. Sakata, M. Morizane, K. Uchihashi, N. Nakamura, S. Kiyama, O. Oota, Prog. Photovolt. **8**, 503 (2000)
3. M. Taguchi, A. Terakawa, E. Maruyama, M. Tanaka, Prog. Photovolt. **13**, 481 (2005)
4. M. Taguchi, E. Maruyama, M. Tanaka, Jpn. J. Appl. Phys. **47**, 814 (2008)
5. T. Mishima, M. Taguchi, H. Sakata, E. Maruyama, Sol. Eng. Mater. Sol. Cells **95**, 18 (2011)
6. M. Taguchi, A. Yano, S. Tohoda, K. Matsuyama, Y. Nakamura, T. Nishiwaki, K. Fujita, E. Maruyama, IEEE J. Photovolt. **4**, 96 (2014)
7. K. Masuko, M. Shigematsu, T. Hashiguchi, D. Fujishima, M. Kai, N. Yoshimura, T. Yamaguchi, Y. Ichihashi, T. Mishima, N. Matsubara, T. Yamanishi, T. Takahama, M. Taguchi, E. Maruyama, S. Okamoto, IEEE J. Photovolt. **4**, 1433 (2014)
8. M.A. Green, K. Emery, Y. Hishikawa, W. Warta, E.D. Dunlop, D.H. Levi, A.W.Y. Ho-Baillie, Photovoltaics **25**, 3 (2017)
9. Y. Tsunomura, Y. Yoshimine, M. Taguchi, T. Baba, T. Kinoshita, H. Kanno, H. Sakata, E. Maruyama, M. Tanaka, Sol. Eng. Mater. Sol. Cells **93**, 670 (2009)
10. T. Koida, H. Fujiwara, M. Kondo, Sol. Eng. Mater. Sol. Cells **93**, 851 (2009)
11. Z.C. Holman, A. Descoeudres, L. Barraud, F.Z. Fernandez, J.P. Seif, S. De Wolf, C. Ballif, IEEE J. Photovolt. **2**, 7 (2012)
12. S. De Wolf, A. Descoeudres, Z.C. Holman, C. Ballif, Green **2**, 7 (2012)
13. E. Kobayashi, Y. Watabe, T. Yamamoto, Y. Yamada, Sol. Eng. Mater. Sol. Cells **149**, 75 (2016)
14. H. Fujiwara, M. Kondo, Appl. Phys. Lett. **86**, 032112 (2005)
15. H. Fujiwara, M. Kondo, J. Appl. Phys. **101**, 054516 (2007)
16. H. Fujiwara, M. Kondo, *Proceedings of the IEEE 4th World Conference on Photovoltaic Energy Conversion (WCPEC-4)* (Hawaii, 2006), p. 1443

17. H. Fujiwara, M. Kondo, Appl. Phys. Lett. **90**, 013503 (2007)
18. S. De Wolf, M. Kondo, Appl. Phys. Lett. **90**, 042111 (2007)
19. U.K. Das, M.Z. Burrows, M. Lu, S. Bowden, R.W. Birkmire, Appl. Phys. Lett. **92**, 063504 (2008)
20. R. Gogolin, R. Ferré, M. Turcu, N.-P. Harder, Sol. Eng. Mater. Sol. Cells **106**, 47 (2012)
21. A. Descoeudres, L. Barraud, S. De Wolf, B. Strahm, D. Lachenal, C. Guerin, Z.C. Holman, F. Zicarelli, B. Demaurex, J. Seif, J. Holovsky, C. Ballif, Appl. Phys. Lett. **99**, 123506 (2011)
22. F. Meng, L. Shen, J. Shi, L. Zhang, J. Liu, Y. Liu, Z. Liu, Appl. Phys. Lett. **107**, 223901 (2015)
23. K. Watanabe, N. Matsuki, H. Fujiwara, Appl. Phys. Express **3**, 116604 (2010)
24. N. Matsuki, H. Fujiwara, J. Appl. Phys. **114**, 043101 (2013)
25. Y. Tanaka, N. Matsuki, H. Fujiwara, Thin Solid Films **565**, 222 (2014)
26. H. Fujiwara, T. Kaneko, M. Kondo, Appl. Phys. Lett. **91**, 133508 (2007)
27. H. Fujiwara, T. Kaneko, M. Kondo, Sol. Eng. Mater. Sol. Cells **93**, 725 (2009)
28. J.P. Seif, A. Descoeudres, M. Filipic, F. Smole, M. Topic, Z.C. Holman, S. De Wolf, C. Ballif, J. Appl. Phys. **115**, 024502 (2014)
29. J. Sritharathikhun, H. Yamamoto, S. Miyajima, A. Yamada, M. Konagai, Jpn. J. Appl. Phys. **47**, 8452 (2008)
30. A. Lambertz, V. Smirnov, T. Merdzhanova, K. Ding, S. Haas, G. Jost, R.E.I. Schropp, F. Finger, U. Rau, Sol. Eng. Mater. Sol. Cells **119**, 134 (2013)
31. H. Zhang, K. Nakada, S. Miyajima, M. Konagai, Phys. Status Solidi RPL **9**, 225 (2015)
32. J. Bullock, M. Hettick, J. Geissbuhler, A.J. Ong, T. Allen, C.M. Sutter-Fella, T. Chen, H. Ota, E.W. Schaler, S. De Wolf, C. Ballif, A. Cuevas, A. Javey, Nat. Energy **2**, 15031 (2016)
33. G.E. Jellison Jr., F.A. Modine, Appl. Phys. Lett. **69**, 371 (1996); Erratum, Appl. Phys. Lett. **69**, 2137 (1996)
34. A.S. Ferlauto, G.M. Ferreira, J.M. Pearce, C.R. Wronski, R.W. Collins, X. Deng, G. Ganguly, J. Appl. Phys. **92**, 2424 (2002)
35. H. Fujiwara, *Spectroscopic Ellipsometry: Principles and Applications* (Wiley, West Sussex, UK, 2007)
36. H. Fujiwara, J. Koh, P.I. Rovira, R.W. Collins, Phys. Rev. B **61**, 10832 (2000)
37. J. Koh, Y. Lu, C.R. Wronski, Y. Kuang, R.W. Collins, T.T. Tsong, Y.E. Strausser, Appl. Phys. Letts. **69**, 1297 (1996)
38. C.M. Herzinger, B. Johs, W.A. McGahan, J.A. Woollam, W. Paulson, J. Appl. Phys. **83**, 3323 (1998)
39. T. Yasuda, D.E. Aspnes, Appl. Opt. **33**, 7435 (1994)
40. H. Angermann, W. Henrion, M. Rebien, A. R seler, Sol. Eng. Mater. Sol. Cells **83**, 331 (2004)
41. G.D. Cody, B.G. Brooks, B. Abeles, Sol. Energy Mater. **8**, 231 (1982)
42. J. Perrin, Y. Takeda, N. Hirano, Y. Takeuchi, A. Matsuda, Surf. Sci. **210**, 114 (1989)
43. T.H. Wang, E. Iwaniczko, M.R. Page, D.H. Levi, Y. Yan, H.M. Branz, Q. Wang, Thin Solid Films **501**, 284 (2006)
44. S. Olibet, E. Vallat-Sauvain, L. Fesquet, C. Monachon, A. Hessler-Wyser, J. Damon-Lacoste, S. De Wolf, C. Ballif, Phys. Stat. Solidi A **207**, 651 (2010)
45. K. Nakada, J. Irikawa, S. Miyajima, M. Konagai, Jpn. J. Appl. Phys. **54**, 052303 (2015)
46. A. Morimoto, H. Noriyama, T. Shimizu, Jpn. J. Appl. Phys. **26**, 22 (1987)
47. D. Das, S.M. Iftiquar, A.K. Barua, J. Non-Cryst, Solids **210**, 148 (1997)
48. A. Janotta, R. Janssen, M. Schmidt, T. Graf, M. Stutzmann, L. Görgens, A. Bergmaier, G. Dollinger, C. Hammerl, S. Schreiber, B. Stritzker, Phys. Rev. B **69**, 115206 (2004)
49. A. Janotta, Y. Dikce, S. Linder, M. Schmidt, R. Janssen, M. Stutzmann, J. Appl. Phys. **95**, 4046 (2004)
50. T. Itoh, R. Katayama, K. Yamakawa, K. Matsui, M. Saito, S. Sugiyama, P. Sichanugrist, S. Nonomura, M. Konagai, Jpn. J. Appl. Phys. **54**, 08KB11 (2015)
51. R.A. Street, *Hydrogenated Amorphous Silicon* (Cambridge University Press, New York, 1991)

52. D.E. Polk, J. Non-Cryst. Solids **5**, 365 (1971)
53. D.E. Polk, D.S. Boudreaux, Phys. Rev. Lett. **31**, 92 (1973)
54. D. Weaire, N. Higgins, P. Moore, I. Marshall, Philos. Mag. B **40**, 243 (1979)
55. W. Schülke, Philos. Mag. B **43**, 451 (1981)
56. F. Wooten, K. Winer, D. Weaire, Phys. Rev. Lett. **54**, 1392 (1985)
57. G.D. Cody, C.R. Wronski, B. Abeles, R.B. Stephens, B. Brooks, Solar Cells **2**, 227 (1980)
58. G.F. Feng, M. Katiyar, J.R. Abelson, N. Maley, Phys. Rev. B **45**, 9103 (1992)
59. A.H. Mahan, P. Menna, R. Tsu, Appl. Phys. Lett. **51**, 1167 (1987)
60. E. Bhattacharya, A.H. Mahan, Appl. Phys. Lett. **52**, 1587 (1988)
61. N. Nakamura, T. Takahama, M. Isomura, M. Nishikuni, K. Yoshida, S. Tsuda, S. Nakano, M. Ohnishi, Y. Kuwano, Jpn. J. Appl. Phys. **28**, 1762 (1989)
62. S. Guha, J. Yang, S.J. Jones, Y. Chen, D.L. Williamson, Appl. Phys. Lett. **61**, 1444 (1992)
63. P. D'Antonio, J.H. Konnert, Phys. Rev. Lett. **43**, 1161 (1979)
64. J.C. Knights, G. Lucovsky, R.J. Nemanich, J. Non-Cryst. Solids **32**, 393 (1979)
65. J.B. Boyce, M. Stutzmann, Phys. Rev. Lett. **54**, 562 (1985)
66. Y.J. He, M. Hasegawa, R. Lee, S. Berko, D. Adler, A. Jung, Phys. Rev. B **33**, 5924 (1986)
67. V.G. Bhide, R.O. Dusane, S.V. Rajarshi, A.D. Shaligram, S.K. David, J. Appl. Phys. **62**, 108 (1987)
68. A.H. Mahan, D.L. Williamson, B.P. Nelson, R.S. Crandall, Solar Cells **27**, 465 (1989)
69. A.H.M. Smets, M.C.M. van de Sanden, Phys. Rev. B **76**, 073202 (2007)
70. S. Kageyama, M. Akagawa, H. Fujiwara, Phys. Rev. B **83**, 195205 (2011)
71. S. Kageyama, M. Akagawa, H. Fujiwara, J. Non-Cryst. Solids **358**, 2257 (2012)
72. P. Biswas, R. Atta-Fynn, S.R. Elliott, Phys. Rev. B **93**, 184202 (2016)
73. T. Sekimoto, M. Matsumoto, A. Sagara, M. Hishida, A. Terakawa, J. Non-Cryst. Solids **447**, 207 (2016)
74. W.Y. Ching, D.J. Lam, C.C. Lin, Phys. Rev. B **21**, 2378 (1980)
75. D.A. Papaconstantopoulos, E.N. Economou, Phys. Rev. B **24**, 7233 (1981)
76. K.H. Johnson, H.J. Kolari, J.P. de Neufville, D.L. Morel, Phys. Rev. B **21**, 643 (1980)
77. B. von Roedern, L. Ley, M. Cardona, Phys. Rev. Lett. **39**, 1576 (1977)
78. M. Sato, S.W. King, W.A. Lanford, P. Henry, T. Fujiseki, H. Fujiwara, J. Non-Cryst, Solids **440**, 49 (2016)
79. S. Kageyama, N. Matsuki, H. Fujiwara, J. Appl. Phys. **114**, 233513 (2013)
80. A. Matsuda, K. Nomoto, Y. Takeuchi, A. Suzuki, A. Yuuki, J. Perrin, Surf. Sci. **227**, 50 (1990)
81. H. Fujiwara, Y. Toyoshima, M. Kondo, A. Matsuda, Phys. Rev. B **60**, 13598 (1999)

Chapter 10
Optical Properties of $Cu(In,Ga)Se_2$

Hiroyuki Fujiwara

Abstract In $Cu(In,Ga)Se_2$ (CIGSe) solar cells, a precise control of the CIGSe elemental composition is crucial to achieve high conversion efficiencies. In particular, for CIGSe layers incorporated into solar cells, compositionally graded structures are formed intentionally to suppress the carrier recombination at the front and rear interfaces. In designing complex CIGSe solar cells, the determination and understanding of fundamental CIGSe optical properties are of significant importance. In this chapter, high-precision characterization of CIGSe dielectric functions based on multi-sample spectroscopic ellipsometry analyses is presented. Moreover, this chapter focuses on the variations of the optical properties with the Cu and Ga compositions. From the systematic critical point analyses performed for the extracted dielectric functions, the optical transitions in CIGSe are discussed. This chapter further explains a complete CIGSe optical database, from which the optical constants of CIGSe for arbitrary Cu and Ga compositions can be determined.

10.1 Introduction

Thin-film solar cells based on $Cu(In,Ga)Se_2$ (CIGSe) have been studied extensively [1–18] and large-area CIGSe modules have already been commercialized [1–3]. In recent years, the performance of CIGSe solar cells has been increasing steadily by the improvement of solar cell processing, and the record efficiency of a CIGSe solar cell (22.6% in [4]) is currently highest among thin-film-based polycrystalline solar cells [5]. The superior characteristics of CIGSe solar cells can be understood in part from unique optoelectronic properties arising from a group I-III-VI_2 chalcopyrite structure [19–22].

Figure 10.1a shows the structure of a $CuInSe_2$ (CISe) chalcopyrite crystal determined from density functional theory (DFT) calculation. The crystal structure of CISe consists of the alternating plane of Se and (Cu, In) atoms along the *c* axis

H. Fujiwara (✉)
Gifu University, 1-1 Yanagido, Gifu 501-1193, Japan
e-mail: fujiwara@gifu-u.ac.jp

© Springer International Publishing AG, part of Springer Nature 2018

H. Fujiwara and R. W. Collins (eds.), *Spectroscopic Ellipsometry for Photovoltaics*,
Springer Series in Optical Sciences 212,
https://doi.org/10.1007/978-3-319-75377-5_10

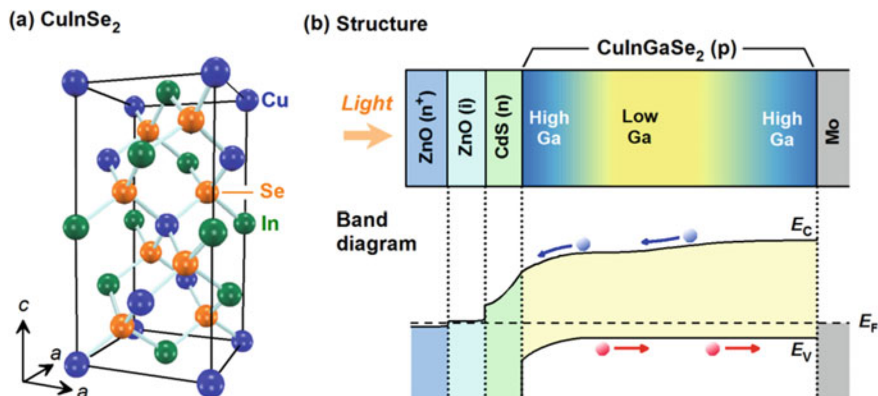

Fig. 10.1 **a** Structure of a $CuInSe_2$ chalcopyrite crystal determined from DFT and **b** structure and band diagram of a high-efficiency CIGSe solar cell fabricated by a conventional three-stage coevaporation process [34]. In (**a**), the arrows show the *a* and *c* axis directions of the unit cell. In the band diagram of (**b**), E_C and E_V show the energy positions of the conduction-band and valence-band edges, respectively, and the formation of a thin $MoSe_2$ layer at the CIGSe/Mo rear interface is neglected. The blue and red circles in (**b**) represent photogenerated electrons and holes, respectively

indicated by the arrow, and some In atoms are replaced with Ga atoms in CIGSe. It can be seen that one Se atom is bonded with two Cu and two In atoms, whereas each Cu and In (or Ga) atom forms tetrahedral bonds with four Se atoms. The structure of the chalcopyrite crystal is quite similar to that of a well-known zinc-blende crystal and, when all the Cu and In atoms are replaced with Zn atoms, for example, the crystal structure reduces to the ZnSe zincblende structure. In other words, group-II atoms in II-VI compounds are simply replaced with group-I and III atoms in I-III-VI_2 chalcopyrites. In the CISe crystal, the Cu-Se bond length is slightly shorter than the In-Se bond length, which can be interpreted by the strong interaction between the Cu 3*d* and Se 4*p* orbitals and the resulting covalent character of the Cu-Se bonds [19]. Moreover, the unit cell structure of CISe in Fig. 10.1a is slightly distorted. Indeed, the experimental lattice parameters of CISe are $a = 5.78$ Å and $c = 11.62$ Å with a *c/a* ratio of 2.01, while $CuGaSe_2$ (CGSe) shows a *c/a* ratio of 1.97 ($a = 5.60$ Å and $c = 11.00$ Å) [20].

It is known well that the band gap (E_g) of CIGSe increases with increasing Ga content $x = \mathrm{Ga}/(\mathrm{Ga} + \mathrm{In})$ [23–29]. In general, for high efficiency CIGSe solar cells, CIGSe absorber layers with E_g of 1.1–1.2 eV ($x = 0.2$–0.3) are used [1, 7–10, 16–18]. One of the surprising features of CIGSe-based materials is a quite large structural tolerance to off stoichiometry particularly for the Cu-deficient layers. In fact, high-efficiency CIGSe solar cells can be fabricated with Cu compositions [$y = \mathrm{Cu}/(\mathrm{Ga} + \mathrm{In})$] in a quite wide range of $y = 0.6$–1.0 [14]. Thus without generating mid-gap deep defects, the Cu composition in CIGSe can be varied rather flexibly [22]. Furthermore, in CIGSe solar cells, intentional doping has not been made as the

Cu-deficient CIGSe layers ($y \sim 0.9$) exhibit desirable *p*-type conductivity with carrier concentrations of 10^{16}–10^{17} cm^{-3} [30].

The presence of the Cu-deficient phase has been explained by the generation of ordered defect complex (ODC) [22]. Specifically, DFT calculations reveal that a defect complex of $2V_{Cu} + In_{Cu}$, consisting of Cu vacancies (V_{Cu}) and the Cu sites replaced with In atoms (In_{Cu}), is formed quite easily, and this specific complex does not create deep states within the gap of CISe [22]. The stable formation of CISe secondary phases, including $CuIn_3Se_5$ and $CuIn_5Se_8$, can also be explained by the introduction of ($2V_{Cu} + In_{Cu}$) defects into the CISe phase with different concentrations. Thus, $CuIn_3Se_5$ and $CuIn_5Se_8$ are often referred to as the ODC phases. So far, the formation of V_{Cu} [31–33] and In_{Cu} [32, 33] in the Cu-poor phases has been confirmed experimentally.

Figure 10.1b shows the structure and band diagram of conventional CIGSe solar cells [34]. In general, a high-efficiency CIGSe solar cell has a structure of ZnO(n)/non-doped ZnO/CdS(n)/CIGSe(p)/Mo [1, 9]. For the preparation of CIGSe absorber layers, a three-stage coevaporation process, in which (Cu, In, Ga, Se) elemental sources are supplied with different combinations, is commonly used [6–8]. This processing allows the formation of a V-shaped Ga profile with a low Ga content in the middle and higher Ga contents at the front and rear sides (see also Fig. 2.8b in Vol. 2). As shown in the band diagram, this V-shaped profile creates pseudo-potentials in the front and rear interface regions. This highly controlled Ga profile has been essential for realizing a high short-circuit current density (J_{sc}), while maintaining a high open-circuit voltage (V_{oc}) in CIGSe solar cells [1, 6–8, 10, 11, 16–18]. In particular, a higher Ga content in the rear region generates a back-surface field (BSF) structure, which is quite effective in suppressing the recombination in the rear interface region [1, 7, 8, 10–12, 14–17]. Moreover, near the CdS/CIGSe front interface, the decrease in the Cu content [1, 35–41] and the increase in E_g [36, 41–43] due to the presence of the ODC phase have been confirmed, although this is not reflected in the band diagram of Fig. 10.1b. It has been established that the formation of the wider-gap Cu-deficient layer at the interface is quite beneficial to reduce the front interface recombination [44].

As mentioned above, the Cu and Ga compositions in CIGSe absorber layers are controlled precisely to maximize the conversion efficiencies. Thus, the understanding of CIGSe optical properties is crucial in interpreting the device characteristics and optimizing CIGSe device structures. Nevertheless, the optical constants reported for CIGSe-based materials have been highly controversial [27–29, 45–57] and, for the variations of *x* and *y* in $Cu_y(In_{1-x}Ga_x)Se_2$, reported dielectric functions show very different trends [25, 28, 29, 51, 55–58]. Quite fortunately, it is found that the inconsistent optical data originate primarily from the effect of rough surfaces (Chap. 6), and accurate optical constants can be obtained when multi-sample spectroscopic ellipsometry (SE) analysis is performed for thin CIGSe layers with smooth surfaces [29]. As a result, recent SE studies on CIGSe show more consistent optical data [29, 55–57].

In this chapter, the multi-sample SE analysis of CIGSe layers based on the self-consistent global error minimization (GEM) scheme [29, 55] is explained in

detail. From the optical data extracted using GEM analyses, the variations of CIGSe optical properties with the Cu and Ga compositions are discussed. This chapter further introduces a CIGSe optical database established earlier [55], which allows the calculation of $Cu_y(In_{1-x}Ga_x)Se_2$ optical constants in a complete two-dimensional compositional space of (x, y).

10.2 GEM Analysis

GEM is a self-consistent approach that allows the high-precision characterization of material optical constants [59, 60]. In this analysis, the optical constants are extracted directly from experimental (ψ, Δ) spectra using the mathematical inversion [60, 61] and thus artifacts originating from inappropriate dielectric function modeling can be avoided. In this section, the basic concept of the mathematical inversion and the analysis procedure of GEM are described. As an example, the GEM analysis of a $CuIn_{1-x}Ga_xSe_2$ layer ($x = 0.38$) is explained.

10.2.1 Mathematical Inversion

Mathematical inversion (point-by-point fitting) [60, 61] is used quite widely for the analyses of various materials. Based on this method, the dielectric function ($\varepsilon = \varepsilon_1 - i\varepsilon_2$) of samples can be determined from (ψ, Δ) spectra without the requirement of dielectric function modeling.

Figure 10.2 summarizes the procedure of the mathematical inversion performed for a thin layer formed on a substrate. If an optical model consisting of an ambient (air)/surface roughness layer/bulk layer/substrate is assumed (Fig. 10.2a), the ellipsometry parameters (ψ, Δ) can be expressed as

$$\tan\psi\ \exp(i\Delta) = \rho(N_0, N_1, N_2, N_3, d_s, d_b, \theta). \tag{10.1}$$

In this equation, only variables used in the calculation are shown. Here, N_j represents the complex refractive index ($N_j = n_j - ik_j$) of the jth layer, whereas d_s and d_b denote the thicknesses of the surface roughness and bulk layers, respectively. The incident angle (θ) and the optical properties of the substrate (N_3) are usually known in advance and the optical constants of the roughness layer (N_1) can be calculated from the Bruggeman effective medium approximation (EMA) assuming a 50:50 vol.% mixture of the bulk layer component and voids (Sect. 3.4.2). In this case, since $N_0 = 1$ (air), the unknown parameters in the optical model become N_2, d_s and d_b.

In the mathematical inversion, the structural parameters (i.e., d_s and d_b) are determined from the SE fitting in a transparent energy region where measured spectra show optical interference effect, as illustrated in Fig. 10.2b. To express the

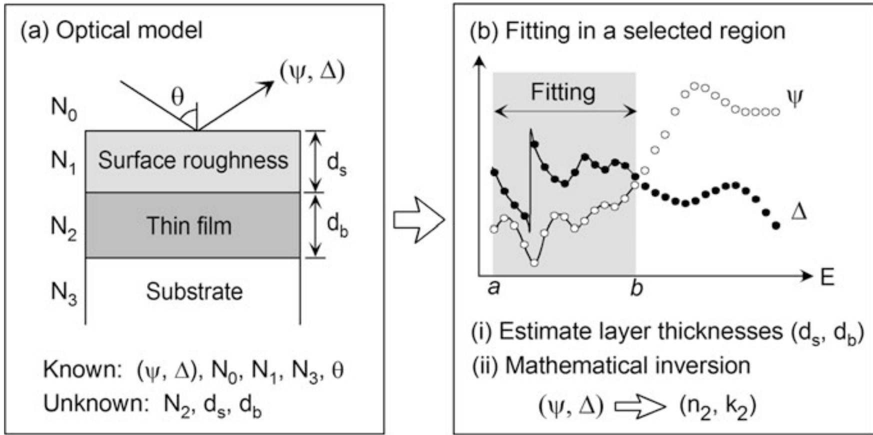

Fig. 10.2 Procedure of SE data analysis using the mathematical inversion: **a** optical model for a thin film formed on a substrate and **b** SE fitting in a selected region

dielectric function in the transparent region (the photon energy (E) range of a–b in Fig. 10.2b), a simple dielectric function model, such as the Tauc-Lorentz model (Sect. 5.3.7), is used, and the SE fitting is carried out in this selected region by including (d_s, d_b) as free parameters. If these structural parameters are deduced successfully from the SE analysis, the unknown parameters in (10.1) become only $N_2 = n_2 - ik_2$. Accordingly, if (10.1) is solved, the measured (ψ, Δ) can be converted directly to (n_2, k_2). This procedure is referred to as the mathematical inversion. In the actual mathematical inversion, the optical constants at each energy are obtained from fitting analysis and, from this process, the mathematical inversion is also called the point-by-point fitting. It should be emphasized that, using the mathematical inversion, the optical constants in the whole measured range can be determined, even though the original SE fitting is carried out in the selected region ($E = a$–b).

10.2.2 Analysis Procedure of GEM

GEM is a data analysis method in which the mathematical inversion is combined with multi-sample analysis [59, 60]. From this method, quite reliable optical data can be extracted by assuming that the dielectric function of an analyzing layer is independent of thickness. The greatest advantage of this method is the accurate determination of a material dielectric function without any dielectric function modeling even when the dielectric function is totally unknown.

Figure 10.3 illustrates the procedure of the GEM analysis. In this analysis, the ellipsometry spectra are obtained first from a thin layer [i.e., $(\psi, \Delta)_{\mathrm{Thin}}$]. For the analysis of these spectra, we assume a simple optical model shown in Fig. 10.3 and

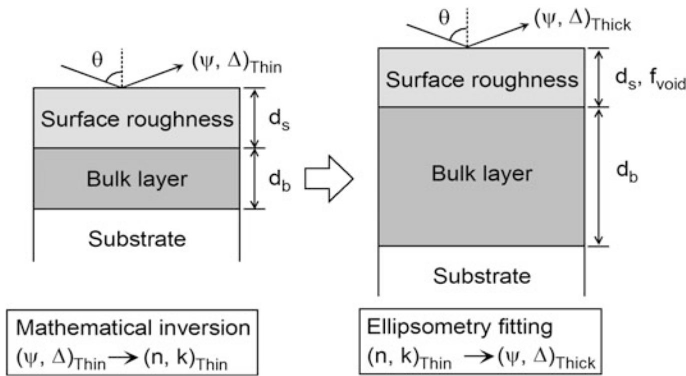

Fig. 10.3 Procedure of GEM analysis. This analysis is consisting of two steps with (i) the mathematical inversion for a thin layer and (ii) ellipsometry fitting for a thicker layer

the optical constants of the surface roughness layer are calculated from EMA assuming the void volume fraction of $f_{\text{void}} = 0.5$. From the procedure described in the previous section, the parameters of (d_s, d_b) can be determined and the mathematical inversion is further performed to extract the optical constants of the thin bulk layer [$(n, k)_{\text{Thin}}$ or (n_2, k_2) in Fig. 10.2b]. Unfortunately, in this conventional approach, it is still difficult to confirm the validity of the SE analysis as $(\psi, \Delta)_{\text{Thin}}$ is converted directly to $(n, k)_{\text{Thin}}$ in this case.

In the second step of the GEM analysis, the extracted optical constants $(n, k)_{\text{Thin}}$ are applied further for the analysis of the ellipsometry spectra obtained from a thicker layer [$(\psi, \Delta)_{\text{Thick}}$]. In this SE analysis, f_{void} can be used as a free parameter since f_{void} may increase in a thicker layer (Fig. 6.2). From the SE analysis of $(\psi, \Delta)_{\text{Thick}}$ using $(n, k)_{\text{Thin}}$ and three fitting parameters (d_s, f_{void}, d_b), the mean-squared error (MSE) described in Sect. 3.5.2 is determined. The overall SE analysis of Fig. 10.3 is repeated by employing different pairs of (d_s, d_b) for a thin layer, so that MSE in the $(\psi, \Delta)_{\text{Thick}}$ fitting is minimized. In the GEM analysis, therefore, the mathematical inversion is performed using trial values of (d_s, d_b) and the fitting analysis in a transparent region (Fig. 10.2b) is not always necessary.

Figure 10.4 illustrates the variation of MSE in the $(\psi, \Delta)_{\text{Thick}}$ fitting with (d_s, d_b) used for the mathematical inversion of $(\psi, \Delta)_{\text{Thin}}$. In this analysis, MSE is expressed using the two-dimensional plane of (d_s, d_b) and the contour of MSE shows a circle shape [60]. When appropriate (d_s, d_b) values are employed for the mathematical inversion of $(\psi, \Delta)_{\text{Thin}}$, the realistic optical constants are extracted, minimizing MSE in the fitting analysis of $(\psi, \Delta)_{\text{Thick}}$. In contrast, when inappropriate (d_s, d_b) values are employed, artifacts (or anomalous structures) appear in the extracted dielectric function, resulting in the increase in MSE. In other words, the accurate optical constants can be determined from (d_s, d_b) that minimize MSE. This is the basic concept of GEM analysis. As confirmed from the above procedure, in this analysis, $(n, k)_{\text{Thin}}$ of a bulk layer are obtained self-consistently assuming that the bulk-layer optical properties are independent of a layer thickness. Very reliable

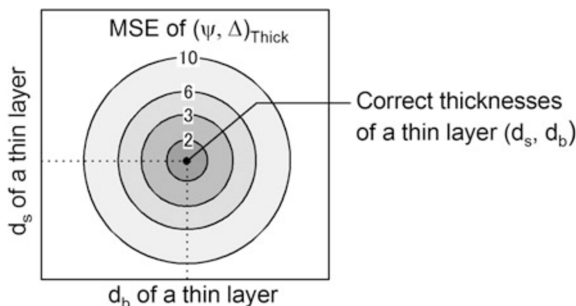

Fig. 10.4 Variation of MSE in the $(\psi, \Delta)_{\text{Thick}}$ fitting with (d_s, d_b) values used for the mathematical inversion of $(\psi, \Delta)_{\text{Thin}}$

optical data are obtained from this approach since SE fitting quality degrades significantly when the optical response is not modeled properly and the optical model is oversimplified [62–64] (see also Chaps. 6 in Vol. 1 and 4 in Vol. 2). The GEM analysis can be implemented by using more than two sets of SE spectra obtained from different layer thicknesses. If there is an interface layer or a compositionally graded structure, however, the optical properties change toward the growth direction and the analysis becomes difficult. From the GEM analysis, the presence of such non-ideal structures can also be detected as MSE will not converge in this case.

10.2.3 GEM Analysis of CIGSe

Here, as an example, the GEM analysis of polycrystalline $Cu_yIn_{1-x}Ga_xSe_2$ layers ($x = 0.38$, $y = 0.90$) [29] is described. In this analysis, to avoid the effect of rough surfaces formed in thick CIGSe samples, two CIGSe layers with very thin thicknesses (around 25 and 40 nm) were characterized, and the two sets of the SE spectra (i.e., $(\psi, \Delta)_{25\text{nm}}$ and $(\psi, \Delta)_{40\text{nm}}$) were obtained from these samples. As described in Chap. 6, SE shows quite high sensitivity for roughness structures and the analysis of smooth samples is of paramount importance to eliminate analysis artifacts such as non-zero ε_2 or absorption coefficient (α) in an energy region below E_g. The CIGSe samples used for the SE analyses were deposited on crystalline Si (c-Si) substrates using a single coevaporation process of Cu, In, Ga, and Se elementary sources at 520 °C. Although the c-Si substrates are covered with thin native oxide layers (2 nm), the optical response of the SiO_2 layer has been neglected in the analysis due to the SiO_2 thickness reduction by the CIGSe growth.

Figure 10.5 shows (a) the dielectric function of the polycrystalline CIGSe ($x = 0.38$, $y = 0.90$) extracted from the thin CIGSe layer [$(\psi, \Delta)_{25\text{nm}}$] using the mathematical inversion and (b) the (ψ, Δ) spectra obtained from the thicker CIGSe layer [$(\psi, \Delta)_{40\text{nm}}$] deposited under the identical growth conditions [29]. The CIGSe dielectric function of Fig. 10.5a [$(\varepsilon_1, \varepsilon_2)_{25\text{nm}}$] corresponds to $(n, k)_{\text{Thin}}$ in Fig. 10.3 and was obtained using $d_b = 21.2$ nm and $d_s = 5.5$ nm assuming $f_{\text{void}} = 0.5$. It can

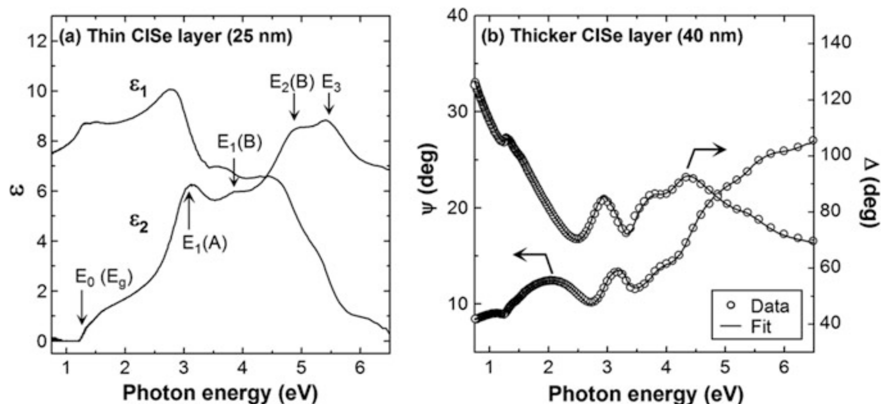

Fig. 10.5 **a** Dielectric function of the polycrystalline CIGSe (x = 0.38, y = 0.90) extracted from the thin CIGSe layer [$(\psi, \Delta)_{25nm}$] using the mathematical inversion and **b** the (ψ, Δ) spectra obtained from the thicker CIGSe layer [$(\psi, \Delta)_{40nm}$] deposited under the identical growth conditions [29]. In (**a**), the transition energies are shown by the arrows. In (**b**), the open circles show the experimental data and the solid lines indicate the calculated result obtained using the CIGSe dielectric function of (**a**)

be seen that the extracted dielectric function is quite smooth and the ε_2 values are almost completely zero in the energy region below $E_g(E_0)$. The four transition peaks at 3.09 eV, 3.87 eV, 4.86 eV and 5.48 eV in the ultraviolet (UV) region are labeled as $E_1(A)$, $E_1(B)$, $E_2(B)$ and E_3, respectively, using the notation of Alonso et al. [48].

In Fig. 10.5b, the solid lines show the result of the fitting for $(\psi, \Delta)_{40nm}$ using $(\varepsilon_1, \varepsilon_2)_{25nm}$ shown in Fig. 10.5a. From this fitting analysis, d_b = 42.5 ± 0.1 nm, d_s = 8.9 ± 0.1 nm and f_{void} = 0.71 ± 0.01 were obtained. The excellent fitting to the experimental spectra confirms that the optical model used for the SE analysis is appropriate. To justify the SE result further, the cross-sectional transmission electron microscope (TEM) image shown in Fig. 10.6 has been obtained from the CIGSe sample of Fig. 10.5b [29]. As confirmed from this TEM image, the CIGSe layer is quite uniform toward the growth direction and is consisting of small grains with a size ranging from 20 to 40 nm. More importantly, the SE thicknesses indicated by the dotted lines in Fig. 10.6, show remarkable agreement with the TEM results. Accordingly, all the SE results of Figs. 10.5 and 10.6 are quite consistent.

It has been observed that the surface oxidation of CISe and CGSe layers leads to the formation of In_2O_3 and Ga_2O_3 near the surface [65–67]. Furthermore, in the surface region of CIGSe layers, the Cu-deficient layers are present [1, 35–41, 50], although there has been little agreement on the thickness of the Cu-poor region [1, 39, 40, 50]. However, good fitting observed in Fig. 10.5b confirms that the optical response of the roughness region can be approximated by using a single EMA layer. If there is a large contribution of the surface oxide and other phase-modulated layers, anomalous features are expected to appear in the mathematically-inverted

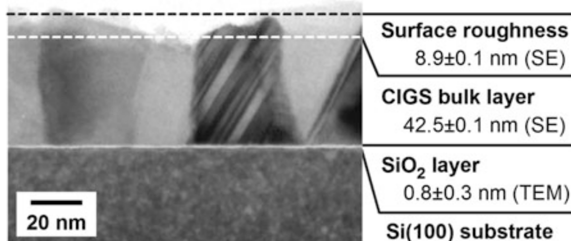

Fig. 10.6 Cross-sectional TEM for the CIGSe sample of Fig. 10.5b [29]. The dotted lines show the bulk and surface roughness layer thicknesses determined by SE

dielectric function and the analysis using this dielectric function will not provide the sufficiently good fitting to the other experimental spectra. Thus, GEM analysis is quite useful when the layer structure is complicated and the optical model used in SE analysis needs to be justified.

In the above GEM analysis, quite thin polycrystalline layers were analyzed to suppress the roughness effect. One drawback of this approach is that the optical properties of small-sized grains are characterized in this case. As known widely [68, 69], the width of transition peaks is inversely proportional to the grain size and ε_2 peaks become broader for smaller grains. As a result, compared with other studies [25, 28, 48], the optical transitions in the E_g regime are slightly broad in Fig. 10.5a. However, the determination of accurate optical constants (or α) is generally more important than the slight variation in absorption features. It has been demonstrated that the dielectric functions obtained from the thin CIGSe layers provide excellent fittings in the external quantum efficiency (EQE) analysis of CIGSe solar cells (Sect. 2.2.3 in Vol. 2) and the SE analysis of thick CIGSe layers (Sect. 4.3.4 in Vol. 2).

10.3 Dielectric Function of CIGSe

In this section, the dielectric functions of various CIGSe-based materials with different Ga and Cu compositions, determined from the GEM analyses, are shown. From the dielectric functions, the optical transition energies are further characterized using critical point (CP) analysis. Based on these results, a general picture of the optical transitions in CIGSe materials is presented.

10.3.1 Variations with the Ga and Cu Composition

To determine the changes of $Cu_y(In_{1-x}Ga_x)Se_2$ optical properties with the alloy compositions (x, y), two CIGSe layers having different thicknesses have been

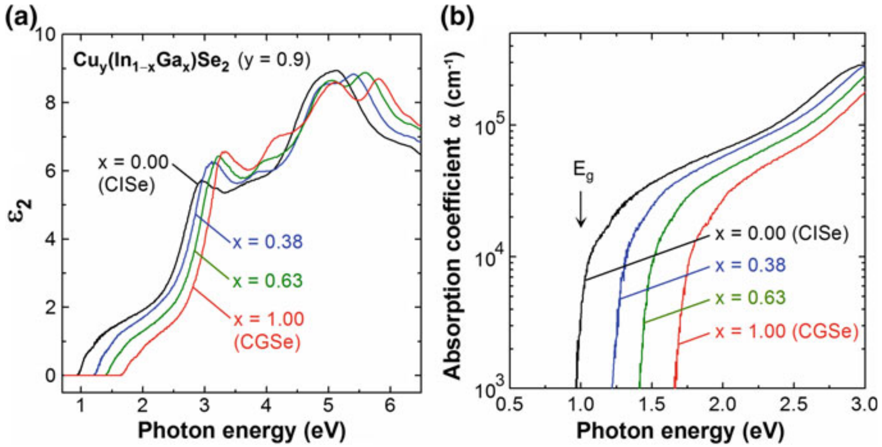

Fig. 10.7 Variations of **a** the ε_2 and **b** the α spectra with x of the $Cu_yIn_{1-x}Ga_xSe_2$ ($y \sim 0.9$), determined from the GEM analyses [29]. In (**b**), the arrow shows the E_g position of the CISe

analyzed for each Ga and Cu compositions [29], so that the dielectric functions can be obtained in a self-consistent approach using GEM.

Figure 10.7 shows the variations of (a) the ε_2 and (b) the α spectra with x of the $Cu_y(In_{1-x}Ga_x)Se_2$ ($y \sim 0.9$), determined from the GEM analyses [29]. The compositions x and y indicate those obtained from electron probe microanalyzer (EPMA). The complete optical data of CISe and CGSe are shown in Figs. 8.24 and 8.25 (Vol. 2), respectively. The ε_2 spectrum of $x = 0.38$ in Fig. 10.7a corresponds to that of Fig. 10.5a. All the dielectric functions show $\varepsilon_2 = 0$ below E_g and the ε_2 peak energies shift quite systematically toward higher energies with increasing x.

The α spectra of Fig. 10.7b are consistent with the ε_2 spectra of Fig. 10.7a. Since CIGSe is a direct transition semiconductor [19–21], α increases sharply near E_g. In particular, with increasing x, the α spectrum shifts toward higher energies due to E_g widening. It can be seen that the α values of CIGSe near E_g are in the range of 10^4 cm^{-1}, which are far smaller than high α values ($\sim 10^5$ cm^{-1}) reported in [45]. Nevertheless, the high α values exceeding 10^5 cm^{-1} have been attributed to artifacts generated by strong surface light scattering [29] (see Fig. 6.8). In all the α spectra of Fig. 10.7b, on the other hand, the small increase in α can be observed at around 0.2 eV above the sharp absorption edge near E_g. As known widely [25, 28, 47, 48], this additional absorption is caused by the spin-orbit splitting near the valence band top (Sect. 4.4.1).

Figure 10.8 shows the pseudo-ε_2 spectra ($\langle\varepsilon_2\rangle$) obtained from a CISe single crystal [48]. In this figure, the uniaxial optical anisotropy characterized by light polarizations perpendicular ($E\perp c$) and parallel ($E\parallel c$) to the c axis in Fig. 10.1a is shown. The components of $E\perp c$ and $E\parallel c$ are also referred to as the ordinary ray and extraordinary ray, respectively [60]. Since the spectra of Fig. 10.8 are pseudo-spectra, the influence of near-surface structures, such as roughness and

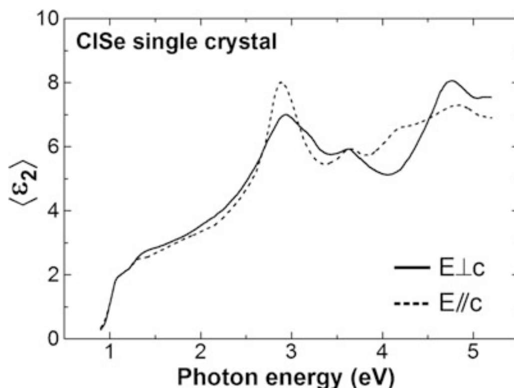

Fig. 10.8 $\langle \varepsilon_2 \rangle$ spectra obtained from a CISe single crystal [48]. In this figure, two spectra for the ordinary ray (electric field perpendicular to the c axis: $E \perp c$) and extraordinary ray (electric field parallel to the c axis: $E \| c$) are shown. The c axis direction of the chalcopyrite crystal is indicated in Fig. 10.1a

mechanical damage caused by polishing, is included in the spectra. It can be confirmed that the CISe shows anisotropic optical properties at $E > 2.5$ eV. In the case of polycrystalline CIGSe materials, the optical properties are isotropic due to random orientation of crystal grains [29] and the optical constants of isotropic chalcopyrite crystals can be approximated as $(\varepsilon_{\|} + 2\varepsilon_{\perp})/3$ from the contributions of the a and c axis directions. Thus, the ε_2 spectrum of the polycrystalline CISe in Fig. 10.7a resembles the spectrum calculated assuming $(\varepsilon_{\|} + 2\varepsilon_{\perp})/3$. In Fig. 10.8, however, the $\langle \varepsilon_2 \rangle$ spectra of the single crystal show slightly sharp absorption features near E_g, compared with the polycrystalline CISe, due to the grain size effect mentioned earlier.

Figure 10.9 shows the variations of (a) the ε_2 and (b) the α spectra with y of the $Cu_yIn_{1-x}Ga_xSe_2$-based layer in a range of $0.36 \leq y \leq 1.34$ with a constant $x \sim 0.4$ [29, 55]. When the samples were prepared under the condition of $y > 1$, however, the segregation of a metallic Cu_xSe phase occurs [70, 71], resulting in the structure of Cu_xSe/CIGS/substrate [29]. For $y = 1.02$ in Fig. 10.9a, a KCN treatment [72, 73] was performed to remove the Cu_xSe layer and to prepare the sample of $y \sim 1$ with $x \sim 0.4$. For $y = 1.34$ in Fig. 10.9b, on the other hand, the SE analysis was carried out without removing the Cu_xSe layer assuming a uniform film structure.

When the y composition is varied, the amplitude of the dielectric function shows a relatively large change with almost no shifts of the ε_2 peak positions in the UV region. In particular, the amplitude of the $E_1(A)$ transition decreases significantly at lower y and the E_3 transition peak disappears when $y = 0.36$. The shape of the ε_2 spectrum for $y = 0.36$ is quite similar to that reported for $Cu(InGa)_3Se_5$ ($y = 0.33$) [74] and $Cu(InGa)_5Se_8$ ($y = 0.20$) [75, 76]. The slightly low ε_2 amplitude of $y = 1.02$ at $E > 4.5$ eV could be an artifact originating from surface roughening caused by KCN etching.

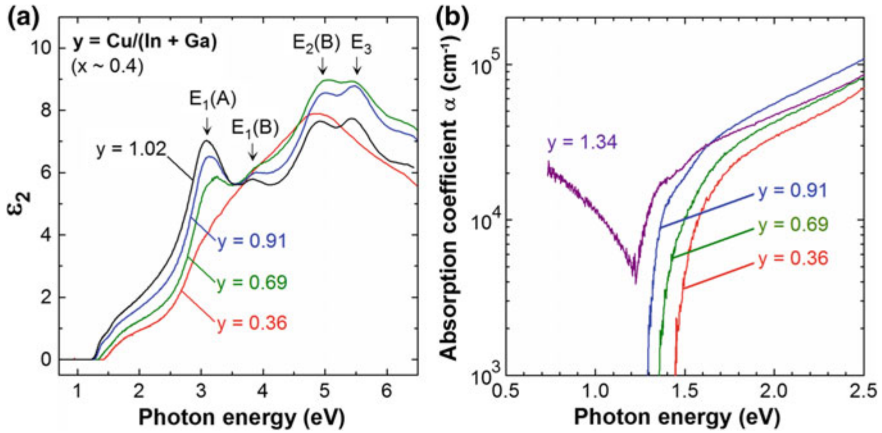

Fig. 10.9 Variations of **a** the ε_2 and **b** the α spectra with y of the $Cu_yIn_{1-x}Ga_xSe_2$-based layer ($x \sim 0.4$), determined from the GEM analyses [29, 55]

In Fig. 10.9b, as y decreases, the band-edge absorption shifts toward higher energies, accompanied by the reduction of α in the visible region. When $y = 1.34$, however, a large change in the ε_2 spectrum can be seen in the energy region below E_g. In this sample, the Cu_xSe overlayer is present and the increase in α at lower energies can be attributed to the effect of free carrier absorption in a semi-metallic Cu_xSe phase [70, 71]. The Cu_xSe is a degenerate p-type semiconductor with quite high hole concentrations of $\sim 10^{22}$ cm^{-3} [77]. From the strong free carrier absorption, therefore, the presence of the Cu_xSe component can be detected. However, the absolute α values of $y = 1.34$ are not reliable as the simplified optical model is used without incorporating the contribution of the Cu_xSe overlayer.

10.3.2 E_g and CP Analyses

The band-edge absorption of direct transition semiconductors is approximated by $\alpha E = A(E - E_g)^{1/2}$ [78] and thus E_g can be determined by plotting $(\alpha E)^2$ versus E. Figure 10.10 shows the E_g analysis performed for the α spectra of Fig. 10.7b using the $(\alpha E)^2 - E$ plot [29]. In this figure, good linearities can be seen and E_g is estimated from the energy position at $(\alpha E)^2 = 0$. These analyses lead to $E_g = 1.00 \pm 0.01$ eV ($x = 0.00$) and $E_g = 1.70 \pm 0.01$ eV ($x = 1.00$). Similar E_g values ranging from 0.94 and 1.04 eV have also been reported for CISe [23, 26–28, 45–50, 52, 53, 56, 79–82].

Figure 10.11 summarizes E_g obtained from this procedure as a function of (a) x and (b) y of the CIGSe-based layer [29]. The variation of E_g with x is almost completely linear without the E_g bowing effect and is expressed simply by

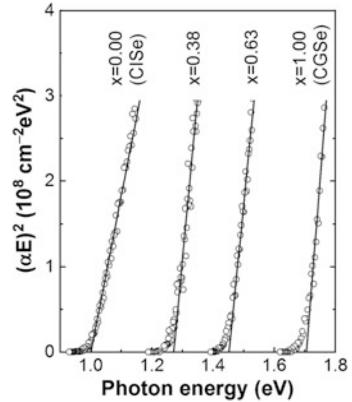

Fig. 10.10 E_g analysis results for the α spectra of Fig. 10.7b [29]. Solid lines show linear fits to the experimental data (open circles)

$E_g(x) = 1.00 + 0.71x$ eV. When the energy position at $\alpha = 10^3$ cm^{-1} is plotted for x, a similar linear variation is observed [29].

In Fig. 10.11b, the E_g values of the various CIGSe-based layers ($0.36 \leq y \leq 1.40$) with a fixed $x \sim 0.4$ are summarized. When the free carrier absorption is present, E_g was obtained by removing the contribution using the Drude model (Sect. 18.2.2). In the Cu deficient layers, however, the linearities in the $(\alpha E)^2 - E$ analysis degrade, suggesting the tail state formation in these layers. In Fig. 10.11b, we observe a systematic linear variation of E_g with y, which can be expressed by $E_g(y) = 1.64 - 0.34y$ eV ($y \leq 1$). This result clearly supports E_g widening in the Cu deficient layers. When $y > 1.0$, on the other hand, E_g becomes constant, as the excess Cu atoms are consumed for the Cu_xSe phase formation with a constant chemical composition in the CIGSe phase.

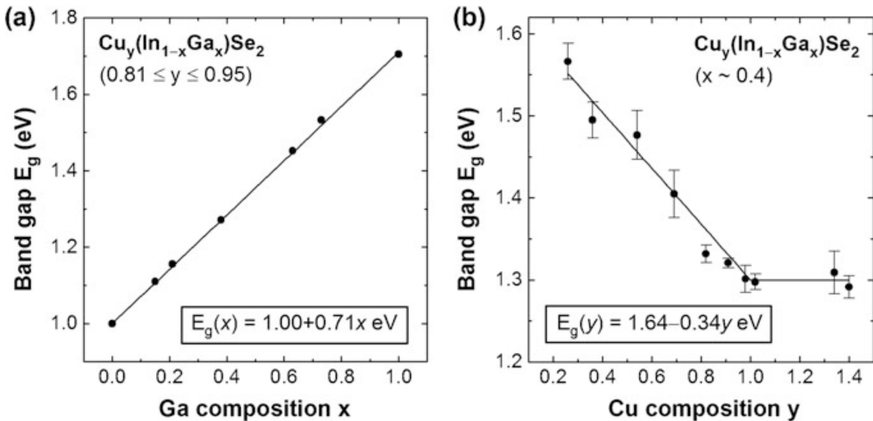

Fig. 10.11 E_g values obtained from the $(\alpha E)^2 - E$ analysis as a function of **a** x and **b** y of the various CIGSe-based layers [29]. In (**a**), the y values are fixed at ~0.9, whereas the x values are fixed at ~0.4 in (**b**)

To characterize the optical transitions in the UV region, a standard CP analysis (Sect. 4.3.1) has been performed for the dielectric functions of the CIGSe-based layers in Figs. 10.7 and 10.9. In the CP analysis, the second derivative spectra expressed by the following theoretical formulas are used:

$$\frac{d^2\varepsilon}{dE^2} = n(n-1)A\ \exp(i\phi)(E - E_\mathrm{p} + i\Gamma)^{n-2}(n \neq 0), \tag{10.2}$$

$$\frac{d^2\varepsilon}{dE^2} = A\ \exp(i\phi)(E - E_\mathrm{p} + i\Gamma)^{-2}(n = 0), \tag{10.3}$$

where A, ϕ, E_p, and Γ show the amplitude, phase, position and width of the peak [83, 84]. The joint density of state (DOS) around CP depends on the band structure, and the CP is classified into one dimension ($n = -1/2$), two dimension ($n = 0$) and three dimension ($n = 1/2$) according to the wave vector involved in the optical transition (Fig. 4.6). Furthermore, $n = -1$ is employed in (10.2) when an optical transition exhibits excitonic behavior.

From the CP analysis using the second derivative spectra, the specific feature of CP can be characterized selectively. In the second derivative spectra, however, the spectral noise in experimental dielectric functions is enhanced drastically. To suppress the noises, CP analyses have been performed using modeled (smoothened) dielectric functions [29, 85]. For this purpose, dielectric function models, including the Lorentz model [29] and Tauc-Lorentz model [85], have been employed. From the modeled dielectric function, quite smooth second-derivative spectra can be obtained. One drawback of this approach is that small absorption features may be eliminated in the process of dielectric function modeling. As an alternative method, smoothing of experimental data based on smoothing polynomials [86, 87] has been employed. In this approach, however, inappropriate choice of smoothening parameters leads to the distortion of the second-derivative spectra.

Figure 10.12a shows an example of ε_2 modeling using the Lorentz peaks [29]. In this figure, the open circles show the experimental ε_2 spectrum of the CISe in Fig. 10.7a and the solid lines indicate the calculation result obtained using five Lorentz oscillators in the region of $E = 2.5$–6.5 eV, which provides sufficiently good fitting to the experimental spectrum. Figure 10.12b shows the second-derivative ε_1 and ε_2 spectra of the CISe obtained from the modeled dielectric function (open circles) and the CP fitting analysis (solid lines) [29]. In this CP analysis, the excellent fitting between the semi-experimental and calculated spectra is confirmed when the excitonic transitions ($n = -1$) are assumed for all the critical points of $E_1(A)$, $E_1(B)$, $E_2(B)$ and E_3. In other studies [25, 48, 53], the CP structures have been fitted assuming the two-dimensional line shape ($n = 0$).

From the analysis procedure of Fig. 10.12, the CP energies (E_p) of various CIGSe-based layers are determined. Figure 10.13 summarizes the variations of the CP transition energies with (a) x and (b) y in the CIGSe-based layer [29]. For the

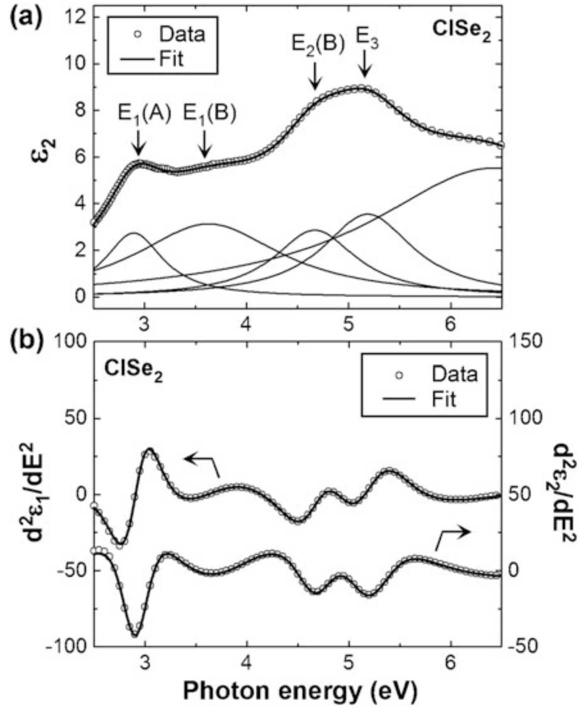

Fig. 10.12 **a** Modeling of the CISe dielectric function using the Lorentz peaks and **b** CP analysis of the CISe dielectric function [29]. In (**a**), the open circles show the experimental ε_2 spectrum of the CISe in Fig. 10.7(**a**) and the solid lines indicate the calculation result using five Lorentz oscillators in the region of E = 2.5–6.5 eV. In (**b**), the second-derivative spectra of the CISe (open circles) were obtained from the modeled dielectric function in (**a**), and the fitted spectra calculated from (10.2) assuming $n = -1$ (solid lines) show good agreement

increase in x ($y \sim 0.9$), all the transition energies increase quite linearly. As a result, the energy positions of the critical points are expressed simply by

$$E_0 = (1.00 + 0.71x) - 0.34(y - 0.90)\ \text{eV}, \tag{10.4}$$

$$E_1(A) = 2.94 + 0.39x\ \text{eV}, \tag{10.5}$$

$$E_1(B) = 3.71 + 0.49x\ \text{eV}, \tag{10.6}$$

$$E_2(B) = 4.71 + 0.44x\ \text{eV}, \tag{10.7}$$

$$E_3 = 5.24 + 0.64x\ \text{eV}. \tag{10.8}$$

Equation (10.4) has been derived by combining the results of Fig. 10.11a, b [55]. In this case, however, it is assumed that the slope of 0.34 for y is independent of x. As confirmed from Fig. 10.13a, the energy shift value for x depends on the CP.

On the other hand, the CP energies of all the UV transitions are independent of y ($x \sim 0.4$) (Fig. 10.13b) and only the E_0 position shifts toward higher energies with decreasing y, as described in (10.4). These trends can be confirmed directly from the variation of the optical spectrum in Fig. 10.9.

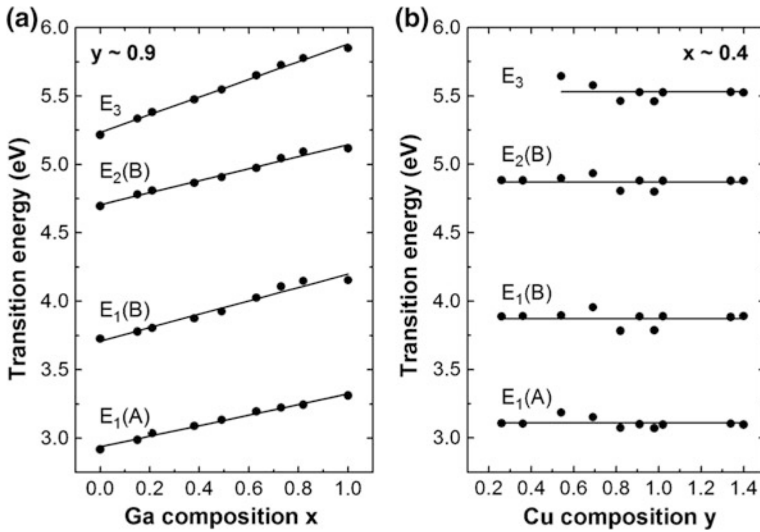

Fig. 10.13 Transition energies obtained from the CP analyses as a function of **a** *x* and **b** *y* in the CIGSe layers [29]

10.3.3 Optical Transition

The band structures [19–21, 88–90] of a Cu-In-Ga-Se system have been calculated based on DFT and the optical transitions have also been investigated theoretically [27, 28, 47, 48]. In DFT calculations within local-density approximation (LDA), E_g is underestimated seriously and the band calculation of CISe using LDA leads to $E_g \sim 0$ eV [19, 20]. Although improved DFT calculation methods that reproduce E_g of various semiconductors have been developed [90–92], the calculation cost of these high-level DFT methods is rather high. On the other hand, the relative band positions within the valence and conduction bands do not vary significantly with the DFT calculation method [90, 93]. In fact, the DOS of the CISe valence band deduced from LDA shows good agreement with that obtained experimentally from X-ray photoelectron spectroscopy [19]. Accordingly, if the small E_g estimated from LDA is corrected using the experimental value of E_g, the optical transition analysis can be made relatively easily based on the simple LDA.

Figure 10.14 shows the band structure of CISe obtained after the E_g correction [29]. In this figure, all the conduction bands calculated from LDA [19] have been shifted toward higher energies so that E_g matches with the experimental E_g value of $E_g = 1.00$ eV (CISe). For the representation of the energy levels in the chalcopyrite Brillouin zone (BZ), the notations of Alonso et al. [48] are adopted. Although the I-III-VI_2 chalcopyrite structure is similar to II-VI binary semiconductors, the unit cell size of the chalcopyrite crystal is larger than that of the zincblende crystal. As a result, zone folding of the zincblende BZ occurs, reducing the volume of the

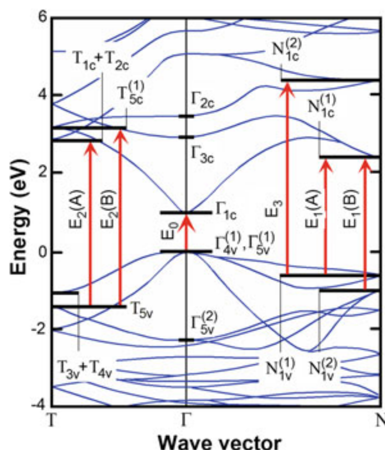

Fig. 10.14 Band structure of CISe [29]. The optical transitions in CISe are indicated by arrows. The energy positions of the conduction bands obtained from LDA [19] have been adjusted using the experimental E_g value of 1.00 eV

chalcopyrite BZ by a factor of four, compared with the zincblende BZ, and the symmetry points N and T are generated by this zone folding (see Fig. 4.3). By the effect of the tetragonal distortion (crystal field), the valence states at the Γ and N points are split into $\left[\Gamma_{4v}^{(1)},\Gamma_{5v}^{(1)}\right]$ and $\left[N_{1v}^{(1)},N_{1v}^{(2)}\right]$, respectively (Fig. 4.5) [19, 48]. In the band calculation of [19], the spin-orbit interaction is neglected and there are only two energy levels near the valence band top [i.e., $\Gamma_{4v}^{(1)},\Gamma_{5v}^{(1)}$], instead of three levels depicted in Fig. 4.5. It should be noted that the energy states $\left[\Gamma_{2c},\Gamma_{3c},\Gamma_{5v}^{(2)}\right]$ at the Γ point are pseudo-direct and are created by the zone folding of the X point in the zincblende BZ [19, 48].

The arrows in Fig. 10.14 represent the major interband transitions in CISe [29]. All the strong optical transitions in the UV region can be assigned to the interband transitions at the N and T points. More specifically, the E_1 and E_2 transitions occur at the N and T points, respectively [48], while the E_3 transition has been attributed to the transition to deeper conduction bands at the N point [29]. Table 10.1 summarizes the transition energies determined from the E_g and CP analyses of the CISe single crystal (Fig. 10.8) [48] and the CISe polycrystal (Fig. 10.12a), together with the theoretical values obtained from the band structure of Fig. 10.14. It can be confirmed that the DFT result shows excellent agreement with the experimental results, confirming the validity of the overall transition analysis.

10.3.4 Effect of Compositions

Figure 10.15 illustrates the variations of valence and conduction bands with x and y in CIGSe-based materials. Unlike binary compounds, such as ZnSe and GaAs, the band structure of CIGSe is perturbed strongly by the presence of the Cu 3d

Table 10.1 Optical transition energies in a CISe single crystal [48] and a CISe polycrystal [29]. The energy levels and the transitions in the chalcopyrite BZ are indicated in Fig. 10.14. In the case of the CISe single crystal, the optical transitions for the ordinary ray ($E \perp c$) and extraordinary ray ($E \| c$) are shown. The numerical data of the table are taken from [29]

Label	Transition	Theory (eV)	Single crystal (eV)		Polycrystal (eV)
			$E \perp c$	$E \| c$	
E_0	$\Gamma_{4v}^{(1)} \to \Gamma_{1c}$	1.00	1.04	1.04	1.00
$E_1(A)$	$N_{1v}^{(1)} \to N_{1c}^{(1)}$	3.22	2.90	2.82	2.92
$E_1(B)$	$N_{1v}^{(2)} \to N_{1c}^{(1)}$	3.59	3.63	3.64	3.73
$E_2(A)$	$T_{5v} \to T_{1c} + T_{2c}$	4.25	4.71		
$E_2(B)$	$T_{5v} \to T_{5c}^{(1)}$	4.56		4.84	4.70
E_3	$N_{1v}^{(1)} \to N_{1c}^{(2)}$	5.20			5.22

electrons [19, 80]. It is well established that the valence band of CIGSe is derived from the cation *d* (Cu 3*d*) and anion *p* (Se 4*p*) states, whereas the conduction band is generated by the cation *s* (In 5*s* or Ga 4*s*) and anion *sp* (Se 4*s*/4*p*) states [19–22, 89, 90]. In particular, DFT calculations revealed that the hybridization of Cu 3*d* and Se 4*p* orbitals results in the generation of the bonding and antibonding bands below valence band maximum (VBM) [22, 90]. As depicted in Fig. 10.15, the anion *p* and cation *d* states repel each other and this interaction moves the VBM toward higher energies, leading to the E_g shrinkage in CIGSe-based materials [19, 20]. This *p-d* coupling effect is inversely proportional to the energy separation between the anion *p* and cation *d* states ($\Delta E_{p\text{-}d}$ in Fig. 10.15) and becomes negligible when $\Delta E_{p\text{-}d}$ is large [20]. In the case of CISe, the E_g reduction caused by the *p-d* interaction has been estimated to be ~0.7 eV [20].

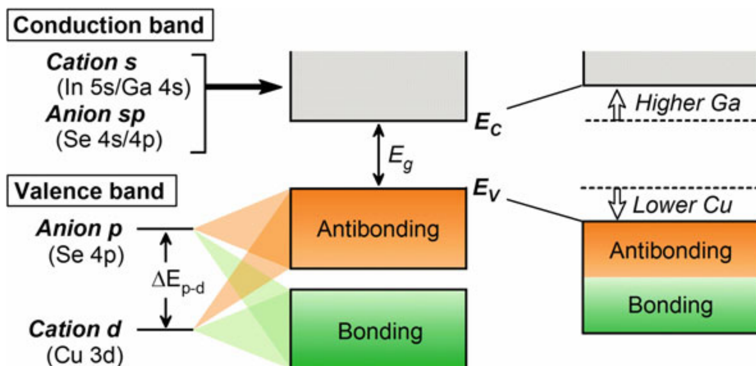

Fig. 10.15 Variations of valence and conduction bands with the Ga and Cu compositions in CIGSe-based materials. By the interaction between the anion *p* and cation *d* states, the bonding and antibonding bands are formed. In the figure, $\Delta E_{p\text{-}d}$ represents the energy separation between the *p-d* states

When the Cu content is low, however, the *p*-*d* coupling effect becomes weaker and E_g widening occurs due to the downward shift of the VBM position [22], as illustrated in Fig. 10.15. This phenomenon explains the increase in E_g with decreasing *y*, observed in Fig. 10.11b. Quite interestingly, among the five transitions in Fig. 10.14, only the E_0 transition at the Γ point shows the change with *y*, as expressed in (10.4)–(10.8). The reduction of the α values in the Cu-deficient layers can be interpreted by the smaller DOS in the valence band, since the partial DOS of the Cu 3d states is quite large, compared with that of the Se 4*p* states [21, 89].

The linear increase in E_g with decreasing *y* further supports the formation of ODC mentioned in Sect. 10.1. For the Cu-In-Se system, there exist the Cu-deficient phases of $Cu_2In_4Se_7$ ($y = 0.5$) [94, 95], $CuIn_3Se_5$ ($y = 0.33$) [96–100] and $CuIn_5Se_8$ ($y = 0.2$) [75, 76, 101–104], in addition to $CuInSe_2$. If these phases exist separately and the segregation of different phases occurs in the Cu deficient layers, the distinct features of each phase should be observed. Accordingly, the smooth variation of E_g with *y* indicates that the structural change with *y* occurs continuously by the introduction of $2V_{Cu} + In_{Cu}$ defect complex. The linear increase of E_g with *y* has also been confirmed from the DFT calculation of CISe [22]. In CIGSe layers fabricated by the three-stage process, the formation of the Cu-deficient layer widens E_g near the CdS/CIGSe interface [36, 41–43], reducing the recombination in the front interface region [44], as described in Sect. 10.1.

So far, the variation of CIGSe optical properties with *x* has been investigated quite extensively [23–29, 51, 55–58]. As illustrated in Fig. 10.15, when the Ga content is increased, the conduction band minimum (CBM) shifts toward higher energy, resulting in the increase in E_g [88, 105]. The band structures of CISe and CGSe are essentially similar [19, 21, 90], and only the CBM position changes with *x* since the influence of the group-III cations is limited to the conduction band. In fact, it has been confirmed experimentally that the energy position of CBM moves toward higher energies almost linearly with *x*, whereas that of VBM is independent of *x* [81]. Consequently, when the V-shaped Ga-profile is formed by the three stage process, the BSF structure is generated in the rear interface region due to the modification of the CBM position, as shown in Fig. 10.1b.

10.4 CIGSe Optical Database

Based on the fundamental optical properties described in the previous section, a formalism that allows the calculation of CIGSe optical constants for arbitrary (*x*, *y*) has been established [55]. This method expresses the variation of the CIGSe dielectric function with *x* and *y* by (i) the energy shift model [106] and (ii) spectral averaging, respectively. In this section, the developed CIGSe optical database is explained in detail.

10.4.1 Energy Shift Model

The energy shift model has been applied successfully for the dielectric function calculation of various semiconductor alloys including $Al_{1-x}Ga_xAs$ [106] and $Si_{1-x}Ge_x$ [107]. In this model, the dielectric function of a target composition is deduced by shifting the energy positions of reference dielectric functions [106]. Figure 10.16 illustrates the calculation procedure of the ε_2 spectrum [$\varepsilon_2(E)$] by the energy shift model [55]. In this example, $\varepsilon_2(E)$ of a target Ga composition of $x_t = 0.2$ is calculated from a reference $\varepsilon_2(E)$ of $x = 0.0$ (CISe), and $\varepsilon_2(E)$ of $x = 0.0$ is slided toward higher energy, so that the CP energies match with those of x_t. As confirmed from (10.4)–(10.8), the energy shift of the transition peak with x depends on each CP, and the energy spacing between the optical transitions needs to be adjusted when $\varepsilon_2(E)$ is shifted toward higher energy. For example, the CP energies of E_0 and $E_1(A)$ for $x = 0.0$ ($y = 0.9$) are 1.00 and 2.94 eV, respectively. In this case, the energy separation of these transitions (i.e., $\Delta E_{01} = E_1(A) - E_0$) is 1.94 eV, whereas ΔE_{01} is 1.88 eV for $x = 0.2$. In the $\varepsilon_2(E)$ calculation for $x_t = 0.2$, therefore, $\varepsilon_2(E)$ of $x = 0.0$ in an energy range of 1.00–2.94 eV is transferred to 1.14–3.02 eV ($x_t = 0.2$) by uniformly reducing the energy spacing of the partial spectrum. As a result, in the energy shift model, the spectral shape is adjusted while maintaining consistency in the CP energies given by (10.4)–(10.8). The effect of the tail absorption below E_0 can also be incorporated into the calculation by simply sliding the ε_2 contribution in this regime toward higher energy assuming a constant energy range for the tail absorption (ΔE in Fig. 10.16) [106]. Nevertheless, the effect of the tail-state absorption is quite small in CIGSe due to the sharp absorption onset near E_g (see Fig. 1.6). In the energy shift model, the corresponding ε_1 spectrum is calculated by the same manner.

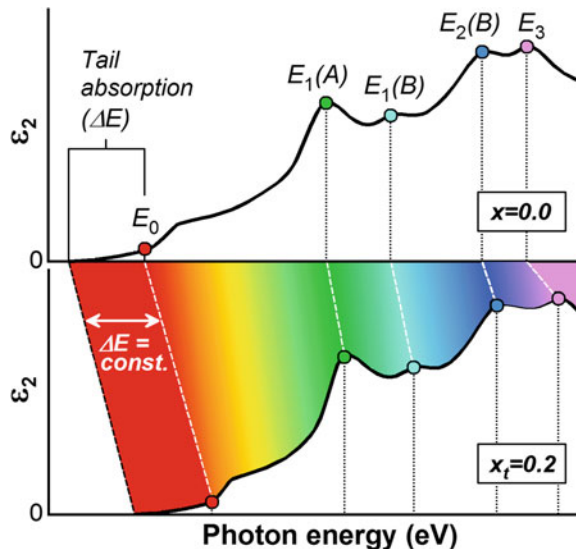

Fig. 10.16 Calculation procedure of the CIGSe ε_2 spectrum by the energy shift model [55]. In this figure, $\varepsilon_2(E)$ for a target Ga composition of $x_t = 0.2$ is calculated from a reference $\varepsilon_2(E)$ of $x = 0.0$ (CISe) by taking the shift of the CP energies (closed circles) into account

10.4.2 Calculation of CIGSe Optical Constants

The effect of the y composition can further be modeled by using a spectral averaging method [55]. In particular, the amplitude of $\varepsilon_2(E)$ reduces gradually with decreasing y (Fig. 10.9a). Accordingly, the CIGSe dielectric function for an arbitrary y can be expressed as a simple spectral average of two dielectric functions with higher and lower Cu contents than a target y composition (y_t). This method can be combined with the energy shift model quite easily. Figure 10.17a shows the calculation method of the CIGSe dielectric function for arbitrary (x_t, y_t) compositions [55]. In Fig. 10.17a, the dielectric function [$\varepsilon(E)$] of target compositions (x_t, y_t) is calculated from three reference dielectric functions indicated by the open circles at (x_1, y_1), (x_1, y_2), and (x_2, y_2).

In the calculation of Fig. 10.17a, the compositional effect of x is calculated first by applying the energy shift model. Specifically, the CP energies of the two dielectric functions at (x_1, y_2) and (x_2, y_2) are shifted to those of (x_t, y_2), and $\varepsilon(E)$ at (x_t, y_2) [i.e., $\varepsilon_{xt,y2}(E)$] is determined as a weighted average of the shifted spectra:

$$\varepsilon_{xt,y2}(E) = \varepsilon_{x1,y2}(E_{\mathrm{shift}}) \frac{|x_t - x_2|}{|x_2 - x_1|} + \varepsilon_{x2,y2}(E_{\mathrm{shift}}) \frac{|x_t - x_1|}{|x_2 - x_1|} \tag{10.9}$$

where $\varepsilon_{x1,y2}(E_{\mathrm{shift}})$ and $\varepsilon_{x2,y2}(E_{\mathrm{shift}})$ denote the dielectric functions obtained after the energy-shift adjustment. When two dielectric functions with higher and lower x values are employed, $\varepsilon(E)$ of a target composition can be calculated more

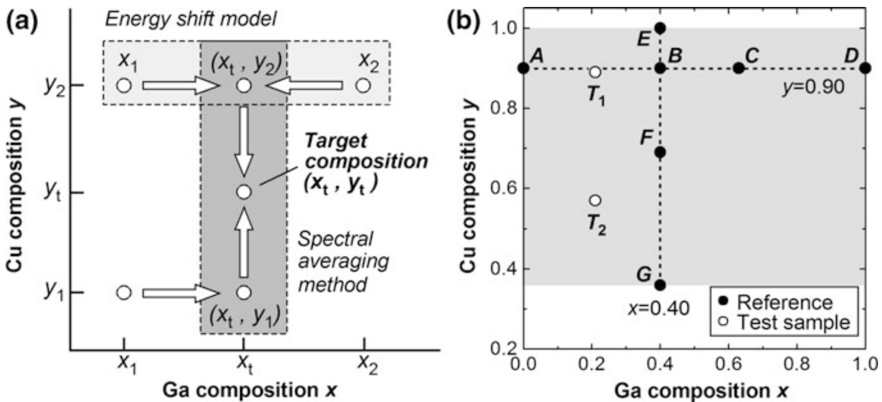

Fig. 10.17 a Calculation method of the CIGSe dielectric function for arbitrary (x_t, y_t) compositions and **b** compositions of reference samples used for $\varepsilon(E)$ calculation (closed circles) [55]. In (**a**), the CIGSe dielectric function at the target compositions of (x_t, y_t) is calculated by the energy shift model for the variation of x and the spectral averaging method for the variation of y. In (**b**), the capital letter shows the reference-sample name and the open circles show the compositions of test samples (T_1 and T_2)

accurately. For the y_t calculation, $\varepsilon(E)$ at (x_t, y_1) [$\varepsilon_{xt,y1}(E)$] is also calculated from the composition of (x_1, y_1). Finally, $\varepsilon(E)$ at (x_t, y_t) is determined as a weighted average (spectral averaging) of the two dielectric functions of $\varepsilon_{xt,y1}(E)$ and $\varepsilon_{xt,y2}(E)$:

$$\varepsilon_{xt,\,yt}(E) = \varepsilon_{xt,\,y1}(E)\frac{|y_t - y_2|}{|y_2 - y_1|} + \varepsilon_{xt,\,y2}(E)\frac{|y_t - y_1|}{|y_2 - y_1|}. \tag{10.10}$$

It should be noted that only the amplitude is modified in the calculation of (10.10). In the actual calculation, the $\varepsilon_1(E)$ and $\varepsilon_2(E)$ contributions of $\varepsilon_{xt,yt}(E)$ are obtained separately. From the above procedure, CIGSe optical constants can be deduced in a two-dimensional compositional space of (x, y).

Figure 10.17b shows the (x, y) compositions of CIGSe-based reference samples used for the dielectric function calculation (closed circles) [55]. In this figure, the compositions of test samples (T_1 and T_2) are also indicated (open circles). The samples of A, C and D in the figure correspond to those in Fig. 10.7, whereas the optical properties of samples E, F and G are summarized in Fig. 10.9. For the sample B, the dielectric function shown in Fig. 8.26 (Vol. 2) is used. In the coevaporation process of CIGSe-based layers, the precise composition control is difficult, and the actual compositions of the samples deviate slightly from the intended compositions of $y = 0.9$ for the variation of x and $x = 0.4$ for the variation of y. In the CIGSe optical database calculation, therefore, the (x, y) compositions of these samples are assumed to be $y = 0.9$ (samples A–D) and $x = 0.4$ (samples B, E–G) since the x or y composition of the reference optical data needs to be identical in the above calculation. As a result, the developed calculation procedure has inherent maximum deviations of 3 at.% for x and 6 at.% for y.

For the optical database calculation, CIGSe dielectric functions were parameterized completely up to a photon energy of 6.5 eV assuming several transition peaks expressed by the Tauc-Lorentz model (Sect. 5.3.7) and, in Chap. 8 (Vol. 2), the results of the dielectric function modeling for sample A (Fig. 8.24 in Vol. 2), sample B (Fig. 8.26 in Vol. 2), sample D (Fig. 8.25 in Vol. 2), sample F (Fig. 8.27 in Vol. 2) and sample G (Fig. 8.28 in Vol. 2) are summarized with their Tauc-Lorentz model parameters [55]. As confirmed from Fig. 10.17b, for the composition range of $y > 0.69$ ($0 \leq x \leq 1.0$), the dielectric function calculation is carried out using three reference dielectric functions, while only two reference data (the samples F and G) are employed in the region of $0.36 < y < 0.69$ ($0 \leq x \leq 1.0$).

Figure 10.18 shows the change of $\varepsilon_2(E)$ with (a) x and (b) y, obtained from the calculation procedure shown in Fig. 10.17 [55]. In Fig. 10.18a, the y value is fixed at 0.9 and the $\varepsilon_2(E)$ spectrum is calculated by applying only the energy shift model using the reference data of the samples A–D. In Fig. 10.18b, $\varepsilon_2(E)$ is deduced by using spectral averaging of the reference samples of B and E–G assuming $x = 0.4$. In Fig. 10.18, the white lines represent the E_g positions. It can be seen that the variations of the CIGSe dielectric function with (x, y) shown in Figs. 10.7 and 10.9 can be reproduced quite well by the developed model. The continuous shift of the α

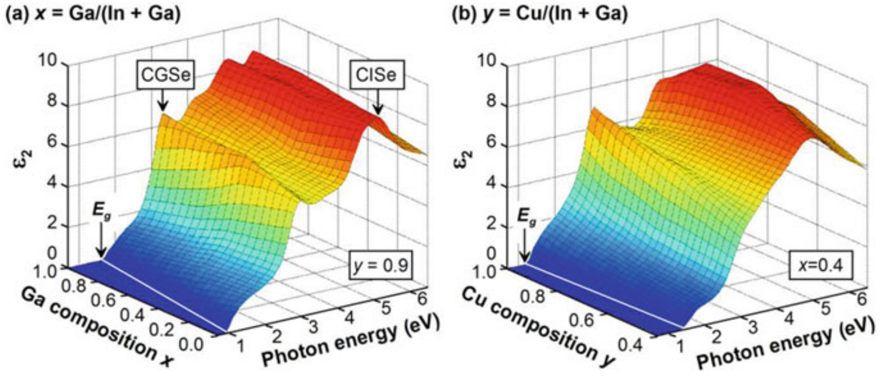

Fig. 10.18 Variation of $\varepsilon_2(E)$ with **a** x and **b** y, obtained from the CIGSe optical database [55]. In (**a**) and (**b**), the values of $y = 0.9$ and $x = 0.4$ are assumed, respectively. The energy spacing of $\varepsilon_2(E)$ is 0.1 eV, and the spectra were calculated with compositional steps of 5 at.% in (**a**) and 2.5 at.% in (**b**). The white lines represent the E_g positions

spectrum with x (Fig. 10.7b) due to E_g widening can also be expressed properly from the above calculation method [55].

To confirm the validity of the CIGSe optical database, the dielectric functions of the two test samples in Fig. 10.17b have been calculated. Figure 10.19 shows the ε_2 spectra of (a) T_1 ($x = 0.21$, $y = 0.89$) and (b) T_2 ($x = 0.21$, $y = 0.57$) [55]. The open circles show the experimental spectra extracted from the GEM analyses of thin layers (~25 nm) and the solid lines represent the results calculated from the CIGSe optical database. In the calculation, $\varepsilon(E)$ of T_1 is deduced using three reference spectra (the samples A, B, and F), whereas $\varepsilon(E)$ of T_2 is obtained using two reference spectra (the samples F and G). It can be seen that $\varepsilon_2(E)$ calculated for T_1 shows excellent agreement with the experimental spectrum in the whole energy range, while the overall agreement degrades slightly in the case of T_2 due to the limitation of the reference spectra. In Fig. 10.19, however, the calculated CP energies reproduce the experimental CP energies quite well, confirming that the CP energies vary with x but are independent of y for the $E_1(A)$, $E_1(B)$, $E_2(B)$ and E_3 transitions.

Similar analyses have been performed for other CIGSe-based samples with different (x, y) compositions and the systematic analysis shows that the calculated $\varepsilon(E)$ deviates slightly from the experimental $\varepsilon(E)$ when (x_t, y_t) locate away from (x, y) of the reference samples [55]. The fitting quality degrades particularly in the y region of $0.36 \leq y < 0.69$, as shown in Fig. 10.19b For the CIGSe samples of $y > 0.69$ ($0 \leq x \leq 1.0$), however, excellent agreement between the experimental and calculated spectra has been confirmed [55]. Thus, the above method can be employed to calculate the CIGSe dielectric function in a composition range commonly applied for the solar cell fabrication ($x = 0.2$–0.3 and $y \sim 0.9$) [1, 7–10, 16–18].

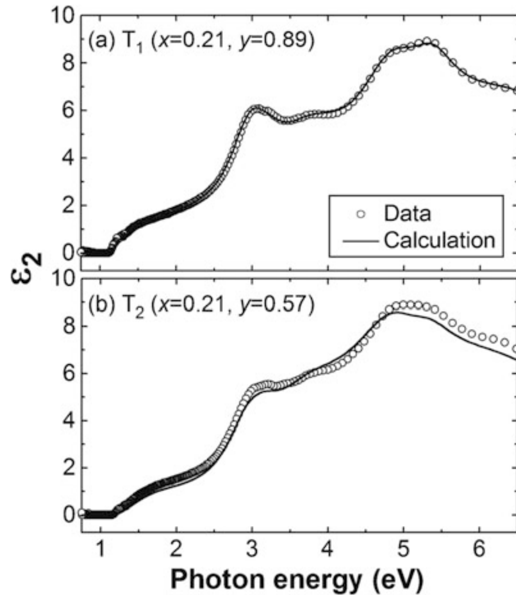

Fig. 10.19 ε_2 spectra of the test samples: **a** T_1 ($x = 0.21$, $y = 0.89$), **b** T_2 ($x = 0.21$, $y = 0.57$) [55]. The open circles show the experimental spectra, whereas the solid lines indicate the results calculated from the CIGSe optical database

From the established model, the dielectric function, (n, k) and α for arbitrary CIGSe compositions can readily be obtained. The CIGSe optical data in a range of $0 \leq x \leq 1.0$ at $y = 0.9$, calculated from the above procedure, are summarized in Fig. 8.26 (Vol. 2) with the tabulated optical constants (Tables 8.62, 8.64, and 8.74–8.82 in Vol. 2). This CIGSe optical database has been applied for an explicit optical simulation of the state-of-the-art CIGSe solar cells fabricated by a three-stage process [17]. When the α values calculated from the optical database are employed, the EQE spectrum of the CIGSe solar cell can be reproduced almost perfectly (Sect. 2.2.3 in Vol. 2). Furthermore, it has been demonstrated that the compositional and structural characterizations of CIGSe-based layers can be performed using the above calculation method (Sect. 4.3.4 in Vol. 2). On the other hand, the CIGSe optical database for x has also been constructed using a different approach, in which parameter values extracted from the dielectric function modeling are expressed as a function of x [56].

References

1. S. Niki, M. Contreras, I. Repins, M. Powalla, K. Kushiya, S. Ishizuka, K. Matsubara, Prog. Photovolt. **18**, 453 (2010)
2. K. Kushiya, Y. Tanaka, H. Hakuma, Y. Goushi, S. Kijima, T. Aramoto, Y. Fujiwara, Thin Solid Films **517**, 2108 (2009)

3. M. Powalla, G. Voorwinden, D. Hariskos, P. Jackson, R. Kniese, Thin Solid Films **517**, 2111 (2009)
4. P. Jackson, R. Wuerz, D. Hariskos, E. Lotter, W. Witte, M. Powalla, Phys. Status Solidi RRL **10**, 583 (2016)
5. M.A. Green, K. Emery, Y. Hishikawa, W. Warta, E.D. Dunlop, D.H. Levi, A.W.Y. Ho-Baillie, Prog. Photovolt. **25**, 3 (2017)
6. A.M. Gabor, J.R. Tuttle, D.S. Albin, M.A. Contreras, R. Noufi, A.M. Hermann, Appl. Phys. Lett. **65**, 198 (1994)
7. A.M. Gabor, J.R. Tuttle, M.H. Bode, A. Franz, A.L. Tennant, M.A. Contreras, R. Noufi, D. G. Jensen, A.M. Hermann, Sol. Eng. Mater. Sol. Cells **41/42**, 247 (1996)
8. M.A. Contreras, J. Tuttle, A. Gabor, A. Tennant, K. Ramanathan, S. Asher, A. Franz, J. Keane, L. Wang, R. Noufi, Sol. Eng. Mater. Sol. Cells **41/42**, 231 (1996)
9. U. Rau, H.W. Schock, Appl. Phys. A **69**, 131 (1999)
10. T. Dullweber, U. Rau, M.A. Contreras, R. Noufi, H. Schock, IEEE Trans. Electron Devices **47**, 2249 (2000)
11. T. Dullweber, O. Lundberg, J. Malmstrom, M. Bodegard, L. Stolt, U. Rau, H.W. Schock, J. H. Werner, Thin Solid Films **387**, 11 (2001)
12. O. Lundberg, M. Bodegard, J. Malmstrom, L. Stolt, Prog. Photovolt. **11**, 77 (2003)
13. M. Gloeckler, J.R. Sites, J. Appl. Phys. **98**, 103703 (2005)
14. O. Lundberg, M. Edoff, L. Stolt, Thin Solid Films **480–481**, 520 (2005)
15. J. Mattheis, P.J. Rostan, U. Rau, J.H. Werner, Sol. Eng. Mater. Sol. Cells **91**, 689 (2007)
16. A. Chirilă, S. Buecheler, F. Pianezzi, P. Bloesch, C. Gretener, A.R. Uhl, C. Fella, L. Kranz, J. Perrenoud, S. Seyrling, R. Verma, S. Nishiwaki, Y.E. Romanyuk, G. Bilger, A.N. Tiwari, Nat. Mater. **10**, 857 (2011)
17. T. Hara, T. Maekawa, S. Minoura, Y. Sago, S. Niki, H. Fujiwara, Phys. Rev. Appl. **2**, 034012 (2014)
18. P. Jackson, D. Hariskos, R. Wuerz, O. Kiowski, A. Bauer, T.M. Friedlmeier, M. Powalla, Phys. Status Solidi RRL **9**, 28 (2015)
19. J.E. Jaffe, A. Zunger, Phys. Rev. B **28**, 5822 (1983)
20. J.E. Jaffe, A. Zunger, Phys. Rev. B **29**, 1882 (1984)
21. S. Siebentritt, M. Igalson, C. Persson, S. Lany, Prog. Photovolt. **18**, 390 (2010)
22. S.B. Zhang, S. Wei, A. Zunger, H. Katayama-Yoshida, Phys. Rev. B **57**, 9642 (1998)
23. T. Tinoco, C. Rincon, M. Quintero, G.S. Perez, Phys. Status Solidi A **124**, 427 (1991)
24. S. Wei, A. Zunger, J. Appl. Phys. **78**, 3846 (1995)
25. M.I. Alonso, M. Garriga, C.A. Durante Rincon, E. Hernandez, M. Leon, Appl. Phys. A **74**, 659 (2002)
26. S. Han, F.S. Hasoon, J.W. Pankow, A.M. Hermann, D.H. Levi, Appl. Phys. Lett. **87**, 151904 (2005)
27. C.A. Durante Rincon, E. Hernandez, M.I. Alonso, M. Garriga, S.M. Wasim, C. Rincon, M. Leon, Mater. Chem. Phys. **70**, 300 (2001)
28. P.D. Paulson, R.W. Birkmire, W.N. Shafarman, J. Appl. Phys. **94**, 879 (2003)
29. S. Minoura, K. Kodera, T. Maekawa, K. Miyazaki, S. Niki, H. Fujiwara, J. Appl. Phys. **113**, 063505 (2013)
30. R. Noufi, R. Axton, C. Herrington, S.K. Deb, Appl. Phys. Lett. **45**, 668 (1984)
31. C. Rincon, S.M. Wasim, G. Marin, J.M. Delgado, J.R. Huntzinger, A. Zwick, J. Galibert, Appl. Phys. Lett. **73**, 441 (1998)
32. C. Stephan, S. Schorr, M. Tovar, H. Schock, Appl. Phys. Lett. **98**, 091906 (2011)
33. S. Yamazoe, H. Kou, T. Wada, J. Mater. Res. **26**, 1504 (2011)
34. A. Nakane, H. Tampo, M. Tamakoshi, S. Fujimoto, K.M. Kim, S. Kim, H. Shibata, S. Niki, H. Fujiwara, J. Appl. Phys. **120**, 064505 (2016)
35. I. Repins, M.A. Contreras, B. Egaas, C. DeHart, J. Scharf, C.L. Perkins, B. To, R. Noufi, Prog. Photovolt. **16**, 235 (2008)
36. D. Schmid, M. Ruckh, F. Grunwald, H.W. Schock, J. Appl. Phys. **73**, 2902 (1993)

37. R. Herberholz, U. Rau, H.W. Schock, T. Haalboom, T. Godecke, F. Ernst, C. Beilharz, K.W. Benz, D. Cahen, Eur. Phys. J. AP **6**, 131 (1999)
38. Y. Yan, K.M. Jones, J. Abushama, M. Young, S. Asher, M.M. Al-Jassim, R. Noufi, Appl. Phys. Lett. **81**, 1008 (2002)
39. D. Liao, A. Rockett, Appl. Phys. Lett. **82**, 2829 (2003)
40. I.M. Kotschau, H.W. Schock, J. Phys. Chem. Solids **64**, 1559 (2003)
41. M. Bar, I. Repins, M.A. Contreras, L. Weinhardt, R. Noufi, C. Heske, Appl. Phys. Lett. **95**, 052106 (2009)
42. M. Morkel, L. Weinhardt, B. Lohmuller, C. Heske, E. Umbach, W. Riedl, S. Zweigart, F. Karg, Appl. Phys. Lett. **79**, 4482 (2001)
43. M. Bar, S. Nishiwaki, L. Weinhardt, S. Pookpanratana, O. Fuchs, M. Blum, W. Yang, J.D. Denlinger, W.N. Shafarman, C. Heske, Appl. Phys. Lett. **93**, 244103 (2008)
44. T. Nishimura, S. Toki, H. Sugiura, K. Nakada, A. Yamada, Appl. Phys. Express **9**, 092301 (2016)
45. W. Horig, H. Neumann, H. Sobotta, Thin Solid Films **48**, 67 (1978)
46. J.R. Tuttle, D. Albin, R.J. Matson, R. Noufi, J. Appl. Phys. **66**, 4408 (1989)
47. T. Kawashima, S. Adachi, H. Miyake, K. Sugiyama, J. Appl. Phys. **84**, 5202 (1998)
48. M.I. Alonso, K. Wakita, J. Pascual, M. Garriga, N. Yamamoto, Phys. Rev. B **63**, 075203 (2001)
49. S. Han, C. Persson, F.S. Hasoon, H.A. Al-Thani, A.M. Hermann, D.H. Levi, Phys. Rev. B **74**, 085212 (2006)
50. S. Han, F.S. Hasoon, A.M. Hermann, D.H. Levi, Appl. Phys. Lett. **91**, 021904 (2007)
51. S. Theodoropoulou, D. Papadimitriou, K. Anestou, C. Cobet, N. Esser, Semicond. Sci. Technol. **24**, 015014 (2009)
52. A. Kreuter, G. Wagner, K. Otte, G. Lippold, A. Schindler, M. Schubert, Appl. Phys. Lett. **78**, 195 (2001)
53. T. Begou, J.D. Walker, D. Attygalle, V. Ranjan, R.W. Collins, S. Marsillac, Phys. Status Solidi RRL **5**, 217 (2011)
54. V. Ranjan, T. Begou, S. Little, R.W. Collins, S. Marsillac, Prog. Photovolt. **22**, 77 (2014)
55. S. Minoura, T. Maekawa, K. Kodera, A. Nakane, S. Niki, H. Fujiwara, J. Appl. Phys. **117**, 195703 (2015)
56. P. Aryal, A. Ibdah, P. Pradhan, D. Attygalle, P. Koirala, N.J. Podraza, S. Marsillac, R.W. Collins, J. Li, Prog. Photovolt. (2016). https://doi.org/10.1002/pip.2774
57. A. Loubat, C. Eypert, F. Mollica, M. Bouttemy, N. Naghavi, D. Lincot, A. Etcheberry, Appl. Surf. Sci. **421**, 643 (2017)
58. G.W. El Haj Moussa, M. Ajaka, M. El Tahchi, E. Eid, C. Llinares, Phys. Status Solidi A **202**, 469 (2005)
59. H. Fujiwara, J. Koh, P.I. Rovira, R.W. Collins, Phys. Rev. B **61**, 10832 (2000)
60. H. Fujiwara, *Spectroscopic Ellipsometry: Principles and Applications* (Wiley, West Sussex, UK, 2007)
61. D.E. Aspnes, A.A. Studna, E. Kinsbron, Phys. Rev. B **29**, 768 (1984)
62. M. Akagawa, H. Fujiwara, J. Appl. Phys. **110**, 073518 (2011)
63. D. Murata, T. Yuguchi, H. Fujiwara, Thin Solid Films **571**, 756 (2014)
64. H. Fujiwara, S. Fujimoto, M. Tamakoshi, M. Kato, H. Kadowaki, T. Miyadera, H. Tampo, M. Chikamatsu, H. Shibata, Appl. Surf. Sci. **421**, 276 (2017)
65. L.L. Kazmerski, O. Jamjoum, P.J. Ireland, S.K. Deb, J. Vac. Sci. Technol. **19**, 467 (1981)
66. L.L. Kazmerski, O. Jamjoum, J.F. Wager, P.J. Ireland, K.J. Bachmann, J. Vac. Sci. Technol., A **1**, 668 (1983)
67. R. Wurz, M. Rusu, T. Schedel-Niedrig, M.C. Lux-Steiner, H. Bluhm, M. Havecker, E. Kleimenov, A. Knop-Gericke, R. Schlogl, Surf. Sci. **580**, 80 (2005)
68. G.F. Feng, R. Zallen, Phys. Rev. B **40**, 1064 (1989)
69. S. Boultadakis, S. Logothetidis, S. Ves, J. Appl. Phys. **73**, 914 (1993)
70. J.R. Tuttle, D.S. Albin, R. Noufi, Solar Cells **27**, 231 (1989)

71. V. Ranjan, R.W. Collins, S. Marsillac, Phys. Status Solidi RRL **6**, 10 (2012)
72. C. Guillen, J. Herrero, J. Electrochem. Soc. **141**, 225 (1994)
73. C. Guillen, J. Herrero, Sol. Eng. Mater. Sol. Cells **43**, 47 (1996)
74. M. Leon, R. Serna, S. Levcenko, G. Gurieva, J.M. Merino, E.J. Friedrich, E. Arushanov, J. Appl. Phys. **104**, 093507 (2008)
75. S. Levcenko, L. Duran, G. Gurieva, M.I. Alonso, E. Arushanov, C.A. Durante Rincon, M. Leon, J. Appl. Phys. **107**, 033502 (2010)
76. M. Leon, R. Serna, S. Levcenko, G. Gurieva, J.M. Merino, E.J. Friedrich, S. Lehmann, T. Schedel-Niedrig, S. Schorr, M.C. Lux-Steiner, E. Arushanov, Phys. Status Solidi C **6**, 1078 (2009)
77. T. Ohtani, Y. Tachibana, J. Ogura, T. Miyake, Y. Okada, Y. Yokota, J. Alloys Comp. **279**, 136 (1998)
78. H.G. Tompkins, E.A. Irene (eds.), *Handbook of Ellipsometry* (William Andrew, New York, 2005)
79. S. Chichibu, T. Mizutani, K. Murakami, T. Shioda, T. Kurafuji, H. Nakanishi, S. Niki, P. J. Fons, A. Yamada, J. Appl. Phys. **83**, 3678 (1998)
80. J.L. Shay, B. Tell, H.M. Kasper, L.M. Schiavone, Phys. Rev. B **7**, 4485 (1973)
81. M. Turcu, U. Rau, Thin Solid Films **431–432**, 158 (2003)
82. C. Rincon, J. Gonzalez, G.S. Perez, Phys. Status Solidi B **108**, K19 (1981)
83. P. Lautenschlager, M. Garriga, S. Logothetidis, M. Cardona, Phys. Rev. B **35**, 9174 (1987)
84. P. Lautenschlager, M. Garriga, L. Vina, M. Cardona, Phys. Rev. B **36**, 4821 (1987)
85. M. Shirayama, H. Kadowaki, T. Miyadera, T. Sugita, M. Tamakoshi, M. Kato, T. Fujiseki, D. Murata, S. Hara, T.N. Murakami, S. Fujimoto, M. Chikamatsu, H. Fujiwara, Phys. Rev. Applied **5**, 014012 (2016)
86. A. Savitzky, J.E. Golay, Anal. Chem. **26**, 1627 (1964)
87. J. Steinier, Y. Termonia, J. Deltour, Anal. Chem. **44**, 1906 (1972)
88. S. Wei, S.B. Zhang, A. Zunger, Appl. Phys. Lett. **72**, 3199 (1998)
89. Y. Li, W. Fan, H. Sun, X. Cheng, P. Li, X. Zhao, J. Appl. Phys. **109**, 113535 (2011)
90. Y. Zhang, X. Yuan, X. Sun, B. Shih, P. Zhang, W. Zhang, Phys. Rev. B **84**, 075127 (2011)
91. M. Shishkin, M. Marsman, G. Kresse, Phys. Rev. Lett. **99**, 246403 (2007)
92. M. Marsman, J. Paier, A. Stroppa, G. Kresse, J. Phys. Condens. Mater **20**, 064201 (2008)
93. J. Paier, R. Asahi, A. Nagoya, G. Kresse, Phys. Rev. B **79**, 115126 (2009)
94. T. Tanaka, N. Tanahashi, T. Yamaguchi, A. Yoshida, Sol. Eng. Mater. Sol. Cells **50**, 13 (1998)
95. M. Leon, S. Levcenko, A. Nateprov, A. Nicorici, J.M. Merino, R. Serna, E. Arushanov, J. Phys. D. **40**, 740 (2007)
96. T. Negami, N. Kohara, M. Nishitani, T. Wada, Jpn. J. Appl. Phys. **33**, L1251 (1994)
97. G. Marin, S. Tauleigne, S.M. Wasim, R. Guevara, J.M. Delgado, C. Rincon, A.E. Mora, G. S. Perez, Mater. Res. Bull. **33**, 1057 (1998)
98. C. Rincon, S.M. Wasim, G. Marin, I. Molina, J. Appl. Phys. **93**, 780 (2003)
99. M. Leon, R. Serna, S. Levcenko, A. Nateprov, A. Nicorici, J.M. Merino, E. Arushanov, Phys. Status Solidi A **203**, 2913 (2006)
100. M. Leon, R. Serna, S. Levcenko, A. Nicorici, J.M. Merino, E.J. Friedrich, E. Arushanov, J. Appl. Phys. **103**, 103503 (2008)
101. L. Duran, S.M. Wasim, C.A. Durante Rincon, E. Hernandez, C. Rincon, J.M. Delgado, J. Castro, J. Contreras, Phys. Status Solidi A **199**, 220 (2003)
102. C. Rincon, S.M. Wasim, G. Marin, R. Marquez, L. Nieves, G.S. Perez, E. Medina, J. Appl. Phys. **90**, 4423 (2001)
103. S. Levcenko, N.N. Syrbu, E. Arushanov, V. Tezlevan, R. Fernandez-Ruiz, J.M. Merino, M. Leon, J. Appl. Phys. **99**, 073513 (2006)
104. L. Duran, J. Castro, J. Naranjho, J.R. Fermin, C.A. Durante Rinon, Mater. Chem. Phys. **114**, 73 (2009)

105. S. Chen, A. Walsh, J.-H. Yang, X.G. Gong, L. Sun, P.-X. Yang, J.-H. Chu, S.-H. Wei, Phys. Rev. B **83**, 125201 (2011)
106. P.G. Snyder, J.A. Woollam, S.A. Alterovitz, B. Johs, J. Appl. Phys. **68**, 5925 (1990)
107. H. Yao, J.A. Woollam, P.J. Wang, M.J. Tejwani, S.A. Alterovitz, Appl. Surf. Sci. **63**, 52 (1993)

Chapter 11
Real Time and In-Situ Spectroscopic Ellipsometry of $Cu_yIn_{1-x}Ga_xSe_2$ for Complex Dielectric Function Determination and Parameterization

Abdel-Rahman A. Ibdah, Puruswottam Aryal, Puja Pradhan, Sylvain Marsillac, Nikolas J. Podraza and Robert W. Collins

Abstract Real time spectroscopic ellipsometry (RTSE) has been applied to characterize the structural evolution and final structural properties of ~50–60 nm thin film $Cu_y(In_{1-x}Ga_x)Se_2$ (CIGS) solar cell absorber layers deposited by single stage co-evaporation onto crystalline silicon wafer substrates. Two series of depositions were explored; the first spans the range of copper atomic fraction $y = [Cu]/([In] + [Ga])$ of $0.45 < y < 1.20$ for fixed gallium atomic fraction $x = [Ga]/([In] + [Ga]) = 0.30$ and the second spans the range of $0 \leq x < 0.50$ with fixed $y \sim 0.90$, as measured by energy dispersive X-ray spectroscopy. Systematic variations in the structural evolution with y reveal that near stoichiometric films undergo significant roughening typically associated with crystallite nucleation and growth whereas films with low and high Cu contents undergo significant smoothening during coalescence typically associated with disordered films or surface regions. The final film structural parameters determined from RTSE enable accurate determination of complex dielectric functions at the deposition temperature and at room temperature based on in-situ SE measurements performed immediately after the deposition process and after film cooling, respectively. Critical point (CP) analysis applying a standard lineshape was performed by fitting twice differentiated dielectric functions. Thus, the resulting CP resonance energies were obtained in accordance with the standardized procedures developed for research on the optical properties of semiconductors. An analytical expression describing the complex dielectric functions of the CIGS films over the range 0.75–3.8 eV was

A.-R. A. Ibdah · P. Aryal · P. Pradhan · N. J. Podraza (✉) · R. W. Collins
Department of Physics & Astronomy and Center for Photovoltaics Innovation & Commercialization, University of Toledo, Toledo, OH 43606, USA
e-mail: Nikolas.Podraza@utoledo.edu

R. W. Collins
e-mail: robert.collins@utoledo.edu

S. Marsillac
Virginia Institute of Photovoltaics, Old Dominion University, Norfolk, VA 23529, USA

© Springer International Publishing AG, part of Springer Nature 2018

H. Fujiwara and R. W. Collins (eds.), *Spectroscopic Ellipsometry for Photovoltaics*,
Springer Series in Optical Sciences 212,
https://doi.org/10.1007/978-3-319-75377-5_11

developed that incorporates photon energy independent parameters associated with four CP resonances, a modified Lorentz oscillator as a broad background between CPs, and a sub-bandgap Urbach tail. The procedure for fitting the dielectric functions by this expression was stabilized by fixing the CP energies deduced in the CP analysis. Polynomials describing the dependence on the Cu content y and the Ga content x for each of the photon energy independent parameters were obtained by fitting the plots of these parameter values as functions of y and x. The utility of the dielectric function expression and associated polynomials has been demonstrated through ex-situ spectroscopic ellipsometry (SE) applications in which the compositional parameters of x and y for a ~450 nm CIGS film have been mapped over a 10 cm × 10 cm sample area. Although the dielectric functions have been deduced from ~50–60 nm films on ideal smooth substrates, they have been effective in serving as a database for compositional analysis of much thicker films, as well as films on Mo coated glass substrates in the solar cell configuration.

11.1 Introduction

The performance of $Cu_y(In_{1-x}Ga_x)Se_2$ (CIGS) solar cells depends on the stoichiometry and alloy composition, defined by the copper and gallium atomic ratios in the CIGS absorber layer [1]. High efficiency CIGS absorbers are typically fabricated at high temperature with a Cu content less than stoichiometric (i.e. <25 at.%). An excess in the Cu content in CIGS thin films has been reported to yield residual copper selenide ($Cu_{2-x}Se$) at the surface and within grain boundaries, which can form short circuit paths and degrade the solar cell efficiency [1, 2]. On the other hand, a low Cu content in the CIGS absorbers has been reported to yield mixed phases, which also degrade device efficiency [1, 3]. High performance CIGS solar cells with efficiency >20% can be produced within compositional space that includes a gallium ratio (x) from ~0.25 to 0.35 and a copper ratio (y) from ~0.80 to 0.95, where $x = [Ga]/([In] + [Ga])$ and $y = [Cu]/([In] + [Ga])$ [4]. In this chapter, a spectroscopic ellipsometry (SE) investigation of a series of CIGS thin films with different Cu contents at fixed Ga content ($x \sim 0.3$) is described in detail [5]. Real time spectroscopic ellipsometry (RTSE) analysis is employed to monitor thin film growth and deduce the structural evolution, whereas in-situ SE is used to deduce the complex dielectric functions at the deposition temperature and at room temperature. The final dielectric function results from a similar series of films as a function of Ga content at fixed Cu content ($y \sim 0.90$) are also reviewed in this chapter [6, 7]. Independent parameterizations of the dielectric functions from the Cu and Ga series of depositions versus y and x, respectively, are reported and compared at the crossing point of $(y, x) = (0.90, 0.30)$. These parameterizations are demonstrated to be useful in mapping CIGS stoichiometry and composition using ex-situ SE.

11.2 Experimental Details

Two series of CIGS thin films, the first with different Cu contents (y = 0.00, 0.47, 0.70, 0.82, 0.88, 0.96, 1.05, and 1.18) for fixed $x = 0.30 \pm 0.01$ and the second with different Ga contents (x = 0.00, 0.12, 0.26, 0.30, 0.37, and 0.48) for fixed $y = 0.90 \pm 0.03$, were deposited onto crystalline silicon (c-Si) wafers using a one stage co-evaporation process at a substrate temperature of 570 °C [5–7]. The substrate temperature was measured using a thermocouple attached to the reverse side of the substrate. The c-Si substrates were measured using in-situ SE at room temperature and at the deposition temperature prior to heating of the evaporation sources. The deposition time was controlled to 50–60 s with a substrate shutter. In this time, the thickness of each deposited CIGS film was very thin, ~50–60 nm, in order to ensure a smooth film surface and to suppress any effects of compositional non-uniformity versus depth. Adopting this strategy, the complex dielectric function of the CIGS bulk layer could be obtained accurately [8]. During the depositions, the temperature of the Se source was maintained at 260 °C resulting in an evaporation rate of ~2 nm/s. The evaporation rates of Cu, In, and Ga were measured in real time using electron impact emission spectroscopy (EIES) previously calibrated to a quartz crystal monitor. The controlled evaporation rates of Cu, In, and Ga along with the corresponding source temperatures during the two series of depositions are shown in Table 11.1. The compositions identifying the samples were measured ex-situ using energy dispersive X-ray spectroscopy (EDX).

The deposition shut-down procedure was found to critically affect the nature of the thin CIGS layer and its surface [5–7]. Once the desired film thickness is reached, the deposition is terminated by closing a shutter to the substrate and reducing the source temperatures for In, Ga, and Cu in order to stop co-evaporation. Then the substrate shutter is opened and in-situ SE data are acquired for the deposited films at the deposition temperature of 570 °C. The temperature is then decreased to 350 °C over a time period of 10 min while maintaining Se evaporation so as to prevent CIGS film evaporation. Once the substrate temperature of 350 °C is reached, Se evaporation is terminated, the substrate shutter is closed, and the substrate heater is turned off, allowing the sample to cool to room temperature. In order to prevent pressurizing the deposition system with Se which could result in deposition of a thin layer of amorphous Se on the CIGS surface, the chamber is kept under vacuum until evaporation from the Se source is essentially zero and the base pressure inside the chamber is in the lower range of 10^{-7} Torr. Once these conditions are reached, the high vacuum valve is closed. If this procedure is not carefully followed, an undesirable loss of CIGS thickness can occur via slow evaporation between the real time and in-situ SE measurements, or amorphous Se can form on the CIGS surface during cooling. If the amorphous Se forms, then it can be removed by evaporation upon heating the sample under vacuum to ~250 °C.

In this study, RTSE was performed during CIGS film growth using a multichannel rotating-compensator spectroscopic ellipsometer (J. A. Woollam Co., M2000-DI) with acquisition and repetition times of 0.1 s. Analysis of the RTSE

Table 11.1 Controlled elemental deposition rates of Cu, In, and Ga and the corresponding evaporation source temperatures used during deposition of the one stage CIGS films with eight different Cu contents *y* and six different Ga contents *x*. The temperature of the Se source was maintained at 260 °C, resulting in an evaporation rate of ~2 nm/s. An asterisk indicates an estimated value [5, 6]

y	Oxide thickness (nm)	Cu		In		Ga	
		Rate (nm/s)	Temp (°C)	Rate (nm/s)	Temp (°C)	Rate (nm/s)	Temp (°C)
0.00	1.39 ± 0.004	0.000	500	0.200	939	0.050	876*
0.47	1.40 ± 0.004	0.060	1156	0.200	939	0.050	876*
0.70	1.49 ± 0.004	0.080	1171	0.200	939	0.050	876*
0.82	1.51 ± 0.004	0.090	1189	0.200	939	0.050	876
0.88	1.44 ± 0.004	0.100	1206	0.200	939	0.050	876*
0.96	1.48 ± 0.004	0.110	1215	0.200	939	0.050	876
1.05	1.40 ± 0.004	0.120	1224	0.200	939	0.050	876*
1.18	1.40 ± 0.004	0.140	1243	0.200	939	0.050	876*
x	Oxide thickness (nm)	Cu		In		Ga	
		Rate (nm/s)	Temp (°C)	Rate (nm/s)	Temp (°C)	Rate (nm/s)	Temp (°C)
0.00	1.58 ± 0.009	0.080	1267	0.160	911	0.000	700
0.12	1.49 ± 0.007	0.090	1272	0.145	908	0.015	978
0.26	1.60 ± 0.007	0.095	1279	0.135	905	0.035	994
0.30	1.44 ± 0.004	0.100	1206	0.200	939	0.050	876
0.37	1.62 ± 0.011	0.100	1284	0.130	898	0.055	1012
0.48	1.47 ± 0.009	0.110	1295	0.120	894	0.070	1031

data provided the evolution of the film structure. Upon completion of film fabrication, in-situ SE for determination of the complex dielectric functions (ε_1, ε_2) was performed at the deposition temperature of 570 °C and at room temperature, using a 9.0 s acquisition time in both cases for greater signal averaging. The resulting room temperature dielectric functions (ε_1, ε_2) were parameterized using critical point oscillators [9], and the oscillator parameters were expressed in terms of *y* or *x* by polynomial fitting.

11.3 Data Analysis and Results: Effect of Cu Content

11.3.1 RTSE of CIGS Growth Versus Cu Content at 570 °C

Prior to analyzing the RTSE and in-situ SE data set for a given deposition, the substrate must be analyzed. This analysis begins with a determination of the thickness of the native oxide layer covering the *c*-Si substrate in a room temperature

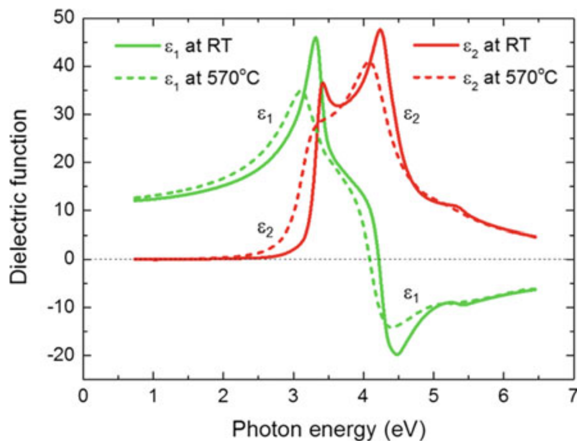

Fig. 11.1 Complex dielectric functions (ε_1, ε_2) of a crystalline silicon substrate at room temperature (RT) and at 570 °C obtained by mathematical inversion of SE data. Both inversions apply the native oxide layer thickness determined from room temperature SE data [5]

measurement. The oxide thickness is then assumed to remain unchanged upon heating the *c*-Si under vacuum to the deposition temperature of 570 °C. Thus, the resulting thickness is used in SE analyses based on numerical inversion, performed point-by-point across the spectra [10], to determine the complex dielectric functions of the *c*-Si at room temperature and at the deposition temperature. The resulting dielectric functions for a typical *c*-Si substrate at these temperatures are shown in Fig. 11.1. The oxide layer thickness in this case was determined at room temperature as 1.40 nm. For the different depositions, the oxide thicknesses varied from 1.39 to 1.62 nm as indicated in Table 11.1. Figure 11.2 depicts the optical model used to fit both RTSE and in-situ SE data. As shown, the CIGS film is divided into two layers, bulk and surface roughness layers of thickness d_b and d_s, respectively. The void volume percentage f_v in the roughness layer is also varied in the fitting procedure.

In order to analyze the RTSE data collected for a given deposition of this study, the initial focus is on the final RTSE (ψ, Δ) spectra measured at the deposition endpoint in the high speed mode (0.1 s acquisition time). Trial values are assigned to the structural parameters in the model of Fig. 11.2 for the film at this endpoint, including the bulk layer thickness d_b, the surface roughness layer thickness d_s, and the void content f_v in the surface roughness layer. These trial values provide sufficient information such that a trial CIGS dielectric function can be obtained from

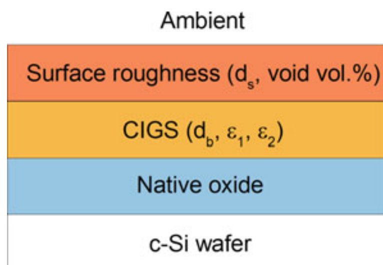

Fig. 11.2 Schematic of the optical model used for analysis of RTSE data during film deposition and in-situ SE data after deposition for CIGS films with different Cu and Ga contents

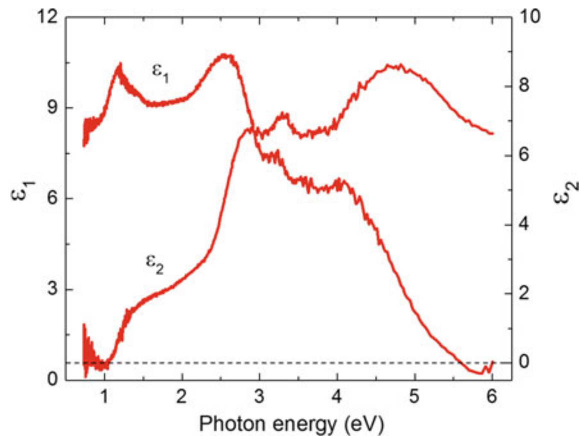

Fig. 11.3 Complex dielectric function (ε_1, ε_2) at 570 °C obtained by RTSE (acquisition time: 0.1 s) for a CIGS layer applying numerical inversion with incorrect CIGS layer thicknesses, yielding artifacts in the spectra over the range of 3–4 eV. These representative results are for the CIGS film with Cu content $y = 0.88$ and Ga content $x = 0.30$ [5]

the final RTSE (ψ, Δ) spectra by numerical inversion. An example of such a trial dielectric function at the substrate temperature of 570 °C is shown in Fig. 11.3 for the CIGS film with Cu content $y = 0.88$ and Ga content $x = 0.30$. These (ε_1, ε_2) spectra exhibit considerable noise due to the very short acquisition time of 0.1 s. In addition, artifacts arising from the *c*-Si substrate are observed in the 3–4 eV spectral range due to the incorrect assignments of ($d_b = 47.0$ nm, $d_s = 10.0$ nm, $f_v = 50$ vol.%) for the three structural parameters. In spite of the artifacts, the inverted dielectric function can be used to deduce the best fit (d_b, d_s, f_v) values as functions of time by least squares regression analysis of data collected throughout bulk layer growth ($d_b > 0.1$ nm). The time dependence of the mean square error (MSE) is also determined, describing the overall quality of the fit to the structural evolution. This analysis step is based on the assumption that the inverted bulk layer dielectric function does not change over the analyzed time range.

Of primary interest in this initial step of the analysis procedure is the time dependence of the MSE from the least squares regression analysis. In fact, the time-averaged MSE is used to evaluate the validity of the trial endpoint structural parameters and the corresponding inverted complex dielectric function [11]. The correct choices for the endpoint parameters are those generating a global minimum in the time-averaged MSE describing the fit for the structural evolution. In this analysis procedure, the number of data values is $2MN$, with M (ψ, Δ) spectra collected versus time and N spectral positions. The model of Fig. 11.2 includes $3M + 2N$ free parameters, three structural variables (d_b, d_s, f_v) at each time and two dielectric function variables (ε_1, ε_2) at each photon energy. Because the number of spectral positions N is large, the analysis is possible even for a relatively small number M of spectra collected versus time. A check of this overall analysis procedure is based on an inspection of the final inverted dielectric function. Artifacts in the dielectric function should be eliminated with the correct assignment of endpoint (d_b, d_s, f_v) values, and in addition, ε_2 should decrease gradually to zero with

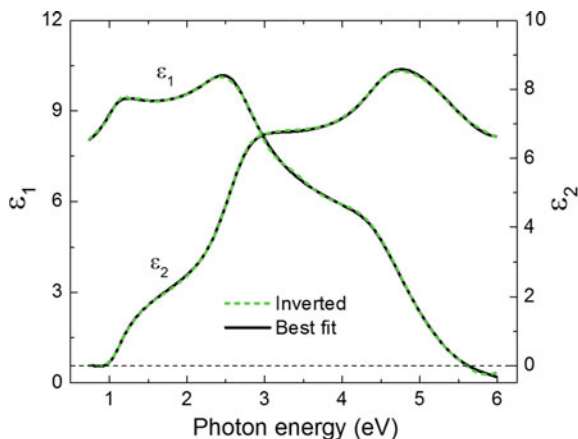

Fig. 11.4 Complex dielectric function (ε_1, ε_2) at 570 °C obtained by in-situ SE (acquisition time: 9 s) for CIGS with Cu content $y = 0.90$ and Ga content $x = 0.26$. The best fit optical model over the photon energy range of 0.75–6.00 eV incorporates four critical point oscillators and one modified Lorentz oscillator. The best fit parameters appear in Table 11.2 [5]

decreasing photon energy below the CIGS bandgap (as long as $y \leq 1$, implying no measurable $Cu_{2-x}Se$ phase) [12].

The same global best fit values of (d_b, d_s, f_v) obtained from RTSE at the end of each deposition were also applied in the analysis of the in-situ SE data collected after deposition using the much longer acquisition time of ~9.0 s. From these best fit structural parameters, the CIGS complex dielectric function (ε_1, ε_2) at 570 °C was determined for each film by numerical inversion. Because the in-situ SE data acquisition time was much longer than that required for the dynamic RTSE measurements, the noise in (ε_1, ε_2) is reduced significantly. Such noise is evident in the inversion of RTSE data shown in Fig. 11.3. The positive impact of the long measurement time is shown in Fig. 11.4 for the deposition with $y = 0.90$ and $x = 0.26$ from the Ga series. Here the dielectric function is presented over the range 0.75–6.0 eV, as obtained by inversion from in-situ SE data collected at 570 °C after deposition. It is evident here that no artifacts are present for the assignment of the best fit endpoint values of (d_b, d_s, f_v), and ε_2 decreases to zero with decreasing energy below the bandgap of the CIGS material. These results indicate that no structural changes have occurred between the final RTSE and the in-situ SE measurements at deposition temperature, an important finding considering the high temperature.

Examples of the in-situ SE (ψ, Δ) spectra acquired at 570 °C are shown in Fig. 11.5 for four CIGS films with Cu contents of $y = 0.47$, 0.70, 0.88, and 1.05. The solid lines in Fig. 11.5 were obtained by using numerically inverted dielectric functions in a simulation with fixed bulk and surface roughness layer thicknesses and roughness layer void contents that correspond to the final film structure as deduced from the RTSE analysis. If the numerical inversion is successfully applied, then the data and simulation should closely coincide. Any deviations are attributed to termination errors in the inversion routine which involves iterative approximation [10]. The values of the final bulk and surface roughness layer thicknesses used in these analyses for the entire Cu series are shown in Table 11.3, and the inverted

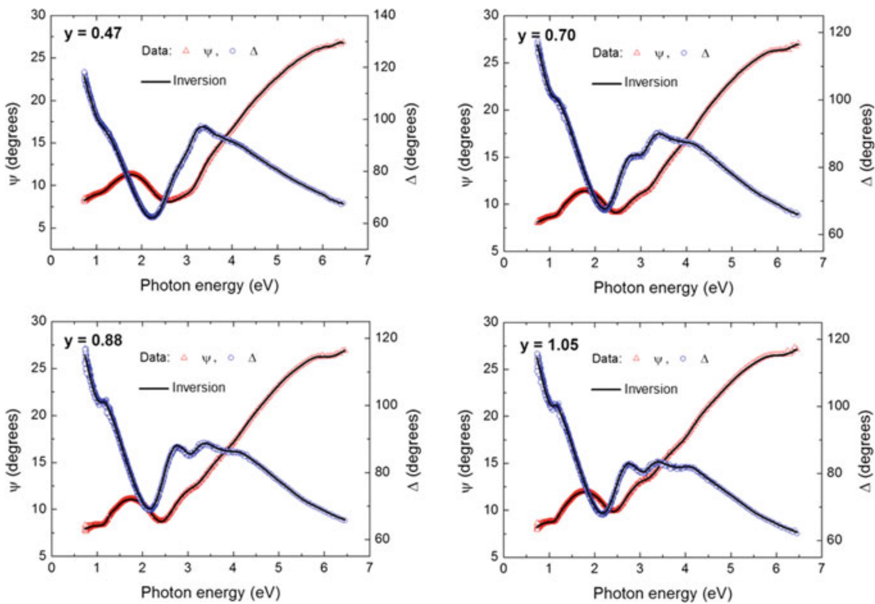

Fig. 11.5 Experimental ellipsometry angles ψ (triangles) and Δ (circles) plotted as functions of photon energy along with the inverted results (lines) for selected CIGS films with Cu contents of $y = 0.47$, 0.70, 0.88, and 1.05 measured at the end of the depositions. These in-situ SE data were acquired at the deposition temperature of 570 °C as determined by a thermocouple attached to the back of the substrate. The inverted dielectric functions that correspond to these results are shown in Fig. 11.6 [5]

dielectric functions that correspond to these SE simulations are shown individually for the four samples with Cu contents of $y = 0.47$, 0.70, 0.88, and 1.05 in Fig. 11.6. For ease of comparison, all dielectric functions are shown together in Fig. 11.7. The dielectric function spectra of CIGS in Figs. 11.6 and 11.7 exhibit a clear dependence on the deposited film Cu content in the range of the absorption onset.

As an evaluation of the validity of the dielectric function spectra inverted from in-situ SE data, these spectra were fitted using an analytical model consisting of four critical point (CP) oscillators and a single Tauc gap modified Lorentz oscillator as a background [9]. This model was adopted because it was found in previous studies to describe accurately the dielectric functions of CIGS layers of the Ga series at 570 °C [6, 7]. The expressions used for these oscillator terms will be presented in the next sub-section; here the focus is on identification of accurate dielectric functions for analysis of the structural evolution. The analytical model uses the oscillator parameters in the left column of Table 11.2. All parameters were allowed to vary in the fitting procedure, with the exception of the constant ε_1 contribution $\varepsilon_{1,\infty}$ which was fixed at unity, and the Tauc gap, which was linked to the lowest energy CP bandgap. The best fit to the dielectric function inverted from in-situ SE data is shown in Fig. 11.4 for the CIGS bulk layer with $y = 0.90$ and $x = 0.26$, and the oscillator parameters are listed in

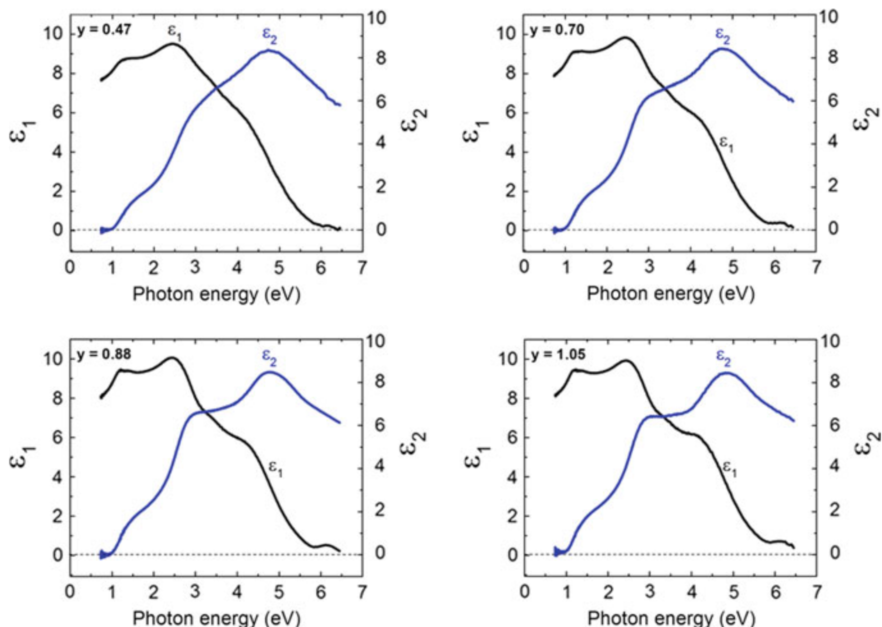

Fig. 11.6 Complex dielectric functions (ε_1, ε_2) at 570 °C obtained by inversion of in-situ SE data as in Fig. 11.5 collected after the deposition for CIGS films with Cu ratios y of 0.47, 0.70, 0.88, and 1.05. Parameterized versions of these results as in Fig. 11.4 and Table 11.2 were used to analyze the RTSE data assuming thickness independent dielectric functions [5]

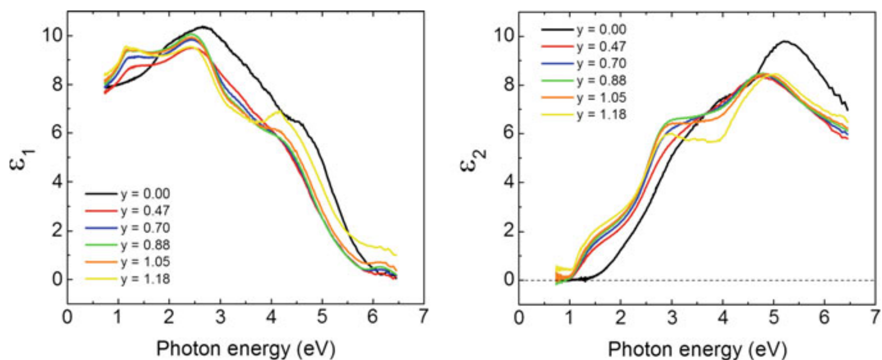

Fig. 11.7 Complex dielectric functions at 570 °C obtained by inversion, including ε_1 (left) and ε_2 (right), from in-situ SE measurements performed after deposition for CIGS films with compositions y of 0.00, 0.47, 0.70, 0.88, 1.05, and 1.18. The results were parameterized as in Fig. 11.4 and Table 11.2 and then used to analyze RTSE data assuming thickness independent dielectric functions. For clarity, the spectra for individual ratios y are presented in Fig. 11.6 [5]

Table 11.2 Critical point (CP) and Tauc gap modified Lorentz (T-L) oscillator parameters for a temperature of 570 °C obtained by fitting the dielectric function for a CIGS film with composition $y = 0.90$ and $x = 0.26$ over the spectral range from 0.75 to 6.00 eV. All parameters were varied in the fitting procedure, with the exception of the constant contribution $\varepsilon_{1,\infty}$ to the real part which was fixed at unity, and the T-L bandgap which was linked to the CP_a bandgap [5]

Parameter	CP_a	CP_b	CP_c	CP_d	T-L
A_n	3.679 ± 0.038	2.894 ± 0.049	6.116 ± 0.136	9.841 ± 0.218	10.817 ± 0.407
E_n (eV)	1.062 ± 0.012	2.618 ± 0.021	4.427 ± 0.123	5.475 ± 0.147	$E_0 = 6.693 \pm 0.240$ eV $E_g = 1.062 \pm 0.012$ eV
Γ_n (eV)	0.366 ± 0.017	0.905 ± 0.054	0.942 ± 0.094	5.187 ± 0.316	1.380 ± 0.018
ϕ_n (degree)	−66.12 ± 0.96	−51.92 ± 0.73	−18.92 ± 0.82	51.29 ± 0.44	–
μ_n	0.229 ± 0.044	0.863 ± 0.053	0.277 ± 0.052	1.141 ± 0.113	–

Table 11.2. The limitation of the spectra obtained by inversion is that they can exhibit fluctuations and systematic instrument or alignment errors; however, close fits with physics-based analytical models as in Fig. 11.4 provide support for the validity of these dielectric functions.

It is of interest to compare the different depositions for an understanding of the effect of Cu incorporation on the growth evolution of the films. The time evolution of the structural parameters for each CIGS film can be obtained by least squares regression analysis, applying the dielectric function deduced by inversion at the final RTSE endpoint using the best fit endpoint (d_b, d_s, f_v) [11]. High precision is needed in the analysis of the evolution of (d_b, d_s, f_v), however, in order to detect small differences that may occur between one deposition and the next. Based on these considerations, improved results for the structural evolution are anticipated by applying parameterized dielectric functions at 570 °C, as in Fig. 11.4 (solid lines) and Table 11.2, deduced by fitting the much smoother dielectric functions obtained by in-situ SE. (Compare dielectric functions in Figs. 11.3 and 11.4.) Application of the parameterized dielectric functions has led to plots of the bulk and surface roughness layer thicknesses versus time and the void content versus time over the complete time range of deposition that show clear, systematic variations with the CIGS Cu content.

Figure 11.8 depicts RTSE data collected using the fast data acquisition mode at t = 0.201 min and t = 0.601 min after the onset of deposition for the CIGS film of this study with a Cu content of y = 0.88 and a Ga content of x = 0.30. Also shown are the best fits to the data at the two different times that contribute to the structural evolution plots to be presented. The quality of the RTSE data sets in Fig. 11.8 is poorer relative to the in-situ SE data sets in Fig. 11.5 due to the short acquisition time of 0.1 s used for the RTSE data, compared to 9.0 s used for the in-situ SE data acquired after deposition for determination of the dielectric function. In Fig. 11.9, final results are shown for the CIGS film of Fig. 11.8, including the time evolution of the surface roughness void volume percentage as well as the bulk and surface

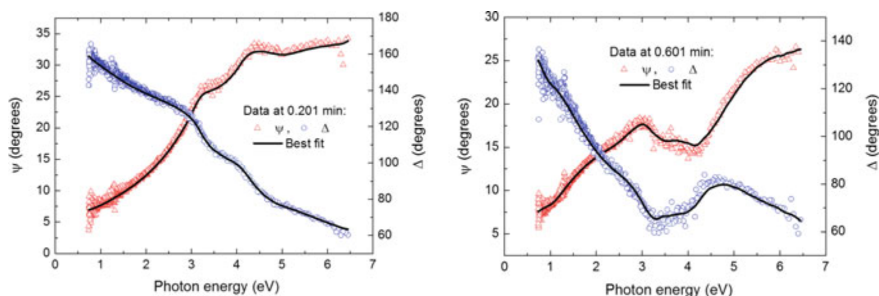

Fig. 11.8 Experimental ellipsometric angles ψ (triangles) and Δ (circles) versus photon energy along with the best fits (solid lines) for a CIGS film with Cu content of y = 0.88 and Ga content x = 0.30 measured at two different times, t = 0.201 min (left) and t = 0.601 min (right), during film growth at the deposition temperature of 570 °C. These RTSE data were collected in 0.1 s using the fast data acquisition mode [5]

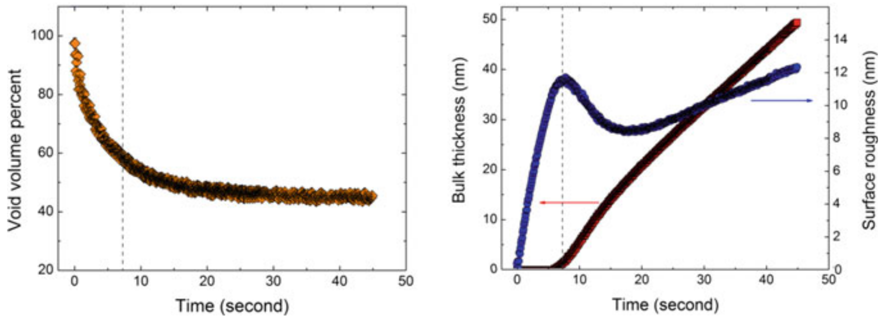

Fig. 11.9 Time evolution of (left) the void volume percentage in the surface roughness layer and (right) the bulk and surface roughness layer thicknesses during deposition of the CIGS film with a Cu content $y = 0.88$ and a Ga content $x = 0.30$ on native oxide covered *c*-Si at a substrate temperature of 570 °C. The vertical lines indicate the onset of nuclei coalescence [5]

roughness layer thicknesses [5]. The associated structural evolution plots of surface roughness layer thickness as a function of bulk layer thickness for the six CIGS films with different Cu contents are shown together for comparison in Fig. 11.10. In Fig. 11.11, the results are shown individually for the bulk layer thickness range $\leq$ 50 nm. The maximum and minimum values of the surface roughness layer thickness before and after coalescence, respectively, are shown and plotted versus *y* in Fig. 11.12. Also plotted in Fig. 11.12 is the difference between the maximum and the minimum, which is a measure of the degree of coalescence. The endpoint void contents in the surface roughness for CIGS films with different Cu contents are given in Table 11.3 with values of 26, 48, and 18 vol.% for

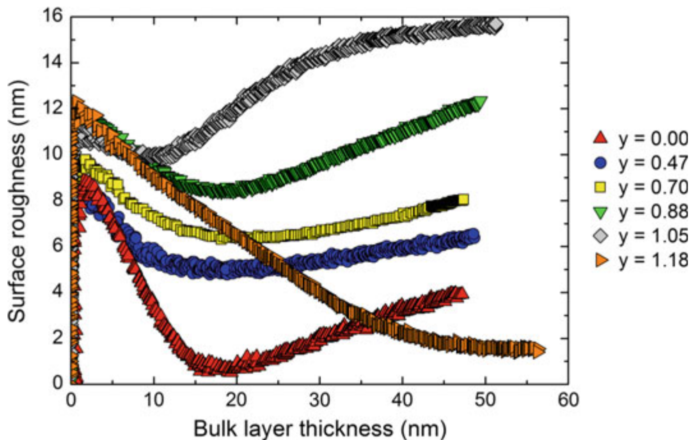

Fig. 11.10 Evolution of surface roughness layer thickness as a function of bulk layer thickness from RTSE studies of CIGS films with six different Cu contents $y = 0.00$, 0.47, 0.70, 0.88, 1.05, and 1.18. For clarity, the results are shown individually in Fig. 11.11 [5]

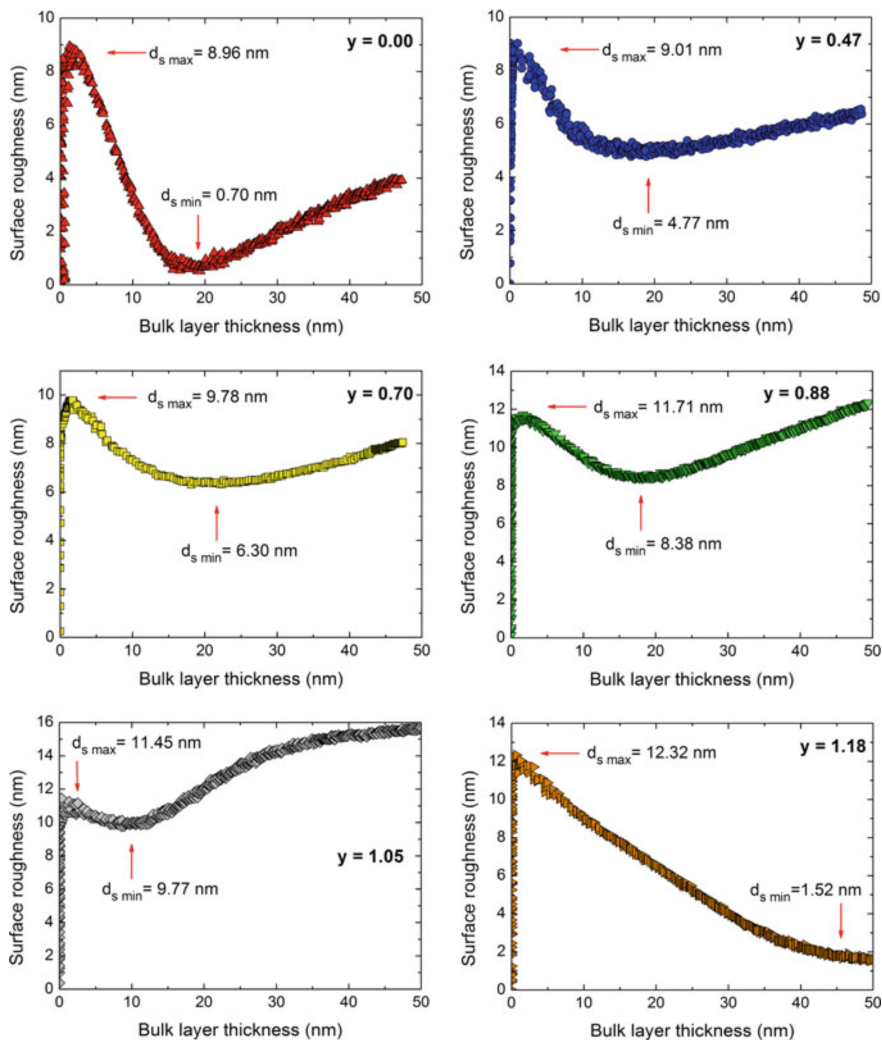

Fig. 11.11 Evolution of surface roughness layer thickness as a function of bulk layer thickness obtained in RTSE studies of CIGS films with six different Cu contents $y = 0.00$, 0.47, 0.70, 0.88, 1.05 and 1.18. For clarity, the results are shown individually for bulk layer thickness $\leq$ 50 nm, with indicated surface roughness layer thickness at the maximum value before coalescence and at the minimum value after coalescence [5]

$y = 0.00$, 0.88, and 1.18, respectively. Thus, a systematic trend in the endpoint void content is observed with a maximum near $y = 0.9$. Among the CIGS samples of the Cu series, that with $y = 0.88$ is of special interest in terms of structural evolution, as this composition is near the center of the range 0.80–0.95 yielding the highest efficiency solar cells [1].

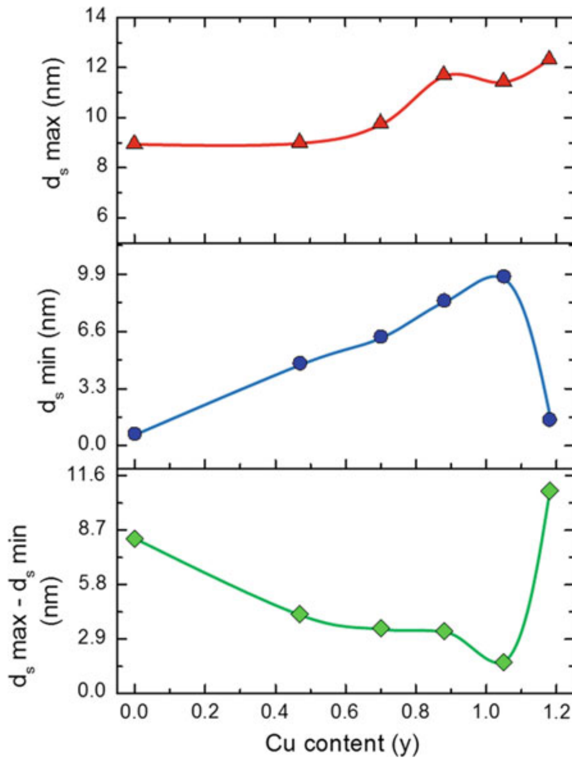

Fig. 11.12 Surface roughness layer thickness value at the maximum before coalescence, at the minimum after coalescence, and the difference between the two values from RTSE studies of CIGS depositions with Cu contents of $y = 0.00$, 0.47, 0.70, 0.88, 1.05 and 1.18 [5]

Table 11.3 Final bulk and surface roughness layer thicknesses along with the surface roughness layer void volume percentages for CIGS thin films fabricated with eight different Cu contents. In the analysis of the in-situ SE data collected at 570 °C and at room temperature, these structural parameters were fixed, enabling numerical inversion to determine the complex dielectric functions (ε_1, ε_2) at the two temperatures [5]

Cu content y	Final bulk layer thickness (nm)	Final surface roughness layer thickness (nm)	Final void vol.% in surface roughness layer
0.00	49.7 ± 0.1	4.1 ± 0.1	26.3 ± 0.2
0.47	51.2 ± 0.1	6.2 ± 0.1	32.2 ± 0.1
0.70	49.1 ± 0.1	8.1 ± 0.1	35.6 ± 0.1
0.82	54.6 ± 0.1	10.2 ± 0.1	38.5 ± 0.1
0.88	49.5 ± 0.1	12.4 ± 0.1	42.3 ± 0.1
0.96	57.3 ± 0.1	14.9 ± 0.1	47.6 ± 0.1
1.05	51.4 ± 0.1	15.7 ± 0.1	31.9 ± 0.1
1.18	58.2 ± 0.1	1.3 ± 0.1	17.7 ± 0.1

For all Cu compositions y, the thickness of the surface roughness layer initially increases with time at zero bulk layer thickness, indicating a clustering process characteristic of nucleation. The surface roughness thickness then passes through a maximum versus time at values ranging from 9.0 to 12.3 nm depending on y. The maximum in surface roughness is followed by a smoothening trend, indicating nuclei coalescence, before the surface begins to roughen again. This later stage roughening trend was observed for all deposited films except for that of $y = 1.18$ for which the surface roughness is continuously smoothening after the initial maximum surface roughness value of 12.3 nm. This trend may be explained by the presence of excess copper selenide ($Cu_{2-x}Se$) phase around the CIGS grains which results in a smoothening of the surface for the deposited film. The differences in the observed nucleation, coalescence, and growth characteristics for the deposited CIGS films with different Cu contents are indications of different characteristics of the structural evolution [13].

In general, for polycrystalline films, a direct comparison of the surface roughness layer thickness values for films of similar bulk layer thickness can provide an indication of the relative grain sizes in the films; (for this behavior in CIGS, see [14]). In fact, the surface roughness thickness is expected to increase with an increase in the average grain size for the deposited film. For the case of CIGS, it has been proposed that the grain size increases with increasing Cu content. The relationship between surface roughness and grain size is difficult to generalize over the full range of y, however, since the CIGS material undergoes various phase compositional changes which can also influence the film microstructure as the Cu content increases from $y = 0$ to $y = 1$ and above [3, 15]. For CIGS films with Cu ratios $y < 1.0$, chalcopyrite type phases, i.e. $Cu(In, Ga)Se_2$ and $Cu(In, Ga)_3Se_5$, are present depending on the Cu content of the film. For $y > 1$, it has been widely reported that the presence of the $Cu_{2-x}Se$ phase during film deposition promotes the growth of large grains in CIGS [1]. The situation in this case is complex as well because the excess Cu in CIGS films with increasing Cu ratios $y > 1.0$ will be present in the form of $Cu_{2-x}Se$ which increases in volume fraction. At sufficiently high levels, this phase is believed to form at the grain boundaries and fill in the voids present within the surface roughness layer due to its liquid-like mobility at the 570 °C deposition temperature [1, 2, 15, 16]. Thus, a very smooth surface may be possible for $y > 1.0$ in spite of a large grain size associated with the chalcopyrite phase.

Applying this general discussion for guidance, the different CIGS films fabricated in this study can be compared in terms of their surface roughness thicknesses and void contents considering bulk layer thicknesses increasing to ~50–60 nm. It is suggested that the CIGS film with $y = 0$, i.e. $(In_{0.70}Ga_{0.30})_2Se_3$, exhibits the smallest grain size among the films deposited versus y. In fact, this film with $y = 0$ may be a highly disordered phase based on the nature of the dielectric function in Fig. 11.7, which shows no clear evidence of a bandgap resonance feature. This conclusion is also supported by the observed coalescence of the initial nuclei to a surface that is almost atomically smooth as shown in Figs. 11.10 and 11.11. Such smoothening behavior has been observed for the deposition of amorphous semiconductors under high precursor surface mobility conditions optimized for

electronic performance [17]. It should be noted that $(In_{1-x}Ga_x)_2Se_3$ films measured by RTSE at similar thicknesses of ~50 nm, but at a substrate temperature of 400 °C, as is used for the first stage of three stage CIGS, also lack bandgap resonance features [18]. Again, the absence of these features is characteristic of a highly disordered semiconductor.

With the increase in Cu content for $0 < y < 1$, coalescence results in an increasingly rough surface in Fig. 11.10, suggesting crystallite development during coalescence and bulk layer growth. Consistent with this trend, a bandgap resonance feature near 1.25 eV emerges for $y = 0.47$, as shown in Figs. 11.6 and 11.7. The proposed development of crystallites with increasing y is accompanied by an increase in void content in the roughness layer, which is typical of crystallites protruding from the surface that are increasing in size. Based on these observed features, the CIGS films with $y = 0.47$ and 0.70 appear to exhibit smaller grain sizes than that of $y = 0.88$. The CIGS films with $y = 0.47$ and 0.70 are also likely to incorporate $Cu(In, Ga)_3Se_5$ as one of the secondary phases, whereas the CIGS film with $y = 0.88$ is expected be single phase crystalline chalcopyrite.

Based on reported structural studies of CIGS films with different Cu contents [1, 2, 19], the CIGS films with $y = 1.05$ and $y = 1.18$ are expected to be chalcopyrite with $Cu_{2-x}Se$ as a secondary phase. The amount of $Cu_{2-x}Se$ present in the film is proportional to the difference between the measured Cu content (i.e. $y = 1.05$ or $y = 1.18$) and that of stoichiometric CIGS ($y = 1$). This is proposed on the basis of the increasing ε_2 with y below the bandgap [12]. Among the deposited films, those with $y = 1.05$ and $y = 1.18$ exhibit the maximum and minimum surface roughness layer thicknesses, respectively, at the end of deposition with a decreasing void fraction in the roughness layer with the increase in y above $y = 1$ (see Table 11.3). Among the CIGS films studied by RTSE, the one with $y = 1.05$ has a Cu content that is closest to stoichiometric CIGS. This film has a small amount of $Cu_{2-x}Se$ which may play a role in promoting growth of large CIGS grains but with minimal effects on smoothening of the surface roughness layer. Some densification of the surface roughness layer is observed, however. On the other hand, the significant amount of $Cu_{2-x}Se$ present in the film with $y = 1.18$ has a pronounced effect on decreasing the measured thickness of the surface roughness layer while decreasing the void fraction in the layer as well. As a result, trends in the surface roughness evolution obtained from the RTSE analysis for CIGS films with $y > 1$ are found to be consistent with expectations based on previously developed understanding of the phase and structural evolution of CIGS [14].

11.3.2 CIGS at Room Temperature

After RTSE during CIGS film deposition and after in-situ SE measurement at 570 °C, the sample was cooled to room temperature. Additional in-situ SE data acquired after cooling were used to extract the dielectric functions at room temperature. The same optical model shown in Fig. 11.2 was used to analyze the room temperature SE data.

The dielectric function was obtained by numerical inversion using the previously determined values of the bulk and surface roughness layer thicknesses and the void volume fraction in the roughness layer. These values are shown in Table 11.3 and are initially assumed to remain unchanged when the films are cooled to room temperature. For the Cu series, no artifacts were found in the resulting room temperature dielectric functions when applying the endpoint (d_b, d_s, f_v) values. In addition, ε_2 decreases gradually to near zero with decreasing photon energy below the bandgap for these inversions. These observations support the validity of the assumption that the (d_b, d_s, f_v) values are unchanged after deposition and even upon cooling the sample. For samples of the Ga series, it was necessary to reheat the samples to remove Se, and then make additional small adjustments to d_b and d_s in order to eliminate artifacts from the room temperature dielectric functions [7].

Data and simulations in (ψ, Δ) from in-situ SE measurements performed at room temperature are shown in Fig. 11.13 for the completed CIGS films with different Cu contents. The inverted dielectric functions at room temperature that correspond to these SE data and simulations are shown individually for the eight films with Cu contents of $y = 0.00$, 0.47, 0.70, 0.82, 0.88, 0.96, 1.05, and 1.18 for clarity in Fig. 11.14. As noted earlier, if the numerical inversion is successfully applied, then the data and simulations in Fig. 11.13 should closely coincide. Again, any observed deviations are attributed to termination errors in the numerical inversion routine. For comparison, the dielectric functions are shown together in Fig. 11.15.

The motivation of this study is to represent these room temperature complex dielectric functions for CIGS as analytical functions of Cu content y using a sum of mathematical oscillators describing the critical point (CP) features [20]. These features represent the lowest energy (bandgap) and higher energy resonances associated with interband transitions within the material. The CP energies can be obtained by applying an expression that is intended to correctly describe the line-shapes of the transitions at the band structure CPs [9, 21, 22]. In order to enhance the sensitivity to the CP features and resolve weak CPs, the second derivatives of the dielectric functions with respect to photon energy were taken first. The spectra in $d^2\varepsilon/dE^2$ were calculated numerically from the inverted dielectric functions and then fitted by least-squares regression analysis to extract the CP energies. An example is shown in Fig. 11.16 for the CIGS sample with composition $y = 0.88$ and $x = 0.30$. Here, the numerically calculated spectra in the second derivative of the dielectric function near the bandgap are shown for this sample along with the best fit of these spectra. Prior to calculating the second derivative spectra, however, it was necessary to smooth the data; for this purpose, a fast Fourier transform filter was applied.

The second derivative fitting method shown in Fig. 11.16 is based on the assumption that in the neighborhood of the nth CP, the complex dielectric function can be represented by the following equation [9]:

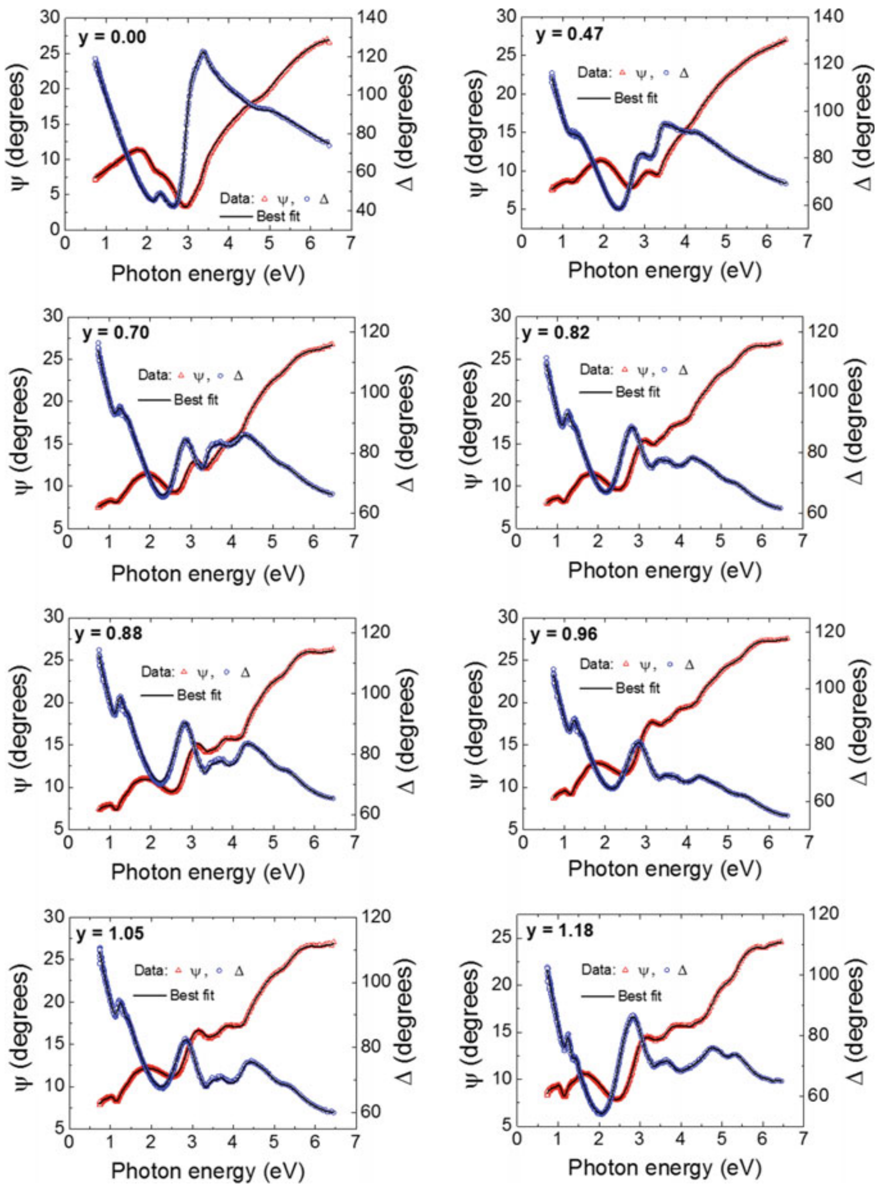

Fig. 11.13 Ellipsometry angles ψ (triangles) and Δ (circles) plotted as functions of photon energy from measurements performed in vacuum at room temperature for CIGS films with Cu contents of y = 0.00, 0.47, 0.70, 0.82, 0.88, 0.96, 1.05, and 1.18. Simulations of the measurements are also included (lines). The inverted dielectric functions that correspond to these simulations are shown in Fig. 11.14 [5]

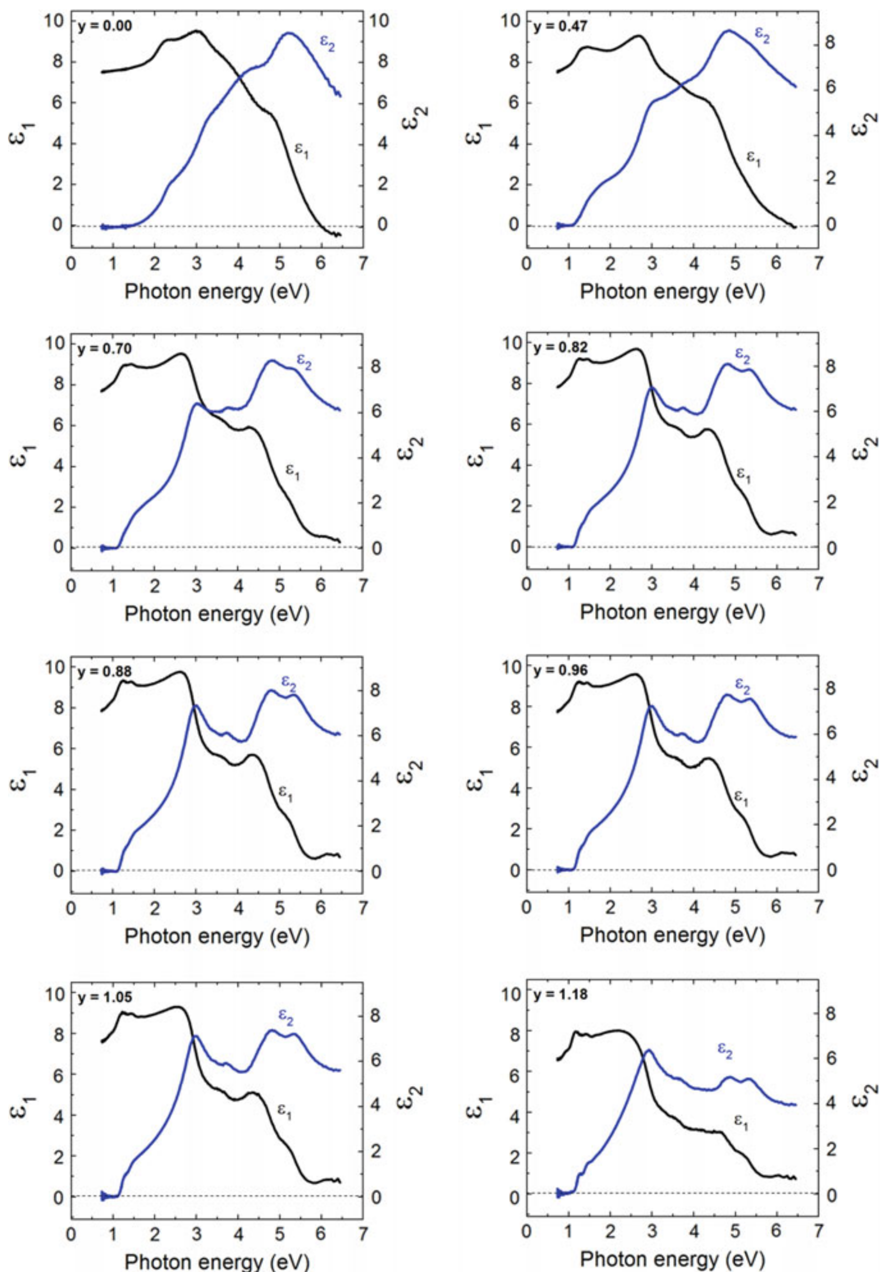

Fig. 11.14 Complex dielectric functions (ε_1, ε_2) at room temperature for CIGS films with Cu ratios y of 0.00, 0.47, 0.70, 0.82, 0.88, 0.96, 1.05, and 1.18. The results were obtained by numerical inversion of in-situ SE data using the bulk and surface roughness layer thicknesses and the void volume percentage values given in Table 11.3 [5]

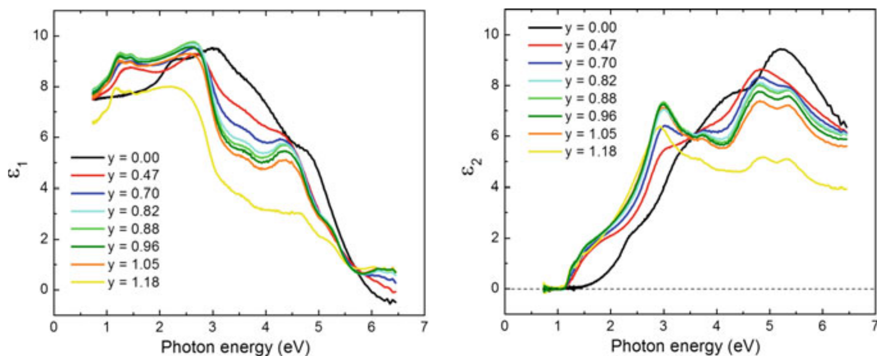

Fig. 11.15 Real and imaginary parts of the dielectric functions, ε_1 (left) and ε_2 (right), at room temperature obtained for CIGS films with Cu compositions y of 0.00, 0.47, 0.70, 0.82, 0.88, 0.96, 1.05, and 1.18. These spectra were obtained from in-situ SE data applying numerical inversion using the bulk and surface roughness layer thicknesses and the void volume percentages in Table 11.3. For clarity, the spectra are shown individually in Fig. 11.14 [5]

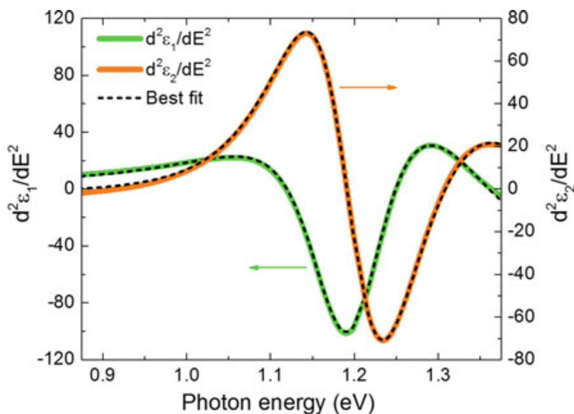

Fig. 11.16 A fit to the second derivative of the real and imaginary parts of the dielectric function at room temperature applying (11.1) in the neighborhood of the critical point E_0(A, B) for the CIGS sample with composition $y = 0.88$ and $x = 0.30$ [5]

$$\varepsilon(E) = A_n(\Gamma_n/2)^{\mu_n}\, e^{i\phi_n}\, [E_n - E - i(\Gamma_n/2)]^{-\mu_n} \quad (11.1)$$

where A_n is the amplitude, E_n the CP bandgap, Γ_n the broadening parameter, ϕ_n the phase angle, and μ_n is the exponent. Equation (11.1) is twice differentiated and the resulting equation is fitted to extract these five parameters. In this analysis, the CPs E_0(A) and E_0(B) were not resolvable and were treated as a single CP represented by the notation E_0(A, B). For the eight dielectric function spectra shown in Figs. 11.14 and 11.15, the room temperature CP energies obtained in the best fit are listed in Table 11.4. The positions of six CPs, designated E_0(A, B), E_0(C), E_1(A), E_1(B), E_2(A), and E_3 were identified for the CIGS spectra with Cu contents y in the range of 0.47–1.18. For the CIGS material with $y = 0$, which corresponds to

$(In_{0.70}Ga_{0.30})_2Se_3$, only the E_0(A, B) CP was analyzed since higher energy features could not be clearly identified for a film of the deposited thickness. It should also be noted that, in a comparison of Tables 11.2 and 11.4, E_0(C) and the weak CP E_1(B) could not be resolved at 570 °C.

The lowest CP energy E_0(A, B), which defines the bandgap energy of the material, is plotted versus the Cu content y in Fig. 11.17 for the range $0.47 \leq y \leq 1.18$. These room temperature bandgap data were fitted to an equation of the form:

$$E_g(y) = a + by + cy(y - 1), \tag{11.2}$$

and the following result was obtained [5]:

$$E_g(y) = [1.578 - 0.394y + 0.307y(y - 1)]\,\text{eV}; \quad 0.47 \leq y \leq 1.18. \tag{11.3}$$

Due to the large difference in bandgap energy between $E_g(y = 0.00)$ and $E_g(y = 0.47)$ and the different overall shape of the dielectric function for $y = 0$, $E_g(y = 0.00)$ was excluded from the fit using (11.2). It can be observed from these results that the addition of Cu over the range $0.47 \leq y \leq 1.18$ is associated with a continuous decrease in the bandgap of CIGS.

In order to estimate the bandgap of CIGS at 570 °C for comparison with the room temperature results, the in-situ SE spectra acquired at 570 °C after deposition were fitted over the photon energy range from 0.75 to 3 eV for the CIGS film with $y = 0$ and 0.75–2 eV for films with $y > 0$. A sum of two CP oscillators in the form of (11.1) was used to simulate the bandgap transition and the next highest energy transition nearby, and all fitting parameters were allowed to vary. The resonance energy of the lowest CP, i.e. E_0(A, B), defines the bandgap. The best fit bandgaps both at the deposition temperature and at room temperature are listed in Table 11.5 for CIGS films with different Cu contents; also shown are the estimated temperature coefficients of the bandgap. These coefficients were calculated under the assumption of a linear dependence of the bandgap on temperature from 20 to 570 °C. Results for the 570 °C bandgap as a function of Cu content y for $y \geq 0.47$ are shown in Fig. 11.18 and compared to those for the room temperature bandgap deduced from the CP analysis. The 570 °C bandgap data for Cu contents $y \geq 0.47$ were fitted to (11.2) and the following result was obtained [5]:

$$E_g(y) = [1.212 - 0.109y + 0.028y(y - 1)]\,\text{eV}; \quad 0.47 \leq y \leq 1.18. \tag{11.4}$$

The energy of the second CP oscillator resulted in a broad background without a clear trend due to the significant broadening that occurs at the deposition temperature.

The room temperature dielectric function spectra of Figs. 11.14 and 11.15 for the CIGS films with Cu contents of $y = 0.47$, 0.70, 0.82, 0.88, 0.96 and 1.05 were parameterized using an oscillator model. The resulting oscillator parameters of the dielectric function spectra were then expressed as polynomial equations in y [5, 20]. This method yields mathematical expressions for the complex dielectric function

Table 11.4 Resonance energies at room temperature for the six critical points E_0(A, B), E_0(C), E_1(A), E_1(B), E_2(A), and E_3 obtained from CP analyses of CIGS dielectric functions deduced from in-situ SE measurements. The dielectric functions were obtained at room temperature for CIGS samples with eight different Cu contents and were twice differentiated as illustrated in Fig. 11.16 to obtain these results [5]

Composition *y*	CP_1 E_0(A, B) (eV)	CP_2 E_0(C) (eV)	CP_3 E_1(A) (eV)	CP_4 E_1(B) (eV)	CP_5 E_2(A) (eV)	CP_6 E_3 (eV)
0.00	2.238 ± 0.09	–	–	–	–	–
0.47	1.315 ± 0.008	1.505 ± 0.019	2.802 ± 0.014	3.747 ± 0.019	4.851 ± 0.018	5.370 ± 0.023
0.70	1.243 ± 0.006	1.454 ± 0.016	2.889 ± 0.010	3.753 ± 0.014	4.837 ± 0.015	5.374 ± 0.017
0.82	1.210 ± 0.006	1.430 ± 0.013	2.923 ± 0.009	3.756 ± 0.012	4.808 ± 0.014	5.363 ± 0.015
0.88	1.196 ± 0.005	1.420 ± 0.010	2.938 ± 0.008	3.757 ± 0.013	4.795 ± 0.014	5.358 ± 0.012
0.96	1.191 ± 0.006	1.416 ± 0.012	2.931 ± 0.008	3.750 ± 0.013	4.806 ± 0.015	5.351 ± 0.014
1.05	1.185 ± 0.007	1.409 ± 0.009	2.921 ± 0.006	3.740 ± 0.013	4.823 ± 0.014	5.341 ± 0.010
1.18	1.179 ± 0.008	1.388 ± 0.009	2.914 ± 0.007	3.712 ± 0.011	4.844 ± 0.016	5.331 ± 0.009

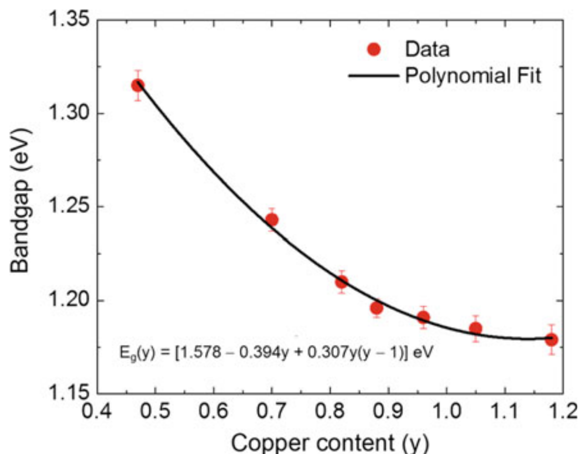

Fig. 11.17 A plot of the bandgap at room temperature as a function of Cu content y for CIGS films with Cu contents in the range of $0.47 \leq y \leq 1.18$. The bandgaps were obtained from CP analyses of the room temperature dielectric functions as shown in Fig. 11.16 [5]

Table 11.5 Bandgaps at room temperature deduced from CP analysis of the dielectric functions of CIGS films of different Cu contents y from Table 11.4. Also provided for comparison are the bandgaps at 570 °C deduced from fits to the dielectric functions obtained from in-situ SE data by inversion. Temperature coefficients of the bandgap for CIGS films of different Cu contents y are determined from these results assuming linear temperature dependences of the bandgaps. Dielectric functions at high temperature were unavailable for samples with $y = 0.82$ and 0.96 [5]

Cu content (y)	CP_1 E_0(A, B) (eV) at 20 °C	CP_1 E_0(A, B) (eV) at 570 °C	Temp. coefficient (eV/°C $\times$ 10^{-4})
0.00	2.238 ± 0.09	1.877 ± 0.023	−6.564
0.47	1.315 ± 0.008	1.152 ± 0.018	−2.964
0.70	1.243 ± 0.006	1.135 ± 0.013	−1.964
0.82	1.210 ± 0.006	N/A	N/A
0.88	1.196 ± 0.005	1.110 ± 0.009	−1.564
0.96	1.191 ± 0.006	N/A	N/A
1.05	1.185 ± 0.007	1.102 ± 0.009	−1.509
1.18	1.179 ± 0.008	1.089 ± 0.011	−1.709

spectra of CIGS for any given y value with $x = 0.30$. A parameterization of this type can be challenging if the entire composition and photon energy ranges are used. In fact, for films that are rough, the higher energy photons are absorbed solely within the roughness layer, and the microstructural variations due to the changes in roughness mask the variations that may occur in the dielectric function. As a result, the highest energy region can be excluded, implying a less challenging parameterization, with a minimal loss of useful information. In this study, the room temperature dielectric function spectra over the photon energy range from 0.75 to 3.8 eV were parameterized for CIGS with Cu content in the range of $0.47 \leq y \leq 1.05$. The optical model applies four CP oscillators, representing the CPs E_0(A, B), E_0(C), E_1(A), and E_1(B), along with one Tauc gap modified Lorentz (T-L) oscillator,

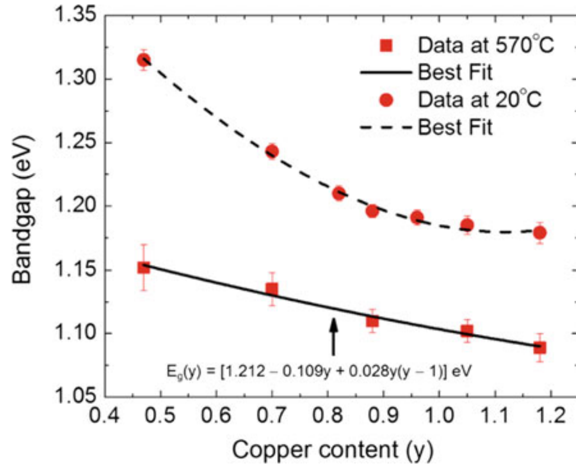

Fig. 11.18 A plot of the bandgap at 570 °C as a function of Cu content *y* for CIGS films measured with Cu contents in the range of $0.47 \le y \le 1.18$ (squares). The bandgaps were obtained from fits of in-situ SE spectra acquired at the end of deposition. Plotted for comparison are the room temperature bandgaps deduced from CP analyses of dielectric functions obtained by in-situ SE after cooling the sample (circles) [5]

the latter representing a broad background dielectric response between the CPs [5–7]. The T-L oscillator may be attributed to interband transitions that occur between bands that are not parallel, in contrast to the higher energy CPs which describe parallel-band transitions at van Hove singularities. In the parameterization, the extracted CP energies shown in Table 11.4 were used as fixed parameters in order to stabilize the regression analysis. Presented in Fig. 11.19 are the plots of these fixed CP energies as functions of *y* used in the parameterization of the dielectric functions for the CIGS compositions $y = 0.47$, 0.70, 0.82, 0.88, 0.96, and 1.05. These plots also include the higher energy CPs E_2(A) and E_3, which are not used in the parameterization. All such CPs are fitted with polynomial expressions that enable determination of all six energies at room temperature given the value of *y* for the CIGS sample.

The discussion now focuses on the details of the parameterization of the CIGS dielectric function versus Cu content *y* using both CP and modified Lorentz oscillators. The CP oscillator was presented in (11.1). The Tauc gap modified Lorentz (T-L) oscillator is given by [9]:

$$\varepsilon_2(E) = \begin{cases} \dfrac{A_{\mathrm{TL}} E_{\mathrm{TL}} \Gamma_{\mathrm{TL}}}{\left[(E_{\mathrm{TL}}^2 - E^2)^2 + \Gamma_{\mathrm{TL}}^2 E^2\right]} \cdot \dfrac{(E - E_g)^2}{E} & E > E_g \\ 0 & E \le E_g \end{cases}; \tag{11.5a}$$

$$\varepsilon_1(E) = \varepsilon_{1,\infty} + \frac{2}{\pi} \mathrm{P} \int_{E_g}^{\infty} \frac{\xi\, \varepsilon_2(\xi)}{\xi^2 - E^2} \mathrm{d}\xi, \tag{11.5b}$$

and incorporates four energy independent parameters including the Lorentz oscillator amplitude (A_{TL}), energy (E_{TL}), and broadening (Γ_{TL}), and the Tauc bandgap (E_g). As indicated by (11.5b), $\varepsilon_1(E)$ is determined through a Kramers-Kronig

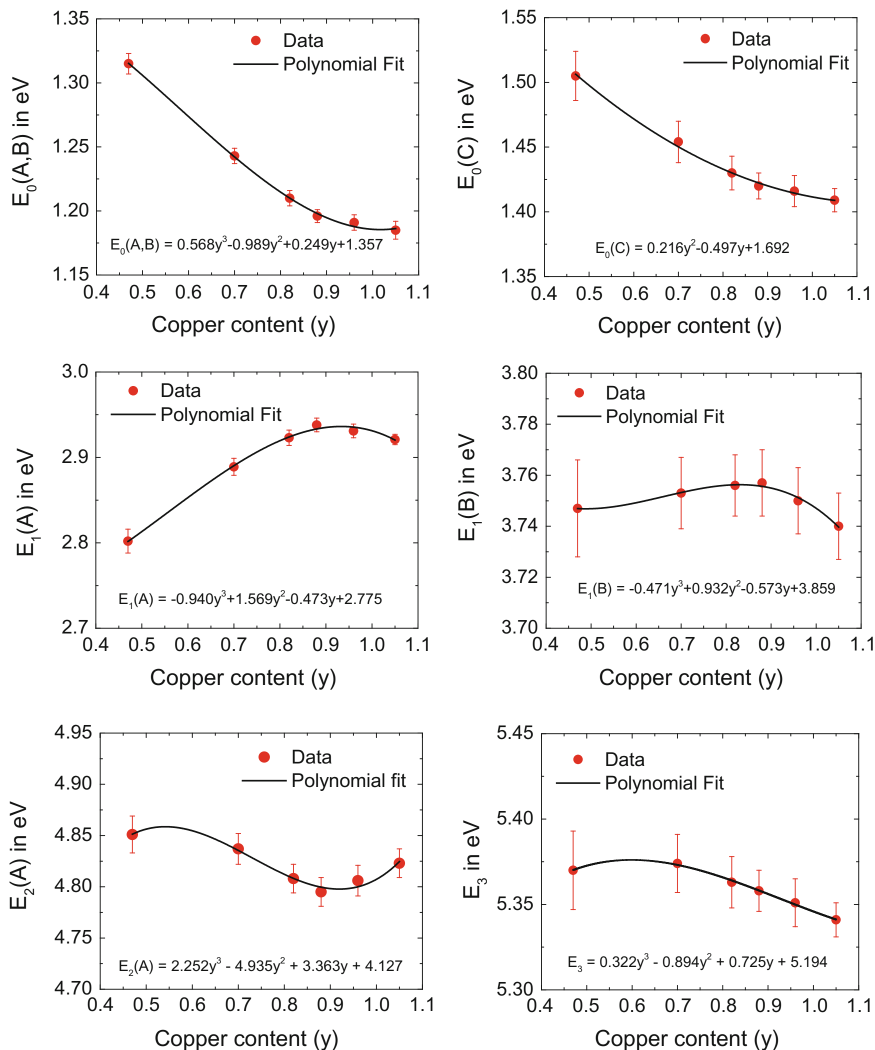

Fig. 11.19 Plots of critical point (CP) resonance energies of CIGS at room temperature as functions of Cu content y (circles) for six CPs: E_0(A, B), E_0(C), E_1(A), E_1(B), E_2(A), and E_3 along with polynomial fits (lines) with the polynomial expressions provided in units of eV. The resonance energies were obtained from CP analysis of in-situ SE spectra acquired at room temperature for CIGS films with six different Cu contents y = 0.47, 0.70, 0.82, 0.88, 0.96, and 1.05 [5]

integral which can be evaluated analytically [9]. Some CP and T-L oscillator parameters were allowed to vary in the parameterization versus y whereas others were fixed. As noted in the previous paragraph, the CP energies were fixed to the values deduced from the room temperature CP analysis. As a result, the Tauc gap value E_g for each dielectric function was coupled to the fixed value of E_0(A, B) to

ensure that no absorption is generated by the Lorentz oscillator below the bandgap. A constant contribution to the real part of the dielectric function, indicated as $\varepsilon_{1,\infty}$ in (11.5b), was varied during the fitting. The dielectric function of CIGS material with $y = 0.88$ and $x = 0.30$ was fitted first and the deduced oscillator parameter values for Γ_{CP1}, μ_{CP1}, Γ_{CP4}, ϕ_{CP4}, μ_{CP4}, and E_{TL} were then fixed for all samples at the values obtained in that analysis.

Fits of the room temperature dielectric functions of the six CIGS materials with $y = 0.47, 0.70, 0.82, 0.88, 0.96$, and 1.05 are shown in Fig. 11.20, and the values of the free and fixed parameters for the four CP oscillators are provided in Table 11.6. The parameter values of the Tauc gap modified Lorentz oscillator along with the constant term $\varepsilon_{1,\infty}$ are listed in Table 11.7. Figure 11.21 shows the CP oscillator parameters that were allowed to vary in the fitting procedure plotted as functions of CIGS Cu content y, along with best polynomial fits. Plots of the free parameters of the modified Lorentz oscillator and the parameter $\varepsilon_{1,\infty}$ as functions of y along with their polynomial fits are shown in Fig. 11.22 and Fig. 11.23, respectively. The deduced polynomial expressions for the CP and modified Lorentz oscillator parameters, and $\varepsilon_{1,\infty}$ in terms of Cu content y of the CIGS material are summarized in Table 11.8. Because the coefficients in Table 11.8 are given in terms of $\Delta y = y - 0.90$, the zero-order polynomial coefficient $a_{0i}(0.90, 0.30)$ for the ith parameter is the value appropriate for the composition $y = 0.90$ and $x = 0.30$. The obtained expressions are functions of only one variable (y), and enable generation of the CIGS dielectric function for any specified Cu content in the range of $0.47 \leq y \leq 1.05$.

Thus, the variable parameters in Tables 11.4, 11.6, and 11.7 are fitted using polynomial expressions of the form

$$P_i(y, 0.30) = \sum_{n=1}^{N_i} a_{ni}(y - 0.90)^n + a_{0i}(0.90, 0.30). \tag{11.6}$$

Here $P_i(y, 0.30)$ describes the ith parameter sought in this study as a function of the Cu content y for $x = 0.30$, with a_{ni} serving as the polynomial coefficients. In addition, N_i is the order of the polynomial required to fit the parameter $P_i(y, 0.30)$ as a function of y. Finally, $a_{0i}(0.90, 0.30)$ is the value of the same parameter, for the hypothetical sample of composition $y = 0.90$ and $x = 0.30$, which is of greatest interest.

The parameterization results for the dielectric functions of CIGS materials in terms of the Cu content y shown in Table 11.8 can be improved further by replacing the imaginary part of each generated CIGS dielectric function below the bandgap $E_0(\mathrm{A, B})$ with an Urbach tail [9]. This is done to ensure that the imaginary parts of the generated CIGS dielectric functions for different Cu contents approach zero in the sub-bandgap region. An Urbach tail is an absorption tail whereby $\alpha(E)$ decreases exponentially with decreasing photon energy E below $E_0(\mathrm{A, B})$. The Urbach tail parameterization can be described by:

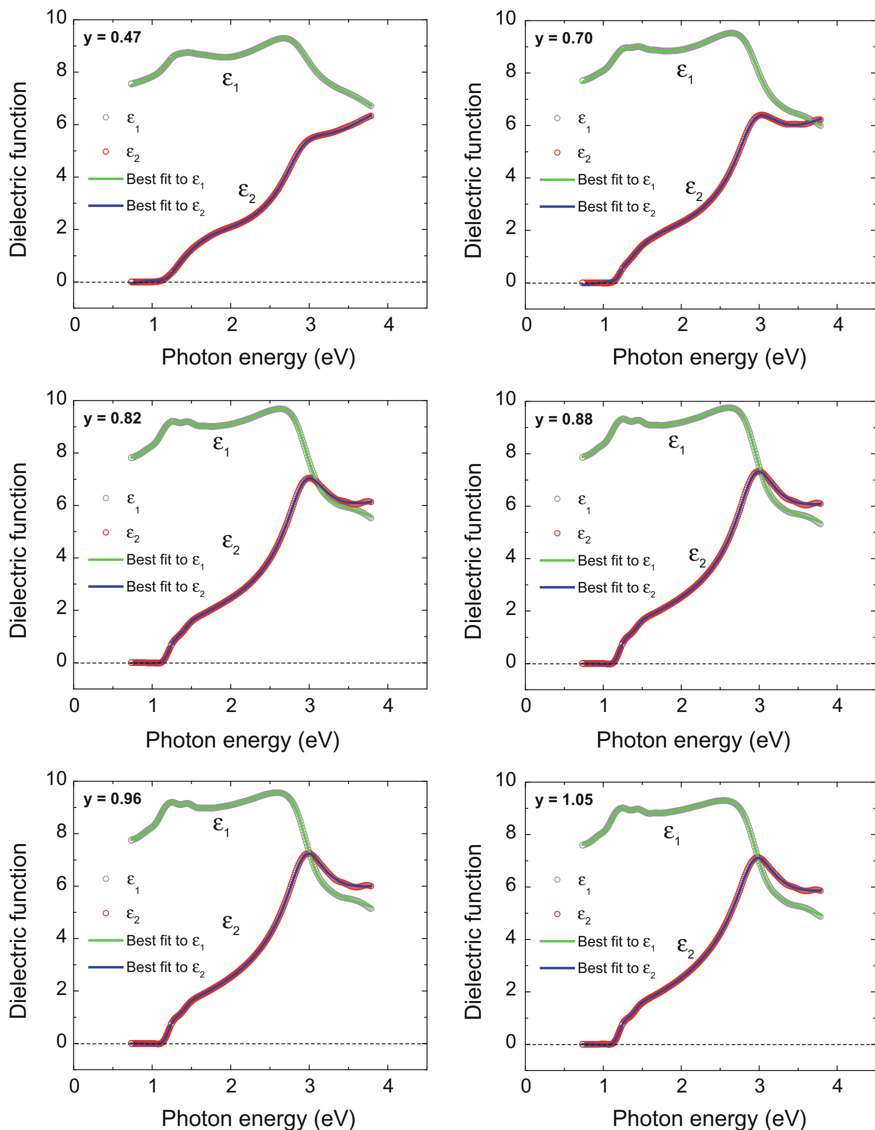

Fig. 11.20 Fits to room temperature dielectric functions obtained from in-situ measurements of CIGS films with six different Cu contents $y = 0.47, 0.70, 0.82, 0.88, 0.96$, and 1.05. The dielectric function model is given as a sum of four critical point oscillators and one modified Lorentz oscillator serving as a background [5]

Table 11.6 Parameter values for the critical points obtained from fits to room temperature dielectric functions over the spectral range from 0.75 to 3.80 eV for CIGS films with Cu contents y = 0.47, 0.70, 0.82, 0.88, 0.96, and 1.05. The listed values without confidence limits were fixed in the fitting procedure. Resonance energies E_0(A, B), E_0(C), E_1(A), and E_1(B) were fixed at values obtained from CP analysis [5]

Oscillator	y	A_n	E_n (eV)	Γ_n (eV)	ϕ_n (degree)	μ_n
CP_1 E_0(A, B)	0.47	0.461 ± 0.057	1.315	0.077	0.31 ± 1.19	0.302
	0.70	0.955 ± 0.042	1.243	0.077	−19.72 ± 0.87	0.302
	0.82	1.185 ± 0.038	1.210	0.077	−29.07 ± 0.88	0.302
	0.88	1.284 ± 0.033	1.196	0.077	−33.07 ± 0.88	0.302
	0.96	1.267 ± 0.036	1.191	0.077	−31.32 ± 0.89	0.302
	1.05	1.242 ± 0.035	1.185	0.077	−28.71 ± 0.91	0.302
CP_2 E_0(C)	0.47	2.454 ± 0.078	1.505	0.563 ± 0.054	−3.63 ± 1.08	0.365 ± 0.076
	0.70	2.135 ± 0.049	1.454	0.453 ± 0.047	−0.03 ± 0.91	0.319 ± 0.052
	0.82	1.940 ± 0.047	1.430	0.450 ± 0.044	1.66 ± 0.82	0.297 ± 0.046
	0.88	1.856 ± 0.045	1.420	0.449 ± 0.042	2.38 ± 0.75	0.288 ± 0.044
	0.96	1.875 ± 0.046	1.416	0.405 ± 0.043	0.56 ± 0.73	0.285 ± 0.045
	1.05	1.903 ± 0.046	1.409	0.340 ± 0.040	−2.64 ± 0.69	0.281 ± 0.046
CP_3 E_1(A)	0.47	1.852 ± 0.145	2.802	0.605 ± 0.052	−34.34 ± 2.04	0.723 ± 0.016
	0.70	2.670 ± 0.136	2.889	0.617 ± 0.048	−15.59 ± 1.32	0.807 ± 0.015
	0.82	3.225 ± 0.132	2.923	0.623 ± 0.043	−5.34 ± 1.28	0.855 ± 0.013
	0.88	3.463 ± 0.127	2.938	0.625 ± 0.034	−0.95 ± 1.19	0.876 ± 0.011
	0.96	3.407 ± 0.128	2.931	0.627 ± 0.041	−0.17 ± 1.25	0.888 ± 0.012
	1.05	3.072 ± 0.129	2.921	0.630 ± 0.039	1.01 ± 1.21	0.906 ± 0.013
CP_4 E_1(B)	0.47	0.162 ± 0.018	3.747	0.516	159.21	3.000
	0.70	0.120 ± 0.014	3.753	0.516	159.21	3.000
	0.82	0.101 ± 0.015	3.756	0.516	159.21	3.000
	0.88	0.093 ± 0.012	3.757	0.516	159.21	3.000
	0.96	0.088 ± 0.014	3.750	0.516	159.21	3.000
	1.05	0.080 ± 0.013	3.740	0.516	159.21	3.000

$$\alpha(E) = \alpha_0 \exp[(E - E_t)/E_u] \tag{11.7}$$

for $E < E_t$, where E_u is the Urbach absorption tail slope and E_t is the transition energy below which the behavior is observed. Equation (11.7) can be expressed in terms of ε_2 approximately as:

$$\varepsilon_2(E) = \varepsilon_2(E_t) \exp[(E - E_t)/E_u], \tag{11.8}$$

an equation which ignores algebraic prefactors of energy based on the assumption that the energy range of the Urbach tail is narrow. Although $\varepsilon_2(E)$ is modified according to (11.8) in the sub-bandgap region, ε_1 is assumed to be unaffected due to

Table 11.7 Values of Tauc gap modified Lorentz oscillator parameters obtained from fits to room temperature CIGS dielectric functions with Cu contents y = 0.47, 0.70, 0.82, 0.88, 0.96, and 1.05 over the spectral range of 0.75 to 3.80 eV along with the photon-energy-independent parameter $\varepsilon_{1,\infty}$. The listed values without confidence limits were fixed during fitting. The values of E_g were fixed to the resonance energies E_0(A, B) deduced from CP analysis. This oscillator serves to simulate the broad background in the dielectric function between critical points [5]

y	A_{TL} (eV)	E_{TL} (eV)	Γ_{TL}(eV)	E_g (eV)	$\varepsilon_{1,\infty}$
0.47	86.16 ± 2.54	6.234	9.325 ± 0.321	1.315	0.104 ± 0.029
0.70	80.50 ± 2.43	6.234	10.064 ± 0.276	1.243	0.403 ± 0.026
0.82	79.29 ± 2.45	6.234	10.408 ± 0.272	1.210	0.542 ± 0.024
0.88	78.78 ± 2.39	6.234	10.556 ± 0.265	1.196	0.602 ± 0.022
0.96	80.63 ± 2.38	6.234	10.922 ± 0.273	1.191	0.535 ± 0.025
1.05	83.42 ± 2.47	6.234	11.471 ± 0.277	1.185	0.377 ± 0.027

its weak Kramers-Kronig integral contribution. The value of $\varepsilon_2(E_t)$ in (11.8) is chosen for continuity of $\varepsilon_2(E)$ at the transition energy E_t, and the value of E_u can be chosen such that $d\varepsilon_2/dE$ is continuous at E_t. Thus, theoretically the Urbach tail can be incorporated into the dielectric function model without the addition of free parameters [23].

The Urbach transition energy E_t was set equal to the resonance energy for the first CP oscillator E_0(A,B) from Table 11.8. Then $\varepsilon_2(E_t)$ and E_u can be determined uniquely from the continuity requirement of ε_2 and $d\varepsilon_2/dE$ at the photon energy E_t according to

$$\varepsilon_2(E = E_t) = \varepsilon_2[E_0(\mathrm{A,B})], \tag{11.9}$$

$$\left.\frac{d\varepsilon_2}{dE}\right|_{E=E_0(\mathrm{A,B})} \approx \frac{2A_1\mu_1}{\Gamma_1}\sin\left[\phi_1 + (\pi/2)(\mu_1+1)\right], \tag{11.10}$$

where the subscript “1” designates the first or bandgap CP whose contribution to $d\varepsilon_2/dE$ at $E_t = E_0$(A, B) is dominant compared to higher energy CPs and the smoothly varying T-L term. For this deposition series in y, only the Urbach tail in the data was fitted, and $\varepsilon_2(E_t)$ was defined by the ε_2 parameterization. This approach yields the following relationship between E_u and y:

$$E_u(y) = \left[0.335y^2 - 0.680y + 0.373\right]\mathrm{eV}, \tag{11.11}$$

which exhibits a minimum at y = 1.01, very close to the stoichiometric composition—in accord with expectations. A plot of E_u as a function of y is shown in Fig. 11.24, and analytically defined ε_2 spectra incorporating the Urbach tail are shown in Fig. 11.25 for samples deposited in this study with six different Cu contents 0.47 $\leq y \leq$ 1.05.

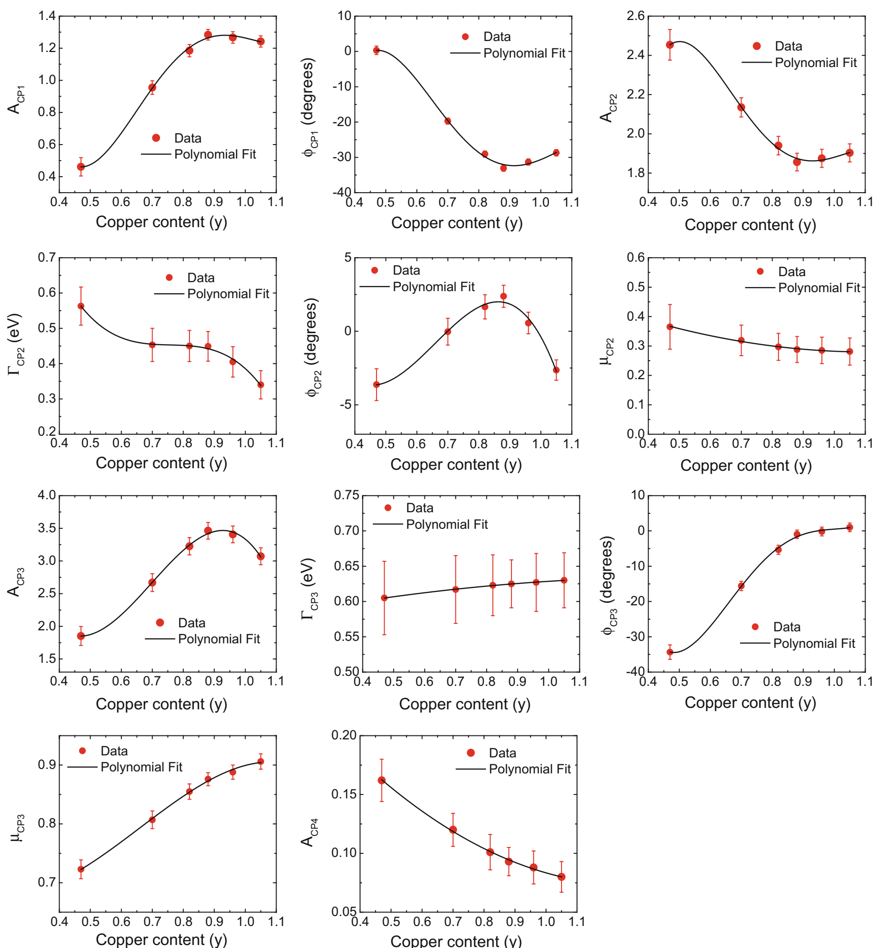

Fig. 11.21 Plots of the CP oscillator free parameters that were allowed to vary in the fitting procedure for CIGS dielectric functions versus Cu content y (circles), where $0.47 \leq y \leq 1.05$, along with best polynomial fits (lines). The oscillators CP_1, CP_2, CP_3, and CP_4 represent the E_0(A, B), E_0(C), E_1(A), and E_1(B) transitions, respectively. For these transitions, the resonance energies were fixed to the values obtained from CP analysis. The values of the fixed and varied CP parameters are shown in Table 11.6, and the equations of the polynomial fits are shown in Table 11.8 [5]

The CIGS sample with composition $y = 1.18$ was excluded from the parameterization of the CIGS dielectric functions versus Cu content since this highest Cu composition failed to follow the clear trends set by the lower compositions. This dielectric function was parameterized separately, however, using the same procedure with the same number of oscillators. First, the resonance energies E_0(A, B),

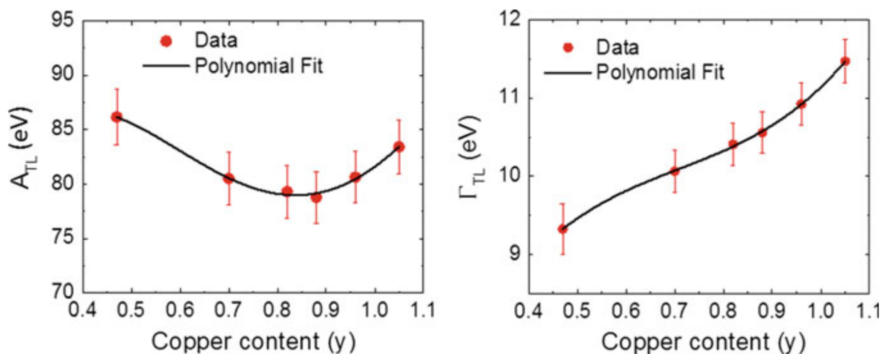

Fig. 11.22 Plots of the amplitude and broadening parameters of the Tauc gap modified Lorentz oscillator as functions of y (circles), where $0.47 \leq y \leq 1.05$, along with the best polynomial fits (lines). The values of the fixed and variable parameters are shown in Table 11.7, and the equations of the polynomial fits are shown in Table 11.8 [5]

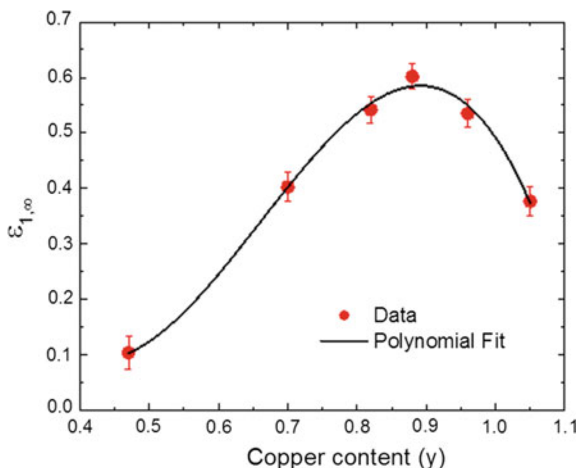

Fig. 11.23 Plot of $\varepsilon_{1,\infty}$ as a function of y (circles) along with the best fit polynomial (line). The values of $\varepsilon_{1,\infty}$ are shown in Table 11.7, and the equation of the corresponding polynomial fit is shown in Table 11.8 [5]

E_0(C), E_1(A), and E_1(B) were fixed at values obtained from the CP analysis, and the T-L gap was fixed at the value of E_0(A, B). In addition, Γ_{CP1}, μ_{CP1}, μ_{CP4}, and the resonance energy E_{TL} were fixed at 0.077 eV, 0.302, 3.00, and 6.234 eV, respectively, which are either the same or very close to the values used in the parameterization over the range $0.47 \leq y \leq 1.05$. In contrast to the lower y parameterization, $\varepsilon_{1,\infty}$ was fixed at unity for $y = 1.18$. The fitting results are shown in Fig. 11.26, and the oscillator parameters are summarized in Table 11.9.

Table 11.8 Equations for the parameters of the critical points, the Tauc gap modified Lorentz oscillator, and $\varepsilon_{1,\infty}$ in terms of the difference Δy in Cu content from $y = 0.90$, i.e. $\Delta y = y - 0.90$. Because the coefficients are given in terms of Δy, the zero-order coefficient of the ith parameter $a_{0i}(0.90,\ 0.30)$ is the value appropriate for the composition of greatest interest $y = 0.90$ and $x = 0.30$

Oscillator	Parameter	Expression in terms of y
CP_1 E_0(A, B)	A	$31.03(\Delta y)^4 + 7.838(\Delta y)^3 - 5.893(\Delta y)^2 + 0.379(\Delta y) + 1.280$
	E (eV)	$0.568(\Delta y)^3 + 0.5446(\Delta y)^2 - 0.1510(\Delta y) + 1.1941$
	Γ (eV)	0.077
	ϕ (degree)	$-1240.9(\Delta y)^4 - 253.04(\Delta y)^3 + 279.67(\Delta y)^2 - 7.37(\Delta y) - 32.28$
	μ	0.302
CP_2 E_0(C)	A	$-29.63(\Delta y)^4 - 6.384(\Delta y)^3 + 5.232(\Delta y)^2 - 0.307(\Delta y) + 1.858$
	E (eV)	$0.216(\Delta y)^2 - 0.1082(\Delta y) + 1.4197$
	Γ (eV)	$-4.333(\Delta y)^3 - 1.8481(\Delta y)^2 - 0.2844(\Delta y) + 0.4373$
	ϕ (degree)	$-167.84(\Delta y)^3 - 121.460(\Delta y)^2 - 8.423(\Delta y) + 1.845$
	μ	$0.212(\Delta y)^2 - 0.0904(\Delta y) + 0.2889$
CP_3 E_1(A)	A	$-33.12(\Delta y)^3 - 20.144(\Delta y)^2 + 1.172(\Delta y) + 3.447$
	E (eV)	$-0.94(\Delta y)^3 - 0.969(\Delta y)^2 + 0.067(\Delta y) + 2.935$
	Γ (eV)	$-0.032(\Delta y)^2 + 0.0344(\Delta y) + 0.6259$
	ϕ (degree)	$1351.7(\Delta y)^4 + 378.12(\Delta y)^3 - 199.04(\Delta y)^2 + 29.56(\Delta y) - 0.979$
	μ	$-0.746(\Delta y)^3 - 0.5382(\Delta y)^2 + 0.2690(\Delta y) + 0.8782$
CP_4 E_1(B)	A	$0.139(\Delta y)^2 - 0.1038(\Delta y) + 0.0920$
	E (eV)	$-0.471(\Delta y)^3 - 0.3397(\Delta y)^2 - 0.0399(\Delta y) + 3.7549$
	Γ (eV)	0.516
	ϕ (degree)	159.21
	μ	3.000
Background T-L	A (eV)	$-151.8(\Delta y)^4 + 17.52(\Delta y)^3 + 101.15(\Delta y)^2 + 12.45(\Delta y) + 79.44$
	E (eV)	6.234
	Γ (eV)	$13.98(\Delta y)^3 + 7.976(\Delta y)^2 + 3.935(\Delta y) + 10.653$
	E_g (eV)	$0.568(\Delta y)^3 + 0.5446(\Delta y)^2 - 0.1510(\Delta y) + 1.1941$
	$\varepsilon_{1,\infty}$	$-9.885(\Delta y)^3 - 7.1275(\Delta y)^2 - 0.1200(\Delta y) + 0.5842$
	E_u (eV)	$0.335(\Delta y)^2 - 0.0770(\Delta y) + 0.0324$

11.4 Results: Effect of Ga Content

It is also desirable to express the complex dielectric function spectra of CIGS analytically for any given Ga content x as well [7, 20] In the work presented here, the available dielectric function spectra at room temperature for the samples with $y = 0.90 \pm 0.03$ and $x = 0.0, 0.12, 0.26, 0.30, 0.37$, and 0.48 were fitted from 0.75 to 3.8 eV using the standard model of four critical point (CP) oscillators and one Tauc gap modified Lorentz (T-L) oscillator serving as a background. The resonance energies of the four CP oscillators, E_0(A, B), E_0(C), E_1(A), and E_1(B), were fixed to the values deduced from CP analysis. The bandgap of the T-L oscillator was also

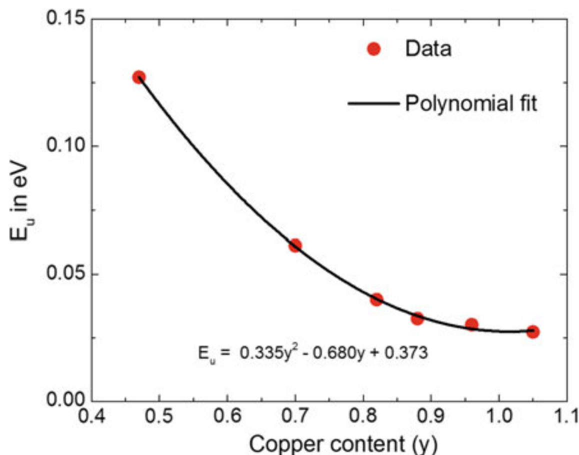

Fig. 11.24 Urbach absorption tail slope E_u as a function of Cu content y deduced from room temperature dielectric functions of CIGS samples with $0.47 \leq y \leq 1.05$ [5]

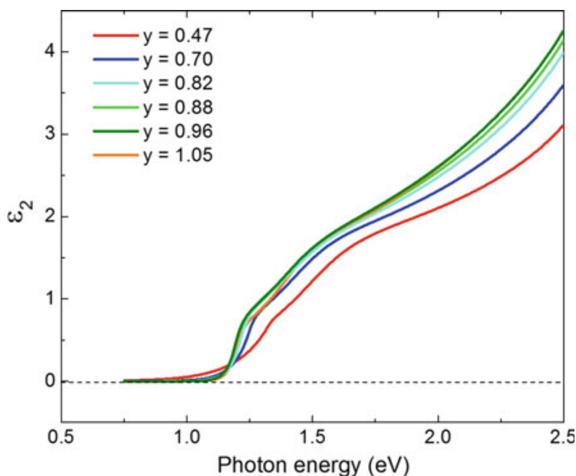

Fig. 11.25 A plot of ε_2 spectra at room temperature as functions of photon energy with an Urbach tail added below the bandgap for CIGS samples of different Cu contents $0.47 \leq y \leq 1.05$. The Urbach tail parameter of $\varepsilon_2(E_t)$ has been selected to ensure continuity of ε_2 as a function of photon energy [5]

coupled to the value of E_0(A, B), the resonance energy of the first CP oscillator that defines the bandgap of the material. All other parameters were allowed to vary in the fitting procedure for the composition $x = 0$, which exhibited the most clearly defined CPs. For all other compositions, it was necessary to fix some of the parameters to the values obtained for the composition $x = 0$ so that desired smooth variations in the fitting parameter values as functions of x could be obtained.

The fixed parameters included three of the four CP broadening parameters, in fact those of E_0(A, B), E_0(C), and E_1(B). The assumption of fixed broadening parameter values independent of x may appear to be an over-simplification in the model, especially for the bandgap CP E_0(A, B); however, the low energy side of the E_0(A, B) CP has been replaced by an Urbach tail. As a result of this replacement, sensitivity to Γ_{CP1} is lost because the remaining high energy side of the E_0(A, B) CP

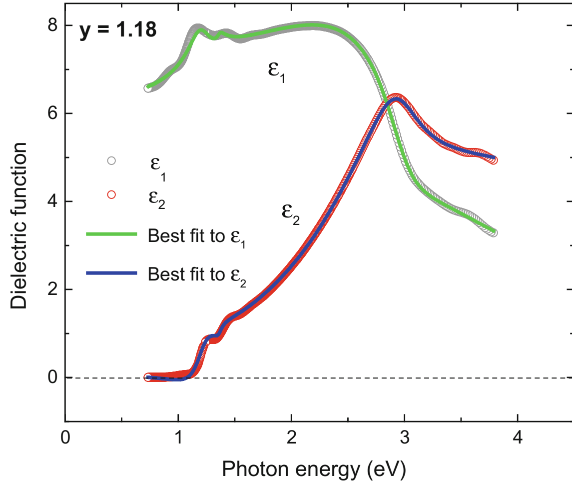

Fig. 11.26 Fit to the dielectric function at room temperature for CIGS with Cu content $y = 1.18$. The dielectric function model includes a sum of four critical point oscillators and one Tauc gap modified Lorentz oscillator serving as a background [5]

Table 11.9 Values of critical point (CP) and Tauc gap modified Lorentz oscillator parameters obtained from fitting the room temperature dielectric function over the range of 0.75–3.80 eV for CIGS with a Cu content $y = 1.18$. The listed values without confidence limits were fixed in the fit. Resonance energies E_0(A, B), E_0(C), E_1(A), and E_1(B) were fixed at values obtained from CP analysis [5]

Oscillator	A	E (eV)	Γ (eV)	ϕ (degree)	μ
CP_1 E_0(A, B)	1.242 ± 0.089	1.179	0.077	−28.71 ± 1.38	0.302
CP_2 E_0(C)	1.903 ± 0.076	1.388	0.340 ± 0.064	−2.64 ± 1.84	0.281 ± 0.056
CP_3 E_1(A)	3.072 ± 0.194	2.914	0.630 ± 0.082	1.01 ± 2.66	0.906 ± 0.073
CP_4 E_1(B)	0.080 ± 0.037	3.712	0.516 ± 0.095	159.21 ± 3.75	3.000
Background T-L	A_{TL} (eV)	E_{TL} (eV)	Γ_{TL} (eV)	E_g (eV)	$\varepsilon_{1,\infty}$
	83.42 ± 3.59	6.234	11.471 ± 0.383	1.179	1.000

tends to overlap the next higher energy E_0(C) CP. For the parameterization in terms of x, in particular, an Urbach absorption tail is needed if one seeks to apply the parameterization to simulate external quantum efficiency (EQE) measurements due to the high sensitivity of EQE to weak absorption in the CIGS. For the Ga series of CIGS depositions, E_t was also chosen to be equal to the E_0(A, B) lowest bandgap energy, as in the analyses of the Cu series. Also for the Ga series, the fit to the data incorporated both $\varepsilon_2(E_t)$ and E_u parameters that define the Urbach absorption tail, and both parameters were fitted versus composition x. In contrast, for the Cu series of CIGS depositions, only the Urbach tail slope was fitted and $\varepsilon_2(E_t)$ was defined by the parameterization as described in Sect. 11.4.

The advantage of the parameterization approach presented here is that the resonance energies of the oscillators are obtained using the standard CP lineshapes

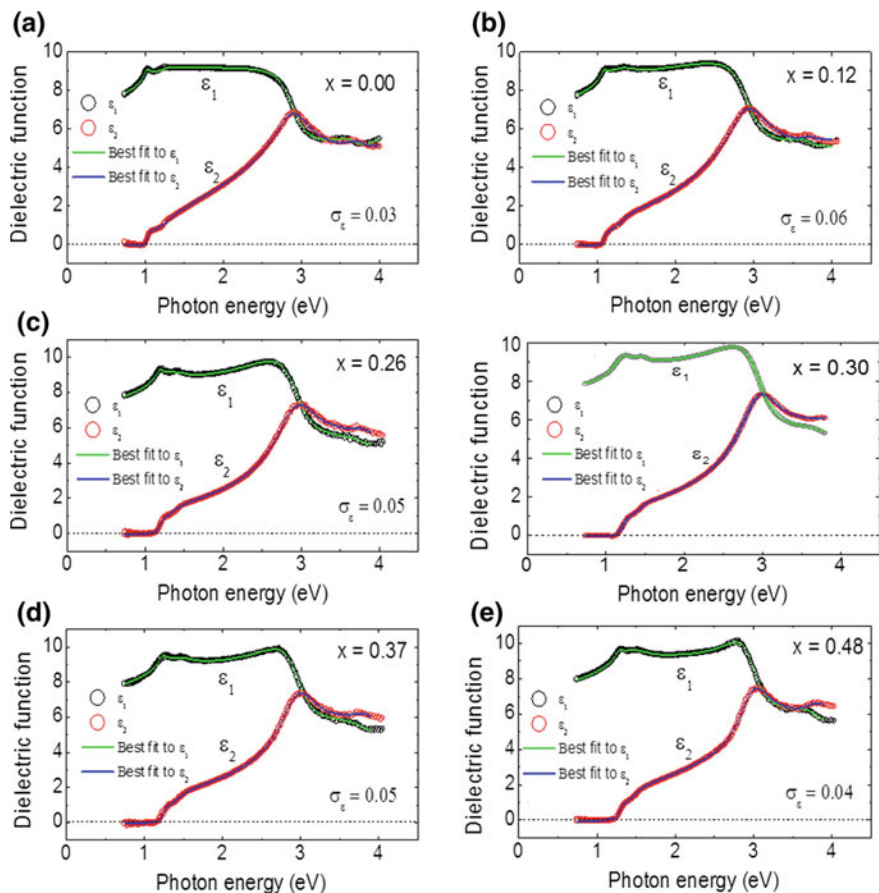

Fig. 11.27 Fits to room temperature dielectric functions of CIGS films having compositions $x = 0.0$, 0.12, 0.26, 0.30, 0.37, and 0.48. The dielectric function model employed a sum of four critical point oscillators and one Tauc gap modified Lorentz oscillator serving as a background. The quality of the fit was evaluated by root-mean-square-deviation σ_{ε}, which is also given in the panels [6]

widely used in the semiconductor community, and thus, they can be compared with results obtained by the standard methodology. Parameterization with non-standard lineshapes can be considered purely mathematical simulations as the individual energy values may not necessarily represent the true bandgaps of the materials studied. The dielectric functions predicted on the basis of the parameterization in this study are closely simulated and can be used in applications such as the compositional mapping and depth profiling of three-stage co-evaporated CIGS [7, 24], with examples given in Sect. 11.6. Fits to the dielectric functions for $x = 0.0$, 0.12, 0.26, 0.30, 0.37, and 0.48 are shown in Fig. 11.27, and the values of the free and fixed CP parameters are tabulated in Table 11.10. The values of T-L parameters along with the $\varepsilon_{1,\infty}$ term are provided in Table 11.11.

Table 11.10 Critical point (CP) parameter values obtained from fits to room temperature dielectric function spectra over the spectral range from 0.75 to 3.8 eV along with fixed values (those without confidence limits). Resonance energies were fixed at the values obtained from CP analysis whereas other fixed parameters including Γ, ϕ, and μ derive from the $x = 0$ best fit [6]

Oscillator	x	A	E (eV)	Γ (eV)	ϕ (degrees)	μ
CP_1 E_0(A,B)	0.00	1.382 ± 0.232	1.025	0.077 ± 0.044	−32.57 ± 5.35	0.302 ± 0.153
	0.12	1.383 ± 0.047	1.079	0.077	−32.40 ± 2.10	0.302
	0.26	1.326 ± 0.037	1.185	0.077	−32.95 ± 1.09	0.302
	0.30	1.284 ± 0.033	1.196	0.077	−33.07 ± 0.88	0.302
	0.37	1.201 ± 0.041	1.232	0.077	−33.52 ± 2.35	0.302
	0.48	1.074 ± 0.032	1.281	0.077	−33.87 ± 2.73	0.302
CP_2 E_0(C)	0.00	1.920 ± 0.372	1.241	0.449 ± 0.225	−56.47 ± 9.39	0.288 ± 0.086
	0.12	1.564 ± 0.057	1.321	0.449	−25.67 ± 2.90	0.288
	0.26	1.741 ± 0.086	1.399	0.449	−0.81 ± 3.16	0.288
	0.30	1.856 ± 0.045	1.420	0.449	2.38 ± 0.75	0.288
	0.37	2.112 ± 0.066	1.452	0.449	6.17 ± 2.46	0.288
	0.48	2.579 ± 0.051	1.496	0.449	3.84 ± 1.48	0.288
CP_3 E_1(A)	0.00	4.694 ± 0.544	2.893	0.436 ± 0.120	57.86 ± 9.36	0.431 ± 0.112
	0.12	4.149 ± 0.100	2.914	0.572 ± 0.013	32.28 ± 1.39	0.630 ± 0.011
	0.26	3.752 ± 0.129	2.932	0.646 ± 0.033	5.90 ± 4.17	0.826 ± 0.013
	0.30	3.463 ± 0.127	2.938	0.625 ± 0.034	−0.95 ± 1.19	0.876 ± 0.011
	0.37	3.055 ± 0.158	2.948	0.571 ± 0.027	−12.22 ± 3.62	0.950 ± 0.009
	0.48	2.720 ± 0.142	2.962	0.485 ± 0.039	−28.04 ± 3.17	1.039 ± 0.012
CP_4 E_1(B)	0.00	0.136 ± 0.055	3.652	0.516 ± 0.297	159.21 ± 13.53	3.000 ± 0.991
	0.12	0.112 ± 0.019	3.687	0.516	159.21	3.000
	0.26	0.095 ± 0.012	3.741	0.516	159.21	3.000
	0.30	0.093 ± 0.012	3.757	0.516	159.21	3.000
	0.37	0.090 ± 0.009	3.789	0.516	159.21	3.000
	0.48	0.090 ± 0.014	3.841	0.516	159.21	3.000

Table 11.11 Parameter values of the Tauc gap modified Lorentz oscillator obtained from fits to room temperature dielectric function spectra over the spectral range from 0.75 to 3.8 eV. Also shown is the best fit value of the photon energy independent $\varepsilon_{1,\infty}$ term. The values without confidence limits were fixed in the analysis either at the E_0(A, B) bandgap value from CP analysis (E_g) or at the values from the $x = 0$ fit (E_{TL}) [6]

x	A_{TL} (eV)	E_{TL} (eV)	Γ_{TL} (eV)	E_g (eV)	$\varepsilon_{1,\infty}$
0.00	50.48 ± 9.05	6.234 ± 0.838	8.773 ± 1.093	1.025	1.690 ± 0.324
0.12	58.94 ± 4.61	6.234	8.663 ± 0.235	1.079	1.171 ± 0.040
0.26	71.70 ± 3.39	6.234	9.737 ± 0.265	1.185	0.749 ± 0.032
0.37	91.45 ± 4.56	6.234	11.730 ± 0.326	1.232	0.412 ± 0.033
0.48	105.76 ± 4.32	6.234	12.533 ± 0.267	1.281	0.000 ± 0.040

The free oscillator parameters presented in Tables 11.10 and 11.11 were plotted versus x and polynomial best fits were obtained. This can be done by fitting the variable parameters in Tables 11.10 and 11.11 using polynomial expressions of the form

$$P_i(0.90,\, x) = \sum_{n=1}^{N_i} b_{ni}(x - 0.30)^n + b_{0i}(0.90,\, 0.30) \tag{11.12}$$

where $P_i(0.90, x)$ describes the ith parameter as a function of the Ga content x for $y = 0.90$ with b_{ni} serving as the polynomial coefficients. Here N_i is the order of the polynomial required to fit the parameter $P_i(0.90, x)$ as a function of x. In addition, $b_{0i}(0.90, 0.30)$ is the value of the constant coefficient for the ith parameter of the hypothetical sample with composition $y = 0.90$ and $x = 0.30$, which can be compared directly with the corresponding result from (11.6) for the Cu series.

The plots of the energies deduced from CP analysis are shown in Fig. 11.28, and all the free CP and background T-L parameters are shown as functions of x in Fig. 11.29. In all, 24 oscillator parameters and the energy independent $\varepsilon_{1,\infty}$ are used, 17 through polynomial equations in terms of composition x and 8 through manually fixed parameter values. The overall results are summarized in Table 11.12. Of particular interest among the polynomials in Table 11.12 is the

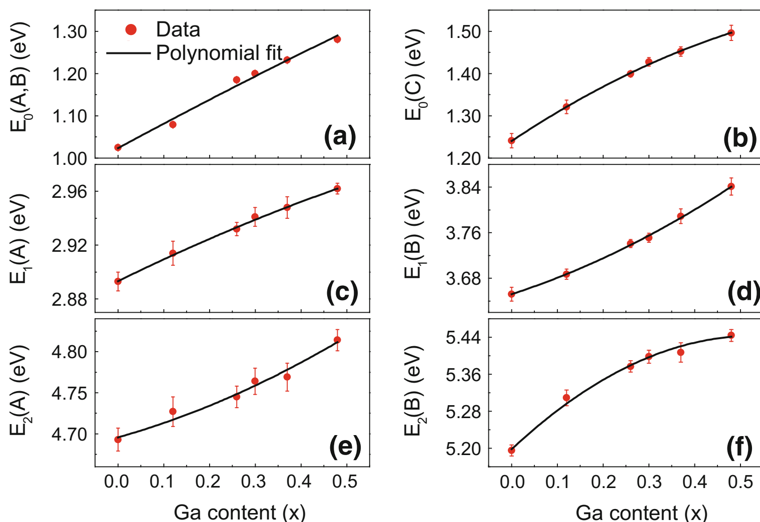

Fig. 11.28 Critical point (CP) energies and their 90% confidence limits plotted as functions of the Ga content x for a set of CIGS thin films. These results are deduced from CP analyses of dielectric function spectra obtained in-situ at room temperature. The solid lines are second order polynomial fits to the data [7]. Reproduced with permission from John Wiley & Sons, Ltd

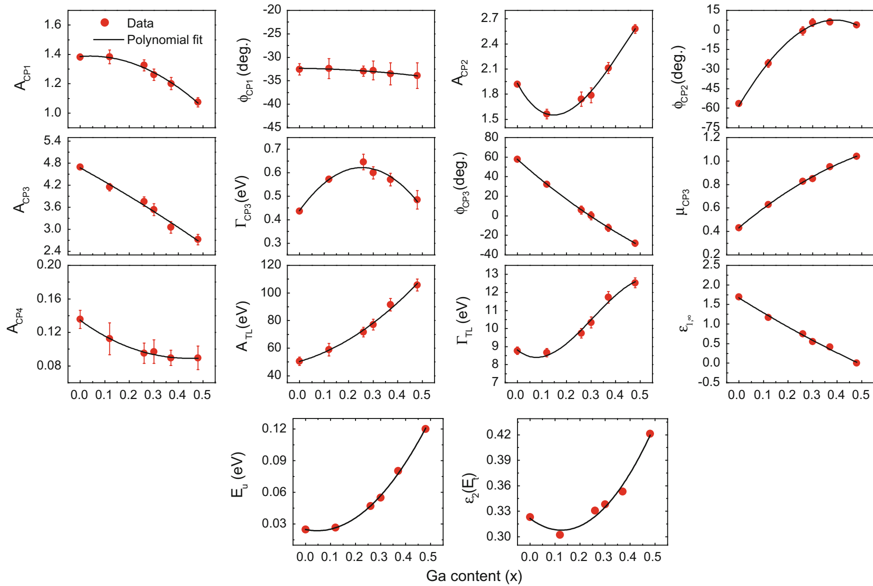

Fig. 11.29 Photon energy independent oscillator parameters plotted as functions of x ($0 \leq x < 0.5$) (points). The subscripts CP1, CP2, CP3, and CP4 represent the E_0(A, B), E_0(C), E_1(A), and E_1(B) critical points, respectively, and TL represents the background Tauc gap modified Lorentz oscillator. Also shown are the Urbach parameters including the absorption tail slope E_u and ε_2 at $E = E_t$ as functions of x. For each parameter presented, the best fit polynomial function is also plotted (lines) [7]. Reproduced with permission from John Wiley & Sons, Ltd

Urbach slope parameter E_u, which is found to exhibit a minimum near $x = 0.04$ and increases with x, which is likely an effect of alloy-induced broadening. Through the expressions of Table 11.12, the number of parameters that can represent each dielectric function over the 0.75–3.8 eV has now been reduced from twenty-five to one, the composition x. A similar approach was reported previously for hydrogenated amorphous $Si_{1-x}Ge_x$ alloys and metastable polycrystalline $CdTe_{1-x}S_x$ alloys for the purposes optical depth profiling by RTSE [25, 26]. It is important to emphasize that the approach followed in this study to obtain expressions for the CIGS dielectric functions in terms of compositional parameters uses the physically justifiable CP oscillators. Because the CP expression of (11.1) is derived from the band structure based on the assumption of parabolic bands in $E(\mathbf{k})$ and a constant momentum matrix element, the fixed and variable oscillator parameters reflect to some extent band structure characteristics of the studied CIGS films.

Table 11.12 Critical point and Tauc gap modified Lorentz oscillator parameters, as well as $\varepsilon_{1,\infty}$, E_u, and $\varepsilon_2(E_t)$ described by second or third order polynomials of composition x. The values of fixed parameters are also provided. The expressions for oscillator parameters are valid for $0 \leq x < 0.5$ over the photon energy range of 0.75 eV $\leq E \leq$ 3.80 eV for ε_1 and $E_t < E \leq$ 3.80 eV for ε_2. Below E_t, ε_2 is given as an Urbach tail generated by E_u and $\varepsilon_2(E_t)$. The coefficients are given in terms of $\Delta x = x - 0.30$; thus, the zero-order coefficient $b_{0i}(0.90, 0.30)$ of the ith parameter is the value appropriate for the composition $y = 0.90$ and $x = 0.30$

Oscillator	Parameter	Expression in terms of x
CP_1 E_0(A,B)	A	$-1.66(\Delta x)^2 - 0.860(\Delta x) + 1.277$
	E (eV)	$-0.063(\Delta x)^2 + 0.547(\Delta x) + 1.194$
	Γ (eV)	0.077
	ϕ (degree)	$-5.411(\Delta x)^2 - 3.993(\Delta x) - 33.040$
	μ	0.302
CP_2 E_0(C)	A	$-16.30(\Delta x)^3 + 7.320(\Delta x)^2 + 3.352(\Delta x) + 1.836$
	E (eV)	$-0.388(\Delta x)^2 + 0.487(\Delta x) + 1.421$
	Γ (eV)	0.449
	ϕ (degree)	$-412.96(\Delta x)^2 + 78.14(\Delta x) + 3.410$
	μ	0.288
CP_3 E_1(A)	A	$-0.953(\Delta x)^2 - 4.256(\Delta x) + 3.484$
	E (eV)	$-0.049(\Delta x)^2 + 0.138(\Delta x) + 2.939$
	Γ (eV)	$-2.840(\Delta x)^2 - 0.264(\Delta x) + 0.615$
	ϕ (degree)	$85.44(\Delta x)^2 - 167.64(\Delta x) - 0.640$
	μ	$-1.02(\Delta x)^2 + 1.148(\Delta x) + 0.869$
CP_4 E_1(B)	A	$0.239(\Delta x)^2 - 0.0656(\Delta x) + 0.0938$
	E (eV)	$0.278(\Delta x)^2 + 0.427(\Delta x) + 3.755$
	Γ (eV)	0.516
	ϕ (degree)	159.21
	μ	3.000
Tauc gap modified Lorentz	A (eV)	$137.3(\Delta x)^2 + 134.0(\Delta x) + 78.2$
	E (eV)	6.232
	Γ (eV)	$-88.91(\Delta x)^3 + 2.344(\Delta x)^2 + 14.242$ $(\Delta x) + 10.478$
	E_g (eV)	$-0.063(\Delta x)^2 + 0.547(\Delta x) + 1.194$
	$\varepsilon_{1,\infty}$	$1.008(\Delta x)^2 - 3.308(\Delta x) + 0.586$
	E_u (eV)	$0.499(\Delta x)^2 + 0.260(\Delta x) + 0.0582$
	$\varepsilon_2(E_t)$	$0.886(\Delta x)^2 + 0.311(\Delta x) + 0.334$

11.5 Comparison and Discussion of Results

Of interest is a comparison of the fitting strategies for the Cu and Ga composition series. In the study versus x, the fixed values of the oscillator parameters were identified in a fit to the dielectric function of the CIGS material with $x = 0$ and $y = 0.90$. For $x > 0$, it was advantageous to fix the exponent of the second E_0(C) CP (at $\mu_{CP2} = 0.288$). In the study versus y, however, improved results were obtained by varying this parameter, which varied monotonically from $\mu_{CP2} = 0.359$ at $y = 0.5$ to $\mu_{CP2} = 0.282$ at $y = 1$. Also in the study versus x, the second CP broadening parameter was fixed at $\Gamma_{CP2} = 0.449$ eV. Improved results were obtained versus y by varying this parameter, which decreased monotonically from $\Gamma_{CP2} = 0.533$ eV at $y = 0.5$ to $\Gamma_{CP2} = 0.386$ eV at $y = 1$.

The depositions of the Cu stoichiometry series and the Ga alloy composition series were performed independently with one member of the Cu series added to the Ga series as indicated by the deposition conditions listed in Table 11.1 [5, 6]. This provides an opportunity to check the reproducibility of the deposition and accuracy of the parameterization at the $y = 0.90$, $x = 0.30$ crossing point of greatest interest. Direct comparison is facilitated by expressions of the best fit polynomials in Tables 11.8 and 11.12 in terms of $\Delta y = y - 0.90$ and $\Delta x = x - 0.30$. Then the constant terms in the parameterizations versus y and x should agree. A comparison is shown in Table 11.13 for the oscillator parameters of CIGS with $y = 0.9$, $x = 0.3$ from the Ga variation series (first data column) and Cu variation series (second data column). All values are in agreement to better than 3% with the exception of two higher energy CP phase parameters and the Urbach tail slope. The CP energies are in particularly good agreement at the crossing point of the two parameterizations. The percentage difference between the two phase parameters is high because these parameters are close to zero; the absolute difference in both cases is less than 2°. Thus, the most significant difference is in the Urbach tail slope. The value of E_u predicted from the Cu parameterization at $y = 0.9$ is 0.0324 eV whereas the corresponding result for the Ga parameterization is 0.0591 eV. This difference may result from a difference in the quality of the very thin CIGS material in the two deposition series.

Figure 11.30 provides a visual representation of the differences in Table 11.13 both in terms of (ψ, Δ) and in terms of the dielectric function. In this figure, the Ga parameterization was used to generate a predicted dielectric function for CIGS material with Ga ratio of $x = 0.30$ which was compared (without free parameters) to the dielectric function measured at room temperature for the sample of the Cu series with $x = 0.30$ and Cu ratio $y = 0.88$. In addition, the (ψ, Δ) spectra measured in-situ at room temperature were also modeled based on a simulation applying the structural parameters of Tables 11.1 and 11.3. The largest deviations in the spectra occur at the upper limit of the parameterization near 4 eV and in ε_1 near the two

Table 11.13 Critical point and T-L oscillator parameter values, as well as $\varepsilon_{1,\infty}$, that provide a best fit of the room temperature dielectric function of CIGS for $x = 0.30$ and $y = 0.90 \pm 0.03$ from the parameterization of the Ga series and for $x = 0.30 \pm 0.01$, $y = 0.90$ from the parameterization of the Cu series

Parameter type	Parameter	Ga series ($x = 0.30$, $y = 0.90 \pm 0.03$)	Cu series ($x = 0.30 \pm 0.01$, $y = 0.90$)	Percent difference $(P_{Ga} - P_{Cu})/P_{Cu}$ x (100%)
CP_1 E_0(A,B)	A_{CP1}	1.277	1.280	−0.2
	E_{CP1} (eV)	1.194	1.1941	0
	Γ_{CP1} (eV)	0.077	0.077	–
	ϕ_{CP1} (degree)	−33.04	−32.28	2.4
	μ_{CP1}	0.302	0.302	–
CP_2 E_0(C)	A_{CP2}	1.836	1.858	−1.2
	E_{CP2} (eV)	1.421	1.4197	0.1
	Γ_{CP2} (eV)	0.449	0.4373	2.7
	ϕ_{CP2} (degree)	3.410	1.845	85
	μ_{CP2}	0.288	0.2889	−0.3
CP_3 E_1(A)	A_{CP3}	3.484	3.447	1.1
	E_{CP3} (eV)	2.939	2.935	0.1
	Γ_{CP3} (eV)	0.615	0.6259	−1.7
	ϕ_{CP3} (degree)	−0.640	−0.979	−35
	μ_{CP3}	0.869	0.8782	−1.0
CP_4 E_1(B)	A_{CP4}	0.0938	0.09120	2.9
	E_{CP4} (eV)	3.755	3.7549	0
	Γ_{CP4} (eV)	0.516	0.516	–
	ϕ_{CP4} (degree)	159.21	159.21	–
	μ_{CP4}	3.000	3.000	–
T-L	A_{TL} (eV)	78.2	79.44	−1.6
	E_{TL} (eV)	6.232	6.234	–
	Γ_{TL} (eV)	10.478	10.653	−1.6
	$E_{g(TL)}$ (eV)	1.194	1.1941	0
Constant	$\varepsilon_{1,\infty}$	0.586	0.5842	0.3
Urbach	E_u (eV)	0.0582	0.0324	80

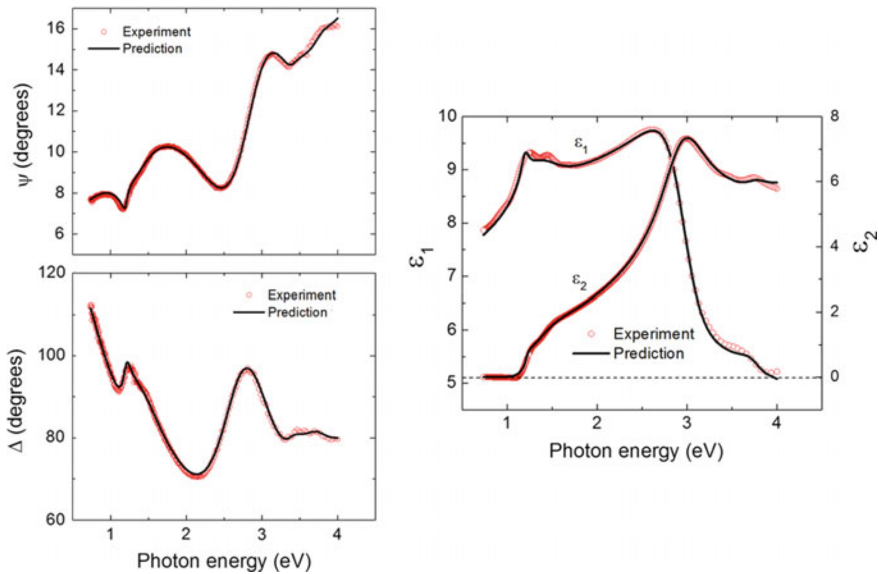

Fig. 11.30 The ellipsometric spectra in (ψ, Δ) measured in-situ at room temperature for a CIGS film with a Ga ratio x of 0.30 and a Cu ratio y of 0.88. The solid lines represent a prediction with structural parameters given in Tables 11.1 and 11.3. In this prediction, the parameterization in the Ga content x was used with $x = 0.30$, valid for photon the energy range of 0.75–3.80 eV. The measured room temperature dielectric function (ε_1, ε_2) corresponding to the (ψ, Δ) results are shown in comparison with the predicted dielectric function generated from parameterization results of the Ga series [5, 6]. No free parameters were used in the predictions

lowest energy CPs. The latter deviations are reduced through the ~1–3% differences in the amplitude and broadening parameters associated with the Cu parameterization.

11.6 Applications

The analytical forms of the CIGS dielectric function given in terms of composition parameters have many useful applications in CIGS photovoltaics technology. When this methodology is applied to maps of SE (ψ, Δ) data collected over the area of a CIGS film, maps of the film composition, bulk layer thickness, and surface roughness layer thickness can be deduced simultaneously [24]. Mapping can also be applied to completed device structures, and the resulting information can be correlated with the performance of small area cells point-by-point to identify local process-property-performance relationships. Furthermore, the multilayer stack structural parameters and associated component material dielectric functions from the database, all deduced by SE, enable simulations of the solar cell external

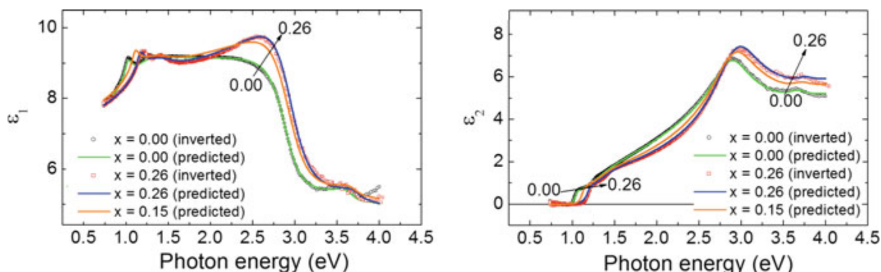

Fig. 11.31 The real parts (left) and imaginary parts (right) of the dielectric function ε of CIGS generated from the equations presented in Table 11.12 for compositions $x = 0.00$, 0.15, and 0.26. Inverted ε spectra for $x = 0.00$ and $x = 0.26$ are also shown [6]

quantum efficiency (EQE) [27–29]. A comparison of the simulated results with the experimental EQE provides insights into the origins of recombination losses. Finally, the database enables the determination of compositional profiles of graded CIGS layers fabricated in multistage processes, and how profile parameters vary over the area of a solar cell structure.

It should be emphasized that the expressions presented in Sects. 11.3 and 11.4 are only valid for $0.45 < y \leq 1.05$, and $0 \leq x < 0.5$. Because the optimum y and x values for solar cells are in the ranges 0.8–0.95 and 0.25–0.35, respectively, the database ranges are selected for simulations of the most relevant device configurations. They are also applicable for optical simulations of narrow gap $CuInSe_2$ and CIGS of low Ga content absorbers for possible use in the bottom cell of a tandem solar cell. To demonstrate simulation capabilities, Fig. 11.31 shows the real and imaginary parts of the dielectric functions ε_1 and ε_2 predicted from the parameters of the analytical expressions for the compositions $x = 0.00$, 0.15, and 0.26 along with inverted ε_1 and ε_2 spectra for $x = 0.00$ and $x = 0.26$. Additional simulations are shown Figs. 11.32 and 11.33 which present (ε_1, ε_2) generated from the

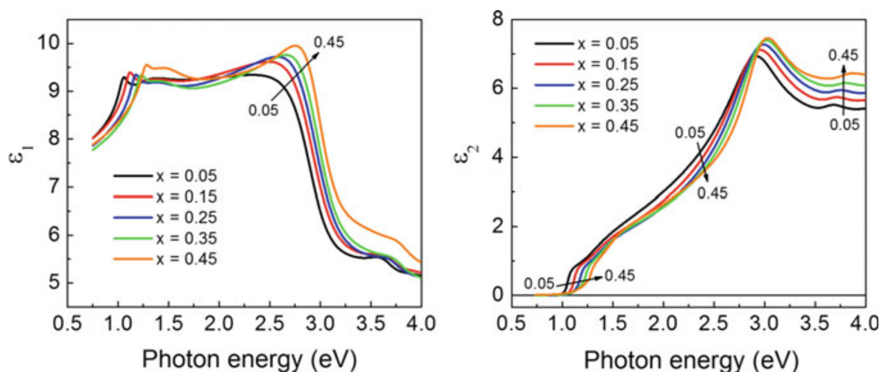

Fig. 11.32 Simulations of room temperature dielectric functions for CIGS films of different composition x with $y = 0.90$ as generated from the set of equations presented in Table 11.12 [5]

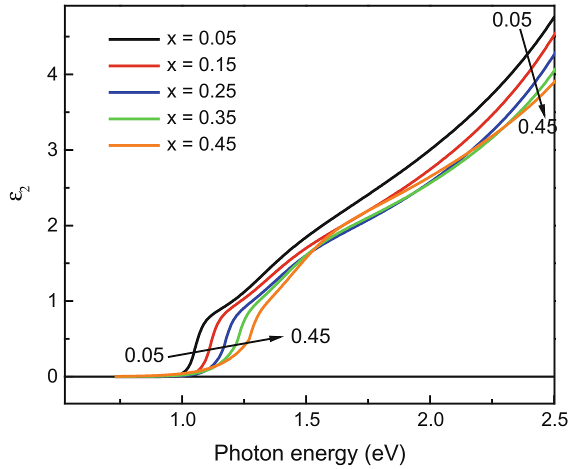

Fig. 11.33 Simulations of ε_2 at room temperature as functions of photon energy for CIGS samples of different selected Ga contents x with Cu content $y = 0.90$. This plot highlights the absorption onset region where the transition from the Urbach tail to the lowest energy CP feature occurs [5]

polynomials of Table 11.12 for different compositions ranging from $x = 0.05$ to $x = 0.45$. Figure 11.33 highlights the absorption onset region in ε_2 where the transition occurs from the Urbach tail to the lowest energy CP.

An application of the parameterization will be provided that involves approximation methods for solution of the inverse problem, i.e. determining y and x along with structural parameters of thickness through least squares regression analysis fitting of mapping SE data [5]. In this application, a CIGS thin film was fabricated using one stage co-evaporation onto a 10 cm × 10 cm native oxide coated *c*-Si wafer at 570 °C. An ex-situ SE mapping measurement was performed at room temperature using AccuMap-SE (J. A. Woollam Co.) instrumentation which is equipped with a high-speed multichannel spectroscopic ellipsometer (Model M2000-DI).

The SE data were fitted to deduce the CIGS bulk layer thickness and surface roughness layer thickness along with composition parameters. The surface roughness layer was modeled using the Bruggeman effective medium approximation as a mixture of the underlying (CIGS) and overlying (void) materials. In the fitting procedure, the void fraction in the surface roughness layer was allowed to vary in order to simulate variations in the surface microstructure. For the CIGS material, the two different dielectric function parameterizations were used to extract Ga and Cu contents in the CIGS film. The equations that describe the CIGS dielectric function for different Ga contents and a Cu content of $y = 0.90 \pm 0.03$ are summarized in Table 11.12, and the equations that describe the dielectric function for different Cu contents for a Ga content of $x = 0.30 \pm 0.01$ are summarized in Table 11.8. For the map in Ga content x in Fig. 11.34, a constant Cu content was assumed since the variation in that parameter was relatively small ~±0.06 over a significant fraction of the total area, with much of the center of the sample at $y = 0.88$. Similarly, for the map in Cu content y in Fig. 11.35, a constant Ga content was assumed since its variation was also small ~±0.02 over a significant

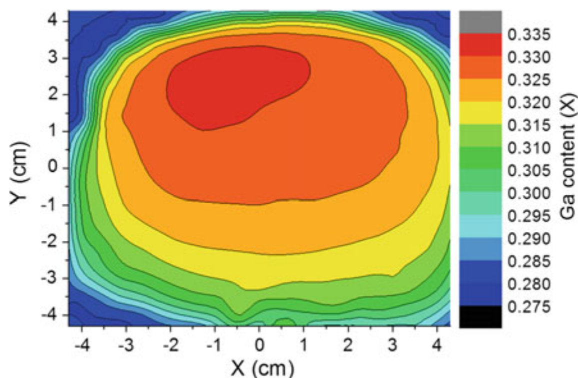

Fig. 11.34 Map of Ga content x determined by ex-situ SE for an ~450 nm thick CIGS layer deposited on a 10 cm × 10 cm c-Si substrate. In the one-stage co-evaporation process, the Ga source was located beneath the 570 °C substrate near the bottom left corner of the map [5]

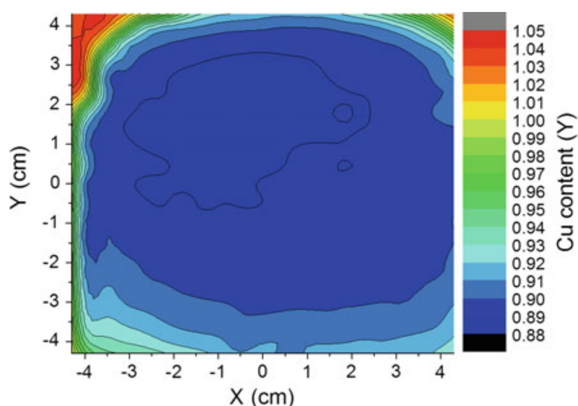

Fig. 11.35 Map of Cu content y determined by ex-situ SE for an ~450 nm thick CIGS layer deposited on a 10 cm × 10 cm c-Si substrate. In the one-stage co-evaporation process, the Cu source was located near the top left corner of the map [5]

fraction of the total area. In this case, a large area of the center of the sample exhibits a Ga content of $x = 0.315–0.335$. Maps of the CIGS bulk and surface roughness layer thicknesses in Fig. 11.36 were deduced from the latter SE analysis due to the weaker variation in Ga content which was not taken into account in the modeling. An approach has been developed to extract x and y simultaneously using relationships that cover the area of two-dimensional (x, y) space [22].

The greatest uncertainty in the use of the equations in Tables 11.8 and 11.12 arises from the fact that the dielectric functions on which they were based were obtained from very thin films (~50–60 nm) deposited on ideal c-Si wafer substrates. The advantages of this approach are associated with the smooth substrate/film interfaces and the thinner roughness layers which lead to higher accuracy dielectric functions. The disadvantage arises from the possible lack of relevance of the dielectric functions to thicker films or films deposited on Mo coated glass substrates, as such films may have different grain structures. Comparison studies using EDX, as well as Auger electron spectroscopy and secondary ion mass spectroscopy depth profiling, have demonstrated the validity of the parameterizations in a wide variety of applications. Here, the focus is on a thicker film, ~350 nm, deposited on c-Si and

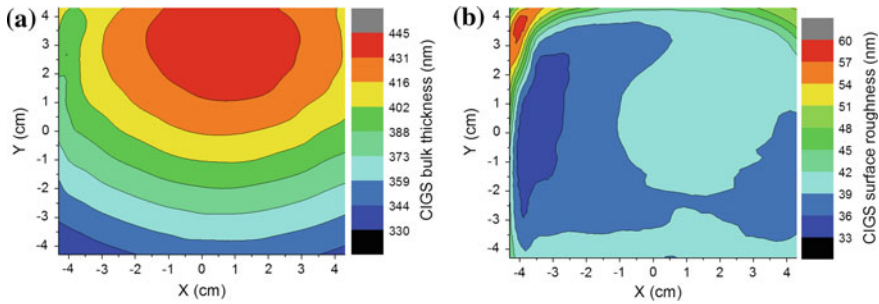

Fig. 11.36 Maps of the **a** CIGS bulk layer thickness and **b** surface roughness layer thickness for a 10 cm × 10 cm CIGS coated *c*-Si substrate obtained simultaneously with that of Fig. 11.35. This result was obtained assuming a surface roughness layer dielectric function deduced by using the Bruggeman effective medium approximation with a variable volume fraction of void in the layer [5]

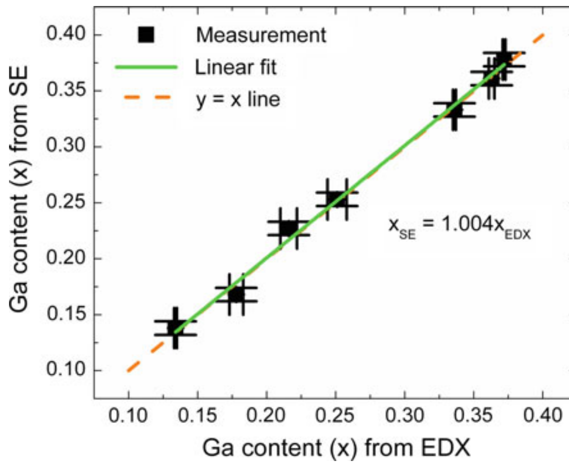

Fig. 11.37 Correlation plot between the Ga contents *x* from EDX and from mapping SE over the surface of a 350 nm CIGS thin film deposited on a *c*-Si wafer. Each data point represents EDX and SE measurements performed at the same location whereas multiple data points arise from measurements at different locations on the surface. The horizontal error bars represent the maximum change in *x* from EDX if the sample is moved by 1 mm from the measurement point. The vertical error bars represent the confidence limits in the SE analysis [7]. Reproduced with permission from John Wiley & Sons, Ltd

mapped for Ga content. In this example, the Ga composition values deduced by mapping SE over a non-uniform surface were found to be consistent with EDX, as demonstrated by the correlation plot in Fig. 11.37. In this figure, the horizontal error bars represent the maximum change in EDX composition if the sample is moved by 1 mm from the measurement location where SE is also performed. The vertical error

bars are the confidence limits in the mapping SE analysis. This close agreement demonstrates the relevance of the ε spectra of Figs. 11.20 and 11.27 deduced for ~50–60 nm thick layers in correctly representing the ε spectra for thicker layers (~350 nm). As a result the EDX-SE calibration performed on the basis of the ~50–60 nm thick CIGS films measured by in-situ SE and the associated parameterization both apply for films of much greater thickness as well.

11.7 Summary

The outcomes of broadest interest described in this chapter are the systematic parameterizations of the complex dielectric functions of $Cu_y(In_{1-x}Ga_x)Se_2$ (CIGS), the first spanning the Cu atomic fraction $y = [Cu]/([In] + [Ga])$ range of $0.45 < y \leq 1.05$ for fixed Ga atomic fraction $x = [Ga]/([In] + [Ga]) \sim 0.30$, and the second spanning the range $0 \leq x < 0.50$ with $y \sim 0.90$. Calibration between the SE and composition is performed through energy dispersive X-ray spectroscopy. Table 11.14 summarizes the three major methodologies for real time and in-situ spectroscopic ellipsometry (SE) applied in this chapter, and the data outcomes of the associated SE analyses. Dielectric function parameterization has been

Table 11.14 Real time and in-situ measurement and analysis methodologies described in this chapter. The useful outcome of each analysis is provided

Measurement approach and temperature	Spectral range(s)	Analysis methodology	Complex dielectric function model	Useful outcome
RTSE with 0.1 s acquisition time; sample at $T = 570$ °C	0.75–6.5 eV	Multi-time fitting of (ψ, Δ) with time range of ~30 s	None assumed; ~700 pairs of $(\varepsilon_1, \varepsilon_2)$ values determined by inversion of (ψ, Δ)	Structural evolution, $d_b(t)$, $d_s(t)$, $f_v(t)$ and final values $d_b(t_f)$, $d_s(t_f)$, $f_v(t_f)$
in-situ SE single acquisition, with 9 s acquisition time; sample at $T = 570$ °C	0.75–6.5 eV	Inversion of (ψ, Δ) with fixed structural parameters; analytical fit	$(\varepsilon_1, \varepsilon_2)$ modeled with: 2CP analytical expression near bandgap	Inverted $(\varepsilon_1, \varepsilon_2)$; Bandgap CP energies; Temperature coefficient of bandgap
in-situ SE single acquisition, with 9 s acquisition time; sample at $T = 20$ °C	0.75–6.5 eV (inversion) 0.75–3.8 eV (parameterization)	Inversion of (ψ, Δ) with fixed structural parameters; analytical fit	$(\varepsilon_1, \varepsilon_2)$ modeled with: CP analysis and parameterization with Urbach + 1T-L + 4CP	Inverted $(\varepsilon_1, \varepsilon_2)$; CP energies; Dielectric function parameters

preceded by a number of steps involving determination of (i) the evolution and final structural properties of the films by real time SE (RTSE), (ii) inverted dielectric functions obtained in-situ at deposition and room temperatures based on the RTSE structural parameters, (iii) critical point (CP) energies from the twice differentiated dielectric functions, and (iv) best fit parameters in an analytical model of the dielectric function deduced with the fixed CP energies for fitting stability. In this overall analysis, additional useful information on the optimum procedure for in-situ determination of the structural parameters and dielectric function of CIGS was obtained. Key results of this four-step analysis are described in the following paragraphs.

CIGS films having different Cu and Ga contents prepared by the one stage co-evaporation process were studied by RTSE performed at the deposition temperature (570 °C). Analysis of the RTSE measurements yielded the bulk and surface roughness layer thickness evolution during the growth of CIGS films with different Cu and Ga contents at 570 °C. The focus of this chapter was the systematic variation in the structural evolution as a function of the Cu content. It was found that films nearest the stoichiometric composition with $y = 1$ exhibited the maximum surface roughness thickness after coalescence and the weakest coalescence effect, effects which in polycrystalline thin films in general correspond to the greatest initial grain growth. Cu free $(In_{1-x}Ga_x)_2Se_3$ and Cu rich films exhibit the strongest coalescence effects in the former case possibly due to a highly disordered semiconductor phase and in the latter case due to the role of a $Cu_{2-x}Se$ phase. The results found here are consistent with previous RTSE studies for films of different x suggesting that the films undergoing the largest roughening characteristic of grain growth exhibit higher solar cell performance.

By depositing very thin films, ~50–60 nm in bulk layer thickness, on crystalline silicon wafer substrates, and performing in-situ measurements for the purpose of extracting CIGS layer dielectric functions, the primary limitations to the accuracy of the results are overcome. First, in-situ measurements eliminate the possibility of oxidation and contamination of the film surface, which can have a significant effect on the dielectric function determination. A more important second limitation in determining dielectric functions of CIGS films, however, arises from the correction of the SE data for the effect of surface roughness. Thin roughness is modeled as an individual layer with its dielectric function approximated by an effective medium theory. The ~50–60 nm thick films exhibit thinner surface roughness layers (<16 nm) relative to thick films which lessen the impact of the corrections and improve confidence in the results. Also due to the large data set, RTSE provides the structural parameters of the final film, including the roughness layer thickness and void content, with a high degree of confidence. As a result, high quality dielectric function spectra for 50–60 nm thick films of different Cu and Ga contents have been obtained by in-situ SE at 570 °C and at room temperature by inversion of (ψ, Δ) data.

Critical point analyses were performed on the resulting dielectric function spectra obtained for CIGS films measured in-situ at both deposition and room temperatures, which yield average temperature coefficients of the CIGS bandgap for

the different stoichiometries and compositions. The locations of the room temperature CP resonance energies, including the bandgap energy, from CP analyses were fixed in a dielectric function parameterization up to 3.8 eV. The dielectric function model included a combination of four CP oscillators of different energies, a Tauc gap modified Lorentz oscillator serving as a background, and an Urbach tail below the bandgap defined by the lowest energy CP oscillator. Expressions describing the dependence of each of the oscillator parameters on the Cu content y and Ga content x were obtained by fitting the plots of these parameter values as functions of y and x to polynomial functions. Since all the dielectric function parameters are expressed in terms of x or y, the dielectric function spectra can be generated for any given composition over the range of Cu atomic fraction $y = [\mathrm{Cu}]/([\mathrm{In}] + [\mathrm{Ga}])$ of $0.45 < y \leq 1.05$ for Ga atomic fraction $x = [\mathrm{Ga}]/([\mathrm{In}] + [\mathrm{Ga}]) \sim 0.30$ and over the range $0 \leq x < 0.50$ for $y \sim 0.90$. The two parameterizations obtained from independent series of CIGS depositions versus y and x show good agreement at the crossing point, confirming the stability and reproducibility of the methodology that extends from film deposition to SE analysis.

The established capability of calculating (ε_1, ε_2) from y or x enables solution of the inverse problem, determining y or x along with structural parameters of thickness through least squares regression analysis fitting of SE data. This capability has a wide variety of applications in CIGS technology, including compositional mapping and depth profiling using ex-situ SE measurements. In this study, maps of Cu stoichiometry and Ga composition are demonstrated for a single thicker (~450 nm) CIGS deposition on a Si wafer exhibiting thicker roughness as well (~40 nm). Good agreement between mapping SE and energy dispersive X-ray spectroscopy (EDX) has been obtained in such mapping applications. This indicates that although the parameterized dielectric functions derive from 60 nm thin films, they are suitable for the analysis of much thicker films as well. Good agreement is also obtained between ex-situ SE determination and Auger electron spectroscopy as well as secondary ion mass spectroscopy of bandgap profiles in the CIGS absorber layers of CIGS solar cells fabricated by three-stage co-evaporation. This indicates that although the parameterized dielectric functions derive from films on *c*-Si substrates, they are also suitable for CIGS layers deposited on Mo in the solar cell configuration.

References

1. W.N. Shafarman, S. Siebentritt, L. Stolt, in *Handbook of Photovoltaic Science and Engineering*, ed. by A. Luque, S. Hegedus, 2nd edn. (Wiley, New York, NY, 2011), Chapter 13, p. 546
2. T.-P. Hsieh, C.-C. Chuang, C.-S. Wu, J.-C. Chang, J.-W. Guo, W.-C. Chen, in *Proceedings of the 34th IEEE Photovoltaics Specialists Conference (PVSC)*, June 7–12, 2009, Philadelphia, PA (IEEE, New York, NY, 2009), p. 886

3. C. Stephan, *Structural Trends in Off Stoichiometric Chalcopyrite Type Compound Semiconductors*. Ph.D. Dissertation, Freie Universität Berlin, Helmholtz-Zentrum Berlin, Germany, 2011
4. M. Powalla, W. Witte, P. Jackson, S. Paetel, E. Lotter, R. Würz, F. Kessler, C. Tschamber, W. Hempel, D. Hariskos, R. Menner, A. Bauer, S. Spiering, E. Ahlswede, T. Magorian Friedlmeier, D. Blazquez-Sanchez, I. Klugius, W. Wischmann, IEEE J. Photovolt. **4**, 440 (2014)
5. A.-R. Ibdah, *Optical Physics of Cu(In, Ga)Se_2 Solar Cells and Their Components*. Ph.D. Dissertation, University of Toledo, Toledo, OH, USA, 2017
6. P. Aryal, *Optical and Photovoltaic Properties of Copper Indium-Gallium Diselenide Materials and Solar Cells*. Ph.D. Dissertation, University of Toledo, Toledo, OH, USA, 2014
7. P. Aryal, A.-R. Ibdah, P. Pradhan, D. Attygalle, P. Koirala, N.J. Podraza, S. Marsillac, R.W. Collins, J. Li, Prog. Photovolt.: Res. Appl. **24**, 1200 (2016)
8. J.D. Walker, H. Khatri, V. Ranjan, S. Little, R. Zartman, R.W. Collins, S. Marsillac, in *Proceedings of the 34th IEEE Photovoltaic Specialists Conference (PVSC)*, 7–12 June 2009, Philadelphia, PA (IEEE, New York, NY, 2009), p. 1154
9. R.W. Collins, A.S. Ferlauto, in *Handbook of Ellipsometry*, ed. by H.G. Tompkins, E.A. Irene, (William Andrew, Norwich, NY, 2005), Chapter 2, p. 93
10. W.G. Oldham, Surf. Sci. **16**, 97 (1969)
11. I. An, Y.M. Li, H.V. Nguyen, C.R. Wronski, R.W. Collins, Appl. Phys. Lett. **59**, 2543 (1991)
12. S. Marsillac, V. Ranjan, S. Little, R.W. Collins, in *Proceedings of the 35th IEEE Photovoltaic Specialists Conference (PVSC)*, 20–25 June 2010, Honolulu, HI (IEEE, New York NY, 2010), p. 866
13. V. Ranjan, R.W. Collins, S. Marsillac, Phys. Stat. Sol. RRL **6**, 10 (2012)
14. P. Pradhan, P. Aryal, A.-R. Ibdah, K. Aryal, J. Li, N. J. Podraza, S. Marsillac, R.W. Collins, in *Proceedings of the 40th IEEE Photovoltaics Specialists Conference (PVSC)*, 8–13 June 2014, Denver, CO (IEEE, New York, NY, 2014), pp. 2060–2065
15. M.A. Contreras, J. Tuttle, A. Gabor, A. Tennant, K. Ramanathan, S. Asher, A. Franz, J. Keane, L. Wang, J. Scofield, R. Noufi, *Proceedings of the First World Conference on Photovoltaic Energy Conversion*, 5–9 Dec 1994, Waikoloa, HI (IEEE, New York, 1994), p. 68
16. H. Liu, X. Shi, F. Xu, L. Zhang, W. Zhang, L. Chen, Q. Li, C. Uher, T. Day, G.J. Snyder, Nature Mat. **11**, 422 (2012)
17. J. Koh, A.S. Ferlauto, P.I. Rovira, C.R. Wronski, R.W. Collins, Appl. Phys. Lett. **75**, 2286 (1999)
18. P. Pradhan, D. Attygale, P. Aryal, N.J. Podraza, A.S. Ferlauto, S. Marsillac, R.W. Collins, *Proceedings of the 39th IEEE Photovoltaics Specialists Conference*, 16–21 June 2013, Tampa, FL (IEEE, New York, NY, 2013), p. 414
19. S. Siebentritt, L. Gütay, D. Regesch, Y. Aida, V. Deprédurand, Sol. Ener. Mater. Sol. Cells **119**, 18 (2013)
20. S. Minoura, T. Maekawa, K. Kodera, A. Nakane, S. Niki, H. Fujiwara, J. Appl. Phys. **117**, 195703 (2015)
21. M.I. Alonso, M. Garriga, C.A. Durante Rincón, E. Hernández, M. León, Appl. Phys. A **74**, 659 (2002)
22. S. Minoura, K. Kodera, T. Maekawa, K. Miyazaki, S. Niki, H. Fujiwara, J. Appl. Phys. **113**, 063505 (2013)
23. A.S. Ferlauto, G.M. Ferreira, J.M. Pearce, C.R. Wronski, R.W. Collins, X.M. Deng, G. Ganguly, J. Appl. Phys. **92**, 2424 (2002)
24. P. Aryal, D. Attygalle, P. Pradhan, N.J. Podraza, S. Marsillac, R.W. Collins, IEEE J. Photovolt. **3**, 359 (2013)
25. N.J. Podraza, C.R. Wronski, M.W. Horn, R.W. Collins, in *Amorphous and Polycrystalline Thin-Film Silicon Science and Technology—2006*, Materials Research Society Symposium Proceedings, vol. 910, ed. by S. Wagner, V. Chu, H.A. Atwater, K. Yamamoto, H.-W. Zan, (MRS, Warrendale, PA, 2006), p. 259

26. J. Li, N.J. Podraza, R.W. Collins, Phys. Stat. Sol (a) **205**, 901 (2008)
27. P. Aryal, J. Chen, Z. Huang, L.R. Dahal, M.N. Sestak, D. Attygalle, R. Jacobs, V. Ranjan, S. Marsillac, R.W. Collins, in *Proceedings of the 37th IEEE Photovoltaics Specialists Conference,* 19–24 June 2011, Seattle, WA (IEEE, New York NY, 2011), p. 2241
28. A. Nakane, H. Tampo, M. Tamakoshi, S. Fujimoto, K.M. Kim, S. Kim, H. Shibata, S. Niki, H. Fujiwara, J. Appl. Phys. **120**, 064505 (2016)
29. A.-R. Ibdah, P. Koirala, P. Aryal, P. Pradhan, S. Marsillac, A.A Rockett, N.J. Podraza, R.W. Collins, Appl. Surf. Sci. (2017). https://doi.org/10.1016/j.apsusc.2016.12.236

Chapter 12 $Cu_2ZnSn(S,Se)_4$ and Related Materials

Sukgeun Choi

Abstract $Cu_2ZnSn(S,Se)_4$ and related multinary compounds in the kesterite crystal structure are considered promising light-absorbing materials for thin-film photovoltaic (PV) device technology because of their earth abundance, desired opto-electronic properties, and non-toxic nature of constituent elements. In the past few years, spectroscopic ellipsometry (SE) has been applied to characterize the optical functions and related physical properties of this new class of PV absorber materials. This chapter presents SE-determined optical function spectra of $Cu_2ZnSn(S,Se)_4$ and related compounds and discusses associated scientific and technical issues. Detailed information on the measurement strategies is also provided, so that interested readers can adopt the same methods for their own studies.

12.1 Introduction

12.1.1 Emergence of $Cu_2ZnSn(S,Se)_4$-Based Solar Cells

Over the last few decades, significant advancements have been made in thin-film photovoltaic (PV) technologies. CdTe, $CuIn_xGa_{1-x}Se_2$, and a-Si solar cells have been recognized as the major technologies. However, concern has arisen over the inherent limit on device performance for a-Si, toxicity of Cd, and possible price escalation of the rare elements In and Te. Thus, there is interest in recruiting new absorber materials with desired opto-electronic properties and low procurement cost for next-generation thin-film solar cells.

Among a number of promising candidate materials, copper zinc tin sulfide (Cu_2ZnSnS_4)-based I_2-II-IV-VI_4 quaternary compounds have received considerable attention [1]. In fact, the PV effect in Cu_2ZnSnS_4 has been observed by Ito and Nakazawa as early as 1988 [2], and Friedlmeier et al. [3] reported a power

S. Choi (✉)
Department of Electrical and Computer Engineering, University of California, Santa Barbara, CA 93106-9560, USA
e-mail: sukgeunc@gmail.com

© Springer International Publishing AG, part of Springer Nature 2018

H. Fujiwara and R. W. Collins (eds.), *Spectroscopic Ellipsometry for Photovoltaics*, Springer Series in Optical Sciences 212,
https://doi.org/10.1007/978-3-319-75377-5_12

conversion efficiency (PCE) of 2.3% from a ZnO/n-CdS/Cu_2ZnSnS_4 device in 1997. However, studies of Cu_2ZnSnS_4 for PV device applications were rather sporadic thereafter until Todorov et al. at IBM [4] reported a 9.6%-efficiency device in 2010. The bandgap (E_0) energy spanning from ~1.0 to ~1.5 eV and large optical absorption coefficients of ~10^4 cm^{-1} make $Cu_2ZnSn(S,Se)_4$ suitable for high-performance solar cells. Furthermore, the earth-abundance of constituent elements can potentially pave a new pathway toward gigawatt (GW)-scale mass production of solar-cell panels. Despite their relatively brief history in thin-film PV, $Cu_2ZnSn(S,Se)_4$ technology has rapidly advanced and its PCE has already reached as high as 12.6% [5].

12.1.2 Fundamental Physical Properties of $Cu_2ZnSn(S,Se)_4$

$Cu_2ZnSn(S,Se)_4$ and related materials are often called *kesterite solar-cell materials* because their representative crystal structure is kesterite (KS, space group: $I\bar{4}$). However, it has been known [6] for some time that rearrangements of Cu and Zn atomic positions can result in different structural phases such as stannite (ST, space group: $I\bar{4}2m$) and primitive-mixed CuAu (PMCA, space group: $P\bar{4}2m$) phases. Figure 12.1 shows the three possible variations for the $Cu_2ZnSn(S,Se)_4$ crystal structure. It is anticipated that the optical properties for all three structures are biaxially anisotropic where the properties along the *a* and *b* directions are different from those in the *c* direction. For polycrystalline-phase $Cu_2ZnSn(S,Se)_4$ thin films, however, the grains are randomly oriented and the anisotropy generally does not become a critical problem in SE studies.

Since the results from theoretical studies suggested that the KS phase is thermodynamically stable, it has long been considered that $Cu_2ZnSn(S,Se)_4$ compounds

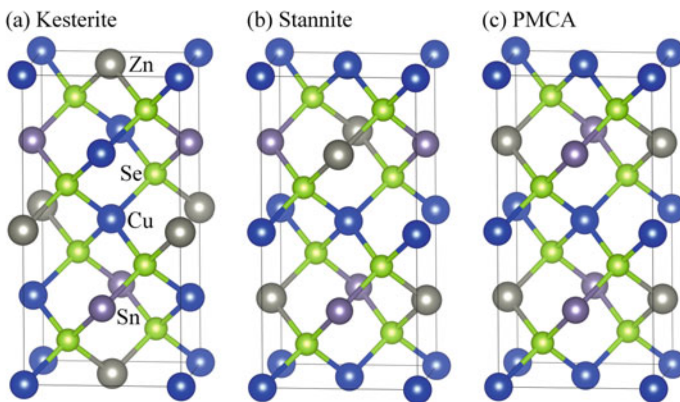

Fig. 12.1 Atomic structures of $Cu_2ZnSnSe_4$ in **a** kesterite (KS), **b** stannite (ST), and **c** primitive-mixed CuAu (PMCA) phases

form with ordered KS phase. However, it has recently been shown that the formation energies for the three phases are not much different (only a few meV/atom) [7]. Hence, even small changes in the synthesis methods and conditions can make $Cu_2ZnSn(S,Se)_4$ crystals with any of the three ordered phases (KS, ST, and PMCA) or their disordered version [8]. Indeed, it has been experimentally evidenced [9–11] that $Cu_2ZnSn(S,Se)_4$ may form in a disordered KS phase. The cation-sites disordering in $Cu_2ZnSn(S,Se)_4$ is an important issue because it may adversely influence device performance [12] by reducing the E_0 energy and extending the band tail to lower photon energy. In comparison studies with the electronic structure calculations, the ε spectra determined by SE suggest structural disorders in $Cu_2ZnSnSe_4$ [9], which will be discussed later in this chapter.

Among a number of desired characteristics for a good single-junction PV absorber material summarized in Table 12.1, optical properties of the material are of great importance. Other properties can be potentially tailored to some extent during the growth and device fabrication procedures. Accurate optical characterization of materials thus plays a crucial role in developing new PV materials. The E_0 energies of $Cu_2ZnSn(S,Se)_4$ reported in early studies show a large disagreement [13], which is in part due to (1) difference in the crystalline structure and quality of materials and (2) inconsistent interpretation of experimental data. In the last few years, the crystalline quality and our knowledge of physical and chemical properties of $Cu_2ZnSn(S,Se)_4$ have been greatly improved. The E_0 energies of Cu_2ZnSnS_4 and $Cu_2ZnSnSe_4$ are now established to be ~1.5 and ~1.0 eV, respectively.

The absorption coefficients α for $Cu_2ZnSnSe_4$ and related materials are compared in Fig. 12.2. The α values right above the E_0 are mostly in the low to mid 10^4 cm^{-1} range. More detailed information on fundamental physical properties of Cu_2ZnSnS_4 and $Cu_2ZnSnSe_4$ can be found in [18].

Figure 12.3 shows the electronic band structure of KS-phase $Cu_2ZnSnSe_4$, which was calculated by using the full-potential linearized augmented-plane wave (FPLAPW) generalized gradient approximation (GGA + U) method.

Table 12.1 Selected properties required for high-performance single-junction solar cell absorber materials

Category	Desired characteristics
Optical	• Direct bandgap (1.0–1.5 eV) • Large absorption coefficients (>10^4 cm^{-1})
Electrical	• Optimum carrier concentrations (10^{15}–10^{16} cm^{-3}) • High carrier mobilities (long carrier lifetime and large diffusion coefficients)
Structural	• Large (>1-μm) grain size • Benign grain boundaries • Phase purity • Absence of mid-gap defects
Economic/ Environmental	• Earth abundance (low procurement cost) • Non-toxic nature of constituent element
Reliability	• Long-term stability

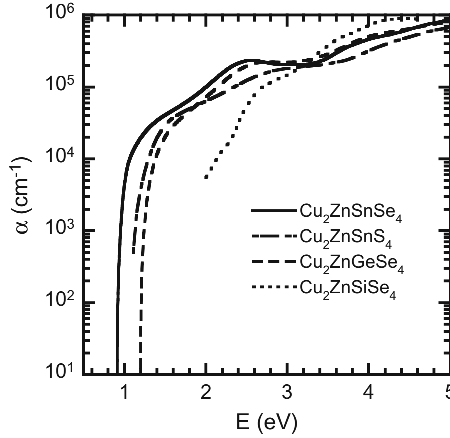

Fig. 12.2 Comparison of absorption coefficient α spectra for $Cu_2ZnSnSe_4$ [14], Cu_2ZnSnS_4 [15], $Cu_2ZnGeSe_4$ [16], and $Cu_2ZnSiSe_4$ [17] in logarithm scale

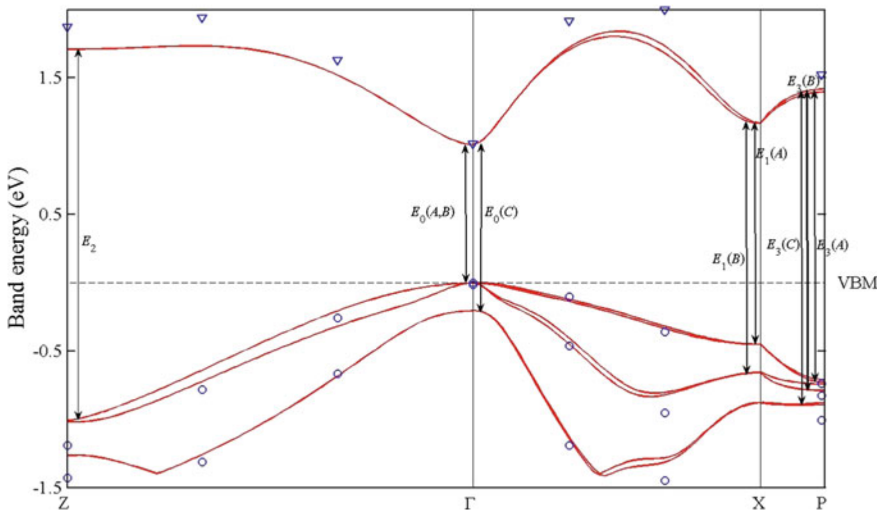

Fig. 12.3 Calculated electronic energy band structure for KS-$Cu_2ZnSnSe_4$

Open symbols are obtained from *GW* calculations. The high symmetric points Γ (0, 0, 0), Z (0, 0, 1), X (½, ½, 0), and P (½, ½, ½) are indicated. The separation of $E_0(A)$ and E_0(B) transitions is caused by crystal-field splitting (Δ_{CF}), and the $E_0(A)$ and E_0(C) transitions by spin-orbit splitting (Δ_{SO}). The Δ_{CF} values have been predicted to be −36, 84, −7, and 68 meV for KS-Cu_2ZnSnS_4, ST-Cu_2ZnSnS_4, KS-$Cu_2ZnSnSe_4$, and ST-$Cu_2ZnSnSe_4$, respectively. The Δ_{SO} values have been predicted to be −27, 24, 198, and 220 meV for KS-Cu_2ZnSnS_4, ST-Cu_2ZnSnS_4, KS-$Cu_2ZnSnSe_4$, and ST-$Cu_2ZnSnSe_4$, respectively

[19]. For KS-Cu_2ZnSnS_4, the Δ_{CF} and Δ_{SO} values are not much different. Thus, experimental data may show two transitions, $E_0(A)$ and $E_0(B, C)$, or a single transition $E_0(A, B, C)$ depending on the spectral resolution. On the other hand, KS-$Cu_2ZnSnSe_4$ exhibits a Δ_{SO} value 10 times larger than KS-Cu_2ZnSnS_4 but a very small Δ_{CF} value, which can result in the observation of $E_0(A, B)$ and $E_0(C)$ transitions in experiments, as implied in Fig. 12.3. Details of the electronic structures of $Cu_2ZnSnSe_4$ and Cu_2ZnSnS_4 are given in [19].

12.1.3 Spectroscopic Ellipsometric Studies of $Cu_2ZnSn(S,Se)_4$ and Related Compounds

Accurate knowledge of the optical properties of materials is very important for (1) designing PV device structures [20, 21], (2) modeling the device performance [22, 23], and (3) better understanding the electronic structure of the absorber materials [24]. SE has thus been used to study a wide variety of PV materials and devices, which is well addressed throughout this book. For $Cu_2ZnSn(S,Se)_4$ and related compounds, numerous SE studies have been reported, some of which are introduced in this chapter. The scope of reported studies ranged from determination of optical function spectra to investigation of energy band structures. Various spectral analysis methods were employed, which include the standard lineshape analysis of second-energy-derivative data, Adachi's Model Dielectric Function approach, and general oscillator model. Details of the lineshape analysis method and general oscillator models are given in Chaps. 4 and 5, respectively.

12.2 Strategies in Sample Preparation

The primary goal of this chapter is to provide fundamental optical function data and discuss associated physics problems for $Cu_2ZnSn(S,Se)_4$-based PV materials. To achieve this goal, however, accurate data acquisition is a prerequisite. Some of the materials presented in this chapter have been measured with special preparation procedures of the film/substrate interface and film surface to improve data quality and make the data modeling procedure simpler. Thus, brief descriptions of the sample preparation methods need to be given. In this section, I first introduce the *pseudobulk* method, which makes a semiconductor thin film optically a bulk crystal. This trick is particularly useful when one needs optical function data near the E_0 without the complicated multilayer analysis procedures. SE is known to be a surface sensitive technique. While the high surface sensitivity certainly makes SE a very powerful technique for real-time monitoring of physical and chemical changes on the surface of a material, it adversely affects the accuracy of the bulk optical

properties when the surface overlayers present. I next discuss chemomechanical polishing procedures that reduce artifacts from the surface-overlayers in the SE data. In principle, the strategies introduced in this section can also be applied to other polycrystalline thin-film materials.

12.2.1 Pseudobulk Approach

In optical characterization of thin-film materials grown on flat substrates using SE, the light is reflected from the film/substrate interface as well as the front surface of film. If the substrate is optically transparent (such as a glass) and its backside is flat, then the light is also reflected from the backside. But, for the sake of simplicity, let us assume that the backside reflections have been experimentally suppressed by known methods [25].

The light reflected from the film surface and film/substrate interface interfere with each other, which generates oscillations below the E_0 of the film material. If the absorption coefficients are small and the film is thin, the oscillations are seen even in the above-E_0 energy region. When the optical information on both substrate and film are available, the oscillations can be removed mathematically by the multilayer analysis. In reality, however, a number of non-ideality factors may exist, which include (1) possible formation of unknown thin layer at the film/substrate interface, (2) variation of the film thickness, and (3) complicated optical nature of the substrate material such as anisotropy and inhomogeneity. Consequently, accurate determination of the near-E_0 optical function data often becomes a non-trivial task and the model-determined E_0 energy can be somewhat influenced by the type of model functions and initial fitting parameters.

A direct method has recently been developed although it is still rather empirical. Here, the front surface of substrate is first mechanically roughened using abrasive alumina powder followed by the deposition of a film on top of it. During SE measurements, the incident beam travelling through the thin film backscatters in arbitrary directions at the rough film/substrate interface, which suppresses the secondary reflections to the detector. As a result, the thin film now becomes a "pseudobulk" with a semi-infinite optical thickness, and the absorption edge can be clearly seen without being obscured by thickness fringes. Figure 12.4 compares the schematics and the imaginary part of the corresponding *pseudodielectric function* $<\varepsilon> = <\varepsilon_1> - i<\varepsilon_2>$ spectra, which are simulated, of a-Si on three different structures of glass substrate—(a) standard flat surfaces, (b) suppression of backside reflection (roughened backside), and (c) pseudobulk approach (roughened front side).

However, some drawbacks also exist. First, the thin-film characteristic is completely lost and no film thickness information can be obtained. Second, for variable-angle SE measurements of thin films, it is known [26] that the accuracy of modeling can be improved when transmittance data are tied with SE results, which is unfortunately not an option here. Third, the film needs to be thicker than at least

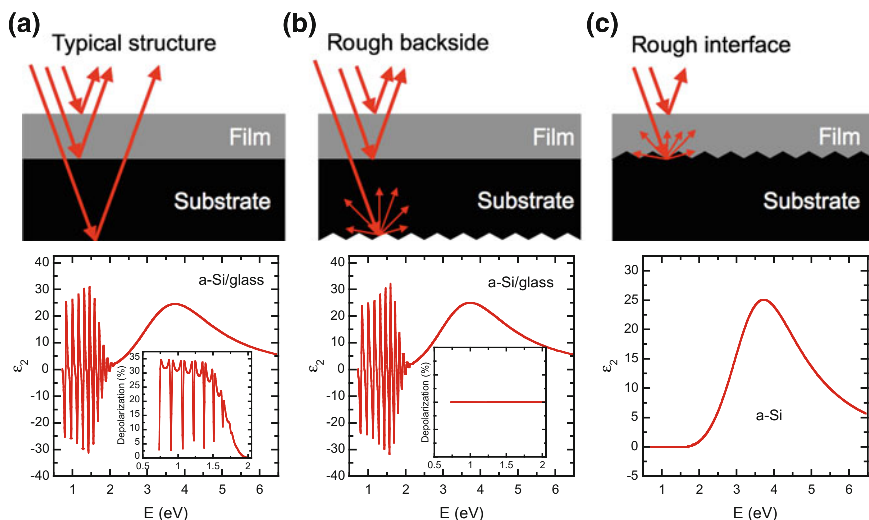

Fig. 12.4 Comparison of the simulated <ε_2> spectra of a-Si/glass in three structures (Insets for **a** and **b**: Depolarization spectra). **a** Typical flat surfaces: Both thickness fringes and incoherent backside reflection (causing depolarization) present. **b** Suppression of backside reflection: Thickness fringes still exist owing to the interference of reflections from surface and film/substrate interface, but the depolarization is avoided. **c** Pseudobulk method: The probing light reaching the film/substrate interface is not collected by the detector. Thickness fringe and depolarization do not show

the vertical roughness of the substrate. Otherwise, the reflected light may contain the information from both film and substrate. Fourth, the pseudobulk approach may not be applicable for single-crystalline epitaxial growth.

It is also noted that the level of surface roughness needs to be carefully controlled by selecting the optimum particle size of abrasive powders. Small roughness makes the light reflected from the film/substrate interface still affect the SE data, and effective-medium approximation (EMA) [27] will need to be considered. On the other hand, if the roughness is too big, a very thick film needs to be grown to completely cover the macroscopically roughed substrate surface.

12.2.2 Chemomechanical Polishing

Characterization or removal of surface overlayer has long been one of the key subjects in SE studies. The surface overlayer generally appears in the form of microscopic roughness, native oxides, organic contaminants, or a combination of the preceding. Presence of a thick surface overlayer usually weakens the ε_2 especially in the high-energy region and also results in nonzero ε_2 below the E_0. Two approaches have been developed to reduce the artifacts in SE data from surface

overlayers: Aspnes has developed an in situ wet chemical etching method [28] to remove the overlayers to the maximum extent possible, which is particularly useful when the identity and properties of the overlayer are unknown. When the optical information of the overlayer is already available (such as the native oxides of Si), the overlayer artifacts can be mathematically corrected by the multilayer analysis.

Surface roughness of $Cu_2ZnSn(S,Se)_4$ thin films varies from sample to sample, which also depends on the growth methods. For the films prepared by the co-evaporation method, roughness of the as-grown surface is typically 60 nm or larger [9]. Such a large surface roughness makes the film less reflective and thus worsens the signal-to-noise ratio in the measured data. In an attempt to improve surface quality sufficient for SE characterization, the film surface has been chemomechanically polished which resulted in the root-mean-square roughness of 3 nm or smaller [9]. Figure 12.5a, b show the atomic force microscopic images of the surface for $Cu_2ZnSnSe_4$ thin film before and after the chemomechanical polishing, respectively. The corresponding $<\varepsilon_2>$ spectra are presented in Fig. 12.5c.

Chemomechanical polishing (or chemomechanical planarization) equipment is available commercially. A wide variety of polishing pads (either abrasive discs or polishing cloths) and polishing slurries (alumina and colloidal silica suspensions for example) exist, and the selection of products should be made depending on the

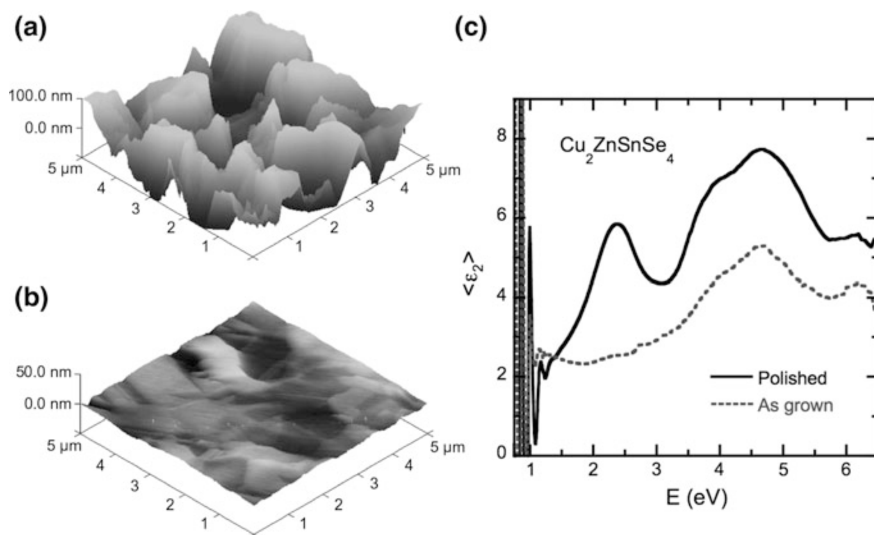

Fig. 12.5 Atomic force microscopic images of $Cu_2ZnSnSe_4$ film **a** before and **b** after the chemomechanical polishing. The estimated surface roughness for "as grown" and "polished" surfaces are 70.9 and 2.7 nm, respectively. **c** Effects of chemomechanical polishing on the $<\varepsilon_2>$ spectrum of $Cu_2ZnSnSe_4$. Data for the polished and as-grown surface are represented by solid and dotted lines, respectively. The polishing procedure clearly improved the data and more optical structures are better resolved

initial roughness of the surface and hardness of the material. For the $Cu_2ZnSnSe_4$ film shown in Fig. 12.5, a non-crystallizing colloidal silica suspension with 0.05-μm particles and a high-density, non-woven, low-nap porous polyurethane polishing cloth have been used. The revolution-per-minute (RPM) value of the polishing wheel was 200. At this speed, a highly reflective surface of $Cu_2ZnSnSe_4$ can be achieved after 30 s–3 min of polishing depending on the initial surface roughness. It is noted that the colloidal silica particles are typically suspended in a liquid of ~10 pH. Thus, some specific elements or compounds may be preferentially removed during the chemomechanical polishing process.

Pseudobulk and chemomechanical polishing methods have been used in the studies discussed in Sects. 12.3.1 ($Cu_2ZnSnSe_4$), 12.4.1 ($Cu_2ZnGeSe_4$), and 12.4.3 (Cu_2SnSe_3).

12.3 Studies of $Cu_2ZnSnSe_4$ and Cu_2ZnSnS_4

12.3.1 $Cu_2ZnSnSe_4$

$Cu_2ZnSnSe_4$ has been studied by SE over wide photon energies ranging from 0.5 to 9.0 eV using a vacuum-ultraviolet (VUV) ellipsometer [9]. Chemomechanical polishing followed by wet-chemical etching with a 50 vol% solution of NH_4OH in deionized water rendered the $<\varepsilon>$ data least influenced by surface overlayers, which was verified by X-ray photoemission spectroscopic (XPS) analysis. Seven spectral features related to the electronic band-to-band transitions were observed in the SE data, and their electronic origins were identified based on the results from the calculations within the *GW* quasi-particle approximation. However, the $Cu_2ZnSnSe_4$ film used in [9] has been grown on a soda-lime glass substrate coated with Mo. Therefore, the optical properties near the E_0 could not be studied thoroughly for the reasons explained in Sect. 12.2.1. Later, the pseudobulk approach was employed in their study and temperature-dependent E_0 energy of $Cu_2ZnSnSe_4$ was obtained [14]. Figure 12.6 shows the cross-sectional scanning electron microscopic (SEM) image of the $Cu_2ZnSnSe_4$ thin film that has been grown on the

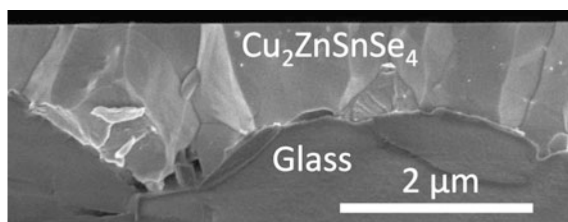

Fig. 12.6 Cross-sectional SEM image of $Cu_2ZnSnSe_4$ film prepared by the pseudobulk method. The film surface was chemomechanically polished. The structure resembles the schematic shown in Fig. 12.4c

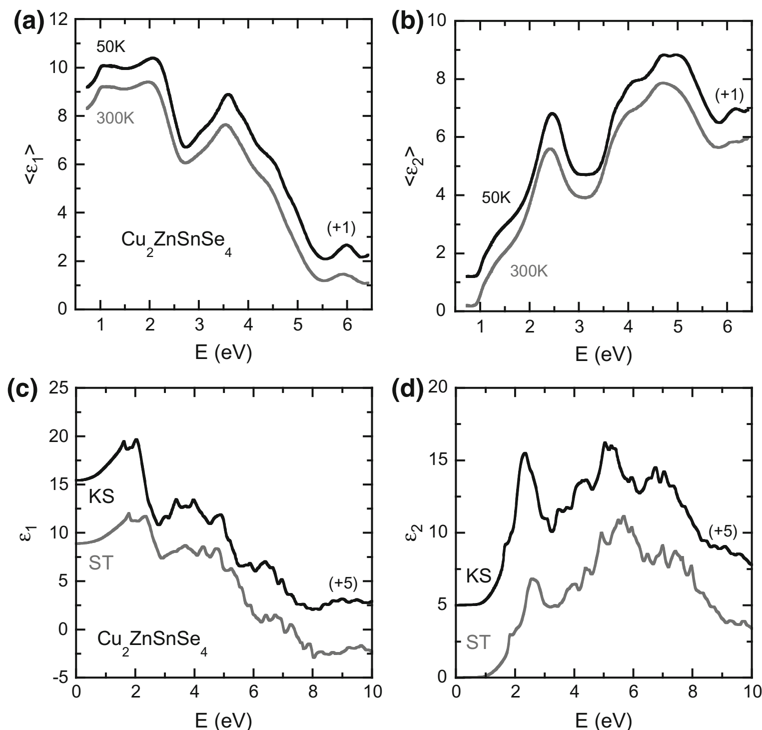

Fig. 12.7 Real (**a**) and imaginary (**b**) parts of the SE-determined <*ε*> spectra for $Cu_2ZnSnSe_4$ taken at 50 and 300 K. For clarity, the 50 K spectra are offset upward by 1. Real (**c**) and imaginary (**d**) parts of the calculated ε spectra for $Cu_2ZnSnSe_4$ with the kesterite (KS) and stannite (ST) phases. The KS-phase data are offset upward by 5 in (**c**) and (**d**). *Note* The experimental spectra ((a) and (b)) are limited at ~6.5 eV whereas the calculated data cover up to 10 eV

roughened surface of a glass substrate followed by chemomechanical polishing. To roughen the glass surface, 9-μm-diameter Al_2O_3 particles have been used, which resulted in a surface roughness of 530 nm determined by a 50 × 50 μm^2 scale atomic force microscopic analysis.

Real $<\varepsilon_1>$ and imaginary $<\varepsilon_2>$ parts of $<\varepsilon>$ spectra for $Cu_2ZnSnSe_4$ recorded at 50 K and 300 K are presented, respectively, in Fig. 12.7a, b. It is noted that the 50 K spectra are moved upward by 1. The optical structures, especially appeared in the photon energies between 3.5 and 6.0 eV, are better resolved in the data acquired at 50 K. Application of the pseudobulk method and post-growth chemomechanical polishing of the surface render the clear observation of bandgap onset in the $<\varepsilon_2>$ data without the multilayer analysis. The $<\varepsilon>$ spectra taken at 300 K agree well with the results reported by others [29–31]. Hirate et al. [31] studied $Cu_2ZnSnSe_4$ thin films (<50 nm) grown on Si substrates at 370 °C. The surface roughness for such thin films was small enough (<19 nm) to directly apply the multilayer model and they obtained the optical function spectra of $Cu_2ZnSnSe_4$

without post-growth surface polishing procedures. Their model-determined E_0 energy seems slightly smaller than the value determined in the study with the pseudobulk approach. The observed discrepancy may be caused in part by the difference in the structural properties, as the thin films used in [31] have been grown at a much lower temperature than the co-deposition process adopted in [9, 14] ($T_g \sim 500$ °C). In addition, the modeled ψ and Δ spectra appeared slightly off from the experimental data below 3 eV, which possibly had a minor effect on the model-determined E_0 value as well.

For comparison, the calculated ε spectra of $Cu_2ZnSnSe_4$ with the KS and ST structures are also given in Fig. 12.7c, d. Here, the ε components in the a, b, and c axes are averaged mathematically (i.e., $[\varepsilon_a + \varepsilon_b + \varepsilon_c]/3$) to better describe the ε data of the polycrystal-phase material. The agreement between the $<\varepsilon>$ spectra and calculated ε data is overall very reasonable.

Figures 12.7b, d show that the ε_2 spectra consist of a distinct feature at ~2.5 eV and a main broad structure starting from ~4.0 eV. It is interesting to notice in Fig. 12.7d that the amplitude of the feature at ~2.5 eV is clearly weaker than that of the main broad structure for the ST phase. However, the results of calculations suggest that the same structure for the KS phase appears as strong as the main broad feature. In this regard, SE-determined $<\varepsilon_2>$ spectra shown in Fig. 12.7b look similar to the ST-phase data rather than the KS-phase one, which implies that the $Cu_2ZnSnSe_4$ film may not form with the pure (ordered) KS-phase.

To obtain accurate interband-transition critical point (CP) energies and their temperature dependence, the second-energy-derivative $d^2<\varepsilon>/dE^2$ spectra were calculated numerically using the Savitzky-Golay type linear filtering algorithm [32]. The transition energies are obtained by fitting the $d^2<\varepsilon>/dE^2$ data to the standard CP lineshape expressions [33, 34]:

$$\frac{d^2\varepsilon}{dE^2} = \begin{cases} n(n-1)Ae^{i\Phi}(E-E_0+i\Gamma)^{n-2}, & n \neq 0 \\ Ae^{i\Phi}(E-E_0+i\Gamma)^{-2}, & n = 0 \end{cases} \tag{12.1}$$

where A is the amplitude, E_0 is the threshold energy, Γ is the broadening parameter, and Φ is the excitonic phase angle. The exponent n has the values −1, −½, 0, and +½ for excitonic, one-, two-, and three-dimensional lineshapes, respectively. Details of the standard lineshape analysis method are given in Chap. 4.

Figure 12.8 shows the calculated $d^2<\varepsilon>/dE^2$ data taken at 50 K with the best-fit curves from 0.75 to 5.0 eV. The open circles represent $d^2<\varepsilon_1>/dE^2$ calculated numerically from the SE data. For clarity, $d^2<\varepsilon_2>/dE^2$ results are not shown, but the quality of the fits is similar. The solid and dash-dotted lines are the best-fit curves for the real and imaginary parts, respectively. Optical structures are better resolved in the derivative spectra and the presence of $E_0(A, B)$ and E_0(C) CPs are obvious. As discussed in Sect. 12.1.2, the Δ_{CF} value of 7 meV is beyond the limit of spectral resolution in this study, and thus the $E_0(A)$ and $E_0(B)$ appear as a singlet. However, the predicted Δ_{SO} value of 0.2 eV is large enough to observe, which is indeed clearly seen in Fig. 12.8. The fit-determined CP energies for $Cu_2ZnSnSe_4$ at 50 K are listed in Table 12.2. It is noted that the low-temperature data resolved six CP structures between 2.0 and 5.0 eV

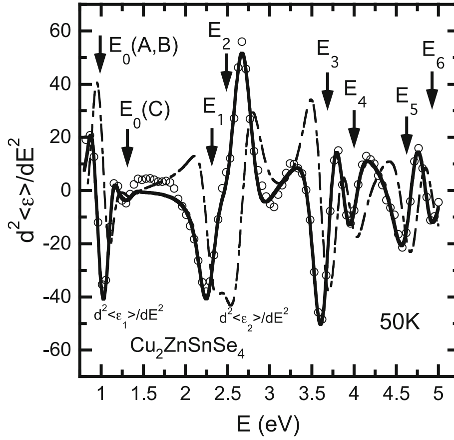

Fig. 12.8 Best-fit curves for the d^2<ε_1>/dE^2 (solid line) and d^2<ε_2>/dE^2 (dash-dotted line) of $Cu_2ZnSnSe_4$ at 50 K. Open circles represent the data for d^2<ε_1>/dE^2. To show the quality of the fits clearly, only 20% of the data points are shown and the d^2<ε_2>/dE^2 are not displayed. Energies of each CP are indicated by arrows and labeled in a numeric order

Table 12.2 Critical-point energies in eV for $Cu_2ZnSnSe_4$ at 50 K

CP	$E_0(A, B)$	$E_0(C)$	E_1	E_2	E_3	E_4	E_5	E_6
E (eV)	0.99	1.30	2.28	2.67	3.65	3.94	4.69	4.85

(above-bandgap CP structures) whereas only four CP structures have been found in the room-temperature d^2<ε>/dE^2 spectra of [9] in the same spectral range.

The data were fitted to the single Bose-Einstein oscillators in order to obtain temperature dependencies of the $E_0(A, B)$ and $E_0(C)$ energies. The oscillators are described by [35]:

$$E(T) = E(0) - a\left[1 + \frac{2}{\exp[\Theta/T] - 1}\right] \tag{12.2}$$

where $E(0)$ represents the zero-temperature energy, and a is a fitting variable related to the strength of electron-phonon interactions. Θ is the average energy of phonons divided by the Boltzmann constant k_B. Figure 12.9 shows experimental data (filled dots) together with best-fit lines (solid lines). The fit-determined parameters $E(0)$, a, and Θ are listed in Table 12.3.

While the decrease of E_0 energy with increasing temperature is consistent with the cases for many semiconducting materials [36], the amount of change was found to be relatively small for $Cu_2ZnSnSe_4$. For semiconductors, there are two major factors influencing the temperature dependence of E_0 energy: (1) the variation of bond length with the changes of unit-cell volume and (2) the variation of

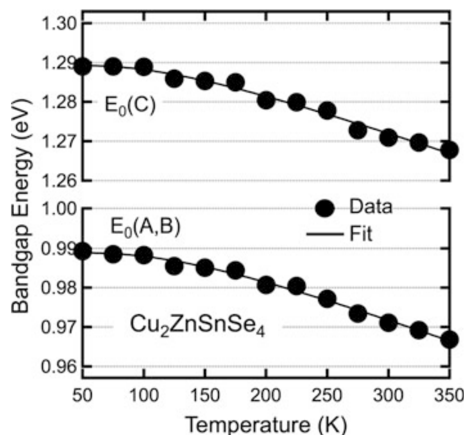

Fig. 12.9 Temperature dependencies of the $E_0(A, B)$ and $E_0(C)$ energies in the temperature range between 50 and 350 K [14]. Filled dots represent the transition energies as shown in Fig. 12.5, and solid lines are the best fits of energies to the single Bose-Einstein oscillator

Table 12.3 Fit-determined Bose-Einstein oscillator parameters $E(0)$, a, and Θ for the $E_0(A, B)$ and $E_0(C)$ CP energies

CP	E_0 (eV)	a (eV)	Θ (K)	Lineshape
$E_0(A, B)$	1.01 ± 0.01	0.02 ± 0.01	397.8 ± 54.7	2-D Min.
$E_0(C)$	1.31 ± 0.01	0.02 ± 0.01	365.6 ± 70.3	3-D M_2

interactions between electrons and phonons [37]. Wei et al. have shown that the volume deformation does not significantly change the E_0 energy of Cu-containing chalcopyrite-phase materials including $CuIn_{1-x}Ga_xSe_2$, while the effect is more apparent for zinc-blende semiconductors [38]. The difference can be attributed to the relatively large structural freedom in chalcopyrite-phase semiconductors. Since the change in the internal coordinate of the cell u can adjust the bond lengths, the change in volume does not play a major role. Moreover, Cu-containing semiconductors possess a large coupling of anion-p and Cu-d states, and the large coupling effectively cancels the change in unit-cell volume because the sign of two effects are opposite. A weak dependence of transition energies on temperature has indeed been experimentally observed for $CuIn_{1-x}Ga_xSe_2$ [38]. As the two material systems exhibit similar structural and opto-electronic properties, it is not surprising to find that $Cu_2ZnSnSe_4$ also shows a weak dependence of the $E_0(A, B)$ and $E_0(C)$ transition energies on temperature. In fact, a recent electroreflectance study of $Cu_2ZnSnSe_4$ [39] shows a similar result on the temperature dependence of E_0 transition energy, where the overall shift of E_0 energy was found to be only ~13 meV between 100 and 300 K.

$Cu_2ZnSnSe_4$ possesses a strong ionic characteristic, which in part explains the observed relatively weak electron-phonon interaction (the small a value in

Table 12.3). For $Cu_2ZnSnSe_4$, the *s*-*s* coupling and *p*-*p* coupling are both weak, which are associated with the volume change at the conduction-band minimum and the valence-band maximum, respectively. The volume change at the valence-band maximum is further reduced by a large anion-*p* and Cu-*d* coupling because the effects of the *p*-*d* coupling and normal *p*-*p* coupling are against each other.

As shown in Fig. 12.9, the E_0 energies are nearly temperature independent in the temperature range below 100 K but they change relatively fast at higher temperature. This is probably due to the fact that the number of available phonons is limited at low temperature. Also, the dependence of E_0 on temperature is largely governed by the volume and *p*-*d* coupling, but the effects are negligible as the two components cancel each other. At higher temperature, however, more phonons are available, which makes the electron-phonon interaction stronger. Therefore, the temperature dependence of E_0 becomes more apparent at high temperature.

It is important to identify the electronic origins of the above-bandgap optical structures shown in the ε spectrum to better understand the electronic structure of materials and the relative strength of interband transitions, which is typically done by comparing the calculated spectra and experimental data [9, 31]. One prominent structure appears at around 2.5 eV (E_1 and E_2 transitions in Fig. 12.8), which is reported to consist of $\mathrm{Cu}\left(3d_{xz}+3d_{yz}\right)\rightarrow \mathrm{Se}(4p_z)$, $\mathrm{Se}(4p_x+4p_y)\rightarrow \mathrm{Cu}\left(3d_{z^2}+3d_{x^2-y^2}\right)$, and $\mathrm{Se}(4p_x + 4p_y) \rightarrow \mathrm{Sn}(5s)$ transitions. The net effect is that the Cu(3*d*) electronics in the uppermost two valence bands are excited to the Sn (5*s*) orbital in the lowest conduction band. The E_3 transition at 3.65 eV involves the $\mathrm{Cu}(3d_{xy} + 3d_{xz}) \rightarrow \mathrm{Sn}(5p_x)$, $\mathrm{Cu}(3d_{xy} + 3d_{yz}) \rightarrow \mathrm{Sn}(5p_z)$, and $\mathrm{Cu}(3d_{yz} + 3d_{xz}) \rightarrow \mathrm{Sn}(5p_z)$ transitions with the net result of $\mathrm{Cu}(3d) \rightarrow \mathrm{Sn}(5p)$. The E_4 transition at 3.94 eV contains the $\mathrm{Cu}(3d) \rightarrow \mathrm{Sn}(5s)$ transition occurring at the Z-point of the Brillouin zone (BZ). The Cu(3*d*) state in $Cu_2ZnSnSe_4$ is expected to span over a wide energy range of the upper valence band and split into two peaks in the density of states spectrum owing to the *p*-*d* repulsion. The E_4 transition is corresponding to the lower Cu(3*d*) peak to Sn(5*s*) state. Other possible contributions include $\mathrm{Cu}(3d_{xy} + 3d_{xz}) \rightarrow \mathrm{Sn}(5p_x)$ and $\mathrm{Cu}(3d_{xy} + 3d_{yz}) \rightarrow \mathrm{Sn}(5p_y)$ occurring at the Γ-point of the BZ. High-energy transitions E_5 and E_6 contain numerous contributions over a wide region of the BZ. Due to the close locations of multiple transitions, it is challenging to unambiguously identify the origins of those transitions.

12.3.2 Cu_2ZnSnS_4

Optical properties of Cu_2ZnSnS_4 have also been determined by Levcenko et al. [40]. They reported the ε, N, and α spectra in the spectral range of 0.8–4.7 eV. Using the Model Dielectric Function method developed by Adachi and Taguchi [41], they obtained the E_0 energy of 1.44 eV, which agrees well with the theoretically predicted value of ~1.5 eV [19], and two above-bandgap CP structures at 2.82 and 3.86 eV.

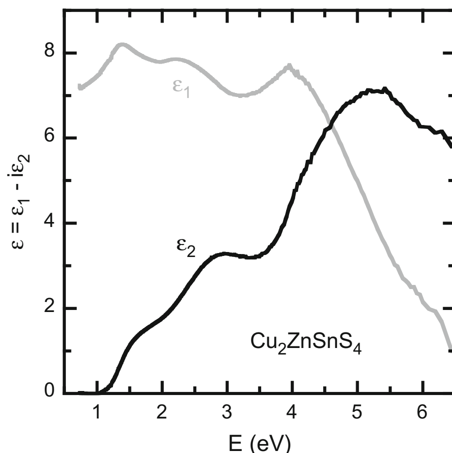

Fig. 12.10 Real (light gray) and imaginary (black) parts of the ε spectrum of Cu_2ZnSnS_4 [15]

Li and coworkers [42] developed the two-side measurement approach to better model the surface overlayers and extract accurate optical function data of a polycrystalline Cu_2ZnSnS_4 thin film grown on a fused quartz substrate over the extended photon energies ranging from 0.73 to 6.5 eV. The ε spectrum of Cu_2ZnSnS_4 obtained by the direct numerical inversion is presented in Fig. 12.10. By analyzing the lineshapes of $d^2\langle\varepsilon\rangle/dE^2$ spectra, they obtained the E_0 energy of 1.32 eV and four above-bandgap CP energies at 2.92, 3.92, 4.96, and 5.62 eV.

Crovetto et al. [15] studied Cu_2ZnSnS_4 thin layers grown by pulsed-laser deposition technique at various growth temperatures. They found that the surface overlayer of Cu_2ZnSnS_4 consists of complicated surface topography and a mix of different phases that is distinguished from the underlying Cu_2ZnSnS_4. The observation of a complex Cu_2ZnSnS_4 surface overlayer is consistent with the results from [15]. They also observed that Cu_2ZnSnS_4 films formed in the amorphous phase at the growth temperature of 25 °C, whereas the films grown at high temperature (425 °C) exhibited better crystalline quality but apparently experienced the phase separation.

Dependencies of the E_0 (1.51 eV) and two above-bandgap CP energies of Cu_2ZnSnS_4 on temperature have been investigated by Li et al. [43] from transmittance measurements over a wide temperature range of 8–300 K. The data were analyzed with the Bose-Einstein model (12.2), and the a and Θ parameters for the E_0 were determined to be 55.9 meV and 523 K, respectively. The a parameter of 55.9 meV for Cu_2ZnSnS_4 is a few times larger than that for $Cu_2ZnSnSe_4$ (~20 meV) [14]. The observed difference in the a parameters between Cu_2ZnSnS_4 and $Cu_2ZnSnSe_4$ is somewhat expected. S-containing compounds generally exhibit a higher phonon frequency than the corresponding Se-containing ones. Therefore, a larger Θ value is expected for S-containing compounds although the two compounds show similar $dE(T)/dT$ values. A similar trend has been observed for the a parameter between $CuGaSe_2$ (23 meV) [44] and $CuGaS_2$ (54–88 meV) [45].

12.4 Studies of Other Related Compounds

Even though the kesterite solar cell technology has been developed from $Cu_2ZnSn(S,Se)_4$, alteration of chemical elements would be beneficial for optimizing material properties and simplifying synthesis/fabrication procedures, which will further enhance device performance and reduce manufacturing cost. For some of the alternative compounds, SE has been used not only to obtain the optical function data but also to better understand the electronic energy band structure and related physical properties of the kesterite materials system.

12.4.1 $Cu_2ZnGeSe_4$

$Cu_2ZnSnSe_4$ solar cells have recently shown a rapidly increasing PCE, but the record PCE of 11.6% [46] is still much lower than those of CdTe (22.1%) and $CuInGaSe_2$ (22.6%) devices [47]. The E_0 energy suitable for a PV absorber material is known to lie between 1.1 and 1.4 eV [48]. Thus, it has been of great interest to increase the E_0 (~1.0 eV) of $Cu_2ZnSnSe_4$. Among a number of options available, alloying $Cu_2ZnSnSe_4$ with S to form $Cu_2ZnSnS_xSe_{4-x}$ has been the most successful, which indeed enhanced the PCE to 12.6% [5]. $Cu_2ZnGeSe_4$ formed by replacing Sn in $Cu_2ZnSnSe_4$ with Ge can be an alternative way of increasing E_0. There are also some additional advantages:

- The formation energies for (Sn, Ge) compounds are lower than the (Se, S) compounds.
- Addition of Ge increases the E_0 energy as a result of lifting the conduction-band minimum upward whereas 30% increase of the E_0 energy with S alloying is achieved by lowering the valence-band maximum. These two different alloying approaches result in similar E_0 energy values but different conduction-band offsets to the buffer layer, from which the carrier recombination mechanisms at the interface between buffer and absorber layers can be better examined.
- The increase of E_0 can be achieved without formation of an unwanted ZnS secondary phase.

In the SE study of $Cu_2ZnGeSe_4$ reported in [49], a 4.3-μm-thick polycrystalline film has been grown on a mechanically roughened surface of soda-lime glass by thermal co-evaporation method with elemental Cu, Zn, Ge, and Se as source materials. Room-temperature VUV-SE spectra were recorded over a wide spectral range between 0.7 and 9.0 eV with the spectral resolution of 0.01 eV. The angle of incidence was 70°.

Figure 12.11 shows the results. The three-phase model has been employed to analyze SE data, which consists of the ambient, a surface-layer (a 3.1-Å-thick Bruggeman EMA layer), and the $Cu_2ZnGeSe_4$ crystal. The model structure is essentially the same as the case for bulk specimen. Unlike the typical multilayer

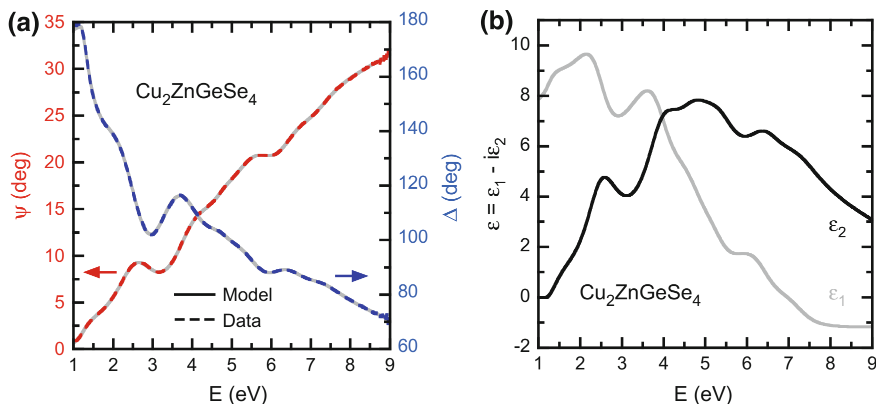

Fig. 12.11 **a** Dashed lines are experimental data and solid lines represent the best-fit curves for ψ and Δ of $Cu_2ZnGeSe_4$. **b** The real (light gray) and imaginary (black) parts of modeled ε spectrum [16]

analysis procedure, we need neither optical information of substrate nor thickness of $Cu_2ZnGeSe_4$ film here. The rough film-substrate interface does not generate coherent reflections back to the optics component as explained in Sect. 12.2.1. The modeled ε spectrum of $Cu_2ZnGeSe_4$ consists of eight Tauc-Lorentz (T-L) oscillators. Figure 12.11b displays the ε spectrum that is in a good agreement with the results from the SE study [16] of a $Cu_2ZnGeSe_4$ bulk polycrystal (1.2–4.6 eV) and the predictions made by electronic structure calculations [17]. The spectroscopic feature appeared at around 2.5 eV is originated mainly from the transition from the Cu 3*d*–Se 4*p* anti-bonding states in the valence band to the Ge 5*s*–Se 4*p* anti-bonding states in the conduction band. As a matter of fact, this particular structure is a characteristic feature in the optical function spectra for $Cu_2ZnSnSe_4$ and related compounds.

The fit-determined E_0 energy of 1.25 eV for $Cu_2ZnGeSe_4$ appears slightly smaller than the theoretically predicted value of 1.5 eV [50] and the result (1.41 eV) from the other SE study [17]. As in the case of other kesterite solar cell materials, however, a large discrepancy has been found [16] among the experimentally determined E_0 energies of $Cu_2ZnGeSe_4$, which vary from 1.29 to 1.6 eV.

12.4.2 $Cu_2ZnSiSe_4$

In the previous section, we discussed the replacement of Sn with Ge as one way to increase the E_0 of $Cu_2ZnSnSe_4$. In general, Si-containing compounds exhibit larger E_0 than the same compound with Ge. Thus, the E_0 of $Cu_2ZnSnSe_4$ can also be optimized by using even smaller amounts of Si than Ge. It should be noted, however, that the Si-Se binary compound is metastable and reacts violently with

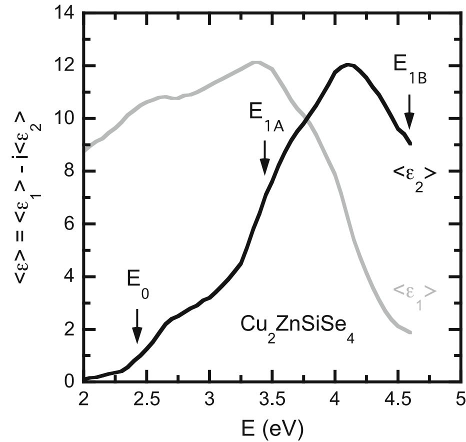

Fig. 12.12 Real (light gray) and imaginary (black) parts of the <ε> spectrum of $Cu_2ZnSiSe_4$, which are digitized from [17]

H_2O, which produces highly toxic H_2Se. Therefore, vacuum deposition of $Cu_2Zn(Sn_{1-x}Si_x)Se_4$ thin films should be carefully planned and carried out.

León et al. [17] studied optical properties of $Cu_2ZnSiSe_4$ bulk crystal using SE over the photon-energy range from 1.2 to 4.6 eV. Figure 12.12 shows the real and imaginary parts of <ε> for $Cu_2ZnSiSe_4$ digitized from [17]. The vertical arrows indicate the model-determined energies of three optical transitions, E_0 = 2.42 eV, E_{1A} = 3.44 eV, and E_{1B} = 4.59 eV. Apparently, the E_0 of 2.42 eV is too large for a single-junction PV absorber material. However, this result suggests that only 9 atomic % of Si is needed in $Cu_2Zn(Sn_{1-x}Si_x)Se_4$ solid solution to obtain E_0 of 1.1 eV when the bandgap bowing is not considered.

A non-zero <ε_2> value below the E_0 is probably due to the residual surface overlayers. Although chemomechanical polishing of the surface has been performed, which is similar to the method described in Sect. 12.2.2, a small amount of microscopic roughness may still exist or the surface can be quickly re-contaminated depending on the chemical nature of constituent elements. Nevertheless, it is known [51] that effects of surface overlayers on the determination of CP energies are insignificant. Therefore, the reported CP energies are valid.

12.4.3 Cu_2SnSe_3

The presence of unwanted secondary phases is one of the technical challenges in the development of quaternary or quinary $Cu_2ZnSn(S,Se)_4$-based PV devices. Ternary alternatives with similar material properties may lighten this problem. For example, a diamond-like I_2-IV-V_3 ternary compound, Cu_2SnSe_3 was considered a potential PV absorber material [52, 53]. This idea was driven in part by its reported E_0 energy of 0.84 eV [54] that does not deviate much from the optimum E_0 energy range of 1.1 to 1.4 eV for single-junction solar cells. However, the results from electronic

structure calculations predict that the E_0 of Cu_2SnSe_3 is much smaller, 0.35–0.4 eV [55, 56].

Two recent SE studies [31, 57] of Cu_2SnSe_3 support the results from theoretical studies. Fit-determined E_0 energy for a thick monoclinic-phase film and a thin cubic-phase film are 0.49 and 0.68 eV, respectively. For those two SE studies, two different instruments were used to take data in the spectral ranges of visible/ultraviolet and infrared separately, so that the E_0 lying in the low-energy region was clearly resolved. In [58], the pseudobulk method and chemomechanical polishing procedures were adopted. Figure 12.13 shows real and imaginary parts of the ε spectrum modeled with nine Tauc-Lorentz oscillators for monoclinic-phase Cu_2SnSe_3 from 0.30 to 6.45 eV, where the artifacts from a 4.1-nm-thick residual surface overlayer was mathematically corrected using the Bruggeman EMA. Owing to the polycrystalline nature of the sample with no preferential orientation of grains used in this study, anisotropy was not observed. Therefore, the ε spectrum shown in Fig. 12.13 can be regarded as a mathematical average of three ε spectral components for a monoclinic-phase crystal.

Overall, the ε spectrum shown in Fig. 12.13 is similar to that reported in [31]. However, one clear difference exists between the two data sets, which is the strong free-carrier absorption observed in [31]. By analyzing data with the conventional Drude formula, the authors extracted the carrier concentration of 1.6×10^{20} cm^{-3} for the 20-nm-thick film and 2.5×10^{19} cm^{-3} for the 60-nm-thick film. The optimum carrier concentration for a single-junction PV absorber layer is in the range of 10^{15}–10^{16} cm^{-3}, as listed in Table 12.1. In addition to the small E_0 energy, its large carrier concentration implies that Cu_2SnSe_3 may not be suitable for solar cell applications.

First-principles total energy and band structure calculations [51] predict that the E_0 of Cu_2SnS_3 is larger by ~0.5 eV than that of Cu_2SnSe_3. The lower E_0 in Cu_2SnSe_3 can be explained by the fact that (1) the higher Se 4*p* level than S 3*p* level

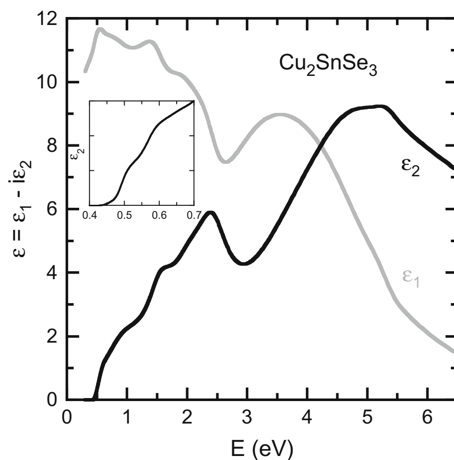

Fig. 12.13 Real (light gray) and imaginary (black) parts of the <ε> spectrum of Cu_2SnSe_3 [58]. Inset: The ε_2 spectrum from 0.4 to 0.7 eV shows the E_0 at ~0.5 eV

lifts up the valence-band maximum and (2) the larger size of Se than S lowers the conduction-band minimum state consisting of anti-bonding anion *s* and Sn *s* conduction-band minimum. A similar argument can be applied to explain the observed difference of ~0.5 eV in E_0 between $Cu_2ZnSnSe_4$ and Cu_2ZnSnS_4. The E_0 of ~1.0 eV has been predicted by theory [51] and confirmed by experiments [58, 59] for Cu_2SnS_3. As far as the E_0 is concerned, Cu_2SnS_3 may thus be a better choice than Cu_2SnSe_3 for single-junction solar cell applications. Detailed information on the optical properties of Cu_2SnS_3 has not yet been reported, and a systematic SE study is highly desired.

12.5 Summary and Outlook

In this chapter we reviewed SE-determined optical properties of $Cu_2ZnSn(S,Se)_4$ and related compounds, $Cu_2ZnGeSe_4$, $Cu_2ZnSiSe_4$, and Cu_2SnSe_3, which are considered promising absorber materials for next-generation thin-film photovoltaic devices. In addition to providing optical function data and discussing related physics, two data-acquisition strategies were also introduced: The pseudobulk method reduces complications in the multilayer analysis and helps to accurately extract the near-bandgap optical functions. Chemomechanical polishing procedures improve data quality by removing the surface overlayers including microscopic roughness.

The complex dielectric function spectra for many $Cu_2ZnSn(S,Se)_4$ and related materials were found to consist mainly of a distinct optical structure residing at ~1.5 eV above the bandgap and a broad structure in the high-energy region. From temperature-dependent SE studies of $Cu_2ZnSnSe_4$ and Cu_2ZnSnS_4, it was observed that their bandgap energies increase with decreasing temperature as for many semiconductors, but the change appears to be very small in particular below 100 K. The weak temperature dependence of bandgap energy was explained in terms of the atomic structure and electronic interactions for kesterite-phase compounds.

Small discrepancies were noticed in the optical function data and bandgap energies among the reported studies for this new class of materials, which can in part be attributed to the various types of structural imperfections including the presence of secondary phases and cation-sites disorder as well as to the different structural phases—kesterite, stannite, or primitive-mixed CuAu. It is thus important that characterization of structural properties is included in order to accurately relate SE-determined optical functions to the structural nature of the material. Raman spectroscopy, scanning-electron microscopy, and X-ray diffraction are some of the techniques typically used with SE characterization of kesterite solar cell materials. Comparison of SE-determined optical function spectra with the theoretical data is another means of assessing the structural property of the material, from which the electronic origins of major spectroscopic features shown in SE spectra can be identified.

Kesterite solar cell technology has been developed based on $Cu_2ZnSn(S,Se)_4$. However, substituting some elements in $Cu_2ZnSn(S,Se)_4$ or alloying it with other elements can improve our understanding of the bulk and interface properties of the material, optimize device structure by tailoring the bandgap energy, and reduce the manufacturing cost. For example, replacing Sn in $Cu_2ZnSnSe_4$ with Ge increases the bandgap and possibly cation-sites disorder, whereas replacing Cu in $Cu_2ZnSnSe_4$ with Au will also increase the bandgap but decrease the disorder. Optical properties for many of the alternating compounds have not yet been well studied. Furthermore, it is witnessed that the list of compounds keeps getting longer with many new promising contestants. SE is expected to continue playing an important role in characterizing the optical properties of new materials in the kesterite solar cell family. It is hoped that this book chapter provides interested readers technical information and reference data for developing $Cu_2ZnSn(S,Se)_4$-based compounds for the next-generation thin-film solar cells.

Acknowledgements The author acknowledges Jian Li (Univ. of Toledo) for his critical contributions to the development of the pseudobulk method and Ingrid Repins (NREL) for valuable discussions on kesterite solar cell technology as well as providing $Cu_2ZnSnSe_4$, $Cu_2ZnGeSe_4$, and Cu_2SnSe_3 thin film samples. Suhuai Wei (Beijing Computation Science Research Center, China) is acknowledged for discussions on the electronic structure of kesterite-phase compounds. Figure 12.1 was prepared by Ji-Sang Park (Imperial College London, UK) and the energy band structure of $Cu_2ZnSnSe_4$ shown in Fig. 12.3 was provided by Hanyue Zhao and Clas Persson (Univ. of Oslo, Norway). The author thanks David Aspnes (North Carolina State Univ.) for helpful discussions on surface preparations and Lynn Gedvilas (Colorado School of Mines) for technical editing.

References

1. See for example, *Copper Zinc Tin Sulfide-Based Thin Film Solar Cells*, ed. by K. Ito (Wiley, Chichester, UK, 2015)
2. K. Ito, T. Nakazawa, Jpn. J. Appl. Phys. **27**, 2094 (1988)
3. T.M. Friedlmeier, N. Wieser, T. Walter, H. Dittrich, H.W. Schock, *Proceedings of the 14th European Conference of Photovoltatic Science and Engineering and Exhibition* (Bedford, UK, 1997), p. 1242
4. K. Todorov, K.B. Reuter, D.B. Mitzi, Adv. Mater. **22**, E156 (2010)
5. W. Wang, M.T. Winkler, O. Gunawan, T. Gokmen, T.K. Todorov, Y. Zhu, D.B. Mitzi, Adv. Mater. **4**, 1301465 (2014)
6. S. Chen, X.G. Gong, A. Walsh, S.-H. Wei, Appl. Phys. Lett. **94**, 041903 (2009)
7. C. Persson, J. Appl. Phys. **107**, 053710 (2010)
8. G. Rey, A. Redinger, J. Sendler, T.P. Weiss, M. Thevenin, M. Guennou, B. El Adib, S. Siebentritt, Appl. Phys. Lett. **105**, 112106 (2014)
9. S.G. Choi, H.Y. Zhao, C. Persson, C.L. Perkins, A.L. Donohue, B. To, A.G. Norman, J. Li, I. L. Repins, J. Appl. Phys. **111**, 033506 (2012)
10. S. Schorr, Sol. Energy Mater. Sol. Cells **95**, 1482 (2011)
11. T. Washio, H. Nozaki, T. Fukano, T. Motohiro, K. Jimbo, H. Katagiri, J. Appl. Phys. **110**, 074511 (2011)
12. T. Gokmen, O. Gunawan, T.K. Todorov, D.B. Mitzi, Appl. Phys. Lett. **103**, 103506 (2013)

13. For example, see S. Ahn, S. Jung, J. Gwak, A. Cho, K. Shin, K. Yoon, D. Park, H. Cheong, J. H. Yun, Appl. Phys. Lett. **97**, 021905 (2010)
14. S.G. Choi, T.J. Kim, S.Y. Hwang, J. Li, C. Persson, Y.D. Kim, S.-H. Wei, I.L. Repins, Sol. Energy Mater. Sol. Cells **130**, 375 (2014)
15. A. Crovetto, A. Cazzaniga, R.B. Ettlinger, J. Schou, O. Hansen, Thin Solid Films **582**, 203 (2015)
16. M. León, S. Levcenko, R. Serna, A. Nateprov, G. Gurieva, J.M. Merino, S. Schorr, E. Arushanov, Mater. Chem. Phys. **141**, 58 (2013)
17. A.P. Litvinchuk, Phys. Status Solidi B. https://doi.org/10.1002/pssb.201552415 (in press)
18. S. Adachi, *Copper Zinc Tin Sulfide-based Thin Film Solar Cells*, ed. by K. Ito (Wiley, Chichester, UK, 2015) Chap. 7
19. C. Persson, R. Chen, H. Zhao, M. Kumar, D. Huang, *Copper Zinc Tin Sulfide-based Thin Film Solar Cells*, ed. by K. Ito (Wiley, Chichester, UK, 2015) Chap. 4
20. B.G. Lee, S. Li, G. von Gastrow, M. Yli-Koski, H. Savin, V. Malinen, J. Skarp, S. Choi, H.M. Branz, Thin Solid Films **550**, 541 (2014)
21. M.A. Steiner, J.F. Geisz, I. García, D.J. Friedman, A. Duda, S.R. Kurtz, J. Appl. Phys. **113**, 123109 (2013)
22. M. Law, M.C. Beard, S. Choi, J.M. Luther, M.C. Hanna, A.J. Nozik, Nano Lett. **8**, 3904 (2008)
23. T. Hara, T. Maekawa, S. Minoura, Y. Sago, S. Niki, H. Fujiwara, Phys. Rev. Appl. **2**, 034012 (2014)
24. J.-S. Park, S. Choi, Y. Yan, Y. Yang, J.M. Luther, S.-H. Wei, P. Parilla, K. Zhu, J. Phys. Chem. Lett. **6**, 4304 (2015)
25. R.A. Synowicki, Phys. Status Solidi (c) **5**, 1085 (2008)
26. J.N. Hilfiker, N. Singh, T. Tiwald, D. Convey, S.M. Smith, J.H. Baker, H.G. Tompkins, Thin Solid Films **516**, 7979 (2008)
27. G.E. Jellison Jr., L.A. Boatner, D.H. Lowndes, R.A. McKee, M. Godbole, Appl. Opt. **33**, 6053 (1994)
28. D.E. Aspnes, A.A. Studna, Appl. Phys. Lett. **39**, 316 (1981)
29. S. Ozaki, T. Namba, Phys. Status Solidi C **9**, 2403 (2012)
30. M. León, S. Levcenko, R. Serna, I.V. Bodnar, A. Nateprov, M. Guc, G. Gurieva, N. Lopez, J. M. Merino, R. Caballero, S. Schorr, A. Perez-Rodriguez, E. Arushanov, Appl. Phys. Lett. **105**, 061909 (2014)
31. Y. Hirate, H. Tampo, S. Minoura, H. Kadowaki, A. Nakane, K.M. Kim, H. Shibata, S. Niki, H. Fujiwara, J. Appl. Phys. **117**, 015702 (2015)
32. A. Savitzky, M.J.E. Golay, Anal. Chem. **36**, 1627 (1964)
33. M. Cardona, *Modulation Spectroscopy, Suppl. 11 of Solid State Physics* (Academic, New York, 1969), p. 119
34. D.E. Aspnes, *Handbook of Semiconductors*, ed. by M. Balkanski, vol. 2 (North-Holland, Amsterdam, 1980), p. 109
35. M. Cardona, M.L.W. Thewalt, Rev. Mod. Phys. **77**, 1173 (2005)
36. R. Pässler, J. Appl. Phys. **89**, 6235 (2001)
37. J.C. Phillips, G. Lukovsky, *Bonds and Bands in Semiconductors*, 2nd edn. (Momentum Press, New York, 2009)
38. S.G. Choi, R. Chen, C. Persson, T.J. Kim, S.Y. Hwang, Y.D. Kim, L.M. Mansfield, Appl. Phys. Lett. **101**, 261903 (2012)
39. J. Krustok, T. Raadik, M. Grossberg, S. Giraldo, M. Neuschitzer, S. López-Marino, E. Saucedo, Mater. Sci. Semicond. Process. **39**, 251 (2015)
40. S. Levcenko, G. Gurieva, M. Guc, A. Nateprov, Mold. J. Phys. Sci. **8**, 173 (2009)
41. S. Adachi, T. Taguchi, Phys. Rev. B **43**, 9569 (1991)
42. J. Li, H. Du, J. Yarbrough, A. Norman, K. Jones, G. Teeter, F.L.J. Terry, D. Levi, Opt. Exp. **20**, A327 (2012)
43. W. Li, K. Jiang, J. Zhang, X. Chen, Z. Hu, S. Chen, L. Sun, J. Chu, Phys. Chem. Chem. Phys. **14**, 9936 (2012)

44. A. Meeder, A. Jäger-Waldau, V. Tezlevan, E. Arushanov, T. Schedel-Niedrig, MCh. Lux-Steiner, J. Phys. **15**, 6219 (2003)
45. J. Bhosale, A.K. Ramdas, A. Burger, A. Muñoz, A.H. Romero, M. Cardona, R. Lauck, R.K. Kremer, Phys. Rev. B **86**, 195208 (2012)
46. Y.S. Lee, T. Gershon, O. Gunawan, T.K. Todorov, T. Gokmen, Y. Virgus, S. Guha, Adv. Energy Mater. **5**, 1401372 (2015)
47. M.A. Green, K. Emery, Y. Hishikawa, W. Warta, E.D. Dunlop, D.H. Levi, A.W.Y. Ho-Baillie, Prog. Photovolt. Res. Appl. **25**, 3 (2017)
48. W. Shockley, H.J. Queisser, J. Appl. Phys. **32**, 510 (1961)
49. S.G. Choi, J.-S. Park, A.L. Donohue, S.T. Christensen, B. To, C. Beall, S.-H. Wei, I.L. Repins, Phys. Rev. Appl. **4**, 054006 (2015)
50. S. Chen, X.G. Gong, A. Walsh, S.-H. Wei, Phys. Rev. B **79**, 165211 (2009)
51. Y.W. Jung, T.H. Ghong, Y.D. Kim, D.E. Aspnes, Appl. Phys. Lett. **91**, 121903 (2007)
52. K.M. Kim, H. Tampo, H. Shibata, S. Niki, Thin Solid Films **536**, 111 (2013)
53. M. Ahmadi, S.S. Pramana, S.K. Batabyal, C. Boothroyd, S.G. Mhaisalkar, Y.M. Lam, Inorg. Chem. **52**, 1722 (2013)
54. G. Marcano, C. Rincón, L.M. de Chalbaud, D.B. Bracho, G. Sánchez, Pérez. J. Appl. Phys. **90**, 1847 (2001)
55. Y.-T. Zhai, S. Chen, J.-H. Yang, H.-J. Xiang, X.-G. Gong, A. Walsh, J. Kang, S.-H. Wei, Phys. Rev. B **84**, 075213 (2011)
56. L. Xi, Y.B. Zhang, X.Y. Shi, J. Yang, X. Shi, L.D. Chen, W. Zhang, J. Yang, D.J. Singh, Phys. Rev. B **86**, 155201 (2012)
57. S.G. Choi, J. Kang, J. Li, H. Haneef, N.J. Podraza, C. Beall, S.-H. Wei, S.T. Christensen, I.L. Repins, Appl. Phys. Lett. **106**, 043902 (2015)
58. D. Tiwari, T.K. Chaudhuri, A.I.P. Conf, Proc. **1349**, 1295 (2011)
59. D.M. Berg, R. Djemour, L. Gütay, G. Zoppi, S. Siebentritt, P.J. Dale, Thin Solid Films **520**, 6291 (2012)

Chapter 13
Real Time and Mapping Spectroscopic Ellipsometry for CdTe Photovoltaics

Prakash Koirala, Jian Li, Nikolas J. Podraza and Robert W. Collins

Abstract Real time spectroscopy ellipsometry (RTSE) has been implemented in studies of the structural evolution during magnetron sputtering of the polycrystalline CdS and CdTe thin film components of CdS/CdTe solar cells on glass substrates coated in turn with transparent conducting oxide (TCO) top contact layers. RTSE provides detailed information on various structural features identified during CdS and CdTe film growth. These include (i) formation of the TCO/CdS interface as the surface modulations of the high resistivity transparent (HRT) layer are filled with the depositing CdS during its initial growth; (ii) evolution of the CdS bulk layer thickness and associated surface roughness layer thickness; (iii) formation of the CdS/CdTe interface as the depositing CdTe fills the modulations of the CdS surface, resulting in the heterojunction; and (iv) evolution of the CdTe bulk layer and surface roughness layer thicknesses. The structural and optical models established in the analysis procedures for RTSE data acquired from the film side at a single location on the solar cell surface are also applied in the analysis of ex situ mapping spectroscopic ellipsometry (M-SE) data acquired in through-the-glass mode over the entire area of the completed solar cell structure. In fact, M-SE has been applied to generate maps in the effective thicknesses (or volumes/area) of layer components over the 225 cm^2 areas of the solar cell structures for spatial correlation with the performance of arrays of 256 dot cells fabricated over the same areas. The results of such M-SE studies are presented in detail including those from several investigations designed for process optimization of the CdS/CdTe solar cell on TCO-coated glass. In the solar cell fabrication process, the CdS/CdTe structure is subjected to various processing steps after deposition of the heterojunction materials. The first steps include an anneal of the structure with simultaneous $CdCl_2$ exposure of the CdTe film surface, followed by a deposition of ultrathin Cu by thermal evaporation on the CdTe surface. The additional steps that complete the

P. Koirala · J. Li · N. J. Podraza (✉) · R. W. Collins
Department of Physics & Astronomy and Center for Photovoltaics Innovation & Commercialization, University of Toledo, Toledo, OH 43606, USA
e-mail: Nikolas.Podraza@utoledo.edu

R. W. Collins
e-mail: robert.collins@utoledo.edu

© Springer International Publishing AG, part of Springer Nature 2018

H. Fujiwara and R. W. Collins (eds.), *Spectroscopic Ellipsometry for Photovoltaics*, Springer Series in Optical Sciences 212,
https://doi.org/10.1007/978-3-319-75377-5_13

device include a deposition of a metal back contact layer and a final anneal to promote the diffusion of Cu into the underlying CdTe. M-SE studies are described for CdS/CdTe solar cells fabricated with different thicknesses of the CdTe absorber layer within the range from 0.5 to 2.5 μm, focusing initially on the influence of the $CdCl_2$ treatment duration which ranges from 5 to 30 min. In addition, processing-property-performance relationships are identified and presented for the CdS top window layer and the Cu back contact layer; the effective thickness of each layer is critical for the optimization of the solar cells. Relationships between the solar cell performance parameters and the effective thicknesses from M-SE analysis for solar cells fabricated under different processing conditions are demonstrated to facilitate process optimization.

13.1 Introduction

Simulating accurate optical characteristics, including reflectance and layer absorbance spectra, for the CdTe solar cell is a challenge considering that the cell incorporates as many as four glass coatings associated with the transparent conducting oxide (TCO) top contact, at least two semiconductor layers forming the heterojunction, and one or more layers associated with the back contact [1]. In addition, the CdTe solar cell is fabricated in the superstrate configuration, implying that the solar irradiance passes through the glass before entering the multilayer cell structure. Both deposition and post-deposition processes have significant impacts on the optical characteristics of the layers in this superstrate structure. The challenges in optical analysis and simulation arise from the interrelated effects of the process dependences, including film stack or substrate dependences. First, complications arise due to variations in what are nominally referred to as "bulk layer optical properties". Such properties are not uniquely defined and can be affected by the deposition and processing procedures, which lead to variations in the void volume fraction, average size of the polycrystalline grains and their orientations, as well as strain in the films. In addition, for transparent conducting oxides, variations can occur in the characteristics of the free carriers, such as their concentration and mobility. Databases of optical properties have been collected relevant for CdTe and CdS deposited and treated under different conditions [2–7]. The effects of measurement temperature on these semiconductor optical properties, as may be required for on-line measurements, have also been explored. The variations in the doped SnO_2 transparent conducting oxide (TCO) optical properties are generally known, in particular, those that control the near-infrared and near-ultraviolet transmission [2, 7–11]. The effects of measurement temperature in modifying the SnO_2 optical properties, however, have been established only recently through results presented in [11]. Further complications arise due to the effects of underlying films or substrates and, particularly, the effects of the interfaces in the film stack which generate challenges in designing realistic models of the optical behavior of the stack. In standard existing models of interface regions, simple effective medium mixtures of

the adjacent materials of the multilayer have been applied successfully [2, 10]. Separating the effects of interface roughness and inter-diffusion is an important next step, however, in establishing a more realistic metrology. Advances in this direction may be made through in-depth analysis of optical data acquired in real time during film growth.

The motivation for this research is two-fold. First, realistic structural and optical models of the CdTe solar cell are required if quantitative on-line optical monitoring with high accuracy and reproducibility is to be successful. Ideally, such models should incorporate all possible variability in the optical properties of the bulk and interface layers, including the effects of measurement temperature. In this case, the capabilities of spectroscopic ellipsometry (SE) in measuring the ratio $\rho = r_p/r_s$ for the film stack, where r_p and r_s are the p and s complex amplitude reflection coefficients, respectively, comprise a powerful approach for analysis of the stack based on realistic structural and optical models of the device [12]. Second, analysis based on the detailed models as described is also required if an in-depth understanding of the external quantum efficiency (EQE) of the solar cell is to be achieved. In this application, the depth distribution of the electric field associated with the optical wave within the layers of the multilayer structure is sought so that the absorbances of the layers can be calculated. Then the EQE can be predicted assuming all the electron-hole pairs that are generated within the active absorber layer components are separated and all the separated carriers are collected [13]. Differences observed between the predicted EQE and the measurement, evaluated versus the photon energy, provide information on electronic losses. Furthermore, an EQE prediction capability can be applied to mapping measurements performed over large areas in order to calculate subcell current output and evaluate quantitatively the impact of non-uniformities.

13.2 Real Time Spectroscopic Ellipsometry

The focus of this section involves the use of real time SE (RTSE) to analyze the formation of interfaces (i) between the topmost TCO layer on the glass substrate and the CdS layer, as well as (ii) between the CdS layer and the CdTe layer of the heterojunction during deposition, employing CdS layers sputtered at different Ar pressures. The goal of these studies is to quantify differences in the structural evolution of the thin films, and to analyze the optical nature of the heterojunction interface for the different CdS deposition conditions.

13.2.1 Experimental Methods

The thin film polycrystalline CdS and CdTe were deposited by radio frequency (rf) magnetron sputtering on TEC™ 15 glass samples 5 cm × 5 cm in size. The TEC™ 15 glass was additionally coated with a high resistivity transparent

(HRT) SnO_2 layer before the sputter depositions. The deposition conditions common to the CdS and CdTe layers were as follows: substrate temperature, 250 °C; rf sputtering power, 200 W; and Ar gas flow, 23 standard cm^3/min (sccm). For CdS film deposition, the Ar pressure (p_{Ar}) for sputtering was set at different values within the range from 5 to 50 mTorr, with 5 mTorr fixed intervals. For CdTe film deposition, p_{Ar} was fixed at 10 mTorr. Out of twenty differently processed samples, the first set of ten samples was prepared by depositing the CdS layers at ten different p_{Ar} values for 12 min each (referred to as the "constant time series"), and the CdTe layers for 120 min each. For these samples, the resulting CdS effective thickness values were within the range 500–1400 Å, and the targeted CdTe effective thickness value was 2 μm. For the second set, the CdS deposition times were varied within the range of ~8–34 min for the layers deposited at ten different p_{Ar} values in an attempt to maintain a constant final effective thickness of ~1200 Å (referred to as the "constant thickness series"). As in the constant time series, the CdTe layers were deposited for 120 min for a thickness of 2 μm. The effective thickness is defined as the deposited material volume per unit area of substrate. Thus, the effective thickness accounts for the interface roughness, bulk, and surface roughness components.

In situ SE data were acquired on the substrates at room temperature prior to heating and film deposition using a rotating-compensator multichannel ellipsometer spanning a spectral range from 0.75 to 6.5 eV (Model M2000-DI, J. A. Woollam Co., Inc). Such data were also acquired on the substrates at the deposition temperature, followed by RTSE measurements during the sputter depositions of the CdS and CdTe thin films. For RTSE, the time interval between acquisitions of successive spectra was 2.4 s. During this time, increases in effective thickness of (4.8, 1.6) Å are observed for the CdS deposited at the fixed p_{Ar} settings of (5, 50) mTorr, respectively, and an increase of 6.6 Å is observed for the CdTe depositions. Figure 13.1 depicts a schematic of the magnetron sputter deposition system used for semiconductor layer depositions with provisions for RTSE data acquisition.

A series of processing steps was applied to as-deposited multilayer structures that resulted in operating solar cell devices [1]. In this study, the steps include post-deposition exposure of the CdTe surface to $CdCl_2$ vapor in a dry air ambient at a temperature of 387 °C for 30 min, followed by the deposition by thermal evaporation of a 30/300 Å Cu/Au bilayer on the CdTe surface by using a metal mask. After back contact deposition, the structure was annealed at a temperature of 150 °C for 45 min to ensure Cu diffusion into the underlying CdTe. These steps resulted in 36 individual dot cells over the 5 cm × 5 cm area, each with an area of 0.125 cm^2. The performance of each of the 36 solar cells was evaluated under AM 1.5 illumination. Table 13.1 summarizes the details of fabrication for the completed devices.

13.2.2 Optical Model with Dielectric Functions

Figure 13.2 is a simplified schematic of the CdTe solar cell structure including the component layers and their representative thicknesses, as indicated on the diagram.

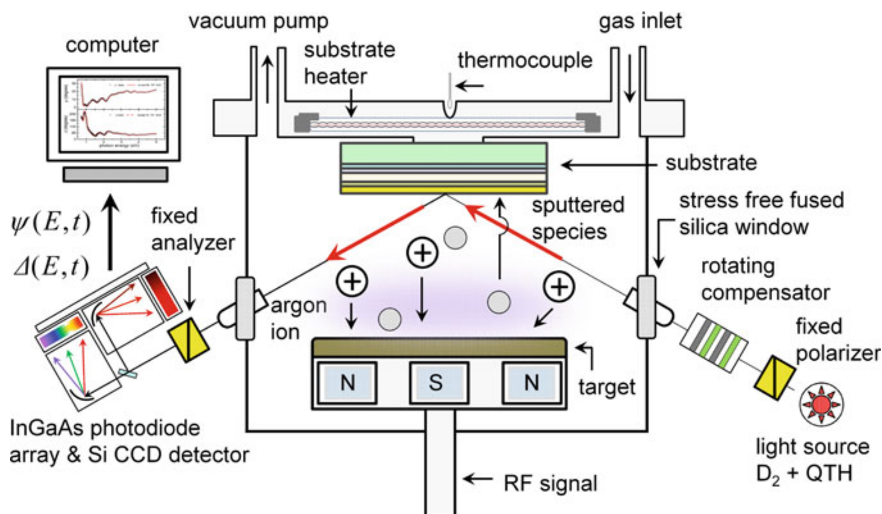

Fig. 13.1 Magnetron sputter deposition system with the capability of performing real time spectroscopic ellipsometry measurements. In the lower right corner are the polarization generation components of the ellipsometer, including a broadband source of light, a polarizer, and a rotating compensator. Shown in the lower left corner are the polarization detection components including a fixed analyzer, spectrographs, and irradiance detectors. A personal computer is used to analyze the detector output and calculate the ellipsometry spectra in (ψ, Δ)

Quantitative analysis of RTSE data during CdS/CdTe deposition becomes possible if the thicknesses of all the component layers of the substrate structure are known along with the layers' complex dielectric functions at the elevated deposition temperature of 250 °C. Prior to each CdS deposition on the (TEC™ 15)/HRT substrate, in situ SE data were acquired on the substrate both at room temperature and at the deposition temperature as described in Sect. 13.2.1. These in situ SE data were analyzed using the optical model shown in Fig. 13.2, indicated in the schematic by (TEC™ 15)/HRT, but without the overlying semiconductor layers and metal back contact. Also a roughness layer was added to the SnO_2 HRT surface in the optical model, as shown in the left column of Table 13.2.

In the analysis of each individual (TEC™ 15)/HRT substrate, the thicknesses are expected to differ from sample location to location for a given run, and from run to run in production. Spatial and run-to-run variations may also occur in the optical parameters that describe the dielectric functions. As a result, the thicknesses of all the component layers were used as variable parameters in the analysis of in situ SE data collected for each (TEC™ 15)/HRT substrate at room temperature. Selected dielectric function parameters were also varied for the SnO_2:F and HRT layers, which were the thickest of the four layers in Fig. 13.2. In contrast, for the soda-lime glass (SLG), thin SnO_2, and thin SiO_2, database dielectric functions at room temperature were used from [7, 11], as defined by fixed parameters. To analyze the SE data acquired at the deposition temperature of 250 °C, the layer thicknesses were

Table 13.1 Device fabrication conditions for the complete CdTe solar cell in the superstrate configuration. The process involves sputter deposition of CdS and CdTe layers on (TEC™ 15)/HRT surfaces, followed by a 30 min $CdCl_2$ treatment step. Devices are completed by depositing 30/300 Å thicknesses of Cu/Au through a mask that defines the back contact area of a single dot cell. The Ar sputtering pressure (p_{Ar}) for CdS was fixed within the range of 5–50 mTorr, using intervals of 5 mTorr. The Ar pressure for all CdTe depositions was fixed at 10 mTorr. The effective thicknesses of CdS were found to be in the range 500–1400 Å for a constant time series and was targeted as 1200 Å for a constant thickness series. The deposition times for these two series were 12 min and 8–34 min, respectively. The targeted effective thickness of CdTe was 2 μm, obtained over a deposition time of 120 min

Deposition process and parameters	CdS layer	CdTe layer
Substrate structure	NSG Pilkington (TEC™ 15)/HRT	(TEC™ 15)/ HRT/CdS
Deposition temperature (°C)	250	250
Base pressure at deposition temperature (Torr)	1.6×10^{-7}	1.6×10^{-7}
Gas flow rate (Ar) (sccm)	23	23
Deposition Ar pressure	5–50 mTorr, at intervals of 5 mTorr	10 mTorr
RF power (W)	200	200
Target-to-substrate distance (cm)	14	14
Deposition time	Constant time series: 12 min constant thickness series: 8–34 min	120 min
Maximum in effective thickness at center of a 5 cm × 5 cm (RTSE) or 15 cm × 15 cm (M-SE) substrate	Constant time series: 500–1400 Å constant thickness series: 1000–1400 Å	2 μm
$CdCl_2$ treatment	Saturated aqueous solution of $CdCl_2$ applied to CdTe surface; heated in 0.5 ft^3/min of dry air for 30 min at 387 °C	
Copper intended effective thickness	30 Å	
Gold intended effective thickness	300 Å	
Back contact annealing step	45 min at 150 °C	

fixed to the values obtained from analysis of the in situ SE data at room temperature for the same substrate. In addition, the set of variable optical parameters representing the dielectric functions of the SnO_2:F and HRT layers at elevated temperature were the same set as those varied in the analysis of room temperature data. For the SLG, SnO_2, and SiO_2, database dielectric functions at 250 °C were again used from [7, 11]. One approach for limiting the number of variable parameters in the modeling at the two temperatures involves linking the room and deposition temperature optical parameters according to the known temperature coefficients of

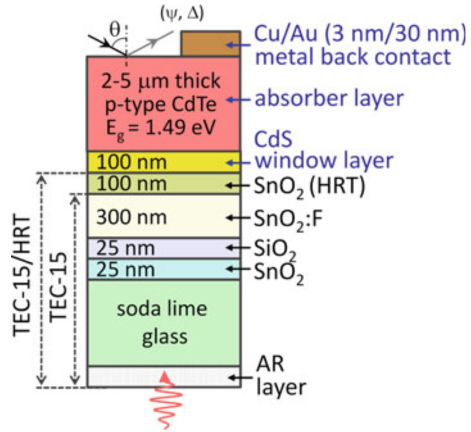

Fig. 13.2 Schematic of a CdTe solar cell of the type analyzed in this RTSE study. The starting structure for CdS/CdTe deposition corresponds to a commercial TEC™ 15 glass substrate coated with a high resistivity transparent (HRT) layer. Although an anti-reflection (AR) coating can be used at the front side of the glass to improve performance, it was not applied in this study

the parameters, determined as described in [11]. In fact, these temperature coefficients are expected to exhibit less variability.

In the analysis of the in situ SE data acquired at room temperature for the (TEC™ 15)/HRT substrates, two different substrate types were found, distinguished primarily by a difference in the SnO_2:F layer thickness. For different samples of the same type, much smaller variations in SnO_2:F layer thickness and dielectric function parameters were found in the best fits. Table 13.2 lists the thicknesses of the component layers for typical samples indicated as type I and type II. Values of the square root of the mean square error (RMSE) in the table were obtained as measures of the quality of the best fit in least-squares regression analysis. The RMSE used in these studies is defined by the expression

$$\sigma_{NCS} = \sqrt{\frac{1}{3n-p}\sum_{i=1}^{n}\left[\left(\frac{N_i^{(e)} - N_i^{(c)}}{\sigma_{N,i}^{(e)}}\right)^2 + \left(\frac{C_i^{(e)} - C_i^{(c)}}{\sigma_{C,i}^{(e)}}\right)^2 + \left(\frac{S_i^{(e)} - S_i^{(c)}}{\sigma_{S,i}^{(e)}}\right)^2\right]}, \tag{13.1}$$

where $i = 1, \ldots, n$ designates the spectral points and p is the numbers of fitting parameters; $N = \cos 2\psi$, $C = \sin 2\psi \cos\Delta$, and $S = \sin 2\psi \sin\Delta$. The SE angles (ψ, Δ) are given by $\tan\psi \exp(i\Delta) \equiv r_p/r_s$, i.e. the p-to-s ratio of the complex amplitude reflection coefficients. The quantities $\sigma_{j,i}^{(e)}$, with $j = N, C, S$, are estimates of measurement uncertainty for N, C, and S. These estimates are taken to be 10^{-3} for the high-speed, multichannel spectroscopic ellipsometer used in this study (M2000-DI, J. A. Woollam Co., Inc) [14].

In developing the database of the substrate materials in [11], the dielectric function for SLG versus photon energy E has been modeled using a five parameter Sellmeier equation with the resonance energies of the two oscillators positioned

Table 13.2 Example sets of structural parameters for types I and II (TEC™ 15)/HRT substrates and the sources of the dielectric functions for the component layers of the substrates. These results were determined in the analyses of in situ SE data collected at room temperature prior to sample heating and CdS deposition. Dielectric functions for the SnO_2, SnO_2:F, and HRT layers are modeled using the combination of a constant contribution ε_{1o}, a Drude term, and one or two critical point oscillators. The best fit variable parameters including thicknesses and surface roughness layer compositions are listed along with their confidence limits. Substrates for all depositions analyzed by RTSE were type II with the exception of those from the constant CdS thickness series with p_{Ar} in the range of 35–50 mTorr

Layer	Dielectric functions	Layer thickness	
		(TEC™ 15)/HRT substrate: type I	(TEC™ 15)/HRT substrate: type II
HRT surface roughness	EMA of HRT/void with variable volume fractions	383 ± 3 Å (0.63 ± 0.01/0.37 ± 0.01)	397 ± 3 Å (0.63 ± 0.01/0.37 ± 0.01)
HRT	Fixed and variable parameters defined as in Table 13.4 [11]	856 ± 6 Å	838 ± 5 Å
SnO_2:F		3058 ± 12 Å	3287 ± 11 Å
SiO_2	Reference data [7]	298 ± 6 Å	305 ± 5 Å
SnO_2	Reference data of Table 13.3 [11]	261 ± 5 Å	260 ± 5 Å
SLG		Semi-infinite	Semi-infinite
RMSE (σ_{NCS})		21	20

below and above the spectral range of the measurements. The resulting parametric equation for the dielectric function is given by

$$\varepsilon = \varepsilon_{1o} + \sum_{i=1}^{2} A_i E_i^2 / (E_i^2 - E^2) \tag{13.2}$$

where ε_{1o} is a constant additive term, A_i and E_i are the amplitudes and resonance energies of the *i*th oscillator that, along with ε_{1o}, define the Sellmeier equation [15]. The absorption is neglected in reflection SE, leading to a real expression in (13.2) for the SLG. For the SnO_2 layer at the interface to the SLG in the (TEC™ 15)/HRT substrate, the analytical expression representing the dielectric function consists of a sum that incorporates a constant term in ε_1, an intraband term based on the Drude free electron formula, and an interband term based on one or more transitions of electrons between parabolic bands in $E(\boldsymbol{k})$ space, as follows [15]

$$\varepsilon(E) = \varepsilon_{1o} + \varepsilon_D(E) + \sum_n A_n \{\exp(i\phi_n)\}\{(\Gamma_n/2)/[E_n - E - i(\Gamma_n/2)]\}^{\mu_n}. \tag{13.3}$$

The second term derives from the Drude equation,

$$\varepsilon_D(E) = \frac{-\hbar^2}{\varepsilon_0 \rho (\tau \cdot E^2 + i\hbar E)}, \tag{13.4}$$

where $\hbar = h/2\pi$ with h as Planck's constant, ε_0 is the permittivity of free space, τ is the mean free time for charge carrier scattering, and ρ is the electrical resistivity given by $\rho = m_e^*/Ne^2\tau = 1/e\mu N$. In this expression for the resistivity, m_e^* is the effective mass of the charge carrier, which is the electron in this case, e is electron charge, and μ and N are the free electron mobility and concentration, respectively. The third term in (13.3), which is the interband term, is described as a sum of critical point (CP) oscillators where A_n, E_n, Γ_n, μ_n, and ϕ_n are the amplitude, resonance energy, broadening parameter, exponent, and phase of the *n*th CP oscillator, respectively.

Table 13.3 lists the parameters of these analytical equations representing the dielectric function of the SLG (13.2) and that of the SnO_2 layer (13.3) located directly on top of the SLG, both from the database of [11]. The parameters of Table 13.3 were applied for the analysis of the in situ SE data acquired at room temperature and at the deposition temperature of 250 °C for both types of substrates. These parameters were also fixed throughout the analyses of the individual (TEC™ 15)/HRT substrates used for the RTSE studies. Figure 13.3 shows the associated dielectric function spectra for these materials as generated by the parameters of Table 13.3 applying (13.2) and (13.3). The SiO_2 layer dielectric function from previous studies was used in these substrate analyses [7].

Table 13.3 Parameters that describe (13.2) and (13.3) representing the dielectric functions of the SLG and the SnO_2 layer, respectively, from the database of [11]. The two sets of parameter values are appropriate for room temperature and for the elevated deposition temperature of 250 °C, and are applicable to both (TEC™ 15)/HRT substrate types of Table 13.2

Layer	Parameters	Room temperature	T = 250 °C
Glass	ε_{1o}	1.591	1.943
	A_1 (unitless)	0.655	0.304
	E_1 (eV)	9.576	8.118
	A_2 (unitless)	0.012	0.012
	E_2 (eV)	0.556	0.556
SnO_2	ε_{1o}	1.688	1.594
	ρ (10^{-4} Ω-cm)	42.268	42.268
	τ (fs)	5.362	5.362
	A_0 (unitless)	1.515	1.613
	E_0 (eV)	4.256	4.197
	Γ_0 (eV)	0.586	0.706
	ϕ_0 (°)	3.259	3.259
	μ_0	0.283	0.283
	A_1 (unitless)	1.439	1.439
	E_1 (eV)	5.144	5.144
	Γ_1 (eV)	1.184	1.184
	ϕ_1 (°)	−6.490	−6.490
	μ_1	0.209	0.209

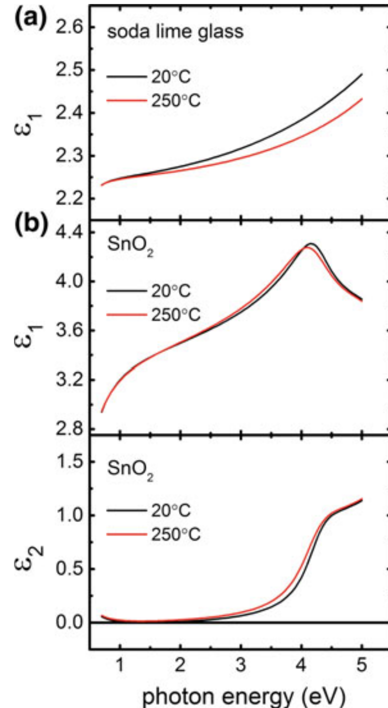

Fig. 13.3 Plots of the analytical expressions for the components of (TEC™ 15)/HRT including **a** the real dielectric function of the SLG and **b** the real (top) and imaginary (bottom) parts of the dielectric function of the SnO_2 adjacent to the SLG. These expressions, obtained from fits to measurements at room temperature and at the CdS/CdTe deposition temperature of 250 °C, are applied for all substrates used in CdS/CdTe deposition

Equation (13.3) was also applied for parameterization of the dielectric functions of the SnO_2:F and HRT layers. Characteristic parameters of the analytical expressions representing the dielectric functions of these layers are listed in Table 13.4 as examples of the analysis results obtained for both types of substrates at room temperature and at the CdS/CdTe deposition temperature of 250 °C [11]. In these results for the two temperatures, the structural parameters were fixed from the room temperature analysis and a subset of optical property parameters was varied. This results in temperature coefficients for the variable parameters of the HRT and the SnO_2:F, as also provided in Table 13.4. Once the temperature coefficients have been identified, the analysis of the measurements at room and deposition temperatures can be linked to ensure that the known temperature dependences of the parameters are followed, even though the specific values themselves are varied from sample to sample. It is noted in Table 13.4 that the dielectric function of the HRT layer includes only one CP oscillator in the analytical expression from the database, compared to two for the SnO_2:F layer. Because the HRT could be measured only in the complete (TEC™ 15)/HRT configuration, which includes three underlying layers, it was more challenging to determine an accurate representation of its dielectric function, given the variability in the underlying SnO_2:F. It was more challenging as well to determine the variation with measurement temperature. As a result, a simplified model was used for the HRT dielectric function compared with that of SnO_2:F.

The parameters with confidence limits in Table 13.4 are those used as variables in the least-squares regression analysis of each substrate with the remaining parameters being fixed at the database values. The selection of the variable and fixed parameters in the substrate analysis for RTSE is based on sensitivity considerations; the fixed parameters are those that affect the data less sensitively. The fixed parameters for the HRT dielectric function include both Drude parameters, due to the high resistivity and low electron concentration of the HRT, as well as the phase and exponent of the CP. For the SnO_2:F, all the parameters of the second high energy CP were fixed, along with the phase and exponent of the bandgap CP. Figure 13.4 shows corresponding dielectric function spectra for the representative results of Table 13.4 at the two temperatures.

Next the variation in the parameters with measurement temperature will be discussed briefly in order to assess the temperature coefficients. Because the Drude term for the HRT layers of both sample types is quite weak due to its high resistivity, the two Drude parameters ρ and τ must be fixed at the two temperatures. For the SnO_2:F, however, ρ increases with measurement temperature according to the temperature coefficient of 4.46×10^{-7} Ω cm/K as a result of a decrease in scattering time τ, as $\tau \propto T^{-1}$, due to phonon scattering. For both the HRT and SnO_2:F, the resonance energy E_0 of the interband transition decreases whereas the associated broadening parameter Γ_0 increases with increasing measurement temperature; both are expected trends. The constant contributions to the real part of the dielectric functions in Table 13.4 show decreasing trends with increasing temperature for the HRT and SnO_2:F whereas the amplitude A_0 shows opposing trends. For A_0, it is expected that the SnO_2:F trend is a better representation due to the difficulty of

Table 13.4 Parameters of the analytical expressions that represent the dielectric functions of the SnO_2:F and HRT layers for a typical (TEC™ 15)/HRT substrate. The two sets of parameter values correspond to room temperature and 250 °C deposition temperature. Parameters with confidence limits serve as variables along with layer thicknesses during in situ SE analyses of the substrates used for RTSE studies. Dielectric function parameters without confidence limits are fixed and their values obtained from a previous dielectric function database, which was also used for the SLG and thin SnO_2 layer of Table 13.3 [11]. The variable parameters at the two temperatures can be linked to ensure temperature coefficients consistent with those of the previous database

Layers	Parameter	Room temperature	250 °C	Temperature coefficient
HRT	ε_{1o}	3.883 ± 0.042	3.856 ± 0.042	-1.15×10^{-4} K^{-1}
	ρ	2.104×10^{-3} Ω-cm	2.104×10^{-3} Ω-cm	–
	τ	5.362 fs	5.362 fs	–
	A_0	1.503 ± 0.087	1.373 ± 0.079	-5.65×10^{-4} K^{-1}
	E_0	4.918 ± 0.031 eV	4.880 ± 0.031 eV	-1.66×10^{-4} eV/K
	Γ_0	1.009 ± 0.072 eV	1.269 ± 0.091 eV	1.13×10^{-3} eV/K
	ϕ_0	−9.060°	−9.060°	–
	μ_0	1.000	1.000	–
SnO_2:F	ε_{1o}	3.377 ± 0.041	3.323 ± 0.040	-2.32×10^{-4} K^{-1}
	ρ	(4.219 ± 0.202) × 10^{-4} Ω-cm	(5.245 ± 0.249) × 10^{-4} Ω-cm	4.46×10^{-7} Ω-cm/K
	τ	6.533 ± 0.364 fs	5.439 ± 0.304 fs	-4.75×10^{-3} fs/K
	A_0	1.053 ± 0.062	1.111 ± 0.065	2.52×10^{-4} K^{-1}
	E_0	4.871 ± 0.030 eV	4.807 ± 0.030 eV	-2.76×10^{-4} eV/K
	Γ_0	1.185 ± 0.082 eV	1.521 ± 0.105 eV	1.46×10^{-3} eV/K
	ϕ_0	−79.124°	−79.124°	–
	μ_0	1.538	1.538	–
	A_1	2.014	2.014	–
	E_1	6.237	6.237	–
	Γ_1	1.810	1.810	–
	ϕ_1	0.842	0.842	–
	μ_1	0.962	0.962	–

characterizing the temperature dependence of the dielectric function of the HRT as a component of a complicated multilayer stack. In spite of the challenge of analyzing the HRT, results for the HRT temperature coefficients with the exception of that for A_0 are reasonably consistent with the more accurately determined results for SnO_2:F.

The $\varepsilon(E)$ spectra of CdS and CdTe were expressed as a sum of a constant real contribution, a background Tauc-Lorentz (T-L) oscillator, and multiple critical point (CP) oscillators, according to

$$\varepsilon(E) = \varepsilon_{1o} + \varepsilon_{(\mathrm{TL})}(E) + \sum_n A_n\{\exp(i\phi_n)\}\{(\Gamma_n/2)/[E_n - E - i(\Gamma_n/2)]\}^{\mu_n} \quad (13.5)$$

The first and third terms were described previously in relation to (13.3). The second term in (13.5) $\varepsilon_{(\mathrm{TL})}(E)$ is the background T-L oscillator term added to simulate the smooth variation of the dielectric function in regions between CPs. This oscillator term can be expressed as

$$\varepsilon_{(\mathrm{TL})}(E) = \varepsilon_{1(\mathrm{TL})}(E) - i\varepsilon_{2(\mathrm{TL})}(E), \quad (13.6a)$$

where

$$\varepsilon_{2(\mathrm{TL})}(E) = \begin{cases} \frac{A_{\mathrm{TL}}E_{\mathrm{TL}}\Gamma_{\mathrm{TL}}}{[(E_{\mathrm{TL}}^2 - E^2)^2 + \Gamma_{\mathrm{TL}}^2 E^2]} \cdot \frac{(E - E_g)^2}{E} & ; \quad E > E_g \\ 0 & ; \quad E \le E_g \end{cases} \quad (13.6b)$$

Here A_{TL}, E_{TL}, and Γ_{TL} are the Lorentz oscillator amplitude, resonance energy, and broadening parameter, respectively, and E_g is the Tauc bandgap [15]. The real part of the dielectric function $\varepsilon_{1(\mathrm{TL})}$ in (13.6a) is derived from $\varepsilon_{2(\mathrm{TL})}$ in (13.6b) through the Kramers-Kronig relationship. The imaginary part in (13.6b) is forced to zero below the bandgap E_g of the Tauc-Lorentz oscillator.

Below E_0, defined as the resonance energy of the lowest energy CP, the imaginary part of (13.5) is replaced by an Urbach tail described by

$$\varepsilon_{2(U)} = \varepsilon_2(E_0)\exp[(E - E_0)/E_u]; E \le E_0, \quad (13.7)$$

where E_u is the Urbach energy [15]. By ensuring that both $\varepsilon_2(E)$ and its first derivative are continuous at $E = E_0$, no additional free parameters are needed for addition of the Urbach tail. Alternatively, one can also fit the $\varepsilon_2(E)$ data below E_0 to determine E_u whereby $\varepsilon_2(E_0)$ is again determined by continuity of ε_2 at E_0. The contribution of the Urbach tail to $\varepsilon_1(E)$ in (13.5) can be neglected for CdS and CdTe.

The dielectric functions analyzed using this approach were obtained in separate experiments in which 500–1000 Å layers of CdS and CdTe were deposited on *c*-Si substrates and measured in situ after deposition at the elevated temperatures.

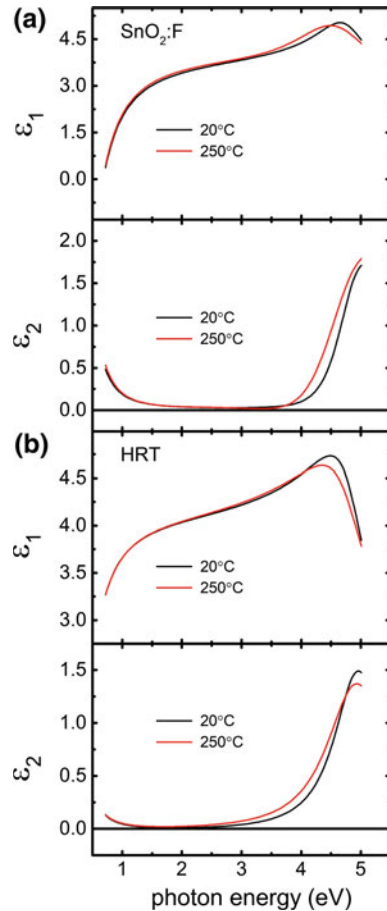

Fig. 13.4 Plots of analytical expressions for the dielectric functions versus photon energy for representative **a** SnO_2:F and **b** HRT layer components of the (TEC™ 15)/HRT substrate. Results are provided for the dielectric functions of the two layers obtained both at room temperature and at the CdS/CdTe deposition temperature of 250 °C

The best fit results are shown in Fig. 13.5. In the analyses of the RTSE data collected during the sputter depositions of CdS and CdTe at 250 °C, the dielectric functions shown in Fig. 13.5 for elevated temperature were used, along with those obtained for the substrate layers (those of Fig. 13.4 being illustrative). These dielectric functions are fixed throughout the RTSE analysis in which interface formation and structural evolution of the CdS and CdTe films are characterized. In situ data were also acquired after the completion of the depositions probed by RTSE and after cooling the solar cell structure to room temperature.

It should be emphasized that the CdS and CdTe dielectric functions were deduced from thin layer depositions on smooth substrates. As will be demonstrated in Sect. 13.3 the dielectric functions of these materials depend on processing and likely on the substrate as well. Thus, the results of Fig. 13.5 serve as a starting point for structural analysis of RTSE data. For in-depth analysis, however, it is important to describe the dielectric function in terms of a set of physical parameters such as

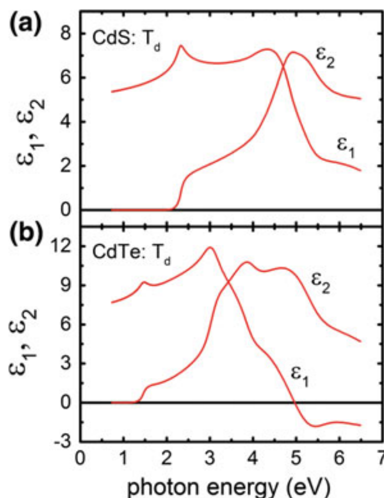

Fig. 13.5 Plots of analytical expressions that describe the dielectric functions of **a** CdS and **b** CdTe appropriate for a deposition temperature of 250 °C. These results were obtained in fits to the dielectric functions deduced for films deposited on crystalline silicon wafer substrates and measured in situ before cooling

stress and crystalline grain size that is smaller in number than the set of optical parameters in (13.5). This is a challenging goal for future scientific study.

13.2.3 Structural Evolution of CdS/CdTe

Figure 13.6 is a schematic representation of interface formation between a rough underlying film and an over-depositing film. Thus, this model is appropriate for the analysis of RTSE data acquired during the structural evolution of CdS on HRT and CdTe on CdS. As film growth is initiated, the depositing film begins to fill the void space within the modulations of the surface roughness layer of the underlying film. Simultaneously, the peaks in the surface roughness of the underlying film are coated with the depositing material, generating a roughness layer associated with the growing film. Initially, the volume fraction of depositing material in this new surface roughness layer is small. As the deposition proceeds and the depositing material roughness layer increases in thickness and in material volume fraction, the void space at the interface is essentially filled by the depositing material (with the possibility of some voids trapped there). A bulk layer component of the growing film first develops in association with the following three film growth features: (i) the interface layer with the underlying film approaches complete or stabilized filling; (ii) the roughness layer thickness on the growing film approaches that on the underlying film as an indication of conformal coverage of the underlying film; and (iii) the volume fraction of the roughness layer material component for the growing film approaches that of the underlying film in the interface layer also due to conformal coverage.

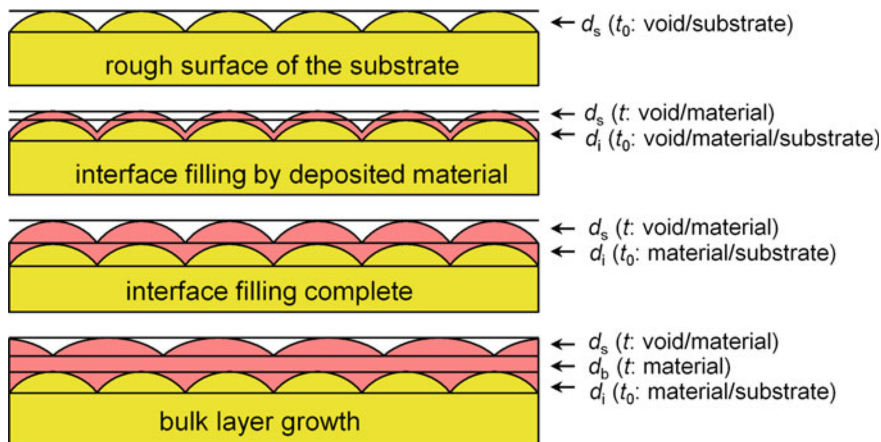

Fig. 13.6 Optical models representing the structural evolution of the CdS and CdTe thin film semiconductor materials deposited on rough underlying materials, as relevant for the analysis of the RTSE data of this study. When the deposition is initiated, the depositing material begins to fill the voids in the roughness layer on the surface of the substrate. Simultaneously a surface roughness region forms as a component of the growing film. As the deposition continues, the voids in the underlying roughness are replaced by the depositing material which then leads to the appearance of a bulk layer

Characterization of an interface interaction that may lead to $CdS_{1-x}Te_x$ and $CdTe_{1-x}S_x$ alloys at the CdS/CdTe interface, as has been done previously for CdS/CdTe deposition on *c*-Si [16] is not yet possible with this approach. The challenge in the present study arises from the microscopically rough HRT, serving as the underlying substrate layer. The rough HRT layers lead to rough CdS/CdTe interfaces which dominate over the interface interaction. In contrast, such interactions were detectable using virtual interface analysis of RTSE data acquired during similar CdS/CdTe depositions on atomically smooth *c*-Si substrates [16].

Figure 13.7a shows typical SE data acquired on a type II substrate at room temperature before heating the substrate to the deposition temperature. The corresponding best fit is based on the multilayer structure shown in Fig. 13.7b. The thicknesses of the component layers of the substrate and the variable parameters in the dielectric functions of the SnO_2:F and HRT were determined in this analysis. (The structural parameters also appear in Table 13.2 as the type II column.) The SE data acquired on the substrate at the deposition temperature were also analyzed. The typical substrate analysis shown in Fig. 13.7 is relevant for the sample whose CdS and CdTe layers were subsequently deposited using p_{Ar} settings of 20 and 10 mTorr and deposition times of 14.6 and 120 min, respectively. Thus, this specific deposition corresponds to a member of the constant CdS thickness series of solar cell structures.

RTSE data acquired during the deposition of each CdS layer were analyzed by fixing the thicknesses of the component layers for the substrate to the values

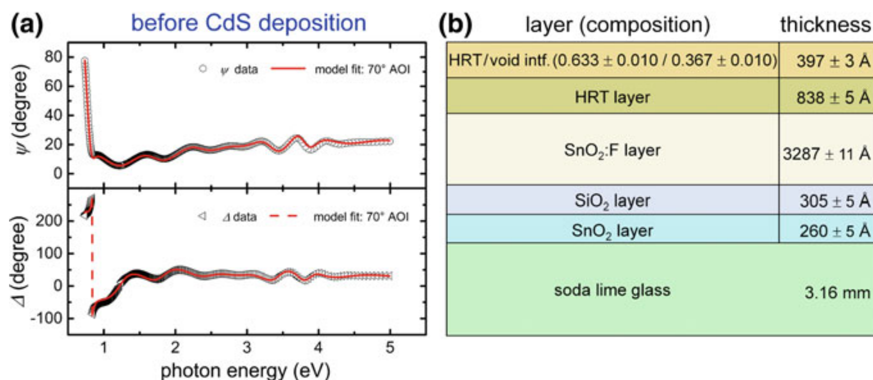

Fig. 13.7 **a** In situ SE measurement results at room temperature and best fit analysis results presented in the form of (ψ, Δ) spectra for a (TEC™ 15)/HRT substrate before the deposition of a CdS film from the constant thickness series using p_{Ar} = 20 mTorr. Also included in **b** are the structural model, the best fit structural parameters, and their confidence limits

obtained from the room temperature SE analysis, as illustrated in Fig. 13.7. Also in the RTSE analysis, the dielectric function parameters for the substrate component layers were fixed to the values obtained by analysis of in situ SE at the deposition temperature using previously identified variable and fixed parameters, as in Tables 13.3 and 13.4. No changes in the underlying properties of the HRT layer are assumed to occur during the deposition of the CdS. Because the RTSE data were analyzed by using a fixed set of CdS and CdTe dielectric functions obtained near the appropriate deposition temperature, the model does not take into consideration possibilities that the dielectric functions of the CdS and CdTe layers evolve with thickness, or that interactions occur at the HRT/CdS and CdS/CdTe interfaces other than interface filling. Figure 13.8a shows RTSE experimental data collected at t = 7.4 min during the 14.6 min CdS deposition on the (TEC™ 15)/HRT substrate structure at 250 °C. The corresponding best fit is also shown in Fig. 13.8a, with Fig. 13.8b providing the best fit structural model including the layer thicknesses and the interface and surface roughness compositions. This CdS deposition is a member of the constant thickness series using p_{Ar} = 20 mTorr, and so the fixed substrate structure is that shown in Fig. 13.7b. Thus, structural parameters without confidence limits are the fixed parameters as determined from SE analysis of the (TEC™ 15)/HRT substrate at room temperature from Fig. 13.7b.

Figure 13.9 depicts a complete set of results for RTSE analysis of the 14.6 min CdS deposition on the (TEC™ 15)/HRT substrate surface. The in situ substrate analysis and the analysis at t = 7.4 min during this deposition were provided in Figs. 13.7 and 13.8. Thus, the deposition is a member of the constant CdS thickness series corresponding to p_{Ar} = 20 mTorr for the CdS film deposition. The surface roughness thickness on the top-most HRT layer at t = 0 was that obtained in the room temperature analysis of Fig. 13.7. The information obtained in the least squares regression analysis and depicted in Fig. 13.9 includes the evolution with

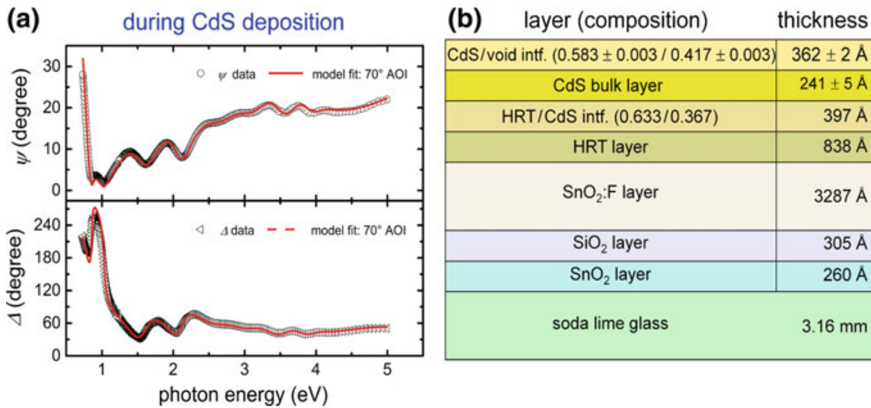

Fig. 13.8 **a** RTSE measurement results at the deposition temperature and best fit analysis results presented in the form of (ψ, Δ) spectra for CdS thin film growth on a (TEC™ 15)/HRT substrate. The measurement was performed at t = 7.4 min during the CdS deposition of Figs. 13.7 and 13.9, a member of the CdS constant thickness series using p_{Ar} = 20 mTorr. Shown in **b** are the structural model, the best fit thickness and composition variables, and their confidence limits. The values without confidence limits were fixed in the analysis from a study of the underlying (TEC™ 15)/HRT substrate

time of (a) the thickness of the CdS bulk layer; (b) the CdS volume fraction within the modulations of the HRT surface as these modulations evolve from HRT surface roughness to HRT/CdS interface roughness; (c) the CdS volume fraction within the roughness layer on the CdS surface; and (d) the thickness of the roughness layer on the CdS surface. Also shown in Fig. 13.9e is the evolution with time of the RMSE. The latter results can be applied to evaluate the validity of the structural and optical models developed to describe the growth process.

At t = 0 in Fig. 13.9, the top-most HRT layer on the substrate exhibits a rough surface quantified by a roughness layer thickness of 397 ± 3 Å, as determined from the room temperature analysis. The CdS structural evolution on this rough HRT surface, depicted schematically in Fig. 13.6, exhibits an interface filling regime (0 < t < 3.7 min) and a bulk layer growth regime (3.7 < t < 14.6 min) separated by the vertical broken line in Fig. 13.9. When a shutter initially blocking the sputtered flux is opened to begin the CdS deposition on the HRT surface, the interface filling regime is described by two characteristics that evolve simultaneously. First, the free space (voids) associated with the valleys in the surface roughness of the top-most HRT layer fills with CdS material. The volume fraction of CdS within the developing interface layer is designated f_i(CdS). Second, the peaks in the HRT surface roughness are covered by CdS conformally such that a CdS roughness layer is formed. The thickness and CdS volume fraction for this roughness layer are designated d_s(CdS) and f_s(CdS), respectively. Upon completion of interface filling, which occurs when f_i(void) → 0 or at t = 3.7 min in Fig. 13.9 (vertical broken line), the onset of bulk layer growth is observed, as characterized by the appearance of the first monolayer [d_b(CdS) ~3 Å]. At this point the volume

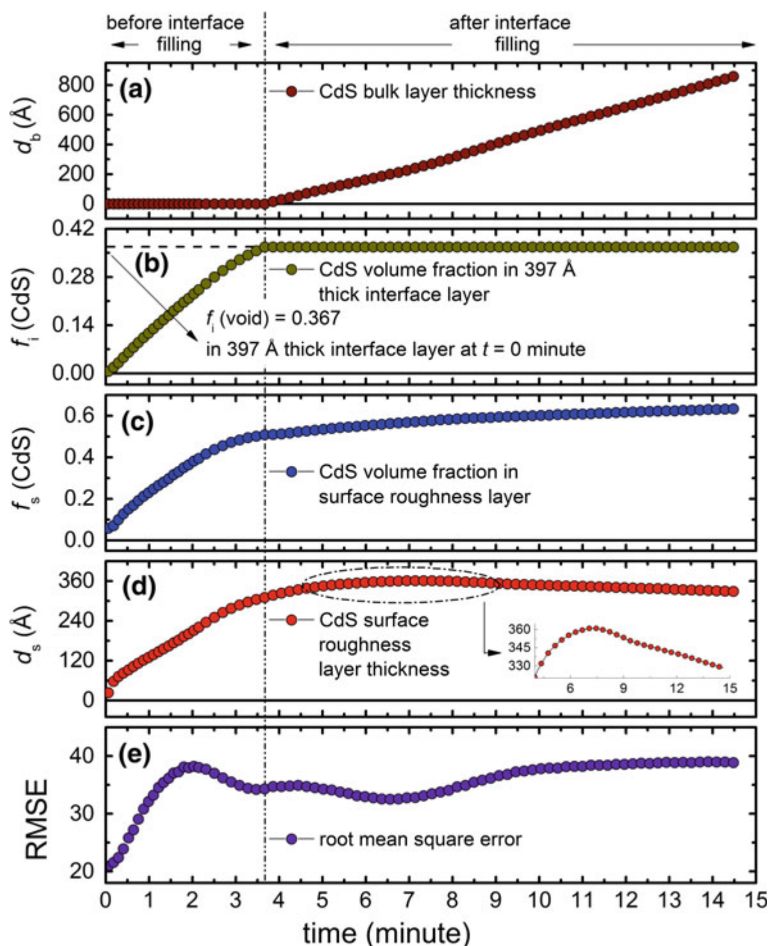

Fig. 13.9 Structural parameters from analysis of RTSE measurements performed during the growth of a CdS film to a final effective thickness of ~1200 Å on the surface of a rough HRT coated substrate. This deposition was a member of the constant thickness series with $p_{\mathrm{Ar}} = 20$ mTorr. The panels include **a** the thickness of the CdS bulk layer; **b** the volume fraction of CdS within the HRT/CdS interface layer; **c** the volume fraction of CdS within the CdS surface roughness layer; **d** the thickness of the CdS surface roughness layer; and **e** the RMSE, which is used to evaluate the quality of the fit to the RTSE results

fraction of CdS within the CdS surface roughness layer is given by f_s(CdS) = 0.51. For $t > 3.7$ min, the CdS volume fraction within the HRT/CdS interface roughness layer is fixed at its completely-filled value of f_i(CdS) = 0.367 ± 0.010. During the bulk layer growth regime, $3.7 < t < 14.6$ min, the thickness of the bulk layer d_b(CdS) increases from the monolayer scale to 871 ± 6 Å. A constant deposition rate for the CdS bulk layer thickness is reached once the surface characteristics stabilize. During the bulk layer growth regime, the CdS content in the roughness

layer on the CdS surface increases, and its thickness passes through a maximum, which occurs at $t = 7.4$ min in Fig. 13.9.

The RTSE results exhibit high sensitivity to the structural development of the deposited layer, as indicated both by the interface filling regime and by the bulk and surface roughness evolution. As indicated in Fig. 13.9, a CdS component as low as 5 vol.% can be observed in the initial stages of substrate-induced evolution of the CdS surface roughness ($d_s < 20$ Å) as the HRT is conformally covered. Shown in Fig. 13.10a are the experimental ellipsometry spectra (ψ, Δ) and the results of the best fit at $t = 14.6$ min, i.e. at the end of the CdS deposition, at the deposition temperature. The schematic in Fig. 13.10b includes the best fit thicknesses and compositions of the component layers deduced in the analysis of the RTSE data for the final CdS film. In fact, the CdS surface nature and its roughness at the end of the deposition is expected to impact the characteristics of the heterojunction, as this junction is generated by the over-deposition of the CdTe on the rough CdS surface. Two results of interest can be identified from these analysis results. First, the effective thickness of CdS (or its volume/area) can be determined at the end of deposition according to $d_{\rm eff} = f_i({\rm CdS})d_i + d_b + f_s({\rm CdS})d_s = 1225 \pm 9$ Å. This value matches closely the intended thickness of 1200 Å. This thickness affects the quantum efficiency in the near ultraviolet to green region of the solar spectrum (0.35–0.55 μm) and, thus, to a lesser extent the (current-density)-voltage characteristics of the heterojunction diode. Second, the surface roughness layer thickness and the CdS volume fraction are given in Fig. 13.10b at the end of deposition, by d_s(CdS) ~328 ± 3 Å and f_s(CdS) ~0.634 ± 0.004, respectively. These final roughness layer characteristics appear to be controlled predominantly by the corresponding characteristics of the roughness on the underlying HRT layer. This conclusion is drawn by comparing the results of Fig. 13.10 to RTSE results for the structural evolution and final roughness thickness of a series of CdS films deposited on smooth *c*-Si substrates. For the latter results, the roughness layer thicknesses were in the range of 5–25 Å after thin film coalescence and relatively stable during the growth of ~1000 Å thick films [6, 17].

Corresponding results have been obtained in RTSE studies of CdTe deposition on (TEC™ 15)/HRT/CdS to form the solar cell's heterojunction. Figure 13.11a shows experimental RTSE data at $t = 60.7$ min and the corresponding best fit during CdTe deposition by magnetron sputtering on the (TEC™ 15)/HRT/CdS substrate structure at the elevated temperature. The sample was from the constant CdS thickness series using $p_{\rm Ar} = 20$ mTorr for the underlying CdS deposition. Figure 13.11b shows the optical model with layer thicknesses and composition determined from the RTSE analysis. Parameters without confidence limits are those fixed as determined from SE analysis of the underlying (TEC™ 15)/HRT/CdS structure at the end of CdS deposition at the deposition temperature, as in Fig. 13.10b.

Figure 13.12 summarizes the results of the RTSE studies of CdTe deposited on the CdS surface, the latter with a ~328 Å surface roughness layer thickness. The panels include: (a) the thickness of the CdTe bulk layer; (b) the volume fraction of CdTe within the CdS/CdTe interface, which saturates at the onset of bulk layer

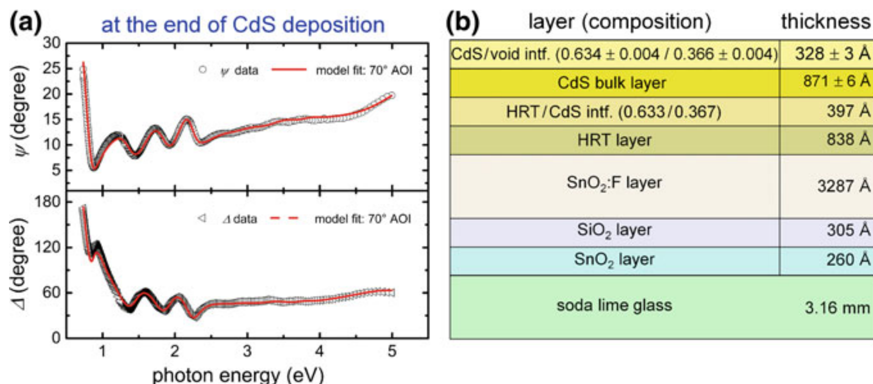

Fig. 13.10 **a** RTSE measurement results at the deposition temperature and the corresponding best fit analysis results presented in the form of the (ψ, Δ) spectra for the (TEC™ 15)/HRT/CdS structure of Figs. 13.7, 13.8, and 13.9 from the constant thickness series using p_{Ar} = 20 mTorr. The measurement was performed at t = 14.6 min, i.e. at the end of the deposition. Also shown in **b** are the structural model, the best fit variable parameters, and their confidence limits. The values without confidence limits were fixed in the analysis from a study of the underlying (TEC™ 15)/HRT substrate

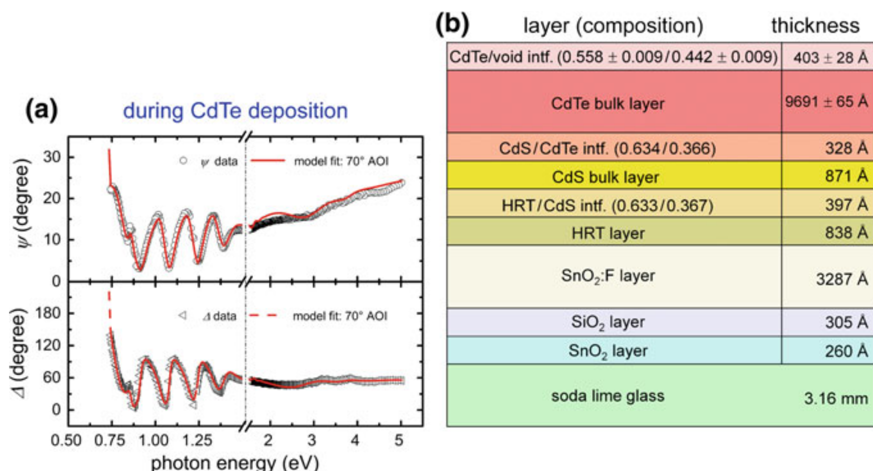

Fig. 13.11 **a** RTSE measurement and best fit analysis results presented in the form of the (ψ, Δ) spectra for the (TEC™ 15)/HRT/CdS/CdTe structure of Fig. 13.12. Also shown in **b** are the structural model, the best fit variable parameters, and their confidence limits. The measurements were obtained during the deposition of the CdTe film at t = 60.7 min on the structure obtained in the constant CdS thickness series using p_{Ar} = 20 mTorr for the CdS deposition

growth; (c) the volume fraction of CdTe within the roughness layer on the CdTe surface; (d) the thickness of the surface roughness layer on the growing film; and (e) the RMSE. The starting CdS sample is the same as that of Figs. 13.9 and 13.10,

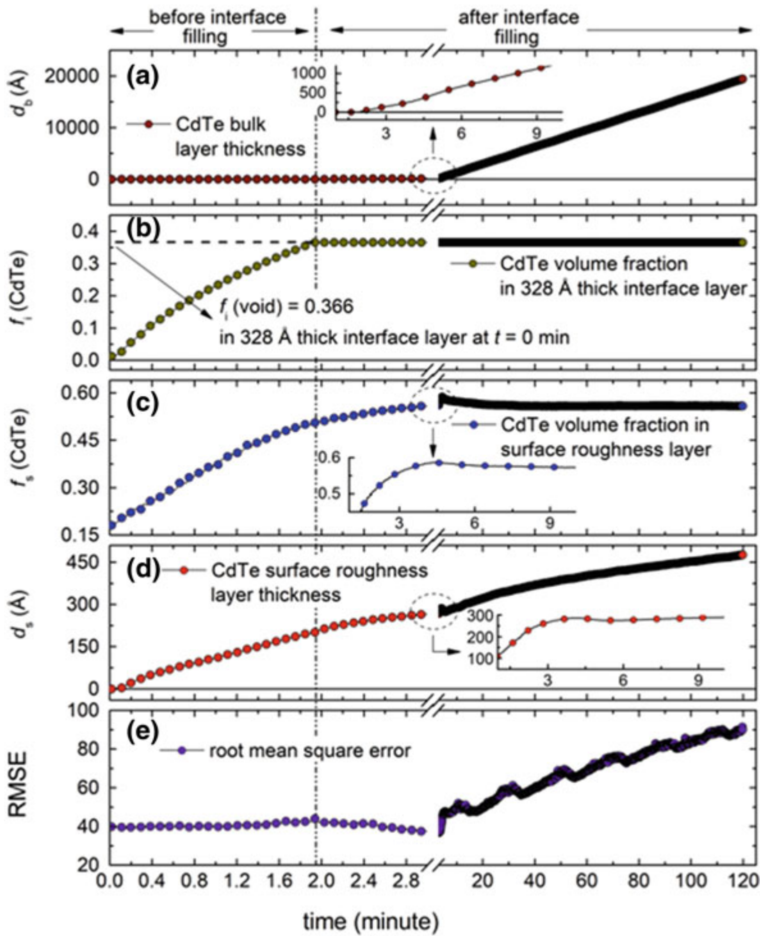

Fig. 13.12 Structural parameters obtained in an analysis of RTSE data that characterize the sputter deposition of a 2 μm thick CdTe film on the rough surface of CdS, the latter prepared as a member of the constant thickness series with p_{Ar} = 20 mTorr. The panels include **a** the thickness of the CdTe bulk layer; **b** the volume fraction of CdTe within the CdS/CdTe interface roughness layer; **c** the volume fraction of CdTe within the roughness layer on the CdTe surface; **d** the thickness of the CdTe surface roughness layer; and **e** the RMSE, which is used to evaluate the quality of the fit to the RTSE results

and so is a member of the constant CdS thickness series with p_{Ar} = 20 mTorr. In Fig. 13.12, the CdTe deposition on the CdS film surface follows the analogous process as for CdS deposition on the HRT film surface. Upon opening the shutter to initiate the CdTe deposition, the void space within the surface roughness valleys of the underlying CdS is filled with the depositing CdTe material. Simultaneously, the depositing CdTe forms a surface roughness layer of its own via conformal coverage of the peaks in the underlying CdS surface roughness. The volume fractions of

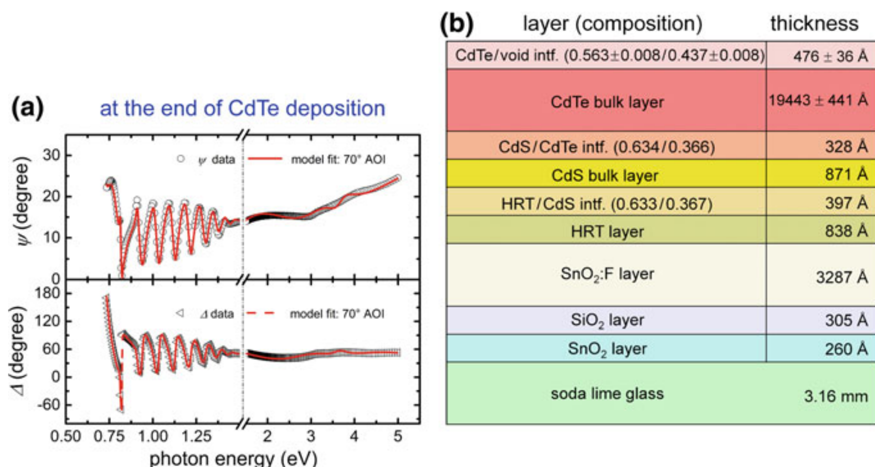

Fig. 13.13 **a** RTSE measurement results at the deposition temperature and the best fit analysis results presented in the form of the (ψ, Δ) spectra for the (TEC™ 15)/HRT/CdS/CdTe structure at the end of the CdTe film deposition. Shown in **b** are the structural model, the best fit variable parameters, and their confidence limits. These results were obtained for the deposition of Fig. 13.12 with the underlying structure from the CdS constant thickness series using $p_{\mathrm{Ar}} = 20$ mTorr in the CdS deposition

CdTe within the interface and surface layers increase with time in the first ~2 min of the deposition. Once the CdS/CdTe interface filling process is complete, the CdTe bulk layer begins to form, covering the CdS/CdTe interface layer. These features of the structural evolution are evident in Fig. 13.12 with the vertical broken line separating the interface filling and bulk layer growth regimes. Shown in Fig. 13.13 are the experimental ellipsometry spectra (ψ, Δ) at the end of the deposition, acquired at the deposition temperature, along with the results of the best fit to these spectra.

In efforts to improve the existing structural and optical models, as assessed by reductions in the time-averaged RMSE, one may consider first the possibility of a dependence of the complex dielectric functions of CdS and CdTe on structure size or thickness. This effect has been investigated in RTSE studies of CdS and CdTe film growth on smooth silicon wafer substrate surfaces. In the RTSE investigation, the largest change in the ε spectra as a function of thickness occurs for $d_b < 500$ Å and is associated with the oscillator amplitude parameters [6]. This indicates a change in void volume fraction, an effect not included in the models of Figs. 13.6, 13.9, and 13.12 due to the use of fixed dielectric functions and the constraint of complete interface filling in the adopted models. Further such complications in the structural and optical models have been explored through analysis of ex situ variable angle SE measurements. This analysis includes modifications in the ε spectra for the underlying HRT and overlying CdS layers as a result of atomic inter-diffusion [11]. Generally, the effects on the (ψ, Δ) spectra generated by inter-diffusion are found to be much weaker than those of the overall film structural

evolution, characterized by the processes of interface filling, substrate-induced roughness development, and bulk layer growth as applied in the existing models. In the future, the analysis may be extended to include effects of atomic inter-diffusion, in conjunction with complementary ex situ materials analysis as in previous studies [2], in efforts to reduce the time-average of the RMSE to values less than that achieved in Figs. 13.9 and 13.12. In the CdTe deposition process, for example, it is important to determine the extent to which Te diffuses into the underlying CdS, and S diffuses into the overlying CdTe. This may be possible by fixing the less critical structural parameters, and allowing changes with time in the optical parameters of a fixed thickness region of the CdS, including its surface layer component. Similarly, the optical parameters of the growing CdTe could be allowed to vary with time. Such efforts would be facilitated using parameterizations that describe the effect of small values of x in $CdS_{1-x}Te_x$ and in $CdTe_{1-x}S_x$ on the optical parameters that describe their dielectric functions [16].

13.2.4 Application: Role of Ar Pressure in CdS Sputter Deposition

Figure 13.14 shows the deposition rate given in terms of effective thickness plotted as a function of p_{Ar} for CdS layers deposited on (TEC™ 15)/HRT substrates using the deposition parameters listed in Table 13.1. This calculation is based on RTSE data analyses as in Fig. 13.9. The RTSE data were obtained during the CdS depositions of the constant time series. The plot shows an exponential decrease in the deposition rate with increasing pressure. Thus, throughout the pressure range, the sputtered species undergo multiple collisions between the target and substrate, separated by 14 cm, with increasing numbers of collisions occurring with

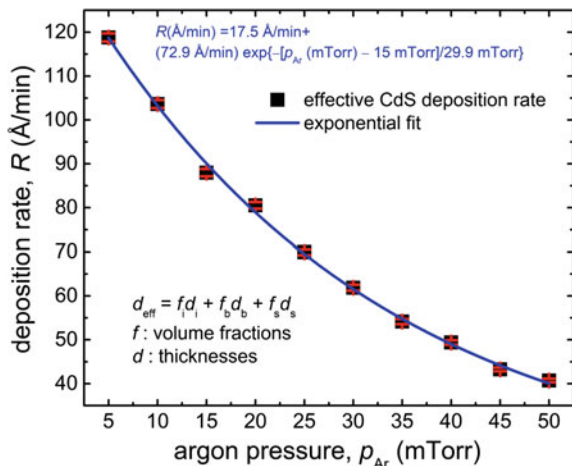

Fig. 13.14 The CdS deposition rate in term of effective thickness plotted versus Ar pressure. These results are obtained by analyzing the RTSE data acquired during the 12 min of the constant time series for CdS depositions on (TEC™ 15)/HRT. The deposition rate decreases exponentially with pressure according to the expression given at the top of the figure

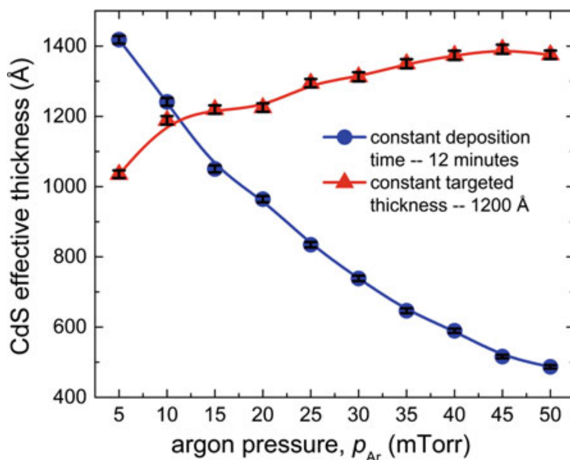

Fig. 13.15 The CdS effective thicknesses at the end of deposition as deduced by RTSE analysis plotted as functions of the CdS p_{Ar} value over the range 5–50 mTorr. Circles denote CdS depositions of the constant time series (12 min deposition time), and the triangles denote CdS depositions of the constant thickness series (1200 Å target effective thickness)

increasing pressure. As a result of enhanced scattering of the precursor species in the gas phase, the deposition rate decreases continuously with increasing pressure.

Figure 13.15 shows the final CdS effective thicknesses plotted versus p_{Ar} for twenty different samples deposited on (TEC™ 15)/HRT using ten different p_{Ar} values for two different time durations. Samples with CdS layers deposited for the constant time interval of 12 min exhibit CdS effective thicknesses ranging from ~1400 to 500 Å as the pressure is increased, and the CdS samples deposited for variable durations in an attempt to achieve a constant targeted thickness of 1200 Å exhibit effective thicknesses in the range of ~1000–1400 Å. These values were calculated by analyzing the RTSE data at the end of CdS deposition using the model similar to that in Fig. 13.10b. The RTSE measurement point corresponds to a location near the center of the 5 cm × 5 cm sample.

RTSE provides accurate thickness values during solar cell fabrication for monitoring and control capabilities, which are particularly useful when applied to CdS layer deposition. In addition, RTSE results can reveal small differences that may occur in the structural evolution due to differences in the deposition parameters. RTSE data collected during the CdS depositions at different Ar pressures p_{Ar} were analyzed by using the analogous models to those shown in Figs. 13.6, 13.8, and 13.9. Figure 13.16 shows a plot of CdS roughness layer thickness, d_s(CdS) versus CdS bulk layer thickness d_b(CdS) for the constant time and constant thickness series. When the deposition is initiated, the interface filling process begins as in Fig. 13.9. Only after the completion of HRT/CdS interface filling, does the bulk component of the CdS layer begin to appear. The surface roughness layer, on the other hand, is increasing from the beginning of the deposition. Hence, at the point when the first bulk monolayer appears, a ~275–315 Å thick surface roughness layer already exists, covering the underlying HRT film. As the bulk layer grows, the surface layer thickness continues to increase and attains a maximum value near a bulk layer thickness of d_b(CdS) ~ 250 Å. For the sample of the

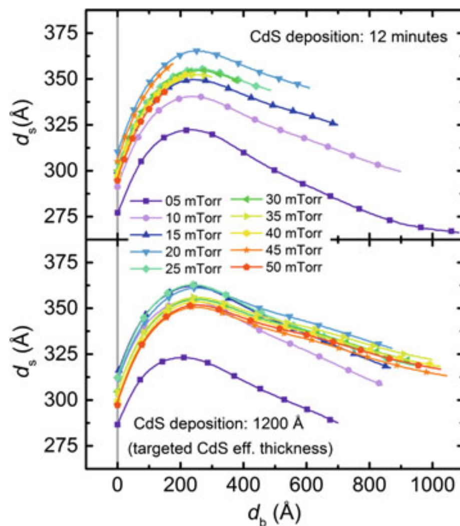

Fig. 13.16 The CdS surface roughness layer thickness plotted versus CdS bulk layer thickness for two sets of samples prepared with p_{Ar} values over the range 5–50 mTorr. The panel at the top shows the CdS depositions of the constant time series with 12 min deposition duration, and the panel at the bottom shows the CdS depositions of the constant thickness series with intended effective thickness of ~1200 Å

constant thickness series with p_{Ar} = 20 mTorr, the maximum in surface roughness is also highlighted in the inset of Fig. 13.9d. For the samples of the constant time series deposited at $p_{Ar} > 35$ mTorr, the deposition ends before the surface roughness on CdS attains its maximum value. This occurs due to the reduction in deposition rate in Fig. 13.14, which leads to a much slower growth evolution and a thinner bulk layer at the end of the deposition as in Fig. 13.15. For the samples with thicker bulk layers, upon further deposition beyond the maximum in d_s, a weak coalescence effect occurs, resulting in a somewhat smoother surface relative to the observed maximum. The features of CdS surface roughness evolution appear to be characteristic of the underlying (TEC™ 15)/HRT surface used in the device configuration. In contrast to the results in Fig. 13.16, similar CdS sputter depositions on *c*-Si exhibit stable roughness layers in the range of 5–25 Å after nucleation and coalescence [17]. Thus, the effect of Ar deposition pressure in controlling the CdS surface roughness is relatively small compared to that of the underlying substrate. Figure 13.16 shows that the structure incorporating CdS prepared at an Ar pressure ~20 mTorr exhibits the largest surface roughness layer thickness in both series, whereas the samples prepared at lower and higher p_{Ar} exhibit smoother surfaces. In fact, the CdS films deposited at 5 mTorr show the smoothest surfaces of all, throughout the bulk growth regime. Similarly smooth surfaces in the low Ar pressure deposition are observed for both series.

Figure 13.17 shows the thickness of the CdS surface roughness layer and the volume fraction of CdS within the roughness layer, both at the onset of bulk layer evolution, plotted versus the p_{Ar} setting for the CdS deposition. The maximum value of the CdS roughness layer thickness and the value of the CdS volume fraction within the layer at this maximum are also plotted versus p_{Ar}. The scatter in the d_s values in this plot is likely to arise due to variations in the surface roughness

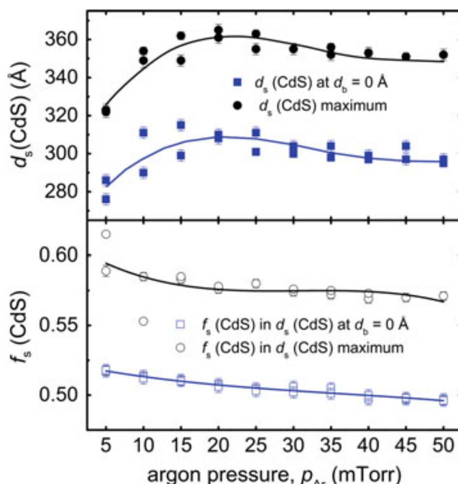

Fig. 13.17 Thickness of the roughness layer on the CdS surface and the volume fraction of CdS within the roughness layer both plotted as functions of the Ar pressure used in CdS magnetron sputtering. These results were obtained for both deposition series at the onset of CdS bulk layer growth (squares); corresponding results at the maximum in the CdS roughness layer thickness are also shown (circles)

on the underlying HRT. Because the roughness layer thickness on the CdS surface is less than that on the HRT surface (see Table 13.2, for example), one must conclude that the CdS deposition smoothens the evolving surface to a certain extent under all conditions of Ar pressure; however, there remains a dominant influence of the HRT. The results show that such smoothening relative to the HRT is enhanced most strongly at low p_{Ar}, and is also enhanced relatively weakly with increasing p_{Ar} above $p_{Ar} = 20$ mTorr. The trend at low pressure can be associated with a smoothening effect induced by bombardment of the surface by incoming sputtered film precursors, which can lead to preferential resputtering or removal of the atoms from the asperities on the CdS surface. The trend at high pressure can be associated with a smoothening effect generated by scattering of film precursors in the gas phase which randomizes the directionality of the sputtered precursors. The results in Fig. 13.17 for the material volume fractions in the CdS roughness layers demonstrate that these layers are more compact at the low Ar pressures, consistent with the proposed bombardment effect. The roughness layers also become more compact as the deposition proceeds, as illustrated in Fig. 13.9.

Figure 13.18 shows a plot of the final roughness layer thickness on the CdS surface at the end of the deposition for all the samples of the constant thickness series, i.e. when the target effective thickness is 1200 Å. These results are plotted versus the surface roughness layer thickness on the associated (TEC™ 15)/HRT substrate. Due to the incomplete evolution of the surface roughness layer, a similar comparison as that of Fig. 13.18 is not possible for the samples of the constant time series. The results of Fig. 13.18 indicate that, although the magnitude of the surface roughness at the end of the CdS deposition is controlled primarily by the roughness on the surface of the underlying HRT layer, effects depending on p_{Ar} are observed at a finer level. It is clear here as in Fig. 13.16 that the smoothest surfaces at the end of deposition are obtained at the lowest pressures, and the roughness thickness passes through a maximum with increasing pressure. A maximum in roughness

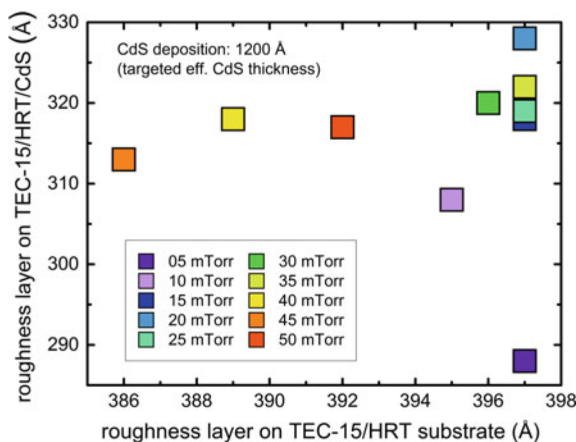

Fig. 13.18 Surface roughness layer thicknesses at the end of deposition for CdS having a target effective thickness of 1200 Å. These results are plotted versus the surface roughness layer thicknesses on the (TEC™ 15)/HRT substrates for all the samples of the constant thickness series. The magnitude of the roughness on the CdS surface is controlled primarily by the roughness on the surface of the underlying HRT layer. At lower and higher deposition p_{Ar}, however, smoothening appears to be induced by bombardment and by gas phase scattering of precursors, respectively, and exert measurable effects on the final CdS roughness thickness. The scatter in the roughness layer thickness on the (TEC™ 15)/HRT arises predominantly from the type I substrates (35–50 mTorr depositions)

thickness at p_{Ar} = 20 mTorr suggests smoothening induced by bombardment at the lowest pressures and smoothening induced by gas phase scattering of precursors at high pressures. Because it is likely that the grains in the polycrystalline CdS film extend above the surface and contribute to the roughness, it is possible that the maximum roughening of the 20 mTorr CdS deposition reflects the largest grain growth processes.

The nature of the surface roughness on the CdS layer at the end of its deposition is likely to influence the formation of the heterojunction with CdTe. For evaluation of the effect of Ar pressure in CdS deposition on photovoltaic device performance, a total of 36 dot cells were fabricated on each of the 5 cm × 5 cm structures of the two ten-member series in which the Ar pressure in CdS deposition was a variable, resulting in 36 × 20 = 720 dot cell devices. The CdS effective thickness values for each of the 20 structures are shown in Fig. 13.15. These thickness values correspond to the RTSE monitoring point which lies at the center of the sample. From the center of the sample to the edge for each of these 5 cm × 5 cm samples, there exists an ~10% effective thickness non-uniformity.

In an attempt to clarify the effect of Ar pressure in the deposition of CdS, four solar cell performance parameters versus thickness were analyzed for different groupings of p_{Ar} according to p_{Ar} = 5, 10, 17.5 ± 2.5, 30 ± 5, and 45 ± 5 mTorr. Figure 13.19 shows the CdS effective thickness at which the highest cell efficiency is obtained (top panel) as well as the highest efficiency value itself (bottom panel),

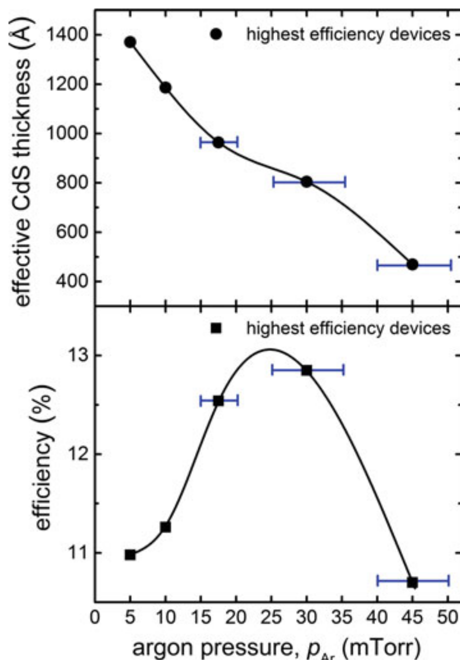

Fig. 13.19 CdS effective thickness at which the highest cell efficiency is obtained (top panel) and the highest efficiency value (bottom panel) both plotted versus the CdS p_{Ar} grouping value. These results summarize available cell performance data for the depositions of Fig. 13.15

both plotted versus the CdS p_{Ar} value that characterizes the grouping. From these results, one observes that the optimum CdS effective thickness decreases with increasing CdS Ar pressure at least from 1400 to 800 Å with the increase of p_{Ar} from 5 to 25 mTorr. This behavior in Fig. 13.19, top panel, may arise if high pressure provides improved coverage of the HRT/CdS interface due to more randomly directed incoming flux, enabling thinner CdS. The maximum efficiency occurs in the intermediate pressure range where CdS exhibits the largest roughness attributed to enhanced crystallite growth. In this range, the energies of the incoming precursors may be large enough to promote surface mobility, but not so large as to generate damage to the underlying atomic layers. A two-step CdS deposition process of high pressure followed by intermediate pressure is suggested by these results.

13.3 Mapping Spectroscopic Ellipsometry of CdTe Solar Cells

The ability to characterize the structural, optical, and electrical properties of the CdTe solar cell component layers and to control these properties throughout the several solar cell processing steps over large areas, is critically important for the optimization of devices and the scale up of new processes [1]. The first steps in the optimization of thin film solar cells involve the measurement of component layer

thicknesses, compositions, and optical properties, as these characteristics determine the maximum possible short-circuit current density value for the device. Spectroscopic ellipsometry (SE), as a non-invasive optical analysis method, is capable of determining the properties of the critical thin films in CdTe technology, such as those of the CdS heterojunction partner and the Cu back contact component, with thickness sensitivity approaching the monolayer level in measurements performed over large areas.

In Sect. 13.2, the application of in situ real time SE was described for monitoring of CdS and CdTe deposition by magnetron sputtering on the TCO-coated glass surfaces used in solar cell fabrication. In this section, ex situ mapping SE (M-SE) will be described for similarly prepared solar cells. These measurements are performed over larger substrates, 15 cm × 15 cm in size, onto which arrays of dot cells 16 × 16 in number have been fabricated [18]. With this M-SE capability, the 15 cm × 15 cm device structures can be analyzed at different stages during their fabrication. Thus, mapping by M-SE enables evaluation of the uniformity in the structural and optical parameters of the component layers over the full area of the device structure after each deposition and processing step. Also in this section, results are presented for the device performance parameters using different CdTe absorber layer thicknesses in correlation with the effective thickness of the CdS, the $CdCl_2$ treatment duration, and the effective thickness of the Cu back contact interlayer. Such correlations can take advantage of the non-uniformities in thin film deposition and processing to facilitate and expedite performance optimization.

13.3.1 Experimental Methods

Magnetron sputtering processes were used to deposit CdS and CdTe thin films onto TEC™ 15 substrates 15 cm × 15 cm in size, in turn coated with layers of high resistivity transparent conducting oxides (HRT layers). The fixed conditions for the CdS and CdTe depositions include a substrate temperature of 250 °C; an rf power of 200 W; and an Ar flow of 23 sccm. The Ar pressures (p_{Ar}) were set at values of 15 mTorr for the CdS depositions and 10 mTorr for CdTe depositions. In the standard solar cell fabrication process, CdS and CdTe deposition times of 12 and 120 min led to the targeted effective thickness values of 1200 Å and 2 μm, respectively. Ex situ M-SE was performed on the as-deposited samples using a commercially-available mapping system (AccuMap-SE, J.A. Woollam Co., Inc) [19, 20]. With this system, measurement of the as-deposited multilayer stack can be performed over the full device structure area of 225 cm^2 at the 256 locations where dot cells are fabricated. The M-SE instrument employs a rotating compensator for polarization modulation and a multichannel detector to achieve spectroscopic data acquisition at the high speeds required for mapping at a large number of spatial positions. M-SE was performed in a through-the-glass measurement mode. Thus, the device structure was illuminated from the glass side, and the only beam collected is that undergoing a single pair of passes through the glass, and thus a single

reflection from the back glass/film-stack interface. To avoid incoherent mixing of beams in these M-SE measurements, the first reflection, occurring from the ambient/glass interface, is blocked as are the reflections that undergo more than a single pair of passes through the glass. The details of the data acquisition and analysis techniques in through-the-glass mode can be found in the literature [21, 22].

The as-deposited solar cell structure was subjected to a $CdCl_2$ treatment step, which involved applying a $CdCl_2$ aqueous solution to the surface of the deposited CdTe and annealing the structure in dry air at 387 °C. For the standard structure with a targeted CdTe effective thickness of 2 μm, annealing was performed for 30 min. After the $CdCl_2$ treatment step, the device structure was again mapped by M-SE in through-the-glass mode at the locations where dot cells were subsequently fabricated. The $CdCl_2$-treated structure was completed by deposition of an intended Cu effective thickness of ~30 Å for the standard CdTe thickness and a Au thickness of ~300 Å, both using thermal evaporation without breaking the vacuum between the two metal layers. A mask was used for the deposition of the metal layers, which resulted in 256 individual dot cells each having an area of 0.125 cm^2. Next the structure with the metallic back contact dots was annealed at 150 °C over 45 min for Cu diffusion into the adjacent CdTe film. The (current-density)-voltage characteristic of each of the individual dot cells was measured under AM 1.5 illumination. When fabricating CdTe solar cells with thinner absorbers (<2 μm) various processing steps are adjusted to achieve optimum solar cell performance including reductions in the $CdCl_2$ treatment time and in the Cu layer thickness [23].

As an illustration of the M-SE capabilities, studies of the processing-property-performance relationships have been undertaken with different CdTe absorber layer thicknesses, and the results are presented in this section. In these studies, three different solar cell device structures were fabricated, each covering the area of a 15 cm × 15 cm (TEC™ 15)/HRT substrate using CdTe deposition times of 120, 72, and 43 min for intended effective thicknesses of the absorber layer of 2.0, 1.2, and 0.7 μm, respectively. The CdS deposition time of 12 min was fixed for each of the three structures. Each structure was cut into four pieces 7.5 cm × 7.5 cm in size so that four different $CdCl_2$ treatment times could be evaluated for a given CdTe thickness. These four treatment times were set within the three ranges of 18–30 min, 11–18 min, and 5–11 min for the three 15 cm × 15 cm structures with intended CdTe effective thicknesses of 2.0, 1.2, and 0.7 μm, respectively. The three structures were measured by M-SE before and after the $CdCl_2$ treatments. The M-SE measurements after treatment required reassembly of the four pieces. Back contacts were fabricated through a mask onto the three reassembled device structures with intended Cu effective thicknesses of 30 Å, 18 Å, and 11 Å for the structures with CdTe effective thicknesses of 2.0, 1.2, and 0.7 μm, respectively. An intended 300 Å thick layer of Au was then deposited through the same mask onto each reassembled device structure. The structure with back contacts was finally subjected to the standard 45 min anneal at 150 °C.

An additional sample structure incorporating 256 dot cells was fabricated in a modified process using a (TEC™ 15)/HRT substrate 15 cm × 15 cm in size. The

purpose of this structure is to reduce correlations between the CdS and CdTe effective thicknesses that occur due to the similarity of non-uniformity patterns generated by the deposition system. In the standard deposition process, the sample is transferred after CdS deposition from the CdS chamber to the CdTe chamber via linear translation without exposure to vacuum. In this process, the non-uniformity patterns of the two layers coincide. In the modified process, the sample was cooled to room temperature after CdS deposition and transferred to the load lock unit. Then the chamber was vented and the sample was rotated by 90° while minimizing the exposure time to the atmosphere. The sample was then returned to the deposition chamber for CdTe film growth. The effect of this modification was to decouple the correlations in the non-uniformity patterns of the two layer thicknesses. The structure from this modified process was mapped in similar fashion as the other samples of this study.

For all device fabrications, separate calibration experiments using M-SE were required because of the thinness of the Cu layer. In these experiments, CdTe depositions were performed by sputtering to the intended bulk layer thickness of ~200 Å onto SLG substrates 15 cm × 15 cm in size, followed by thin Cu depositions by thermal evaporation. This process is designed to simulate the spatial distribution in the Cu deposition rate, given in terms of effective thickness, over the 15 cm × 15 cm area of the cell structure. This distribution is used for effective thickness calibration given the different Cu deposition times used for the device structures with different CdTe effective thicknesses. M-SE measurements were performed on the resulting calibration samples immediately upon their removal from the deposition system in order to minimize the oxidation of Cu in the laboratory atmosphere and the possible diffusion of Cu into the underlying ~200 Å CdTe layer. For the intended Cu effective thicknesses of 11 Å and 18 Å, used for the device structures with CdTe effective thicknesses of 0.7 μm and 1.2 μm, respectively, the calibration from the thermal evaporation with an intended Cu effective thickness of 30 Å was applied. Thus, the calibrated thicknesses are scaled by factors of 0.37 and 0.60, respectively, in accordance with the reduced Cu deposition times used for these two device structures.

13.3.2 Dielectric Function Model for CdS and CdTe

For ex situ M-SE of solar cell structures, a database of the complex dielectric functions at room temperature is required for the solar cell components. In Sect. 13.2, this database has been described for the (TEC™ 15)/HRT components. In this section, the focus is on the CdS and CdTe components and their observed variability with processing. Identified variability arises from voids, in-plane film stress, and grain size or defect concentration, whose effects can be evaluated on the basis of the critical point (CP) amplitudes, energies, and broadening parameters, respectively. Alloying can also influence these CP parameters, resulting in complications that generate analysis challenges for alloy materials. For both CdS and

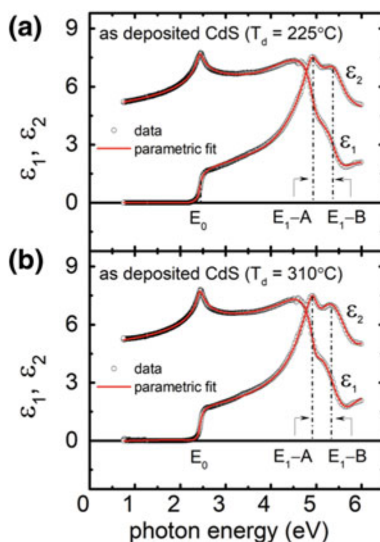

Fig. 13.20 Room temperature complex dielectric functions of CdS thin films deposited at substrate temperatures of 225 and 310 °C. These dielectric functions were obtained in separate experiments in which CdS layers were prepared by sputtering to thicknesses of ~500 Å on crystalline Si wafer substrates at elevated temperatures and measured in situ immediately after cooling to room temperature. The solid lines show parametric fits applying (13.5)–(13.7)

CdTe, approaches exist for parameter reduction when expressing the dielectric function in the form of an analytical function of oscillator parameters. For example, the oscillator amplitudes and energies, as well as the broadening parameters associated with the multiple CPs can be linked to single values of the void fraction, in-plane film stress, and excited carrier mean free path. For the four CPs in CdTe this can lead to a reduction in the number of free parameters by a total of nine in fits of ex situ M-SE data that incorporate an analytical model for the dielectric function as a sum of four CPs.

As examples for CdS, Fig. 13.20 shows real and imaginary parts of the complex dielectric functions for the bulk layers of two films sputter deposited at substrate temperatures of 225 and 310 °C, and measured in situ after cooling to room temperature. Also shown in Fig. 13.20 are the best fit dielectric functions applying (13.5)–(13.7) with parameters given in Table 13.5. Similarly, as examples for CdTe, Figs. 13.21a, b show real and imaginary parts of the complex dielectric functions at room temperature for sputter-deposited CdTe on a crystalline Si wafer in as-deposited and $CdCl_2$-treated states. For these CdTe dielectric functions, the film was deposited at 215 °C, cooled and measured in situ before exposure to laboratory ambient. After removal from the deposition system, the sample was annealed at 387 °C with $CdCl_2$ exposure, cooled and remeasured ex situ in the laboratory environment. The SE data collected on the as-deposited and $CdCl_2$-treated CdTe were analyzed using the inversion method, and the resulting dielectric functions were fitted applying the parameterized model given by (13.5)–(13.7). The film stress and excited carrier mean free path could be deduced consistently from the set of CP energies and broadening parameters, respectively [4–6, 24]. Also shown in Fig. 13.21c are the complex dielectric function spectra for single crystal

Table 13.5 Parameters from (13.5)–(13.7) representing room temperature complex dielectric functions of CdS thin films deposited at 225 and 310 °C. These dielectric functions were obtained in separate experiments in which ~500 Å CdS layers were deposited by sputtering on crystalline Si wafer substrates at elevated temperatures and measured in situ immediately after cooling to room temperature

Layer		Oscillators	Parameters						
			A_n	E_n (eV)	Γ_n (eV)	ϕ_n (°)	μ_n	E_g (eV)	ε_{1o}
CdS	T_d = 225 °C	CP (E_0)	6.781 ± 0.038	2.418 ± 0.002	0.091 ± 0.006	−23.124 ± 0.259	0.103		−1.590 ± 0.052
		CP (E_1-A)	2.092 ± 0.036	4.939 ± 0.004	0.234 ± 0.019	56.519 ± 1.613	0.777		
		CP (E_1-B)	5.920 ± 0.044	5.381 ± 0.009	0.702 ± 0.018	83.537 ± 2.212	0.489		
		T-L	116.520 ± 3.531 eV	6.262	5.495 ± 0.177			3.501	
		Urbach absorption	E_0 (eV)				E_u (eV)		
			2.418 ± 0.002				0.041 ± 0.004		
	T_d = 310 °C	CP (E_0)	6.949 ± 0.031	2.422 ± 0.002	0.071 ± 0.004	−22.774 ± 0.212	0.103		−1.5825 ± 0.0435
		CP (E_1-A)	2.133 ± 0.029	4.920 ± 0.003	0.212 ± 0.004	51.162 ± 1.292	0.777		
		CP (E_1-B)	6.151 ± 0.065	5.460 ± 0.006	0.641 ± 0.018	99.537 ± 1.511	0.489		
		T-L	128.612 ± 2.470 eV	6.262	4.947 ± 0.114			3.501	
		Urbach absorption	E_0 (eV)				E_u (eV)		
			2.422 ± 0.002				0.036 ± 0.002		

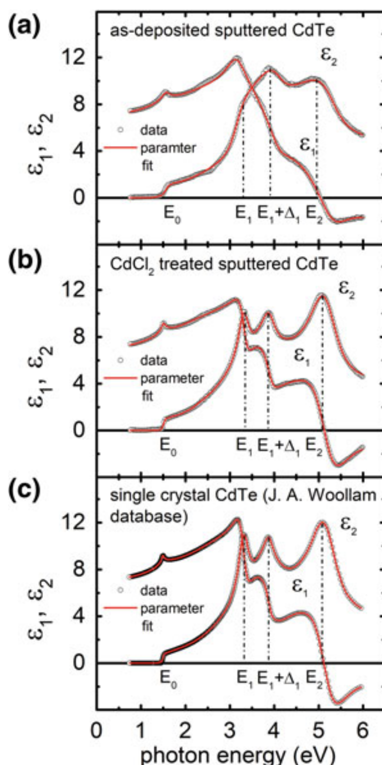

Fig. 13.21 Room temperature dielectric functions for **a** an as-deposited polycrystalline CdTe film measured in situ and **b** the same film after $CdCl_2$–treatment measured ex situ. The film was deposited to a thickness of ~1000 Å on a single crystal Si substrate at a temperature of 215 °C. **c** Dielectric function spectra are also shown for single crystal CdTe from a commercial software database (J. A. Woollam Co., Inc). Parametric forms of the inverted dielectric functions for the polycrystalline CdTe films and the database dielectric function for single crystal CdTe were obtained by applying (13.5)–(13.7)

CdTe and the best fit applying the same parameterization. The resulting CP energies for single crystal CdTe are consistent with zero stress, and the CP broadening parameters serve as a lower limit established by electron-phonon scattering at the measurement temperature. Table 13.6 lists the parameters in (13.5)–(13.7) for the best fit dielectric function spectra shown in Fig. 13.21.

This parameterization has critical applications in the analysis of completed multilayer solar cells by film side and through-the-glass SE. These applications can also be extended to on-line monitoring capabilities enabling characterization of material thickness, microstructure, and electronic quality. The analytical expression of the CdTe dielectric function incorporating photon energy independent variable parameters has been employed for M-SE analysis of sputter deposited as well as commercial CdTe panels as will be discussed in the following sections of this chapter.

Table 13.6 Parameters from (13.5)–(13.7) representing the room temperature dielectric function of a CdTe layer deposited at 215 °C and measured in situ after cooling. Also tabulated are the parameters for the same sample after $CdCl_2$ treatment, which involves annealing at 387 °C under $CdCl_2$ exposure, obtained by ex situ measurement after cooling to room temperature. The parameters of the analytical expression for the dielectric function of single crystal CdTe measured at room temperature are included, as well

Layer		Oscillators	Parameters						
			A_n	E_n (eV)	Γ_n (eV)	ϕ_n (°)	μ_n	E_g (eV)	ε_{1o}
CdTe	Single crystal CdTe	CP (E_0)	7.433 ± 0.036	1.491 ± 0.003	0.041 ± 0.005	−20.543 ± 0.103	0.048		−3.113 ± 0.031
		CP (E_1)	4.884 ± 0.015	3.310 ± 0.001	0.299 ± 0.003	−6.372 ± 0.149	1.089		
		CP ($E_1 + \Delta_1$)	7.345 ± 0.012	3.894 ± 0.001	0.286 ± 0.010	77.137 ± 0.169	0.377		
		CP (E_2)	5.319 ± 0.010	5.160 ± 0.001	0.923 ± 0.006	−31.006 ± 0.073	1.560		
		T-L	70.586 ± 0.221 eV	4.790	4.770 ± 0.016			1.710	
		Urbach absorption	E_0 (eV)				E_u (eV)		
			1.491 ± 0.002				0.035 ± 0.002		
	$CdCl_2$-treated	CP (E_0)	7.569 ± 0.129	1.493 ± 0.007	0.061 ± 0.011	−17.132 ± 0.304	0.048		−3.523 ± 0.110
		CP (E_1)	4.099 ± 0.049	3.300 ± 0.004	0.308 ± 0.026	−16.281 ± 0.611	1.089		
		CP ($E_1 + \Delta_1$)	6.041 ± 0.039	3.894 ± 0.008	0.300 ± 0.009	88.677 ± 0.740	0.377		
		CP (E_2)	5.035 ± 0.034	5.209 ± 0.008	0.951 ± 0.007	−29.052 ± 0.274	1.560		
		T-L	85.299 ± 0.888 eV	4.790	5.308 ± 0.063			1.710	
		Urbach absorption	E_0 (eV)				E_u (eV)		
			1.493 ± 0.007				0.036 ± 0.001		
	As-deposited	CP (E_0)	9.920 ± 0.142	1.547 ± 0.004	0.117 ± 0.023	−10.874 ± 0.202	0.048		−5.091 ± 0.119
		CP (E_1)	2.407 ± 0.033	3.145 ± 0.018	0.627 ± 0.025	−97.902 ± 0.986	1.089		
		CP ($E_1 + \Delta_1$)	6.321 ± 0.051	4.107 ± 0.021	0.570 ± 0.026	128.86 ± 0.837	0.377		
		CP (E_2)	2.219 ± 0.023	5.290 ± 0.026	1.100 ± 0.048	28.126 ± 0.724	1.560		
		T-L	95.260 ± 0.782 eV	4.790	4.238 ± 0.027			1.710	
		Urbach absorption	E_0 (eV)				E_u (eV)		
			1.547 ± 0.004				0.097 ± 0.004		

13.3.3 Maps of SnO_2:F and CdTe Properties

Figure 13.22 shows (ψ, Δ) spectra (points) identified with a single location excerpted from sets of through-the-glass M-SE measurements on a standard CdTe device structure 15 cm × 15 cm in size. Results are presented for the same location (a) before and (b) after an optimized $CdCl_2$ treatment. By standard, it is meant that the intended effective thicknesses of the CdS and CdTe layers were 1200 Å and 2 μm, respectively, the $CdCl_2$ treatment time was 30 min, and the intended Cu effective thickness was 30 Å. The best fits in Fig. 13.22 (lines) provide both the optical and structural parameters of the multilayer device structures using the

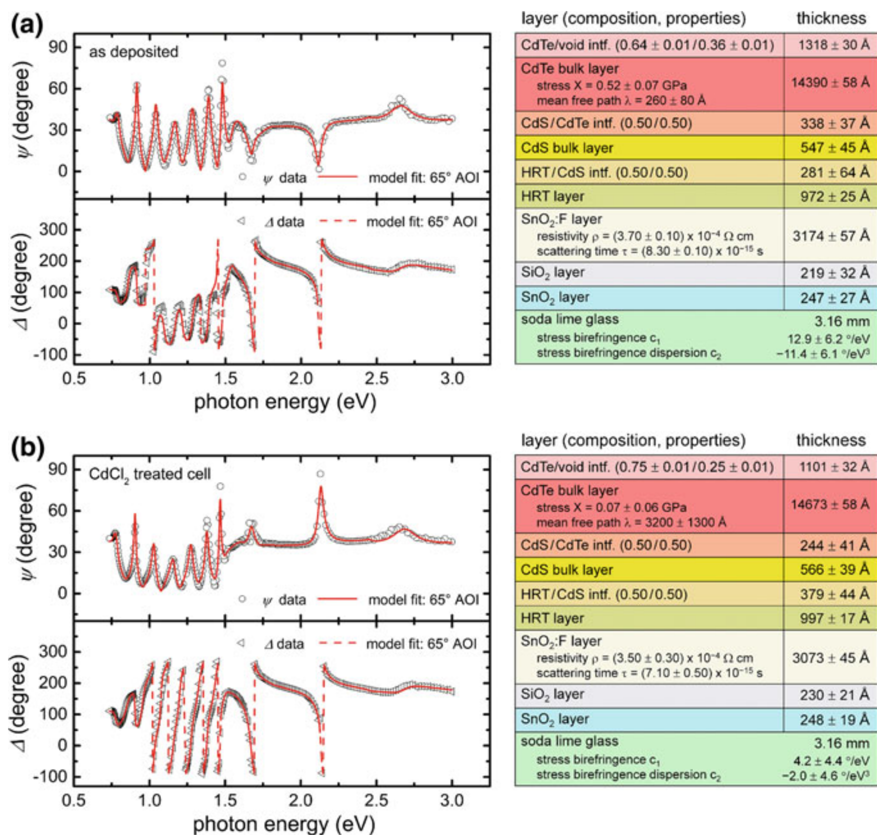

Fig. 13.22 Experimental through-the-glass ellipsometry spectra (points) and associated best fit results (lines) for a representative dot cell location within an array of 16 × 16 devices, each cell having an area of 0.125 cm^2. Parts **a** and **b** correspond to SE data and analysis results for the device structure before and after $CdCl_2$ treatment, respectively. Structural models and corresponding best fit parameters along with their confidence limits from the SE analyses are shown on the right side of each figure. A 65° angle of incidence (AOI) was employed for both pairs of spectra

Table 13.7 Physical and electrical characteristics for as-deposited and $CdCl_2$-treated CdTe and for TEC™ 15 SnO_2:F, as determined from analyses of M-SE data at one location on the standard solar cell structure mapped in Figs. 13.23 and 13.24. The CdTe parameters derive from a CP model of the E_0 bandgap transition, with relationships between the CP energy and stress and between the broadening parameter and excited carrier mean free path given elsewhere [4, 5]. The parameters of the SnO_2:F material define the Drude model for the free electron component of the dielectric function, with an assumed electron effective mass of $m_e* = 0.38\ m_e$, where m_e is the free electron mass [25]

	Optical parameter deduced from M-SE analysis				
Layer	Bandgap, E_0 (eV)	Compressive stress (GPa)		Broadening, Γ_0 (eV)	Mean free path (Å)
As-deposited CdTe	1.524 ± 0.005	0.46 ± 0.06		0.090 ± 0.009	195 ± 51
$CdCl_2$-treated CdTe	1.505 ± 0.004	0.20 ± 0.06		0.056 ± 0.003	634 ± 177
Layer	Resistivity, ρ (10^{-4} Ω-cm)	Scattering time, τ (10^{-15} s)	Carrier concentration (10^{20} cm^{-3})	Mobility (cm^2/Vs)	Sheet resistance (Ω/sq.)
SnO_2:F before CdS/CdTe deposition	3.36 ± 0.13	7.28 ± 0.22	5.51 ± 0.38	34 ± 1	10.6 ± 0.4
SnO_2:F after CdS/CdTe deposition	3.59 ± 0.48	7.04 ± 0.52	5.34 ± 1.13	33 ± 2	11.4 ± 1.5
SnO_2:F after $CdCl_2$ treatment	4.02 ± 0.41	6.34 ± 0.65	5.29 ± 1.10	29 ± 3	12.8 ± 1.3

procedure demonstrated in detail previously [22]. Extensions of the analyses to the entire M-SE data sets provide the variations in the parameters over the entire areas of the device structures before and after $CdCl_2$ treatment.

Table 13.7 shows results obtained by M-SE before and after CdS/CdTe deposition and after $CdCl_2$ treatment for the (4 cm, 4 cm) location on the maps of Figs. 13.23 and 13.24. These results are obtained in the analysis of a sample structure different from that in the study of Fig. 13.22. First, the discussion focuses on the SnO_2:F TCO layer in Table 13.7. For this layer, the resistivities and scattering times define the Drude formula for the free electron component of its complex dielectric function [15]. Upon deposition of the CdS/CdTe on the (TEC™ 15)/HRT surface, Table 13.7 suggests that the resistivity and the free electron scattering time of the SnO_2:F remain unchanged within the confidence limits, and this leads to similar conclusions for the electron concentration and electron mobility, deduced assuming an electron effective mass of $m_e* = 0.38m_e$, where m_e is the free electron mass [25]. Comparison of the SnO_2:F parameters before CdS/CdTe deposition with those obtained after $CdCl_2$ treatment suggests an increase in resistivity and a decrease scattering time slightly outside the confidence limits, which leads to a decrease in mobility and an increase in sheet resistance. The

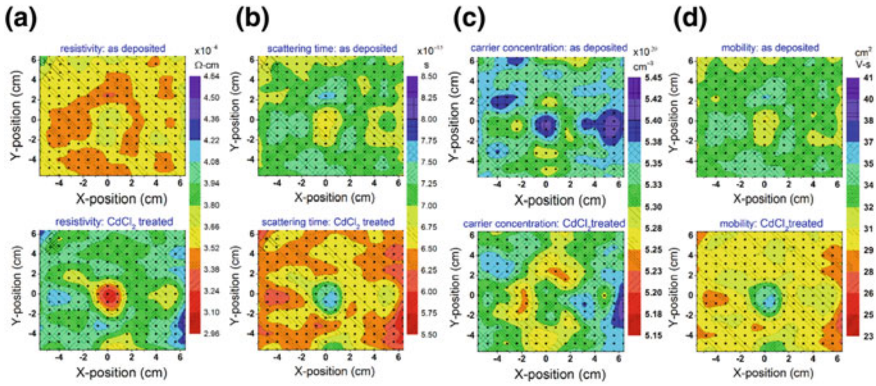

Fig. 13.23 Maps for the **a** resistivity ρ, **b** scattering time τ, **c** carrier concentration N, and **d** mobility μ that describe the SnO_2:F layer of the (TEC™ 15)/HRT substrate. Results are shown for the SnO_2:F layer of as-deposited (top figures) and $CdCl_2$-treated (bottom figures) (TEC™ 15)/HRT/CdS/CdTe sample structures

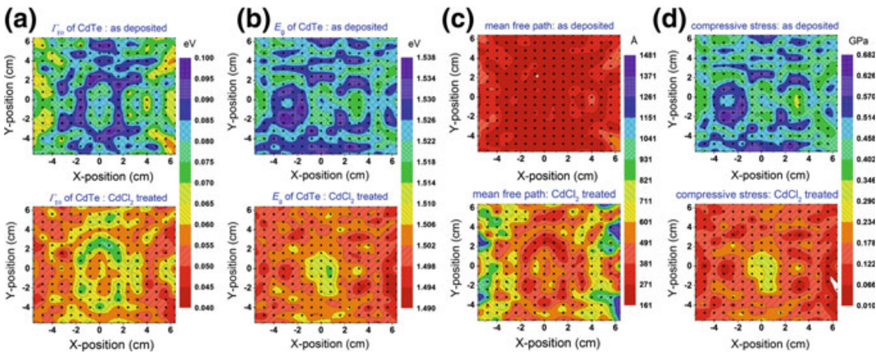

Fig. 13.24 Maps of the **a** broadening parameter Γ_{E0} and **b** bandgap E_0 of the lowest energy CP in the CdTe dielectric function; **c** excited carrier mean free path, and **d** in-plane compressive stress for as-deposited (top figures) and $CdCl_2$-treated (bottom figures) structures. The maps in the mean free path and in-plane compressive stress were determined from the maps in the broadening parameter and bandgap, respectively, for as-deposited and $CdCl_2$-treated structures using the relationships in [4, 5]

infrared spectral range provides much greater sensitivity to the Drude and associated derived parameters, but does not allow a mapping capability at present.

Next, the focus turns to the optical parameters in Table 13.7 associated with the CdTe layer before and after $CdCl_2$ treatment, obtained simultaneously with the SnO_2:F properties in the next-to-last and last rows of the table, respectively. The bandgap energy E_0 and broadening Γ_{E0} are parameters associated with a CP model for the lowest energy or bandgap transition, designated E_0. The decrease in E_0 observed in Table 13.7 upon $CdCl_2$ treatment, from 1.524 to 1.505 eV, is consistent with stress relaxation within the plane of the CdTe film from a value of 0.46 GPa to a

value of 0.20 GPa [5]. The decrease in Γ_{E0} observed upon $CdCl_2$ treatment, from 0.090 to 0.056 eV, suggests an increase in the mean free path of the excited carriers from ~200 to 600 Å [4]. Considering that the dominant effect limiting the mean free path in polycrystalline films is grain boundary or defect scattering, the decrease in Γ_{E0} can be attributed to grain growth or to defect reduction that occurs in the $CdCl_2$ treatment process.

For the sample of Table 13.7, Fig. 13.23 depicts the maps of the resistivity ρ and scattering time τ, along with the derived carrier concentration N and mobility μ for the SnO_2:F layer of the substrate before and after the $CdCl_2$ treatment of the overlying CdS/CdTe heterojunction. The map in Fig. 13.23a shows that the resistivity ρ of the SnO_2:F layer tends to increase and the scattering time τ tends to decrease upon $CdCl_2$ treatment. Most changes are small and within the confidence limits when considered on a point-by-point basis. The carrier concentration is found to be less affected upon treatment although there are some regions on the map in Fig. 13.23c where the carrier concentration has decreased. The map in Fig. 13.23d shows that the mobility μ for the carriers has decreased from an average value of ~33 to 30 $cm^2/V\ s$ between the as-deposited and $CdCl_2$-treated devices, however, for most points the difference is within the confidence limits. Figure 13.24 depicts the corresponding maps of the broadening parameter Γ_{E0} and the lowest energy bandgap E_0 for the as-deposited and $CdCl_2$-treated device structures. The reduction in the broadening parameter of the CP and the decrease in its resonance energy with $CdCl_2$ treatment are observed with relative uniformity over the ~12 cm × 12 cm area of the measurements. The parameters derived from E_0 and Γ_{E0} for CdTe, namely the stress and electron mean free path, respectively, are also given in Fig. 13.24. In the map of the stress, however, it is notable that for the $CdCl_2$-treated structure, a residual region of higher stress (~0.3 GPa) is observed at the sample center, likely due in part to a CdTe layer of larger thickness that is present in this region as will be demonstrated in the next sub-section.

13.3.4 Maps of CdS/CdTe/Cu Structures

Figure 13.25 shows four device structures fabricated for solar cell processing-property-performance correlation studies. Figure 13.26 shows maps of the CdTe effective thickness spanning areas of ~150 cm^2 for the four $CdCl_2$-treated structures with deposition times of 120, 72, and 43 min, and 110 min, respectively. These results were obtained from analyses of through-the-glass SE maps. Effective thickness is defined as the volume of deposited material per unit area of substrate and includes CdTe contributions from the CdS/CdTe interface layer at the heterojunction, the CdTe bulk layer, and the CdTe surface roughness layer located at the back of the device structure. The maps reveal reproducible non-uniformity patterns that are elliptical in shape. The minimum thickness occurs in the upper right corner, and this minimum is ~40% smaller than the maximum thickness near the center of the device structure. In Fig. 13.27, an illustrative CdS effective

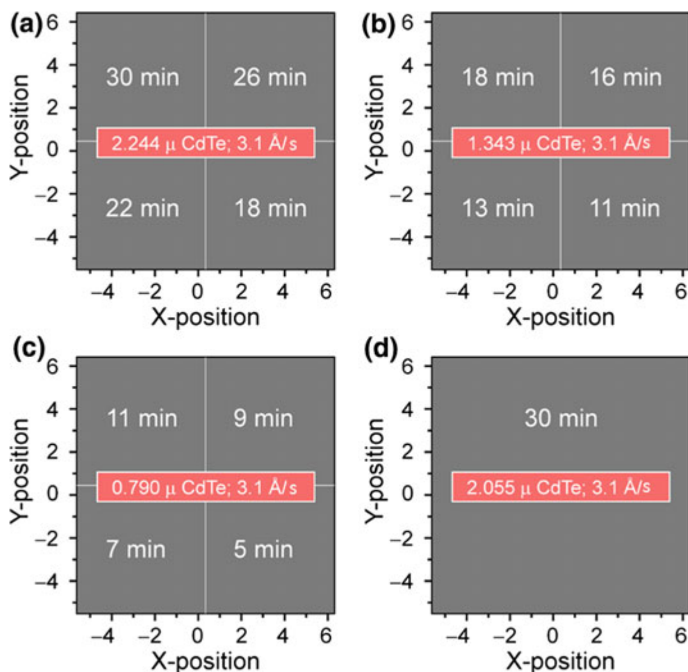

Fig. 13.25 Schematics of four device structures fabricated using (**a**–**c**) a CdS deposition time of 12 min for each structure and different CdTe deposition times of **a** 120 min, **b** 72 min, and **c** 43 min for the first three structures, and **d** a CdS deposition time of 11 min and CdTe deposition time of 110 min for the fourth structure. Each of the device structures (**a**–**c**) was cut into four samples which were exposed to $CdCl_2$ treatments for individual times over the ranges of **a** 18–30 min, **b** 11–18 min, and **c** 5–11 min. The fourth device structure **d** was subjected to a $CdCl_2$ treatment for 30 min. The four cut samples from each of the first three device structures were reassembled for Cu/Au back contact deposition with intended Cu thicknesses of **a** 30, **b** 18, and **c** 11 Å and (**a**–**c**) a fixed Au thickness of 300 Å. The back contact depositions for the fourth device structure **d** included an intended Cu thickness of 30 Å and a Au thickness of 300 Å. A total of 256 dot cells, each having an area of 0.125 cm^2, was fabricated on each of the three reassembled device structures and the fourth structure as well

thickness map is shown for one of the four structures, the one with the CdTe deposition time of 43 min and intended CdTe effective thickness of 0.7 μm. The thickness map for CdS shows greater non-uniformity than the CdTe effective thickness map, as the former spans a range of 700 Å about 1000 Å (or an edge-to-center effective thickness range of 650–1350 Å). The CdS and CdTe show similar elliptical patterns in the thickness as a result of the similarity of the separate sputtering chambers used for CdTe and CdS deposition.

As Cu is incorporated in the form of an ultrathin layer in the first fabrication step of the back contact, the thickness of the Cu layer within the device structure requires monolayer level control in order to optimize device performance. In these studies, due to the design of the equipment, the evaporation process generates significant non-uniformity in the effective thickness of the Cu layer over the

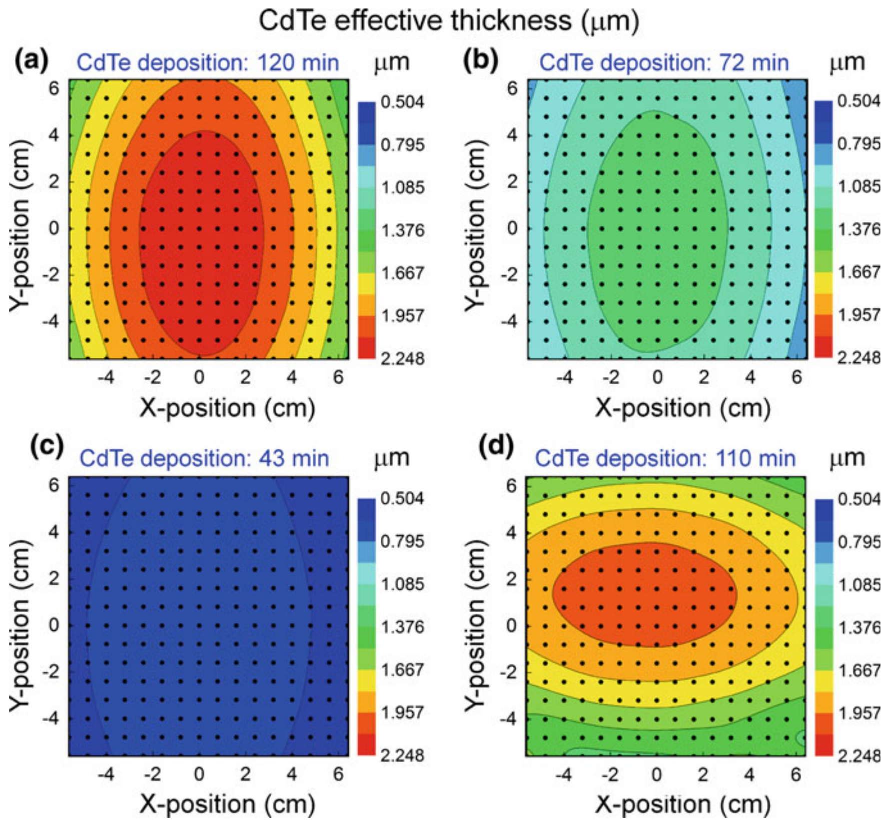

Fig. 13.26 Maps in the effective thickness of CdTe over ~12 cm × 12 cm areas for four $CdCl_2$-treated solar cell device structures. Four sets of structures, each incorporating 256 dot cells, were fabricated with targeted CdTe effective thicknesses of **a** 2.0 μm, **b** 1.2 μm, **c** 0.7 μm, and **d** 1.9 μm by depositing CdTe for 120 min, 72 min, 43 min, and 110 min, respectively. The fourth sample was rotated by 90° between CdS and CdTe depositions, yielding a rotated non-uniformity pattern with respect to a reference orientation

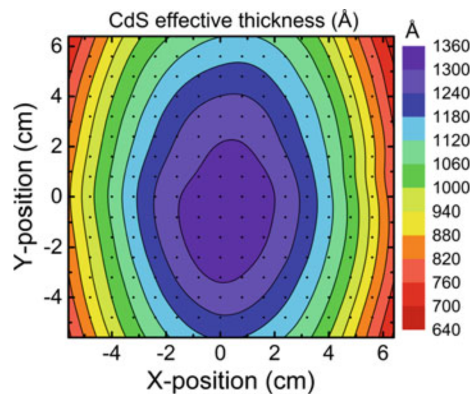

Fig. 13.27 An illustrative effective thickness map for the CdS layer spanning an ~12 cm × 12 cm area as obtained for the $CdCl_2$-treated CdS/CdTe solar cell structure of Fig. 13.25 having an intended CdTe effective thickness of 0.7 μm

15 cm × 15 cm area of the device structure. Such thickness non-uniformity can be used to advantage, however, for the purposes of optimization as will be described in the next sub-section.

Due to the roughness on the surface of the CdTe device structure, standard processing of the back contact is not suitable for accurate mapping in calibrations of the effective thickness of Cu deposited by evaporation over the surface area of the CdTe film. In fact, standard processing includes thermal evaporation of an ultrathin Cu layer of intended effective thickness ~30 Å, followed by a Au layer of intended thickness ~300 Å. In an attempt to calibrate the evaporation process of the ultrathin Cu layer, CdTe films with intended bulk layer thicknesses of ~200 Å were deposited by sputtering onto SLG plates 15 cm × 15 cm, the same size as that used in the fabrication of the solar cell structures. A CdTe film 200 Å in bulk layer thickness exhibits a minimum in the surface roughness thickness which enables accurate analyses of M-SE data for the SLG/CdTe/Cu samples obtained after ~30 Å Cu depositions. For relevance to the solar cell structures, the Cu evaporation was performed under the same conditions as those used for the devices [18]. M-SE data were acquired from the Cu film side over the 256 standardized dot cell locations on the 15 cm × 15 cm SLG/CdTe/Cu structures to deduce the distributions of the Cu effective thickness which serve as a calibration. Figure 13.28a shows illustrative experimental and best fit (ψ, Δ) spectra over the photon energy range from 0.73 to 5.50 eV at a single location on a SLG/CdTe/Cu sample which used a thicker Cu layer for model development. The best fit applies the SE model shown in the inset of Fig. 13.28a. An identical model was applied in the analysis of a full set of M-SE data for intended ~30 Å Cu, and a map of the effective thickness

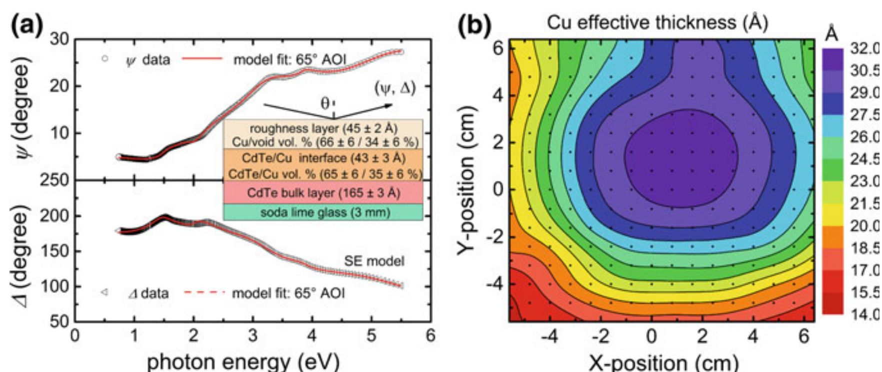

Fig. 13.28 **a** Ellipsometry data (ψ, Δ) and corresponding best fit analysis results for a single location on a 15 cm × 15 cm SLG/CdTe/Cu sample. The multilayer stack in the inset represents the SE model developed in the data analysis along with the layer parameters deduced as the best fit. The key result is the Cu effective thickness which is the product of layer thickness and the Cu volume fraction in the layer, summed over the two layers that include Cu. Thus, the Cu effective thickness is given by (0.35) (43 Å) + (0.66) (45 Å) = 45 Å for the location in **a**. AOI in **a** refers to the angle of incidence. **b** Map of Cu effective thickness depicted over the ~150 cm^2 area of a SLG/CdTe/Cu sample at 256 dot cell positions

of the Cu layer over the full SLG panel was obtained. Because the effective thickness is the volume/area, it can be determined as the product of Cu volume fraction and layer thickness, summed over the two layers in the model that contain Cu; the final results are shown in Fig. 13.28b. In order for this Cu calibration to be valid, the three 15 cm × 15 cm structures that were cut into fours, as shown in Fig. 13.25 for different $CdCl_2$ treatments, required reassembly of the four samples.

13.3.5 Application: Structure-Performance Correlations for Devices

Thickness non-uniformities exist for the three device structures in Figs. 13.25a–c, in addition to the intended thickness differences in the CdTe layer obtained through differences in the deposition time. As depicted in Figs. 13.26, 13.27, and 13.28, these non-uniformities are characteristic of the sputtering and evaporation systems and the associated deposition processes. Figure 13.29a shows correlation plots for CdS effective thickness versus CdTe effective thickness at 256 dot cell locations for the three structures. The resulting ranges of the CdTe effective thickness for the 3 × 256 dot cells are 1.39–2.24 µm, 0.84–1.34 µm, and 0.50–0.79 µm for the device structures with intended effective thickness values of 2.0, 1.2, and 0.7 µm, respectively. A range of 690–1350 Å is obtained for the effective thickness of CdS when the intended thickness is 1200 Å. Figure 13.29a reflects the close correlations of the effective thicknesses of CdS in Fig. 13.27 with those of CdTe in Figs. 13.26a–c, which may lead to challenges in separating their effects on device performance. The approach for overcoming these challenges involves fabricating a set of cell structures with the same intended CdTe thicknesses and largely different CdS thicknesses, as a companion set to those of Figs. 13.25a–c. As an alternative approach involving just one deposition, the device structure of Fig. 13.25d was fabricated by rotating the sample by 90° between the CdS and CdTe depositions. Figure 13.29b includes a correlation plot of CdS effective thickness versus CdTe effective thickness at 256 dot cell positions for this fourth sample. For these 256 dot cells, the deduced CdTe effective thickness spans the range 1.286–2.055 µm for the intended effective thickness of 1.9 µm; the effective thickness of CdS spans the range of 550–1200 Å for the intended thickness of 1100 Å. This correlation plot in Fig. 13.29b (circles) is superimposed on that of Fig. 13.29a for the structure of Fig. 13.25a with the intended 2 µm thick CdTe layer (squares). In this comparison, only the results are used from the 64 dot cell locations in the upper left quadrant of Fig. 13.25a with the corresponding 30 min $CdCl_2$ treatment time. A weaker correlation occurs in Fig. 13.29b for the sample of Fig. 13.25d as can be seen from a direct comparison of the maps in Figs. 13.27 and 13.26d.

Figure 13.30 shows solar cell performance parameters of open-circuit voltage V_{OC}, short-circuit current density J_{SC}, fill-factor *FF*, and efficiency ($V_{OC} \times J_{SC} \times FF$) correlated with the effective thickness of the CdTe layer for the devices of

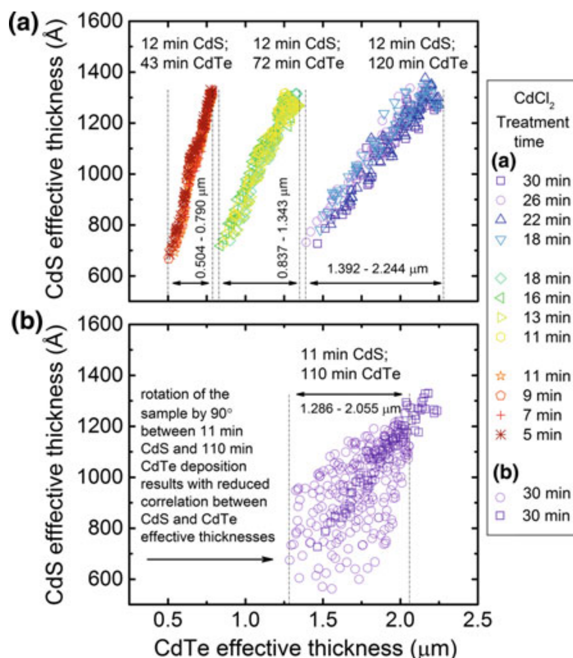

Fig. 13.29 **a** CdS effective thicknesses are plotted versus CdTe effective thicknesses for three device structures with (12 min CdS; 43 min CdTe), (12 min CdS; 72 min CdTe), and (12 min CdS; 120 min CdTe). The data points are shape-coded to indicate the $CdCl_2$ treatment time. A set of 256 dot cells is fabricated over the deposition area and pairs of thicknesses are associated spatially with each device. **b** CdS effective thickness is plotted versus CdTe effective thickness for the device structure with 11 min CdS and 110 min CdTe depositions (circles). The $CdCl_2$ treatment time was 30 min for this device structure. By rotating the sample by 90° between the CdS and CdTe depositions, the correlation in **b** between the two thicknesses was reduced as compared with the structure of **a** with 64 dot cell locations having 12 min CdS and 120 min CdTe depositions, and a $CdCl_2$ treatment time of 30 min (squares)

Figs. 13.25a–c with different $CdCl_2$ treatment times. In an attempt to optimize the $CdCl_2$ treatment time for the different CdTe absorber layer thicknesses, devices were treated over different durations, ranging from 5 to 30 min as indicated in Fig. 13.25. The $CdCl_2$ treatment times are identified by the different data point shapes. Considerable scatter in the data in these plots exists because, for a given CdTe effective thickness, the CdS and Cu effective thicknesses also vary. The effects of these parameters will be depicted through correlations presented later in this section. In addition, fabrication yield is not 100% and some cells are subject to varying degrees of shunting due to pinholes and substrate surface contamination. In the following, the effect of CdS/CdTe/Cu processing and properties on the observed maximum solar cell performances will be discussed based correlations such as those established by M-SE in Fig. 13.30.

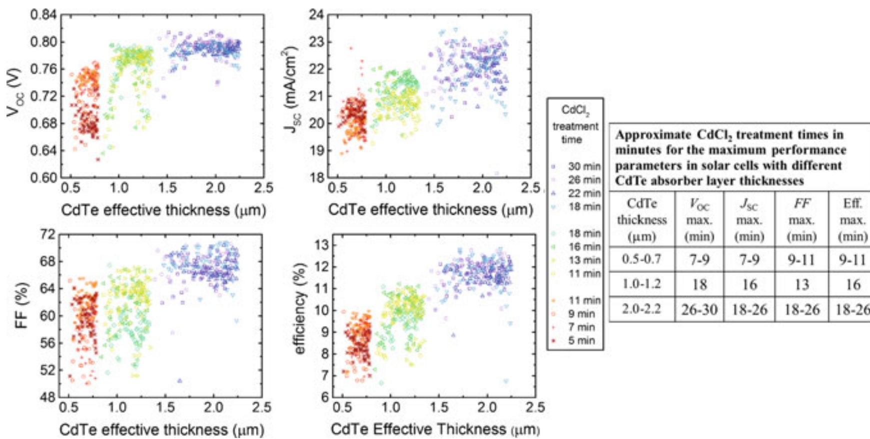

Approximate $CdCl_2$ treatment times in minutes for the maximum performance parameters in solar cells with different CdTe absorber layer thicknesses

CdTe thickness (μm)	V_{OC} max. (min)	J_{SC} max. (min)	*FF* max. (min)	Eff. max. (min)
0.5-0.7	7-9	7-9	9-11	9-11
1.0-1.2	18	16	13	16
2.0-2.2	26-30	18-26	18-26	18-26

Fig. 13.30 Plots of device performance parameters including V_{OC}, J_{SC}, *FF*, and efficiency in correlation with the CdTe effective thickness as obtained from M-SE analysis of $CdCl_2$-treated devices. The data point shape distinguishes the different values of the $CdCl_2$ treatment time which was reduced for structures with thinner CdTe layers. The table at right shows the approximate treatment times yielding the highest efficiency devices

The scatter plot for V_{OC} in Fig. 13.30 (top) shows that the highest values occur over the CdTe effective thickness range from 1.5 to 2.1 μm for a 30 min $CdCl_2$ treatment. Over this range, Fig. 13.29a shows that the CdS effective thickness varies between 800 and 1200 Å. Thus, there appears to be a relatively wide range of CdS and CdTe effective thicknesses over which V_{OC} is maximized. For the three device structures with thin, intermediate, and thick CdTe, the treatment times of 7–9, 18, and 26–30 min, respectively, tend to maximize V_{OC}. It appears that further improvements in V_{OC} may be possible by increasing the treatment time for the device structures with intended CdTe effective thicknesses of 1.2 and 2.0 μm. In fact, the decrease in V_{OC} with the reduction in CdTe thickness from 2.0 to 1.2 μm appears to be caused by the reduction in treatment time and not by the reduction in CdTe thickness. This conclusion is supported by the observation that for an 18 min $CdCl_2$ treatment, V_{OC} does not depend on CdTe effective thickness over the range spanning from 2.2 to 0.9 μm, covering the data for the two device structures with CdTe thicknesses of 2.0–1.2 μm. Only for CdTe effective thicknesses <1 μm does V_{OC} appear to decrease with decreasing CdTe thickness, as indicated by the data for the 11 min $CdCl_2$ treatment, which is common to the two sample structures with thicknesses of 1.2 and 0.7 μm. This decrease is reflected in a downward sloping envelope of maximum V_{OC} observed for CdTe effective thicknesses <0.8 μm in Fig. 13.30.

Additional observations can be made from the V_{OC} correlations based on poor performing cell results. First, it is clear that a 5 min treatment is insufficient for the

deposition with intended 0.7 μm CdTe thickness. Second, for the two device structures with the thinner CdTe layers, a much larger variation in V_{OC} is observed. This may be due to a higher sensitivity of the performance of thin CdTe to properties such as the CdS and Cu thicknesses. In other words, there may be narrower ranges of these parameters over which high V_{OC} can be reached for thin CdTe, in contrast to the behavior for thick CdTe. This suggests that greater fabrication control may be needed for solar cells with thin CdTe absorber layers.

The short-circuit current density J_{SC} maps in Fig. 13.30 show that the highest J_{SC} values occur over the CdTe effective thickness range from 1.5 to 2.2 μm for 18–26 min $CdCl_2$ treatments, clearly shorter than the time required to optimize V_{OC}. For the two device structures with intended CdTe layer thicknesses of 1.2 and 0.7 μm, the optimum treatment times are 16 and 7–9 min, respectively, excluding the outlying points for cells with thin CdTe layers. For devices with CdTe layer thickness <1.6 μm, J_{SC} shows a decreasing trend with decreasing CdTe layer thickness as expected. For the thinnest structures in the series, the outlying J_{SC} values for 7 min treatment times may result from additional current collection outside the area of the dot cell; these devices have low *FF* and efficiency.

The scatter plot for fill-factor *FF* in Fig. 13.30 shows that the highest values occur over a narrow CdTe effective thickness range near 2.1 μm for the range of $CdCl_2$ treatment times spanning 18–26 min. At this CdTe thickness, Fig. 13.29 shows that the CdS effective thickness is ~1250 Å. For the devices with thin, intermediate, and thick CdTe, the treatment times of 9–11, 13, and 18–26, respectively, tend to maximize *FF*. It appears that further improvements in *FF* may be possible for the device structure with the intended CdTe thickness of 0.7 μm by increasing the treatment time. In fact, the reduction in the *FF* with the decrease in intended CdTe thickness from 1.2 to 0.7 μm may be due to the reduction in treatment time and not due to the reduction in CdTe thickness. This conclusion is supported by the observation that for the 11 min $CdCl_2$ treatment, the *FF* does not depend sensitively on CdTe effective thickness over the range spanning from 1.3 to 0.5 μm, covering the data for the two device structures with intended CdTe thickness from 1.2 to 0.7 μm. Similar to the observations for V_{OC}, it is found that a reduction in CdTe thickness leads to greater scatter in the values for the *FF*. A summary of the optimization of $CdCl_2$ treatment is presented in the table in Fig. 13.30.

Figure 13.31 shows correlations between each of the device parameters (V_{OC}, *FF*, J_{SC}, efficiency) and the effective thickness of the CdTe layer for the three device structures with the CdS effective thickness identified by the shape of the data points. The data pattern reflects the correlations in Fig. 13.29a and limits the accessible information from the individual performance parameters. The scatter plot for V_{OC} reveals that in the CdTe thickness range of 2 μm, a weak maximum is observed in the CdS thickness range of 1150–1300 Å. As the CdTe thickness decreases to 1.5 μm, V_{OC} first decreases and then increases again with a maximum in the CdS thickness range of 800–900 Å. This same optimum CdS thickness is also observed as the CdTe thickness decreases to 1 μm. Below 1 μm, the effect of CdS thickness on V_{OC} is difficult to evaluate due to its correlation with CdTe thickness.

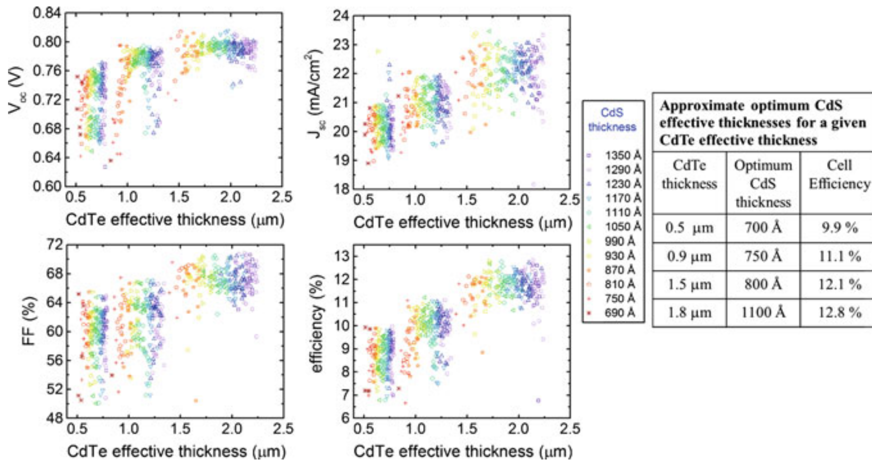

Approximate optimum CdS effective thicknesses for a given CdTe effective thickness

CdTe thickness	Optimum CdS thickness	Cell Efficiency
0.5 μm	700 Å	9.9 %
0.9 μm	750 Å	11.1 %
1.5 μm	800 Å	12.1 %
1.8 μm	1100 Å	12.8 %

Fig. 13.31 Plots of device performance parameters including V_{OC}, J_{SC}, *FF*, and efficiency in correlation with the effective thickness values of the CdTe. The effective thickness values of the CdS are distinguished by the data point shape. The table at right shows the approximate CdS effective thicknesses yielding the highest efficiency devices of different CdTe thicknesses

The behavior of J_{SC} in Fig. 13.31 is also difficult to evaluate in this case as a result of outlying points, possibly due to localized occurrences of current collection outside the areas of the dot cells. Excluding such points, the trend in J_{SC} for CdTe thicknesses below 1.5 μm is dominated by the variation in CdTe thickness with much less influence from the variation in CdS thickness. Even in the CdTe thickness range of 1.7–2.2 μm where collection from the CdTe is nearly complete, J_{SC} is not clearly dependent on the CdS thickness. Given complete absorption in the CdTe, an increase in J_{SC} is expected with decreasing CdS thickness due to reduced absorption by the inactive CdS layer on the blue side of the solar spectrum. The observations suggest that other competing effects may occur, for example, deep absorption losses at the back of the CdTe layer that increase with the decrease in CdTe thickness and thus CdS thickness.

The effect of CdS effective thickness on the *FF* and efficiency in Fig. 13.31 will be considered next. By comparing the *FF* for similar CdTe effective thicknesses that derive from the maximum and minimum values of two different structures, one can evaluate the role of CdS thickness. In this comparison, the CdS thicknesses derive from the outer edges and the center and are largely different. As a result, one can observe that the CdS thickness generating the optimum *FF* decreases with decreasing CdTe thickness. The accumulated effect of these solar cell parameter variations suggests that as the CdTe thickness is reduced, the highest efficiency cells incorporate reduced thickness CdS, as well, as indicated by the large efficiency steps between the three data sets. The observed trend generates flat regions in the efficiency maximum envelope over the ranges 1.7–2.2, 0.9–1.3, and 0.5–0.8 μm as the decrease in collection with decreasing CdTe thickness is balanced by an

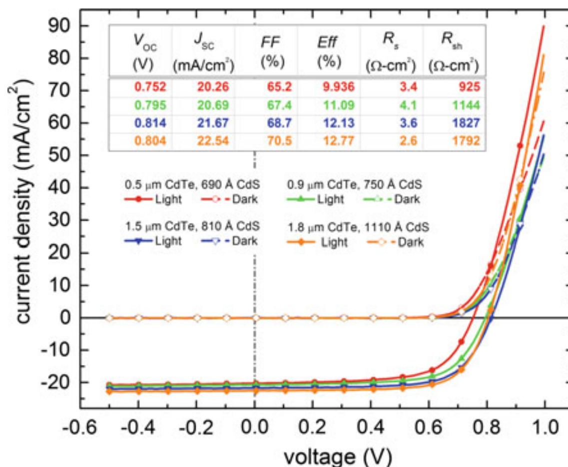

Fig. 13.32 (Current-density)-voltage (J-V) characteristics and deduced performance parameters for the four highest performing solar cells having CdTe effective thicknesses ranging from 0.5 to 1.8 μm. The results show the decrease in optimum effective thickness of CdS with the thinning of the CdTe. The area of each solar cell is 0.125 cm^2

increase in the *FF* with decreasing CdS thickness (which is correlated with the CdTe thickness). Thus, the trend in the efficiency arises predominantly from the trend in the *FF*. For devices with ~1.8, 1.5, 0.9, and 0.5 μm CdTe layers, for example, optimum efficiencies are obtained with ~1100, 800, 750, and 700 Å CdS layers, respectively, as summarized in the table of Fig. 13.31. It is clear, however, that reasonable device performance results over a relatively wide range in the CdS thickness for a selected CdTe thickness. Figure 13.32 shows the light and dark (current-density)-voltage (J-V) characteristics for the four highest efficiency devices obtained under AM 1.5 illumination.

Next, the impact of the effective thickness of Cu on the solar cell performance parameters will be discussed. In Fig. 13.33 additional plots are presented that depict correlations of the device performance with the CdTe effective thickness. In this case, the Cu effective thickness is distinguished by data point shape. Among the device parameters, V_{OC} shows the clearest effects of Cu thickness. For CdTe thicknesses in the narrow ranges of (1.9–2.1 μm, 1.4–1.6 μm, 0.9–1.1 μm), the Cu effective thicknesses span the ranges of (20–30 Å, 15–25 Å, 8–15 Å), respectively. Within these ranges, maximum V_{OC} is observed for Cu effective thicknesses of (26–28 Å, 22–24 Å, 11–13 Å). Finally, for the CdTe thickness range of 0.5–0.6 μm, the highest V_{OC} is obtained for the minimum Cu thickness of 6 Å. Figure 13.33 demonstrates similar behavior for the final cell efficiency, as well, revealing that the optimum effective thickness of Cu decreases with decreasing effective thickness of CdTe. In this case, for devices with ~2, 1.5, 1.0, and 0.5 μm thick layers of CdTe, the highest efficiency is obtained with ~29, 22, 11, and 6 Å thick layers of Cu, respectively, or a Cu:CdTe ratio of effective thicknesses in the range $(1.1\text{–}1.5) \times 10^{-3}$.

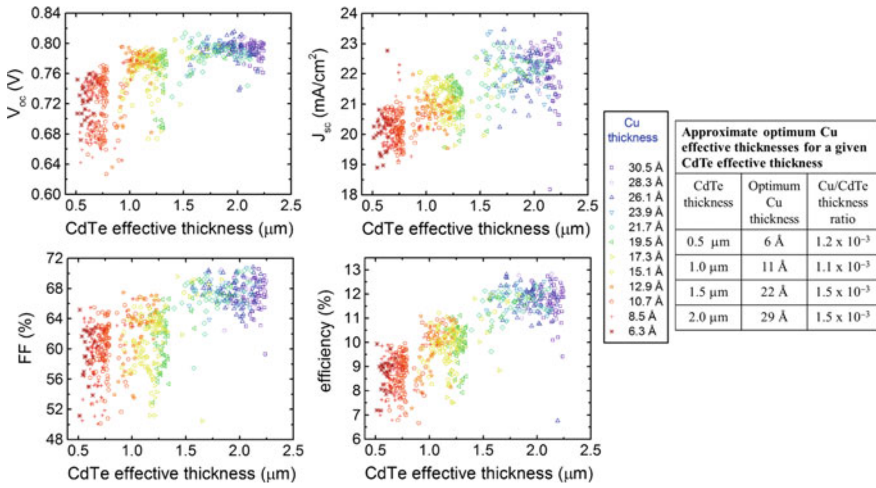

Approximate optimum Cu effective thicknesses for a given CdTe effective thickness		
CdTe thickness	Optimum Cu thickness	Cu/CdTe thickness ratio
0.5 µm	6 Å	1.2×10^{-3}
1.0 µm	11 Å	1.1×10^{-3}
1.5 µm	22 Å	1.5×10^{-3}
2.0 µm	29 Å	1.5×10^{-3}

Fig. 13.33 Plots of device performance parameters including V_{OC}, J_{SC}, *FF*, and efficiency in correlation with the CdTe effective thickness. The Cu effective thickness values are distinguished by the data point shape. The table at right shows the approximate Cu effective thicknesses yielding the highest efficiency devices

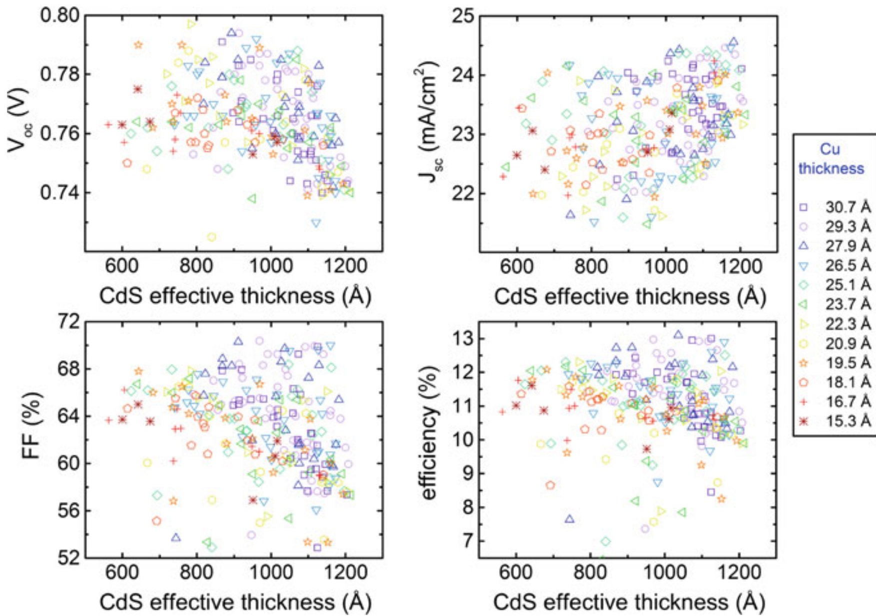

Fig. 13.34 Plots of device performance parameters including V_{OC}, J_{SC}, *FF*, and efficiency in correlation with the CdS effective thickness for the (11 min CdS; 110 min CdTe) sample fabricated in a process designed to reduce the correlation between the two thicknesses. The Cu effective thickness values are identified by the data point shape

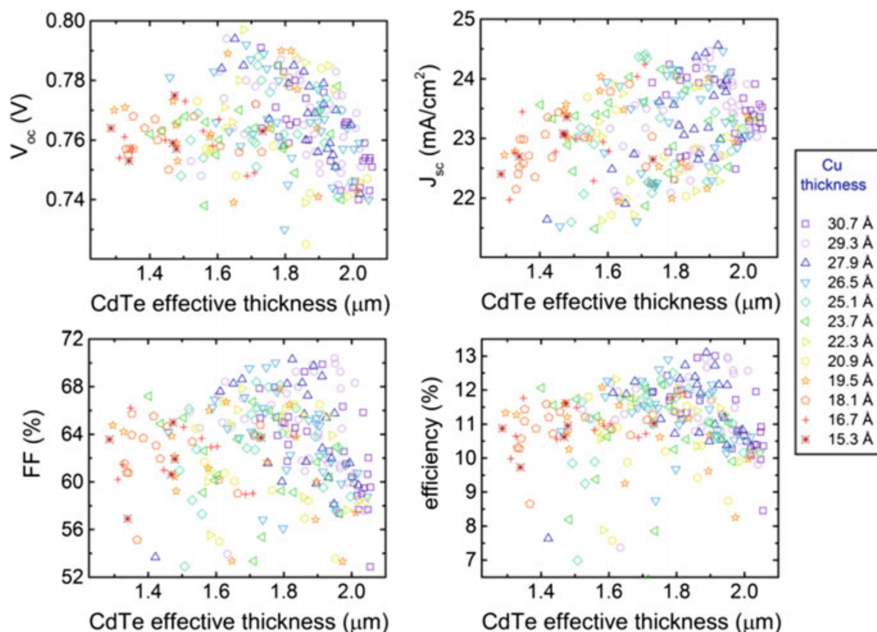

Fig. 13.35 Plots of device performance parameters including V_{OC}, J_{SC}, FF, and efficiency in correlation with the CdTe effective thickness for the (11 min CdS; 110 min CdTe) sample fabricated in a process designed to reduce the correlation between the two thicknesses. The Cu effective thickness values are identified by the data point shape

Figures 13.34 and 13.35 show the plots of the device performance parameters including V_{OC}, J_{SC}, FF, and efficiency in correlation with the CdS and CdTe effective thicknesses for the sample with CdS deposited for 11 min and CdTe deposited for 110 min. This sample was fabricated in an attempt to reduce the correlation between the CdS and CdTe thicknesses as shown in Fig. 13.29. The scatter plots for V_{OC} in Figs. 13.34 and 13.35 show a clear maximum value occurring at CdS and CdTe effective thicknesses of ~800–1000 Å and ~1.6–1.8 μm, respectively. Cu thicknesses in the range from 20 to 30 Å contribute to this maximum V_{OC}. This behavior can be compared with the previously presented results in Fig. 13.31 which plots the correlation between the V_{OC} value and the CdTe effective thickness for various effective thicknesses of the CdS layer, considering the sample prepared with 12 min CdS and 120 min CdTe. In Fig. 13.31, evidence for a weak maximum in V_{OC} appears near CdS and CdTe thicknesses of ~800–900 Å and 1.5–1.6 μm, respectively; the best treatment time is 30 min as shown in Fig. 13.30 and the best Cu thickness of 22–24 Å is shown in Fig. 13.33. From the scatter plots for V_{OC} in Figs. 13.30, 13.31, and 13.33, however, the maximum in V_{OC} is much broader than that in Fig. 13.35 with CdTe effective thicknesses in the range of 1.5–2.1 μm yielding high V_{OC} for the corresponding

30 min $CdCl_2$-treated devices. The variations in CdS effective thickness across this broad maximum are also broad, spanning the range of 800–1200 Å. The identification of a more clearly defined CdTe effective thickness for maximum V_{OC} appears possible due to the larger number of cells spanning a wider range of CdS effective thickness for the given CdTe effective thickness as shown in Fig. 13.29b. In contrast, in Fig. 13.31, the close correlation between the two thicknesses likely contributes to the observed broad maximum.

The maximum overall efficiency in Figs. 13.34 and 13.35 results from a CdTe thickness of 1.9 μm, a CdS thickness of 950–1150 Å, and a Cu thickness of 28–30 Å. These results obtained from a less correlated set of CdS and CdTe thicknesses are consistent with those of the correlated set of Figs. 13.31 and 13.33 and illustrate the ability of M-SE to expedite the development of processing-property-performance relationships from a single non-uniform device structure.

13.4 Mapping Spectroscopic Ellipsometry for Full Scale Solar Modules

As an extension of the mapping SE (M-SE) capability, an as-deposited pre-production CdTe solar panel 60 cm × 120 cm in size was studied, provided by Calyxo USA. Off-line though-the-glass mapping was performed at the fixed angle of incidence of 65° using a commercial M-SE system (AccuMap-SE, J. A. Woollam Co.) based on the rotating-compensator multichannel principle [19, 20]. The map consists of sets of (ψ, Δ) spectra from 0.75 to 3.5 eV at 861 spatial locations. The panel structure incorporates stratified layers of TEC™/HRT/CdS/CdTe; the Pilkington TEC™ glass consists of a sequence of four layers on the 3.2 mm thick SLG. The layers on SLG from bottom to top include SnO_2 (~250 Å), SiO_2 (~250 Å), a thicker layer of SnO_2:F (~3000 Å), and a high resistivity transparent layer (HRT; ~300 Å). Deposited on the TEC™/HRT panel are the layers of CdS and CdTe by an atmospheric pressure vapor deposition process to thicknesses of ~1000 Å and several microns, respectively [26]. The M-SE data acquired on the panel were analyzed by considering the optical model shown on the right side of Fig. 13.22. Owing to the relatively thick CdTe layer and its large surface roughness on this panel, the probe light reaching the back in a through-the-glass SE measurement does not reflect specularly from CdTe/air interface. As a result, the optical model used to analyze this panel is further simplified in comparison with that of the sputter deposited CdTe solar cell structures, to the extent that the CdTe bulk layer is assumed to be semi-infinite.

Figure 13.36 shows key parameters extracted from analysis of the through-the-glass M-SE data. The upper two maps in the figure show bulk layer and effective thicknesses for the SnO_2:F and HRT layers, respectively. The lower two maps show parameters associated with the semiconductor layers over-deposited on

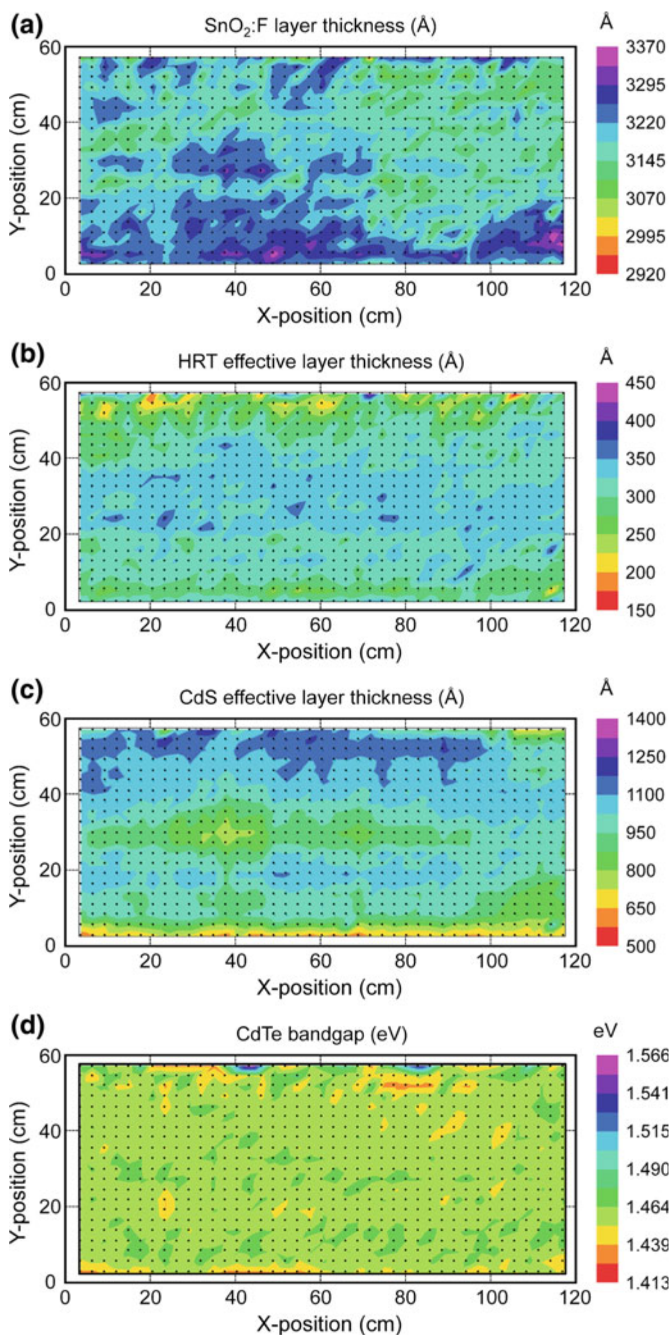

Fig. 13.36 Maps of **a** SnO_2:F bulk layer thickness, **b** HRT effective thickness, **c** CdS effective thickness, and **d** CdTe bandgap for a 60 cm × 120 cm pre-production CdTe solar cell structure as determined from through-the-glass SE analysis (This panel was provided courtesy of Kenneth Kormanyos, Calyxo USA.)

the TEC™/HRT structure in the superstrate configuration. Figure 13.36c shows the map of CdS effective thickness which is a critical parameter in controlling the device performance. Knowledge of this parameter facilitates determination of the external quantum efficiency spectra and locally collected current. Another key parameter map depicted in Fig. 13.36d is that of the CdTe bandgap. The bandgap of CdTe in the case of this high temperature deposition is influenced both by stress and by S in-diffusion which reduces the bandgap due to the bowing effect in $CdTe_{1-x}S_x$ alloys. By assuming that the S content reaches the solubility limit at the deposition temperature, then the stress in the layer can be determined based on the bandgap. Thus, it may be possible to develop maps of film stress at it evolves during processing even in this complicated optical structure. A few outlier data points exist at the edges of the maps as observed in the bandgap figure which may be generated as a result of warpage due to the thermal cycle during pre-production process evaluation or as a result of localized defects at the edges. One of the challenges in large area mapping involves the planarity of the panel. Warpage can lead to misalignments in the reflected beam. If reflected beam collection is still possible under these circumstances, warpage in orthogonal directions can lead to changes in the angle of incidence and the plane of incidence, the latter shifting the azimuthal angle calibrations. Various approaches can be applied to address these issues.

13.5 Summary

Application of real time spectroscopic ellipsometry (RTSE) has been presented for the study of the structural evolution of CdS and CdTe during the sputter deposition of these semiconducting layers on (TEC™ 15)/HRT substrates. The RTSE data were analyzed by implementing an appropriate optical model that applies a dielectric function database obtained at the elevated temperature of deposition. The HRT layer on the substrate exhibits an ~400 Å thick roughness layer, as determined by analysis of SE data obtained at room temperature before CdS deposition. As the deposition is initiated, an interface filling process begins and a surface roughness layer on the CdS simultaneously increases from the start of the deposition. Upon completion of the interface filling process, the bulk layer forms and evolves in thickness. At the time when the first bulk monolayer appears, a ~300 Å thick surface roughness layer has developed on the CdS, conformally covering the underlying HRT film. As the deposition continues, the surface layer thickness continues to increase and attains a maximum value at the bulk layer thickness of d_b(CdS) ~250 Å. Upon further deposition, a weak coalescence effect occurs resulting in a slightly smoother surface as compared to the initial bulk growth regime. A similar structural evolution was observed for the CdTe layer deposited on the CdS layer.

Variations in the Ar pressure (p_{Ar}) used for the CdS deposition have been explored, along with studies of its effects on the structural evolution and photovoltaic device performance. Although the structural evolution of the CdS is

dominated by the underlying roughness on the HRT, smaller changes with Ar pressure occur consistent with simple concepts of the sputtering process. The lowest Ar pressures promote the smoothest CdS surfaces, implying that under these conditions the growing film can suppress the substrate-induced roughness effects. This likely occurs due to the bombardment of the surface by the incoming atomic and molecular species which suppresses asperities, increases surface diffusion, and smoothens the surface. As the Ar pressure used in CdS deposition increases, the roughness on the CdS first increases and then decreases, irrespective of the CdS thickness. The increase may be associated with the reduced momentum per atom carried by the arriving species which suppresses bombardment generated smoothening. At high pressures, the sputtered species are likely to be thermalized arriving with low momentum; however, under these conditions flux directionality is lost which may enable smoothening via a reduction in self-shadowing. The highest performance solar cells are obtained in the intermediate range in which case the incident momentum per arriving species is optimized such that the mobility of surface atoms is promoted, but without damage to the underlying layers. In this intermediate range, it is likely that the growth of crystalline grains with a reduced density of defects occurs during the process.

Ex situ mapping spectroscopic ellipsometry (M-SE) has been applied as well in a through-the-glass optical configuration for characterization of the structure of CdTe solar cells. M-SE deduced structural characteristics of the solar cells, varied by changing the process parameters, have been correlated with performance characteristics of solar cells. The results of these correlations demonstrate that when deposition processes yield non-uniformities in layer thicknesses, M-SE can be performed to map basic structural parameters, enabling the development of processing-property-performance correlations on a spatial basis. As a result, solar cell optimization can be expedited in a relatively small number of depositions. In this study, the effects on device performance of the M-SE determined CdTe absorber, CdS window, and Cu back contact effective thicknesses have been explored through four CdS/CdTe depositions. Three different intended CdTe thicknesses were used with a single non-uniform CdS deposition process having a range of thicknesses over the substrate area, and three Cu/Au back contact fabrication processes were used with different intended Cu thicknesses. Of particular importance is the use of mapping SE to calibrate the deposited Cu thickness, as changes at the monolayer level exert an influence on the device performance. In addition to layer thicknesses, the $CdCl_2$ treatment time was also varied and twelve different $CdCl_2$ treatments of different durations were explored. In this study, a total of $256 \times 4 = 1024$ small area solar cells were evaluated and their performances correlated with the effective layer thicknesses as deduced by M-SE and with the $CdCl_2$ treatment time.

Three key results of the M-SE processing-property-performance spatial correlations can be summarized as follows. First, as the CdTe thickness is reduced, the highest efficiency cells are obtained with reduced thickness CdS. For solar cell devices with CdTe layers ranging from 2 μm to 0.5 μm in effective thickness, the highest efficiencies are obtained with CdS layers ranging from ~1300 to 700 Å in

effective thickness. Although this behavior arises predominantly from the trend in the *FF,* it is found that reasonable device performance parameters result over a relatively wide range of ~±200 Å in the CdS effective thickness for a given CdTe effective thickness. The optimum $CdCl_2$ treatment time for solar cells with a 2 μm thick absorber represents a trade-off between optimum V_{OC}, which requires longer treatments and optimum *FF* which requires shorter treatments. This behavior suggests that during treatment, the annealing of small grains and passivation of grain boundary defects by Cl tend to proceed as a diffusion process from the back of the device toward the junction. This trade-off disappears as the CdTe thickness decreases below 1 μm, and treatment times for optimum V_{OC} and *FF* approach one another. Finally, the optimum Cu thickness in forming the back contact is found to be consistent with a Cu:CdTe effective thickness ratio of $(1.3 \pm 0.02) \times 10^{-3}$ as the CdTe absorber layer thickness is reduced over the range from 2 to 0.5 μm.

The M-SE metrology has been extended to characterize commercial CdTe photovoltaic panels in a through-the-glass measurement configuration. M-SE analysis on the panel results in parameter maps associated with optical and structural properties of the layer stack in the device configuration. The information extracted in such analyses can be used for optimization purposes by spatially correlating local device properties and performance. The results can also be applied in predictions of the local external quantum efficiency as well as the photocurrent generated in individual subcells.

References

1. B.E. McCandless, J.R. Sites, *Handbook of Photovoltaic Science and Engineering*, 2nd edn., ed. by A. Luque, S. Hegedus (Wiley, New York, NY, 2011), Chapter 14, pp. 600–641
2. J. Chen, J. Li, C. Thornberry, M.N. Sestak, R.W. Collins, J.D. Walker, S. Marsillac, A.R. Aquino, A. Rockett, *Proceedings of the 34th IEEE Photovoltaic Specialists Conference*, Philadelphia, PA, 7–12 June 2009 (IEEE, New York, NY, 2009), pp. 1748–1753
3. S. Kohli, V. Manivannan, J.N. Hilfiker, P.R. McCurdy, R.A. Enzenroth, K.L. Barth, W. P. Smith, R. Luebs, J. Kephart, W.S. Sampath, *Proceedings of the 35th IEEE Photovoltaic Specialists Conference*, Honolulu, HI, 20–25 June 2010 (IEEE, New York, NY, 2010), pp. 1951–1954
4. J. Li, J. Chen, R.W. Collins, Appl. Phys. Lett. **97**, 181909 (2010)
5. J. Li, J. Chen, R.W. Collins, Appl. Phys. Lett. **99**, 061905 (2011)
6. J. Li, *Real Time Spectroscopic Ellipsometry Studies of Thin Film Materials and Structures for Photovoltaic Applications*, Ph.D. Dissertation (The University of Toledo, Toledo, OH, 2010)
7. J. Chen, *Spectroscopic Ellipsometry Studies of II–VI Semiconductor Materials and Solar Cells*, Ph.D. Dissertation (The University of Toledo, Toledo, OH, 2010)
8. R. Kykyneshi, J. Zeng, D.P. Cann, *Handbook of Transparent Conductors*, ed. by D.S. Ginley, H. Hosono, D.C. Paine (Springer, New York, NY, 2010), Chapter 6, pp. 171–191
9. K. von Rottkay, M. Rubin, *Materials Research Society Symposium Proceedings; Thin Films for Photovoltaic and Related Device Applications*, vol. 426, ed. by A. Catalano, C. Eberspacher, D.S. Ginley, T.M. Peterson, H.W. Schock, T. Wada (MRS, Warrendale, PA, 1996), pp. 449–454

10. J. Chen, J. Li, D. Sainju, K.D. Wells, N.J. Podraza, R.W. Collins, *Proceedings of the 2006 IEEE 4th World Conference on Photovoltaic Energy Conversion*, Waikoloa, HI, 7–12 May 2006 (IEEE, New York, NY, 2006), pp. 475–478
11. P. Koirala, *Multichannel Spectroscopic Ellipsometry for CdTe Photovoltaics: From Materials and Interfaces to Solar Cells*, Ph.D. Dissertation (The University of Toledo, Toledo, OH, 2015)
12. H. Fujiwara, *Spectroscopic Ellipsometry: Principles and Applications* (Wiley, Chichester, UK, 2007)
13. P. Aryal, J. Chen, Z. Huang, L.R. Dahal, M.N. Sestak, D. Attygalle, R. Jacobs, V. Ranjan, S. Marsillac, R.W. Collins, *Proceedings of the 37th IEEE Photovoltaic Specialists Conference,* Seattle, WA, 19–24 June 2011 (IEEE, New York, NY, 2011), pp. 2241–2246
14. B. Johs, C.M. Herzinger, Phys. Status Solidi (c) **5**, 1031 (2008)
15. R.W. Collins, A.S. Ferlauto, *Handbook of Ellipsometry*, ed. by H.G. Tompkins, E.A. Irene (William Andrew, Norwich, NY, 2005), Chapter 2, pp. 93–236
16. J. Li, N.J. Podraza, R.W. Collins, Phys. Status Solidi (a) **205**, 901 (2008)
17. J. Li, J. Chen, M.N. Sestak, C. Thornberry, R.W. Collins, *Proceedings of the 34th IEEE Photovoltaic Specialists Conference*, Philadelphia, PA, 7–12 June 2009 (IEEE, New York NY, 2009), pp. 1982–1987
18. P. Koirala, J. Chen, X. Tan, N.J. Podraza, S. Marsillac, A.A. Rockett, R.W. Collins, *Proceedings of the 39th IEEE Photovoltaic Specialists Conference*, Tampa, FL, 16–21 June 2013 (IEEE, New York, NY, 2013), pp. 1987–1991
19. B.D. Johs, J. Hale, N.J. Ianno, C.M. Herzinger, T. Tiwald, J.A. Woollam, *Proceedings of SPIE; Optical Metrology Roadmap for the Semiconductor, Optical, and Data Storage Industries II*, vol. 4449, ed. by A. Duparre, B. Singh (SPIE, Bellingham WA, 2001), pp. 41–57
20. Z. Huang, J. Chen, M.N. Sestak, D. Attygalle, L.R. Dahal, M.R. Mapes, D.A. Strickler, K.R. Kormanyos, C. Salupo, R.W. Collins, *Proceedings of the 35th IEEE Photovoltaic Specialists Conference*, Honolulu, HI, 20–25 June 2010 (IEEE, New York, NY, 2010), pp. 1678–1683
21. J. Chen, P. Aryal, J. Li, M.N. Sestak, L.R. Dahal, Z. Huang, R.W. Collins, *Proceedings of the 37th IEEE Photovoltaic Specialists Conference*, Seattle, WA, 19–24 June 2011 (IEEE, New York, NY, 2011), pp. 3486–3491
22. P. Koirala, J. Li, H.P. Yoon, P. Aryal, S. Marsillac, A.A. Rockett, N.J. Podraza, R.W. Collins, Prog. Photovolt. Res. Appl. **24**, 1055 (2016)
23. V. Plotnikov, A.C. Vasko, A.D. Compaan, X. Liu, K.A. Wieland, R.M. Zeller, J. Li, R. W. Collins, *Materials Research Society Symposium Proceedings; Thin-Film Compound Semiconductor Photovoltaics-2009*, vol. 1165, ed. by A. Yamada, C. Heske, M.A. Contreras, M. Igalson, S.J.C. Irvine (MRS, Warrendale, PA, 2009), pp. 383–392
24. J. Li, M.N. Sestak, J. Chen, R.W. Collins, IEEE J. Photovolt. **1**, 187 (2011)
25. B. Stjerna, E. Olsson, C.G. Granqvist, J. Appl. Phys. **76**, 3797 (1994)
26. F. Becker, H.-J. Frenck, *Photovoltaics International*, vol. 134,12th edn. (2011)

Chapter 14
High Efficiency III–V Solar Cells

Nikolas J. Podraza

Abstract Solar cells based on single junction or multijunction architectures with compound group III–V semiconductor absorbers have very high efficiencies. A review of spectroscopic ellipsometry characterization of component III–V semiconductors (III: Al, Ga, In; V: As, P) in the near infrared to ultraviolet range is provided. Variations in complex dielectric function spectra over the near infrared to ultraviolet have been tracked as functions of composition in ternary and quaternary alloys, compressive or tensile stress reflected in blue-shifting or red-shifting of critical point features, and limitations in the mean free path of carriers detected in critical point broadening. Extensions of ellipsometry measurements to longer wavelengths show sensitivity to free carrier absorption and infrared active phonon modes related to chemical bonding and lattice vibrations. When free carrier absorption is detected, the Drude model can be applied to deduce some electrical transport properties (resistivity, carrier mean scattering time). Measurements collected as functions of applied magnetic field, noted as the optical Hall effect, can yield carrier concentration, mobility, and effective mass. Surface oxidation effects are noted and pathways to either eliminating this contribution to measured ellipsometric spectra or incorporating it into the data analysis procedure are discussed. In situ real time spectroscopic ellipsometry is reviewed for processing monitoring and control. Future outlooks include extension of complex dielectric function databases to incorporate composition, stress, and defects simultaneously as well as accounting for systematic variations in phonon modes and free carrier absorption (due to doping type and concentrations). The challenge for future research is to successfully characterize complete III–V solar cells by spectroscopic ellipsometry in a manner similar to that already done for thin film photovoltaics based on polycrystalline or otherwise disordered materials.

N. J. Podraza (✉)
Department of Physics & Astronomy, University of Toledo, 2801 W. Bancroft Street,
Mailstop 111, Toledo, OH 43606, USA
e-mail: Nikolas.Podraza@utoledo.edu

© Springer International Publishing AG, part of Springer Nature 2018

H. Fujiwara and R. W. Collins (eds.), *Spectroscopic Ellipsometry for Photovoltaics*,
Springer Series in Optical Sciences 212,
https://doi.org/10.1007/978-3-319-75377-5_14

14.1 Background of III–V Photovoltaic Devices

Compound semiconductors from periodic groups III and V are utilized for an array of technological applications including sensors, transistors, laser diodes, microwave electronics, and, of course, photovoltaic devices [1–9]. Typical III–V materials of interest for solar cells are based upon aluminum, gallium, and indium (III: Al, Ga, In) with arsenic and phosphorus (V: As, P). GaAs serves as the basis of most of these solar cells, however ternary (InGaAs, AlGaAs, GaInP, AlInP) and quaternary (AlInGaAs, AlGaInP, InGaAsP) alloys are often exploited to tailor individual layer optical response, e.g. band gap, and crystal structure, e.g. lattice constant [10–26]. These III–V compounds are typically direct band gap semiconductors, meaning that there is significant optical absorption of photons with energies greater than or wavelengths shorter than the band gap, while photons with lower energies or longer wavelengths are not absorbed. Beyond variations in III–V compound properties by alloying and the nature of the intrinsic majority carrier type, these compounds can be *n*-type or *p*-type doped with suitable group IV or group II elements [27–29]. Thin films of these compounds have been made using molecular beam epitaxy (MBE) and more recently metal organic chemical vapor epitaxy (MOCVE). Proper choice of substrate or underlying material for epitaxy ensures that lattice matched or mismatched films can be controllably produced, while the epitaxial nature of the films eliminates undesirable effects due to extended defects like grain boundaries. The full ability to tailor the electrical, optical, and structural characteristics for materials with low levels of defects and mature material processing technology has led to an overall high electronic quality when incorporated properly into devices.

With respect to solar cells, these materials have been applied in both single junction and multijunction configurations, designed for standard one-sun illumination as well as concentration in both terrestrial and space applications. For devices designed to operate under one-sun illumination, fabrication of the solar cell and integration into modules and panels completes the process: the device is exposed to the direct solar irradiance incident onto the active area of the device. In concentrator photovoltaics, a small solar cell is integrated with a large array of reflectors such that higher intensity (>one sun) illumination is incident onto the solar cell. This configuration is desirable for devices made from expensive components and semiconductors that convert incident photons to electron-hole pairs more effectively under greater irradiance. III–V solar cells are used for both these applications, although the overall fabrication process and materials can be somewhat costly.

The highest efficiency concentrator solar cells at the date of writing this article are based on multijunction architectures such as GaInP/GaAs bonded with InGaAsP/InGaAs yielding an efficiency (η) = 46.0% [6], monolithic GaInP/GaAs/InGaAs/InGaAs yielding η = 45.7% [7], and inverted metamorphic GaInP/GaAs/InGaAs yielding η = 44.4% [5]. All of these multijunctions are designed such that incident light enters the final devices first through a wide-band gap sub-cell, followed by sub-cells with increasingly narrow band gap absorbers. With respect to

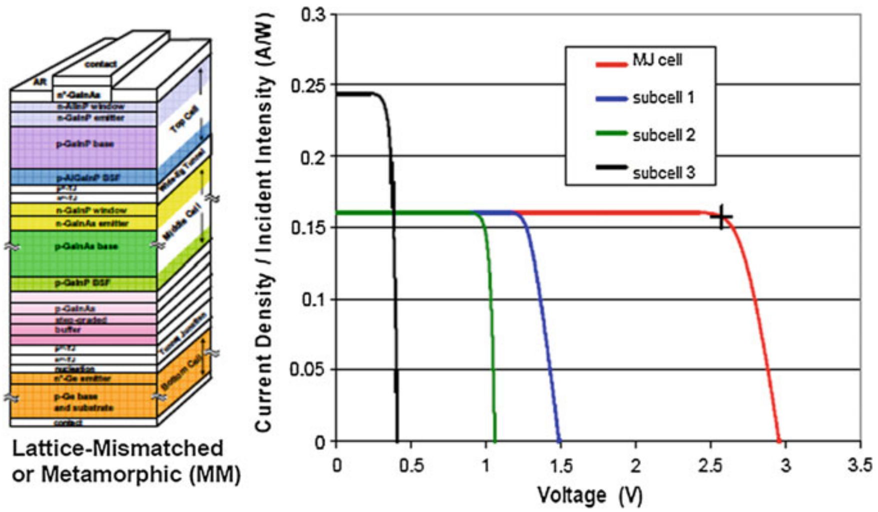

Fig. 14.1 Example schematic for a multijunction III–V based concentrator solar cell. A top cell with a wide band gap absorber (GaInP), a middle cell with an intermediate band gap absorber (InGaAs), and a bottom cell with a narrow band gap absorber (Ge) are combined in a lattice mismatched metamorphic structure here. The individual junction and complete cell current-voltage curves are also shown [2]. Reprinted from ["Band-gap-engineered architectures for high-efficiency multijunction concentrator solar cells," R. R. King, A. Boca, W. Hong, X.-Q. Liu, D. Bhusari, D. Larrabee, K. M. Edmondson, D. C. Law, C. M. Fetzer, S. Mesropian, N. H. Karam EU PVSEC, Hamburg, Germany, (2009)] with permission from EU PVSEC

each sub-cell, photons with energies greater than the absorber band gap may be absorbed while those below the band gap are transmitted through to be absorbed by an underlying sub-cell with a narrower band gap. The multijunctions are designed so that photons not absorbed in one sub-cell will be absorbed in another, enabling collection of a significant fraction of the incident irradiance spectrum, AM 1.5 for terrestrial and AM 0 for space applications [2, 5–9]. In fact, in some cases a germanium (Ge) sub-cell is used both to begin epitaxial growth and serve as the narrowest band gap sub-cell or bottom junction [2]. Figure 14.1 shows an example schematic of a type of multijunction III–V solar cell from [2]. In broad terms, the open circuit voltage (V_{oc}) is additive for this stack, the short circuit current (J_{sc}) is limited by the sub-cell with the least current generated, and the fill factor (FF) is a composite response of the quality of the full device.

The differences in the particular cell fabrication process type (bonding, monolithic, inverted metamorphic) are due to how each of the sub-cells is deposited and the final multijunction structure produced. Bonded devices have junctions separately fabricated and interconnected together. Monolithic devices have multiple junctions deposited on top of each other in the same fabrication process. Inverted metamorphic structures rely on deposition of sub-cells in the "reverse" order onto a starting wafer substrate, then removing the multijunction stack from that substrate

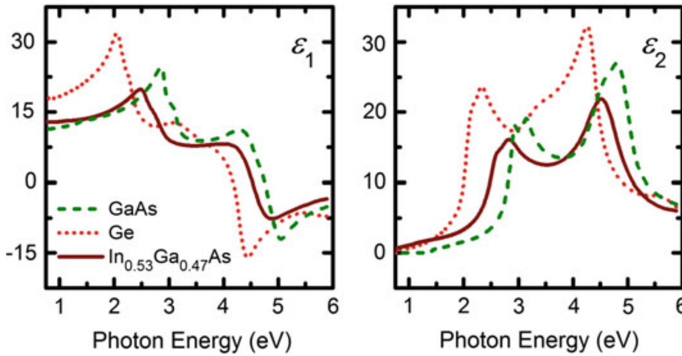

Fig. 14.2 Comparison of spectra in ε for multijunction solar cell components [30]

wafer such that the "first" layers deposited will be the "top" or widest band gap sub-cell of the multijunction. Inspection of Fig. 14.1 shows that a large number of layers are necessary to make high efficiency multijunction devices, and this chapter cannot do justice to the complexity involved in this process or the strengths, weaknesses, and applicability of each device design. Figure 14.2 shows complex dielectric function ($\varepsilon = \varepsilon_1 - i\varepsilon_2$) spectra from the near infrared to ultraviolet for example bottom junction (Ge, InGaAs) and intermediate junction (GaAs) absorber layers. Values of ε_2 are nonzero above the band gap and variations in the absorber layer band gap are evident.

III–V multijunctions also have the highest efficiency under one-sun AM 1.5 illumination with a five-junction 2.17/1.68/1.40/1.06/0.73 eV band gap sub-cell stack yielding $\eta = 38.8\%$ [8, 9]. In fact, the highest efficiency single junction device under one-sun illumination uses a GaAs thin film absorber with $\eta = 28.8\%$ [4, 9]. Figure 14.3 shows a schematic of a single junction GaAs-based device where a variety of III–V contact, window, emitter, and back surface field layers are used to achieve high efficiency. Even with just this single junction, the quantum efficiency, the spectroscopic electrical response of the solar cell, is high across the visible spectrum into the infrared [4]. The high quantum efficiency indicates that each photon incident to the GaAs absorber generates electron-hole pairs and almost all carriers are collected at the respective contact.

Fig. 14.3 Schematic of a thin film GaAs solar cell with carrier concentrations in each GaAs layer listed, after [1]

	Front Contact	
Antireflection Coating	GaAs Contact	10^{19}
30 nm	InGaP Window	
100 nm	GaAs Emitter	10^{18}
2000 nm	GaAs Base	10^{17}
50 nm	AlGaInP Back Surface Field	
300 nm	GaAs Contact	10^{18}
	Back Contact	

14.2 Challenges for Spectroscopic Ellipsometry Measurements and Analysis

Since the 1970s and the development of true spectroscopic ellipsometry, semiconductors have been studied. The III–V compounds, such as those based on GaAs, have been characterized in both thin film and bulk crystal forms over near infrared to ultraviolet spectral ranges [10–22, 24–26, 31–40], with extensions into the vacuum ultraviolet and deeper into the infrared [23, 27–29, 40] now possible. Near infrared to ultraviolet measurements (~1–5 eV) generally provide sensitivity to layer thickness and spectra in ε spanning the electronic transitions, band gap, and sub-gap transparent region. Deeper ultraviolet measurements (~5–9 eV) may be used to identify higher energy critical point transitions, achieve better surface sensitivity, and characterize the absorption features of native oxide or surface layers. On the other hand, infrared and now terahertz (THz) spectral range measurements may lack sensitivity to these surface layers and be conducted in a spectral range well below the band gap (~1 meV up to <1 eV), but provide insights into infrared-active phonon modes arising from chemical structure as well as free carrier absorption even in low carrier concentration semiconductors [23, 27–29, 40].

The most relevant materials for III–V photovoltaics are epitaxial thin films used in the aforementioned single and multijunction solar cell configurations. Even though there is a rich history of characterization and pioneering ellipsometry work was done on these materials, challenges still exist when studying these layers in the solar cell device configuration. Figures 14.1 and 14.3 show that the device structure of multijunction and single junction III–V solar cells requires multiple layers with varying degrees of optical contrast. Ultimately, the sensitivity of spectroscopic ellipsometry, regardless of the spectral range used, depends on the contrast in ε between component materials and layer thicknesses. If there is only a subtle variation in ε between two adjacent materials, the characteristics of a thin layer may be difficult or impossible to discern from its neighboring materials. If the overlying layers are optically opaque over the full measured spectrum, sensitivity to any underlying layers may also be lost.

The layers in III–V solar cells may be chemically different, leading to significant contrast in ε. The final device structure is suited for near infrared to ultraviolet measurements, in that in general the top-most sub-cell material has the widest band gap or is at least not optically opaque allowing light into the absorber layer(s) in the device. The structure desired for a solar cell, with the most light transmitted into the absorber layer(s), is reasonable for near infrared to ultraviolet ellipsometry measurements in that all light is not absorbed partway through the semiconductor stack. Consider the multijunction solar cell, whereby each sub-cell decreases in band gap from the top-most junction to the bottom. Although the top junction is designed to absorb higher photon energy or shorter wavelength light, a significant amount of visible and near infrared light passes through this junction to the underlying sub-cells. Each underlying sub-cell absorbs light with successively lower photon energies or longer wavelengths. The spectrum of incident light not absorbed by the

overlying sub-cells may be severely restricted upon reaching the bottom sub-cell, due to absorption in all overlying layers, but it is still non-zero in intensity in at least part of the infrared spectrum. Thus, features in ε in the vicinity of the band gap may be determined for each absorber and layer thicknesses deduced from the infrared spectrum interference pattern. While the devices are fabricated, measurements may not be so straightforward, as the inverted metamorphic design requires deposition of progressively more absorbing layers from bottom to top. In any configuration the ability to perform in situ or step-wise ellipsometry measurements after the fabrication of each layer is desirable to obtain ε over the full measurable range.

A challenge to these measurements is simply that there are many layers present in high efficiency solar cell device structures. Unlike polycrystalline, amorphous, or otherwise disordered thin film photovoltaics, however, texturing and light scattering are typically not employed in the final device structure. The epitaxial layers are also quite smooth, producing nearly discrete interfaces, which when modeled using Bruggeman effective medium approximations of overlying and underlying materials are quite thin (~<1 nm's). Considering these discrete interfaces and the high crystalline quality of the layers, deducing the full device structure is conceptually simple and acquisition of ellipsometric spectra (in ψ, Δ, or some variant such as complex ρ, N, C, S; etc.) is readily achievable. Analysis of ellipsometric spectra for cubic, isotropic crystals is sufficient for full optical characterization, however generalized ellipsometry or Mueller matrix measurements are required to ascertain the tensor describing ε for anisotropic materials with lower symmetry arising either from the equilibrium crystal structure or distortions of a cubic lattice. Additionally, closer inspection of the sample structures indicate that issues may exist such as the presence of compositionally graded layers that may be difficult to model independently. These graded layers may be modeled discretely which would entail using a simple line shape to describe variation in a parameter, like composition, and a database of ε spanning that range of compositional variations. In fact, for analysis of the full solar cell device structure, databases of spectra in ε for each layer would be useful to limit the free parameters during fitting to those pertaining to structure (layer thicknesses) and internal layer characteristics (composition, strain, degree of disorder).

Although there has been significant work on III–V semiconductors in the near infrared to ultraviolet range, developing parametric models for ε incorporating direct band gaps, like those found in these materials, is not trivial. In Chap. 5, a variety of methods for modeling crystalline optical response are discussed, including those based upon B-Splines and incorporating critical points. Physically realistic information should be able to be deduced from spectra in ε and its parameters, including information such as chemical content in alloys reflected in the amplitude and composite shape of ε itself [11, 13–19, 21, 22, 25], shifts in critical point energies due to compressive and tensile stress [19], and broadening of the critical points associated with a reduction in the mean free path of electrons [19, 35, 38]. Sensitivity to these variations simultaneously can be difficult to achieve, and a full database incorporating all these effects to ε has not been established. Nevertheless, there has been extensive work in database development and detecting

trends in ε with composition for a variety of ternary and quaternary alloys, as well as interpretations of the meanings of variations in critical point energies and broadenings.

In the infrared and THz ranges, the predominate optical features stem from phonon modes and free carrier absorption, both of which can be modeled using existing parametric expressions for ε. Transverse optical (TO) and longitudinal optical (LO) phonon modes can be described using the factorized or Lowndes model applied to parameterize ε [41–44]. Features in both ε and the loss function ($1/\varepsilon$) can alternately be parameterized using Lorentz oscillators. Regardless of the parameterization of ε, the detection of phonon modes provides additional information on the lattice and chemical bonding vibrational modes, which can be intimately linked to composition [23, 29, 40]. The Drude model is most directly applied to study free carrier absorption [27, 28, 40, 45]. The extension of the spectral range into the infrared and then deeper into the THz allows for the extraction of free carrier absorption, and associated electrical transport properties (scattering time, resistivity). When the free carrier absorption feature is detectable, measurements conducted as a function of applied magnetic field can be used to deduce carrier concentration, mobility, and effective mass via the optical Hall effect [28, 46].

The near infrared to ultraviolet and the infrared to THz range ellipsometry measurements suffer from different problems. In the near infrared to ultraviolet spectrum, models describing ε require improvement, although sensitivity to thickness effects in ellipsometric spectra stemming from the multiple layers present in the solar cell configuration is retained. However, optical contrast in ε in the near infrared to ultraviolet range may not be detectable as a function of semiconductor doping—essentially it may not be possible to differential *n*- or *p*-doped adjacent layers of the same compound. At longer wavelengths or lower photon energies extending into the infrared and THz, differences in ε based on dopant type and carrier concentration strongly impact the Drude feature providing a pathway to access characteristics of adjacent differently doped layers. Unfortunately, when a sufficiently strong Drude feature absorbs all incident photons, it may not be possible to deduce the free carrier absorption or phonon modes of any underlying layers in a multiple layer stack.

Lastly, many of the seminal ellipsometry measurements of these III–V materials have been made on films deposited on particular substrates ex situ, after sample deposition. For these III–V (and many other) semiconductors, surface oxidation occurs rapidly and results in an overlying layer with distinct optical response from the material of interest. The presence of this oxide introduces additional complexity into data analysis, as there is now an extra material with unknown optical response. Furthermore, if the surface oxide exists on top of an already optically rough surface it may not be possible to separate total optical response of the over-layer into the contributions from the oxide and void in the surface roughness. There are three (or more) ways to account for these types of variations. One way is to use Kramers-Kronig consistent parameterizations of ε for both the underlying material and its native oxide in the data analysis. Another is to perform in situ measurements

of the sample in vacuum after film growth but prior to ambient air exposure. A third is to perform in situ ellipsometry measurements during the removal of the oxide by chemical or mechanical means. In each case the possibility exists to deduce ε for the material and its oxide in the same analysis procedure.

Ultimately, the goal of measuring each film in the final solar cell device structure eliminates the need for accounting for any native oxide as ideally vacuum is not broken between each layer deposition. However, the complexity of the ellipsometric spectra acquired for a complete single junction or multijunction solar cell, each of which contains many individual component layers, makes this an incredibly challenging data analysis problem. Likely the most reasonable solution is to use parametric models of ε developed for single test sample cases to establish a database of the variations of ε possible for each component layer, then apply that database in the analysis of ellipsometric spectra collected for the full multilayer stack comprising the device structure.

14.3 Optical Properties

III–V materials including the binary compound GaAs; ternary InGaAs, AlGaAs, GaInP, and AlInP alloys; and quaternary AlInGaAs, AlGaInP, and InGaAsP alloys are all used within single and multijunction solar cells as emitters, window, back-side field, and base layers. Each material has a direct band gap within the near infrared to the blue visible wavelength range. Above the band gap, electronic critical point transitions in ε are observed. As mentioned in earlier chapters, these critical point features arise from electron transitions between the valence and conduction bands. Below each respective band gap, a material is not absorbing until sufficiently low photon energies or long wavelengths where phonon modes and free carrier absorption appear (see Sect. 14.4). The band gap and higher energy critical points define the imaginary part of ε, ε_2. The real part of ε, ε_1, is related to ε_2 through Kramers-Kronig consistency—in essence both the real and imaginary parts of ε are physically linked together. Each feature in ε can be described by several energy-independent parameters, the type and variety of which are defined in the particular parametric expression (see Chap. 5). Generally, each electronic transition feature is described in terms of a critical point or resonance energy for oscillations of bound electrons, a broadening describing the scattering time of those carriers with a sharper transition indicative of more well ordered material with less scattering, and an amplitude dictated by the number of carriers making the respective transition. A variety of parametric models have been applied for III–V semiconductors. An additional approach involves extracting ε numerically from ellipsometric spectra when all layer thicknesses and ε of all but the material of interest are known.

The band gap and higher energy critical points are defined by the composition and lattice structure of each III–V compound. Basically, these electronic transitions are controlled by the composition of the semiconductor, the lattice may be

manipulated by strain and shift the critical point energy, and each critical point broadening may be increased by the presence of defects which limit the carrier mean free path. As such the measured spectra in ε for a III–V material will be influenced by its chemical composition, any distortions in the lattice parameters due to compressive or tensile stress, and the relative density of defects which cause scattering of charge carriers. In principle, suitable analysis and modeling of ε yields quantitative or at least qualitative information about each of these physical properties. The ability to access these properties comes from a thorough understanding of ε as a function of composition, strain, and defects present and are enabled through the development of databases describing ε as a function of one or more of these physical parameters.

14.3.1 Composition Dependence

The composition dependence of ε for ternary and quaternary alloys is the most studied of these potential effects [11, 13–19, 21, 22, 25]. Figures 14.4 and 14.5 show example variations in ε for quaternary $In_{1-x}Ga_xAs_yP_{1-y}$ [11, 14, 15] and $Al_xGa_{1-x}InP$ alloys [18, 21, 22], although expressions for InGaAs [25], AlGaAs [13, 15, 16], AlInGaAs [17], GaInP [19, 22], AlInP [22], and others have been published. Overall effects to note are that differences in the composition strongly shift some critical point energies as well as the band gap. In Fig. 14.5, addition of aluminum to GaInP results in blue shifting of the E_0 band gap and the E_1 critical point transition energy. The E_2 transition remains relatively unaffected. The overall amplitude of each feature in ε_2 does not significantly change at each transition, although the precise value of ε_2 at a given photon energy will vary. Spectra in ε in

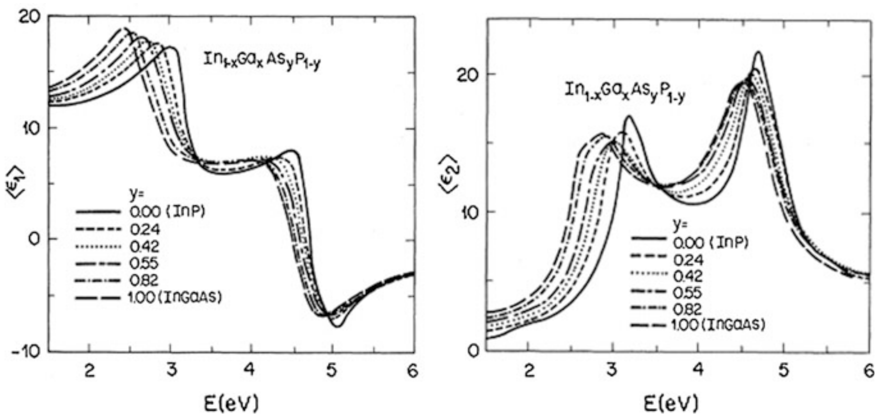

Fig. 14.4 <ε> spectra for $In_{1-x}Ga_xAs_yP_{1-y}$ as functions of y [11]. Reprinted figures with permission from [S. M. Kelso, D. E. Aspnes, M. A. Pollack, and R. E. Nahory, *Physical Review B* **26**, 6669–6681 (1982)] Copyright (1982) by the American Physical Society

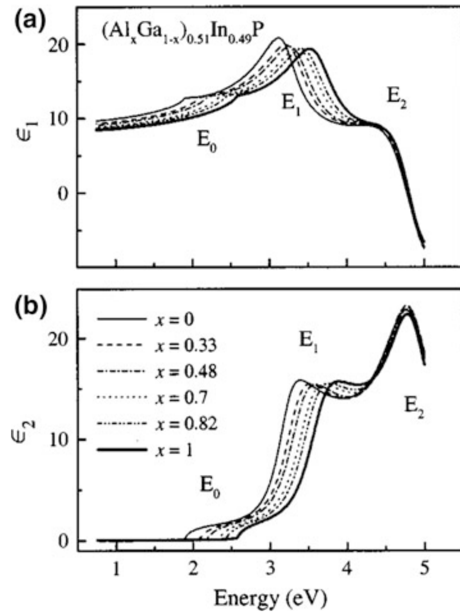

Fig. 14.5 ε spectra for $(Al_xGa_{1-x})_{0.51}In_{0.49}P$ as functions of x [22]. Reprinted from [M. Schubert, J. A. Woollam, G. Leibiger, B. Rheinlander, I. Pietzonka, T. Sab, and V. Gottschalch, *Journal of Applied Physics* **86**, 2025–2033 (1999)], with permission of AIP Publishing

Fig. 14.4 span from that of InGaAs to InP, with significant shifts in the band gap, higher energy critical points, and the overall amplitude of such features. The particular shifts are dictated by the impact of alloying on the electronic band structure, in that the addition of new elements into a III–V semiconductor in sufficient quantities can modify the energy gap between the valence and conduction bands. When the gap between the bands is smaller, the band gap energy and critical points closer to the band gap shift to lower energy. The opposite holds true when the gap between the bands becomes larger. For electronic transitions sufficiently greater than the band gap energy, the overall amplitude and position may vary less, however that depends on the particular constituent elements. Overall, the critical point features and band gap in ε provide a reflection of electronic band structure.

When spectra in ε are described using parametric models, trends in the energy-independent parameters, such as the critical point resonance energies, are tracked as a function of compositional variations. Identification of trends in parameters describing ε with composition based on polymeric expressions means that a collection of energy-independent parameters can be predicted for intermediate data points in the series of materials defining the database of ε. Thus, chemical composition, such as InP and InGaAs ratio in Fig. 14.4 and Al content in Fig. 14.5, can be used as a fit parameter in ellipsometric analysis. This type of capability enables detection of compositional variations arising during respective experiments, such as the result of spatial non-uniformities when mapping ellipsometry is applied over a sample area and as a function of thickness when in situ real time

spectroscopic ellipsometry measurements are conducted during film growth. This capability has been applied to thin film polycrystalline $Cu_yIn_{1-x}Ga_xSe_2$ as described in Chap. 10 (this volume), and 6 (Vol. 2).

14.3.2 Compressive and Tensile Stress

Compositional changes affect the band structure of an alloy, shifting the electronic transitions observed in ε. More subtle effects, however, are observed even if two samples have the same composition but exhibit different stress or strain effects. Either compressive or tensile stress distorts the lattice structure of a material, and like any force can be applied isotropically or along a particular direction. For isotropic crystals, these external forces can generate optical anisotropy in that the crystal lattice is compressed and stretched along different principle axes. Even when birefringence and dichroism are not immediately detected, shifts in the critical point energies can occur. Typically, tensile stress increases the interatomic distance of atoms in the crystal lattice in the in-plane direction, resulting in a red-shift of the critical point features to longer wavelength or lower photon energies. Conversely, when compressive stress reduces that interatomic distance, blue-shifting of the critical point features to shorter wavelength or higher photon energies occurs. The governing physics of stress on critical point features is described in Chap. 13 for CdTe.

Figure 14.6 shows shifts in the E_1 and $E_1 + \Delta_1$ critical point energies for epitaxial $In_xGa_{1-x}P$ as a function of indium content, x [19]. The data for epitaxial films are compared against unstrained bulk and film samples to show that the critical point energy shifts are not attributed to compositional variations. In particular, there

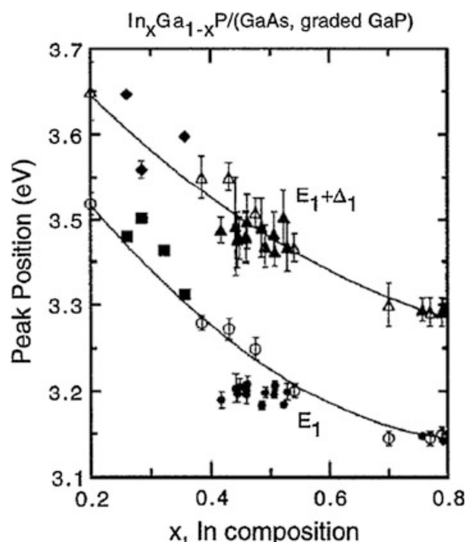

Fig. 14.6 E_1 and $E_1 + \Delta_1$ critical point energies for $In_xGa_{1-x}P$. Solid lines correspond to the open symbol points for unstrained samples. Solid symbols show deviation in critical point energies for strained epitaxial films [19]. Reprinted from [H. Lee, D. Biswas, M. V. Klein, H. Morkoc, D. E. Aspnes, B. D. Choe, J. Kim, and C. O. Griffiths, *Journal of Applied Physics* **75**, 5040–5051 (1994)], with permission of AIP Publishing

is a substantial difference between the E_1 critical points in x ~0.4–0.5 strained films. For samples with well-defined stoichiometry, shifts in critical points may be attributed solely to stress. Unfortunately, when compositional variations are introduced it can be difficult to separate variations in ε due to stress and alloying. When properly accounted, stress effects can be incorporated into a database describing ε so that this structurally meaningful property can be extracted optically. This procedure has been applied to CdTe films discussed in Chap. 13, and although the films are polycrystalline a similar approach would be valid here.

14.3.3 Defects

Stress and composition may alter the lattice and band structure to varying degrees, resulting in shifts in the critical point energy transitions. Additional changes in ε may be described in terms of limitations in the mean free path of carriers due to defects. In polycrystalline materials, a version of the Scherrer formula is often used to deduce "grain size" from the width or broadening of respective critical point features as described in Chap. 13 for polycrystalline CdTe. As the broadening of the respective critical point feature increases, the mean free path of electrons and average time between scattering events decrease. For polycrystalline samples, narrower features with lower broadening ultimately approach that of the corresponding single crystal. This analysis is analogous to that used in determining grain size from x-ray diffraction (XRD).

It should be noted, however, that the broadening of a critical point feature or even of a XRD peak does not directly indicate grain size, but rather just the mean distance over which an electron can travel before being scattered. In the absence of grain boundaries, or with a sufficiently high defect concentration within a crystalline grain, the mean free path of electrons can be limited by point and line defects in the material. For epitaxial thin films like the III–V layers used in solar cells, the dominant thermodynamically stable defect type may influence the broadening of the critical point transitions.

In essence, larger broadening is equivalent to a smaller mean free path of electrons and a shorter time between carrier scattering events. These scattering events are due to deviations in the crystal lattice from equilibrium, i.e. increased concentrations of point or lattice defects present. Figure 14.7 illustrates a simulation of broadening of the E_1 and $E_1 + \Delta_1$ critical points of GaAs due to a 20–50% decrease in the scattering time or mean free path of carriers compared to reference spectra in ε [30]. Variations in defect density may occur due to deposition conditions leading to growth variations [19] or post-deposition processing [35, 38]. For example, Snyder et al. [35, 38] reported broadening of critical point energies in GaAs due to chemical etching and plasma damage. This type of critical point broadening may occur concurrently with strain induced in the crystal lattice as in Lee et al. [19] or compositional variations (antisite defects, etc.). Robust understanding of ε as a function of both composition and strain allow for the mean free

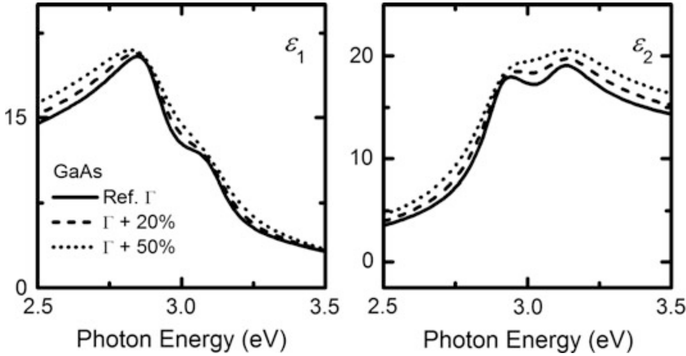

Fig. 14.7 Simulated critical point broadening schematic for the E_1 and $E_1 + \Delta_1$ critical point transitions in GaAs [30] where each transition is broadened by an additional 20 and 50% relative to their reference values to simulate a reduction in the mean free path of carriers

path of electrons to be deduced from measured ε. Large variations in broadening due to grain size in CdTe has been incorporated into the database of ε such that "grain size" serves as a single fit parameter describing shifts in the broadening for each critical point over the visible to ultraviolet spectral range. Broadening increases due to point and line defects in epitaxial and bulk III–V semiconductors will likely be smaller, due to the more localized extent of these defects compared to grain boundaries, but can potentially be measured and used to qualify crystal damage, defects, and disorder.

14.3.4 Temperature Dependence

As a final note on all these possible variations in ε, its temperature dependence must be considered. Variations in critical point energy position, broadening, and amplitude may be used to deduce composition, strain, and defects assuming that all comparison spectra in ε are measured at the same temperature. The temperature dependence on the critical point energies and associated parameters are well studied for III–V semiconductors [26, 32], with databases of temperature dependent ε developed [34, 36]. In general, variations in ε with temperature may be comparable in magnitude to small shifts in composition and strain. To compare subtle variations in ε, or the parameters describing it, temperature must be considered in all analyses. Of course, when measurements are conducted at "room temperature" and there is not a significant variation, ~several °C, the effects can be weak and may be within the error of the measurement and analysis. However, significant deviations in ε are expected when comparing spectra collected at room temperature and at high temperatures, several hundred °C, used in III–V semiconductor fabrication and must be considered for any in situ measurement of film growth or processing.

14.4 Infrared and THz Spectroscopic Ellipsometry

A significant amount of information can be deduced about material composition and structure from near infrared to ultraviolet measurements, however advances in spectroscopic ellipsometer instrumentation over the recent decades have made longer wavelength measurements, and deduction of features in ε, far more accessible. Fourier transform infrared (FTIR) based spectroscopic ellipsometers enable detection of phonon modes [23, 27, 29] and free carrier absorption [27, 28] in moderately doped semiconductors, as has been mentioned previously. More recently developed THz range spectroscopic ellipsometry enables detection of lower frequency phonon modes and free carrier absorption in more lightly doped semiconductors [46]. In both cases phonon modes detected are linked to the internal chemical bonding and lattice structures in the material, and are represented in ε by either variations on Lorentz and Gaussian broadened oscillators or a factorized Lowndes model expression. These phonon absorption features are more directly linked to chemical bonding compared to visible and ultraviolet range critical point energies where compositional changes are only detected through variations in the band structure. Free carrier absorption is typically described based on the Drude model, whereby infrared and THz range ellipsometric spectra (or visible range ellipsometric spectra for metals) can be described in terms of layer resistivity and mean free carrier scattering time [45]. When free carrier absorption is observed, additional ellipsometry measurements made as a function of applied magnetic field may be used to determine carrier concentration, mobility, and effective mass from the magnetic field dependence of the Drude oscillator parameters. This ability is called the optical Hall effect and is gaining popularity in deducing electrical transport properties from non-contacting optical measurements [28, 46]. Alternately, either carrier concentration, mobility, or effective mass can be fixed and used to deduce the other two quantities from standard measurements.

14.4.1 Infrared Active Phonon Modes

Phonon modes represented in ε are ascribed to infrared active chemical bonding or lattice vibrations. TO modes manifest as peaks in ε_2 while LO modes generally appear as peaks in the imaginary part of $1/\varepsilon$. The utility in identification of these mode positions is that they can identify the presence of particular chemical bonding in III–V semiconductors [23, 27, 29]. The amplitude of these features is correlated with the number of those bonds present per unit volume in the material and their transition strength. Often these features can be detected from ψ, Δ spectra directly, as inflection points at appropriate photon energies even with an oscillating interference fringe pattern present. Figure 14.8 shows measured spectra in ψ for an InGaAsP film, where features due to InP, AlP, and GaP are identified [23]. This example measurement is also sensitive to peaks in the underlying GaAs substrate.

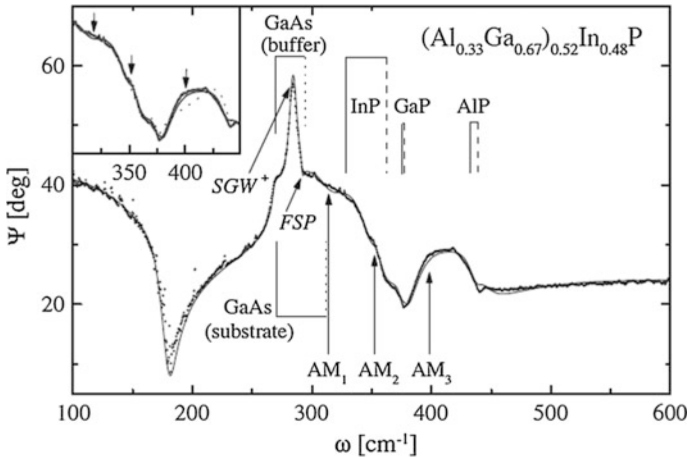

Fig. 14.8 Example phonon modes detected in infrared extended ellipsometric spectra for an $(Al_{0.33}Ga_{0.67})_{0.52}In_{0.48}P$ epitaxial layer [23]. Reprinted figure with permission from [T. Hofmann, G. Leibiger, V. Gottschalch, Ines Pietzonka, and M. Schubert, *Physical Review B* **64**, 155206 (2001)] Copyright (2001) by the American Physical Society

With a full analysis, spectra in ε are fit to deduce the phonon mode parameters, typically the TO mode resonance energy or frequency, the LO mode resonance energy or frequency, and the respective broadening associated with each. Sometimes it is difficult to distinguish the broadening for the TO and LO modes independently, so only a common broadening can be identified [41–44].

14.4.2 Free Carrier Absorption and Electrical Transport

Interpretation of free carrier absorption in ε is particularly interesting as it provides a means of identifying some electrical transport properties optically, without deposition and pattering of contact layers or concern about forming an Ohmic contact. Standard measurements rely on interpretation of the Drude feature to obtain material resistivity and carrier mean free scattering time—two free parameters linked to transport in addition to however many other free parameters may be present in the fit [23, 27, 29, 40]. From the Drude parameters, one can deduce any two of carrier concentration, mobility, and effective mass if the third is fixed from other measurements [27, 40, 45]. Typically, effective carrier mass is fixed in order to optically obtain mobility and carrier concentration. With standard electrical measurements these properties may be difficult to obtain for each layer in a multiple layer sample. The potential to determine these quantities from a technique like spectroscopic ellipsometry, which is sensitive to both ε and thickness of each layer, is attractive. With a suitable analysis, it may be possible to identify multiple effects

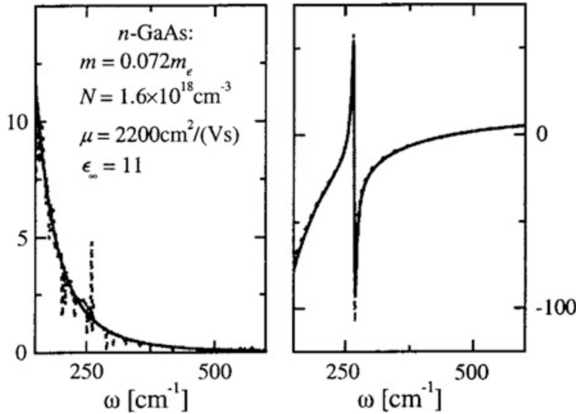

Fig. 14.9 Free carrier response in n-type GaAs yields carrier concentration, mobility, and effective mass from analysis of the magneto-optic ε tensor from far infrared ellipsometry measurements. Imaginary (left) and real (right) parts of ε_{xx} shown [28]. Reprinted from [M. Schubert, T. Hofmann, and C. M. Herzinger, *Journal of the Optical Society of America A* **20**, 347–356, (2003)] with permission from The Optical Society

such as sensitivity to carrier concentration and mobility of both "heavy" and "light" holes in p-type GaAs [27].

To overcome the limitation of requiring a fixed effective carrier mass in interpreting parameters from the Drude model, ellipsometric measurements are being compared as a function of applied magnetic field [28, 46]. Variations in ε as a function of magnetic field strength and direction are analyzed to deduce all three parameters independently: carrier concentration, mobility, and effective mass. These measurements are referred to as the optical Hall effect and provide more information than standard electrical Hall effect measurements that yield only concentration and mobility. Figure 14.9 shows spectra in ε along the "xx" direction of the magneto-optic tensor for n-type GaAs as obtained from analysis of magnetic field dependent far infrared ellipsometry measurements [28]. A Drude feature due to free carrier absorption is observed where ε_2 amplitude increases with decreasing frequency. A TO mode peak in ε_2 is also discerned near a frequency of 270 cm^{-1}. This data demonstrates sensitivity in resolving both phonon mode and free carrier absorption contributions to ε simultaneously.

The nature of spectroscopic ellipsometry may enable variations in ε with magnetic field to be identified for multiple layers in a thin film stack or device structure —such as a III–V solar cell. The full potential of this technique is great and it is currently being used for a wide range of material systems. However, possible limitations exist in that these longer wavelength or lower photon energy measurements require there to be significant contrast in ε between the layer of interest and all overlying and underlying materials to produce reliable results. Furthermore, a highly doped over-layer or even a material with strong TO modes may absorb all light over a portion of the incident spectrum, so that sensitivity to all underlying layers can be lost in that spectral range.

14.5 In Situ and Real Time Spectroscopic Ellipsometry

Static ex situ measurements over the THz, infrared, and near infrared to ultraviolet spectrums provide a huge amount of information pertaining to the properties of an epitaxial thin film including the band gap, higher energy electronic transitions, phonon modes, and free carrier absorption during intentional alloying or doping and sometimes unintentional variations in film stress and defect density. Accessing these properties after the films have been deposited involves measuring the sample on a spectroscopic ellipsometer in ambient. Most samples are modeled as homogeneous thin films with some degree of surface roughness or interfaces formed where applicable. Overall, however, the samples may not be this well-behaved after deposition. These semiconductors oxidize quickly upon exposure to the ambient [10, 12, 25, 31, 37, 39, 47]. Deposition of ternary and quaternary alloys involves multiple types of atoms occupying similar lattice sites, so the deposition fluxes of each source can vary with time during the deposition and result in the formation of compositional and optical property gradients [48]. In situ and real time spectroscopic ellipsometry, typically over the near infrared to ultraviolet range, provide the tools necessary to understand both oxidation and compositional inhomogeneities with thickness by accessing changes in the measured ellipsometric spectra during post-deposition processes or growth [48, 49]. A variety of analysis techniques exist, which have been described for disordered material systems in other chapters. Here we will highlight techniques already applied to III–V semiconductors.

14.5.1 Surface Oxidation

The primary complication in the measurement of any III–V sample post-deposition is the quality of the sample surface. Once the sample leaves vacuum and the deposition chamber, the surface can oxidize (~1–10's nm thick) and impact the measured ellipsometric spectra [10, 12, 25, 31, 37, 39, 47]. This type of consideration is minimized with stacks of layers, such as those found in the complete solar cell configurations, as each layer is deposited on top of the last ideally without breaking vacuum until the final layer. Unfortunately, many of the samples used for fundamental studies consist of only a single thin film on a substrate or an exposed top layer material in the sample stack. When the deposition equipment allows, in situ spectroscopic ellipsometry measurements can be made after the sample is deposited, but prior to leaving vacuum or an otherwise inert atmosphere. Most deposition systems are not equipped for in situ ellipsometry measurements, however more details regarding these measurements will be discussed in the context of real time spectroscopic ellipsometry. For samples deposited in an arbitrary system and characterized in ambient, the oxide must still be considered.

Two primary problems with ex situ static measurements are that there are two unknown contributions: the film and its native oxide and that the surface layer may

consist of atomic to microscopic scale roughness in addition to the native oxide. Solutions to the oxide and surface roughness issues can take two approaches: (i) parametric modeling of ε for the film and its surface layer using Kramers-Kronig consistent expressions and effective medium approximations as necessary and/or (ii) measuring ellipsometric spectra before and after a post-deposition process to remove the native oxide which has formed and/or reduce the magnitude of surface roughness. The primary disadvantage of (i) is that it further complicates the optical and structural model used to analyze spectra. The precise contributions of both surface roughness and the oxide may still not be disentangled, particularly for thin layers [40]. For (ii), chemical etching of the native oxide and mechanical-electro-chemical etching of the surface roughness have been successfully applied to improve the sample quality [12, 25, 31, 39, 47]. However, if not properly done, the surface quality may degrade or defects may be introduced into the bulk material causing deviations in measured ε.

Figure 14.10 shows $<\varepsilon>$ for a GaAs single crystal both before and after a 1 nm native oxide has grown on a discreet clean interface [10, 12]. There is a significant difference observed with a relatively small amount of oxidation. For III–V semiconductors like GaAs, a successful strategy involves applying bromine-methanol etches to samples while they are otherwise kept in an inert atmosphere such as dry nitrogen. In situ spectroscopic ellipsometry measurements are conducted during this etching process (oxide removal) and continued after exposure to atmosphere (oxide regrowth). The largest magnitude and sharpest features resolved in $<\varepsilon>$ are indicative that the oxide surface layer has been removed and yield a very good approximation, if not the true value, for ε of the III–V material. Ellipsometric measurements of the sample when oxidized, either before etching or after regrowth,

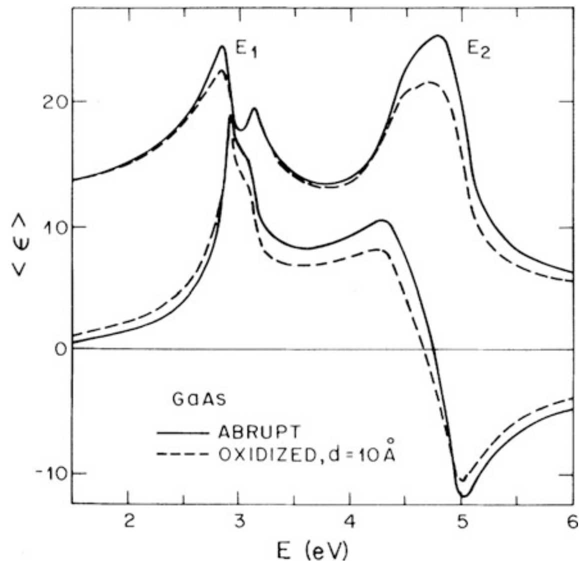

Fig. 14.10 $<\varepsilon>$ spectra for GaAs single crystal with and without a 1 nm thick oxide [10, 12]. Reprinted figure with permission from [D. E. Aspnes and A. A. Studna, *Physical Review B* **27**, 985–1009 (1983)] Copyright (1983) by the American Physical Society

can be analyzed using reference ε obtained from removal for the III–V material to determine the optical response of the oxide using simultaneous analysis of multiple measurements with varying thicknesses of oxide acquired [10, 37]. Spectroscopic ellipsometry measurements in this type of in situ configuration can be performed using either spectral scanning or multichannel instruments, as data acquisition time may not be an issue depending on the oxidation rate and equipment setup (purging, etc.).

The approach using in situ ellipsometry and chemical etching of the native oxide is quite elegant, however windows at oblique angles of incidence on a deposition system or load-lock enable measurements to be made while the sample is still under vacuum or in otherwise inert atmosphere, prior to any oxidation. Surface roughness still remains a consideration, but the near infrared to ultraviolet ε can be obtained from parametric models where the surface roughness may be represented as an effective medium approximation of the underlying material and void if in-plane features are sufficiently smaller than the wavelength of probing light. Measurements conducted both before and after exposing the sample to laboratory ambient or a reactive gas atmosphere can identify the formation of the oxide in a similar approach as described previously for etching.

14.5.2 Deposition Monitoring and Control

Use of multichannel, high-speed spectroscopic ellipsometers enables full spectra in ψ, Δ to be acquired on time scales ~1 s [48–52]. As typical deposition rates of III–V semiconductors, and many other thin films described earlier, may be ~0.1–10 nm/s, ellipsometric spectra can be acquired in situ, in real time during thin film growth when the ellipsometer is able to be mounted on the deposition chamber. Time dependent ellipsometric spectra allow for different analysis methodologies not reliant upon parametric models. In one such case, the time dependence of bulk and surface roughness layer thickness and a time-independent spectra in ε are simultaneously obtained by analyzing multiple sets of ellipsometric spectra simultaneously. Numerical inversion is used to generate ε under test sets of thickness values. The numerically inverted ε are then used to fit ellipsometric spectra collected at other times with thicknesses or other structural characteristics as free parameters. The approach is repeated for many test sets of ε obtained from various combinations of thicknesses, until the set of structural parameters are identified yielding ε which can fit other time points with the lowest spectrally averaged mean square error (σ). This approach is described as the global sum-of-σ ($\Sigma\sigma$) minimization procedure, and similar methodologies are adapted for multi-time analyses [53, 54]. This type of approach has been widely successful in characterizing the growth of other thin film materials for solar cells, as described in other chapters of this book.

The shortcoming of $\Sigma\sigma$-minimization and similar multi-time analyses is the assumption of a homogeneous ε with thickness. However, through the time dependence of the mean square error, regimes where the optical and structural model does not provide a reasonable fit to the experimental data can be identified.

These regions can then be analyzed with more complicated models or procedures. For samples exhibiting inhomogeneities with thickness, either from composition or structural transitions, a virtual interface analysis approach may be appropriate [55–58]. In virtual interface analysis, the time dependence of the ellipsometric spectra is modeled in such a way that the ε, the growth rate, and surface roughness is deduced for only the top outer-layer of a growing sample. A set of ellipsometric spectra collected at an earlier time is numerically inverted using a test surface roughness thickness and assuming a semi-infinite underlying surface referred to as the pseudo-substrate. A later time point is analyzed using this pseudo-substrate and the change with time of the ellipsometric spectra is used to deduce the aforementioned properties of the outer-layer. The difference in time between the later time point and that used to obtain the pseudo-substrate, along with the instantaneous deposition rate, controls the thickness of the outer-layer. A minimum outer-layer thickness is the amount of depositing material accumulated between ellipsometric spectra collected at two successive time points. This approach is iterated based upon different pseudo-substrates from assuming test surface roughness thicknesses, until a time averaged minimum in the mean square error is obtained. A parameterization of ε as a function of the variable parameter, possibly composition in III–V alloys, can be used to reduce the complexity and fit parameters within the model during virtual interface analysis in addition to fitting each set of ellipsometric spectra collected singly.

If such a model is not available, other methods can be used to provide the real time monitoring of thickness dependent material properties desired. For example, in ternary or quaternary alloys multiple deposition fluxes may occur simultaneously, although the rate at which each atomic species is incorporated into the film may be different. This difference results in compositional non-uniformities with thickness, i.e. the layer may become either deficient or rich in a component throughout the accumulated thickness even if the source fluxes remain constant. Trepk et al. [48] used Fourier coefficients related to the measured ψ, Δ spectra to track composition in $In_xGa_{1-x}As$ films. The spectra collected near 3.3 eV has the largest difference with respect to composition over their accessible spectral range. Time dependent variations in the Fourier coefficients are tracked and related to the lattice mismatch and composition from XRD measurements as shown in Fig. 14.11. This information is then used to interpret the Fourier coefficients output from the ellipsometer, and with no additional analysis could yield the composition of the outer surface of the growing film. The composition output from the in situ real time spectroscopic ellipsometry collected during growth is used in a feedback loop to control the relative source fluxes to maintain the desired composition of $x = 0.523$, which was confirmed for the film by XRD measurements. Ex situ measurements may have simply reported an average value, while in reality a gradient could be present. Overall this real time monitoring and control enabled by in situ real time spectroscopic ellipsometry is impressive, as variations in composition with thickness using fixed source fluxes may have remained otherwise undetected.

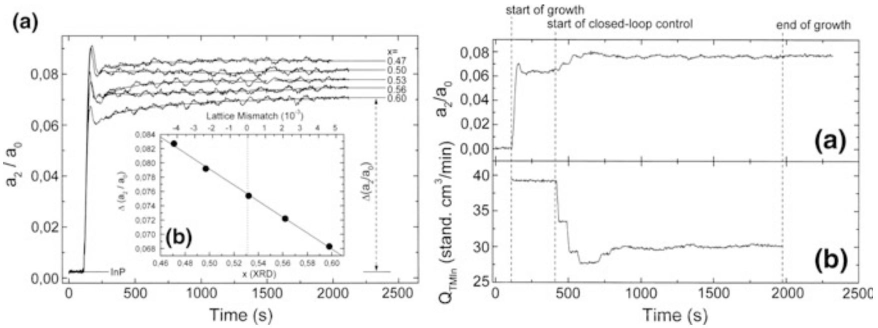

Fig. 14.11 **a** Fourier coefficient ratios of ellipsometric spectra obtained for $In_xGa_{1-x}As$ growth on InP for different In content, *x*, as calibrated by XRD. **b** Example trimethylindium (TMIn) flux control using in situ ellipsometric data to produce a composition $x = 0.523$ [48]. Reprinted from [*Thin Solid Films*, **313–314**, T. Trepk, M. Zorn, J.-T. Zettler, M. Klein, and W. Richter, "Spectroscopic ellipsometry applied for in-situ control of lattice matched III–V growth in MOVPE," 496–500] Copyright (1998) with permission from Elsevier

14.6 Future Outlook

In terms of solar cells, III–V photovoltaics are going to continue to be a topic of intense research interest. Higher efficiency of multijunction devices are sought by using combinations of new quaternary and quinary alloys and increasing the number of junctions. Potentially up to six sub-cells can realistically be used in a multijunction, each of which can contain an equivalent number of contact, emitter, base, and other component layers [2, 8]. Efficiency improvements in these more complicated structures, or even a better understanding of failure mechanisms, can be determined by precise layer control enabled by spectroscopic ellipsometry measurements. Even single junction thin film III–V solar cells are being evaluated for large area applications [4]. In that scenario mapping ellipsometric measurements may be used to determine spatial non-uniformity.

Barriers to addressing current and future problems do exist. The number of layers in III–V solar cells can be large, and some components only have subtly different optical responses in the near infrared to ultraviolet. Differences do exist, however, at longer wavelengths as reflected in phonon modes and free carrier absorption. Two possible pathways for immediate impact on III–V solar cell characterization are:

(1) Development of optical and structural models for complete III–V solar cell structures suitable for use in analysis of ellipsometric spectra.
(2) Expansion of existing databases of ε to include variations due to composition, stress, and defects. Inclusion of infrared and THz spectral range features and their variations should also be investigated.

These two tracks will advance understanding of devices and materials in the same way that spectroscopic ellipsometry has for solar cells based on

polycrystalline and other disordered materials as described in other chapters of this book. In particular, simultaneous analysis of spectra spanning from deeper into the infrared to the ultraviolet will include both electronic transitions and phonon modes. Shifts in the position of electronic transitions due to variations in the band structure upon alloying or applied stress should be compared to shifts in the phonon modes under these same conditions. These comparisons may make it easier to identify "compensating" behavior in the visible range electronic transitions affected by both composition and stress simultaneously.

An existing understanding of III–V materials for photovoltaics and other applications, and the very rich comprehensive literature on ellipsometry characterization of these semiconductors already exist. This knowledge base means that investigation of new III–V alloys can be done in an existing framework and used to augment databases of ε already in existence. To push the measurements and analyses further only requires sufficient research time and effort. So get to work!

References

1. J.J. Schermer, G.H. Bauhuis, P. Mulder, E.J. Haverkamp, J. van Deelen, A.T.J. van Niftrik, P. K. Larsen, Thin Solid Films **511–512**, 645 (2006)
2. R.R. King, A. Boca, W. Hong, X.-Q. Liu, D. Bhusari, D. Larrabee, K.M. Edmondson, D.C. Law, C.M. Fetzer, S. Mesropian, N.H. Karam, *Proceedings of the 24th European Photovoltaic Solar Energy Conference*, 55 (2009)
3. G.J. Bauhuis, P. Mulder, E.J. Haverkamp, J.C.C.M. Huijben, J.J. Schermer, Sol. Energy Mater Sol. Cells **93**, 1488 (2009)
4. B.M. Kayes, H. Nie, R. Twist, S.G. Spruytte, F. Reinhardt, I.C. Kizilyalli, G.H. Higashi, *Proceedings of the 37th PV Specialists Conference*, 4 (2011)
5. Press Release, Sharp Corporation, http://sharp-world.com/corporate/news/120531.html. Accessed 31 May 2012
6. Press Release, Fraunhofer Institute for Solar Energy Systems, http://www.ise.fraunhofer.de/en/press-and-media/press-releases/pressreleases-2014/new-world-record-for-solar-cell-efficiencyat-46-percent. Accessed 1 Dec 2014
7. Press Release, National Renewable Energy Laboratory, 16 Dec 2014, NR-4514
8. P.T. Chiu, D.L. Law, R.L. Woo, S. Singer, W.D. Hong, Z. Zakaria, J.C. Boisvert, S. Mesroian, R.R. King, N.H. Karam, *Proceedings of the 40th PV Specialists Conference*, 11 (2014)
9. M.A. Green, K. Emery, Y. Hishikawa, W. Warta, E.D. Dunlop, Prog. PV Res. Appl. **24**, 3 (2016)
10. D.E. Aspnes, G.P. Schwartz, G.J. Gaultieri, A.A. Studna, B. Schwartz, J. Electrochem. Soc. **128**, 590 (1981)
11. S.M. Kelso, D.E. Aspnes, M.A. Pollack, R.E. Nahory, Phys. Rev. B **26**, 6669 (1982)
12. D.E. Aspnes, A.A. Studna, Phys. Rev. B **27**, 985 (1983)
13. S. Adachi, Phys. Rev. B **38**, 12345 (1988)
14. S. Adachi, Phys. Rev. B **39**, 12612 (1989)
15. S. Adachi, J. of Appl. Phys. **66**, 6030 (1989)
16. P.G. Snyder, J.A. Woollam, S.A. Alterovitz, B. Johs, J. of Appl. Phys. **68**, 5925 (1990)
17. H.W. Dinges, H. Burkhard, R. Losch, H. Nickel, W. Schlapp, Mater. Sci. Eng. **21**, 174 (1993)
18. S. Adachi, H. Kato, A. Moki, K. Ohtsuka, J. of Appl. Phys. **75**, 478 (1994)

19. H. Lee, D. Biswas, M.V. Klein, H. Morkoc, D.E. Aspnes, B.D. Choe, J. Kim, C.O. Griffiths, J. of Appl. Phys. **75**, 5040 (1994)
20. C.M. Herzinger, P.G. Snyder, B. Johs, J.A. Woollam, J. of Appl. Phys. **77**, 1715 (1995)
21. S. Ozaki, S. Adachi, M. Sato, K. Ohtsuka, J. of Appl. Phys. **79**, 439 (1996)
22. M. Schubert, J.A. Woollam, G. Leibiger, B. Rheinlander, I. Pietzonka, T. Sab, V. Gottschalch, J. of Appl. Phys. **86**, 2025 (1999)
23. T. Hofmann, G. Leibiger, V. Gottschalch, I. Pietzonka, M. Schubert, Phys. Rev. B **64**, 155206 (2001)
24. S. Zollner, J. Appl. Phys. **90**, 515 (2001)
25. Y.S. Ihn, T.H. Ghong, Y.D. Kim, S.J. Kim, D.E. Aspnes, T. Yao, B.H. Koo, J. Korean Phys. Soc. **42**, S242 (2003)
26. S. Adachi, *Properties of Semiconductor Alloys: Group-IV, III–V, and II-VI Semiconductors* (Wiley, West Sussex, 2009)
27. S. Zangooie, M. Schubert, D.W. Thompson, J.A. Woollam, Appl. Phys. Lett. **78**, 937 (2001)
28. M. Schubert, T. Hofmann, C.M. Herzinger, J. Opt. Soc. Am. A **20**, 347 (2003)
29. T. Hofmann, M. Schubert, G. Leibiger, V. Gottschalch, Appl. Phys. Lett. **90**, 182110 (2007)
30. Reference spectra obtained from the J.A. Woollam Co. database
31. D.E. Aspnes, H.J. Stocker, J. Vac. Sci. Tech. **21**, 413 (1982)
32. P. Lautenschlager, M. Garriga, S. Logothetidis, M. Cardona, Phys. Rev. B **35**, 9174 (1987)
33. S. Alterovitz, P.G. Snyder, K.G. Merkel, J.A. Woollam, D.C. Radulescu, L.F. Eastman, J. Appl. Phys. **63**, 5081 (1988)
34. H. Yao, P.G. Snyder, J.A. Woollam, J. Appl. Phys. **70**, 3261 (1991)
35. G.F. Feng, R. Zallen, J.M. Epp, J.G. Dillard, Phys. Rev. B **43**, 9678 (1991)
36. S. Zollner, M. Garriga, J. Kircher, J. Humlicek, M. Cardona, G. Neuhold, Phys. Rev. B **48**, 7915 (1993)
37. S. Zollner, Appl. Phys. Lett. **63**, 2523 (1993)
38. P.G. Snyder, N.J. Ianno, B. Wigert, S. Pittal, B. Johs, J.A. Woollam, Mater. Res. Soc. Symp. Proc. **378**, 689 (1995)
39. G.Y. Seong, C.Y. Bang, Y.D. Kim, J. Wang, D.E. Aspnes, B.H. Koo, T. Yao, J. Korean Phys. Soc. **39**, S389 (2001)
40. I. Subedi, M. Slocum, D. Forbes, S. Hubbard, N.J. Podraza, Appl. Surf. Sci. **421**, 813 (2017)
41. R.P. Lowndes, Phys. Rev. B **1**, 2754 (1970)
42. A. Kasic, M. Schubert, S. Einfeldt, D. Hommel, T. Tiwald, Phys. Rev. B **62**, 7365 (2000)
43. M. Schubert, T.E. Tiwald, C.M. Herzinger, Phys. Rev. B **61**, 8187 (2000)
44. M. Schubert, *Infrared Ellipsometry on Semiconductor Layer Structures: Phonons, Plasmons, and Polaritons* (Springer, Berlin, 2004)
45. T.E. Tiwald, D.W. Thompson, J.A. Woollam, W. Paulson, R. Hance, Thin Solid Films **313–314**, 661 (1998)
46. T. Hofmann, C.M. Herzinger, J.L. Tedesco, D.K. Gaskill, J.A. Woollam, M. Schubert, Thin Solid Films **519**, 2593 (2011)
47. H.J. Stocker, D.E. Aspnes, Appl. Phys. Lett. **42**, 85 (1983)
48. T. Trepk, M. Zorn, J.-T. Zettler, M. Klein, W. Richter, Thin Solid Films **313–314**, 496 (1998)
49. M. Ebert, K.A. Bell, S.D. Yoo, K. Flock, D.E. Aspnes, Thin Solid Films **364**, 22 (2000)
50. J. Lee, P.I. Rovira, I. An, R.W. Collins, Rev. Sci. Instrum. **69**, 1800 (1998)
51. B. Johs, J.A. Woollam, C.M. Herzinger, J. Hilfiker, R. Synowicki, C.L. Bungay, SPIE Proc. **CR 72**, 29 (1999)
52. C. Chen, I. An, G.M. Ferreira, N.J. Podraza, J.A. Zapien, R.W. Collins, Thin Solid Films **455–456**, 14 (2004)
53. Y. Cong, I. An, K. Vedam, R.W. Collins, Appl. Opt. **30**, 2692 (1991)
54. P. Aryal, A. Ibdah, P. Pradhan, D. Attygalle, P. Koirala, N.J. Podraza, S. Marsillac, R.W. Collins, J. Li, Prog. PV Res. Appl. **24**, 1200 (2016)

55. D.E. Aspnes, J. Opt. Soc. Am. A **10**, 974 (1993)
56. H. Fujiwara, J. Koh, R.W. Collins, Thin Solid Films **313–314**, 474 (1998)
57. A.S. Ferlauto, G.M. Ferreira, R.J. Koval, J.M. Pearce, C.R. Wronski, R.W. Collins, M.M. Al-Jassim, K.M. Jones, Thin Solid Films **455–456**, 665 (2004)
58. N.J. Podraza, J. Li, C.R. Wronski, E.C. Dickey, M.W. Horn, R.W. Collins, Phys. Stat. Sol. A **205**, 892 (2008)

Chapter 15
Organic Solar Cells

Maria Isabel Alonso and Mariano Campoy-Quiles

Abstract Organic solar cells attract both scientific and economic interest due to their potential for clean and cost-effective photovoltaic energy conversion. Continuous evolution of this field relies on materials research, including synthesis of new compounds and fine control over film microstructure, as well as improved device architectures. In this context, spectroscopic ellipsometry is a helpful characterization tool, stretching over material preparation, device structure, and device modelling. This chapter will provide a general perspective of aspects that can be investigated by ellipsometry in these systems. The acquired insights enhance our capability to understand and model the optoelectronic properties of photovoltaic devices.

15.1 Introduction

The field of organic solar cells or photovoltaics (OPV) is in continuous development mainly driven by its advantageous traits: environment-friendly low-cost generation of energy owing to the possibility of large area manufacturing of flexible, light-weight, semi-transparent devices with low energy payback times. Progress in this field is largely based on the design of new materials, control of microstructure and the improvement of device geometries. In this context, spectroscopic ellipsometry is gaining attention for the characterization and optimization of layered devices. The technique can be helpful to evaluate new active materials, obtain detailed depth profiles of material composition, and study solid-state microstructure of organic semiconductors, which can be very varied depending on

M. I. Alonso (✉) · M. Campoy-Quiles
Institut de Ciència de Materials de Barcelona (ICMAB-CSIC), Campus UAB, 08193 Bellaterra, Spain
e-mail: isabel.alonso@icmab.es

© Springer International Publishing AG, part of Springer Nature 2018

H. Fujiwara and R. W. Collins (eds.), *Spectroscopic Ellipsometry for Photovoltaics*, Springer Series in Optical Sciences 212,
https://doi.org/10.1007/978-3-319-75377-5_15

the physical phase and molecular orientation, so that the device optical properties emerge as a combination of both chemical nature and solid state packing.

The device architectures developed for OPVs take into account the particular properties of organic semiconductors. Active layers must be thin to optimize the efficiency of charge extraction. This is partly due to the large binding energies of photoexcited electron-hole pairs (called excitons) and their short diffusion length, L_D ~20 nm, before recombination. Such excitons need to reach the p-n (or donor-acceptor, D-A) junction to dissociate into free charges. Once this charge transfer process happens, the charge extraction is also hindered by a very low charge-carrier mobility that limits the effective charge separation and collection. Since sufficient layer thickness is needed to absorb a reasonable amount of photons, in planar junctions a thickness compromise must be met. Fortunately, organic semiconductors have relatively strong absorption coefficients and operational thicknesses are not too large. It is also possible to tailor the active compounds via chemical synthesis to reach improved matching with the solar spectrum. The device architecture that addresses the mentioned drawbacks is the bulk heterojunction concept shown in Fig. 15.1, in which D and A compounds are blended to increase the available interface and to shorten the distance from any point to an interface. The morphology and phase separation in the blend are critical to OPV performance

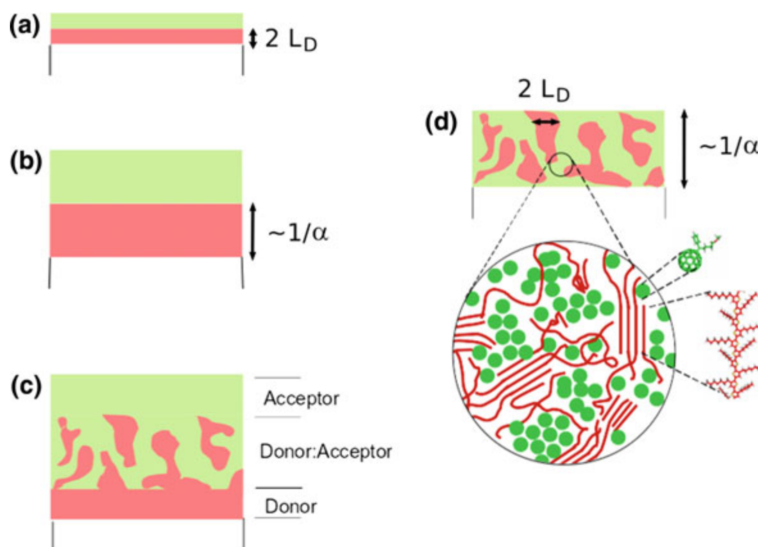

Fig. 15.1 Schematics of the active layer for several device configurations based on donor-acceptor (D-A) junctions. The main absorber is assumed to be the donor (red region). The two relevant lengths for planar junctions are given in (**a**) and (**b**), where L_D represents the exciton diffusion length and α the maximum value of absorption coefficient of the donor. **c** Bulk heterojunction with vertical phase separation region which is detailed in (**d**) assuming a P3HT: PCBM blend

and in favorable cases can be evaluated by SE. As a non-invasive tool, SE can also be applied in situ and in real-time to evaluate film deposition kinetics, to monitor temporal changes in morphology such as those occurring during post-deposition treatments, and even be an in-line monitoring tool to assess organic photovoltaic thin film microstructure during roll-to-roll processing [1, 2].

15.2 Ellipsometric Characterization of Organic Semiconductors

In this section, we focus on the optical properties of single-phase materials that form the active layers of OPVs. The visible range spectra of organic semiconductors generally exhibit several bands that predominantly comprise electronic transitions between π-electron levels and their vibronic sidebands. Measured transitions display lineshapes resulting from a Poisson distribution of the oscillator strength over the series of vibronic replicas, described by a Huang-Rhys parameter. The frequencies of vibrations that couple to electronic states are usually high, giving rise to large total bandwidths. The intermolecular interactions, different conformations or states of order further broaden the spectral features resulting in asymmetric absorption bands and shoulders. Commonly, the analysis of these vibronically structured peaks is kept simple and they are modelled as asymmetrically broadened electronic transitions [3]. Fitting of ellipsometric spectra of films has been already described in Chap. 3 and common strategies for the particular case of polymer semiconductors have been recently reviewed [4]. Here, we describe results obtained in different organic semiconductor materials. We consider first single crystal molecular semiconductors, as useful model substances. Then, we turn to thin films which are obtained using two main methodologies: thermal evaporation and solution processing. In all two cases the processing conditions or choice of the substrates have a large influence on the resulting microstructure, impacting the corresponding optical properties. Typically, molecules with low molecular weight are insoluble but relatively ordered films can be obtained by vacuum evaporation in favorable conditions. Crystal polymorphism is, however, an issue to be dealt with. For high molecular weights, typically polymeric chains, solution processing methods are employed and the resulting films are as a rule of thumb more disordered. Therefore, structural aspects acquire high importance when characterizing organic films for OPVs.

15.2.1 Single Crystals

The study of single crystal molecular materials is interesting from two perspectives. Firstly, it offers access to unique fundamental phenomena in solid state optical

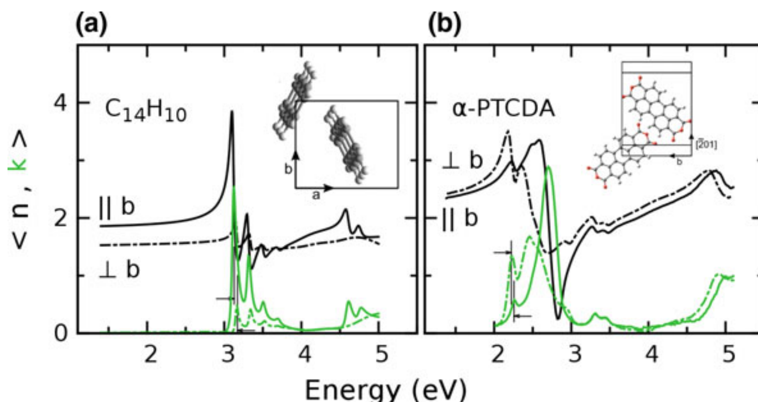

Fig. 15.2 Ellipsometric spectra of **a** Anthracene (001) and **b** α-PTCDA (102) single crystal cleaved surfaces given as pseudo-values <*n*> and <*k*> . The unit cells projected on the measured planes are given as insets. In both cases, the monoclinic b axis is on the plane and the unit cells contain two inequivalent molecules, giving rise to Davydov splittings. The latter are indicated on the lower excitonic peaks by vertical lines and arrows

properties. Secondly, it provides helpful references to understand the optical properties of other organic semiconductors more common to OPV application. The main objective in single crystal ellipsometry is to determine the dielectric tensor. In the case of molecular single crystals this objective has been hampered by the lack of appropriate single crystals as well as by the difficulty of reliably determining the dielectric tensor of low symmetry crystals. Some OPV relevant single crystalline materials have been investigated using ellipsometry including for instance tetracene [5], pentacene [6], and fullerite (C_{60}) [7]. The C_{60} crystal is cubic at room temperature and therefore optically isotropic. The rest of crystals are anisotropic, crystallize usually in monoclinic or triclinic systems and the dielectric tensor cannot be diagonalized in a fixed coordinate axes set [8]. Exact treatments taking into account all degrees of freedom of the dielectric tensor allowed by symmetry have been applied in part of the spectrum to two prototypical organic semiconductors which are model compounds for organic optoelectronics: Anthracene and the perylene derivative PTCDA (perylene tetracarboxylic dianhydride). Both crystallize in monoclinic systems. Historically, the photovoltaic effect in organic semiconductors was first measured in anthracene. However, it is not currently used for OPV because of its high band gap, which is partly due to rather weak intermolecular interactions in the crystal leading to optical spectra of strong molecular character, as shown in Fig. 15.2. In spite of this, the crystalline molecular arrangement in anthracene, with a monoclinic angle of 124.7°, has a large impact into its dielectric tensor components. In particular, the phenomena of dispersion of principal axes of the dielectric tensor and non-coincidence for axes of the real and imaginary part of the tensor are well marked in anthracene [9]. The intermolecular interactions are stronger in PTCDA, for which the band character of the electronic structure is rather

extended. The availability of detailed ellipsometric studies of single crystal PTCDA allowed testing refined theories of electronic structure of this class of semiconductors [10]. The monoclinic angle in PTCDA is 98.8°, close to orthogonal, but nevertheless the low symmetry manifests in the dielectric tensor [11]. In both mentioned examples the unit cells contain two molecules and the lowest singlet excitons display similar Davydov splittings (cf. Sect. 4.5.2) of the order of 40 meV. The observation of these fine splittings is considered a signature of crystalline perfection.

15.2.2 Vacuum Evaporated Films

The active layers in early OPV designs were composed by low molecular weight organic materials, i.e., small molecules or pigments. The initially studied structures were similar to inorganic devices, with planar heterojunctions deposited by thermal evaporation. The active films of these OPVs were usually combinations of metallo-phthalocyanines (MPc) with M = Cu, Zn acting as donor materials and perylene derivatives such as PTCBI (perylene tetracarboxylic bisbenzimidazole) and PTCDA acting as acceptors. An immediate evolution was to implement fullerenes C_{60} and later on C_{70} as acceptors since their spherical shape is advantageous to produce suitable blends with the mostly planar MPc molecules [12]. Hence, fullerenes remain the most chosen acceptors for bulk heterojunction (BHJ) devices despite their relatively limited spectral overlap with the solar spectrum. In the context of BHJs, the field of OPV is dominated by solution processed polymeric films (see Sect. 15.2.3). However, the more precise control both in molecule synthesis and purification, film morphology, and reproducibility in device fabrication offered by vacuum deposited small molecules maintains a sustained research activity in the field. Improvements in performance are seeked in multilayer architectures with multiple heterojunctions and tandem configurations. The increased complexity and cost of the multilayers should be balanced by a higher achievable efficiency. These systems are also regarded as models to obtain a fundamental understanding of the efficiency limiting mechanisms in OPVs. Compared to solution processing, upscaling can be more difficult for thermally evaporated systems needing vacuum. Roll-to-roll compatible vacuum technologies do, however, exist.

Ellipsometric characterization plays a central role in the development of new materials and improved structures, helping to evaluate both the spectral match and the film morphology, i.e., molecular orientation in films, polymorphism and interdiffusion between layers. The reference systems are MPc/fullerene combinations. Thus, research efforts to improve the overall spectral overlap with the solar spectrum are aimed to examine new donors as well as new acceptors to combine

with fullerenes or to substitute them. In addition, optical anisotropy must be evaluated [13] to optimize in-plane absorption [14]. Even if the symmetry of single crystals is monoclinic or triclinic, films always display some disorder and the effective symmetry is at most orthorhombic [4] but normally is tetragonal. Hence, in most cases, only two components fully describe the uniaxial optical response of films with the most usual situation of the optic axis perpendicular to the film surface. Many donors other than MPcs have been considered including diindenoperylene (DIP) [13], squaraines [15], as well as more complicated molecules designed with different moieties to tailor an improved performance [16]. Comparatively, less non-fullerene small molecule acceptors are capable of providing improved efficiencies. Among others, perfluorinated analogs of phthalocyanines [17] and subPcs [18] have been considered because fluorine acts as electron-withdrawing group and reduces the HOMO level of the molecules which become effective acceptors whereas the spectral match remains quite suitable. Figure 15.3 shows the anisotropic optical functions of perfluorinated CuPc films. Different polymorphs result from deposition at different substrate temperatures: films deposited on unheated substrates display a spectrum similar to that of CuPc whereas films deposited on heated substrates show a strong redshifted exciton. Spectroscopic details can be related to the local arrangements of neighboring molecules. In all known CuPc polymorphs the molecular stacks are rather eclipsed forming H-aggregates. Such a redshifted exciton is the signature of staggered molecular stacks or J-aggregates, as observed in bulk $F_{16}CuPc$. Interestingly, the concepts of H- and J-aggregation have been extended to respectively describe interchain and intrachain coupling in conjugated polymers [19].

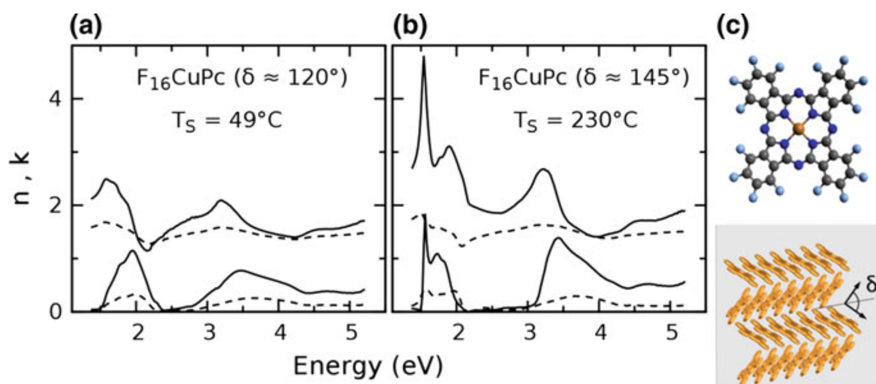

Fig. 15.3 Optical functions of two films of $F_{16}CuPc$ deposited at different substrate temperatures. The observed effective optical anisotropy was uniaxial. Solid (dashed) lines give the ordinary (extraordinary) optical component obtained by point-by-point fitting. In **a** the substrate was not directly heated, in **b** it was kept at 230 °C. **c** Schemes of the molecular structure and of the film arrangement, where different crystal polymorphs are given by the herringbone angle δ

15.2.3 Solution Processed Films

As mentioned above, most organic films for OPVs are deposited from solution because this alternative offers many advantages, including low cost, high flexibility, low thermal budget and up-scalability. Different techniques such as spin coating, blade coating, inkjet printing and screen printing are often used to deposit conjugated polymers and soluble versions of small molecules. In particular the fullerene derivatives PCBM (Phenyl-C(60,70)-butyric acid methyl ester) depicted in Fig. 15.4 along with some usual donor polymers.

The optical properties of polymer films can be quite complex. In addition to the basic molecular nature of the polymer, the particular conformation is decisive to determine the effective optical properties of the film, given by both the spectral features (resulting from the electronic density of states) and the anisotropy (resulting from orientation). Even in a single-component film, a multi-phase morphology can occur. Because of the abundant morphological variations in polymers, it is pertinent to apply a physical parameterization of the dielectric function that allows describing structural variations and transformations by varying the model parameters. Systematic comparisons of the fitting quality of different dispersion models to the ellipsometry data for films of conjugated polymers coincide in concluding that asymmetric lineshapes are the most suited. The case of P3HT as the most important polymer in the context of OPV is illustrative. Arwin and Jansson [20] found that the best description of its optical properties was given by modified Lorentzian resonances which consist in adding a phase to a Lorentzian oscillator. This is a phenomenological approximation to account for asymmetric lineshapes that arise from the interacting electrons and local vibrational modes subjected to inhomogeneous broadening. In addition, the excitonic model is able to describe the

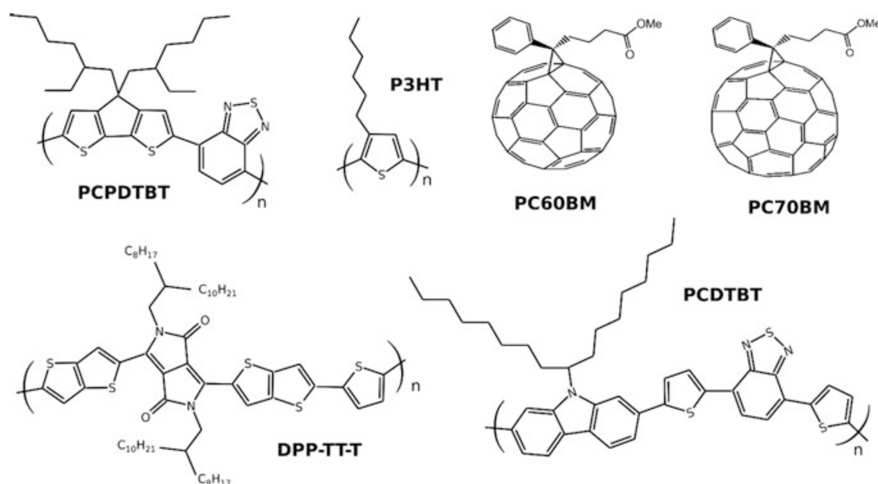

Fig. 15.4 Molecular structures of typical solution-processed OPV materials

expected underlying physics. However, the full spatial localisation represented by excitons might be incomplete to describe the electronic wavefunction of highly crystalline conjugated polymers such as regioregular P3HT, with possible delocalization in up to two dimensions [21]. To account for different dimensionality, the general standard critical point (SCP) lineshapes described in Chaps. 4 and 5 are the natural extension. This model was shown to be superior to other analytical representations of the dielectric function of polymeric thin films [3]. It was shown that analysis of ellipsometric measurements using the SCP model gave results consistent with the anticipated physics: The electronic wavefunctions for highly crystalline films or containing chains with planar conformations displayed 1D/2D delocalization [3] in contrast to localized excitons for amorphous polymeric films. Zhokhavets and co-workers [22] also employed a 1D density of states to describe anisotropic spin-coated thin films of poly(3-octylthiophene) (P3OT). From this model, they obtained a value of around 0.6 eV for the exciton binding energy (E_b), in fairly good agreement with E_b values obtained with other techniques. Gurau and co-workers [23] conducted a combined multi-technique study of the anisotropy of P3HT and P3OT films and used SE to correlate the spectral changes and degree of order in the films. They analyzed their data in terms of critical points using derivative spectra and tried to correlate the fine structure observed in the spectra with the local order in terms of Franck-Condon progressions. Other descriptions of the dielectric function of P3HT include explicit modelling of this fine structure by a Huang-Rhys vibronic envelope [24]. However, it has been pointed out that the Huang-Rhys description is probably too simple, not adequate to provide a satisfactory explanation of the evolution of the spectrum with local order [23]. A more complex theory has been recently developed for P3HT based on weakly coupled

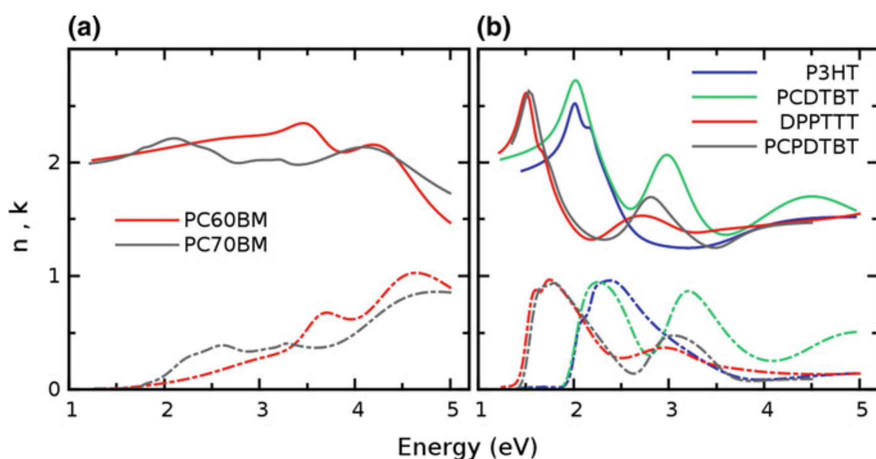

Fig. 15.5 Refractive index n and extinction coefficient k for several solution processed materials. **a** Acceptors, **b** donors

H-aggregates. This alternative model allows to extract relevant parameters such as an interchain bandwidth and intrachain order (conjugation length) from the polymer absorbance [25].

As shown in Fig. 15.5 for some usual donors and acceptors, the refractive index of thin film solution processed organic semiconductor ranges between 1.7 and 2.1, while typical maximum extinction coefficients reach values about $k = 1$. We note that solution processed polymers may exhibit preferential molecular orientation leading to uniaxial anisotropy. The in-plane index (shown in Fig. 15.5b) is then higher than the out-of-plane (extraordinary) index [26].

15.3 Device Architectures

Organic photovoltaics belong to the third generation solar cell class in which a thin film of a highly absorbing direct semiconductor is sandwiched between two metals with different work functions, one of which is transparent to allow light go through. Given the aforementioned characteristics of free carrier generation in organic semiconductors, the active layer can be either a bilayer (p-n heterojunction), a bulk-heterojunction (BHJ), or a p-i-n like structure formed by embedding a mixed layer in between two layers of the pure components. These architectures are depicted in Fig. 15.6a, b and c, respectively. While BHJs are the preferred choice for solution processed cells, active layers comprising several layers with different degrees of mixing can be obtained by thermal evaporation.

Historically, in the most conventional device architecture, often called “normal” or “standard” geometry, light reaches the active layer through the anode. In the so-called “inverted” geometry depicted in Fig. 15.6d, light reaches the active layer through the cathode. The anode and cathode are defined by the choice of electrodes, but also, importantly, by introducing electron and hole blocking layers,

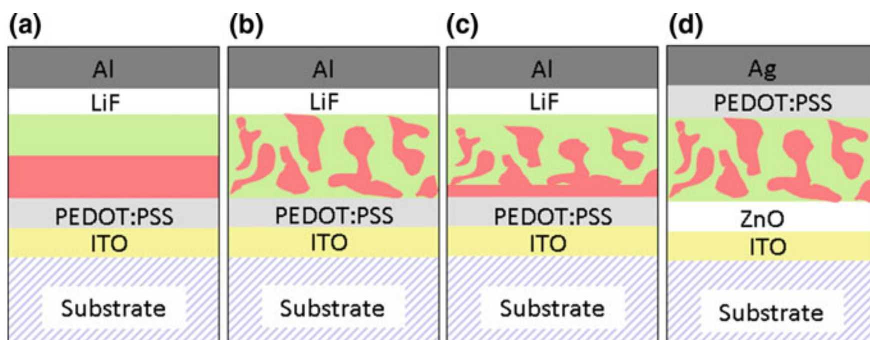

Fig. 15.6 Schematic representation of the most common device architectures. **a**–**c** display standard structures in which the active materials are combined in different ways, namely **a** bilayer planar junction, **b** bulk heterojunction, and **c** combination of both as a bilayer with a wide intermixed zone. **d** Inverted structure with bulk heterojunction

respectively. The conductive polymer PEDOT:PSS is typically used as electron blocking layer which besides shifting the work function of the corresponding metal electrode, helps planarizing the surface of the contact for the correct subsequent deposition of the active layer. In the inverted structure, surfactants are used in order for the water based dispersion of PEDOT:PSS to be properly deposited on top of the typically hydrophobic active layer. Alternatively, evaporated or solution processed MoO_3 has also been used as electron blocking layer. Typical hole blocking layers include calcium, LiF, ZnO and TiOx. The latter two can be deposited using physical methods, but also from precursor solutions using wet deposition methods (from spin coating to roll-to-roll compatible slot dye coating).

In the context of device architectures, ellipsometry provides information at different levels. First, it helps to assess the structure itself, giving non-destructive estimates of thicknesses for the different layers of the stack. It also enables the monitoring of morphological aspects, such as buried interfaces, intermixing between different layers, or the appearance of phase separation between components. Finally, ellipsometry provides the required optical parameters used as input in the modeling and optimization of organic photovoltaics.

15.3.1 Vertical Structures

Within the described device architectures, vertical structure arises not only by design, as in advanced tandem organic photovoltaic cells [27] containing complex engineered multilayer stacks, but also unintentionally, in form of surface roughness, interphase boundaries and segregation within one layer, and intermixing at the interface between adjacent layers. The design of optimal devices for photovoltaic applications requires an accurate control of both the dielectric function and vertical structure because effects such as anisotropy and optical cavity interference can be dominant for light absorption in solar cells [28, 29]. Rigorous modelling is crucial to improve the understanding of the internal photon conversion efficiency and allows design improvements [30]. Although some structural features like interphase mixing and segregation may be not too important to alter photonic behavior, their impact on electrical performance is significant, as they strongly affect injection and recombination properties [31].

Evaluation of vertical structures relies on structural models built from multilayers containing effective medium approximations (EMAs) to account for the mixed layers, as described in (3.9). Typical mixed layers include surface roughness with sub-wavelength features, composed by the underlying material and void. This approximation gives good results in many situations, particularly if the rough overlayer is thinner than about 10% of the total film thickness. For thicker rough overlayers, conventional ellipsometric results may still be reliable with more complex analysis protocols and be well correlated to structural techniques [32, 33]. Optical contrast is required for a successful evaluation of depth profiles by SE. For conjugated polymers, the contrast in the spectral transparency region is usually poor

but the technique can take advantage of absorption contrast in films of the order of the absorption depth. Typical suitable thicknesses are in the range of 0.1 to 0.01 times the incident wavelength. In all cases, the availability of accurate reference dielectric functions eases the interpretation of the data. The study of photovoltaic devices can be simplified by examining bilayer films as model systems. Organic bilayers are often partially miscible and interlayers are generally present. Experiments that require a sharp interface can benefit from a critical validation of film structure by ellipsometry, for instance in order to determine the exciton diffusion length [34].

Bilayers obtained by solution processing commonly have a diffuse interface because it is problematic to find orthogonal (incompatible) solvents for depositing layers sequentially. The first deposited layer may partially (or totally) dissolve when a second layer is put on top resulting in a mixed interfacial layer. Interfacial mixing can also appear to some extent for bilayers formed by thermally evaporating the top layer or after an annealing step. Ferenczi et al. explored interdiffusion for bilayers composed of PCBM and P3HT [35]. A solvent-free stamp transfer process was used to deposit the top PCBM layer so that the as-prepared bilayers showed sharp interfaces. Subsequent thermal annealing caused the formation of a broad mixed layer capped by a fullerene and a P3HT single component layers. The resulting triple stack showed much better performance as a photodiode than the as-prepared bilayers. Analysis of the ellipsometric data evidenced the intermixing and the obtained vertical profiles allowed to model the photodiode spectral response satisfactorily [35].

15.3.2 Bulk Heterojunctions

The protocol to produce the technologically relevant BHJ structure, see Figs. 15.6b, d, is to form a mixed layer by spin coating from a solution already containing two materials. In essence, the optical properties of the resulting blend film can be represented using an EMA such as the Bruggeman model of (3.9). In most cases, the assumptions inherent to an EMA model are justifiable. These comprise the situation that the components are well mixed (on a scale below 0.1 the wavelength) and that any additional optical excitations such as interface charge transfer have negligible spectral weight [36]. Hence, these models work well as an approximation and are very useful to deal with structural parameters. However, some basic suppositions of the EMA models might be invalid in some cases [37, 38]. For instance, the mixing process may lead to domains of the pristine materials with a different microstructure than that of the single material films used to obtain reference dielectric functions. In particular, the amount of anisotropy or the extent of crystallinity have been shown to vary and are also dependent on the processing conditions. For instance, the n and k values for P3HT:PCBM blends strongly depend on annealing conditions and weight fraction, as shown in Fig. 15.7. In addition, since most organic materials are somewhat miscible [39], for all practical purposes a ternary system is formed, made up of nearly pure

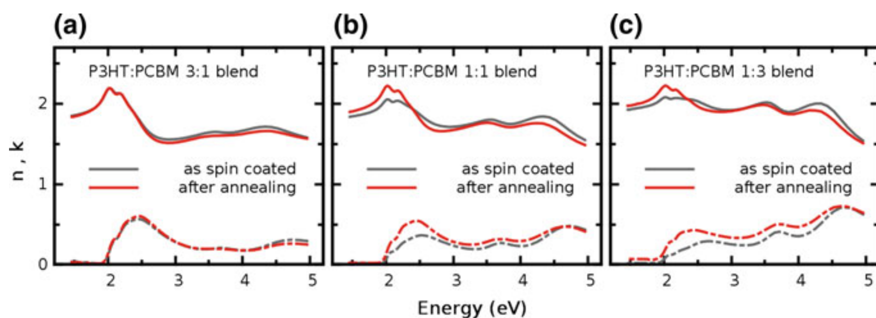

Fig. 15.7 Refractive index *n* and extinction coefficient *k* for P3HT:PCBM blends spin coated at 4000 rpm before and after 15 min of annealing at 140 °C. Larger changes for larger PCBM contents upon annealing are related in this case to the variation of depth profile and degree of crystallinity of the polymer

domains of each material plus a fine intermixed blend of both. More refined models including those structural modifications such as effective ternary mixing [40, 41] or anisotropic inclusions [42] must be used or further developed in order to find out the dielectric function of the blends from those of the constituent materials. As a matter of fact, the most accurate alternative is, probably, to consider the blend film as a different material system, comparable to an alloy system, and determine its particular dielectric function as though it was a new compound [28, 43]. A helpful option for that is to build flexible material functions, like are frequently used when dealing with alloys [38], based upon data libraries that gather diverse ways of processing reference films. In this way, satisfactory models of both the morphology and the anisotropy should be attainable and allow to deduce detailed profiles [43]. Having said that, the heterogeneity of such films can also yield a spatial variation of the dielectric function, producing averaged results that depend to some extent on the measurement spot loci and size.

In spite of not always being the most precise description, using the dielectric function of the pristine components to model blend materials is a rather reliable procedure to investigate structural homogeneity. For example, the vertical phase separation in blends of P3HT and PCBM has been successfully evaluated using VASE [40, 44, 45], and the same for other photovoltaic systems such as APFO3:PCBM [38] and PCPDTBT:PC70BM [46]. For this purpose, the blend films were analyzed by decomposing the profiles in several sublayers with their corresponding dielectric functions deduced from an EMA model allowing for different compositions of the two materials. Appealingly, as-spin-coated films were seen to exhibit an intrinsic amount of vertical phase separation, and it was revealed that this segregation increased when exposing the film to temperature or solvent vapor [44]. Moreover, ellipsometry was useful to explore the dependence of the specific depth profile on a diversity of conditions related to the hydrophilicity of the substrate [43, 44], variable processing history [44], the crystallinity of the polymer [47],

and the composition ratio of the blend [38, 45], as illustrated in Fig. 15.7. Conducting PEDOT:PSS layers with a component of un-complexed PSS were also found to exhibit vertical concentration profiles that could be characterized using ellipsometry [48].

15.3.3 Full Devices

Since ellipsometry is highly sensitive to film thickness and layer morphology, this technique is especially suited as a non invasive tool to monitor device quality. Figure 15.8 shows an example of the use of ellipsometry to assess the homogeneity of an organic photovoltaic module in inverted geometry, see Fig. 15.6d, as it was being built. Ellipsometry was first measured at several loci over a 4 cm^2 sample after the deposition of the blocking layer (glass/ITO/ZnO), then after the deposition of the active layer (P3HT:PCBM) and finally after the deposition of the hole conducting layer (modified PEDOT:PSS). The data clearly show that the last layer is not homogeneous and it should be reformulated to improve the wettability of PEDOT:PSS on top of the hydrophobic active layer.

A complete device often has a metallic electrode on top of the PEDOT:PSS layer deposited by thermal evaporation or screen printing. Evaluation of the full device requires, then, measuring through the glass. In this case, the available spectral range is smaller (due to the UV absorption of a ca 1 mm thick glass substrate). Flexible samples are typically supported on PET substrates. These are highly anisotropic [49], which complicates the analysis of the ellipsometric angles.

Besides quality control, ellipsometry is regularly used to obtain the input parameters that are needed in order to model and optimize the organic photovoltaic devices. Contrary to other photovoltaic technologies, charge transport in organic

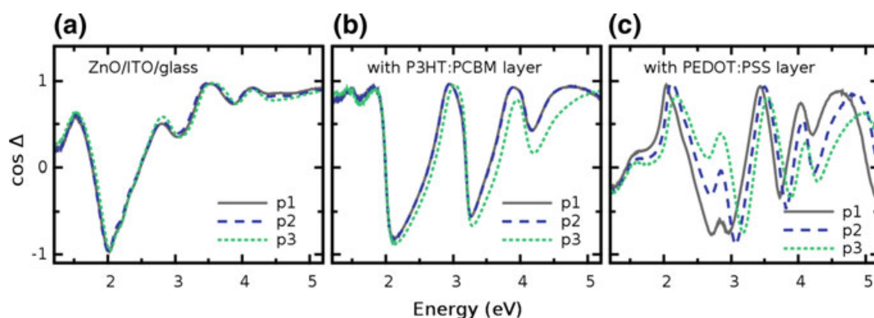

Fig. 15.8 Raw ellipsometry spectra (cos *Δ*) of an organic solar cell structure with inverted geometry as represented in Fig. 15.6d. ITO was coated by sputtering and the other three layers from solution by knife coating. Measurements on three different points across the sample at various stages: **a** ZnO/ITO/glass sample, **b** P3HT:PCBM/ZnO/ITO/glass sample, and **c** PEDOT:PSS/P3HT:PCBM/ZnO/ITO/glass sample

semiconductors is typically poor, with mobilities several orders of magnitude lower than that of amorphous silicon. This imposes a limitation with respect to how thick the active layer can be: thicker films absorb more light, but charges generated too far from the electrodes may recombine before they can be collected. The optimum film thicknesses for the multilayer stack will then be related to the absorption coefficient of the materials, electron and hole mobilities of the active layer and the degree of (unintentional) doping [50].

In this context, ellipsometry can provide the complex refractive index for each of the relevant materials. With this input information, the electric field distribution within the active layer can be determined, and thus the profile of photogenerated excitons [29]. An electric model is then used to estimate the charge collection depending on the recombination rates and transport properties of the system. In this way, optimum film thicknesses can be determined theoretically. In most cases, the optimum thickness for the active layer corresponds to that of the first optical interference maximum for low mobility semiconductors (70–100 nm), and to the second interference maximum for materials whose transport is better (ca 225 nm) [50–52]. This type of modeling can be used to explore also the suitability of this technology for specific applications, such as greenhouses [53] and color tunable photovoltaics for building integrated generation [54].

15.4 Monitoring Organic Solar Cells

Ellipsometry is a non invasive and relatively fast technique (measurement time ≤ 1 s), and thus it is useful to monitor changes in film properties via in situ experiments. Two main types of information can be accessed, either dynamic or thermodynamic. Examples of the former include the study of film formation from solution or the structural changes induced by post-deposition treatments. Thermodynamic aspects such as miscibility limit, phase transition temperatures or even full phase diagrams have also been investigated.

15.4.1 Monitoring Thermal Stability

In the context of bulk heterojunction solar cells, the glass transition is one of the key parameters to understand the thermal stability of the cell. If the operational temperature (up to 85 °C) is higher than the glass transition temperature, the morphology of the blend, and thus performance, will change with operation time, which is unacceptable for most applications. Providing access to the glass transition of the material in thin film form is, therefore, a very useful contribution from ellipsometry to this field. This is especially so if we consider the large number of reports that show that phase transition temperatures of geometrically confined polymers differ from the bulk values obtained by Differential Scanning Calorimetry (DSC) [55–57].

Whereas some of the studies require analysis of the full set of ellipsometric data as a function of time, it has been pointed out that for small variations in morphology or thickness (such as those typically occurring while thermally annealing), the ellipsometric angles themselves depend approximately linearly with film thickness [4]. This observation opens up the opportunity of retrieving useful pieces of information directly from the raw ellipsometry data. This includes the determination of the glass transition temperature of thin films using the kink that appears in the evolution of ψ with temperature, which reflects the different coefficients of thermal expansion before and after the glass transition [39].

Besides the glass transition temperature, in-situ ellipsometry can be employed to characterize thoroughly the phase evolution in quasi-isothermal experiments, including the determination of crystallization and liquid crystalline temperatures. Some examples in the literature include PFO [55], F8BT [55], P3HT [58], APFO3 [56], APFO9 [56], pBTTT [59], and PCDTBT [60]. The full phase diagram for photovoltaic blends consisting of the low band gap polymer APFO3 and fullerene (PCBM) were deduced using ellipsometry in combination with polarized microscopy [39]. For this, the temperature dependence of the ellipsometric angles was recorded for several polymer: fullerene compositions. The phase diagram was then constructed and revealed a eutectic behavior including a lyotropic phase. This study provided information on the miscibility limit of both compounds, and demonstrated that the miscibility limit depends on the molecular weight of the polymer. The authors correlated the high glass transition temperatures with the high thermal stability of the corresponding devices and also the miscibility limit with the recombination probability for the blends.

15.4.2 Monitoring Morphology Evolution

As it has been mentioned throughout this chapter, the way in which donor and acceptor molecules pack in the solid state to form the blend film is a critical aspect for the operation of organic photovoltaics. The two materials should form a finely interpenetrated network to allow charge generation and extraction. Optimum domain sizes are around 10–20 nm, furthermore, the domain purity is crucial to avoid charge recombination leading to performance loss. Being so critical, a myriad of methods to control the film morphology have emerged. These include control of the drying kinetics during solution deposition via solvent mixtures, use of solvent saturated atmospheres, varying stage or solution temperature, or the use of additives. Alternatively, the structure of some blend films can be modified after deposition using treatments such as thermal or vapor annealing.

The time scales of deposition and post deposition treatments are very different, being a few seconds for the former, and several minutes for the later. In both cases, in situ ellipsometry can offer insights into morphology evolution, as exemplified in Fig. 15.9. This is because the optical features associated to isolated molecules, molecular aggregates and crystalline domains are all different.

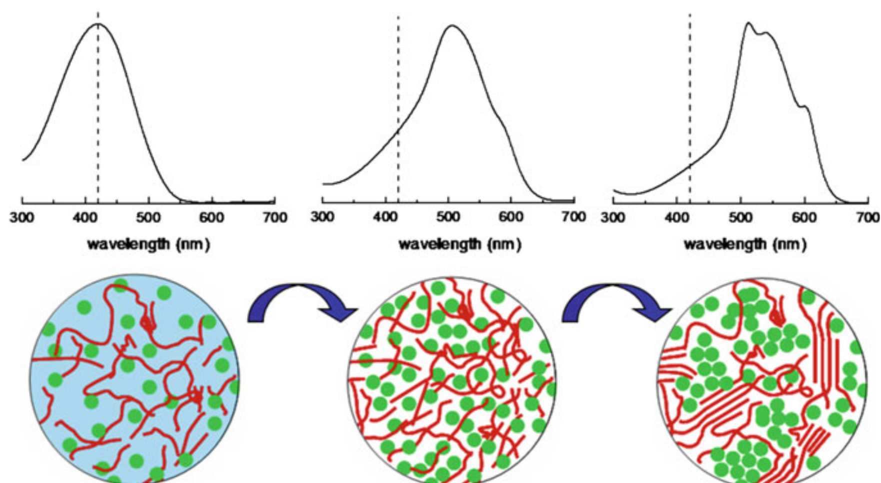

Fig. 15.9 Schematic representation of the evolution of a polymer-fullerene blend upon thermal annealing. The spectra illustrate qualitative changes in extinction coefficient curves that may help to monitor morphology changes in real time

For the workhorse bulk heterojunction material system P3HT:PCBM, ellipsometric studies have been carried out by exposing the films to saturated atmosphere of solvent vapor [44]. The ellipsometric data exhibited variations due to changes in oscillator strength and density, which were used to deduce the onset of polymer crystallization. Subsequent lateral and vertical diffusion of fullerene molecules [44, 45, 61] yielded finally a blend structure offering superior solar cell performance. Similarly, Wang et al. [62] have ellipsometrically monitored the evolution of these blends upon thermal annealing. Three distinct regimes were identified. First, the solvent trapped within the film evaporated, followed by the polymer crystallization and finally, the phase separation of the two components.

The bilayer geometry constitutes a useful system to study microstructure evolution. In this case, two layers of the pure constituents are deposited sequentially, typically first the polymer and then the fullerene from an orthogonal solvent or thermally evaporated on top of the polymer film. This system is valuable because the starting point is very well defined (pure vertical domains of each component) and then upon application of an external stimulus, such as temperature, the morphology evolves. The kinetics of molecular diffusion, as well as the miscibility limit have been studied by measuring ellipsometry on bilayers [35, 63]. In a study comprising two polymers and four different fullerenes, ellipsometry enabled to understand how mixing only occurred above the glass transition of the polymer, and was consistent with swelling of the polymer by the fullerene [63]. For absorbing materials, the limitation here is that films ought to be thin enough to enable optical access to the bottom layer. The use of ellipsometry to investigate polymer film swelling by penetrants has been recently reviewed by Ogieglo and colleagues [64].

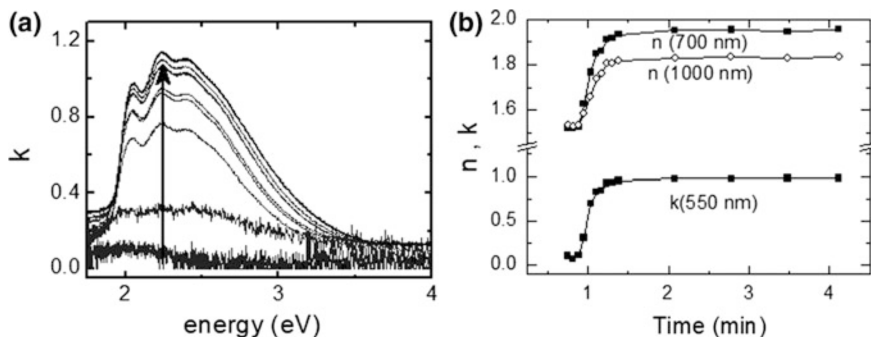

Fig. 15.10 Dependence of the optical constants of a P3HT film upon drying. **a** Spectral changes of the extinction coefficient. The arrow marks the wavelength of maximum absorption, 550 nm. **b** Time evolution of *n* and *k* at selected wavelengths

The characterization of thin film changes during fast deposition processes is yet more challenging due to the very wide timescales (from milliseconds to minutes) and the fast changing film properties, starting from the few microns thick wet film down to the 100 nm thick dried film. Other deposition methods have also been explored, such as dip coating [65] (see Fig. 15.10) and knife coating [66, 67]. It is worth noting that high speed photometry was also used to monitor the spin-coating process of non-conjugated polymer blends [68]. Polarized photometry has also allowed to monitor the layer-by-layer growth of small molecule films [69].

The drying kinetics of a knife-coated P3HT:PCBM film was explored by combining in situ ellipsometry and X-ray measurements [66]. This encouraging report revealed different steps in film formation. In the wet film, the polymer chains start to crystallize by way of heterogeneous nucleation when the concentration of polymer surpasses 50%. Due to the remaining solvent, a self-annealing step takes place. This evolution is monitored by following the ellipsometrically deduced film thickness and extinction coefficients. As a first approximation, the changes in thickness and refractive index during annealing or in the last stages of film formation can be rationalized in terms of variations in film density (ρ) and polarizability (μ) [61, 65, 70]. For a given system with an accessible transparent spectral window, the variation in refractive index far from the absorption edge can be approximated as:

$$\frac{n_t^2 - 1}{n_0^2 - 1} \cong \frac{\mu_t \rho_t}{\mu_0 \rho_0} \tag{15.1}$$

Equation (15.1) has been used to correlate the values of density and polarizability with the length of the polymer side chains in different films [71], and to compare the values before and after thermal annealing [44, 71] as well as during deposition [65]. For the case of post-deposition treatments, the film mass at two given times has to be conserved, and then the previous equation can be rewritten as:

$$\frac{n_t^2 - 1}{n_{t=0}^2 - 1} \cdot \frac{d_t}{d_{t=0}} \cong \frac{\mu_t}{\mu_{t=0}} \tag{15.2}$$

By analyzing the time dependent ellipsometry data, the refractive index and thickness can be found independently. Then, this relationship allows to estimate the polarizability variations occurring during a post deposition treatment and correlate them to the morphology of the film. These variations may be originated, for instance, by the evolution of the average degree of molecular orientation upon annealing [65].

Clearly, the development of in-situ ellipsometry for the characterization of organic solar cells films during deposition or annealing is at an early stage, so far. The very reassuring already reported results, however, encourage further investigations to cast light into such topics as the effect of additives, molecular weight, or crystallization tendency.

15.4.3 Monitoring Fabrication

Besides the great sensitivity to small thickness and/or dielectric function changes, the new generation of commercially available ellipsometers equipped with CCD detection are also very fast, with acquisition times around 50 ms. In situ characterization of layers and stacks *in-line* during roll-to-roll processing has, therefore, become a reality.

Indeed, two groups have already built stand alone in-line ellipsometers into lab scale roll-to-roll systems devoted to the fabrication of organic photovoltaics [1, 2]. The advancements introduced by one such system have been protected via patent filing [72]. Very fast data acquisition, processing and analysis are key features of these pieces of equipment. In order to have access to the full width of the rolling web, the optics of the ellipsometer are scanned (translated) perpendicularly to the roll to roll moving direction. Alternatively, an expanded beam geometry coupled to a 2D detector with no moving parts has also been proposed for in-line quality monitoring during roll-to-roll manufacturing [73].

15.4.4 Monitoring Degradation

Stability is one of the key challenges to overcome before organic photovoltaics can reach the market. Besides the aforementioned thermal stability, photodegradation and chemical stability need to be addressed. Interestingly, most common degradation pathways affecting the active layer in OPVs, such as chain scission or shortening, conjugation breaking via defects, etc., result in a reduction of conjugation length, yielding blue shifted absorption and loss in vibronic sideband

spectral resolution. The absorption spectrum, therefore, reflects the degree of degradation of a given material. Note, cautiously, that the electronic processes are affected by degradation much more strongly via trap formation, in such a way that an absorption loss of less than 3% might be associated to the same degree of degradation than a solar cell efficiency loss of 80%.

In a pioneering work on photooxidation of polythiophenes from 1994, Arwin and Jansson proposed the ex situ ellipsometric determination of the absorption coefficient as an easy magnitude measurement to detect degradation [20]. They observed how photodegradation resulted in a loss of oscillator strength, and a broadening of absorption. Similar studies have been conducted on other polymers, such as MHPPV [74] and small molecules, such as Alq3 [75]. The structural stability of polymer/fullerene blends has also been assessed via ellipsometry [76]. These authors find that the vertical composition profile evolves over time, with fullerene molecules accumulating at the surface. This has a clear effect on the corresponding solar cells as a fullerene rich interface can act as an electron conducting layer.

There is plenty of room for further studies of the stability in this type of systems. In particular, in situ real time investigation of the degradation of photovoltaic systems under controlled oxygen, humidity and temperature conditions might prove very useful. In the case of lead halide perovskite based hybrid photovoltaics, ellipsometry has been used in situ while exposing the material to water vapor [77] revealing a reversible hydration process. Similar studies applied to organic photovoltaics will help to increase our understanding of the degradation pathways and how to cut them short.

15.5 Hybrid Approaches

For the sake of completeness, we mention briefly the use of ellipsometry for characterization of hybrid active layers in solar cells. Current organic-inorganic mixed approaches evolved from the concept of dye-sensitized solar cells. These electrochemical or Grätzel cells are composed by a mesoporous titania matrix with a thin layer of dye attached to the surface and embedded in an electrolyte solution. The thickness and porosity of the mesoporous TiO_2 have a relevant effect on the cell performance and can be characterized by ellipsometry [78]. Evolution of this concept to solid state brings hybrid approaches closer to the concept of bulk heterojunctions, like that represented in Fig. 15.1c where a hole-transporting polymer (frequently spiro-MeOTAD) replaces the electrolyte. In other studies, infiltration of a donor polymer to replace both the dye and the electrolyte has been considered, where the inorganic semiconductor TiO_2 acts as the acceptor. These vertically mixed heterojunctions are efficiently characterized by SE [78] also in this case. Another widely used acceptor is ZnO. Optical properties of blends between ZnO and several polymers such as P3HT have been investigated by SE and have been successfully correlated to the color of full devices [79]. Effective medium

approximations have been applied to study structural aspects in polymer-quantum dot blend films [80] which are also used in hybrid solar cell concepts. Last but not least, lead halide perovskite-based solar cells evolved from the same hybrid concept. Chapter 16 is devoted to this hybrid kind of solar cells due to the current enormous interest and intense activity in this field of research.

15.6 Summary

In this chapter we have reviewed a representative selection of significant examples regarding the use of spectroscopic ellipsometry for the characterization of organic semiconductors applied to solar cells. Throughout the chapter, we have detailed the particularities of organic semiconductors that ultimately define the device architectures and indicated which aspects can be characterized by ellipsometry both regarding material preparation and device structure. First, we have described the ellipsometric characterization of single-phase materials that form the active layers of OPVs including single crystals and films of small molecules and polymers. We have further outlined the use of ellipsometry for the characterization of device-quality layers such as films with vertical structure, either a single blend layer or sequentially deposited layers. Also, we have pointed out the real time in situ application of ellipsometry to monitor film deposition processes and post-deposition treatments. Finally, we have commented on characterization aspects of organic-inorganic hybrid solar cell materials. In all cases, an accurate knowledge of the dielectric functions of the materials, enabled by the use of ellipsometry, is essential to understand and model the optoelectronic properties of photovoltaic devices. Moreover, advanced ellipsometry can provide fundamental information about the structural configuration of the thin films, along with the phase separation of components, the quality of interfaces, and characteristics of molecular kinetics for the fabrication processes.

Acknowledgements The authors thank Ms. Andrea Pitillas help in the preparation of devices studied in Fig. 15.8 and the Spanish Ministry of Economy and Competitiveness for funding through grants MAT2012-37776, MAT2015-70850-P, and the “Severo Ochoa” Programme for Centres of Excellence in R&D (SEV-2015-0496).

References

1. M.V. Madsen, K.O. Sylvester-Hvid, B. Dastmalchi, K. Hingerl, K. Norrman, T. Tromholt, M. Manceau, D. Angmo, F.C. Krebs, J. Phys. Chem. C **115**, 10817 (2011)
2. S. Logothetidis, D. Georgiou, A. Laskarakis, C. Koidis, N. Kalfagiannis, Sol. Ener. Mater. Sol. Cells **112**, 144 (2013)
3. M. Campoy-Quiles, J. Nelson, D.D.C. Bradley, P.G. Etchegoin, Phys. Rev. B **76**, 235206 (2007)

4. M. Campoy-Quiles, M.I. Alonso, D.D.C. Bradley, L.J. Richter, Adv. Funct. Mater. **24**, 2116 (2014)
5. S. Tavazzi, L. Raimondo, L. Silvestri, P. Spearman, A. Camposeo, M. Polo, D. Pisignano, J. Chem. Phys. **128**, 154709 (2008)
6. D. Faltermeier, B. Gompf, M. Dressel, A.K. Tripathi, J. Pflaum, Phys. Rev. B **74**, 125416 (2006)
7. P. Milani, M. Manfredini, G. Guizzetti, F. Marabelli, M. Patrini, Solid State Commun. **90**, 639 (1994)
8. M.I. Alonso, M. Garriga, Thin Solid Films **455–456**, 124 (2004)
9. O. Arteaga, M. Garriga, M.I. Alonso, unpublished (2017)
10. L. Gisslén, R. Scholz, Phys. Rev. B **80**, 115309 (2009)
11. M.I. Alonso, M. Garriga, J.O. Ossó, F. Schreiber, R. Scholz, Thin Solid Films **571(**Part 3), 420 (2014)
12. C. Schünemann, D. Wynands, L. Wilde, M.P. Hein, S. Pfützner, C. Elschner, K.-J. Eichhorn, K. Leo, M. Riede, Phys. Rev. B **85**, 245314 (2012)
13. U. Heinemeyer, A. Hinderhofer, M.I. Alonso, J.O. Ossó, M. Garriga, M. Kytka, A. Gerlach, F. Schreiber, Phys. Status Solidi A **205**, 927 (2008)
14. C. Schünemann, D. Wynands, K.-J. Eichhorn, M. Stamm, K. Leo, M. Riede, J. Phys. Chem. C **117**, 11600 (2013)
15. G. Chen, D. Yokoyama, H. Sasabe, Z. Hong, Y. Yang, J. Kido, Appl. Phys. Lett. **101**, 083904 (2012)
16. L.-Y. Lin, Y.-H. Chen, Z.-Y. Huang, H.-W. Lin, S.-H. Chou, F. Lin, C.-W. Chen, Y.-H. Liu, K.-T. Wong, J. Am. Chem. Soc. **133**, 15822 (2011)
17. M.I. Alonso, M. Garriga, J.O. Ossó, F. Schreiber, E. Barrena, H. Dosch, J. Chem. Phys. **119**, 6335 (2003)
18. H. Gommans, T. Aernouts, B. Verreet, P. Heremans, A. Medina, C.G. Claessens, T. Torres, Adv. Funct. Mater. **19**, 3435 (2009)
19. F.C. Spano, C. Silva, Annu. Rev. Phys. Chem. **65**, 477 (2014)
20. H. Arwin, R. Jansson, Electrochim. Acta **39**, 211 (1994)
21. R. Osterbacka, C.P. An, X.M. Jiang, Z.V. Vardeny, Science **287**, 839 (2000)
22. U. Zhokhavets, R. Goldhahn, G. Gobsch, W. Schliefke, Synth. Met. **138**, 491 (2003)
23. M.C. Gurau, D.M. Delongchamp, B.M. Vogel, E.K. Lin, D.A. Fischer, S. Sambasivan, L. J. Richter, Langmuir **23**, 834 (2007)
24. A.J. Morfa, T.M. Barnes, A.J. Ferguson, D.H. Levi, G. Rumbles, K.L. Rowlen, J. van de Lagemaat, J. Polym. Sci. B: Polym. Phys. **49**, 186 (2011)
25. J. Clark, J.-F. Chang, F.C. Spano, R.H. Friend, C. Silva, Appl. Phys. Lett. **94**, 163306 (2009)
26. M. Campoy-Quiles, P.G. Etchegoin, D.D.C. Bradley, Phys. Rev. B **72**, 045209 (2005)
27. T. Ameri, G. Dennler, C. Lungenschmied, C.J. Brabec, Energy Environ. Sci. **2**, 347 (2009)
28. N.K. Persson, H. Arwin, O. Inganäs, J. Appl. Phys. **97**, 034503 (2005)
29. L.A.A. Pettersson, L.S. Roman, O. Inganäs, J. Appl. Phys. **86**, 487 (1999)
30. G.F. Burkhard, E.T. Hoke, S.R. Scully, M.D. McGehee, Nano Lett. **9**, 4037 (2009)
31. L.-M. Chen, Z. Hong, G. Li, Y. Yang, Adv. Mater. **21**, 1434 (2009)
32. M. Akagawa, H. Fujiwara, J. Appl. Phys. **110**, 073518 (2011)
33. D. Lehmann, F. Seidel, D.R.T. Zahn, Springerplus **3**, 82 (2014)
34. J.D.A. Lin, O.V. Mikhnenko, J. Chen, Z. Masri, A. Ruseckas, A. Mikhailovsky, R.P. Raab, J. Liu, P.W.M. Blom, M.A. Loi, C.J. Garcia-Cervera, I.D.W. Samuel, T.-Q. Nguyen, Mater. Horiz. **1**, 280 (2014)
35. T.A.M. Ferenczi, J. Nelson, C. Belton, A.M. Ballantyne, M. Campoy-Quiles, F.M. Braun, D. D.C. Bradley, J. Phys. Condens. Matter **20**, 475203 (2008)
36. K. Vandewal, K. Tvingstedt, A. Gadisa, O. Ingänas, J.V. Manca, Nat. Mater. **8**, 904 (2009)
37. U. Zhokhavets, R. Goldhahn, G. Gobsch, M. Al-Ibrahim, H.K. Roth, S. Sensfuss, E. Klemm, D.A.M. Egbe, Thin Solid Films **444**, 215 (2003)
38. M. Campoy-Quiles, C. Müller, M. Garriga, E. Wang, O. Inganäs, M.I. Alonso, Thin Solid Films **571(**Part 3), 371 (2014)

39. C. Müller, J. Bergqvist, K. Vandewal, K. Tvingstedt, A.S. Anselmo, R. Magnusson, M.I. Alonso, E. Moons, H. Arwin, M. Campoy-Quiles, O. Inganäs, J. Mater. Chem. **21**, 10676 (2011)
40. I. Burgues-Ceballos, M. Campoy-Quiles, L. Francesch, P.D. Lacharmoise, J. Polym. Sci. B Polym. Phys. **50**, 1245 (2012)
41. S. Engmann, V. Turkovic, P. Denner, H. Hoppe, G. Gobsch, J. Polym. Sci. B Polym. Phys. **50**, 1363 (2012)
42. S. Engmann, V. Turkovic, G. Gobsch, H. Hoppe, Adv. Ener. Mater. **1**, 684 (2011)
43. D.S. Germack, C.K. Chan, R.J. Kline, D.A. Fischer, D.J. Gundlach, M.F. Toney, L.J. Richter, D.M. DeLongchamp, Macromolecules **43**, 3828 (2010)
44. M. Campoy-Quiles, T. Ferenczi, T. Agostinelli, P.G. Etchegoin, Y. Kim, T.D. Anthopoulos, P.N. Stavrinou, D.D.C. Bradley, J. Nelson, Nat. Mater. **7**, 158 (2008)
45. T. Agostinelli, S. Lilliu, J.G. Labram, M. Campoy-Quiles, M. Hampton, E. Pires, J. Rawle, O. Bikondoa, D.D.C. Bradley, T.D. Anthopoulos, J. Nelson, J.E. Macdonald, Adv. Funct. Mater. **21**, 1701 (2011)
46. A. Guerrero, B. Doerling, T. Ripolles-Sanchis, M. Aghamohammadi, E. Barrena, M. Campoy-Quiles, G. Garcia-Belmonte, ACS Nano **7**, 4637 (2013)
47. M. Campoy-Quiles, V. Randon, M. Mróz, M. Jarzaguet, M. Garriga, J. Cabanillas-González, Org. Photonics Photovolt. **1**, 11 (2013)
48. T. Ino, T. Hayashi, T. Fukuda, K. Ueno, H. Shirai, Phys. Status Solidi C **8**, 3025 (2011)
49. S. Logothetidis, Polymeric substrates and encapsulation for flexible electronics: bonding structure, surface modification and functional nanolayer growth. Rev. Adv. Mater. Sci. **10**, 387 (2005)
50. F. Deledalle, T. Kirchartz, M.S. Vezie, M. Campoy-Quiles, P. Shakya Tuladhar, J. Nelson, J. R. Durrant, Phys. Rev. X **5**, 011032 (2015)
51. D.W. Sievers, V. Shrotriya, Y. Yang, J. Appl. Phys. **100**, 114509 (2006)
52. A.J. Moulé, J.B. Bonekamp, K. Meerholz, J. Appl. Phys. **100**, 094503 (2006)
53. C.J.M. Emmott, J.A. Rohr, M. Campoy-Quiles, T. Kirchartz, A. Urbina, N.J. Ekins-Daukes, J. Nelson, Energy Environ. Sci. **8**, 1317 (2015)
54. R. Betancur, P. Romero-Gomez, A. Martinez-Otero, X. Elias, M. Maymó, J. Martorell, Nat. Photon. **7**, 995 (2013)
55. M. Campoy-Quiles, M. Sims, P.G. Etchegoin, D.D.C. Bradley, Macromolecules **39**, 7673 (2006)
56. C. Müller, L.M. Andersson, O. Peña-Rodriguez, M. Garriga, O. Inganäs, M. Campoy-Quiles, Macromolecules **46**, 7325 (2013)
57. A. Roigé, M. Campoy-Quiles, J.O. Ossó, M.I. Alonso, L.F. Vega, M. Garriga, Synth. Met. **161**, 2570 (2012)
58. D. Cheyns, K. Vasseur, C. Rolin, J. Genoe, J. Poortmans, P. Heremans, Nanotechnology **19**, 424016 (2008)
59. D.M. DeLongchamp, R.J. Kline, Y. Jung, E.K. Lin, D.A. Fischer, D.J. Gundlach, S.K. Cotts, A.J. Moad, L.J. Richter, M.F. Toney, M. Heeney, I. McCulloch, Macromolecules **41**, 5709 (2008)
60. T. Wang, A. Pearson, A.D.F. Dunbar, P.A. Staniec, D.C. Watters, D. Coles, H. Yi, A. Iraqi, D.G. Lidzey, R.A.L. Jones, Eur. Phys. J. E **35**, 129 (2012)
61. D. Nassyrov, C. Mueller, A. Roigé, I. Burgues-Ceballos, J.O. Ossó, D.B. Amabilino, M. Garriga, M.I. Alonso, A.R. Goñi, M. Campoy-Quiles, J. Mater. Chem. **22**, 4519 (2012)
62. T. Wang, A.J. Pearson, D.G. Lidzey, R.A.L. Jones, Adv. Funct. Mater. **21**, 1383 (2011)
63. D. Leman, M.A. Kelly, S. Ness, S. Engmann, A. Herzing, C. Snyder, H.W. Ro, R.J. Kline, D. M. DeLongchamp, L.J. Richter, Macromolecules **48**, 383 (2015)
64. W. Ogieglo, H. Wormeester, K.-J. Eichhorn, M. Wessling, N.E. Benes, Prog. Polym. Sci. **42**, 42 (2015)
65. M. Campoy-Quiles, M. Schmidt, D. Nassyrov, O. Peña, A.R. Goñi, M.I. Alonso, M. Garriga, Thin Solid Films **519**, 2678 (2011)

66. T. Wang, A.D.F. Dunbar, P.A. Staniec, A.J. Pearson, P.E. Hopkinson, J.E. MacDonald, S. Lilliu, C. Pizzey, N.J. Terrill, A.M. Donald, A.J. Ryan, R.A.L. Jones, D.G. Lidzey, Soft Matter **6**, 4128 (2010)
67. B. Schmidt-Hansberg, M.F.G. Klein, K. Peters, F. Buss, J. Pfeifer, S. Walheim, A. Colsmann, U. Lemmer, P. Scharfer, W. Schabel, J. Appl. Phys. **106**, 124501 (2009)
68. S.Y. Heriot, R.A.L. Jones, Nat. Mater. **4**, 782 (2005)
69. U. Heinemeyer, K. Broch, A. Hinderhofer, M. Kytka, R. Scholz, A. Gerlach, F. Schreiber, Phys. Rev. Lett. **104**, 257401 (2010)
70. S. Heun, R.F. Mahrt, A. Greiner, U. Lemmer, H. Bassler, D.A. Halliday, D.D.C. Bradley, P.L. Burn, A.B. Holmes, J. Phys. Condens. Matter **5**, 247 (1993)
71. T. Kreouzis, D. Poplavskyy, S.M. Tuladhar, M. Campoy-Quiles, J. Nelson, A.J. Campbell, D. D.C. Bradley, Phys. Rev. B **73**, 235201 (2006)
72. S. Logothetidis, Method for in-line determination of film thickness and quality during printing processes for the production of organic electronics, 2014, US Patent App. 14/113,125
73. A. Shan, M. Fried, G. Juhasz, C. Major, O. Polgar, A. Nemeth, P. Petrik, L.R. Dahal, Jie Chen, Zhiquan Huang, N.J. Podraza, R.W. Collins, IEEE J. Photovolt. **4**, 355 (2014)
74. R.F. Bianchi, D.T. Balogh, M. Tinani, R.M. Faria, E.A. Irene, J. Polym. Sci. B Polym. Phys. **42**, 1033 (2004)
75. S. Kumar, V.K. Shukla, A. Tripathi, Thin Solid Films **477**, 240 (2005)
76. S. Engmann, V. Turkovic, H. Hoppe, G. Gobsch, Synth. Met. **161**, 2540 (2012)
77. A.M.A. Leguy, Y. Hu, M. Campoy-Quiles, M.I. Alonso, O.J. Weber, P. Azarhoosh, M. van Schilfgaarde, M.T. Weller, T. Bein, J. Nelson, P. Docampo, P.R.F. Barnes, Chem. Mater. **27**, 3397 (2015)
78. A.J. Moulé, H.J. Snaith, M. Kaiser, H. Klesper, D.M. Huang, M. Grätzel, K. Meerholz, J. Appl. Phys. **106**, 073111 (2009)
79. D. Duché, F. Bencheikh, S. Ben Dkhil, M. Gaceur, N. Berton, O. Margeat, J. Ackermann, J. J. Simon, L. Escoubas, Sol. Ener. Mater. Sol. Cells **126**, 197 (2014)
80. M. Schädel, K.F. Jeltsch, P. Niyamakom, F. Rauscher, Y. Zhou, M. Krüger, K. Meerholz, J. Polym. Sci. B Polym. Phys. **50**, 75 (2012)

Chapter 16
Organic-Inorganic Hybrid Perovskite Solar Cells

Hiroyuki Fujiwara, Nikolas J. Podraza, Maria Isabel Alonso, Masato Kato, Kiran Ghimire, Tetsuhiko Miyadera and Masayuki Chikamatsu

Abstract Quite high efficiencies exceeding 20% have been realized in solar cells incorporating organic-inorganic hybrid perovskites ($APbX_3$), which have a unique structure with a center cation [A = $CH_3NH_3{}^+$, $HC(NH_2)_2^+$] located within a $PbX_3{}^-$ cage (X = I, Br, Cl). Superior characteristics of hybrid perovskite solar cells can be understood from the nature of optical transitions and the efficient carrier collection in the device. From these points of view, this chapter provides details on optical properties of various hybrid perovskite materials and carrier dynamics in the solar cells. In particular, based on the first-principles analyses of different perovskite materials, we present universal rules that allow the unified interpretation of the optical absorption phenomenon in $APbX_3$ perovskites. The external quantum efficiency (EQE) analysis further reveals that high short-circuit current densities (>20 mA/cm^2) observed in the perovskite solar cells originate from electric-field-assisted carrier collection and the suppressed optical losses in the devices. Although hybrid perovskites have quite favorable characteristics for solar cells, these materials exhibit rather intense phase change upon exposure to humid air. In this chapter, the degradation process of $CH_3NH_3PbI_3$ in humid air, characterized by applying ellipsometry technique, is further presented and discussed.

H. Fujiwara (✉) · M. Kato
Gifu University, 1-1 Yanagido, Gifu 501-1193, Japan
e-mail: fujiwara@gifu-u.ac.jp

N. J. Podraza · K. Ghimire
University of Toledo, Toledo, OH 43606, USA

M. I. Alonso
Institut de Ciència de Materials de Barcelona (ICMAB-CSIC), Campus UAB, 08193 Bellaterra, Spain

T. Miyadera · M. Chikamatsu
Research Center for Photovoltaics, National Institute of Advanced Industrial Science and Technology, 1-1-1 Umezono, Tsukuba 305-8568, Japan

© Springer International Publishing AG, part of Springer Nature 2018

H. Fujiwara and R. W. Collins (eds.), *Spectroscopic Ellipsometry for Photovoltaics*, Springer Series in Optical Sciences 212,
https://doi.org/10.1007/978-3-319-75377-5_16

16.1 Introduction

Research into organic-inorganic hybrid perovskite solar cells is progressing rapidly and quite remarkable conversion efficiencies exceeding 20% have already been realized by using hybrid perovskite light absorbers [1–4]. The operation of a hybrid perovskite solar cell was first demonstrated by Kojima et al. using methylammonium lead iodide ($MAPbI_3$, $CH_3NH_3PbI_3$) in 2009 [5]. Although the conversion efficiency of this solar cell was 3.8%, later the efficiency was improved to 10.9% in 2012 [6], leading to drastic expansion of the researches on hybrid perovskite photovoltaic devices [7–14].

In the last few years, formamidinium lead iodide [$FAPbI_3$, $HC(NH_2)_2PbI_3$], which exhibits higher thermal stability, has been applied to solar cells as an alternative hybrid perovskite material [1–4, 15–17]. However, this perovskite is intrinsically unstable and a cubic $FAPbI_3$ crystal (α-$FAPbI_3$) shows a gradual phase transformation into a transparent δ-$FAPbI_3$ phase having a one-dimensional crystal structure [18, 19]. Quite fortunately, $FAPbI_3$-based perovskites can be stabilized by including a small amount of MA^+ and Cs^+ and, as a result, a variety of hybrid perovskites ($APbX_3$) consisting of mixed center cations (A = MA^+, FA^+, Cs^+) with different PbX_3^- cages (X = I, Br) have been developed [1–4, 20–24]. To date, quite high conversion efficiencies over 20% have been demonstrated in (FA, MA)Pb(I, Br)$_3$ and (FA, MA, Cs)Pb(I, Br)$_3$ solar cells [1–4].

Figure 16.1 shows basic crystal structures of $MAPbI_3$ and $FAPbI_3$ hybrid perovskites: (a) $MAPbI_3$ (pseudocubic), (b) $MAPbI_3$ (tetragonal) and (c) α-$FAPbI_3$ (pseudocubic). These crystal structures represent the optimized crystal structures obtained from the density functional theory (DFT) calculation using the Perdew-Burke-Ernzerhof (PBE) scheme [25] within the cubic (Fig. 16.1a, c) and tetragonal (Fig. 16.1b) bases [26, 27]. The arrows indicate the directions of the *a*, *b*, and *c* axes of the unit cells. It can be seen that hybrid perovskite compounds in Fig. 16.1 have a unique combination of the organic A-site center cation with the inorganic cage consisting of PbI_3^-. At room temperature, $MAPbI_3$ single crystals show a tetragonal structure [9, 28, 29]. However, the $MAPbI_3$ crystals become cubic above 57 °C [9]. For $FAPbI_3$, there are two different phase structures at room temperature (i.e., α-$FAPbI_3$ and δ-$FAPbI_3$) [15, 18, 29] of which δ-$FAPbI_3$, that will be shown later, is the most stable crystal structure at room temperature [18, 19].

In Fig. 16.1a, c, the unit cells have pseudocubic structures with the lattice parameters of a = 6.306 Å, b = 6.291 Å and c = 6.310 Å ($MAPbI_3$) and a = 6.416 Å, b = 6.236 Å, and c = 6.353 Å (α-$FAPbI_3$). Thus, the unit cell sizes of $MAPbI_3$ and α-$FAPbI_3$ are quite similar. However, a of α-$FAPbI_3$ is expanded slightly, compared with b and c, due to the steric effect of FA^+, while the lattice parameters are almost the same in $MAPbI_3$. These values are comparable to the experimental values of a = 6.259 Å ($MAPbI_3$) [9] and a = 6.362 Å (α-$FAPbI_3$) [19].

In the DFT-optimized structures obtained assuming 0 K, MA^+ and FA^+ interact with I atoms, forming hydrogen bonds expressed by I···H–N, and the orientation and location of the center cation are determined primarily by this hydrogen bonding

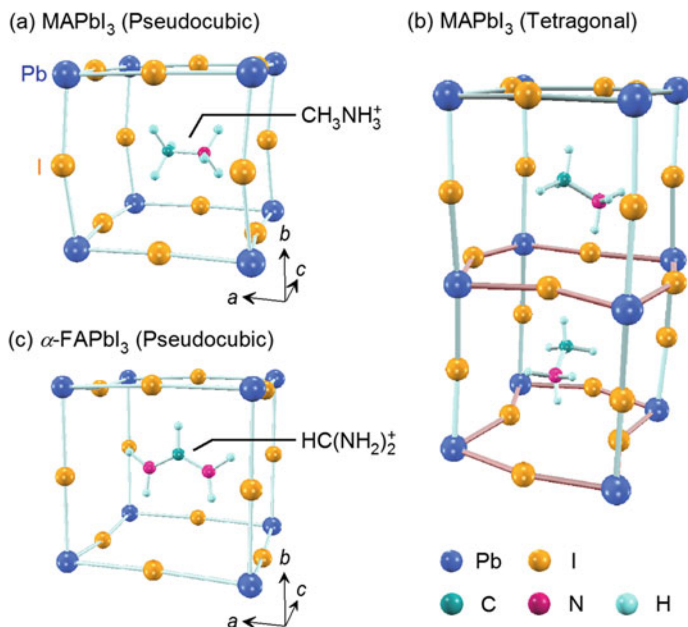

Fig. 16.1 Crystal structures of $MAPbI_3$ and $FAPbI_3$ hybrid perovskites determined by DFT calculations using PBE: **a** $MAPbI_3$ (pseudocubic) [26], **b** $MAPbI_3$ (tetragonal) and **c** α-$FAPbI_3$ (pseudocubic) [27]. The arrows indicate the *a*, *b*, and *c* axes of the pseudocubic unit cells. In **b**, the in-plane Pb–I networks are shown by the thin red color

interaction [19, 26, 27, 30–33]. Nevertheless, it has been confirmed experimentally that, at room temperature, MA^+ and FA^+ reorient quite rapidly (0.5–14 ps) inside the Pb–I network [19, 34–40]. In Fig. 16.1, on the other hand, the I–Pb–I angle is slightly bent and, in the tetragonal phase, the I–Pb–I bond angle changes rather significantly. It has been reported that the introduction of the large center cation leads to the formation of collinear I–Pb–I bonds, which are closer to 180° [41]. Quite interestingly, the collinear bond formation induces the slight band gap (E_g) reduction [30, 41, 42], which has been explained by the anti-bonding character of the Pb–I bond [41, 42].

Figure 16.2 shows a basic structure of a hybrid perovskite ($MAPbI_3$) solar cell [6, 8, 10, 12]. This solar cell consists of a glass substrate, SnO_2:F transparent conductive oxide (TCO), TiO_2 electron transport layer (ETL), light absorber ($MAPbI_3$), spiro-OMeTAD hole transport layer (HTL) and back metal electrode (Au or Ag). The spiro-OMeTAD is an organic compound (see Fig. 9.18 in Vol. 2), which is employed quite commonly in hybrid perovskite solar cells [6, 8] and can be formed by spin coating. For the fabrication of the solar cells, commercial glass substrates on which TCO (SnO_2:F) layers are formed (TEC-8 or TEC-15,

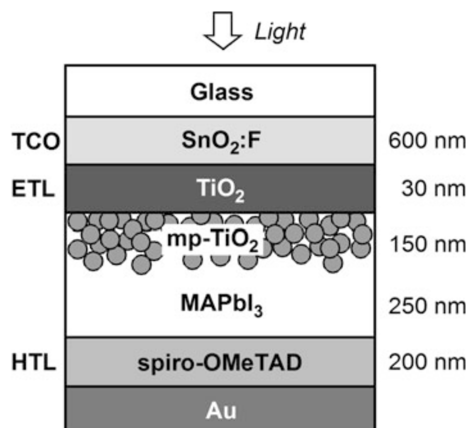

Fig. 16.2 Basic structure of a hybrid perovskite ($MAPbI_3$) solar cell fabricated by spin coating. In this structure, the $MAPbI_3$ absorber layer is inserted between the mesoporous (mp)-TiO_2 electron transport layer (ETL) and spiro-OMeTAD hole transport layer (HTL)

Pilkington) are used widely (see Chap. 18). On this SnO_2:F/glass substrate, a dense (compact) TiO_2 layer, followed by a porous (mesoporous; mp) TiO_2 layer, is formed prior to the perovskite layer fabrication [6, 8]. One quite remarkable feature of hybrid perovskite solar cells is that high efficiency devices can be made by adopting a rather simple solution-based process, combined with low temperature annealing at ~100 °C [6, 7, 12]. Accordingly, by further developing hybrid perovskite solar cells, low-cost production of large-area solar cell modules could be realized.

In this chapter, we will overview the optical characteristics of unique hybrid perovskite compounds and the operational principles of the solar cells (Sects. 16.2 and 16.3, H. Fujiwara, M. Kato, T. Miyadera and M. Chikamatsu). Moreover, this chapter describes spectroscopic ellipsometry (SE) characterization of hybrid perovskite structures based on real-time measurements (Sect. 16.4, N. J. Podoraza and K. Ghimire). One of the drawbacks of hybrid perovskite solar cells is a rather strong degradation in humid air, and the degradation phenomenon and its mechanism are discussed in Sect. 16.5 (M. I. Alonso).

16.2 Optical Properties

16.2.1 Optical Constants of Hybrid Perovskites

For $MAPbI_3$, many inconsistent optical data have been reported [26, 43–52] (see Fig. 1.3). However, the disagreement observed among the reported optical constants can primarily be attributed to the influence of roughness component (Chap. 6). Since spectroscopic ellipsometry (SE) is a surface-sensitive technique, the fabrication

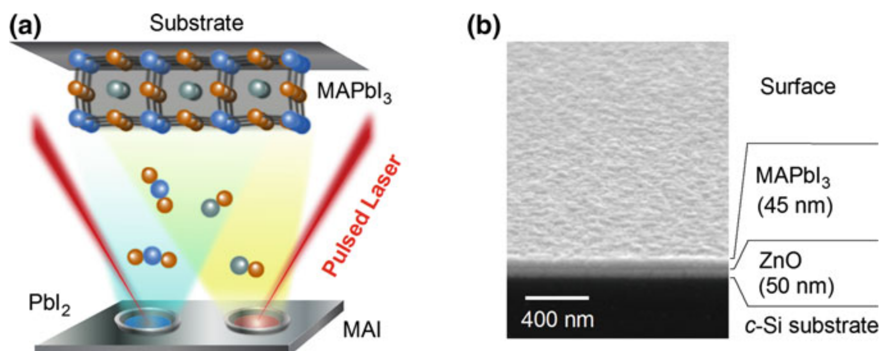

Fig. 16.3 **a** Schematic of the laser evaporation process and **b** a scanning electron microscope (SEM) image of the $MAPbI_3$/ZnO/*c*-Si structure [26]

of samples with smooth surfaces is essential for reliable SE characterization. For the preparation of smooth $MAPbI_3$ and α-$FAPbI_3$ layers, a laser evaporation technique shown in Fig. 16.3a has been applied [26, 53]. In this technique, PbI_2 and MAI (or FAI) source materials are heated by a near-infrared laser, and the evaporation rates of the source materials are controlled precisely by adjusting the pulsed-laser power and frequency. By using this technique, an ultrasmooth $MAPbI_3$ layer shown in Fig. 16.3b can be formed [26] and, in this sample, a thin ZnO layer is provided to improve film adhesion on a crystalline Si (*c*-Si) substrate. For the suppression of surface roughening and structural non-uniformity in the growth direction, characterization of thin layers (45 nm in Fig. 16.3b) is quite effective (Chap. 6). The $MAPbI_3$ and α-$FAPbI_3$ layers fabricated by laser evaporation show sharp X-ray diffraction peaks, which are consistent with the perovskite pseudocubic phases, and the formation of secondary PbI_2 phase is negligible [26, 27].

Unfortunately, $MAPbI_3$ [51, 54–59] and α-$FAPbI_3$ [16, 21, 23, 29] exhibit significant degradation in humid air (Sect. 16.5). Thus, to avoid the air exposure, the samples were transferred from the deposition system to the SE measurement system using a N_2-filled plastic bag. From this procedure, the SE spectra of the pristine $MAPbI_3$ and α-$FAPbI_3$ were measured without exposing the samples to humid air at all [26, 27], although the high-energy spectra of $MAPbI_3$ ($E \geq 4.75$ eV) were obtained after the short-time air exposure (~20 s) at 40% relative humidity [26].

Moreover, to determine reliable optical constants of hybrid perovskites, the SE analyses have been performed using a global error minimization (GEM) scheme [26, 27], in which the dielectric function is determined self-consistently using more than two samples having different layer thicknesses on substrates [60, 61] (Sect. 10.2). In this method, the dielectric function is obtained first from a thin layer and the extracted dielectric function is then applied for the SE analysis of a thicker

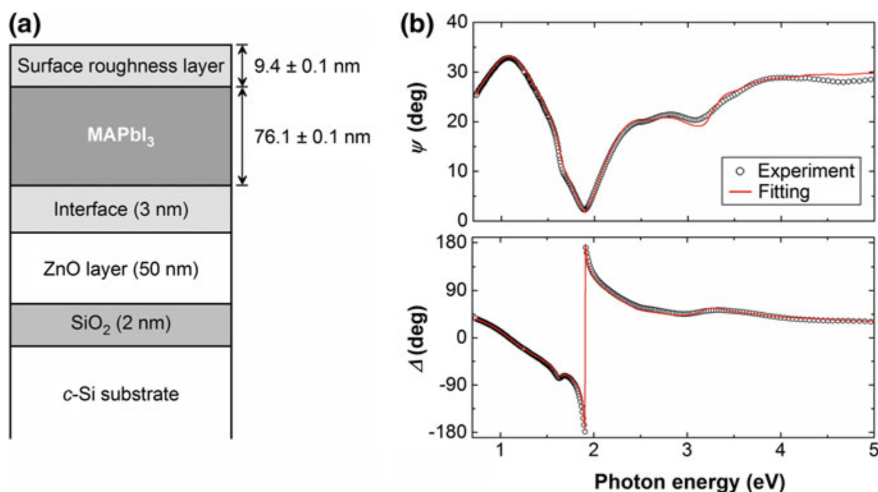

Fig. 16.4 **a** Optical model and **b** (ψ, Δ) ellipsometry spectra for a $MAPbI_3$ (85 nm)/ZnO (50 nm)/SiO_2 (2 nm)/*c*-Si structure [26]. The solid lines show the fitting result calculated using the $MAPbI_3$ dielectric function extracted from the thinner layer (45 nm). In **a**, the layer thicknesses determined from the SE analysis of **b** are shown. In **b**, the SE measurement was carried out in a N_2 environment without exposing the sample to air at an angle of incidence of 75°

layer (or layers) under the assumption that the bulk-layer optical properties are independent of the layer thickness. In the actual GEM analyses of the hybrid perovskites, a pair of samples with thicknesses in a range of 45–200 nm have been employed [26, 27].

Figure 16.4 shows an example of GEM analysis performed for $MAPbI_3$ [26]. In this case, two samples with $MAPbI_3$ layer thicknesses of 45 nm (Fig. 16.3b) and 85 nm were used and two sets of ellipsometry spectra were obtained from these samples [i.e., $(\psi, \Delta)_{45nm}$ and $(\psi, \Delta)_{85nm}$]. For this SE analysis, an optical model shown in Fig. 16.4a has been assumed. The interface and SiO_2 layers correspond to the surface roughness of the ZnO layer and the native oxide of the *c*-Si substrate, respectively. The ZnO surface roughness can be characterized from the SE analysis of a ZnO/SiO_2/*c*-Si structure (see Sect. 18.3.2). The optical properties of the surface roughness layer are calculated as a 50:50 vol.% mixture of the bulk layer and voids by applying the Bruggeman effective-medium approximation (EMA) [60, 61] (see Sects. 3.4.2 and 6.1), while a 50:50 vol.% mixture of $MAPbI_3$ and ZnO is assumed for the interface layer.

Figure 16.4b shows experimental SE spectra of $(\psi, \Delta)_{85nm}$ and the solid lines represent the fitting result calculated using the $MAPbI_3$ dielectric function extracted from $(\psi, \Delta)_{45nm}$ [26]. The calculated spectra show excellent fitting to the experimental spectra, confirming the validity of the analysis. The layer thicknesses determined from the SE analysis of Fig. 16.4b are also summarized in Fig. 16.4a. In the subsequent analysis, the final dielectric function is extracted from $(\psi, \Delta)_{45nm}$ by adjusting the $MAPbI_3$ bulk layer thickness slightly since the ε_2 values obtained

from the above analysis show very small negative values ($\varepsilon_2 \sim -0.05$) at $E < E_g$. In particular, the bulk layer thickness is increased slightly (~5% of total thickness) so that the ε_2 values at $E < E_g$ become completely zero. Such minor adjustment is often necessary due to the imperfection of samples. It should be noted that the surface-roughness layer thickness of 2.9 ± 0.1 nm obtained from the SE analysis of $(\psi, \Delta)_{45\mathrm{nm}}$, shows reasonable agreement with the root-mean-square roughness of 4.6 nm observed in AFM. Thus, the overall ellipsometry analysis can be justified by comparing the roughness values characterized from SE and AFM (Fig. 6.1b). It has been confirmed that thermal annealing (80 °C for 45 min) of a $MAPbI_3$ sample does not change the SE result significantly, while annealing at a higher temperature (100 °C for 45 min) leads to PbI_2 formation by the MAI desorption [26].

Figure 16.5 summarizes (a) the ε_2 spectra and (b) the α spectra of $MAPbX_3$ and α-$FAPbI_3$. The optical functions of $MAPbI_3$ [26] and α-$FAPbI_3$ [27] have been determined from the GEM analyses of the laser-evaporated layers (i.e., Figure 16.4 for $MAPbI_3$), whereas those of $MAPbBr_3$ and $MAPbCl_3$ have been obtained from the SE analyses of the single crystals [52]. The complete optical data of these materials are also shown in Chap. 10 in Vol. 2. In Fig. 16.5a, when the X-site halogen atom is changed, the whole dielectric function shifts toward higher energy with the gradual reduction of the ε_2 amplitude for the lighter halogen atom. In this case, a high-energy transition peak observed at 3.24 eV in $MAPbI_3$ splits into two peaks in $MAPbBr_3$ and $MAPbCl_3$. The sharp absorption peaks of $MAPbBr_3$ and $MAPbCl_3$, observed near the E_g regions, originate from excitonic transitions [62] and the excitonic peaks become more pronounced in $MAPbCl_3$.

Quite interestingly, the ε_2 amplitude of α-$FAPbI_3$ is roughly half of that of $MAPbI_3$ at E <3 eV, even though the overall ε_2-spectral shape is independent of

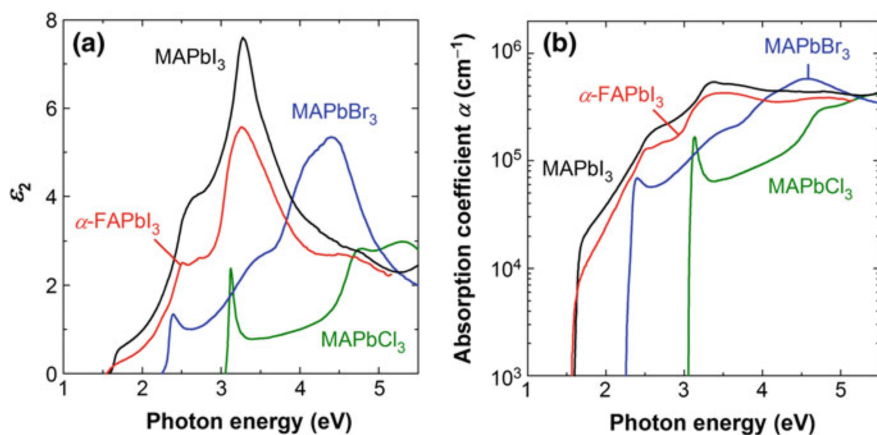

Fig. 16.5 **a** ε_2 spectra and **b** α spectra of $MAPbX_3$ (X = I, Br, Cl) and α-$FAPbI_3$. The reported optical data of $MAPbI_3$ [26], α-$FAPbI_3$ [27], $MAPbBr_3$ [52], and $MAPbCl_3$ [52] are shown. The results of α-$FAPbI_3$ and $MAPbI_3$ were obtained from the GEM analyses of polycrystalline layers, whereas those of $MAPbBr_3$ and $MAPbCl_3$ were extracted from the single crystals

the center cation. Accordingly, the replacement of the A-site cation has a large influence on the absorption strength. In fact, the α values of α-FAPbI$_3$ are notably smaller than those of MAPbI$_3$ and, at 1.7 eV, α of α-FAPbI$_3$ is half of that of MAPbI$_3$ (Fig. 16.5b). The lower light absorption observed in α-FAPbI$_3$ explains why thicker absorber layers (~500 nm) are generally necessary for FAPbI$_3$-based perovskite solar cells [1–4], compared with MAPbI$_3$ solar cells (typically ~300 nm) [7]. The low α values observed in α-FAPbI$_3$ have also been confirmed based on external quantum efficiency (EQE) analysis of a α-FAPbI$_3$ solar cell [27]. The results of Fig. 16.5 show clearly that the A-site cation (MA$^+$ and FA$^+$) modifies the oscillator strength of the optical transition (or ε_2 amplitude), while the X-site halogen atom determines the transition energy.

Often, high conversion efficiencies demonstrated in MAPbI$_3$ solar cells are attributed to quite high α in MAPbI$_3$ [13, 63, 64]. Nevertheless, many α values reported earlier for MAPbI$_3$ have been overestimated seriously due to the influence of surface roughness (see Fig. 1.3 and Chap. 6), and the actual α values of MAPbI$_3$ in Fig. 16.5b are comparable to those of CuInGaSe$_2$, GaAs, and CdTe absorbers (Fig. 1.6). In other words, the α values of α-FAPbI$_3$ are lower than major solar-cell materials. Since hybrid perovskite layers fabricated by spin-coating processes are generally thin (<1 μm), the optical confinement is of significant importance particularly in FAPbI$_3$-based solar cells (see also Sect. 16.3).

Figure 16.6 summarizes (a) the dielectric functions and (b) the α spectra of hybrid-perovskite secondary phases including PbI$_2$ [26], MAI [26] and δ-FAPbI$_3$ [27], together with those of MAPbI$_3$ and α-FAPbI$_3$ in Fig. 16.5. As confirmed from Fig. 16.6, PbI$_2$ exhibits ε_2 peaks at 2.51, 2.97, 3.26, 3.90, and 4.33 eV, where the rather sharp peak at 2.51 eV has been attributed to an excitonic transition [65, 66]. On the other hand, the visible light absorption in MAI and δ-FAPbI$_3$ is quite weak.

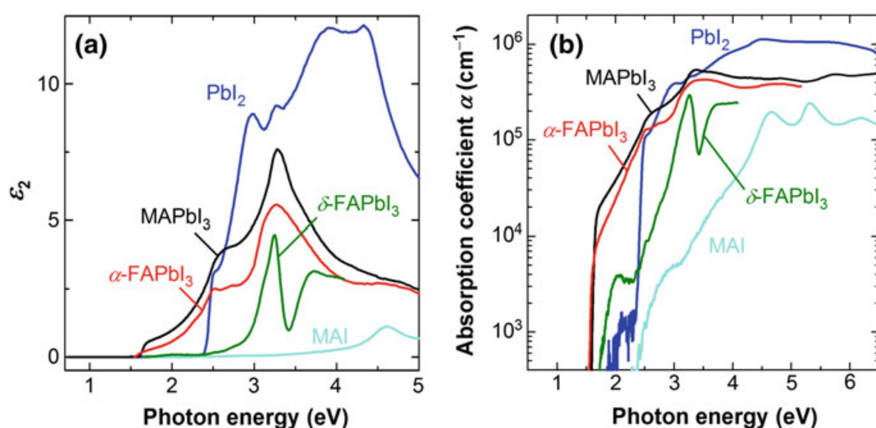

Fig. 16.6 **a** ε_2 spectra and **b** α spectra of hybrid-perovskite secondary phases including PbI$_2$ [26], MAI [26] and δ-FAPbI$_3$ [27], together with those of MAPbI$_3$ and α-FAPbI$_3$ in Fig. 16.5

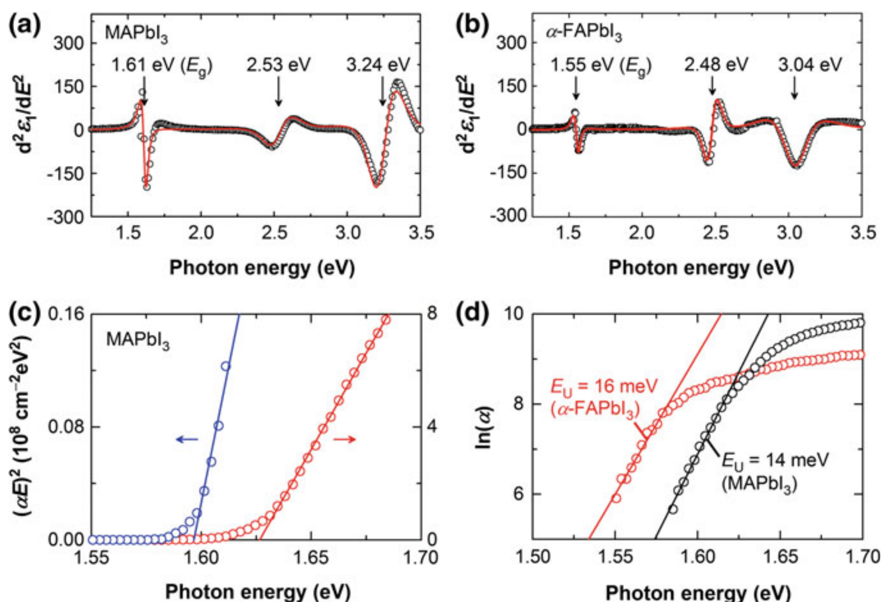

Fig. 16.7 Critical point (CP) analyses of **a** $MAPbI_3$ [26] and **b** α-$FAPbI_3$ [27] dielectric functions, together with **c** E_g analysis for $MAPbI_3$ using the $(\alpha E)^2 - E$ plot [26] and **d** analysis of the Urbach energy (E_U) assuming $\ln(\alpha) \propto E/E_U$. In the CP analyses of **a** and **b**, the open circles denote the experimental data and the solid lines represent the theoretical fittings. From the CP analyses, E_g values are determined to be 1.61 ± 0.01 eV ($MAPbI_3$) and 1.55 ± 0.01 eV (α-$FAPbI_3$). These E_g values correspond to the transition energies of E_0. In **c**, the E_g analysis results for two different $(\alpha E)^2$ regions are shown, which result in different E_g values. The open circles show the experimental data and the solid lines represent the linear fitting results

Figure 16.7 presents the critical point (CP) analyses of (a) $MAPbI_3$ [26] and (b) α-$FAPbI_3$ [27] dielectric functions. As described in Sect. 4.3.1, the CP analysis is used commonly to determine the optical transition energies and E_g accurately. For the CP analyses of $MAPbI_3$ in Fig. 16.7a and α-$FAPbI_3$ in Fig. 16.7b, a procedure described in Sect. 10.3.2 has been employed. Briefly, in this CP analysis, the second-derivative spectra calculated from the modeled dielectric functions (Chap. 10 in Vol. 2) are employed to suppress the spectral noise and the theoretical fitting to these spectra is then carried out. The open circles in Fig. 16.7a, b show the $d^2\varepsilon_1/dE^2$ spectrum obtained from the modeled dielectric functions, while the solid lines represent the fitting results calculated from (10.2) and (10.3). From the CP analysis, E_0 (E_g) of $MAPbI_3$ is found to be 1.61 ± 0.01 eV, while the peak transition energies in the high energy region are determined to be E_1 = 2.53 ± 0.01 eV and E_2 = 3.24 ± 0.01 eV [26]. The CP analysis of α-$FAPbI_3$ has been implemented assuming only three transitions at $E \leq 3.5$ eV, which results in the CP energies of 1.55 ± 0.01, 2.48 ± 0.01, and 3.04 ± 0.01 eV [27]. The CP energy of 1.55 ± 0.01 eV corresponds to E_g of α-$FAPbI_3$. Thus, E_g of α-$FAPbI_3$ changes only slightly, if compared with $MAPbI_3$.

On the other hand, E_g can be analyzed more conveniently using a $(\alpha E)^2$–E plot. In Fig. 16.7c, an example of this E_g analysis, performed for the α spectrum of $MAPbI_3$, is shown [26]. In this analysis, the E_g value is determined from the intercept, but the analysis implemented using different $(\alpha E)^2$ regions gives different E_g values. Thus, the reliability of this analysis is rather low. Moreover, when the effect of surface roughness is underestimated in SE analyses, E_g is also underestimated (see Fig. 1.3). Accordingly, slightly smaller E_g values reported for $MAPbI_3$ (1.50–1.61 eV in [10, 12, 16, 29, 54, 67]) and α-$FAPbI_3$ (1.43–1.53 eV in [4, 15–17, 21, 29, 68]) could be interpreted by (i) the uncertainty in the E_g analysis and (ii) the contribution of surface roughness.

In Fig. 16.7d, from the α spectrum of $MAPbI_3$ and α-$FAPbI_3$, the Urbach energy (E_U) is further determined assuming $\alpha \propto \exp(E/E_U)$ [i.e., $\ln(\alpha) \propto E/E_U$]. The E_U values of $MAPbI_3$ and α-$FAPbI_3$ estimated from this simple analysis are 14 meV [26] and 16 meV [27], respectively, confirming the sharp absorption onset near E_g in hybrid perovskites [45].

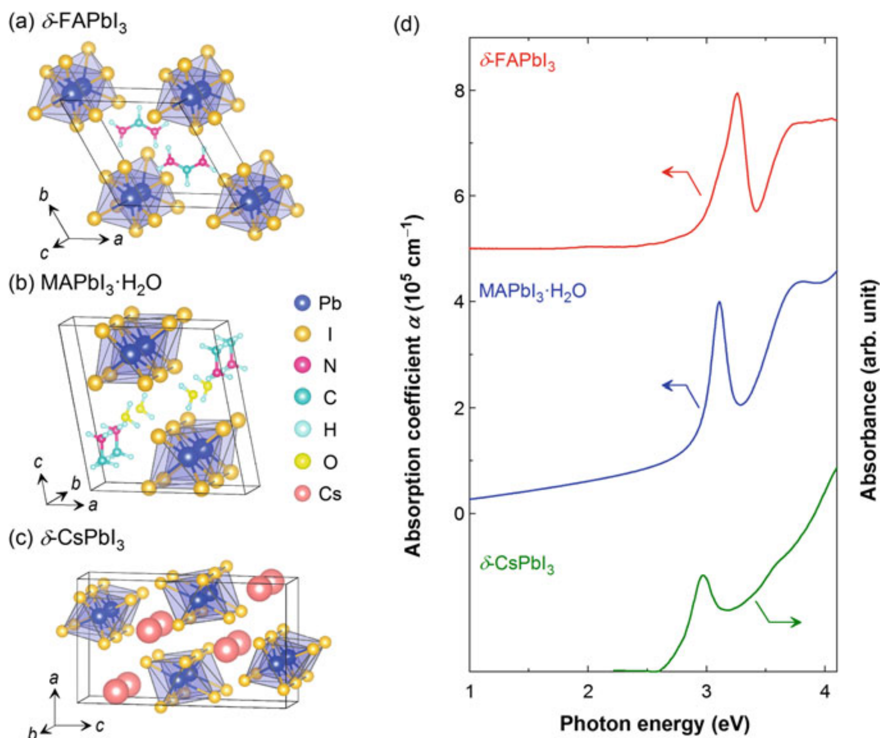

Fig. 16.8 Crystal structures of **a** δ-$FAPbI_3$, **b** $MAPbI_3 \cdot H_2O$ and **c** δ-$CsPbI_3$ and **d** their α spectra. The DFT-derived crystal structure (δ-$FAPbI_3$) and reported crystal structures of $MAPbI_3 \cdot H_2O$ [69] and δ-$CsPbI_3$ [29] are shown. All the crystals have similar one-dimensional crystal structures. In this figure, the α spectra reported for δ-$FAPbI_3$ [27], $MAPbI_3 \cdot H_2O$ [51] and δ-$CsPbI_3$ [70] are summarized. The α spectrum of δ-$FAPbI_3$ is shifted by 5×10^5 cm^{-1} for clarity

In Fig. 16.8, the crystal structures and α spectra of δ-$FAPbI_3$, $MAPbI_3 \cdot H_2O$ and orthorhombic $CsPbI_3$ (δ-$CsPbI_3$) are shown. The crystal structure of δ-$FAPbI_3$ in Fig. 16.8a is derived from the DFT calculation, while the reported crystal structures of $MAPbI_3 \cdot H_2O$ [69] and δ-$CsPbI_3$ [29] are shown in Fig. 16.8b, c, respectively. All the crystal phases have one-dimensional crystal structures consisting of PbI_6 octahedra, although the crystal structure of δ-$FAPbI_3$ is slightly different from the other two. It should be noted that, at room temperature, δ-$FAPbI_3$ and δ-$CsPbI_3$ are the most stable phases of $FAPbI_3$ and $CsPbI_3$ [22]. On the other hand, it has been confirmed that the $MAPbI_3 \cdot H_2O$ phase is formed by the exposure of $MAPbI_3$ to humid air [51] (Sect. 16.5).

It can be seen from Fig. 16.8d that the reported α spectra of $MAPbI_3 \cdot H_2O$ [51] and δ-$CsPbI_3$ [70] are quite similar to that of δ-$FAPbI_3$. In fact, all these materials show similar absorption peaks at E = 3.0–3.3 eV with weak shoulder peaks at 3.6–3.8 eV. The sharp peak at 3.1 eV in $MAPbI_3 \cdot H_2O$ has been attributed to the excitonic transition [51]. The DFT calculations confirmed that the interaction between the neighboring PbI_6 octahedrons contributes to reduce E_g and, as a result, E_g of $MAPbI_3$ with three-dimensional PbI_6 structure is much smaller, compared with two-dimensional PbI_2 and one-dimensional $MAPbI_3 \cdot H_2O$ crystals [59].

16.2.2 Optical Transitions in Hybrid Perovskites

To understand the light absorption in hybrid perovskite crystals, the optical transition analyses have been implemented using DFT. In particular, the dielectric functions of $MAPbI_3$, $MAPbBr_3$ and α-$FAPbI_3$ can be reproduced quite well assuming simple pseudocubic structures based on DFT within PBE [26, 27]. Moreover, universal rules that allow the unified interpretation of the light absorption in $APbX_3$-type perovskites have been established [27]. In this section, these results obtained from the DFT analyses are introduced.

Figure 16.9 summarizes the DFT-derived crystal structures of (a) $MAPbI_3$ [26], (b) α-$FAPbI_3$ [27] and (c) $MAPbBr_3$ [27], and corresponding DFT dielectric functions of (d) $MAPbI_3$ [26], (e) α-$FAPbI_3$ [27] and (f) $MAPbBr_3$ [27]. The crystal structures of $MAPbI_3$ and α-$FAPbI_3$ in Fig. 16.9 are identical to those shown in Fig. 16.1. The arrows indicate the a, b, and c axes of the unit cells. In the optimized structures, the C–N bonds of MA^+ in $MAPbI_3$ and $MAPbBr_3$ are aligned to be almost parallel to the a axis, whereas the N–C–N plane of FA^+ in α-$FAPbI_3$ is parallel to the a-b plane (or the line connecting two N atoms of FA^+ is parallel to the a axis). The orientation of FA^+ in α-$FAPbI_3$ (Fig. 16.9b) is consistent with the experimental result [19].

In Fig. 16.9d–f, the experimental dielectric functions shown in Fig. 16.5 (open circles) are compared with the DFT-derived dielectric functions (solid lines). The theoretical dielectric functions have been obtained assuming the different polarization states with directions parallel to the a, b and c axes in Fig. 16.9a–c, and the arrows indicated in Fig. 16.9d–f represent the transition (CP) energies in the

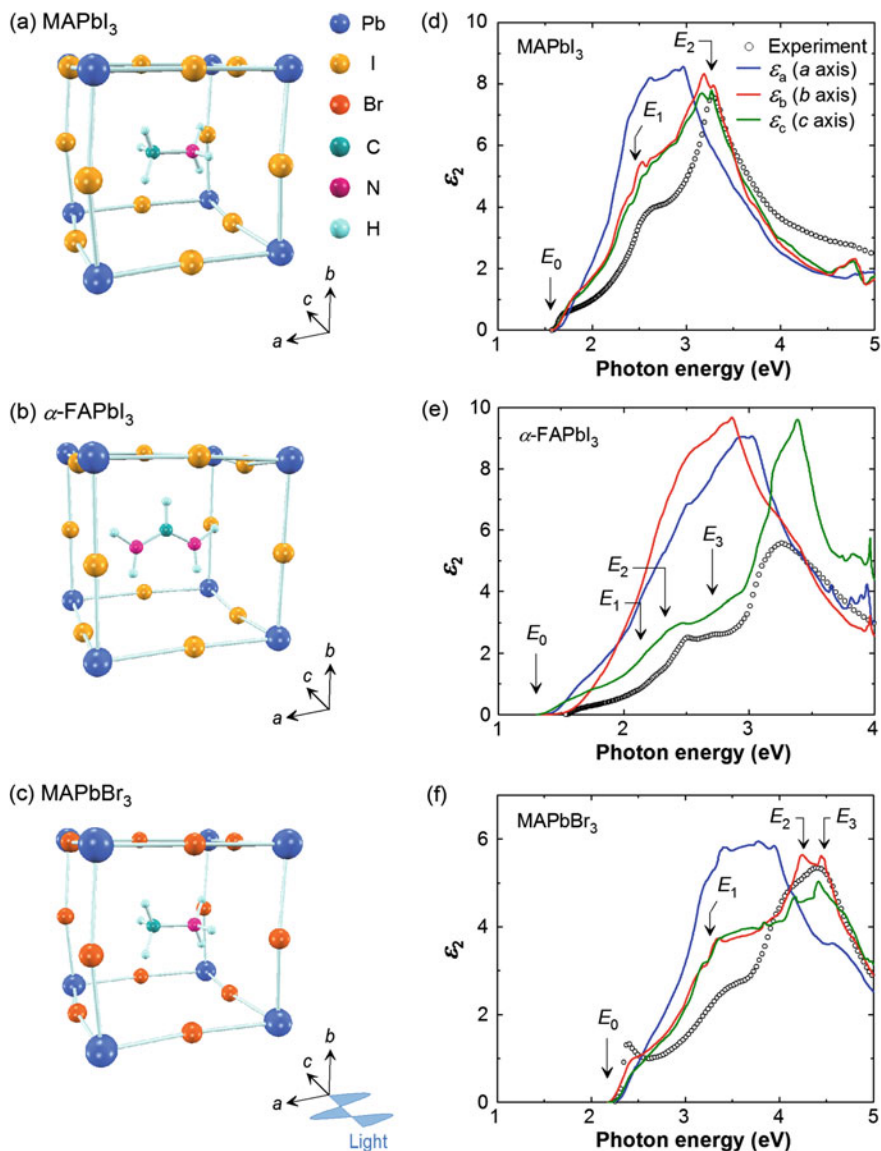

Fig. 16.9 Pseudocubic crystal structures of **a** $MAPbI_3$, **b** α-$FAPbI_3$ and **c** $MAPbBr_3$ obtained from the DFT calculations, and ε_2 spectra of **d** $MAPbI_3$, **e** α-$FAPbI_3$ and **f** $MAPbBr_3$, obtained from the experiments (open circles) and DFT calculations (solid lines). In **a**–**c**, the arrows indicate the a, b, and c axes of the unit cells. In **d**–**f**, the experimental results correspond to those shown in Fig. 16.5, and ε_a, ε_b and ε_c represent the ε_2 spectra calculated assuming the light polarization along the a, b, and c axes in **a**–**c**, respectively. On the ε_2 spectra, the transition energies determined by the DFT analyses (see Fig. 16.10) are indicated. In **f**, the DFT spectra of $MAPbBr_3$ have been shifted toward higher energy by 0.22 eV to obtain better matching with the experimental spectrum. The experimental and DFT data are taken from [26] ($MAPbI_3$) and [27] (α-$FAPbI_3$ and $MAPbBr_3$)

Brillouin zone described below. For $MAPbBr_3$, however, all the calculated spectra have been shifted toward higher energy by 0.22 eV to match the DFT result with the experimental result. The DFT calculations show that all the perovskite compounds have highly anisotropic optical characteristics. In the case of $MAPbI_3$, for example, the dielectric function for the a axis polarization (ε_a) is quite different to those for the b and c axes (ε_b and ε_c), and similar trends can be confirmed for $MAPbBr_3$. It can be seen that the overall shapes of ε_b and ε_c obtained for $MAPbI_3$ and $MAPbBr_3$ show remarkable agreement with those of the experimental spectra. In the case of α-$FAPbI_3$, the ε_2 spectra for the a and b axes (ε_a and ε_b) exhibit different shapes from that for the c axis (ε_c), and the shape of ε_c agrees well with the experimental dielectric function.

In Fig. 16.9d–f, the CP energies ($E_{0\text{-}3}$) of $MAPbI_3$, $MAPbBr_3$ and α-$FAPbI_3$, deduced from the DFT calculations, show excellent agreement with the experimental results, and all the fine absorption features observed experimentally in these perovskites are reproduced quite well. However, the band-edge excitonic transition observed in $MAPbBr_3$ at 2.4 eV is not reproduced in the calculation result as the DFT calculations in Fig. 16.9 have been performed without incorporating electron-hole interactions (or exciton formation). Consequently, the calculated ε_2 becomes lower than the experimental ε_2 near the E_g region. In contrast, excellent matching is observed between the experimental and DFT spectra for $MAPbI_3$ and α-$FAPbI_3$, confirming that the contribution of excitons in the light absorption process is negligible in these materials [26, 27]. Non-excitonic nature of $MAPbI_3$ has already been confirmed and discussed quite extensively [47, 71, 72].

Figure 16.10 shows the band structure and the density of states (DOS) of (a) $MAPbI_3$ [26] and (b) α-$FAPbI_3$ [27], calculated from the pseudocubic structures of Fig. 16.9a, b, respectively. For the band structures, the corresponding Brillouin zone is shown in the inset and the partial DOS of each material is also shown. The V_j and C_j in these figures denote the jth valence and conduction bands from the valence band maximum (VBM) and the conduction band minimum (CBM), respectively. In both $MAPbI_3$ and α-$FAPbI_3$, V_1 consists of the Pb 6s and I 5p states, whereas C_1 is dominated by Pb 6p [9, 26, 64, 73, 74], as confirmed from the corresponding partial DOS. The band structures of $MAPbI_3$ and α-$FAPbI_3$ are quite similar, but α-$FAPbI_3$ has an additional conduction band at ~2.9 eV due to the π-state of the sp^2 C atom in FA^+. The insets of Fig. 16.10a also show the charge density profiles of $MAPbI_3$ for the designated energy regions of $E = 1.4 \sim 1.6$ eV (CBM), $E = -0.2 \sim 0.0$ eV (VBM), and $E = -0.6 \sim -0.4$ eV. Because of the antibonding nature of Pb–I [75], the charge densities near VBM are localized on the Pb (6s) and I (5p), while the charge density near CBM is dominated by Pb 6p. In the band structures of Fig. 16.10, the energy positions of $M_{1\text{-}3}$ and those of $X_{1\text{-}3}$ differ slightly because the assumed cubic crystal is distorted and the resulting reciprocal lattices ($a^* = 2\pi/a$, $b^* = 2\pi/b$, $c^* = 2\pi/c$) are different. In particular, the α-$FAPbI_3$ unit cell is distorted largely due to the steric effect of FA^+ and the energy differences of $M_{1\text{-}3}$ and $X_{1\text{-}3}$ are larger in α-$FAPbI_3$ than in $MAPbI_3$.

The arrows in Fig. 16.10a, b represent the interband transitions that occur at high symmetry points in the pseudocubic Brillouin zone. These optical transitions have

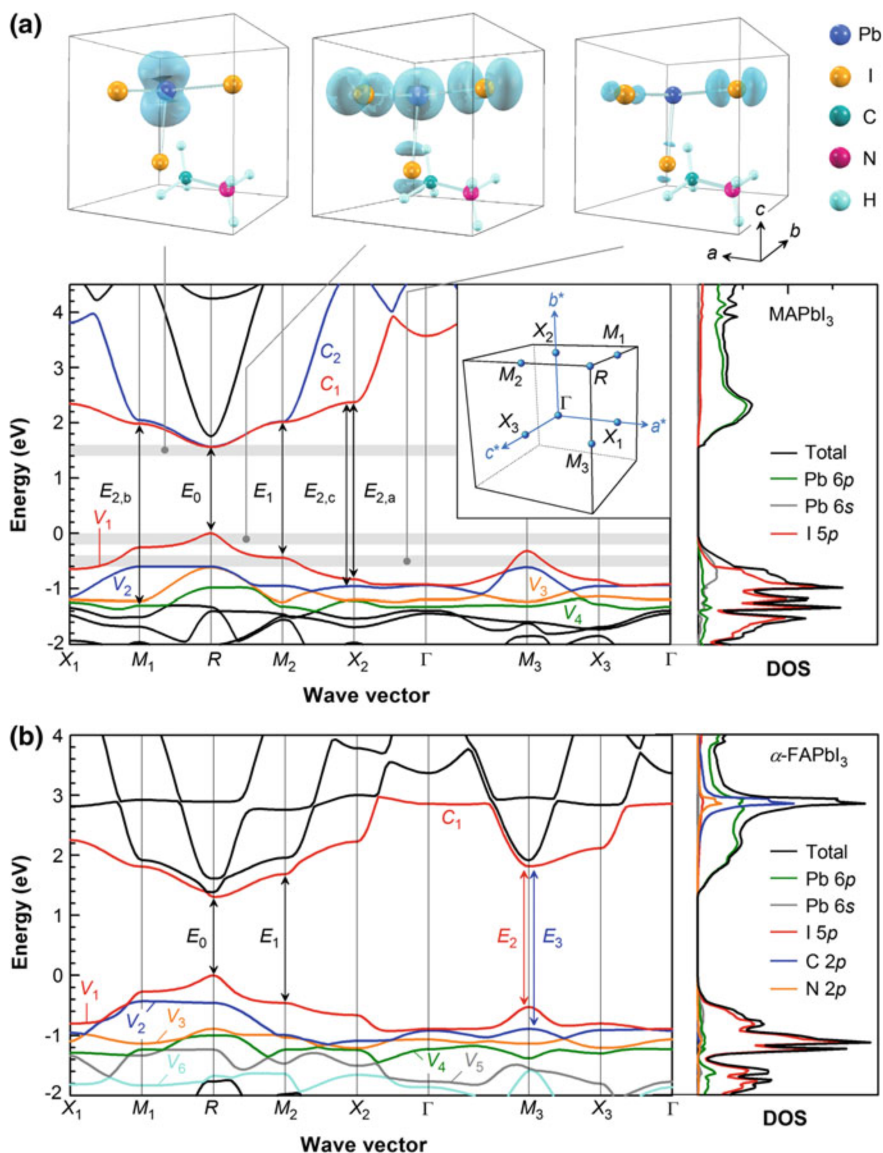

Fig. 16.10 Band structure and DOS of **a** $MAPbI_3$ [26] and **b** α-$FAPbI_3$ [27] pseudocubic crystals. In **a** and **b**, V_j and C_j denote the jth valence and conduction bands from VBM and CBM, respectively, and the partial DOS distributions are also indicated. The optical transitions determined by the polarization-dependent DFT analyses are indicated by arrows and the energy positions of these transitions are shown in Fig. 16.9. The inset of **a** shows the high symmetry points in the Brillouin zone defined by the reciprocal lattices ($a^* = 2\pi/a$, $b^* = 2\pi/b$, $c^* = 2\pi/c$) of the assumed pseudocubic structure and the charge density profiles for the designated energy regions of $E = -0.2 \sim 0.0$ eV (VBM), $E = 1.4 \sim 1.6$ eV (CBM) and $E = -0.6 \sim -0.4$ eV

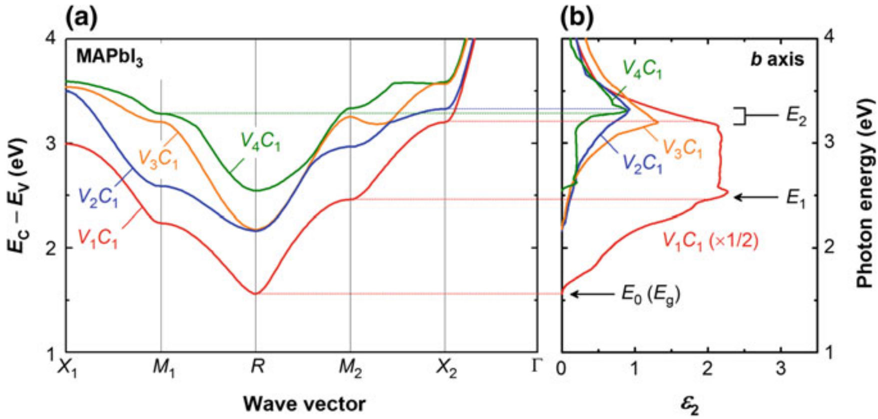

Fig. 16.11 **a** Energy separation between the conduction and valence bands ($E_C - E_V$) in $MAPbI_3$ and **b** contributions of various interband transitions to the ε_2 spectrum of $MAPbI_3$. In **a**, V_jC_1 ($j \leq 4$) denote the interband transitions of $V_j \rightarrow C_1$ in Fig. 16.10a. In **b**, the ε_2 contributions of V_jC_1 for the b axis (i.e., ε_b) are shown, and the amplitude of the ε_2 spectrum for the V_1C_1 transition is reduced to half for clarity. The data reported in [77] are shown

been characterized by calculating the dielectric response of each interband transition by DFT [26, 27], as described below. The energy positions of the arrows in Fig. 16.9d–f correspond to the interband transition energies obtained from the corresponding band structures. In the case of $MAPbI_3$, however, the E_2 transition consists of three components and each component is labeled using the subscript of a, b or c. It can be seen that $MAPbI_3$ [9, 26, 64] and α-$FAPbI_3$ [27, 76] are direct transition semiconductors with the E_0 (E_g) transition at the R point (cubic symmetry) and other hybrid perovskites also show direct gaps [27, 76]. The transition energies of $E_{0\text{-}3}$ obtained from the band structures show remarkable agreement with the experimental values, as confirmed from Fig. 16.9d–f.

Figure 16.11 shows the optical transition analysis performed for $MAPbI_3$ [77]. In this analysis, the energy separation between the conduction and valence bands ($E_C - E_V$) is calculated first for each interband transition of $V_j \rightarrow C_k$. In Fig. 16.11a, the calculated results for V_jC_1 ($j \leq 4$) of Fig. 16.10a are shown, where V_jC_1 denote the transition of $V_j \rightarrow C_1$. The ε_2 contributions induced by the V_jC_1 transitions are calculated further (Fig. 16.11b) and are compared with the energy separations in Fig. 16.11a. From this procedure, the optical transitions at high symmetry points that satisfy van Hove singularities [78] in **k** space (i.e., $\nabla_{\mathbf{k}}[E_C(\mathbf{k}) - E_V(\mathbf{k})] = 0$) have been determined. It can be seen from Fig. 16.11b that the optical transition in the visible region is dominated by the V_1C_1 transition. In Fig. 16.11b, the ε_2 contributions for the b-axis component (i.e., ε_b in Fig. 16.9d) are shown and, in this case, only the transitions at the R, M_1, M_2, and X_2 points are allowed (i.e., b* component of the Brillouin zone). From these assumptions, the CP energies observed in the ε_2 spectrum of $MAPbI_3$ are assigned to the interband transitions of V_1C_1 at the R (E_0 transition), M_2 (E_1 transition) and X_2 ($E_{2,a}$ transition) points.

Moreover, the ε_2 peaks for the V_2C_1 and V_4C_1 transitions are attributed to the transitions of V_4C_1 at the M_1 point ($E_{2,\mathrm{b}}$ transition) and V_2C_1 at the X_2 point ($E_{2,\mathrm{c}}$ transition). The CP energies observed in Fig. 16.11a, however, deviate slightly from the exact peak positions confirmed in the calculated ε_2 spectra and thus slight ambiguity remains. Similar optical transition analyses have been made for α-$FAPbI_3$ and $MAPbBr_3$ [27].

The above DFT analysis and partial DOS in Fig. 16.10 indicate that direct semiconductor-type transitions occur within the PbI_3^- component in $MAPbI_3$ and α-$FAPbI_3$ in the visible region (E < 4 eV), supporting the efficient carrier generation in these semiconductors [26, 27, 77]. By applying the self-consistent *GW* (sc*GW*) approximation, the optical transition analyses of $MAPbX_3$ have been performed and slightly different assignments have been proposed for $MAPbI_3$ [52]. It should be emphasized that the DFT-derived dielectric function changes rather significantly depending on calculation (approximation) method. As examples, Fig. 16.12 compares the α spectra of (a) $MAPbI_3$ and (b) α-$FAPbI_3$ calculated by DFT using different approximations. In these figures, the α values in linear and

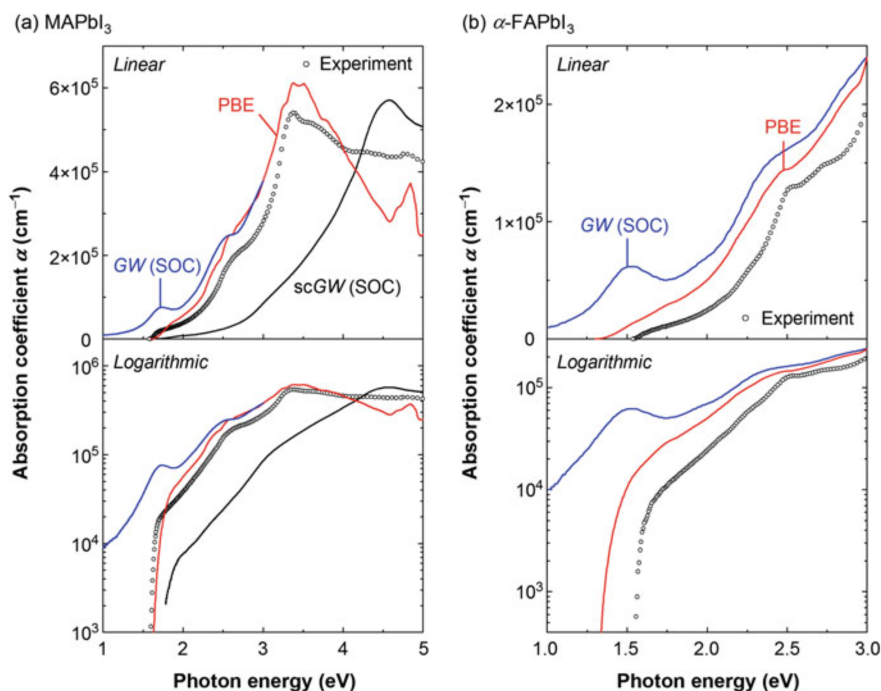

Fig. 16.12 α spectra of **a** $MAPbI_3$ and **b** α-$FAPbI_3$ calculated by DFT using different approximations: PBE ($MAPbI_3$ [26] and α-$FAPbI_3$ [27]), *GW* approximation with SOC [30], and self-consistent *GW* (sc*GW*) approximation with SOC [52]. In **a** and **b**, the α values in linear and logarithmic scales are shown. The absolute α values of the *GW* (SOC) results [30] are deduced by assuming that the α values at 3.0 eV are identical to those of the PBE results

logarithmic scales are summarized. For $MAPbI_3$, the DFT calculation results obtained within PBE [26], the *GW* approximation [30], and the sc*GW* approximation [52] are shown. In the *GW* and sc*GW* calculations, the effect of the spin-orbit coupling (SOC) [79] has been taken into account. For the *GW*-SOC results [30], however, only relative α values have been reported, and the absolute α values are deduced by assuming that the α values at 3.0 eV are identical to those of the PBE results. All the DFT calculations reproduce E_g of $MAPbI_3$ successfully, as discussed previously [52, 73, 80–82]. In general, E_g is underestimated seriously in PBE [83]. For hybrid perovskites, however, the E_g values calculated by PBE agree quite well with the experimental values, which has been attributed to the cancellation of errors in the DFT calculations [52, 73, 79]. On the other hand, if the SOC interaction is not considered in the *GW* and sc*GW*, the E_g values are overestimated seriously [52, 80–82].

The sc*GW* approximation is generally accepted as the most advanced DFT calculation method. However, the transition energies of the α spectrum obtained from the sc*GW*-SOC occur at higher energies and the absolute α values are much smaller, compared with the experimental result. In the *GW*-SOC results of $MAPbI_3$ and α-$FAPbI_3$, small peaks appear near E_g and the absorption features near the fundamental band edge are not reproduced well. As known widely [30, 52, 79–81], when the DFT calculations are implemented by incorporating SOC, all the bands split into two bands and the band structure becomes slightly indirect (or pseudo-direct). Thus, the α peak observed in the *GW*-SOC results could be attributed to the SOC effect. It has been confirmed that the SOC-induced band splitting near the fundamental gap is quite sensitive to the orientation and position of the A-site cation [84–86].

In contrast, the absolute α values and peak energies, deduced from the PBE calculations, show excellent agreement with the experimental spectra, although E_g of α-$FAPbI_3$ is underestimated. At least at this stage, therefore, the PBE calculations provide the best matching with the experimental data. Moreover, the PBE results reproduce the experimental tail-state absorption quite well with similar Urbach energies ($E_U \sim 15$ meV). This is rather surprising as the DFT spectra are obtained assuming a perfect crystal structure with no phonon interaction (0 K). Accordingly, the room-temperature optical spectra of the hybrid perovskites, obtained from the experiments, exhibit ideal sharp absorption feature with quite suppressed tail-state absorption.

16.2.3 Universal Rules for Light Absorption in $APbX_3$ Perovskites

The large α reduction induced by the replacement of MA^+ with FA^+ in $APbI_3$ (Fig. 16.5) and the strong optical anisotropy confirmed in the DFT calculations (Fig. 16.9) are found to originate from the strong interaction of the A-site cation

with the X-site halogen atom [27]. In particular, the visible light absorption in $APbX_3$ varies rather significantly depending on the A-site cation species. Here, we discuss the optical absorption phenomena in hybrid perovskites based on more detailed DFT analyses using PBE [27].

Figure 16.13 represents the charge density profiles of (a) α-$FAPbI_3$, (b) $MAPbI_3$ and (c) $CsPbI_3$ in the energy region of $-0.6 \sim -0.4$ eV from VBM ($E = 0$ eV). In this figure, the charge density indicated by the colors decreases with the order of red > yellow > green > blue with red being the highest. These results have been obtained from the DFT-optimized structures (see Fig. 16.9 for $MAPbI_3$ and α-$FAPbI_3$). The charge density of $MAPbI_3$ has already been shown in the inset of Fig. 16.10a.

The charge densities of the selected energy region ($-0.6 \sim -0.4$ eV) correspond to the valence electron states that involve in the E_1 transition in $MAPbI_3$ (2.46 eV) and the E_2 transition in α-$FAPbI_3$ (2.34 eV), as confirmed from the V_1 energy positions at the M points in Fig. 16.10. Here, the valence charge states at the M points are considered specifically, as the visible light absorption at ~2 eV in the hybrid perovskites is characterized by the interband transitions near the M point (V_1C_1). Since the transition probability is determined by the interaction of incoming polarized light with the valence state [see (4.2)], the optical absorption can be studied more directly based on the valence electron (wave function) in the corresponding energy range. Although the conduction states are also important in determining the transition probability, the effect of the Pb-derived conduction bands is treated as a constant contribution in this analysis.

In Fig. 16.13, the charge density profiles of $APbI_3$ in the same energy region ($-0.6 \sim -0.4$ eV) are shown, but the distribution of the I-5p charge densities varies significantly depending on the cation species. More specifically, the I-5p valence electron of α-$FAPbI_3$ concentrates on the I atoms along the a and b axes, and the valence charges of these I atoms ($Q_{I,a}$ and $Q_{I,b}$, respectively) are far larger than that of the c axis direction ($Q_{I,c}$). In the case of $MAPbI_3$, the valence charge distribution is more uniform, even though $Q_{I,a}$ is larger than $Q_{I,b}$ and $Q_{I,c}$, while quite homogeneous charge distribution ($Q_{I,a} \sim Q_{I,b} \sim Q_{I,c}$) can be seen for $CsPbI_3$.

It has been confirmed that the distribution of $Q_{I,a\text{-}c}$ is modified strongly by the hydrogen bonding interaction expressed by $I(\delta^-)\cdots H(\delta^+)$–$N(\delta^-)$ [27], where δ^+ and δ^- denote the positive and negative partial charges, respectively, and the magnitude of δ is determined mainly by the electronegativity. In particular, the hydrogen bondings of $I\cdots H$–N, indicated by the dotted lines in Fig. 16.13a, b, lead to the reduction of the N–I distance [26, 33]. In the case of $MAPbI_3$, for example, the N atom position of MA^+ is located more closely to the b-c plane due to the hydrogen bondings formed with the I atoms in the b and c axis directions. The result of Fig. 16.13 shows clearly that the distribution of $Q_{I,a\text{-}c}$ is governed primarily by the N–I distance and $Q_{I,a\text{-}c}$ decreases significantly when the N–I distance is smaller. This electrostatic interaction between the N and I atoms, referred to as the anti-coupling effect hereafter, plays a critical role for the interpretation of the visible light absorption in hybrid perovskites. In α-$FAPbI_3$, the

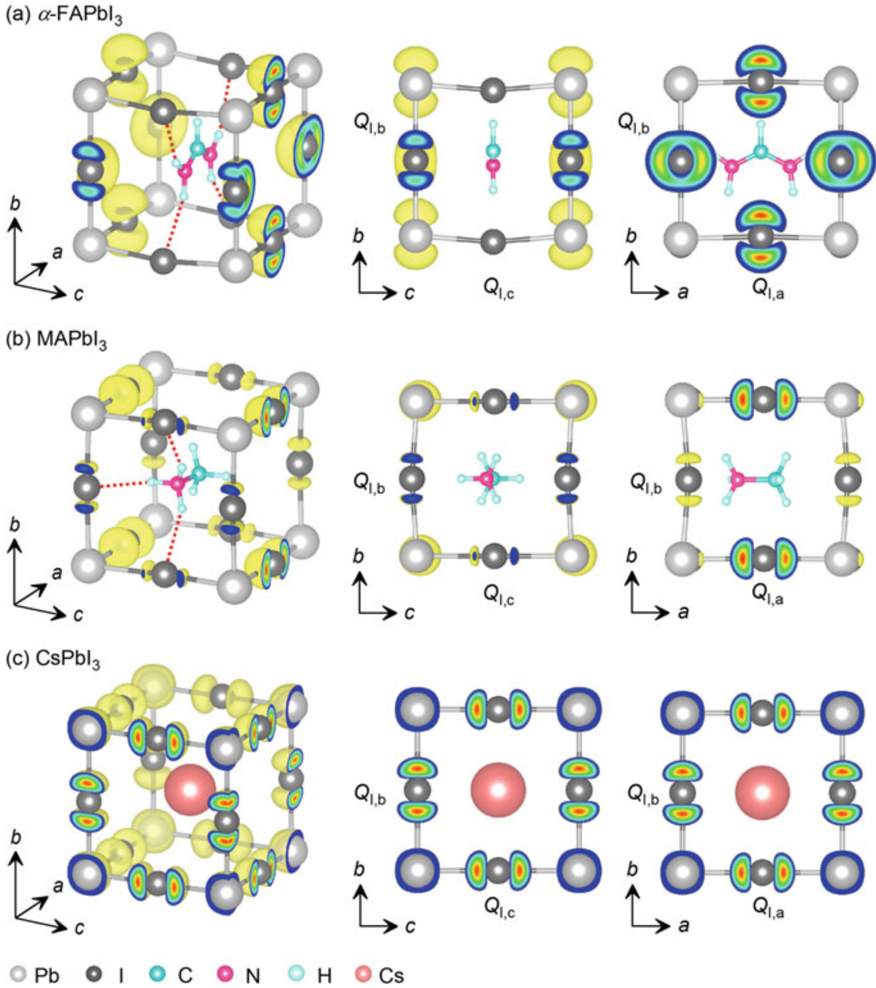

Fig. 16.13 Charge density profiles of **a** α-FAPbI$_3$, **b** MAPbI$_3$ and **c** CsPbI$_3$ in the energy region of $-0.6 \sim -0.4$ eV from VBM ($E = 0$ eV). These profiles represent the valence charge densities for the E_2 transition (α-FAPbI$_3$) and the E_1 transition (MAPbI$_3$ and CsPbI$_3$) at the M point (V_1C_1). The charge density decreases with the order of red > yellow > green > blue with red being the highest. The arrows show the a, b, and c axes of the unit cells, and the valence charges of the I atoms along the a, b, and c axes are indicated as $Q_{\mathrm{I},a}$, $Q_{\mathrm{I},b}$ and $Q_{\mathrm{I},c}$, respectively. For α-FAPbI$_3$ and MAPbI$_3$, the data reported in [27] are shown

intense anti-coupling effect leads to the significant reduction of $Q_{\mathrm{I},c}$ due to the short distance between the I (c axis) and N atoms. As a result, the valence charge of I 5p concentrates on the a-b plane. In MAPbI$_3$, smaller $Q_{\mathrm{I},b}$ and $Q_{\mathrm{I},c}$, compared with $Q_{\mathrm{I},a}$, can also be interpreted by the strong anti-coupling interaction as the N-I

distance is shorter for the I atoms on the *b* and *c* axes. In contrast, the anti-coupling interaction is negligible in $CsPbI_3$ due to the lack of the hydrogen bonding.

The highly anisotropic optical transitions at the *M* point, observed in the DFT results of Fig. 16.9, can be understood based on the above anti-coupling effect. In the case of α-$FAPbI_3$, for example, the ε_2 value at 2.34 eV corresponds to the E_2 transition, and ε_b shows the highest ε_2 value at this energy, while ε_c shows the lowest value (Fig. 16.9e). As confirmed from Fig. 16.13a, the charge density distribution of $Q_{I,a}$ is oriented along the *b* axis, increasing the polarizability and the resulting ε_2 value significantly in this direction. Consequently, ε_b of α-$FAPbI_3$ exhibits the maximum ε_2 value, while very low $Q_{I,c}$ results in very small ε_c. In the case of $MAPbI_3$, the distribution of $Q_{I,a}$ is aligned along the *a* axis, leading to the higher ε_a value at 2.46 eV (E_1 transition), compared with ε_b and ε_c (Fig. 16.9d). Moreover, the similar ε_2 values of ε_b and ε_c are consistent with the corresponding charge densities ($Q_{I,b} \sim Q_{I,c}$) shown in Fig. 16.13b. In contrast, $CsPbI_3$ shows negligible optical anisotropy because of the uniform charge distribution of $Q_{I,a\text{-}c}$. Moreover, when the N atom position of MA^+ is shifted intentionally and is placed at the center position of the C–N bond in Fig. 16.13b, the charge density distribution of $-0.6 \sim -0.4$ eV becomes more uniform and the strong anisotropic behavior disappears [27]. Accordingly, the anti-coupling effect is induced primarily by the I···H–N hydrogen bonding interaction.

In Fig. 16.9, among the ε_2 spectra calculated for different light polarizations, the ε_2 spectrum having the lowest ε_2 values in the visible region shows the best match with the experimental data. This result indicates that the visible-light absorption in the actual hybrid perovskites is modified significantly by the strong anti-coupling effect. In other words, although the Pb-derived conduction band (C_1) is independent of the A species, the electronic states of the I atoms are influenced strongly by the hydrogen bonding of the A-site cation.

Figure 16.14 summarizes the dielectric functions of (a) α-$FAPbX_3$, (b) $MAPbX_3$ and (c) $CsPbX_3$ (X = I, Br, Cl) obtained from DFT calculations [27]. These dielectric functions have been obtained by replacing the A-site cation in identical PbI_3^-, $PbBr_3^-$ and $PbCl_3^-$ structures that are deduced from the structural optimization of $MAPbX_3$. In this figure, however, only the ε_2 spectra of ε_c (α-$FAPbX_3$) and ε_b ($MAPbX_3$ and $CsPbX_3$) are shown, and the bars indicate the energy positions of the E_1 transition at the M_2 point (V_1C_1). It should be noted that, when the PbX_3^- structures derived from $MAPbX_3$ are assumed, the energies of the E_1 and E_2 transitions in α-$FAPbX_3$ become almost identical. It can be seen that the shapes of the ε_2 spectra are similar when the ε_2 spectra of the same X are compared. Nevertheless, the ε_2 amplitude varies systematically with the A-site cation, independent of X, due to the presence of the anti-coupling effect. In particular, the ε_2 value of the E_1 transition, indicated by the bar, increases notably as the hydrogen bonding interaction becomes weaker.

For the variation of the ε_2 amplitude with the A-site cation, more quantitative analyses have been made. Figure 16.15 shows the ε_2 values for the E_1 transitions in $APbX_3$, which corresponds to the ε_2 values indicated by the bars in Fig. 16.14a–c, as a function of the valence charge ratio expressed by Q_X/Q_{Total} [27]. Here,

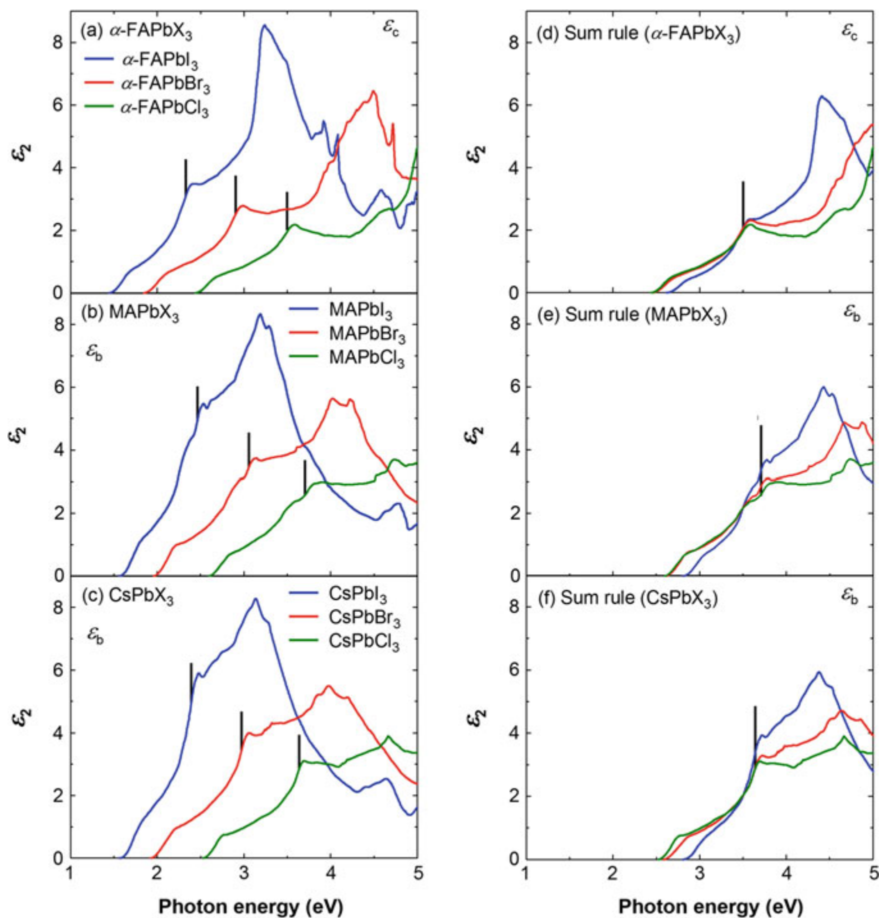

Fig. 16.14 ε_2 spectra of **a** α-$FAPbX_3$, **b** $MAPbX_3$, and **c** $CsPbX_3$ (X = I, Br, Cl) calculated from DFT, together with the corresponding ε_2 spectra of **d** α-$FAPbX_3$, **e** $MAPbX_3$, and **f** $CsPbX_3$ obtained by applying the sum rule for $APbI_3$ and $APbBr_3$. In the figures, only the ε_2 spectra for ε_c (α-$FAPbX_3$) and ε_b ($MAPbX_3$ and $CsPbX_3$) are shown. The bars indicate the energy positions of the E_1 transition at the M_2 point (V_1C_1). The ε_2 spectra of **a**–**c** have been obtained by replacing the A-site cation in the identical PbX_3^- structures determined from the structural optimization of $MAPbX_3$. The data reported in [27] are shown

Q_X/Q_{Total} represents the relative magnitude of each X-site valence charge (i.e., $Q_{X,a}$, $Q_{X,b}$ or $Q_{X,c}$) with respect to the total charge of $APbX_3$ (Q_{Total}). For the calculation of Q_X/Q_{Total}, the energy ranges that correspond to the E_1 transitions have been selected. In Fig. 16.15, the results for ε_a, ε_b and ε_c in each $APbX_3$ are plotted and the solid lines show the linear fitting results. It can be seen that the ε_2 value increases linearly with Q_X/Q_{Total}, confirming the presence of a universal rule for the effect of the A-site cation. As a result, the ε_2 value of ε_a, ε_b or ε_c in $APbX_3$ increases when the corresponding $Q_{X,a}$, $Q_{X,b}$ or $Q_{X,c}$ becomes larger.

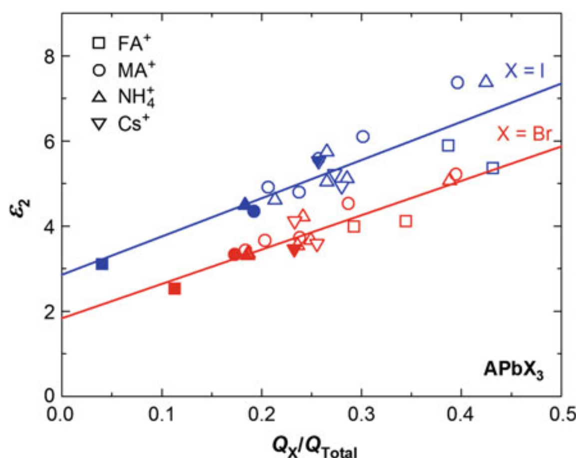

Fig. 16.15 ε_2 values for the E_1 transition at the M_2 point (V_1C_1) in $APbX_3$ (A = FA^+, MA^+, NH_4^+, Cs^+; X = I, Br) as a function of the valence charge ratio expressed by Q_X/Q_{Total}. The Q_X represents the valence charge of the X-site atom along the a, b, and c axes and is calculated by selecting an energy region that corresponds to the E_1 transition at the M_2 point (V_1C_1), whereas Q_{Total} denotes the total charge of $APbX_3$ in the same energy region. The closed symbol shows the plot for the lowest Q_X/Q_{Total} in each $APbX_3$. The data reported in [27] are shown

The closed symbol in Fig. 16.15 shows the ε_2 value for the lowest Q_X/Q_{Total} in each $APbX_3$. As we have seen in Fig. 16.9, the experimental ε_2 values are reproduced when the strong anti-coupling effect is considered (i.e., the lowest ε_2 values in the DFT spectra). Accordingly, the ε_2 values of the closed symbols approximate the light absorption strengths in the hybrid perovskites. These ε_2 values lead to a straightforward conclusion; the anti-coupling interaction strengthens with increasing number of N atoms in the center cation. Since FA^+ has two N atoms, a quite large anti-coupling interaction occurs in α-$FAPbX_3$, which in turn reduces the visible-light absorption significantly, as observed in the experimental α spectra (see Fig. 16.5b). In contrast, Cs^+ is stabilized at the center position of the PbX_3^- cage (Fig. 16.13c) and shows the weak anti-coupling effect. Consequently, the visible light absorption increases in the order $FA^+ < MA^+ < Cs^+$.

As confirmed from Fig. 16.9, the experimental ε_2 spectra of α-$FAPbI_3$, $MAPbI_3$ and $MAPbBr_3$ do not match those calculated assuming optical isotropy [i.e., $(\varepsilon_a + \varepsilon_b + \varepsilon_c)/3$] and the overall visible absorption in these perovskites is minimized by the anti-coupling interaction. As mentioned earlier, MA^+ and FA^+ in the PbI_3^- reorient rapidly with a time scale of 0.5–14 ps at room temperature [19, 34–40]. In the DFT calculation that assumes 0 K, however, the cation position is fixed completely and the effect of the cation reorientation is neglected. Even in this case, excellent agreement can be seen between the experimental and DFT results. This result supports the fact that the N–I distance is close and the anti-coupling phenomenon persists even at room temperature. In particular, the molecular dynamics (MD) simulations reveal that the orientation of the center cation is not completely

random [35–40], and MA^+ and FA^+ are preferentially directed toward the face center position of the cubic structure [36, 37, 39, 40] by maintaining the stable I–H (or I–N) distance even at elevated temperature [36, 38–40]. Accordingly, the anti-coupling effect observed in the room-temperature optical spectrum can be interpreted by the strong hydrogen bonding effect of MA^+ and FA^+.

On the other hand, the optical effect of X on the ε_2 spectrum of hybrid perovskites can be modeled according to the sum rule [27], given by the following expression [78]:

$$\int E\varepsilon_2(E)\mathrm{d}E \ = \ \text{const.} \tag{16.1}$$

When the ε_2 spectrum is shifted toward higher energy by ΔE, the sum rule requires that the ε_2 peak amplitude reduces to $E/(E + \Delta E)$ because $\int E\varepsilon_2(E)\mathrm{d}E = \int (E + \Delta E_\mathrm{g})\varepsilon_2(E + \Delta E_\mathrm{g})\mathrm{d}E$. As confirmed from Fig. 16.14a–c, with decreasing halogen mass (I > Br > Cl), the whole ε_2 spectrum shifts toward higher energy and the ε_2 amplitude decreases. Such spectral changes induced by the X replacement can be expressed by applying (16.1). Figure 16.14 shows the ε_2 spectra of (d) α-$FAPbX_3$, (e) $MAPbX_3$ and (f) $CsPbX_3$ obtained from the calculations assuming the sum rule [27]. In these results, the ε_2 spectra of $APbI_3$ and $APbBr_3$ are shifted so that the E_1 transition energies match those of $APbCl_3$. In this case, the amplitude of the shifted ε_2 spectra is reduced further by applying the sum rule. Under these assumptions, the ε_2 values for the E_1 transition become similar and all the spectra show reasonable overlap in a low energy region (<3.7 eV). Accordingly, the ε_2 amplitude variation induced by X can simply be interpreted by the change in the transition energy.

16.3 Operating Principles of Hybrid Perovskite Solar Cells

In this section, to understand the working principles of hybrid perovskite solar cells, we will examine the photocarrier generation/collection in $MAPbI_3$ solar cells based on (i) the internal quantum efficiency (IQE) simulation of a standard solar cell [26], performed by the optical admittance method assuming a perfectly flat structure (Sect. 2.2 in Vol. 2) and (ii) the characterization of the optical and recombination losses in $MAPbI_3$ solar cells [87], determined from the EQE analysis using the e-ARC method (Sect. 2.3 in Vol. 2). These IQE and EQE calculations have been performed using the $MAPbI_3$ optical constants shown in Fig. 16.5 (see also Fig. 10.2 in Vol. 2).

16.3.1 Optical Simulation of a $CH_3NH_3PbI_3$ Solar Cell

Figure 16.16a shows the IQE and internal absorptance (IA) spectra for a $MAPbI_3$ solar cell consisting of glass/SnO_2:F (600 nm)/TiO_2 (200 nm)/$MAPbI_3$ (400 nm)/ spiro-OMeTAD (500 nm)/Ag [26]. The *IQE* and *IA* spectra can be calculated by $IQE = EQE/(1 - R)$ and $IA = A/(1 - R)$, where R and A represent the reflectance

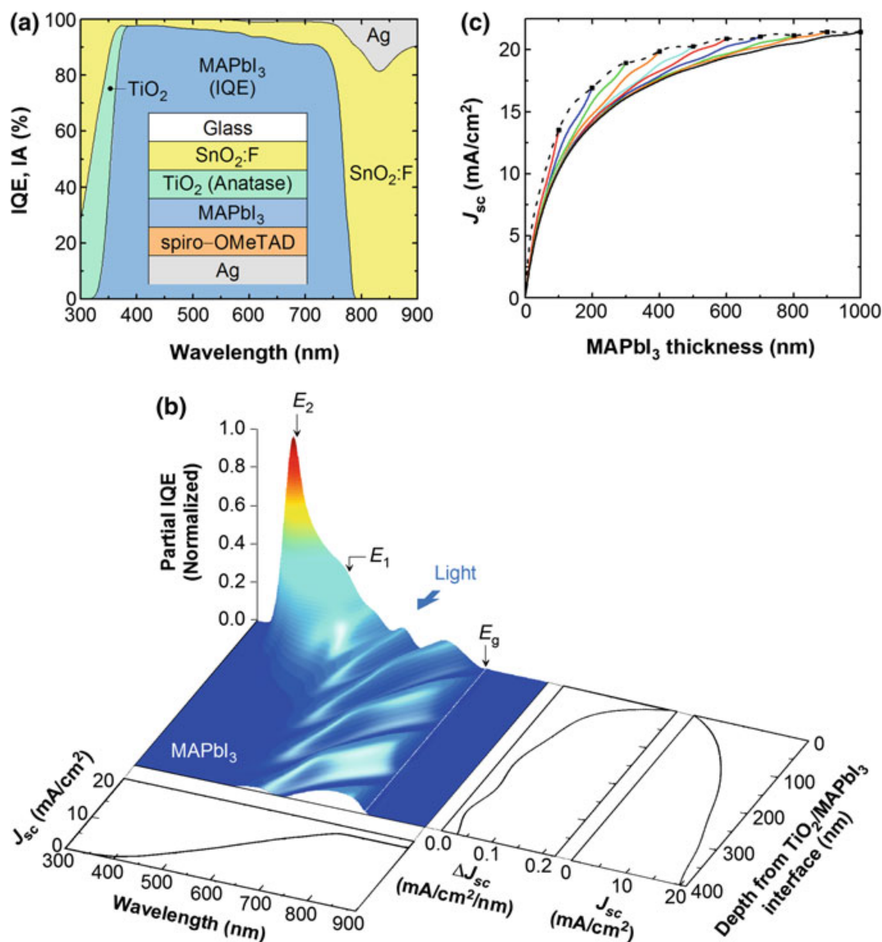

Fig. 16.16 **a** IQE spectrum of the $MAPbI_3$ layer and IA spectra of the component layers in the glass/SnO_2:F (600 nm)/TiO_2 (200 nm)/$MAPbI_3$ (400 nm)/spiro-OMeTAD (500 nm)/Ag structure [26], **b** normalized partial IQE spectra for the $MAPbI_3$, and **c** integrated J_{sc} for perovskite solar cells with discrete $MAPbI_3$ thicknesses from 100 to 1000 nm [26]. In **b**, ΔJ_{sc} shows the J_{sc} component generated within the 1-nm-thick $MAPbI_3$ sublayer, and integrated J_{sc} values relative to the depth from the TiO_2 interface and λ are also shown. The arrows in **b** show the E_g (E_0), E_1, and E_2 positions. In **c**, the solid circles denote the end points of the $MAPbI_3$ thickness and the dotted line shows the J_{sc} values obtained by varying the $MAPbI_3$ layer thickness in the solar cell

and absorptance of the solar cell structure, respectively. By assuming a perfectly flat structure, the R and EQE spectra can be calculated directly using (2.18) and (2.26) in Vol. 2, respectively. In the optical simulation of Fig. 16.16a, the effect of the multiple light reflection/transmission within the glass substrate is neglected (Sect. 2.2.2 in Vol. 2) and 100% collection efficiency of generated carriers is assumed for the perovskite layer. This simulation result can be reproduced by using the optical constants of glass (Fig. 13.1 in Vol. 2), TiO_2 (Fig. 11.12 in Vol. 2), $MAPbI_3$ (Fig. 10.2 in Vol. 2), spiro-OMeTAD (Fig. 9.18 in Vol. 2) and Ag (Fig. 12.6 in Vol. 2) summarized in Part II of Vol. 2. For the SnO_2:F layer [26], however, we assume the Drude parameters of $A_D = 0.919$ eV and $\Gamma = 0.129$ eV, which correspond to $N_{opt} = 1.2 \times 10^{20}$ cm^{-3} and $\mu_{opt} = 49$ cm^2/(Vs) (see Sect. 18.3.4), together with the band-edge Tauc-Lorentz parameters of $A = 44.55$ eV, $C = 12.00$ eV, $E_g = 3.30$ eV and $E_0 = 7.00$ eV [see (5.32)]. The above calculation shows that the average R value in the visible region ($\lambda = 400 \sim 700$ nm) is ~ 15% and a strong interference effect appears in the R and EQE spectra due to the assumed flat structure.

As shown in Fig. 16.16a, for the SnO_2:F, the strong light absorption occurs at $E \geq 3.3$ eV ($\lambda \leq 375$ nm) due to the interband transition, whereas the light absorption at $\lambda > 375$ nm indicates the contribution by the free carrier absorption (Chap. 18). The TiO_2 layer shows the interband transition at $\lambda < 385$ nm. Since E_g of spiro-OMeTAD (2.95 eV) is higher than that of $MAPbI_3$, the light absorption in this layer is negligible. In addition, the light absorption in the Ag back electrode occurs mainly in the λ region below E_g of $MAPbI_3$ due to the strong light transmission in this regime. In Fig. 16.16a, IQE of $MAPbI_3$ is quite high in a wide λ region of 400–700 nm and the IQE maximum in this range is limited by the free carrier absorption of the SnO_2:F layer.

Under AM1.5G conditions, J_{sc} of the solar cell is 19.9 mA/cm^2 with a reflection loss of 3.6 mA/cm^2 and parasitic optical losses of 1.3 mA/cm^2 (SnO_2:F), 0.3 mA/cm^2 (TiO_2), and 0.1 mA/cm^2 (Ag) in the energy region above $E_g = 1.61$ eV ($MAPbI_3$). When a natural texture is present, the front light reflection is suppressed and J_{sc} of the $MAPbI_3$ solar cell increases further.

To visualize carrier generation within the $MAPbI_3$ layer, partial IQE spectra are calculated by dividing the $MAPbI_3$ layer into 400 sublayers (i.e., 1-nm thick sub-layer). In Fig. 16.16b, the partial IQE spectra calculated for different depths from the interface and wavelengths are shown. These IQE values are normalized relative to the maximum IQE value and, if the partial IQE spectra are integrated, the IQE spectrum of Fig. 16.16a can be obtained. The arrows in Fig. 16.16b denote the λ positions that correspond to the E_g (E_0), E_1 and E_2 transitions. In the E_2 transition regime, the partial IQE is limited by light absorption in the upper SnO_2:F and TiO_2 layers. At $E \geq E_1$, the partial IQE exhibits rapid decay with increasing depth because of strong light absorption within $MAPbI_3$. In contrast, in the region of $E_0 \leq E < E_1$, the IQE values are low because of the smaller α values and photocarriers are generated uniformly throughout the entire $MAPbI_3$ layer with the appearance of the optical interference effect. In this region, the electrons and holes that are generated near the front and rear interfaces, respectively, need to travel

through the whole $MAPbI_3$ layer. Therefore, the high J_{sc} of 20 mA/cm^2 observed experimentally supports the efficient carrier collection within the whole absorber layer.

In Fig. 16.16b, ΔJ_{sc} shows the J_{sc} component generated within the 1-nm-thick $MAPbI_3$ sublayer, and the integrated J_{sc} values relative to the depth are also shown. The integrated values obtained for each λ are also indicated. The calculation result of ΔJ_{sc} confirms the intense carrier generation near the TiO_2 interface and J_{sc} increases gradually at larger depth by the carrier collection in the low α region ($E_0 \leq E < E_1$). It should be emphasized that the contribution of J_{sc} at $\lambda \geq 500$ nm accounts for 73% of the total J_{sc}, confirming that the longer wavelength response is critical to realize a high J_{sc} [47].

Figure 16.16c summarizes the change in J_{sc} with $MAPbI_3$ thickness [26]. The solid lines indicate the integrated J_{sc} estimated from $MAPbI_3$ layers with discrete thicknesses ranging from 100 to 1000 nm, and the end points are shown by the solid circles. The dotted line in this figure shows the J_{sc} values obtained by changing the $MAPbI_3$ layer thickness. In Fig. 16.16c, the difference in J_{sc} observed between the dotted line and the solid line for the 1000 nm thickness indicates the influence of the back-side reflection. When the absorber thickness is 400 nm, for example, the contribution of J_{sc} improved by the back-side reflection is 2.4 mA/cm^2. Accordingly, the effect of the back-side reflection is relatively large in the hybrid solar cell and the light is absorbed effectively even in the thin layers. The optimum thickness of 400 nm confirmed in Fig. 16.16c can therefore be interpreted as a consequence of the optical confinement effect. The enhanced light absorption is particularly necessary for tandem-type solar cells and the EQE simulation of a $MAPbI_3$ top cell confirms the importance of the strong optical confinement in the long-wavelength regime (Fig. 6.8).

16.3.2 Carrier Loss Mechanisms

The optical and recombination losses in $MAPbI_3$ solar cells can be evaluated from the EQE analyses using the e-ARC method (Sect. 2.3 in Vol. 2). The ARC method is a calculation method developed originally for the estimation of the optical losses in submicron-textured solar cells, whereas the extended ARC (e-ARC) method further allows the analysis of the recombination loss. Here, from the recombination losses deduced from the e-ARC analyses [87], carrier recombination dynamics in $MAPbI_3$ solar cells are discussed.

Figure 16.17 shows the optical models for $MAPbI_3$ solar cells (a) with an HTL [88] and (b) with no HTL [89], and the corresponding EQE analysis results are shown in (c) and (d), respectively [87]. The solar cell with the HTL has a structure of glass/SnO_2:F/TiO_2/$MAPbI_3$/polytriarylamine(PTAA)/Au and shows a high efficiency of 17.6% (V_{oc} = 1.1 V, J_{sc} = 20.5 mA/cm^2 and FF = 0.78) [88]. This device incorporates the PTAA layer as the HTL and has a simple structure without a mesoporous TiO_2 layer. In the optical model of Fig. 16.17a, a complicated structure

of SnO_2:F/SiO_2/SnO_2/glass (TEC-8, see Fig. 18.25) has been simplified to a SnO_2:F (600 nm)/glass structure [26] and the layer thicknesses were deduced directly from the SEM images. In the optical model, however, the PTAA layer thickness is assumed to be zero, since the optical constants of the PTAA layer are unknown and the optical effect of the wide-gap PTAA layer ($E_g \sim 3$ eV) is negligible. For the calculation, the optical constants of SnO_2:F (Fig. 11.11 in Vol. 2), TiO_2 (Fig. 11.12 in Vol. 2), $MAPbI_3$ (Fig. 10.2 in Vol. 2) and Au (Fig. 12.8 in Vol. 2) have been used. In the EQE analyses, the carrier recombination in the TiO_2/$MAPbI_3$ interface region is further assumed. This recombination is modeled by simply dividing a $MAPbI_3$ bulk layer into two layers and treating a thin layer located at the TiO_2 interface as a "dead layer" that allows no carrier extraction (see Fig. 16.17a).

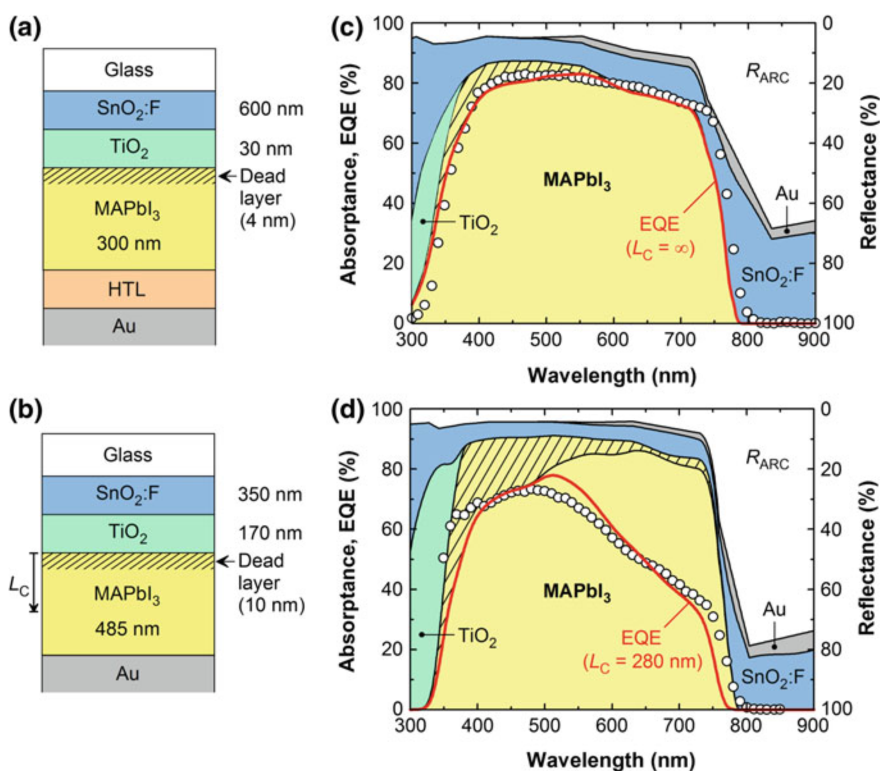

Fig. 16.17 Optical models for $MAPbI_3$ solar cells **a** with an HTL [88] and **b** with no HTL [89], and the corresponding EQE analysis results for the $MAPbI_3$ solar cells **c** with the HTL and **d** with no HTL. In **a** and **b**, the values represent the layer thicknesses in the optical model, and the thickness of the HTL layer in **a** is assumed to be zero. For the $MAPbI_3$ layers, the presence of optical dead layers near the TiO_2 interfaces is assumed. In **c** and **d**, the EQE analyses are carried out based on the e-ARC method using the carrier collection length (L_C) as a fitting parameter. The calculated EQE spectra are shown by red lines. The hatched-line regions show the EQE losses originating from the front dead layers. The analysis data are taken from [87]

In Fig. 16.17c, the absorptance spectra of the solar-cell component layers calculated using the optical model of Fig. 16.17a are shown. The R_{ARC} shows the reflectance deduced from the ARC method, and the R_{ARC} spectrum includes the contribution of light scattering generated in the textured solar cell (see Sect. 2.2.3 in Vol. 2). In this figure, the yellow-colored region shows the light absorption in the $MAPbI_3$, and the hatched-line region corresponds to the EQE loss caused by the front dead layer. The red line indicates the EQE spectrum calculated by e-ARC, from which the carrier collection length (L_C) can be determined. In the EQE analysis using the e-ARC method, the L_C value modeled by $H(\lambda) = 1 - \exp[-\alpha(\lambda)L_C]$ is used as a fitting parameter, where $H(\lambda)$ and $\alpha(\lambda)$ are the carrier collection efficiency and absorption coefficient spectrum of the absorber layer, respectively. In this simple model, L_C shows a meaningful value only when L_C is smaller than the layer thickness and we obtain $L_C = \infty$ when all the carriers are collected (see Fig. 2.14 in Vol. 2). In Fig. 16.17c, the calculated EQE spectrum shows good agreement with the experimental result (open circles) when the thickness of the dead layer is 4 nm with $L_C = \infty$, indicating that the dominant recombination occurs only near the TiO_2 interface and the carrier loss near the HTL interface is negligible.

On the other hand, the slight disagreement of the calculated EQE, observed at $\lambda = 720$–800 nm, can be attributed to the calculation errors of R_{ARC}. Specifically, when the layer thickness of solar cells is thin, the interference fringe becomes large and the calculation of R_{ARC} by the ARC method fails near the E_g region where R shows a sharp increase. This problem can be avoided if the experimental R spectrum obtained from an actual solar cell is used in (2.26) in Vol. 2. In the analysis of Fig. 16.17c, however, the error in the R_{ARC} calculation affects J_{sc} only slightly (0.4 mA/cm^2).

The solar cell with no HTL shown in Fig. 16.17b has a structure of glass/SnO_2:F/compact TiO_2/mesoporous TiO_2-$MAPbI_3$/$MAPbI_3$/Au [89]. Quite fortunately, the optical response of the mesoporous TiO_2-$MAPbI_3$ mixed-phase layer can be expressed as the two separate flat layers of the TiO_2 and $MAPbI_3$ [26]. In this analysis, the TiO_2 volume fraction within the mesoporous layer is assumed to be 30% (porosity 70%).

Figure 16.17d shows the result of the EQE analysis performed for the solar cell with no HTL [87]. It can be seen that the experimental EQE spectrum of this solar cell is quite different, compared with the solar cell with the HTL. In particular, the EQE response in the longer λ region decreases significantly when an HTL is not present [90–93]. The red line in this figure represents the EQE spectrum calculated assuming the carrier recombination in the front and rear interface regions using e-ARC. This EQE analysis reveals that the thickness of the front recombination layer is 10 nm with $L_C = 280$ nm. Thus, the above result confirms that the carrier collection is hindered strongly when the HTL is not present and the effect of the carrier recombination appears primarily as the reduction of the EQE response in the low α region ($\lambda > 600$ nm).

Figure 16.18 shows the band diagrams proposed for $MAPbI_3$ solar cells (a) with an HTL (spiro-OMeTAD) and (b) with no HTL [87]. It can be seen that, in $MAPbI_3$ solar cells, the electrons and holes generated within the absorber layer are collected

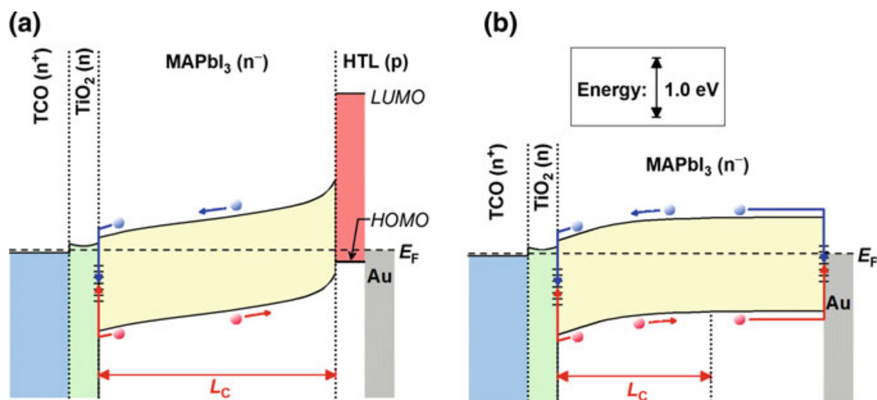

Fig. 16.18 Band diagrams proposed for $MAPbI_3$ solar cells with an HTL (spiro-OMeTAD) and with no HTL [87]. In this figure, L_C represents the carrier collection length determined from the EQE analyses of Fig. 16.17

in the front and rear electrodes without any potential barriers [6]. It is generally assumed that the operation of $MAPbI_3$ solar cells occurs by the formation of a *p-i-n* type structure [11, 94–97], as confirmed by the electron-beam induced current (EBIC) [94, 98] and Kelvin probe force microscopy [95] characterizations. However, the carrier type of $MAPbI_3$ layers is basically *n*-type, and the Fermi level (E_F) of a standard $MAPbI_3$ locates more closer to CBM with an electron concentration of $\sim 10^{17}$ cm^{-3} [99]. When the $MAPbI_3$ layer shows *n*-type conductivity, the electric field is expected to concentrate at the $MAPbI_3(n)$/HTL(p) interface with a weak electric field at the $TiO_2(n)/MAPbI_3(n)$ interface, as illustrated in Fig. 16.18a. Thus, the relatively strong front-carrier recombination near the TiO_2 interface can be interpreted by the weaker electric field in this region. In contrast, the carrier recombination in the solar-cell bottom region is suppressed most likely due to the presence of the strong electric field near the HTL. From the above results, the electric-field-assisted carrier collection by the formation of a p-n^--n type structure has been proposed for $MAPbI_3$ solar cells [87]. The rapid degradation of the solar cell characteristics upon air exposure could be attributed, in part, to the elimination of the strong electric field in the rear p-n junction region.

When the HTL is not present, however, the flat-band formation is expected to occur by the absence of the electric field in the bottom region (Fig. 16.18b), as evidenced by EBIC [98]. In this device, the photocarrier collection occurs through the carrier diffusion, and the intensified recombination in the rear interface region lowers the EQE response in the longer λ region [87, 92]. The lower V_{oc} observed in $MAPbI_3$ solar cells with no HTL [90–92, 100] can be interpreted by the smaller built-in potential.

Earlier DFT studies of $MAPbI_3$ revealed that mid-gap states are not created by the vacancy/interstitial-type defects in $MAPbI_3$ [64, 101, 102], although the formation of complex defects is still possible [103]. Moreover, in the grain boundary

region of $MAPbI_3$, the PbI_2-rich phase having larger E_g is formed, suppressing the carrier recombination in the grain boundary region effectively [104]. In $MAPbI_3$ solar cells, therefore, the carrier recombination is generally considered to occur in the interface regions. Nevertheless, V_{oc} of $MAPbI_3$ solar cells varies with the grain size [105], suggesting the possible recombination in the grain boundary region.

Figure 16.19 illustrates the optical and recombination losses in the $MAPbI_3$ solar cell with an HTL [87], determined from the EQE analysis of Fig. 16.17c. The numerical values in the figure represent the corresponding current densities in units of mA/cm^2. The maximum J_{sc} value attainable under AM1.5G conditions is also shown and, from the ratio of output J_{sc} divided by the maximum attainable J_{sc} value, the optical gain of this solar cell is determined to be 70% (18.7 mA/cm^2). This particular solar cell shows a large reflection loss (3.2 mA/cm^2) due to the lack of an anti-reflection coating and a rather flat layer structure with a thin absorber-layer thickness (~300 nm). The parasitic absorption by the front TCO layer, originating mainly from free carrier absorption, reduces J_{sc} further by 3 mA/cm^2. The parasitic absorption of the TCO can be reduced largely by employing high-mobility TCO layers (Chap. 19). The recombination loss indicated in this figure corresponds to the interface recombination in the TiO_2 interface region.

It should be emphasized that the $MAPbI_3$ solar cell shows quite small overall optical losses, compared with other photovoltaic devices including $CuInGaSe_2$ (Fig. 2.11b in Vol. 2), $Cu_2ZnSnSe_4$ (Fig. 2.15b in Vol. 2) and CdTe (Fig. 2.21b in Vol. 2) solar cells. In particular, the parasitic absorption within the TiO_2 and HTL layers is negligible and the major optical loss occurs only in the front TCO layer, which can be optimized further. Thus, a quite high conversion efficiency reported

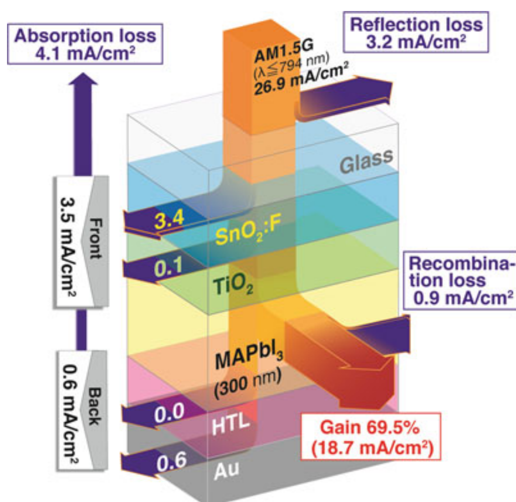

Fig. 16.19 Optical and recombination losses deduced from the EQE analysis performed for the $MAPbI_3$ solar cell shown in Fig. 16.17c [87]. The numerical values represent the corresponding current densities in units of mA/cm^2. The maximum J_{sc} value attainable under AM1.5G conditions is also indicated. The optical gain shows the ratio of output J_{sc} divided by the maximum attainable J_{sc} value

for $MAPbI_3$ solar cells (~20%) can be understood partly by the low parasitic absorption within the solar cell component layers [26].

As a result, the excellent performance of $MAPbI_3$ hybrid solar cells can be interpreted as being due to a combination of (a) high α values comparable to those of $CuInGaSe_2$ and CdTe (Fig. 1.6), (b) E_g being close to the optimum value of 1.4 eV (Fig. 1.5 in Vol. 2) and the sharp absorption onset near E_g (low E_U) (Fig. 16.6), which is expected to reduce the open-circuit voltage loss (see Fig. 1.7b in Vol. 2) [45], (c) efficient free carrier generation by non-excitonic semiconductor-type transitions within the PbI_3^- component in the whole visible region (Fig. 16.9), (d) low levels of carrier recombination by electric-field assisted carrier collection (Figs. 16.17 and 16.18) and (e) the high optical confinement and low parasitic absorption in the solar cells (Figs. 16.16 and 16.19).

16.4 Real Time Spectroscopic Ellipsometry of Thin Film Perovskites

Real time spectroscopic ellipsometry (RTSE) monitoring enables fundamental studies of (i) the growth evolution of both perovskite thin films ($MAPbI_3$ and related materials) and component materials (PbI_2 and other inorganics, MAI and other organics) as well as (ii) the stability of the resultant films post-deposition. These studies enable detection of phase instabilities and changes in composition and structure occurring either during growth as a function of different deposition conditions or after deposition as a function of external stimuli known to cause perovskite decomposition or phase changes.

There are several methods already employed for perovskite deposition, each with their own region of parameter space yielding optimized materials for devices. Some of these methods are more easily adapted to RTSE monitoring of film growth than others. One case study described here will involve vapor deposition of $MAPbI_3$ enabled by evaporation of PbI_2 in a MAI vapor rich vacuum chamber. Figure 16.20 shows a schematic of a vacuum chamber outfitted with windows for in situ RTSE measurements during evaporation of PbI_2, MAI, and other source materials. This evaporation-based approach has multiple utility: (i) PV device quality $MAPbI_3$ can be made as films and layers in functioning solar cells and (ii) fundamental studies of the component materials MAI and PbI_2 are also enabled. Figure 16.21 shows spectra in ε for component MAI and PbI_2 as obtained from RTSE measurements of their respective component films with analysis using a multiple time point approach to obtain the most average spectra in ε for each film [106, 107]. For single component materials like MAI and PbI_2, multiple time and global sum-of-σ (Σσ) minimization approaches are suitable for ascertaining ε as well as the time evolution of structural parameters such as bulk layer and surface

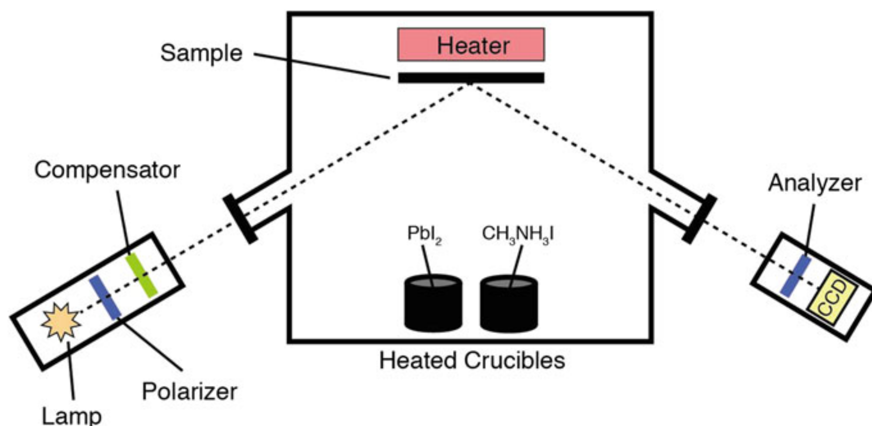

Fig. 16.20 Schematic for real time spectroscopic ellipsometry (RTSE) monitoring of $MAPbI_3$ from multi-source vapor deposition. Adapted from [106]

roughness thickness, as has been detailed for other PV absorber and component materials in other chapters. Spectra in ε for $MAPbI_3$ shown in Fig. 16.21 has been obtained using a divided spectral range analysis [108] for ellipsometric spectra collected ex situ from a vapor deposited film. This particular sample had relatively high crystalline quality, but a small fraction of PbI_2 also present as confirmed with x-ray diffraction and analysis of ellipsometric spectra using ε for phase-pure solution deposited $MAPbI_3$ and PbI_2 in a Bruggeman effective medium approximation [107].

Due to the optical contrast between MAI, PbI_2, and $MAPbI_3$ shown in Fig. 16.21, it is possible to deduce some relative fractional components of each in a phase-segregated multi-component film from ellipsometric spectra. When

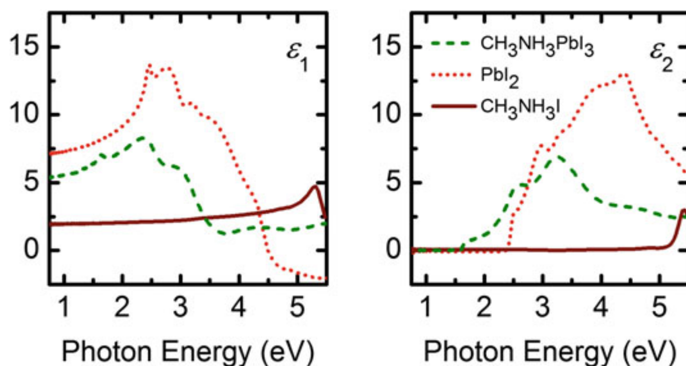

Fig. 16.21 Reference spectra in ε for vapor deposited PbI_2, MAI, and $MAPbI_3$ used for analysis of RTSE data collected during growth and degradation [107]

ellipsometric spectra are collected in situ as a function of time, like RTSE, it is possible to better understand the dynamics of what occurs—namely the appearance or disappearance of particular components. Two case studies to be investigated here involve monitoring (i) vapor deposition of perovskite films enabled by in situ RTSE measurements and (ii) degradation of a film post-deposition upon exposure to laboratory ambient air. For studies of growth evolution, the deposition system must be adaptable to in situ RTSE via appropriate windows and a clear beam-path. In the case of post-deposition changes in films, all that is required is that a sample be first produced and that the post-deposition environment enables in situ ellipsometry measurements. Here we have applied the simplest post-deposition environment possible, namely leaving the sample exposed to laboratory ambient conditions while mounted upon a spectroscopic ellipsometer.

16.4.1 RTSE During Vapor Deposition

As the first example, consider RTSE measurements collected in situ during thin film vapor deposition using MAI and PbI_2 sources. The intended film composition is predominately polycrystalline $MAPbI_3$, possibly with some other components to manipulate the grain boundary chemistry. If not in the appropriate region of deposition parameter space, it is likely to produce significant amounts of phase-segregated PbI_2 + MAI instead of the desired perovskite. These phase segregated regions have been observed near the substrate/film and film/ambient interfaces, possibly where interfacial effects impact perovskite stability. The relative amounts of all components may vary with time during deposition. For vapor deposited materials, changes in source-to-substrate throw distance and deposition sequence (simultaneous or alternating source fluxes) can manipulate the final relative amounts of each component. By analyzing vapor deposited films prepared under a variety of conditions, a relatively flexible structural model has been developed to analyze ellipsometric spectra as shown in Fig. 16.22 [106]. The model itself relies on (i) a known substrate, with optical properties and structure most directly obtained from an ellipsometry measurement prior to film deposition, (ii) a substrate-adjacent Bruggeman effective medium approximation (EMA) layer consisting of PbI_2 + MAI, (iii) a $MAPbI_3$ layer, (iv) a EMA layer of PbI_2 + $MAPbI_3$ + void, and (v) a surface roughness EMA layer of 0.5 void and 0.5 PbI_2 + MAI material fractions. Reference spectra in ε shown in Fig. 16.21 are used for the component materials in this structure. To aid in interpretation of the results, individual layer thicknesses and material fractions are combined into effective material thicknesses (d_{eff}) by multiplying each layer thickness (d) by the relative material fraction within that layer (f) such that $d_{\mathrm{eff}} = d \times f$. These effective material thicknesses of $MAPbI_3$, PbI_2 and MAI near the substrate, and surface PbI_2 and MAI are calculated from the sum of effective material thicknesses of each layer.

Figure 16.23 shows effective thicknesses of the phase segregated PbI_2 and MAI near the film surface and near the substrate as well as the $MAPbI_3$ component [106].

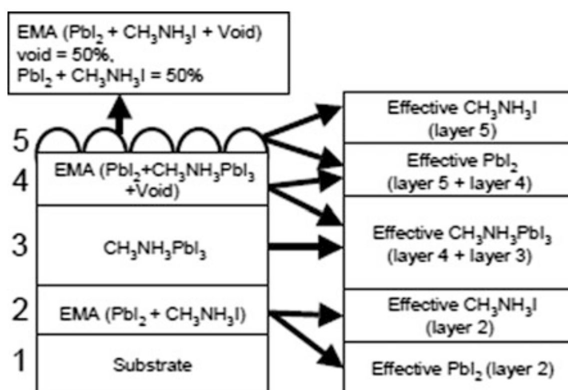

Fig. 16.22 Structure model used in analysis of RTSE data collected during vapor deposition and post-deposition degradation. The layered structure for analysis of ellipsometric spectra consists of (1) a known substrate, (2) a substrate-adjacent Bruggeman effective medium approximation (EMA) layer consisting of PbI_2 + MAI, (3) a $MAPbI_3$ layer, (4) a EMA layer of PbI_2 + $MAPbI_3$ + void, and (5) a surface roughness EMA layer of 0.5 void and 0.5 PbI_2 + MAI material fractions. The effective material thicknesses of $MAPbI_3$, PbI_2 and MAI near the substrate, and surface PbI_2 and MAI are calculated from the sum of the layer thicknesses weighted by the respective material fraction. Adapted from [106, 107]

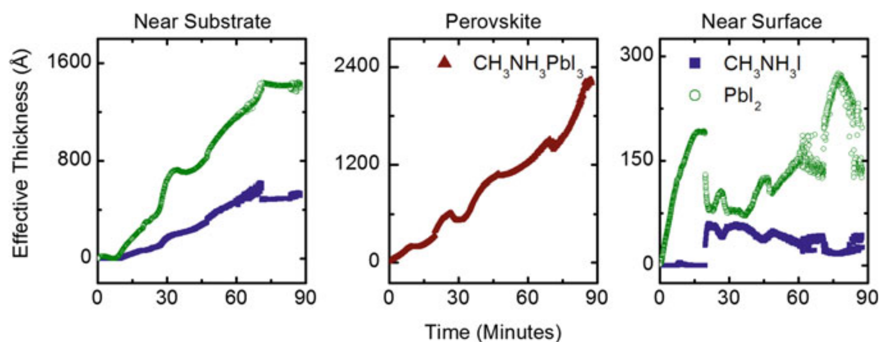

Fig. 16.23 Growth evolution from RTSE in the form of effective material thicknesses of $MAPbI_3$, PbI_2 and MAI near the substrate, and surface PbI_2 and MAI as functions of time during vapor deposition [106]

This particular sample has been made on thermal oxide (250 Å thick) coated crystal silicon with a throw distance of 50 cm and MAI and PbI_2 sources heated to 100 and 300 °C, respectively. For the first ~10 min of the deposition, $MAPbI_3$ grows with some excess surface PbI_2. $MAPbI_3$ thickness increases throughout the deposition, however at 10 min of growth effective thicknesses of PbI_2 and MAI near the substrate begin to increase. After ~20 min variable amounts of both PbI_2 and MAI appear on the film surface. The appearance of significant amounts of both PbI_2 and MAI near the surface and substrate interfaces implies that moderately thin $MAPbI_3$

grown under these conditions may not be stable. After sufficient time has passed, ~72 min, the near-substrate PbI_2 and MAI effective thicknesses stabilize and the $MAPbI_3$ thickness deposition rate increases.

To summarize, RTSE analysis of *this deposition* shows three stages: (i) an initial thin $MAPbI_3$ layer with a slightly lower growth rate from 0–10 min, (ii) continued $MAPbI_3$ growth accompanied by phase segregation of MAI and PbI_2 from 10–72 min, and (iii) stabilization of MAI and PbI_2 effective thicknesses and an increase in growth rate for $MAPbI_3$ from 72 min until the end of the deposition. Samples prepared under different deposition conditions have shown immediate appearance of MAI and PbI_2 components with the perovskite, appearance of these components followed by formation of the perovskite, or different behaviors for each component layer. The ability to apply RTSE during vapor deposition shows the possibility of real time monitoring and control of film composition. These types of RTSE measurements have been made both on test substrates for underlying smoothness and structural simplicity (e.g. oxide covered crystal silicon and glass) and in the superstrate PV device configuration on rough SnO_2:F coated glass with an electron selective layer (ESL).

16.4.2 RTSE Post-deposition

As mentioned elsewhere in this chapter, these perovskites may undergo reversible or irreversible changes with temperature variations, applied bias, exposure to moisture and humidity, and under ultraviolet light. In principle, in situ spectroscopic ellipsometry enables monitoring of the changes in optical response and structure for samples prepared by any deposition method if the measurements can be conducted in a suitably controlled environment so that "before" and "after" characteristics are observed. In situ RTSE enables data to be collected during the respective process, whatever it may be. Temperature controlled stages, biased electrical contacts on films, environmental chambers, and unpolarized intense light sources can be readily applied to these kinds of samples. The sample may begin to change immediately upon exposure to laboratory ambient conditions. This exposure to laboratory ambient, nominally room temperature ~20 °C, illuminated, and relative humidity ~50%, may cause a $MAPbI_3$ perovskite to change and decompose into its constituent components PbI_2 and MAI.

In situ RTSE has been performed on a vapor deposited initially predominately $MAPbI_3$ film prepared on soda lime glass placed on an ellipsometer [107]. Ellipsometric spectra have been collected every 5 min for 48 h. To fit ellipsometric spectra at each measurement time, reference ε from Fig. 16.21 and the structural model from Fig. 16.22 used to describe RTSE of vapor deposition growth have been applied to describe phase segregation and film decomposition. The behavior of the sample post-deposition in ambient laboratory conditions shows similarities to that observed for un-optimized material during growth. Namely, phase segregated MAI and PbI_2 components accumulate near the substrate/film and film/ambient

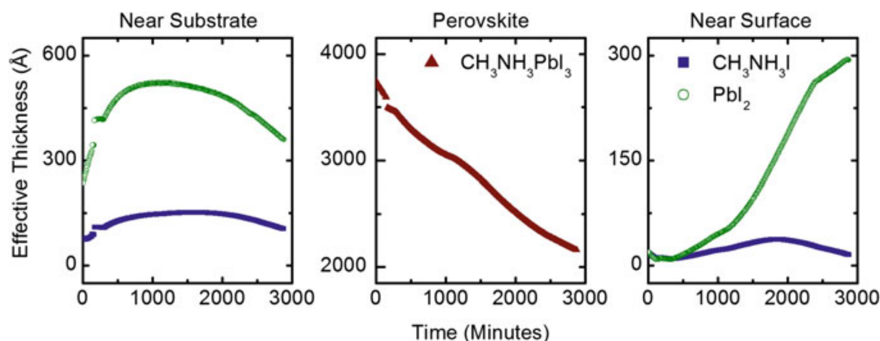

Fig. 16.24 Effective material thicknesses of $MAPbI_3$, PbI_2 and MAI near the substrate, and surface PbI_2 and MAI as functions of time during post-deposition exposure in laboratory ambient conditions monitored by RTSE [107]

interfaces. Effective material component thicknesses are shown in Fig. 16.24. It is clear that the $MAPbI_3$ effective thickness decreases with time over the RTSE measurements. This decrease in effective $MAPbI_3$ thickness occurs with initial increases in the MAI and PbI_2 effective thicknesses near the substrate and surface, implying that phase segregation of the perovskite has occurred. After about 1500–2000 min have passed, the amount of MAI and PbI_2 components near the substrate begin to decrease while the PbI_2 near the surface continues to increase and the surface MAI thickness is much lower in magnitude. The sum of all PbI_2 increases with time, $MAPbI_3$ decreases with time, and MAI first increases then weakly decreases. This indicates that as some of the perovskite is decomposing, the constituents may be reacting.

An interesting observation comes from the quality of the fit over the course of decomposition, represented by the mean square error (MSE) in Fig. 16.25. Reference spectra in ε are used over the full measurement time, however the quality of the fit decreases (MSE increases) at later times. Recent work has shown that changes in the perovskite component optical properties can reduce and stabilize the MSE [109]. A possible explanation for the changes in ε observed may be related to the sum of the effective MAI thicknesses. When considering the density and expected amount of MAI and PbI_2 produced by decomposition of $MAPbI_3$, the

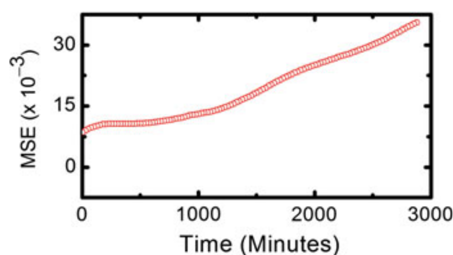

Fig. 16.25 Mean square error (MSE) as a function of time for fits to RTSE data collected during post-deposition exposure to laboratory ambient conditions, with results in Fig. 16.24 [109]

effective thicknesses shown in Fig. 16.24 imply that some MAI is not accounted in the model. Process parameter dependent phase diagrams for these perovskites [110] indicate that a "stacked perovskite sheet" structure consisting of thin perovskite layers interspaced by MAI exists. This explanation possibly accounts for the missing effective MAI thickness, and the transition from perovskite to stacked perovskite sheet structure could be responsible for the variation in ε needed to reduce MSE of RTSE data fitting at later times during degradation.

16.5 Characterization of Degradation in Hybrid Perovskite Materials

One of the key aspects to achieve the full potential of PV devices based on hybrid perovskites is to control the stability of these materials. Up to date, different fabrication protocols can be followed resulting in different film morphologies which might lead to variable degradation pathways [111]. However, most approaches to produce materials, mainly low-temperature evaporation or solution-based, are apt to result in similar high-performance materials and subsequent devices with rather comparable efficiencies and lifetimes. Several environmental factors such as humidity, heat, and illumination can compromise the stability both of the perovskite materials, in particular $MAPbI_3$, and of the solar cell devices. The effect of humidity as the main degradation agent has been investigated by SE, and different results have been detected, from reversible hydration to irreversible decomposition of $MAPbI_3$ [51]. The perovskite structure of $MAPbI_3$ is depicted in Fig. 16.26a. Two hydrated $MAPbI_3$ crystal phases form by water incorporation with either one or two water molecules per formula unit. The monohydrate and dihydrate crystal structures are shown in Fig. 16.26b, c, respectively.

In the seminal work by Leguy et al. [51], solution-processed perovskite films, single crystals and full devices were exposed to high relative humidity (RH) around 75% (±5%). The hydration mechanism was first investigated optically by SE on single crystals of $MAPbI_3$. The crystals were exposed to a humid ambient with

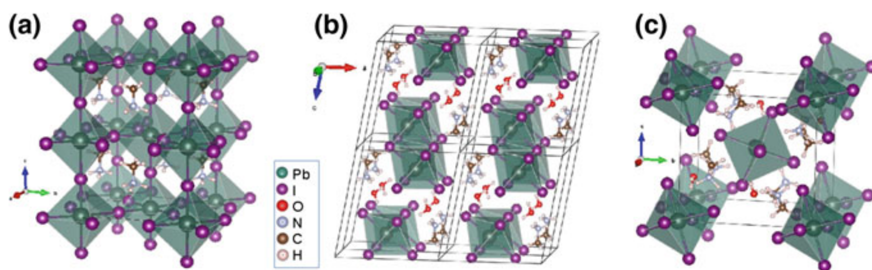

Fig. 16.26 Crystal structures of the phases related to hydration of $MAPbI_3$: **a** pristine perovskite phase, **b** $MAPbI_3 \cdot H_2O$ (monohydrate), and **c** $MAPbI_3 \cdot 2H_2O$ (dihydrate)

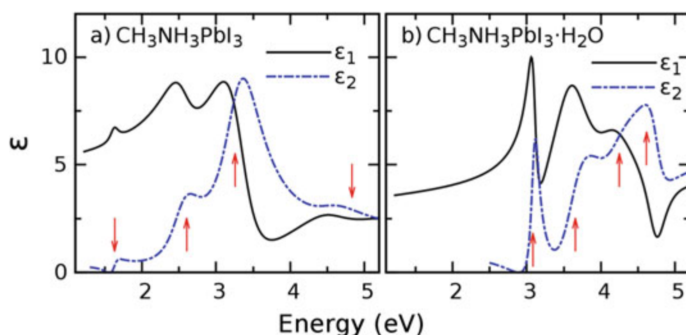

Fig. 16.27 Dielectric functions determined by ellipsometry of **a** $MAPbI_3$ single crystal and **b** $MAPbI_3 \cdot H_2O$ monohydrate phase. Data from [51]. Values of ε_2 in the sub-bandgap region are spurious, due to the modelling. Arrows indicate the energies of the main critical points obtained from fits to second derivative spectra [51, 52].

nitrogen as carrier gas at room temperature (21 °C). Figure 16.27 shows the dielectric function determined in a crystal before (a) and after 60 h of exposure (b) to the humid ambient. The effect of water was to form a new crystal structure identified by X-ray diffraction as the monohydrate $MAPbI_3 \cdot H_2O$, see Fig. 16.26b. The initially black $MAPbI_3$ crystal with band gap ~1.6 eV becomes transparent (whitish) in the wet ambient, with a band gap of ~3.1 eV.

When subsequently exposed to a dry atmosphere, the crystal instantly starts to convert back to the initial structure, as displayed in Fig. 16.28, with the process ending in the full recovery of the material. The spectra measured both during hydration or dehydration can be well understood by an effective Bruggeman mixture of the two phases, therefore suggesting that water is highly mobile within the perovskite lattice with the transformation occurring more or less homogeneously throughout the sample. Both from diffraction and SE investigations it appears that dehydration is faster than hydration. However, the time needed for the transformation depends from the initial material condition: the presence of defects such as pores or grain boundaries facilitate water diffusion through the sample. Consequently, the transformation of thin polycrystalline films starts almost instantaneously [51, 59] because water penetrates more efficiently within the grains than in compact single crystals. The study on thin films [51] lead to the following equations for the hydration of $MAPbI_3$:

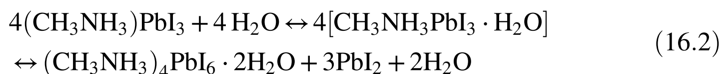

$$\begin{aligned} &4(CH_3NH_3)PbI_3 + 4\,H_2O \leftrightarrow 4[CH_3NH_3PbI_3 \cdot H_2O] \\ &\leftrightarrow (CH_3NH_3)_4PbI_6 \cdot 2H_2O + 3PbI_2 + 2H_2O \end{aligned} \tag{16.2}$$

Equation (16.2) describes a two-step process in which the crystal structure of $MAPbI_3$ is first saturated with one water molecule per unit cell, followed by the insertion of a second water molecule upon longer exposure to humidity. Accordingly, the monohydrate is an intermediate product that can be easily converted back

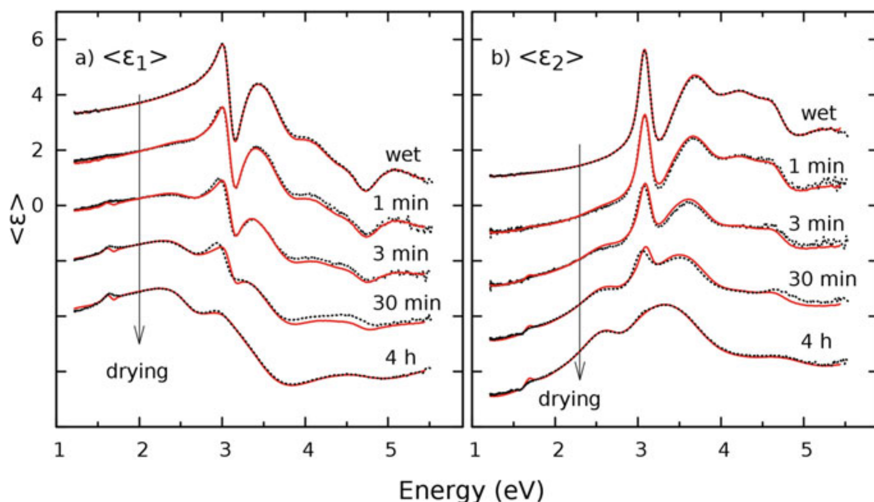

Fig. 16.28 Ellipsometric spectra presented as pseudo-dielectric functions measured during the back-conversion from a $MAPbI_3 \cdot H_2O$ monohydrate crystal to the pristine $MAPbI_3$ phase, see [51]. Dotted lines display the experimental results and solid lines the simulations based on an effective Bruggeman mixture of the two phases and voids. The chosen time intervals represent approximately equidistant volume fractions, i.e., variations of 0.25 in hydrate content upon drying from 1 (wet) to 0. The vertical scale corresponds to the uppermost spectrum and the rest are shifted downwards by steps of −2 for clarity

to $MAPbI_3$. However, when the reaction is driven further to the right of the stoichiometric equation (16.2), the formation of the dihydrated crystal phase initiates the decomposition with formation of PbI_2 and release of water ending in an irreversible degradation of the film. In polycrystalline film material the transformation is reversible up to a certain point before any dihydrate formation. Later, both reactions may happen simultaneously at different film locations. For instance, decomposition may appear at grain boundaries while there are still grains of pristine $MAPbI_3$. In [51], this situation was detected after a monohydrate content in the film of about 20% was reached. Then, the roughness increased dramatically with formation of needle-like structures which are presumably the dihydrate. Therefore, the exact degradation pathways depend on the sample morphology. Furthermore, temperature and illumination also play a role but the interplay of all causes is not well established yet. A decisive factor is whether water condensation occurs on the surface of the film or not [51, 111]. If water condensation is avoided, the process is reversible in films and even in solar cells, where the photovoltaic performance of "degraded" devices was recovered with a simple drying step under a nitrogen stream for a few hours [51].

Shirayama et al. [59] have characterized the degradation processes of ultra-smooth MAPI thin films prepared by a laser evaporation technique. In this study, the exposure of the $MAPbI_3$ samples to humid air was carried out under ordinary room illumination. They observed that at 75% RH, the surface reaction

was quite rapid and the mirror-like surface of the pristine $MAPbI_3$ layer became whitish within 20 s after the air exposure. Unfortunately, reliable optical characterization of this process was quite difficult due to the extensive developed roughness and further analysis was not made. The authors monitored the film changes at RH of 40%, observing by SEM that even at this relatively low RH value [112], large structural changes in the near-surface region take place after a short exposure. The changes in optical functions are displayed in Fig. 16.29 as pseudo-dielectric imaginary part $<\varepsilon_2>$. Although SEM indicated a much faster surface transformation, changes in the optical properties start to be evident at times beyond 2 h. In particular, absorption features that coincide with those of a PbI_2 reference start to appear clearly while the band gap transition at 1.6 eV gradually disappears with the exposure time until at $t \geq 24$ h, the bandgap is located at 2.4 eV, consistent with that of PbI_2. Even if during the initial degradation process ($t \leq 3$ h) the change of the $<\varepsilon_2>$ spectrum is rather small, the E_2 peak shows a distinct peak shift which has been related to the formation of the hydrate phase in the surface region. In contrast to the film thickness increase during hydration observed in [51], at low RH [59] a reduction of the total layer thickness was observed. This was explained by the concurrence of a desorption reaction in addition to the hydration reactions of (16.2). The thickness reduction occurs according to:

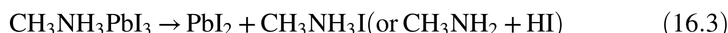

$$CH_3NH_3PbI_3 \rightarrow PbI_2 + CH_3NH_3I(\mathrm{or}\, CH_3NH_2 + HI) \quad (16.3)$$

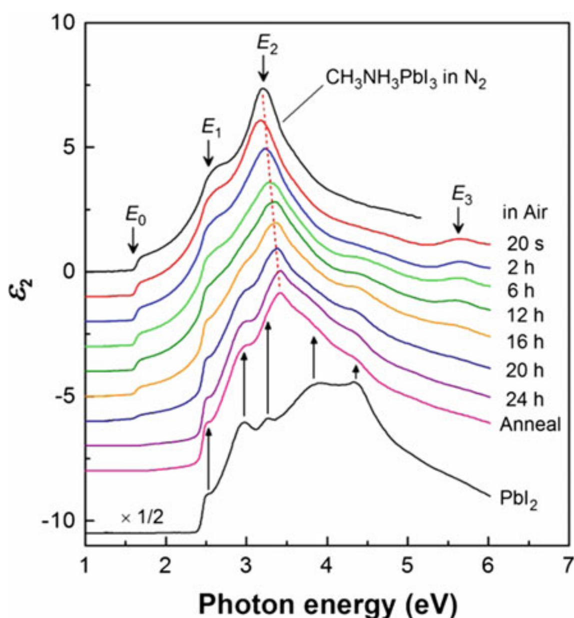

Fig. 16.29 Variation of ε_2 reported in [59] for a $MAPbI_3$ thin film during exposure to air at 40% RH. The spectra of $MAPbI_3$ in N_2 and of a PbI_2 film are plotted for reference. The degraded sample spectrum does not change after a thermal annealing at 100 °C, indicating its stability

In this study it was emphasized that the time scale of the $MAPbI_3$ degradation observed at 40% RH (1 day) starts from the surface and is much faster than that reported in earlier studies at similar RH (1 month) without illumination [113]. This correlates quite well with the efficiency loss observed in actual solar cells (1–2 days at 55% RH) [54]. Accordingly, the degradation of hybrid perovskite solar cells in humid air is most likely caused by the rapid changes near the interfaces that conform the devices. In fact, the contacts performance has been found to degrade faster than the perovskite active layer itself [114].

As a conclusion of these studies, it seems that the degradation processes depend strongly both on the morphology of the samples and on the ambiental conditions, but mainly on the latter. Although humidity is an essential parameter, also temperature and illumination are important degradation agents. Structural studies combined with SE measurements provide insight into the degradation pathways. SE monitoring can be very helpful to follow the changes, allowing to identify the degradation species and to keep track of the thickness and roughness variations associated to these changes.

Acknowledgements N. J. Podraza and K. Ghimire would like to acknowledge D. Zhao, A. Cimaroli, Y. Ke, F. Hong, T. Shi, and Prof. Y. Yan for providing samples and materials; M. Junda for graphical assistance; and the National Science Foundation for financial support (CHE-1230246). M. I. Alonso acknowledges financial support from the Spanish Ministry of Economy and Competitiveness, through grants CSD2010-00044, MAT2015-70850-P, and the "Severo Ochoa" Programme for Centres of Excellence in R&D (SEV-2015-0496).

References

1. W.S. Yang, J.H. Noh, N.J. Jeon, Y.C. Kim, S. Ryu, J. Seo, S.I. Seok, Science **348**, 1234 (2015)
2. D. Bi, W. Tress, M.I. Dar, P. Gao, J. Luo, C. Renevier, K. Schenk, A. Abate, F. Giordano, J.-P. Correa Baena, J.-D. Decoppet, S.M. Zakeeruddin, M.K. Nazeeruddin, M. Grätzel, A. Hagfeldt, Sci. Adv. **2**, e1501170 (2016)
3. M. Saliba, T. Matsui, J.-Y. Seo, K. Domanski, J.-P. Correa-Baena, M.K. Nazeeruddin, S.M. Zakeeruddin, W. Tress, A. Abate, A. Hagfeldt, M. Grätzel, Energy Environ. Sci. **9**, 1989 (2016)
4. T.J. Jacobsson, J.-P. Correa-Baena, M. Pazoki, M. Saliba, K. Schenk, M. Grätzel, A. Hagfeldt, Energy Environ. Sci. **9**, 1706 (2016)
5. A. Kojima, K. Teshima, Y. Shirai, T. Miyasaka, J. Am. Chem. Soc. **131**, 6050 (2009)
6. M.M. Lee, J. Teuscher, T. Miyasaka, T.N. Murakami, H.J. Snaith, Science **338**, 643 (2012)
7. M. Liu, M.B. Johnston, H.J. Snaith, Nature **501**, 395 (2013)
8. J. Burschka, N. Pellet, S.-J. Moon, R. Humphry-Baker, P. Gao, M.K. Nazeeruddin, M. Grätzel, Nature **499**, 316 (2013)
9. T. Baikie, Y. Fang, J.M. Kadro, M. Schreyer, F. Wei, S.G. Mhaisalkar, M. Grätzel, T. J. White, J. Mater. Chem. A **1**, 5628 (2013)
10. P. Gao, M. Grätzel, M.K. Nazeeruddin, Energy Environ. Sci. **7**, 2448 (2014)
11. M.A. Green, A. Ho-Baillie, H.J. Snaith, Nat. Photon. **8**, 506 (2014)
12. H.S. Jung, N.-G. Park, Small **11**, 10 (2015)

13. T.M. Brenner, D.A. Egger, L. Kronik, G. Hodes, D. Cahen, Nat. Rev. Mater. **1**, 15007 (2016)
14. J.S. Manser, J.A. Christians, P.V. Kamat, Chem. Rev. **116**, 12956 (2016)
15. T.M. Koh, K. Fu, Y. Fang, S. Chen, T.C. Sum, N. Mathews, S.G. Mhaisalkar, P.P. Boix, T. Baikie, J. Phys. Chem. C **118**, 16458 (2014)
16. G.E. Eperon, S.D. Stranks, C. Menelaou, M.B. Johnston, L.M. Herz, H.J. Snaith, Energy Environ. Sci. **7**, 982 (2014)
17. S. Pang, H. Hu, J. Zhang, S. Lv, Y. Yu, F. Wei, T. Qin, H. Xu, Z. Liu, G. Cui, Chem. Mater. **26**, 1485 (2014)
18. Q. Han, S.-H. Bae, P. Sun, Y.-T. Hsieh, Y. Yang, Y.S. Rim, H. Zhao, Q. Chen, W. Shi, G. Li, Y. Yang, Adv. Mater. **28**, 2253 (2016)
19. M.T. Weller, O.J. Weber, J.M. Frost, A. Walsh, J. Phys. Chem. Lett. **6**, 3209 (2015)
20. N. Pellet, P. Gao, G. Gregori, T.-Y. Yang, M.K. Nazeeruddin, J. Maier, M. Grätzel, Angew. Chem. Int. Ed. **53**, 3151 (2014)
21. J.-W. Lee, D.-H. Kim, H.-S. Kim, S.-W. Seo, S.M. Cho, N.-G. Park, Adv. Energy Mater. **5**, 1501310 (2015)
22. Z. Li, M. Yang, J.-S. Park, S.-H. Wei, J.J. Berry, K. Zhu, Chem. Mater. **28**, 284 (2016)
23. C. Yi, J. Luo, S. Meloni, A. Boziki, N. Ashari-Astani, C. Grätzel, S.M. Zakeeruddin, U. Röthlisberger, M. Grätzel, Energy Environ. Sci. **9**, 656 (2016)
24. D.P. McMeekin, G. Sadoughi, W. Rehman, G.E. Eperon, M. Saliba, M.T. Hörantner, A. Haghighirad, N. Sakai, L. Korte, B. Rech, M.B. Johnston, L.M. Herz, H.J. Snaith, Science **351**, 151 (2016)
25. J.P. Perdew, K. Burke, M. Ernzerhof, Phys. Rev. Lett. **77**, 3865 (1996)
26. M. Shirayama, H. Kadowaki, T. Miyadera, T. Sugita, M. Tamakoshi, M. Kato, T. Fujiseki, D. Murata, S. Hara, T.N. Murakami, S. Fujimoto, M. Chikamatsu, H. Fujiwara, Phys. Rev. Appl. **5**, 014012 (2016)
27. M. Kato, T. Fujiseki, T. Miyadera, T. Sugita, S. Fujimoto, M. Tamakoshi, M. Chikamatsu, H. Fujiwara, J. Appl. Phys. **121**, 115501 (2017)
28. D. Shi, V. Adinolfi, R. Comin, M. Yuan, E. Alarousu, A. Buin, Y. Chen, S. Hoogland, A. Rothenberger, K. Katsiev, Y. Losovyj, X. Zhang, P.A. Dowben, O.F. Mohammed, E.H. Sargent, O.M. Bakr, Science **347**, 519 (2015)
29. C.C. Stoumpos, C.D. Malliakas, M.G. Kanatzidis, Inorg. Chem. **52**, 9019 (2013)
30. A. Amat, E. Mosconi, E. Ronca, C. Quarti, P. Umari, M.K. Nazeeruddin, M. Grätzel, F. De, Angelis. Nano Lett. **14**, 3608 (2014)
31. J.-H. Lee, N.C. Bristowe, P.D. Bristowe, A.K. Cheetham, Chem. Commun. **51**, 6434 (2015)
32. J.H. Lee, J.-H. Lee, E.-H. Kong, H.M. Jang, Sci. Rep. **6**, 21687 (2016)
33. J.S. Bechtel, R. Seshadri, A. Van der Ven, J. Phys. Chem. C **120**, 12403 (2016)
34. R.E. Wasylishen, O. Knop, J.B. Macdonald, Solid State Commun. **56**, 581 (1985)
35. E. Mosconi, C. Quarti, T. Ivanovska, G. Ruani, F. De Angelis, Phys. Chem. Chem. Phys. **16**, 16137 (2014)
36. A. Mattoni, A. Filippetti, M.I. Saba, P. Delugas, J. Phys. Chem. C **119**, 17421 (2015)
37. A.M.A. Leguy, J.M. Frost, A.P. McMahon, V.G. Sakai, W. Kochelmann, C. Law, X. Li, F. Foglia, A. Walsh, B.C. O'Regan, J. Nelson, J.T. Cabral, R.F. Barnes, Nat. Commun. **6**, 7124 (2015)
38. M.A. Carignano, A. Kachmar, J. Phys. Chem. C **119**, 8991 (2015)
39. A.A. Bakulin, O. Selig, H.J. Bakker, Y.L.A. Rezus, C. Müller, T. Glaser, R. Lovrincic, Z. Sun, Z. Chen, A. Walsh, J.M. Frost, T.L.C. Jansen, J. Phys. Chem. Lett. **6**, 3663 (2015)
40. M.A. Carignano, Y. Saeed, S.A. Aravindh, I.S. Roqan, J. Even, C. Katan, Phys. Chem. Chem. Phys. **18**, 27109 (2016)
41. M.R. Filip, G.E. Eperon, H.J. Snaith, F. Giustino, Nat. Commun. **5**, 5757 (2014)
42. J. Kim, S.-C. Lee, S.-H. Lee, K.-H. Hong, J. Phys. Chem. C **119**, 4627 (2015)
43. G. Xing, N. Mathews, S. Sun, S.S. Lim, Y.M. Lam, M. Grätzel, S. Mhaisalkar, T.C. Sum, Science **342**, 344 (2013)

44. S. Sun, T. Salim, N. Mathews, M. Duchamp, C. Boothroyd, G. Xing, T.C. Sum, Y.M. Lam, Energy Environ. Sci. **7**, 399 (2014)
45. S. De Wolf, J. Holovsky, S.-J. Moon, P. Löper, B. Niesen, M. Ledinsky, F.-J. Haug, J.-H. Yum, C. Ballif, J. Phys. Chem. Lett. **5**, 1035 (2014)
46. G. Xing, N. Mathews, S.S. Lim, N. Yantara, X. Liu, S. Dharani, M. Grätzel, S. Mhaisalkar, T.C. Sum, Nat. Mater. **13**, 476 (2014)
47. Q. Lin, A. Armin, R.C.R. Nagiri, P.L. Burn, P. Meredith, Nat. Photon. **9**, 106 (2015)
48. J.M. Ball, S.D. Stranks, M.T. Hörantner, S. Hüttner, W. Zhang, E.J.W. Crossland, I. Ramirez, M. Riede, M.B. Johnston, R.H. Friend, H.J. Snaith, Energy Environ. Sci. **8**, 602 (2015)
49. P. Löper, M. Stuckelberger, B. Niesen, J. Werner, M. Filipič, S.-J. Moon, J.-H. Yum, M. Topič, S. De Wolf, C. Ballif, J. Phys. Chem. Lett. **6**, 66 (2015)
50. Y. Jiang, M.A. Green, R. Sheng, A. Ho-Baillie, Sol. Eng. Mater. Sol. Cells **137**, 253 (2015)
51. A.M.A. Leguy, Y. Hu, M. Campoy-Quiles, M.I. Alonso, O.J. Weber, P. Azarhoosh, M. van Schilfgaarde, M.T. Weller, T. Bein, J. Nelson, P. Docampo, P.R.F. Barnes, Chem. Mater. **27**, 3397 (2015)
52. A.M.A. Leguy, P. Azarhoosh, M.I. Alonso, M. Campoy-Quiles, O.J. Weber, J. Yao, D. Bryant, M.T. Weller, J. Nelson, A. Walsh, M. van Schilfgaarde, P.R.F. Barnes, Nanoscale **8**, 6317 (2016)
53. T. Miyadera, T. Sugita, H. Tampo, K. Matsubara, M. Chikamatsu, A.C.S. Appl, Mater. Interfaces. **8**, 26013 (2016)
54. J.H. Noh, S.H. Im, J.H. Heo, T.N. Mandal, S.I. Seok, Nano Lett. **13**, 1764 (2013)
55. G. Niu, X. Guo, L. Wang, J. Mater. Chem. A **3**, 8970 (2015)
56. T. Leijtens, G.E. Eperon, N.K. Noel, S.N. Habisreutinger, A. Petrozza, H.J. Snaith, Adv. Energy Mater. **5**, 1500963 (2015)
57. G. Murugadoss, S. Tanaka, G. Mizuta, S. Kanaya, H. Nishino, T. Umeyama, H. Imahori, S. Ito, Jpn. J. Appl. Phys. **54**, 08KF08 (2015)
58. T.A. Berhe, W.-N. Su, C.-H. Chen, C.-J. Pan, J.-H. Cheng, H.-M. Chen, M.-C. Tsai, L.-Y. Chen, A.A. Dubale, B.-J. Hwang, Energy Environ. Sci. **9**, 323 (2016)
59. M. Shirayama, M. Kato, T. Miyadera, T. Sugita, T. Fujiseki, S. Hara, H. Kadowaki, D. Murata, M. Chikamatsu, H. Fujiwara, J. Appl. Phys. **119**, 115501 (2016)
60. H. Fujiwara, J. Koh, P.I. Rovira, R.W. Collins, Phys. Rev. B **61**, 10832 (2000)
61. H. Fujiwara, *Spectroscopic Ellipsometry: Principles and Applications* (Wiley, West Sussex, 2007)
62. N. Kitazawa, Y. Watanabe, Y. Nakamura, J. Mater. Sci. **37**, 3585 (2002)
63. W.-J. Yin, T. Shi, Y. Yan, Adv. Mater. **26**, 4653 (2014)
64. W.-J. Yin, J.-H. Yang, J. Kang, Y. Yan, S.-H. Wei, J. Mater. Chem. A **3**, 8926 (2015)
65. J. Bordas, J. Robertson, A. Jakobsson, J. Phys. C **11**, 2607 (1978)
66. E. Doni, G. Grosso, G. Harbeke, E. Meier, E. Tosatti, Phys. Stat. Sol. (b) **68**, 569 (1975)
67. Y. Yamada, T. Nakamura, M. Endo, A. Wakamiya, Y. Kanemitsu, Appl. Phys. Express **7**, 032302 (2014)
68. A. Binek, F.C. Hanusch, P. Docampo, T. Bein, J. Phys. Chem. Lett. **6**, 1249 (2015)
69. F. Hao, C.C. Stoumpos, Z. Liu, R.P.H. Chang, M.G. Kanatzidis, J. Am. Chem. Soc. **136**, 16411 (2014)
70. O.N. Yunakova, V.K. Miloslavskii, E.N. Kovalenko, Opt. Spectrosc. **112**, 91 (2012)
71. Y. Yamada, T. Nakamura, M. Endo, A. Wakamiya, Y. Kanemitsu, IEEE J. Photovolt. **5**, 401 (2015)
72. A. Miyata, A. Mitioglu, P. Plochocka, O. Portugall, J.T.-W. Wang, S.D. Stranks, H.J. Snaith, R.J. Nicholas, Nat. Phys. **11**, 582 (2015)
73. E. Mosconi, A. Amat, M.K. Nazeeruddin, M. Grätzel, F. De Angelis, J. Phys. Chem. C **117**, 13902 (2013)
74. F. Brivio, A.B. Walker, A. Walsh, APL Mater. **1**, 042111 (2013)
75. T. Umebayashi, K. Asai, T. Kondo, A. Nakao, Phys. Rev. B **67**, 155405 (2003)
76. D. Li, J. Meng, Y. Niu, H. Zhao, C. Liang, Chem. Phys. Lett. **627**, 13 (2015)

77. H. Fujiwara, S. Fujimoto, M. Tamakoshi, M. Kato, H. Kadowaki, T. Miyadera, H. Tampo, M. Chikamatsu, H. Shibata, Appl. Surf. Sci. **421**, 276 (2017)
78. M.P. Marder, *Condensed Matter Physics* (Wiley, Hoboken, 2010)
79. J. Even, L. Pedesseau, J.-M. Jancu, C. Katan, J. Phys. Chem. Lett. **4**, 2999 (2013)
80. P. Umari, E. Mosconi, F. De Angelis, Sci. Rep. **4**, 4467 (2014)
81. F. Brivio, K.T. Butler, A. Walsh, M. van Schilfgaarde, Phys. Rev. B **89**, 155204 (2014)
82. E. Menéndez-Proupin, P. Palacios, P. Wahnón, J.C. Conesa, Phys. Rev. B **90**, 045207 (2014)
83. M. Marsman, J. Paier, A. Stroppa, G. Kresse, J. Phys. Condens. Matter **20**, 064201 (2008)
84. C. Quarti, E. Mosconi, F. De Angelis, Chem. Mater. **26**, 6557 (2014)
85. C. Motta, F. El-Mellouhi, S. Kais, N. Tabet, F. Alharbi, S. Sanvito, Nat. Commun. **6**, 7026 (2015)
86. C. Motta, F. El-Mellouhi, S. Sanvito, Phys. Rev. B **93**, 235412 (2016)
87. A. Nakane, H. Tampo, M. Tamakoshi, S. Fujimoto, K.M. Kim, S. Kim, H. Shibata, S. Niki, H. Fujiwara, J. Appl. Phys. **120**, 064505 (2016)
88. J.H. Heo, D.H. Song, H.J. Han, S.Y. Kim, J.H. Kim, D. Kim, H.W. Shin, T.K. Ahn, C. Wolf, T.-W. Lee, S.H. Im, Adv. Mater. **27**, 3424 (2015)
89. J. Shi, J. Dong, S. Lv, Y. Xu, L. Zhu, J. Xiao, X. Xu, H. Wu, D. Li, Y. Luo, Q. Meng, Appl. Phys. Lett. **104**, 063901 (2014)
90. L. Etgar, P. Gao, Z. Xue, Q. Peng, A.K. Chandiran, B. Liu, MdK Nazeeruddin, M. Grätzel, J. Am. Chem. Soc. **134**, 17396 (2012)
91. H. Zhou, Y. Shi, Q. Dong, H. Zhang, Y. Xing, K. Wang, Y. Du, T. Ma, J. Phys. Chem. Lett. **5**, 3241 (2014)
92. W. Tress, N. Marinova, O. Inganäs, M.K. Nazeeruddin, S.M. Zakeeruddin, M. Graetzel, Adv. Energy Mater. **5**, 1400812 (2014)
93. A.R.B.M. Yuoff, M.K. Nazeeruddin, J. Phys. Chem. Lett. **7**, 851 (2016)
94. E. Edri, S. Kirmayer, A. Henning, S. Mukhopadhyay, K. Gartsman, Y. Rosenwaks, G. Hodes, D. Cahen, Nano Lett. **14**, 1000 (2014)
95. V.W. Bergmann, S.A.L. Weber, F.J. Ramos, M.K. Nazeeruddin, M. Grätzel, D. Li, A.L. Domanski, I. Lieberwirth, S. Ahmad, R. Berger, Nat. Commun. **5**, 5001 (2014)
96. W. Tress, N. Marinova, T. Moehl, S.M. Zakeeruddin, M.K. Nazeeruddin, M. Grätzel, Energy Environ. Sci. **8**, 995 (2015)
97. Y. Zhang, M. Liu, G.E. Eperon, T.C. Leijtens, D. McMeekin, M. Saliba, W. Zhang, M. de Bastiani, A. Petrozza, L.M. Herz, M.B. Johnston, H. Lin, H.J. Snaith, Mater. Horiz. **2**, 315 (2015)
98. E. Edri, S. Kirmayer, S. Mukhopadhyay, K. Gartsman, G. Hodes, D. Cahen, Nat. Commun. **5**, 3461 (2014)
99. Q. Wang, Y. Shao, H. Xie, L. Lyu, X. Liu, Y. Gao, J. Huang, Appl. Phys. Lett. **105**, 163508 (2014)
100. E.J. Juarez-Perez, M. Wuβler, F. Fabregat-Santiago, K. Lakus-Wollny, E. Mankel, T. Mayer, W. Jaegermann, I. Mora-Sero, J. Phys. Chem. Lett. **5**, 680 (2014)
101. W.-J. Yin, T. Shi, Y. Yan, Appl. Phys. Lett. **104**, 063903 (2014)
102. J. Kim, S.-H. Lee, J.H. Lee, K.-H. Hong, J. Phys. Chem. Lett. **5**, 1312 (2014)
103. M.L. Agiorgousis, Y.-Y. Sun, H. Zeng, S. Zhang, J. Am. Chem. Soc. **136**, 14570 (2014)
104. Q. Chen, H. Zhou, T.-B. Song, S. Luo, Z. Hong, H.-S. Duan, L. Dou, Y. Liu, Y. Yang, Nano Lett. **14**, 4158 (2014)
105. H.D. Kim, H. Ohkita, H. Benten, S. Ito, Adv. Mater. **28**, 917 (2016)
106. K. Ghimire, A. Cimaroli, F. Hong, T. Shi, N. Podraza, Y. Yan, in *Proceedings of the 42nd Photovoltaic Specialists Conference* (2015) p. 1
107. K. Ghimire, D. Zhao, A. Cimaroli, W. Ke, Y. Yan, N.J. Podraza, J. Phys. D **49**, 405102 (2016)
108. L. Karki Gautam, H. Haneef, M.M. Junda, D. B. Saint John, N. J. Podraza Thin Solid Films **571**, 548 (2014)

109. K. Ghimire, D. Zhao, A. Cimaroli, W. Ke, M. Junda, Y. Yan, N. Podraza, in *Proceedings of the 43rd Photovoltaic Specialists Conference* (2016) p. 89
110. Z. Song, S.C. Watthage, A.B. Phillips, B.L. Tompkins, R.J. Ellingson, M.J. Heben, Chem. Mater. **27**, 4612 (2015)
111. P. Docampo, T. Bein, Acc. Chem. Res. **49**, 339 (2016)
112. C. Müller, T. Glaser, M. Plogmeyer, M. Sendner, S. Döring, A.A. Bakulin, C. Brzuska, R. Scheer, M.S. Pshenichnikov, W. Kowalsky, A. Pucci, R. Lovrinčić, Chem. Mater. **27**, 7835 (2015)
113. I. Deretzis, A. Alberti, G. Pellegrino, E. Smecca, F. Giannazzo, N. Sakai, T. Miyasaka, A. La Magna, Appl. Phys. Lett. **106**, 131904 (2015)
114. F. Matsumoto, S.M. Vorpahl, J.Q. Banks, E. Sengupta, D.S. Ginger, J. Phys. Chem. C **119**, 20810 (2015)

Chapter 17
Solar Cells with Photonic and Plasmonic Structures

Peter Petrik

Abstract The research on solar cells based on photonic, plasmonic and various nanostructured materials has been increasing in the recent years. A wide range of nanomaterial approaches are applied from photonic crystals to plasmonics, to trap light and enhance the absorption as well as the efficiency of solar cells. The first part of this chapter presents examples on applications that utilize nanostructured materials for photovoltaics. In the second part, ellipsometry related metrology issues are discussed briefly, dividing the topic in two major parts: effective medium and scatterometry approaches.

17.1 Introduction

Writing a complete overview on nanomaterials for solar cells in frame of a book chapter is naturally an impossible mission, since the field is already huge. Figure 17.1 shows the number of articles written on photonic crystals or plasmonic materials in the past two and a half decade. These activities clearly started to grow at the beginning of the 90s, followed by applications in the field of photovoltaics, with a delay of one decade or more. The increase of the plasmonic activities doesn't seem to stop, while the photonic crystal activities tend to reach saturation. Taking into account the size of the field, in this book chapter we only can make an attempt to present and discuss several relevant, interesting and mostly recent examples.

P. Petrik (✉)
Institute for Technical Physics and Materials Science, Centre for Energy Research, Hungarian Academy of Sciences, Budapest, Hungary
e-mail: petrik.peter@energia.mta.hu

© Springer International Publishing AG, part of Springer Nature 2018

H. Fujiwara and R. W. Collins (eds.), *Spectroscopic Ellipsometry for Photovoltaics*, Springer Series in Optical Sciences 212,
https://doi.org/10.1007/978-3-319-75377-5_17

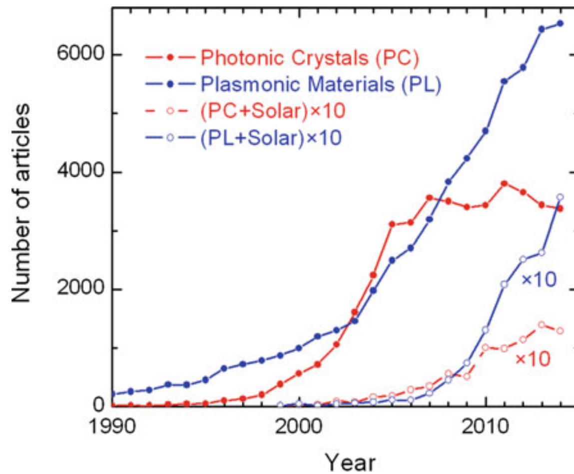

Fig. 17.1 Articles over the years, having different nanomaterial related words (as shown in the legend) together with the phrases of "solar cell" or "photovoltaics" in the title, abstract or keywords

17.2 Nanostructure-Based Solar Cells

To enhance solar cell efficiency, two major types of nanomaterial-based structures are developed. The first approach is to use structuring on the scale of the wavelength of illumination to improve light trapping by scattering. These methods utilize texturing (see Chap. 2 in Vol. 2) and photonic crystal-based structures. The second approach of using nanomaterials is to achieve resonance and conversion effects to enhance absorption in a well controlled wavelength range, as in plasmonics. In the following subsection most recent examples are collected from a selection of the widely investigated types of nanomaterials [1] for photovoltaics. For some of the discussed topics, comprehensive review articles are available (e.g. [2–4]), thus the reader is advised to consult those reports for further information.

17.2.1 Nanostructured Surfaces and Photonic Crystals

Optimal trapping [5–11], absorption enhancement [12–15] (Fig. 17.2), luminescence [16, 17], light harvesting [18] and improved efficiency [19, 20] of solar cells have been demonstrated in numerous works using front and backside [21, 22] nanostructures based on the photonic approach using gratings [23], nanospheres [24], colloids [25], nanotubes [26], textured surfaces (Fig. 17.3) or other structures. Besides amorphous [28–31] or crystalline [32] silicon-based [33] thin film photovoltaics, organic [34–36], thermal [37, 38], Ge-based [39], dye-sensitized [40, 41] or tandem [42] cells and solar collectors [43] are also important targets of the research. A crucial issue is to find high quality, efficient and cost effective thin film

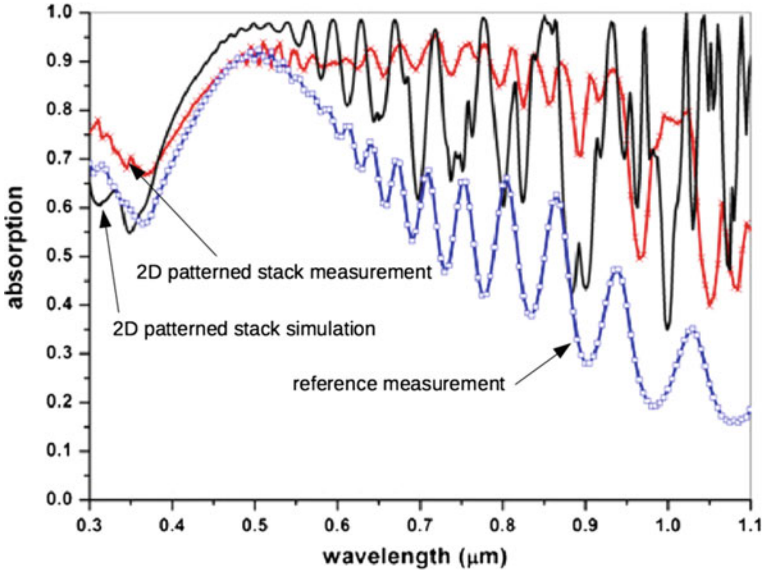

Fig. 17.2 Comparison of measured and simulated absorption spectra using 2D pattern stacks in a thin film c-Si solar cell. Reprinted from [14]

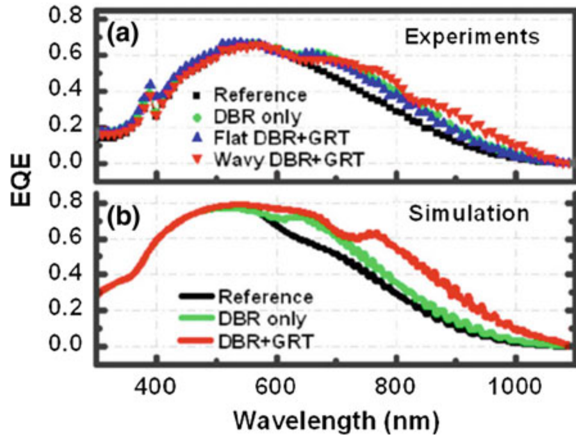

Fig. 17.3 Simulated and experimental external quantum efficiencies (EQE) of a 5 μm thick silicon solar cell using a distributed back reflector (DBR), a DBR plus grating (DBR + GRT), and a reference with only an SiO_2 back layer. Reprinted from [27]

preparation methods in order to create disordered [44–46] or ordered [47] structures based on self-assembly [48], 3D epitaxy [49], nanoimprint [50, 51] and a broad range of other means of layer formation. In most cases the wavelength range of light getting into the device are controlled or converted.

17.2.2 Plasmonic Nanostructures

The number of publications in plasmonics [52] exhibited a significant growth already from the beginning of the 90s with a further increased slope from 2004, as shown in Fig. 17.1. The utilization of plasmonics in photovoltaics [3, 53–55] (open circles in Fig. 17.1) shows a delay of almost a decade, but it continues to grow even today. Similar to the photonic crystal approach, plasmonics is used to trap light [56] and to manipulate the wavelength [57] captured by the device. Besides the silicon based devices the organic applications are also remarkable [58–60]. Both the used materials (Au [61], Ag [57, 62], Al [63], etc.) and structures (plane plasmonic layers [64] and different nanoparticle shapes [54]) cover a broad range.

17.2.3 Nanoparticles and Quantum Dots

Besides quantum dots [65, 66] and quasi-spherical particles [24], numerous "exotic" shapes have been calculated and demonstrated, including nanorods and nanotubes [67], nanobowls [68] and nanoholes [69], prepared mainly by colloidal [70, 65] and self assembly [71] methods. The used materials cover a broad range as well, including Au [72].

17.2.4 Metamaterials

Metamaterials [73], hyperbolic metamaterials [74, 75], often combined with plasmonics [76] are also widely used and demonstrated as absorbers [55, 77, 78], concentrators [79], or selective materials [80] for solar cells [81] and photovoltaics [82].

17.2.5 Nano- and Microwires

Nano- [83–85] or microwire [86] solar cells have been demonstrated in versatile configurations including silicon, hybrid [87] and dye sensitized multilayer form [88]. Numerous calculations have been performed in order to support the design [89], and the absorption capabilities [90, 91]. The applications cover a broader field beyond photovoltaics, such as optoelectronics [92] or plasmonics [93].

17.2.6 Device Performance

In most of the above investigations, the driving force is the solar cell performance. The absorption of light and the resulting gain in efficiency is demonstrated. In some cases the optimization of the parameters, such as the absorber thickness [94], the passivation [95], the patterning [96, 97] or devetting [98] are explicitly investigated in terms of device performance.

17.3 Characterization of Nanomaterials

Ellipsometry has mainly been used for the characterization of thin layers or layer stacks of optical quality. This means that the layers are homogeneous on the scale of the wavelength of illumination, and the boundaries are perfectly plane and well-defined. Therefore, the main application of ellipsometry has long been the investigation of thin films for microelectronic devices. Solar cells are usually also thin film systems of electronic devices. However, as the above examples show, photonic structures are emerging as light trapping and absorption enhancement solutions, which are inhomogeneous on the scale of illumination. On the one hand, this is a disadvantage from the ellipsometric point of view, because the usual effective medium models cannot be used, and also because most ellipsometers utilize specular configuration, which are not able to measure higher order diffractions. On the other hand, Mueller matrix ellipsometry [99, 100] is able to obtain the scattered response in zero order, which enables the measurement of the dimensions of the structures, when proper scatterometry or diffraction optical models are used. In this case, a significant advantage is that some geometrical parameters can also be determined from the models, which is not possible with effective medium models, or only with limitations [101]. Furthermore, ellipsometric scatterometry configurations are also emerging that support the measurement of higher order scattering responses [102]. In the following subsections, these main research directions will be discussed briefly.

17.3.1 Effective Medium Methods in Specular Configuration

The nanoparticles and nanostructures are often small enough to respond as an effective medium, causing no scattering. This is the quasi static limit [103, 104], which (in a certain size range) can also be used to estimate the characteristic periodicity in the materials by only using effective medium models [101]. In case of known phases and proper databases, the dispersion of the components of the nanostructures is known, and only the volume fraction(s) and thickness(es) have to

be used as fit parameters (e.g. poly- [105] or porous silicon [106]). In most cases, the dispersions have to be parameterized (see Chap. 3 of this book). Many analytical models are available in the literature for the most important materials, such as silicon [107, 108], CdTe and CdS [109], ZnO [110], metals [104] and organic materials [111]. The proper effective medium models have to be selected carefully, which is especially important in the case of noble metals for plasmonic applications [112].

17.3.2 Direct Methods

Besides the general effective medium approaches of fitting the thicknesses and the volume fractions of known components of the layers [113], there are some direct methods that don't require the parameterization of the dielectric function. In case of homogeneous semiconductor layers with known thicknesses the dielectric function can be determined by direct inversion with a subsequent "fine tuning" of the layer thickness. It was shown that the proper thickness can be chosen by checking whether the imaginary part of the dielectric function smoothly approaches zero toward the lower photon energies near the gap [114–116]. This method cannot only be used with direct inversion [117] but it can also be combined with the B-Spline parameterization [118], which usually allows fitting the layer thickness as well and using special criteria, such as $\varepsilon_2 > 0$ or the Kramers-Kronig consistency.

Direct (model-free) methods can be considered not only for the dielectric function, but also for its in-depth variation within the layer. Vertical changes can usually be modeled using grading or special functions [119, 120]. However, if the material has a large variation of absorption as a function of the wavelength (e.g. for semiconductors), this fact can be used for a depth scan, when the fitted wavelength is varied properly [101].

17.3.3 Surface Correction

For the accurate determination of optical properties the surface roughness [121], a possible surface contamination [122] and any other unintentional surface overlayers (e.g. native oxide [123]) have to be taken into account correctly. The parameterization of the dielectric function combined with the multi-sample and multiple-angles of incidence approach improves the accuracy and the reliability of the data significantly [124]. Figure 17.4 shows an example of different surface corrections applied for ZnO [116]. In this case, it can clearly be distinguished, whether an (absorbing) overlayer or a surface roughness is the proper approach for the correction. The layer thickness was also fitted, which can be checked by the criterion for the imaginary part of the dielectric function [116] as mentioned above.

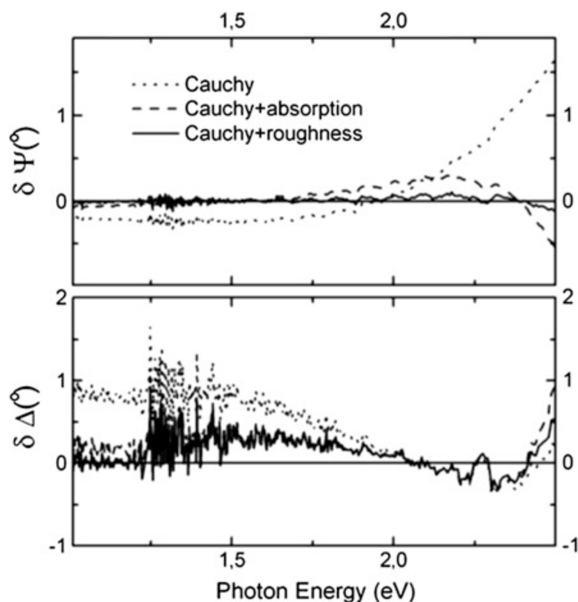

Fig. 17.4 Differences between the measured and calculated spectra of a Si/(10 nm SiO_2)/(50 nm ZnO) layer system using a simple Cauchy model (for the ZnO layer in the restricted wavelength range shown on the graph), a Cauchy model with absorption, and a Cauchy model without absorption but using a surface roughness in the wavelength range below the band gap. The angle of incidence was 65. Reprinted from [116]

17.3.4 Ellipsometry and Mueller Polarimetry in Specular Configuration

The vast majority of scatterometric applications in ellipsometry are utilizing only the zero order diffraction, using specular reflection [125, 127]. In spite of lacking in higher order response of the sample, the spectroscopic information together with the polarimetric data is sufficient for a high-sensitivity measurement even for numerous fit parameters [127].

The instrumentation is usually based on dual rotating compensator configurations that are capable of measuring all the Mueller matrix elements [99, 100] (see also Fig. 17.5). However, even a single rotating compensator ellipsometer or general ellipsometry can provide useful information on photonic structures using the rigorous coupled wave analysis [129, 126], effective medium methods [101], or both, to build libraries for fast evaluation [130].

17.3.5 Ellipsometric Scatterometry

Goniometric scatterometry is a mature method that usually utilizes a bright single-wavelength source and a high-precision goniometer [130–132]. There is a great motivation for the improvement of the sensitivity, speed and accuracy, as well as its validation [133, 134]. Modern lithography is approaching the line width of

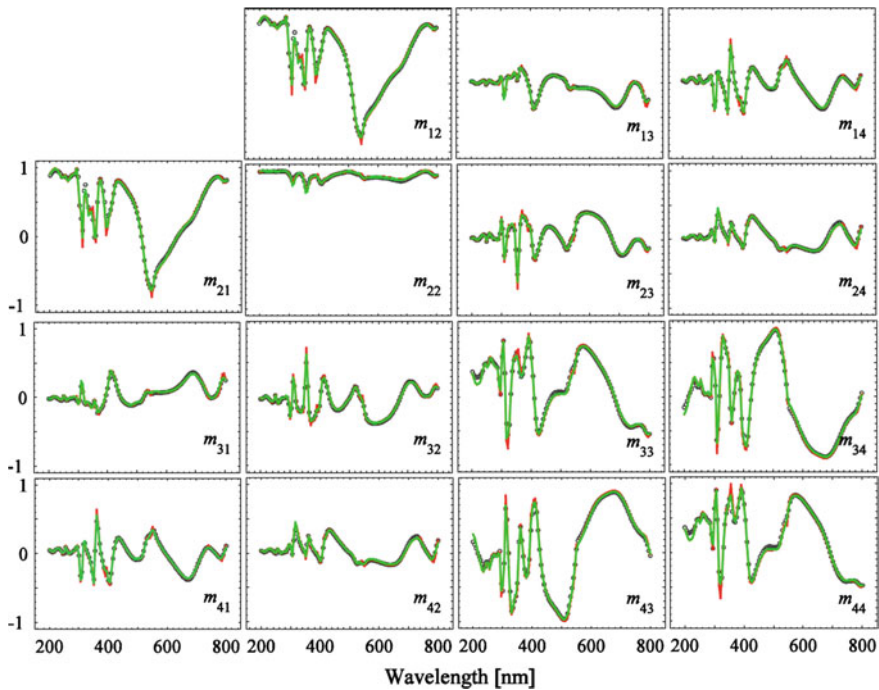

Fig. 17.5 Fit on the Mueller matrix spectra of a nanoimprinted grating with a line width of 351 nm, height of 468 nm, and side wall angle of 87°. Dots denote measured points. The red and green lines correspond to calculations without and with depolarization effects, respectively, due to finite spectral bandwidth, numerical aperture and layer thickness non-uniformity. Reprinted from [127]

10 nm, which requires sensitivity and accuracy (validated measurement) of one nanometer or below. The efforts to improve instrumentation advance into different directions, including the extension of the wavelength range [135], azimuth angles [136] or simultaneous measurement of many scattering directions using configurations such as Fourier scatterometry [137–141].

Both goniometric and Fourier scatterometry can be combined with ellipsometry, as demonstrated in [130] and [102], respectively. The goniometric method usually applies one wavelength, which is a significant disadvantage compared to spectroscopic Mueller polarimetry, even when the latter is applied only in the zero order specular configuration. In the configuration shown in [102] (Fig. 17.6), Fourier ellipsometry is also applied monochromatically, but a large range of polar (0–64° using a lens with a numerical aperture of 0.9) and azimuthal (0–180°) angles can be measured simultaneously. Besides the almost one order of magnitude increase in sensitivity—compared to regular Fourier scatterometry—there are numerous other advantages, such as the lack of need for a coherent source and wave front reference measurements, as in the case of standard Fourier scatterometry [140].

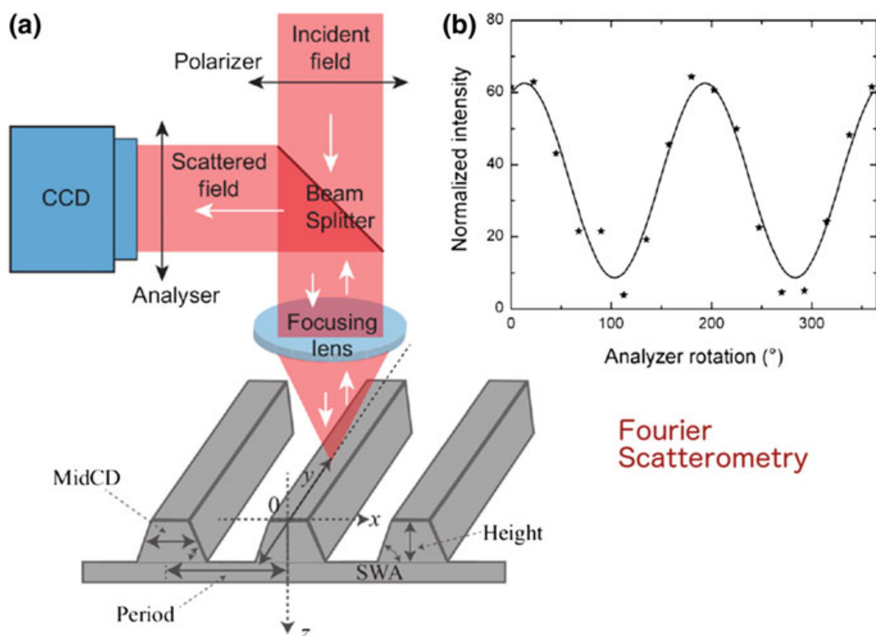

Fig. 17.6 **a** Setup of ellipsometric Fourier scatterometry. **b** Normalized intensity at an arbitrary pixel of the CCD detector as a function of polarizer rotation. Reprinted from [102]

17.4 Summary and Outlook

The number of publications on nanomaterials for solar applications keeps increasing in the past almost 10 years. Dimensional optical metrology has been improved and developed into new directions to meet the increasing need for accurate material characterization. From the metrology point of view the validation of the measurements is a general problem, because most reference methods like electron or scanning probe microscopy are local measurements, which can only be compared with the optical measurements on larger (usually millimeters or hundreds of micrometers) spots if proper calibration standards are created and checked using different validated methods [135]. There is a continuous development, not only for instrumentation, but also for computation using rigorous [128] and finite element [142] methods. In most cases (especially for Fourier scatterometry), not only accuracy and convergence, but the speed of evaluation is also a crucial issue, which requires optimization for algorithms and measurement configurations.

References

1. Z.R. Dai, Z.W. Pan, Z.L. Wang, Adv. Funct. Mater. **13**, 9 (2003)
2. F. Priolo, T. Gregorkiewicz, M. Galli, T.F. Krauss, Nat. Nanotechnol. **9**, 19 (2014)
3. H.A. Atwater, A. Polman, Nat. Mater. **9**, 205 (2010)
4. M. Florescu, H. Lee, I. Puscasu, M. Pralle, L. Florescu, D.Z. Ting, J.P. Dowling, Sol. Energy Mater. Sol. Cells **91**, 1599 (2007)
5. S.B. Mallick, M. Agrawal, P. Peumans, Opt. Expr. **18**, 5691 (2010)
6. S. Basu Mallick, N.P. Sergeant, M. Agrawal, J.-Y. Lee, P. Peumans, MRS Bull. **36**, 453 (2011)
7. D.M. Callahan, J.N. Munday, H.A. Atwater, Nano Lett. **12**, 214 (2012)
8. V.E. Ferry, A. Polman, H.A. Atwater, ACS Nano **5**, 10055 (2011)
9. C. Trompoukis, I. Abdo, R. Cariou, I. Cosme, W. Chen, O. Deparis, A. Dmitriev, E. Drouard, M. Foldyna, E. G.- Caurel, I. Gordon, B. Heidari, A. Herman, L. Lalouat, K.-D. Lee, J. Liu, K. Lodewijks, F. Mandorlo, I. Massiot, A. Mayer, V. Mijkovic, J. Muller, R. Orobtchouk, G. Poulain, P. Prod'Homme, P.R. i Cabarrocas, C. Seassal, J. Poortmans, R. Mertens, O. El Daif, V. Depauw, Phys. Status Solidi **212**, 140 (2015)
10. C. van Lare, F. Lenzmann, M.A. Verschuuren, A. Polman, Nano Lett. **15**, 4846 (2015)
11. M.-C. van Lare, A. Polman, ACS Photon. **2**, 822 (2015)
12. I.E. Khodasevych, L. Wang, A. Mitchell, G. Rosengarten, Adv. Opt. Mater. **3**, 852 (2015)
13. Y. Park, E. Drouard, O. El Daif, X. Letartre, P. Viktorovitch, A. Fave, A. Kaminski, M. Lemiti, C. Seassal, Opt. Expr. **17**, 14312 (2009)
14. X. Meng, V. Depauw, G. Gomard, O. El Daif, C. Trompoukis, E. Drouard, C. Jamois, A. Fave, F. Dross, I. Gordon, C. Seassal, Opt. Expr. **20**, 465 (2012)
15. Y. Xu, Y. Xuan, J. Nanopart. Res. **17**, 314 (2015)
16. A. Shalav, B.S. Richards, M.A. Green, Sol. Energy Mater. Sol. Cells **91**, 829 (2007)
17. R. Reisfeld, Opt. Mater. (Amst). **32**, 850 (2010)
18. S. Colodrero, A. Mihi, J.A. Anta, M. Ocan, H. Míguez, J. Phys. Chem. C **113**, 1150 (2009)
19. P. Bermel, C. Luo, L. Zeng, L.C. Kimerling, J.D. Joannopoulos, Opt. Expr. **15**, 16986 (2007)
20. A. Chutinan, N.P. Kherani, S. Zukotynski, Opt. Expr. **17**, 8871 (2009)
21. S. Jain, V. Depauw, V.D. Miljkovic, A. Dmitriev, C. Trompoukis, I. Gordon, P. Van Dorpe, O. El Daif, Prog. Photovolt. Res. Appl. **23**, 1144 (2015)
22. J. Krc, M. Zeman, S.L. Luxembourg, M. Topic, Appl. Phys. Lett. **94**, 6 (2009)
23. J.G. Mutitu, S. Shi, C. Chen, T. Creazzo, A. Barnett, C. Honsberg, D.W. Prather, Opt. Expr. **16**, 15238 (2008)
24. J. Grandidier, R.A. Weitekamp, M.G. Deceglie, D.M. Callahan, C. Battaglia, C.R. Bukowsky, C. Ballif, R.H. Grubbs, H.A. Atwater, Phys. Status Solidi **210**, 255 (2013)
25. A. Mihi, H. Mı, H. Míguez, J. Phys. Chem. B **109**, 15968 (2005)
26. C.T. Yip, H. Huang, L. Zhou, K. Xie, Y. Wang, T. Feng, J. Li, W.Y. Tam, Adv. Mater. **23**, 5624 (2011)
27. L. Zeng, P. Bermel, Y. Yi, B. Alamariu, K. Broderick, J. Liu, C. Hong, X. Duan, J. Joannopoulos, L.C. Kimerling, Appl. Phys. Lett. **93**, 221105 (2008)
28. G. Gomard, E. Drouard, X. Letartre, X. Meng, A. Kaminski, A. Fave, M. Lemiti, E. Garcia-Caurel, C. Seassal, J. Appl. Phys. **108**, 1 (2010)
29. B. Curtin, R. Biswas, V. Dalal, Appl. Phys. Lett. **95**, 231102 (2009)
30. O. El Daif, E. Drouard, G. Gomard, A. Kaminski, A. Fave, M. Lemiti, S. Ahn, S. Kim, P. Roca, I. Cabarrocas, H. Jeon, C. Seassal, Opt. Expr. **18**, 293 (2010)
31. V.E. Ferry, M.A. Verschuuren, C. Van Lare, R.E.I. Schropp, H.A. Atwater, A. Polman, Nano Lett. **11**, 4239 (2011)
32. V. Depauw, X. Meng, O. El Daif, G. Gomard, L. Lalouat, E. Drouard, C. Trompoukis, A. Fave, C. Seassal, I. Gordon, IEEE J. Photovolt. **4**, 215 (2014)

33. E.D. Kosten, B.K. Newman, J.V. Lloyd, A. Polman, H.A. Atwater, IEEE J. Photovolt. **5**, 61 (2015)
34. D.-H. Ko, J.R. Tumbleston, L. Zhang, S. Williams, J.M. DeSimone, R. Lopez, E.T. Samulski, Nano Lett. **9**, 2742 (2009)
35. R. Betancur, P. Romero-Gomez, A. Martinez-Otero, X. Elias, M. Maymó, J. Martorell, Nat. Photon. **7**, 995 (2013)
36. J.R. Tumbleston, D.H. Ko, E.T. Samulski, R. Lopez, Appl. Phys. Lett. **94**, 18 (2009)
37. S.Y. Lin, J. Moreno, J.G. Fleming, Appl. Phys. Lett. **83**, 380 (2003)
38. P. Nagpal, S.E. Han, A. Stein, D.J. Norris, Nano Lett. **8**, 3238 (2008)
39. I. Prieto, B. Galiana, P. a. Postigo, C. Algora, L.J. Martínez, I. Rey-Stolle, Appl. Phys. Lett. **94**, 25 (2009)
40. A. Mihi, M.E. Calvo, J.A. Anta, H. Miguez, J. Phys. Chem. C **112**, 13 (2008)
41. N. Tétreault, M. Grätzel, Energy Environ. Sci. **5**, 8506 (2012)
42. A. Bielawny, J. Üpping, P.T. Miclea, R.B. Wehrspohn, C. Rockstuhl, F. Lederer, M. Peters, L. Steidl, R. Zentel, S.-M. Lee, M. Knez, A. Lambertz, R. Carius, Phys. Status Solidi **205**, 2796 (2008)
43. V. Hody-Le Caër, E. De Chambrier, S. Mertin, M. Joly, M. Schaer, J.L. Scartezzini, a. Schüler, Renew. Energy **53**, 27 (2013)
44. F. Pratesi, M. Burresi, F. Riboli, K. Vynck, D.S. Wiersma, Opt. Expr. **21**, 460 (2013)
45. K. Vynck, M. Burresi, F. Riboli, D.S. Wiersma, Nat. Mater. **11**, 1017 (2012)
46. S. Colodrero, A. Mihi, L. Häggman, M. Ocaña, G. Boschloo, A. Hagfeldt, H. Míguez, Adv. Mater. **21**, 764 (2009)
47. K.-Q. Peng, X. Wang, X. Wu, S.-T. Lee, Appl. Phys. Lett. **95**, 143119 (2009)
48. C.E.R. Disney, S. Pillai, C.M. Johnson, M.A. Green, ACS Photon. **2**, 1108 (2015)
49. E.C. Nelson, N.L. Dias, K.P. Bassett, S.N. Dunham, V. Verma, M. Miyake, P. Wiltzius, J.A. Rogers, J.J. Coleman, X. Li, P.V. Braun, Nat. Mater. **10**, 676 (2011)
50. C. Trompoukis, O. El Daif, V. Depauw, I. Gordon, J. Poortmans, Appl. Phys. Lett. **101**, 1–5 (2012)
51. I. Abdo, C. Trompoukis, J. Deckers, V. Depauw, L. Tous, D. Van Gestel, R. Guindi, I. Gordon, O. El Daif, IEEE J. Photovolt. **4**, 1261 (2014)
52. J. Zhang, L. Zhang, W. Xu, J. Phys. D Appl. Phys. **45**, 113001 (2012)
53. K.R. Catchpole, A. Polman, Opt. Expr. **16**, 21793 (2008)
54. K.R. Catchpole, A. Polman, Appl. Phys. Lett. **93**, 191113 (2008)
55. Y. Cui, Y. He, Y. Jin, F. Ding, L. Yang, Y. Ye, S. Zhong, Y. Lin, S. He, Laser Photon. Rev. **8**, 495 (2014)
56. V.E. Ferry, M.A. Verschuuren, H.B.T. Li, E. Verhagen, R.J. Walters, R.E.I. Schropp, H.A. Atwater, A. Polman, Opt. Expr. **18**, 237 (2010)
57. X. Li, C. Jia, B. Ma, W. Wang, Z. Fang, G. Zhang, X. Guo, Sci. Rep. **5**, 14497 (2015)
58. J. Weickert, R.B. Dunbar, H.C. Hesse, W. Wiedemann, L. Schmidt-Mende, Adv. Mater. **23**, 1810 (2011)
59. W.C.H. Choy, X. Ren, IEEE J. Sel. Top. Quant. Elect. **22**, 4100209 (2016)
60. L. Chen, S. Wang, C. Han, Y. Cheng, L. Qian, Synth. Met. **209**, 544 (2015)
61. A. de León, E. Arias, I. Moggio, C. Gallardo-Vega, R. Ziolo, O. Rodríguez, S. Trigari, E. Giorgetti, C. Leibig, D. Evans, J. Colloid Interf. Sci. **456**, 182 (2015)
62. H.-L. Hsu, T.-Y. Juang, C.-P. Chen, C.-M. Hsieh, C.-C. Yang, C.-L. Huang, R.-J. Jeng, Sol. Energy Mater. Sol. Cells **140**, 224 (2015)
63. L. Yang, S. Pillai, M. a Green, Sci. Rep. **5**, 11852 (2015)
64. H.K. Singh, B. Arunachalam, S. Kumbhar, P. Sharma, C.S. Solanki, Plasmonics **11**, 323 (2015)
65. X. Lan, S. Masala, E.H. Sargent, Nat. Mater. **13**, 233 (2014)
66. C.S.S. Sandeep, S. ten Cate, J. M. Schins, T.J. Savenije, Y. Liu, M. Law, S. Kinge, A. J. Houtepen, L.D. a Siebbeles, Nat. Commun. **4**, 2360 (2013)
67. V.V. Kislyuk, O.P. Dimitriev, Nanorods and nanotubes for solar cells. J. Nanosci. Nanotechnol. **8**, 131 (2008)

68. R.-N. Sun, K.-Q. Peng, B. Hu, Y. Hu, F.-Q. Zhang, S.-T. Lee, Appl. Phys. Lett. **107**, 013107 (2015)
69. K. Peng, X. Wang, L. Li, X. Wu, S. Lee, J. Am. Chem. Soc. **132**, 6872 (2010)
70. F. Meinardi, H. McDaniel, F. Carulli, A. Colombo, K. a. Velizhanin, N.S. Makarov, R. Simonutti, V.I. Klimov, S. Brovelli, Nat. Nanotechnol. **178**, 1 (2015)
71. C. Hägglund, G. Zeltzer, R. Ruiz, I. Thomann, H.B.R. Lee, M.L. Brongersma, S.F. Bent, Nano Lett. **13**, 3352 (2013)
72. M. Losurdo, M.M. Giangregorio, G.V. Bianco, A. Sacchetti, P. Capezzuto, A.G. Bruno, Sol. Energy Mater. Sol. Cells **93**, 1749 (2009)
73. N.I. Zheludev, Opt. Photon. News, 30 (2011)
74. E.E. Narimanov, H. Li, Y.A. Barnakov, T.U. Tumkur, M.A. Noginov, Opt. Expr. **21**, 215 (2013)
75. D. Ji, H. Song, X. Zeng, H. Hu, K. Liu, N. Zhang, Q. Gan, Sci. Rep. **4**, 4498 (2014)
76. J. Hao, J. Wang, X. Liu, W.J. Padilla, L. Zhou, M. Qiu, Appl. Phys. Lett. **96**, 251104 (2010)
77. C. Wu, B.N. Iii, J. John, A. Milder, B. Zollars, S. Savoy, G. Shvets, J. Opt. **14**, 024005 (2012)
78. K. Liu, B. Zeng, H. Song, Q. Gan, F.J. Bartoli, Z.H. Kafa, Opt. Commun. **314**, 48 (2014)
79. J. Yang, M. Huang, C. Yang, Z. Xiao, P. Jinhui, Opt. Expr. **17**, 19656 (2009)
80. H. Wang, L. Wang, Opt. Expr. **21**, 13311 (2013)
81. Y. Wang, T. Sun, T. Paudel, Y. Zhang, Z. Ren, K. Kempa, Nano Lett. **12**, 440 (2011)
82. S. Molesky, C.J. Dewalt, Z. Jacob, Opt. Expr. **21**, 96 (2013)
83. T. Stelzner, M. Pietsch, G. Andra, F. Falk, E. Ose, S. Christiansen, Nanotechnology **19**, 295203 (2008)
84. L. Tsakalakos, J. Balch, J. Fronheiser, B.A. Korevaar, O. Sulima, J. Rand, L. Tsakalakos, J. Balch, J. Fronheiser, B.A. Korevaar, Appl. Phys. Lett. **91**, 233117 (2015)
85. M. Law, L.E. Greene, J.C. Johnson, R. Saykally, Nat. Mater. **4**, 455 (2005)
86. C. Sugnaux, A. D. Mallorquí, J. Herriman, H.-A. Klok, and A.F. i Morral, Adv. Funct. Mater. **25**, 3958 (2015)
87. J. Huang, C. Hsiao, S. Syu, J. Chao, C. Lin, Sol. Energy Mater. Sol. Cells **93**, 621 (2009)
88. C. Xu, J. Wu, U.V. Desai, D. Gao, J. Am. Chem. Soc. **133**, 8122 (2011)
89. O.L. Muskens, J.G. Rivas, R.E. Algra, E.P.A.M. Bakkers, A. Lagendijk, Nano Lett. **8**, 2638 (2008)
90. L. Cao, J.S. White, J. Park, J.A. Schuller, B.M. Clemens, M.L. Brongersma, Nat. Mater. **8**, 643 (2009)
91. E. Garnett, P. Yang, Nano Lett. **10**, 1082 (2010)
92. T. Khudiyev, M. Bayindir, Sci. Rep. **4**, 7505 (2014)
93. Y. Yang, J. Qing, J. Ou, X. Lin, Z. Yuan, D. Yu, X. Zhou, X. Chen, Sol. Energy **122**, 231 (2015)
94. K. Islam, F.I. Chowdhury, A.K. Okyay, A. Nayfeh, Sol. Energy **120**, 257 (2015)
95. C. Trompoukis, O. El Daif, P. Pratim Sharma, H. Sivaramakrishnan Radhakrishnan, M. Debucquoy, V. Depauw, K. Van Nieuwenhuysen, I. Gordon, R. Mertens, J. Poortmans, Prog. Photovolt. Res. Appl. **23**, 734 (2015)
96. A. Herman, C. Trompoukis, V. Depauw, O. El Daif, O. Deparis, J. Appl. Phys. **112**, 11 (2012)
97. I. Abdo, C. Trompoukis, L. Tous, R. Guindi, I. Gordon, O. El Daif, IEEE J. Photovolt. **5**, 1319 (2015)
98. T. Fleetham, J.-Y. Choi, H.W. Choi, T. Alford, D.S. Jeong, T.S. Lee, W.S. Lee, K.-S. Lee, J. Li, I. Kim, Sci. Rep. **5**, 14250 (2015)
99. P.S. Hauge, J. Opt. Soc. Am. **68**, 1519 (1978)
100. R.W. Collins, J. Koh, J. Opt. Soc. Am. **16**, 1997 (1999)
101. P. Petrik, E. Agocs, J. Volk, I. Lukacs, B. Fodor, P. Kozma, T. Lohner, S. Oh, Y. Wakayama, T. Nagata, M. Fried, Thin Solid Films **571**, 579 (2014)
102. P. Petrik, N. Kumar, M. Fried, B. Fodor, G. Juhasz, S.F. Pereira, S. Burger, H.P. Urbach, J. Eur. Opt. Soc. Rapid Publ. **10**, 15002 (2015)

103. W.G. Egan, D.E. Aspnes, Phys. Rev. B **26**, 5313 (1982)
104. T.W.H. Oates, H. Wormeester, H. Arwin, Prog. Surf. Sci. **86**, 328 (2011)
105. P. Petrik, M. Fried, Ellipsometry of Semiconductor Nanocrystals, in *Ellipsometry at the Nanoscale*, ed. by M. Losurdo, K. Hingerl (Springer, Heidelberg, 2012), p. 583
106. E. Vazsonyi, E. Szilagyi, P. Petrik, Z.E. Horvath, T. Lohner, M. Fried, G. Jalsovszky, P. Petrik, T. Lohner, M. Fried, G. Jalsovszky, E. Szilagyi, P. Petrik, Z.E. Horvath, T. Lohner, M. Fried, G. Jalsovszky, Thin Solid Films **388**, 295 (2001)
107. P. Petrik, Phys. B Condens. Mat. **453**, 2 (2014)
108. P. Petrik, M. Fried, E. Vazsonyi, P. Basa, T. Lohner, P. Kozma, Z. Makkai, J. Appl. Phys. **105**, 024908 (2009)
109. J. Li, J. Chen, M.N. Sestak, R.W. Collins, IEEE J. Photovolt. **1**, 187 (2011)
110. J. Springer, A. Poruba, M. Vanecek, S. Fay, L. Feitknecht, N. Wyrsch, J. Meier, A. Shah, T. Repmann, O. Kluth, H. Stiebig, B. Rech, *Proceedings of 17th European Photovoltanics Solary Energy Conference*, vol. 1 (2001)
111. K. Hinrichs, K. Eichhorn, *Ellipsometry of Functional Organic Surfaces and Films* (Heidelberg, 2014)
112. H. Wormeester, T.W.H. Oates, Thin films of nanostructured noble metals, in *Ellipsometry at the Nanoscale*, ed. by M. Losurdo, K. Hingerl (Springer, Berlin Heidelberg, 2013) p. 225
113. D.E. Aspnes, Thin Solid Films **89**, 249 (1982)
114. D.E. Aspnes, A.A. Studna, E. Kinsbron, Phys. Rev. B **29**, 768 (1984)
115. H. Arwin, D. E. Aspnes, J. Vac. Sci. Technol. A Vacuum Surf. Film. **2**, 1316 (1984)
116. E. Agocs, B. Fodor, B. Pollakowski, B. Beckhoff, A. Nutsch, M. Jank, P. Petrik, Thin Solid Films **571**, 684 (2014)
117. R.W. Collins, A.S. Ferlauto, Optical physics of materials, in *Handbook of Ellipsometry*, ed. by E.G. Irene, H.G. Tomkins (Norwich, NY, William Andrew, 2005)
118. B. John, J. S. Hale, Phys. Stat. Sol. **205**, 715 (2008)
119. P. Petrik, O. Polgár, M. Fried, T. Lohner, N.Q. Khánh, J. Gyulai, O. Polgár, M. Fried, T. Lohner, N.Q. Khánh, J. Gyulai, J. Appl. Phys. **93**, 1987 (2003)
120. P. Kozma, B. Fodor, A. Deak, P. Petrik, Langmuir **26**, 16122 (2010)
121. D.E. Aspnes, J.B. Theeten, F. Hottier, Phys. Rev. B **20**, 3292 (1979)
122. E. Strein, D. Allred, Thin Solid Films **517**, 1011 (2008)
123. E.A. Irene, SiO_2 Films, in *Handbook of Ellipsometry*, ed. by E.G. Irene, H.G. Tomkins (Norwich, NY, William Andrew, 2005)
124. C.M. Herzinger, B. Johs, W.A. McGahan, J.A. Woollam, W. Paulson, J. Appl. Phys. **83**, 3323 (1998)
125. H.-T. Huang, W. Kong, F.L. Terry, Appl. Phys. Lett. **78**, 3983 (2001)
126. G.R. Muthinti, B. Peterson, A.C. Diebold, Proc. SPIE **8324**, 83240O (2012)
127. X. Chen, S. Liu, C. Zhang, H. Jiang, Z. Ma, T. Sun, Z. Xu, Opt. Expr. **22**, 15165 (2014)
128. M.G. Moharam, D.A. Pommet, E.B. Grann, J. Opt. Soc. Am. **12**, 1077 (1995)
129. P.C.Y. Huang, R.C.J. Chen, F. Chen, B. Perng, J. Shieh, SPIE Proc. **6152**, 1 (2006)
130. T.A. Germer, C.C. Asmail, Rev. Sci. Instrum. **70**, 3688 (1999)
131. M. Wurm, F. Pilarski, B. Bodermann, Rev. Sci. Instrum. **81**, 023701 (2010)
132. P.-E. Hansen, S. Burger, Proc. SPIE Int. Soc. Opt. Eng. **8789**, 87890R (2013)
133. B. Bodermann, P.-E. Hansen, S. Burger, M.-A. Henn, H. Gross, M. Bär, F. Scholze, J. Endres, M. Wurm, SPIE Proc. **8466**, 84660E–1 (2012)
134. E. Agocs, B. Bodermann, S. Burger, G. Dai, J. Endres, P.-E. Hansen, L. Nielson, M.H. Madsen, S. Heidenreich, M. Krumrey, B. Loechel, J. Probst, F. Scholze, V. Soltwisch, M. Wurm, SPIE Proc. **9556**, 955610 (2015)
135. M. Wurm, S. Bonifer, B. Bodermann, J. Richter, Meas. Sci. Technol. **22**, 094024 (2011)
136. M. Foldyna, T.A. Germer, B.C. Bergner, R.G. Dixson, Thin Solid Films **519**, 2633 (2011)
137. P. Boher, M. Luet, T. Leroux, J. Petit, P. Barritault, J. Hazart, P. Chaton, SPIE Proc. **5375**, 1302 (2004)
138. O. El Gawhary, N. Kumar, S.F. Pereira, W.M.J. Coene, H.P. Urbach, Appl. Phys. B **105**, 775 (2011)

139. N. Kumar, P. Petrik, G.K.P. Ramanandan, O. El Gawhary, S. Roy, S.F. Pereira, W.M. J. Coene, H.P. Urbach, Opt. Expr. **22**, 24678 (2014)
140. J. Endres, N. Kumar, P. Petrik, M. Henn, S. Heidenreich, S.F. Pereira, H.P. Urbach, B. Bodermann, SPIE Proc. **9132**, 913208 (2014)
141. S. Roy, N. Kumar, S.F. Pereira, H.P. Urbach, J. Opt. **15**, 75707 (2013)
142. S. Burger, L. Zschiedrich, J. Pomplun, F. Schmidt, B. Bodermann, *Proceedings of SPIE 8681, Metrology Inspections Process Control Microlithography XXVII*, vol. 8681, p. 868119 (2013)

Chapter 18
Transparent Conductive Oxide Materials

Hiroyuki Fujiwara and Shohei Fujimoto

Abstract For most of solar cell devices, a transparent conductive oxide (TCO) electrode is a vital component. Nevertheless, free carrier and interband transitions that occur within TCO layers reduce the short-circuit current density (J_{sc}) rather significantly. Thus, the suppression of the parasitic optical absorption in TCO layers is crucial in improving solar cell efficiencies. The free carrier absorption in all TCO materials can be described by the simple Drude model in which absorption characteristics of free electrons are expressed based on two parameters: i.e., optical carrier concentration and optical mobility. From these parameters, the carrier transport properties of TCO materials can further be studied. In this chapter, the optical transitions and physics of free electrons in various TCO materials are reviewed. In particular, the variation of TCO optical constants with carrier concentration is explained in detail. This chapter further introduces ellipsometry analyses of various TCO layers. The ellipsometry characterization examples described here include the analyses of standard (thin) layers, thicker layers, and textured layers. From the absorption features derived from theoretical treatments summarized in this chapter, J_{sc} loss in actual solar cells can be estimated.

18.1 Introduction

Transparent conductive oxide (TCO) electrodes are generally incorporated into solar cells as front electrodes. Although a standard crystalline Si (c-Si) solar cell does not have any TCO layers, this is exceptional and almost all thin-film solar cells have TCO layers. In addition, TCO layers are also incorporated into c-Si heterojunction solar cells with hydrogenated amorphous silicon (a-Si:H) layers. Figure 18.1 summarizes the solar cell structures of (a) $CuIn_{1-x}Ga_xSe_2$ (CIGSe), (b) $CH_3NH_3PbI_3$ (n-p type), (c) $CH_3NH_3PbI_3$ (p-n type), (d) CdTe, (e) a-Si:H/c-Si and (f) MoO_x/a-Si:H/c-Si. The thicknesses of the solar-cell component layers in this

H. Fujiwara (✉) · S. Fujimoto
Gifu University, 1-1 Yanagido, Gifu 501-1193, Japan
e-mail: fujiwara@gifu-u.ac.jp

© Springer International Publishing AG, part of Springer Nature 2018

H. Fujiwara and R. W. Collins (eds.), *Spectroscopic Ellipsometry for Photovoltaics*,
Springer Series in Optical Sciences 212,
https://doi.org/10.1007/978-3-319-75377-5_18

figure are adopted by referring to the reported values for CIGSe [1], $CH_3NH_3PbI_3$ [2, 3], CdTe [4] and c-Si heterojunction [5, 6] solar cells.

For the fabrication of solar cells, ZnO:Al, In_2O_3:Sn (ITO) and SnO_2:F front-TCO layers are commonly applied. As shown in Fig. 18.1c, e, TCO layers are also employed as rear electrodes of solar cells (i) to enhance carrier extraction [3], (ii) to improve back-side reflection by absorber/TCO/metal structures [7] and (iii) to fabricate tandem-type solar cells [8, 9]. The necessity of TCO electrodes in solar cell devices, however, is a serious drawback and the short-circuit current density (J_{sc}) decreases by 5–20% due to the parasitic light absorption within TCO layers (see Sect. 2.6.2 in Vol. 2). In four-terminal tandem solar cells, the effect of the TCO light absorption becomes even more problematic as there are at least three TCO layers in this case; i.e., two TCO layers (front and rear) in the top cell and one front

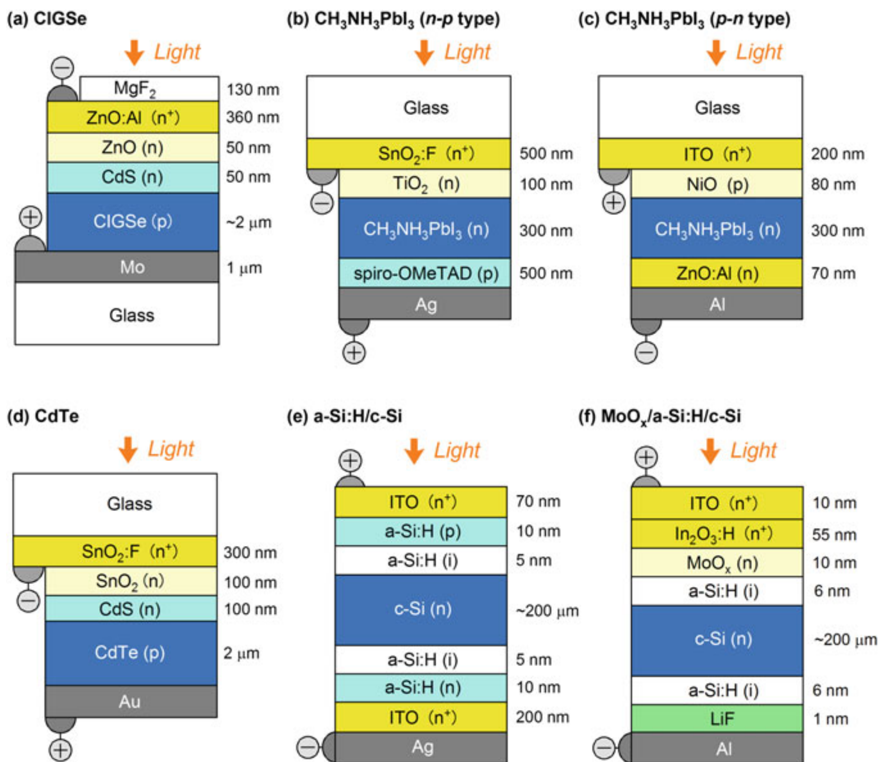

Fig. 18.1 Solar cell structures of **a** CIGSe, **b** $CH_3NH_3PbI_3$ (n-p type), **c** $CH_3NH_3PbI_3$ (p-n type), **d** CdTe, **e** a-Si:H/c-Si and **f** MoO_x/a-Si:H/c-Si. The thicknesses of the solar-cell component layers are adopted by referring to the reported values for CIGSe [1], $CH_3NH_3PbI_3$ [2, 3], CdTe [4] and c-Si heterojunction [5, 6] solar cells. In the figure, TCO layers are shown by the yellow color, whereas the absorber and doped layers are indicated by the blue colors. The carrier types of each layer are also indicated. The operating principles of hybrid perovskite solar cells [i.e., (**b**) and (**c**)] are discussed in Sect. 16.3. The spiro-OMeTAD layer in (**b**) is a hole-transport organic layer (Fig. 9.18 in Vol. 2) and has a p-like character

TCO layer in the bottom cell [9]. To maximize solar-cell conversion efficiencies, therefore, the suppression of the TCO parasitic absorption is crucial.

So far, for photovoltaic devices, a variety of TCO materials have been employed. Figure 18.2 summarizes the valence and conduction band positions of various TCO materials determined experimentally. In this figure, the energy positions reported in [10, 11] are shown with the sequence of their work function ϕ. As confirmed from Fig. 18.2, most of TCO materials show n-type characteristics. However, NiO is a p-type TCO material and has been applied as a hole injection layer (Fig. 18.1c). High work-function materials, such as MoO_3 (MoO_x) and V_2O_5, can be used as hole injection layers [12–14] or alternative materials of p-type semiconductor layers [6, 15, 16].

Figure 18.3 summarizes the absorption coefficient (α) spectra of various TCO materials employed for solar cell fabrication. These α spectra versus photon energy (E) and wavelength (λ) represent those calculated from the modeled dielectric functions described in Chap. 11 (Vol. 2). The α spectrum of SnO_2:F has been extracted from a commercialized substrate (TEC-15, Fig. 11.11 in Vol. 2) [17]. As illustrated in Fig. 18.3, the light absorption in the TCO materials is categorized into two major factors: namely, (i) optical transition from the valence to conduction bands (i.e., interband transition), which occurs typically in a high energy region ($E > 2.5$ eV) and (ii) free carrier absorption (FCA) at lower energy. The FCA is induced by free electrons present within the TCO (Sect. 18.2.2) and the FCA shows a quite broad absorption feature ranging from visible to near infrared. It should be noted that the FCA of the ITO, ZnO:Ga and SnO_2:F in Fig. 18.3 is determined primarily by the electron concentration and not by material properties (Sect. 18.2.1). Furthermore, the FCA in TCO materials varies significantly with the mobility, and high-mobility TCO layers exhibit quite small FCA (Chap. 19). In fact, the FCA of the H-doped In_2O_3 (In_2O_3:H) in Fig. 18.3 is suppressed quite well ($\alpha \sim 300$ cm^{-1} at $\lambda = 800$ nm) due to higher electron mobility exceeding 100 cm^2/(V s) [18, 19], compared with ITO ($\alpha \sim 4400$ cm^{-1} at $\lambda = 800$ nm). On the other hand, TiO_2 does not exhibit strong light absorption in visible region and

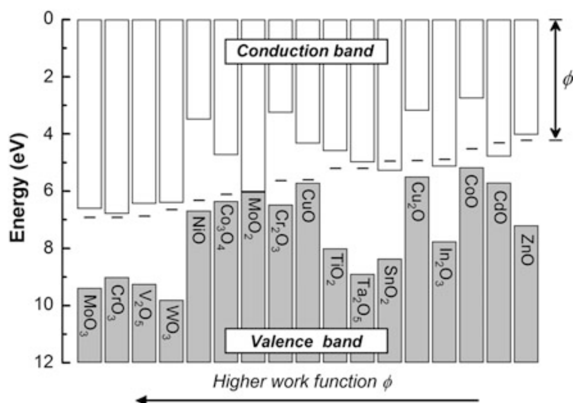

Fig. 18.2 Valence and conduction band positions of various TCO materials determined experimentally. Numerical data are taken from [10, 11]. In this figure, the energy positions are shown with the sequence of their work function ϕ

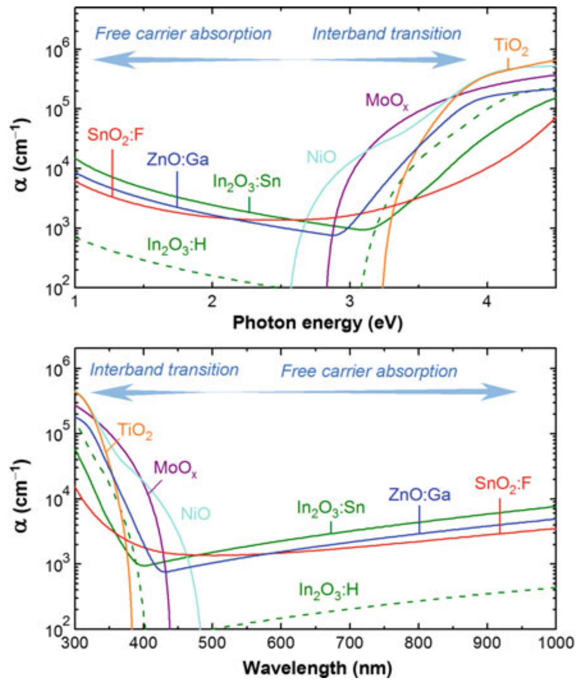

Fig. 18.3 α spectra of various TCO materials. These α spectra represent those calculated from the modeled dielectric functions described in Chap. 11 (Vol. 2): SnO_2:F (Fig. 11.11 in Vol. 2), ZnO:Ga (Fig. 11.19 in Vol. 2), ITO (Fig. 11.5 in Vol. 2), In_2O_3:H (Fig. 11.3 in Vol. 2), NiO (Fig. 11.9 in Vol. 2), MoO_x (Fig. 11.8 in Vol. 2) and TiO_2 (Fig. 11.12 in Vol. 2). The α spectrum of SnO_2:F has been extracted from a commercialized substrate (TEC-15, Pilkington) [17]. The regions of the interband transition and the free carrier absorption (FCA) are also indicated

the parasitic absorption in TiO_2 layers is negligible (Fig. 16.19). The high conversion efficiencies observed in hybrid perovskite solar cells (~20%) arise in part from the superior optical characteristics of TiO_2 (Sect. 16.3.2) [20, 21].

Figure 18.4 shows the schematic structures of (a) superstrate-type and (b) substrate-type solar cells. In superstrate solar cells, the light is illuminated from the substrate side and a relatively thick TCO front layer (300–600 nm) is required to lower series resistance sufficiently. In this case, rather strong parasitic absorption occurs in the thick TCO layer due to FCA, reducing J_{sc} notably (see Fig. 2.23 in Vol. 2, for example). It can be noticed that the $CH_3NH_3PbI_3$ and CdTe solar cells shown in Fig. 18.1 are the superstrate-type solar cells. In substrate-type solar cells, on the other hand, the thickness of TCO front layers can be reduced when metal-grid electrodes are formed on the TCO layers. In the case of c-Si heterojunction solar cells, metal-grid electrodes have been adopted and quite thin TCO layers (~70 nm) can be employed (see Fig. 18.1e). In large-area thin film modules, however, the application of grid electrodes is difficult and thick TCO layers are used even for substrate-type solar cells, including CIGSe solar cells [22, 23]. Thus, the suppression of FCA is quite important to improve solar cell and module efficiencies.

In a-Si:H/c-Si solar cells, a thin TCO front layer with a thickness of d = 70 nm also acts as an anti-reflection layer. As illustrated in Fig. 18.4b, when the phase difference between the incident light and reflected light passing through the TCO layer is π, the light waves overlap deconstructively and the reflectance decreases. As known well [24, 25], λ of the light decreases to $\lambda' = \lambda/n$ in a medium with a

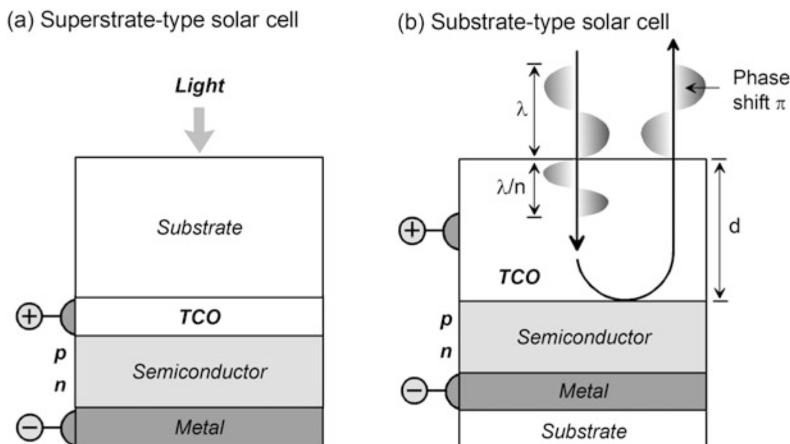

Fig. 18.4 Schematic structures of **a** superstrate-type and **b** substrate-type solar cells. In (**b**), λ indicates the wavelength of the incident light, whereas n and d denote the refractive index and thickness of the TCO layer, respectively. The phase shift of the reflected light is π and satisfies the anti-reflection condition

refractive index n. Since the optical pass length within the TCO layer is $2d$, the anti-reflection condition is satisfied when $2d = \lambda'/2$. Accordingly, if $\lambda = 560$ nm and $n = 2$ in the TCO layer, the TCO thickness that satisfies the anti-reflection condition is estimated by

$$d = \frac{1}{2} \cdot \frac{1}{2} \cdot \frac{\lambda}{n} = 70\,\text{nm}. \tag{18.1}$$

As a result, in TCO/a-Si:H/c-Si solar cell structures, the reflectance becomes zero at $\lambda \sim 560$ nm when $d \sim 70$ nm [26, 27].

As confirmed from Fig. 18.1, many solar cells have TCO bilayer structures (i) to improve the characteristics of TCO/semiconductor interfaces [3, 4], (ii) to eliminate the parasitic light absorption in doped semiconductor layers [6, 15, 16], and (iii) to reduce the FCA in TCO layers [6, 16]. In general, a non-doped TCO layer with higher resistivity is inserted at a TCO/semiconductor interface [1–4] to suppress the interface recombination and to form a favorable band alignment at the interface (see Fig. 18.1a–d). In CIGSe solar cells [1, 22, 23], ZnO:Al/ZnO(non-doped) bilayer structures have been used widely (Fig. 18.1a), whereas non-doped SnO_2 layers have been incorporated into CdTe solar cells (Fig. 18.1d).

More recently, doped semiconductor layers that show strong light absorption are replaced with TCO layers [6, 15, 16]. For this purpose, a MoO_x layer having a high workfunction (see Fig. 18.2) has been used instead of an a-Si:H p layer in a-Si:H/c-Si heterojunction solar cells (see Fig. 18.1e, f). In $CH_3NH_3PbI_3$ hybrid perovskite (Fig. 18.1b) and dye-sensitized solar cells, a SnO_2:F/TiO_2 bilayer has been adopted

widely [2, 28] and the TiO_2 electron transport layer can be considered as a replacement of a n-type semiconductor layer. For hybrid perovskite solar cells, the application of ITO/NiO bilayer structures has also been reported [3, 29] (see Fig. 18.1c), although slight parasitic absorption occurs in the NiO layer due to a small E_g of NiO (see Fig. 18.3).

To suppress the FCA in a TCO layer, a stacked structure of an ITO layer (10 nm) and a high-mobility In_2O_3:H layer (60 nm) has been employed [6, 16]. In this case, a thin ITO layer with a high carrier concentration is taking a role of a contact layer, whereas the In_2O_3:H with less FCA acts as a carrier transport layer [30]. As mentioned above, in four-terminal tandem solar cells, the suppression of the FCA becomes even more critical and advanced TCO structures may be required.

In large-area solar cell modules, on the other hand, the high structural uniformity of TCO layers is quite important to achieve high module efficiencies. In particular, the thin film module is consisting of elementary cells having a striped shape, and these elementary cells are integrated by using a laser or mechanical scribing technique (see Fig. 4.2 in Vol. 2). In the modules, all the elementary cells are connected electrically in series, and the total module current is determined by an elementary cell that shows the lowest current. Accordingly, the structural non-uniformity of the TCO layer directly affects the total output power of the module.

For the module production, a thicker TCO layer is used as mentioned above and thickness non-uniformity tends to increase. For the inspection of such non-uniformities, spectroscopic ellipsometry (SE) provides an ideal tool with which layered structures and optoelectronic properties can be characterized non-destructively. Figure 18.5 shows a SE characterization result obtained from a

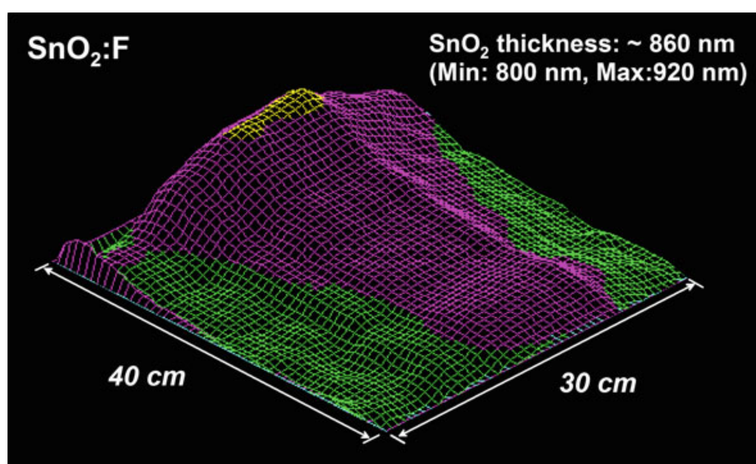

Fig. 18.5 Thickness inhomogeneity of a SnO_2:F layer formed on a large-area glass substrate with a size of 40 × 30 cm^2 [31]. The SnO_2:F layer thickness at each point was characterized by SE. The maximum thickness of the SnO_2:F layer is 920 nm, while the minimum thickness is 800 nm

large-area SnO_2:F-coated glass substrate with a size of 40 × 30 cm^2 [31]. In this analysis, the thickness inhomogeneity of the SnO_2:F layer is determined by a standard SE analysis. It can be seen that the SnO_2:F layer with a thickness of ~ 860 nm shows an irregular thickness variation of 15%. If the module is fabricated using this substrate, J_{sc} in the central region decreases due to a thicker SnO_2:F layer. For the interpretation of the module efficiencies, therefore, SE characterization is quite helpful.

In this chapter, we will review the overall optical characteristics of TCO materials. Specifically, the interpretation and modeling of FCA in TCO layers are described in details. This chapter provides SE analysis examples for various TCO layers and structures. Furthermore, we discuss the effect of carrier concentration on the optoelectronic properties of TCO materials.

18.2 Optical Properties of TCO Materials

The understanding of the optical transitions in TCO materials forms a basis for the interpretation of optical losses in solar cell devices. In this section, quite general optical properties of TCO materials are introduced. The modeling of TCO dielectric functions described here is critical to perform accurate SE analyses as well as optical device simulation of solar cells.

18.2.1 Optical Transitions in TCO Materials

As we have seen in Fig. 18.3, two separate absorption processes (i.e., interband transition and FCA) exist in the TCO. Figure 18.6 illustrates the optical transitions due to the interband transition and FCA. In many doped and some non-doped TCO layers, the free carrier concentration (N_f) is quite high (typically $N_f > 10^{18}$ cm^{-3}) and, in this case, the Fermi level (E_F) locates inside the conduction band due to the upward shift of E_F (see also ϕ in Fig. 18.2). This conduction band filling with free electrons leads to a semiconductor-to-metal transition and the TCO materials exhibit metallic optical properties. Quite interestingly, since the conduction band is partially occupied with electrons, the optical transition from the valence to the conduction band does not occur in the energy range corresponding to the band gap (E_g) and the light absorption in this range is negligible ($\varepsilon_2 \sim 0$). However, the interband optical transition does occur to the vacant conduction band states above E_F, and the photon energy required for the interband transition (E_{inter}) becomes much larger than E_g. Since the E_F position moves upward with increasing N_f, the absorption onset shifts toward higher energy with N_f. This high-energy shift of the absorption edge is referred to as the Burstein-Moss shift.

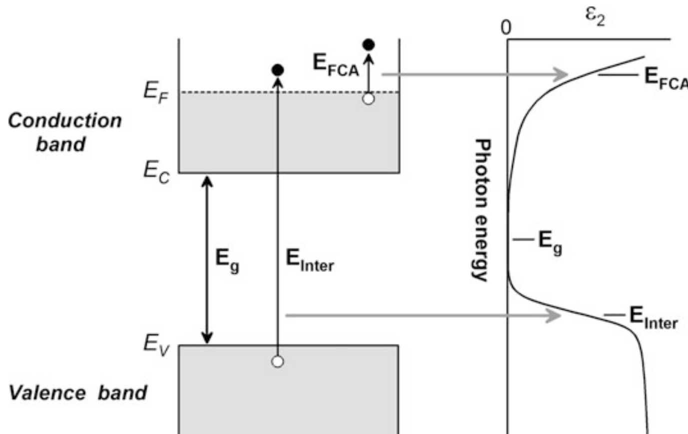

Fig. 18.6 Optical transition processes in TCO materials and the corresponding ε_2 spectrum. The E_F shows the Fermi level and E_V (E_C) denotes the maximum (minimum) energy position of the valence (conduction) band. The E_{Inter} and E_{FCA} represent the transition energies for the interband transition and free carrier absorption (FCA), respectively, while E_g is the band gap of the TCO

The free electrons in the conduction band also absorb light, and the FCA in the TCO occurs from the filled states to the empty states within the conduction band. In Fig. 18.6, E_{FCA} represents the transition energy of FCA. It should be emphasized that FCA increases at lower energies (or longer wavelengths) and ε_2 increases significantly in this region. Consequently, the optical absorption of the TCO can be described by superimposing two separate absorption processes attributed to the interband and free-electron transitions.

Figure 18.7 shows the ε_2 spectra of (a) non-doped and (b) doped ZnO, In_2O_3 and SnO_2 layers. The complete optical data of the TCO materials [1, 17, 32, 33] are summarized in Chap. 11 (Vol. 2). In Fig. 18.7a, the onset of the absorption is basically consistent with E_g, and E_g becomes larger in the order ZnO $<$ In_2O_3 $<$ SnO_2. Thus, to suppress the parasitic light absorption induced by the interband transition, the application of SnO_2 is more favorable. On the other hand, the ε_2 peak of non-doped ZnO observed at 3.45 eV originates from excitonic transition [34–36].

In Fig. 18.7b, the ε_2 spectra of the doped TCO layers with N_f in a range of (3.5–7.0) $\times$ 10^{20} cm^{-3} [33] are shown. These ε_2 spectra correspond to the α spectra shown in Fig. 18.3. It can be seen that the absorption edge of the doped TCO materials shifts toward higher energies, compared with the corresponding non-doped materials, due to the Burstein-Moss effect. In particular, the SnO_2:F shows quite small interband optical absorption below 4 eV ($\lambda > 310$ nm). For solar cell fabrication, doped ZnO (ZnO:Al or ZnO:Ga) layers with $N_f = 2 \times 10^{20}$ cm^{-3} have been used [1, 21], while ITO and SnO_2:F layers with $N_f = 5 \times 10^{20}$ cm^{-3} are employed for a-Si:H/c-Si [26, 37] and hybrid perovskite [20] solar cells.

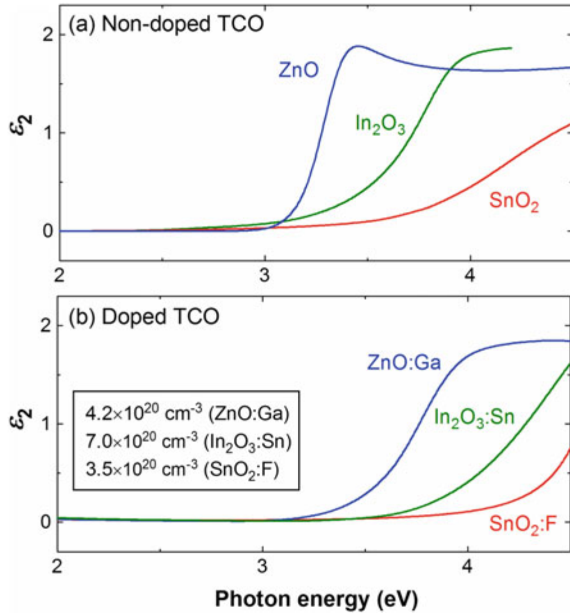

Fig. 18.7 ε_2 spectra of **a** non-doped and **b** doped ZnO, In_2O_3 and SnO_2 layers. The optical data of the TCO materials were taken from those shown in Chap. 11 (Vol. 2): ZnO (Fig. 11.16 in Vol. 2) [1], In_2O_3 (Fig. 11.2 in Vol. 2), SnO_2 (Fig. 11.10 in Vol. 2) [32], ZnO:Ga (Fig. 11.19 in Vol. 2) [33], ITO (Fig. 11.5 in Vol. 2) [33], and SnO_2:F (Fig. 11.11 in Vol. 2) [17]. The α spectra of the doped TCO layers have been shown in Fig. 18.3. The free (optical) carrier concentrations ($N_f = N_{opt}$) of each doped layer are also indicated. The high-energy shift of the ε_2 spectra by doping is caused by the Burstein-Moss effect

Figure 18.8 summarizes the variation of (a) the dielectric function and (b) the α spectrum with N_f in ZnO:Ga layers [33]. The N_f values were determined by electrical (Hall) measurements, and the carrier properties characterized by Hall measurements will be referred to as the Hall carrier concentration (N_{Hall}) and Hall mobility (μ_{Hall}) in this chapter. As shown in Fig. 18.8a, by the effect of FCA, the ε_2 values at low energies increase drastically with increasing N_f (N_{Hall}), while the ε_1 values reduce with N_f. The energy position of $\varepsilon_1 = 0$ is called plasma energy (E_p), from which the effective mass (m^*) of the TCO can be estimated (Sect. 18.3.3). Since ε can be related to complex refractive index $N = n - ik$ by $\varepsilon = N^2$ (1.15), n becomes ~2 ($\varepsilon_1 \sim 4$) in a low energy region when N_f is low. However, the slight increase in FCA leads to the large reduction in ε_1 (or n). When N_f is high, the reduction of ε_1 is rather significant even in the visible region (~2 eV).

In Fig. 18.8a, the whole ε_1 and ε_2 spectra move toward higher energy with increasing N_f due to the Burstein-Moss effect. In Fig. 18.3, compared with the In_2O_3:H, the ITO shows the blue shift of the band-edge absorption, which also represents the Burstein-Moss shift in the In_2O_3. Accordingly, by the change of N_f, the interband and free carrier optical transitions vary, modifying the whole dielectric function significantly. It can be noticed from Fig. 18.8a that the ZnO excitonic peak becomes broader as N_f increases. This effect has been explained by screening of the exciton Coulomb attraction by free electrons [33, 38, 39].

In Fig. 18.8b, the corresponding α spectra of the ZnO:Ga are shown. These results were obtained from simple conversion of the dielectric functions of Fig. 18.8a using (1.13) and (1.19). In conventional spectral ranges used for

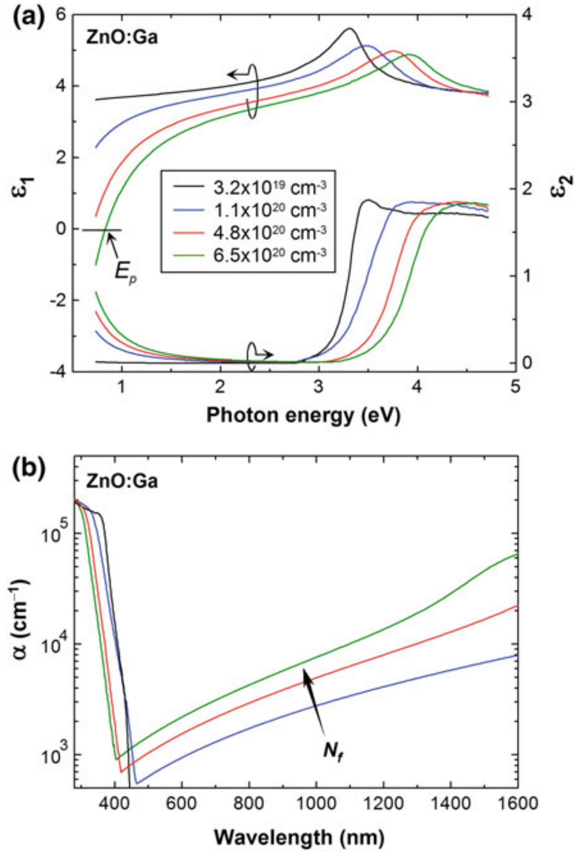

Fig. 18.8 Variation of **a** the dielectric function and **b** the α spectrum with free carrier concentration (N_f) in ZnO:Ga layers [33]. The N_f values correspond to the Hall carrier concentrations (i.e., $N_f = N_{Hall}$). In (**a**), E_p represents the plasma energy. In (**b**), the α values versus λ are shown

quantum efficiency (QE) measurements (λ = 300–1200 nm, for example), the influence of the interband transition is rather limited. However, the FCA in the visible and near-infrared region increases remarkably with increasing N_f and the corresponding QE decreases by the parasitic FCA. Since FCA is enhanced notably in longer λ (low E), the optical loss originating from the FCA becomes more severe in low-E_g solar cells due to the wider spectral responses [21]. For these solar cells, therefore, the suppression of the FCA is of significant importance.

18.2.2 Drude Model

Quite fortunately, the FCA in various TCO materials can be expressed completely by the Drude model (see also Sect. 5.3.4). Figure 18.9 illustrates a scattering process of a free electron by point defects, from which the Drude model is derived. When an electromagnetic wave advances into a TCO, a free electron is accelerated

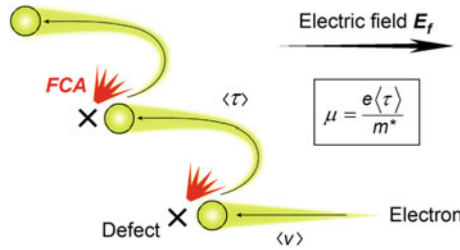

Fig. 18.9 Free-electron scattering process assumed in the Drude model. When a free electron is scattered by a point defect, free carrier absorption (FCA) occurs under light illumination. The free electron has a mean speed of $\langle v \rangle$ and is scattered repeatedly with a mean time interval of $\langle \tau \rangle$. The μ, e and m^* represent the drift mobility, electron charge and effective mass, respectively

by the electric field (E_f) and the electron drifts along the opposite direction of E_f with a mean speed of $\langle v \rangle$. However, if there are scattering centers, such as point and extended defects, the electron is scattered with a mean time interval of $\langle \tau \rangle$. Whenever the electron is scattered, the accelerated electron loses its acceleration completely and the FCA occurs. Accordingly, the FCA within TCO materials is enhanced as the electron and defect concentrations increase.

The motion of the free electron in Fig. 18.9 is described simply by

$$F_{fe} = m^* \frac{dv}{dt} = m^* \frac{\langle v \rangle}{\langle \tau \rangle}, \tag{18.2}$$

where m^* represents the effective mass of an electron. On the other hand, $\langle v \rangle$ is proportional to E_f and can be described as $\langle v \rangle = -\mu E_f$, where μ is drift carrier mobility.

From the above equations and the electrostatic force, $F = -eE_f$, where e is the electron charge, we obtain an important relation:

$$\mu = e\langle \tau \rangle / m^*. \tag{18.3}$$

Thus, μ is proportional to $\langle \tau \rangle$, and FCA is suppressed in high-mobility TCO layers, as a longer interval time between scatterings reduces the opportunity of FCA. For the reduction of the parasitic FCA in solar cells, therefore, the application of high-mobility TCO layers is quite effective (Chap. 19). For TCO materials incorporated into solar cells, the TCO resistivity, given by $\rho = (eN_f\mu)^{-1}$, needs to be lowered to decrease the sheet resistance. In this case, however, higher N_f leads to a drastic increase in FCA. Accordingly, to realize low ρ while suppressing FCA, the combination of higher μ and lower N_f is quite favorable even though the optical loss induced by the interband transition increases due to the smaller Burstein-Moss shift at lower N_f.

When a free electron is driven by E_f of an incident electromagnetic wave [$E_f = E_{f0}\exp(i\omega t)$], the equation of motion for the free electron is expressed by

$$m^* \frac{d^2x}{dt^2} = -F_{fe} + F_{em} = -\frac{m^*}{\langle\tau\rangle}\frac{dx}{dt} - eE_{f0}\exp(i\omega t) \tag{18.4}$$

where F_{em} shows the electromagnetic force of the incident light ($F_{em} = -eE_f$) and ω is the angular frequency of the electromagnetic wave [25]. In (18.4), the minus sign for F_{fe} represents the acceleration loss by carrier scattering. Equation (18.4) describes the forced oscillation of an electron by the ac electric field of the electromagnetic wave and, as a result, the electron oscillates at the same frequency as the ac electric field [i.e., $\exp(i\omega t)$]. Thus, if the solution of (18.4) is assumed to be $x = a\exp(i\omega t)$, we obtain $dx/dt = ia\omega\exp(i\omega t)$ and $d^2x/dt^2 = -a\omega^2\exp(i\omega t)$. By substituting these into (18.4) and setting $\gamma = \langle\tau\rangle^{-1}$, we get

$$a = -\frac{eE_{f0}}{m^*}\left(\frac{1}{-\omega^2 + i\gamma\omega}\right). \tag{18.5}$$

On the other hand, from the dipole moment of $\mu_{di} = qx$, the dielectric polarization is given by $P = \sum\mu_{di}$ [25, 40]. Thus, for free electrons in unit volume, we obtain $P = -exN_f$ by setting $q = -e$. Since $x = a\exp(i\omega t)$, the relation of $P = e^2N_fE_f/\{m^*(-\omega^2 + i\gamma\omega)\}$ is further derived using $E_f = E_{f0}\exp(i\omega t)$.

As shown in (1.20), the complex dielectric constant of media is expressed by $\varepsilon = 1 + P/(\varepsilon_0 E_f)$, where ε_0 is the free space permittivity [25, 40]. As a result, we obtain

$$\varepsilon = 1 - \frac{e^2N_f}{\varepsilon_0 m^*}\left(\frac{1}{\omega^2 - i\gamma\omega}\right). \tag{18.6}$$

This equation represents the Drude model.

Figure 18.10 illustrates the oscillation of free electrons in a TCO. Now imagine that free electrons and equal amount of ionized impurities exist in a cuboid with the

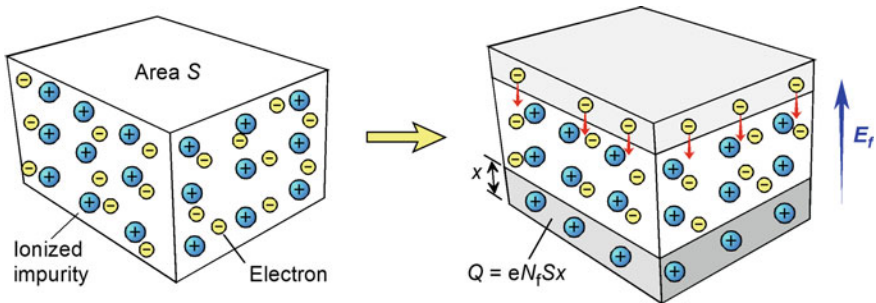

Fig. 18.10 Plasma oscillation induced by free electrons in a TCO. The amounts of free electrons and ionized impurities are equal. The free electrons exist in a cuboid with the surface area S and are displaced by a distance x. The Q represents the total charge of the charged layer

surface area S, and further suppose that all the electrons move upward by a distance x. This collective motion of the electrons forms a capacitance-like structure and generates E_f between the electron and ionized impurity layers. The total charge of this layer is given simply by $Q = eN_f Sx$ where Sx shows the volume of the charged layers. From Gauss's law, E_f generated by the collective motion of the electrons is expressed by

$$E_f = \frac{Q}{\varepsilon_p S} = \frac{eN_f}{\varepsilon_p} x, \tag{18.7}$$

where ε_p is the permittivity of the TCO. This ε_p is further described as $\varepsilon_p = \varepsilon_\infty \varepsilon_0$, where ε_∞ is the high-frequency dielectric constant (Fig. 1.5). The motion of the free electron under the presence of E_f can then be modeled as

$$m^* \frac{d^2 x}{dt^2} = -eE_f = -\frac{e^2 N_f}{\varepsilon_p} x. \tag{18.8}$$

After E_f is generated by the upward motion of the free electrons, these electrons receive the electrostatic force in the opposite direction, as indicated by the arrows in Fig. 18.10, and all the electrons start to move downward. However, the electrons may move a little too far and overshoot the ionized impurity layer, which in turn generates a capacitance-like structure again, but with the opposite polarity. In other words, the collective oscillation of the free electrons continues to occur with an oscillation frequency know as the plasma frequency. Here, we assume that this oscillation is expressed by $x = \exp(i\omega_p t)$, where ω_p is the plasma angular frequency. The insertion of this x into (18.8) leads to

$$\omega_p = \left(\frac{e^2 N_f}{\varepsilon_\infty \varepsilon_0 m^*} \right)^{1/2}. \tag{18.9}$$

If both sides of (18.9) are multiplied by $\hbar$, the following equation is obtained using $E = \hbar\omega$:

$$E_p = \hbar\omega_p = \left(\frac{e^2 \hbar^2 N_f}{\varepsilon_\infty \varepsilon_0 m^*} \right)^{1/2}. \tag{18.10}$$

As shown in Fig. 18.8, the actual value of E_p can be determined experimentally.

On the other hand, if the numerator and the denominator of the second term of (18.6) are multiplied by $\hbar^2$, we obtain the well-known Drude expression [33]:

$$\varepsilon = 1 - \frac{A_D}{E^2 - i\Gamma E}, \tag{18.11}$$

where

$$A_D = \varepsilon_\infty E_p^2 = \frac{e^2 \hbar^2 N_{opt}}{\varepsilon_0 m^*} \tag{18.12}$$

and $\Gamma = \hbar\gamma$. In the above equation, the optical carrier concentration (N_{opt}) is used instead of N_f to specify the carrier concentration characterized by (18.12). From (18.3), $\gamma = \langle\tau\rangle^{-1}$ and $\Gamma = \hbar\gamma$, we also get

$$\Gamma = \frac{e\hbar}{\mu_{opt} m^*}, \tag{18.13}$$

where μ_{opt} shows the optical mobility [33]. If (A_D, Γ) values are extracted experimentally from the SE analysis, (N_{opt}, μ_{opt}) can further be determined if m^* is known (Sect. 18.3.3).

For the Drude expression of (18.11), when the unit of electronvolt (eV) is used, e^2 in (18.12) and e in (18.13) need to be removed. For example, if $N_{opt} = 5 \times 10^{20}$ cm^{-3}, μ_{opt} = 30 cm^2/(V s) and $m^* = 0.3 m_0$, where m_0 is the free electron mass, A_D and Γ in the unit of eV are calculated as

$$A_D = \frac{(1.055 \times 10^{-34})^2 (5 \times 10^{26})}{(8.854 \times 10^{-12})(0.3 \times 9.109 \times 10^{-31})} = 2.30\,\text{eV}, \tag{18.14a}$$

$$\Gamma = \frac{(1.055 \times 10^{-34})}{(0.3 \times 9.109 \times 10^{-31})(30 \times 10^{-4})} = 0.13\,\text{eV}. \tag{18.14b}$$

Note that the units of N_{opt} and μ_{opt} in (18.14) are m^{-3} and m^2/(V s), respectively.

18.2.3 Modeling of TCO Dielectric Functions

The dielectric functions of various TCO materials can be modeled by combining the Drude model with other models that express the interband transition [18, 19, 33, 41–49]. For modeling of TCO interband transitions, the Tauc-Lorentz (TL) model (Sect. 5.3.7) has been applied extensively [18, 19, 33, 41–44], based on the work of Rovira et al. [41]. In this case, the dielectric function of the TCO is expressed by

$$\varepsilon(E) = \varepsilon_D(E) + \varepsilon_{TL}(E), \tag{18.15}$$

where $\varepsilon_D(E)$ and $\varepsilon_{TL}(E)$ indicate the dielectric functions calculated by the Drude and TL models, respectively. When the Drude model is combined with other models, $\varepsilon_D(E)$ is described by removing one from (18.11):

$$\varepsilon_{\mathrm{D}}(E) = -\frac{A_{\mathrm{D}}}{E^2 - i\Gamma E} = \left(-\frac{A_{\mathrm{D}}}{E^2 + \Gamma^2}\right) - i\left(\frac{A_{\mathrm{D}}\Gamma}{E^3 + \Gamma^2 E}\right). \tag{18.16}$$

The transformation of the above equation can be carried out by multiplying ($E^2 + i\Gamma E$) to the numerator and the denominator of $A_{\mathrm{D}}/(E^2 - i\Gamma E)$.

Figure 18.11 illustrates the modeling of a TCO dielectric function by (18.15). Since $\varepsilon(E) = \varepsilon_1(E) - i\varepsilon_2(E)$, $\varepsilon_1(E)$ and $\varepsilon_2(E)$ shown in Fig. 18.11a are calculated from $-A_{\mathrm{D}}/(E^2 + \Gamma^2)$ and $A_{\mathrm{D}}\Gamma/(E^3 + \Gamma^2 E)$, respectively. Thus, $\varepsilon_1(E)$ of ε_{D} shows negative values, whereas ε_2 increases at lower energies. The A_{D} and Γ of the Drude model essentially correspond to the amplitude and broadening parameters, although the ε_2 amplitude is determined by $A_{\mathrm{D}}\Gamma$, as confirmed from (18.16).

In the TL model shown in Fig. 18.11b, the dielectric function is expressed from five free parameters: the amplitude parameter (A), broadening parameter (C), Tauc optical gap (E_g), peak transition energy (E_0), and energy-independent contribution to $\varepsilon_1(E)$ [$\varepsilon_1(\infty)$], respectively [50] (Sect. 5.3.7). In general, at sufficiently low energies, the real part (ε_1) of $\varepsilon_{\mathrm{TL}}(E)$ shows a constant value known as the high-frequency dielectric constant (ε_∞) (see Fig. 1.5). Note that ε_∞ and $\varepsilon_1(\infty)$ are different values and ideally we obtain $\varepsilon_1(\infty) = 1$.

In Fig. 18.11c, the TCO dielectric function described by (18.15) is shown. The variation of the high-energy part is described predominantly by $\varepsilon_{\mathrm{TL}}(E)$ but ε_1 decreases and ε_2 increases at low energies due to the contribution of the Drude term.

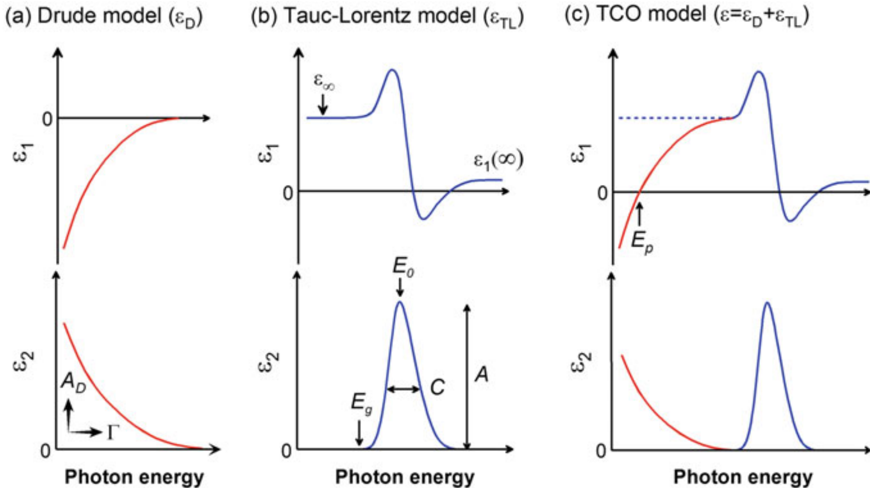

Fig. 18.11 Dielectric function modeling for TCO materials based on the Drude and Tauc-Lorentz (TL) models: **a** the Drude model ε_{D}, **b** the TL model $\varepsilon_{\mathrm{TL}}$ and **c** the TCO model described by $\varepsilon = \varepsilon_{\mathrm{D}} + \varepsilon_{\mathrm{TL}}$. In (**a**), A_{D} and Γ show the amplitude and broadening parameters, respectively. In (**b**), ε_∞ represents the high-frequency dielectric constant and the TL model is expressed by a total of five parameters: the amplitude parameter (A), broadening parameter (C), Tauc optical gap (E_g), peak transition energy (E_0), and energy-independent contribution to $\varepsilon_1(E)$ [$\varepsilon_1(\infty)$]

Notice that the ε_2 spectrum corresponds to that shown in Fig. 18.6 and the increase in ε_2 at low E shows FCA. Although a single TL peak is assumed in Fig. 18.11, to model the interband transition of TCO materials accurately, a few TL peaks need to be assumed (see Chap. 11 in Vol. 2). It can be understood from Fig. 18.11c that the ε_1 spectrum below the interband transition regime can be modeled by

$$\varepsilon_1(E) = \varepsilon_\infty - \frac{A_D}{E^2 + \Gamma^2} \tag{18.17}$$

using (18.16). Accordingly, by plotting ε_1 versus $1/(E^2 + \Gamma^2)$, ε_∞ can be determined from an intercept [33, 51, 52].

18.3 Analyses of TCO Layers

In this section, the SE analysis of an ITO layer using the Drude and TL models is introduced as a TCO analysis example. The detailed analysis of the FCA further enables us to determine m^*, which becomes critical when (N_{opt}, μ_{opt}) are deduced from (A_D, Γ). In particular, the increase of m^* with N_f due to the effect of the nonparabolicity of TCO conduction bands is discussed. The Burstein-Moss shift observed in actual TCO materials is further addressed.

18.3.1 SE Measurement

The SE measurements of TCO samples can be performed using a standard measurement configuration [33, 41]. However, TCO layers are often formed on transparent glass substrates and the influence of the back-side reflection needs to be considered in this case. Figure 18.12 shows the SE measurements of TCO samples with (a) thin (1 mm) and (b) thick (4 mm) glass substrates. When the thin glass substrate is employed, the light beam reflected on the TCO film side overlaps with the light beam reflected on the glass back side, and both light beams are detected by the detector. Unfortunately, a rather complex SE analysis is necessary in the case of Fig. 18.12a and the effect of the incoherent light beam generated by the back-side reflection should be taken into account explicitly in the analysis [53]. For module production, however, thick glass substrates are used and the two light beams are separated spatially, as illustrated in Fig. 18.12b. In this structure, only the probe light reflected on the TCO surface is detected and the influence of the back-side reflection can be neglected [42].

Even when thin glass substrates are employed, the effect of the glass back-side reflection can be eliminated by (i) using a focused optical beam [43], (ii) roughening the glass-substrate rear side or (iii) pasting a semitransparent white tape (Scotch tape) onto the back side of the glass substrate [54]. The use of the white

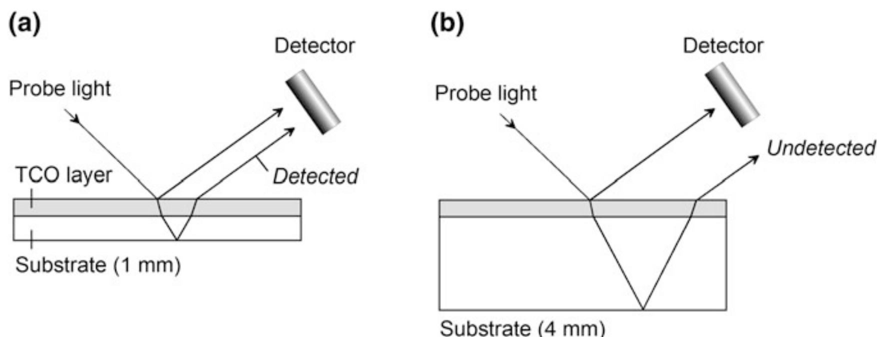

Fig. 18.12 SE measurements of TCO samples with **a** thin (1 mm) and **b** thick (4 mm) glass substrates. In the case of the thin glass substrate, the effect of the back-side reflection needs to be considered in the SE analysis unless the back-side reflection is suppressed

tape, which does not damage the glass substrate, is quite easy and favorable, although the back-side reflection component may not be eliminated completely.

For the accurate characterization of TCO dielectric functions, c-Si substrates with rough (unpolished) back surface provide ideal substrates, as the optical constants of c-Si are well known, the surface is atomically flat, and there is no back-side reflection. Unfortunately, in this case, the electrical measurements of TCO layers become difficult due to conductive c-Si substrates. Thus, c-Si substrates coated with insulating SiO_2 layers (50 nm) have also been used [33], as described in the next section. To confirm the effect of the back-side reflection on the SE analysis, the dielectric functions extracted from TCO layers formed on glass and c-Si substrates can be compared, although the substrate conductivity may alter the optical properties of prepared TCO layers particularly in the case of sputtering depositions.

18.3.2 SE Analysis of an ITO Layer

Here, as a SE analysis example, we will see the dielectric function analysis of an ITO layer formed on a c-Si substrate coated with a SiO_2 thermal oxide (50 nm) [33]. In this SE analysis, a rather thin ITO layer (70 nm) has been characterized to avoid the effect of strong dependence of FCA on film thickness. In particular, TCO layers often show a notable increase of N_f with layer thickness (see Sect. 18.4.2). In the analysis of thick TCO layers (~300 nm, for example), a more complicated SE analysis may need to be performed by modeling the exact N_f variation in the growth direction (Fig. 18.22). Accordingly, for accurate characterization of TCO layers, SE analyses of thinner layers are quite preferable.

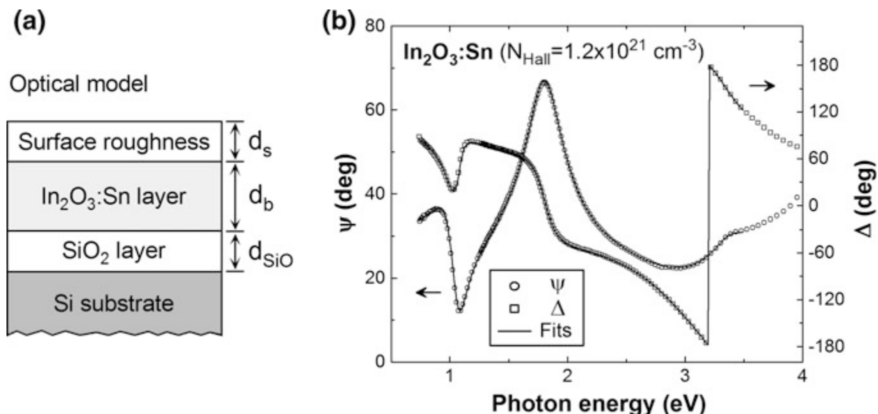

Fig. 18.13 **a** Optical model for a sputter-deposited ITO layer formed on a SiO_2/c-Si substrate and **b** (ψ, Δ) spectra obtained from the ITO sample (open circles) and the result of the SE fitting analysis (solid lines) [33]. The Hall carrier concentration of the sample is $N_{Hall} = 1.2 \times 10^{21}$ cm^{-3}. In (**a**), d_s, d_b and d_{SiO} indicate the thicknesses of the surface roughness, bulk and SiO_2 layers, respectively. In (**b**), the incident angle of the SE measurement is $\theta = 70.6°$

Figure 18.13a shows the optical model for a sputter-deposited ITO layer formed on the SiO_2/c-Si substrate. This c-Si substrate has an unpolished back surface and the effect of the back-side reflection that occurs at <1.2 eV in c-Si [55] can be neglected. The optical properties of the c-Si and SiO_2 are known (Chap. 8 in Vol. 2) and the SiO_2 layer thickness (d_{SiO}) can be determined from the SE analysis performed prior to the ITO deposition. The optical properties of the surface roughness layer can be calculated from those of the TCO bulk layer by applying the Bruggeman effective medium approximation (EMA) assuming that the void volume fraction within the roughness layer is $f_{void} = 0.5$ (see Sects. 3.4.2 and 6.1). In the above case, the unknown parameters of the optical model are the surface roughness layer thickness (d_s), bulk layer thickness (d_b), and dielectric function of the ITO layer. When the ITO dielectric function is expressed by the Drude and TL models, the SE analysis is performed using a total of nine parameters [i.e., d_s, d_b, $(A_D, \Gamma)_{Drude}$, $(\varepsilon_1(\infty), A, C, E_g, E_0)_{TL}$]. In this analysis example, however, the number of the analysis parameters is reduced to eight by assuming $\varepsilon_1(\infty) = 1$.

Figure 18.13b shows the (ψ, Δ) spectra obtained from the ITO sample [33]. The electrical measurement of the sample confirmed $N_{Hall} = 1.2 \times 10^{21}$ cm^{-3}. The peak position of ψ observed at ~2 eV in Fig. 18.13b represents the layer thickness and shifts toward lower energies with increasing thickness. On the other hand, a sharp spectral feature observed at $E < 1.5$ eV is caused by the FCA. The solid lines show the result calculated from the SE fitting analysis. In the analysis of Fig. 18.13b, the analyzed energy region was limited at $E < 3.5$ eV because the interband transition cannot be modeled completely using a single TL peak. From the above SE analysis, the thickness parameters of $d_s = 35.8 \pm 1.6$ Å and $d_b = 685.7 \pm 1.2$ Å were determined. In this case, we can further perform the

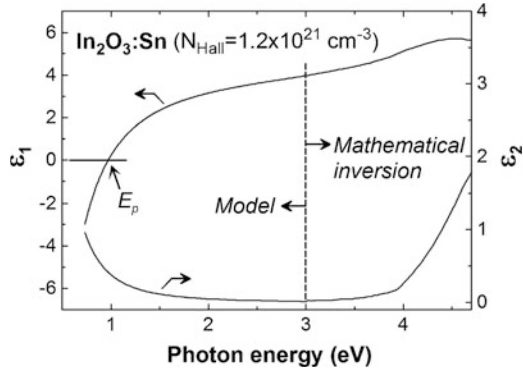

Fig. 18.14 Dielectric function of the ITO layer obtained from the SE analysis of Fig. 18.13b [33]. The high energy spectra ($E > 3$ eV) have been extracted using the mathematical inversion, while the modeled dielectric function is shown in a low energy region ($E < 3$ eV). From the energy position of $\varepsilon_1 = 0$, the plasma energy (E_p) is determined

mathematical inversion (see Sect. 10.2.1) to extract the dielectric function of the ITO in the whole measured region.

Figure 18.14 shows the dielectric function of the ITO layer extracted using the mathematical inversion [33]. At lower energies ($E < 3.0$ eV), however, to eliminate spectral noise, the dielectric function calculated from (18.15) using the extracted parameters of $A_D = 3.786 \pm 0.007$ eV, $\Gamma = 0.102 \pm 0.001$ eV, $A = 111.4 \pm 7$ eV, $C = 11.7 \pm 2$ eV, $E_g = 3.13 \pm 0.02$ eV, $E_0 = 9.6 \pm 0.2$ eV with $\varepsilon_1(\infty) = 1$ is shown. From the energy position of $\varepsilon_1 = 0$, E_p is determined to be 0.970 eV. It can be seen that the dielectric function of the ITO is essentially similar to those of doped ZnO shown in Fig. 18.8a. The above procedure has been used quite extensively to determine the optical constants of ITO [33], In_2O_3:H [18], ZnO:Al [1], ZnO:Ga [33], SnO_2:F [41, 42] layers, and all the ZnO:Ga dielectric functions shown in Fig. 18.8a have been obtained from similar SE analyses of the thin layers (~70 nm).

18.3.3 Analysis of Effective Mass

The m^* value of TCO materials can be evaluated directly from (18.10), if (E_p, ε_∞, N_f) are known [33]. As mentioned earlier, by plotting ε_1 versus $1/(E^2 + \Gamma^2)$, ε_∞ is obtained from the intercept at $1/(E^2 + \Gamma^2) = 0$ using the relation of (18.17). Figure 18.15a shows ε_1 of ZnO:Ga layers as a function of $1/(E^2 + \Gamma^2)$. The two ε_1 spectra of Fig. 18.15a correspond to those shown in Fig. 18.8a, and the solid lines indicate linear fits to the experimental results. In these analyses, the Γ values extracted from the SE analyses were employed. However, Γ is rather small ($\Gamma \sim 0.1$ eV), compared with E, and the effect of Γ is minor [33]. In Fig. 18.15a, ε_1 varies linearly versus $1/(E^2 + \Gamma^2)$, and the ε_∞ values are determined to be ~4, although ε_∞ decreases slightly with increasing N_{Hall}. The ε_∞ can also be obtained from the TL parameters. In this case, ε_∞ is simply determined from the ε_1 value of $\varepsilon_{TL}(E)$ at low energies. The above two analyses lead to similar values of ε_∞ [33].

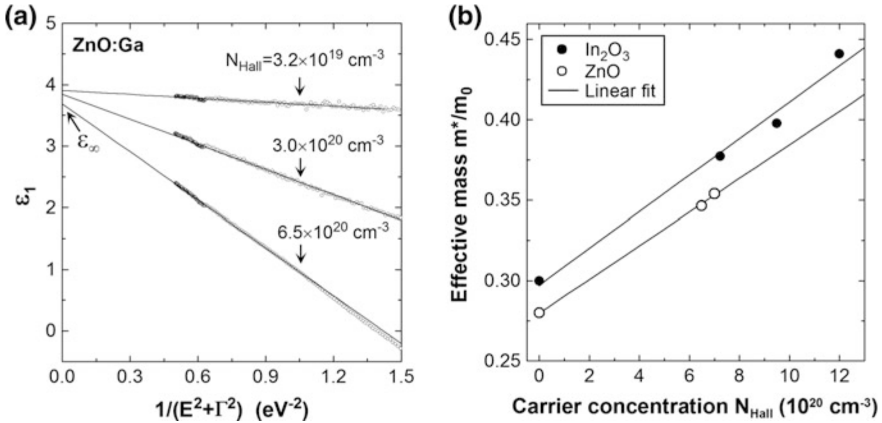

Fig. 18.15 **a** ε_1 of ZnO:Ga layers with different N_{Hall} values as a function of $1/(E^2 + \Gamma^2)$ and **b** m^*/m_0 of ZnO:Ga and ITO obtained from (18.10) as a function of N_{Hall} [33]. In the analysis of (**a**), the high frequency dielectric constant ε_∞ is determined from the intercept [i.e., $1/(E^2 + \Gamma^2) = 0$]. In (**b**), the solid lines show the results of the linear fitting analyses

Since E_{p} can be determined experimentally, if we assume that $N_{\mathrm{f}} = N_{\mathrm{Hall}}$, m^* is estimated from (E_{p}, ε_∞, N_{Hall}) using (18.10). Figure 18.15b shows m^*/m_0 of ZnO:Ga and ITO obtained from this procedure as a function of N_{Hall} [33]. In this figure, as the m^* values at $N_{\mathrm{f}} = N_{\mathrm{Hall}} = 0$ (i.e., m_0^*), reported values of $m_0^* = 0.28m_0(\mathrm{ZnO})$ [56] and $m_0^* = 0.3m_0(\mathrm{In_2O_3})$ [57] are shown. It can be seen that m^* shows a distinct increase with N_{Hall}.

When the two parameters (A_{D}, m^*) are known, N_{opt} can further be determined by applying (18.12). Figure 18.16 shows N_{opt} estimated from A_{D} assuming (a) fixed m^* values of $m^* = m_0^* = 0.28m_0(\mathrm{ZnO})$ and $m^* = m_0^* = 0.30m_0(\mathrm{In_2O_3})$ and (b) linear increases of m^* shown in Fig. 18.15b, plotted as a function of N_{Hall} [33]. When m^* is fixed, the agreement between N_{opt} and N_{Hall} is poor, and N_{opt} is underestimated seriously at high N_{Hall}. In contrast, when the variation of m^* with N_{Hall} is taken into account, N_{opt} shows remarkable agreement with N_{Hall} (Fig. 18.16b). This result provides clear evidences that (i) m^* of TCO materials increases with N_{f} and (ii) $N_{\mathrm{f}} = N_{\mathrm{Hall}} = N_{\mathrm{opt}}$ [33]. On the other hand, μ_{opt} can also be evaluated from (Γ, m^*) using (18.13). From the comparison between μ_{opt} and μ_{Hall}, the carrier transport mechanism can further be studied (Sect. 18.4).

At lower N_{f} ($N_{\mathrm{Hall}} < 2 \times 10^{20}$ cm^{-3} in Fig. 18.16), the analysis of FCA becomes increasingly difficult owing to smaller FCA in TCO materials. Sensitivity for FCA can be improved greatly if the SE spectral region is extended toward lower energies (or longer wavelengths) [18, 58–60]. When infrared and terahertz SE instruments are applied, we can characterize FCA generated by N_{f} in ranges of $>10^{18}$ cm^{-3} [18, 58] and $>10^{15}$ cm^{-3} [59, 60], respectively.

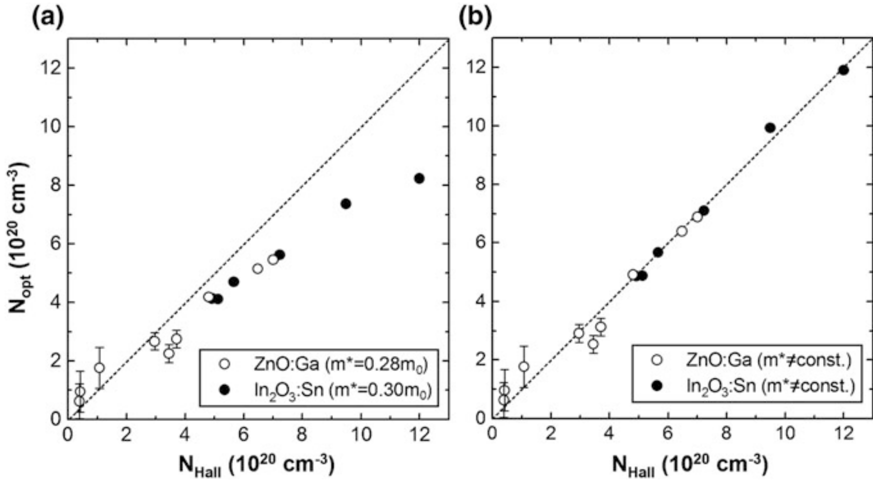

Fig. 18.16 Optical carrier concentration (N_{opt}) estimated from A_D assuming **a** fixed m^* values of $m^* = m_0^* = 0.28m_0(\text{ZnO})$ and $m^* = m_0^* = 0.30m_0(\text{In}_2\text{O}_3)$ and **b** linear increases of m^* shown in Fig. 18.15b, plotted as a function of the Hall carrier concentration (N_{Hall}) [33]

18.3.4 Nonparabolicity of TCO Conduction Bands

The increase in m^* observed in doped TCO materials has been explained by the nonparabolicity of the conduction band [33, 56–58, 61–73]. Figure 18.17 explains the nonparabolic conduction band in k space. In general, the variation of the conduction band near the bottom is assumed to be parabolic [i.e., $E = \hbar^2 k^2/(2m_0^*)$] [40]. However, this assumption is valid only near the conduction band minimum (CBM) and the conduction band cannot be expressed properly by $E = \hbar^2 k^2/(2m_0^*)$ when k is away from of the CBM [71].

The variation of the conduction band in k space can be approximated more realistically by incorporating higher order terms [66]:

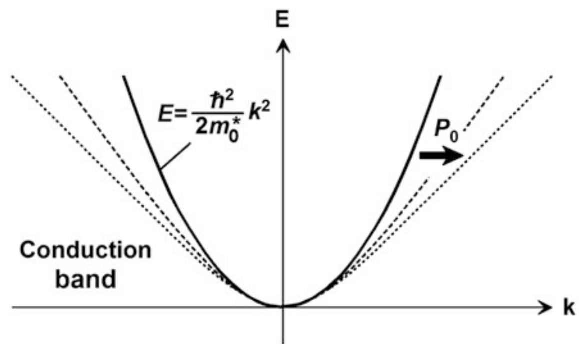

Fig. 18.17 Nonparabolic conduction band in k space. The P_0 represents a nonparabolicity parameter and $E = \hbar^2 k^2/(2m_0^*)$ when $P_0 = 0$

$$\frac{\hbar^2}{2m_0^*}k^2 = E + P_0E^2 + P_1E^3 \ldots, \tag{18.18}$$

where P_j represent nonparabolicity parameters, and m_0^* shows m^* at the CBM. In general, to describe the nonparabolicity of TCO conduction bands, only the parameter P_0 is taken into account by neglecting higher contributions (i.e., $P_1 = 0$) [63]. In this case, by solving (18.18) for E, we get

$$E = \frac{1}{2P_0}\left[-1 + \left(1 + 2P_0\frac{\hbar^2k^2}{m_0^*}\right)^{1/2}\right]. \tag{18.19}$$

The variation of the conduction band with increasing P_0 is shown in Fig. 18.17. It can be seen that, when P_0 is increased, the change of E versus k becomes more linear, as observed in the band structures of TCO materials [74].

On the other hand, from the curvature of the conduction band, m^* can be determined using the following relation [40, 75]:

$$m^* = \hbar^2k/(\mathrm{d}E/\mathrm{d}k). \tag{18.20}$$

By inserting (18.19) into (18.20) and using the Fermi wave vector $k = (3\pi^2N_\mathrm{f})^{1/3}$, an important relation is derived [63]:

$$m^*(N_\mathrm{f}) = m_0^*\left[1 + 2P_0\frac{\hbar^2}{m_0^*}(3\pi^2N_\mathrm{f})^{2/3}\right]^{1/2}. \tag{18.21}$$

The above expression shows the nonlinear variation of m^* with N_f. Although the linear variation of m^* with N_f was confirmed in Fig. 18.15b, m_0^* values in this figure were determined from different analyses [56, 57] and ambiguity remained for m_0^*. Later, m^* of In_2O_3 at lower N_f ($\sim10^{18}$ cm^{-3}) was characterized by applying infrared SE, and it has been found that m_0^* of In_2O_3 is much lower ($m_0^* = 0.18m_0$) [58] and m_0^* of $0.30m_0$ shown in Fig. 18.15b is overestimated seriously.

Figure 18.18 summarizes the variation of the effective mass (m^*/m_0) with N_Hall of In_2O_3 [58], ITO [33], SnO_2:F [72] and ZnO in (a) logarithmic and (b) linear scales. In this figure, the result of In_2O_3 indicated by closed circles has been determined from infrared and visible/ultraviolet SE measurements [58], and open circles for ITO [33], which correspond to m^* of Fig. 18.15b, show good agreement with the trend of [58]. For SnO_2:F, m^* values determined from SE analyses [72] are shown. Unfortunately, m^* values reported for ZnO are highly controversial [33, 56, 65–71]. In Fig. 18.18, therefore, the m^* values extracted from the ZnO data of Fig. 18.16 are shown. Specifically, if we assume $N_\mathrm{opt} = N_\mathrm{Hall}$, m^* can be estimated

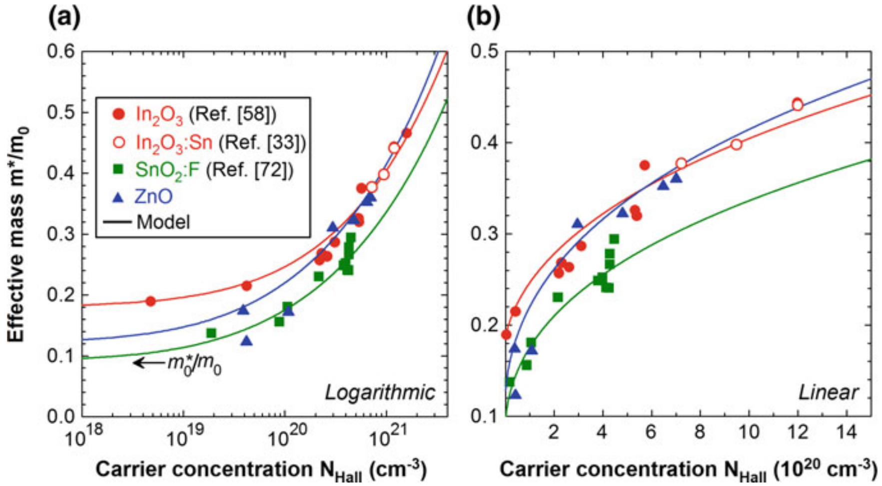

Fig. 18.18 Variation of effective mass (m^*/m_0) with N_{Hall} of In_2O_3 [58], ITO [33], SnO_2:F [72] and ZnO in **a** logarithmic and **b** linear scales. The result of ITO (open circles) corresponds to m^* shown in Fig. 18.15b. The m^* of ZnO is determined from the result of Fig. 18.16 assuming $N_{opt} = N_{Hall}$. The solid lines represent the fitting results obtained from (18.21)

directly from (18.12). In this analysis, however, two data points with $N_{Hall} \sim 4 \times 10^{20}$ cm^{-3} in Fig. 18.16, which show poor agreement with N_{opt}, are excluded.

It can be seen from Fig. 18.18 that m^* is 0.1–0.2 in a low N_{Hall} range and increases drastically at $N_{Hall} > 10^{20}$ cm^{-3}. More importantly, the increasing trend is rather independent of TCO materials, and all the TCO materials show similar values of m^*/m_0= 0.25–0.35 at $N_{Hall} \sim 5 \times 10^{20}$ cm^{-3}, which is a typical N_{Hall} in solar cells. In particular, it can be seen that the m^* values of In_2O_3 and ZnO are almost identical at $N_{Hall} > 2 \times 10^{20}$ cm^{-3}. The solid lines in Fig. 18.18 represent the calculation results obtained from the fitting analyses using (18.21) [58, 72]. In the fitting for ZnO, the parameters were adjusted so that the fitting quality in a region of (3–7) $\times 10^{20}$ cm^{-3} improves, as this range is more important in solar cell application. As confirmed from Fig. 18.18, the variation of m^* with N_{Hall} is approximated well by (18.21).

Table 18.1 summarizes the two parameters $(m_0^*/m_0, P_0)$ extracted from the analyses for In_2O_3 [58], SnO_2 [72], and ZnO. The unit of P_0 in the table is eV^{-1} and, in the actual calculation using (18.21), the value of $P_0/(1.609 \times 10^{-19})$ needs to be used. For example, when N_f (N_{opt}) of ITO is 5×10^{20} cm^{-3}, m^*/m_0 is calculated from

Table 18.1 Parameter values of TCO conduction-band nonparabolicity

TCO materials	m_0^*/m_0	P_0 (eV^{-1})	Reference
In_2O_3	0.18	0.5	[58]
SnO_2	0.09	0.8	[72]
ZnO	0.12	0.9	–

$$\frac{m^*}{m_0} = 0.18\left[1 + \frac{2(0.5)(1.055\times10^{-34})^2(3\pi^2\times5\times10^{26})^{2/3}}{(1.609\times10^{-19})(0.18\times9.109\times10^{-31})}\right]^{1/2} = 0.34. \quad (18.22)$$

Consequently, from (m_0^*, P_0), the Drude parameters (A_D, Γ) are obtained by

$$A_D = \frac{\hbar^2 N_{opt}}{\varepsilon_0 m_0^*}\left[1 + 2P_0\frac{\hbar^2}{m_0^*}(3\pi^2 N_{opt})^{2/3}\right]^{-1/2} \text{eV}, \quad (18.23)$$

$$\Gamma = \frac{\hbar}{\mu_{opt} m_0^*}\left[1 + 2P_0\frac{\hbar^2}{m_0^*}(3\pi^2 N_{opt})^{2/3}\right]^{-1/2} \text{eV}. \quad (18.24)$$

Conversely, by solving (18.23) for N_{opt}, we can express N_{opt} by

$$N_{opt} = \left[a + \left(\frac{1}{6} + \frac{2b^3}{\eta^2}\right)\eta\right]^{1/2}, \quad (18.25)$$

where

$$a = \left(m_0^*\right)^2 \varepsilon_0^2 A_D^2/\hbar^4, \quad (18.26a)$$

$$b = 2(3\pi^2)^{2/3} P_0 m_0^* \varepsilon_0^2 A_D^2/\hbar^2, \quad (18.26b)$$

$$\eta = \left[108ab^3 + 12b^3(-12b^3 + 81a^2)^{1/2}\right]^{1/3}. \quad (18.26c)$$

Note that η in (18.26c) becomes a complex number. By applying (18.25), N_{opt} can be determined from A_D assuming a nonparabolic TCO conduction band, if m_0^* and P_0 are known. Finally, μ_{opt} is determined from (Γ, N_{opt}) using (18.24).

18.3.5 Analysis of Interband Transition

As we have seen in Figs. 18.7 and 18.8, the band-edge absorption shifts toward higher energy with increasing N_f. Figure 18.19 summarizes the band-gap shift (ΔE_g) observed in In_2O_3 and ZnO as functions of (a) N_f and (b) $N_f^{2/3}$. The numerical

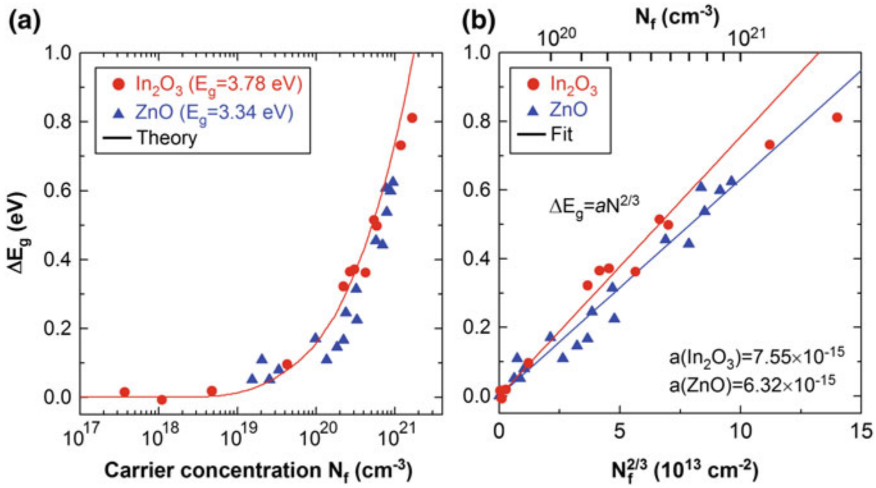

Fig. 18.19 Band-gap shift (ΔE_g) of In_2O_3 and ZnO as functions of **a** N_f and **b** $N_f^{2/3}$. The numerical data were taken from [58] (In_2O_3) and [76] (ZnO). The E_g values of In_2O_3 and ZnO are 3.78 eV [58] and 3.34 eV [76], respectively. In (**a**), the solid line for In_2O_3 shows the result of theoretical calculation using (18.28) [58]. In (**b**), the solid lines represent the results of linear fitting analyses assuming $\Delta E_g = aN_f^{2/3}$. The slopes obtained from the analyses are also indicated

data of this figure were taken from [58] (In_2O_3) and [76] (ZnO), and the E_g values of In_2O_3 and ZnO have been estimated to be 3.78 eV [58] and 3.34 eV [76], respectively. It can be seen from Fig. 18.19a that In_2O_3 and ZnO show similar variations and ΔE_g increases drastically at $N_f > 10^{20}$ cm^{-3}.

The increase in ΔE_g is essentially caused by the Burstein-Moss effect explained in Fig. 18.6, and the Burstein-Moss shift (ΔE_{BM}) can be approximated by

$$\Delta E_{BM} = \frac{\hbar^2}{2m_{eh}^*}(3\pi^2 N_f)^{2/3}, \tag{18.27}$$

where m_{eh}^* is the reduced effective mass given by $(m_{eh}^*)^{-1} = (m_e^*)^{-1} + (m_h^*)^{-1}$, and m_e^* and m_h^* denote the effective masses of the electron and hole, respectively [74, 77]. Although band-gap widening by the Burstein-Moss effect is calculated by (18.27), the actual shift of E_g does not follow this equation. This has been interpreted by a band-gap shrinkage that occurs simultaneously with band-gap widening [58, 76–78]. The band-gap narrowing (also known as band-gap renormalization) is induced by many-body effects including electron-electron and electron-ion interactions [58, 76, 78].

When the band-gap widening by the Burstein-Moss effect and the band-gap narrowing by the band-gap renormalization (ΔE_{BR}) are considered, ΔE_{g} is described by the following equation [58, 78]:

$$\Delta E_{\mathrm{g}} = \Delta E_{\mathrm{BM}} + \Delta E_{\mathrm{BR}}. \tag{18.28}$$

In the above equation, ΔE_{BM} is a positive value, while ΔE_{BR} is a negative value. Thus, the actual band-edge shift with increasing N_{f} is offset by ΔE_{BR} and becomes smaller. In Fig. 18.19a, the solid line for In_2O_3 shows the result obtained from explicit theoretical calculation using (18.28) [58]. This analysis shows that, at $N_{\mathrm{f}} = 5 \times 10^{20}$ cm^{-3}, $\Delta E_{\mathrm{BM}} = 0.9$ eV and $\Delta E_{\mathrm{BR}} = -0.4$ eV, which result in $\Delta E_{\mathrm{g}} = 0.5$ eV. Accordingly, ΔE_{g} is influenced rather significantly by the many-body effects.

The Burstein-Moss theory of (18.27) shows that the band-edge absorption shifts linearly with $N_{\mathrm{f}}^{2/3}$. In fact, as confirmed from Fig. 18.19b, the variation of ΔE_{g} exhibits a linear dependence on $N_{\mathrm{f}}^{2/3}$ and is expressed simply by $\Delta E_{\mathrm{g}} = aN_{\mathrm{f}}^{2/3}$, where a is a proportionality constant. The fitting analyses performed for the data of Fig. 18.19b using this equation lead to $a = 7.55 \times 10^{-15}$ eV cm^2 (In_2O_3) and 6.32×10^{-15} eV cm^2 (ZnO). By applying these relations, the shift of TCO dielectric functions with N_{f} can be described to some extent.

18.4 Carrier Transport Properties

As shown above, the electrical properties of TCO layers can be characterized from FCA even without the requirement of forming electrodes on samples. From μ_{opt} obtained from the FCA analysis, the carrier transport properties in TCO layers can further be studied. In this section, we focus on the carrier scattering mechanism in ZnO layers and discuss the ionized impurity and grain boundary scatterings in the ZnO. In particular, to reveal the effect of grain boundary scattering, the SE analysis of a thick ZnO:Al layer has been performed by taking N_{f} variation toward the growth direction into account [44]. The influence of humidity on the grain-boundary carrier transport in sputter-deposited ZnO:Al layers is also described.

18.4.1 Carrier Scattering in TCO

Free electrons in TCO materials are scattered by ionized impurities and grain boundaries. Figure 18.20 schematically shows (a) the ionized impurity and

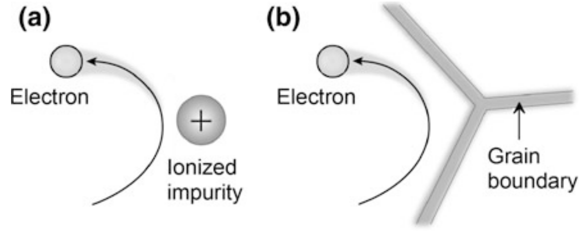

Fig. 18.20 **a** Ionized impurity and **b** grain boundary scatterings

(b) grain boundary scatterings. By considering the nonparabolicity of the TCO conduction band, the ionized impurity scattering is expressed by

$$\mu_{\text{ion}} = \frac{3\varepsilon_s^2 \varepsilon_0^2 h^3}{(m^*)^2 e^3} \left(\frac{N_f}{N_{\text{ion}} Z^2} \right) \frac{1}{F}, \tag{18.29}$$

where

$$F = \left[1 + 4\frac{\phi_1}{\phi_0}\left(1 - \frac{\phi_1}{8}\right) \right] \ln(1+\phi_0) - \frac{\phi_0}{1+\phi_0} - 2\phi_1\left(1 - \frac{5\phi_1}{16}\right), \tag{18.30a}$$

$$\phi_0 = \frac{\varepsilon_s \varepsilon_0 h^2 (3\pi^2 N_f)^{1/3}}{m^* e^2}, \tag{18.30b}$$

$$\phi_1 = 1 - m_0^*/m^*. \tag{18.30c}$$

The ε_s, N_{ion} and Z denote the static dielectric constant, ionized impurity concentration, and charge of the ionized impurity, respectively [56, 63]. The ε_s includes the contribution of the atomic polarization in an infrared region, in addition to the electric polarization in the visible/ultraviolet region, and thus $\varepsilon_s \geq \varepsilon_\infty$ (see Fig. 1.5). In (18.29), substitutional doping leads to $Z = 1$, while the charge of oxygen vacancies is $Z = 2$. The m^* in the above equations is described by (18.21). Although (18.29) and (18.30a), (18.30b), (18.30c) are complicated, from this model, the variation of μ_{ion} with N_f is calculated using ε_s, N_{ion} and m^* (or m_0^* and P_0).

For the description of grain boundary scattering in TCO materials, different models have been applied [71–74, 79]. Here, based on the work of [73], we use a simple model in which the electron scattering at grain boundaries is expressed from a dislocation density N_{dis} [80, 81]:

$$\mu_{\text{grain}} = \frac{4ea^2}{\pi^2 \hbar N_{\text{dis}}} \left(\frac{3N_f}{\pi} \right)^{2/3} \left(1 + \frac{\phi_0}{2} \right)^{3/2}, \tag{18.31}$$

where a is a lattice parameter and ϕ_0 is given by (18.30b). From μ_{ion} and μ_{grain} described above, the total mobility (μ_{total}) in the TCO can be obtained by applying Matthiessen's rule [82]:

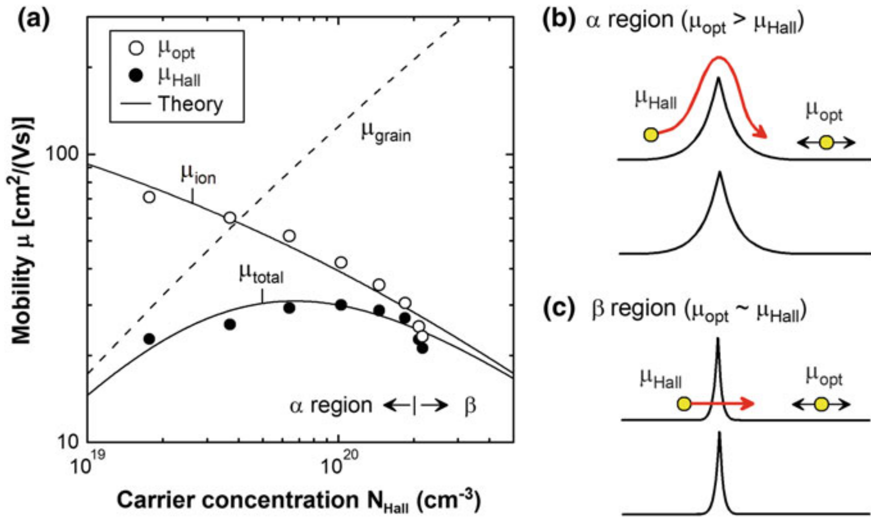

Fig. 18.21 **a** Change of μ_{opt} and μ_{Hall} in ZnO:B layers as a function of N_{Hall}, and carrier transport in **b** the α region ($\mu_{\text{opt}} > \mu_{\text{Hall}}$) and **c** the β region ($\mu_{\text{opt}} \sim \mu_{\text{Hall}}$). The experimental data of (**a**) were taken from [83, 84] but the μ_{opt} values have been corrected by taking the nonparabolicity of the conduction band into account. The μ_{ion}, μ_{grain} and μ_{total} in (**a**) are calculated from (18.29), (18.31) and (18.32), respectively

$$\frac{1}{\mu_{\text{total}}} = \frac{1}{\mu_{\text{grain}}} + \frac{1}{\mu_{\text{ion}}}. \tag{18.32}$$

The above equation simply shows that μ_{total} is essentially limited by a carrier scattering process with the lowest mobility.

Figure 18.21a shows the change of μ_{opt} and μ_{Hall} in ZnO:B layers as a function of N_{Hall}. The experimental data were taken from [83, 84]. In the reported analysis, however, the μ_{opt} values were deduced using a fixed m^* of $0.28m_0$. This m^* value is much higher than those obtained from the relation shown in Fig. 18.18. When m^* is overestimated, the corresponding μ_{opt} reduces. Accordingly, in Fig. 18.21a, μ_{opt} values were recalculated by applying (18.13) and (18.21) assuming $N_{\text{opt}} = N_{\text{Hall}}$, and the corrected values are plotted as a function of N_{Hall}.

The solid and dotted lines of Fig. 18.21a show the results calculated from (18.29)–(18.32). For these calculations, $\varepsilon_s = 9$ [85] and $a = 4.2$ Å, which corresponds to the average value of the a and c axis parameters ($a = 3.2$ Å and $c = 5.2$ Å in ZnO [74]), are used. The electron scattering analysis of Fig. 18.21a was performed assuming that μ_{opt} is not influenced by μ_{grain} since free carriers do not exist in the grain boundary region. In this case, we obtain a relation of $\mu_{\text{opt}} = \mu_{\text{ion}}$ from (18.32) and the variation of μ_{opt} is expressed from (18.29). For μ_{ion}, a good fitting is obtained when a fixed ratio of $N_{\text{ion}}/N_{\text{f}} = 7.7$ ($Z = 1$) is used. If $Z = 2$ is assumed, we obtain $N_{\text{ion}}/N_{\text{f}} = 1.9$. Thus, N_{ion} deduced from the above analysis is

higher than N_f, and μ_{opt} (μ_{ion}) decreases significantly with increasing N_f due to the increase in the number of scattering centers. Although phonon scattering is neglected in the analysis, its effect is relatively small [56, 70].

On the other hand, μ_{Hall} is affected by the grain boundary scattering as the electrons travel across the grain boundaries in electrical measurements, and thus we observe $\mu_{Hall} = \mu_{total}$. In fact, μ_{Hall} generally shows substantially lower values, compared with μ_{opt}, when the carrier transport is hindered considerably by grain boundaries [33, 44, 68–70, 72, 83, 84]. If μ_{ion} estimated from the above analysis is applied to (18.32), μ_{total} shows excellent agreement with μ_{Hall} when N_{dis} in (18.31) is 2.6×10^{12} cm^{-2}. The result of Fig. 18.21a supports that $\mu_{opt} = \mu_{ion}$ and $\mu_{Hall} = \mu_{total}$. Based on the variation of μ_{opt} and μ_{Hall} with N_f, therefore, carrier scattering mechanisms can be studied in detail.

In Fig. 18.21a, it can be seen that $\mu_{opt} > \mu_{Hall}$ at $N_f < 2 \times 10^{20}$ cm^{-3} (α region), while $\mu_{opt} \sim \mu_{Hall}$ at $N_f > 2 \times 10^{20}$ cm^{-3} (β region). Indeed, μ_{opt} at $N_f \sim 2 \times 10^{19}$ cm^{-3} is 71 cm^2/(V s) and is three times larger than μ_{Hall} at the same N_f [i.e., 23 cm^2/(V s)]. This is caused by lower μ_{grain} at lower N_f, and this phenomenon can be understood by considering a potential barrier formation at grain boundaries (Fig. 18.21b). More specifically, when N_f is low, the width of the grain-boundary potential barrier becomes wider, hindering the carrier transport (i.e., μ_{Hall}) significantly, while the free electrons exist inside the grain and are not influenced by the grain boundary. As a result, we observe $\mu_{opt} > \mu_{Hall}$ in the α region [83, 84].

However, at high N_f, the barrier width becomes quite thin and the tunneling of the electron through the potential barrier occurs (Fig. 18.21c). In this case, μ_{Hall} is no longer affected by the grain boundary as μ_{grain} increases [83, 84]. Thus, the effect of grain boundary scattering can be evaluated directly from the μ_{Hall}/μ_{opt} ratio, and this approach is quite effective in characterizing the potential barrier formation at grain boundaries. For carrier scattering in ZnO, more detailed analyses have also been reported [56, 79].

It should be emphasized that the FCA in TCO materials is determined by (μ_{opt}, N_{opt}), while the series resistance of TCO layers is determined by (μ_{Hall}, N_{Hall}). In other words, the parasitic FCA and the resulting J_{sc} reduction is influenced by μ_{opt} (see Fig. 18.9), whereas the fill factor (FF) of solar cells is influenced strongly by μ_{Hall} and may decrease if μ_{Hall} is too low. When N_f in the α region is employed, therefore, the effect of the grain boundary scattering needs to be considered. For ZnO:Al layers incorporated into solar cells, N_f of 2×10^{20} cm^{-3} has been applied [1, 21] and the effect of the grain boundary scattering is minor.

18.4.2 Thickness Variation of Grain Boundary Scattering

The electrical properties of TCO films often show strong thickness dependence [44, 86–91]. In the SE analysis described in Sect. 18.3.2, a thin layer (~70 nm) was characterized to avoid such dependence. When the optical properties of a thin layer

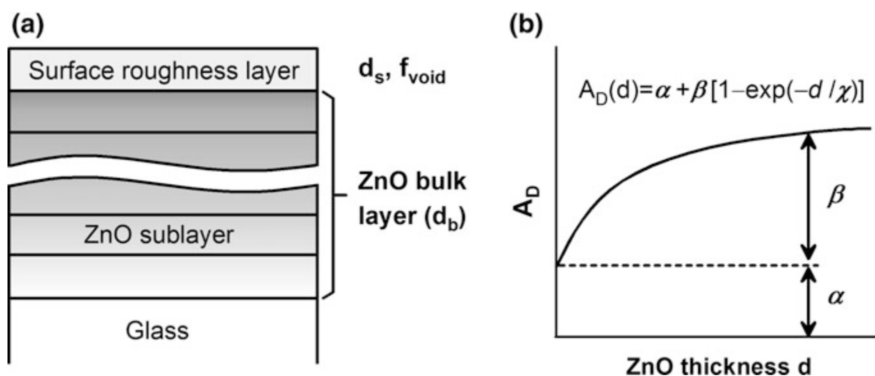

Fig. 18.22 **a** Optical model used for the SE analyses of thick ZnO:Al layers with different thicknesses (100–1600 nm) and **b** modeling of A_D variation along the ZnO growth direction. The optical model of (**a**) consists of surface roughness layer/ZnO bulk layer/glass substrate. In the analysis, the ZnO bulk layer is divided into sublayers with a thickness of ~100 nm, and A_D of each sublayer is calculated from the expression indicated in (**b**)

vary toward the growth direction, a multilayer optical model should be used in the data analysis. Here, we will see the effect of the grain boundary scattering in a thick ZnO:Al layer, determined by the multilayer SE analysis [44].

Figure 18.22 shows an optical model used for the SE analyses of sputter-deposited ZnO:Al layers with various thicknesses in a range of 100–1600 nm. This optical model consists of surface roughness layer/ZnO bulk layer/glass substrate but a multilayer model is used for the ZnO bulk layer to express the change in the FCA. The structural parameters of this model are essentially the same as that of Fig. 18.13 (i.e., d_s, d_b, f_{void}).

The dielectric function of the ZnO:Al can be expressed by the Drude and TL models. To model the continuous variation of the FCA along the growth direction, A_D at the ZnO thickness d is described by

$$A_D(d) = \alpha + \beta[1 - \exp(-d/\chi)], \tag{18.33}$$

where α, β and χ are fitting parameters [44]. In the actual analysis, A_D of each ZnO sublayer was calculated from (18.33) assuming a constant A_D within the ZnO sublayer (~100 nm), while the Drude parameter Γ was treated as a thickness-independent parameter.

For the TL model, to reduce the number of free analytical parameters, fixed values of $C = 12$ eV, $E_0 = 7$ eV and $\varepsilon_1(\infty) = 1$ were used and only two parameters (A, E_g) were varied in the SE analysis. For the surface roughness layer, $f_{void} = 0.5$ was assumed. As a result, a total of eight analytical parameters were employed in the SE analysis: i.e., (d_s, d_b) for the ZnO layer structure, (A, E_g) for the TL model, (α, β, χ, Γ) for the Drude model.

Figure 18.23 shows the (ψ, Δ) spectra obtained experimentally from the 1600-nm thick ZnO:Al layer (open circles) and fitting results (solid lines) obtained

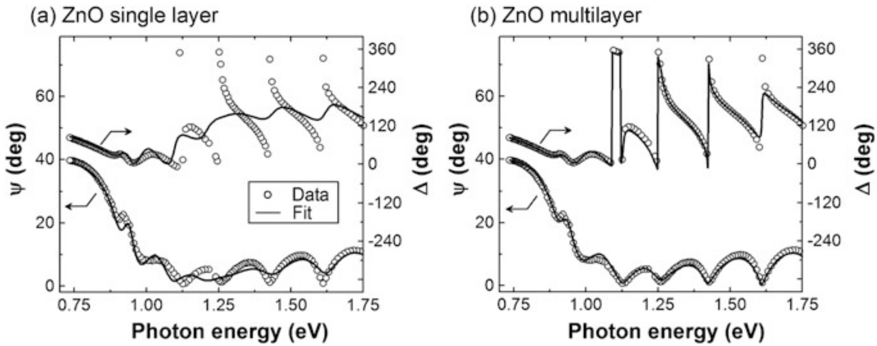

Fig. 18.23 (ψ, Δ) spectra obtained experimentally from the 1600-nm thick ZnO:Al layer (open circles) and fitting results (solid lines) obtained when the SE analyses were performed assuming **a** a single ZnO bulk layer and **b** the ZnO multilayer shown in Fig. 18.22 [44]. The incident angle of the SE measurement is $\theta = 55°$

when the SE analyses were performed assuming (a) a single ZnO bulk layer and (b) the ZnO multilayer shown in Fig. 18.22 [44]. In the case of Fig. 18.23a, the optical response of the ZnO bulk layer was calculated by simply setting $\beta = 0$ in (18.33) [i.e., $A_D(d) = \alpha$]. It can be seen from Fig. 18.23 that the fitting quality improves drastically when the ZnO multilayer model is used.

Figure 18.24 shows (a) carrier concentration (N_{opt}, N_{Hall}) and (b) mobility (μ_{opt}, μ_{Hall}) as a function of d [44]. The variation of N_{opt} was obtained from the multilayer SE analysis of the thick ZnO layer (1600 nm), whereas the N_{Hall} values were determined from the individual ZnO:Al samples with different thicknesses. In Fig. 18.24a, N_{opt} increases rapidly up to 500 nm and saturates at $d > 1000$ nm, which shows excellent correlation with N_{Hall}. In Fig. 18.24b, (μ_{opt}, μ_{Hall}) obtained from each ZnO sample are shown. The plots of $\mu_{Hall,deg}$ indicate μ_{Hall} obtained after wet air treatment (85 °C and 85% relative humidity for 1000 h). It is clear that μ_{opt} shows a constant value of ~50 cm^2/(V s), whereas μ_{Hall} increases gradually from $d = 500$ nm. Furthermore, when the changes in N_{opt} at $d \leq 300$ nm and $d \geq 1000$ nm are linearly extrapolated, we observe a cross point at a similar thickness of 500 nm, as indicated by the dotted lines in Fig. 18.24a. These results imply that the structural transition occurs at a transition thickness of $d_t = 500$ nm. In Fig. 18.24b, a rather small value of $\mu_{Hall}/\mu_{opt} \sim 0.4$ at $d < d_t$ shows that the grain boundary scattering is the dominant carrier scattering process in this regime. In contrast, μ_{Hall}/μ_{opt} approaches unity at $d > d_t$, and the effect of μ_{grain} becomes negligible.

Figure 18.24c shows the cross-sectional transmission electron microscopy (TEM) image of the ZnO:Al(1600 nm)/glass substrate structure [44]. The white lines in the figure represent the thicknesses of each layer as estimated from the SE analysis of Fig. 18.23b and the position of the ZnO:Al bulk layer deduced from SE shows excellent agreement with the actual structure. For the surface roughness, however, d_s determined from SE is rather small. In general, the sensitivity for surface roughness decreases in the SE analysis of transparent materials with low

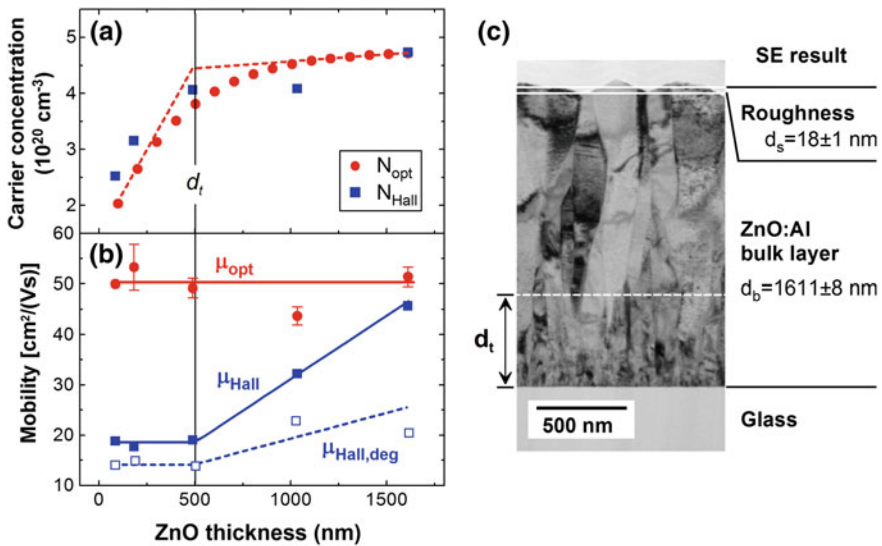

Fig. 18.24 **a** Carrier concentration (N_{opt}, N_{Hall}) and **b** mobility (μ_{opt}, μ_{Hall}) as a function of ZnO thickness, and **c** cross-sectional TEM image of the ZnO:Al(1600 nm)/glass substrate structure [44]. In (**a**), $\mu_{Hall,deg}$ shows μ_{Hall} obtained after the exposure to wet air (85% relative humidity) at 85 °C for 1000 h. The d_t represents the thickness of the ZnO transition layer (500 nm) with high-density grain boundaries

refractive indices since the difference of optical constants between the bulk layer and EMA surface roughness layer becomes small [25]. In this case, d_s of TCO layers tends to be underestimated in the SE analyses, particularly when the surface is rough [41, 44, 53].

The TEM image of the ZnO layer reveals that a sharp structural transition occurs at d_t. At $d < d_t$, the presence of high-density grain boundaries can be seen, whereas the columnar growth of the larger grain occurs at $d > d_t$. Thus, the thickness variation of the carrier transport properties can be understood from the density of the grain boundaries at each thickness. In particular, the smaller (N_{opt}, N_{Hall}) values at $d < d_t$ are most likely caused by the electron-trap formation at the grain boundaries. Density of such defects decreases as the grain size becomes larger and N_{opt} (N_{Hall}) saturates when the ZnO grains are well developed. The variation of the μ_{Hall}/μ_{opt} ratio is quite consistent with the grain boundary density in the ZnO. The increase of the conductivity with d generally saturates at ~500 nm [86, 87, 91–93]. Accordingly, the value of d_t = 500 nm appears to be a universal value for poly-crystalline ZnO layers formed on glass substrates.

When the ZnO layers were treated by wet air (85% relative humidity), the ZnO layers show large degradation. In this case, the change of μ_{opt} is minor [44], but μ_{Hall} decreases significantly to the value indicated by $\mu_{Hall,deg}$. This result provides direct confirmation that the reduction in μ_{Hall} is caused by enhanced grain boundary scattering. Previously, it has been confirmed that the columnar ZnO grain structure

with a strong *c*-axis orientation enhances the degradation under a high humidity condition [94]. During the exposure, therefore, the H_2O/O_2 species diffuse through the ZnO grain boundaries and modify the electronic states at the grain boundary. The enhanced carrier scattering at the ZnO grain boundary by the H_2O/O_2 exposure has been confirmed widely [84, 94–96]. Unfortunately, the ZnO degradation observed in wet air environment is expected to reduce the long-term stability of the large-area modules.

18.5 SE Analysis of Textured TCO Layers

Textured SnO_2:F [41–43, 97–100] and ZnO:Al [44, 99–101] layers have been incorporated into solar cells to enhance the light absorption in the devices by light scattering. Glass substrates coated with textured SnO_2:F layers have already been

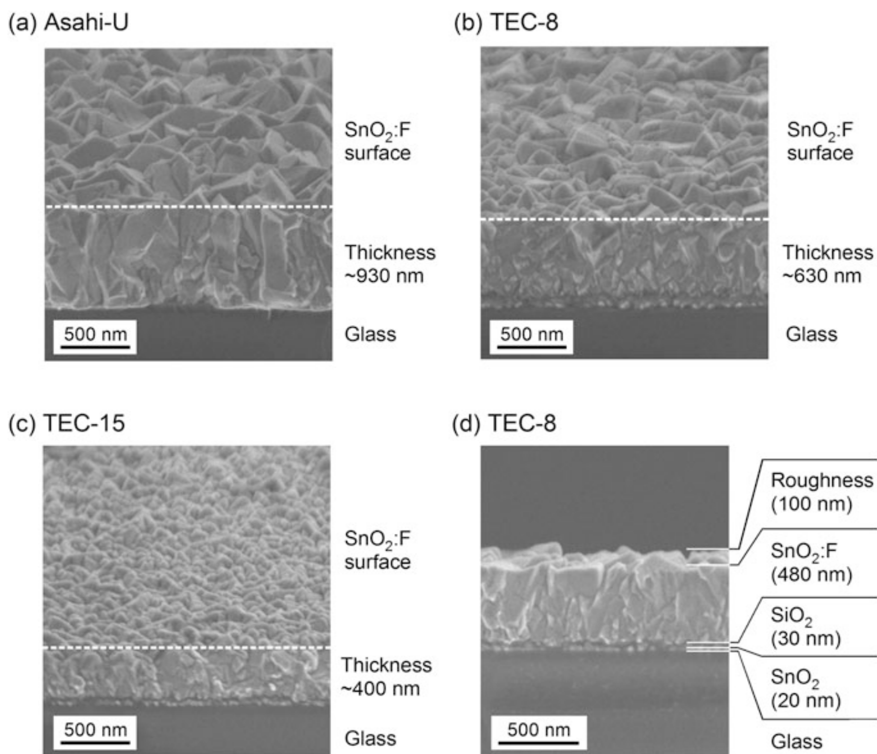

Fig. 18.25 Surface images of **a** Asahi-U, **b** TEC-8, and **c** TEC-15 substrates, and **d** cross-sectional image of the TEC-8 substrate, obtained from SEM observations. The thicknesses indicated in (**a**–**c**) correspond to the total thicknesses of each structure. In (**d**), the SnO_2:F/SiO_2 (30 nm)/SnO_2(20 nm)/glass structure of the TEC glass substrates can be confirmed

commercialized (Asahi-U and TEC glass substrates) and employed widely for solar cell fabrication [2, 4, 17, 97–99].

Figure 18.25 shows the surface images of (a) Asahi-U, (b) TEC-8, and (c) TEC-15 substrates, and (d) the cross-sectional image of the TEC-8 substrate, obtained from scanning electron microscopy (SEM) observations. The Asahi-U substrate has a structure of SnO_2:F/SnO_2/SiO_2/glass, and the thin SiO_2 layer with a thickness of 50 nm is a diffusion barrier, provided to suppress the migration of alkali-metal ions from the glass substrate [102]. Although the SiO_2 layer is not visible in the SEM, the presence of this layer can be confirmed in the TEM images (Fig. 4.19 in Vol. 2) [103]. On the other hand, TEC glass substrates (TEC-8 and TEC-15) have a structure of SnO_2:F/SiO_2/SnO_2/glass [4, 17]. In the TEC glass substrates, the SiO_2 and SnO_2 layers have been introduced to suppress the interference color change caused by thickness inhomogeneity. Table 18.2 summarizes the structure and electric properties of the Asahi-U and TEC substrates.

The layer thicknesses indicated in Fig. 18.25 correspond to the total layer thicknesses of each structure. The surface textures of the Asahi-U and TEC-8 substrates are rather similar and the texture size of these substrates is comparable to λ of the visible region (~500 nm). In this case, light scattering occurs on the texture surface and, consequently, these substrates show a relatively high haze value of

Table 18.2 Structure and electric properties of Asahi-U and TEC glass substrates. The layer thicknesses have been determined from SE analyses described in Sects. 18.5.1 and 18.5.2

	Asahi-U[a]	TEC-8	TEC-15
Structure	SnO_2:F/SnO_2/SiO_2/ glass	SnO_2:F/SiO_2/SnO_2/ glass	SnO_2:F/SiO_2/SnO_2/ glass
SnO_2:F thickness[b] (nm)	752	517	302
SnO_2 thickness (nm)	130	19	17
SiO_2 thickness (nm)	50[c]	30	26
Roughness[d] (nm)	46	54	34
Haze (%)	12	12[e]	<1[e]
N_{Hall} (cm^{-3})	2.9×10^{20}	5.3×10^{20} [f]	5.6×10^{20} [f]
μ_{Hall} [$cm^2/(V\ s)$]	32	28[f]	21[f]
ρ_{Hall}[g] (Ω)	6.7×10^{-4}	4.2×10^{-4}	5.3×10^{-4}
R_{sheet}[h] (Ω/sq.)	8.6	7.7	16.6

[a]Data are taken from [43]
[b]Thickness corresponds to $d_{F1} + d_{F2}$ (see Figs. 18.26 and 18.27)
[c]Thickness of a SiO_2 alkali barrier layer [103]
[d]Thickness of d_s (see Figs. 18.26 and 18.27)
[e]Data are taken from [104]
[f]Data are adopted from [105]
[g]Resistivity calculated from $\rho_{Hall} = (eN_{Hall}\mu_{Hall})^{-1}$
[h]Sheet resistance calculated from $R_{sheet} = \rho_{Hall}/d_{total}$. Here, d_{total} is the total SnO_2:F thickness given by $d_{total} = 0.5d_s + d_{F1} + d_{F2}$ (see Sects. 18.5.1 and 18.5.2)

12% (see Table 18.2). On the other hand, the layer thickness of the TEC-15 is much thinner and the texture is very small with a low haze value of <1% [104]. The N_{Hall} of the Asahi-U is slightly lower ($N_{Hall} \sim 3 \times 10^{20}$ cm^{-3}) [43], compared with the TEC glass substrates ($N_{Hall} \sim 5 \times 10^{20}$ cm^{-3}) [105]. However, due to the thicker SnO_2:F layer in the Asahi-U substrate, the Asahi-U and TEC-8 substrates show a similar sheet resistance of $R_{sheet} \sim 8$ Ω/sq. [104–107].

In general, when a texture size has the same dimension as λ of the SE light probe, a rather complicated optical model is necessary in the SE analysis (Chaps. 6 in Vol. 1 and 4 in Vol. 2). Quite fortunately, for textured TCO layers, SE analyses can be performed using conventional optical models incorporating a single surface-roughness layer, as we have seen in the previous section. In this case, however, d_s is underestimated (see Fig. 18.24c). Moreover, for the accurate characterization of the commercial textured SnO_2:F substrates, the variation of N_{opt} toward the growth direction needs to be modeled properly.

In this section, the structure and optoelectronic properties of the Asahi-U and TEC glass substrates, characterized by SE, are described. By applying these results, optical simulation of solar cells (Chap. 2 in Vol. 2) and SE characterization of solar cell structures formed on these substrates (Chap. 4 in Vol. 2) can further be carried out.

18.5.1 Analysis of an Asahi-U Substrate

Figure 18.26a shows an optical model used for the SE analysis of the Asahi-U substrate [43]. Since the textured SnO_2 layer of the Asahi-U substrate is formed by a three step process [102, 108], the SnO_2 bulk layer is divided into a total of three sublayers (i.e., SnO_2:F layer 1, SnO_2:F layer 2, SnO_2). The SnO_2 layer in the model represents a SnO_2 layer with low FCA, whereas the two SnO_2:F layers show distinct FCA due to high carrier concentrations (~10^{20} cm^{-3}). In the optical model, the presence of the SiO_2 alkali-barrier layer is neglected, as the optical properties of this layer are similar to those of the glass substrate [103]. In Fig. 18.26a, d_{F1}, d_{F2} and d_t denote the layer thicknesses of the SnO_2:F-1, SnO_2:F-2 and SnO_2 layer, respectively.

The dielectric functions of the SnO_2:F layers can be calculated using the Drude and TL models. However, to suppress the number of free parameters, the SE analysis of the Asahi-U substrate has been carried out by using fixed values of [$C = 12$ eV, $E_0 = 7$ eV, $E_g = 3.0$ eV, $\varepsilon_1(\infty) = 2.2$] for the SnO_2:F-1, [$A = 15$ eV, $C = 12$ eV, $E_0 = 7$ eV, $E_g = 3.0$ eV, $\varepsilon_1(\infty) = 3.3$] for the SnO_2:F-2, and [$C = 12$ eV, $E_0 = 9$ eV, $E_g = 3.0$ eV, $\varepsilon_1(\infty) = 1$, $A_D = 1.0$ eV, $\Gamma = 1 \times 10^{-4}$ eV] for the SnO_2 transparent layer. As a result, the SE fitting was implemented using a total of nine analytical parameters: d_s, (d_{F1}, A, A_D, Γ) in the SnO_2:F-1, (d_{F2}, A_D, Γ) in the SnO_2:F-2, and d_t. In addition, the optical properties of the surface roughness layer were calculated from EMA assuming $f_{void} = 0.5$.

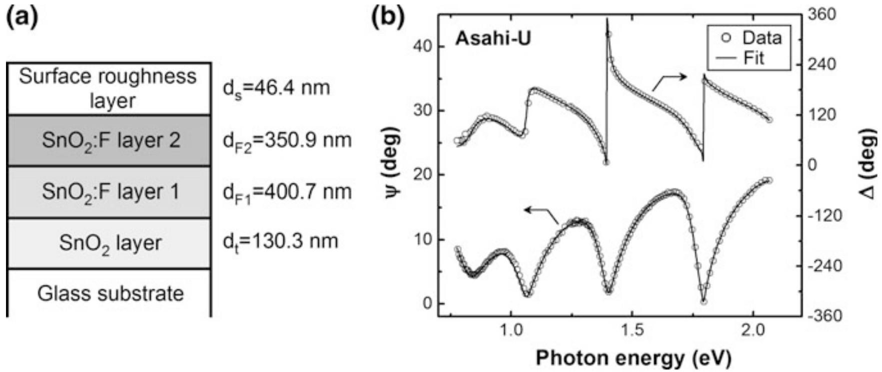

Fig. 18.26 **a** Optical model used for the SE analysis of the Asahi-U substrate and **b** ellipsometry spectra obtained from the Asahi-U substrate (open circles) and the result of the SE fitting analysis (solid lines) [43]. The incident angle of the SE measurement is $\theta = 55°$

Figure 18.26b shows the ellipsometry spectra obtained from the Asahi-U substrate [43]. The solid lines represent the calculation result obtained using the optical model of Fig. 18.26a. In Fig. 18.26b, the good agreement between the experimental and calculated spectra can be seen. When only one layer is used for SnO_2:F, instead of the two SnO_2:F layers shown in Fig. 18.26a, the fitting quality at $E < 1$ eV degrades due to the oversimplified modeling of FCA. As a result, the structural parameters are determined to be $d_s = 46.4$ nm, $d_{F2} = 350.9$ nm, $d_{F1} = 400.7$ nm, and $d_t = 130.3$ nm (see Fig. 18.26a). The total thickness (~900 nm) shows excellent agreement with that deduced from SEM.

The Drude parameters obtained from the analysis are ($A_D = 1.050$ eV, $\Gamma = 0.266$ eV) for the SnO_2:F-1 and ($A_D = 1.273$ eV, $\Gamma = 0.170$ eV) for the SnO_2:F-2. By applying (18.24) and (18.25), the optical carrier properties are estimated to be [$N_{opt1} = 1.5 \times 10^{20}$ cm^{-3}, $\mu_{opt1} = 22.5$ cm^2/(V s)] for the SnO_2:F-1, and [$N_{opt2} = 1.9 \times 10^{20}$ cm^{-3}, $\mu_{opt2} = 32.8$ cm^2/(V s)] for the SnO_2:F-2. From the N_{opt} values and thicknesses of each layer, the average optical carrier concentration (N_{ave}) and the average optical resistivity can be calculated by

$$N_{ave} = \sum_j N_{opt,j} d_j / \sum_j d_j, \tag{18.34}$$

$$\rho_{ave} = \sum_j d_j / \left(\sum_j d_j / \rho_{opt,j} \right), \tag{18.35}$$

where d_j, $N_{opt,j}$, and $\rho_{opt,j}$ show the thickness, N_{opt} and ρ_{opt} of the jth SnO_2:F layer. For the calculation of ρ_{ave}, the parallel connection of conductive layers is assumed, and $\rho_{opt,j}$ in (18.35) is given by $\rho_{opt,j} = (eN_{opt,j}\mu_{opt,j})^{-1}$. In the case of Fig. 18.26, the contribution of the roughness layer can also be included as $d_j = 0.5d_s$ using 50

vol.% of void assumed for d_s [43]. From N_{ave} and ρ_{ave}, the average optical mobility μ_{ave} is determined by

$$\mu_{ave} = (eN_{ave}\rho_{ave})^{-1} \quad (18.36)$$

The N_{ave} and μ_{ave} obtained from (18.34) and (18.36) are 1.7×10^{20} cm^{-3} and 28.1 cm^2/(V s), which show good agreement with $N_{Hall} = 2.9 \times 10^{20}$ cm^{-3} and $\mu_{Hall} = 32.2$ cm^2/(V s).

The above result confirms that the FCA analysis of the textured SnO_2:F layer can be performed using a standard procedure [42, 43]. By applying the above analysis, the mapping characterization of Asahi-U substrates has been performed [43]. In particular, from the mapping result of the Drude parameters, non-uniformity of the electric properties in textured SnO_2:F layers can be characterized.

18.5.2 Analysis of TEC Substrates

Figure 18.27a shows an optical model used for the SE analysis of a TEC-8 substrate. In this optical model, an additional SiO_2 layer is inserted between SnO_2:F and SnO_2 layers in the model of Fig. 18.26a. The SnO_2:F bulk layer is divided into two sublayers, similar to the case of the Asahi-U analysis. For the analysis of the TEC-8, reported optical constants of glass (Fig. 13.1 in Vol. 2), SiO_2 (Fig. 8.3 in Vol. 2), and SnO_2 (Fig. 11.10 in Vol. 2) were used. For the SnO_2:F layers, the Drude parameters in each SnO_2:F layer were employed as fitting parameters, while using fixed TL parameters extracted from a TEC-15 substrate [17] (see Table 11.23 in Vol. 2). In the analysis, Γ of the SnO_2:F sublayers was assumed to be constant.

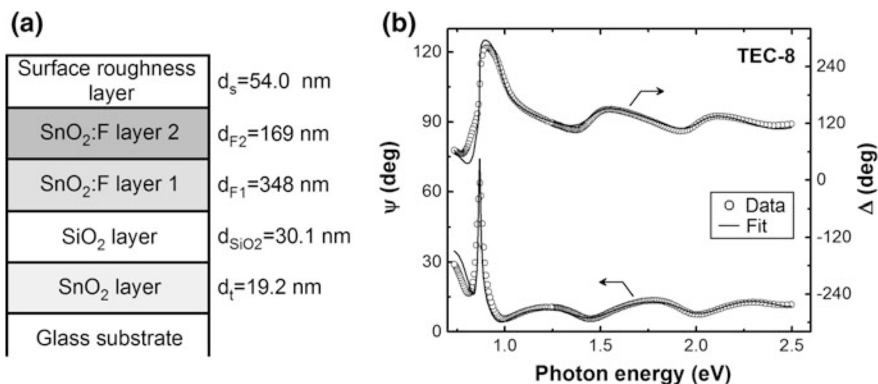

Fig. 18.27 **a** Optical model used for the SE analysis of the TEC-8 substrate and **b** ellipsometry spectra obtained from the TEC-8 substrate (open circles) and the result of the SE fitting analysis (solid lines). The incident angle of the SE measurement is $\theta = 55°$

When f_{void} in the roughness layer is incorporated as an additional free parameter, the SE analysis can be performed using a total of nine parameters: i.e., d_s, d_{F1}, d_{F2}, d_{SiO}, d_t, A_D (SnO_2:F-1), A_D (SnO_2:F-2), Γ and f_{void}.

Figure 18.27b indicates the SE fitting analysis for the TEC-8 substrate shown in Fig. 18.25b. The open circles show the experimental spectra and the solid lines represent the calculation result obtained using the optical model of Fig. 18.27a. It can be seen that the fitted spectra show good agreement with the experimental spectra. The slight disagreement observed at ~0.8 eV is caused by insufficient modeling of the FCA variation within the SnO_2:F bulk layer, and the fitting quality can be improved by further increasing the number of the SnO_2:F sublayers, although the SE analysis becomes more difficult in this case. The structural parameters extracted from this SE analysis are $d_s = 54.0 \pm 0.3$ nm, $f_{void} = 42.5 \pm 0.3$ vol.%, $d_{F2} = 169 \pm 3$ nm, $d_{F1} = 348 \pm 4$ nm, $d_{SiO2} = 30.1 \pm 0.3$ nm, and $d_t = 19.2 \pm 0.4$ nm, as indicated in Fig. 18.27a. On the other hand, the Drude parameters of the SnO_2:F sublayers are determined to be $A_D = 2.108$ eV (SnO_2:F-1), $A_D = 1.858$ eV (SnO_2:F-2) and $\Gamma = 0.082$ eV, which correspond to $N_{opt1} = 3.9 \times 10^{20}$ cm^{-3} and $N_{opt2} = 3.2 \times 10^{20}$ cm^{-3} with $\mu_{opt1} = 55.9$ cm^2/(V s) and $\mu_{opt2} = 58.8$ cm^2/(V s). The value of $N_{ave} = 3.6 \times 10^{20}$ cm^{-3}, obtained by applying (18.34), is consistent with $N_{Hall} \sim 5 \times 10^{20}$ cm^{-3} of TEC-8 substrates [105–107], whereas μ_{ave} of the TEC-8 shows a higher value [56.8 cm^2/(V s)], compared with μ_{Hall} of ~25 cm^2/(V s) [105–107]. In the SnO_2:F layer of the TEC-8 substrate, therefore, grain boundary scattering is rather significant.

The basic structure and the optoelectronic properties of TEC-15 substrates are quite similar to those of TEC-8 substrates (see Table 18.2). The SE analysis of this substrate can be performed using the same optical model shown in Fig. 18.27a. However, the total SnO_2:F thickness of the TEC-15 is thinner (300 nm), compared with the TEC-8 (520 nm), and d_s of the TEC-15 is smaller (34 nm) than that of the TEC-8 (54 nm) due to the smaller-size texture of the TEC-15 substrates.

When solar cells fabricated on the TEC-8 and TEC-15 substrates are compared, J_{sc} is expected to decrease in the solar cells fabricated on the TEC-8 substrates since the thicker SnO_2:F layer leads to increased J_{sc} loss due to FCA. However, the larger texture of the TEC-8 substrates may compensate the J_{sc} loss. On the other hand, R_{sheet} of the TEC-8 substrate (8 Ω/sq.) is lower than that of the TEC-15 substrate (17 Ω/sq.). Thus, solar cells with the TEC-8 substrates may show improved FF with lower J_{sc}, if compared with solar cells with the TEC-15 substrates.

References

1. T. Hara, T. Maekawa, S. Minoura, Y. Sago, S. Niki, H. Fujiwara, Phys. Rev. Appl. **2**, 034012 (2014)
2. M. Liu, M.B. Johnston, H.J. Snaith, Nature **501**, 395 (2013)
3. J. You, L. Meng, T.-B. Song, T.-F. Guo, Y. Yang, W.-H. Chang, Z. Hong, H. Chen, H. Zhou, Q. Chen, Y. Liu, N. De Marco, Y. Yang, Nat. Nanotech. **11**, 75 (2016)

4. P. Koirala, J. Li, H.P. Yoon, P. Aryal, S. Marsillac, A.A. Rockett, N.J. Podraza, R.W. Collins, Prog. Photovolt. **24**, 1055 (2016)
5. J.P. Seif, A. Descoeudres, M. Filipic, F. Smole, M. Topic, Z.C. Holman, S. De Wolf, C. Ballif, J. Appl. Phys. **115**, 024502 (2014)
6. J. Bullock, M. Hettick, J. Geissbuhler, A.J. Ong, T. Allen, C.M. Sutter-Fella, T. Chen, H. Ota, E.W. Schaler, S. De Wolf, C. Ballif, A. Cuevas, A. Javey, Nat. Energy **1**, 15031 (2016)
7. X.L. Chen, B.H. Xu, J.M. Xue, Y. Zhao, C.C. Wei, J. Sun, Y. Wang, X.D. Zhang, X.H. Geng, Thin Solid Films **515**, 3753 (2007)
8. J. Meier, J. Spitznagel, U. Kroll, C. Bucher, S. Fay, T. Moriarty, A. Shah, Thin Solid Films **451–452**, 518 (2004)
9. L. Kranz, A. Abate, T. Feurer, F. Fu, E. Avancini, J. Lockinger, P. Reinhard, S.M. Zakeeruddin, M. Gratzel, S. Buecheler, A.N. Tiwari, J. Phys. Chem. Lett. **6**, 2676 (2015)
10. M.T. Greiner, M.G. Helander, W.-M. Tang, Z.-B. Wang, J. Qiu, Z.-H. Lu, Nat. Mater. **11**, 76 (2012)
11. H. Hosono, T. Kamiya, in *Technology of Transparent Conductive Oxides* (in Japanese), ed. by Japan Society for the Promotion of Science, Chapter 4 (Ohmsha, Tokyo, 2014), pp. 109–140
12. G. Li, C.-W. Chu, V. Shrotriya, J. Huang, Y. Yang, Appl. Phys. Lett. **88**, 253503 (2006)
13. M. Kroger, S. Hamwi, J. Meyer, T. Riedl, W. Kowalsky, A. Kahn, Appl. Phys. Lett. **95**, 123301 (2009)
14. Z. He, C. Zhong, S. Su, M. Xu, H. Wu, Y. Cao, Nat. Photonics **6**, 591 (2012)
15. C. Battaglia, X. Yin, M. Zheng, I.D. Sharp, T. Chen, S. McDonnell, A. Azcatl, C. Carraro, B. Ma, R. Maboudian, R.M. Wallace, A. Javey, Nano Lett. **14**, 967 (2014)
16. J. Geissbuhler, J. Werner, S. Martin de Nicolas, L. Barraud, A. Hessler-Wyser, M. Despeisse, S. Nicolay, A. Tomasi, B. Niesen, S. De Wolf, C. Ballif, Appl. Phys. Lett. **107**, 081601 (2015)
17. J. Chen, J. Li, C. Thornberry, M.N. Sestak, R.W. Collins, J.D. Walker, S. Marsillac, A.R. Aquino, A. Rockett, in *Proceedings of the 34th IEEE PVSC* (IEEE, New York, 2009), p. 1748
18. T. Koida, M. Kondo, K. Tsutsumi, A. Sakaguchi, M. Suzuki, H. Fujiwara, J. Appl. Phys. **107**, 033514 (2010)
19. T. Koida, Phys. Status Solidi A. **214**, 1600464 (2017)
20. M. Shirayama, H. Kadowaki, T. Miyadera, T. Sugita, M. Tamakoshi, M. Kato, T. Fujiseki, D. Murata, S. Hara, T.N. Murakami, S. Fujimoto, M. Chikamatsu, H. Fujiwara, Phys. Rev. Appl. **5**, 014012 (2016)
21. A. Nakane, H. Tampo, M. Tamakoshi, S. Fujimoto, K.M. Kim, S. Kim, H. Shibata, S. Niki, H. Fujiwara, J. Appl. Phys. **120**, 064505 (2016)
22. For a review, see S. Niki, M. Contreras, I. Repins, M. Powalla, K. Kushiya, S. Ishizuka, K. Matsubara, Prog. Photovolt. **18**, 453 (2010)
23. M. Powalla, G. Voorwinden, D. Hariskos, P. Jackson, R. Kniese, Thin Solid Films **517**, 2111 (2009)
24. E. Hecht, *Optics*, 4th edn. (Addison Wesley, San Francisco, 2002)
25. H. Fujiwara, *Spectroscopic Ellipsometry: Principles and Applications* (Wiley, West Sussex, UK, 2007)
26. H. Fujiwara, M. Kondo, J. Appl. Phys. **101**, 054516 (2007)
27. D. Zhang, I.A. Digdaya, R. Santbergen, R.A.C.M.M. van Swaaij, P. Bronsveld, M. Zeman, J.A.M. van Roosmalen, A.W. Weeber, Sol. Energy Mater. Sol. Cells **117**, 132 (2013)
28. B. O'Regan, M. Gratzel, Nature **353**, 737 (1991)
29. K.-C. Wang, J.-Y. Jeng, P.-S. Shen, Y.-C. Chang, E.W. Diau, C.-H. Tsai, T.-Y. Chao, H.-C. Hsu, P.-Y. Lin, P. Chen, T.-F. Guo, T.-C. Wen, Sci. Rep. **4**, 4756 (2014)
30. L. Barraud, Z.C. Holman, N. Badel, P. Reiss, A. Descoeudres, C. Battaglia, S. De Wolf, C. Ballif, Sol. Energy Mater. Sol. Cells **115**, 151 (2013)
31. Unpublished results of S. Yamaguchi (SCREEN Semiconductor Solutions Co., Ltd.) and Y. Sugimoto (SCREEN Holdings Co., Ltd.)

32. H.S. So, J.-W. Park, D.H. Jung, K.H. Ko, H. Lee, J. Appl. Phys. **118**, 085303 (2015)
33. H. Fujiwara, M. Kondo, Phys. Rev. B **71**, 075109 (2005)
34. H. Yoshikawa, S. Adachi, Jpn. J. Appl. Phys. **36**, 6237 (1997)
35. G.E. Jellison Jr., L.A. Boatner, Phys. Rev. B **58**, 3586 (1998); Erratum, Phys. Rev. B **65**, 049902 (2001)
36. A.B. Djurisic, Y. Chan, E.H. Li, Appl. Phys. A **76**, 37 (2003)
37. Z.C. Holman, M. Filipic, A. Descoeudres, S. De Wolf, F. Smole, M. Topic, C. Ballif, J. Appl. Phys. **113**, 013107 (2013)
38. D.E. Aspnes, A.A. Studna, E. Kinsbron, Phys. Rev. B **29**, 768 (1984)
39. C. Tanguy, Phys. Rev. B **60**, 10660 (1999)
40. C. Kittel, *Introduction to Solid State Physics* (Wiley, New York, 1986)
41. P.I. Rovira, R.W. Collins, J. Appl. Phys. **85**, 2015 (1999)
42. M. Akagawa, H. Fujiwara, J. Appl. Phys. **112**, 083507 (2012)
43. Y. Sago, H. Fujiwara, Jpn. J. Appl. Phys. **51**, 10NB01 (2012)
44. K. Sago, H. Kuramochi, H. Iigusa, K. Utsumi, H. Fujiwara, J. Appl. Phys. **115**, 133505 (2014)
45. T. Gerfin, M. Gratzel, J. Appl. Phys. **79**, 1722 (1996)
46. R.A. Synowicki, Thin Solid Films **313–314**, 394 (1998)
47. K. Zhang, A.R. Forouhi, I. Bloomer, J. Vac. Sci. Technol. A **17**, 1843 (1999)
48. L. Meng, E. Crossan, A. Voronov, F. Placido, Thin Solid Films **422**, 80 (2002)
49. M. Losurdo, Thin Solid Films **455–456**, 301 (2004)
50. G.E. Jellison Jr., F.A. Modine, Appl. Phys. Lett. **69**, 371 (1996); Erratum, Appl. Phys. Lett. **69**, 2137 (1996)
51. E. Shanthi, V. Dutta, A. Banerjee, K.L. Chopra, J. Appl. Phys. **51**, 6243 (1980)
52. E. Shanthi, A. Banerjee, V. Dutta, K.L. Chopra, J. Appl. Phys. **53**, 1615 (1982)
53. S. Yamaguchi, Y. Sugimoto, H. Fujiwara, Thin Solid Films **534**, 149 (2013)
54. R.A. Synowicki, Phys. Status Solidi C **5**, 1085 (2008)
55. K. Forcht, A. Gombert, R. Joerger, M. Kohl, Thin Solid Films **302**, 43 (1997)
56. K. Ellmer, J. Phys. D Appl. Phys. **34**, 3097 (2001)
57. Z.M. Jarzebski, Phys. Status Solidi A **71**, 13 (1982)
58. M. Feneberg, J. Nixdorf, C. Lidig, R. Goldhahn, Z. Galazka, O. Bierwagen, J.S. Speck, Phys. Rev. B **93**, 045203 (2016)
59. T. Nagashima, M. Hangyo, Appl. Phys. Lett. **79**, 3917 (2001)
60. T. Hofmann, C.M. Herzinger, A. Boosalis, T.E. Tiwald, J.A. Woollam, M. Schubert, Rev. Sci. Instrum. **81**, 023101 (2010)
61. R. Clanget, Appl. Phys. **2**, 247 (1973)
62. Y. Ohhata, F. Shinoki, S. Yoshida, Thin Solid Films **59**, 255 (1979)
63. T. Pisarkiewicz, K. Zakrzewska, E. Leja, Thin Solid Films **174**, 217 (1989)
64. T. Minami, H. Sato, K. Ohashi, T. Tomofuji, S. Takata, J. Cryst. Growth **117**, 370 (1992)
65. S. Brehme, F. Fenske, W. Fuhs, E. Nebauer, M. Poschenrieder, B. Selle, I. Sieber, Thin Solid Films **342**, 167 (1999)
66. D.L. Young, T.J. Coutts, V.I. Kaydanov, A.S. Gilmore, W.P. Mulligan, J. Vac. Sci. Technol. A **18**, 2978 (2000)
67. W.M. Kim, I.H. Kim, J.H. Ko, B. Cheong, T.S. Lee, K.S. Lee, D. Kim, T.-Y. Seong, J. Phys. D **41**, 195409 (2008)
68. F. Ruske, A. Pflug, V. Sittinger, B. Szyszka, D. Greiner, B. Rech, Thin Solid Films **518**, 1289 (2009)
69. T. Yamada, H. Makino, N. Yamamoto, T. Yamamoto, J. Appl. Phys. **107**, 123534 (2010)
70. J.S. Kim, J.-H. Jeong, J.K. Park, Y.J. Baik, I.H. Kim, T.-Y. Seong, W.M. Kim, J. Appl. Phys. **111**, 123507 (2012)
71. A.A. Ziabari, S.M. Rozati, Phys. B **407**, 4512 (2012)
72. G. Rey, C. Ternon, M. Modreanu, X. Mescot, V. Consonni, D. Bellet, J. Appl. Phys. **114**, 183713 (2013)

73. C. A. Niedermeier, S. Rhode, K. Ide, H. Hiramatsu, H. Hosono, T. Kamiya, M. A. Moram, Phys. Rev. B **95**, 161202 (2017)
74. D.S. Ginley (ed.), *Handbook of Transparent Conductors* (Springer, New York, 2010)
75. R.E. Hummel, *Electronic Properties of Materials*, 4th edn. (Springer, New York, 2011)
76. J.A. Sans, J.F. Sanchez-Royo, A. Segura, G. Tobias, E. Canadell, Phys. Rev. B **79**, 195105 (2009)
77. I. Hamberg, C.G. Granqvist, J. Appl. Phys. **60**, R123 (1986)
78. B.E. Sernelius, K.-F. Berggren, Z.-C. Jin, I. Hamberg, C.G. Granqvist, Phys. Rev. B **37**, 10244 (1988)
79. N. Sommer, J. Hupkes, U. Rau, Phys. Rev. Appl. **5**, 024009 (2016)
80. D.C. Look, C.E. Stutz, R.J. Molnar, K. Saarinen, Z. Liliental-Weber, Solid State Commun. **117**, 571 (2001)
81. D.C. Look, H. Lu, W.J. Schaff, J. Jasinski, Z. Liliental-Weber, Appl. Phys. Lett. **80**, 258 (2002)
82. B.L. Anderson, R.L. Anderson, *Fundamentals of Semiconductor Devices* (McGraw-Hill, New York, 2005)
83. J. Steinhauser, S. Fay, N. Oliveira, E. Vallat-Sauvain, C. Ballif, Appl. Phys. Lett. **9**, 142107 (2007)
84. S. Fay, J. Steinhauser, S. Nicolay, C. Ballif, Thin Solid Films **518**, 2961 (2010)
85. E.F. Venger, A.V. Melnichuk, L.Y. Melnichuk, Y.A. Pasechnik, Phys. Status Solidi B **188**, 823 (1995)
86. T. Minami, H. Sato, H. Nanto, S. Takata, Jpn. J. Appl. Phys. **24**, L781 (1985)
87. S. Major, A. Banerjee, K.L. Chopra, Thin Solid Films **125**, 179 (1985)
88. B.H. Choi, H.B. Im, J.S. Song, K.H. Yoon, Thin Solid Films **193–194**, 712 (1990)
89. Y. Shigesato, S. Takaki, T. Haranou, Appl. Surf. Sci. **48/49**, 269 (1991)
90. J. Hu, R.G. Gordon, J. Appl. Phys. **72**, 5381 (1992)
91. Y. Qu, T.A. Gessert, K. Ramanathan, R.G. Dhere, R. Noufi, T.J. Coutts, J. Vac. Sci. Technol. A **11**, 996 (1993)
92. C. Agashe, O. Kluth, J. Hupkes, U. Zastrow, B. Rech, M. Wuttig, J. Appl. Phys. **95**, 1911 (2004)
93. N. Ehrmann, R. Reineke-Koch, Thin Solid Films **519**, 1475 (2010)
94. O. Nakagawara, Y. Kishimoto, H. Seto, Y. Koshido, Y. Yoshino, T. Makino, Appl. Phys. Lett. **89**, 091904 (2006)
95. T. Minami, T. Miyata, Y. Ohtani, T. Kuboi, Phys. Status Solidi RRL **1**, R31 (2007)
96. T. Minami, T. Kuboi, T. Miyata, Y. Ohtani, Phys. Status Solidi A **205**, 255 (2008)
97. M. Kambe, M. Fukawa, N. Taneda, K. Sato, Sol. Energy Mater. Sol. Cells **90**, 3014 (2006)
98. T. Matsui, A. Bidiville, K. Maejima, H. Sai, T. Koida, T. Suezaki, M. Matsumoto, K. Saito, I. Yoshida, M. Kondo, Appl. Phys. Lett. **106**, 053901 (2015)
99. K. Ding, T. Kirchartz, B.E. Pieters, C. Ulbrich, A.M. Ermes, S. Schicho, A. Lambertz, R. Carius, U. Rau, Sol. Energy Mater. Sol. Cells **95**, 3318 (2011)
100. M. Zeman, O. Isabella, S. Solntsev, K. Jager, Sol. Energy Mater. Sol. Cells **119**, 94 (2013)
101. B. Rech, H. Wagner, Appl. Phys. A **69**, 155 (1999)
102. K. Sato, Y. Gotoh, Y. Wakayama, Y. Hayashi, K. Adachi, H. Nishimura, Reports Res. Lab. Asahi Glass Co. Ltd, **42**, 129 (1992)
103. S. Yamaguchi, Y. Sugimoto, H. Fujiwara, Thin Solid Films **565**, 222 (2014)
104. Pilkington TEC glass performance data
105. D. Bhachu, M.R. Waugh, K. Zeissler, W.R. Branford, I.P. Parkin, Chem. Eur. J. **17**, 11613 (2011)
106. J.W. Bowers, H.M. Upadhyaya, S. Calnan, R. Hashimoto, T. Nakada, A.N. Tiwari, Prog. Photovolt. **17**, 265 (2009)
107. C.K.T. Chew, C. Salcianu, P. Bishop, C.J. Carmalt, I.P. Parkin, J. Mater. Chem. C **3**, 1118 (2015)
108. A. Luque, S. Hegedus (eds.), *Handbook of Photovoltaic Science and Engineering* (Wiley, West Sussex, UK, 2011)

Chapter 19
High-Mobility Transparent Conductive Oxide Layers

Takashi Koida

Abstract Transparent conductive oxides (TCOs) are wide band gap degenerated semiconductors popularly used in devices. Most commonly, TCO films are employed as transparent electrodes in flat-panel displays, thin-film solar cells, light-emitting diodes, and electrochromic windows. The development of high-performance optoelectronic devices has stimulated research on TCO films; namely, the improvement of the electrical and/or optical properties of existing TCO materials, the development of alternative TCO materials composed of naturally abundant and low-cost metals, and the development of new multifunctional TCOs that can improve device performance. TCO materials can be binary (In_2O_3, ZnO, SnO_2, CdO, and Ga_2O_3) or multicomponent (In-Zn-O, Zn-Sn-O, and In-Ga-Zn-O). To develop and refine TCOs, we must understand their electron transport mechanisms and optical properties. The dielectric functions of TCO films can be elucidated by spectroscopic ellipsometry (SE). Moreover, by analyzing the dielectric functions at infrared wavelengths, we can evaluate the optical effective mass and the relaxation time of free electrons in TCO films. From the relationship between effective mass and carrier density, we can determine the curvature of the energy band as a function of Fermi energy, which reveals the fundamental nature of the material. Meanwhile, the relaxation time helps us to understand the dominant scattering mechanism of free carriers in the films and how to improve the film fabrication process. This chapter presents an analytical SE procedure for TCO layers, focusing on high-mobility TCOs and their advantages. The superior electrical transport and optical properties of TCO thin films and solar cells installed with TCO electrodes are also discussed.

T. Koida (✉)
Research Center for Photovoltaics, National Institute of Advanced Industrial Science and Technology, 1-1-1 Umezono, Tsukuba 305-8568, Japan
e-mail: t-koida@aist.go.jp

© Springer International Publishing AG, part of Springer Nature 2018

H. Fujiwara and R. W. Collins (eds.), *Spectroscopic Ellipsometry for Photovoltaics*, Springer Series in Optical Sciences 212,
https://doi.org/10.1007/978-3-319-75377-5_19

19.1 Introduction

19.1.1 Optical and Electrical Properties of Transparent Conductive Oxide Layers

Transparent conductive oxide (TCO) films are widely used in the flat-panel displays and low-emittance windows. Recently, TCO films have also been employed as transparent electrodes in optoelectronic applications such as thin-film solar cells, light-emitting diodes, electrochromic windows, and oxide thin-film transistors. Research on TCO films has been stimulated by the ongoing development of high-performance optoelectronic devices. For example, solar cells with high conversion efficiency require highly conductive electrodes that are transparent to both visible and near-infrared (NIR) wavelengths. TCO is incorporated in thin-film solar cells based on various materials (Si, CdTe, $Cu(In,Ga)Se_2$, organic, and perovskite) and in a-Si:H/c-Si heterojunction solar cells. The configurations of a photovoltaic module based on a substrate-type thin-film $Cu(In,Ga)Se_2$ and an a-Si:H/c-Si heterojunction solar cell are presented in Fig. 19.1. In the former, lateral transport is prevented by the high sheet resistance of the solar cell absorbers; in the latter, it is prevented by the doped a-Si:H layers. Therefore, TCO is required to provide photo-generated carriers to the next subcell in the thin-film photovoltaic module and to the metal grids in heterojunction solar cells. Because of its role as a window electrode, TCO must exhibit low sheet resistance ($R_{\text{sheet}} = 1/Ne\mu t$) to minimize the power losses through Joule heating. The sheet resistance R_{sheet} of the TCO largely determines the subcell width in the photovoltaic module and the pitch of the metal grids in the heterojunction solar cell. The R_{sheet} can be reduced by increasing the carrier density N of the free electrons, the electron mobility μ, or the thickness t of the TCO film. However, increasing N and t reduces the transmittance of the TCO layer by free carrier absorption or metal-like reflection, thereby increasing the optical loss of the solar cell. Furthermore, in heterojunction solar cells, the TCO layer acts as an antireflection layer. Therefore, the t of the front TCO is typically fixed at about 75 nm to decrease reflection of the solar cells at around 550 nm. The constraints on N and t imply that in order to increase the transmittance while lowering the R_{sheet}, we must substantially increase the μ.

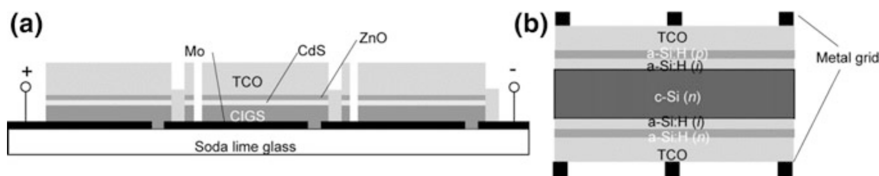

Fig. 19.1 Schematic of **a** $Cu(In,Ga)Se_2$ (CIGS) based thin-film photovoltaic module and **b** an a-Si:H/c-Si heterojunction solar cell

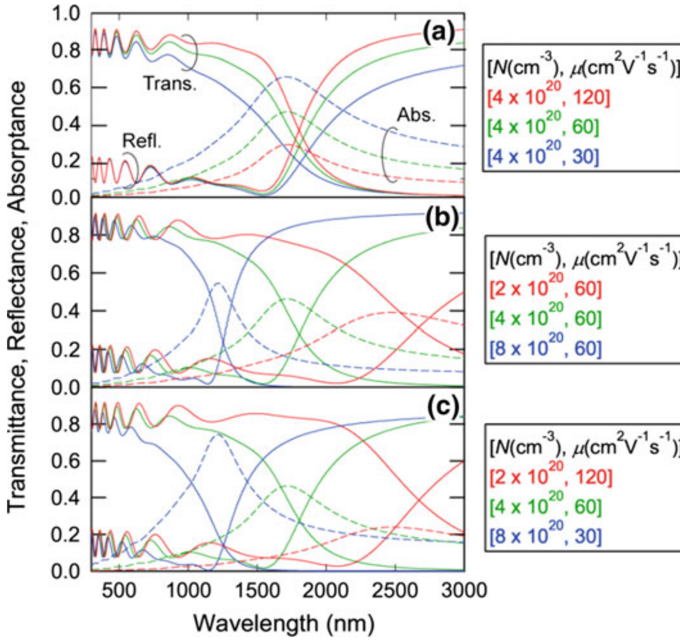

Fig. 19.2 Simulated transmittance, reflectance, and absorption spectra of 500-nm-thick TCO films on glass with **a** $N = 4 \times 10^{20}$ cm^{-3} and μ varied as 30, 60, and 120 cm^2 V^{-1} s^{-1}; **b** $\mu = 60$ cm^2 V^{-1} s^{-1} and N varied as 2×10^{20}, 4×10^{20}, and 8×10^{20} cm^{-3}, and **c** $R_{\text{sheet}} = 5.2$ Ω/sq with varying N and μ

We now relate the optical properties of TCO films to their electrical properties. Figure 19.2 shows the calculated transmittance, reflectance, and absorptance spectra of 500-nm-thick TCO films on glass. In panel (a), μ is varied (30, 60, 120 cm^2 V^{-1} s^{-1}) while N is fixed at 4×10^{20} cm^{-3}; in panels (b) and (c), μ and R_{sheet} are fixed at 60 cm^2 V^{-1} s^{-1} and 5.2 Ω/sq, respectively, while N is varied as 2×10^{20}, 4×10^{20}, and 8×10^{20} cm^{-3}. The optical model was an air/TCO/glass system, and the optical constants of TCO were calculated by the Drude model ((19.2) and (19.5), as described later). The high-frequency permittivity (ε_∞) and electron effective mass (m^*) of the TCO were assumed as 4 and 0.3 m_0, respectively, where m_0 is the free electron mass. The optical constants of the TCO layers corresponding to Fig. 19.2a–c; namely, the complex dielectric functions (ε_1: real part, ε_2: imaginary part) and complex refractive index (n: refractive index, k: extinction coefficient), are presented in panels (a)–(c) and (d)–(f) of Fig. 19.3, respectively. The behavior of these optical constants will be explained later. In constructing Fig. 19.2, the n and k values of the glass were fixed at 1.5 and 0, respectively. As observed in Fig. 19.2a, increasing the μ decreases the peak height of the absorption and the full width at half maximum (FWHM), but does not affect the wavelength of the absorption peak. Instead, the wavelength depends strongly on N, as observed in Fig. 19.2b. Decreasing N reduces the height of the absorption

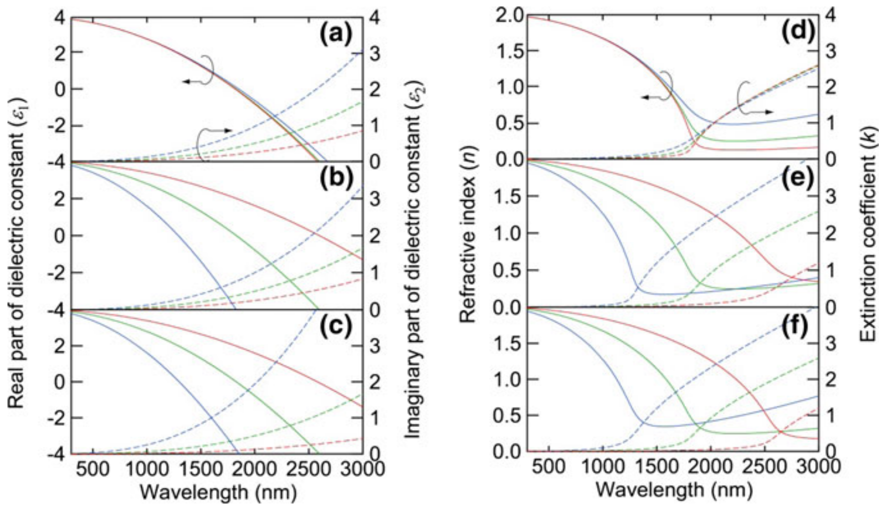

Fig. 19.3 **a–c** Dielectric functions and **d–f** optical constants of the TCO layers corresponding to panels **a–c** of Fig. 19.2. The complex optical constants were calculated by the Drude model (19.2) and (19.5)

peaks and moves them to longer wavelengths, while also increasing their FWHMs. Consequently, when the R_{sheet} is fixed, TCO films with lower N and higher μ absorb less strongly at visible and NIR wavelengths (Fig. 19.2c).

19.1.2 High-Mobility TCO Layers

As described in the previous subsection, the critical parameters for realizing both low R_{sheet} and high transmittance are N and μ. This section investigates the effective values of N and μ in In_2O_3-based TCOs. In general, N can be controlled over a wide range by varying the dopant concentration, whereas μ is limited by the carrier scattering processes, including those of phonons and impurities. Additional scattering may arise from structural imperfections such as grain boundaries and dislocations in thin films. Furthermore, surface and interface roughness may also scatter free electrons in very thin films. Single crystals of the TCO material provide a model system for TCO characterization, because crystals grown under equilibrium conditions have minimal point defects and extended defects. However, conventional TCO films doped with high concentrations of impurities cannot be fabricated under equilibrium conditions because of their low solid solubility limit. Therefore, the materials are typically fabricated by epitaxial growth on lattice-matched substrates. Here, a supersaturated solid solution occurs as a result of the highly non-equilibrium growth process. The defect density is much lower in epitaxial films than in conventional polycrystalline TCO films grown on glass at

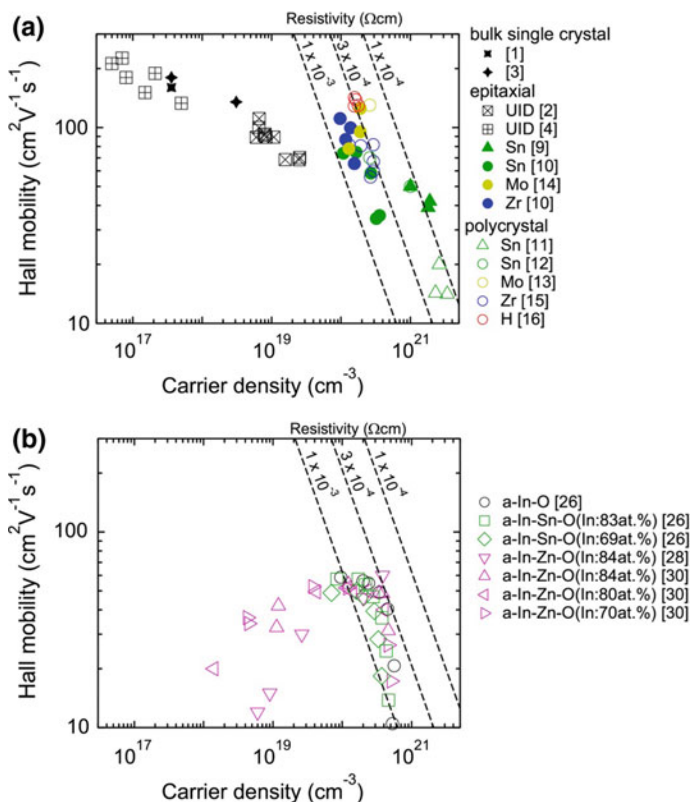

Fig. 19.4 **a** Hall mobility versus Hall carrier density in In_2O_3-based TCO. Results are plotted for bulk single crystals, unintentionally doped (UID) and impurity doped epitaxial films on yttria-stabilized zirconia, and impurity doped polycrystalline films on glass. Data were sourced from Weiher [1] and Galazka et al. [3] (bulk samples), Koida and Kondo [2] and Bierwagen and Speck [4] (UID epitaxial films), Ohta et al. [9] and Koida and Kondo [10] (Sn-doped expitaxial films), Warmsingh et al. [14] (Mo-doped epitaxial films), Koida and Kondo [10] (Zr-doped expitaxial films), Ishibashi et al. [11] and Shigesato et al. [12] (Sn-doped polycrystalline films), Meng et al. [13] (Mo-doped polycrystalline films), Koida and Kondo [15] (Zr-doped polycrystalline films), and Koida et al. [16] (H-doped polycrystalline films). **b** Hall mobility versus Hall carrier density in In_2O_3-based amorphous TCO films. Data for a-In-O and a-In-Sn-O were extracted from Utsumi et al. [26] and data for a-In-Zn-O films were extracted from Martins et al. [28] and Leenheer et al. [30]

low temperature; consequently, the properties of epitaxial films provide a benchmark for characterizing heavily doped materials.

Figure 19.4a plots the electrical properties of three crystalline In_2O_3-based TCOs; bulk single crystal, epitaxial films on single crystalline yttria-stabilized zirconia, and polycrystalline films on glass. The bulk and unintentionally doped (UID) In_2O_3 show high μ (~200 $cm^2\ V^{-1}\ s^{-1}$) at $N \sim 1 \times 10^{17}\ cm^{-3}$, and the μ decreases monotonically as N increases from 5×10^{16} to $3 \times 10^{19}\ cm^{-3}$ [1–4]. The origin of the large residual carrier density in bulk and UID epitaxial films has

been debated. Experimentally, N can be controlled by varying the oxygen partial pressure during the film growth and post-growth annealing. Hence, the residual carrier density could be sourced from oxygen vacancy-type defects. On the other hand, in theoretical investigations of native and extrinsic defects [5–8], another candidate source for free carriers is hydrogen impurities incorporated from the growth environment. When epitaxial [9, 10] and polycrystalline [11, 12] In_2O_3 films are doped with Sn, their N increases and their resistivity reduces to the order of 1×10^{-4} Ω cm (Fig. 19.4a). Moreover, μ decreases from 75 to 15 as N increases from 1×10^{20} to 3×10^{21} cm^{-3}, primarily because of scattering by ionized impurities. However, some In_2O_3-based films exhibit high μ (> 100 cm^2 V^{-1} s^{-1}) even at N values around 10^{20} cm^{-3}. To date, simultaneous high μ and low resistivity has been achieved by two major approaches. In the first approach, the concentration of a suitable dopant is optimized to reduce the effects of ionized impurities and neutral scattering. Alternatively, the structure can be controlled to reduce the grain boundary scattering. In Fig. 19.4a, In_2O_3 doped with Mo [13, 14], Zr [10, 15] or H [16] exhibits higher μ than Sn-doped In_2O_3 (ITO). The μ is also increased in In_2O_3 doped with W [17] or Ti [10]. The high μ in these films has been attributed to the low scattering cross-section of the dopant impurities [18], suppressed scattering from oxygen interstitials [19], and suppressed oxygen deficiencies in the In_2O_3 host material [10, 15, 16]. In Mo-doped In_2O_3 films with high μ, the relaxation time (τ) of the free electrons is long and m^* (~0.32 m_0) is insensitive to carrier densities between 4×10^{19} and 6×10^{20} cm^{-3} [19]. Here, μ is defined by Drude theory as $\mu = e\tau/m^*$. Moreover, theoretical calculations have revealed that the d-states of Mo do not hybridize with the s-states of In; consequently, the m^* remains similar to that of UID In_2O_3 [20]. Structural control is also important for attaining high μ, especially in films grown on glass at low temperature. In In_2O_3:H films, the μ is increased by H doping and forming large crystal grain structures by solid phase crystallization processes [16]. The films are free from strain and the grain size is of submicrometer order, far exceeding the mean free path of free electrons. The parameters m^* and τ, as will be described in Sect. 19.2.3. Ce and H co-doped In_2O_3 films fabricated via solid phase crystallization [21] also exhibit high μ.

Amorphous structures can effectively eliminate grain boundary scattering. Typical In_2O_3-based amorphous films such as a-In-O [12, 22], a-In-Sn-O [12, 23], and a-In-Zn-O [24, 25] exhibit low resistivity with relatively high μ (~50 cm^2 V^{-1} s^{-1}) and moderate N ($1–3 \times 10^{20}$ cm^{-3}) [26–30]. As revealed by grazing incidence X-ray scattering and the X-ray absorption fine structure, edge- and corner-sharing In-O_6 octahedral and/or In-O_n polyhedral units are preserved in a-In-O [31], a-In-Zn-O [32], and a-In-Ga-Zn-O [33]. The high μ in amorphous conducting oxides can be explained by the extended spherical In (5 s) orbitals, which are insensitive to local structures [34–37]. Figure 19.4b plots the electrical properties of a-In-O, a-In-Sn-O [26], and a-In-Zn-O [28, 30] films with different metal compositions. The N–μ trend is independent of the metal composition, but depends on the oxygen partial pressure during growth, which controls the N. The N–μ trend differs from that of crystalline In_2O_3 shown in Fig. 19.4a; notably, the μ of a-TCOs

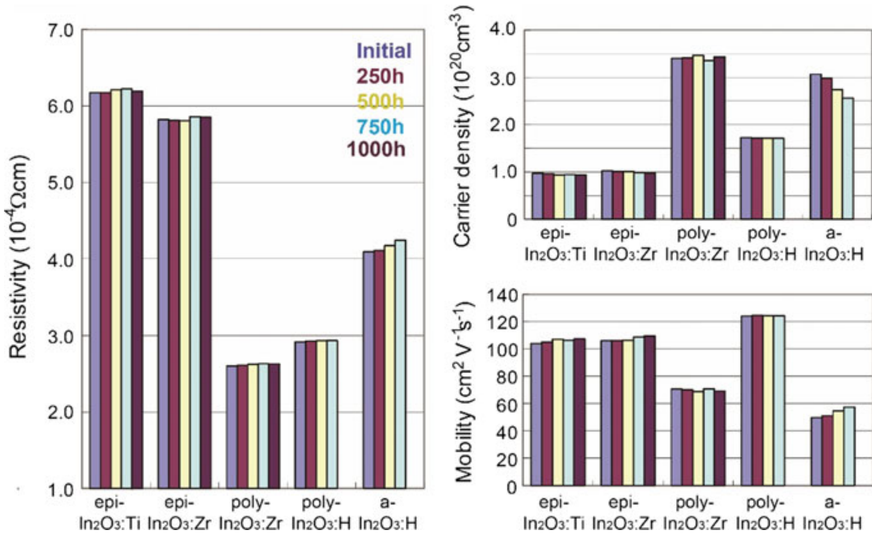

Fig. 19.5 Changes in electrical properties after the damp heat test (85 °C, 85% RH). Results are plotted for 250-nm-thick Ti- and Zr-doped expitaxial In_2O_3 [10], 260-nm-thick Zr-, 240-nm-thick H-doped polycrystalline In_2O_3 [15], and 240-nm-thick H-doped amorphous In_2O_3 films. The impurity compositions (fabrication temperatures) are 0.3 at.% (650 °C) for Ti- and Zr-doped In_2O_3 epitaxial films, 0.3 at.% (650 °C) for Zr- and 3 at.% (200 °C) for H-doped In_2O_3 polycrystalline films. The impurity composition of unheated H-doped In_2O_3 amorphous film is 4 at.%

decreases as N decreases below 10^{19} cm^{-3}. This difference is attributed to scattering by charged structural defects [28] and/or percolation conduction over the distribution of potential barriers around the conduction band edge, which is associated with random Zn distribution [38].

In addition to superior electrical properties, stability is an important requirement of photovoltaic applications. Although modules can be stabilized under typical environmental conditions by proper encapsulation, stabilizing the TCO itself could lower the encapsulation costs and enable a light and flexible structure without glass/glass lamination. Figure 19.5 presents the changes in the electrical properties of various films after an accelerated aging test in damp heat (85 °C, 85% RH). The tested films were Ti- and Zr-doped In_2O_3 epitaxial films grown on yttria-stabilized zirconia [10], Zr- [10] and H-doped [16] In_2O_3 polycrystalline films grown on glass, and H-doped In_2O_3 amorphous film [16]. All of the films fabricated under optimized growth conditions remain stable under the test conditions. The optical and electrical properties of a-In-Zn-O thin films are also stable to damp heat [39]. However, the electrical conductivity of polycrystalline films was sometimes affected by grain boundaries under certain conditions. For example, Fig. 19.6

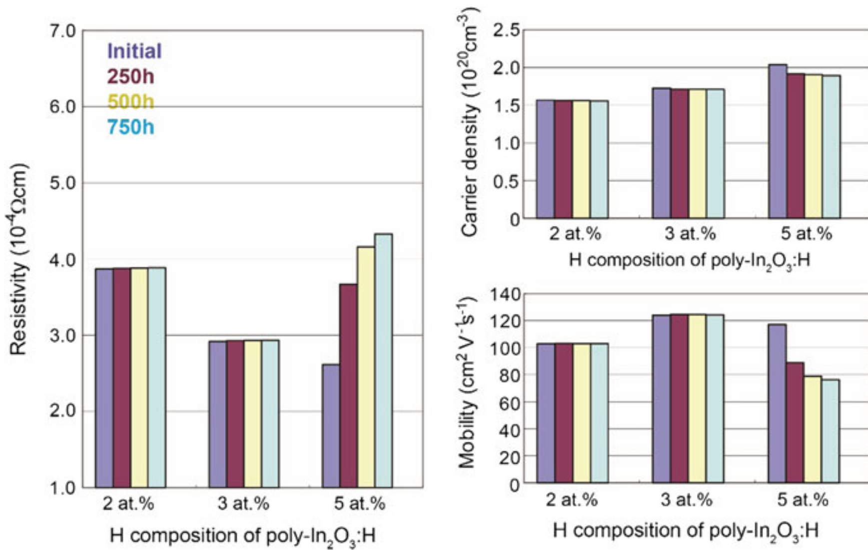

Fig. 19.6 Changes in electrical properties of 240-nm-thick crystallized In_2O_3:H films with different H compositions subjected to a damp heat test (85 °C, 85% RH) [40, 44]. The films were deposited by sputtering under different H_2O vapor pressures (5×10^{-5}, 1×10^{-4}, and 5×10^{-4} Pa) without substrate heating and crystallized by post-annealing at 200 °C

shows the changes in the electrical properties of polycrystalline films doped with different H compositions [40] during a damp heat test. At H compositions of 2 and 3 at.% the films remain stable, but at an H composition of 5 at.%, the mobility reduces, and the carrier density slightly decreases after the dump heat test. To prepare the polycrystalline films, amorphous films were deposited without substrate heating by sputtering an In_2O_3 ceramic target in the presence of H_2O vapor. Solid-phase crystallization was then induced at 200 °C. The H_2O partial pressure controlled the H composition, and also influenced the microscopic structure of the as-deposited films and crystallite size of the post-annealed films [41–44]. These results indicate that excess H_2O-related molecules inside films may form unstable grain boundaries during the crystallization process, enhancing the grain boundary scattering of free electrons after the damp heat test [44]. Furthermore, in substrate-type thin-film photovoltaic modules (for example), the front TCO covers the rough surface of the solar cell absorbers and integrated structures, as illustrated in Fig. 19.1a. Inhomogeneous growth on the rough surface could influence the stability, especially in polycrystalline TCOs [45]. Therefore, the development of TCOs with both high μ and high stability is important.

19.2 Spectroscopic Ellipsometry Analysis of High-Mobility TCO Layers

19.2.1 SE Analysis for TCO Layers

This subsection is devoted to the spectroscopic ellipsometry (SE) data analysis of TCO films. SE analysis reveals the surface roughness, thickness, and dielectric functions of the TCO films. Furthermore, by analyzing the dielectric functions, we can determine the m^* and optical relaxation time (τ_{opt}) of the films. These parameters are essential for understanding the electrical and optical properties of the TCOs and for developing high-μ TCO materials. From the value of relaxation time, we can better understand the dominant scattering mechanism of free carriers in the films and suggest improvements to the fabrication process. Finally, by relating m^* to N, we can derive the curvature of the energy bands as a function of the Fermi energy, which reveals the fundamental nature of the material.

To model the dielectric function of the TCO layer, we combine the Drude and Tauc–Lorentz (TL) models [46] as

$$\varepsilon(E) = \varepsilon_{TL}(E) + \varepsilon_{D}(E). \tag{19.1}$$

The TL model is expressed in Sect. 5.3.7, and the Drude model is given by

$$\varepsilon_D(E) = -\frac{A_D}{E^2 - i\Gamma_D E} = -\frac{A_D}{E^2 + \Gamma_D^2} - i\frac{A_D\Gamma_D}{E^3 + \Gamma_D^2 E}, \tag{19.2}$$

where A_D and Γ_D denote the oscillator amplitude and broadening parameter, respectively, expressed as follows:

$$A_D = \frac{\hbar^2 e^2 N_{opt}}{m^* \varepsilon_0} \tag{19.3}$$

$$\Gamma_D = \frac{\hbar}{\tau_{opt}} = \frac{\hbar e}{m^* \mu_{opt}}. \tag{19.4}$$

The dielectric function based on the TL and Drude model is also described in Sect. 18.2.3 and illustrated in Fig. 18.11. In (19.3) and (19.4), $\hbar$, ε_0, N_{opt} and μ_{opt} are the reduced Plank's constant, free space permittivity, optical carrier density, and optical mobility, respectively. Once Γ_D is known, τ_{opt} can be obtained. Also, if m^* is known, N_{opt} and μ_{opt} can be obtained from A_D and Γ_D. Alternatively, the TL model, which provides good fits to the experimental data of various TCO films [47, 48], computes the dielectric function from five parameters (A_{TL}, C, E_T, E_0, and $\varepsilon_1(\infty)$), representing the amplitude, broadening parameter, Tauc optical gap, peak transition energy, and energy-independent contribution to the real part of the

dielectric function, respectively. At sufficiently low energies, the real part of the dielectric function of the TL model is constant and equal to ε_∞. Under this condition, the real part of the dielectric function reduces to

$$\varepsilon_1(E) = \varepsilon_\infty - \frac{A_D}{E^2 + \Gamma_D^2}. \quad (19.5)$$

Thus, ε_∞ is the y-intercept of an ε_1 versus $1/(E^2 + \Gamma_{\mathrm{D}}^2)$ plot.

In Fig. 19.3a–c of Sect. 19.1.1, we described the behaviors of the dielectric functions of a TCO for different combinations of N_{opt} and μ_{opt}, with ε_∞ and m^* of the TCO set to 4 and 0.3 m_0, respectively. As shown in these plots, ε_1 decreases with increasing wavelength and crosses zero at the plasma energy (E_{p}), defined as the maximum energy at which free electrons can follow a disturbing electromagnetic field. At $E \sim E_{\mathrm{p}}$ the absorption is large, as shown in Fig. 19.2a–c, and Γ_{D}^2 in the TCO becomes negligibly smaller than E^2. Therefore, from (19.5), E_{p} can be written as

$$E_p = \left(\frac{A_D}{\varepsilon_\infty}\right)^{\frac{1}{2}} = \left(\frac{\hbar^2 e^2 N_{\mathrm{opt}}}{m^* \varepsilon_\infty \varepsilon_0}\right)^{\frac{1}{2}}. \quad (19.6)$$

Equation (19.6) indicates that E_{p} depends on N_{opt}, but not on μ_{opt}. The same phenomenon is observed in Fig. 19.3a–c. Because E_{p} can be experimentally obtained and ε_∞ can be determined from (19.5), m^* can be deduced if N_{opt} is also known; that is, if the numbers of optically active carriers (N_{opt}) and electrically active carriers (N_{Hall}) are equal.

19.2.2 Dielectric Functions of In_2O_3:H Layers

This subsection presents the SE analysis of two TCO films; amorphous H doped In_2O_3 (a-In_2O_3:H) and polycrystalline (poly-) In_2O_3:H [49]. Theoretically, H forms a shallow donor state in TCO materials such as In_2O_3 [50], ZnO [5, 8], SnO_2 [6], and CdO [6]. In In_2O_3, interstitial hydrogen (H_i^+) and substitutional hydrogen at oxygen sites (H_O^+) have been theoretically confirmed as shallow donors [50]. Muon spin rotation and relaxation spectroscopy measurements have revealed that implanted muons, with analogous properties to those of hydrogen, also act as shallow donors in In_2O_3 [51], ZnO [52], SnO_2 [51], and CdO [53]. When bulk In_2O_3 single crystals are annealed in hydrogen, a thin (~0.06 mm) conducting layer forms with a carrier density of 1.6×10^{19} cm^{-3}, and the free-carrier absorption is correlated with OH vibrational modes [54]. Post-annealed solid-phase crystallized In_2O_3:H films grown by sputtering [16, 55], ion plating with DC arc discharge [21], and atomic layer deposition [56] present as n-type degenerated semiconductors with $N \sim 10^{20}$ cm^{-3} and high μ (>100 cm^2 V^{-1} s^{-1}).

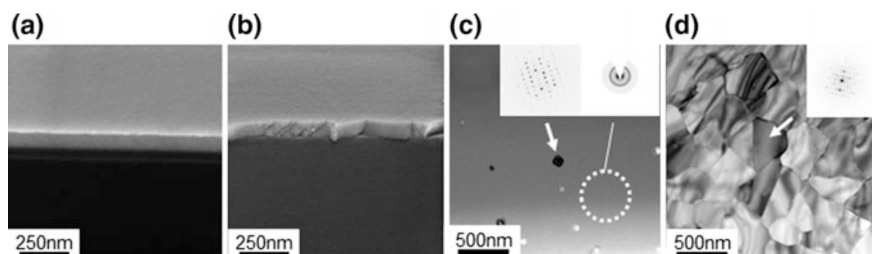

Fig. 19.7 Cross-sectional SEM images (Bird's eye view) of **a** a-In_2O_3:H and **b** poly-In_2O_3:H films grown on SiO_2 coated Si. Plan-view TEM images of **c** a-In_2O_3:H and **d** poly-In_2O_3:H films [49]. Insets in **c** and **d** show the nano-beam electron diffraction patterns and a selective area-electron diffraction pattern

Panels (a) and (b) of Fig. 19.7 show cross sectional SEM images (bird's eye views) of a-In_2O_3:H and poly-In_2O_3:H films, respectively, grown on SiO_2-coated Si. Plan-view TEM images of the same films are shown in panels (c) and (d), respectively (insets show the nano-beam electron diffraction patterns and a selected area electron diffraction pattern). The a-In_2O_3:H film was fabricated at room temperature by sputtering an In_2O_3 ceramic target in the presence of H_2O vapor. The poly-In_2O_3:H film was fabricated by post-annealing the amorphous film in vacuum at 250 °C. Whereas the a-In_2O_3:H film is generally amorphous with isolated crystalline grains, poly-In_2O_3:H film exhibits a decidedly grained structure with an average grain size of approximately 440 nm. The lattice parameters measured by X-ray diffraction were similar to those of In_2O_3 powder [41], indicating that the film was strain-free. The H composition of the a-In_2O_3:H and poly-In_2O_3:H films was ~3 at.%. From Hall measurements in the van der Pauw configuration, the N_{Hall} (μ_{Hall}) values of the a-In_2O_3:H and poly-In_2O_3:H films were determined as 4.64×10^{20} cm^{-3} (41.5 cm^2 V^{-1} s^{-1}) and 1.74×10^{20} cm^{-3} (122 cm^2 V^{-1} s^{-1}), respectively.

Figure 19.8a shows the optical model for the SE analysis of the In_2O_3:H layers. The optical model comprises a stacked air–surface roughness layer/TCO/SiO_2/crystalline Si. The rear surface of the c-Si substrate was roughened to eliminate the backside reflection at photon energies below and close to the Si bandgap. To simplify the SE analysis, the thickness and optical constants of the SiO_2 film were measured in the SiO_2/Si substrate prior to deposition, and fixed during the TCO characterization. Given the constant depth of the TCO in SEM and TEM observations, we also assumed a homogenously deep dielectric function of the TCO layer. An inhomogeneously deep TCO layer with strong thickness dependence demands a multilayered structure in the data analysis [57]. SE spectra were measured from ultraviolet to IR wavelengths using two rotating-compensator ellipsometry systems, one operating at 200–1700 nm, and the other operating from 1.7 to 30 μm. TCO films with low carrier density are not easily analyzed by the Drude model at visible and NIR wavelengths because of insufficient free carrier absorption (FCA). IR-SE is a useful alternative in such cases.

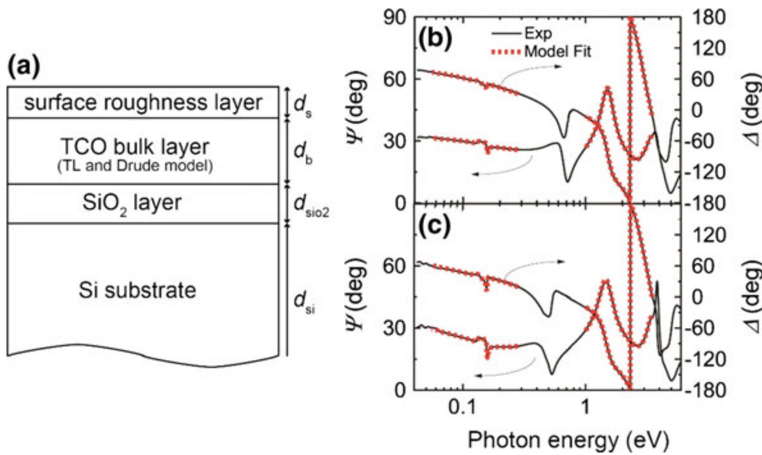

Fig. 19.8 **a** Optical model of In_2O_3:H layers used in the SE analysis. SE spectra of **b** a-In_2O_3:H, and **c** poly-In_2O_3:H films measured at 70° incident angle [49]. Dotted lines in the ranges $1 \leq E \leq 3.5$ eV and $0.055 \leq E \leq 0.28$ eV are fitting curves based on the Tauc–Lorentz and Drude models, respectively

Panels (b) and (c) of Fig. 19.8 show the SE spectra of the a-In_2O_3:H and poly-In_2O_3:H films, respectively, acquired at 70° incidence. The spectral features at $E \leq 1$ eV arise from the FCA, whereas those at $E \geq 3$ eV arise from absorption transitions between the valence and conduction band states. The dotted lines at $1 \leq E \leq 3.5$ eV and $0.055 \leq E \leq 0.28$ eV are linear regression fits using the TL and Drude models, respectively (see previous subsection). The higher energy region ($1 \leq E \leq 3.5$ eV) was selected to avoid the complicated structure of dielectric functions at even higher energies ($E > 3.5$ eV) and the FCA effects at lower energies ($E < 1$ eV). The $\varepsilon_1(\infty)$ and C were fixed at 1 and 12, respectively. The free parameters in the fitting were d_s, d_b, A_{TL}, E_T, and E_0, where d_s and d_b represent the thicknesses of the surface roughness and TCO bulk layers, respectively. The lower energy region ($0.055 \leq E \leq 0.28$ eV) was analyzed by the Drude model. In this energy range, we avoid the effect of phonon absorptions by In_2O_3 ($E < 0.055$ eV) and the O-H vibration lines of the H-dopants ($E \sim 0.4$ eV). The film thicknesses were extracted from the above fittings. The free parameters were A_D and Γ_D. As demonstrated in Fig. 19.8b, c, both models provide good fits to the experimental spectra. The analysis parameters are summarized in Table 19.1.

Table 19.1 Fitting parameters obtained by modeling the dielectric functions of a-In_2O_3:H and poly-In_2O_3:H films by the Tauc–Lorentz and Drude models. Hydrogen composition of both films is ~3 at.%

Film	Thickness		TL model			Drude model	
	d_s (nm)	d_b (nm)	A_{TL} (eV)	E_T (eV)	E_0 (eV)	A_D (eV)	Γ_D (eV)
a-In_2O_3:H	1.73	73.61	171.4	2.86	5.35	1.591	0.0777
poly-In_2O_3:H	1.59	74.14	254.7	3.28	4.31	0.759	0.0331

When the thickness of each layer in the optical model is known, the dielectric function at each wavelength can be mathematically derived by inverting the measured SE spectra using the Fresnel equations. Figure 19.9 plots the dielectric functions of the films obtained from the mathematical inversion on a logarithmic scale over the measured photon energies (Fig. 19.9a) and on a linear scale at photon energies above 2 eV (Fig. 19.9b). The dotted lines are the dielectric functions fitted by the TL and Drude models in the $1 \leq E \leq 3.5$ eV and the $0.055 \leq E \leq 0.28$ eV ranges, respectively. The fitting curves agree with the mathematically inverted spectra even in the unfitted photon energy region ($0.28 < E < 1$ eV), confirming the consistency of the fitting models and the parameters summarized in Table 19.1.

As shown in the ε_2 spectra of Fig. 19.9b, both films strongly absorb at $E \geq 3$ eV. The onset energy of the absorption is higher in the poly-In_2O_3:H film than in the a-In_2O_3:H film. Recently, the band structure and optical transitions in crystalline In_2O_3 have been clarified by first-principles calculations and photoemission spectroscopy [58–60]. The direct bandgap of In_2O_3 is 2.9 eV, and optical transitions from the valence band maximum (VBM) to the conduction band minimum (CBM) in the dipole approximation are forbidden by the symmetry of the bixbyite crystal. The experimentally observed onset of absorption corresponds to transitions from the lower lying valence band states (~0.8 eV below the VBM) to the CBM [58]. The dielectric function of bixbyite In_2O_3 has also been theoretically calculated [59, 61]. Conversely, optical transitions that are forbidden by the symmetric bixbyite structure can occur in the disordered structure of an amorphous film. Therefore, the onset energy might largely differ between the a-In_2O_3:H and poly-In_2O_3:H films. The onset energy in both films is also influenced by the

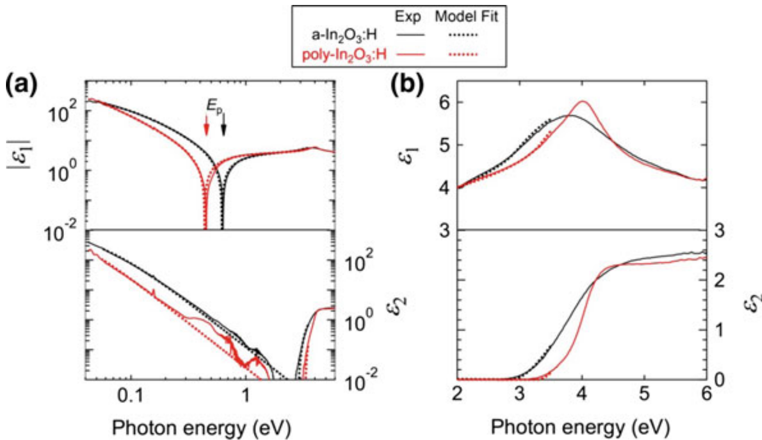

Fig. 19.9 **a** Dielectric functions of the films obtained by mathematical inversion, plotted on a logarithmic scale over the measured photon energy [49]. **b** Linear-scale dielectric functions of the films at photon energies above 2 eV. Dotted lines in the region $0.055 \leq E \leq 3.5$ eV are the dielectric functions fitted by the Tauc–Lorentz and Drude models over $1 \leq E \leq 3.5$ eV and $0.055 \leq E \leq 0.28$ eV, respectively

Table 19.2 Physical properties of the a-In_2O_3:H and poly-In_2O_3:H films obtained in the SE analysis, and the Hall mobility (μ_{Hall}) and Hall carrier density (N_{Hall}) extracted from Hall measurements

Film	SE						Hall	
	E_p (eV)	ε_∞	m^*/m_0	τ_{opt} (s)	μ_{opt} ($cm^2V^{-1}s^{-1}$)	N_{opt} (cm^{-3})	μ_{Hall} ($cm^2V^{-1}s^{-1}$)	N_{Hall} (cm^{-3})
a-In_2O_3:H	0.635	4.26	0.373	8.47×10^{-15}	40.0	4.30×10^{20}	41.5	4.64×10^{20}
poly-In_2O_3:H	0.453	4.23	0.336	1.99×10^{-14}	104	1.85×10^{20}	108	2.12×10^{20}

E_p Plasma energy; ε_∞ high-frequency dielectric constant; m^*/m_0 effective mass; τ_{opt} optical relaxation time; μ_{opt} optical mobility; N_{opt} optical carrier density

Burstein–Moss effect [40, 49]. Both films exhibit low ε_2 and are transparent in the $1.5 \leq E \leq 3$ eV region. As shown in Fig. 19.9a, ε_2 rises monotonically in the range $E < 1.5$ eV, while ε_1 decreases and crosses zero at E_p. Below E_p, ε_1 is negative. At $E \ll E_p$, ε_1 becomes highly negative and the film reflects light. The E_p values are given in Table 19.2. Because of its lower carrier density, the poly-In_2O_3:H film exhibits lower E_p than the a-In_2O_3:H film. Moreover, the In_2O_3 lattices of poly-In_2O_3:H absorb phonons at $E < 0.055$ eV. In a-In_2O_3:H film, such phonon absorptions are hindered by the large FCA. The mathematically inverted spectra of the poly-In_2O_3:H film also display broad ε_2 peaks at $E \sim 0.4$ eV, which are ignored in the optical model. The intensity of the broad peak gradually decreased with decreasing H content in poly-In_2O_3:H films [49]; therefore, the peak is attributed to H-doping and OH vibrational lines. The O-H vibrational line at 3306 cm^{-1} and several additional OH lines have also been observed for In_2O_3 single crystals annealed in an H_2 atmosphere. These measurements were made by a Fourier-transform IR spectrometer at low temperature. In theoretical calculations, the 3306 cm^{-1} line was attributed to interstitial H, and the additional OH lines were ascribed either to additional configurations of the interstitial H or to defects containing H-trapped In vacancies [54, 62].

19.2.3 Analysis of Dielectric Functions of In_2O_3:H Layers

We now analyze the dielectric functions of the films using Drude theory. According to (19.5), ε_∞ can be obtained as the ε_1 at $1/(E^2 + \Gamma_D^2) = 0$. Figure 19.10 plots the ε_1 values of the films as functions of $1/(E^2 + \Gamma_D^2)$. The Γ_D is extracted from the SE analysis shown in Table 19.1. Dotted lines are fitted to the experimental results. The increased ε_1 at $1/(E^2 + \Gamma_D^2) \sim 0.1$ is affected by transitions between the valence and conduction band states, which is not considered in the Drude theory.

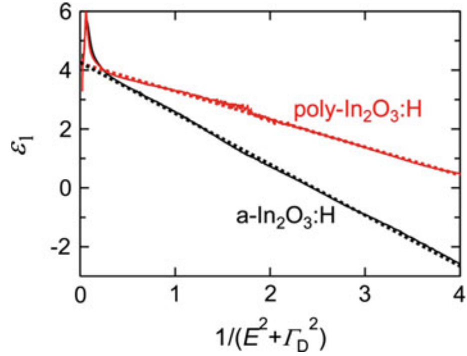

Fig. 19.10 ε_1 versus $1/(E^2 + \Gamma_D^2)$ in the In_2O_3:H layers [49]. Dotted lines show the best-fit curves

In the lower energy region, ε_1 linearly decreases with $1/(E^2 + \Gamma_D^2)$. The extracted ε_∞ values are listed in Table 19.2. Provided that $N_{opt} = N_{Hall}$, we can determine the m^*/m_0 of the films from ε_∞ and E_p, as shown in Table 19.2. Figure 19.11 plots the electrical properties (N_{Hall}, μ_{Hall}) of the a-In_2O_3:H and poly-In_2O_3:H films (panel a), and m^*/m_0 as functions of N_{Hall} in In_2O_3:H-based films (panel b); namely, a-In_2O_3:H films [43] grown under various oxygen partial pressures and poly-In_2O_3:H films [49] post-annealed at different temperatures. The m^*/m_0 values of both films were obtained by the same procedure. The observed gradual increase in m^* with N_{Hall} is attributed to the degeneracy and non-parabolicity of the conduction band, which exert large influence in heavily doped TCO films [63–66]. Moreover, at similar N_{Hall}, the m^* values of the a-In_2O_3:H films are quite similar to those of crystallized In_2O_3:H, reflecting the similar CBM structures in the a-In_2O_3:H films and crystallized In_2O_3:H, and the weak effect of structural disorder on m^*. First-principles density functional theory reveals a highly dispersed conduction band primarily derived from In (5 s) orbitals [33, 35–37].

The similar m^* in the a-In_2O_3:H and poly-In_2O_3:H films implies that the μ_{Hall} differs by significant differences in τ. As shown in Table 19.2 and Fig. 19.11c, the τ_{opt} obtained from Γ_D largely differs between the a-In_2O_3:H and poly-In_2O_3:H films. The μ_{opt} and N_{opt} values, determined by inserting Γ_D, m^*, and A_D into (19.4) and (19.3), respectively, are also summarized in Table 19.2. We find that μ_{opt} and N_{opt} favorably agree with μ_{Hall} and N_{Hall}, respectively. In the plots of μ_{opt} versus N_{Hall} for a-In_2O_3:H and poly-In_2O_3:H films, the μ_{Hall} and μ_{opt} are also close (Fig. 19.11a). Therefore, the electron mobility must be limited by (i) scattering inside the amorphous matrix of a-In_2O_3:H films, and (ii) in-grain scattering rather than grain boundary scattering in poly-In_2O_3:H films. It should be emphasized that in polycrystalline materials with grain sizes much larger than the mean free path of free electrons (~10 nm), μ_{opt} represents the average mobility within the grains, excluding the effects of grain boundaries. Because the grain boundaries hinder the carrier transport, the μ_{opt} is generally higher than μ_{Hall} at densities around 10^{20} cm^{-3}. For example, in polycrystalline B-doped ZnO films grown by low-pressure chemical vapor deposition, μ_{opt} is higher than μ_{Hall} at N_{Hall} below 1.5×10^{20} cm^{-3} [67]. In polycrystalline Al-doped ZnO films grown by reactive magnetron

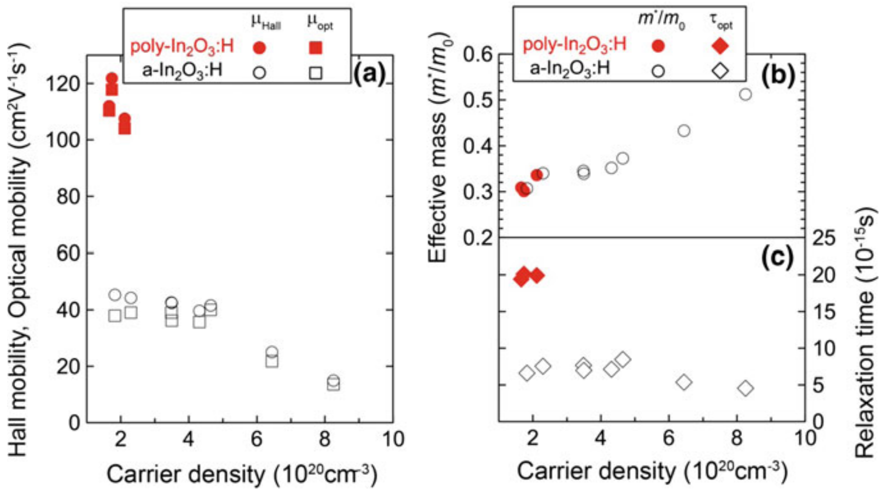

Fig. 19.11 **a** Hall and optical mobilities of a-In_2O_3:H [43] and poly-In_2O_3:H [49] films as functions of carrier density. **b** Effective masses (m^*/m_0) and **c** carrier relaxation times in a-In_2O_3:H [43] and poly-In_2O_3:H [49] films as functions of carrier density

sputtering, the same phenomenon is observed at N_{Hall} below 5×10^{20} cm^{-3} [68]. Conversely, the mobility in poly-In_2O_3:H films is not limited by grain boundary scattering, at least for N around 1×10^{20} cm^{-3}, because the grain size is very much larger than the mean free path of electrons. Instead, the mobility is limited by impurities and phonon scattering inside the grains. According to the temperature dependence of μ_{Hall}, crystallization reduces the ionized impurity scattering but increases the phonon scattering effects [16]. The scattering rates of phonons, ionized impurities, and neutral impurities can be theoretically calculated. By comparing the experimental and theoretical values of τ, we can elucidate the transport mechanism of the materials [66, 69, 70] and suggest improvements to the film fabrication.

19.3 Application of High-Mobility TCO Layers to Solar Cells

In this subsection, we investigate how high-mobility TCO reduces the optical losses in an a-Si:H/c-Si heterojunction solar cell [71]. The structure of the heterojunction solar cell is Ag grid/TCO (72 nm thick)/a-Si:H *p* layer (3 nm thick)/a-Si:H *i* layer (4 nm thick)/*n*-type c-Si (525 μm thick)/Al (Fig. 19.12a). The cell is simply structured and lacks a textured c-Si and back surface field (BSF). Optical losses in heterojunction solar cells typically include reflection loss at the front TCO/a-Si:H interface and absorption losses within the TCO. Although reflection loss can be

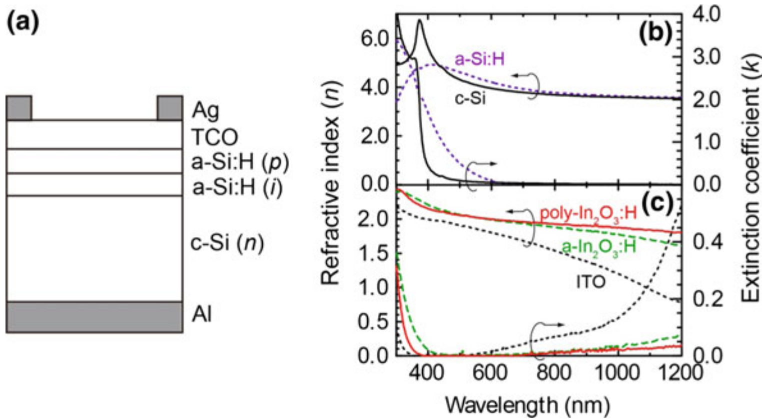

Fig. 19.12 **a** Structure of a heterojunction solar cell. Right panels plot the refractive index (*n*) and extinction coefficient (*k*) of **b** a-Si:H (dotted lines) and c-Si (full lines) and **c** poly-In_2O_3:H (full lines), a-In_2O_3:H (dashed lines), and ITO layers (dotted lines) [71]

reduced by adopting a textured structure [72], a high-μ TCO material with appropriate *n* and *k* will substantially reduce both the reflection and absorption losses.

Panels (b) and (c) of Fig. 19.12 plot the wavelength dependencies of *n* and *k*, respectively, in a-Si:H, c-Si, and three TCO layers [71]. The TCOs are ~72-nm-thick poly-In_2O_3:H, a-In_2O_3:H, and polycrystalline Sn doped In_2O_3 (ITO) films, with respective electrical properties [resistivity (Ω cm), N_{Hall} (cm^{-3}) and μ_{Hall} (cm^2 V^{-1} s^{-1})] of [2.94×10^{-4}, 1.51×10^{20}, 141], [3.47×10^{-4}, 3.27×10^{20}, 55.0] and [2.32×10^{-4}, 1.51×10^{21}, 17.9]. Note that the resistivities, and hence the R_{sheet}s, of the three TCO films are very similar. In all of the TCO layers, *k* increases and *n* decreases at longer wavelengths under the effects of FCA. The behavior and changing parameter values can be explained by the N_{opt} and μ_{opt} of the TCO layers, as shown in Fig. 19.3d–f. The changes are smaller in the poly-In_2O_3:H layers than in the ITO layer, because the influences of FCA in the In_2O_3:H layer are well suppressed by the low *N* and high μ. Figure 19.13a presents the external quantum efficiency (QE) and specular reflectance spectra of the solar cells installed with the three TCO films [71]. The reflectance spectra of the solar cells in Fig. 19.13a were calculated at normal incidence using the optical constants in Fig. 19.12b, c. The calculated reflectance spectra reasonably agreed with the measured spectra. The reflectance in Fig. 19.13a is basically determined by the interference effect in the air/TCO/a-Si:H structure. The 72-nm-thick TCO layers almost cancel the reflectance at 560–590 nm. At longer wavelengths, however, the anti-reflection property is diminished, and the reflectance increases significantly. In this wavelength region, the light reflection is largely contributed by the TCO/a-Si:H interface, which essentially governs the front reflectance of the solar cell. In turn, the reflectance at this interface is increased by the strong FCA in the TCO,

which reduces the n at longer wavelengths. Thus, FCA suppression can effectively reduce the front reflectance in solar cells. Consequently, the solar cells installed with poly-In_2O_3:H show lower reflectance and higher external QE values in the visible and NIR wavelengths (>600 nm) than ITO-based solar cells. The absorption loss within the TCO also manifests in the QE spectra. The internal QE calculated from the external QE and reflectance spectra are presented in Fig. 19.13b. The internal QE varies among the three cells at shorter wavelengths (<400 nm) because the optical band gap differs among the TCO films, as shown in Fig. 19.12c. More importantly, the internal QE at visible and NIR wavelengths (400–1000 nm) is higher in the poly-In_2O_3:H-based solar cell than in the ITO-based solar cell, due to the smaller k in the In_2O_3:H layer. Reflection and absorption proved equally important for improving the short circuit current density (J_{sc}) in these cells, and both losses largely affected the J_{sc}. In these solar cells, which lacked a BSF structure, the internal QE at longer wavelengths is rather limited by rear surface recombination [73]. In heterojunction solar cells [74–76] with BSF or front-surface field and textured structures, the QE is amplified at wavelengths over 1000 nm. Moreover, the spectral sensitivity, J_{sc} and fill factor have been improved by applying a high-mobility In_2O_3:H- and/or In_2O_3-based TCO as the front TCO. The rear TCO in bifacial solar cells must meet similar requirements, as shown in Fig. 19.1a. Conversely, in heterojunction solar cells with full rear metallization, the rear TCO must form an optical layer that minimizes the absorption of evanescent waves in the metal reflector [77]. Because the lateral transport is constrained by the rear metal, this layer behaves like the rear dielectric layer in rear-passivated diffused-junction Si solar cells.

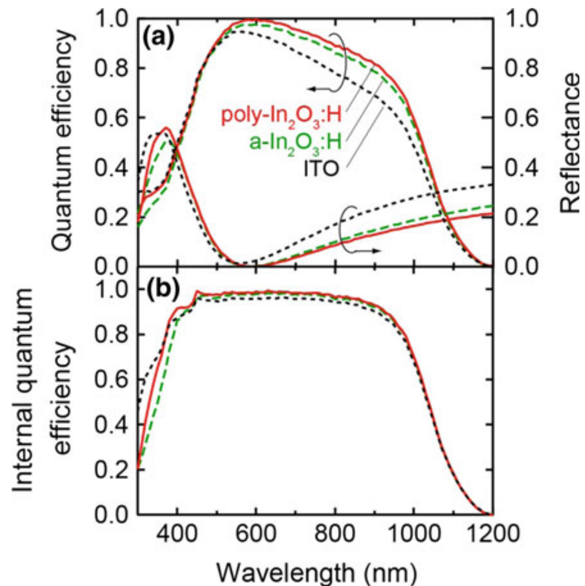

Fig. 19.13 Spectra of **a** external quantum efficiency (QE) and **b** internal QE of a-Si:H/c-Si heterojunction solar cells with front TCOs composed of poly-In_2O_3:H (full lines), a-In_2O_3:H (dashed lines), and ITO layers (dotted lines) [71]. Panel (**a**) also shows the calculated reflectance spectra of the heterojunction solar cells

High-μ TCO has also been applied to thin-film solar cells, such as conventional and mechanical stack solar cells. The structure of the conventional solar cell is TCO/absorber/TCO/rear reflector, whereas the top and/or middle cells of a mechanical stacked solar cell are structured as TCO/absorber/TCO. These structures are similar to those of a heterojunction solar cell with full rear metallization and a bifacial heterojunction solar cell, respectively. Therefore, the FCA in TCO causes similar optical losses in both types of thin-film solar cells. In thin-film Si and CdTe solar cells, the front electrode is typically composed of ZnO- or SnO_2-based TCO in a superstrate-type structure, whereas in Cu(In,Ga)Se_2 solar cells, ZnO-based TCO is typically installed in a substrate-type structure. To date, improving the TCO properties to increase the conversion efficiency of solar cells has received widespread attention. However, the development of SnO_2- and ZnO-based TCO films with high μ at $N \sim 10^{20}$ cm^{-3} remains challenging. On the other hand, various solar cells have been installed with high-μ CdO- and In_2O_3-based TCOs. Examples are the CdTe solar cell with Cd_2SnO_4 [78], Cu(In,Ga)Se_2 solar cells with In_2O_3:Ti [79] and a-In-Zn-O [39], a bifacial Cu(In,Ga)Se_2 solar cell with an In_2O_3:Ti rear electrode and an ITO front electrode [80], a superstrate-type nc-Si:H solar cell with In_2O_3:Mo and a textured ZnO [81], a superstrate-type a-Si:H/nc-Si:H micromorph thin-film Si solar cell with In_2O_3:H and a textured transparent substrate [82], a substrate-type μc-Si:H solar cell with In_2O_3:H [83], and a dye sensitized solar cell with In_2O_3:Ti [84]. In these solar cells, the spectral sensitivity is improved at longer wavelengths and/or the NIR transmission is improved in the top cell of mechanical stacked solar cells.

References

1. R.L. Weiher, J. Appl. Phys. **33**, 2834 (1962)
2. T. Koida, M. Kondo, J. Appl. Phys. **99**, 123703 (2006)
3. Z. Galazka, K. Irmscher, M. Pietsch, T. Schulz, R. Uecker, D. Klimma, R. Fornaria, Cryst. Eng. Commun. **15**, 2220 (2013)
4. O. Bierwagen, J.S. Speck, Appl. Phys. Lett. **97**, 072103 (2010)
5. C.G. Van de Walle, Phys. Rev. Lett. **85**, 1012 (2000)
6. C. Kilic, A. Zunger, Appl. Phys. Lett. **81**, 73 (2002)
7. S. Lany, A. Zunger, Phys. Rev. Lett. **98**, 045501 (2007)
8. A. Jannotti, C.G. Van de Walle, Phys. Rev. B **76**, 165202 (2007)
9. H. Ohta, M. Orita, M. Hirano, H. Tanji, H. Kawazoe, H. Hosono, Appl. Phys. Lett. **76**, 2740 (2000)
10. T. Koida, M. Kondo, J. Appl. Phys. **101**, 063713 (2007)
11. S. Ishibashi, Y. Highchi, Y. Ota, K. Nakamura, J. Vac. Sci. Technol. A **8**, 1403 (1990)
12. Y. Shigesato, Y. Hayashi, T. Haranoh, Appl. Phys. Lett. **61**, 73 (1992)
13. Y. Meng, X. Yang, H. Chen, J. Shen, Y. Jiang, Z. Zhang, Z. Hua, Thin Solid Films **394**, 218 (2001)
14. C. Warmsingh, Y. Yoshida, D.W. Readey, C.W. Teplin, J.D. Perkins, P.A. Parilla, L.M. Gedvilas, B.M. Keyes, D.S. Ginley, J. Appl. Phys. **95**, 3831 (2004)
15. T. Koida, M. Kondo, J. Appl. Phys. **101**, 063705 (2007)
16. T. Koida, H. Fujiwara, M. Kondo, Jpn. J. Appl. Phys. **28**, L685 (2007)

17. P.F. Newhouse, C.-H. Park, D.A. Keszler, J. Tate, P.S. Nyholm, Appl. Phys. Lett. **87**, 112108 (2005)
18. S. Calnan, A.N. Tiwari, Thin Solid Films **518**, 1839 (2010)
19. Y. Yoshida, D.M. Wood, T.A. Gessert, T.J. Coutts, Appl. Phys. Lett. **84**, 2097 (2004)
20. J.E. Medvedeva, Phys. Rev. Lett. **97**, 086401 (2006)
21. E. Kobayashi, Y. Watabe, T. Yamamoto, Appl. Phy. Expr. **8**, 015505 (2015)
22. J.R. Bellingham, W.A. Phillips, C.J. Adkins, J. Phys. Condens. Matt. **2**, 6207 (1990)
23. S. Ishibashi, Y. Higuchi, Y. Ohta, K. Nakamura, J. Vac. Sci. Technol. A **8**, 1399 (1990)
24. A. Kaijo, Display Imag. **4**, 143 (1996)
25. T. Minami, T. Kakumu, S. Takata, J. Vac. Sci. Technol. A **14**, 1704 (1996)
26. K. Utsumi, H. Iigusa, R. Tokumaru, P.K. Song, Y. Shigesato, Thin Solid Films **445**, 229 (2003)
27. H. Nakazawa, Y. Ito, E. Matsumoto, K. Adachi, N. Aoki, Y. Ochiai, J. Appl. Phys. **100**, 093706 (2006)
28. R. Martins, P. Barquinha, A. Pimentel, L. Pereira, E. Fortunato, Phys. Status Solidi A **202**, R95 (2005)
29. B. Yaglioglu, Y.-J. Huang, H.-Y. Yeom, D.C. Paine, Thin Solid Films **496**, 89 (2006)
30. A.J. Leenheer, J.D. Perkins, M.F.A.M. van Hest, J.J. Berry, R.P, O'Hayre, D.S. Ginley, Phys. Rev. B **77**, 115215 (2008)
31. F. Utsuno, H. Inoue, I. Yasui, Y. Shimane, S. Tomai, S. Matsuzaki, K. Inoue, I. Hirosawa, M. Sato, T. Honma, Thin Solid Films **496**, 95 (2006)
32. F. Utsuno, H. Inoue, I. Yasui, Y. Shimane, T. Shibuya, K. Yano, K. Inoue, I. Hirosawa, M. Sato, T. Honma, Thin Solid Films **516**, 5818 (2008)
33. K. Nomura, T. Kamiya, H. Ohta, T. Uruga, M. Hirano, H. Hosono, Phys. Rev. B **75**, 035212 (2007)
34. H. Hosono, N. Kikuchi, N. Ueda, H. Kawazoe, J. Non-Cryst, Solids **198–200**, 165 (1996)
35. J. Robertson, Phys. Stat. Solidi B **245**, 1026 (2008)
36. T. Kamiya, K. Nomura, M. Hirano, H. Hosono, Phys. Stat. Solidi A **206**, 860 (2009)
37. A. Walsh, J.L.F. Da Silva, S.-H Wei, Chem. Mater. **21**, 5119 (2009)
38. R. Martins, P. Almeida, P. Barquinha, L. Pereira, A. Pimentel, I. Ferriera, E. Fortunato, J. Non-Cryst, Solids **352**, 1471 (2006)
39. J.D. Perkins, T. Gennett, J.E. Leisch, R. Sundaramoorthy, I.L. Repins, M.F.A.M. van Hest, D.S. Ginley, *35th IEEE Photovoltaic Specialists Conference* (2010), pp. 989–991
40. T. Koida, H. Sai, H. Shibata, M. Kondo, The proceedings of AM-FPD 12, in *The Nineteenth International Workshop on Active-Matrix Flatpanel Displays and Devices–TFT Technologies and FPD Materials* (2012), pp. 45–48
41. M. Ando, E. Nishimura, K. Onisawa, T. Minemura, J. Appl. Phys. **93**, 1032 (2003)
42. T. Koida, H. Fujiwara, M. Kondo, J. Non-Cryst, Solids **354**, 2805 (2008)
43. T. Koida, H. Shibata, M. Kondo, K. Tsutsumi, A. Sakaguchi, M. Suzuki, H. Fujiwara, J. Appl. Phys. **111**, 063721 (2012)
44. T. Koida, Physica Status Solidi A. **214**, 1600464 (2017)
45. D. Greiner, S.E. Gledhill, Ch. Koble, J. Krammer, R. Klenk, Thin Solid Films **520**, 1285 (2011)
46. P.I. Rovira, R.W. Collins, J. Appl. Phys. **85**, 2015 (1999)
47. R.A. Synowicki, Thin Solid Films **313–314**, 394 (1998)
48. H. Fujiwara, M. Kondo, Phys. Rev. B **71**, 075109 (2005)
49. T. Koida, M. Kondo, K. Tsutsumi, A. Sakaguchi, M. Suzuki, H. Fujiwara, J. Appl. Phys. **107**, 033514 (2010)
50. S. Limpijumnong, P. Reunchan, A. Janotti, C.G. Van de Walle, Phys. Rev. B **80**, 193202 (2009)
51. P.D.C. King, R.L. Lichti, Y.G. Celebi, J.M. Gil, R.C. Vilão, H.V. Alberto, J. Piroto Duarte, D.J. Payne, R.G. Egdell, I. McKenzie, C.F. McConville, S.F.J. Cox, T.D. Veal, Phys. Rev. B **80**, 081201 (2009)

52. S.F.J. Cox, E.A. Davis, S.P. Cottrell, P.J.C. King, J.S. Lord, J.M. Gil, H.V. Alberto, R.C. Vilao, J. Piroto Duarte, N. Ayres de Campos, A. Weidinger, R.L. Lichti, S.J.C. Irvine, Phys. Rev. Lett. **86**, 2601 (2001)
53. S.F.J. Cox, J.S. Lord, S.P. Cottrell, J.M. Gil, H.V. Alberto, A. Keren, D. Prabhakaran, R. Scheuermann, A. Stoykov, J. Phys. Condens. Matt. **18**, 1061 (2006)
54. W. Yin, K. Smithe, P. Weiser, M. Stavola, W. Beall Fowler, L. Boatner, S.J. Pearton, D.C. Hays, S.G. Koch, Phys. Rev. B **91**, 075208 (2015)
55. C. Battaglia, J. Escarre, K. Soderstrom, L. Erni, L. Ding, G. Bugnon, A. Billet, M. Boccard, L. Barraud, S.D. Wolf, F.-J. Haug, M. Despeisse, C. Ballif, Nano Lett. **11**, 661 (2010)
56. B. Macco, Y. Wu, D. Vanhemel, W.M.M. Kessels, Phys. Status Solidi RRL **8**(12), 987 (2014)
57. R.A. Synowicki, Thin Solid Films **313–314**, 394 (1998)
58. A. Walsh, J.L.F. Da Silva, S.-H. Wei, C. Korber, A. Klein, L.F.J. Piper, A. DeMasi, K.E. Smith, G. Panaccione, P. Torelli, D.J. Payne, A. Bourlange, R.G. Egdell, Phys. Rev. Lett. **100**, 167402 (2008)
59. F. Fuchs, F. Bechstedt, Phys. Rev. B **77**, 155107 (2008)
60. P.D.C. King, T.D. Veal, F. Fuchs, ChY Wang, D.J. Payne, A. Bourlange, H. Zhang, G.R. Bell, V. Cimalla, O. Ambacher, R.G. Egdell, F. Bechstedt, C.F. McConville, Phys. Rev B **79**, 205211 (2009)
61. SZh Karazhanov, P. Ravindran, P. Vajeeston, A. Ulyashin, T.G. Finstad, H. Fjellvag, Phys. Rev. B **76**, 075129 (2007)
62. J.B. Varley, H. Peelaers, A. Janotti, C.G. Van de Walle, J. Phys, Condens. Matter **23**, 334212 (2011)
63. R. Clanget, Appl. Phys. **2**, 247 (1973)
64. Y. Ohhata, F. Shinoki, S. Yoshida, Thin Solid Films **59**, 255 (1979)
65. T. Pisarkiewicz, K. Zakrzewska, E. Leja, Thin Solid Films **174**, 217 (1989)
66. M. Chen, Z.L. Pei, X. Wang, Y.H. Yu, X.H. Liu, C. Sun, L.S. Wen, J. Phys. D Appl. Phys. **33**, 2538 (2000)
67. J. Steinhauser, S. Fay, N. Oliveira, E. Vallat-Sauvain, D. Zimin, U. Kroll, C. Ballif, Phys. Stat. Sol. A **205**, 1983 (2008)
68. F. Ruske, A. Pflug, V. Sttinger, B. Szyszka, D. Greiner, B. Rech, Thin Solid Films **518**, 1289 (2009)
69. K. Ellmer, R. Mientus, Thin Solid Films **516**, 4620 (2008)
70. N. Preissler, O. Bierwagen, A.T. Ramu, J.S. Speck, Phys. Rev B **88**, 085305 (2013)
71. T. Koida, H. Fujiwara, M. Kondo, Appl. Phys. Express **1**, 041501 (2008)
72. M. Tanaka, M. Taguchi, T. Matsuyama, T. Sawada, S. Tsuda, S. Nakano, H. Hanafusa, Y. Kuwano, Jpn. J. Appl. Phys. **31**, 3518 (1992)
73. T. Sawada, N. Terada, S. Tsuge, T. Baba, T. Takahama, K. Wakisaka, S. Tsuda, S. Nakano, in *IEEE 1st World Conference on Photovoltaic Energy Conversion, 1994 on Conference Record of the 24 the IEEE Photovoltaic Specialists Conference* (1994), pp. 1219–1226
74. L. Barraud, Z.C. Holman, N. Badel, P. Reiss, A. Descoeudres, C. Battaglia, S. De Wolf, C. Ballif, Sol. Energy Mater. Sol. C **115**, 151 (2013)
75. M. Taguchi, A. Yano, S. Tohoda, K. Matsuyama, Y. Nakamura, T. Nishiwaki, K. Fujita, E. Maruyama, IEEE J. Photovolt. **4**, 96 (2014)
76. T. Watahiki, T. Furuhata, T. Matsuura, T. Shinagawa, Y. Shirayanagi, T. Morioka, T. Hayashida, Y. Yuda, S. Kano, Y. Sakai, Appl. Phys. Expr. **8**, 021402 (2015)
77. Z.C. Holman, M. Filipic, A. Descoeudres, S. De Wolf, F. Smole, M. Topic, C. Ballif, J. Appl. Phys. **113**, 013107 (2013)
78. X. Wu, J. Zhou, A. Duda, J.C. Keane, T.A. Gessert, Y. Yan, R. Noufi, Prog. Photovolt. **14**, 471 (2006)
79. A.E. Delahoy, L. Chen, M. Akhtar, B. Sang, S. Guo, Sol. Energy **77**, 785 (2004)
80. T. Miyano, R. Hashimoto, Y. Kanda, T. Mise, T. Nakada, in *Proceedings of the Technical Digest of 17th International Photovoltaic Science and Engineering Conference* (2007), p. 806

81. J.A.A. Selvan, A.E. Delahoy, S. Guo, Y.-M. Li, Sol. Energy Mater. Sol. Cells **90**, 3371 (2006)
82. C. Battaglia, L. Erni, M. Boccard, L. Barraud, J. Escarre, K. Soderstrom, G. Bugnon, A. Billet, L. Ding, M. Despeisse, F.-J. Haug, S. De Wolf, C. Ballif, J. Appl. Phys. **109**, 114501 (2011)
83. T. Koida, H. Sai, M. Kondo, Thin Solid Films **518**, 2930 (2010)
84. J.W. Bowers, H.M. Upadhyaya, S. Calnan, R. Hashimoto, T. Nakada, A.N. Tiwari, Prog. Photovolt. **17**, 265 (2008)

Index

A
Absorbance, 358
Absorber layer, 359
Absorbing films, 85
Absorbing region, 82
Absorption coefficient, 10, 67, 206, 207, 212, 223, 335
Absorption features, 124
Atomic Force Microscopy (AFM), 157
a-In-O, 570
a-In-Sn-O, 570
a-In-Zn-O, 570
Al, 185
AlAs, 13
Al_2O_3, 222
Alloy composition, 282
Amorphous, 570, 577
Amorphous networks, 227
Amorphous semiconductors, 232
Amplitude ratio, 3
Analysis flow, 59
Analysis strategies, 80
Analyzer, 23
Anderson localization, 108, 112
Angle of incidence, 19
Anisotropic, 442, 451
Anisotropic optical transition, 482
Anisotropy, 447
Anomalous dispersion, 79, 120, 121
Anthracene, 442
Antibonding orbitals, 92
Anti-coupling effect, 480
Anti-reflection, 581
Anti-reflection coating, 26, 186
Anti-reflection layer, 526
Ar pressure, 360
Ar sputtering pressure, 362
Asahi-U, 556, 557
a-$Si_{1-x}Ge_x$:H, 175
a-Si:H/c-Si, 227, 523
a-Si:H network model, 242
a-Si:H/c-Si heterojunction solar cell, 227, 580
a-SiO:H, 229, 244
a-TCO, 570
Atmospheric pressure vapor deposition, 408
Atomic polarization, 12
Auger electron spectroscopy, 325

B
Back contact, 360
Back-contact solar cell, 228
Back-reflector, 186
Back-side reflection, 488, 524, 538
Back-Surface Field (BSF), 228, 255
Band diagram, 490
Band-edge absorption, 264
Band gap, 62, 177, 213, 301, 367
Bandgap energy, 122, 395
Band-gap renormalization, 548
Bandgap transition, 395
Band structure, 208, 297, 475
Band structure of CISe, 268
Basis-spline (b-spline), 148
Beer's law, 10
Bloch wave function, 95
Bonding orbitals, 92
Bose-Einstein oscillators, 344
Brillouin Zone (BZ), 93, 208, 475
Broadband source, 21
Broadening parameter, 367

© Springer International Publishing AG, part of Springer Nature 2018

H. Fujiwara and R. W. Collins (eds.), *Spectroscopic Ellipsometry for Photovoltaics*,
Springer Series in Optical Sciences 212,
https://doi.org/10.1007/978-3-319-75377-5

Bruggeman effective medium approximation, 68, 156, 178, 326
Bulk heterojunction, 440, 443, 449
Bulk layer, 358
Bulk layer growth, 374
Bulk layer thickness, 375
Burstein-Moss effect, 547, 578
Burstein-Moss shift, 529

C
Carrier concentration, 396
Carrier mean free path, 389
Carrier mobility, 533
Carrier scattering, 568
Carrier scattering mechanism, 548
Carrier transport properties, 548
Cauchy, 80, 130, 148, 218
$CdCl_2$ treatment, 358
CdS, 357
$CdS_{1-x}Te_x$, 380
CdS/CdTe/Cu structures, 396
CdS/CdTe solar cell, 357
CdS film deposition, 360
CdS thickness, 372
CdTe, 357, 523
CdTe absorber layer, 386
CdTe dielectric function, 370
CdTe film deposition, 360
CdTe solar cell, 360
CdTe solar panel, 408
$CdTe_{1-x}S_x$, 380
CdTe thickness, 387
$CH_3NH_3PbI_3$, 6, 166, 464, 523
$CH_3NH_3PbI_3$ solar cell, 168, 486
Chalcopyrite, 93
Chalcopyrite-phase semiconductors, 345
Chalcopyrite structure, 253
Characterization, 513
Character tables, 106
Charge density, 480
Charge dipoles, 116
Chemical etching, 340
Chemomechanical polishing, 340, 341
Chi-Square, 75
CIGS, 283
CIGS bandgap, 287
CIGSe, 13, 157, 253, 523
CIGSe optical database, 271
CIGS films having different Cu and Ga contents, 328
CIGS technology, 329
CISe, 159, 262
Coalescence, 292
Cody gap, 232, 245
Cody-Lorentz function, 141
Cody-Lorentz oscillator, 179
Co-evaporation, 281
Compensator, 21
Complex amplitude reflection coefficient, 19, 359
Complex dielectric constant, 11
Complex dielectric function, 175, 327
Complex index of refraction, 26
Complex phasor, 24
Complex refractive index, 10, 205
Composites, 67
Composition, 373
Compositional profile, 323
Composition-shifting algorithm, 69
Conduction Band Minimum (CBM), 475
Conductive materials, 134
Conductivity, 123
Confidence limit, 79, 232, 367
Conformal coverage, 371
Conjugated molecules, 110
Conjugation, 91
Conjugation length, 112, 456
Constitutive relation, 116
Correlation, 78
CP broadening parameter, 313
CP energies, 343, 347
CP lineshape, 314
CP parameters, 388
Critical Point (CP), 63, 90, 99, 208, 209, 261, 343, 446, 471
Critical point analysis, 266, 281, 328, 471
Critical point models, 143
Critical point oscillator, 284, 365
Critical Point Parabolic Band (CPPB), 143
Crystal field, 106
Crystal-field splitting, 336
Crystalline grain size, 371
Crystalline Silicon (c-Si), 202, 227
c-Si textures, 233
$CsPbI_3$, 473, 480
$CsPbX_3$, 482
$Cu(In,Ga)Se_2$, 106, 253
$Cu_2ZnSiSe_4$, 350
$Cu_2ZnSn(S,Se)_4$, 334
Cu_2ZnSnS_4, 335, 346, 347
$Cu_2ZnSnSe_4$, 335, 337, 341, 343–345, 348
$CuInSe_2$, 159, 323
$Cu_y(In_{1-x}Ga_x)Se_2$, 281, 327
Cubic smoothing splines, 102
Cu deposition, 388
Cu diffusion, 360

(Current-density)-voltage characteristics, 376
$Cu_{2-x}Se$, 287
Cu_2SnS_3, 351
Cu_2SnSe_3, 350
Cu stoichiometry, 329
Cu thickness, 405
Cu_xSe, 264
$Cu_y(In_{1-x}Ga_x)Se_2$ (CIGS) solar cells, 282

D
Damp heat, 571
Data analysis, 59, 73
Data fitting, 73, 74
Data interpretation, 61
Davydov splitting, 111, 443
Dead layer, 489
Defects, 185
Defect scattering, 396
Degradation, 457
Degradation in hybrid perovskite, 499
Density Functional Theory (DFT), 96, 268, 473
Density Of State (DOS), 475
Depolarization, 25
Deposition rate, 284, 375
Deposition temperature, 362
Detectors, 22
Device fabrication, 362
Device performance, 513
Diamond lattice, 202
Dielectric constant, 117
Dielectric function, 11, 66, 98, 116, 124, 205, 209, 281, 285, 360
Dielectric function model, 5
Dielectric polarization, 11
Dielectrics, 20
Dielectric tensor, 442
Dimensionality, 100
Dipole matrix element, 179
Dipole moment, 11
Dipole response, 117
Direct bandgap, 122
Direct conversion, 73
Direct interband transitions, 98
Direct inversion, 514
Direct methods, 514
Direct-transition semiconductor, 13, 264
Dispersion, 513
Dispersion equations, 67
Dispersion relations, 127
Doped a-Si:H, 185
Doping, 212, 216
Double group, 96
Drude equation, 365
Drude model, 134, 394, 532, 573
Drude term, 188
Drude theory, 570
Dye-sensitized, 457

E
e-ARC method, 488
Effective mass, 95, 100, 541
Effective medium, 448
Effective-Medium Approximation (EMA), 67, 86, 156, 256, 339
Effective medium methods, 513
Effective thickness, 195, 360
Effect of roughness, 155
Efficiency, 384
E_g analysis, 264, 472
Electrical resistivity, 365
Electric field, 2, 71
Electric polarization, 12
Electromagnetic wave, 9
Electron concentration, 367
Electronic band structure, 90
Electronic losses, 359
Electronic structure, 337, 346
Electronic structure calculations, 349
Electronic transitions, 122
Electron impact emission spectroscopy, 283
Electron mobility, 365
Electron scattering time, 394
Electron selective layer, 497
Electron Transport Layer (ETL), 465
Ellipsometer, 361
Ellipsometric scatterometry, 515
Ellipsometry, 1, 19
Ellipsometry angles, 19
Ellipsometry measurement, 71
Ellipsometry parameter, 3
EMA multilayer model, 157
Empty lattice model, 95
Energy dispersive X-ray spectroscopy, 281
Energy shift model, 272
Epitaxial growth, 237
$\varepsilon_1(\infty)$, 127
EQE simulation, 168
Evaluating results, 77
Exciton Coulomb attraction, 531
Excitons, 440
External quantum efficiency, 20, 175, 359
Extinction coefficient, 9, 19, 66, 116, 213, 214
Extraordinary, 262
Extra roughness correction, 163

F
$FAPbI_3$, 464, 469, 473
$FAPbX_3$, 482

Fast data acquisition, 291
Features in SE data, 61
Fermi golden rule, 98
Fermi wave vector, 544
Fill-factor, 400
Fitting parameters, 75
Flat-band formation, 491
Flexible substrates, 176
Formamidinium lead iodide, 464
Franck-Condon, 110, 446
Free Carrier Absorption (FCA), 13, 525, 529, 566, 576, 581
Free carriers, 123, 134
Free electron, 365
Frenkel excitons, 111
Fresnel's equations, 71
Fullerenes, 443
Full Width at Half Maximum (FWHM), 132, 137

G
Ga composition, 329
GaP, 13
Gaussian, 137
Gaussian-Broadened Polynomial Superposition (GBPS) parametric dispersion model, 145
Ge, 13
Generalized critical point oscillator, 190
Generalized form of ellipsometry, 25
Germanium, 83
Glass transition, 452
Global Error Minimization (GEM), 159, 255, 467
Global minimum, 77
Grain boundary, 570, 580
Grain boundary scattering, 549, 579
Grain size, 295
Growth evolution, 382
GW approximation, 479

H
H-aggregates, 444, 447
Hall carrier concentration, 531
Hall mobility, 531
Harmonic oscillator model, 135
$HC(NH_2)_2PbI_3$, 464
Heterojunction, 357
Heterojunction diode, 376
Heterojunction solar cell, 523
High-frequency dielectric constant, 13, 537
Highly disordered semiconductor, 296
High Resistivity Transparent (HRT) layer, 357
Hole injection layer, 525
Hole Transport Layer (HTL), 465, 490
Huang-Rhys, 446
Huang-Rhys parameter, 110, 441
Hybrid perovskite, 463
Hybrid perovskite solar cell, 465, 485
Hybrid solar cell, 458
Hydrogenated amorphous silicon, 175, 227
Hydrogenated amorphous silicon-germanium alloy, 175
Hydrogenated nanocrystalline Si:H, 176
Hydrogenated silicon, 176
Hydrogen bonding interaction, 480

I
Imaging spectroscopic ellipsometry, 19
Incident angle, 3
Index of refraction, 19, 66, 116
Indirect absorption, 210
Indirect bandgap, 122
Indirect interband transitions, 98
Indirect-transition semiconductor, 13
Indium Tin Oxide (ITO), 134, 524, 539, 544, 581
$(In_{0.70}Ga_{0.30})_2Se_3$, 301
$(In_{1-x}Ga_x)_2Se_3$, 296
Inhomogeneous broadening, 108, 112
In_2O_3, 530, 544, 546, 568, 574, 581
In_2O_3:H, 525
In_2O_3:Sn, 524
In_2O_3:Sn (ITO), 185
In-plane film stress, 388
In-situ, 452, 453
In-situ SE, 287, 360
Interband optical transition, 13
Interband transition, 297, 346, 367, 525
Inter-diffusion, 359
Interface, 357
Interface filling, 373
Interface interaction, 372
Interface layer, 359
Interface roughness, 183, 359
Interfacial mixing, 449
Interference enhancement, 85
Interference features, 61
Intersystem crossing, 109
Inverse approach, 65
"Inverted" geometry, 447
Investigated spectral range, 126
Ionized impurity scattering, 549
Irradiance, 23
Irreducible representations, 92
Island formation, 234

J
J-aggregates, 444
Joint Density of States (JDOS), 99
Jones vector, 70

K
Kesterite, 342
Kesterite solar-cell, 334
KP method, 96
Kramers-Kronig (KK), 203, 219
Kramers-Kronig consistency, 79
Kramers-Kronig integral, 305
Kramers-Kronig relations, 99, 120, 369

L
Least-squares regression analysis, 286, 363
Levenberg-Marquardt, 102
Light intensity, 10
Light scattering, 86, 164
Linear detector array, 24
Linear polarization, 23
Liquid silicon, 217
Local minima, 77
Local network structure, 240
Lorentz oscillator, 27, 179, 287, 369
Lorentz oscillator model, 132

M
m^*, 579
Macfarlane, 214
Magnetron sputtering, 359
MAI, 470
Many-body effects, 103
$MAPbBr_3$, 469
$MAPbCl_3$, 469
$MAPbI_3$, 464, 469, 473
$MAPbX_3$, 482
Mapping, 28, 322
Mapping spectroscopic ellipsometry, 27, 180, 326, 357
Mathematical inversion, 163, 256, 541
Matthiessen's rule, 549
Maxwell's equations, 11
Mean-Squared Error (MSE), 75, 77, 182, 258, 363
Measurement, 60
Merit function, 75
Metal back contact, 361
Metals, 20
Metamaterials, 512
Methylammonium lead iodide, 464
Microscopic roughness, 28
Microstructure, 295
Microvoid formation, 239
Minimum deviation, 203
Mobility, 568, 579
Mobility edge, 108
Model, 65
Model calculations, 70
Model Dielectric Functions (MDFs), 144
Molecular materials, 441
Molecular solids, 111
Momentum matrix element, 179
MoO_x, 523
Morphology, 212, 216
Mott-Wannier excitons, 103
MSE profile, 77
Mueller matrix, 182
Mueller polarimetry, 515, 516
Multichannel detector, 386
Multichannel rotating-compensator spectroscopic ellipsometer, 283
Multichannel spectroscopic ellipsometer, 363
Multilayer analysis, 340
Multilayer model, 552
Multilayer stack, 28
Multiple angle of incidence SE, 177
Multiple measurement strategy, 27
Multi-sample analyses, 6, 257
Multi-sample SE analysis, 255
Multi-spot analysis, 182
Multi-time analysis, 180

N
Nano- and microwires, 512
Nanocrystal (NC), 107
Nanomaterials, 509
Nanoparticles, 512
Nanorods, 512
Nanostructured surfaces, 510
Nanotubes, 512
Nc-Si:H, 176
Network structure, 240
NiO, 525
N-i-p solar cell, 177
Non-linear least-squares regression, 27
Nonparabolicity of TCO, 543
Nonparabolicity parameters, 544
Non-uniformity, 359, 384
Normal dispersion, 79, 120
N-type, 185
Nucleation, 295, 382
Numerical derivatives, 102
Numerical inversion, 286

O
One interface system, 26
On-line monitoring, 391

Open-circuit voltage, 400
Optical anisotropy, 262, 479
Optical carrier concentration, 536
Optical constants, 9, 66
Optical constants of hybrid perovskites, 466
Optical depth profiling, 318
Optical functions, 116
Optical functions of silicon, 206
Optical loss, 580
Optical mobility, 536
Optical model, 5, 285, 361
Optical properties of a-Si:H, 239
Optical properties of silicon, 203
Optical properties of TCO, 529
Optical property parameters, 367
Optical transition, 209, 473
Ordered Defect Complex (ODC), 255
Ordinary ray, 262
Organic solar cells, 439
Oscillator amplitude, 379
Oscillator parameter, 301, 305
Oscillator strength, 470
Oversimplification of optical model, 155

P
Parallel-band transition, 304
Parameterization, 282, 306, 327
Parameterized dielectric function, 291
Parametric Semiconductor (PSEMI) model, 145
Partial IQE, 487
Patterning, 513
PbI_2, 470
P-d coupling effect, 270
PEDOT:PSS, 448
Perdew-Burke-Ernzerhof (PBE), 473
Periodicity, 513
Perylene Tetracarboxylic Dianhydride (PTCDA), 442
Phase difference, 3
Phase separation, 440, 450
Phase variation, 72
Phase velocity, 66
Phonon, 210, 212
Phonon absorption, 13, 123, 578
Phonon scattering, 367
Photon energy, 63
Photonic crystals, 509, 510
Photovoltaics, 20
P3HT, 445, 446
Phthalocyanines, 444
P3HT:PCBM, 454, 455
P3HT:PCBM blends, 449
π-electron, 91, 109, 441
Plane of incidence, 23, 70
Plasma angular frequency, 535
Plasma energy, 531, 574
Plasma-enhanced chemical vapor deposition, 179
Plasmonic materials, 509
Plasmonic nanostructures, 512
Plasmonics, 512
Point-by-point fitting, 77, 83, 163, 256
Polarizability, 482
Polarization, 3, 11, 70
Polarization ellipse, 21
Polarization state, 19
Polarization state detector, 20
Polarization state generator, 20
Polarizer, 21
Pole, 128
Polycrystalline, 106, 357
Polycrystalline CdS, 384
Polycrystalline CdTe, 391
Polycrystalline film, 295
Polymer chain, 112
Polymer films, 445
Polynomial, 147
P-polarization, 2
Primitive-mixed CuAu, 334
Principles of ellipsometry, 2
Processing-property-performance relationship, 358
Process optimization, 358
Process-property-performance relationship, 322
Pseudobulk approach, 341
Pseudobulk method, 337
Pseudo-dielectric function, 63, 73, 204, 237
Pseudo-potential, 96
ψ and Δ, 60, 71
p-type a-Si:H, 185
p-type TCO, 525
PV manufacturing, 176
PV production line, 175
p-wave, 71

Q
Quantum and dielectric confinement, 107
Quantum dots, 512
Quasi-electrons, 95

R
Ray, 262
Real-time control, 234
Real time ellipsometry, 19
Real Time Spectroscopic Ellipsometry (RTSE), 19, 179, 281, 357, 493

Reciprocal-space analysis, 103
Reflectance, 4, 21, 358
Reflection, 70
Reflectivity, 203, 206, 207
Refraction, 70
Refractive index, 9, 66, 116, 206, 213, 214, 223
Regression analysis, 65, 74
Relaxation time, 573
Resistivity, 533
Resonance, 118
Resonant energy, 128
Resonant wavelength, 128
Retarder, 22
Roll-to-roll, 456
Roll-to-roll photovoltaics, 175
Root-mean-square roughness, 157
Rotating compensator, 23, 361
Rotating-compensator multichannel ellipsometer, 182, 360
Roughness layer, 361
Rough surface, 6, 155
RTSE monitoring, 384

S

Scattering time, 185, 367
Scatterometry, 516
Schott glass, 129
Schrödinger equation, 94
Secondary ion mass spectroscopy, 325
Second derivative spectra, 266
SE data, 60
Selection rules, 98
Self-consistent GW, 478
Sellmeier, 80, 128, 218
Sellmeier equation, 363
SE mapping, 324
Semiconductors, 20
Semiconductor-to-metal transition, 529
SE spectra, 61
Sheet resistance, 394
Short-circuit current density, 400
Shunting, 401
Si:H, 13, 176
SiO_2, 361
SiH_2 formation, 241
Silicon, 201
Silicon dioxide, 222
Silicon-Germanium alloys, 89
Silicon nitride, 219–221
Single crystal CdTe, 391
Single crystals, 202
Single group, 96
Single-junction solar cells, 176
Slater-Koster contact exciton, 103
Small molecule, 443
Smoothing polynomials method, 102
SnO_2, 358, 530, 583
SnO_2:F, 361, 524, 544
Soda-lime glass, 361
Solar cell, 176, 360
Solar cell optimization, 411
Solar cell performance, 384
Solar grade, 202
Solar module, 408
Solar spectrum, 26
Space group, 93
Spectral averaging method, 273
Spectrograph, 24, 361
Spectrometer, 24
Spectroscopic ellipsometer, 22, 324
Spectroscopic ellipsometry, 5, 19, 175, 204, 282, 359
sp^3 hybridization, 91
sp^2 hybridization, 91
Spin-Orbit Coupling (SOC), 96, 479
Spin-orbit splitting, 262, 336
Spline function, 148
S-polarization, 2
Sputtering, 360
Stability, 571
Stainless steel, 182
Standard CP lineshape expressions, 343
"Standard" geometry, 447
Stannite, 334, 342
Static dielectric constant, 12, 549
Steel foil substrates, 177
Stoichiometric CIGS, 296
Stoichiometry, 282
Strain, 358
Stranski-Krastanov, 234
Stress, 212
Structural disorders, 335
Structural evolution, 291, 293, 359
Structural model, 373
Structural parameters, 367
Structure-performance correlations, 400
Substrate-type solar cell, 526
Sum rule, 485
Supercell, 107
Superstrate configuration, 25, 358
Superstrate-type solar cell, 526
Surface contamination, 514
Surface correction, 514
Surface overlayers, 514
Surface roughness, 6, 86, 159, 285, 340, 357, 514
Surface roughness evolution, 296, 382

Surface roughness layer, 371
Surface roughness layer thickness, 178, 376
S-wave, 71

T
Table of characters, 92
Tabulated lists, 67
Tandem solar cells, 178
Tauc bandgap, 304
Tauc gap, 232
Tauc gap modified Lorentz (T-L) oscillator, 290
Tauc law, 139
Tauc-Lorentz model, 138
Tauc-Lorentz oscillator, 179, 349, 369
Tauc-Lorentz (T-L), 219, 573
TEC-15, 359, 556
TEC-8, 556
TEC substrates, 559
Temperature, 212
Temperature coefficient, 215, 367
Temperature coefficients of the CIGS bandgap, 328
Temperature dependence, 344, 345
Terahertz SE, 542
Textured c-Si, 233
Textured surface, 86
Textured TCO, 555
Texturing, 222
Thermal evaporation, 388
Thermal stability, 452
Thickness, 19, 177, 285, 358
Thickness calibration, 388
Thickness non-uniformity, 86, 399
Thickness sensitivity, 6
Thin film, 218, 357
Thin film coalescence, 376
Thin-film photovoltaic, 176, 333
Thin-film solar cell, 583
Third generation solar cell class, 447
Three-stage coevaporation, 255
Through-the-glass measurement, 25, 386
Tight-binding, 95
TiO_2, 525
(TL) model, 573
Translational symmetry, 93, 107
Transmission, 203
Transmittance, 26
Transparent Conductive Oxide (TCO), 20, 64, 123, 175, 357, 523, 566
Transparent thin films, 80
Two-dimensional detector array, 24
Two interface system, 26
Two-modulator generalized ellipsometer, 223

U
Urbach absorption, 131, 142
Urbach energy, 369, 472
Urbach tail, 179, 306, 369

V
Valence Band Maximum (VBM), 475
Valence electron, 91, 480
Validation, 517
Van Hove singularities, 90, 99, 477
Vapor deposition, 495
Variable angle of incidence spectroscopic ellipsometry, 27
Vertical changes, 514
Vibrational modes, 123
Virtual interface analysis, 372
V_2O_5, 525
Void content, 285
Void volume fraction, 358
Volmer-Weber, 234

W
Wavelength, 19
Wet-chemical etching, 341
Wigner-Eckart theorem, 98
Work function, 525
Wurtzite, 92

Z
Zinc blende, 92
ZnO, 185, 530, 544, 546, 583
ZnO:Al, 524, 552
ZnO:Ga, 531, 541
Zone-folding, 95, 106